STABLE ISOTOPES AS TRACERS OF COPPER CORROSION IN THE ATMOSPHERE AND SOIL ENVIRONMENT: A GEOGRAPHIC STUDY ON BROCHANTITE AND MALACHITE FORMATIONS ON HISTORIC AND ARCHAEOLOGICAL MATERIAL USING $\delta^{18}O$, $\delta^{13}C$ and $\delta^{2}H$

A thesis presented

by

Daniela Alicia Boos Pedroza

to

Research Laboratory for Archaeology and the History of Art

in partial fulfilment of the requirements

for the degree of

Doctor of Philosophy

In the subject of

Archaeological Science

St. Hugh's College

University of Oxford



Hilary 2020

Dedicated to my grandmothers,

Virginia Boos

and

María Pedroza López

ACKNOWLEGEMENTS

Firstly, I would like to express my sincere gratitude to my supervisor, Professor Mark Pollard, for the continuous support of my doctoral study, for his patience, motivation, and immense knowledge. His guidance helped me throughout the research and writing of this thesis.

Besides my supervisor, I would like to thank the members of my Transfer of Status, Confirmation and final viva committees, for their insightful comments and encouragement, but also for the hard questions and critique.

Most of my DPhil was funded by the Mexican government scholarship, Consejo Nacional de Ciencia y Tecnología (CONACyT), and I am extremely grateful for this support. Further financial assistance was provided by the University of Oxford Counselling Service, St. Hugh's College, the School of Archaeology, my partner, and family. Thank you for providing me with the necessary funds to carry out my research.

Sample collection was a tremendous task that involved many people. I thank the University of Alabama in Tuscaloosa and the cities of Ottawa, Vienna, and Oxford for my brochantite samples. The malachite samples were sent to Oxford from around the world, and I thank all the individuals involved in this process, including those at the Institute of Archaeology of University College London, the Ashmolean Museum, State of Alaska Office of History and Archaeology, Canterbury Archaeological Trust, A.M. Art Conservation, Museum of London, Wiltshire Conservation Service, as well as several friends, colleagues and visiting scholars at the School of Archaeology, University of Oxford.

Sample processing and lab work would not have been possible without contributions from the many knowledgeable, patient and caring experts at the British Geological Survey, Godwin Laboratory for Palaeoclimate Research at the University of Cambridge, and the following departments at the University of Oxford: Earth Sciences, Inorganic Chemistry, Organic Chemistry, Geography, Research Laboratory for Archaeology and the History of Art, and the Oxford Luminescence Dating Laboratory.

Warm thanks go to my family and friends, even if they did not directly help with my research, because they offer support by being in my life.

Stable Isotopes as Tracers of Copper Corrosion in the Atmosphere and Soil Environment: A Geographic Study on Brochantite and Malachite Formations on Historic and Archaeological Material Using $\delta^{18}O$, $\delta^{13}C$ and $\delta^{2}H$

ABSTRACT

A refined methodology using light stable isotopes in precipitation to determine the formation location of copper minerals is tested, for the eventual use on archaeological bronzes that corroded in the soil environment. To do this, $\delta^{18}O$ in historic brochantite and archaeological malachite is used to determine whether the region in which these common minerals formed may be identified when the $\delta^{18}O$ is a function of the $\delta^{18}O$ in meteoric water and temperature. The waters in each phase of the hydrologic cycle have distinct isotopic compositions and can yield information on climate or water provenance. The possibility that this $\delta^{18}O$ study can be supplemented by including the hydroxyl-$\delta^{2}H$ in brochantite or $\delta^{13}C$ in malachite is explored as sub-studies.

This study shows no significant difference between the $\delta^{18}O_{SO4}$ in brochantite, and the $\delta^{18}O_{SO4}$ variances are about equal among the cities considered. Furthermore, there is no statistically significant correlation between $\delta^{18}O_{SO4}$ or hydroxyl-$\delta^{2}H$ and the $\delta^{18}O$ in precipitation, precipitation amount, pH, surface temperature, latitude, or age of deposit. About 50% of brochantite's $\delta^{18}O_{SO4}$ is sourced from local meteoric water. Of the three $SO_2 \rightarrow SO_4$ pathways that contribute oxygen in brochantite, oxygen percentages can be calculated for two pathways at a time.

The malachite data shows significant difference between the geographic groups surveyed, but does not suggest a statistically significant relationship between the $\delta^{18}O$ or $\delta^{13}C$ in malachite and the $\delta^{18}O$ in local precipitation or surface temperature. A significant relationship is apparent between $\delta^{18}O$ and $\delta^{13}C$ with some clustering within sample sites. Therefore, a comprehensive study into the $\delta^{13}C$ of malachite would be worthwhile. Climate-focused research also shows potential.

This work can be used to advise on authenticity issues or guide in provenance studies when choosing between suspected sites. Further refinement is necessary before it may be adopted for cases without suspected formation sites.

TABLE OF CONTENTS

Acknowledgements……iii

Abstract……iv

Table of Contents……v

List of Figures……viii

List of Tables……xviii

Chapter 1
Introduction

1.1. Project Rationale……1
1.2. Copper Corrosion Minerals……2
1.2.1. Description of Brochantite, $Cu_4SO_4(OH)_6$……3
1.2.2. Description of Malachite, $Cu_2CO_3(OH)_2$……4
1.3. $\delta^{18}O$, $\delta^{13}C$ and $\delta^{2}H$ ……7
1.4. Project Significance……10
1.5. The Gaps in Current Research……10
1.5.1. Brochantite……10
1.5.2. Malachite……11
1.6. Thesis Aims and Objectives……14
1.6.1. Brochantite Study……14
1.6.2. Malachite Study……16
1.7. Thesis Structure……17

Chapter 2
The Driving Forces of Metallic Corrosion

2.1. Introduction……19
2.2. Metal Corrosion and Electrochemistry……19
2.2.1. Thermodynamics and Kinetics of Aqueous Corrosion……20
2.2.2. The Activity Series and Pourbaix Diagrams……22
2.3. Summary……27

Chapter 3
The Effects of Observed Global Cycles

3.1. Introduction……28
3.2. Water in the Atmosphere: Observed Stable Isotope Effects During Precipitation……28
3.2.1. Rayleigh Rainout Effect……28
3.2.2. The Regional and Temporal Effects……31
3.3. Soil Profiles and Classification of Subsurface Waters……34
3.3.1. Understanding Soil Temperature and pH……36
3.4. Oxygen and the Oxygen Cycle……37
3.4.1. Tropospheric Ozone……38
3.4.2. Upsetting the Oxygen Cycle……39
3.4.3. Isotope Fractionation Through the Oxygen Cycle……39
3.4.4. The Isotope ($\Delta^{17}O$) Anomaly……40

3.5. Sulfur in the Atmosphere....42
3.6. Carbon and the Carbon Cycle....44
3.6.1. Carbonate Equilibrium....45
3.6.2. Carbon Isotopes Throughout the Environment....46
3.6.3. Carbon Isotopes in Malachite Ores....49
3.7. Summary....50

Chapter 4
Formation, Stability and Isotopy of Brochantite and Malachite

4.1. Introduction....52
4.2. Brochantite, $Cu_4SO_4(OH)_6$....52
4.2.1. Formation of Atmospheric Sulfates and Brochantite....53
4.2.2. Stability and Thermal Decomposition of Brochantite....56
4.2.3. Isotopy of Atmospheric Sulfates and Brochantite....60
4.3. Malachite, $Cu_2CO_3(OH)_2$....66
4.3.1. Formation of Supergene Carbonate Minerals and Malachite....66
4.3.2. Stability and Thermal Decomposition of Malachite....70
4.3.3. Isotopy of Supergene Carbonates and Malachite....72

Chapter 5
Sampling and Methodology

5.1. Analytical Procedure for the Brochantite Study....75
5.1.1. Sample Collection Criteria....75
5.1.2. Sample Processing and Material Characterization....79
5.1.3. Isolation of Brochantite and Its Sulfate Oxygen....83
5.1.4. Measurement of $\delta^{18}O$ in $BaSO_4$....86
5.1.5. Hydroxyls: A Pilot Study on δ^2H....87
5.1.5. Statistical Analyses of Brochantite Data....89
5.2. Analytical Procedure for the Malachite Study....89
5.2.1. Sample Acquisition....90
5.2.2. Sample Processing of Malachite Samples....91
5.2.3. Sample Batches and Purity....96
5.2.4. Environmental Classifications Used for the Malachite Sample Regions....97
5.2.5. Site Profiles....99
5.2.6. Isolation of Malachite Crystals and Measurement of $\delta^{18}O$ and $\delta^{13}C$....119
5.2.7. Statistical Analyses on Malachite Data....121
5.3. Summary....121

Chapter 6
XRD and Stable Isotope Results for Brochantite

6.1. Material Characterization: XRD Results....125
6.2. Brochantite $\delta^{18}O$ Results....127
6.2.1. Presentation of Raw Data and Descriptive Statistics....127
6.2.2. Incorporation of Environmental Parameters....130
6.2.3. Calculating % Contributions from Heterogeneous & Homogeneous Pathways....137
6.3. Raw Data and Descriptive Statistics for Hydroxyl-δ^2H....143

6.3.1. Correlation Statistics with Hydroxyl-δ^2H and Environmental Parameters……146
6.4. Summary……..148

Chapter 7
XRD and Stable Isotope Results for Malachite

7.1. Material Characterization: XRD Results……150
7.1.1. Azurite and Atacamite……150
7.2. Malachite δ^{18}O and δ^{13}C Results.....160
7.2.1. Presentation of Raw Data and Descriptive Statistics…….....160
7.2.2. Oxygen Isotope Results: Incorporating Environmental Parameters.....176
7.2.3. Carbon Isotope Results: Incorporating Environmental Parameters.....186
7.3. Summary…….....195

Chapter 8
Discussion and Conclusion

8.1. Thesis Overview…….....197
8.2. $\delta^{18}O_{SO4}$ Study on Historic Brochantite…….... 198
8.3. δ^{18}O and δ^{13}C in Archaeological Malachite…….....200
8.3.1. Comparing to Data from Previous Investigations.....200
8.3.2. Discussion by Geographic Group……....208
8.4. In Conclusion……..221

Works Cited.....224

Appendix A: Sample Catalog for the Brochantite and Malachite Studies.....I

Appendix B: XRD Spectra of the Brochantite Samples.....XII

Appendix C: FTIR Spectra of the Malachite Samples.....LXXIX

Appendix D: XRD Spectra of the Malachite Samples.....CXLII

Appendix E: Binocular Microscope Photographs of All Samples……..…..CCLXV

Appendix F: References for the Environmental Data on Table 5.2.....CCXCVIII

LIST OF TABLES

Table 1.1: Some examples of copper corrosion phases, specific minerals and descriptions. Merged adaptation from Scott 2002, 82, 102, 123, 148, 227, 251; Selwyn 2004, 60. *pg. 2*
Table 1.2: Some basic information on brochantite (Anthony *et al.* 2003, 125; Ralph & Chau 2013). *pg. 4*
Table 1.3: Some basic information on malachite (Chang *et al.* 1996, 291).
Table 1.4: Some of the isotopes used in archaeology, adapted from Pollard 1998b, 286 cited in Pollard *et al.* 2007, 179. *pg. 8*
Table 4.1: Thermal decomposition of geological malachite (adapted from Frost *et al.* 2002, 135). *pg. 72*
Table 5.1: Altitude and long-term weighted means of $\delta^{18}O$ in precipitation at the sampling sites in Gansu (IAEA/GNIP 2019; Wu *et al.* 2010, 1125-1126; Chen *et al.* 2015, 4673 & 4675; Liu *et al.* 2014, 5). *pg. 115*
Table 5.2: Table showing environmental data for each sample region. Refer to Appendix E for citations. *pg. 124*
Table 6.1: Powder XRD results for samples collected from patinated roofs and historic objects that continued to isotopic analysis. All samples were predominantly brochantite, but several samples were mixed phase and required processing to isolate the brochantite and its sulfate oxygen. *pg. 126*
Table 6.2: Full results for $\delta^{18}O$ values and descriptive statistics from the brochantite samples scrapped off patinated copper roofs and historic material. Values marked with an asterisk are outliers according to Grubb's test. These outlying data are excluded from the descriptive statistics. *pg. 128*
Table 6.3: Total $\delta^{18}O$ descriptive statistics for all the brochantite sites combined. Calculations exclude two outliers, marked with an asterisk in **table 6.2**. *pg. 128*
Table 6.4: Paired *t*-test statistics for brochantite $\delta^{18}O$ in four cities, considered two at a time. *pg. 129*
Table 6.5: Presentation of the mean $\delta^{18}O$-SO_4 values for each city next to local environmental parameters, with a focus on precipitation. Apart from the first row, which contains data from this study, information was collected from GNIP for the city of interest (IAEA/WMO 2015). The only exception is the average surface temperature for Tuscaloosa, which was not recorded by GNIP and instead taken from Climate-Data.org (2019). Summer is defined as May through September, inclusive. *pg. 131*
Table 6.6: Presentation of various possible percent contributions of $\delta^{18}O$ from meteoric water, showing seasonal variation. *pg. 137*
Table 6.7: The long-term year and summer mean $\delta^{18}O$ in Tuscaloosa's precipitation is -4.7‰. Therefore, R1 = 6.6‰, R2 = 2.4‰ and R3 = 16.5‰. Using this data along with the mean, lowest and highest $\delta^{18}O_{SO4}$ in brochantite results for Tuscaloosa, the following percent contributions from heterogeneous and homogeneous pathways (considering two pathway pairs at a time, labeled as 1 and 2) were calculated and presented on this table. In the homogeneous pathway, the oxidizer is always assumed to be atmospheric oxygen. The lowest ratio yielded by a sample in Tuscaloosa's data set is lower than the theoretical lowest (6.5‰ and 6.6‰, respectively), which is why a value over 100% was calculated for the heterogeneous pathway of the first pair and no value is given for the corresponding homogeneous pathway. There is no distinction between summer and year for $\delta^{18}O$ data on precipitation in Tuscaloosa because the temperature very seldom drops below freezing. *pg. 140*
Table 6.8: The long-term summer mean $\delta^{18}O$ in Vienna's precipitation is -7.0‰. Therefore, R1 = 5.2‰, R2 = 0.63‰ and R3 = 15.9‰. Using this data along with the mean, lowest and highest $\delta^{18}O_{SO4}$ in brochantite results for Vienna, the following percent contributions from heterogeneous

and homogeneous pathways (considering two pathway pairs at a time, labeled as 1 and 2) were calculated and are presented on this table. In the homogeneous pathway, the oxidizer is always assumed to be atmospheric oxygen. *pg. 140*
Table 6.9: The long-term yearly mean $\delta^{18}O$ in Vienna's precipitation is -9.8‰. Therefore, R1 = 3.5‰, R2 = -1.5‰ and R3 = 15.2‰. Using this data along with the mean, lowest and highest $\delta^{18}O_{SO4}$ in brochantite results for Vienna, the following percent contributions from heterogeneous and homogeneous pathways (considering two pathway pairs at a time, labeled as 1 and 2) were calculated and are presented on this table. In the homogeneous pathway, the oxidizer is always assumed to be atmospheric oxygen. *pg. 141*
Table 6.10: The long-term summer mean $\delta^{18}O$ in Ottawa's precipitation is -8.0‰. Therefore, R1 = 4.6‰, R2 = -0.1‰ and R3 = 15.6‰. Using this data along with the mean, lowest and highest $\delta^{18}O_{SO4}$ in brochantite results for Ottawa, the following percent contributions from heterogeneous and homogeneous pathways (considering two pathway pairs at a time, labeled as 1 and 2) were calculated and are presented on this table. In the homogeneous pathway, the oxidizer is always assumed to be atmospheric oxygen. *pg. 141*
Table 6.11: The long-term yearly mean $\delta^{18}O$ in Ottawa's precipitation is -11.0‰. Therefore, R1 = 2.8‰, R2 = -2.4‰ and R3 = 14.9‰. Using this data along with the mean, lowest and highest $\delta^{18}O_{SO4}$ in brochantite results for Ottawa, the following percent contributions from heterogeneous and homogeneous pathways (considering two pathway pairs at a time, labeled as 1 and 2) were calculated and are presented on this table. In the homogeneous pathway, the oxidizer is always assumed to be atmospheric oxygen. *pg. 141*
Table 6.12: The long-term summer mean $\delta^{18}O$ in Oxford's precipitation is -5.5‰. Therefore, R1 = 6.1‰, R2 = 1.7‰ and R3 = 16.2‰. Using this data along with the mean, lowest and highest $\delta^{18}O_{SO4}$ in brochantite results for Oxford, the following percent contributions from heterogeneous and homogeneous pathways (considering two pathway pairs at a time, labeled as 1 and 2) were calculated and are presented on this table. In the homogeneous pathway, the oxidizer is always assumed to be atmospheric oxygen. *pg. 142*
Table 6.13: The long-term yearly mean $\delta^{18}O$ in Oxford's precipitation is -7.3‰. Therefore, R1 = 5.0‰, R2 = 0.4‰ and R3 = 15.8‰. Using this data along with the mean, lowest and highest $\delta^{18}O_{SO4}$ in brochantite results for Oxford, the following percent contributions from heterogeneous and homogeneous pathways (considering two pathway pairs at a time, labeled as 1 and 2) were calculated and are presented on this table. In the homogeneous pathway, the oxidizer is always assumed to be atmospheric oxygen. *pg. 142*
Table 6.14: Brochantite hydroxyl-$\delta^{2}H$ pilot study results, run in duplicate, apart from the St. Cross Law Building in Oxford, which was used for initial methodology testing and therefore has more data. *pg. 143*
Table 6.15: Showing descriptive statistics for the $\delta^{2}H$ pilot study on brochantite's hydroxyls. The number of samples (n), mean average, standard deviation (SD), standard error (SE), and 95% confidence intervals (CI) for the mean (upper and lower bounds) are based on the data provided in **table 6.13**. *pg. 143*
Table 7.1: Quantitative XRD results of phases present in the Hungarian samples. Eleven Hungarian samples ranged from 46% to 100% malachite. Under a binocular microscope, the malachite crystals appeared mostly teal and emerald-green colored, semi-translucent and semi-glossy. XRD analysis suggested that the most common contaminates included various SiO_2 phases and tenorite. Each primary sample had a correlating B2 sample. XRD characterization suggested that samples B2H2, B2H4 and B2H8 contained more malachite than their primary sample counterparts. Another copper carbonate mineral, azurite, was present in samples B2H3, B2H5, B2H9 and B2H11. *pg. 151*

Table 7.2: Quantitative XRD results of phases present in the Alaskan samples. The primary samples varied from 38% to 100% malachite, and each had correlating B2 samples. Optical microscopy descriptions ranged from classic emerald-green, semi-translucent and semi-glossy crystals to mint-colored, opaque and matte powders. Such descriptions are indicative of varying crystal sizes, with the finer samples appearing lighter in color and milky. XRD analysis suggested that B2US6 contained 1% more malachite than the correlating primary sample. XRD also suggested that US5 and B2US5 consisted of 100% malachite, which was strange because the B2 sample was roughly picked and visual descriptions state that these samples were more contaminated than the other Alaskan samples, with a yellower tint. Another carbonate mineral, calcite, was the dominant phase present in B2US4. *pg. 152*

Table 7.3: Quantitative XRD results of phases present in the Peruvian samples. These samples were dominated by another copper corrosion product, atacamite, and only contained 26% to 48% malachite. Optical microscopy descriptions of the crystals ranged from pine, teal and emerald-green colored, generally darker than the other samples included in the study, semi-translucent and semi-glossy. There was one B2 sample correlated with P2, which contained slightly more malachite, and much more copper (II) chloride hydroxide minerals. Two geological ore samples from the same tomb were also analyzed, though their formation site is uncertain. They were much purer, at 82% to 100% malachite. *pg. 152*

Table 7.4: Quantitative XRD results of phases present in the Cypriot samples. Optical microscopy descriptions suggested yellower, brighter crystals with more opaque and matte appearances than many of the other samples included in this study. Sample RC4 yielded peculiar XRD results as it could have contained anywhere from 27% to 57% malachite, with the rest copper (II) chloride hydroxide minerals. Samples RC7 and RC8 had similar compositions and were contaminated with another carbonate mineral, calcite. Cyprus is represented only with B1 samples. *pg. 153*

Table 7.5: Quantitative XRD results for phases present in Spanish samples. All samples were pure malachite. Optical microscopy of the archaeological sample described emerald-green, semi-translucent, glossy, bubble-shaped crystals. The ores were also emerald-green, semi-translucent and glossy, but had fibrous crystals. The true formation site of the ores is unknown, but believed to be from somewhere in southern Spain (*pers. comm.* Murillo Barroso 2016). *pg. 153*

Table 7.6: Quantitative XRD results for phases present in English samples. Eleven samples contained a range from 25% to 100% malachite, of which five had correlating B2 samples. Optical microscopy was most interesting, with most samples described as emerald-green colored, semi-translucent and semi-glossy, but two samples were very unique. The malachite crystals in E6 and EC4 formed in coils, which is rare. Apart from their coil structures, these samples were visually distinct from each other. E6 was pine-green colored, semi-glossy and semi-translucent. Meanwhile EC4 was mint-green colored, matte and opaque. According to XRD, the main contaminants in the English samples were quartz and atacamite. Samples E3 and EC2 were heavily contaminated with other carbonate minerals (azurite and calcite, respectively). Samples B2EC2 and B2EC5 may have contained more malachite than the primary samples, but were also heavily mixed phase, which makes XRD characterization less reliable. *pg. 154*

Table 7.7: Quantitative XRD results of phases present in Israeli samples. Three samples passed processing, but none had B2 samples. They all had similar compositions, ranging from 43% to 47% malachite with the main contaminants being atacamite and quartz. Samples I2 and I4 had more than three phases present, which complicated XRD analysis and could have hindered reliable characterizations. Optical microscopy descriptions of the samples were very distinct. I1 was mostly turquoise-colored, matte and opaque. I2 was dark teal-green, semi-opaque and semi-glossy. I4 was medium-green and had yellow-tinted areas, was semi-translucent and semi-glossy. *pg. 155*

Table 7.8: Quantitative XRD results for phases present in Chinese samples. Considering China's vast size with wide-ranging environments, the samples were grouped by province. A total of 17 samples in five provinces represent China. Gansu was represented by one pure malachite sample.

Guangxi was represented by four samples ranging from 62% to 100% malachite and two B2 samples. According to XRD, B2CGS3 was pure malachite, and the correlating primary sample was just 71% malachite and contained azurite, which is another copper carbonate mineral. CGS5 also contained azurite. Jiangsu was represented by one sample, which was 94% malachite, as well as a correlating B2 sample. Jiangxi was represented by one pure malachite sample. Ningxia was represented by six samples, of which two had B2 samples. Malachite purity ranged from 42% to 93%, with SiO_2 minerals as the main contaminant. CNM1, CNW2 and CNW3 contained other carbonate phases, and CNW5 was very mix-phase. Ningxia was also represented by four malachite ore samples of uncertain formation origin. *pg. 156*

Table 7.9: Chemical and visual descriptions of the non-malachite minerals identified in the samples, and formation details (Anthony *et al.* 2003). *pg. 157-159*

Table 7.10: Full results for $\delta^{18}O$ and $\delta^{13}C$ values from the archaeological malachite samples. The $\delta^{18}O$ values (VSMOW) range from 21.1‰ – 30.1‰, and the $\delta^{13}C$ values (VPDB) range from -18.1‰ to -8.1‰. Overall mean, standard deviation and coefficient of variation for each data column is shown at the bottom of the table. Data from sample CNW4 is furthest from the rest (in the dark grey boxes), but not an outlier as $p > 0.05$. Apart from the $\delta^{18}O$ values for sample E3, values in grey boxes are furthest from the rest in their geographical group, however not significant outliers (a group requires more than four samples to carry out a Grubb's test). The $\delta^{18}O$ values for sample E3, marked with an asterisk, are significant outliers with $p = 0.04$. *pg. 161*

Table 7.11: Full results for oxygen-18 and carbon-13 values from the Batch Two archaeological malachite samples. The $\delta^{18}O$ values (VSMOW) range from 22.4‰ to 30.9‰, and the $\delta^{13}C$ values (VPDB) range from -18.2‰ to -6.9‰. Overall mean, standard deviation and coefficient of variation for each data column is shown at the bottom of the table. The $\delta^{18}O$ value from sample B2EO and $\delta^{13}C$ value from B2CNW2 are furthest from the rest (dark grey boxes), but not outliers as $p > 0.05$. Isotope values in light grey boxes are furthest from the rest in their geographical group (a group requires more than four samples to carry out a Grubb's test), however not significant outliers. The B2 data set has no outliers. *pg. 162*

Table 7.12: Geographically grouped B1 $\delta^{18}O$ descriptive statistics for malachite. England is presented twice; first using all isotopic data, second excluding the outlying sample (E3). *pg. 163*

Table 7.13: Geographically grouped B2 $\delta^{18}O$ descriptive statistics for malachite. *pg. 163*

Table 7.14: Showing the 29 B1 and B2 $\delta^{18}O$ pairs for archaeological malachite. The mean, standard deviation and coefficient of variation are included to show the strength of central tendencies within pairs and batch data sets, and quantify the amount of dispersion. *pg. 165*

Table 7.15: Geographically grouped B1 $\delta^{13}C$ descriptive statistics for malachite. *pg. 166*

Table 7.16: Geographically grouped B2 $\delta^{13}C$ descriptive statistics for malachite. *pg. 167*

Table 7.17: Showing the 29 B1 and B2 $\delta^{13}C$ pairs for archaeological malachite. The mean, standard deviation and coefficient of variation are included to show the strength of central tendencies within pairs and batch data sets, and quantify the amount of dispersion. *pg. 169*

Table 7.18: Showing the $\delta^{18}O$ and $\delta^{13}C$ results for the B1 and B2 malachite samples that contained azurite in one of the pairs. Asterisks identify the azurite-containing samples. *pg. 170*

Table 7.19: Showing the B1 and B2 sample pairs that contained azurite, and their quantitative XRD material characterizations. *pg. 170*

Table 7.20: Showing the $\delta^{18}O$ results for the B1 and B2 samples that contained atacamite or the related minerals; paratacamite and clinoatacamite. Asterisks identify the samples with more copper (II) chloride hydroxide-containing minerals than the counterpart sample. *pg. 171*

Table 7.21: Showing the B1 and B2 sample pairs that contained a copper (II) chloride hydroxide mineral (atacamite, paratacamite, and clinoatacamite), and their quantitative XRD material characterizations. *pg. 171*

Table 7.22: Table of each sample's estimated formation water $\delta^{18}O$ (based on the data reported in the site profiles section in Chapter 5) and formation temperature (based on the average surface air

temperature at or near the sample's assumed excavation site). Also presented in this table are the calculated formation water $\delta^{18}O$ and temperatures, which were obtained using the estimated values. *pg. 176*
Table 7.23: Table showing Köppen climate classification order for the $\delta^{18}O$ in malachite ranked by increasing mean value. The first letter, in bold, defines the major climate type. Subsequent letters describe climate subtypes. *pg. 186*
Table 7.24: The measured B1 archaeological malachite $\delta^{13}C$ values are presented next to the calculated $\delta^{13}C$ in local soil CO_2, as determined using Melchiorre's ^{13}C fractionation equation. Each sample's estimated formation water $\delta^{18}O$ (based on the data reported and cited in the site profiles section in Chapter 5) and formation temperature (based on the average surface air temperature at or near the sample's assumed excavation site) is also presented. *pg. 191*
Table 7.25: The measured B2 archaeological malachite $\delta^{13}C$ values are presented next to the calculated $\delta^{13}C$ in local soil CO_2, as determined using Melchiorre's ^{13}C fractionation equation. Each sample's estimated formation water $\delta^{18}O$ (based on the data reported and cited in the site profiles section in Chapter 5) and formation temperature (based on the average surface air temperature at or near the sample's assumed excavation site) is also presented. *pg. 192*
Table 7.26: Table showing Köppen climate classification order for the $\delta^{13}C$ in malachite ranked by decreasing mean value. The first letter, in bold, defines the major climate type. Subsequent letters describe climate subtypes. *pg. 193*
Table 8.1: Displaying the number of malachite samples (n) analyzed and statistical interpretations on the relationships between $\delta^{18}O$ and $\delta^{13}C$ for each project or combination of projects shown in **figure 8.1**. *pg. 202*

LIST OF FIGURES

Figure 1.1: A patinated bronze angel statue on the rooftop of the Hofburg Palace in Vienna, Austria, from which a brochantite sample was collected for isotopic analysis. Photo courtesy of the author. *pg. 1*

Figure 1.2: One of the most distinctive features of the Statue of Liberty is its pale green patina, which is mainly composed of brochantite despite having formed by the sea. Image from the Business Insider, Inc. 2013. *pg. 3*

Figure 1.3: Cross section of a malachite specimen, showing bands and rings (image from TimeLine Auctions Limited 2017). *pg. 5*

Figure 1.4: The globular surface of a botryoidal malachite specimen from Shaba, D.R. Congo (image from Friedman 2015). *pg. 5*

Figure 1.5: An example of fibrous malachite excavated from Kasompi Mine in Katanga Province, D.R. Congo (image from Marin Mineral 2017). *pg. 5*

Figure 1.6: Stalagmitic malachite from Mashamba West Mine, D.R. Congo (image from Geology In 2014). *pg. 5*

Figure 1.7: Showing malachite with azurite and quartz. The orange coating is limonite, an iron ore. Specimen excavated from M'Cissi, Alnif, Tinghir Province, Souss-Massa-Draâ Region, Morocco. Image from FossilEra Minerals, 2017. *pg. 6*

Figure 2.1: The general characteristics of voltaic and electrolytic cells (Silberberg 2003, 899). *pg. 21*

Figure 2.2: The activity series of the metals. This list of metals (and H_2) is arranged with the most active metal (strongest reducing agent) at the top and the least active metal (weakest reducing agent) at the bottom (Silberberg 2003, 160). *pg. 23*

Figure 2.3: Immune, active and passive behaviors (Selwyn 2004, 24). *pg. 23*

Figure 2.4, a – b: Pourbaix diagrams for a copper-water system at 25ºC, 1atm and a Cu+ concentration of 10^{-6} M. For the diagram on the left, water is stable within the boundaries set by the broken lines (a) and (b); it can be oxidized to oxygen gas at or above line (b), and it can be reduced to hydrogen gas at or below line (a). The Pourbaix diagram shown on the right is the same as the one on the left, only the regions are labeled as immune, active or passive (Selwyn 2004, 25). *pg. 24*

Figure 2.5: Pourbaix diagram for the system Cu – SO_4 – H_2O at 20ºC with an SO_2 level of 46 ppm, showing brochantite at the center of the grey zone (Scott 2002, 150-151). *pg. 25*

Figure 2.6: Pourbaix diagrams for the system Cu – CO_3 – H_2O at 25ºC with carbon dioxide concentrations of A) 44ppm, B) 440ppm, C) 4400ppm, D) 44000ppm (Scott 2002, 96-7). *pg. 26*

Figure 2.7: A comparatively complex Pourbaix diagram for the system Cu – CO_3 – SO_4 – Cl – H_2O for solutions containing 229ppm CO_2 and 46ppm SO_3 (Scott 2002, 135). *pg. 27*

Figure 3.1: The basic water cycle (Utah State University 2013). *pg. 29*

Figure 3.2: Image depicting the Rayleigh rainout effect on δ^2H and $\delta^{18}O$ (adaptation based on Hoefs 1997 and Coplen *et al.* 2000, cited Arizona Board of Regents 2005). *pg. 29*

Figure 3.3: Image depicting global distribution of $\delta^{18}O$ values (per mil, ‰) in precipitation produced by interpolation of long-term annual means from about 700 GNIP stations (IAEA 1998-2013). *pg. 31*

Figure 3.4: Image of the distribution of $\delta^{18}O$ values (per mil, ‰) in precipitation over continental USA. The latitudinal effect is particularly evident in North America. Distortions to latitudinal gradients are due to continental effects and ocean currents. Beware that the color schemes are reversed between Figures 3.4 and 3.5. Image from Kendall & Coplen 2001 cited in University of Colorado, Boulder. *pg. 32*

Figure 3.5: Weighted monthly $\delta^{18}O$ (‰) distributions over the globe for one year, suggesting a seasonal effect (images from animations by IAEA 1998-2013). *pg. 34*

Figure 3.6: Three examples of different soil profiles, showing general horizons. Clearly the types (and conditions) of soil that form depend to a great extent upon the climate, particularly rainfall and temperature (Harris & Eyre 1994, 2:74; Stott & John 2010, 1153; Wilmott & Jack 2000, 335). *pg. 35*
Figure 3.7: Classification of subsurface waters (Langmuir 1997, 268). The soil zone extends from the ground surface through the major root zone (Mays 2012, 7). The thickness ranges with soil type and vegetation (*ibid.*). The thickness of the intermediate vadose zone ranges from non-existent to over 100m (*ibid.*). Capillary water (with fluctuating water height) is groundwater that has risen and is held above the water table due to capillary forces (Langmuir 1997, 269). Capillary water may be as much as 9 meters thick (Mays 2012, 7). Like the other zones, groundwater depths also range, reaching tens of thousands of meters in sedimentary basins (Langmuir 1997, 269). *pg. 35*
Figure 3.8: The basic oxygen cycle (Alberts *et al.* 2004). *pg. 38*
Figure 3.9: Upper panels: simplified schemes (pool sizes not shown to scale) of the natural global carbon and oxygen cycles where Ph = photosynthesis, Res = respiration, MB = marine biota and DIC = dissolved inorganic carbon (H_2CO_3, HCO_3^-, CO_3^{2-}). Lower panels: corresponding schemes of the cycles of oxygen isotopes in CO_2 and in O_2. Dark blue arrows indicate links to oxygen isotopes in the hydrological cycle. Red whiskers on arrows indicate exchanges during which fractionation processes occur. Heimann 2001, 236. *pg. 45*
Figure 3.10: General ranges of $\delta^{13}C$ values of selected carbon-bearing materials. The modern average $\delta^{13}C$ value of the atmosphere is shown by the filled circle; the pre-anthropogenic value is an open circle (Sharp 2007, 152). *pg. 49*
Figure 3.11: Showing the potential carbon reservoirs. Arrows indicate carbon isotope fractionation between carbon source and resulting carbonate mineral (malachite). The double arrow indicates the range of soil CO_2. Image from Haßler *et al.* 2014, 7. *pg. 50*
Figure 4.1: Diagram distinguishing heterogeneous (aqueous) and homogeneous (gaseous) pathways of SO_2 to sulfate formation. The homogeneous mechanism is suggested to be 1.8 times faster than the heterogeneous oxidation, though heterogeneous pathways predominate (Holt & Kumar 1991, 36; Tanaka *et al.* 1994, 1521). *pg. 54*
Figure 4.2: Illustration of the reactions involved in brochantite formation during patination. R1, R2, R3, and R4 are abbreviations for reactions 1-4. (FitzGerald *et al.* 2006, 2502). *pg. 55*
Figure 4.3: Pourbaix (Stability) diagram for the Cu – SO_3 – H_2O system. A and B indicate the regions in which antlerite (A) and brochantite (B) are stable. Diagram from Leygraf & Graedel 2000, 275. *pg. 57*
Figure 4.4: Above table showing percent mass losses from the decomposition of brochantite. Below table showing the percent weights of decomposition product ions for brochantite. Tables from Tanaka & Koga 1990, 613. *pg. 59*
Figure 4.5: Typical simultaneous TG-DTA and DSC curves for the thermal decomposition of synthetic brochantite at a heating rate of 10K/minute (Koga *et al.* 1997, 1469). *pg. 59*
Figure 4.6: Comparison of sulfates formed by the seven reactions carried out by Holt and collaborators (Holt & Kumar 1991, 35). Curves 1, 2 and 3 involved the aqueous oxidation of SO_2; curves 4, 5, 6, and 7 involved the non-aqueous oxidation of SO_2. The plot also displays isotopic precipitation water data (rain and snow) collected at Argonne, Illinois, October 1976 through March 1978 (*ibid.*). *pg. 61*
Figure 4.7: The $SO_2 \rightarrow SO_4$ Pathway Flowchart. *pg. 63*
Figure 4.8: Isotopic results obtained for precipitation water and for the sulfates dissolved in water. The open data points represent rain; the crossed pointed represent snow. The average monthly temperatures at Argonne, Illinois, 1975-6 are also plotted for comparison (Holt *et al* 1978, 46-7). *pg. 65*

Figure 4.9: Isotopic results for particulate sulfates and water vapor at Argonne, Illinois, 1975-6 (Holt *et al.* 1978, 48). The isotopic results for the water vapor are comparable to those of precipitation sulfate and precipitation water, found on **Figure 4.8**. The $\delta^{18}O$ of particulate sulfate varied randomly with season. *pg. 65*
Figure 4.10: Representation of type I corrosion layering on copper alloys (adapted from Piccardo *et al.* 2007, 241). *pg. 68*
Figure 4.11: Representation of type II corrosion layering on copper alloys (adapted from Piccardo *et al.* 2007, 241). *pg. 69*
Figure 4.12 (A, B & C): Pourbaix diagrams for copper and ionic species: showing the common parameters of $Cu^{2+}=10^{-4}$ M, T=25ºC and P=1013 bar. **A**: today's meteoric water in equilibrium with ~400pppmv atmospheric CO_2 ($P_{CO2}=10^{-3.4}$); **B**: typical groundwater ($P_{CO2}=10^{-2}$) and **C**: typical groundwater ($P_{CO2}=10^{-2}$) with 200mg/l $SO_{3(aq)}$. Adapted from De Putter *et al.* 2010, 98. *pg. 70*
Figure 4.13: Typical TG-DTA-EGA curves for the thermal decomposition of synthetic malachite (20.08 mg) at the heating rate of 10 K/min under flowing dry N_2 (200 cm^3/min) (Koga & Yamada 2005, 348). *pg. 71*
Figure 4.14: Component analysis of the differential thermogravimetric analysis of malachite (Frost *et al.* 2002, 136). *pg. 72*
Figure 4.15: Malachite-water oxygen isotope fractionation as a function of temperature for slow precipitation experiments (Melchiorre 1998, 187). *pg. 74*
Figure 5.1: Weighted annual $\delta^{18}O$ in rainwater isoscape of Europe, with Wallingford (Oxfordshire) and Vienna pointed out (image adapted from IAEA 2001). Oxford's closest meteoric station, which is in Wallingford, has analyzed 417 precipitation samples, yielding a long-term yearly mean oxygen-18 value of -7.3‰ (IAEA/WMO 2018). Vienna has a long-term yearly mean of -9.8‰, based on 600 precipitation measurements (IAEA/WMO 2015). *pg. 77*
Figure 5.2: GNIP map of weighted annual $\delta^{18}O$ in precipitation across North America, showing a clear latitudinal affect (image adapted from IAEA 2001). Asterisks mark the locations of Ottawa and Tuscaloosa. The oxygen-18 values in Ottawa's rainwater, based on 547 samples, have a long-term yearly mean average of -11.0‰ (IAEA/WMO 2015). Tuscaloosa has a young GNIP meteoric station, with 36 precipitation samples yielding a long-term yearly mean $\delta^{18}O$ value of -4.7‰ (*ibid.*). This value contrasts nicely with Ottawa by demonstrating the isotopic latitudinal effect in precipitation. *pg. 78*
Figure 5.3: Copper roofing at Technische Universität Wien (Vienna University of Technology) showing where a patina sample was collected (inside the red circle). Most samples averaged 4-5 cm^2, depending on the corrosion thickness. *pg. 79*
Figure 5.4: Binocular microscope photograph of the Hofburg angel statue (seen in **figure 1.1**) patina sample from Vienna, Austria. Scale: Image width approximately one centimeter. *pg. 81*
Figure 5.5: Binocular microscope photograph of the Vienna University of Technology (seen in **figure 5.3** and **5.8**) roof patina sample from Vienna, Austria. Scale: Image width approximately one centimeter. *pg. 81*
Figure 5.6: Binocular microscope photograph of the West Block Building roof patina sample from Parliament Hill, Ottawa, Canada. Scale: Image width approximately one centimeter. *pg. 81*
Figure 5.7: Binocular microscope photograph of the Presidential Hall (demolished) roof patina sample from Tuscaloosa, Alabama, USA. Scale: Image width approximately one centimeter. *pg. 81*
Figure 5.8: XRD spectrum of the patina sample collected from TU Wien. All the peaks in this spectrum are consistent with those of known brochantite samples, suggesting that this sample is also brochantite. *pg. 82*

Figure 5.9: XRD spectrum of the patina sample collected from the copper roof on Hotel Lord Elgin in Ottawa. The peaks indicate that the sample contains brochantite (red) and antlerite (blue). *pg. 82*
Figure 5.10: XRD spectrum of the patina sample collected from the copper roof on Farrah Hall in Tuscaloosa, Alabama. The peaks indicate that the sample contains brochantite (red) and quartz (blue). *pg. 83*
Figure 5.11: Map showing locations of malachite study regions against the global amount-weighted $\delta^{18}O_{annual}$ in precipitation isoscape. The legend is $\delta^{18}O$ in per mil relative to the VSMOW-SLAP scales (adapted from Terzer *et al.* 2013, 4724). *pg. 91*
Figure 5.12: Binocular microscope photograph of sample CGN2, from the interior surface of a *ding* vessel, Gansu, China. This photograph was taken before picking, yet already has an ideal visual description for malachite. XRD material characterization on the picked sample confirms it is 100% malachite. Scale: Image width approximately one centimeter. *pg. 92*
Figure 5.13: Binocular microscope photograph of sample EC4, from an ingot/Cu cake fragment, mid-late Bronze Age, Bogshole Lane, Broomfield, Kent, UK. These malachite crystals formed coils and curls (now fragmented), which is very rare (Eggert 2007, 57). Scale: Image width approximately one centimeter. *pg. 92*
Figure 5.14: Binocular microscope photograph of sample CGS3, from a *ding* vessel, Guangxi, China. This sample is before picking and mix-phase, showing a considerable amount of blue azurite. Scale: Image width approximately one centimeter. *pg. 92*
Figure 5.15: Binocular microscope photograph of sample I4, from Tel Gezer, Israel. These malachite crystals are coated in soil. An alcohol rinse was used on patina samples like this one. Scale: Image width approximately one centimeter. *pg. 92*
Figure 5.16: Binocular microscope photograph of sample RC4, from Pila Kokkinokremos, Cyprus. This image is included to show the variety of visual descriptions for the unpicked malachite samples. Scale: Image width approximately one centimeter. *pg. 92*
Figure 5.17: Binocular microscope photograph of sample US7, from a round shallow sheet copper vessel, Castle Hill, Sitka, Alaska. This sample contains organic material like wood, and was removed from the study for having too few uncontaminated malachite crystals. Scale: Image width approximately one centimeter. *pg. 92*
Figure 5.18: FTIR spectrum of homogenized sample CGN2 (also shown in figure 5.12), which is considered a pure malachite sample. Appendix C contains full page images of all FTIR spectra. *pg. 94*
Figure 5.19: FTIR spectrum of homogenized sample CHS2, an 11th century BC patina sample from Hunan, China. This sample does not appear to include any malachite, and therefore was eliminated from this study and was not analyzed using XRD. Appendix C contains full page images of all FTIR spectra. *pg. 94*
Figure 5.20: XRD spectrum and details for sample CGN2 (also shown in figure 5.12 and 5.18), which is a pure malachite sample. For all XRD spectra on the malachite samples, refer to Appendix D. *pg. 95*
Figure 5.21: XRD spectrum and details for sample B2H11, which consists of at least four different phases (tenorite, malachite, azurite and graphite). For all XRD spectra on the malachite samples, refer to Appendix D. *pg. 96*
Figure 5.22: Map of Hungary showing locations of major cities, including Debrecen in the east (University of Szeged 2010). *pg. 100*
Figure 5.23: GNIP's weighted annual $\delta^{18}O$ isoscape of precipitation throughout Europe, showing locations of Southern England; Mojácar, Spain; Hungary; and Cyprus. Adapted from IAEA 2001. *pg. 101*

Figure 5.23: GNIP's North American isoscape of $\delta^{18}O_{\text{weighted annual}}$ in precipitation showing a clear latitudinal effect and the location of Sitka, Alaska in a teal-colored zone (defined as -22‰ to -18‰) (IAEA 2001). *pg. 102*
Figure 5.24: $\delta^{18}O$ isoscape based on altitude, latitude, and July to January mean temperatures of Alaska and Yukon. Colors indicate $\delta^{18}O$ values derived from the multiple regression against measured $\delta^{18}O$ values in stream water (yellow circles), test data locations (white circles), and precipitation collection stations (white triangles) from the Lachniet *et al.* (2016) study. This isoscape is draped over hillshade to emphasize topographical details. Adapted from figure 5 in Lachniet *et al.* 2016, 6581. *pg. 103*
Figure 5.25: Map of Peru showing location of Batán Grande in the north (McEwan 2000, 15). *pg. 104*
Figure 5.26: GNIP's South American isoscape of $\delta^{18}O_{\text{weighted annual}}$ in precipitation showing the location of Batán Grande, Peru, in an orange-colored zone (defined as -6‰ to -2‰) (IAEA 2001). *pg. 106*
Figure 5.27: Map of Cyprus showing locations of sample sites and nearby modern cities (adapted from Prio Cyprus 2011). *pg. 107*
Figure 5.28: Map of Spain showing location of Las Pilas in relation to the main mining districts in the area (Murillo-Barroso *et al.* 2017, 1541). *pg. 108*
Figure 5.29: County map of England showing locations of sample sites and Wallingford, where GNIP has a meteoric station (adapted from Garber 2011). *pg. 109*
Figure 5.30: Map showing location of Tel Gezer relative to Jerusalem, Tel Aviv, Ashdod, and Rehovot (Google Maps 04 May 2019). Bet Dagan is about 14 kilometers north of Rehovot, just below the blue Route 1 label by Holon on this map. *pg. 110*
Figure 5.31: The Gat and Dansgaard plot of $\delta^{18}O$ (x-axis) against $\delta^{2}H$ (y-axis, not labeled on plot) in precipitation at Bet Gamal (marked as 22) (1972, 185). Point 20 is Ashdod and 23 represents Jerusalem (179). *pg. 111*
Figure 5.32: GNIP's Asia isoscape of $\delta^{18}O_{\text{weighted annual}}$ in precipitation showing the locations of Israel, Gansu, Ningxia, Jiangsu, Jiangxi and Guangxi in gold and orange-colored zones (defined as -6‰ to -10‰, and -6‰ to -2‰, respectively) (IAEA 2001). *pg. 111*
Figure 5.33: Showing the distribution of annual average precipitation $\delta^{18}O$ in China and the monsoon trajectories. The data are the annual average $\delta^{18}O$ values of the precipitation (Zheng *et al.* 1983 and Liu *et al.* 2008 cited in Zhang *et al.* 2015, 955). *pg. 112*
Figure 5.34: Example of a *ding* cauldron, based on a vessel found at Shaanxi Fufeng Shaochencun, Late Western Zhou (Rawson 1987, 40). *pg. 112*
Figure 5.35: Map of China with Gansu province in red, showing the locations of Zhangye and Lanzhou (adapted from Dedering 2011). *pg. 113*
Figure 5.36: Showing locations and topography of the Wu *et al.* study area and sampling sites in the Heihe River Basin, northern Gansu (2010, 1124). *pg. 114*
Figure 5.37: Showing locations and topography of the Chen *et al.* Lanzhou study region and sampling stations in Lanzhou City and its surrounding area (2015, 4673). *pg. 114*
Figure 5.38: Example of a *hu* wine container, based on an early Eastern Zhou vessel at the British Museum (Rawson 1987, 43). *pg. 115*
Figure 5.39: Map of China, with Guangxi in red, and locations of Liuzhou and Guilin marked (adapted from Dedering 2011). *pg. 116*
Figure 5.40: Map of China, showing Jiangsu in red, and the location of Nanjing marked (adapted from Dedering 2011). *pg. 117*
Figure 5.41: Map of China showing Jiangxi in red and the locations of Niucheng, Ji'an, Yingtan, and Qianyanzhou (adapted from Dedering 2011). *pg. 118*
Figure 5.42: Map of China showing Ningxia in red, and the locations of Yinchuan and Shapotou district (adapted from Dedering 2011). *pg. 119*

Figure 6.1: Plot showing the brochantite $\delta^{18}O$ means (central tendency) for each site represented by a dot, and lines representing the precision of the estimate of the mean (variability, with a 95% confidence interval), plotted in order of increasing mean value. *pg. 129*
Figure 6.2: City scales showing isotopic spread in brochantite $\delta^{18}O_{SO4}$ (‰, VSMOW) results, displayed between $\delta^{18}O$ of atmospheric oxygen (+23.5‰) and the $\delta^{18}O_{H2O}$ of each site (May-September weighted mean average, data from **tables 6.2** and **6.5**). *pg. 132*
Figure 6.3: Scatterplot shows $\delta^{18}O$-SO_4 as a function of the yearly weighted mean $\delta^{18}O$-H_2O ($y=0.05x+7.9$, $R^2=0.01$, $p=0.5$). From left to right, the first column is Ottawa, second is Vienna, third is Oxford and the fourth is Tuscaloosa. *pg. 133*
Figure 6.4: Scatterplot shows $\delta^{18}O$-SO_4 as a function of the summer weighted mean $\delta^{18}O$-H_2O ($y=8.3+0.1x$, $R^2=0.03$, $p=0.4$). This is an alternative illustration of the same information presented in the city scales (**figure 6.2**). From left to right, the first column is Ottawa, second is Vienna, third is Oxford and the fourth is Tuscaloosa. *pg. 134*
Figure 6.5: Scatterplot shows $\delta^{18}O$-SO_4 as a function of the yearly mean precipitation amount at the cities of sampling. From left to right, the first column is Oxford (24.2 inches) with Vienna (24.4 inches) immediately after, third is Ottawa (37.2 inches) and the fourth is Tuscaloosa (55.6 inches). This scatterplot shows no statistically significant correlation, with $y=8-0.02x$, $R^2=0.04$, $p=0.3$. *pg. 135*
Figure 6.6: Scatterplot shows $\delta^{18}O$-SO_4 as a function of the yearly mean surface temperature at the cities of sampling. From left to right, the first column is Ottawa (6.1ºC), followed by Vienna (10.4ºC), third is Oxford (10.6ºC), and the fourth is Tuscaloosa (17.2ºC). This scatterplot shows no statistically significant correlation, with $y=6.9+0.05x$, $R^2=0.04$, $p=0.3$. *pg. 135*
Figure 6.7: Scatterplot shows $\delta^{18}O$-SO_4 as a function of the latitude at the cities of sampling. From left to right, the first column is Tuscaloosa (33.2º), followed by Ottawa (45.3º), third is Vienna (48.2º), and the fourth is Oxford (51.6º). This scatterplot shows no statistically significant correlation, with $y=6.8+0.01x$, $R^2=0.009$, $p=0.6$. *pg. 136*
Figure 6.8: Scatterplot shows $\delta^{18}O$-SO_4 as a function of the yearly average acidity in meteoric water (presented in concentration of H^+) at the cities of sampling (i.e. scatterplot shows $\delta^{18}O$-SO_4 versus pH in local precipitation). This scatterplot shows no statistically significant correlation, with $y=7.9-(2.3x10^4)x$, $R^2=0.05$, $p=0.2$. *pg. 136*
Figure 6.9: Scatterplot shows $\delta^{18}O$-SO_4 as a function of the date of the buildings from which the samples were collected. This scatterplot shows no statistically significant correlation, with $y=15.9-0.004x$, $R^2=0.04$, $p=0.3$. *pg. 137*
Figure 6.10: The $SO_2 \rightarrow SO_4$ Pathway Flowchart. *pg. 139*
Figure 6.11: Duplicate measurement errorplot showing the brochantite hydroxyl- δ^2H (labeled as hydroxyl-D in the plot, with D standing for deuterium) means for each building represented by a dot, and lines representing the precision of the estimate of the mean (with a 95% confidence interval). *pg. 144*
Figure 6.12: Scatterplot of brochantite hydroxyl-δ^2H (using the δ^2H mean from duplicate run values presented in **table 6.13**) against the long term weighted mean δ^2H in local precipitation. Plot includes a regression line summarizing the relationship between these variables through the equation $y=12.3+0.5x$ with $R^2=0.4$, and $p=0.1$. *pg. 145*
Figure 6.13: Scatterplot shows brochantite hydroxyl-δ^2H as a function of the yearly mean precipitation amount at the cities of sampling. From left to right, the first column is Oxford (24.2 inches) with Vienna (24.4 inches) immediately after, third is Ottawa (37.2 inches) and the fourth is Tuscaloosa (55.6 inches). This scatterplot shows no statistically significant correlation, with $y=0.5x-31.2$, $R^2=0.2$, $p=0.3$. *pg. 146*
Figure 6.14: Scatterplot shows brochantite hydroxyl-δ^2H as a function of the yearly mean surface temperature at the cities of sampling. From left to right, the first column is Ottawa (6.1ºC),

followed by Vienna (10.4ºC), third is Oxford (10.6ºC), and the fourth is Tuscaloosa (17.2ºC). This scatterplot shows no statistically significant correlation, with y=2.6x-42.1, R^2=0.4, *p*=0.09. *pg. 146*
Figure 6.15: Scatterplot shows brochantite hydroxyl-δ^2H as a function of the latitude at the cities of sampling. From left to right, the first column is Tuscaloosa (33.2º), followed by Ottawa (45.3º), third is Vienna (48.2º), and the fourth is Oxford (51.6º). This scatterplot shows no statistically significant correlation, with y=33.7-1.05x, R^2=0.2, *p*=0.3. *pg. 147*
Figure 6.16: Scatterplot shows brochantite hydroxyl-δ^2H as a function of the yearly average acidity in meteoric water (presented in concentration of H^+) at the cities of sampling. This scatterplot shows no statistically significant correlation, with y=4.9-($9.7x10^{-5}$)x, R^2=0.3, *p*=0.2. *pg. 147*
Figure 6.17: Scatterplot showing hydroxyl-δ^2H brochantite data as a function of the date of the buildings from which the patina samples were collected. This scatterplot shows no statistically significant correlation, with y=0.2x-($2.9x10^{-2}$), R^2=0.09, *p*=0.5. *pg. 148*
Figure 7.1: Plot showing the B1 malachite δ^{18}O means (central tendency) for each site represented by a dot, and lines representing the precision of the estimate of the mean (variability, with a 95% confidence interval), plotted in order of increasing mean value. This order remains the same when plotted without the English outlier (E3), however the error bars shorten slightly. Jiangsu, Jiangxi, Gansu and Spain are only represented by dots because there is only one data point for each of these geographic groups. *pg. 164*
Figure 7.2: Plot showing the B2 malachite δ^{18}O means (central tendency) for each site represented by a dot, and lines representing the precision of the estimate of the mean (variability, with a 95% confidence interval), plotted in order of increasing mean value. Peru and Jiangsu are only represented by dots because there is just one data point for each of these geographic groups. *pg. 164*
Figure 7.3: Plot showing the B1 malachite δ^{13}C data, plotted in order of increasing mean value. Jiangsu, Jiangxi, Gansu and Spain are only represented by dots because there is just one data point for each of these geographic groups. *pg. 167*
Figure 7.4: Plot showing the B2 malachite δ^{13}C data, plotted in order of increasing mean value. Jiangsu and Peru are only represented by dots because there is just one data point for each of these geographic groups. *pg. 168*
Figure 7.5: In this scatterplot, there a statistically significant linear correlation between B1 δ^{18}O and δ^{13}C from the carbonate in archaeological malachite (y= -0.4x–2.4, $F_{1,47}$=11.0, *p*=0.002, R^2=0.2). *pg. 173*
Figure 7.6: In this B2 scatterplot, there is a negative linear regression between the δ^{18}O and δ^{13}C in the carbonate of archaeological malachite (y = -0.7x+5.6, $F_{1,27}$ = 14.1, *p* = 0.001, R^2 = 0.3). *pg. 175*
Figure 7.7: Scatterplot of Melchiorre's malachite project, showing that plotting the δ^{18}O in malachite ore samples against the δ^{18}O of modern meteoric water has a positive linear relation, and demonstrating that most malachite is precipitated from water with δ^{18}O very close to the modern values (Melchiorre data obtained from table 2.2 in Melchiorre 1998, 97-100). About 70% (R^2 = 0.7) of the variability in $\delta^{18}O_{malachite}$ is matched by the variability in the $\delta^{18}O_{water}$, with an apparent pattern that is statistically significant (*p* < 0.0005). *pg. 177*
Figure 7.8: Scatterplot showing that plotting the δ^{18}O in archaeological malachite samples against the δ^{18}O of modern meteoric water does not suggest a linear relation (*p* = 0.9, statistically insignificant). *pg. 178*
Figure 7.9: A plot of Smith's malachite precipitation results, showing δ^{18}O against formation temperature. There is a strong, negative, linear correlation (r = 0.999, r^2 = 0.998) with a temperature coefficient of −0.22‰ per ºC (Smith 1978, 127 & 130). *pg. 179*
Figure 7.10: Scatterplot of archaeological malachite δ^{18}O data against modern surface temperatures from representative sites. No simple correlations are apparent; suggesting the use of

modern surface temperatures will not always serve as suitable proxies for the formation temperature of malachite. *pg. 180*
Figure 7.11: Scatterplot of the estimated formation temperature, based on average yearly surface temperature, against the calculated formation temperature, determined using $\delta^{18}O$ of local meteoric water. *pg. 182*
Figure 7.12: Only considering samples with known formation sites, this scatterplot is of the estimated formation temperature, based on average yearly surface temperature, against the calculated formation temperature, determined using $\delta^{18}O$ of local meteoric water. *pg. 182*
Figure 7.13: Scatterplot of the calculated $\delta^{18}O$ in formation water, based on surface temperatures near the formation site, against the estimated $\delta^{18}O$ in local meteoric water. *pg. 184*
Figure 7.14: Classification plot of archaeological malachite $\delta^{18}O$ values grouped by Köppen climate type, and presented in hierarchal order. *pg. 185*
Figure 7.15: Scatterplot showing that plotting the B1 $\delta^{13}C_{malachite}$ against the $\delta^{18}O$ of modern meteoric water does not suggest a linear relation ($p = 0.1$, statistically insignificant). Only about 5% ($R^2 = 0.05$) of the variability in $\delta^{13}C_{malachite}$ is matched by the variability in the $\delta^{18}O_{water}$. *pg. 187*
Figure 7.16: Scatterplot showing that plotting the B2 $\delta^{13}C_{malachite}$ against the $\delta^{18}O$ of modern meteoric water does not suggest a linear relation ($p = 0.3$, statistically insignificant). Only about 4% ($R^2 = 0.04$) of the variability in $\delta^{13}C_{malachite}$ is matched by the variability in the $\delta^{18}O_{water}$. *pg. 187*
Figure 7.17: Scatterplot of B1 malachite $\delta^{13}C$ against modern surface temperatures from sites does not suggest a linear relation ($p = 0.3$, statistically insignificant). Only about 3% ($R^2 = 0.03$) of the variability in $\delta^{13}C_{malachite}$ is matched by the variability in the surface temperature. This suggests that the use of modern surface temperatures will not always serve as suitable proxies for the formation temperature of malachite. *pg. 189*
Figure 7.18: Scatterplot of B2 malachite $\delta^{13}C$ against modern surface temperatures from sites does not suggest a linear relation ($p = 0.8$, statistically insignificant). Only about 0.2% ($R^2 = 0.002$) of the variability in $\delta^{13}C_{malachite}$ is matched by the variability in the surface temperature. This suggests that the use of modern surface temperatures will not always serve as suitable proxies for the formation temperature of malachite. *pg. 189*
Figure 7.19: Classification plot of archaeological malachite B1 $\delta^{13}C$ values grouped by Köppen climate type, and presented in hierarchical order. Code: 1-BSh, 2-BSk, 3-BWh, 4-BWk, 5-Csa, 6-Cfa, 7-Cfb. *pg. 194*
Figure 7.20: Classification plot of archaeological malachite B2 $\delta^{13}C$ values grouped by Köppen climate type, and presented in hierarchical order. Code: 1-BSh, 2-BSk, 3-BWh, 4-BWk, 5-Csa, 6-Cfa, 7-Cfb (the B2 set only has samples from BWh, BWk, Cfa and Cfb). *pg. 194*
Figure 8.1: Scatterplot displaying isotopic data from all known malachite investigations. Altogether, the linear correlation between $\delta^{18}O$ and $\delta^{13}C$ can be summarized as: $y = -0.6x + 3.6$, $R^2 = 0.2$, $F_{1,275} = 52.03$, $p = <0.0005$. Independent studies vary in correlation strength, with details available in **table 8.1**. *pg. 201*
Figure 8.2: Scatterplot for Melchiorre's malachite ore data, showing calculated formation temperatures against average modern surface temperatures. A statistically significant linear correlation is apparent. Data from Melchiorre 1998, 97-100. *pg. 205*
Figure 8.3: Scatterplot of Melchiorre's data on $\delta^{18}O$ in malachite ores versus surface temperatures, showing that there is no significant relationship. *pg. 206*
Figure 8.4: Scatterplot of Melchiorre's data on $\delta^{13}C$ in malachite ores versus surface temperatures, showing that there is no significant relationship. *pg. 206*

CHAPTER 1

Introduction

1.1. PROJECT RATIONALE

Metal corrosion is the result of numerous physico-chemical interactions between a metallic substrate and its environment, and should therefore be considered a valuable source of historical material evidence. This doctoral research aims to apply a refined methodology that uses light stable isotopes in meteoric water to determine the formation location of copper corrosion minerals, for the eventual use on unprovenanced archaeological bronzes that corroded in the soil environment. To establish such a methodology, multiple investigations are necessary. This thesis only considers the correlations between the two most common copper corrosion minerals, brochantite and malachite, and their formation environment using $\delta^{18}O$, and to a lesser extent $\delta^{13}C$ and $\delta^{2}H$. Brochantite, $Cu_4SO_4(OH)_6$, is a copper (II) sulfate mineral commonly found on bronze objects exposed to the urban atmosphere. Malachite, $Cu_2CO_3(OH)_2$, is a copper (II) carbonate mineral that typically forms in soil environments. The archaeological and historic samples this research includes are from around the world, and from many different periods ranging from pre-Roman through the 20th century. However, the age of the samples is not especially relevant to this study. This is a geographic study, and how the various regions included in this study compare to one another isotopically is the focus of the project.



Figure 1.1: A patinated bronze angel statue on the rooftop of the Hofburg Palace in Vienna, Austria, from which a brochantite sample was collected for isotopic analysis. Photo by author.

1.2. COPPER CORROSION MINERALS

Before elaborating upon the design of this study, it is important to introduce copper corrosion minerals and the main copper corrosion minerals under investigation: brochantite and malachite.

Usually, metals are found in naturally occurring minerals known as ores. These minerals are classified on the basis of the anion part of their chemical formula. This is because minerals with the same anionic dominant in their composition tend to have a closer family resemblance than those with the same cation (e.g. carbonates tend to be more similar to each other than all minerals containing copper) (Fraser 2011; Nesse 2012, 5). This research project focuses on brochantite, which is a sulfate mineral, and malachite, which is a carbonate mineral. These and other major copper corrosion phases are listed in **table 1.1**, along with examples of specific minerals.

- Oxides, like cuprite, are often the first insoluble products to form on copper and tend to be reddish-brown in color.
- Carbonates, specifically malachite, are the most common corrosion product for buried archaeological bronzes.
- Chlorides are very troublesome for cuprous objects and are known to cause fast-forming and destructive corrosion. Chlorides are also associated with environments nearer the sea.
- Sulfates are mainly products of atmospheric corrosion, the most common of which that is found on copper being brochantite, antlerite, and posnjakite.
- Sulfides on copper are less common but are sometimes reported when the corrosion conditions support sulfate reducing bacteria.
- Nitrates are rare as copper corrosion products because they are mostly water soluble, but when present, copper nitrates are usually associated with artificial patinas.

A Selection of Copper Minerals

Mineral Phase	Mineral Name	Chemical Name	Chemical Formula	Color
oxide	cuprite	copper (I) oxide	Cu_2O	submetallic red
oxide	tenorite	copper (II) oxide	CuO	metallic grey black
carbonate	malachite	copper (II) carbonate hydroxide	$Cu_2CO_3(OH)_2$	pale to dark green
carbonate	azurite	copper (II) carbonate hydroxide	$Cu_3(CO_3)_2(OH)_2$	vitreous blue
chloride	nantokite	copper (I) chloride	CuCl	pale grey-green
chloride	atacamite	copper (II) chloride hydroxide	$Cu_2Cl(OH)_3$	vitreous green
sulfate	brochantite	copper (II) hydroxide sulfate	$Cu_4(OH)_6SO_4$	pale to dark green
sulfate	antlerite	copper (II) hydroxide sulfate	$Cu_3(OH)_4SO_4$	vitreous green
sulfate	posnjakite	copper (II) hydroxide sulfate monohydrate	$Cu_4(OH)_6SO_4 \cdot H_2O$	vitreous green
sulfide	chalcocite	copper (I) sulfide	Cu_2S	metallic blackish grey
nitrate	gerhardtite	copper (II) hydroxide nitrate	$Cu_2NO_3(OH)_3$	transparent green

Table 1.1: Some examples of copper corrosion phases, specific minerals and descriptions. Merged adaptation from Scott 2002, 82, 102, 123, 148, 227, 251; Selwyn 2004, 60.

1.2.1. Description of Brochantite, $Cu_4SO_4(OH)_6$

Brochantite is a green basic copper sulfate mineral named in honor of Professor André-Jean-François-Marie Brochant de Villiers (1772 - 1840), a French geologist and mineralogist of the School of Mines in Paris (Anthony *et al.* 2003, 125). It is the most common and most stable phase to form on the outer corrosion crust of copper alloys exposed to the atmosphere, yet it is rarely an ore (*ibid.*). Brochantite tends to prevail since it can form under a variety of oxidizing conditions provided mild acidity and low Cu(II) and S(VI) aqueous activities (Scott 2002, 152; Zittlau *et al.* 2013, 39). It is found in rural, urban, industrial and marine environments. Even the patina on the Statue of Liberty in New York Harbor, which is surrounded by salty seawater, is predominately brochantite (FitzGerald *et al.* 2006, 2480; Graedel *et al.* 1987, 639). This global recurrence makes brochantite a sensible material for provenance studies. It was also selected for study because it is a very stable mineral (for the limitations on the stability of brochantite, refer to Chapter 4: Formation, Stability and Isotopy of Brochantite and Malachite).

Once formed, sulfates of various isotopic ratios are highly stable with respect to oxygen isotope exchange, which proceeds at an extremely slow rate with any water which they may be subsequently associated (Holt *et al.* 1981a, 804; Holt & Kumar 1991, 27). It is also believed that the isotope ratios may not re-equilibrate during mineral precipitation (Seal *et al.* 2000, 542). This results in the preservation of $\delta^{18}O$, which may reflect the formation mechanism in sulfates (Holt & Kumar 1991, 28). Even in highly acidic rain of pH ~4 at around 10ºC, the half-life of oxygen atom exchange between the sulfate and water is in the order of 600-1000 years (Holt *et al.* 1978, 105; Lloyd 1967 cited in Holt & Kumar 1991, 28).



Figure 1.2: One of the most distinctive features of the Statue of Liberty is its pale green patina, which is mainly composed of brochantite despite having formed by the sea. Image from the Business Insider, Inc. 2013.

General Brochantite Information

Mineral Name	brochantite
Chemical Name	copper (II) hydroxide sulfate
Chemical Formula	$Cu_4SO_4(OH)_6$
Crystal System	monoclinic, space group P (for cubic primitive, with lattice points only at the corners of the cell)
Mohs Hardness	3.5 – 4
Optical Properties	· green (ranging from emerald-green, blackish green, pale green and bluish green) · transparent to translucent · vitreous, somewhat pearly on cleavages
Composition	56.20% Cu 70.35% CuO 35.37% O 17.70% SO_3 7.09% S 11.95% H_2O 1.34% H 100% total oxide 100%
Environment	secondary, formed in arid climates or in rapidly oxidizing copper sulfide deposits under low acidity

Table 1.2: Some basic information on brochantite (Anthony *et al.* 2003, 125; Ralph & Chau 2013).

Besides brochantite, the most common copper sulfates that tend to form during outdoor corrosion are antlerite and posnjakite (though the latter to a lesser extent) (Scott 2002, 147). Posnjakite is identical to brochantite in stoichiometry, except for the water of hydration. Posnjakite tends to be found in younger patinas and is considered to be a transient phase (FitzGerald *et al.* 2006, 2482). It has been thought that posnjakite may coexist with or undergo transformation to brochantite because of its structural similarity, or that it may be a precursor to brochantite (Scott 2002, 153). Work by Selwyn *et al.* (1996) however, has cast doubt on this supposition. Antlerite is stable at a lower pH than brochantite (FitzGerald *et al.* 2006, 2482).

1.2.2. Description of Malachite, $Cu_2CO_3(OH)_2$

The most characteristic physical feature of malachite is its green color, which can form bands or rings that contrast lighter and darker shades. There are many green copper corrosion minerals, and malachite can be distinguished from them by its banding or its effervescence with dilute hydrochloric acid (Chang *et al.* 1996, 293). The name, malachite, is derived from the Greek for 'mallow,' an allusion to its green color and resemblance to the leaves of the mallow plant (Rapp 2002, 108). Yet malachite's optical properties vary considerably, from bright green to almost black, translucent to opaque, and glossy to matte. Though distinct crystals are rare, they accumulate into masses with varying crystal habits. These are usually botryoidal (globular), fibrous and stalactitic. Malachite is likely the first mineral ever smelted, and has been used ornamentally for thousands of years (Rapp 2002, 160). To this day, malachite has economic value and is mined intensively around the world.


1.3


1.4


1.5


1.6

Figure 1.3: Cross section of a malachite specimen, showing bands and rings (image from TimeLine Auctions Limited 2017).
Figure 1.4: The globular surface of a botryoidal malachite specimen from Shaba, D.R. Congo (image from Friedman 2015).
Figure 1.5: An example of fibrous malachite excavated from Kasompi Mine in Katanga Province, D.R. Congo (image from Marin Mineral 2017).
Figure 1.6: Stalagmitic malachite from Mashamba West Mine, D.R. Congo (image from Geology In 2014).

Malachite ore occurs as a common secondary mineral that forms in the oxidation zones of copper deposits, especially in places where limestone is present (Chang *et al* 1996, 289). Malachite is the stable phase in equilibrium with most fresh ground and surface waters in contact with the atmosphere (Woods & Garrels 1986, 182-185). This is due to the high levels of carbon dioxide generated by the oxidation of organic material in surface and sub-surface soil-waters, which favor the stabilization of malachite over brochantite (Selwyn 2004, 65; Woods & Garrels 1986 & 1985). Since many of the same environmental factors apply to buried archaeological copper, the stable phases are also cuprite and malachite (for the limitations on the stability of malachite, refer to Chapter 4: Formation, Stability and Isotopy of Brochantite and Malachite). The first product to form on the metal is cuprite, which preserves the original surface, over which malachite commonly follows. This natural transition of copper to cuprite to malachite is extremely difficult to replicate in a laboratory, making it a good indicator of naturally formed patinas (Scott 2002, 106).

General Malachite Information

Mineral Name	malachite
Chemical Name	copper (II) carbonate hydroxide
Chemical Formula	$Cu_2CO_3(OH)_2$
Crystal System	monoclinic, space group P (for cubic primitive, with lattice points only at the corners of the cell)
Mohs Hardness	3.5 – 4
Optical Properties	· green (from bright green to blackish green) · transparent to opaque, vitreous to dull · commonly banded in masses · often forms in botryoidal, fibrous or stalagmitic masses
Composition	57.48% Cu 71.95% CuO 36.18% O 19.90% CO_2 5.43% C 8.15% H_2O 0.91% H 100% total oxide 100%
Environment	secondary, formed in the oxidizing zones of copper deposits.

Table 1.3: Some basic information on malachite (Chang *et al.* 1996, 291).

Azurite is often associated with malachite and cuprite deposits (see **figure 1.7**). Like malachite, azurite is a copper (II) carbonate hydroxide formed at low temperatures in the presence of carbon dioxide in the soil environment. Azurite, however, is less stable and will occur in favor of malachite in relatively acidic, drier environments with high CO_2 levels. Azurite often alters to malachite when small environmental changes cause hydration or a decrease in carbon dioxide (Melchiorre *et al.* 2000, 621; Scott 2002, 111; Vink 1986, 41). These pseudomorphs of malachite over well-crystallized azurite are common, but the reverse is rare (Woods & Garrels 1986, 184). On copper remains, azurite rarely forms a coherent patina (Scott 2002, 110).



Figure 1.7: Showing malachite with azurite and quartz. The orange coating is limonite, an iron ore. Specimen excavated from M'Cissi, Alnif, Tinghir Province, Souss-Massa-Draâ Region, Morocco. Image from FossilEra Minerals, 2017.

1.3. $\delta^{18}O$, $\delta^{13}C$ AND $\delta^{2}H$

Isotopes are atoms of the same element that have different numbers of neutrons, and consequently different mass numbers. The number of neutrons, therefore, defines the isotope of an element. The chemical properties of an element are primarily determined by the number of electrons, which remains constant between isotopes of the same element. This means that all isotopes of an element have nearly identical chemical behavior. The influential factor between isotopes of the same element surrounds the stability of varying numbers of neutrons in the nucleus (Silberberg 2003, 1046). There is a degree of isotopic instability created by having too many or too few neutrons. These unstable isotopes, better known as radioactive, have a certain probability of decay, which results in the emission of gamma rays and subatomic particles. Conversely, stable isotopes do not spontaneously disintegrate by any known mode of decay.

Radioactive isotopes will change in a predictable direction towards maximum stability. The radionuclides that have been observed to decay at a characteristic rate (defined by half-life) are useful for measurements of time (for example, determining the age of an archaeological object using radiocarbon dating). In archaeology, the application of isotopes has been on biomineral and organic substances to answer questions pertaining to climatic conditions, pollution, diet, dating and provenance (refer to **table 1.4**) (Pollard *et al.* 2007, 179). Using inorganic materials, like metal and environmental samples, several scholars investigated the use of lead isotopes in the 1980s and 90s to suggest provenance (Henderson 2000, 248-58).

Meteoric processes that provide a characteristic fingerprint of their origin affect the stable isotope composition of water (refer to section 3.2). This signature then serves as a natural tracer, which is fundamental in investigating provenance. This work is possible when the minerals are highly stable, resulting in the preservation of stable isotope information, which can therefore reflect the formation conditions (unstable minerals remain reactive, potentially resulting in oxygen isotope exchanges). However, the oxidizing oxygen must be primarily sourced from the local meteoric water, since its values vary geographically, and the remainder must be from atmospheric molecular oxygen, O_2, which has a relatively constant $\delta^{18}O$ composition of 23.5‰.

Isotopes in Archaeology

Element	Isotope ratio	Natural isotopic abundance (%)	Substances studied	Application
Carbon	$^{13}C/^{12}C$	^{12}C=98.89, ^{13}C=1.11	Organic matter, carbonates, biomineralized tissue, soil, CO_2	Diet, plant water-use efficiency, climate and habitat, provenance (ivory, marble)
Hydrogen	$^{2}H/^{1}H$	^{1}H=99.985, ^{2}H(D)=0.015	Water, organic matter (cellulose, collagen, lipids, chitin, peat)	Climate, plant water metabolism
Lead[1]	$^{208}Pb/^{206}Pb$, $^{207}Pb/^{206}Pb$, $^{206}Pb/^{204}Pb$	^{204}Pb=1.4, ^{206}Pb=24.1, ^{207}Pb=22.1, ^{208}Pb=52.4	Geological material, metals, silicates, biominerals, environmental samples	Provenance, pollution sourcing
Nitrogen	$^{15}N/^{14}N$	^{14}N=99.633, ^{15}N=0.366	Organic matter, soil, dissolved NO_3^- and NH_4^+, groundwater	Diet, nitrogen fixation pathways, animal water use, climate, groundwater pollution
Oxygen	$^{18}O/^{16}O$	^{16}O=99.633, ^{17}O=0.037, ^{18}O=0.204	Water, biomineralized carbonates and phosphates, sedimentary phosphates and carbonates, silicates, organic matter	Climate, plant and animal metabolism, ocean temperature, provenance (marble), chronostratigraphy
Strontium	$^{87}Sr/^{86}Sr$	84Sr=0.56, 86Sr=9.86, 87Sr=7.02, 88Sr=82.56	Bone and dental mineral, sediments, seawater	Diet, trophic levels, provenance, dating
Sulfur	$^{34}S/^{32}S$	^{32}S=95.00, ^{33}S=0.76, ^{34}S=4.22, ^{36}S=0.014	Organic matter, hydrocarbons, sulfates, sediments	Diet, pollution

Table 1.4: Some of the isotopes used in archaeology, adapted from Pollard 1998b, 286 cited in Pollard *et al.* 2007, 179.

[1] The isotope ratios given for lead are those usually reported in the archaeological literature, and differ from those used in geologically.

The brochantite study is smaller than the malachite study, serving as a test to determine whether the $\delta^{18}O$ in copper corrosion minerals can show geographic variation as they do in meteoric waters. Since the purpose of this project is to help develop a methodology that could be applied to buried archaeological bronzes, and considering that brochantite tends to form in the open atmosphere, the brochantite study did not extend beyond correlations to the local meteoric water. Brochantite is not as commonly found in in the soil environment, making it an impractical mineral to study extensively for this project. It is also for this reason that the sulfur isotopes in brochantite are not considered, though $\delta^{34}S$ is widely used in ecological and archaeological studies. A more extensive investigation into the possible use of sulfur isotopes as indicators of formation environment could be pursued in the future, for use on less common copper sulfate mineral findings.[1,2] Some information on the sources of sulfur in the atmosphere is available in section 3.5, and the formation of brochantite is addressed in section 4.2.1.

In addition to the $\delta^{18}O$ study, opportunity and resource availability led to measurement of hydroxyl-$\delta^{2}H$ in a small number of brochantite samples and carbonate-$\delta^{13}C$ in the malachite samples. As peripheral sub-studies, these isotopes are explored to determine whether the $\delta^{18}O$ study could be altered or supplemented by also measuring the hydroxyl-$\delta^{2}H$ in brochantite or carbonate-$\delta^{13}C$ in malachite, which could be useful in future investigations. Environmental water should be the only source of oxygen and hydrogen in hydroxyl groups, and the dual isotopes could provide robust data (for more information on the hydroxyl sub-study, refer to section 5.1.5). Since measuring these isotopes in the hydroxyls would require unrealistically large natural brochantite samples (several grams for a single analysis), a pilot study was carried out on only the few brochantite samples that were large enough for the analysis of $\delta^{2}H$. The amount of brochantite needed to measure the hydroxyl-$\delta^{2}H$ is smaller than for hydroxyl-$\delta^{18}O$. Although measuring $\delta^{2}H$ alone may be insufficient, this sub-study was still carried out in anticipation that the hydroxyl-$\delta^{2}H$ data on its own is still informative for whether it does in fact appear that the hydroxyls are meteoric in origin. If yes, then recommendations could be made for further research using large enough samples for measurement of both isotopes in brochantite, and perhaps eventually, in malachite too. These data could be compared to the sulfate-$\delta^{18}O$ in brochantite or the carbonate-$\delta^{18}O$ of malachite.

---

[1] At least one small study has already been published, concluding that the $\delta^{34}S$ values are typically in the region of 4 - 6‰ (CDT) with a mean of 4.7+1.2‰, which indicates that the sulfur in brochantite mainly originates from a similar source despite geographic variation, most likely sulfur contained in air pollutants (Nord *et al.* 2000, 193). This study did not include oxygen isotope measurements.

[2] Isotopic fractionation by sulfate reducing bacteria (SRB) microbiologically influenced corrosion (MIC) has been used to interpret the origin of sulfides in modern and ancient environments (Little *et al.* 1994, 180). Brochantite is not a good choice for this work because it does not fit the profile of copper corrosion minerals influenced by SRB MIC. MIC is a type of localized corrosion that is often fast forming, destructive, and occurs in environments where corrosion would not be predicted (Little & Lee 2007, 1; Little *et al.* 1994, 180). SRBs reduce sulfates, with the most common products on copper being chalcocite (Cu_2S, a black mineral) among other complex sulfide minerals (Little & Lee 2007, 28, 31; Little *et al.* 1994, 180).

Additional data is offered from the opportune measurement of $\delta^{13}C$ in malachite. Although not initially part of the oxygen-18 research project, this peripheral analysis may provide evidence of isotopic correlations to the formation environment in malachite. In this investigation, the $\delta^{13}C$ from the carbonate in malachite is processed in the same way as the $\delta^{18}O$, however future studies could include a more robust procedure. Among other parameters, the $\delta^{13}C$ values are broadly compared to the local carbon reservoirs, which are assumed based on estimated biome and soil descriptions. Carbon within the soil zone has multiple sources, both organic and inorganic in origin. Reduced organic carbon has characteristically low $\delta^{13}C$, and inorganic carbon tends to have high $\delta^{13}C$ values (Yakir 2011, 123; Sharp 2007, 152; for more details refer to section 3.6.3). The $\delta^{13}C$ value of a malachite sample can be used to differentiate between malachite that has inherited a low carbon signature from organic soil CO_2 in a vegetation-dense, temperate climate, or a higher carbon signature from a dry desert with soils more strongly influenced by limestone dissolution or atmospheric CO_2. Therefore, the carbon data is expected to generally reflect the formation soil mineral compositions and the types of plants growing, which is used more as supportive data rather than research pathfinders.

1.4. PROJECT SIGNIFICANCE

This investigation is pursued to test the possibility of creating a methodology that could be used to identify the location of formation soil for metal corrosion minerals, which in turn could be applied to the life history of an object and contribute to provenance studies. Although the corrosion formation location may not be the same as the place where an object was created or used, the corrosion formation location is still part of an object's narrative. Almost all museum collections have objects with incomplete provenance for various reasons, the most scandalous of which include looting and forgeries. The purpose of tracing provenance is normally to provide contextual and circumstantial evidence for an object's original production or discovery. At a more refined level, a methodology for identifying corrosion formation location could be applied where there is a complex history for an object. For example, an artifact could undergo multiple burials, with an initial deposition in a tomb for 200 years, only to be looted and re-buried 500 km away for another 3000 years. Moreover, this study offers the possibility to ascertain whether the corrosion products on a specific object could have been produced naturally by environmental interaction over a period of hundreds or thousands of years, or an artificial patination.

1.5. GAPS IN CURRENT RESEARCH

1.5.1. Brochantite

Measurement of $\delta^{18}O$ in the sulfate of natural brochantite for comparison to $\delta^{18}O$ in the local meteoric water has never been attempted before. The most complete data on the control of $\delta^{18}O$ in sulfate, which was published in a series of papers from the late 1970's through the early

1980's, are that of Holt, Cunningham, Engelkemeir and Kumar.[1] They developed a method of analysis based on $\delta^{18}O$ in atmospheric sulfates and water that allows for estimates of the relative amounts of primary and secondary sulfates at a given receptor site.[2] Sulfates are either primary (sulfates formed within combustion sources before emission into the atmosphere) or secondary (sulfates formed in the atmosphere, principally from SO_2, by atmospheric conversion processes).[3] Although primary sulfates contribute to the total sulfate budget, they are not considered in estimations because they constitute a negligible portion compared to secondary sulfates (Lee & Thiemens 2001, 17362).

The two widely accepted mechanisms by which SO_2 is transformed to secondary sulfate are aqueous-phase (heterogeneous) and gaseous-phase (homogeneous). In the homogeneous process, oxidation precedes hydration (oxidation-hydrolysis), whereas in the heterogeneous process, hydration precedes oxidation (hydrolysis-oxidation) (Holt *et al.* 1979, 44; Novák *et al.* 2007, 706). Although made from the same starting components, the mechanisms responsible for the two transformation processes are entirely different, resulting in sulfate products of distinguishable $\delta^{18}O$ content (Holt *et al.* 1979, 44; Holt & Kumar 1991, 32). There are no experimental data that allow for an isotopic comparison of sulfates clearly formed by the aqueous and gaseous pathways.

1.5.2. Malachite

$\delta^{18}O$ in Malachite Ores

Oxygen isotope studies have been conducted on synthetic and geological malachite, but very little has been done on archaeological or historical malachite. Since the formation pathways between synthetic, geological and archaeological malachite are different (refer to section 4.3.1), the results obtained from synthetic and geological samples cannot be assumed to be totally representative of archaeological malachite as well. One hypothesis of this study is that there could be a stronger correlation between the $\delta^{18}O$ in archaeological malachite samples and the $\delta^{18}O$ of modern meteoric waters used as environmental proxies since the malachite used in this study is much younger than the malachite ores used in previous studies.

Four previous investigations on the use of stable isotopes in malachite have focused on authenticity, provenance and formation temperature. In 1998, E. B. Melchiorre verified that malachite ore is dominantly controlled by the $\delta^{18}O$ values of ambient meteoric waters and surface temperatures, and established an empirical geothermometer (discussed in detail in section 7.2.2). Melchiorre's studies started as a doctoral project, and the same 61 malachite ores from around the world were used in subsequent publications. These samples were mostly collected by Melchiorre, handpicked under a binocular microscope and confirmed as malachite using XRD analysis.

Most malachite forms between 5 and 30ºC (Melchiorre 1998, 222). These temperatures

[1] Holt & Kumar 1991; Holt *et al.* 1978, 1979, 1981a, 1981b, 1982, 1983.
[2] Refer to section 4.2. for details on the work by Holt, Cunningham, Engelkemeir and Kumar.
[3] Refer to section 4.2. for details on relevant sulfate chemistry.

correlate reasonably well with the modern local ambient temperatures, suggesting that all the natural malachite samples formed in equilibrium with waters having low $\delta^{18}O$ values (which are consistent with meteoric values). Moreover, the $\delta^{18}O$ of malachite is dominantly controlled by the temperature and $\delta^{18}O$ of the meteoric water from which the sample formed (Melchiorre 1998, 222, 233). Melchiorre's study used mine water and other water sources in the district of his malachite samples. When this was not feasible, Melchiorre used estimates based on interpolation of the water data in Taylor (1974), Yurtserver and Gat (1981), and A. Andrew (1997) (Melchiorre *et al.* 1999, 252). He reported a simple correlation between malachite $\delta^{18}O$ and the $\delta^{18}O$ of modern meteoric waters nearby, which indicates that the malachite samples precipitated from waters like the modern ones used for the study, and therefore concluded that modern water $\delta^{18}O$ values can serve as a reasonable environmental water proxy (when the malachite samples are young, since meteoric waters can change significantly over longer periods of time) (Melchiorre 1998, 222, 248).

The most recent study on stable isotopes in malachite was by Haßler, Taubald and Markl in 2014. Like Melchiorre, their research was based on ores, but it was not geographically varied and considered several carbonate minerals simultaneously. Instead, Haßler *et al.* focused on a single region in southwest Germany known as the Schwarzwald mining district. Again, sample processing included careful picking under a binocular microscope and only using samples with good XRD material characterizations. The malachite samples used in the Schwarzwald study were deliberately chosen with different textural appearance from deposits at various altitudes and geological settings (49 localities within the Schwarzwald site). As an environmental proxy for the formation water, this study used an estimated average value of -10‰ for all samples, which is based on groundwater collected from the area by the World Meteorological Organization (WMO). For an $\delta^{18}O$ value of water of -10‰, temperatures of 13-31ºC were calculated using Melchiorre's malachite-water oxygen isotope thermometer. The results obtained by Haßler *et al.* suggest the malachite-water oxygen isotope thermometer by Melchiorre is a valuable tool for calculating formation temperatures of copper carbonates, which is also in accordance with the theoretically calculated oxygen isotope fractionation factors between water and carbonate mineral by Chacko and Deines (2008 cited in Haßler *et al.* 2014, 14).

The Haßler *et al.* study shows that Melchiorre's work on $\delta^{18}O$ can serve as a reliable framework upon which to build the archaeological malachite study. Especially encouraging is the fact that the $\delta^{18}O$ in formation water was estimated successfully by Haßler *et al.* using groundwater collected and analyzed by the WMO, which is also responsible for Global Network in Precipitation (GNIP, used and discussed later in this study). These groundwater values yielded reasonable results in Melchiorre's geothermometer equation, prompting this archaeological malachite study that uses estimated $\delta^{18}O$ in local meteoric water to calculate formation temperatures.

$\delta^{13}C$ in Malachite Ores

Previous studies on the controls of $\delta^{13}C$ in malachite have always focused on the carbon reservoirs, and the distinction between organic and inorganic sources. The lack of data and discrepancies in carbon isotope fractionation factors for many heavy metal carbonate minerals like malachite, especially at lower (ambient) temperatures, has limited progress on improving upon these investigations (Haßler *et al.* 2014, 8). Consequently, previous investigations have hardly examined the impact temperature has on $\delta^{13}C$ in malachite. Melchiorre *et al.* believes that carbon isotope exchange between CO_2-malachite is significantly influenced by temperature, but only under certain circumstances. They suggest that in the case of malachite slowly precipitated in ambient temperature ranges, the $\delta^{13}C$ values are not as thermally dependent because bicarbonate is present, but they do not elaborate further (1999, 250).

$\delta^{18}O$ and $\delta^{13}C$ in Archaeological Malachite

The first paper on archaeological malachite was published in 1978 by A. W. Smith, who worked at the British Museum Research Laboratory. His paper, titled "Stable Carbon and Oxygen Isotope Ratios of Malachite from the Patinas of Ancient Bronze Objects," aims to relate the carbon-13 and oxygen-18 ratios to the formation conditions of the malachite patina and to examine the feasibility of using this information as a basis of a new criterion for authenticity. The reasoning behind this study was based on the hypothesis that $\delta^{18}O$ is related to average soil temperature and local water values, and that $\delta^{13}C$ is related to both the source of the dissolved carbonate as well as equilibrium between dissolved carbonate and hydrogen carbonate. Smith selected pieces from the British Museum's collection of provenanced bronze hoards, with objects ranging from England, Italy, Libya and 'Asia', thus enabling the observation of the effects of regional climatic differences in the isotope ratios.

When corroded by waters containing oxygen and carbon dioxide, the copper that is attacked by the water that goes into solution is mostly in the form of cupric bicarbonate. Fractionation can occur between the carbon dioxide and bicarbonate ions, resulting in ^{13}C becoming more concentrated in the bicarbonate solution. Consequently, malachite deposited from bicarbonate solutions might have $\delta^{13}C$ values that are higher than the biogenic CO_2 values of -26‰. This was confirmed by Smith's study. The degree of corrosion of the bronze object studied and the $\delta^{13}C$ of the malachite patina appeared to be related: severely corroded objects had the lowest $\delta^{13}C$, and moderately corroded objects the highest. This would indicate that the consistency of the British data is related to the CO_2 concentration in the soil. When plotted, the results suggest that various sites in Britain have similar oxygen-18 values, but the oxygen-18 ratios of samples from non-British sites display a wide range of values that do not appear to show clear provenance relationships. Nevertheless, his work is encouraging and has motivated further research. Comparing the $\delta^{18}O$ and $\delta^{13}C$ of malachite from the patina of an unknown bronze object with the same ratios from an ancient bronze of known provenance might make it possible to draw some

conclusions about origins. This application, however, has yet to be verified by any practical studies.

Smith's samples were not examined or sorted under a microscope nor analyzed for malachite identification. The main issue with Smith's work is sample purity and identity, and the methodology needs updating. A scraping of green minerals from a bronze object will contain many different phases, and it is believed that isolating the malachite, if present, would provide more refined results that can be used in determining geographic formation region.

In 2005, a MSc student (Pandey 2005) in Archaeological Science at the University of Oxford attempted to carry out further research on Smith's work for his dissertation. The aim was to study the oxygen isotopic variation in corrosion products of copper and its alloys, and its application as a tracer of burial environment. Like Smith and Melchiorre, Pandey's study was based on the anticipation that the source of soil water, which is responsible for corrosion in burial conditions, is mainly meteoric in nature. The meteoric water, therefore, should show an isotopic relationship with that of the soil water. In burial conditions corrosion products are formed through a slow process and should ideally exist in equilibrium with the soil water. This equilibrium would result in an inheritance of isotopic characteristics in corrosion products from the soil water and can be assessed through measuring the isotopic ratios of corrosion products and comparing with that of meteoric water. If this equilibrium is not maintained, then it may be possible to predict that the isotopic signature of soil water is altered from that of the meteoric water either during other natural processes or due to contamination from other isotopic species in the soil.

The Pandey's research had several limitations. Among them:

- The isotopic data for the meteoric water values were not precise. He used averages for the entire country, or continent, of interest rather than exact sites.
- His study was carried out on six samples. Only one sample was used to represent each location, defined as Britain (x 2), Sumatra, Europe, Thailand and Northern Iraq. Some of these regions are very broad, especially the sample from "Europe."
- A combination of FTIR and XRD yielded inconclusive material identifications. All of Pandey's samples were mixed-phase, and only two likely contained malachite.

Inconsistencies in sample descriptions make Pandey's data set difficult to use appropriately. Ultimately the student's results were not able to provide a definite conclusion on the geochemistry of corrosion during burial and the possible factors responsible for it.

The isotopic data collected from all known previous studies on brochantite and malachite was not statistically tested for significance.

1.6. THESIS AIMS AND OBJECTIVES

1.6.1. Brochantite Study

The aim of the brochantite study is to measure the $\delta^{18}O_{SO4}$ in natural brochantite from geographically distinct locations to determine whether there is isotopic variation between sites, as

there is in meteoric waters. Next, the $\delta^{18}O_{SO4}$ in brochantite is compared to the $\delta^{18}O$ in local meteoric water, which serves as a proxy for the formation water, using the Global Network of Isotopes in Precipitation (GNIP) as the source of data. Additionally, the hydroxyl-$\delta^{2}H$, which should be entirely meteoric in origin, is measured in larger samples to determine whether this is a practical methodology that can be used to supplement the $\delta^{18}O_{SO4}$ investigation. Other environmental parameters (temperature, pH, amount of precipitation, and latitude) are also compared to the $\delta^{18}O_{SO4}$ and hydroxyl-$\delta^{2}H$ measurements in brochantite to understand what controls the isotope ratios during formation.

To test the quality and significance of the isotope results in brochantite, the $\delta^{18}O_{SO4}$ and hydroxyl-$\delta^{2}H$ are processed statistically. To determine whether the isotopes ratios are predictable, the strength of the data is quantified, and the variance within groups and between groups is tested for significance. To identify the most influential factors and trends that may be used in provenance and authenticity studies, regression statistics are carried out to look for relationships between the brochantite isotope data and environmental parameters. Finally, a heterogeneous-homogeneous formation pathway flowchart is created to help understand and calculate the percent contributions from aqueous and gaseous formation pathways in the brochantite samples.

The project aims and objectives are accomplished with the following tasks:

1. To collect natural brochantite samples with good geographic variance.

Four cities were chosen for sample collection from patinated copper roofs, which are Oxford (England), Vienna (Austria), Ottawa (Canada) and Tuscaloosa, Alabama (USA).

2. To isolate the sulfate in brochantite for isotope analysis.

The focus of this research is to measure the sulfate $\delta^{18}O$ values in brochantite, which need to be isolated from the other oxygen atoms within the brochantite structure (the hydroxyl oxygen needs to be separated, along with any contaminants). This is done by confirming the presence of brochantite with XRD and reacting dissolved patina with barium chloride ($BaCl_2$) to precipitate $BaSO_4$ that can then be used for isotopic analysis through a mass spectrometer.

3. To carry out a pilot study for the analysis of $\delta^{2}H$ from the hydroxyl groups in brochantite.

None of the previous studies on brochantite or malachite have included isotopic analysis of the hydroxyl isotopes. A reduction on hot zinc was tested, requiring just 8-10mg of patina for $^{2}H/^{1}H$ analysis of water.

4. To statistically process all isotope data from the brochantite samples.

Statistical analysis is conducted to describe the variance, differences, and relationships in the brochantite isotope data, and to use in comparisons with the environmental parameters. This includes paired *t*-tests, Anova, and regression.

5. To create a quantitative flowchart explaining the possible formation pathways for $SO_2 \rightarrow SO_4$.

Since there are no experimental data that allow for an isotopic comparison of sulfates clearly formed by the aqueous and gaseous pathways, a flowchart is created that can be used to calculate estimations. Using the $SO_2 \rightarrow SO_4$ Pathway Flowchart, the percent contributions from heterogeneous and homogeneous pathways are calculated for the isotopically analyzed brochantite samples.

1.6.2. Malachite Study

Similar to the brochantite study, the aim of the malachite study is to measure the $\delta^{18}O$ in archaeological malachite from geographically distinct locations to determine whether there is isotopic variation between sites, as there is in meteoric waters. This was done in two groups, called Batch One and Batch Two, which consist of the same original samples cleaned differently to assess the extent of processing necessary to obtain reliable isotope data, and to help understand the impact of common contaminants. Next, the $\delta^{18}O$ in archaeological malachite is compared to the $\delta^{18}O$ in local meteoric water, which serves as a proxy for the formation water. GNIP offers a strong resource of oxygen-18 ratios in precipitation around the globe. When water collection and its isotope measurement is not an option for personal investigation projects, as is the case for this study, GNIP can serve as a good guide. However, in several cases, alternative published data is used for areas where GNIP is not well established. Simultaneously, the $\delta^{13}C$ is measured to determine whether this information can be used to supplement the $\delta^{18}O$ investigation. Other environmental parameters (temperature and climate) are also compared to the $\delta^{18}O$ and $\delta^{13}C$ measurements in archaeological malachite to understand what controls the isotope ratios during formation.

To test the quality and significance of the isotope results in archaeological malachite, the B1 and B2 $\delta^{18}O$ and $\delta^{13}C$ data are processed statistically. To determine whether the isotope ratios are predictable, the strength of the data is quantified, and the variance within groups and between groups is tested for significance. To identify the most influential factors and trends that may be used in provenance and authenticity studies, regression statistics are carried out to look for relationships between the malachite isotope data and environmental parameters. Finally, the previous malachite studies on ores and archaeological malachite are statistically assessed, and then compared to this project's results. The purpose of doing this is to determine whether there is a detectable isotopic difference between archaeological malachite and ores, and if there is a stronger correlation between archaeological malachite and modern meteoric waters than with malachite ores.

The project aims and objectives are accomplished with the following tasks:

1. To collect archaeological malachite samples with good geographic variance.

For this study, sample acquisition depends on the people working in the country of the archaeological object's origin, who collect and send many of the samples in the malachite study. Object details and archaeological contexts are largely lacking. The post-excavation life cycles of

most of the objects used for corrosion sampling are vague, if at all known. It is possible that they received chemical surface treatments that can taint isotope measurements, or been mislabeled with inaccurate provenances. After processing, forty-nine archaeological malachite samples grouped into twelve formation regions are suitable for isotope analysis. They are: Alaska, USA; northern Peru; Hungary; Cyprus; southern Spain; southern England; Israel and the following Chinese provinces: Gansu, Guangxi, Jiangsu, Jiangxi and Ningxia.

2. To isolate malachite crystals in mix-phase samples for material characterization and isotope analysis.

The focus of this research is to measure the carbonate $\delta^{18}O$ and $\delta^{18}O$ values in archaeological malachite, which need to be isolated from the other minerals present (including other copper corrosion products and soil components) in the original samples. This is done visually by steadily picking out malachite crystals using a needle under a binocular microscope. Prior to mass spectrometry, samples are pulverized with a mortar and pestle and quantitatively characterized with micro-sample XRD. Unsuitable samples are removed throughout this process.

The Batch Two samples are less-processed and more heavily contaminated to test the necessity of meticulous picking.

3. To statistically process all isotope data from the archaeological malachite samples.

Statistics are used to describe the variance, differences, and relationships in the archaeological malachite isotope data, and to use in comparisons with the environmental parameters. This includes paired *t*-tests, Anova, and regression. Similarly, the data from previous malachite studies are statistically evaluated for comparison to this study.

Though these analytical methods are interventive and destructive, they are far less destructive than other isotopic investigations that require samples of the object itself. It will also be more informative as it is the product of the reaction between the object and its corrosive environment. Regardless of the study results, this work emphasizes the need to conserve corrosion products as common practice.

1.7. THESIS STRUCTURE

This doctoral thesis is comprised of eight chapters, as follows:

Chapter 1 establishes the research rationale by situating the project in a broader context. Descriptions for brochantite and malachite are provided, as well as brief classifications of other common copper corrosion minerals. The reasoning behind the isotopes used is introduced, before putting the research into a context that illustrates the types of situations where this work may be applied. Previous investigations are addressed, and the gaps in research to be filled by the thesis aims and objectives are outlined.

Chapter 2 summarizes the basic concepts of copper corrosion as a case of electrochemistry. The driving forces of metallic corrosion are discussed mainly through aqueous thermodynamics to better understand the corrosion pathways relevant to this research.

Chapter 3 focuses on the effects of observed global cycles. These are the natural global systems that influence copper corrosion at the molecular and isotopic level, and support the theory behind the project aims. This includes the water, oxygen and carbon cycles, the observed stable isotope effects throughout these cycles, and the sources of sulfur in the atmosphere.

Chapter 4 utilizes the background information from chapters 2 and 3 to narrow in on brochantite and malachite by thoroughly discussing their formation, stability and isotopy.

Chapter 5 describes the study procedures, from sampling criteria to the laboratory methodologies used for the brochantite and malachite studies.

Chapter 6 presents all XRD and isotope results from the brochantite study. Raw data, descriptive statistics, *t*-tests, Anova and regression analyses are provided with limited discussion, to be elaborated upon in more detail in the final chapter.

Chapter 7 presents all XRD and isotope results from the malachite study. Raw data, descriptive statistics, *t*-tests, Anova and regression analyses are provided with limited discussion, to be elaborated upon in more detail in the final chapter.

Chapter 8 offers a review and final discussion for this thesis, and directly addresses all research aims using findings from this project, with conclusions. The limitations and suggestions for further research are presented last.

CHAPTER 2

The Driving Forces of Metallic Corrosion

2.1. INTRODUCTION

Most metals used in antiquity are not particularly stable. In natural environments, they tend to react with elements derived from inorganic sources and biological organisms. These reactions often yield more stable compounds, but result in the irreversible deterioration of the metal and its properties, apparently eating it away. For this reason, corrosion is often considered undesirable and problematic. Yet metallic corrosion may be exploited for preservation and scientific research, or even deemed as aesthetically desirable (i.e. patina).

What governs the level of corrosion is the combination of the material type and the environment to which it was exposed (a metal/non-metal interface) by an electrochemical reaction. As a necessary precursor to this investigation, this chapter has established the fundamental processes and terminology used when describing copper corrosion, focusing on the thermodynamics of aqueous corrosion, as an example of environmental electrochemistry.

2.2. METAL CORROSION AND ELECTROCHEMISTRY

In order to extract a metal from its mineral ore, a large amount of energy, often in the form of heat, is necessary (Trethewey and Chamberlain 1995, 69). Once separated from its ore, the metal is in an energetically rich state and wants to return to a more stable, lower energy state. Metals do this by releasing energy back into the environment, which is accomplished through a process known as corrosion. Corrosion products have a less coordinated structure than metal, which in appearance and content resembles the parent raw material – the ore. There are four reaction requirements for metal to release energy into its environment:

1. an anode where oxidation processes take place;
2. a cathode where counterbalancing reduction processes take place;
3. an electrical connection that allows electrons to flow from the anode to the cathode;
4. an ionic connection that allows ions to flow between the anode and cathode (i.e. and electrolyte) (Selwyn 2004, 20).

In this section, these corrosion requirements are defined through descriptions of what, how and why certain reactions take place. Traditionally, corrosion formation is classified by its deposition mode, which is referred to as either wet or dry. Where the oxidation of metal occurs by reduction of a species in solution, the corrosion pathway is wet or aqueous. Dry corrosion is

defined as the direct ionization of oxygen by deposition of particulates or aerosols (Cole 2010, 1069, Shreir 1994, 1:18). However, it is best to view corrosion reactions as either being dominated by thermodynamics or kinetics. Thinking of corrosion as either dry and chemical or aqueous and electrochemical is limited considering that most corrosion is the latter. This project focuses on the thermodynamics of aqueous corrosion, but dry and kinetic corrosion mechanisms are briefly described to establish some balance and connections for a better understanding of the pathways relevant to this research.

2.2.1. Thermodynamics and Kinetics of Aqueous Corrosion

The electrochemical reactions that yield metallic corrosion are based on thermodynamics.[1] Thermodynamics deals with the relations between heat and other forms of energy, and the role of entropy in these chemical reactions. It can be used to describe the tendency of a system to corrode by predicting the equilibrium state. Thermodynamics cannot lend information on the detailed reaction pathway or the rate at which the system proceeds to equilibrium. The rate of corrosion is investigated through kinetics, and it is determined by measurement of current density (Trethewey and Chamberlain 1995, 94). Therefore, to better understand the fundamental concepts behind the conditions under which it is possible for metal corrosion to occur, a grasp of thermodynamics and equilibria is integral.

Elaborating further on kinetics, the corrosion rate of a metal is influenced by many factors including the amount of water present, the pH, soil compositions, as well as temperature (Selwyn 2004, 33). Water is a necessary requirement for aqueous corrosion, and the more of it, the easier electrochemical reactions can take place. This is because water serves as an electrolyte, that is, a carrier for ions during corrosive reactions. Therefore, more water allows for greater ion flow. Certain ions are especially corrosive, like the chloride ions typically found nearer the ocean, which lead to bronze disease, a fast developing and destructive formation. The acidity or alkalinity of an environment plays a role in the rate of corrosion because, in general, metals corrode more quickly in acidic conditions where their corrosion products are more likely to be soluble. In alkaline environments, the corrosion products are likely to be insoluble and often form a passivating film that slows corrosion. Temperature influences the rate of corrosion as well: the higher the temperature, the faster the corrosion. Modeling kinetic corrosion is not very practical or easy, especially when the rate is slow (hundreds or thousands of years), though this is not unrealistic in archaeology (Scott 2002, 14). The main issue here is when a particular step in the corrosion process is so slow that thermodynamic equilibrium is never obtained (Scott 2002, 14).

In most archaeological contexts, metallic corrosion is a case of environmental electrochemistry. Electrochemistry is the relationship between chemical change and electrical work (Silberberg 2003, 893). Corrosion occurs when two or more electrochemical reactions take

[1] For the basic principles of thermodynamics, including entropy (*S*) and Gibbs free energy reaction ($\Delta G = G_{(products)} - G_{(reactants)}$), refer to Procter (2010) pp. 2-4 and Silberberg (2003) pp. 865.

place on a metal surface, and results in some of the metal changing from the metallic state to a non-metallic state (e.g. a metal oxide) (Selwyn 2004, 19). Since corroding metals are not at equilibrium, the reaction can be characterized as an electrochemical cell. Two cell types are distinguished based on the general thermodynamic nature of the reactions taking place. Voltaic cells (also known as galvanic) share many similarities with the corrosion process.[1] They do work by releasing free energy from a spontaneous reaction to produce electricity.[2] In comparison, an electrolytic cell absorbs free energy from an electricity source to drive a non-spontaneous reaction. The change in free energy (ΔG) during metal oxidation is a measure of the spontaneity of a process and of the useful energy available from it (Silberberg 2003, 872). It is equal to the work released or absorbed during corrosion. Whether absorbing or releasing free energy, electrochemistry always involves the movement of electrons from one chemical species to another in an oxidation-reduction (redox) reaction (Silberberg 2003, 147 and 893).[3]

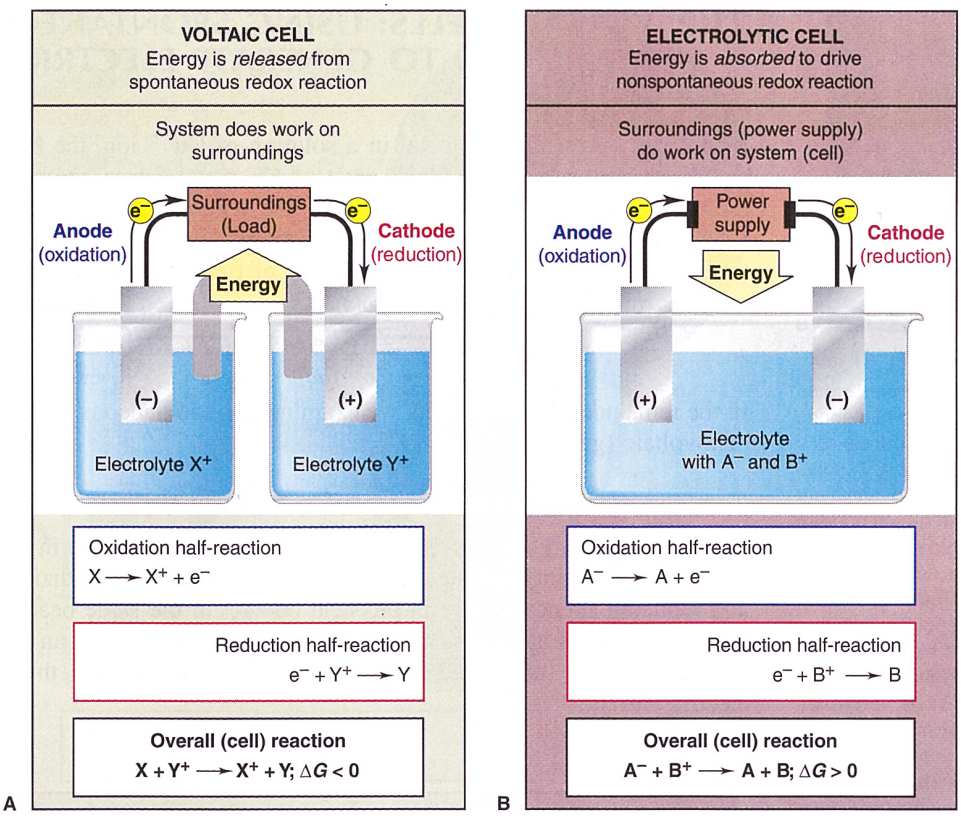


Figure 2.1: The general characteristics of voltaic and electrolytic cells (Silberberg 2003, 899).

As a metal corrodes, the surface becomes covered with a network of local electrochemical cells that are constantly changing, until over time the corrosion becomes fairly uniform over the

[1] For more on the basic principles of cell potential, including the output of a voltaic cell and half-cell potentials, refer to Selwyn (2004) 19 and 22, and Silberberg (2003) 905-906.
[2] For the basic principles of free energy, electrical work, Faraday's Law and the Nernst equation, refer to Silberberg (2003) 917, Trethewey and Chamberlain (1995) 74, and Selwyn (2004) 23 for an understanding within the context of metallic corrosion.
[3] For the basic principles of redox reactions within the metallic corrosion context, refer to McNeil and Selwyn (2001) pp. 605, Selwyn (2004) pp. 20, and Silberberg (2003) pp. 894.

entire surface (Selwyn 2004, 21). Slow-forming cationic corrosion retains the original shape and surface detail of an object because there is a direct relationship between the crystallography of the copper alloy substrate and the corrosion products that orient from it (Cronyn 1990, 167-8; Silberberg 2003, 968). Examples include cuprite for copper and Ag_2O for silver (Scott 1991, 43). Under anionic control, corrosion progresses with a greater change of volume and produces thicker, less coherent products (Cronyn 1990, 167-8). This mineralization results in the solid-state transformation of one corrosion product to another. An example is the alteration of cuprite (Cu_2O) to tenorite (CuO). When anodic and cathodic sites occur at different areas of the same metal surface, the metal is said to corrode normally. However, when the anodic and cathodic sites occur on two different metals, the corrosion is said to be galvanic. When two metals are in contact (two dissimilar metals or phases, such as copper and iron), the noble metal would corrode less than usual. The base metal, in this case the iron, would corrode more than usual. This process would continue until the iron has totally corroded away. This is known as cathodic protection, with the more noble metal acting as a cathode (Cronyn 1990, 171).

2.2.2. The Activity Series and Pourbaix Diagrams

Metals can be ranked by their ability to displace H_2 from various sources or to displace one another from solution. The results of such reactions between metals and water, aqueous acids, and metal-ion solutions form the basis of the activity series of the metals (refer to **figure 2.2**). For those that are stable in water, elements higher on the list can reduce aqueous ions of elements lower down. Copper is one of the least active metals, meaning it is one of the weakest reducing agents, and it cannot displace H_2 from any source in aqueous solution (Silberberg 2003, 160). This means that, during corrosive redox reactions, copper is not oxidized by water. A more powerful oxidant, usually oxygen, is necessary for corrosion to occur (Scott 2002, 34). There is almost always something (typically air, sulfate-producing bacteria, salts) that will cause the water molecules to separate and yield dissociated oxygen to initiate corrosive reactions.

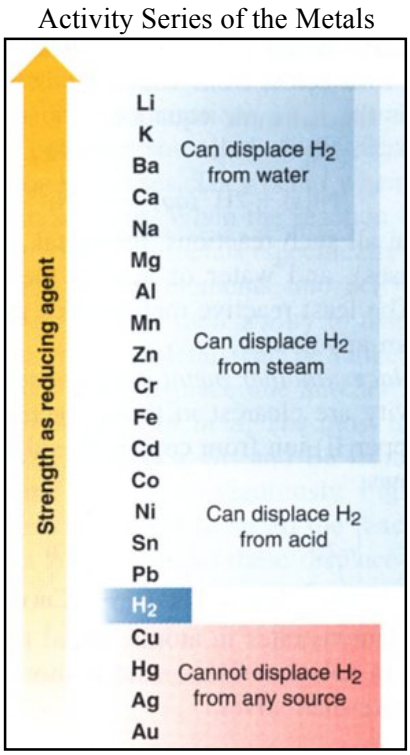


Figure 2.2: The activity series of the metals. This list of metals (and H_2) is arranged with the most active metal (strongest reducing agent) at the top and the least active metal (weakest reducing agent) at the bottom (Silberberg 2003, 160).



Figure 2.3: Immune, active and passive behaviors (Selwyn 2004, 24).

The environmental conditions in which a metal will be actively corroding, immune to corrosion, or possibly passivated, can be calculated using thermodynamic information, and these predictions plotted on Pourbaix diagrams (refer to **figure 2.3**).[1] The basis for Pourbaix diagrams is that electrochemical reactions are the result of chemical species and electrical charges. These valuable diagrams show how a metal should behave in certain environments, including the regions of stability for certain mineral species, by plotting the redox potential (E_h) of a system (its ability to act in either an oxidizing or reducing manner) against its acidity or alkalinity (pH) (Frankel &

[1] There are three possible behaviors of a metal when immersed in a solution: immune, active or passive (Selwyn 2004, 24). Immunity is when there is no reaction or corrosion of the metal. Examples of immune metals found in archaeology are gold and platinum (Scott 1980, 149-150). Active corrosion means that a metal is reacting with its environment and resulting in the deterioration of the material. This is usually characterized by a high weight loss of the metal. Passive corrosion is when the metal corrodes, but a protective corrosion product is formed. Cuprite patinas are examples of protective (passive) corrosion.

Landolt 2003, 16; Scott 2002, 32). The corrosion of many metals, even in simple electrolytes, may consist of more than one reaction, and therefore several different plots may be necessary (Trethewey and Chamberlain 1995, 106). How many depends on the concentration of species at a given temperature.

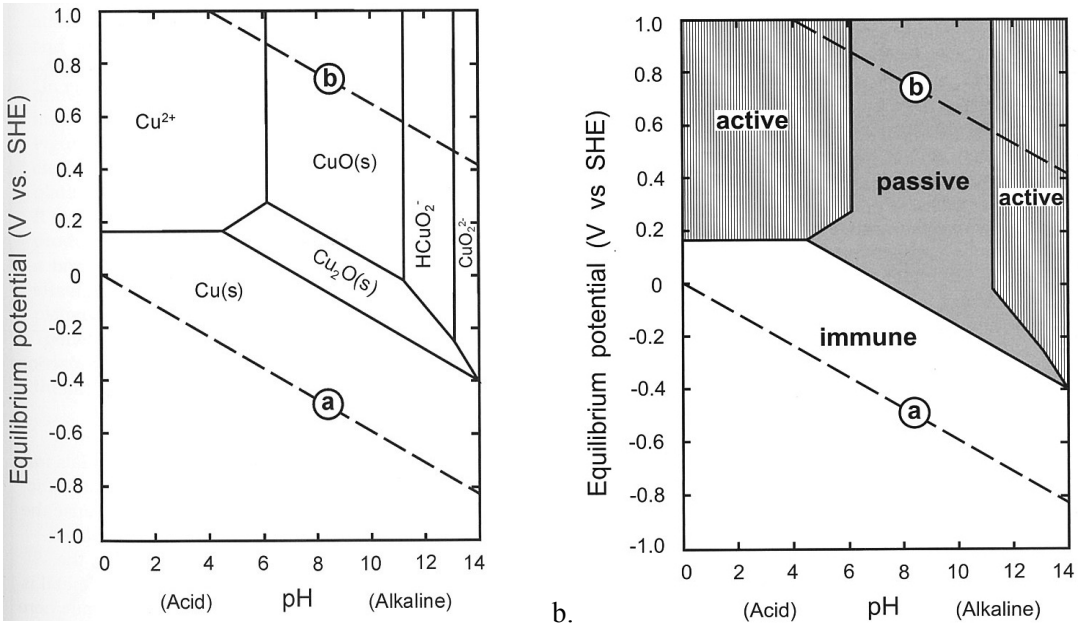


Figure 2.4, a – b: Pourbaix diagrams for a copper-water system at 25ºC, 1atm and a Cu+ concentration of 10^{-6} M. For the diagram on the left, water is stable within the boundaries set by the broken lines (a) and (b); it can be oxidized to oxygen gas at or above line (b), and it can be reduced to hydrogen gas at or below line (a). The Pourbaix diagram shown on the right is the same as the one on the left, only the regions are labeled as immune, active or passive (Selwyn 2004, 25).

In order to construct a metal Pourbaix diagram, the possible reaction products in aqueous solution must be known. In general, a metal will oxidize to form a soluble cation, a soluble anion, or a metal oxide or hydroxide (Frankel & Landolt 2003, 16). Pourbaix diagrams must also consider chemical reactions in which a species containing a metallic element at a given oxidation state changes into another species containing the metallic element in the same oxidation state (Frankel & Landolt 2003, 16-17). The region where the metal is considered stable is the region of immunity, and corrosion is unfavored. Phase fields in which a dissolved cation or oxy-anion is stable are considered regions of corrosion, usually at the acid and alkaline ends of the diagram. Phase fields in which the stable substance is a solid oxide or hydroxide are considered regions of passivity, with the assumption that a protective corrosion will form on the metal surface. Pourbaix diagrams include lines for the cathodic reactions in water; the relative position of these lines to the stable phases indicates the availability of the cathodic reactions for corrosion (Frankel & Landolt 2003, 21). Examples of Pourbaix diagrams for brochantite and malachite are presented in **figures 2.5, 2.6 and 2.7**.

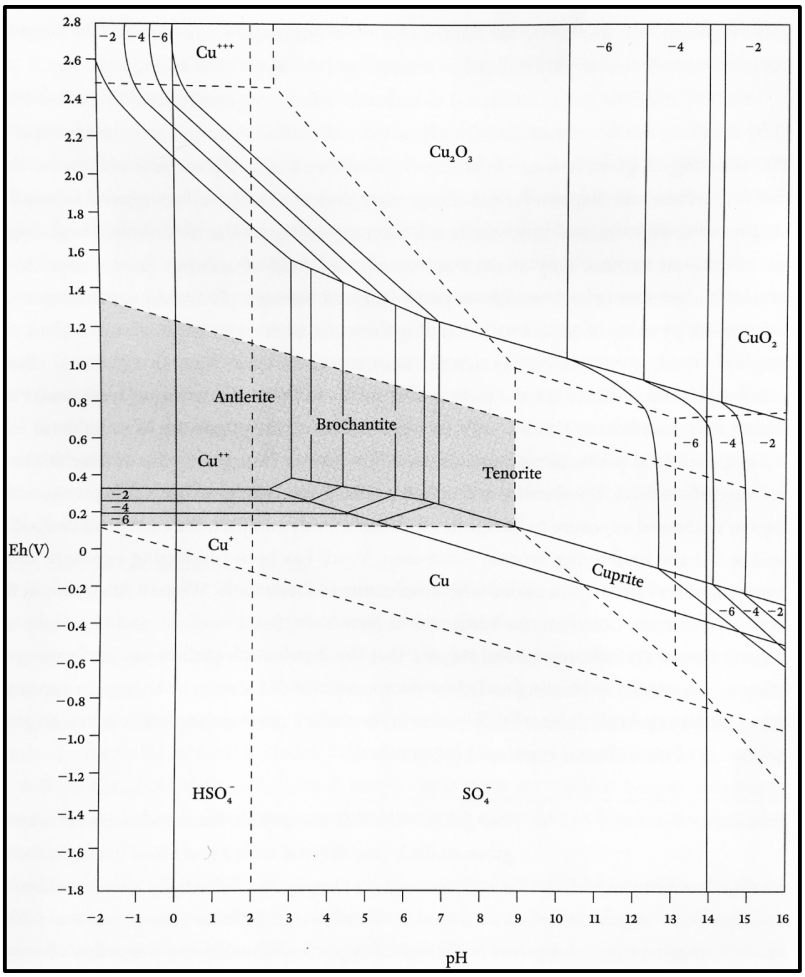


Figure 2.5: Pourbaix diagram for the system Cu – SO_4 – H_2O at 20ºC with an SO_2 level of 46 ppm, showing brochantite at the center of the grey zone (Scott 2002, 150-151).

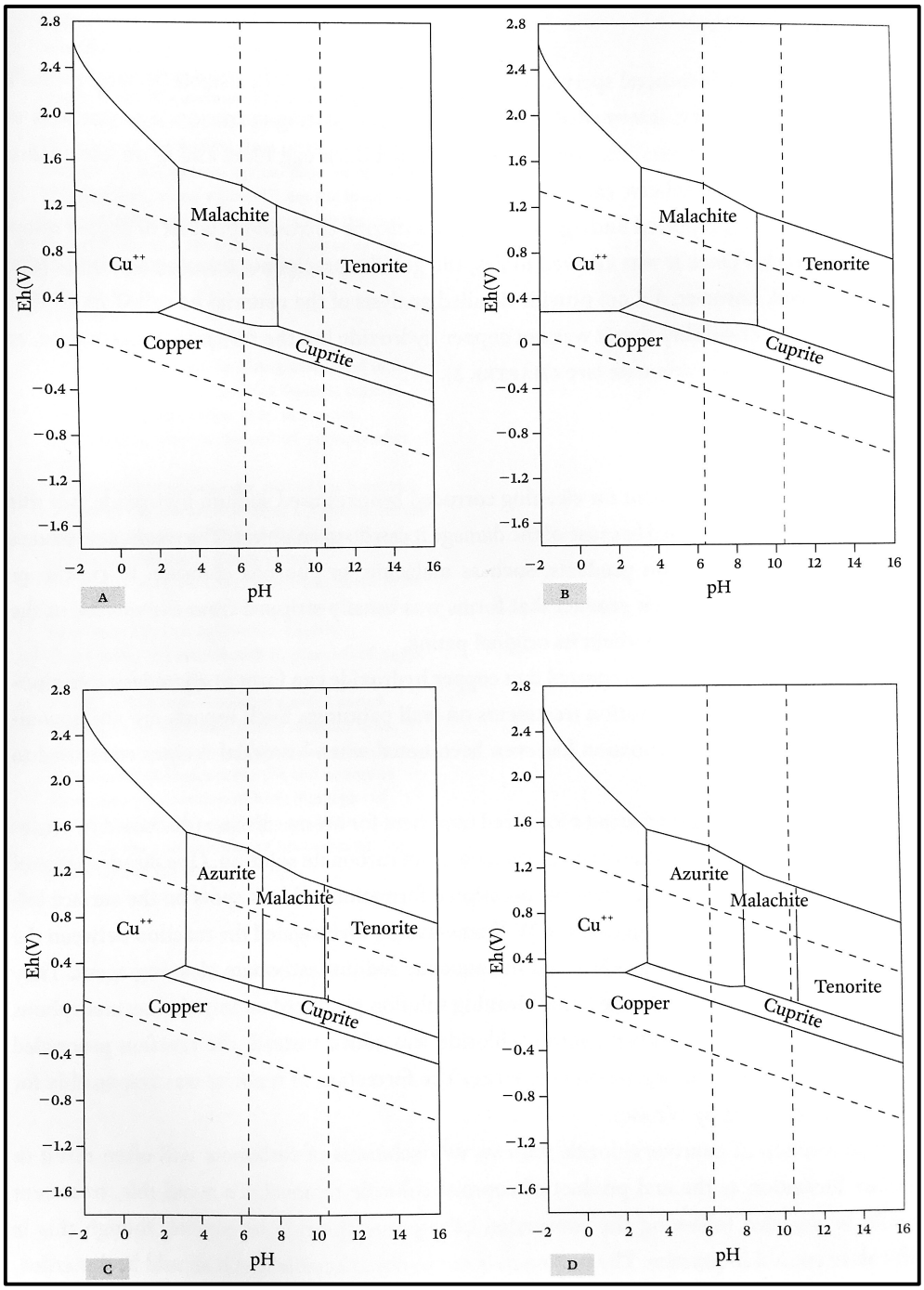


Figure 2.6: Pourbaix diagrams for the system Cu – CO_3 – H_2O at 25ºC with carbon dioxide concentrations of A) 44ppm, B) 440ppm, C) 4400ppm, D) 44000ppm (Scott 2002, 96-7).

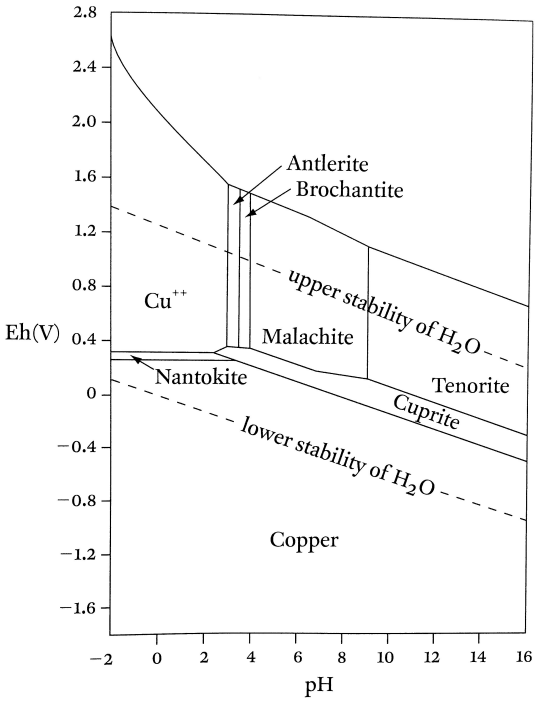


Figure 2.7: A comparatively complex Pourbaix diagram for the system Cu – CO_3 – SO_4 – Cl – H_2O for solutions containing 229ppm CO_2 and 46ppm SO_3 (Scott 2002, 135).

2.3. Summary

Corrosion is the product of a metal and the environment to which it was exposed by an electrochemical reaction. Since corroding metals are not at equilibrium, the reaction can be characterized as an electrochemical cell. More specifically, voltaic cells (also known as galvanic) share many similarities with the corrosion process. They release free energy from a spontaneous reaction to produce electricity, which always involves a redox reaction (Silberberg 2003, 147 & 893). Pourbaix diagrams show how a metal should behave in certain environments, including the regions of stability for certain mineral species, by plotting the redox potential of a system against its pH (Frankel & Landolt 2003, 16; Scott 2002, 32).

CHAPTER 3

The Effects of Observed Global Cycles

3.1. INTRODUCTION

This research aims to investigate correlations between the two most common copper corrosion minerals, brochantite and malachite, and their formation environment using stable isotopes. This is a geographic study, and how the various regions included in this study compare to one another isotopically is the focus of the project. Chapter three begins with the water cycle and flows into atmospheric and soil chemistry, while considering stable isotope utility as tracers. These are the natural global systems that influence copper corrosion at the molecular and isotopic level, and support the theory behind the project aims.

3.2. WATER IN THE ATMOSPHERE: OBSERVED STABLE ISOTOPE EFFECTS DURING PRECIPITATION

3.2.1. Rayleigh Rainout Effect

The terrestrial hydrologic (or water) cycle can be broken down into three essential subsystems: the atmospheric water system, the surface water system, and the subsurface water system.[1] These systems are interconnected through evaporation, precipitation, and water flow through the strata of the earth, all of which includes the phenomena of transport, temporary storage, and sometimes phase changes (gas, liquid, solid) (refer to **figure 3.1)**. Precipitation changes in oxygen and hydrogen isotope composition because the rainout process in clouds (evaporation and condensation) is driven by decreasing temperature, a parameter with both regional and temporal variability. When water evaporates from the earth's surface, the lower isotopologues[2] preferentially escape into the vapor phase. Evaporation is a kinetic fractionation process, meaning it is irreversible, and it is dependent on a large number of factors (Appelo & Postma 2005, 38; Sharp 2007, 74). The opposite occurs upon condensation, an equilibrium fractionation process, with the isotopically higher water molecules preferentially condensing out and leaving a vapor relatively concentrated in water with lower values of $\delta^{18}O$ and $\delta^{2}H$. Therefore, deuterium and oxygen-18 favored precipitation forms and falls, gradually lightening the residual vapor isotopically. This results in subsequent rains that, while isotopically still high relative to the vapor, are low with respect to earlier rains from the same vapor mass (Clark & Fritz 1997, 47). This is

[1] For the basic principles of the water cycle, refer to Clark and Fritz (1997), pp. 47.

[2] Isotopologues are molecules that differ from one another only in isotopic composition (Sharp 2007, 16).

known as the Rayleigh rainout effect, which is a progression towards colder, isotopically-lowered precipitation (*ibid.*).

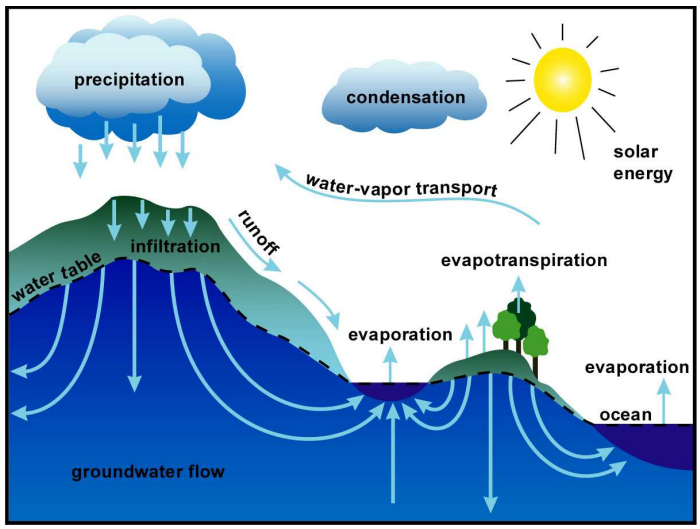


Figure 3.1: The basic water cycle (Utah State University 2013).

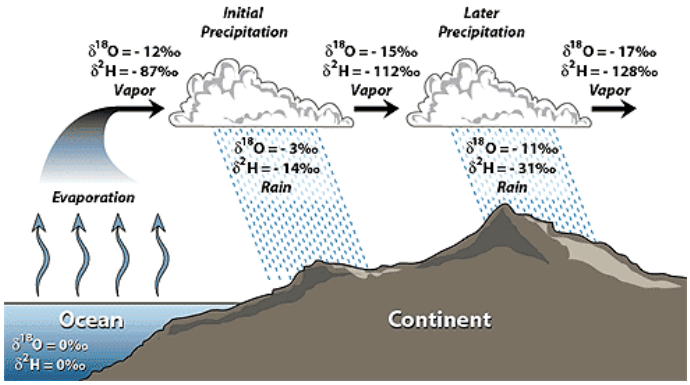


Figure 3.2: Image depicting the Rayleigh rainout effect on δ^2H and $\delta^{18}O$ (adaptation based on Hoefs 1997 and Coplen *et al.* 2000, cited Arizona Board of Regents 2005).

The Rayleigh rainout effect demonstrates that hydrogen and oxygen isotopes are fractionated in proportion during processes concerning evaporation and condensation. Accordingly, the first important isotopic relationship to understand about natural surface waters is the Global Meteoric Water Line (GMWL), which defines the relationship between deuterium[1] (δ^2H or δD) and $\delta^{18}O$ as a worldwide average. In 1961, geochemist Harmon Craig expressed this relationship through the equation:

$$\delta^2H = 8 \cdot \delta^{18}O + 10‰$$

GMWL characterized by a slope of 8 and a certain intercept with the deuterium axis (the δ^2H value at $\delta^{18}O$ = 0‰; this equation was established for the SMOW reference) (Leibundgut *et al.* 2009, 22; Mook 2006, 65).

[1] The names of the hydrogen isotopes: ^1H is protium, ^2H is deuterium and ^3H is tritium.

The GMWL is essentially an average of local or regional meteoric lines (LMWL), which vary in both slope and intercept according to meteorological conditions (Clark & Fritz 1997, 47 and 51). Precision can be added to calculations using the LMWL[1] by basing the data on precipitation only (no surface waters). This is the approach used by the Global Network of Isotopes in Precipitation (GNIP)[2], which has a network of stations worldwide to monitor the global distribution of isotopes in meteoric waters.

The Rayleigh rainout process is driven by decreasing temperature, showing that fractionation factors depend on temperature, and suggesting that where temperature gradients exist, gradients in $\delta^{18}O$ and $\delta^{2}H$ should also be observed. In 1964, paleoclimatologist Willi Dansgaard established a linear relationship between surface air temperatures (not in-cloud temperatures) and $\delta^{18}O$ for mean annual precipitation on a global basis:

$$\delta^{18}O = 0.695\ T_{annual} - 13.6‰\ SMOW$$

and

$$\delta^{2}H = 5.6\ T_{annual} - 100‰\ SMOW$$

If monthly average temperatures are used instead, the global relationship for $\delta^{18}O$ becomes:

$$\delta^{18}O = (0.338 \pm 0.028)\ T_{monthly} - 11.99‰\ VSMOW$$

(Yurtsever & Gat 1981 cited in Clark & Fritz 1997, 64).

The global temperature-$\delta^{18}O$ (T-$\delta^{18}O$) relationship, however, is only an approximation, and on a regional basis it is not perfectly linear. Moreover, the correlation of $\delta^{18}O$ with temperature deviates when using data from short time periods, indicating that single precipitation events are not isotopically representative. Using $\delta^{18}O$ as a proxy for temperature is only successful when considering data sets from seasonal or multi-annual scales (Clark & Fritz 1997, 65).

A relation is often observed between the amount of precipitation and $\delta^{18}O$. This is mostly controlled by secondary evaporation, a kinetic fractionation, which occurs after condensation in the clouds and as precipitation droplets fall to the ground (Clark & Fritz 1997, 50; Mook 2006, 98). In arid climates, there tends to be a high rate of secondary evaporation. Very humid environments are the opposite, where the evaporation from droplets is less extreme. The rate of droplet evaporation partly determines the isotopic composition of the precipitation near ground level, with low rainfall showing higher isotopic compositions than in times of increased precipitation. Although commonly demonstrated on a monthly basis, the amount effect has been observed on much shorter cycles. For instance, it is possible for very strong storms to have less $\delta^{18}O$ and $\delta^{2}H$ in as much as -15‰ (Mook 2006, 97). Moreover, convective storms in North Western Europe have shown changes in $\delta^{18}O$ of -7‰ within an hour (*ibid.*).

[1] Local meteoric water lines vary slightly from one another. GNIP tends to use the VSMOW standard and a revised regression with a slope of 8.17±0.07‰ and an intercept of 11.27±0.65‰ (Clark & Fritz 1997, 47; Leibundgut *et al.* 2009, 22).

[2] GNIP was established in the early 1960's by IAEA in Vienna and the World Meteorological Organization (WMO) in Geneva.

3.2.2. The Regional and Temporal Effects

The Rayleigh rainout process has so far been described as if it were taking place over one location when in reality, air masses move and mix with other traveling air masses, each containing water vapor with unique oxygen and hydrogen compositions. As a result, each rainout from an air mass takes place over a different location, and the further an air mass moves from the water source; the lower the isotopes in meteoric waters. The effects causing regional and temporal variations in $\delta^{18}O$ of precipitation are referred to as the latitude, altitude and continental effects, all of which lead to isotope fractionation that appear influenced by temperature and the amount of precipitation. Moreover, they lead to $\delta^{18}O$ variations in precipitation across the world that can be rather large and distinctive.

Latitude Effect, where $\delta^{18}O$ values lower with increasing latitude

$\delta^{18}O$ values become lower with increasing latitude. This is attributed to temperature, with the equatorial region being warm and the poles much colder, and a vague temperature gradient in the latitudes between, though with much greater fluctuations relative to the equatorial and polar regions. Distortions to latitudinal gradients, which are nicely shown on the map of the United States (**figure 3.4**), are due to continental effects, described next, and ocean currents (Clark & Fritz 1997, 66). For coastal and continental stations in Europe and the USA, the latitude effect is about $\Delta\delta^{18}O \approx$ -0.6‰/degree of latitude, and up to -2‰/degree of latitude in the colder Antarctic continent (Mook 2006, 90). Using amount-weighted means, the observed relation between monthly temperature and isotopic composition for the North Atlantic and European stations from the GNIP network is:

$$\delta^{18}O = (0.521 \pm 0.014)t - (14.96 \pm 0.21)‰$$

where t is the surface temperature in ºC (Mook 2006, 90).

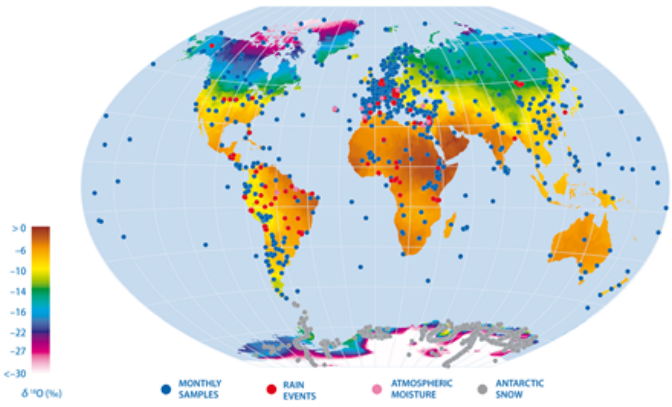


Figure 3.3: Image depicting global distribution of $\delta^{18}O$ values (per mil, ‰) in precipitation produced by interpolation of long-term annual means from about 700 GNIP stations (IAEA 1998-2013).

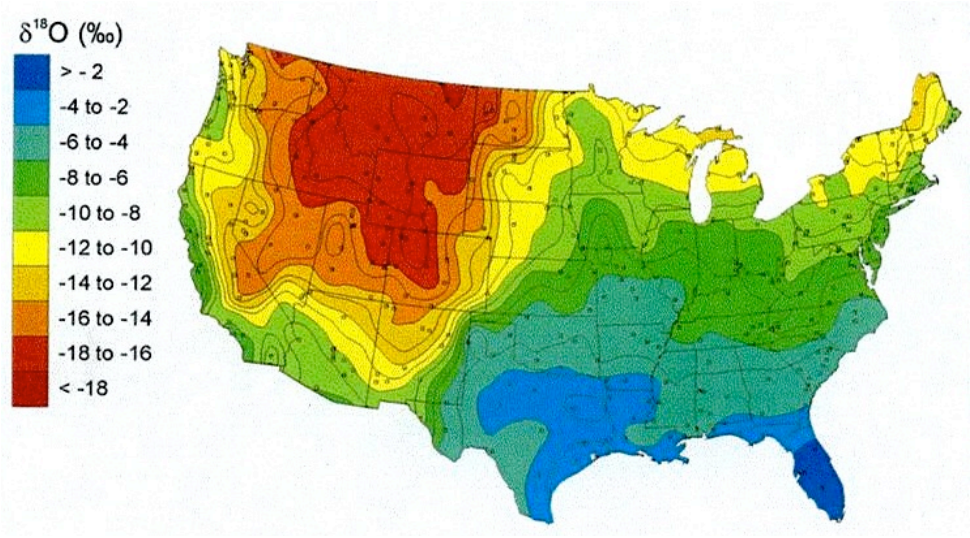


Figure 3.4: Image of the distribution of $\delta^{18}O$ values (per mil, ‰) in precipitation over continental USA. The latitudinal effect is particularly evident in North America. Distortions to latitudinal gradients are due to continental effects and ocean currents. Beware that the color schemes are reversed between Figures 3.3 and 3.4. Image from Kendall & Coplen 2001 cited in University of Colorado, Boulder.

Continental Effect, where the more inland, the lower the $\delta^{18}O$ values

The continental effect is the progressive drop in $\delta^{18}O$ value with increasing distance from the coast. The isotopic composition of precipitation becomes lower because the atmospheric vapor mass needs progressively lower temperatures to rainout (Appelo & Postma 2005, 41). Increased moisture flux (higher wind speed, absolute moisture) will reduce continental effects, while topographic effects and the temperature extremes that characterize continental climates cause isotopic compositions of vapor masses to evolve more quickly (Clark & Fritz 1997, 67; Leibundgut *et al.* 2009, 28). The continental effect can vary considerably from area to area and from season to season, even over low-relief profiles, and modeling can be difficult due to various complications like the mixing of different air masses, the influence of evapotranspiration over continental surfaces, or convective cloud processes (Mook 2006, 92; Leibundgut *et al.* 2009, 28).

Altitude Effect, where higher altitude brings lower $\delta^{18}O$ values

As a general rule, the isotopic composition of precipitation becomes lower as the terrain reaches higher elevations. This is the result of temperature drops typical of higher elevations; however, the altitude effect is different from the latitude effect in terms of temperature correlations because the decreasing pressure of higher altitudes requires a more drastic temperature decrease to reach saturated water vapor pressure (Gat, Mook & Meijer 2000 cited in Leibundgut *et al.* 2009, 26). The resulting change in moisture per change in temperature is smaller than for isobaric[1] condensation (Leibundgut *et al.* 2009, 26). The observed depletion value for $\delta^{18}O$ and the rise in altitude is between -0.1 and -0.36‰ per 100 meters, with a corresponding decrease of about -1 to

[1] Thermodynamic process carried out at constant pressure.

-4‰ for δ^2H (Clark & Fritz 1997, 70; Leibundgut *et al.* 2009, 26). Factors that affect altitude effect include different precipitation generation processes or mixing of air masses with different air trajectories (Leibundgut *et al.* 2009, 26).

Seasonal Effect, where winter brings lower $\delta^{18}O$ values
(in regions with temperate climate)

Seasonal weather fluctuations often lead to varying $\delta^{18}O$ and δ^2H fractionations in precipitation around the world. Seasonal weather fluctuations largely depend on geographic factors such as proximity to the oceans and other large bodies of water that can buffer temperature extremes, the currents and various cycles within those oceans, prevailing winds, and the amount of sunlight (which varies with latitude and affects the local temperature). Observations in the seasonal variation of $\delta^{18}O$ and δ^2H for a given location range from no or little distinction, as is the case in some coastal and equatorial areas where temperature ranges are short, to strong variations, which most often correspond with equally extreme seasonal temperature variation and continentality (Clark & Fritz 1997, 71). The factors that produce a seasonal effect are:

- The temperature of atmospheric moisture in the source region, which will affect fractionation during evaporation;
- Transport processes and the circulation of air masses that cause the advection of moisture from varying origins and modify the isotopic composition; and
- Changes in rainout conditions (ambient temperature, absolute moisture and precipitation phase, i.e. solid, liquid or gas) (Leibundgut *et al*. 2009, 25).

Isotope variations are dependent on local temperature to the extent that it appears as the overriding parameter. For instance, rain in the summer often has isotopically heavier rain than in the winter. However, for both δ values in precipitation, this temperature dependence is generally smaller than the latitude effect. Seasonal effects can be partly masked by the latitude effect (Mook 2006, 92).

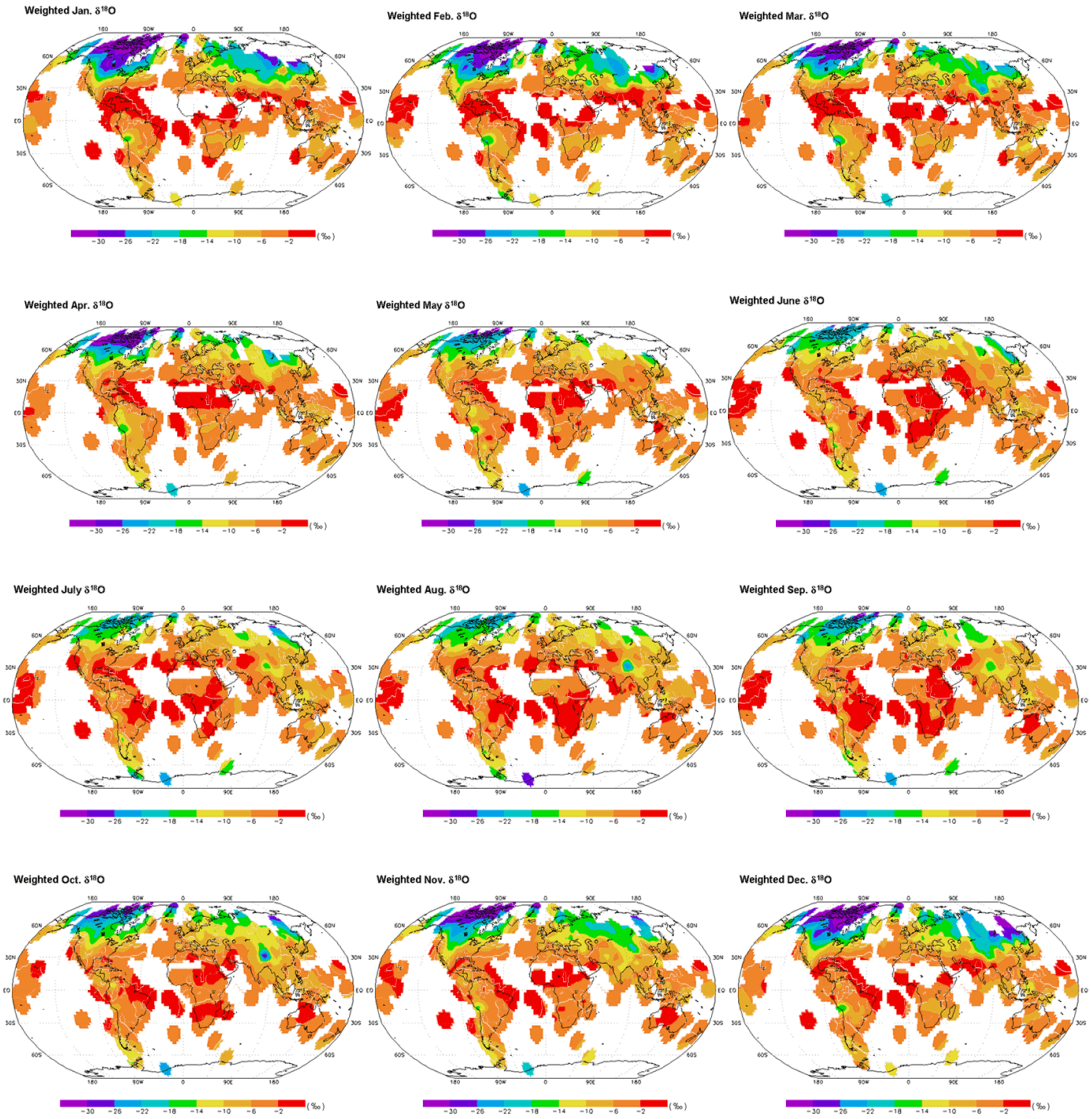


Figure 3.5: Weighted monthly $\delta^{18}O$ (‰) distributions over the globe for one year, suggesting a seasonal effect (images from animations by IAEA 1998-2013).

3.3. SOIL PROFILES AND CLASSIFICATION OF SUBSURFACE WATERS

The downward movement of mineral and organic material within the soil profile produces the horizons (refer to **figure 3.6**), which are determined by how easily the material moves in water and the rate of water movement (Ashman & Puri 2002, 16 and 18). Subsurface waters flow through soil and eventually return to the surface as discharge or runoff, where it continues to circulate the earth's hydrologic cycle. Like the soil profile, the different subsurface waters can be described in layers. In most places, one zone of aeration overlies a single zone of saturation. The water table is an imaginary surface that represents the interface between the saturated and aerated zones, where the core water pressure is atmospheric (Langmuir 1997, 267; Mays 2012, 310). The zone of aeration is above the water table and consists of interstices occupied partially by water and partially by air, which creates an oxidizing environment with water held below atmospheric pressure (Langmuir 1997, 269). Vadose water flows through the zone of aeration, which can be

further subdivided into the soil water zone, the intermediate vadose zone and the capillary zone (**figure 3.7**). Beneath the water table in the zone of saturation, all interstices are filled with water under pressures higher than atmospheric (Langmuir 1997, 269; Mays 2012, 41).

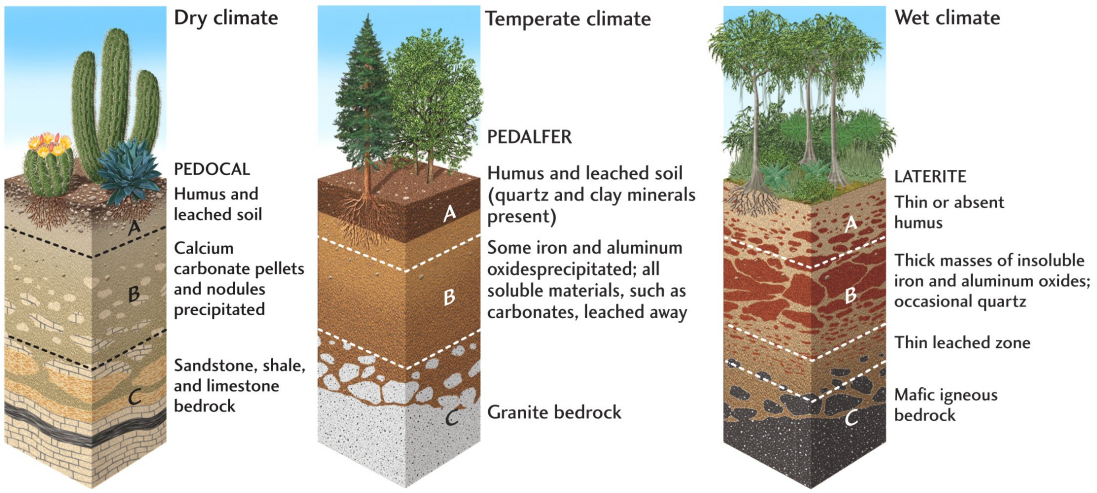


Figure 3.6: Three examples of different soil profiles, showing general horizons. Clearly the types (and conditions) of soil that form depend to a great extent upon the climate, particularly rainfall and temperature (Harris & Eyre 1994, 2:74; Stott & John 2010, 1153; Wilmott & Jack 2000, 335).

Common Classification of Subsurface Waters

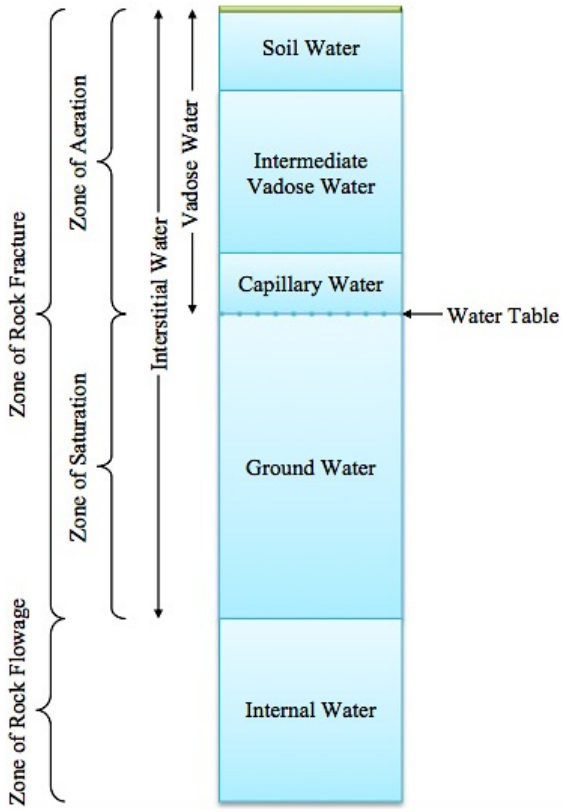


Figure 3.7: Classification of subsurface waters (Langmuir 1997, 268). The soil zone extends from the ground surface through the major root zone (Mays 2012, 7). The thickness ranges with soil type and vegetation (*ibid.*). The thickness of the intermediate vadose zone ranges from non-existent to over 100m (*ibid.*). Capillary water (with fluctuating water height) is groundwater that has risen and is held above the water table due to capillary forces (Langmuir 1997, 269). Capillary water may be as much as 9 meters thick (Mays 2012, 7). Like the other zones, groundwater depths also range, reaching tens of thousands of meters in sedimentary basins (Langmuir 1997, 269).

Meteoric water is the source of most subsurface water, though the percentage of precipitation that directly infiltrates the soil to become vadose- and groundwater is highly variable (Appelo & Postma 2005, 23; Mays 2012, 7; Mook 2006, 135). This is because the subsystems of the global hydrologic cycle (the atmospheric, surface and subsurface water systems) are interconnected processes that lead to infiltration, groundwater recharge, vadose flow and groundwater flow. Precipitation that is not directly infiltrated may be stored at the surface (lakes and reservoirs, snow and ice, overland flow, et cetera) where the lapse of many years or centuries can pass before continuing through the hydrologic cycle, sometimes participating in soil infiltration. Other, artificial contributions of water into the soil environment occur from excess irrigation, seepage from canals and water purposefully added to augment groundwater supplies (Mays 2012, 7).

Much of the water that infiltrates soil does not travel down the zone of aeration, but instead returns to the atmosphere by evaporation or plant transpiration (Mays 2012, 7). The water that stays within the ground moves downward under the action of gravity, collecting dissolved solutes, colloids and small particles along the way (known as vadose circulation) (Williams 1990, 103). Therefore, the distinctive characteristics of groundwater are mainly established in the aerated zone. Once in the saturated zone, water moves in the direction determined by the surrounding hydraulic situation, and depending on the flow path, can remain underground from days to millennia (Mays 2012, 7; Schwartz and Zhang 2003, 35). Groundwater will continue to undergo geochemical evolutions, though less intense and usually much slower than in the aerated zone (Cook & Herczeg 2000, 31).

When enough rain falls to percolate through the soil, the water will react with the soluble components of biological, microbial or human origin, as well as any leached-out earth elements from the weathering parent rock (Harris & Eyre 1994, 2:74, 2:79). However, separate and individual particles are not typically found in soils. Instead, most soils consist of aggregates of particles within a matrix of organic and inorganic colloidal matter (Harris & Eyre 1994, 2:75; Stott & John 2010, 1154). This gives soil a crumb-like structure; leading to friability, more ready penetration of moisture, greater aeration, less erosion by water and wind, and generally greater biological activity (*ibid.*). In any case, based on the most common subsurface cations and anions, the prevalent chemical character in subsurface waters is calcium carbonate, the cations of which can accelerate metallic corrosion. Calcareous soils are predominantly composed of calcium and magnesium and tend to form insoluble oxides with buried copper (Harris & Eyre 1994, 2:79). Alkaline soils are high in sodium and potassium and tend to form carbonates like malachite (*ibid.*).

3.3.1. Understanding Soil Temperature and pH

The sun warms soil surfaces during the day, often making them slightly warmer than the air above it. Since the sun's energy has to be conducted by the subsoil, daily soil temperature fluctuations are greatest at the ground surface and diminishes exponentially with depth (Eash *et al.*

2015, 125). The intensity of these fluctuations varies depending on the vegetative cover and moisture levels, which can reduce the amount of temperature change (Eash *et al.* 2015, 121). Depth is also a factor in the variation of soil temperature over the course of a year, with the highest temperatures normally reached during late summer and the coolest in late winter (Eash *et al.* 2015, 126). At lower depths of 0.5 to 1.5 meters, high and low temperatures lag behind the surface temperatures by two to three months (*ibid.*).

Temperature has a significant impact on the behavior of water in soil, beginning with the physical form (solid, liquid, gas). The physical state of water in turn affects the rate of water movement in soil. Moreover, warm water hastens the dissolution of minerals in the soil, but when paired with excessive rainfall, this can result in leached-out, nutrient-deficient soils (Eash *et al.* 2015, 119). Soil minerals and amount of precipitation also affects the soil pH (Eash *et al.* 2015, 96). Soil pH can refer to the pH of a soil solution (active acidity) or to the solid phases (reserve acidity) (Eash *et al.* 2015, 93). The reserve acidity is the main source of the active acidity and is responsible for the buffering capacity of a soil (Eash *et al.* 2015, 96). Soil reaction is usually less than two pH units on either side of neutral (pH 7) (Eash *et al.* 2015, 93). In semi-arid and arid regions, most soils are alkaline or nearly neutral, whereas clayey soils with high organic matter tend to be more acidic (Eash *et al.* 2015, 96). This is partly because base-forming ions are leached by precipitation and translocated deeper into the soil (*ibid.*). The translocation of soluble minerals and their subsequent accumulation in the profile leads to soil horizons.

Corrosion of buried copper is mainly controlled by the aeration and pH of the soil (Elsner 2011, 558; Stott & John 2010, 1159). Soils with an abundant supply of oxygen and highly acidic conditions are the most corrosive (*ibid.*). Poorly aerated soils lead to the best preservation since protective patinas tend to form (*ibid.*). Most soils range between pH 5 and pH 8, in part depending on the formation of carbonic acid from carbon dioxide and water (Harris & Eyre 1994, 2:79). The environmental conditions in which a metal corrodes can be thermodynamically calculated and plotted on a Pourbaix diagram (refer to section 2.2.2.). Water volumes and oxygen concentrations in soils are inversely related, with the slowest corrosion rates occurring under the most constant water/oxygen ratios. The extent of moisture content can range between conditions comparable to atmospheric towards the surface (except there is a higher carbon dioxide content) and total immersion in zones below the level of permanent ground water (Harris & Eyre 1994, 2:77-78; Stott & John 2010, 1154).

3.4. OXYGEN AND THE OXYGEN CYCLE

Gaseous oxygen typically occurs in air as diatomic (two-atom) molecules, which behave as independent units. The natural abundance of dioxygen (O_2) accounts for about 21% of the Earth's atmosphere by volume and 23% by mass (Knapp 1996, 6). Oxygen is highly chemically reactive, spontaneously forming covalent bonds with atoms of all other elements (except noble elements) to create oxides that are thermodynamically stable over large temperature ranges (Hoefs 1997, 47;

Sawyer 1991, 4; Spiro *et al.* 2012, 49). Oxygen is fundamental for oxidative respiration, its contribution to the ozone shield, and its links to the carbon and hydrological cycles. Moreover, oxygen is central to this project as the principal cause of copper corrosion by way of oxidation-reduction reactions.

Photosynthesis drives the great cycles of CO_2 uptake and O_2 evolution. It is carried out to fuel organism activities, including the production of organic matter essential to their survival and growth (Lane 2002, 23).

$$6CO_{2(g)} + 6H_2O_{(l)} \xrightarrow{\text{solar energy}} C_6H_{12}O_{6(s)} + 6O_{2(g)}$$

Equation generalizing oxygenic photosynthesis (Knapp 1996, 15).

Today, as has been the case for millions of years, the atmosphere's oxygen is almost entirely sourced from photosynthesis by terrestrial vegetation and marine phytoplankton, which are descendants of cyanobacteria and still use chlorophyll to absorb sunlight.

$$C_6H_{12}O_{6(s)} + 6O_{2(g)} \rightarrow 6CO_{2(g)} + 6H_2O_{(l)}$$

The above equation generalizes the oxidation of organic matter (in this case glucose) to yield carbon dioxide and water (Knapp 1996, 15). Notice that this equation is the reverse reaction of photosynthesis.

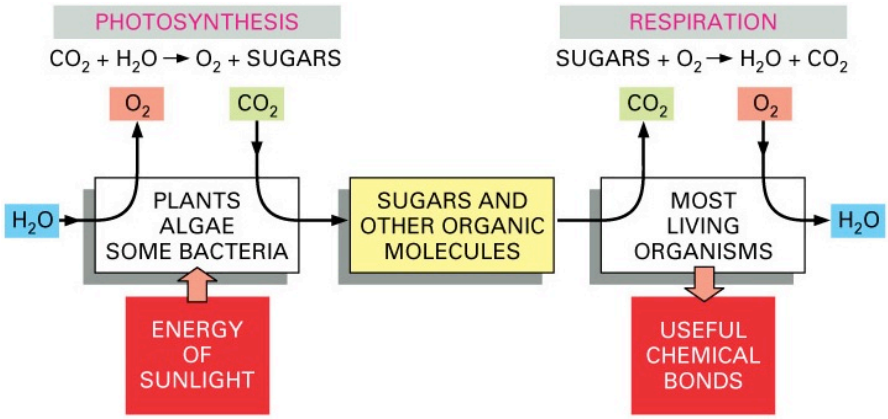


Figure 3.8: The basic oxygen cycle (Alberts *et al.* 2004).

Driven by photosynthesis, the constant regeneration of oxygen by biogeochemical processes between the atmosphere and water, plants and animals, and mineral matter is altogether known as the oxygen cycle. Its influence largely lies in the fundamental linkage points it forms between other biogeochemical cycles such as the carbon and hydrologic cycles.

3.4.1. Tropospheric Ozone

Atmospheric oxygen is actually found in two gaseous forms: dioxygen (O_2) and ozone (O_3). Most ozone is found in a region of the stratosphere called the ozone layer. Although ozone is essential for life on Earth, at ground level (the troposphere) it is considered a poisonous air pollutant. Ozone at the surface is usually a consequence of city traffic. Initiated by the nitrogen in

exhaust gases from vehicle engines, the ozone formed is part of a cycle dependent on the amount of sunlight and hydrocarbons present and the concentration of nitrogen oxides (Knapp 1996, 42; Spellman 2009, 110).[1] It is generally believed that surface ozone concentrations have been increasing and will continue to do so.

Surface ozone plays a role in copper corrosion and the formation of brochantite. Mixtures of ozone, SO_2 and NO_2 have strong synergistic effects that considerably increase the corrosion rate of exposed copper, and more specifically, the formation of cuprite (Baumann 2011, 130; Scott 2002, 46; Selwyn 2004, 63; Strandberg 1998, 3516). An increase in surface ozone concentrations can potentially increase the formation rate of basic copper sulfate minerals like brochantite. It is not known if brochantite concentrations on exposed copper were lower historically (~100-200 years ago) due to lower ozone levels at the surface, or if so, to what degree.

3.4.2. Upsetting the Oxygen Cycle

In addition to the oceanic flux, other hypotheses have been brought forward regarding what controls the O_2 concentrations in modern systems; for example, the possibility that a warming ocean, resulting in increased stratification, may be affecting air-sea gas exchanges (Heimann 2001, 238). Anthropogenic factors are commonly implied since they have altered the chemical composition of the atmosphere, sometimes drastically. A small decrease is suspected in the atmosphere's ability to oxidize as a consequence of profound modifications to the source strengths of volatile organic carbon, carbon monoxide and reactive nitrogen gases due to the increase in fossil fuel consumption and biomass burning (Brasseur & Holland 2001, 32). The magnitude of these various ideas is difficult to assess, in part suggesting that they are small and the oxygen cycle is still efficient. Due to its long residence time, dioxygen cannot be affected by anthropogenic activities on the human timescale (Berner & Berner 2012, 24). It would take tens of thousands of years and drastic, unrealistic conditions for dioxygen concentrations in the atmosphere to change to a meaningful extent (*ibid.*). However, local sulfur dioxide concentrations have increased in the atmosphere as a consequence of human activity (refer to section 3.5.). So have the concentrations of methane, ammonia, carbon monoxide, nitrous oxide and nitrogen oxides. It is therefore possible that the concentration changes of these gases have been affecting what corrosion products form on copper roofs over the last ~200 years. Oxygen's consistency throughout the centuries in source and concentration is partly why it can serve as a tracer in various environmental studies.

3.4.3. Isotope Fractionation Through the Oxygen Cycle

Atmospheric molecular oxygen has a relatively constant isotopic composition with a $\delta^{18}O$ value of 23.5 ± 0.3‰ relative to ocean water (SMOW) (Kroopnick & Craig 1972, 54). This steady off-set between seawater $\delta^{18}O$ and the $\delta^{18}O$ of atmospheric O_2 is known as the Dole effect (Δ:

[1] For the basic principles of tropospheric ozone as a cycle, refer to Knapp (1996) pp. 42, Spellman (2009) pp. 110 and Spiro *et al.* (2012) pp. 60.

$\delta^{18}O_{atm} - \delta^{18}O_{sw} = 23.5 \pm 0.3‰$). Most of this enrichment is dependent on isotopic fractionation during respiration and photosynthesis in the oxygen cycle.[1] The oceanic exchange flux is large, but as described earlier in terms of concentration, only tiny amounts of molecular oxygen are dissolved. The net oceanic exchange is near zero and the overall oceanic influence on atmospheric $\delta^{18}O$ is quite small (Yakir 2011, 134). Likewise, the exchange flux between the troposphere and stratosphere is again large, but with no net flux and a minimal influence on atmospheric $\delta^{18}O$ (Yakir 2011, 134). Fossil fuel and biomass burning fluxes are also relatively small, and to this day their oxygen isotopic compositions are assumed to be that of atmospheric O_2 used in combustion (Yakir 2011, 134).

There are small atmospheric variations in the $\delta^{18}O$ of molecular oxygen. This is correlated to the oxygen isotope variations that take place in the meteoric water cycle, which influence the isotopic composition of leaf water. The mean annual gradients are expected to be on the order of a few per meg (equals 0.001 per mil) (Seibt 1997 cited in Heimann 2001, 242). This observation is relatively recent, and to better understand it, better methods need to be created for the isolation and measurement of the $\delta^{18}O$ in leaf water (Angert & Luz 2001, 1695; Jouzel *et al.* 2002, 310). Other small factors that have an influence on the magnitude of the Dole effect include the solubility fractionation of O_2 isotopomers[2] different isotope effects associated with different pathways of metabolic O_2 consumption, and partial recycling of O_2 in subsurface ocean waters (Blunier *et al.* 2002, 2). In any case, the variations in the $\delta^{18}O$ of atmospheric O_2 are small enough to be disregarded for the purposes of this project.

3.4.4. The Isotope ($\Delta^{17}O$) Anomaly

Most physical, biological and chemical processes on Earth induce mass-dependent fractionation, which yields oxygen-bearing compounds with a fixed correlation between $\delta^{18}O$ and $\delta^{17}O$ (Bao *et al.* 2000, 176; Bao & Reheis 2003, 2). The $\delta^{18}O$ variations are approximately twice as large as the $\delta^{17}O$ variations, as conventionally related using delta notation in the expression: $\delta^{17}O = 0.52\delta^{18}O$ (Bao & Reheis 2003, 2; Lee *et al.* 2002, 194; Savarino *et al.* 2000, 29080). Deviations from this tight relationship are evidence for mass-*independent* fractionation, expressed by $\Delta^{17}O = \delta^{17}O - 0.52\delta^{18}O$, where the coefficient (0.52) is independent of temperature and remains constant through a Rayleigh process, but depends on the molecular weight of the species (Bao *et al.* 2000, 176; Bao & Reheis 2003, 2; Lee *et al.* 2002, 194; Morin *et al.* 2011, 3653; Thiemens 2002, 44; Savarino *et al.* 2000, 29080). This is known as the isotope anomaly of oxygen-bearing species.

---

[1] For the basic principles of oxygen fractionation during photosynthesis, refer to Angert & Luz (2001) pp. 1695, Blunier *et al.* (2002) pp. 2-3, Ehleringer & Vogel (1993) pp. 14, Farquhar & Lloyd (1993) pp. 65, Farquhar *et al.* (1993) pp. 439-440, Guy *et al.* (1993), Heimann (2001) pp. 241, Jouzel *et al.* (2002) pp. 310, Yakir (2011) pp. 133-138, Yakir *et al.* (1993) pp. 533.

[2] Isotopomers, or isotopic isomers, have the same number of each isotope of each element, but at different positions. Isotopomers can be either constitutional isomers (e.g. $CH_2DCH=O$ and $CH_3CD=O$) or isotopic stereoisomers [e.g. (*R*)- and (*S*)-CH_3CHDOH or (*Z*)- and (*E*)-$CH_3CH=CHD$]. IUPAC 1997.

Theoretically, sulfate minerals are produced from thermodynamic and kinetic (including biological) processes that generate mass-dependent compositions, and therefore a $\Delta^{17}O \approx 0‰$ is expected. Yet, positive $\Delta^{17}O$ values have been observed in sulfate minerals found in gypcretes from the central Namib desert and the Miocene volcanic ash-falls in the western United States, indicating a different process is sometimes involved (Bao *et al.* 2000, 176). In addition to these sulfates, a few nitrates and perchlorates have been found in arid and hyper-arid environments where oxyanion acids or salts produced in the atmosphere accumulate and recrystallize over time to become massive ^{17}O-anomalous deposits (Bao 2005, A443). In all of these cases, the isotopic anomalies appear to be linked to reactions involving stratospheric ozone (Bao 2005, A443; Miller 2002, 1881).

Ozone and hydrogen peroxide are atmospheric oxidants known to possess positive $\Delta^{17}O$ values (Bao *et al.* 2000, 176; Savarino *et al.* 2000, 29079). This distinct isotope anomaly is inherited from mass-independent fractionation during formation, and during oxidation reactions, the anomalous oxygen(s) are transferred to non-liable oxyanions including sulfate, nitrate and perchlorate (Bao 2005, A443; Morin *et al.* 2011, 3653). Once these oxyanions are produced, they are resistant to further oxygen exchange (even with water), preserving any anomalous $\Delta^{17}O$ signatures in sulfate minerals (Bao 2005, A443; Bao *et al.* 2000, 177). Therefore, the $\Delta^{17}O$ of a species reflects the fractional importance in its elemental composition of oxygen atoms inherited directly or indirectly from ozone or H_2O_2 (Morin *et al.* 2011, 3653).

If the collected brochantite samples from copper roofs have anomalous $\Delta^{17}O$ signatures, then the amount of oxygen in the sulfate contributed by oxidants other than atmospheric water or molecular oxygen can be calculated. At present, the stable oxygen isotope compositions of ambient oxidants (such as O_3, H_2O_2, NO_x and of free radicals including $^{\bullet}OH$ and $HO^{\bullet}_2$) have not been determined (Holt *et al.* 1981a, 804; Van Stempvoort & Krouse 1994, 451). The oxygen isotopes of water are known to possess a mass-dependent composition (Savarino *et al.* 2000, 29080; Thiemens 2005, A443). The $\Delta^{17}O$ of atmospheric molecular oxygen is negligible and assumed constant, with values insignificantly different from 0‰ ($\Delta^{17}O$ (O_2) = -0.3‰, $\Delta^{17}O$ (H_2O) = -1.0 – 0.0‰, Balkan & Luz, 2003 & 2005). This is important because about 75% of the oxygen in atmospheric sulfates is contributed by water; the remainder is contributed by atmospheric molecular oxygen (refer to section 4.2.3.). However, the amount of oxygen contributed by water can be as low as 60%. In these cases, it is possible that the unaccounted oxygen originates from alternative ambient oxidants with $\Delta^{17}O$ anomalies that transferred to the sulfate product. Positive $\Delta^{17}O$ signatures would be indicative of this hypothesis, however, $\Delta^{17}O$ anomalies cannot be correlated to geographic locations because ozone and H_2O_2 concentrations in the troposphere are not uniform or consistent and vary from day-to-day and place-to-place.

Several investigators have already tested a few reaction pathway hypotheses. These tests have determined that:

- Measurements of the sulfate produced by marcasite (FeS_2) oxidation in the air have no isotope anomaly, indicating that the tropospheric ozone and hydrogen peroxide in rainwater does not significantly transfer positive $\Delta^{17}O$ values to the product sulfate by *in situ* oxidation of surface minerals (Bao *et al.* 2000, 176; Bao & Reheis 2003, 7).
- Surface SO_2 oxidation in the aqueous phase catalyzed by Fe(III) and Mn(II) does not produce $\delta^{17}O$ anomalous sulfate (Bao & Reheis 2003, 7; Savarino *et al.* 2000, 29079).
- The only significant homogeneous oxidation pathway in the atmosphere (SO_2 + $^{\bullet}OH$ and its chain termination reaction, $SO_3 + H_2O$) does not produce mass-independent oxygen isotopic compositions in the yielded sulfate (Savarino 2000, 29079).
- It appears that only aqueous phase oxidation produces a mass-independent oxygen isotopic composition in aerosol sulfate. Isotopic analysis shows that two oxygen atoms from H_2O_2 are found in the product H_2SO_4 and that one oxygen from ozone is transferred to the product sulfate (Savarino *et al.* 2000, 29079).
- No experimental data is available for sulfate derived from SO_2 oxidation on a mineral surface, which is the accepted pathway for the formation of brochantite on exposed copper (Bao & Reheis 2003, 7; Bao *et al.* 2000, 176).

When gaseous SO_2 is deposited into the aqueous layer on a hydroxylated copper surface, the sulfur dioxide will react to form the bisulfite ion, which in the presence of ozone or hydrogen peroxide will further yield bisulfate ions that contain positive $\Delta^{17}O$ values. These bisulfate ions ultimately react with copper ions to form various sulfate minerals, which is a mass-dependent formation. Since $\Delta^{17}O$ is fairly insensitive to mass-dependent fractionation, it is entirely possible for the brochantite samples collected from copper roofs to possess a small $\Delta^{17}O$ anomaly.

A concern about $\Delta^{17}O$ signatures in brochantite is that they may be very small, to the extent that their significance may be challenged. Dealing with small values is complicated by a lack of knowledge on the accurate positions of mass-dependent fractionation lines (MDFL, the coefficient of which is usually presented as 0.52, but this is actually an estimated average) of various isotope exchange reactions, which have become a prerequisite condition for research in $\Delta^{17}O$ anomaly studies (Cao *et al.* 2011, 147; Cao & Liu 2011, 7435). More precise ratios can be determined experimentally if the reaction process is well defined, which in this case it is not, in addition to high-precision analytical capabilities (Cao & Liu 2011, 7435).

3.5. SULFUR IN THE ATMOSPHERE

Sulfur in the troposphere is usually considered an impurity, and its presence varies regionally because its sources are natural and anthropogenic.[1] The principal sulfur-containing compounds in the atmosphere are hydrogen sulfide (H_2S), dimethyl sulfide (DMS, $(CH_3)_2S$), carbon disulfide (CS_2), carbonyl sulfide (COS), sulfur dioxide (SO_2) and sulfur trioxide (SO_3)

[1] For a basic understanding of sulfur-containing atmospheric aerosol particles, refer to Leygraf and Graedel (2000) pp. 59-60, and Vedal and Sullivan (2007) pp. 1488.

(Cole 2010, 1054). Hydrogen sulfide often results from anaerobic digestion by sulfate- or sulfur-reducing bacteria, but still 10% of total H_2S emissions are due to human activity (Fyfe 1994, 2:35). Despite this, concentrations are low and good measurements are difficult, often resulting in the lack of reliable data for the involvement of H_2S in atmospheric corrosion (Leygraf & Graedel 2000, 50). Hydrogen sulfide is slightly soluble in water and it tends to act as a reducing agent and weak acid, giving the hydrosulfide ion HS^- (Leygraf & Graedel 2000, 44). This ion can be used to form metal sulfides. Hydrogen sulfide is also fairly rapidly oxidized to SO_2 (Fyfe 1994, 2:34). Dimethyl sulfide is the most common biological compound emitted into the atmosphere, particularly over oceans by phytoplankton, but it is insoluble in water. Only a small amount of carbon disulfide is emitted by volcanic eruptions and marshes. Where present, it will react with O_2 to form carbon dioxide and hydrogen sulfide. Carbonyl sulfide also forms CO_2 and H_2S by decomposing in the presence of humidity and alkaline compounds. It is the most abundant sulfur compound naturally present in the atmosphere, partly due to its long atmospheric lifetime. Sulfur trioxide (SO_3) is the primary agent in acid rain and is a precursor to sulfuric acid, which is a particularly aggressive electrolyte (Trethewey & Chamberlain 1995, 281). Sulfur dioxide (described in the following paragraphs) can convert to SO_3 with vanadium, a common fuel impurity, as a catalyst (Trethewey & Chamberlain 1995, 282).

The major air pollutant and sulfur-containing compound in the troposphere is sulfur dioxide since it has significant impacts on animal and plant life. It is also a powerful stimulator of atmospheric metal corrosion. Sulfur dioxide is naturally produced from aerial oxidation of H_2S, but most of the air's SO_2 is related to the combustion of fossil fuels (Leygraf & Graedel 2000, 50-1; Fyfe 1994, 2:34). In industrial areas, the anthropogenic source dominates, and sulfur pollution levels are clearly related with the domestic heating cycle (coal) in densely populated countries (Fyfe 1994, 2:34). This can be noted in corrosion rate variations, where corrosion is the heaviest during cold months despite lower average temperatures (Fyfe 1994, 2:35). Due to its adverse health effects on animal and plant life, efforts have been made to reduce SO_2 concentrations in North America and Europe (Scott 2002, 145). In fact, reflecting on the past two centuries, urban air compositions have fluctuated considerably, especially in SO_2 concentrations (*ibid.*).

Sulfur dioxide is moderately soluble in water, yet still 1,300 times more soluble in water than oxygen (Fyfe 1994, 2:39). For this reason, its concentration may be significantly higher than expected from partial pressure considerations (*ibid.*). Furthermore, the solubility of SO_2 makes it a superior cathode reactant than dissolved oxygen despite having a comparatively small atmospheric concentration (*ibid.*). The SO_2 that reacts with water yields sulfuric acid (H_2SO_4). The rest is absorbed into aerosol particles and oxidized into the sulfate ion (SO_4^{2-}) (Leygraf & Graedel 2000, 45-6).

In addition to the described atmospheric sulfur contaminants, there are two main types of saline particles that can serve as strong stimulators in the initiation of corrosion. One is ammonium sulfate and the other is a chloride. Ammonium sulfate is formed in industrial areas where ammonia

and SO_3 or H_2SO_4 aerosols co-exist in appreciable concentrations (Fyfe 1994, 2:35). Other airborne particles interact with tropospheric sulfur in ways that lend to metallic corrosion. The group of interest is the absorbent particles such as charcoal and soot, which have surfaces or infrastructures that absorb sulfur dioxide. By interacting further in water, either by co-absorption of vapor or condensation within the structure, they serve as catalysts in the formation of corrosion. This is the case because soluble corrosion products are retained long enough on a metal surface to be converted into protective, insoluble salts (Fyfe 1994, 2:35).

3.6. CARBON AND THE CARBON CYCLE

Carbon forms a number of mobile, simple compounds in nature (CO, CO_2, CO_3^{2-}, etc.), which take part in the intensive circulation of substances in the geosphere and are in close relationship with water and oxygen cycles of the hydrosphere (Ferronsky & Polyakov 2012, 205). The main carbon reservoirs are in the air (as CO_2), and in the crust (mainly as sedimentary inorganic carbon in the form of carbonates [e.g. limestone and dolomites], organic carbon, and carbon hosted in crystalline rocks) (Sharp 2007, 150; Knapp 1996, 10). Carbon dioxide is also found dissolved in all water (*ibid.*). The main transfers are through the ocean and land (soil and plants; involving photosynthesis, respiration and oxidation), and about half is attributed by human perturbation through the burning of fossil fuels (oxidation).

Dioxygen and carbon dioxygen are closely coupled due to photosynthesis, which uses CO_2 to release O_2 in a cycle that is almost perfectly balanced (to within 0.4%) (Berner & Berner 2012, 24). At first glance, it may appear that the carbon and oxygen cycles are reciprocals (upper panels of **figure 3.9**), but with a closer look, an important difference is found in the oceans. When atmospheric CO_2 enters the ocean, it is buffered by a large carbonate (dissolved inorganic carbon, DIC) system, which has more than 50 times the carbon contained in the air (Heimann 2001, 236). This large oceanic carbon reservoir can dilute any perturbations to atmospheric CO_2 to a considerable extent (*ibid.*). This is not the case for the oxygen cycle, where the molecular oxygen that enters the ocean is dissolved in tiny amounts, and therefore only minimal changes are observed during exchanges with the ocean (*ibid.*). This difference matters when considering anthropogenic reactions that involve and influence carbon dioxide and dioxygen levels in the atmosphere, possibly setting cycles off balance. Specifically, the burning of fossil fuels and emissions from cement production result in an increase of CO_2 concentration, and since these processes require oxygen, they also result in a decreasing trend in atmospheric oxygen (Berner & Berner 2012, 27; Heimann 2001, 237). As described, the excess of CO_2 is largely taken up by the oceans and partly used during photosynthesis for the generation of O_2; yet the oceans have a very small effect on the oxygen balance. The impact of this term to the oxygen cycle is believed to be small (Heimann 2001, 237).

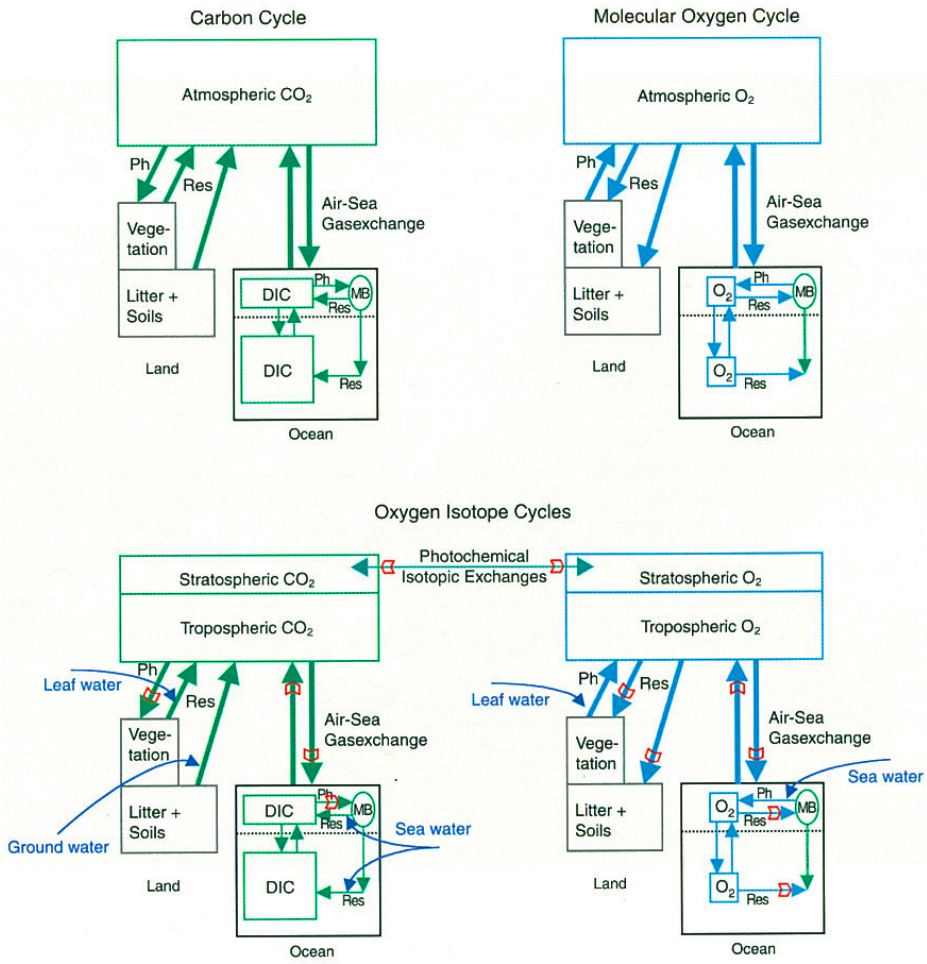


Figure 3.9: Upper panels: simplified schemes (pool sizes not shown to scale) of the natural global carbon and oxygen cycles where Ph = photosynthesis, Res = respiration, MB = marine biota and DIC = dissolved inorganic carbon (H_2CO_3, HCO_3^-, CO_3^{2-}). Lower panels: corresponding schemes of the cycles of oxygen isotopes in CO_2 and in O_2. Dark blue arrows indicate links to oxygen isotopes in the hydrological cycle. Red whiskers on arrows indicate exchanges during which fractionation processes occur. Heimann 2001, 236.

3.6.1. Carbonate Equilibrium

Natural systems always tend towards equilibrium; however, equilibrium is more of a theoretical concept than an attainable state in the natural world, as geochemical parameters are constantly changing. All aqueous systems contain carbonate ions resulting from the dissolution of atmospheric carbon dioxide. The relationships between the various carbonate species ($CO_{2(g)}$ and $H_2O_{(l)}$ at STP) are expressed by the following equilibria reactions:

$$CO_{2(g)} + H_2O \rightleftharpoons H_2CO_3$$

$$H_2CO_3 \rightleftharpoons H^+ + HCO_3^-$$

$$HCO_3^- \rightleftharpoons H^+ + CO_3^{2-}$$

Shifts in carbonate equilibria generally exert a controlling influence on the pH of natural aqueous systems (by production of carbonic acid in equation 1 [above] and conversely, pH change can instigate precipitation or dissolution of carbonate (Fetter 1994 cited in Wilson 2004, 23). High

carbon dioxide concentrations can also result from microbial activity in soils and on the seabed (Edwards 1998, 88). In acidic environments, CO_3^{2-} activity is relatively low, but higher levels in alkaline solutions allow metal carbonates for form (Lindsay 1979 cited in Wilson 2004, 23). Consequently, the solubility of many metal ions is limited under alkaline conditions. Carbonate equilibria has direct implications for the preservation or degradation of archaeological materials, in particular metals and calcareous ceramics.

Many processes involving isotope exchange can be modeled by classical equilibrium thermodynamics, because they are near-equilibrium phenomena. Equilibrium fractionation between two phases is based on the differences in bond strength of the different isotopes of an element. The heavier isotope will form a stronger bond and will be concentrated in the phase with higher bond energy or "stiffness." Fractionation varies regularly with temperature, a relationship that forms the basis for stable isotope thermometry (equilibrium fractionation between two phases generally decreases with increasing temperature). The degree of fractionation is generally larger for elements whose mass ratio is large. The heavy isotope is preferentially partitioned into the site with stiffest bonds (strong and short chemical bonds). Empirical theoretical methods of determining fractionation factors are based on ordering minerals according to their increasing anionic bond strength. Empirical determinations are made by measuring the fractionation between two natural phases, with temperatures either measured (for modern samples) or calculated (for example, with metamorphic rocks).

In an open system, calcium carbonate reacts with water in contact with a gas phase of fixed pCO_2. In an open system complete isotopic equilibrium may ultimately occur between the soil-CO_2 and the inorganic carbon species in solution. The composition then is not influenced by that of the dissolving inorganic carbonate (e.g. calcium carbonate), but is determined by the $\delta^{13}C$ of the soil-CO_2, the relative proportions of the inorganic species and the fractionation factors involved between $CO_{2(g)}$ and the inorganic species. In an open system, CO_2 as well as H_2O can be transferred out of as well as into the soil solution.

In a closed system the water first equilibrates with a carbon dioxide reservoir, is subsequently isolated from the reservoir and finally reacts with the carbonates. In a closed system, the water equilibrates first with the gas phase and is then brought into contact with the inorganic carbonate (e.g. calcium carbonate); no further exchange with the gas reservoir takes place. Therefore, the $\delta^{13}C$ depends on the original composition and the amount of dissolved inorganic carbonate (calcium carbonate), which in turn is determined by pCO_2. A semi-open system (also referred to as closed system) the CO_2 and H_2O transport is only out of the solution.

3.6.2. Carbon Isotopes Throughout the Environment

Carbon Isotopes in the Atmosphere

Atmospheric CO_2, in the long-term, is controlled by the uptake and dissolution of CO_2 in the hydrosphere, its participation in the weathering/sedimentation of carbonate rocks, as well as the

CO_2 released into the atmosphere via tectonic processes and volcanism (Yakir 2011, 118). The short-term CO_2 balance of the atmosphere is dominantly controlled by photosynthesis and the air-sea gas exchange (Yakir 2011, 118, 123).

Carbon dioxide in the air has a $\delta^{13}C$ value around -7‰ (Ferronsky & Polyakov 2012, 208; Yakir 2011, 117). Publications from just 20 years ago state that the $\delta^{13}C$ value is closer to -8‰. Each year the atmospheric $\delta^{13}C$ value becomes lower due to the addition of isotopically light CO_2 produced by the combustion of fossil fuels and, to a lesser extent, deforestation (Long *et al.* 2005, 148; Melchiorre 1998, 235; O'Leary 1993, 20 & 50). Since atmospheric CO_2 provides, directly or indirectly, the fundamental carbon source for most terrestrial and aquatic chemical reactions in the ecosystem, large-scale depletion of atmospheric CO_2 $\delta^{13}C$ produces a substantial change in isotopic baseline for stable carbon isotope studies (Long *et al.* 2005, 149). Although there is a model that applies an estimated correction factor that controls for atmospheric change in CO_2 $\delta^{13}C$, its application introduces additional variability in ratio estimates and, consequently, reduces precision (Long *et al.* 2005).

Organic Carbon Isotopes in Soil CO_2

Down to a certain depth (usually a few meters), the infiltrating water (meteoric in origin) remains in continuous contact with atmospheric CO_2 at a fixed partial pressure. The carbon in this zone is therefore involved in an open dissolution system. The CO_2 in soil may be several orders of magnitude higher than in the atmosphere (Salomons & Mook 1986, 242). Carbon within the soil zone has multiple sources, both organic and inorganic in origin. Carbon dioxide production in the soil depends on the vegetation and on the microbial degradation of organic matter (Salomons & Mook 1986, 242). All of these reactions involve hydrolysis and a change in pH (Herczeg & Edmund 2001, 35). Carbonates are an important constituent of soils because they act as a buffer for pH changes (Salomons & Mook 1986, 239). Below the soil zone, contact with the atmospheric carbonate reservoir is lost and subsequent evolution towards a closed dissolution system takes place. In nature, carbonate dissolution will often take place under mixed conditions (open and closed systems).

If CO_2 reacts with water to form carbonic acid, the soil environment may become chemically very aggressive and attack copper directly, preventing the formation of a protective film (Garrels 1954; Jenks 1948 cited in Scott 2002, 37). Alternatively, CO_2 and water can produce soluble calcium carbonate, which is quite benign and can lend to the protection of bronzes (Scott 2002, 37). The overall pH in groundwater is principally controlled by this $CaCO_3 - H_2O - CO_2$ equilibrium. Since this study is focused on malachite, a protective mineral, it is assumed that the latter reaction between CO_2 and water was dominant. The formation of malachite is detailed in Chapter 4.

The ^{13}C fractionations involved in biological systems and the decomposition of organic matter are extremely complex and are presented here as broad generalizations. Fractionation

between inorganic and biologic organic carbon is very large. Reduced organic carbon has characteristically low $\delta^{13}C$ (-31 to -9‰) because plants fractionate carbon isotopes during photosynthesis with a preferential uptake of $^{12}CO_2$ by photosynthetic enzymes (Yakir 2011, 123). To a large degree, the effects of photosynthesis on carbon fractionation in terrestrial plants are dependent on the carbon fixation pathway of the plant. Most plants, including all woody trees, use Rubisco (Ribulose biphosphate carboxylase/oxygenase) as the primary photosynthetic enzyme, producing three-carbon sugars as the primary product and are therefore called C_3 plants (Yakir 2011, 123-4). The $\delta^{13}C$ of soil CO_2 respired by C_3 plants is -31 to -20‰ (or -30 to -25 in Kendall & Doctor 2011, 201) (Hall & Rao 1999, 118; Melchiorre 1998, 236). About 23% of global plant productivity (mostly grasslands and agriculture) uses PEP-c (phosphor-Enol-Pyruvate-carboxylase) as the primary photosynthetic enzyme, which acts on bicarbonate as a substrate and produces four-carbon organic acids (Yakir 2011, 124). These are called C_4 plants, and the $\delta^{13}C$ of soil CO_2 contributed by C_4 plants is -20 to -10‰ (Hall & Rao 1999, 118; Melchiorre 1998, 236). CAM (Crassulacean Acid Metabolism) plants dominate in very hot, dry climates and include cacti and succulents, yet they are difficult to distinguish from C_3 and C_4 plants (*ibids.*). Since little isotopic fractionation occurs during decay, the $\delta^{13}C$ of soil carbonates (paleosols) is generally controlled by the type of plant (C_3 or C_4) living at (or shortly before) the time of carbonate formation (Sharp 2007, 162).

Dissolved Inorganic Carbon Isotopes in Soil Fluids

Water serves as a dissolvent and carrier for many carbon species. Water will move carbon between reservoirs, and facilitate reactions to form other carbon products. Combined, these are termed "dissolved inorganic carbon," or DIC[1]. The relative concentrations of DIC species are mainly a function of pH, temperature and salinity (Yakir 2011, 121). Carbon dioxide gas can diffuse into water, going into a dissolved or aqueous from ($CO_{2(aq)}$), and then rapidly hydrate to form carbonic acid (H_2CO_3) (Appelo & Postma 2005, 79; Yakir 2011, 121). The primary reactions that produce DIC are: (i) weathering of carbonate minerals by acidic rain or other strong acids; (ii) weathering of silicate minerals by carbonic acid produced by the dissolution of biogenic soil CO_2 by infiltrating rainwater; and (iii) weathering of carbonate minerals by carbonic acid (Kendall & Doctor 2011, 201).

The $\delta^{13}C$ in a fluid is determined by the dissolved carbon species in the fluid (CO_2, H_2CO_3, HCO_3^- and CO_3^{2-}), which are affected by several soil processes and are pH and temperature

[1] Dissolved Inorganic Carbon (DIC) always consists of more than one compound:

gaseous CO_2 with a partial pressure pCO_2
dissolved CO_2
dissolved carbonic acid, H_2CO_3, with a = $[H_2CO_3] + [CO_{2aq}]$
dissolved bicarbonate, HCO_3^-, with b = $[HCO_3^-]$
dissolved carbonate, CO_3^{2-}, with c = $[CO_3^{2-}]$
total dissolved inorganic carbon, DIC, with c total = a + b + c
solid carbonate, like $CaCO_3$

dependent (Hoefs 1997, 97). Fractionation between oxidized inorganic carbon species is generally small (Sharp 2007, 153). This is complicated by the incorporation of organic carbon species. On long timescales, $\delta^{13}C$ values are a function of the balance in deposition of organic matter and inorganic carbonates.

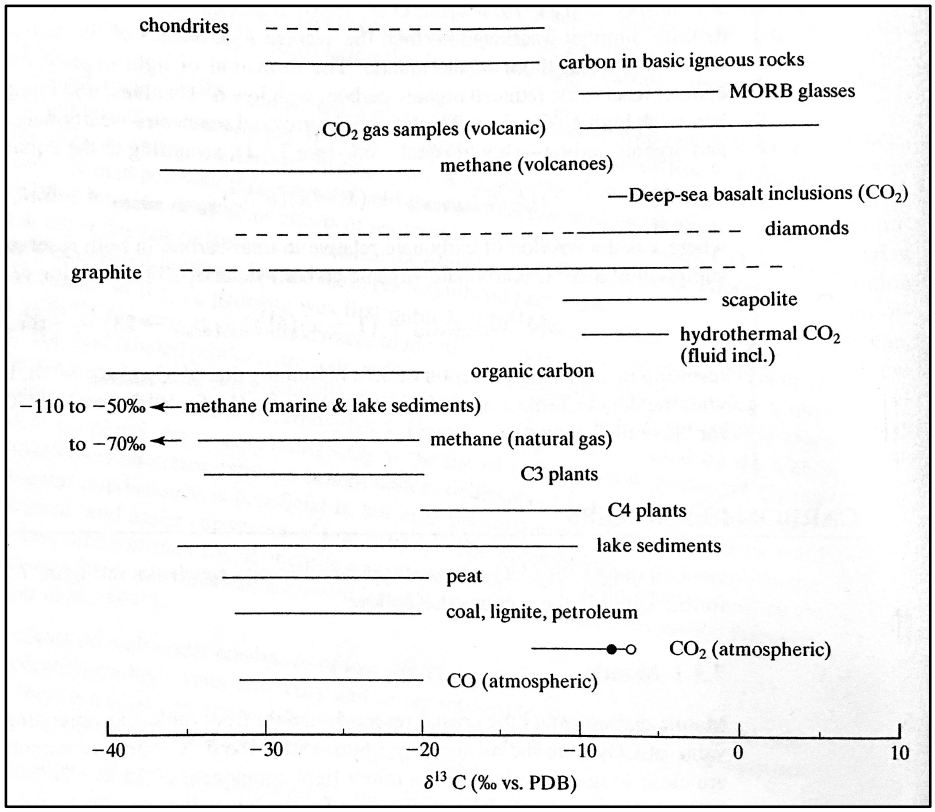


Figure 3.10: General ranges of $\delta^{13}C$ values of selected carbon-bearing materials. The modern average $\delta^{13}C$ value of the atmosphere is shown by the filled circle; the pre-anthropogenic value is an open circle (Sharp 2007, 152).

3.6.3. Carbon Isotopes in Malachite Ores

Assuming that malachite forms in isotopic equilibrium with its carbon source, and that the carbon fractionation between malachite and the carbon source is known, the $\delta^{13}C$ value of a malachite sample can be used to differentiate between malachite that has inherited a light carbon signature from soil CO_2, or a heavier carbon signature from limestone dissolution or atmospheric CO_2.

Melchiorre (1998) reports that the carbon isotope behavior of malachite is within experimental error the same as calcite and HCO_3, and therefore assumes as follows:

$$1000\ln\alpha_{\text{malachite-HCO3}} \approx 1000\ln\alpha_{\text{calcite-HCO3}} = 1.85 + (0.035(T\text{-}20)) \tag{235}$$

The experimental determinations of carbon fractionation between calcite and HCO_3 were determined by Emrich *et al.* in 1970. Haßler *et al.* agree with this fractionation, using it to assume that under equilibrium conditions between atmospheric $CO_{2(g)}$ and the atmosphere (and assuming atmospheric $\delta^{13}C$ is ca. -8‰ at the time of malachite formation), the newly precipitated malachite

should be enriched in heavy isotopes by about Δ = +10.2‰ at 20ºC, and even more at lower temperatures (Δ = +9.7‰ at 10ºC) (Haßler *et al.* 2014, 8; Melchiorre 1998, 236). This would result in $\delta^{13}C$ values around 2.2‰ in carbonates which derive their carbon exclusively from atmospheric CO_2 and values between -21.8‰ and -12.8‰ in those that incorporate carbon from soil CO_2 (refer to **figure 3.11**).

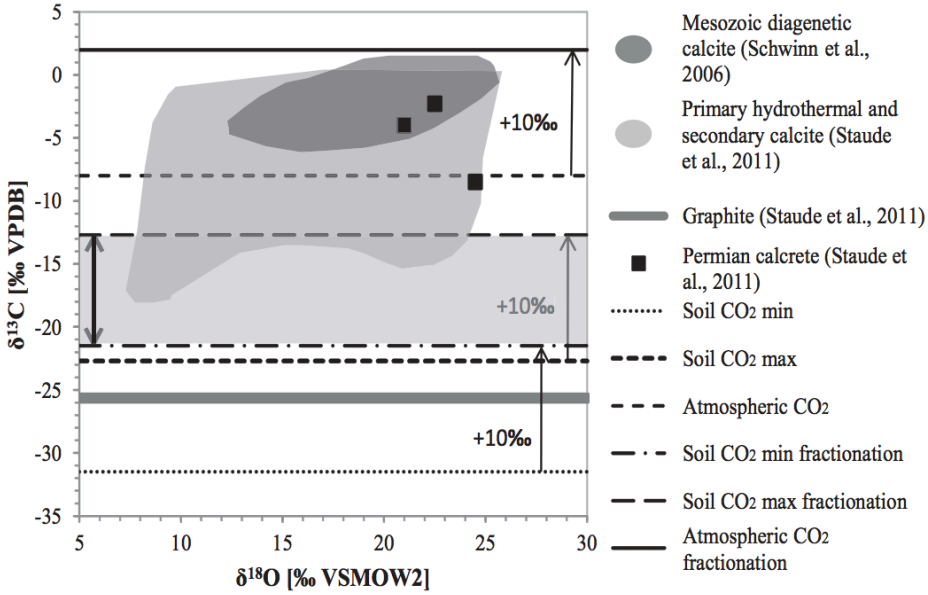


Figure 3.11: Showing the potential carbon reservoirs. Arrows indicate carbon isotope fractionation between carbon source and resulting carbonate mineral (malachite). The double arrow indicates the range of soil CO_2. Image from Haßler *et al.* 2014, 7.

It has been shown in soil carbonate studies by many workers that soil water residence times are generally sufficient for carbon isotope exchange between soil water bicarbonate and soil CO_2 to reach equilibrium (e.g. Cerling 1984, Amundson *et al.* 1988, Quade *et al*. 1989). The carbonate study carried out by Haßler *et al.* reports $\delta^{13}C$ values ranging from 1.0‰ to -21.0‰ (VPDB). Melchiorre's doctoral study on malachite ores reports $\delta^{13}C$ values ranging between -0.75‰ and -19.85‰ (PDB). These results suggest that, for most malachite ores, the source is dominantly vegetation-respired soil CO_2, though higher values represent mixtures that includes some inorganic carbon sources. Melchiorre made no attempt to infer a specific vegetation-type source of carbon for individual malachite samples, as many processes can affect the $\delta^{13}C$ value of a sample, blurring the distinction between C_4, C_3 and CAM. For example, a soil CO_2 produced by C_3 vegetation, where $\delta^{13}C$ is -20‰, could mix with bicarbonate from a buffering marine limestone host with $\delta^{13}C$ around 0‰, and the malachite formed from this solution would have a $\delta^{13}C$ of -10‰. It is hypothesized that similar results would be acquired from archaeological malachite samples.

3.7. Summary

In review, meteoric water is produced as precipitation in the water cycle. The processes involved in the water cycle provide a characteristic fingerprint of their origin and affect the stable isotopic composition of water. This signature therefore serves as a natural tracer, which is

fundamental to investigating the provenance of meteoric waters. It is hypothesized that the global variations in isotopic composition of precipitation is maintained when meteoric water reacts with exposed copper, and that the $\delta^{18}O$ values from copper corrosion products can be used as a tracer.

Driven by photosynthesis, the constant regeneration of oxygen by biogeochemical processes between the atmosphere and water, plants and animals, and mineral matter is altogether known as the oxygen cycle. Its influence largely lies in the fundamental linkage points it forms between other biogeochemical cycles such as the carbon and water cycles. Atmospheric molecular oxygen has a relatively constant isotopic composition with a $\delta^{18}O$ value of 23.5 ± 0.3‰ relative to ocean water (SMOW).

The major air pollutant and sulfur-containing compound in the troposphere is sulfur dioxide since it has significant impacts on animal and plant life. It is also a powerful stimulator of atmospheric metal corrosion. The formation of brochantite through sulfur dioxide is elaborated upon in chapter 4.

Meteoric water is the source of most subsurface water, and like the soil profile, the different subsurface waters can be described in layers. The soil zone extends from the ground surface through the major root zone, with thickness ranging depending on soil type and vegetation. When enough rain falls to percolate through the soil, the water serves as a dissolvent and carrier for many carbon species. Water will move carbon between reservoirs, and facilitate reactions to form other carbon products.

Carbon plays a significant role in copper corrosion and the formation of the carbonate in malachite. Carbon within the soil zone has multiple sources, both organic and inorganic in origin. Reduced organic carbon has characteristically low $\delta^{13}C$, and inorganic carbon tends to have high $\delta^{13}C$ values. The $\delta^{13}C$ value of a malachite sample can be used to differentiate between malachite that has inherited a low carbon signature from organic soil CO_2, or a higher carbon signature from limestone dissolution or atmospheric CO_2.

CHAPTER 4

Formation, Stability and Isotopy of Brochantite and Malachite

4.1. INTRODUCTION

Having provided a project foundation through sections on metallic corrosion, stable isotopes in hydrology, characteristics of the atmosphere and soil as corrosive environments, and general descriptions of brochantite and malachite, it is now appropriate to present the research framework. The aim of Chapter 4 is to describe what is already known about the formation pathways and oxygen isotopy of brochantite and malachite. These copper minerals are discussed chemically through theoretical, empirical and experimental studies carried out on synthetic and natural specimens.

4.2. BROCHANTITE, $Cu_4SO_4(OH)_6$

The general understanding of outdoor corrosion is that exposed copper turns reddish-brown and eventually green over several decades. It was not until after World War I that investigations were properly carried out to identify what mineral phases form (Scott 2002, 48). Brochantite is the most abundant and most stable product formed on exposed copper, largely due to its stability under a wide variety of chemical conditions, and it represents the terminal stage of atmospheric copper corrosion (Nassau *et al.* 1987; Woods & Garrels 1986; Strandberg 1998, 3512). Pourbaix diagrams show that brochantite should be the major corrosion product and basic copper carbonates and chlorides should be minor or absent in temperate outdoor environments (refer to **figures 2.5** and **2.7**). Powder X-ray diffraction (XRD) analyses carried out for this thesis on corrosion samples collected from copper roofs around Ottawa, Oxford, Tuscaloosa and Vienna have also identified the copper (II) hydroxide sulfate mineral, brochantite ($Cu_4SO_4(OH)_6$), as the dominant product. This section aims to inform the reader of the sources and controls of oxygen and sulfur in the atmosphere, and how these elements chemically react with exposed copper to form brochantite. The stability and thermal decomposition of brochantite is presented, as this affects the analytical methodologies used to study the isotopy of atmospheric sulfates and brochantite. Most influential to this doctoral study are the oxygen isotope investigations on atmospheric sulfates of Holt and collaborators, the relevant points of which are discussed.

4.2.1. Formation of Atmospheric Sulfates and Brochantite

Emphasis on SO_2 → Sulfate

There are a variety of mechanisms for sulfate formation, which involve different conditions of kinetic and thermodynamic fractionation of oxygen isotopes that may be related to the oxygen isotope content of the sulfate product. Even the same starting components will produce isotopically varied sulfate products if driven through different reaction pathways.

Understanding the formation pathways for SO_2 is of particular significance because most of the SO_2 in urban air is anthropogenic and because the majority of sulfur compounds pass through oxidation as SO_2 before being converted to sulfate. With regards to this research project, SO_2 is important as one of the most common and powerful stimulators of atmospheric metal corrosion. Sulfates are either primary (sulfates formed within combustion sources before emission into the atmosphere) or secondary (sulfates formed in the atmosphere, principally from SO_2, by atmospheric conversion processes). Although primary sulfates contribute to the total sulfate budget, they are not considered in estimations because they constitute a negligible portion compared to secondary sulfates (Lee & Thiemens 2001, 17362). The two widely accepted mechanisms by which SO_2 is transformed to secondary sulfate are aqueous-phase (heterogeneous) and gaseous-phase (homogeneous). In the homogeneous process, oxidation precedes hydration (oxidation-hydrolysis), whereas in the heterogeneous process, hydration precedes oxidation (hydrolysis-oxidation) (Holt *et al.* 1979, 44; Novák *et al.* 2007, 706). Although made from the same starting components, the mechanisms responsible for the two transformation processes are entirely different, resulting in sulfate products of distinguishable $\delta^{18}O$ content (Holt *et al.* 1979, 44; Holt & Kumar 1991, 32). The competing oxidation pathways of sulfate are affected by several interacting factors during the formation, notably:

1. The relative amounts of $sulfate_{(aq)}$ oxygen incorporated from various oxygen sources (most importantly water, which varies in $\delta^{18}O$ values, and O_2); and
2. Ambient physiochemical conditions, like pH, temperature, atmospheric pressure, atmospheric oxidant concentrations, liquid water content, atmospheric transition metal concentrations, and aerosol surface area.

The heterogeneous sequence of SO_2 dissolved in water begins with rapid hydrolysis according to the chemical equilibrium: $SO_2 + H_2O \rightleftharpoons HSO_3^- + H^+$. The most effective oxidants of SO_2 during heterogeneous oxidation are by hydrogen peroxide, ozone and molecular oxygen (catalyzed by Fe^{3+} or Mn^{2+}). Oxidation by H_2O_2 is not significantly dependent on pH within normal atmospheric ranges (pH 2 – 7), but is favored at low pH (< 5) since O_3 and O_2 (catalyzed by metals) dominate (and become faster) at greater pH (> 5) (Li *et al.* 2013, 592; Savarino *et al.* 2000, 29079; Van Stempvoort & Krouse 1994, 447). In terms of isotopy, H_2O_2 is expected to be richer in water oxygen than in air oxygen, leading to sulfate with lower $\delta^{18}O$ values (Novák *et al.* 2007, 706). Ozone and O_2 lead to higher $\delta^{18}O$ values in sulfate (*ibid.*).

In contrast, the homogeneous sequence starts with gaseous SO_2 reacting with atmospheric species to produce gaseous oxidized compounds, which then react with atmospheric water to form sulfuric acid (Van Stempvoort & Krouse 1994, 447). It is well established that there is only one homogeneous pathway that is significant under atmospheric conditions (Lee & Thiemens 2001, 17361; Li *et al.* 2013, 592; Savarino *et al.* 2000, 29084). It involves initiation by $^{\bullet}OH$ radicals, followed by a chain reaction:

$SO_2 + {}^{\bullet}OH \rightarrow {}^{\bullet}HOSO_2$,

${}^{\bullet}HOSO_2 + O_2 \rightarrow SO_3 + {}^{\bullet}HO_2$,

$SO_3 + H_2O \rightarrow H_2SO_4$ (*ibids.*).

For isotopic variation, the most influential steps are the geochemical processes that initially yield sulfates from other sulfur species, and not the precipitation of a sulfate mineral from dissolved sulfate (Seal II *et al.* 2000, 557). Therefore, the more important processes generally involve the oxidation of sulfide to sulfate, or the reduction of sulfate to sulfide (*ibid.*).

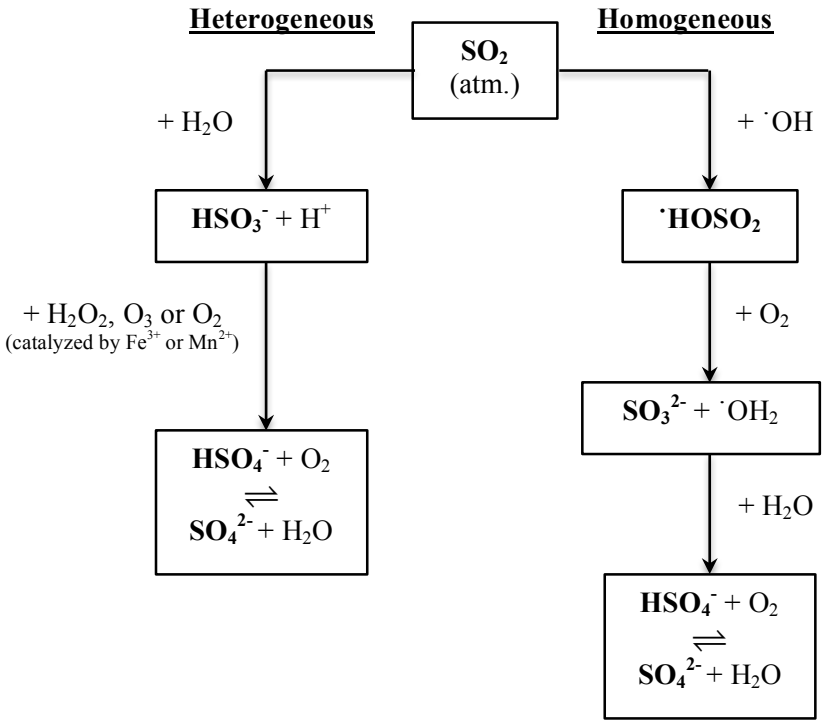


Figure 4.1: Diagram distinguishing heterogeneous (aqueous) and homogeneous (gaseous) pathways of SO_2 to sulfate formation. The homogeneous mechanism is suggested to be 1.8 times faster than the heterogeneous oxidation, though heterogeneous pathways predominate (Holt & Kumar 1991, 36; Tanaka *et al.* 1994, 1521).

Corrosion Mechanisms of Brochantite

For brochantite to form, a source of sulfur and an oxidizer is necessary. The initial stage of atmospheric brochantite formation takes place when exposed copper begins reacting with water, most likely from precipitation or atmospheric water vapor, which provide the oxygen atoms that cause surface hydroxylation. The hydroxyl groups that result serve as sites for subsequent water adsorption in the molecular form, and the first precipitated corrosion mineral, cuprite, is oxidized as shown in reaction 1 (FitzGerald *et al.* 2006, 2501):

Reaction 1: $2Cu + \frac{1}{2}O_2 = Cu_2O$

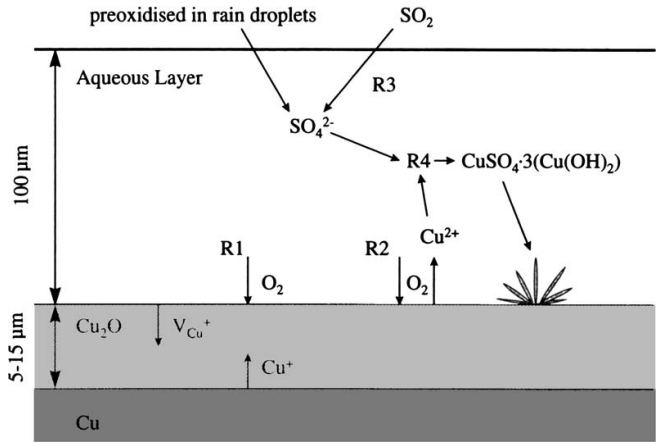


Figure 4.2: Illustration of the reactions involved in brochantite formation during patination. R1, R2, R3, and R4 are abbreviations for reactions 1-4. (FitzGerald *et al.* 2006, 2502).

Reaction 1 is controlled by the diffusion of Cu^+ through the cuprite layer and is equivalent to the dissolution/oxidation rate of cuprite after many years (often decades), whereupon a steady state corrosion rate is reached (FitzGerald *et al.* 2006, 2502). When an aqueous layer is still present, it serves as the electrolyte in electrochemical reactions as well as a solvent for additional atmospheric constituents, gaseous and particulate, which deposit into the liquid layer, either directly or as a component of precipitation. There is an enormous range of species in the atmosphere, yet surprisingly few play an active role in atmospheric corrosion (Leygraf & Graedel 2000, 52). The most relevant gases (and dissolved analogues) are CO_2, O_3, NH_3, NH_2, H_2S, SO_2, HCl and organic acids. Soot deposits also develop from the early periods of exposure. Strong synergistic effects occur with mixtures of SO_2, NO_2 and ozone that considerably increase the corrosion rate of exposed copper (more specifically, cuprite) than the action of the individual pollutants (Baumann 2011, 130; Scott 2002, 46; Selwyn 2004, 63; Strandberg 1998, 3516).

In the following stage, there is a change in liquid layer chemistry, which results from the constituent depositions into the aqueous phase. In this case, surface copper ions from the cuprite are further oxidized in the presence of a layer of surface water via the two partial electrochemical reactions:

Reaction 2: $Cu^+ = Cu^{2+} + e^-$

$\frac{1}{2}O_2 + H_2O + 2e^- = 2OH^-$

Simultaneously atmospheric SO_2 is transformed into sulfate ions as described in the previous section (via heterogeneous and homogeneous pathways), and are temporarily available for reactions:

Reaction 3: $SO_2 + H_2O \rightleftharpoons H^+ + HSO_3^-$ (bisulfite ion in isotopic equilibrium with water)

or

$SO_2 + {}^\bullet OH \rightarrow {}^\bullet HOSO_2$,

${}^\bullet HOSO_2 + O_2 \rightarrow SO_3^{2-} + {}^\bullet HO_2$ (sulfite ion produced via homogeneous pathway)

The sulfite/bisulfite ion can then react with water to form sulfate/bisulfate ions. In heterogeneous formation pathways, which is the predominant mechanism; hydrogen peroxide, ozone or O_2 (catalyzed by metals) in the presence of SO_2 yields the sulfate/bisulfate ion (refer to **figure 4.1**).

$HSO_3^- + [H_2O_2, O_3, \text{or } O_2] \rightleftharpoons HSO_4^- + O_2$ (bisulfate ion)

The supply of sulfates to the surface is not sufficient to account for the quantity of brochantite present on patinas. Brochantite is precipitated by reaction 4, when the pH in the water becomes sufficiently alkaline (refer to **figure 4.3**, a stability diagram):

Reaction 4: $4Cu^{2+} + SO_4^{2-} + 6OH^- \rightarrow CuSO_4 3Cu(OH)_2$

Brochantite thus precipitates from an aqueous surface layer from an oxidative dissolution of some cuprite.

4.2.2. Stability and Thermal Decomposition of Brochantite

Stability

Pourbaix diagrams can be used to show the stability of common copper minerals that contain oxidized sulfur. The $Cu - SO_3 - H_2O$ system is represented on **figure 4.3**. Centered within the rain regime is the region in which brochantite is stable. As moisture layers on metal surfaces begin to evaporate, ionic concentrations increase while pH decreases, moving the system upwards into a region of much wider brochantite stability, as well as towards antlerite stability. Antlerite, $Cu_3SO_4(OH)_4$, is more likely to occur in fog and sheltered areas that favor the accumulation of debris (Scott 2002, 148-9; Selwyn 2004, 64). It also seems to precipitate in conditions with lower pH, though this has been disputed. Worth noting, however, are the diagram's limitations, of which there are two. Firstly, it represents chemical equilibrium, which are unlikely in natural atmospheric conditions and secondly, the diagram applies to pure systems, though in reality other constituents are also present, often in higher concentrations. Once a patina has formed, changes in rainwater chemistry are unlikely to affect its mineral content unless very acidic conditions (<2.5) are encountered (Scott 2002, 55).

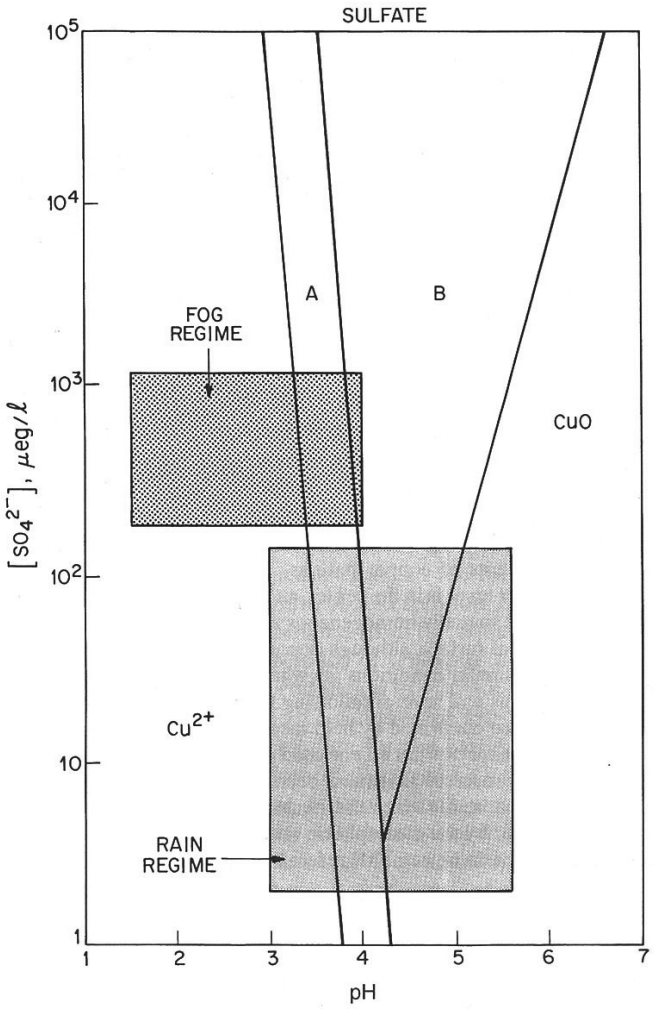


Figure 4.3: Pourbaix (Stability) diagram for the Cu – SO_3 – H_2O system. A and B indicate the regions in which antlerite (A) and brochantite (B) are stable. Diagram from Leygraf & Graedel 2000, 275.

Once formed, sulfates of various isotopic ratios are stable with respect to oxygen isotope exchange, which proceeds at an extremely slow rate, with any water which they may be subsequently associated (Holt *et al*. 1981a, 804; Holt & Kumar 1991, 27). It is also believed that the isotope ratios may not re-equilibrate during mineral precipitation (Seal II *et al.* 2000, 542). This results in the preservation of $\delta^{18}O$ (which may reflect the formation mechanism) in formed sulfates (Holt & Kumar 1991, 28). Even in highly acidic rain of pH ~4 at around 10ºC, the half-life of oxygen atom exchange between sulfate and water is of the order of 600-1000 years (Holt *et al.* 1978, 105; Lloyd 1967 cited in Holt & Kumar 1991, 28).

Thermal Decomposition

Each oxygen in the brochantite molecule is of interest, however those bound in the sulfate, $Cu_4S\underline{\mathbf{O}}_4(OH)_6$, need to be analyzed separately from those in the hydroxyl group, $Cu_4SO_4(\underline{\mathbf{O}}H)_6$. The simplest way to do this is by heating the brochantite until the hydroxyl anions break away.

The temperature at which this happens needs to be identified, and the temperature at which the sulfate breaks away needs to be known as well so that it is not reached during the heat treatment.

The principal for thermal analysis of solid material basically involves the quantitative measurement of the weight change in a sample under controlled heating conditions (Pollard & Heron 1996, 73). Three forms of thermal analysis are commonly carried out: thermogravimetric analysis (TG or TGA), differential thermal analysis (DTA) and differential scanning calorimetry (DSC). Thermogravimetry simply records the weight of a sample as the temperature is raised, thus recording the loss of components such as water, hydroxyl anions or SO_4, while also allowing for the composition to be elucidated (Pollard & Heron 1996, 73-74). In DTA, a sample is measured against an inert reference material as it is heated, allowing phase changes to be monitored as well as chemical changes (*ibid.*). Differential scanning calorimetry is a related technique that allows more quantitative estimates to be made of the thermodynamic heats of transition (*ibid.*).

The relative stabilities of the members of the copper hydroxyl sulfate family, including brochantite as the most common, have been studied on several occasions, but with considerable disagreements. Laboratory studies of the system have generally involved an acid-base titration, with the drop-addition of a hydroxide solution to a copper (II) sulfate solution. The predominant mineral phases and compositions of the basic copper (II) sulfates precipitated are inconsistent among different workers, which is ascribed to varying precipitation conditions such as the concentrations of the solutions mixed, the mixing rate, the pH of the solution, and temperature. Thermogravimetry is useful for characterizing the precipitates obtained under various experimental conditions, however the reported thermal decomposition behaviors are also contradictory and apparently not always reproducible. Another issue is that synthetic posnjakite, which is essentially brochantite with water molecules attached to it, cannot be distinguished from brochantite from the pH titration procedure, but the thermal dehydration of the two minerals is different. A positive identification for brochantite is therefore critical.

The accepted thermal decomposition of synthetic brochantite has been reported to decompose via a stable, dehydrated, amorphous intermediate ($Cu_4O_3SO_4$) to copper (II) oxide with three distinguished thermal behaviors: 1. thermal dehydration, 2. in-situ recrystallization of dehydrated amorphous compound and 3. thermal desulfurization, as follows:

$$Cu(OH)_6SO_4 \xrightarrow{-3H_2O} Cu_4O_3SO_4 \xrightarrow{-SO_3} 4CuO$$

(Tanaka & Koga 1990, 613; Koga *et al.* 1997, 1467-8).

1. Thermal dehydration: The first stage of the decomposition is associated with dehydroxylation, which has two, separate endothermic peaks:

$$Cu_4(OH)_6SO_4 \rightarrow Cu_4O(OH)_4SO_4 + H_2O$$
$$Cu_4O(OH)_4SO_4 \rightarrow Cu_4O_3SO_4 + 2H_2O \quad (ibid.).$$

The first intermediate compound [$Cu_4O(OH)_4SO_4$] was obtained by linearly heating (10 K/min) the brochantite sample to the isothermic (constant temperature) temperature range of 510K [236.85ºC] $\leq T \leq$ 540K [266.85ºC]) for 15 hours (Koga *et al.* 1997, 1468, 1470). The product was allowed to

cool to room temperature in a nitrogen flow atmosphere before being heated to 570K [296.85ºC] ≤ T ≤ 720K [446.85ºC] to initiate the second reaction, which is characterized by a well-distinguished, single peak (DTA and TG) (*ibid.*).

Table 1. The Mass Loss Due to the Successive Decomposition of Synthetic Brochantite

Reaction	Mass Loss, % Observed	Mass Loss, % Calculated[a]
$Cu_4(OH)_6SO_4 \rightarrow Cu_4O_3SO_4 + 3H_2O$	11.87 ± 0.34	11.95
$Cu_4O_3SO_4 \rightarrow 4CuO + SO_3$	17.48 ± 0.19	17.70

[a] Assuming the composition, $Cu_4(OH)_6SO_4$.

Table 2. Determination of Copper(II) and Sulfate Ions in Synthetic Brochantite and Its Decomposition Products

Compound	Weight % Cu^{2+} Obsd.	Cu^{2+} Calcd.	SO_4^{2-} Obsd.	SO_4^{2-} Calcd.
$Cu_4(OH)_6SO_4$	55.67 ± 0.61	56.20	22.07 ± 0.83	21.24
$Cu_4O_3SO_4$	63.01 ± 0.48	63.84	24.31 ± 0.72	24.12
CuO	80.43 ± 0.70	79.90	—	—

Figure 4.4 (combination of above two tables): Above table showing percent mass losses from the decomposition of brochantite. Below table showing the percent weights of decomposition product ions for brochantite. Tables from Tanaka & Koga 1990, 613.

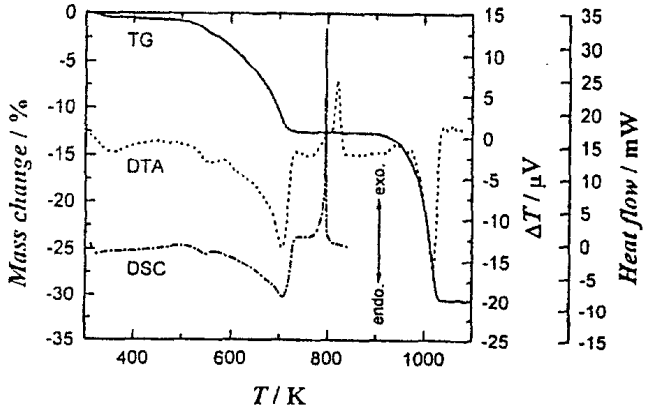


Figure 4.5: Typical simultaneous TG-DTA and DSC curves for the thermal decomposition of synthetic brochantite at a heating rate of 10K/minute (Koga *et al.* 1997, 1469).

2. In-situ recrystallization: Recrystallization of the dehydrated sample was recorded at 763K [489.85ºC] in flowing nitrogen gas for identification (XRD and FTIR) and then in flowing helium for DSC measurements. This confirmed that the stable intermediate product, until now identified as $Cu_4O_3SO_4$, is actually a mixture of CuO and dolerophanite, $CuO{\cdot}CuSO_4$ (Koga *et al.* 1997, 1473; Tanaka & Koga 1990, 613). This crystallization also produced a single, well-distinguished exothermic peak in DSC.

3. Thermal desulfurization: The desulfurization of $Cu_4O_3SO_4$ under isothermal (843K [569.85ºC] ≤ T ≤ 900K [626.85ºC]) and linearly increasing temperature conditions in flowing nitrogen gas were recorded and are represented by the final endothermic peak on **figure 4.5**, as confirmed by chemical analysis and mass loss data (Koga *et al.* 1997, 1469).

4.2.3. Isotopy of Atmospheric Sulfates and Brochantite

Isotopic Studies on Synthetic Sulfates

Analytical methods that use the measurement of $\delta^{18}O$ in sulfates have remained under-exploited. Much is known about oxygen isotopes in the atmosphere and influential factors, making oxygen isotopy a valuable experimental technique. The oxygen isotopes in atmospheric sulfates are of particular interest because, during oxidation, they undergo large fractionations while sulfur isotopes tend to result in relatively small fractionations. As a tool, oxygen isotopy can be applied to atmospheric sulfates to derive their formation mechanisms.

The most complete data on the control of $\delta^{18}O$ in sulfate, which have been published in a series of papers, are that of Holt, Cunningham, Engelkemeir and Kumar (Holt & Kumar 1991; Holt *et al.* 1978, 1979, 1981a, 1981b, 1982, 1983). They developed a method of analysis based on $\delta^{18}O$ values in atmospheric sulfates and water that allows for estimations of the relative amounts of primary sulfates (sulfates formed within combustion sources before emission into the atmosphere) and secondary sulfates (sulfates formed in the atmosphere, principally from SO_2, by hydrolysis-oxidation and oxidation-hydrolysis processes) at a given receptor site (Holt & Kumar 1991, 27). Holt and collaborators used this technique to aid in identifying the source regions that lead to polluted precipitation at a given time. The same analytical framework is investigated here for potential use in determining whether stable oxygen isotope analysis can be used to trace the formation mechanisms of copper sulfate minerals like brochantite.

The methods used by Holt and collaborators involved liquid preparations, preparations in humid air and one high-temperature preparation (intended to simulate primary sulfate formation). Their data were based on the control of $\delta^{18}O$ in sulfate formed by oxidation of the intermediate specie, SO_3^{2-}. The following aqueous-phase reactions were carried out by Holt *et al.* (1982, 51):

$$SO_2 + H_2O \rightleftharpoons SO_2 \cdot H_2O \rightleftharpoons HSO_3^- + H^+$$

Isotopic equilibrium accompanies this chemical equilibrium, and the intermediate species (HSO_3^- and/or SO_3^{2-}) are consequently composed of three oxygen atoms with an average isotopic enrichment that is heavily influenced by the solvent water. During heterogeneous reactions, this isotopic equilibrium essentially reaches completion prior to oxidation (Holt *et al.* 1982, 51). This is not surprising considering water is always in large excess in the atmosphere, whether as vapor or liquid. This also means that the initial $\delta^{18}O$ of emitted SO_2 has no appreciable effect on the $\delta^{18}O$ of secondary sulfates formed in the atmosphere (Holt *et al.* 1982, 51). The bisulfite ion was then reacted with air and Fe^{3+}, air and charcoal, and H_2O_2 to form the sulfate ion (SO_4^{2-}) (*ibid.*). The following nonliquid-phase reactions were carried out by Holt *et al.* (1982, 51):

$$SO_2 + H_2O_{(g)} \rightleftharpoons SO_2 \cdot H_2O$$

To form H_2SO_4, this product was reacted with air and an electric spark (to simulate lightning in the atmosphere), air and NO_2 (simulating NO_x pollution), air and γ-ray (simulating hydroxyl radicals),

and air and charcoal (simulating SO_2 adsorption on soot particles) (Holt & Kumar 1991, 34-5; Holt *et al.* 1982, 51). Finally, the following elevated-temperature reaction sequence accompanied by hydration was carried out to represent primary sulfate formation:

$$SO_2 + \tfrac{1}{2}O_2 \xrightarrow[Pt]{400^\circ \text{ to } 500^\circ} SO_3$$

$$SO_3 + H_2O_{(g)} \rightarrow H_2SO_4$$

(Holt *et al.* 1982, 51)

There are no experimental data that allows for an isotopic comparison of sulfates that were clearly formed by the aqueous and gaseous pathways. However, there is a considerable difference between the oxygen isotopes in the air and those of atmospheric waters (Holt *et al.* 1979, 44). Air oxygen (O_2) has a high $\delta^{18}O$ value of +23.5‰, while atmospheric water has low $\delta^{18}O$ values (0.00‰ for sea water and down to -50‰ for atmospheric water) (Holt *et al.* 1979, 44; Holt & Kumar 1991, 32; Novák *et al.* 2007, 706). As shown in **figure 4.6**, the $\delta^{18}O$ of primary sulfates are much higher and less dependent on the $\delta^{18}O$ of the associated water than secondary sulfates.

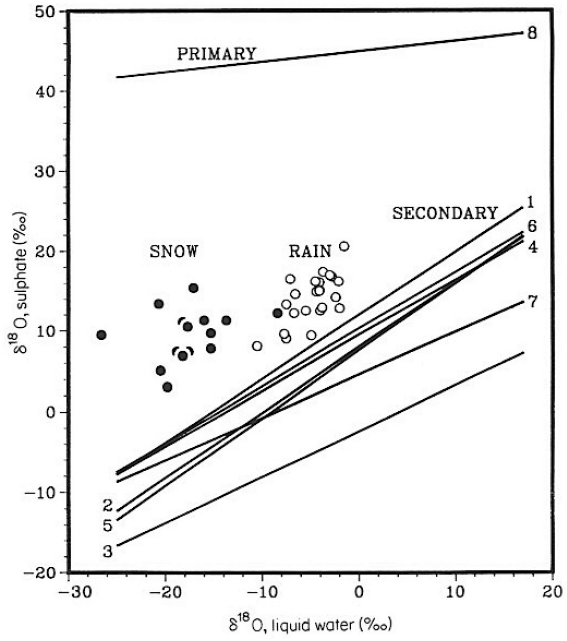


Figure 4.6: Comparison of sulfates formed by the seven reactions carried out by Holt and collaborators (Holt & Kumar 1991, 35). Curves 1, 2 and 3 involved the aqueous oxidation of SO_2; curves 4, 5, 6, and 7 involved the non-aqueous oxidation of SO_2. The plot also displays isotopic precipitation water data (rain and snow) collected at Argonne, Illinois, October 1976 through March 1978 (*ibid.*).

Impressively, Holt and collaborators found that by varying the $\delta^{18}O_{H2O}$ during Fe^{3+}-catalyzed as well as un-catalyzed oxidation of SO_3^{2-} in water exposed to air, the water contributed approximately 75% of the SO_4^{2-} oxygen:

$$\delta^{18}O_{SO4} = \sim 0.75(\delta^{18}O_{H2O}) + K$$

where intercept K was dependent on experimental conditions (Holt *et al.* 1981b, 563-4). Thus, the yielded sulfate ion approaches an isotope content of three oxygen atoms originating from the water and one oxygen atom apparently derived from O_2:

$$SO_3^{2-} + \tfrac{1}{2}O_2 \Rightarrow SO_4^{2-}$$

A different relationship can be obtained from oxidizing SO_2 with hydrogen peroxide in aqueous solution, which yields sulfates with approximately 57% of the oxygen contributed by the water, as described by the following regression curve:

$$\delta^{18}O_{SO4-} = \sim 3/5\ \delta^{18}O_{H2O} + K$$

(Holt *et al.* 1981b, 564).

The 3/5 slope suggests a five-oxygen intermediate is formed (peroxymonosulfurous acid, $H_2O_2 \cdot HSO_3^-$), where the sulfite contributes 3 oxygen isotopically controlled by the water, two from the peroxide (whose O-O bonds remain intact during oxidation) and none from SO_2 (Holt *et al.* 2981b, 564). The main limitation for this pathway is that the $\delta^{18}O$ of H_2O_2 in the Earth's atmosphere is unknown (Van Stempvoort & Krouse 1994, 451). In fact, the $\delta^{18}O$ of most atmospheric oxidants other than O_2 (such as O_3, H_2O_2 and NO_x) and of free radicals (such as $^{\bullet}OH$ and $^{\bullet}HO_2$) have not been determined (Holt *et al.* 1981a, 804). It is perhaps more accurate to state that 60-75% of the oxygen in atmospheric secondary heterogeneous sulfates is contributed by water and its oxygen isotope composition.

The isotopic mechanism for heterogeneous oxidation by ozone remains controversial and needs resolution. There are two different proposed oxidation mechanisms. One is a free radical mechanism that involves $^{\bullet}OH$, $^{\bullet}HSO_3$ and $^{\bullet}HSO_5$ as principal radicals (Savarino *et al.* 2000, 29085). The other is a non-radical mechanism that proceeds via an electrophilic displacement reaction of ozone on the sulfur atoms of the sulfate species in the aqueous phase (*ibid.*). The number of oxygen atoms contributed from ozone to each molecule of sulfate is identical in both mechanisms, that is, ¼ of the sulfate oxygen derives from O_3 (*ibid.*). Ozone and H_2O_2 concentrations in the troposphere are not uniform and vary from day-to-day and place-to-place. Moreover, the stable oxygen isotope compositions of ambient oxidants (such as O_3, H_2O_2, NO_x and of free radicals including $^{\bullet}OH$) have not been determined (Holt *et al.* 1981a, 804; Van Stempvoort & Krouse 1994, 451).

Holt and collaborators also carried out experiments on heterogeneous phase reactions using water vapor rather than liquid water. Like the aqueous reactions, this pathway showed rapid isotopic equilibration between the SO_2 and water vapor. Using different oxidative conditions, including the introduction of a high-voltage spark, gamma radiation, NO_2, and exposure to charcoal, the results varied but fit into the 60-75% range proposed for aqueous-phase reactions (Holt *et al.* 1981b, 630).

Significantly less is understood about the homogeneous pathway. Remembering:

(R1) $SO_2 + {}^{\bullet}OH \rightarrow {}^{\bullet}HOSO_2$,

(R2) $^{\bullet}HOSO_2 + O_2 \rightarrow SO_3 + {}^{\bullet}HO_2$,

(R3) $SO_3 + H_2O \rightarrow H_2SO_4$

In reaction 3, the H_2O and SO_3 combine, suggesting an oxygen contribution from H_2O to sulfate of around 0.25 (one oxygen from H_2O, and the rest from SO_3). Studies by triple oxygen analysis (^{16,17} and ^{18}O) have suggested this ratio is actually a bit lower, at 0.21 ± 0.01 (Savarino *et al.* 2000, 29084). Reaction 2 may be dominated by oxygen isotopic exchange with excess O_2, meaning the SO_3 is controlled by molecular oxygen, which has a constant $\delta^{18}O$ of +23.5‰ (*ibid.*).

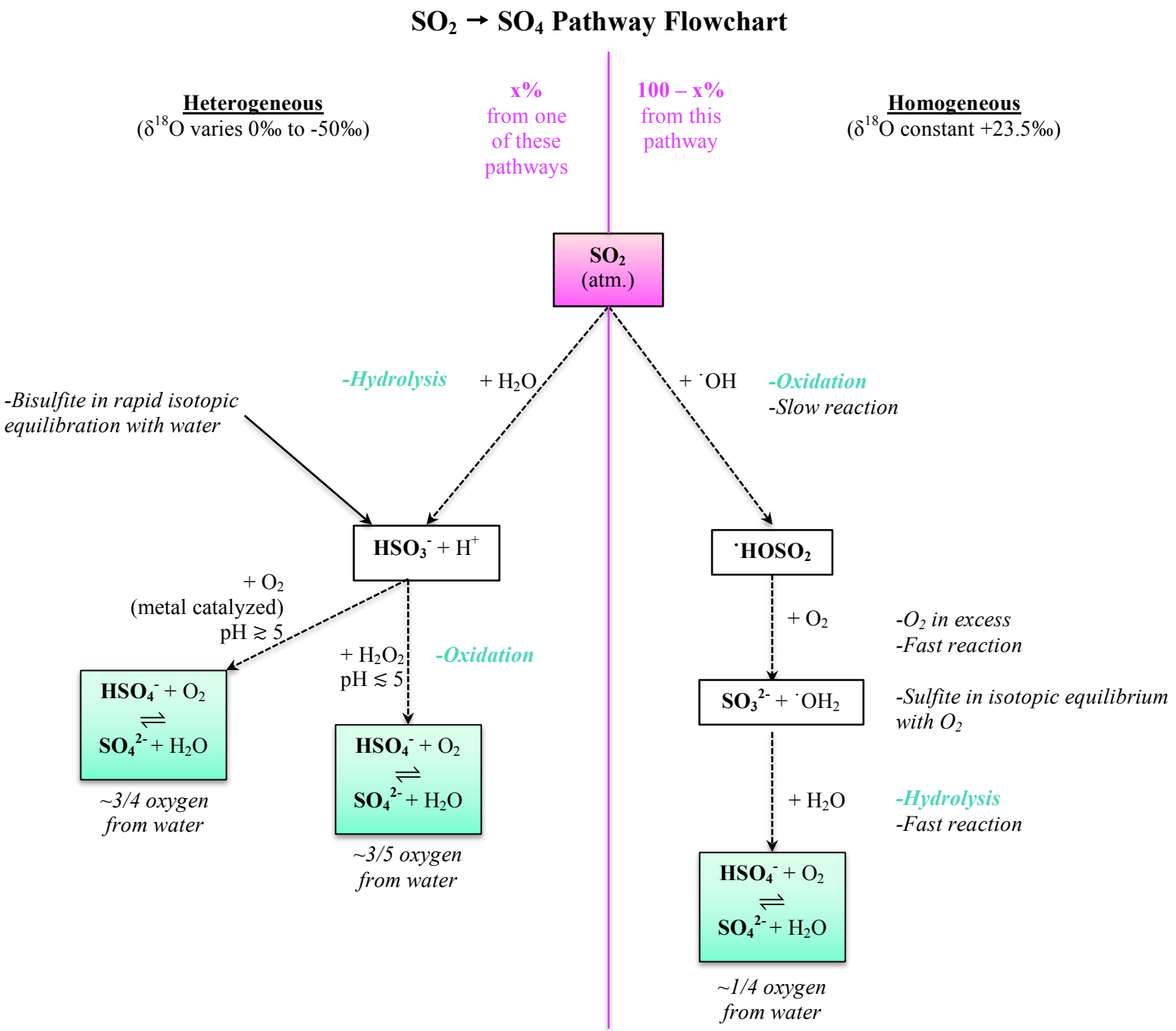

SO2 → SO4 Pathway Flowchart
Heterogeneous
(δ18O varies 0‰ to -50‰)
x%
from one
of these
pathways
100 – x%
from this
pathway
Homogeneous
(δ18O constant +23.5‰)
SO2
(atm.)
-Hydrolysis
+ H2O
+ ˙OH
-Oxidation
-Slow reaction
-Bisulfite in rapid isotopic
equilibration with water
HSO3- + H+
˙HOSO2
+ O2
(metal catalyzed)
pH ≳ 5
+ H2O2
pH ≲ 5
-Oxidation
+ O2
-O2 in excess
-Fast reaction
HSO4- + O2
⇌
SO42- + H2O
~3/4 oxygen
from water
HSO4- + O2
⇌
SO42- + H2O
~3/5 oxygen
from water
SO32- + ˙OH2
-Sulfite in isotopic equilibrium
with O2
+ H2O
-Hydrolysis
-Fast reaction
HSO4- + O2
⇌
SO42- + H2O
~1/4 oxygen
from water

Figure 4.7

Isotopic Studies on Environmental Sulfate

It is worthwhile to compare the laboratory-controlled results with those obtained from different environmental samples, especially considering that these are the conditions under which brochantite is formed on copper roofs. As is the case for aqueous sulfates, the measured isotopic composition of sulfate minerals approximates the isotopic composition of the formation water (Seal *et al.* 2000, 551).

Holt and collaborators carried out analyses on environmental samples, distinguished as precipitation sulfates and particulate sulfates. Isotopic analyses of sulfates in precipitated water have led to at least three significant observations (Holt & Kumar 1991, 34 & 36):

1. The $\delta^{18}O$ of sulfate varies seasonally and in phase with corresponding isotopic variations of the precipitation water. The amplitude of the seasonal variation of $\delta^{18}O$ in precipitation sulfate is about three-quarters that of the precipitation water.
2. The $\delta^{18}O$ of sulfates in precipitation is higher than that of sulfates prepared in the lab by a variety of methods to simulate secondary sulfate formation, and higher than that of sulfates prepared in the lab by high temperature SO_3 formation to simulate primary sulfate formation.
3. Near seacoasts, the $\delta^{18}O$ of precipitation sulfates may be significantly affected by sea spray (Mizutani & Rafter 1969c and Cortecci & Longinelli 1970 cited in Holt & Kumar 1991, 36).

The first and second observations are interesting since they may be applied to the corrosion of exposed copper in urban environments. The copper corrosion samples considered for this investigation are not from marine sites, and therefore the third observation cannot be relevantly discussed.

Referring to the first observation, the amplitude of the sulfate actually varied less than 3/4, closer to about 70%, which is still consistent with the laboratory results that suggest an oxygen isotope correlation between the sulfate and water of about 60-75% (Holt *et al.* 1979, 46). Sulfates formed from water vapor also varied seasonally, but at levels about 10% lower than the corresponding precipitation water vapor (Holt *et al.* 1979, 48). It is hypothesized that this difference is due to the isotopic shift characteristic of the phase change of gaseous to liquid water at ambient temperatures (*ibid.*). The variation of $\delta^{18}O$ with seasonal change particulate sulfate is apparently random; however, the average over a two-year period is close to that of participation sulfates (Holt *et al.* 1979, 48-9; Holt *et al.* 1981a, 805). The differences in $\delta^{18}O$ between precipitation and particulate sulfates in the atmosphere could be due to the prompt removal of precipitation sulfates in rain or snow, whereas particulate sulfates remain in the atmosphere longer (that is, at least long enough to become effectively intermixed with particles with different seasonal origins) (Holt *et al.* 1979, 51-2). Yet, since the two-year average of $\delta^{18}O$ in aerosol and precipitation sulfates is about equal, Holt and collaborators (1981a) postulated that both sulfate

varieties were probably formed by the same heterogeneous oxidation mechanism in the clouds (805).

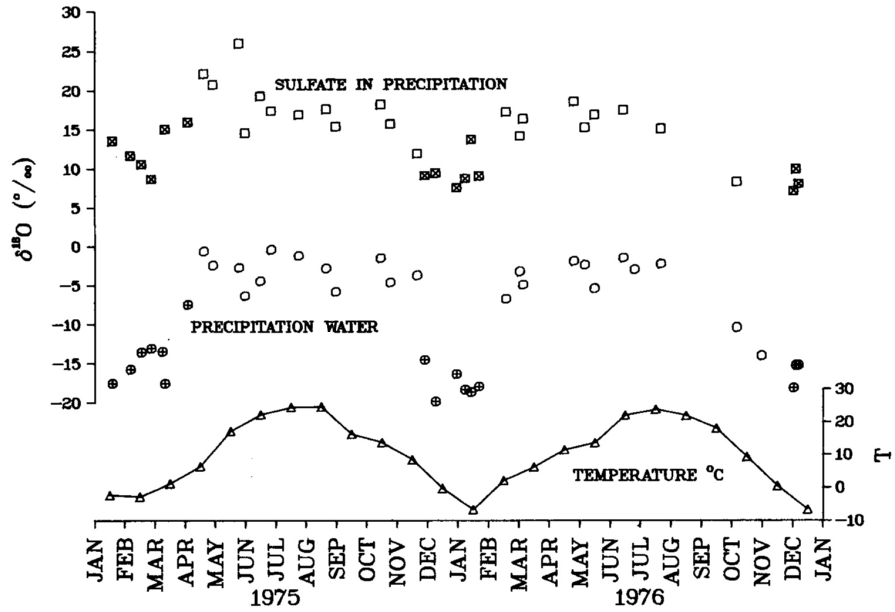


Figure 4.8: Isotopic results obtained for precipitation water and for the sulfates dissolved in water. The open data points represent rain; the crossed pointed represent snow. The average monthly temperatures at Argonne, Illinois, 1975-6 are also plotted for comparison (Holt *et al* 1978, 46-7).

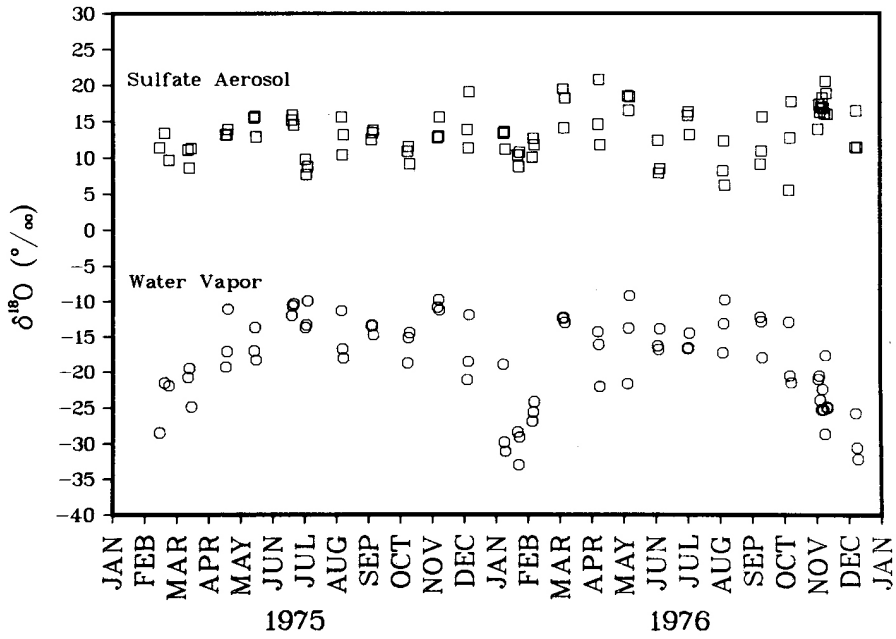


Figure 4.9: Isotopic results for particulate sulfates and water vapor at Argonne, Illinois, 1975-6 (Holt *et al.* 1978, 48). The isotopic results for the water vapor are comparable to those of precipitation sulfate and precipitation water, found on **Figure 4.8**. The $\delta^{18}O$ of particulate sulfate varied randomly with season.

Holt and collaborators regard the discrepancies described for the second observation as simply an indication that atmospheric sulfates have been made via a combination of mechanisms

with components more highly concentrated in $\delta^{18}O$ than was isotopically examined in the laboratory.

Thus far, the oxygen isotopy of secondary sulfates has been discussed. Primary sulfates are generally easily distinguished from secondary sulfates in the atmosphere because primary sulfates tend to be much higher in $\delta^{18}O$ (**figure 4.6**). This also allows their reactive amounts in the atmosphere to be estimated by isotopic analysis (Holt *et al.* 1982, 631). The formation mechanism for primary sulfates begins with sulfur trioxide, which is formed at high temperatures in $SO_2 - O_2 - SO_3$ systems in exhaust gases from smelters, power plants, combustion engines, et cetera, and is continuously emitted into the atmosphere (Holt & Kumar 1984 cited in Holt & Kumar 1991, 32). As the exhausted gases cool, the SO_3 rapidly reacts with combustion-produced water vapor, which is relatively high in $\delta^{18}O$ as a result from its prior high-temperature isotopic equilibration with air oxygen (*ibid.*). Likewise, the hydrated sulfuric acid that is formed has a relatively high $\delta^{18}O$.

4.3. MALACHITE, $Cu_2CO_3(OH)_2$

In the soil environment, the principal copper corrosion product is not a sulfate, but the carbonate mineral, malachite. Malachite commonly occurs naturally in large supergene assemblages around the world, where they have economic value and are intensively mined. On buried copper-alloy substrates, corrosion products form in layers, which often preserve the original surface of the metal. Again, malachite is the favored mineral. Oxygen and carbon isotope studies have been conducted on synthetic and geological malachite, but very little has been done on archaeological or historic malachite. Since the formation pathways between synthetic, geological and archaeological malachite are different, the results obtained from synthetic and geological samples cannot be assumed to be totally representative of archaeological malachite as well. The following sections are focused on synthetic and geological malachite, since these have been studied and published, and serve as references to compare the data obtained from archaeological and historic malachite for this doctoral study.

4.3.1. Formation of Supergene Carbonate Minerals and Malachite

Formation of Geological Malachite

The geological genesis of copper deposits start with a cupric "protore" [*prot* + *ore*], typically an igneous crystalline material containing sufficient disseminated copper sulfides for enrichment into ores (Melchiorre 1998, 24-5). Enrichment occurs when oxidizing meteoric waters percolate through the vadose zone. As these fluids travel downward, they dissolve pyrite (FeS_2) and produce sulfuric acid (Melchiorre 1998, 25). In turn, this acidity dissolves primary copper minerals (usually cuprite or a sulfide) in the protore and increases the environmental copper ion concentration (*ibid.*). The meteoric fluid may also increase in carbon dioxide concentration as it travels through the soil, since it is more abundant than in the atmosphere. These changes in Cu^{2+},

pH and P_{CO2} pass the stability fields of various copper minerals, including malachite (refer to **figure 4.12**).

Voids within a host-rock are also necessary for the formation of malachite (De Putter *et al.* 2010, 99). These voids serve as preferential drains for the circulation of fluids, which can also widen the space. When malachite forms in a calcareous host-rock, a different mechanism occurs in which carbonate is sourced from the dissolution of the rock. In non-calcareous rocks, carbon dioxide is sourced from meteoric fluids or in a form derived from overlaying carbonate formations (De Putter *et al.* 2010, 99). Malachite precipitation can also occur by mixing between copper and bicarbonate solutions and/or by evaporation and saturation (Melchiorre 1998, 26).

Oxide development during the formation of malachite is mainly controlled by the position of the water table, climate and host-rock properties. The position of the water table, which can change over time, usually represents the boundary between oxidizing and reducing environments. High water tables result in smaller oxidation zones, a limiting factor for malachite formation. Temperature can affect malachite formation rate (precipitates more slowly at 10ºC than at 50ºC), with freezing temperatures restricting water flow and enrichment (Melchiorre 1998, 27). The amount of rainfall is another important climatic factor, since little or infrequent precipitation reduces mobility and chemical interactions, while excessive rainfall can cause the water table to rise so rapidly that oxidation mineralization is minimal before the zone is drowned in a low-pH, reducing environment (*ibid.*). The physical properties of the host-rock, like porosity, can enhance or retard oxidation as well.

Corrosion Mechanisms of Archaeological Malachite

Patinated archaeological bronzes have many common morphological features, including tin-enriched corrosion layers. Ancient and historic bronzes can contain up to around 28% tin, but most have tin contents less than 17% (Scott 2002, 400 & 402). Studies on the chemical characteristics and structures of natural patinas formed on buried bronze objects have shown two main types of corrosion structures, depending on whether an original surface (marker layer preserving the original shape of the artifact) is present (Piccardo *et al.* 2007, 240; Robbiola *et al.* 1998, 2090). Often, both types of corrosion are found on the same object. Type I patinas (**figure 4.10**) have even surfaces and are characterized mainly by a bilayer. Type II structures (**figure 4.11**) are characterized by the loss of the original surface and schematically represented in three layers. These corrosion layers bridge the non-equilibrium condition between the metal and soil. The first corrosion products usually show a composition that is nearly in equilibrium with the metal, and the outer layers develop compositions that are in near equilibrium with the soil (Wagner *et al.* 1997, 22).

The formation process for type I corrosion structures is mainly related to the oxidation of the bronze alloy and the selective dissolution of copper (decuprification) (Piccardo *et al.* 2007, 239; Robbiola & Hurtel 1997, 110). Oxidized tin (possibly as SnO_2, occasionally hydrated) has a lower standard Gibbs energy of formation than CuO_2 (-519 and -146kJ/mol at 298K [24.85ºC],

respectively), which means tin dioxide should form more easily than cuprous oxide (Robbiola *et al.* 1998, 2104). This explains the observed tin enrichment of the inner layer of corrosion. Copper oxides and hydroxides are also present. The external layer forms cupric (copper II) compounds with available soil elements (e.g. hydroxycarbonates, hydrosilicates, hydrosulfates). The two layers that form in type I structures have excellent protective properties that preserve the original surface of the artifact by growing into the alloy. Type I structures have been observed on archaeological bronzes with low and high tin contents, but sometimes the inner layer is not present (Robbiola & Hurtel 1997, 109-10).

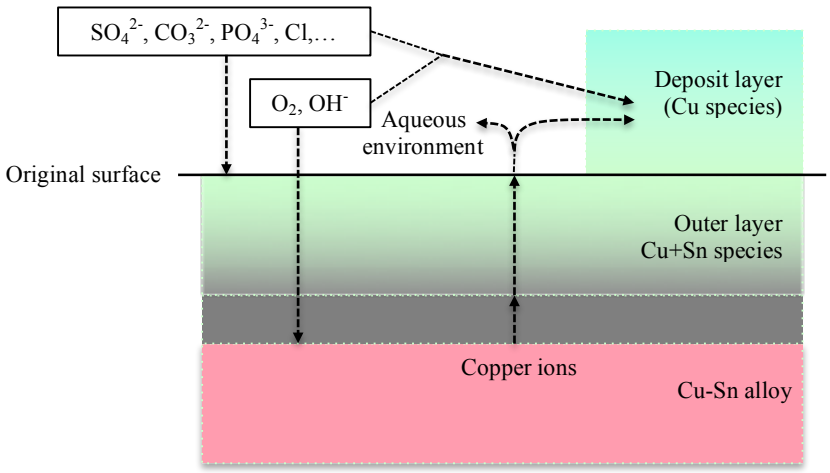


Figure 4.10: Representation of type I corrosion layering on copper alloys (adapted from Piccardo *et al.* 2007, 241).

Type II structures are the effect of more severe corrosive attacks (e.g. pits, crevices and lamellar corrosion) due to a high dissolution rate, which prevents the initial stabilization of tin compounds observed in type I structures. Instead, copper minerals form over the original surface, deforming features. As it thickens, the cuprous corrosion layer will slow alloy dissolution and migration, eventually allowing tin products to stabilize between a cuprous oxide layer and the alloy, creating the inner zone. Therefore, type II is a three-layer structure characterized as follows:

1. The external "green" zone consisting of copper compounds such as malachite. This layer tends to be thicker and rougher than the external layer of type I structures due to the more severe dissolution of the alloy at the beginning of the corrosion process.
2. Cuprous oxide forms the middle layer and serves as an electrical membrane allowing for the transport copper ions outward and environmental anions (O^{2-}, Cl^-) inward.
3. An internal zone formed by tin enrichment and a selective depletion of copper. Chlorinated environments will produce relatively high chloride contents at the internal layer – alloy interface (Piccardo *et al.* 2007, 240; Robbiola *et al.* 1998, 2097).

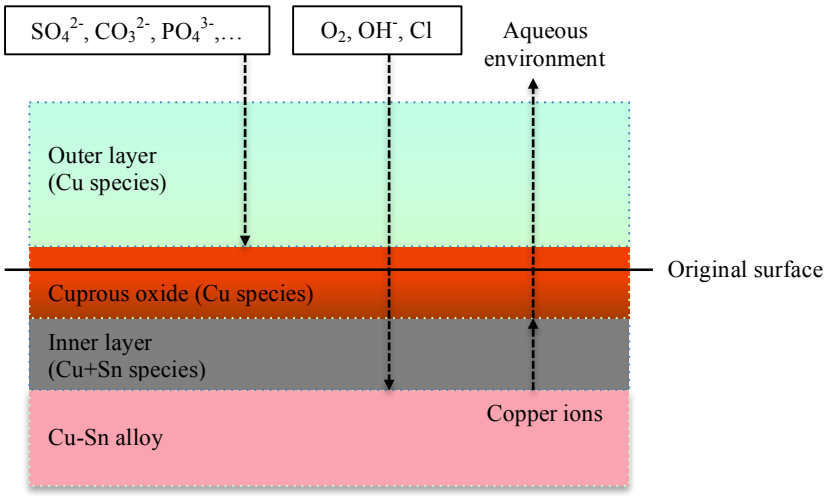


Figure 4.11: Representation of type II corrosion layering on copper alloys (adapted from Piccardo *et al.* 2007, 241).

In both types (I and II), there are ion migration processes (cations out, anions in), decuprification, and the presence of tin compounds acting as structural stabilizers of the patinas (Piccardo *et al.* 2007, 242). These tin compounds tend to be poorly crystallized or amorphous (hydrated tin oxide easily forms gel-like compounds), and their presence cannot be confirmed by the usual methods of characterization (e.g. XRD or IR). To identify the structural types and elements within, previous investigators mainly used cross sections of archaeological artifacts set in resin and polished for SEM-EDXS. It is expected that the more severe the corrosive environment, the more copper is dissolved, resulting in higher Sn/Cu ratios in the corrosion layers.

Both types of corrosion structures are usually found on the same object. As an example for the formation of malachite, cuprite can form epitaxially[1] as a direct reaction of copper with dissolved O_2 or water. Cuprite has a high electrical conductivity and controls the cationic migration of copper ions by allowing them to dissolve from the alloy and travel through the cuprite layer to the surface, where they react with soil species in aqueous solutions (Robbiola & Hurtel 1997, 110, 116; McNeil & Little 1992). If the water has a high concentration of carbon dioxide, then malachite can form over the cuprite. As with geological malachite, the oxidizing meteoric fluids that form carbonate minerals typically descend containing carbon dioxide from the atmosphere, and collect more carbonate species as they pass calcareous formations.

[1] As corrosion products form, they can be grouped into the following events: epitactic, topotactic and reconstructive (Scott 2002, 13). In epitactic mineral growth, the copper alloy substrate serves as a seed crystal for the corrosion products that orient from it. This epitaxial relationship results in the cationic corrosion that retains the original shape and surface detail of an object. Topotactic mineralization results in the solid-state transformation of one corrosion product to another. An example is the alteration of cuprite (Cu_2O) to tenorite (CuO). Cuprite is characteristic of an epitactic product, but during the transformation, the crystal lattice changes and the resulting tenorite does not necessarily reflect the original surface of the object. In a reconstructive event, a corrosion product is completely dissolved or chemically altered to form an entirely different product.

4.3.2. Stability and Thermal Decomposition of Malachite

Pourbaix diagrams indicate that malachite is the stable phase in equilibrium with most fresh ground and surface waters in contact with the atmosphere (Woods & Garrels 1986, 182-185). This is due to the high levels of carbon dioxide generated by the oxidation of organic material in surface and sub-surface soil-waters, which favors the stabilization of malachite over brochantite (Selwyn 2004, 65; Woods & Garrels 1986, 185). Since many of the same environmental factors apply to buried archaeological copper, the stable phases are also cuprite and malachite. This natural transition of copper to cuprite to malachite is extremely difficult to replicate in a laboratory, making it a good indicator of naturally formed patinas (Scott 2002, 106).

The chemistry of the crystallization and stabilization of malachite under all possible conditions is difficult and complex since malachite occurs together with many other species. It is also possible for copper (II) salts to change phase by a process of partial or complete dissolution of the original phase followed by the precipitation of a new phase (Selwyn 2004). The typical environmental conditions for malachite precipitation and stability are described here, however malachite has been observed in nature as the stable phase in areas outside this chemical range. Malachite stability is generally bracketed at low temperatures (thermal decomposition described later in this section), in slightly acidic conditions (pH between approximately 7 and 8), and at P_{CO2} levels between $10^{-1.5}$ and $10^{-2.5}$ atm., which are the conditions commonly found in groundwater (De Putter *et al.* 2010, 98; Vink 1986, 46). At the surface, meteoric water is less acidic and has lower P_{CO2}. These conditions favor other phases, typically brochantite and paratacamite, over malachite. The turning point for malachite formation and stabilization is at pH = 6.95 with a corresponding $P_{CO2} = 10^{-3.45}$ atm. (Vink 1986, 46). **Figure 4.12** shows the variation of the stability of malachite in Pourbaix diagrams, as a function of CO_2 pressure and $SO_{3(aq)}$ concentration. Clearly malachite has a restricted stability field in surface meteoric water compared to groundwater conditions.

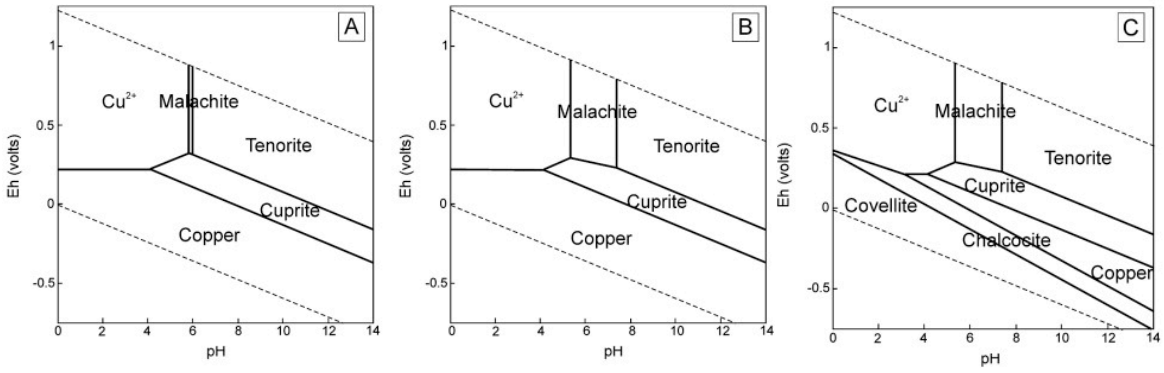


Figure 4.12 (A, B & C): Pourbaix diagrams for copper and ionic species: showing the common parameters of $Cu^{2+} = 10^{-4}$ M, T = 25ºC and P = 1013 bar. **A**: today's meteoric water in equilibrium with ~400pppmv atmospheric CO_2 ($P_{CO2} = 10^{-3.4}$); **B**: typical groundwater ($P_{CO2} = 10^{-2}$) and **C**: typical groundwater ($P_{CO2} = 10^{-2}$) with 200 mg/l $SO_{3\,(aq)}$. Adapted from De Putter *et al.* 2010, 98.

Most research on synthetic malachite suggests it decomposes thermally in a single step to produce carbon dioxide gas, water vapor and tenorite, as follows:

$$Cu_2(OH)_2CO_3 \rightarrow 2CuO + CO_2 + H_2O$$

This step occurs at around 380ºC, with DTA showing a smooth single-step mass-loss trace and a well-shaped single endothermic peak, as shown in **figure 4.13** (Koga & Yamada 2005, 349; Koga *et al.* 1999, 388). The rate of decomposition of synthetic malachite under atmospheric conditions is influenced by the partial pressure of the self-generated gasses, CO_2 and H_2O, which change evolution rates during the reaction (Koga *et al.* 1999, 393; Reading & Dillimore 1994, 119).

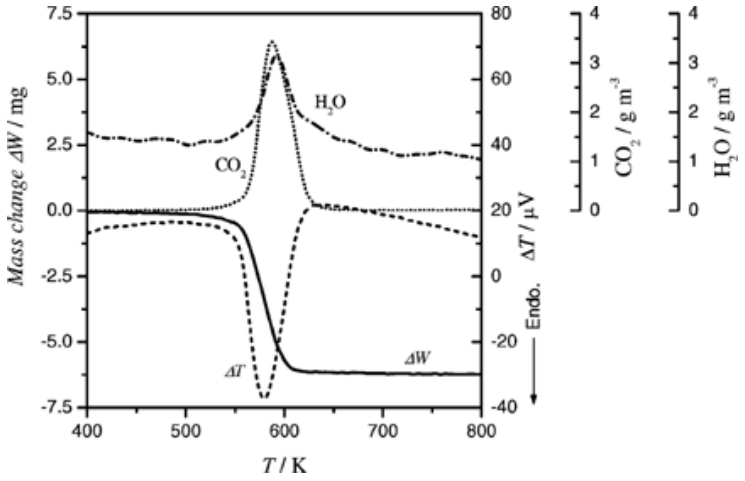


Figure 4.13: Typical TG-DTA-EGA curves for the thermal decomposition of synthetic malachite (20.08 mg) at the heating rate of 10 K/min under flowing dry N_2 (200 cm^3/min) (Koga & Yamada 2005, 348).

Few thermal decomposition studies have been carried out on natural malachite under conditions representative of the supergene environment. Moreover, claims based on empirical studies have suggested that malachite decomposes over a range of temperatures. A convincing study by Frost *et al.* (2002) using natural malachite has a complicated decomposition with six weight loss steps, as shown in **figure 4.14** and described as follows:

1) The first weight loss step is 1.7% of the total weight loss. Mass spectrometry shows that water is the only evolved gas at this point, along with some dehydroxylation.
2) The total weight loss after steps 1 and 2 is 6.9%. This is primarily a dehydroxylation step, with water vapor as the evolved gas. A mechanism is suggested in **table 4.1**.
3) The weight loss for this step is 9.4%. Mass spectrometry shows that both CO_2 and H_2O gasses are evolved at this step, which takes place at 332ºC.

4-5) Observed at 345ºC (step 4) and 432ºC (step 5) involving further loss of hydroxyl units and CO_2, with copper oxide product.

6) Occurring at around 840ºC, this is the step where copper oxide is deoxygenated.

According to this study, dehydroxylation commences at around 250ºC, which continue liberating concurrently with CO_2 gas above 325ºC, and the loss of both gas products completes simultaneously at 450ºC (Frost *et al.* 2002, 141, 143). The theoretical weight loss for malachite is

8.1% for the hydroxyl units and 19.9% for the CO_2, making a total loss of 28% (Frost *et al.* 2002, 139). This study had a measured weight loss of 28.9%, which is close to the theoretical value. The difference may be accounted for by adsorbed water.

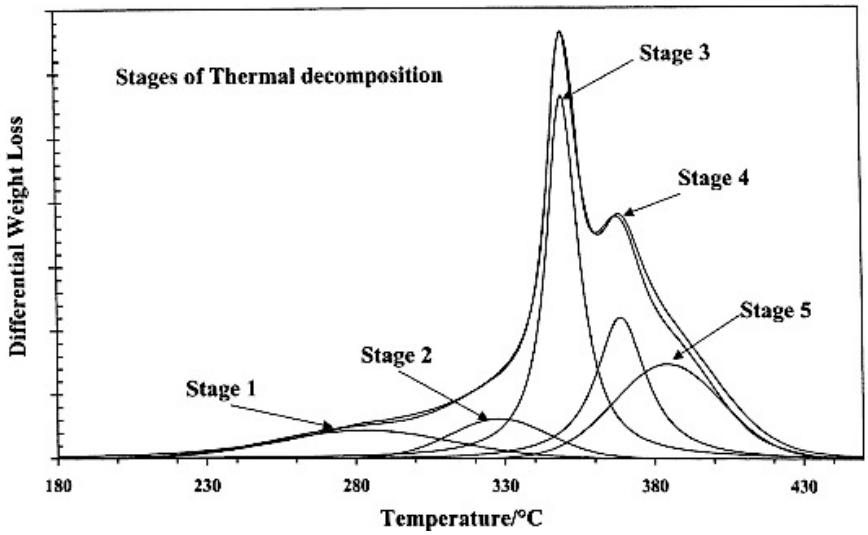


Figure 4.14: Component analysis of the differential thermogravimetric analysis of malachite (Frost *et al.* 2002, 136).

Results of the Stages of the Thermal Decomposition of Malachite

	Temperature[a](°C)	Theoretical weight loss (%)	Proposed thermal reaction of malachite ($Cu^{2+}_2(CO_3)(OH)_2$)
Step 1	250 (1.7)	8.1	Loss of OH units as water
Step 2	321 (5.2)		Loss of OH units—dehydroxylation: $Cu^{2+}_2(CO_3)(OH)_2 \rightarrow 2Cu^{2+}_2(CO_3)_2(OH) + H_2O$
Step 3	332 (9.4)	19.9	$Cu^{2+}_2(CO_3)_2(OH) \rightarrow CuCO_3 + CuO + CO_2+H_2O$
Step 4	345 (5.9)		Loss of water and carbon dioxide: $Cu^{2+}_2(CO_3)_2(OH) \rightarrow CuCO_3 + CO_2 + H_2O$
Step 5	362 (6.7), total decarboxylation = 21.95		Loss of carbon dioxide only: $CuCO_3 \rightarrow CuO + CO_2$
Step 6	842 (6.4)		Loss of oxygen: $CuO \rightarrow Cu_2O + O_2Cu_2O \rightarrow Cu + O_2$

[a] The respective values for weight loss (% per unit area) are given in parentheses.

Table 4.1: Thermal decomposition of geological malachite (adapted from Frost *et al.* 2002, 135).

4.3.3. Isotopy of Supergene Carbonates and Malachite

Malachite will precipitate very close to isotopic equilibrium with its environment. Once formed, oxygen isotopes in low-temperature minerals like malachite do not appear susceptible to isotopic exchange at sedimentary or diagenetic temperatures (<200ºC) (Bird & Chivas 1988; Kyser & Kerrich 1991; Yapp 1991 cited in Zheng 1998). This is due to low solubility and an extremely slow rate of solid-state diffusion at low temperatures, making significant isotope exchange unlikely

(O'Neil 1987 cited in Melchiorre 1998, 233). During formation, oxidizing meteoric fluids typically descend and react with ore minerals, lending to a corresponding diagnostic oxygen isotope signature to the malachite that forms. Being well preserved, the oxygen isotope composition of malachite serves as an important tool when analyzing the formative mechanisms.

Oxygen isotopy of metal carbonates and water has generally been pursued through theoretical calculations, experiments and empirical observations. The $\delta^{18}O$ values of carbonate minerals have been studied to better understand the formation mechanisms of ore depositions, especially to determine equilibrium fractionation factors, yield information about the temperatures of formation, and propose origins and the evolution of ore-forming fluids. However, the relative results for oxygen isotope fractionation between carbonates and water obtained by various investigators are not consistent due to the approaches using several assumptions and corrections that considerably alter the results (Gilg *et al.* 2008, 119). Moreover, theoretical investigations for malachite have not been calculated or presented (*ibid.*).

Experimental studies on the $\delta^{18}O$ values of low-temperature minerals have shown relations to the oxygen isotope composition of the formative meteoric waters by a temperature-dependent fractionation factor (Lawrence & Taylor 1972; Savin 1980; Yapp 1987; Chen *et al.* 1998; Bird *et al.* 1989 cited in Zheng 1998). E. B. Melchiorre is the principal experimental investigator for malachite-water oxygen isotope fractionation. His work verified that natural malachite is dominantly controlled by the $\delta^{18}O$ values of ambient meteoric waters and surface temperatures, and established an empirical geothermometer. Melchiorre was also able to quantitatively demonstrate that malachite forms at temperatures much less than 100ºC (Melchiorre 1998, 247).

Since isotope exchange reactions between carbonates and water at low temperatures are too slow to reach equilibrium, Melchiorre isotopically studied synthetic malachite formed under rapid- and slow-precipitation conditions to define the malachite-water oxygen isotope fractionation factor. When the malachite-water oxygen isotope fractionation factor and the $\delta^{18}O$ of the formation water are known, the precipitation temperature of natural malachite can be quantitatively estimated. This method gives results that are generally consistent with most empirical and theoretical determinations for carbonate-water systems.

Rapid Precipitation

Synthetic malachite was rapidly precipitated from the reaction of $Cu(NO_3)_2$ with Na_2CO_3 solutions in a 1:1 molar ratio (Melchiorre 1998, 179). Melchiorre had problems with experimental reproducibility for the rapidly precipitated malachite. This malachite was also high in $\delta^{18}O$ relative to the slow-precipitated overgrowths that will be discussed next. He suggested that these results could be due to the initial precipitation of georgeite ($Cu_5(CO_3)_3(OH)_4 \cdot 6H_2O$, unstable amorphous form of malachite) in the rapid-precipitation experiments, and that differences in fractionation factors may exist between well-crystallized and poorly crystallized minerals (Melchiorre 1998, 28, 202). Georgeite may complicate the rapid-precipitation experiments because the fractionation between georgeite and water, and between georgeite and malachite may cause the enrichment

between slow- and rapid-precipitation experiments. The rapid-precipitation of malachite is therefore considered unreliable and does not reflect the true equilibrium isotope fractionations.

Slow Precipitation

A copper salt solution was reacted with calcite to slowly precipitate malachite (Melchiorre 1998, 172, 180):

$$2Cu^{2+}_{(aq)} + 2CaCO_{3\,(s)} + H_2O \rightleftharpoons CuCO_3{\cdot}Cu(OH)_{2\,(s)} + CO_{2\,(g)} + 2Ca^{2+}_{(aq)}$$

As shown in the equation above, this reaction releases CO_2 gas, which was distilled and analyzed on an isotopic ratio mass spectrometer (IRMS). The final water was also isotopically measured to provide a check for the integrity of the closed system used, which indicated the slow-precipitation data reached isotopic equilibrium (Melchiorre 1998, 182).

Oxygen fractionation factors for malachite-initial water [$\alpha_{mal\text{-}wi}$] and malachite-final water [$\alpha_{mal\text{-}wf}$] were calculated from the final $\delta^{18}O$ of the malachite product [$\delta^{18}O_{mal}$] and either the initial water $\delta^{18}O$ [$\delta^{18}O_{wi}$], or the final water $\delta^{18}O$ [$\delta^{18}O_{wf}$], using the well-known definition of α as a function of δ-values (Melchiorre 1998, 185):

$$\alpha_{mal\text{-}w} = \left(\frac{1000 + \delta^{18}O_{mal}}{1000 + \delta^{18}O_{w}}\right)$$

Values of $\alpha_{mal\text{-}wi}$ and $\alpha_{mal\text{-}wf}$ do not vary more than a few tenths of a per-mil from each other, as $\delta^{18}O_{wi}$ and $\delta^{18}O_{wf}$ are practically identical. The fractionation factor between malachite and water oxygen [$\alpha_{mal\text{-}w}$] is defined with a best-fit regression for both $\alpha_{mal\text{-}wi}$ and $\alpha_{mal\text{-}wf}$ combined as a function of temperature, as shown in **figure 4.15**. The equation for this line is:

$$1000ln\ \alpha_{\text{oxygen malachite-water}} = 2.66\left(\frac{10^6}{T^2}\right) + 2.66$$

with temperature in kelvin (Melchiorre 1998, 185). The deviation from this best-fit line for values of $1000ln\ \alpha_{mal\text{-}wi}$ and $1000ln\ \alpha_{mal\text{-}wf}$ for individual experiments is less than 1.0‰ (*ibid.*).

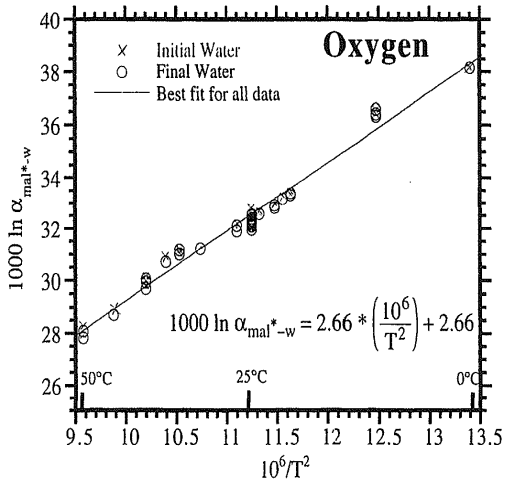


Figure 4.15: Malachite-water oxygen isotope fractionation as a function of temperature for slow precipitation experiments (Melchiorre 1998, 187).

CHAPTER 5

Sampling and Methodology

5.1. ANALYTICAL PROCEDURE FOR THE BROCHANTITE STUDY

A selection of brochantite samples were collected with good geographic variance. In a laboratory, the brochantite sulfate was converted to $BaSO_4$, then pyrolyzed in an elemental analyzer to obtain CO gas, the ^{18}O of which was then measured in a continuous flow isotope ratio mass spectrometer (CF-IRMS). The following sections discuss the reasoning and details for this analytical procedure.

5.1.1. Sample Collection Criteria

An objective for the analytical brochantite study was to create a database of $\delta^{18}O$ values for brochantite from a varying range of geographic sites with clear meteoric $\delta^{18}O$ differences. These values were compared to various local environmental parameters to identify the most influential factors and trends that may be used in provenance and authenticity studies.

To understand the reaction pathway between copper and its oxidizing environment, stable isotope information was extracted from brochantite samples isolated from scrapings off patinated copper roofs with known geographic locations (Oxford, Vienna, Ottawa and Tuscaloosa). It is important to remember that corrosion sampling is an interventive procedure. The brochantite study is focused on copper corrosion products formed in the open atmosphere, which is an unusual condition for archaeological remains. The theoretical framework of the brochantite study was later applied to the burial environment, which is more practical for archaeological remains, however this next step is the subject of a separate research project, presented in this thesis as the malachite study.

Synthetic corrosion samples were briefly considered until it became apparent that the requirements necessary to control various experimental factors as desired were too complex, too expensive or too slow. Synthetic experiments have no guarantee of success in terms of yielding sufficient products for analysis or even the correct products, and time restraints became a considerable problem since natural corrosion formation can take several decades on exposed copper and several years on accelerated tests. Even faster tests involve chemicals and conditions far from natural, which brought on concerns about the reliability of any correlations made between the isotopic data collected from accelerated, synthetic samples and natural samples. Ultimately, as simulating outdoor copper corrosion in a laboratory progressed to include more and more natural environment ingredients, experimental parameters eventually evolved into field tests before settling on outdoor historic and contemporary copper-alloy objects. Corrosion samples from such objects

allow for the direct analysis of naturally oxidized copper in the urban atmosphere. Furthermore, time restraints are no longer an issue and objects that have been exposed and corroding for years, decades and even centuries may be used.

The first consideration was to collect samples from bronze sculptures around Oxford, but as exposed works of art, these tend to have protective coatings, they get cleaned regularly, and their patinas are more likely valued aesthetically, meaning the people responsible are less likely to allow collection of ideal samples. As an alternative solution, the decision was made to collect corrosion samples from copper roofs. The copper used for roofing is relatively pure, tends not to be coated or treated chemically in any way, it has direct contact with rainwater, and it has been left to corrode for several decades. Moreover, estates staff feel much more comfortable with sample collection from roofs even though the patinas are valued aesthetically. Samples were collected around Oxford out of convenience, but since geographic correlations between the $\delta^{18}O$ in the brochantite samples and the $\delta^{18}O$ in local precipitation were anticipated, a sample criterion was based on sample site location. In turn, sample locations were selected based on the availability of local meteoric water data.

Meteoric processes that provide a characteristic fingerprint of their origin affect the stable isotopic composition of water (refer to section 3.2). This signature then serves as a natural tracer, which is fundamental in investigating provenance. Ideally, water samples need to be collected at brochantite formation localities, as was often done by previous investigators. However, this study did not include water sample collection. Instead, meteoric water $\delta^{18}O$ values were found on the Global Network of Isotopes in Precipitation (GNIP).[1] GNIP is part of the International Atomic Energy Agency and collects stable hydrogen and oxygen isotope compositions in precipitation around the world. Although there are now over 1,000 stations collecting meteoric water in more than 125 countries, the data available are still limited (IAEA/WMO 2015). Not all stations measure the $\delta^{18}O$ in their water samples, or only do so sporadically, reporting data from a small number of samples. Nonetheless, GNIP offers a strong resource for oxygen-18 ratios in precipitation around the globe because it is large, has been in operation since 1961, is easily available to the public, and the quality of the data is periodically reviewed (IAEA/WMO 2015). When water collection and its isotope measurement is not an option for personal investigation projects, as would be the case when presented with an unprovenanced bronze, GNIP can serve as a good guide.

[1] For this doctoral project, the Water Isotope System for Data Analysis, Visualization, and Electronic Retrieval (WISER) was employed, which is an application developed by the International Atomic Energy Agency (IAEA) in collaboration with the University of Vienna, and has been designed to visualize and download isotope and related data collected as part of the IAEA-supported projects and global isotope monitoring programs like GNIP.

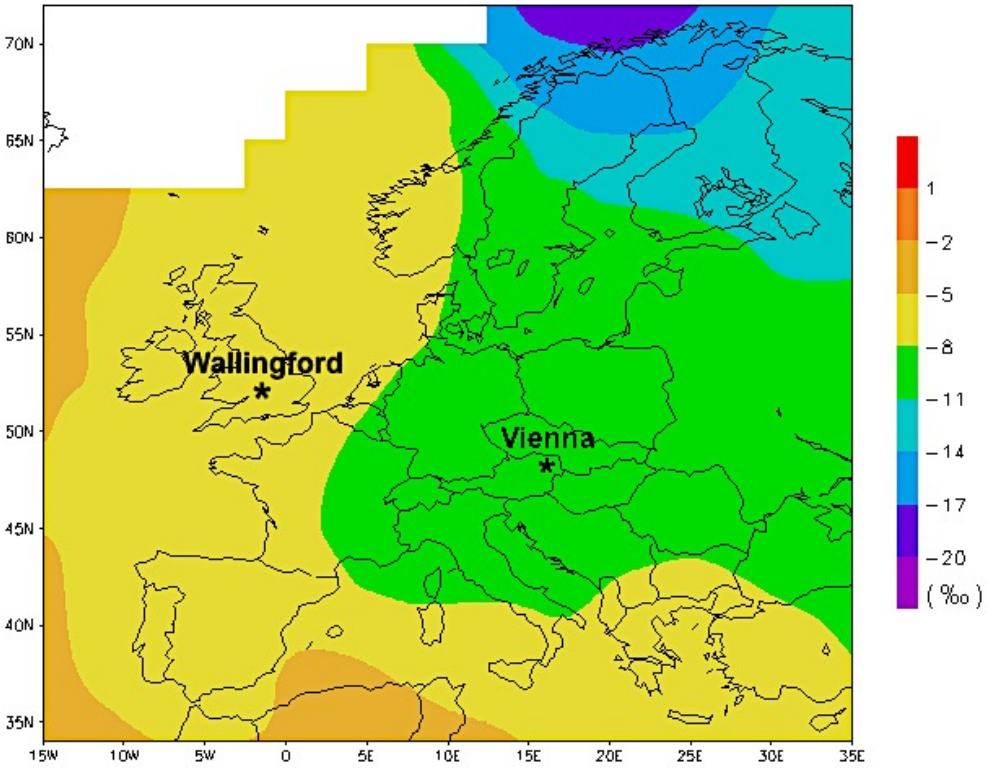


Figure 5.1: Weighted annual $\delta^{18}O$ in rainwater isoscape of Europe, with Wallingford (Oxfordshire) and Vienna pointed out (image adapted from IAEA 2001). Oxford's closest meteoric station, which is in Wallingford, has analyzed 417 precipitation samples, yielding a long-term yearly mean oxygen-18 value of -7.3‰ (IAEA/WMO 2018). Vienna has a long-term yearly mean of -9.8‰, based on 600 precipitation measurements (IAEA/WMO 2015).

After collecting around a dozen copper corrosion samples from Oxford, a trip was arranged to visit Vienna and collect more. Within the green zone presented in **figure 5.1**, which represents a weighted annual $\delta^{18}O$ in rainwater range between -8‰ and -11‰, there is a refined geographic strip along Switzerland, Southern Germany, Austria, and which continues into Eastern Europe, that has the lowest $\delta^{18}O$ values (closer to -11‰) in the rainwater. Since these values differ the most from those in the United Kingdom, this green zone was considered ideal for further sample collection, as it was anticipated that a clear difference would also be apparent in the $\delta^{18}O$ values of the corrosion products. Vienna was chosen because of the number of copper roofs permitted access to and because of the close locality of meteoric stations, which have been collecting and analyzing isotopes in the rainwater longer than any other station in the world. 600 precipitation samples yield a long-term annual mean of -9.8‰ (IAEA/WMO 2015). The oxygen-18 average precipitation values between Oxford and Vienna differ by about 3‰.

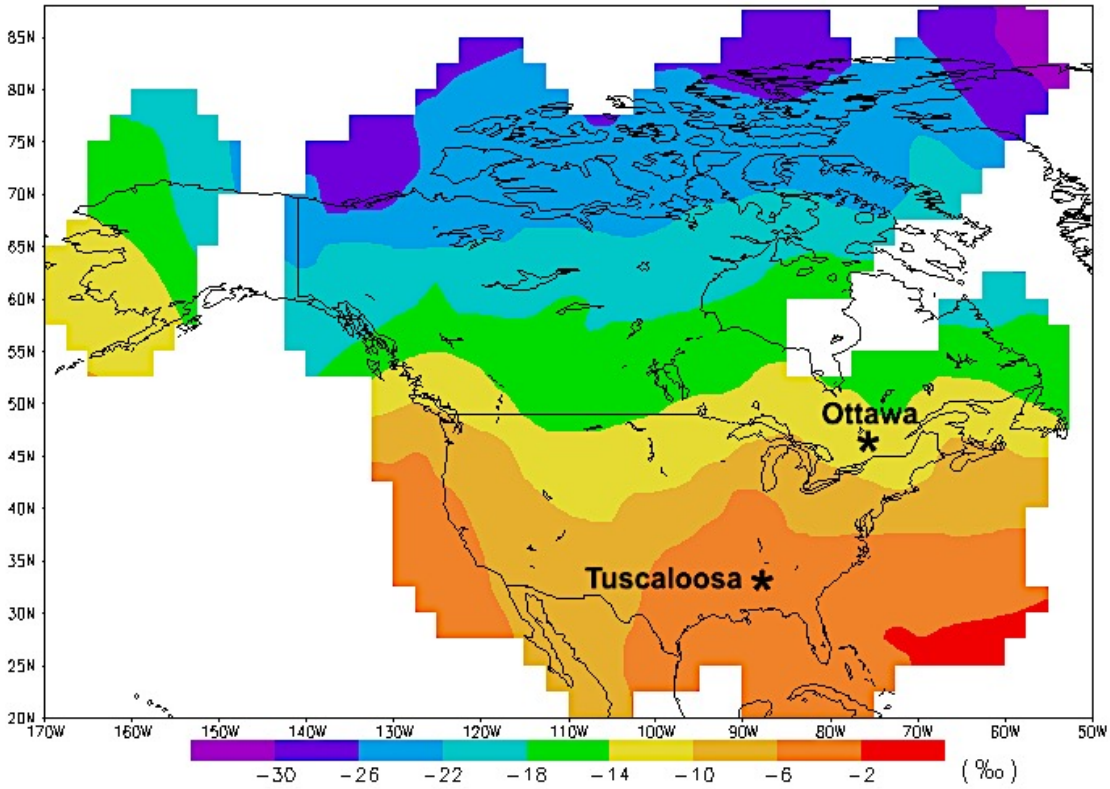


Figure 5.2: GNIP map of weighted annual $\delta^{18}O$ in precipitation across North America, showing a clear latitudinal affect (image adapted from IAEA 2001). Asterisks mark the locations of Ottawa and Tuscaloosa. The oxygen-18 values in Ottawa's rainwater, based on 547 samples, have a long-term yearly mean average of -11.0‰ (IAEA/WMO 2015). Tuscaloosa has a young GNIP meteoric station, with 36 precipitation samples yielding a long-term yearly mean $\delta^{18}O$ value of -4.7‰ (*ibid.*). This value contrasts nicely with Ottawa by demonstrating the isotopic latitudinal effect in precipitation.

To better confirm any possible geographic correlations, sample collection trips to Ottawa, Canada and Tuscaloosa, Alabama, USA were also carried out. In North America, the surface water isotopic concentrations display a clear, latitudinal sequence, with $\delta^{18}O$ values lowering with increasing latitude (refer to **figure 5.2**). Like Vienna, Ottawa has a long-time operating meteoric station and many buildings with copper roofs. The oxygen-18 values in Ottawa's rainwater are lower than Vienna's, with a long-term yearly mean average of -11.0‰ (IAEA/WMO 2015). Tuscaloosa was selected because it has multiple buildings on the University of Alabama campus with patinated copper roofs, and access was granted to collect from them prior to visiting. Moreover, Tuscaloosa has a GNIP meteoric station with a long-term yearly mean average $\delta^{18}O$ value of -4.7‰ (IAEA/WMO 2015), which contrasts Ottawa by nicely demonstrating the isotopic latitudinal effect in precipitation. Sample collection in North America is limiting because there are not a lot of copper roofs, and cities with them tend not to have meteoric stations that measure the $\delta^{18}O$ in rainwater.

5.1.2. Sample Processing and Material Characterization

Corrosion samples were simply scraped off roofing using a small scalpel blade with care not to scratch or collect any of the copper metal below the mineral phases (refer to **figure 5.3**, below). Effort was also made to choose apparently clean areas free of bird droppings, excessive dirt, and soot. The corrosion samples were collected into snap-lidded 1.5 ml centrifuge vials made from colored polypropylene. Due to accessibility or architectural design restraints, there is no consistency in sample area details such as surface angle, amount of sunlight and shade, wind exposure, et cetera; although it has been reported that these details can have an impact on the formation pathways involved (Polikreti *et al.* 2009, 2421). In any case, this information is not known for each sample, particularly in cases where random copper roofing samples (metal included, saved after a roof was replaced), were donated and the person responsible did not know from where the roof sample was cut.

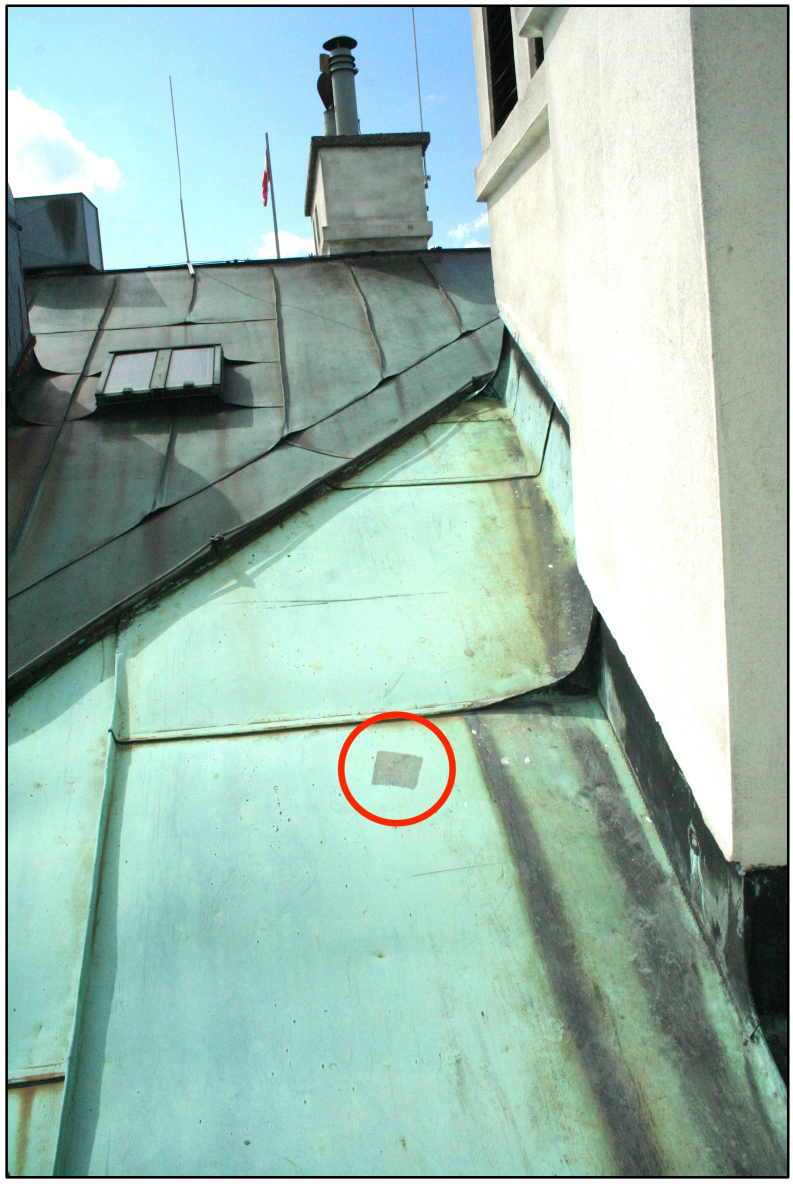
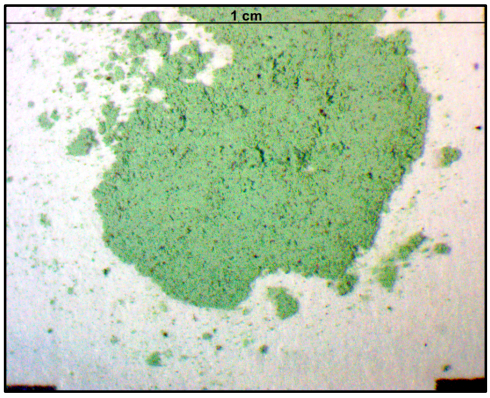


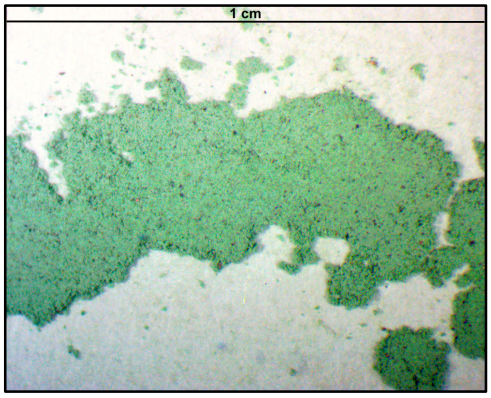
Figure 5.3: Copper roofing at Technische Universität Wien (Vienna University of Technology) showing where a patina sample was collected (inside the red circle). Most samples averaged 4-5 cm^2, depending on the corrosion thickness.

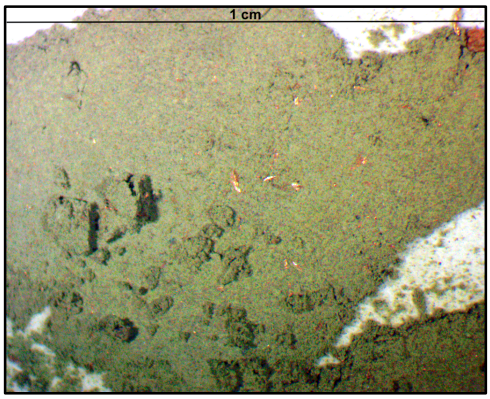
All collected samples were examined visually under a binocular microscope. Most samples were pulverous and appeared to consist of one mineral phase sprinkled by shiny copper metal fragments and dark soot, dirt or other debris (refer to **figures 5.4 and 5.5**). To confirm the identify the mineral phases present in the copper corrosion roof samples as brochantite, powder x-ray diffraction (XRD) was employed.

X-ray diffraction analysis is an instrumental technique used to determine the lattice spacing in crystalline structures by measuring diffraction patterns caused by impinging x-rays with known wavelengths (Pollard *et al.* 2007, 113; Silberberg 2003, 451-2). The spacings between the crystal planes in a lattice determine the angles at which the impinging x-rays, which penetrate the crystal surface at various layers, "reflect" back with either constructive or destructive interference (Cullity & Stock 2001, 94; Pollard *et al.* 2007, 113). In most angle directions, there is no scattering because the scattered rays cancel one another by destructive interference (Cullity & Stock 2001, 93-4; Pollard *et al.* 2007, 113). In very few directions, the scattering is strong and is called diffraction. The direction of the diffracted beams is characteristic of a mineral's unit cell shape and size, and can therefore be used for identification.

Powder XRD is considered the simplest and is the most widely used method for structural identification on inorganic materials. Its advantage is that it is non-destructive, and therefore samples can be used again in other analyses such as FTIR and eventually mass spectrometry (the latter, however, is destructive). XRD involves placing a powder sample of a single or polycrystalline specimen in a suitable holder and in the way of monochromatic radiation (x-rays of a single wavelength). The X'Pert Pro PANalytical PW3719 powder diffractometer at University of Oxford's Chemistry Research Laboratories (CRL) was used with EVA 2, a digital library available at Inorganic Chemistry. Grinding the samples was not necessary because they were already in powder form. The holder was a glass plate with a $2cm^2$ indentation where the powder samples were deposited and scraped flush with the glass surface. The sample-containing glass plates were then horizontally clip-mounted into the instrument and remained fixed during analysis. Monochromatic x-rays were directed down onto the sample at various angles. Each sample run took about 25 minutes. Conveniently, the diffractometer detector automatically sends the results to a computer. Less conveniently, the data had to be moved onto a different computer in Inorganic Chemistry, where the EVA 2 digital library is stored.

5.4 

5.5 

5.6 

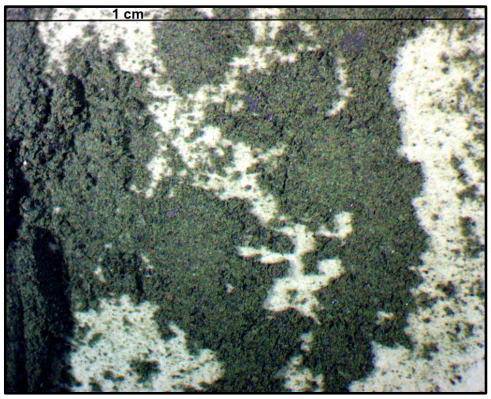
5.7 

Figure 5.4: Binocular microscope photograph of the Hofburg angel statue (seen in **figure 1.1**) patina sample from Vienna, Austria. Scale: Image width approximately one centimeter.
Figure 5.5: Binocular microscope photograph of the Vienna University of Technology (seen in **figure 5.3** and **5.8**) roof patina sample from Vienna, Austria. Scale: Image width approximately one centimeter.
Figure 5.6: Binocular microscope photograph of the West Block Building roof patina sample from Parliament Hill, Ottawa, Canada. Scale: Image width approximately one centimeter.
Figure 5.7: Binocular microscope photograph of the Presidential Hall (demolished) roof patina sample from Tuscaloosa, Alabama, USA. Scale: Image width approximately one centimeter.

Almost 70 samples were collected from patinated roofs and historic objects, but due to financial restraints, only 33 were used for isotopic analysis (catalog for all samples in Appendix A). These were selected based on sample purity and size. The XRD results (provided in Chapter 6, **table 6.1**; for all analyzed samples refer to Appendix B) show that most of the samples are the copper sulfate mineral, brochantite (refer to **figure 5.8**). This is typical of copper objects exposed to the atmosphere in urban environments. Some of the samples also have another mineral phase present, as indicated by peaks that do not match brochantite, which could not always be identified (refer to **figure 5.9** for an example XRD spectrum of brochantite and antlerite, and **figure 5.10** for brochantite and quartz). Sample purification is important because different products may yield different oxygen isotope values, which would then result in mixed data.

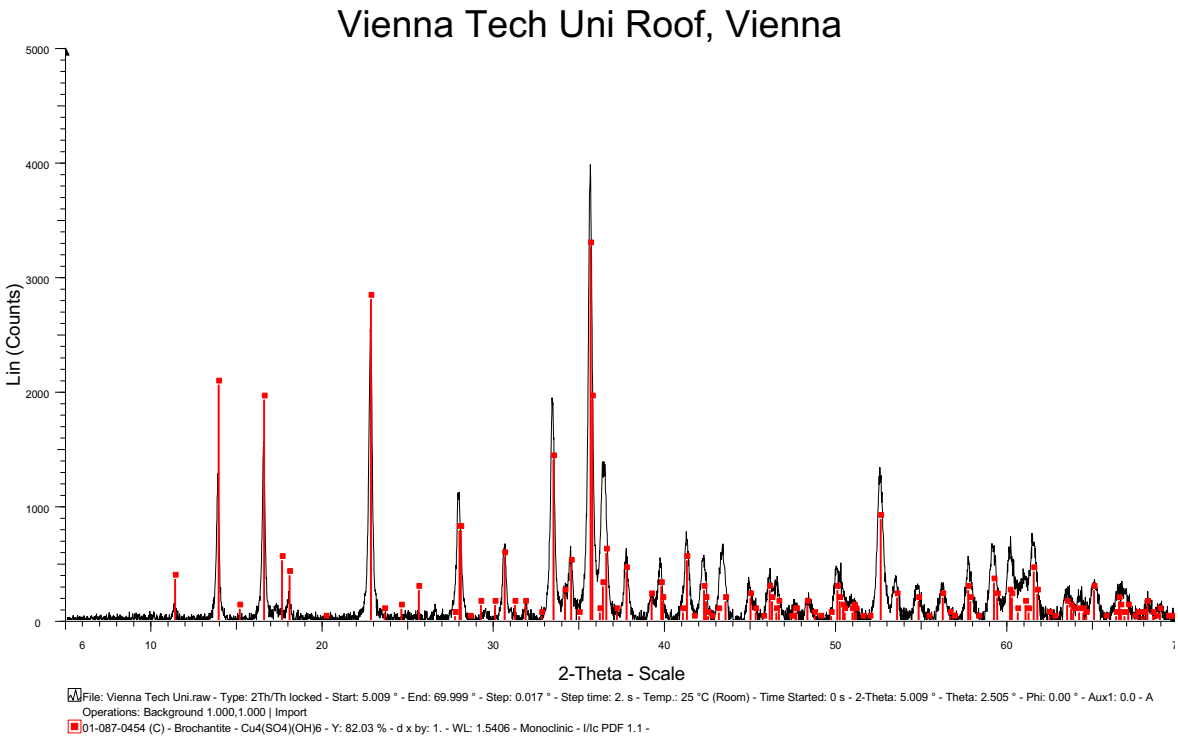


Figure 5.8: XRD spectrum of the patina sample collected from TU Wien. All the peaks in this spectrum are consistent with those of known brochantite samples, suggesting that this sample is also brochantite.

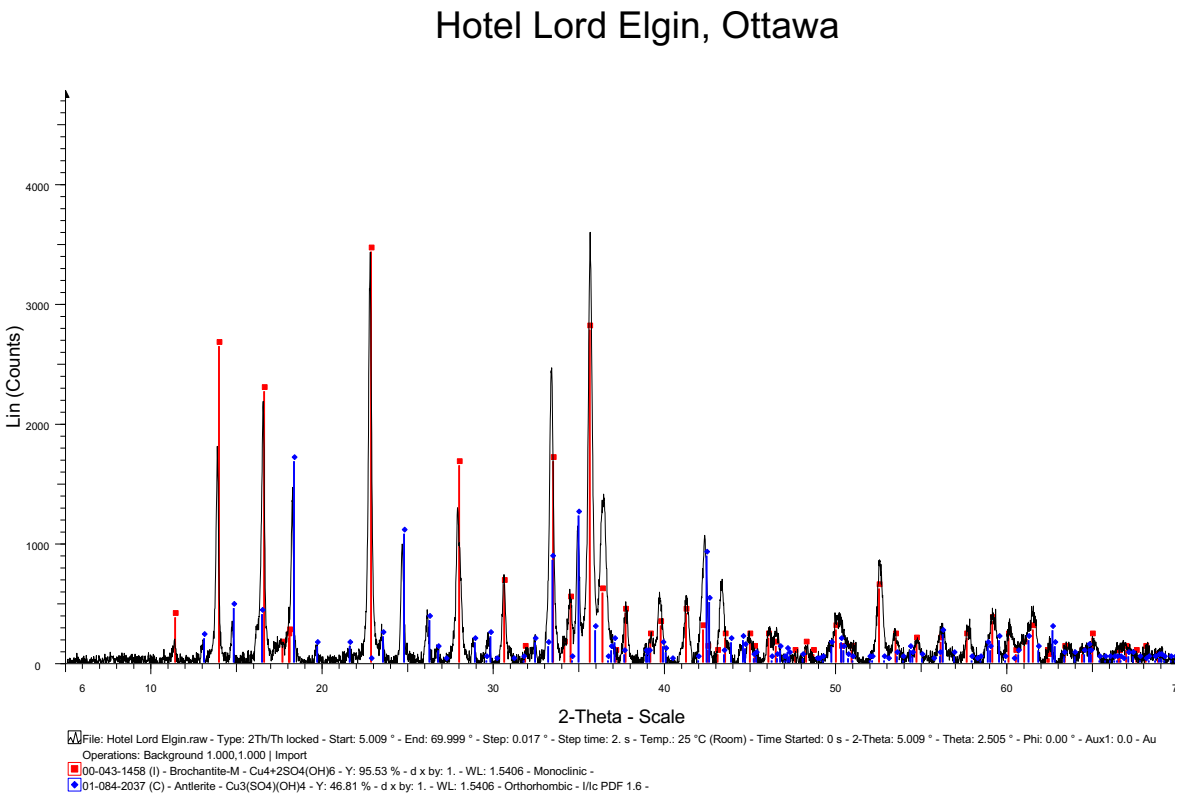


Figure 5.9: XRD spectrum of the patina sample collected from the copper roof on Hotel Lord Elgin in Ottawa. The peaks indicate that the sample contains brochantite (red) and antlerite (blue).

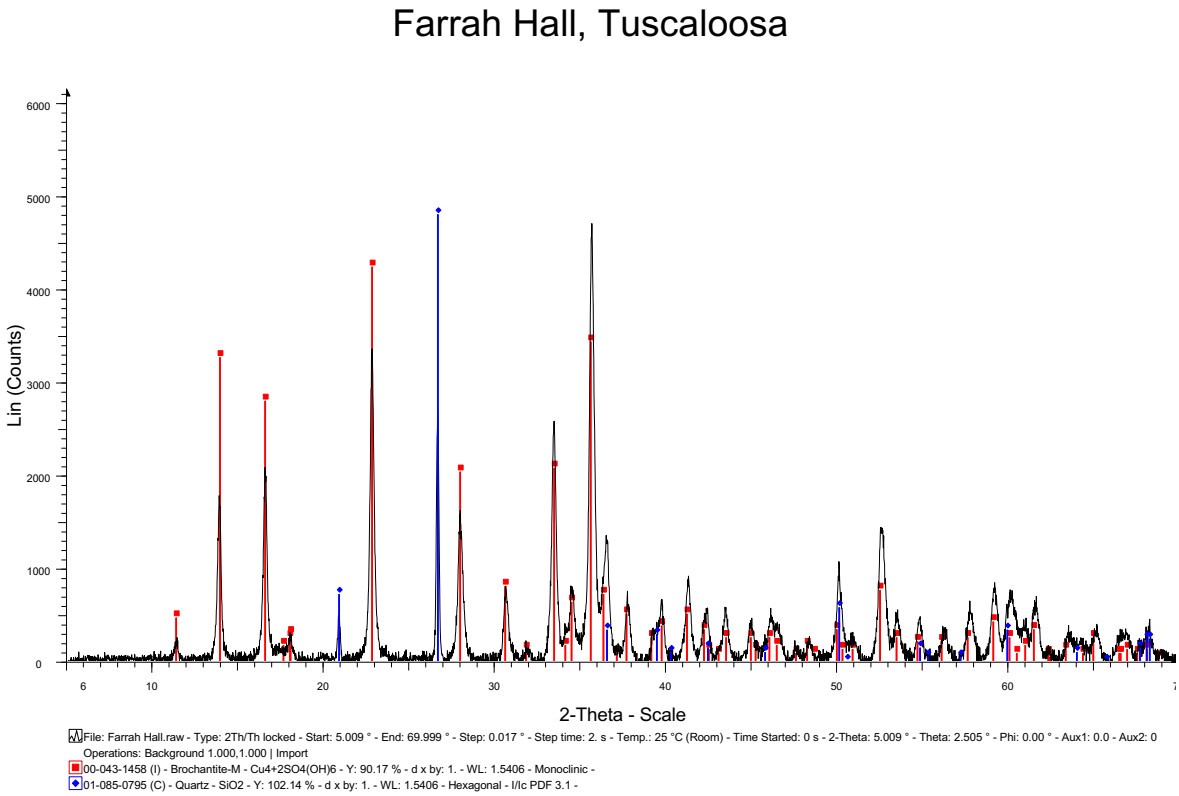


Figure 5.10: XRD spectrum of the patina sample collected from the copper roof on Farrah Hall in Tuscaloosa, Alabama. The peaks indicate that the sample contains brochantite (red) and quartz (blue).

5.1.3. Isolation of Brochantite and Its Sulfate Oxygen

The focus of this research was to measure the sulfate $\delta^{18}O$ values in brochantite, which had to be isolated from the other oxygen atoms within the brochantite structure (the hydroxyl oxygen needed to be removed). Reacting dissolved sulfate with barium chloride ($BaCl_2$) to precipitate $BaSO_4$ that can then be used for isotopic analysis through a mass spectrometer is an isolation method commonly encountered in literature.[1] Barium sulfate is easily acquired by reacting the sample (suspended in distilled water) with dilute acid (HCl or HNO_3 are typical options, but obviously not H_2SO_4 as this introduces a foreign sulfate) and then an excess of barium chloride solution. The acidification of the sample is essential in preventing other barium salts from forming (like carbonates or sulfites) in addition to the $BaSO_4$. This reaction could be carried out on the collected samples as they were, without the need for manual separation or thermal isolation.

[1] As discussed in Chapter 4, Holt and collaborators did a significant amount to work on synthetic, environmental, precipitated and particulate atmospheric sulfates. This work has been applied to the gypsum-rich black crusts that form on historic stone buildings. The black crusts are of conservation concern, and therefore have been extensively studied to elucidate the mechanisms of formation and identify source material. These studies have shown that the oxygen isotopes of gypsum can successfully be used to trace its origin, and the methodology used in these stone-sulfate studies was modified for use in the brochantite study (e.g. Kloppmann *et al.* 2011; Kloppmann *et al.* 2014; Kramar *et al.* 2011; Rivas *et al.* 2014).

Experimental laboratory work, pilot studies and stable isotope measurements were carried out at the British Geological Survey (BGS) Environmental Science Centre in Keyworth, Nottingham in collaboration with Dr. Tim Heaton and Dr. Sarah Bennett. Once a laboratory procedure for precipitating $BaSO_4$ from brochantite was established, sample preparation was carried out at the University of Oxford's Research Laboratory for Archaeology and the History of Art, and only mass spectroscopy was done at BGS.

Laboratory Procedure: Isolation of Brochantite from Copper Roof Patina to Precipitate $BaSO_4$

The laboratory procedure used in this study involved dissolving 30 – 50mg patina samples in 1 M hydrochloric acid, followed by several filtrations to remove any non-sulfate minerals. Barium chloride was added to yield $BaSO_4$ and isolate the sulfate ion of interest. The $BaSO_4$ was converted to CO and analyzed using a high temperature conversion/elemental analyzer–isotope ratio–mass spectrometer (TC/EA-IR-MS). The detailed laboratory procedure is the topic of this section.

Day 1

1. Prepare 100ml of 1M HCl
2. Weigh 5 ~30-50mg patina samples, in duplicate (10 batch total), into 20-50ml screw-top vials
3. Add 5ml 1M HCl to each sample to dissolve sulfates. Solution goes very pale green; some particles sink readily while others are suspended (i.e. near neutral buoyancy)
4. Put samples on mild shaker overnight (speed 290)

Day 2

5. Use Büchner flask with polycarb (glossy side up) attached to a vacuum pump to filter sample. Less than 1mg of undissolved material is removed and discarded, which looks like dust/grit. Sample vial rinsed once, column rinsed twice (using MilliQ). Solution transferred from Büchner flask to 100ml beaker, rinsing flask twice (MilliQ). Sample now has a volume c. 30-40ml and is blue-green. All glassware washed with MilliQ between filtrations/samples.
6. Prepare 'bromine water' from 0.5ml Br_2 in 100ml diH_2O (this can be prepared, under a fume cupboard, during day 1). It is yellow.
7. In the fume cupboard, add 5ml bromine water (oxidizing agent). Solution will turn yellow/brown.
8. Raise solution pH to c. 5.5 with KOH or NaOH (c. 0.5M) using a pH meter. If KOH, add ~500ml, then drop by drop. If NaOH, add ~750ml, then drop by drop. A green flock starts to form (metal hydroxide precipitate)
9. Heat to 50-60ºC for 1 hour (remove excess Br)
10. Add extra KOH/NaOH (~300µl) to raise the pH to 12. A dense teal-black range precipitate forms. Pour samples into 50ml centrifuge tubes, rinsing twice with MilliQ. All tubes need to be roughly same volume to keep centrifuge balanced. Add MilliQ to level samples.

11. Centrifuge (2000 rpm for 5 minutes). Precipitates settle loosely.
12. Syringe filter by decanting solution into 60ml syringe with Luer attachment (25mm filter with 0.45µm nylon membrane) and squirting into 100ml beaker. Rinse once with MilliQ. Discard precipitates. Solution samples are clear colorless.
13. *Carefully* adjust pH to c. 3.5 with HCl (very unstable and sensitive, less than 1ml necessary), ($BaCO_3$ would form if solution not acidic).
14. Heat to 70ºC for about an hour to remove any CO_2
15. Add 4ml 1M $BaCl_2$ under fume cupboard to precipitate $BaSO_4$. This is a thin white precipitate that forms overnight. Keep covered to avoid contamination.

Day 3

16. Filter through polycarb and keep precipitate (the $BaSO_4$). This is an incredibly slow filtration (only around 8 filtrations can be carried out in a day). Place polycarb filter with $BaSO_4$ onto Petri dish and allow drying overnight in an oven. Keep covered to avoid contamination.

Day 4

17. Gently scrape $BaSO_4$ (pearlescent white) onto weighing paper (NOT a petri dish! Sample very difficult to get off glass and significant sample loss would occur). Watch out for contaminants (usually debris/fibers) and remove if found.
18. Weigh $BaSO_4$ yield and store samples in 1.5ml screw-cap glass tubes.
19. Homogenize $BaSO_4$ manually using mortar and pestle
20. Weigh ~0.2-0.3mg homogenized $BaSO_4$ samples, in duplicate, into silver MS capsules. Crush capsule before recording final weight.
21. Store sample capsules for travel to BGS facilities for TC/EA IR-MS.

ALTERNATIVE: Syringe filtration technique can be used to carry out the initial filtration. The result are more finely filtered samples, executed much more quickly with ~10ml less solution, which is convenient. However, syringes are expensive and a new one is required for each filtration. Samples prepared at RLAHA were not syringe filtrated – this was only an option at BGS.

Some of the $BaSO_4$ samples were analyzed with FTIR to check the purity, with concern for carbonate contaminates, but only IR absorptions for the sulfate functional groups were present. Apart from the $BaSO_4$ purity check, the brochantite study only used XRD for material identifications. This was due to limitations in instrument access and financial restrictions. However, FTIR was used extensively in the malachite study, which is discussed later in this chapter.

5.1.4. Measurement of $\delta^{18}O$ in $BaSO_4$

Mass spectroscopy (MS) is the most sensitive detection system possible as it involves counting individual ions using electric and magnetic fields. Mass spectrometers are often coupled with other devices to improve the detection sensitivity, hence the proliferation of "hyphenated techniques" of analysis (e.g. GC-MS, HPLC-MS, or for the brochantite study, TC/EA-IR-MS). Mass spectrometry offers various possibilities and is used in many ways depending on the research aims, but this study focuses on the measurement of stable light isotopes in inorganic material.

The isotopes of light elements are typically measured using a gas isotope mass spectrometer. The mass spectrometer consists of an electron ionization ion source to ionize the gas and accelerate the ions, a flight tube with a magnet for mass separation of the ions and a detector system with Faraday cups at the end of the flight tube to measure the individual isotopic species (Talibova *et al.* 2012, 478). All elements of interest must be converted into a gaseous form in order to be analyzed with this type of mass spectrometer. The ions are separated according to their mass-to-charge ratio in a magnetic sector analyzer and detected with high precision for the determination of isotopes in the sub-parts-per-million (ppm) range (Lebedev 2012, 1; Talibova *et al.* 2012, 478). A computer controls all the steps and processes the data.

Variations in isotopic abundances are relatively small, and simply measuring isotope ratios creates problems when comparing with data from other laboratories, typically because of operational and/or instrumental inconsistencies. Therefore, comparing the variations in isotope concentrations are practiced in place of actual abundance, otherwise known as the apparent ratio (Clark & Fritz 1997, 6). To accomplish this, sample ratios are compared to a reference, allowing for isotopic concentrations to be expressed using the following, universally adopted delta (δ) notation:

$$(\delta, ‰) = \left[\frac{R_{sample}}{R_{standard}} - 1 \right] \times 1000 \text{ for stable isotopes}$$

Standards are obtained through the Isotope Hydrology Section of the International Atomic Energy Agency (IAEA, Vienna, Austria – www.iaea.or.at). For hydrogen and oxygen isotopes in the water cycle, the standard is the Vienna-Standard Mean Ocean Water (VSMOW). Carbon-13 and carbonate-$\delta^{18}O$ are more likely referenced against the Vienna-Pee Dee Belemnite (VPDB), named after and based on the cretaceous marine fossil, *Belemnitella americana* (Clark & Fritz 1997, 9; Herczeg & Edmunds 2000, 511). For convenience, these international reference standards have been assigned δ values of zero. Isotope measurements on water and carbonates are not performed on the original material itself, but on gaseous CO_2 that has reacted with or is derived from the sample (Mook 2006, 56).

This project used two different mass spectrometry facilities. Both incorporated the gas chromatography-based, continuous flow IRMS systems, but required different sample conversion approaches. The $\delta^{18}O_{SO4}$ of brochantite was measured using high temperature conversion, or

combustion, to yield CO gas. The $\delta^{18}O$ and $\delta^{13}C$ in malachite was measured using acidification with orthophosphoric acid to release CO_2 gas.

The $\delta^{18}O_{SO4}$ of brochantite was measured using a high temperature conversion/elemental analyzer–isotope ratio–mass spectrometer (TC/EA-IRMS). The aim of the TC/EA was to convert the samples to reduced gases (CO and H_2) via reduction over glassy carbon at a high temperature in a helium carrier followed by gas chromatographic separation and controlled-continuous transfer into the mass spectrometer source. The TC/EA is the reducing unit, which is equipped with an autosampler, a continuous flow open-split gas control and introduction system, as well as the isotope ratio mass spectrometer. Brochantite samples were weighed in duplicate into silver foil capsules, crimped, and dropped into the 1400ºC furnace using the Thermo Finnigan TC/EA autosampler where it was purged for 10 minutes with helium to remove ambient gases. Gas chromatography was then carried out at 100ºC. Each sample took around ten minutes to run on the Thermo Finnigan DeltaPlus XL IRMS.

Measurements on Standards

The brochantite isotope data reported in this thesis were collected over a period of several months by two different analysts on the same mass spectrometer, and in two distinct batches. The malachite data (discussed in upcoming section 5.2) was collected at the same time in two batches by a third analyst at a completely different facility. Clearly, ensuring data consistency over this length of time is of the utmost importance. For this reason, a laboratory sulfate reference material (or carbonate for the malachite study) is included several times within each batch, some of which to correct for drift, and others as independent secondary standards. Standards and blanks are used for quality control in isotope determinations, by offering a sense of the accuracy and precision of the data. Three reference standards were used for the brochantite study: IAEA-SO-5, NBS-127 and IAEA-SO-6 followed by an empty silver capsule (method blanks). These were grouped and regularly spaced throughout the batch of 40-50 samples (in sequence after about every ten $BaSO_4$ samples). If a sequence of them are seen to drift from the expected values by more than ± ~0.3pm, then either the entire run, or all the samples were the instability is detected, is dropped.

A secondary, multi-point calibration is often carried out against standards, which is used for the correction of instrument measurements. For this research project, interactions with the TC/EA-IRMS and related computer software did not extend beyond loading the sample carousel. Quality control and data processing was entrusted to the analysts, who did not report any issues with the isotope measurements produced. The detailed measurement protocols are assumed to be standard, but needs reviewing.

5.1.5. Hydroxyls: A Pilot Study On δ^2H

The hydroxyl oxygen in brochantite was anaylzed because it was suspected that the δ^2H (occasionally referred to as deuterium in plots) is entirely meteoric in origin. Moreover, since the

chemical bonds in which hydroxyl and non-hydroxyl oxygen are involved are different, their isotopic composition ought to be different (Taylor & Epstein 1962 cited in Gilg *et al.* 2004, 51; Urey 1947 cited in Girard & Savin 1996, 469). This is referred to as intracrystalline oxygen isotope fractionation. If the $\delta^{18}O$ at both sites in a mineral can be determined, the fractionation between them should yield both the temperature and the isotopic composition of the mineral-forming water more accurately than through the non-OH site alone. Studies on clay minerals suggest that hydroxyl oxygen is significantly depleted (up to a few tens of a per-mil) in $\delta^{18}O$ relative to non-hydroxyl oxygen in the same specimen (Gilg *et al.* 2004, 51). These studies also suggest that intracrystalline fractionation decreases with increasing temperature of formation (*ibid.*).

None of the previous studies on brochantite or malachite have included isotopic analysis of the hydroxyl oxygen. The Schwarzwald malachite researchers stated, "We rule out an influence of the oxygen of the OH group [in malachite], since the observed differences in $\delta^{18}O$ nearly perfectly match their fractionation factors determined by Melchiorre *et al.* (2000)," (Haβler *et al.* 2014, 4). In this case, the decision was made not to analyze the hydroxyl oxygen, but the most likely reason for not doing so is limited to sample size and analytical complexity. The potential for exchangeable hydrogen is the main analytical complexity concern. Adsorbed and interlayer water of certain clays, like halloysite ($Al_2Si_2O_5(OH)_4$), exchange isotopically rapidly during degassing at ambient temperatures (Gilg *et al.* 2004, 47). This is especially the case in poorly crystallized formations that seem to retain considerable amounts of interlayer water at temperatures at which dehydroxylation starts (Gilg *et al.* 2004, 49). The hydrogen isotope exchange behavior in brochantite is unknown.

Efforts were made to analyze the hydroxyl $\delta^{18}O$ in some of the brochantite samples collected for this doctoral study. The only known practical method would require dehydrating at a high temperature to provide a minimum of 500 mg of water, and then equilibrating this with CO_2 before measuring the CO_2 $^{18}O/^{16}O$ ratio. This would not only require the use of several grams of sample for a single analysis (impossible requirement: the largest collected brochantite sample is 454 mg), but also would imply oxygen isotope fractionation or exchange during the heating (*pers. comm*. Heaton 2014).

A pilot study was carried out for the analysis of $\delta^{2}H$ from the hydroxyl groups using a method requiring only 8-10 mg of brochantite for $^{2}H/^{1}H$ analysis of water by reduction on hot zinc (modified from Coleman *et al.* 1982). Environmental water should be the only source of O and H in hydroxyl groups and the dual isotopes could provide robust data. This means that analyzing the $\delta^{2}H$ alone may be insufficient. Unfortunately, the brochantite samples collected are not big enough to carry out a full study on the sulfate oxygen and hydroxyl hydrogen, and the hydroxyl study would be incomplete without analyzing the hydroxyl oxygen as well. The patinas that form on archaeological and historic objects tend to be valued aesthetically, and getting permission to collect large enough samples from several sites to carry out all analyses would be impractical. This is why

a pilot study could not be carried out on malachite as well. The hope is that the Schwarzwald malachite researchers were right, and an intracrystalline oxygen isotope study would not be particularly advantageous.

5.1.6. Statistical Analyses on Brochantite Data

The $\delta^{18}O_{SO4}$ data of the brochantite samples were processed statistically. To determine the strength of central tendencies within raw data sets and quantify the amount of dispersion, the standard deviation (SD) was calculated for each city. The extent of variability in relation to the mean, known as the coefficient of variation (CV), was also calculated, as well as the standard error and 95% confidence interval for the mean. Grubb's outlier test was used to identify data points that are inconsistent with the rest in their group.

The brochantite data was analyzed using paired *t*-tests and Anova. A paired *t*-test assesses whether the difference between two related samples can be accounted for by sample error alone (Hawkins 2019, 172). Starting with the null hypothesis that here is no difference between the cities from which the $\delta^{18}O$ values in brochantite come, and using a 5% (0.05) critical significance level, a paired, two-tailed *t*-value can be generated using a statistical software package on a computer (this project uses IBM SPSS, version 25). Analysis of variance (Anova) is an overall test of whether group means differ (Field 2013, 870). It compares the variance between different groups (believed to be due to the independent variable) with the variability within each of the groups (believed to be due to chance) (Pallant 2016, 255).

Regression statistics are carried out to look for relationships between a dependent variable and an independent variable, and it is believed that the relationship might be modelled with a straight line (Hawkins 2019, 220). This was done by plotting the brochantite data against environmental parameters like the $\delta^{18}O$ in local meteoric water, surface temperature, latitude, amount of precipitation and pH.

Finally, the percent contributions from heterogeneous and homogeneous formation pathways were calculated. All statistics results for brochantite are provided in Chapter 6.

5.2. ANALYTICAL PROCEDURE FOR THE MALACHITE STUDY

Like the brochantite study, the objective for the analytical malachite study was to create a database of $\delta^{18}O$ values for archaeological malachite from a varying range of geographic sites with clear meteoric $\delta^{18}O$ differences in precipitation. The malachite study went further by also considering $\delta^{13}C$ values in the malachite carbonate. These values were compared to various local environmental parameters to identify the most influential factors and trends that may be used in provenance and authenticity studies. To understand the reaction pathway between copper and its oxidizing environment, stable isotope information was extracted from malachite samples isolated from scrapings off archaeological artifacts with known geographic locations. Although the aims and objectives of the brochantite and malachite studies were similar, the approach was different.

The approach for the malachite procedure was different from the brochantite study, where cities were selected for sample collection based on their proximity to GNIP stations and the number of patinated copper roofs available. Collecting archaeological samples was much more difficult, and control over sample selection criteria was quickly sacrificed to gain more samples. Moreover, sample processing significantly reduced the number suitable for isotope analysis, which led to a sub-study of analyzing less-processed samples to assess the necessity of such a meticulous methodology. In addition to this, the sub-study proved interesting for unintended reasons by providing information on the formation environments and other carbonate mineral phases.

5.2.1. Sample Acquisition

Sample acquisition depended on people's generosity as a favor. Conservators, archaeologists or other people working in the country of the objects' origin collected many of the samples used in the malachite study. This was necessary because it would not have been financially practical to personally visit each country with potential samples. Although grateful, this resulted in several less-than-ideal samples being collected and sent. Moreover, people often hesitated to do the preliminary work of searching old databases and physically assessing objects, as this can be very time-consuming and inconvenient, which resulted in denied assistance. All this was further complicated by export laws. If an object was rejected, it was usually to do with the objects' value getting compromised (remember collecting from objects is an invasive and destructive procedure). The sample size and quality that people were willing to share was also limiting.

Over 205 samples were acquired for the malachite study (refer to Appendix A for a full sample catalog). Unfortunately, most of these samples had to be eliminated, leaving 49 malachite samples grouped into twelve formation regions for isotopic analyses. These regions provide the malachite study with good geographic variance, and therefore considerable isotopic distribution in the meteoric water (**figure 5.11**). They are: Alaska, USA; northern Peru; Hungary; Cyprus; southern Spain; southern England; Israel and the following Chinese provinces: Gansu, Guangxi, Jiangsu, Jiangxi and Ningxia. Many more samples and objects were evaluated for collection, but were ultimately rejected for various reasons during processing.

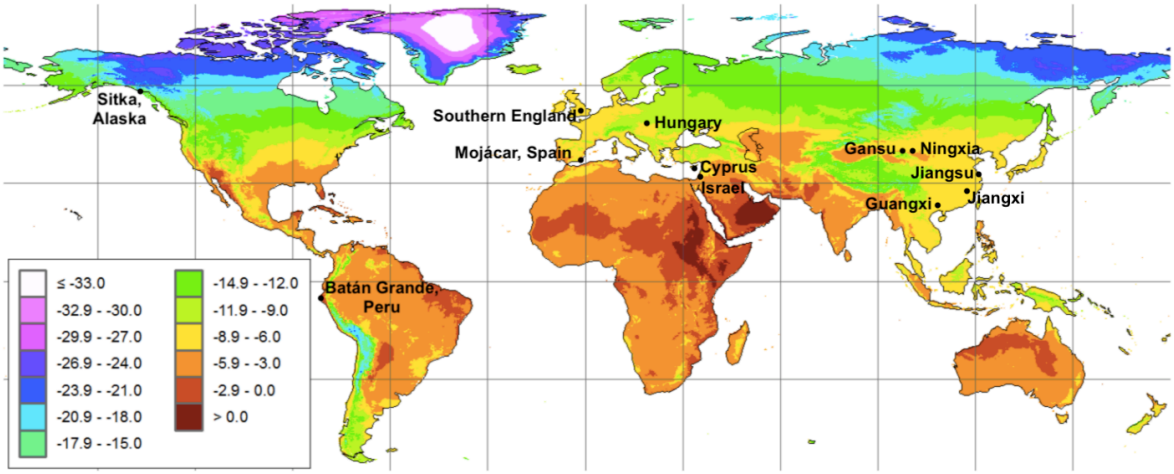


Figure 5.11: Map showing the locations of malachite study regions against the global amount-weighted $\delta^{18}O_{annual}$ in precipitation isoscape. The legend is $\delta^{18}O$ in per mil relative to the VSMOW-SLAP scales (adapted from Terzer *et al.* 2013, 4724).

5.2.2. Sample Processing of Malachite Samples

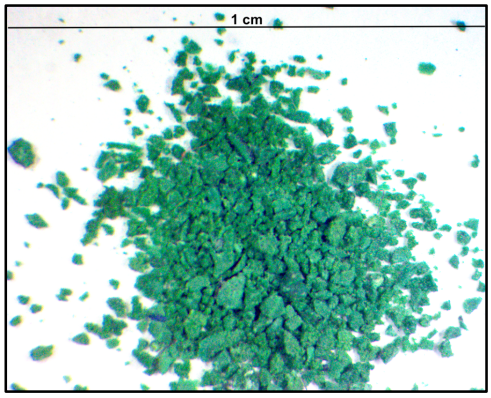
Optical Microscopy and Picking

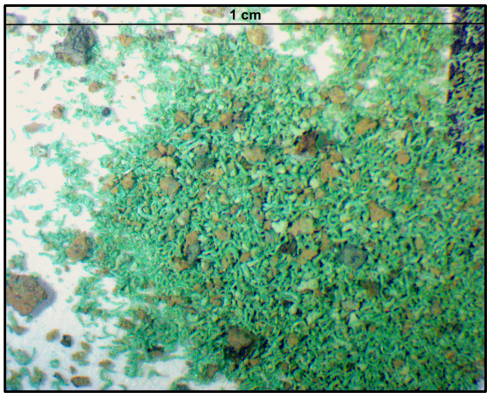
Some of the acquired samples could be eliminated from the malachite study immediately for not containing a green phase or copper minerals in general. Many other samples were removed from the study after a quick assessment under a binocular microscope. The most likely reasons for exclusion included insufficient malachite; malachite crystals were too dirty, or the malachite crystals were too fine for hand-picking.

Picking is a visual assessment. Malachite was visually identified and carefully isolated using a small sewing needle. Often, samples were rinsed with methanol to aid in finding and isolating the malachite crystals from other phases. Many crystals appeared contaminated within the malachite lattice, causing discoloration, or in the midst of a phase change (e.g. azurite → malachite).

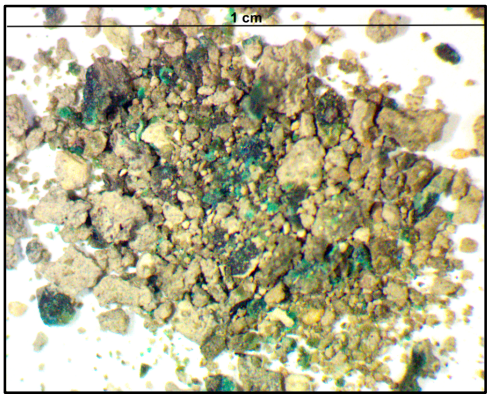
Malachite is known to vary in appearance, as is often seen in banded specimen (refer to section 1.2.2). An ideal malachite sample was perceived as emerald-green, vitreous, semi-translucent and glossy (refer to **figure 5.12**). Such samples were very few. Other good samples were described in personal notes as 'minty' due to a lighter shade, opacity and more matte appearance. Such descriptions suggest smaller crystal sizes or abraded crystal surfaces.

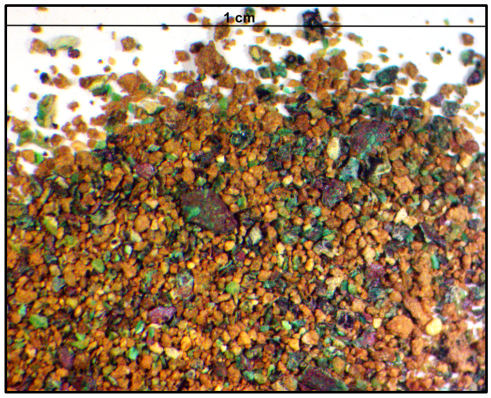
The actual samples collected had much broader visual descriptions and characteristics, even within the same sample (refer to **figures 5.12 – 5.17**). Samples ranged in gloss and opacity; hue, shade and chroma. Crystal shape and size varied considerably, with personal notes containing adjectives like fibrous, coiled, pulverized, porous, bubbly and chipped. The most common visually identified phases other than malachite present in the samples included: cuprite, quartz, sand, rust, azurite, wood, black particles and clay.

5.12 

5.13 

5.14 

5.15 

5.16 

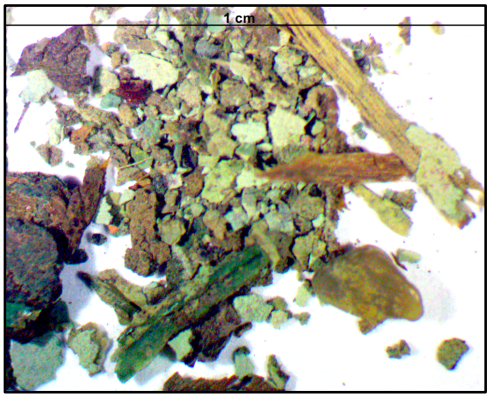
5.17 

Figure 5.12: Binocular microscope photograph of sample CGN2, from the interior surface of a *ding* vessel, Gansu, China. This photograph was taken before picking, yet already has an ideal visual description for malachite. XRD material characterization on the picked sample confirms it is 100% malachite. Scale: Image width approximately one centimeter.

Figure 5.13: Binocular microscope photograph of sample EC4, from an ingot/Cu cake fragment, mid-late Bronze Age, Bogshole Lane, Broomfield, Kent, UK. These malachite crystals formed coils and curls (now fragmented), which is very rare (Eggert 2007, 57). Scale: Image width approximately one centimeter.

Figure 5.14: Binocular microscope photograph of sample CGS3, from a *ding* vessel, Guangxi, China. This sample is before picking and mix-phase, showing a considerable amount of blue azurite. Scale: Image width approximately one centimeter.

Figure 5.15: Binocular microscope photograph of sample I4, from Tel Gezer, Israel. These malachite crystals are coated in soil. An alcohol rinse was used on patina samples like this one. Scale: Image width approximately one centimeter.

Figure 5.16: Binocular microscope photograph of sample RC4, from Pila Kokkinokremos, Cyprus. This image is included to show the variety of visual descriptions for the unpicked malachite samples. Scale: Image width approximately one centimeter.

Figure 5.17: Binocular microscope photograph of sample US7, from a round shallow sheet copper vessel, Castle Hill, Sitka, Alaska. This sample contains organic material like wood, and was removed from the study for having too few uncontaminated malachite crystals. Scale: Image width approximately one centimeter.

Picked samples visually identified as malachite were stored in gelatin capsules. Later, every sample was optically re-assessed under a binocular microscope with fresh descriptions recorded to cross reference with the mix-phase descriptions. Once past optical microscopy (OM), malachite samples were homogenized using a mortar and pestle and weighed. The goal was to collect over 0.50 micrograms of each sample to allow for FTIR, XRD and duplicate runs (0.25-0.50 micrograms each) on a mass spectrometer (refer to Appendix C for FTIR spectra and Appendix D for XRD data on analyzed malachite). The purpose of FTIR and XRD was to confirm the mineral identification of the samples by providing an instrumental assessment to cross-reference with the optical observations.

Material Characterization

Fourier transform infrared (FTIR) is a spectroscopic technique commonly used for material identification. When infrared radiation is absorbed, it causes changes in the electric dipole moment of certain molecules in a sample, which is known as the selection rule since it must occur in order to show IR absorptions as vibrations (Stuart 2004, 5 and 8). Structurally different organic molecules absorb varying radiant energies in the IR region. The frequency pattern of absorption causes certain bonds within a molecule to become excited and jump to a higher vibrational state with increased amplitude (Padías 2007, 57). This results in bonds bending and stretching in distinctive ways, providing supportive data for material characterization (Derrick *et al.* 1999, 4).

By passing infrared radiation through a sample, the fraction for how much of that radiation was absorbed at a specific energy can be determined to obtain an IR spectrum (Stuart 2004, 2). Complexities in an IR spectrum are due to combinations of differing vibrations over a large portion or the entire molecule (Stuart 2004, 10-11). These are called skeletal vibrations and their associated bands on an IR spectrum can correspond to a pattern or fingerprint of the whole molecule as opposed to a specific group within a molecule (Stuart 2004, 10-11). For obvious reasons, fingerprint frequencies are very characteristic for specific molecules, however both group and fingerprint frequencies can provide useful information about a sample.

To gain information from the fingerprint region, the sample's spectrum will need to be compared to an authentic spectrum, which can be found in literature like *The Aldrich Library of FT-IR Spectra* (Padías 2007, 63).

FTIR was not used for detailed characterizations. Due to financial limitations, FTIR served as a filtration step to remove samples that clearly did not contain malachite, as FTIR was far less expensive and more easily accessible than XRD. XRD was considered more ideal for providing reliable characterizations of the malachite and any contaminants, as well as suggesting percent compositions of each phase present. The malachite description tables in Chapter 7 (**tables 7.1 – 7.8**), which discusses the malachite results, present each sample's XRD material characterizations.

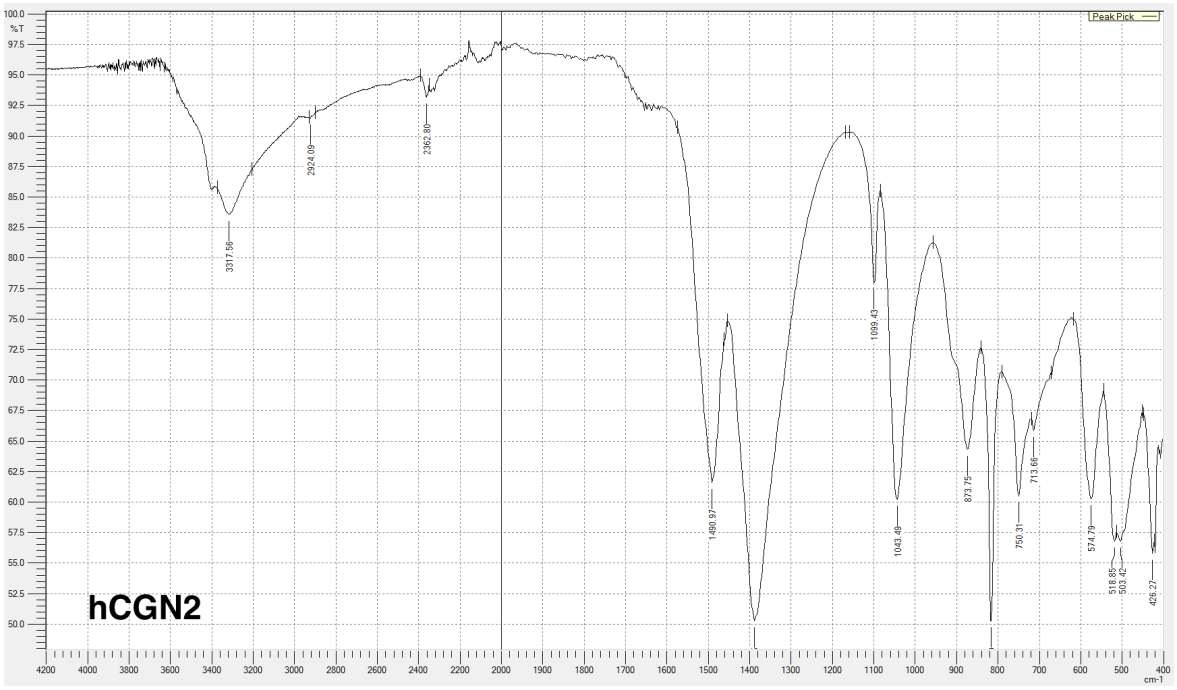


Figure 5.18: FTIR spectrum of homogenized sample CGN2 (also shown in figure 5.12), which is considered a pure malachite sample. Appendix C contains full page images of all FTIR spectra.

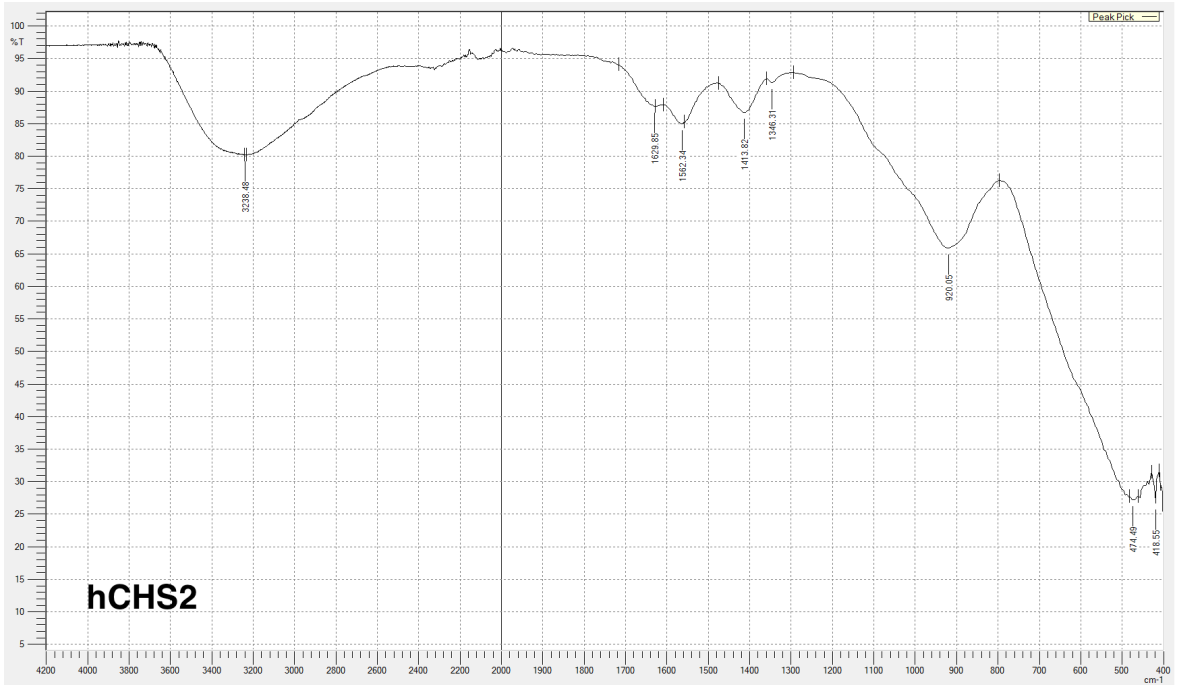


Figure 5.19: FTIR spectrum of homogenized sample CHS2, an 11th century BC patina sample from Hunan, China. This sample does not appear to include any malachite, and therefore was eliminated from this study and was not analyzed using XRD. Appendix C contains full page images of all FTIR spectra.

Different XRD facilities were used for the malachite study because these samples were much smaller than the brochantite samples. At the University of Oxford Department of Earth Sciences, a PANalytical Empyrean Series 2 diffractometer operating at 40 kV and 40 mA with a $Co_{K\alpha}$ source was used for the malachite study as it can scan powdered micro-samples. Samples

were mixed with anhydrous ethanol and deposited on a zero-background single crystal silicon substrate. In the instrument, samples were analyzed while continuously rotated, and data were acquired from 5° to 85° 2theta using a step size of 0.026° which took approximately 20 minutes per sample. Diffraction data were reduced using the HighScore Plus software suite, and mineral identifications were based on correspondence to the International Centre for Diffraction Data Powder Diffraction File 4+ database (and quantified through the reference intensity ratio method).

CGN2

Pattern List

Ref.Code	Mineral Name	SemiQuant[%]	Score	Compound Name	Scale Fac.	Chem. Formula
00-056-0001	Malachite	100	22	Copper Carbonate H..	0.482	Cu2 +2 (C O3) (..

Peak List

Pos.[°2θ]	Height [cts]	FWHMLeft[°2θ]	d-spacing [Å]	Rel. Int. [%]
17.1912	867.01	0.1279	5.98927	54.20
20.3983	1599.58	0.1535	5.05535	100.00
21.7873	161.35	0.6140	4.73659	10.09
27.9404	1151.11	0.1279	3.70791	71.96
34.9500	194.19	0.1535	2.98097	12.14
36.0708	506.55	0.5117	2.89128	31.67
41.5883	454.59	0.1535	2.52148	28.42
42.4910	148.78	0.3070	2.47031	9.30
44.5423	127.63	0.3070	2.36194	7.98
45.5289	110.04	0.3070	2.31339	6.88
49.7392	138.60	0.4093	2.12851	8.67

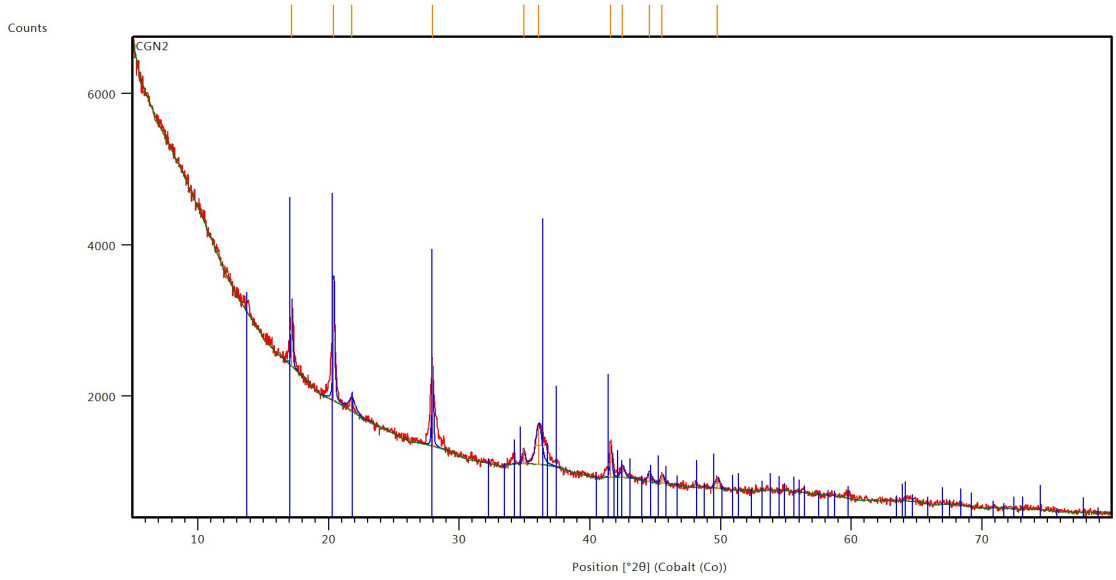


Figure 5.20: XRD spectrum and details for sample CGN2 (also shown in figure 5.12 and 5.18), which is a pure malachite sample. For all XRD spectra on the malachite samples, refer to Appendix D.

Many of the samples contained little or no malachite, or were highly contaminated with several different phases. XRD requires samples with few mineral phases for good, quantitative material identification. It is also possible that visually undetected organic carbon was present. These would not be revealed by XRD. Since many of the malachite samples had more than three phases present, accurate quantitative material identifications were impossible. In most cases, educated judgments could be made to determine the phases most likely present. In other cases, more than one valid option for the composition of a sample was equally plausible (e.g. sample H7

on **table 7.1** could consist of 68% malachite and 32% coesite **or** 85% malachite, 8% coestie and 9% tenorite). Each option could change the suggested amount of malachite present considerably. Sample identification was complicated further when comparisons were attempted between the results offered by FTIR, XRD and the visual assessments, which often did not support one another.

B2H11

Pattern List

Ref.Code	Mineral Name	SemiQuant[%]	Score	Compound Name	Scale Fac.	Chem. Formula
03-065-2309	Tenorite, syn	10	19	Copper Oxide	0.228	Cu O
00-056-0001	Malachite	63	28	Copper Carbonate H..	0.504	Cu2 +2 (C O3) (..
01-070-1579	Azurite	21	Unmatch	Copper Hydroxide C..	0.182	Cu3 (O H)2 (C O..
00-041-1487	Graphite-2H	7	29	Carbon	0.246	C

Peak List

Pos.[°2θ]	Height [cts]	FWHMLeft[°2θ]	d-spacing [Å]	Rel. Int. [%]
13.7702	184.18	0.6140	7.46714	8.46
17.1502	1502.27	0.1279	6.00350	68.97
20.3716	2178.04	0.1279	5.06192	100.00
21.7857	222.89	0.1535	4.73694	10.23
27.9172	1493.17	0.1535	3.71093	68.56
29.2584	372.09	0.1279	3.54429	17.08
30.9455	547.86	0.1023	3.35540	25.15
32.4427	210.66	0.1535	3.20443	9.67
34.2390	188.53	0.3070	3.04096	8.66
34.8473	209.91	0.2047	2.98948	9.64
36.2197	343.68	0.7164	2.87979	15.78
41.5958	618.25	0.1535	2.52104	28.39
42.4841	154.98	0.3070	2.47069	7.12
45.4773	112.71	0.3070	2.31588	5.17
49.6605	144.28	0.2047	2.13166	6.62
54.6684	102.56	0.3070	1.94946	4.71
56.1090	72.36	0.6140	1.90332	3.32
64.4600	65.29	0.8187	1.67846	3.00

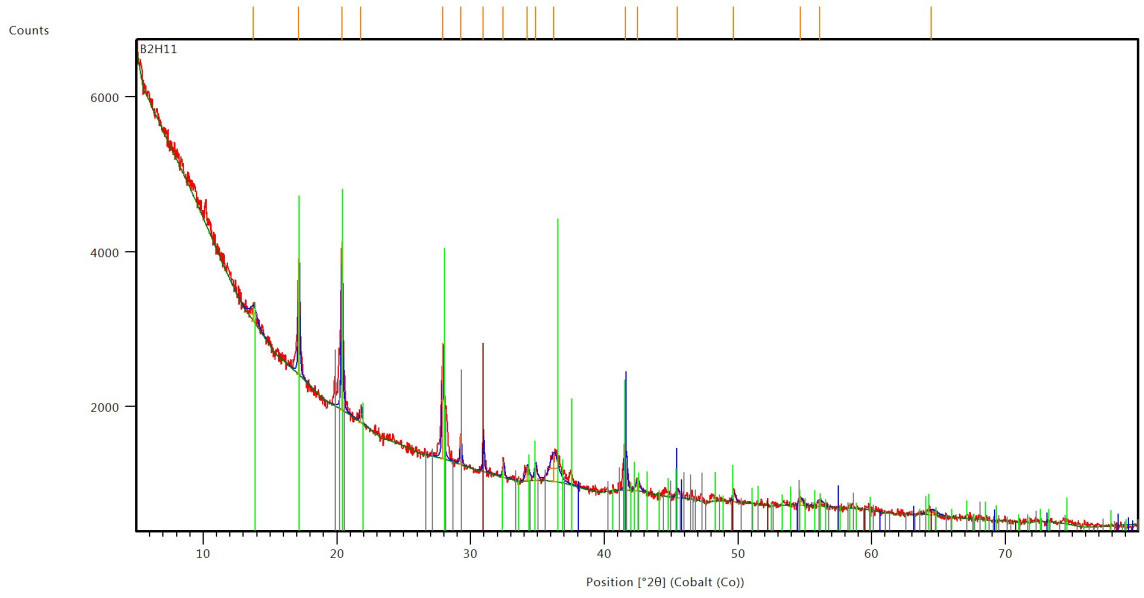


Figure 5.21: XRD spectrum and details for sample B2H11, which consists of at least four different phases (tenorite, malachite, azurite and graphite). For all XRD spectra on the malachite samples, refer to Appendix D.

5.2.3. Sample Batches and Purity

The study started with 205 samples, but picking reduced this number to about 125 for FTIR analysis. FTIR lowered the number of samples suitable for mass spectrometry to just 75, and

XRD further narrowed the archaeological malachite study to 56 samples, and not all of these yielded isotopic data. Processing resulted in the elimination of over 75% of samples.

The decision was made to broaden the malachite study by testing the necessity of such a meticulous picking process by also analyzing less pure samples isotopically. To do this, two malachite study batches were created:

Batch 1 (B1) consisted of the purest malachite samples, as determined by the original sample criteria based on visual assessment, FTIR and XRD. These were predominantly archaeological samples with a few geologically relevant ores for comparison. There was a total of 65 malachite samples, 56 of which were archaeological and nine were ores. These samples were grouped into 12 formation sites.

Batch 2 (B2) consisted of supposedly more contaminated versions of Batch 1 samples to evaluate the level of purity necessary to get reliable stable isotope data on malachite. The degree of contamination and phases present in each B2 sample varied. Not all B2 samples had correlating B1 samples. There were 29 B2 samples, all of them archaeological, from seven different formation sites.

5.2.4. Environmental Classifications Used for the Malachite Sample Regions

Both temperature and the meteoric water conditions can be considered simultaneously through comprehensive forms of environmental classifications. Climate and soil type are the best options because there are several classification systems that can be used for defining them and they tend to be well documented around the world. Among the most common and generally approved include the Köppen Climate Classification system and the Soil Map of the World in conjunction with the World Reference Base (WRB) for Soil Resources, as well as the US Soil Taxonomy system (Buol *et al.* 1998, 6).

The Köppen system offers an empirical approach to classifying climates based on global patterns of precipitation, air temperature and vegetation. It recognizes five major climate types, which are designated with a capital letter: A (tropical), B (dry/arid), C (temperate), D (cold continental) and E (polar) (Chen 2017). These major types can be further divided into subtypes based on the specific seasonal characteristics of precipitation and temperature. Subtypes satisfy the criterion of their parent type and there can only be one climate type in a region (Chen 2017). This is determined using the following hierarchy: ET, EF, BSh, BSk, BWh, BWk, Af, Am, As, Aw, Csa, Csb, Csc, Cwa, Cwb, Cwc, Cfa, Cfb, Cfc, Dsa, Dsb, Dsc, Dsd, Dwa, Dwb, Dwc, Dwd, Dfa, Dfb, Dfc, Dfd (*ibid.*). If the climate satisfies the criterion of both ET and BW, for example, then it is classified as ET. The archaeological malachite samples used in the current study came from two different climates (dry/arid and temperate) and seven different climate subtypes, which are defined as follows:

BSh: hot, semi-arid (Cyprus, Spain)
BSk: cold, semi-arid (Gansu)
BWh: hot desert (Peru)

BWk: cold desert (Ningxia)
Csa: Mediterranean with hot, dry summers (Israel)
Cfa: mild temperate with precipitation generally evenly distributed throughout the year and hot summers (Guangxi, Jiangxi, Jiangsu)
Cfb: mild temperate with precipitation generally evenly distributed throughout the year and warm summers (Hungary, Alaska, England)

Attempting statistics using multidimensional categories like climate is possible when there is a standardized way of identifying them and a widely-used resource available, like the Köppen Climate Classification system. Unfortunately, international communication in soil science is hindered by many uncorrelated, region-limited classification systems. The World Reference Base for Soil Resources (WRB) was developed as an international effort to provide a reference base that could incorporate the numerous soil classification systems into one using names that could be universally recognized (Bridges *et al.* 1998, 6; Buol *et al.* 2011, 390). It provides the terminology used for the Soil Map of the World, which has a scale of 1:5 million (Bridges *et al.* 1998, 6). On the face of it, the WRB appears to be a good, consistent way of classifying soil type in order to attempt correlations with the isotopic ratios in malachite. Most concerning for the current project, however, is that the WRB does not incorporate climatic parameters like soil temperature and moisture as classification criteria (Buol *et al.* 2011, 392). Still, using the WRB was initially pursued to help quantify the extent to which other parameters in soils affect the isotopic ratios in malachite. This was immediately complicated upon realizing that the available information on soil type for the samples in the current study is from a range of soil classification systems, and only one of them is the WRB. Moreover, soil types can vary significantly over small areas, and knowing which one correlates to a sample's microenvironment is almost impossible on a 1:5 million-scale map.

Many other soil classification systems exist, including some that incorporate moisture and temperature, like the US Soil Taxonomy. Completely new in design and nomenclature, the US Soil Taxonomy is a very promising system that is continuously evolving. Its flexibility with the capacity to incorporate new information without having to be destroyed or replaced is causing it to quickly grow in popularity. It aims to provide a system that includes all of the soils in the world, though it is still far from reaching this point, and it does not include all of the soil data necessary for this project. Furthermore, it is not realistic to attempt converting from one soil classification system to another, especially when moving between very different styles with unrelated classification criteria. At present, there appears to be no good way of creating a simple category for soil type to use in statistical studies.

To determine the vegetation present at the formation sites, local biomes were identified and allocated. A biome is a large geographical area of distinctive plant and animal groups, which are adapted to that environment. The climate and geography of a region determines what type of biome can exist in that region. Where an exact site is unknown, biome options are provided on **table 5.2**. The archaeological malachite samples studied are from one of six different biomes, defined as follows:

Alpine: The alpine biome lies just below the snow line of a mountain. It is known for its severe climate with dry, cold conditions and little CO_2, which drastically limits plant presence. Most alpine plants tend to be small and hug the ground, growing and reproducing slowly. Organic decomposition is also slow, resulting in poor soil conditions for further plant growth.
Chaparral: The chaparral is often known as a marquis in Europe, and is characterized as being very hot and dry. Shrubs and low growing plants dominate this biome, but in some areas will extend to larger trees and hard leaf forests, as well as aromatic plants. The vegetation in chaparrals must hold moisture to resist drought.
Deciduous Forest: Deciduous forests are in the temperate zone above the tropical forests and below the coniferous forests. The types of vegetation found in these regions include broad-leaved deciduous trees, some evergreen species, wildflowers, moss, mushrooms, ferns, ginseng and bamboo. The soil is very fertile.
Desert: Most deserts do not have many plants due to the extreme, dry climate. Hot deserts have very little rainfall, or concentrated rainfall during short periods. Cold deserts have lots of snow, and some rain in the spring. Most desert vegetation is scattered, hugging the ground with nutrient-packed, spiny leaves.
Grassland: Grassland biomes are large, rolling terrains of grasses, flowers and herbs. They are found in the middle latitudes, in the interiors of continents. An example grassland is the steppe biome, which is dry and cold, and usually found between deserts and forests. Soils tend to be poor in quality and the regions tend to be windy due to few trees.
Tropical Rainforest: Seventy percent of the plants in rainforests are trees. On the forest floor, organic matter is quickly consumed and broken down by fungi, insects, and other decomposers. The nutrients decomposition creates are immediately taken up by the biomass of the forest. This results in nutrients only being available close to the surface, which is why tree roots do not grow down very far. Instead, trees have adapted by growing buttressed roots up to 30 feet high, or stilt roots that hang down from their trunks and branches.

(Burton 1987; Biomes Group 2004).

5.2.5. Site Profiles

The twelve geographic regions the malachite samples were grouped into are described in the following site profiles. These profiles describe the objects from which the malachite samples were collected, including archaeological contexts where known. These sections also include information on the formation environment where known, and data for site proxies used in calculations. The information from these profiles is condensed and summarized in **table 5.2**.

Hungary

The Hungarian data set has strength in its size. It is comprised of eleven samples, making it one of the most extensive sets of this study. Most of these patina samples came from sickle handles, knife blades and axe heads (Appendix B). Other objects included a harness mount, a pin,

and two strips. Although the patina formation site within Hungary is unknown, these malachite samples came from a collection of corroded bronze objects sold together as a hoard (Broadgate 2001, 4). The implication is that the bronzes were also found together, and corroded in the same spot (*pers. comm.* Northover 2014). Therefore, the isotopic values derived from the malachite on these bronzes should be approximate to one another.

Each Hungarian sample has a correlating B2 sample, which gives this data set extra strength. None of the Hungarian B2 samples were picked under a binocular microscope. Like Smith (1978) and Pandey (2005), the green mineral scrapings were directly analyzed by a mass spectrometer. Visual assessment notes on the original, unpicked samples describe the presence of soil minerals like sand and clay, as well as some organic materials like wood, and in several cases the presence of other copper corrosion minerals. Contaminants varied in proportion, and it was often difficult to define other phases because many of the Hungarian samples were powdery and crumbled easily upon contact with the needle.

Hungary is in the Carpathian Basin in a temperate climate (Cfb) with multiple biomes, mainly alpine and deciduous forest. There is a range of soil types in Hungary, largely brown earth varieties. Since there is no known excavation site for the samples within Hungary, Debrecen was chosen as a proxy for estimating most environmental parameters (**figure 5.22)**. Located at 110 m.a.s.l. (meters above sea level) in the Great Hungarian Plain, Debrecen has a yearly daily air temperature mean of 10.6ºC (Vodila *et al.* 2011, 144-145).



Figure 5.22: Map of Hungary showing locations of major cities, including Debrecen in the east (University of Szeged 2010).

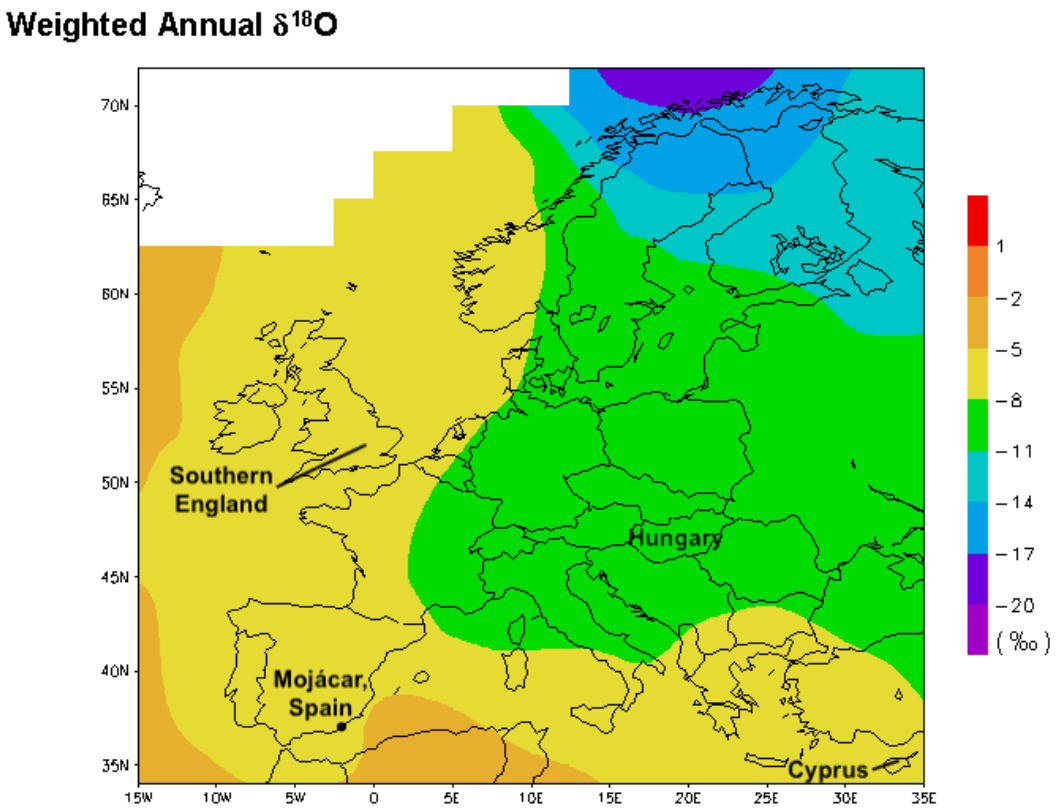


Figure 5.23: GNIP's weighted annual $\delta^{18}O$ isoscape of precipitation throughout Europe, showing locations of Southern England; Mojácar, Spain; Hungary; and Cyprus. Adapted from IAEA 2001.

According to GNIP, Hungary is at the center of a zone where mean $\delta^{18}O$ values in precipitation range between -11‰ to -8‰ (in the green zone on the map, **figure 5.23**). However, Hungary does not currently have meteoric stations endorsed by GNIP. Upon evaluating geographically relevant stations, a published study on a nine-year record of stable isotope ratios in precipitation at Debrecen, Eastern Hungary, was sourced for $\delta^{18}O$ data (Vodila *et al.* 2011). The work analyzed event-based samples collected from the beginning of 2001 to the end of 2009, and produced a $\delta^{18}O$ long-term annual mean of -7.7‰. This value is higher than the green zone range presented by GNIP in **figure 5.23**, but due to a lack of Hungarian data from GNIP, this study proceeded with the $\delta^{18}O$ value presented by Vodila *et al.* (2011).

Sitka, Alaska, USA

Of the twelve samples sent, five were suitable for mass spectrometry. In addition, each Alaskan sample had a correlating B2 sample. The samples were collected from archaeological objects excavated at the Castle Hill site in Sitka, Alaska. Castle Hill is a rock outcrop and the historical site of Tlingit and Russian forts (State of Alaska, 2018). The patina samples came from corroded copper sheets used for straps, lids and unidentified objects (Appendix B). The Alaskan data set was encouraging compared to the others because of its size and good provenance. For this reason, isotopic information derived from these samples was expected to be approximate to one

other and provide a good reflection of the corrosive environment. Into consideration, the Alaskan samples included in this study may not have corroded in soil that is representative of the local natural biome because they were excavated from a historic fort that had been filled (State of Alaska, 2018).

Sitka is located near Juneau on the Alaskan panhandle (**figures 5.23 and 5.24**). Unlike much of inland Alaska, Sitka does not have an arctic climate. It has an oceanic climate (Cfb) with moderate, but generally cool temperatures and abundant precipitation throughout the year (Neal *et al.* 2004, 4). The yearly daily mean temperature for Sitka is 7.4ºC (ranging from 1ºC in January to 13ºC in July and August) (*ibid.*). Sitka's warm, temperate climate is special in a region dominated by more arctic conditions.

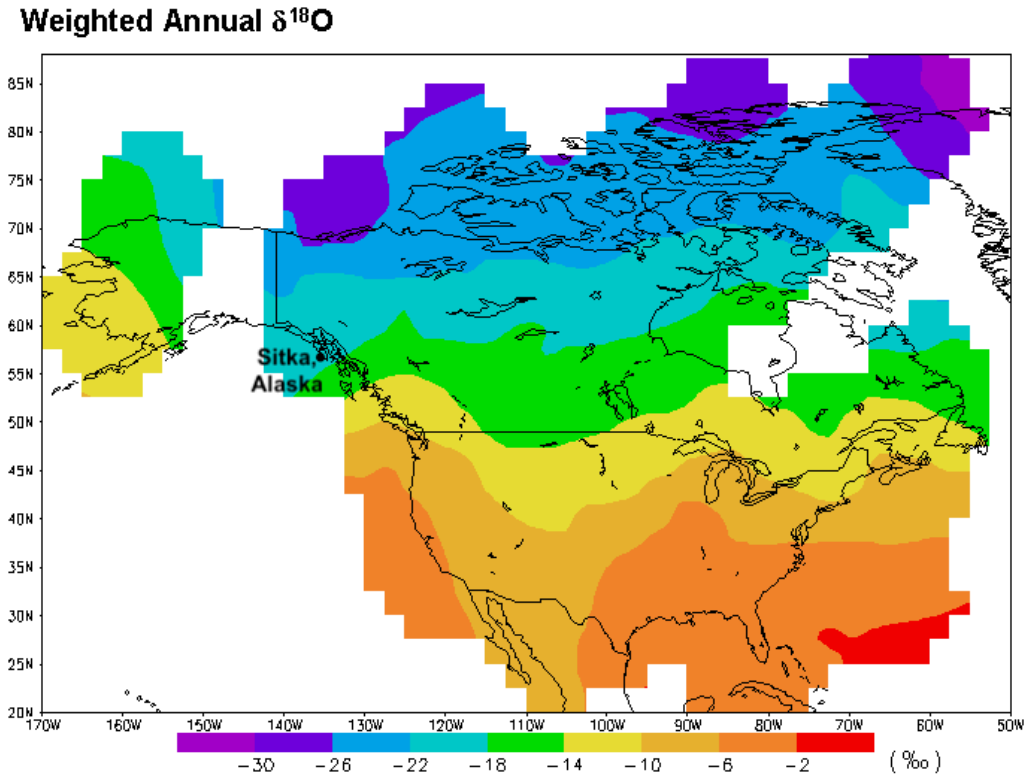


Figure 5.23: GNIP's North American isoscape of $\delta^{18}O_{\text{weighted annual}}$ in precipitation showing a clear latitudinal effect and the location of Sitka, Alaska in a teal-colored zone (defined as -22‰ to -18‰) (IAEA 2001).

Low $\delta^{18}O$ values in meteoric water are characteristic of high latitudes in North America (refer to **figure 5.23**). Geographically, the closest GNIP stations to Sitka are in Bethel, Alaska and Whitehorse, Yukon, Canada. The oxygen isotope data in precipitation from these stations are extremely different (-12.0‰ and -21.4‰, respectively), and their locations suggest climates and susceptibility to environmental parameters that influence isotopes in precipitation in ways that are not applicable to Sitka. In general, the isotope observation network in this region is sparse, resulting in limited data on $\delta^{18}O$ variability across Alaska (Lachniet *et al.* 2016, 6575). An interpolated isoscape map derived from a multiple regression model based on $\delta^{18}O$ in stream waters, altitude, latitude, and July to January mean temperatures of Alaska and Yukon suggest that

the $\delta^{18}O$ value in Sitka is around -11.4‰ (**figure 5.24**) (Lachniet *et al.* 2016, 6581). This is quite different from the GNIP isoscape (**figure 5.23**), which has Sitka in a zone (teal) that is defined as having $\delta^{18}O$ values between -22‰ and -18‰. The study that created an $\delta^{18}O_{water}$ isoscape using stream water observed extreme changes in $\delta^{18}O$ values over short distances, including dramatic decreases from coastal to inland environments (Lachniet *et al.* 2016, 6581). These data show that most of the isotopic distillation of air masses is accomplished from the coast to the first major orographic barrier, which could suggest why Sitka has a significantly higher $\delta^{18}O$ value relative to its closest GNIP station in Whitehorse or regions in the teal zone presented in **figure 5.23** (*ibid.*).

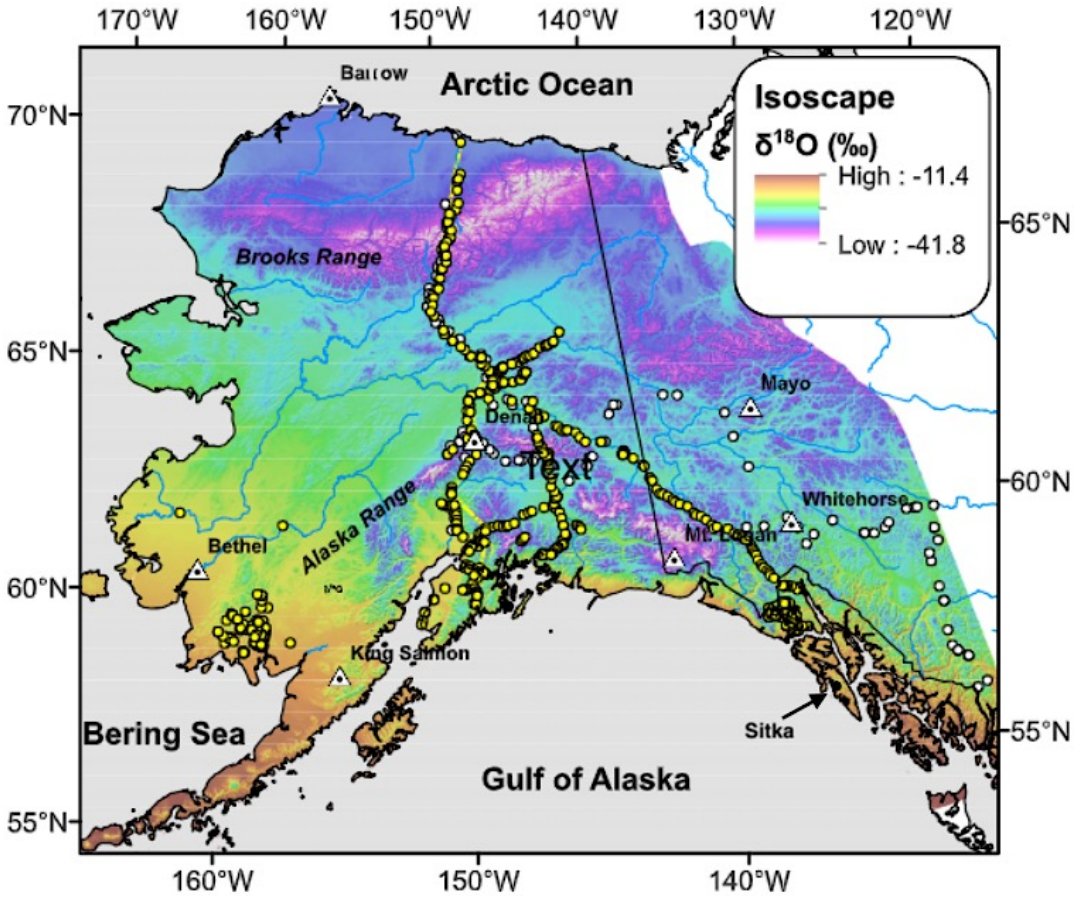


Figure 5.24: $\delta^{18}O$ isoscape based on altitude, latitude, and July to January mean temperatures of Alaska and Yukon. Colors indicate $\delta^{18}O$ values derived from the multiple regression against measured $\delta^{18}O$ values in stream water (yellow circles), test data locations (white circles), and precipitation collection stations (white triangles) from the Lachniet *et al.* (2016) study. This isoscape is draped over hillshade to emphasize topographical details. Adapted from figure 5 in Lachniet *et al.* 2016, 6581.

Batán Grande, Lambayeque, Peru

The Peruvian samples were brought to the Institute of Archaeology, University College London, by a Sicán Archaeological Project conservator for technical analyses (*pers. comm.* Merkel 2010). The Sicán were a civilization that pre-dated the Inca, at the northern coastal site in Batán Grande, Lambayeque (**figure 5.25**). Located about 80 kilometers north of Lima within what is now known as the Poma National Archaeological and Ecological Reserve, Batán Grande is one of

over 30 archaeological sites, many of which were extensively occupied with monumental constructions (Shimada 1995, 12; Shimada & Griffin 1994, 60). This area provided the Sicán with extensive and fertile alluvial plains for irrigation agriculture (Shimada *et al.* 2000, 29). The Pacific coast provided fishing grounds and allowed for maritime trade, and there are convenient mineral deposits in the Andean foothills (Shimada & Merkel 1991, 81; Shimada *et al.* 2000, 29). The patinated copper samples used for analysis were excavated from a massive burial, known as the Huaca Loro East tomb, and abandoned by looters for having too little value compared to the many gold and silver objects that were also entombed. Their exact context within the tomb is therefore not known, but it is possible that they were exposed to a microenvironment isotopically lightened by buried organics like textiles and corpses, as well as the microbes that assisted with decomposition.



Figure 5.25: Map of Peru showing location of Batán Grande in the north (McEwan 2000, 15).

There are only two samples in the Peruvian data set, but they have clear provenance, coming from the same tomb. Sample P2 has a correlating B2 sample, but P3 does not. Two malachite ore samples found at Batán Grande were analyzed isotopically. These samples were

much cleaner than the archaeological samples. The formation site of the ores found in the tomb at Batán Grande is not known, but presumably from the Andean mountains nearby.

Environmental parameters from the closest town, Chiclayo, about 35 kilometers away, were used as proxies for the archaeological site. Chiclayo (and Batán Grande) has a hot desert climate (BWh) near the coast in northern Peru. The yearly daily temperature mean for Chiclayo is 21ºC and it only receives about 21 millimeters of precipitation per year. A soil description could not be found for the Lambayeque area, but a conservator who worked on site and collected the samples used in this study described it as sandy (*pers. comm.* Merkel 2015).

According to the GNIP isoscape map of South America, Batán Grande is in an orange-colored zone, which is defined as having mean $\delta^{18}O$ values in precipitation ranging from -6‰ to -2‰ (**figure 5.26**). The closest GNIP meteoric station to Batán Grande is in Ayabaca, which is inland, has a higher altitude, is much cooler and gets much more rain. These factors considerably affect isotope ratios in rainwater (refer to section 3.2). Including Ayabaca, there are only three stations in Peru that have $\delta^{18}O$ data, and they are all located in very different climates (tropical, equatorial). Stations in neighboring countries are equally unrepresentative. Another station in the desert would be ideal, but there are none along the coast with $\delta^{18}O$ data until Chile. Decidedly, there are no good GNIP station options for Batán Grande. Further investigation revealed that there is generally insufficient $\delta^{18}O$ data for northern coastal Peru, making a formula-based estimate of $\delta^{18}O_{water}$ the only feasible option at this time (Turner *et al.* 2013, 34). $\delta^{18}O_{water}$ data was drawn from an archaeological study by Turner *et al.* (2013) on the $\delta^{18}O$ in human bone carbonate from individuals buried in Chotuna-Huaca de los Sacrificios, Lambayeque. Using a modified formula from Dupras and Schwarza (2001),[1] estimations for $\delta^{18}O$ of the imbibed water were determined by Turner *et al.* to have a mean of -5.1‰ (2013, 33).

[1] $(\delta^{18}O_{carbonate} - 31.2) / 0.78 = \delta^{18}O_{water}$ (Turner *et al.* 2013, 33).

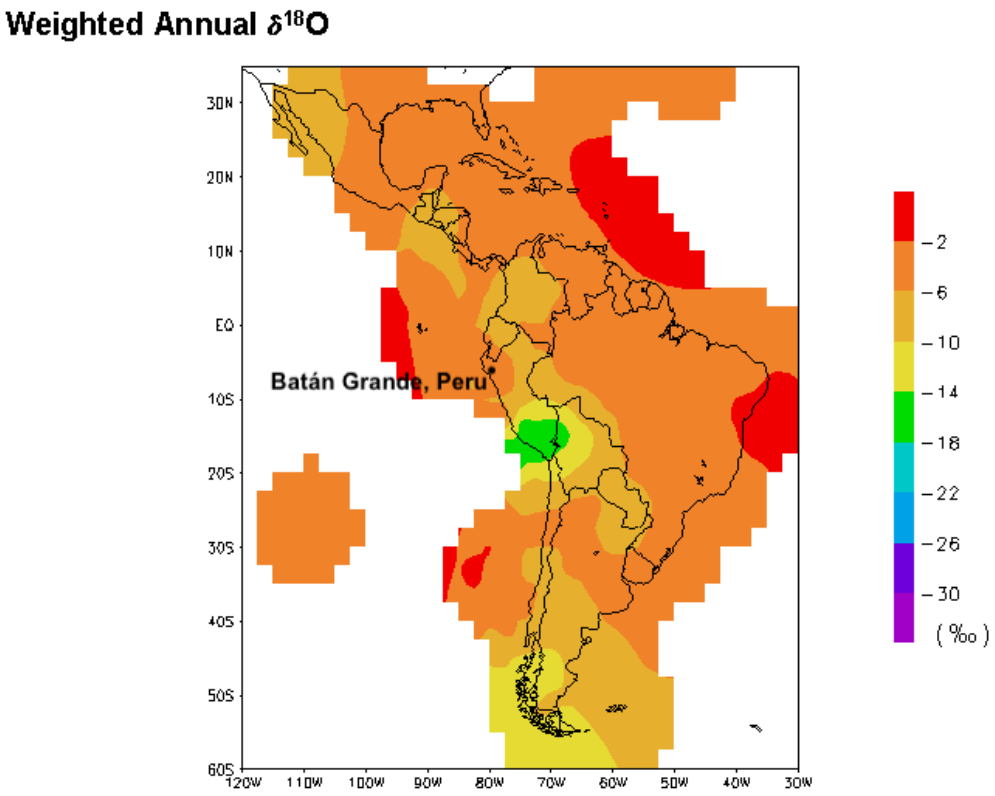


Figure 5.26: GNIP's South American isoscape of $\delta^{18}O_{weighted\ annual}$ in precipitation showing the location of Batán Grande, Peru, in an orange-colored zone (defined as -6‰ to -2‰) (IAEA 2001).

Episkopi and Pyla-Kokkinokremos, Cyprus

Fifteen samples were originally sent for analysis, but many were removed from the malachite study because they were mixed with sulfate products, mainly brochantite. Still, the Cypriot data set is moderate, consisting of three samples with good provenance. Two samples are from the Frankish (Lusignan, 1192-1489 AD) period village of Episkopi near Limassol, and one sample is from a late Bronze Age settlement at Pyla Kokkinokremos near Larnaca (Karageorghis and Demas 1984, 2-5). There are no B2 samples for Cyprus.

Since all samples are from similar latitude, altitude and climate, they were combined to represent southern, coastal Cyprus. Cypriot soils in the sample regions are typically calcaric and generally low in organic matter, particularly for coastal Episkopi (Cyprus 1970). In contrast, Pyla-Kokkinokremos is somewhat inland on a rocky plateau, which may have resulted in slightly different soil and plant prevalence (Soteriades & Grivas 1970; Karageorghis & Demas 1984, 3). The yearly daily mean temperature for Larnaca is 19.5ºC and 18.7ºC for Limassol (refer to **table 5.2**).



Figure 5.27: Map of Cyprus showing locations of sample sites and nearby modern cities (adapted from Prio Cyprus 2011).

In the GNIP isoscape map of Europe (**figure 5.22**), Cyprus is in a yellow zone, which is defined with $\delta^{18}O$ values in precipitation between -8‰ and -5‰. There are three GNIP stations in Cyprus and they are all inland. Data from these stations have weighted mean $\delta^{18}O$ values in precipitation of -5.9‰ (Nicosia), -6.7‰ (Halefka) and -6.7‰ (Prodhromos).[1] The station in Nicosia is the only station that is in the same climate as the sample sites (BSh). Halefka and Prodhromos meteoric stations are in forests at high altitudes in the Csa climate.

Las Pilas, Mojácar, Spain

Six samples were analyzed on a mass spectrometer, but just one Spanish archaeological sample contained enough malachite to yield isotopic data. The sample was collected from an axe head excavated in Las Pilas, near the current city of Mojácar, in Almería, southern Spain. It does not have a correlating B2 sample. This study also included two malachite ores found at Las Pilas.

More samples were collected from southern Spain than any other country, however instrumental characterization repeatedly suggested that most of the samples were not malachite. This was surprising at first because the Spanish samples had exemplary visual descriptions for malachite. Powder XRD suggested that the green mineral present in these samples was a copper (II) chloride hydroxide, like atacamite.

[1] For the Cypriot meteoric stations only, the long-term weighted average $\delta^{18}O$ in precipitation was not provided by GNIP. Instead, the long-term values presented in this thesis were calculated personally by taking the mean of the yearly weighted averages reported by GNIP.

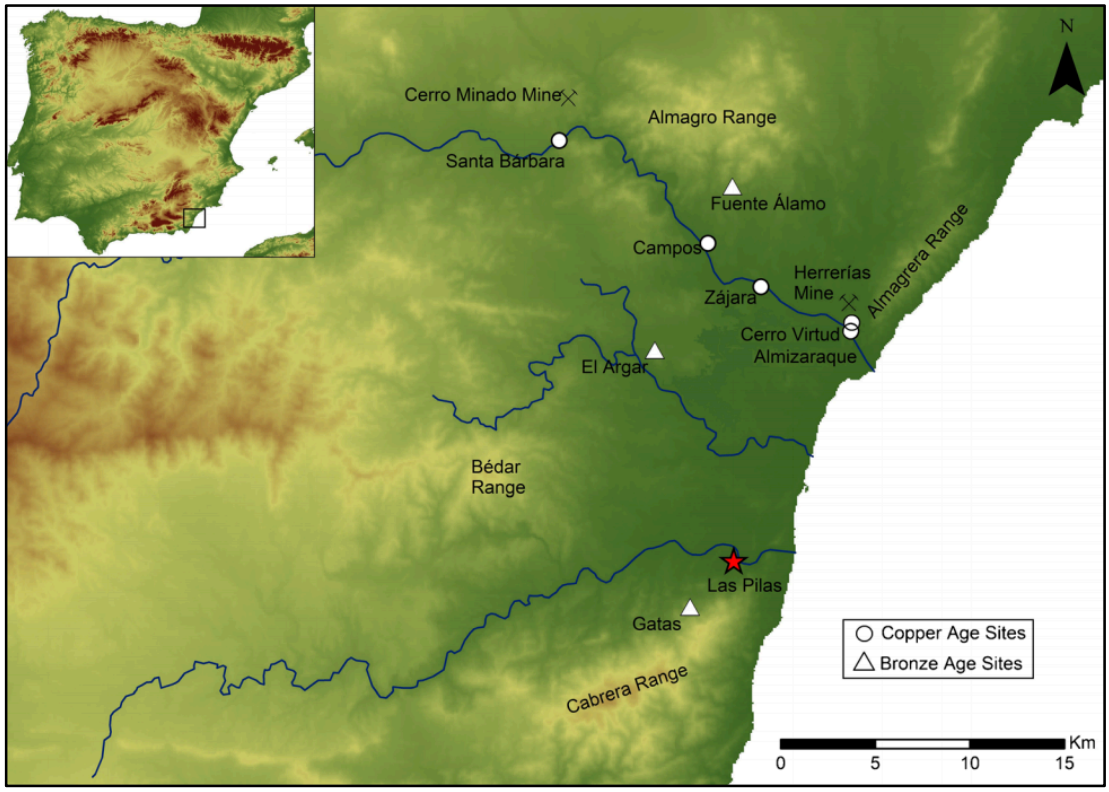


Figure 5.28: Map of Spain showing location of Las Pilas in relation to the main mining districts in the area (Murillo-Barroso *et al.* 2017, 1541).

Occupation at Las Pilas took place during the third millennium BC, or Early Copper Age (Murillo-Barroso 2017, 1541). The Las Pilas archaeological site is on top of a plateau 30 m.a.s.l., close to the estuary of the river Aguas and flanked by two watercourses flowing into it (Murillo-Barroso 2017, 1540). Mojácar is in the most arid region of Europe, marked by irregular and unpredictable rainfall, and a yearly daily mean temperature of 20ºC (climate BSh) (Castro *et al.* 2000, 149). The area is in a chaparral with sierozem soil.

The closest GNIP meteoric station is at the Almería airport, which is located along the coast of the Almería Gulf. It is in a similar climate and a good match for the representation of Las Pilas. The GNIP map in **figure 5.22** of $\delta^{18}O$ values in precipitation across Europe shows Mojácar in a yellow zone, which is defined as -8‰ to -5‰. GNIP's Almería station reports a long-term weighted mean of -5.5‰. Another study carried out by the Spanish Network of Isotopes in Precipitation (SNIP) yielded a higher $\delta^{18}O$ value of -4.3‰, though this study is much less extensive, being based on two years of data collection as opposed to GNIP's 11 years (Araguas-Araguas and Diaz Teijeiro 2005, 176).

Southern England

England is one of the strongest data sets of the study because of its size (11 samples, like Hungary) and because each sample included has a known provenance. There are six B2 samples for England. Corrosion samples were collected by conservators working on coin hoards from Malmsbury (Wiltshire), Pewsey (Wiltshire), and Boldre (Hampshire). Conservators also collected

corrosion samples from unidentified copper alloy objects found at archaeological excavations in London during the 1980's. Near Canterbury, Kent, corrosion was obtained from historic copper alloy objects found at archaeological sites, as well as ingot cake fragments from the mid- to late Bronze Age. A socketed axe head from a hoard excavated in Oxford and treated in the 1880's with a wax coating was also sampled. Together they represent southern England, which has a temperate oceanic climate (Cfb). In general, the natural vegetation of the British Isles deciduous forest, dominated by oak (Shorter *et al.* 1969). Human occupation has left only scattered woodlands, with trees that lose their leaves every year and thrive in mild and wet conditions (*ibid.*).

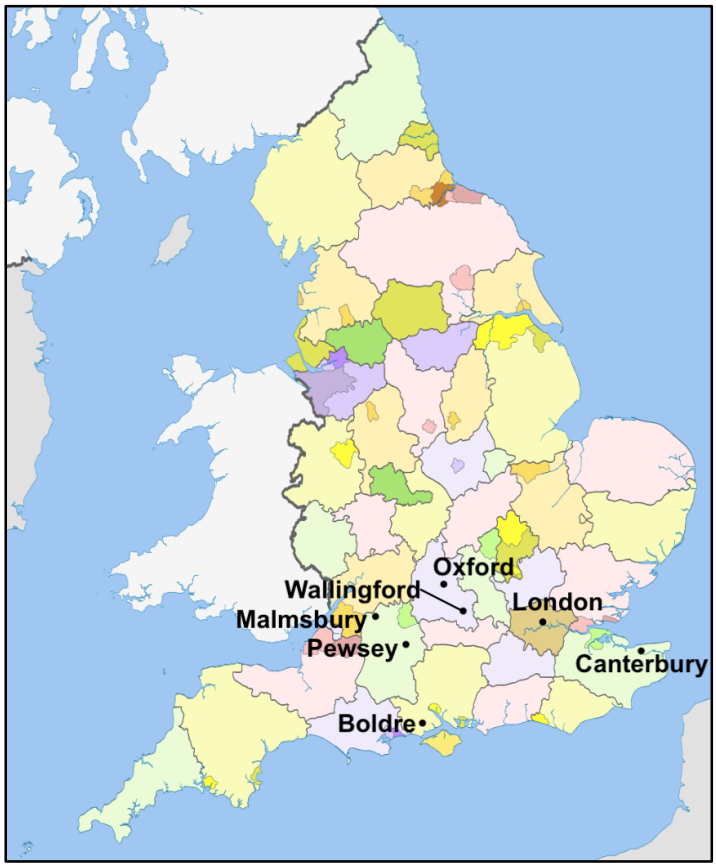


Figure 5.29: County map of England showing locations of sample sites and Wallingford, where GNIP has a meteoric station (adapted from Garber 2011).

In the GNIP map of Europe in **figure 5.22**, England is in a yellow zone, defined as having $\delta^{18}O$ values in precipitation ranging from -8‰ to -5‰. Wallingford, Oxfordshire, has the best-fit meteoric station for all the sample sites included in the English data set. The long-term weighted mean $\delta^{18}O$ value at Wallingford is -7.3‰, with an average yearly temperature of 10.6ºC.

Tel Gezer, Israel

Nine archaeological samples from Israel were procured, of which only three were selected for isotopic analysis. These samples are from Tel Gezer, which is a 33-acre archaeological site in the foothills of the Judean Mountains roughly halfway between Jerusalem and Tel Aviv (**figure 5.30**). One of three cities fortified by Solomon, Tel Gezer was continuously occupied from the

Bronze through Hellenistic Periods (Tel Gezer Project 2019). The context of the samples used in this study is not known, and it is possible that they were collected from objects that were used and buried during different periods. There are no B2 samples for Israel.

Estimated surface temperatures and $\delta^{18}O$ in meteoric water was collected for Bet Dagan, which is close to Tel Gezer, but on the coastal plain closer to Tel Aviv. The two sites have the same Mediterranean climate (Csa) with a similar amount of precipitation per year and the same average air temperatures (19.4ºC). Apart from being closer to the coast, the main difference is altitude with Bet Dagan at 30 meters and Tel Gezer at around 215 meters above sea level.

Bet Dagan is the home of the Israel Meteorological Service and its GNIP station offers the best known stable isotope in precipitation dataset for Israel. Moreover, this station is the closest to Tel Gezer. Other routine precipitation sampling campaigns have augmented the GNIP data, particularly with samples from Rehovot. Rehovot is about equally distant from the coast as Bet Dagan, with an altitude of 50 meters. All of Israel is in a gold-colored zone (defined as -6‰ to -10‰) in the precipitation $\delta^{18}O$ isoscape map presented in **figure 5.32**. However, narrowed data suggests higher $\delta^{18}O$ values, with a weighted mean of -5.2‰ for Bet Dagan (GNIP 2019) and -5.4‰ for Rehovot (Gat *et al.* 2005, 100-101). Another study from 1972 sampled precipitation at Bet Gamal, which is nearby and, like Tel Gezer, has a higher altitude. This study did not provide numerical data for Bet Gamal, but did present a plot that suggests the mean isotope composition is between -5.5‰ and -5.8‰ (**figure 5.31**, Gat & Dansgaard 1972, 185).



Figure 5.30: Map showing location of Tel Gezer relative to Jerusalem, Tel Aviv, Ashdod, and Rehovot (Google Maps 2019). Bet Dagan is about 14 kilometers north of Rehovot, just below the blue Route 1 label by Holon on this map.

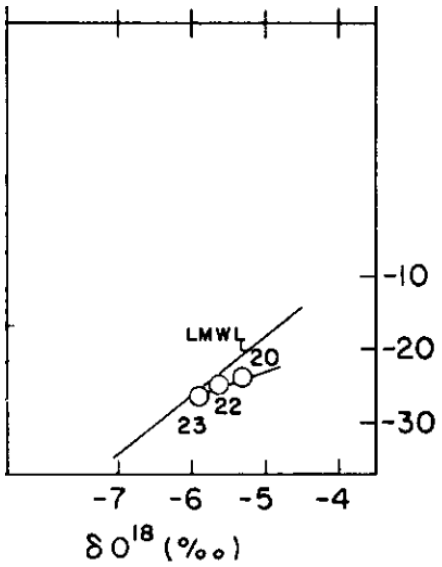


Figure 5.31: The Gat and Dansgaard plot of $\delta^{18}O$ (x-axis) against $\delta^{2}H$ (y-axis, not labeled on plot) in precipitation at Bet Gamal (marked as 22) (1972, 185). Point 20 is Ashdod and 23 represents Jerusalem (179).

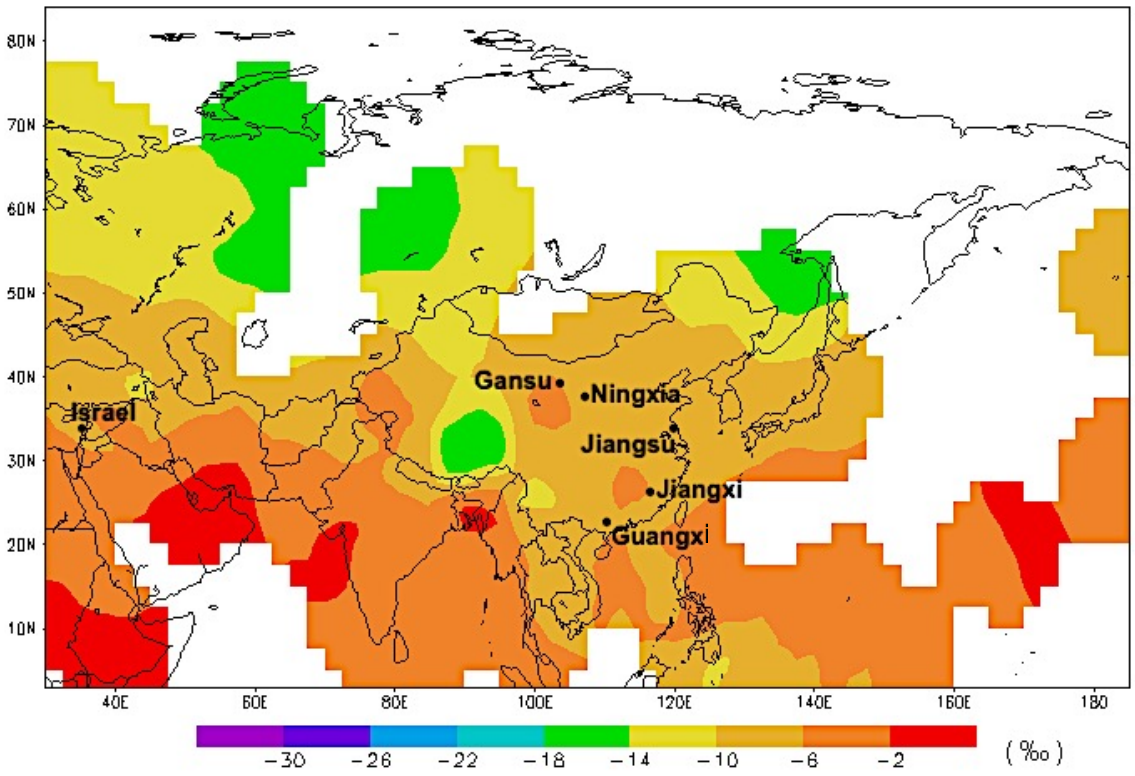


Figure 5.32: GNIP's Asia isoscape of $\delta^{18}O_{\text{weighted annual}}$ in precipitation showing the locations of Israel, Gansu, Ningxia, Jiangsu, Jiangxi and Guangxi in gold and orange-colored zones (defined as -6‰ to -10‰, and -6‰ to -2‰, respectively) (IAEA 2001).

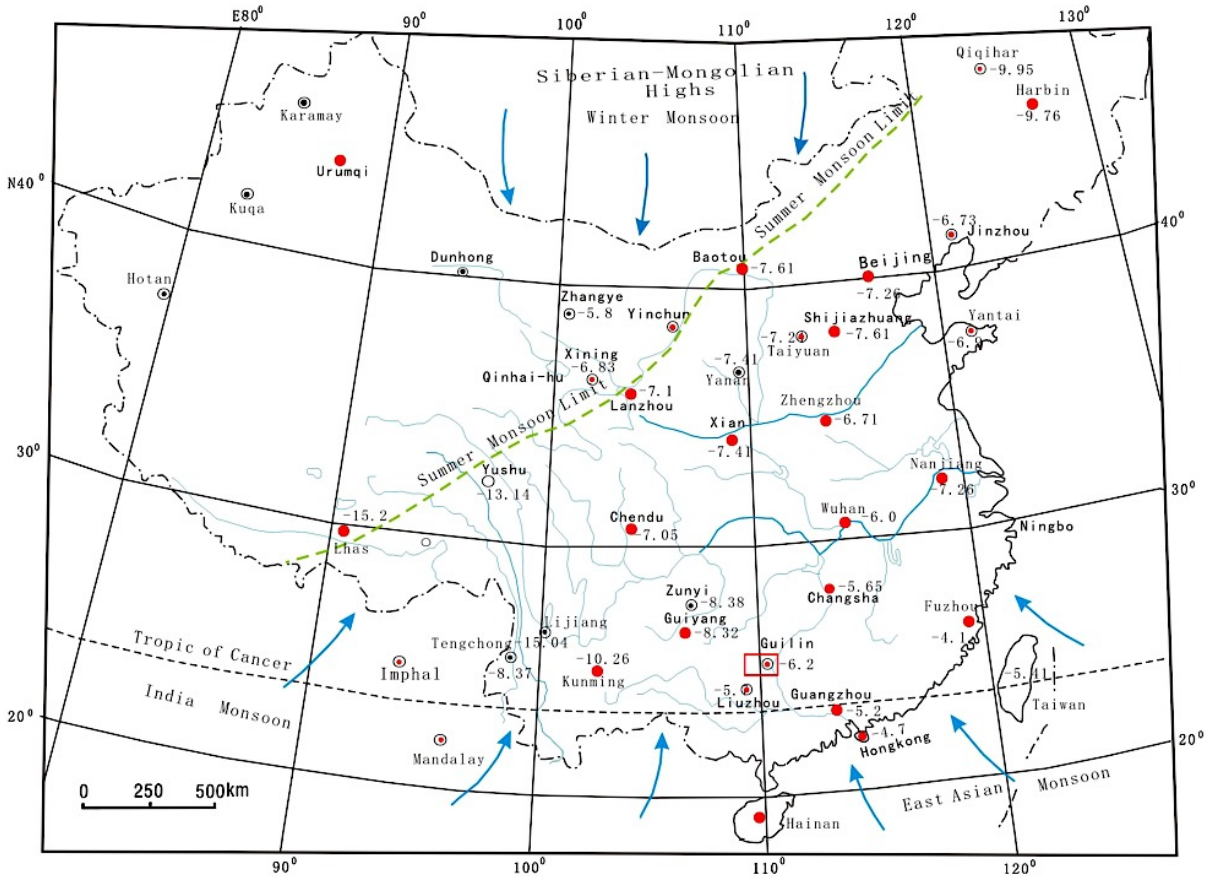


Figure 5.33: Showing the distribution of annual average precipitation $\delta^{18}O$ in China and the monsoon trajectories. The data are the annual average $\delta^{18}O$ values of the precipitation (Zheng *et al.* 1983 and Liu *et al.* 2008 cited in Zhang *et al.* 2015, 955).

Gansu, China

There is only one malachite sample assumed to be from Gansu, and its excavation site within Gansu is unknown. The patina sample came from the interior surface of a *ding* vessel. *Dings* are ancient Chinese ritual cauldrons, mainly used for cooking meat (Li 1995, 16). They are either three-legged and round, or four-legged and rectangular, and may or may not have a lid (**figure 5.34**) (*ibid.*). These vessels were commonly imitated from the Song dynasty (medieval period onwards), and the context of the *ding* used in this study is not known (Sena 2019, 96-109). There is no B2 sample for Gansu.

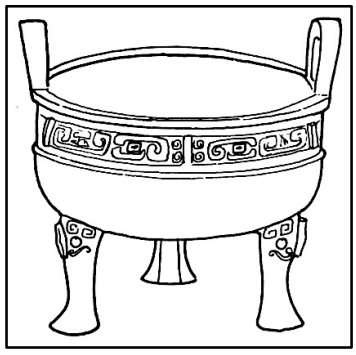


Figure 5.34: Example of a *ding* cauldron, based on a vessel found at Shaanxi Fufeng Shaochencun, Late Western Zhou (Rawson 1987, 40).

Gansu is a long province on the junction of the Loess and Tibetan Plateaus in north-central China with considerable latitudinal, climate and soil type range. Part of the Gobi Desert is in the northern-most region of Gansu, but the landscape in the south is very mountainous. On the GNIP isoscape map of $\delta^{18}O$ in precipitation in **figure 5.32**, Gansu is predominantly in a gold-colored zone, defined as -6‰ to -10‰, and partly in an orange zone, defined as -2‰ to -6‰. This data is mainly from two meteoric stations: Lanzhou and Zhangye. Lanzhou is the capital of Gansu, and has a cold, semi-arid climate (BSk) with an average yearly air temperature of 10ºC. It is about 1500 meters above sea level and has a GNIP $\delta^{18}O$ long-term yearly mean of -4.8‰. Farther north, Zhangye's GNIP station shares very similar environmental parameters with Lanzhou, but has a higher $\delta^{18}O$ long term yearly value of -5.7‰. Expanding on the GNIP data, two studies on the variation of stable isotopes in precipitation in Gansu are also considered, as well as the CHNIP data at Linze. Northwest of Zhangye, the Heihe River Basin was studied by Wu *et al.* (2010) via Xishui, Yingluoxia, Ganzhou, Pingchuan, Zhenyixia, and Juiguan (mapped in **figure 5.36**, data on **table 5.1**). Lanzhou City and the surrounding area was studied by Chen *et al.* (2015), specifically at Yongdeng, Gaolan, Yuzhong, and Lanzhou City (mapped in **figure 5.37**, data on **table 5.1**). Since the Gansu patina sample has no known provenance, isotopic data in precipitation from all of these sites are considered as potential formation environments.



Figure 5.35: Map of China with Gansu province in red, showing the locations of Zhangye and Lanzhou (adapted from Dedering 2011).

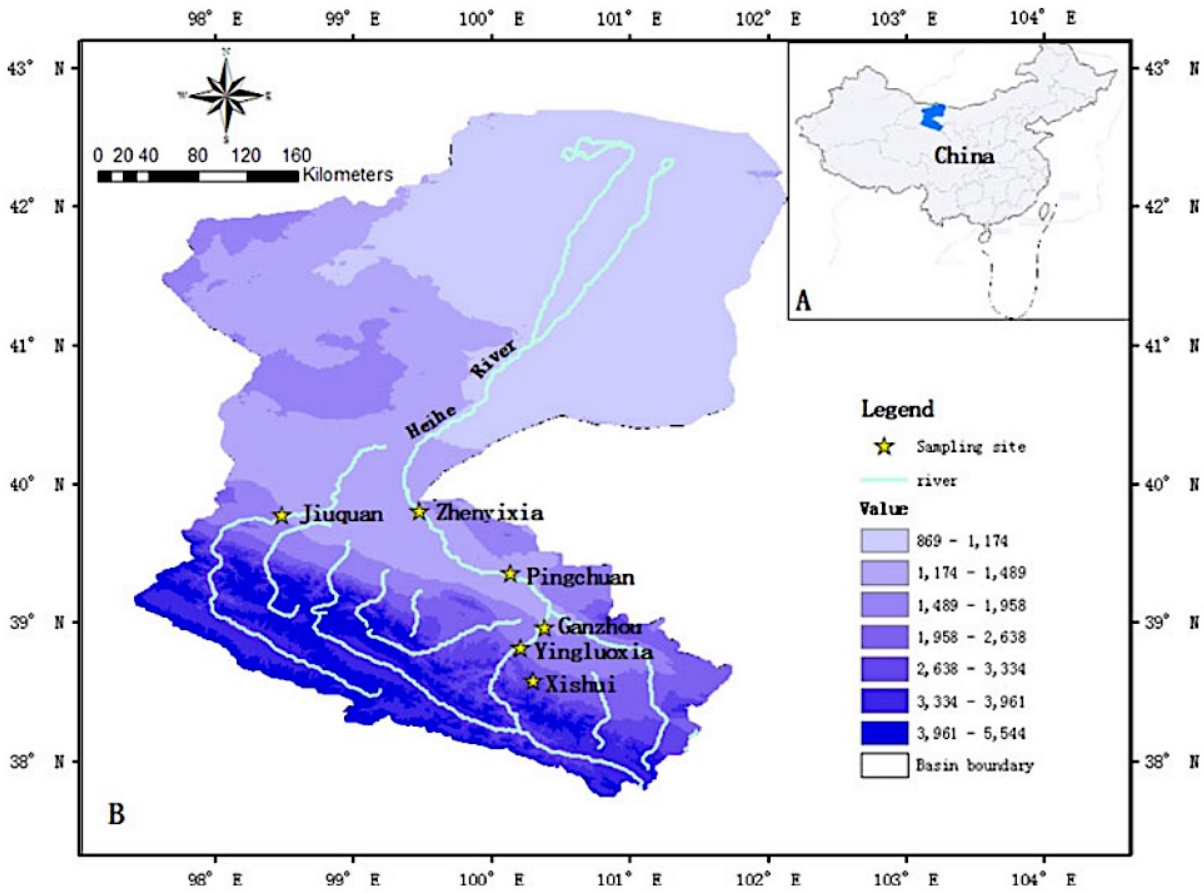


Figure 5.36: Showing locations and topography of the Wu *et al.* study area and sampling sites in the Heihe River Basin, northern Gansu (2010, 1124).

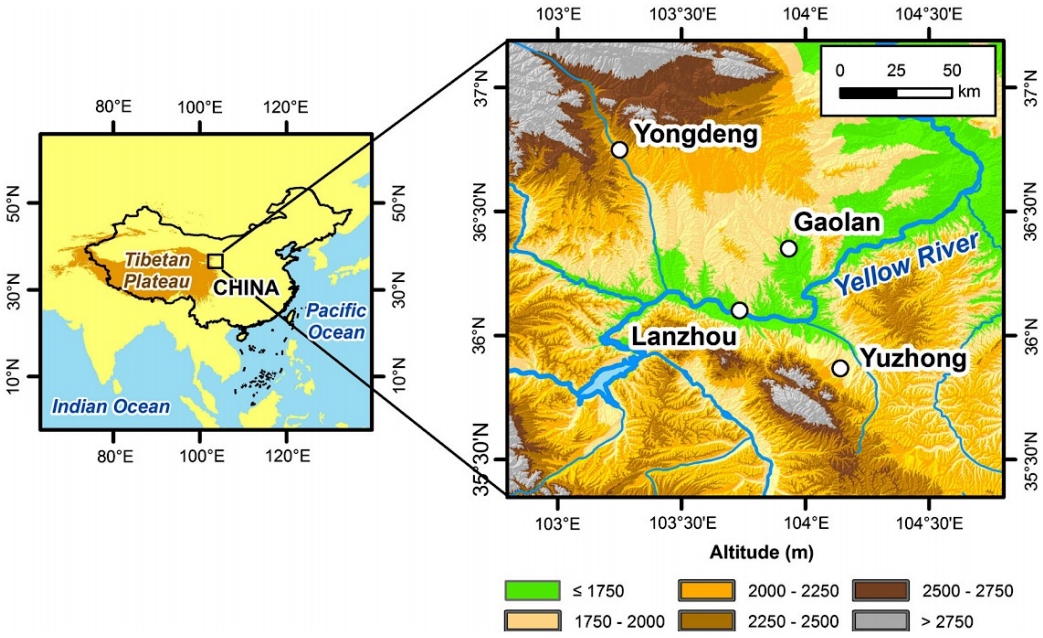


Figure 5.37: Showing locations and topography of the Chen *et al.* Lanzhou study region and sampling stations in Lanzhou City and its surrounding area (2015, 4673).

Station	Altitude (m.a.s.l.)	$\delta^{18}O$ (‰) w. mean
Yongdeng	2118.8	-5.4
Gaolan	1668.5	-5.6
Lanzhou	1548	-5.7
Lanzhou (GNIP)	1522	-4.8
Yuzhong	1874.4	-9.3
Xishui	2569	-9.2
Yingluoxia	1698	-6.5
Ganzhou	1526	-5.7
Pingchuan	1382	-4.4
Zhenyixia	1276	-2.2
Jiuquan	1480	-11.3
Zhangye (GNIP)	1490	-5.7
Linze (CHNIP)	1375	-6.2

Table 5.1: Altitude and long-term weighted means of $\delta^{18}O$ in precipitation at the sampling sites in Gansu (IAEA/GNIP 2019; Wu *et al.* 2010, 1125-1126; Chen *et al.* 2015, 4673 & 4675; Liu *et al.* 2014, 5).

Guangxi, China

There are four archaeological malachite samples from Guangxi, but their excavation sites within Guangxi are unknown. Two samples were collected from *ding* vessels (refer to the profile on Gansu for a description), one from a *hu* vessel, and the fourth was simply described as being from the interior base of an object. *Hu* vessels are ritual, pear-shaped wine containers (Rawson 1987, 41; Li 1995, 35). Some *hu* wine containers have ladles attached to them (Li 1995, 35). It is possible that the samples are from multiple sites, and one of the *ding* samples may not actually be from Guangxi. There are two B2 samples for Guangxi, which were roughly picked using a needle under a binocular microscope.

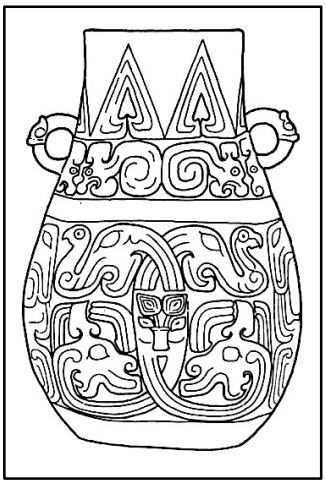


Figure 5.38: Example of a *hu* wine container, based on an early Eastern Zhou vessel at the British Museum (Rawson 1987, 43).



Figure 5.39: Map of China, with Guangxi in red, and locations of Liuzhou and Guilin marked (adapted from Dedering 2011).

Guangxi is in south central China. It is partly mountainous and in a monsoon influenced subtropical climate (Cfa) (Zhang *et al.* 2015, 954). Consequently, the effects of latitude and season on isotopic compositions are significant (Ke *et al.* 2013, 62). There are two GNIP stations in Guangxi, at Guilin and Liuzhou, which are in the northeast of the province and at low altitudes (Liuzhou is at 103 m.a.s.l. and Guilin at 381 m.a.s.l.). The GNIP $\delta^{18}O_{water}$ isoscape presented in **figure 5.32** shows Guangxi in a gold-colored zone, which is defined as -6‰ to -10‰. More specific GNIP data reports Guilin as having a long-term $\delta^{18}O$ weighted average of -6.2‰ and surface temperature of 19ºC. Liuzhou is -6.4‰ with the same average surface temperature of 19ºC. The map in **figure 5.33** similarly has Guilin labeled as having an annual average $\delta^{18}O$ value of -6.2‰, but Liuzhou has a higher $\delta^{18}O$ value at -5‰. A more recent study on stable isotopes in precipitation by Zhang *et al.* determined that the weighted average $\delta^{18}O_{water}$ in Guilin is -5.8‰, with an annual average temperature of 19.2ºC (2015, 953).

Jiangsu, China

One archaeological sample is representing Jiangsu, and its exact provenance within Jiangsu is unknown. The sample was collected from a *ding* vessel leg (**figure 5.34**). There is a correlating B2 sample for Jiangsu.



Figure 5.40: Map of China, showing Jiangsu in red, and the location of Nanjing marked (adapted from Dedering 2011).

Jiangsu is a small, coastal, eastern-central province in China. It is mostly flat and covered with plains and deciduous forest. The climate is mainly monsoon influenced tropical (Cfa), but the far north transitions into a humid continental climate (Dwa). The GNIP $\delta^{18}O$ in precipitation isoscape of Asia (**figure 5.32**) shows Jiangsu in the gold-colored zone, which is defined as -6‰ to -10‰. This is based on precipitation samples collected at the capital of Jiangsu, Nanjing. Nanjing is located on the lower reaches of the Yangtze River, surrounded by low hilly terrain with an average altitude of 25 m.a.s.l. and a mean annual air temperature of 16ºC (14.6ºC reported by GNIP) (Tang *et al.* 2015, 4295). The GNIP station at Nanjing reports a long-term weighted mean $\delta^{18}O$ in precipitation of -8.0‰. In comparison, the map in **figure 5.33** has Nanjing labeled with an annual average $\delta^{18}O$ value of -7.3‰. Another study focused on stable isotopes in precipitation at Nanjing reported a weighted mean $\delta^{18}O$ in the summer monsoon season of -9.1‰, and -4.9‰ for the non-monsoon season (Tang *et al.* 2015, 4297).

Jiangxi, China

Jiangxi is represented with one archaeological malachite sample, described as being collected from a 13-11th century vessel at the Niucheng archaeological site in Xingan, which is located at the center of Jiangxi province. There is no B2 sample for Jiangxi.



Figure 5.41: Map of China showing Jiangxi in red and the locations of Niucheng, Ji'an, Yingtan, and Qianyanzhou (adapted from Dedering 2011).

Jiangxi is in the south east of China, surrounded by mountains, but itself is flat in the north with some hills in the south. Ji'an is the closest city to the archaeological site, with a humid subtropical climate (Cfa). Jiangxi does not have any GNIP meteoric stations, but the GNIP map in **figure 5.32** shows Jiangxi in gold-colored and orange zones, which are defined as having average $\delta^{18}O$ values in precipitation between -6‰ and -10‰, and -2‰ to -6‰, respectively. **Figure 5.33** does not display any stations in Jiangxi, however there are two CHNIP stations at Yingtan and Qianyanzhou (**figure 5.41**). Yingtan has an altitude of 45 m.a.s.l., a mean surface temperature of 18.4ºC, and an average $\delta^{18}O$ value in precipitation of -5.6‰ (Liu *et al.* 2014, 5). Qianyanzhou has an altitude of 76.4 m.a.s.l., a mean surface temperature of 17.9ºC, and an average $\delta^{18}O$ value in precipitation of -4.5‰ (*ibid.*).

Ningxia, China

Five of the six malachite samples from Ningxia were collected from slag fragments found on the ground surface at the west of the region near the Gobi Desert. The sixth sample is from a museum object, a tube fragment, with no known site and is only suspected to be from Ningxia. Three of the archaeological malachite samples were roughly picked and analyzed towards the B2 study. Four malachite ore samples were collected from Ningxia for comparison to the archaeological malachite samples. The ores were found at the ground surface near the Gobi Desert, as the archaeological samples, but this not likely the formation site of the ores.



Figure 5.42: Map of China showing Ningxia in red, and the locations of Yinchuan and Shapotou district (adapted from Dedering 2011).

Ningxia is a small autonomous region in north central China with a diverse geography. On the GNIP map in **figure 5.32**, Ningxia is in a gold-colored zone, defined as having $\delta^{18}O$ values in precipitation between -6‰ and -10‰. There is only one GNIP meteoric station in Ningxia, located in the capital city, Yinchuan. Yinchuan is unlike the environment from which most of the malachite samples formed. It is in a high altitude and is sheltered from nearby deserts by the Helan Mountains. It is therefore suspected that any isotopic data on the precipitation at Yinchuan is not applicable to the malachite samples used in this study. However, CHNIP has a suitable station in the Shapotou district, Zhongwei, which is noted for the Tengger Desert, and boarders Inner Mongolia to the north. The Shapotou station is 1350 m.a.s.l., has average yearly surface temperature of 10.9ºC, and a mean $\delta^{18}O$ value in precipitation of -7.2‰ (Liu *et al.* 2014, 5).

5.2.6. Isolation of Malachite Crystals and Measurement of $\delta^{18}O$ and $\delta^{13}C$

The focus of this research was to measure the carbonate $\delta^{18}O$ values in malachite, the crystals of which requiring manual isolation from a mixed-phase patina sample by steadily using a sewing needle under a under a binocular microscope. Picked samples were tested for material characterization using FTIR and XRD, which identified many unsuitable samples. In total, 96 B1 and B2 samples passed for isotope analysis. The $\delta^{18}O$ and $\delta^{13}C$ in the carbonate of the malachite samples were determined by the standard method of reaction with 100% orthophosphoric acid at

70ºC to release the CO_2 gas, which was purified and analyzed on an IRMS. A detailed lab procedure is the topic of this section.

Laboratory Procedure:

1) Hand-pick malachite samples using a sewing needle under a binocular microscope, then grind them to a mesh powder using an agate mortar.
2) Confirm material identification on picked samples by FTIR and XRD. Remove samples containing sulfur from the study.
3) Weigh out samples between 0.25-0.50 mg. Manually load samples into 10ml round-bottomed borosilicate exetainers. Seal using butyl rubber septa (Labco).
4) Place exetainers into an aluminium tray kept at 70.0 ± 0.1ºC.
5) Exetainers automatically flushed with 5.0 He by penetrating the septa using a double-hole needle at a flow rate of 120ml/min.
6) 4-6 drops of phosphoric acid (density 1.91) are automatically deposited in each exetainer using the autosampler and a stainless-steel capillary needle attached to an acid pump, while the second needle transfers the evolved gas from a neighboring vial into the GasBench II driven by a small stream of He (0.5-1ml/min) (~60 minutes per sample).
7) Water is removed using Nafion traps. CO_2 is separated from other components using a gas chromatographic column (Poraplot Q with fused-silica tubing, 25m x 0.32mm) heated to 70ºC. The CO_2 passes via an open split into the mass spectrometer.

- Reference standards: calcite was CarraraZ with Fletton Clay as a secondary standard, CO_2 was CP grade, followed by blanks (empty exetainers).
- Since the Phosphoric Acid Fractionation Factor (PAFF) is unknown for malachite, the oxygen isotope data is corrected using PAFF value for calcite (=1.008176 at 90ºC, DasSharma *et al.* 2002).
- The reason for choosing a reaction temperature of 70ºC is that PAFF not only depends on the nature of the carbonate cation but also heavily on grain size (Al-Aasm *et al.* 1990), since PAFF is caused by a kinetic fractionation process. This effect is minimized when using higher temperatures.
- The entire calibration is based directly on standard materials that are part of each run rather than solving fractionation equations for the acid-based reaction. In other words, there is no need to know the stable isotopic composition of the CO_2 reference gas a prior, nor the acid fractionation factor at the given temperature of the reaction. Therefore, the CO_2 gas is in oxygen isotope equilibrium with the experimental solution and does not need to be acid fractionation-corrected.
- For natural samples, the amount of CO_2 gas yielded by sample acidification was compared with insoluble residue left after sample acidification, to evaluate the purity of malachite mineral separates.

For this research project, interactions with the GasBench II and related computer software did not extend beyond weighing a small selection of malachite samples into exetainers. Quality control and data processing was entrusted to the analysts, and the detailed measurement protocols are assumed to be standardized, but needs reviewing.

Stable isotope measurements were carried out on a ThermoFinnigan GasBench II equipped with a CTC Combi-Pal autosampler and linked to a Delta 5 mass spectrometer at the Godwin Laboratory for Paleoclimate Research in the Department of Earth Sciences at the University of Cambridge. Eight of the samples run did not produce enough CO_2 to make measurements. These were repeated using much larger samples, but still not enough CO_2 was collected to measure. This was odd because the XRD results on these samples suggested that they contained sufficient malachite to carry out isotopic analyses. In these cases, however, the malachite percentages were around 25%, and with more than three phases present, a good XRD assessment can be difficult. It is possible that the XRD results were inaccurate and that the true quantities of malachite present were indeed too low for isotope analysis.

5.2.7. Statistical Analyses on Malachite Data

The isotope data from the malachite samples were processed statistically. The same approach that was used on the brochantite study was used for the malachite study. This included descriptive statistics (mean, standard deviation, coefficient of variation, the standard error and 95% confidence interval for the mean). Grubb's outlier test was used to identify data points that are inconsistent with the rest in their group. This work is presented in writing, tables and plots in Chapter 7, which covers the malachite results.

The malachite data was also analyzed using paired *t*-tests and Anova to assess the difference between two related samples and compare the variance between different groups. Groups being tested include the B1 and B2 datasets to assess the necessity of meticulous picking and understand the impact of typical contaminants.

Regression statistics were carried out to look for relationships between the malachite data and environmental parameters like the $\delta^{18}O$ in local meteoric water and surface temperature, which served as proxies for the formation conditions. A geothermometer equation based on the equilibrium $\delta^{18}O$ fractionation between malachite and water was also investigated through regression analysis.

5.3. SUMMARY

This chapter is divided into two parts; the first dedicated to the brochantite study, and the second to the malachite study.

Brochantite

To understand the reaction pathway between copper and its oxidizing environment, stable isotope information was extracted from brochantite samples isolated from scrapings off patinated copper roofs with known geographic locations (Oxford, Vienna, Ottawa and Tuscaloosa). This study did not include water sample collection. Instead, meteoric water $\delta^{18}O$ values were found on the Global Network of Isotopes in Precipitation (GNIP). To confirm the identify the mineral phases present in the copper corrosion roof samples as brochantite, powder x-ray diffraction (XRD) was employed.

The laboratory procedure used in this study involved dissolving 30 – 50mg patina samples in 1 M hydrochloric acid, followed by several filtrations to remove any non-sulfate minerals. Barium chloride was added to yield $BaSO_4$ and isolate the sulfate ion of interest. The $BaSO_4$ was converted to CO and analyzed using a high temperature conversion/elemental analyzer–isotope ratio–mass spectrometer (TC/EA-IR-MS). The isotopic data from the brochantite samples were processed statistically, with results presented in Chapter 6.

The hydroxyl oxygen in brochantite was measured because it was suspected that the δ^2H is entirely meteoric in origin. A pilot study was also carried out for the analysis of δ^2H from the hydroxyl groups using a method requiring only 8-10 mg of brochantite for $^2H/^1H$ analysis of water by reduction on hot zinc. The hydroxyl oxygen in brochantite was measured because it was suspected that the δ^2H is entirely meteoric in origin. These measurements were processed statistically and are also presented in Chapter 6.

Malachite

The objective for the analytical malachite study was to create a database of $\delta^{18}O$ values for archaeological malachite from a varying range of geographic sites with clear meteoric $\delta^{18}O$ differences in precipitation. The malachite study went further by also considering $\delta^{13}C$ values in the malachite carbonate. These values were compared to various local environmental parameters to identify the most influential factors and trends that may be used in provenance and authenticity studies.

People working in the country of the objects' origin collected many of the samples used in the malachite study. This was necessary because it would not have been financially practical to personally visit each country with potential samples. Over 205 samples were acquired for the malachite study (refer to Appendix A for a full sample catalog). The samples offered the malachite study with good geographic variance, and considerable isotopic distribution in the meteoric water.

Malachite was visually identified under a binocular microscope and carefully isolated using a small sewing needle. Once past optical microscopy (OM), malachite samples were homogenized using a mortar and pestle and weighed. FTIR served as a filtration step to remove samples that clearly did not contain malachite, as FTIR is far less expensive and more easily accessible than XRD. XRD provided reliable characterizations of the malachite and any contaminants, as well as suggesting percent compositions of each phase present.

Processing resulted in the elimination of over 75% of samples, leaving 49 malachite samples grouped into twelve formation regions for isotopic analysis. They are: Alaska, USA; northern Peru; Hungary; Cyprus; southern Spain; southern England; Israel and the following Chinese provinces: Gansu, Guangxi, Jiangsu, Jiangxi and Ningxia.

Testing the necessity of such a meticulous picking process by also analyzing less pure samples isotopically. To do this, two malachite study batches were created. Batch one (B1) consisted of the purest malachite samples, as determined by the original sample criteria based on visual assessment, FTIR and XRD. Batch two (B2) consisted of supposedly more contaminated versions of B1 samples to evaluate the level of purity necessary to get reliable stable isotope data on malachite. The degree of contamination and phases present in each B2 sample varied. Not all B2 samples had correlating B1 samples.

Environmental details on the twelve formation regions, including climate classification, soil type and biome, are provided in the site profiles section. These profiles also include data for $\delta^{18}O$ in local meteoric water and surface temperatures that were used in calculations through the geothermometer equation. This information is condensed and is presented in **table 5.2**, on the following page. Where known, information regarding the objects from which the samples came and archaeological contexts are provided.

The $\delta^{18}O$ and $\delta^{13}C$ in the carbonate of the malachite samples were determined by the standard method of reaction with 100% orthophosphoric acid at 70ºC to release the CO_2 gas, which was purified and analyzed on an IRMS. The isotope data from the malachite samples were processed statistically, with the results presented in Chapter7.

Region	Latitude	Altitude (m.a.s.l.)	Average Yearly Surface Temperature (ºC)	Yearly Mean Precipitation (mm)	Köppen Climate	Biome	Soil Description
Debrecen, Hungary	47.5	110	10.6	600	Cfb	Deciduous Forest, Alpine	Brown Earth
Sitka, Alaska	57.1	18	7.4	3350	Cfb	Coastal Alpine	Lithosol, Boggy
Chiclayo, Peru	-6.8	100	21.0	20	BWh	Desert, Desert Scrub	Unknown dry
Limassol and Larnaca, Cyprus	~35	~61.5	19.5, 18.7	420	BSh	Chaparral, Grassland	Calcaric, Cambisols, Lithosols, Regosols
Mojácar, Spain	37.1	30	20.0	200	BSh	Chaparral	Sierozems
Southern England	51.5	55.5	10.6	700	Cfb	Deciduous Forest	Brown Calcareous Earths, Rendzinas
Bet Dagan, Israel	31.9	217	19.4	550	Csa	Grassland	Brown and Pale Rendzinas
Lanzhou, Gansu	36.0	1500	10.0	300	BSk	Alpine, Desert, Grassland	Sierozems, Grey-Cinnamon Soils, Warped Irrigated Soils
Guilin, Guangxi	25.3	103	19.0	1888	Cfa	Rainforest, Alpine	Red Earths, Limestone Soils
Nanjing, Jiangsu	32.1	25.0	16.0	1090	Cfa	Deciduous Forest	Yellow-Brown Earths, Paddy Soils
Niucheng, Jiangxi	27.9	45	18.4	1519	Cfa	Rainforest	Red Earths, Yellow-Brown Earths
Shapotou District, Zhongwei, Ningxia	38.5	1350	9.0	186	BWk	Desert, Grassland	Sierozems, Aeolian Sandy Soils

Table 5.2: Table showing environmental data for each sample region. Refer to Appendix F for citations.

CHAPTER 6

XRD and Stable Isotope Results for Brochantite

6.1. MATERIAL CHARACTERIZATION: XRD RESULTS

As described in section 5.1.2, XRD provided reliable characterizations of the brochantite samples, including the identification of contaminants. Only the samples used for stable isotope analysis are provided in the XRD results **table 6.1**. A full list of samples collected and analyzed is available in Appendix A.

Tuscaloosa, Alabama, USA

Building	*XRD ID*
Carmichael Hall vent	brochantite, quartz
Presidential Hall	brochantite, quartz
Farrah Hall	brochantite, quartz
Wilson Hall	brochantite, quartz
Bidgood Hall	brochantite, one unidentified peak
Gallalee Hall	brochantite, quartz
Bryce Hospital (Reception)	brochantite, quartz
Bryce Hospital (Women's Wing)	brochantite, one unidentified peak

Vienna, Austria

Building	*XRD ID*
Linke Sheet	brochantite, 2 unidentified peak
Burgtheater Chimney	brochantite, one unidentified peak
Karlskirche	brochantite
Hofburg angel base	brochantite
Peterskirche	brochantite, one unidentified peak
Votivekirche	brochantite
Vienna Tech. Uni	brochantite

Oxford, UK

Building	*XRD ID*
Old Observatory	brochantite
Rhodes Mandela	brochantite
Corpus Christi	brochantite
New College	brochantite
Oriel Library	brochantite
St. Cross Law vent	brochantite
Philosophy Centre	brochantite
Rhodes House (Oriel)	brochantite
St. Cross Law roof	brochantite

Ottawa, Ontario, Canada

Building	*XRD ID*
Confederation Bldg.	brochantite
Booth House	brochantite
Wellington Bldg.	brochantite
Center Block (Wojdan)	brochantite, cuprite
American Embassy	brochantite
St. Joseph's Parish	brochantite
Hotel Lord Elgin	brochantite, antlerite
Bruyère Hospital	brochantite, cuprite
Center Block (Selwyn)	brochantite

Table 6.1: Powder XRD results for samples collected from patinated roofs and historic objects that continued to isotopic analysis. All samples were predominantly brochantite, but several samples were mixed phase and required processing to isolate the brochantite and its sulfate oxygen.

6.2. BROCHANTITE $\delta^{18}O_{SO4}$ RESULTS

6.2.1. Presentation of Raw Data and Descriptive Statistics

The following tables (**table 6.2 and 6.3**), quartered to isolate data for each city, contains the $\delta^{18}O$ values (VSMOW) for the 33 analyzed $BaSO_4$ samples. The measured $BaSO_4$ samples were derived from $CuSO_4$, as described in Chapter 5, section 5.1.3. The $\delta^{18}O$ values range from 4.7‰ (Wellington Building in Ottawa) to 13.8‰ (Presidential Hall in Tuscaloosa, outlier). Excluding outliers from this point forward, the city mean for the $\delta^{18}O$ data ranges from 7.0 ± 1.4‰ in Ottawa to 7.7 ± 0.5‰ in Oxford. To determine the strength of central tendencies within raw data sets and quantify the amount of dispersion, the standard deviation (SD) was calculated for each city. The extent of variability in relation to the mean, known as the coefficient of variation (CV), is also provided, as well as the standard error. Oxford has the lowest standard deviation (SD = 0.5‰) and coefficient of variation (CV = 6.5%), meaning that its data points are close to the mean. Ottawa has the highest standard deviation (SD = 1.4‰) and coefficient of variation (CV = 19.4%), meaning that its data points are farthest spread.

Grubb's outlier test finds the single most outlying data point. These are marked with an asterisk in **table 6.3** and identified by the outlier test significance probability, *p*. A *p*-value reflects the probability of getting a value for the statistic equal to or more extreme than the one calculated in a hypothesis test, if the null hypothesis is true (Hawkins 2019, 98). A null hypothesis will say that there is no pattern in the data; for example, that there is no difference between samples or no relationship between variables (Hawkins 2019, 96). If the outlier significance probability, *p*, is lower than or equal to a chosen threshold value, then the marked data point is an outlier (Hawkins 2019, 99). Common threshold values for *p* are 0.05 or 0.01 (*ibid.*). The smaller the *p* value is, the more certain it is that the data point is an outlier (*ibid.*). The Tuscaloosa data set has one outlier (Presidential Hall, $p = 0.003$), which is well below both common threshold values. Oxford also has one outlier (Oriel Library, $p = 0.001$). Vienna and Ottawa have no significant outliers ($p > 0.05$), but Peterskirche (Vienna) and Wellington Building (Ottawa) are furthest from the rest in their groups. The two outliers are removed from the calculations presented for the brochantite results.

Tuscaloosa, Alabama, USA

Building	$\delta^{18}O$ *(‰, VSMOW)*
Carmichael Hall vent	6.5
Presidential Hall	13.8*
Farrah Hall	7.2
Wilson Hall	7.7
Bidgood Hall	6.9
Gallalee Hall	8.6
Bryce Hospital (Reception)	6.5
Bryce Hospital (Women's Wing)	8.4
Mean	7.4
SD	0.9
CV (%)	12.2
Standard Error	0.3

Vienna, Austria

Building	$\delta^{18}O$ *(‰, VSMOW)*
Linke Sheet	7.3
Burgtheater Chimney	8.3
Karlskirche	7.5
Hofburg angel base	7.4
Peterskirche	9.2
Votivekirche	8.5
Vienna Tech. Univ.	6.8
Mean	7.9
SD	0.8
CV (%)	10.6
Standard Error	0.3

Oxford, UK

Building	$\delta^{18}O$ *(‰, VSMOW)*
Old Observatory	7.4
Rhodes Mandela	8.2
Corpus Christi	7.3
New College	7.8
Oriel Library	11.5*
St. Cross Law vent	7.3
Philosophy Centre	7.4
Rhodes House (Oriel)	8.6
St. Cross Law roof	7.9
Mean	7.7
SD	0.5
CV (%)	6.5
Standard Error	0.2

Ottawa, Ontario, Canada

Building	$\delta^{18}O$ *(‰, VSMOW)*
Confederation Bldg.	8.5
Booth House	7.3
Wellington Bldg.	4.7
Center Block (Wojdan)	7.8
American Embassy	6.2
St. Joseph's Parish	8.0
Hotel Lord Elgin	5.2
Bruyere Hospital	8.2
Center Block (Selwyn)	6.8
Mean	7.0
SD	1.4
CV (%)	19.4
Standard Error	0.5

Table 6.2: Full results for $\delta^{18}O$ values and descriptive statistics from the brochantite samples scrapped off patinated copper roofs and historic material. Values marked with an asterisk are outliers according to Grubb's test. These outlying data are excluded from the descriptive statistics.

	N	**Mean**	**SD**	**CV (%)**	**Standard Error**
Total	31	7.5	1.0	13.1	0.2

Table 6.3: Total $\delta^{18}O$ descriptive statistics for all the brochantite sites combined. Calculations exclude two outliers, marked with an asterisk in **table 6.2**.

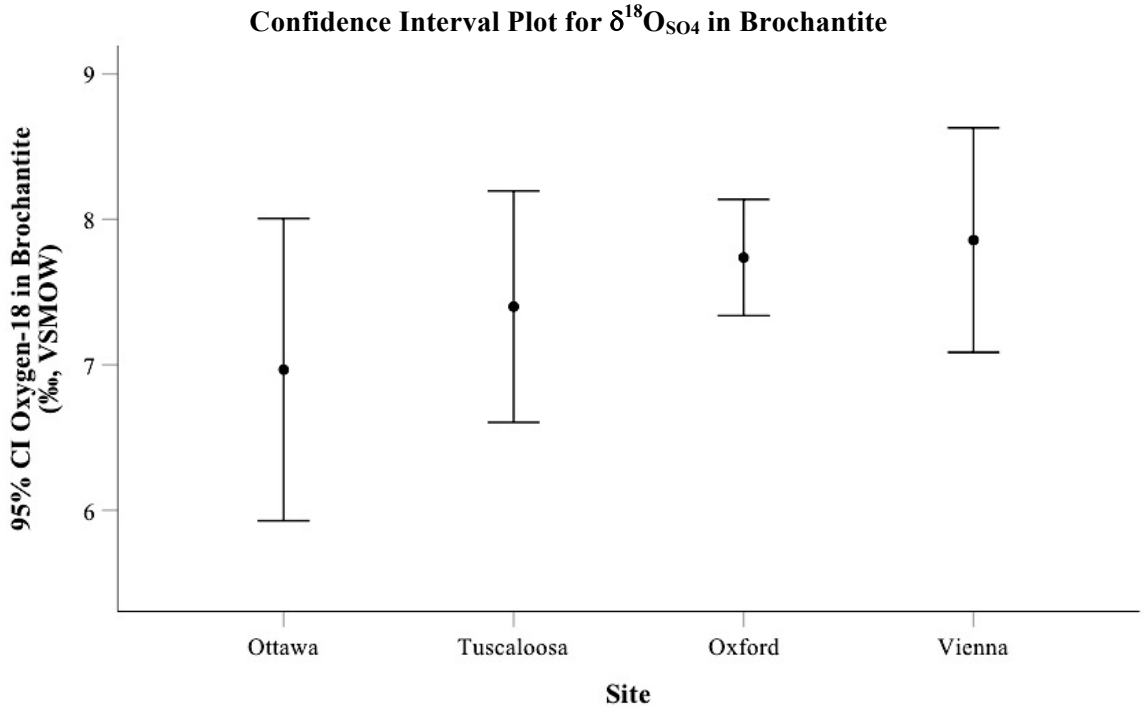


Figure 6.1: Plot showing the brochantite $\delta^{18}O$ means (central tendency) for each site represented by a dot, and the lines representing the precision of the estimate of the mean (variability, with a 95% confidence interval), plotted in order of increasing mean value.

A paired *t*-test assesses whether the difference between two related samples can be accounted for by sample error alone (Hawkins 2019, 172). Starting with the null hypothesis that here is no difference between the cities from which the $\delta^{18}O$ values in brochantite come, and using a 5% (0.05) critical significance level, a paired, two-tailed *t*-value can be generated using a statistical software package on a computer (this project uses IBM SPSS, version 25). For Tuscaloosa and Vienna, there is no significant statistical difference between the $\delta^{18}O$ values of the two sites (t_6=-1.1, p=0.3, 95% CI [-1.5, 0.6]). Statistics for the city comparisons using the paired *t*-test are presented in **table 6.4**, first repeating the statistics for Tuscaloosa and Vienna to demonstrate the table structure. All *p*-values are greater than 0.05, therefore we can accept the null hypothesis that there is no statistically significant difference between the $\delta^{18}O$ values of these city comparisons.

City Pair	*t*	df	*p*	95% CI Upper	95% CI Lower
Tuscaloosa-Vienna	-1.1	6	0.3	0.6	-1.5
Tuscaloosa-Oxford	-0.9	6	0.4	0.5	-1.1
Tuscaloosa-Ottawa	0.7	6	0.5	2.6	-1.5
Vienna-Oxford	0.3	6	0.8	1.2	-0.9
Vienna-Ottawa	1.8	6	0.1	-0.4	2.5
Oxford-Ottawa	1.3	7	0.2	2.1	-0.6

Table 6.4: Paired *t*-test statistics for brochantite $\delta^{18}O$ in four cities, considered two at a time.

Analysis of variance (Anova) is an overall test of whether group means differ (Field 2013, 870). It compares the variance between different groups (believed to be due to the independent variable) with the variability within each of the groups (believed to be due to chance) (Pallant 2016, 255). When these are divided, an F-ratio is calculated, which is the statistic used for an Anova (*ibid.*). Large F-ratios indicate that there is more variability between groups than there is within each group, and we can reject the null hypothesis stating that the means are equal (*ibid.*). There are two different degrees of freedom (df) to report in association with an F-ratio, based on the group variabilities (Hawkins 2019, 198). Between groups variance degrees of freedom are one less than the number of groups (*ibid.*). Within-group degrees of freedom are the total samples minus the number of groups (*ibid.*). The brochantite $\delta^{18}O$ value variances are roughly equal among the sites: $F_{3, 27} = 1.7$, $p = 0.2$. Again, if the p value is greater than 0.05, then the assumption of homogeneity of variance has not been violated, as is the case for the brochantite data.

Paired t-tests and Anova calculations have revealed that there is no statistical difference between the $\delta^{18}O$ values in the sulfate of brochantite samples collected from four distinct geographic sites around the world. The fact that the $\delta^{18}O$ variance is roughly equal among the sites could suggest reaction preferences with meteoric water that lead to homogenization in the $\delta^{18}O_{SO4}$ of brochantite. To understand what controls the oxygen ratios in brochantite, further statistical analyses were carried out using linear regression with various environmental parameters, including the $\delta^{18}O$ in local precipitation, pH and surface temperature.

6.2.2. Incorporation of Environmental Parameters

To explore whether the geographic region in which brochantite formed may be identified to some extent through the $\delta^{18}O$ in brochantite as a function of the $\delta^{18}O$ in local meteoric water, GNIP isotope precipitation data was used for comparison to the brochantite data. The following table (**table 6.5**, next page) presents the mean $\delta^{18}O$-SO_4 values for each city next to local environmental conditions, with a focus on precipitation. The isotopic spread is not as drastic in mean $\delta^{18}O_{SO4}$ values in brochantite as it is in the mean $\delta^{18}O_{H2O}$ between sites.

Mean $\delta^{18}O$ in Brochantite and Local Environmental Data

	Vienna	Tuscaloosa	Oxford	Ottawa
Mean $\delta^{18}O$-SO_4 (‰, VSMOW)	7.9	7.4	7.7	7.0
Mean $\delta^{18}O$-H_2O (Annual, ‰, VSMOW)	-9.8	-4.7	-7.3	-11.0
Mean $\delta^{18}O$-H_2O (Summer, ‰, VSMOW)	-7.0	-4.7	-5.5	-8.0
Average Precipitation Amount (Inches)	24.4	55.6	24.2	37.2
Average pH of Precipitation	4.7	5.0	5.0	4.5
Average Surface Temperature (ºC)	10.4	17.2	10.6	6.1
Latitude	48.2	33.2	51.6	45.3

Table 6.5: Presentation of the mean $\delta^{18}O$-SO_4 values for each city next to local environmental parameters, with a focus on precipitation. Apart from the first row, which contains data from this study, information was collected from GNIP for the city of interest (IAEA/WMO 2015). The only exception is the average surface temperature for Tuscaloosa, which was not recorded by GNIP and instead taken from Climate-Data.org (2019). Summer is defined as May through September, inclusive.

The following four scales (**figure 6.2,** next page), one for each city, plot the $\delta^{18}O_{SO4}$ for each brochantite sample isotopically analyzed. The + marks at each end of the scales represent the local $\delta^{18}O$ in summer precipitation (scale left), which varies geographically, and the $\delta^{18}O$ in atmospheric oxygen, which has a constant value of +23.5‰ (scale right). Summer is defined as May – September, inclusive. This study focuses on the summer because corrosion is assumed to be very slow during winter due to temperature drops and oxidizing water sometimes freezing solid. All sample points lie approximately in the middle of their scales and have positive values. This indicates that both $\delta^{18}O$-H_2O and $\delta^{18}O$-O_2 contribute about equally to the $\delta^{18}O$-SO_4 in brochantite.

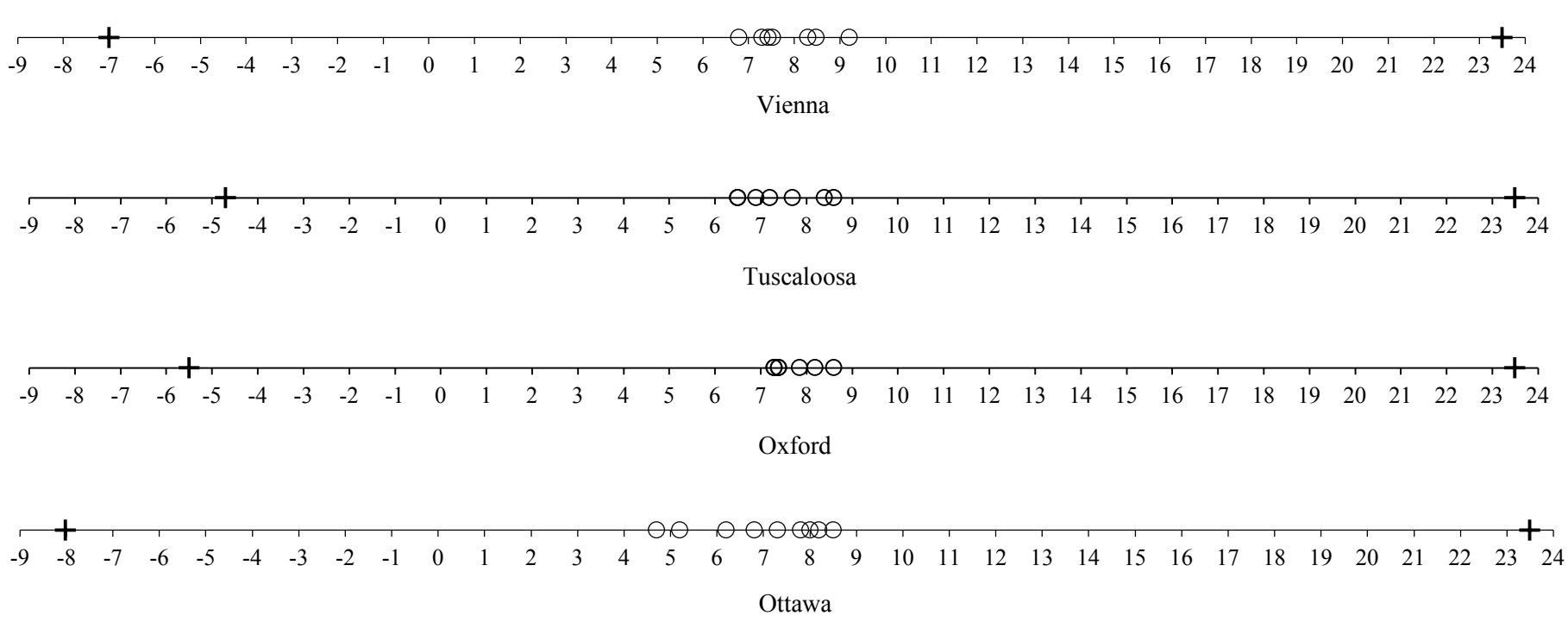


Figure 6.2: City scales showing isotopic spread in brochantite $\delta^{18}O_{SO4}$ (‰, VSMOW) results, displayed between $\delta^{18}O$ of atmospheric oxygen (+23.5‰) and the $\delta^{18}O_{H2O}$ of each site (May-September weighted mean average, data from **tables 6.2** and **6.5**).

Linear regression models are used to summarize the relationship between two variables, in this case the $\delta^{18}O$ values in brochantite with an environmental parameter, by using a straight sloping line with an equation, y=bx+c (dependent variable = slope x independent variable + intercept) (Hawkins 2019, 213). As the slope value approaches 0, the linear relationship reduces and cannot be used for prediction. The coefficient of determination (R^2) for regression is a measure of how much the dependent variable varies with the independent variable (Hawkins 2019, 214). It only makes sense to consider R^2 values if the relationship is significant, which is why a *p*-value needs to be considered in conjunction with R^2 values.

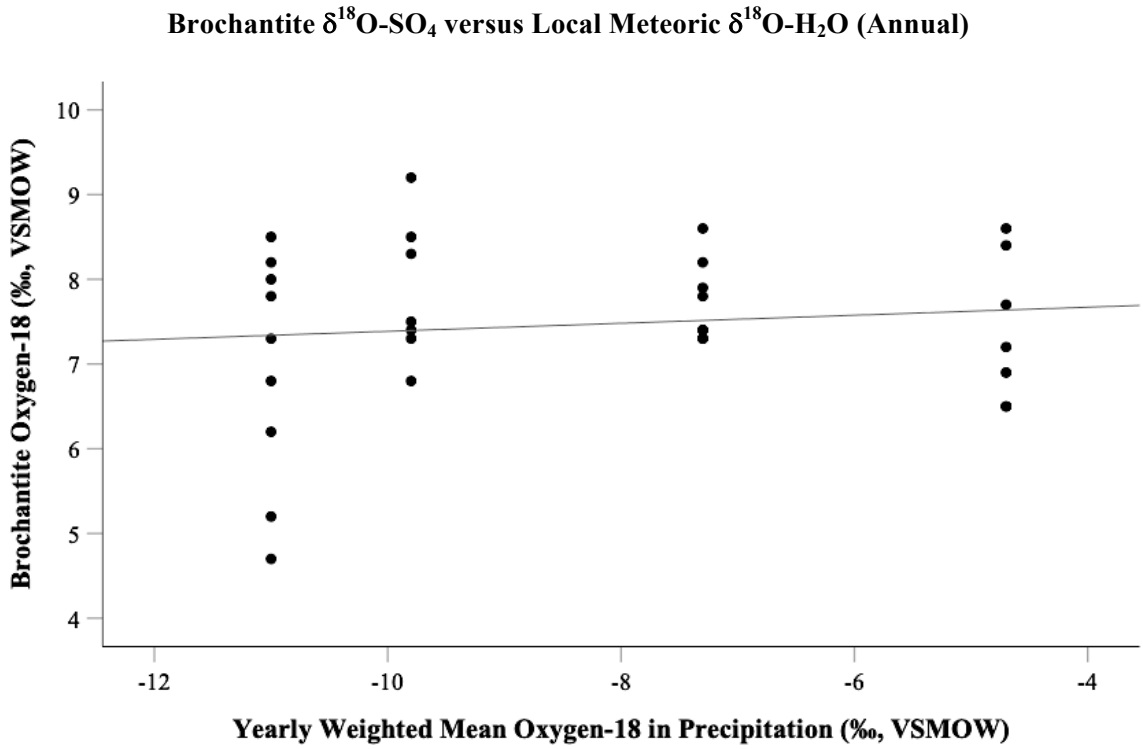


Figure 6.3: Scatterplot shows $\delta^{18}O\text{-}SO_4$ as a function of the yearly weighted mean $\delta^{18}O\text{-}H_2O$ (y=0.05x+7.9, R^2=0.01, *p*=0.5). From left to right, the first column is Ottawa, second is Vienna, third is Oxford and the fourth is Tuscaloosa.

When the brochantite $\delta^{18}O$ data is plotted against the yearly weighted mean $\delta^{18}O$ in local precipitation, there appears to be an insignificant, positive correlation (*p*=0.5, **figure 6.3**). A slightly better correlation, yet still statistically insignificant, is apparent when the $\delta^{18}O$ in brochantite is plotted against the $\delta^{18}O$ in mean summer precipitation (y=8.3+0.1x, R^2=0.03, *p*=0.4, **figure 6.4**, following page).

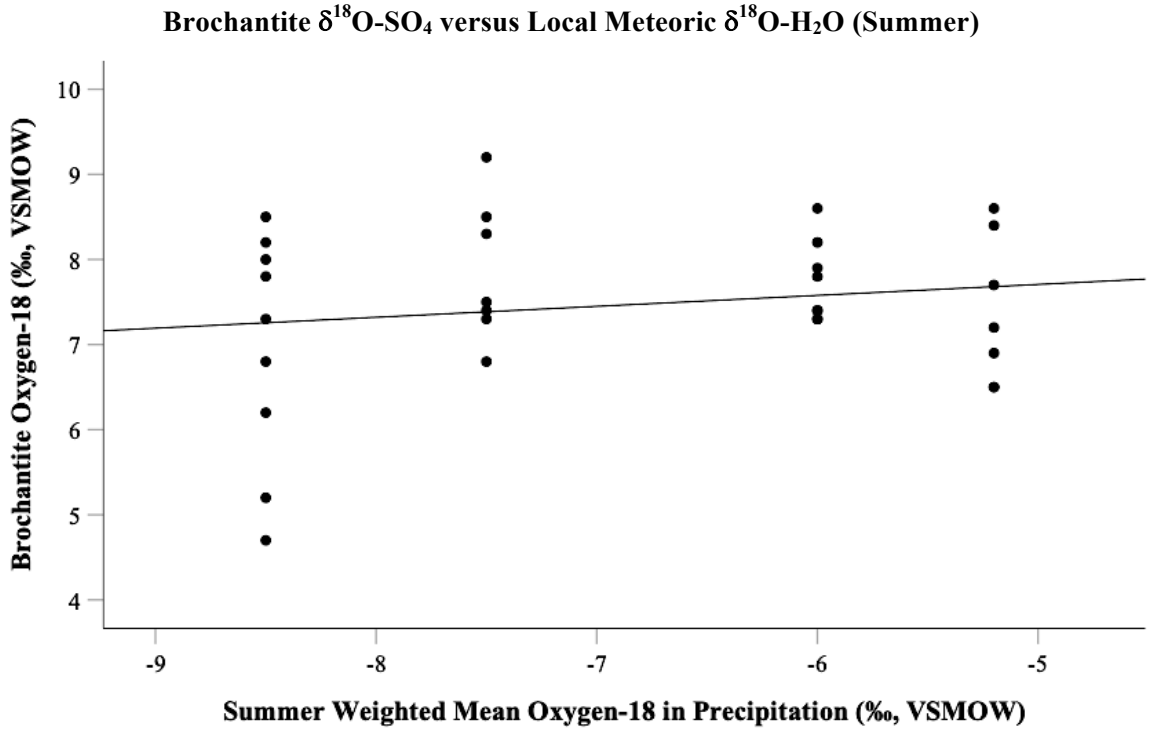


Figure 6.4: Scatterplot shows $\delta^{18}O\text{-}SO_4$ as a function of the summer weighted mean $\delta^{18}O\text{-}H_2O$ ($y=8.3+0.1x$, $R^2=0.03$, $p=0.4$). This is an alternative illustration of the same information presented in the city scales (**figure 6.2**). From left to right, the first column is Ottawa, second is Vienna, third is Oxford and the fourth is Tuscaloosa.

In attempts to find an environmental parameter that has a more statistically significant relationship with the $\delta^{18}O$ values in brochantite, the data was correlated to average surface temperature, latitude, average amount of precipitation, and the average pH of the meteoric water for the cities included in the study (data in **table 6.4**). The following scatterplots show these correlations, with the pH in meteoric water having the strongest, yet still statistically insignificant, correlation ($R^2=0.05$, $p=0.2$). Latitude showed the weakest correlation with $\delta^{18}O$ in brochantite ($R^2=0.009$, $p=0.6$).

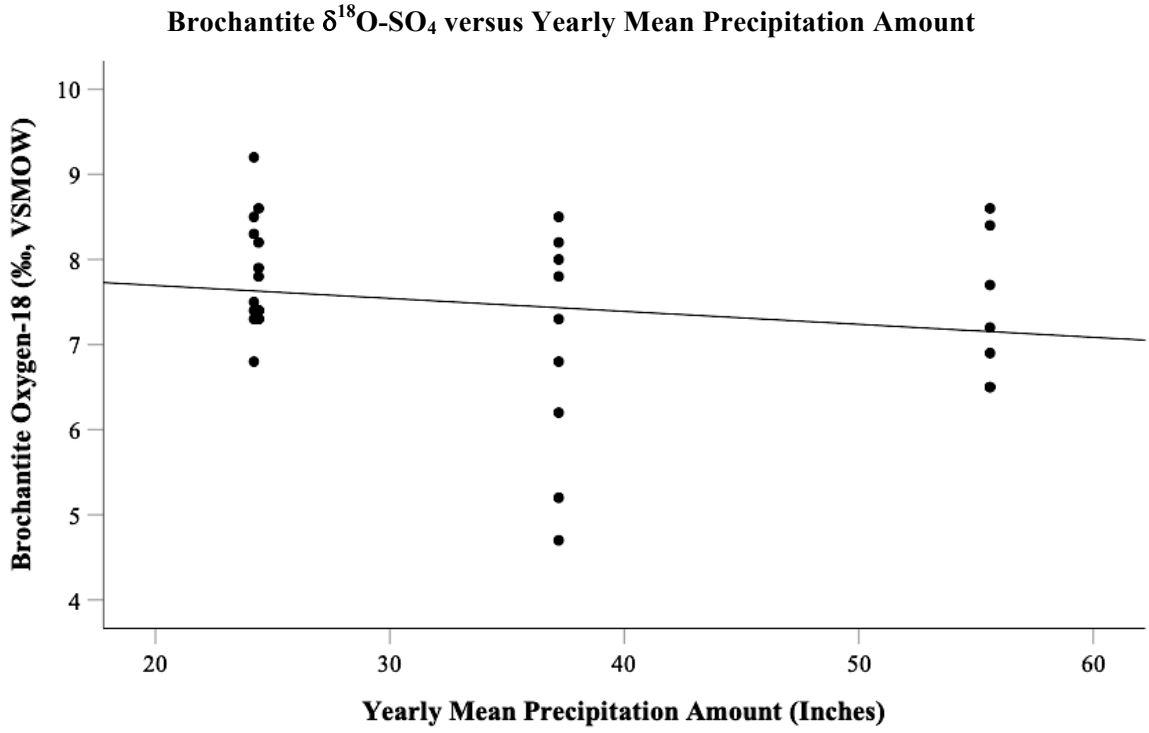


Figure 6.5: Scatterplot shows $\delta^{18}O\text{-}SO_4$ as a function of the yearly mean precipitation amount at the cities of sampling. From left to right, the first column is Oxford (24.2 inches) with Vienna (24.4 inches) immediately after, third is Ottawa (37.2 inches) and the fourth is Tuscaloosa (55.6 inches). This scatterplot shows no statistically significant correlation, with y=8-0.02x, R^2=0.04, *p*=0.3.

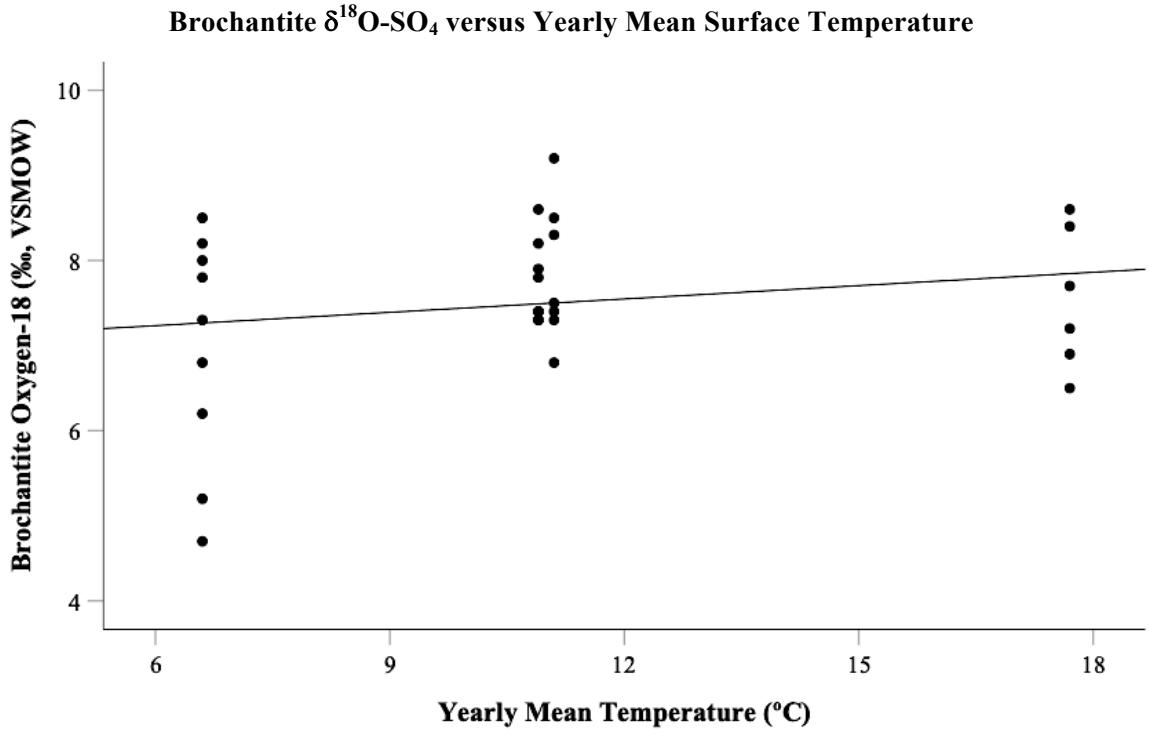


Figure 6.6: Scatterplot shows $\delta^{18}O\text{-}SO_4$ as a function of the yearly mean surface temperature at the cities of sampling. From left to right, the first column is Ottawa (6.1ºC), followed by Vienna (10.4ºC), third is Oxford (10.6ºC), and the fourth is Tuscaloosa (17.2ºC). This scatterplot shows no statistically significant correlation, with y=6.9+0.05x, R^2=0.04, *p*=0.3.

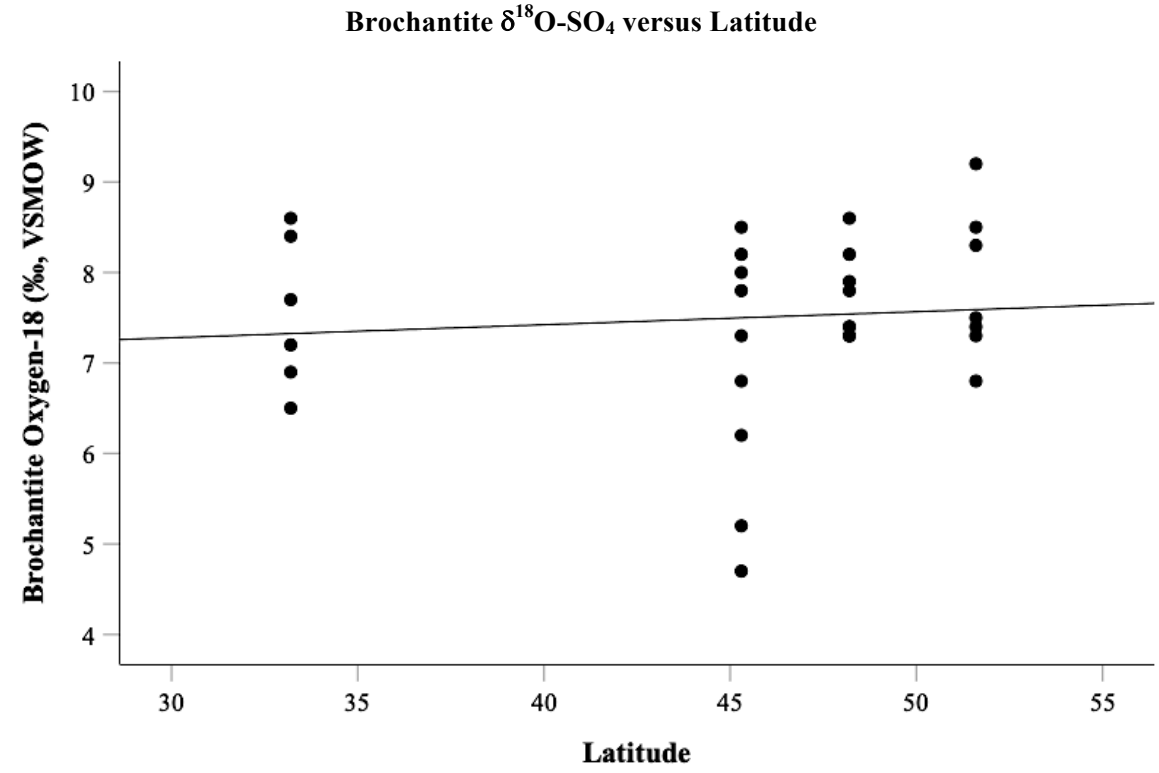


Figure 6.7: Scatterplot shows δ^{18}O-SO_4 as a function of the latitude at the cities of sampling. From left to right, the first column is Tuscaloosa (33.2º), followed by Ottawa (45.3º), third is Vienna (48.2º), and the fourth is Oxford (51.6º). This scatterplot shows no statistically significant correlation, with y=6.8+0.01x, R^2=0.009, *p*=0.6.

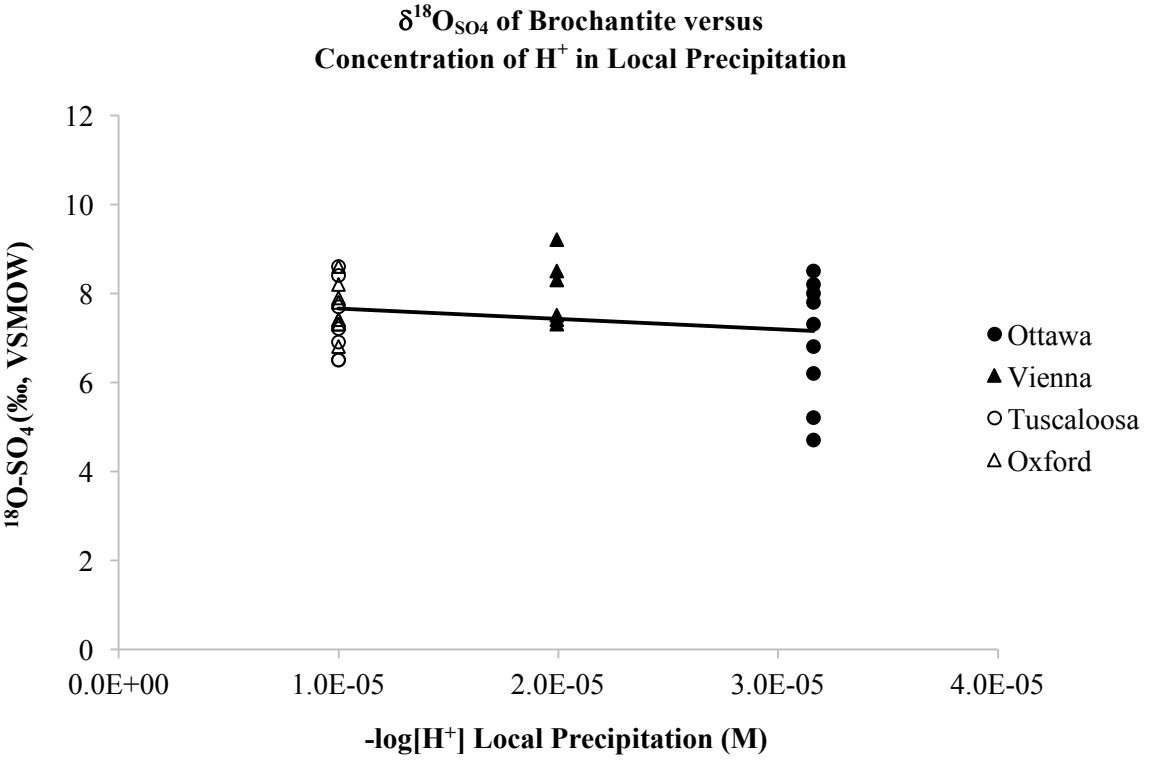


Figure 6.8: Scatterplot shows δ^{18}O-SO_4 as a function of the yearly average acidity in meteoric water (presented in concentration of H^+) at the cities of sampling (i.e. scatterplot shows δ^{18}O-SO_4 versus pH in local precipitation). This scatterplot shows no statistically significant correlation, with y=7.9-(2.3x10^4)x, R^2=0.05, *p*=0.2.

Finally, the age of the brochantite deposits (if known; estimated by the year the copper roof was built) were plotted against the $\delta^{18}O\text{-}SO_4$ values.

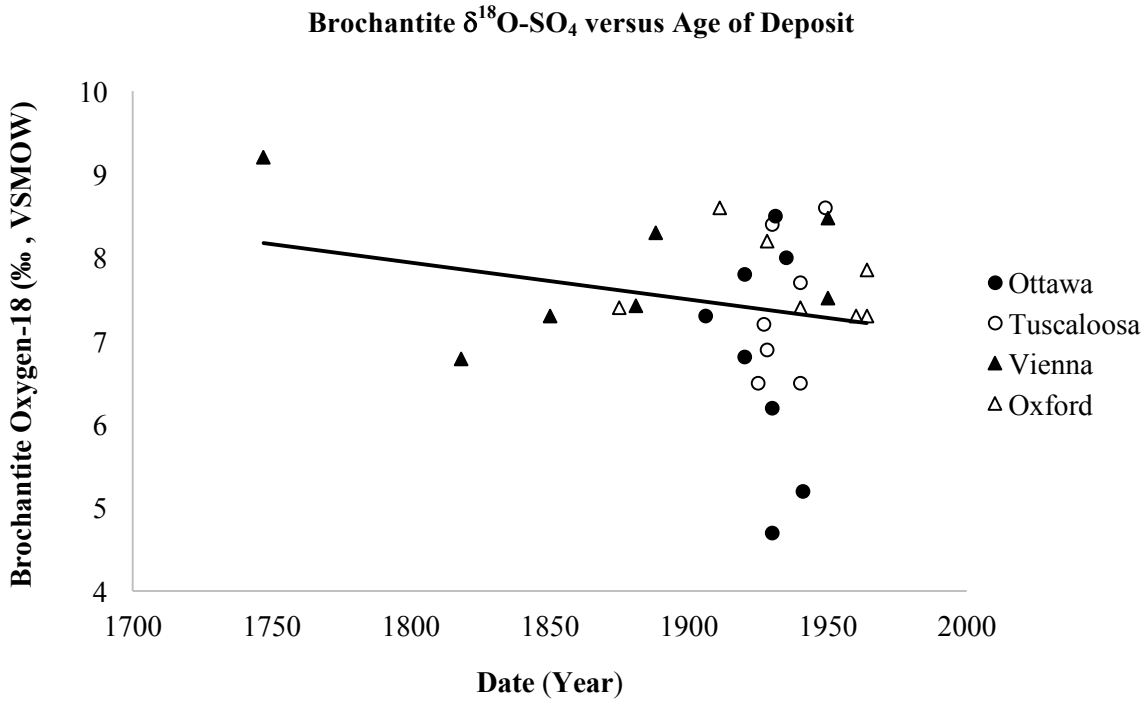


Figure 6.9: Scatterplot shows $\delta^{18}O\text{-}SO_4$ as a function of the date of the buildings from which the samples were collected. This scatterplot shows no statistically significant correlation, with y=15.9-0.004x, R^2=0.04, *p*=0.3.

6.2.3. Calculating Percent Contributions from Heterogeneous and Homogeneous Pathways

A flowchart was created and presented in Chapter 4 (offered again on the following page as **figure 6.10**) that allows for estimations of isotopic oxidation pathways in secondary sulfates. In this section, the flowchart is used algebraically. Beginning with the following relationship, the contributions of each oxygen source was calculated, and the results are presented in the table below.

$$\%\ \text{contribution from water} = \frac{\text{sample } \delta^{18}\text{O value (‰)} - 23.5‰}{\text{precipitation } \delta^{18}\text{O value (‰)} - 23.5‰}$$

Percent Contribution of ^{18}O from Water

	Tuscaloosa	Ottawa	Oxford	Vienna
Year Mean, %	57.1	47.9	51.4	47.0
Summer Mean, %	57.1	52.5	54.5	51.3
Year Low, %	36.2	43.5	40.3	43.0
Summer Low, %	36.2	47.6	53.1	46.9
Year High, %	63.5	54.5	54.4	50.2
Summer High, %	63.5	59.7	57.6	54.8

Table 6.6: Presentation of various possible percent contributions of $\delta^{18}O$ from meteoric water, showing seasonal variation.

Referencing the flowchart on page 139, the following relationships were used to calculate the percent contribution range for each pathway, total heterogeneous to total homogeneous, from sulfur dioxide to sulfate:

Heterogeneous Pathways:

R1) For H_2O_2 oxidation: $\frac{3(\text{precipitation } \delta^{18}O) + 2(23.5‰)}{5}$ = lowest possible value, representing a theoretical case where all reactions go through this pathway.

R2) For O_2 (metal catalyzed) oxidation: $\frac{3(\text{precipitation } \delta^{18}O) + 23.5‰}{4}$ = highest possible value, representing a theoretical case where all reactions go through this pathway.

Homogeneous Pathway:

R3) $\frac{(\text{precipitation } \delta^{18}O) + 3(23.5‰)}{4}$ = value represents a theoretical case where all reactions go through this pathway.

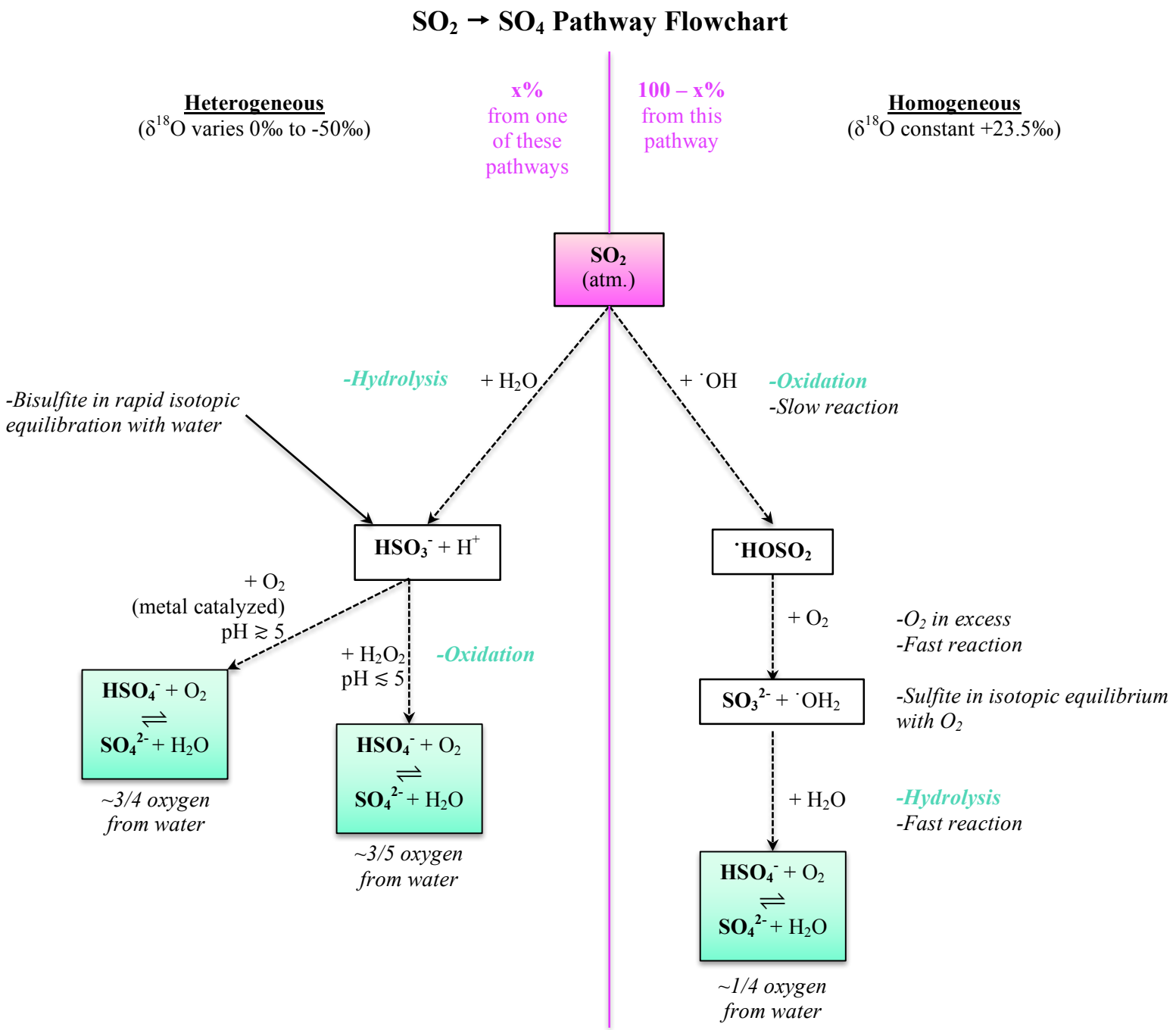

SO2 → SO4 Pathway Flowchart
Heterogeneous
(δ18O varies 0‰ to -50‰)
x%
from one
of these
pathways
100 – x%
from this
pathway
Homogeneous
(δ18O constant +23.5‰)
SO2
(atm.)
-Hydrolysis
+ H2O
+ ·OH
-Oxidation
-Slow reaction
-Bisulfite in rapid isotopic
equilibration with water
HSO3- + H+
·HOSO2
+ O2
(metal catalyzed)
pH ≳ 5
+ H2O2
pH ≲ 5
-Oxidation
+ O2
-O2 in excess
-Fast reaction
HSO4- + O2
⇌
SO42- + H2O
~3/4 oxygen
from water
HSO4- + O2
⇌
SO42- + H2O
~3/5 oxygen
from water
SO32- + ·OH2
-Sulfite in isotopic equilibrium
with O2
+ H2O
-Hydrolysis
-Fast reaction
HSO4- + O2
⇌
SO42- + H2O
~1/4 oxygen
from water

Figure 6.10

Any data should fall between the theoretical values (between any one heterogeneous pathway and the homogeneous pathway). There is no known way to determine percent contributions from all three pathways simultaneously. Considering two pathway pairs at a time (1. homogeneous and heterogeneous using O_2 (metal catalyzed) or 2. homogeneous and heterogeneous using H_2O_2), the following percent contributions were calculated for each city's $\delta^{18}O\text{-}SO_4$ mean, high and low for the summer and for the year.

$$\%\ \text{contribution from heterogeneous pathway} = \frac{\text{R3 value (‰)} - \text{sample } \delta^{18}\text{O value (‰)}}{\text{R3 value (‰)} - \text{R1 or R2 value (‰)}} \times 100$$

% contribution from homogeneous pathway = 100 – above value

Tuscaloosa Percent Contributions from Heterogeneous (aq) and Homogeneous (g) Pathways

	$\delta^{18}O_{SO4}$ (‰, VSMOW)	1 (aq, %)	1 (g, %)	2 (aq, %)	2 (g, %)
Mean	7.4	91.1	8.1	64.5	35.5
Lowest	6.5	100.9	-	70.7	29.3
Highest	8.6	20.2	79.8	49.6	50.4

Table 6.7: The long-term year and summer mean $\delta^{18}O$ in Tuscaloosa's precipitation is -4.7‰. Therefore, R1 = 6.6‰, R2 = 2.4‰ and R3 = 16.5‰. Using this data along with the mean, lowest and highest $\delta^{18}O_{SO4}$ in brochantite results for Tuscaloosa, the following percent contributions from heterogeneous and homogeneous pathways (considering two pathway pairs at a time, labeled as 1 and 2) were calculated and presented on this table. In the homogeneous pathway, the oxidizer is always assumed to be atmospheric oxygen. The lowest ratio yielded by a sample in Tuscaloosa's data set is lower than the theoretical lowest (6.5‰ and 6.6‰, respectively), which is why a value over 100% was calculated for the heterogeneous pathway of the first pair and no value is given for the corresponding homogeneous pathway. There is no distinction between summer and year for $\delta^{18}O$ data on precipitation in Tuscaloosa because the temperature very seldom drops below freezing.

Vienna Summer Percent Contributions from Heterogeneous (aq) and Homogeneous (g) Pathways

	$\delta^{18}O_{SO4}$ (‰, VSMOW)	1 (aq, %)	1 (g, %)	2 (aq, %)	2 (g, %)
Mean	7.9	74.3	25.7	52.6	47.4
Lowest	6.8	85.1	14.9	59.6	40.4
Highest	9.2	62.4	37.6	43.7	56.3

Table 6.8: The long-term summer mean $\delta^{18}O$ in Vienna's precipitation is -7.0‰. Therefore, R1 = 5.2‰, R2 = 0.63‰ and R3 = 15.9‰. Using this data along with the mean, lowest and highest $\delta^{18}O_{SO4}$ in brochantite results for Vienna, the following percent contributions from heterogeneous and homogeneous pathways (considering two pathway pairs at a time, labeled as 1 and 2) were calculated and are presented on this table. In the homogeneous pathway, the oxidizer is always assumed to be atmospheric oxygen.

Vienna Annual Percent Contributions from Heterogeneous (aq) and Homogeneous (g) Pathways

	$\delta^{18}O_{SO4}$ (‰, VSMOW)	1 (aq, %)	1 (g, %)	2 (aq, %)	2 (g, %)
Mean	7.9	62.9	37.1	44.0	56.0
Lowest	6.8	72.1	27.9	50.5	49.5
Highest	9.2	51.3	48.7	35.9	64.1

Table 6.9: The long-term yearly mean $\delta^{18}O$ in Vienna's precipitation is -9.8‰. Therefore, R1 = 3.5‰, R2 = -1.5‰ and R3 = 15.2‰. Using this data along with the mean, lowest and highest $\delta^{18}O_{SO4}$ in brochantite results for Vienna, the following percent contributions from heterogeneous and homogeneous pathways (considering two pathway pairs at a time, labeled as 1 and 2) were calculated and are presented on this table. In the homogeneous pathway, the oxidizer is always assumed to be atmospheric oxygen.

Ottawa Summer Percent Contributions from Heterogeneous (aq) and Homogeneous (g) Pathways

	$\delta^{18}O_{SO4}$ (‰, VSMOW)	1 (aq, %)	1 (g, %)	2 (aq, %)	2 (g, %)
Mean	7.0	78.4	21.6	54.9	45.1
Lowest	4.7	99.0	1.0	69.3	30.7
Highest	8.5	64.0	35.4	45.2	54.8

Table 6.10: The long-term summer mean $\delta^{18}O$ in Ottawa's precipitation is -8.0‰. Therefore, R1 = 4.6‰, R2 = -0.1‰ and R3 = 15.6‰. Using this data along with the mean, lowest and highest $\delta^{18}O_{SO4}$ in brochantite results for Ottawa, the following percent contributions from heterogeneous and homogeneous pathways (considering two pathway pairs at a time, labeled as 1 and 2) were calculated and are presented on this table. In the homogeneous pathway, the oxidizer is always assumed to be atmospheric oxygen.

Ottawa Annual Percent Contributions from Heterogeneous (aq) and Homogeneous (g) Pathways

	$\delta^{18}O_{SO4}$ (‰, VSMOW)	1 (aq, %)	1 (g, %)	2 (aq, %)	2 (g, %)
Mean	7.0	65.4	34.6	45.8	54.2
Lowest	4.7	84.2	15.8	58.9	41.1
Highest	8.5	52.7	47.3	36.9	63.1

Table 6.11: The long-term yearly mean $\delta^{18}O$ in Ottawa's precipitation is -11.0‰. Therefore, R1 = 2.8‰, R2 = -2.4‰ and R3 = 14.9‰. Using this data along with the mean, lowest and highest $\delta^{18}O_{SO4}$ in brochantite results for Ottawa, the following percent contributions from heterogeneous and homogeneous pathways (considering two pathway pairs at a time, labeled as 1 and 2) were calculated and are presented on this table. In the homogeneous pathway, the oxidizer is always assumed to be atmospheric oxygen.

Oxford Summer Percent Contributions from Heterogeneous (aq) and Homogeneous (g) Pathways

	$\delta^{18}O_{SO4}$ (‰, VSMOW)	1 (aq, %)	1 (g, %)	2 (aq, %)	2 (g, %)
Mean	7.7	84.2	15.8	58.6	41.4
Lowest	7.3	88.1	11.9	61.7	38.3
Highest	8.6	24.8	75.2	47.6	52.4

Table 6.12: The long-term summer mean $\delta^{18}O$ in Oxford's precipitation is -5.5‰. Therefore, R1 = 6.1‰, R2 = 1.7‰ and R3 = 16.2‰. Using this data along with the mean, lowest and highest $\delta^{18}O_{SO4}$ in brochantite results for Oxford, the following percent contributions from heterogeneous and homogeneous pathways (considering two pathway pairs at a time, labeled as 1 and 2) were calculated and are presented on this table. In the homogeneous pathway, the oxidizer is always assumed to be atmospheric oxygen.

Oxford Annual Percent Contributions from Heterogeneous (aq) and Homogeneous (g) Pathways

	$\delta^{18}O_{SO4}$ (‰, VSMOW)	1 (aq, %)	1 (g, %)	2 (aq, %)	2 (g, %)
Mean	7.7	75.0	25.0	52.6	47.4
Lowest	7.3	79.0	21.0	55.3	44.7
Highest	8.6	33.3	66.7	46.8	53.2

Table 6.13: The long-term yearly mean $\delta^{18}O$ in Oxford's precipitation is -7.3‰. Therefore, R1 = 5.0‰, R2 = 0.4‰ and R3 = 15.8‰. Using this data along with the mean, lowest and highest $\delta^{18}O_{SO4}$ in brochantite results for Oxford, the following percent contributions from heterogeneous and homogeneous pathways (considering two pathway pairs at a time, labeled as 1 and 2) were calculated and are presented on this table. In the homogeneous pathway, the oxidizer is always assumed to be atmospheric oxygen.

6.3. RAW DATA AND DESCRIPTIVE STATISTICS FOR HYDROXYL-δ^2H

A pilot study was carried out for the analysis of δ^2H from the hydroxyl groups in brochantite. This work was carried out to determine whether it is possible to measure δ^2H in relatively small brochantite samples (8 – 10mg), and if the data produced made statistical suggestions in relation to various environmental parameters that would make further research using larger samples for measurement of δ^{18}O in addition to the δ^2H worthwhile. Environmental water should be the only source of O and H in hydroxyl groups and the dual isotopes could provide robust data.

Hydroxyl-δ^2H Pilot Study Results

Sample City	Sample Site	δ^2H 1 (‰, VSMOW)	δ^2H 2 (‰, VSMOW)	δ^2H 3 (‰, VSMOW)	δ^2H 4 (‰, VSMOW)
Ottawa	Confederation Building	-14.0	-13.8	-	-
Ottawa	Booth House	-38.1	-38.3	-	-
Tuscaloosa	Carmichael Hall vent	-19.4	-14.6	-	-
Tuscaloosa	Former Bryce Hospital	20.5	25.2	-	-
Oxford	St Cross Law Building	-10.3	-7.5	-11.3	-9.1
Oxford	Rhodes-Mandela House	-13.0	-18.3	-	-
Vienna	Hofburg angel statue base	-22.5	-26.5	-	-
Vienna	Gilded roof sheet	-0.8	-16.8	-	-

Table 6.14: Brochantite hydroxyl-δ^2H pilot study results, run in duplicate, apart from the St. Cross Law Building in Oxford, which was used for initial methodology testing and therefore has more data.

Hydroxyl-δ^2H Pilot Study Descriptive Statistics – Measurement Error

Site	N	Mean (‰, VSMOW)	SD	SE	95% CI Lower Bound	95% CI Upper Bound
Confederation Building, Ottawa	2	-13.9	0.1	0.1	-15.2	-12.6
Boothe House, Ottawa	2	-38.2	0.1	0.1	-39.5	-36.9
Carmichael Hall, Tuscaloosa	2	-17.0	3.4	2.4	-47.5	13.5
Bryce Hospital, Tuscaloosa	2	22.9	3.3	2.4	-7.0	52.7
St. Cross Law Building, Oxford	4	-9.6	1.6	0.8	-12.2	-6.9
Rhodes-Mandela House, Oxford	2	-15.7	3.7	2.7	-49.3	18.0
Hofburg Angel, Vienna	2	-24.5	2.8	2.0	-49.9	0.9
Gilded Roof Sheet, Vienna	2	-8.8	11.3	8.0	-110.5	92.9
Total	18	-12.7	16.1	3.8	-20.7	-4.7

Table 6.15: Showing descriptive statistics for the δ^2H pilot study on brochantite's hydroxyls. The number of samples (n), mean average, standard deviation (SD), standard error (SE), and 95% confidence intervals (CI) for the mean (upper and lower bounds) are based on the data provided in **table 6.14**.

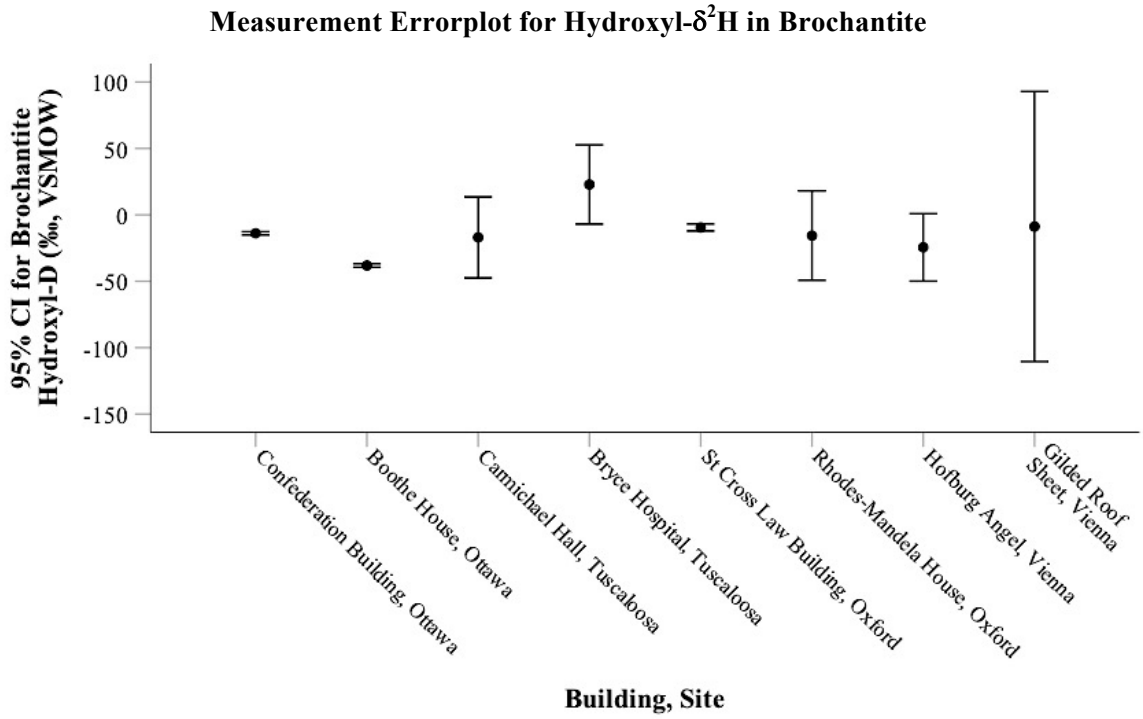


Figure 6.11: Duplicate measurement errorplot showing the brochantite hydroxyl- δ^2H (labeled as hydroxyl-D in the plot, with D standing for deuterium) means for each building represented by a dot, and the lines representing the precision of the estimate of the mean (with a 95% confidence interval).

6.3.1. Correlation Statistics with Hydroxyl-δ^2H and Environmental Parameters:

The long-term weighted mean average δ^2H values for the cities included in this study are available through the GNIP database, which are -74.8‰ for Ottawa, -69.5‰ for Vienna, -49.4‰ for Wallingford (Oxfordshire), and -20.3‰ for Tuscaloosa (IAEA/WMO 2019).

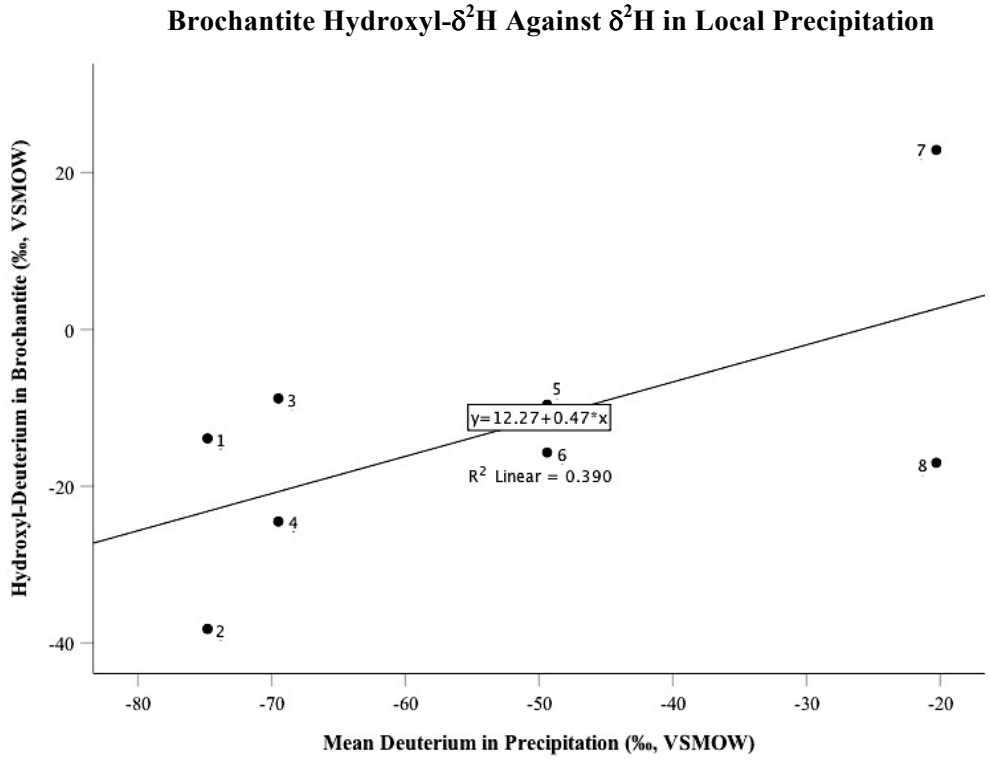


Figure 6.12: Scatterplot of brochantite hydroxyl-δ^2H (using the δ^2H mean from duplicate run values presented in **table 6.13**) against the long term weighted mean δ^2H in local precipitation. Plot includes a regression line summarizing the relationship between these variables through the equation y=12.3+0.5x with R^2=0.4, and p=0.1.

The regression relationship shown in **figure 6.12**, $R^2 = 0.4$, seems better than the relationships between $\delta^{18}O_{SO4}$ and the $\delta^{18}O$ in local meteoric water (annual $R^2 = 0.08$, summer $R^2 = 0.09$). However, the statistical significance between all relationships is about the same ($p_{deuterium} = 0.1$, $p_{18O\ annual} = 0.1$, $p_{18O\ summer} = 0.09$). In all cases $p > 0.05$, and the significance of these relationships are considered insignificant, but the δ^2H pilot study consists of little data. Further investigation would be interesting, but this work is not possible within the scope of this thesis because the samples collected are far too small for δ^2H analysis.

In an attempt to find an environmental parameter that has a more statistically significant relationship with the δ^2H values in brochantite, the data was again correlated to average surface temperature, latitude, average amount of precipitation, and the average pH of the meteoric water for the cities included in the study (data on **table 6.4**). The following scatterplots show these correlations, with the yearly mean surface temperature at the city of formation having the strongest,

yet still statistically insignificant, correlation (R^2=0.4, p=0.09). The age of the brochantite, determined by the year the roof was installed, showed the weakest correlation with δ^2H in brochantite (R^2=0.09 p=0.5).

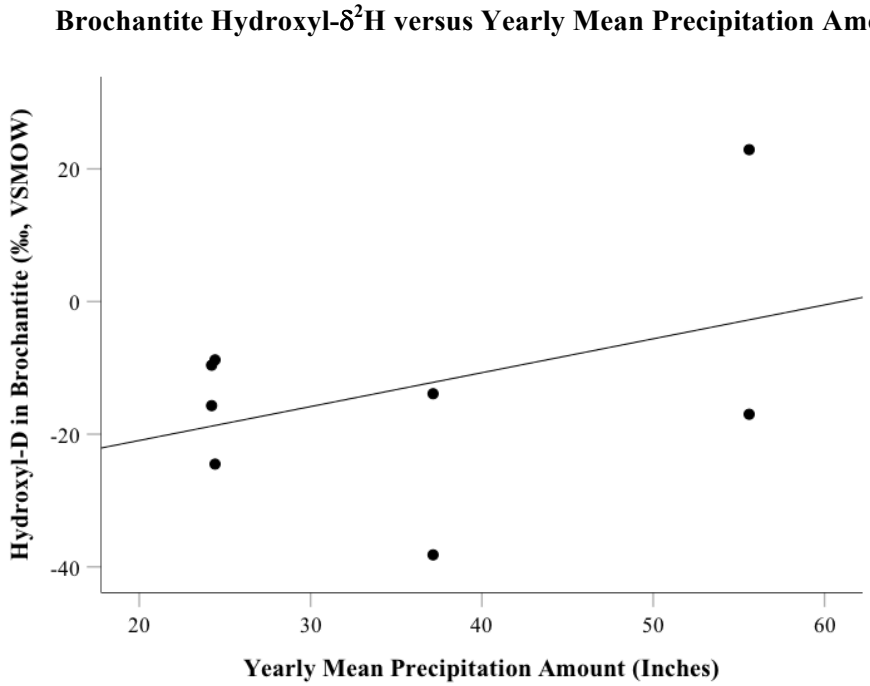


Figure 6.13: Scatterplot shows brochantite hydroxyl-δ^2H as a function of the yearly mean precipitation amount at the cities of sampling. From left to right, the first column is Oxford (24.2 inches) with Vienna (24.4 inches) immediately after, third is Ottawa (37.2 inches) and the fourth is Tuscaloosa (55.6 inches). This scatterplot shows no statistically significant correlation, with y=0.5x-31.2, R^2=0.2, p=0.3.

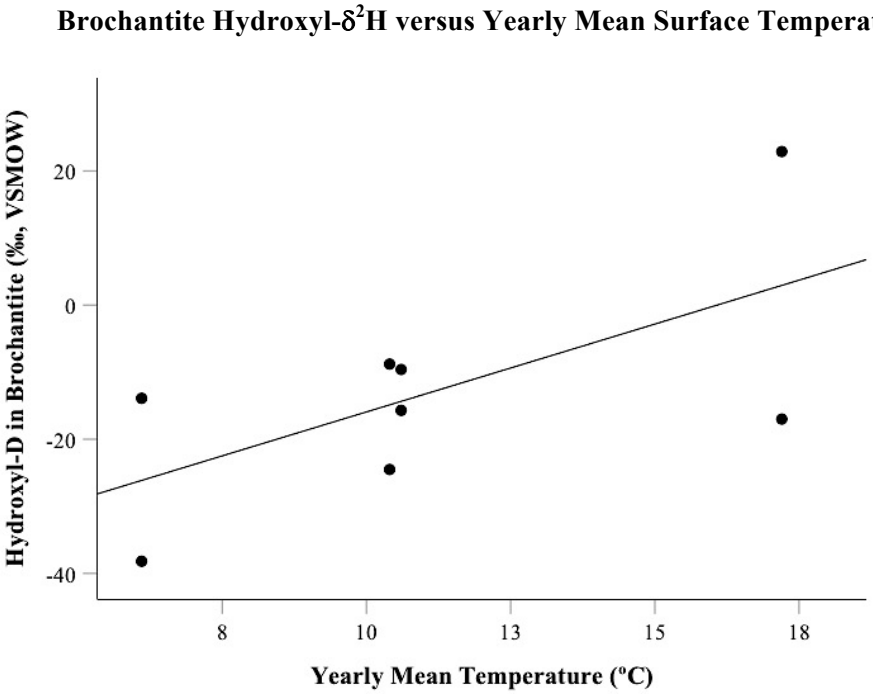


Figure 6.14: Scatterplot shows brochantite hydroxyl-δ^2H as a function of the yearly mean surface temperature at the cities of sampling. From left to right, the first column is Ottawa (6.1ºC), followed by Vienna (10.4ºC), third is Oxford (10.6ºC), and the fourth is Tuscaloosa (17.2ºC). This scatterplot shows no statistically significant correlation, with y=2.6x-42.1, R^2=0.4, p=0.09.

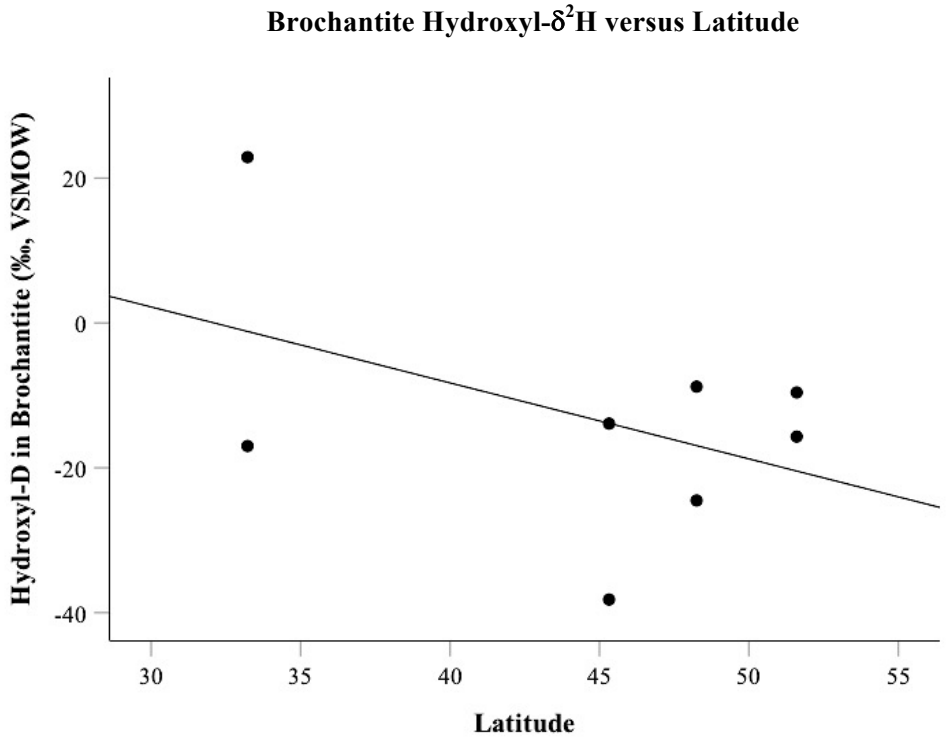


Figure 6.15: Scatterplot shows brochantite hydroxyl-δ^2H as a function of the latitude at the cities of sampling. From left to right, the first column is Tuscaloosa (33.2º), followed by Ottawa (45.3º), third is Vienna (48.2º), and the fourth is Oxford (51.6º). This scatterplot shows no statistically significant correlation, with y=33.7-1.05x, R^2=0.2, *p*=0.3.

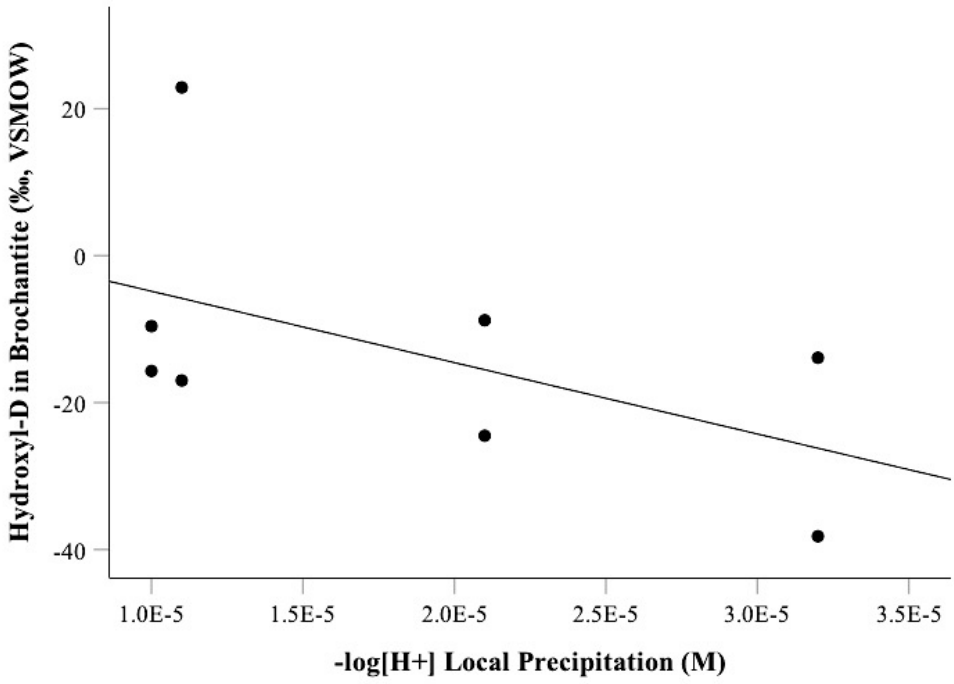


Figure 6.16: Scatterplot shows brochantite hydroxyl-δ^2H as a function of the yearly average acidity in meteoric water (presented in concentration of H^+) at the cities of sampling. This scatterplot shows no statistically significant correlation, with y=4.9-(9.7x10^{-5})x, R^2=0.3, *p*=0.2.

Finally, the age of the brochantite deposits (estimated by the year the copper roof was installed) were plotted against the hydroxyl-δ^2H values.

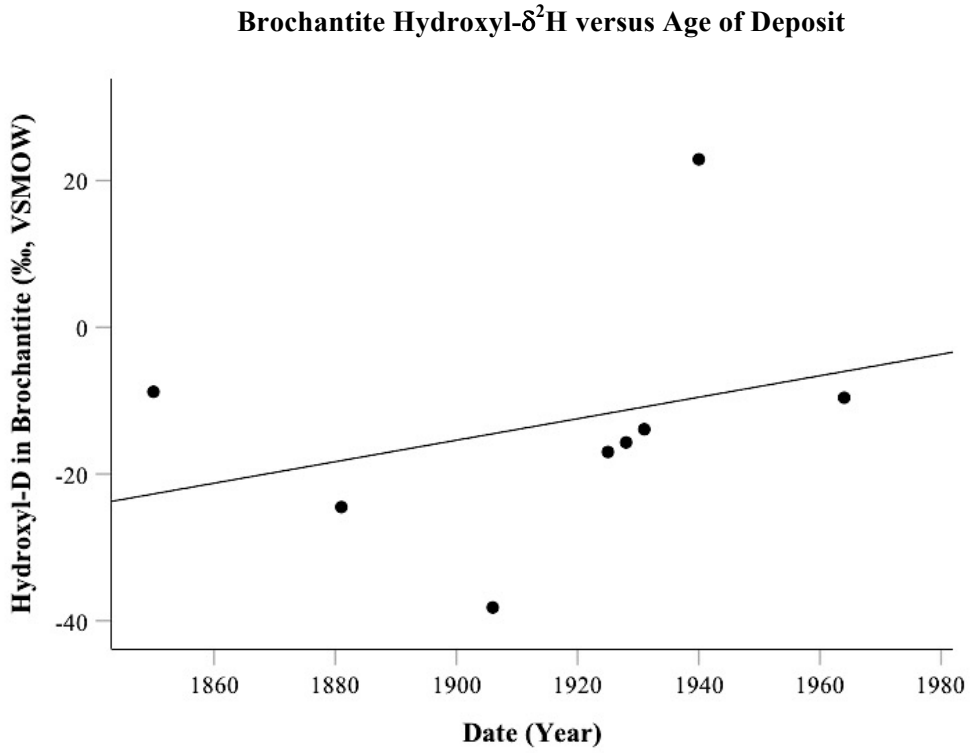


Figure 6.17: Scatterplot showing hydroxyl-δ^2H brochantite data as a function of the date of the buildings from which the patina samples were collected. This scatterplot shows no statistically significant correlation, with y=0.2x-(2.9x10^{-2}), R^2=0.09, *p*=0.5.

6.4. Summary

Powder XRD confirmed that the patina samples scraped from copper roofs around Oxford, Ottawa, Vienna and Tuscaloosa are brochantite, but sometimes mixed with other phases like quartz, cuprite and antlerite (**table 6.1**). The sulfate in the brochantite was isolated by reacting the dissolved samples with barium chloride to precipitate $BaSO_4$ (section 5.1.3). Thirty-Three $BaSO_4$ samples were analyzed isotopically to look for variance in the $\delta^{18}O_{SO4}$ values between the sample sites, as do the $\delta^{18}O_{H2O}$ values in the local precipitation, and to understand what controls the oxygen isotope ratios in the sulfate of brochantite (**table 6.2**). The $\delta^{18}O_{SO4}$ results were statistically analyzed using paired *t*-tests, Anova and linear regression. Since all *p*-values are greater than the critical value of 0.05, the conclusion is that there is no statistically significant difference between the $\delta^{18}O_{SO4}$ values in brochantite (**table 6.4**). Moreover, Anova results show that the brochantite $\delta^{18}O_{SO4}$ variances are roughly equal among the cities: $F_{3, 27} = 1.7$, $p = 0.2$.

Linear regression models were used to summarize the relationship between the $\delta^{18}O_{SO4}$ values in brochantite and an environmental parameter. There is no statistically significant correlation between brochantite $\delta^{18}O_{SO4}$ and the yearly weighted mean $\delta^{18}O_{H2O}$ in local precipitation: y=7.9+0.05x, R^2=0.01, *p*=0.5 (**figure 6.3**). The correlation between $\delta^{18}O_{H2O}$ in local precipitation and $\delta^{18}O_{SO4}$ in brochantite improves slightly when only considering summer

precipitation, though ultimately still insignificant: y=8.3+0.1x, R^2=0.03, *p*=0.4, **figure 6.4**. Scatterplots for brochantite $\delta^{18}O_{SO4}$ against the yearly mean precipitation amount, pH, surface temperature, latitude, and age of deposit (**figures 6.5 – 6.9**) were also analyzed and show no significant correlations. The strongest linear correlation is between $\delta^{18}O_{SO4}$ and the pH in meteoric water (y=7.9-(2.3x10^4)x, R^2=0.05, *p*=0.2), and the weakest is between $\delta^{18}O_{SO4}$ and latitude (y=6.8+0.01x, R^2=0.009, *p*=0.6).

A flowchart (**figure 6.10**) was created for this project that allows for estimations of isotopic oxidation pathways in secondary sulfates by calculating the percent contributions from heterogeneous and homogeneous pathways. After determining the percent contribution of ^{18}O in brochantite from water (**table 6.6**), and considering two pathway pairs at a time (1. homogeneous and heterogeneous using O_2 (metal catalyzed) or 2. homogeneous and heterogeneous using H_2O_2), the percent contributions were calculated for each city's $\delta^{18}O_{SO4}$ mean, high and low for the summer and for the year (**tables 6.7 – 6.13**). Using summer meteoric water data, the mean values suggest about half (51.3 – 57.1%) of the oxygen-18 in brochantite's sulfate is sourced from the local formation waters. Of the oxygen-18 sourced from water, about 44-91% of it was incorporated through an aqueous-phase pathway of SO_2 to SO_4. Values closer to 44% would suggest O_2 is the favored mechanism, whereas values nearer 91% would imply H_2O_2 is predominant. The pH of the local precipitation is the best-known lead in determining which heterogeneous pathway is most likely. If the pH is less than 5, the O_2 (metal catalyzed) pathway is favored. If the pH is greater than 5, the H_2O_2 pathway is favored. It is believed that both heterogeneous pathways are contributing, with preference of unknown magnitude for H_2O_2.

A pilot study was carried out for the analysis of δ^2H from the hydroxyl groups in brochantite (**table 6.14**). As with the $\delta^{18}O_{SO4}$ statistics, linear regression models were again used to summarize the relationship between the δ^2H values in brochantite and an environmental parameter. There is no statistically significant correlation between brochantite δ^2H and the $\delta^{18}O$ in local meteoric water, pH, average surface temperature, latitude, or amount of precipitation for the cities included in the study (**figures 6.12 – 6.17**). The yearly mean surface temperature at the city of formation has the strongest correlation (R^2=0.4, *p*=0.09). The age of the brochantite, determined by the year the roof was installed, showed the weakest correlation with δ^2H in brochantite (R^2=0.09 *p*=0.5). Ultimately, the δ^2H pilot study consists of little data and analyzing the δ^2H alone is insufficient. The hydroxyl study would benefit from analyzing the hydroxyl oxygen as well, but the brochantite samples collected are not big enough to carry out a full study on the sulfate oxygen and hydroxyl hydrogen.

CHAPTER 7

XRD and Stable Isotope Results for Malachite

7.1. MATERIAL CHARACTERIZATION: XRD RESULTS

As described in section 5.2.2, XRD provided reliable characterizations of the malachite samples, including the identification of contaminants. This instrumental technique also suggested percent compositions for each phase present in the samples. The following malachite description tables (**tables 7.1 – 7.8**), grouped by region of formation, present each sample's XRD material characterizations. Only the samples that contained malachite and passed inspection for stable isotope analysis are provided. A full list of samples collected and analyzed is available in Appendix A. The final table in this section (**table 7.9**) offers descriptions for the non-malachite minerals identified in the malachite samples used in the study.

7.1.1. Azurite and Atacamite

Since it is difficult to isolate pure malachite samples, it is important to understand the isotopic influence of the common contaminants found in patina samples from archaeological bronzes. Although the purpose of mass spectroscopy was to analyze the $\delta^{18}O$ and $\delta^{13}C$ in the carbonate of malachite, this step also served as a filter. Any mineral that survived manual picking and XRD would also have had to decompose similarly to malachite at 70ºC in orthophosphoric acid. The minerals that did not break down to release gas phase products were left in the exetainer and not analyzed isotopically. However, it is reasonable to assume that there are many minerals capable of reacting similarly to malachite, leading to data pollution, but they are difficult to identify. Only azurite and atacamite are discussed because they are common and there are multiple cases where it appears that they had an impact on the overall $\delta^{18}O$ or $\delta^{13}C$ values in malachite samples.

Azurite is copper (II) carbonate hydroxide mineral that is often found under malachite in a pseudomorphic state. There are seven B1 and B2 pairs that contained azurite, which are H3, H5, H9, H11, EO2, CGS3 and CNM1 (refer to **tables 7.1 – 7.8** for exact compositions). Atacamite is a copper (II) chloride hydroxide and looks very similar to malachite, making it difficult to distinguish during visual assessments for the isolation of malachite. There are seven B1 and B2 pairs that contained atacamite, which are H6, US1, US6, P2, EC5, EO2 and CNW2 (refer to **tables 7.1 – 7.8** for exact compositions). Samples RC4, P3, CNW2, CNW3, EC8 and E7 also contained atacamite, but without B2 samples, it is not possible to assess its impact on the overall oxygen isotope ratios. The isotopic impact these contaminants have on the malachite samples used in this study is addressed statistically in the following sections.

Hungary

Sample ID	XRD (B1)	XRD (B2)
H1	84% malachite, 10% tenorite, 6% quartz	57% malachite, 27% quartz, 14% tenorite, 2% cuprite
H2	59% malachite, 41% quartz **or** 54% malachite, 46% graphite	75% malachite, 25% SiO_2, plus unidentified peaks
H3	84% malachite, 16% quartz **or** 77% malachite, 14% quartz, 9% tenorite	60% malachite, 23% quartz, 13% azurite, 4% cuprite + more peaks
H4	56% malachite, 44% SiO_2	69% malachite, 23% quartz, 8% tenorite
H5	69% malachite, 19% graphite, 12% halite	40% malachite, 29% quartz, 17% jadeite, 14% azurite
H6	100% malachite	23% malachite, 23% quartz, 55% atacamite
H7	68% malachite, 32% coesite **or** 85% malachite, 8% coesite, 6% tenorite	84% malachite, 16% SiO_2
H8	58% malachite, 42% SiO_2	68% malachite, 22% SiO_2, 9% iron oxide.
H9	100% malachite	66% malachite, 15% quartz and 19% azurite
H10	100% malachite	35% malachite, 65% SiO_2 **or** 59% malachite, 25% quartz, 16% cuprite
H11	46% malachite, 54% sodalite	44% malachite, 35% SiO_2, 15% azurite, 7% tenorite

Table 7.1: Quantitative XRD results of phases present in the Hungarian samples. Eleven Hungarian samples ranged from 46% to 100% malachite. Under a binocular microscope, the malachite crystals appeared mostly teal and emerald-green colored, semi-translucent and semi-glossy. XRD analysis suggested that the most common contaminants included various SiO_2 phases and tenorite. Each primary sample had a correlating B2 sample. XRD characterization suggested that samples B2H2, B2H4 and B2H8 contained more malachite than their primary sample counterparts. Another copper carbonate mineral, azurite, was present in samples B2H3, B2H5, B2H9 and B2H11.

Sitka, Alaska, USA

Sample ID	XRD (B1)	XRD (B2)
US1	43% malachite, 57% atacamite	21% malachite, 5% cuprite, 52% calcite, 7% quartz, 14% atacamite,
US2	100% malachite	65% malachite, 35% quartz
US3	100% malachite	87% malachite, 13% cuprite
US5	100% malachite	100% malachite
US6	38% malachite, 47% atacamite, 16% quartz	39% malachite 28% quartz, 23% cuprite, 10% atacamite

Table 7.2: Quantitative XRD results of phases present in the Alaskan samples. The primary samples varied from 38% to 100% malachite, and each had correlating B2 samples. Optical microscopy descriptions ranged from classic emerald-green, semi-translucent and semi-glossy crystals to mint-colored, opaque and matte powders. Such descriptions are indicative of varying crystal sizes, with the finer samples appearing lighter in color and milky. XRD analysis suggested that B2US6 contained 1% more malachite than the correlating primary sample. XRD also suggested that US5 and B2US5 consisted of 100% malachite, which was strange because the B2 sample was roughly picked and visual descriptions state that these samples were more contaminated than the other Alaskan samples, with a yellower tint. Another carbonate mineral, calcite, was the dominant phase present in B2US4.

Batán Grande, Lambayeque, Peru

Sample ID	XRD (B1)	XRD (B2)
P2	26% malachite, 28% atacamite, 41% SiO_2, 5% cuprite	29% malachite, 24% paratacamite, 38% atacamite and 8% quartz
P3	48% malachite, 51% atacamite	None
P6g (ore)	100% malachite	None
P7g (ore)	82% malachite, 18% quartz	None

Table 7.3: Quantitative XRD results of phases present in the Peruvian samples. These samples were dominated by another copper corrosion product, atacamite, and only contained 26% to 48% malachite. Optical microscopy descriptions of the crystals ranged from pine, teal and emerald-green colored, generally darker than the other samples included in the study, semi-translucent and semi-glossy. There was one B2 sample correlated with P2, which contained slightly more malachite, and much more copper (II) chloride hydroxide minerals. Two geological ore samples from the same tomb were also analyzed, though their formation site is uncertain. They were much purer, at 82% to 100% malachite.

Episkopi and Pyla-Kokkinokremos, Republic of Cyprus

Sample ID	XRD (B1)	XRD (B2)
RC4	27-57% malachite, 36-73% copper (II) chloride hydroxide minerals	None
RC7	65% malachite, 35% calcite	None
RC8	68% malachite, 32% calcite	None

Table 7.4: Quantitative XRD results of phases present in the Cypriot samples. Optical microscopy descriptions suggested yellower, brighter crystals with more opaque and matte appearances than many of the other samples included in this study. Sample RC4 yielded peculiar XRD results as it could have contained anywhere from 27% to 57% malachite, with the rest copper (II) chloride hydroxide minerals. Samples RC7 and RC8 had similar compositions and were contaminated with another carbonate mineral, calcite. Cyprus is represented only with B1 samples.

Las Pilas, Mojácar, Spain

Sample ID	XRD (B1)	XRD (B2)
SES9	100% malachite	None
SES1g (ore)	100% malachite	None
SES2g (ore)	100% malachite	None

Table 7.5: Quantitative XRD results for phases present in Spanish samples. All samples were pure malachite. Optical microscopy of the archaeological sample described emerald-green, semi-translucent, glossy, bubble-shaped crystals. The ores were also emerald-green, semi-translucent and glossy, but had fibrous crystals. The true formation site of the ores is unknown, but believed to be from somewhere in southern Spain (*pers. comm.* Murillo Barroso 2016).

Southern England

Sample ID	XRD (B1)	XRD (B2)
E2	100% malachite	100% malachite
E3	41% malachite, 59% azurite	None
E4	100% malachite	None
E6	64% malachite, 36% quartz	38% malachite, 45% quartz, 17% diopside ($CaMg(SiO)_3$)
E7	25% malachite, 68% atacamite, 7% quartz	None
EC2	34% malachite, 32% calcite, 34% quartz	45% malachite, 55% quartz and unidentified peaks
EC4	97% malachite, 2% iron oxide, 1% graphite	83% malachite, 18% quartz
EC5	36% malachite, 8% quartz, 56% atacamite	54% malachite, 46% atacamite
EC7	90% malachite, 10% graphite **or** 77% malachite and 23% quartz	None
EC8	50% malachite, 48% atacamite, 2% quartz	None
EO2	64% malachite, 3% cristobalite, 33% atacamite	36% malachite, 61% azurite, 3% SiO_2

Table 7.6: Quantitative XRD results for phases present in English samples. Eleven samples contained a range from 25% to 100% malachite, of which five had correlating B2 samples. Optical microscopy was most interesting, with most samples described as emerald-green colored, semi-translucent and semi-glossy, but two samples were very unique. The malachite crystals in E6 and EC4 formed in coils, which is rare. Apart from their coil structures, these samples were visually distinct from each other. E6 was pine-green colored, semi-glossy and semi-translucent. Meanwhile EC4 was mint-green colored, matte and opaque. According to XRD, the main contaminants in the English samples were quartz and atacamite. Samples E3 and EC2 were heavily contaminated with other carbonate minerals (azurite and calcite, respectively). Samples B2EC2 and B2EC5 may have contained more malachite than the primary samples, but were also heavily mixed phase, which makes XRD characterization less reliable.

Tel Gezer, Israel

Sample ID	XRD (B1)	XRD (B2)
I1	43% malachite, 57% anatacamite	None
I2	47% malachite, 36% atacamite, 17% quartz + couple unidentified peaks	None
I4	47% malachite, 43% atacamite, 2% cuprite, 7% quartz	None

Table 7.7: Quantitative XRD results of phases present in Israeli samples. Three samples passed processing, but none had B2 samples. They all had similar compositions, ranging from 43% to 47% malachite with the main contaminants being atacamite and quartz. Samples I2 and I4 had more than three phases present, which complicated XRD analysis and could have hindered reliable characterizations. Optical microscopy descriptions of the samples were very distinct. I1 was mostly turquoise-colored, matte and opaque. I2 was dark teal-green, semi-opaque and semi-glossy. I4 was medium-green and had yellow-tinted areas, was semi-translucent and semi-glossy.

China

Sample ID	XRD (B1)	XRD (B2)
Gansu		
CGN2	100% malachite	None
Guangxi		
CGS2	71% malachite, 19% pyromorphite, 10% SiO_2 + one unidentified peak, possibly another SiO_2	None
CGS3	81% malachite, 19% azurite + one unidentified peak	100% malachite
CGS4	100% malachite	89% malachite, 11% cuprite + one unidentified peak
CGS5	62% malachite, 28% azurite, 10% SiO_2 + one unidentified peak	None
Jiangsu		
CJN	94% malachite, 4% sodalite	None
Jiangxi		
CJS	100% malachite	None
Ningxia		
CNM1	42% malachite, 38% azurite, 20% quartz	3% malachite, 87% SiO_2
CNW1	93% malachite, 7% coesite	None
CNW2	87% malachite, 2% paratacamite, 12% dolomite	59% malachite, 39% azurite, 2% clinoatacamite
CNW3	60% malachite, 21% calcite, 16% atacamite, 3% quartz	None
CNW4	90% malachite, 10% coesite	None
CNW5	76% malachite, 23% SiO_2, 2% tenorite + couple unidentified peaks, one is clay	None
CNWg1	96% malachite, 4% quartz	None
CNWg2	100% malachite	None
CNWg3	82% malachite, 18% quartz	None
CNWg4	63% malachite, 37% quartz	None

Table 7.8: Quantitative XRD results for phases present in Chinese samples. Considering China's vast size with wide-ranging environments, the samples were grouped by province. A total of 17 samples in five provinces represent China. Gansu was represented by one pure malachite sample. Guangxi was represented by four samples ranging from 62% to 100% malachite and two B2 samples. According to XRD, B2CGS3 was pure malachite, and the correlating primary sample was just 71% malachite and contained azurite, which is another copper carbonate mineral. CGS5 also contained azurite. Jiangsu was represented by one sample, which was 94% malachite, as well as a correlating B2 sample. Jiangxi was represented by one pure malachite sample. Ningxia was represented by six samples, of which two had B2 samples. Malachite purity ranged from 42% to 93%, with SiO_2 minerals as the main contaminant. CNM1, CNW2 and CNW3 contained other carbonate phases, and CNW5 was very mix-phase. Ningxia was also represented by four malachite ore samples of uncertain formation origin.

Non-Malachite Minerals Identified in Samples

Mineral Name	Chemical Formula	Visual Description	Polymorphism or Associations	Occurrence
Anatacamite	$Cu_2(OH)_3Cl$	Emerald-green, transparent, vitreous	Polymorphous with atacamite, botallackite and clinoatacamite	In the oxidation zone of a polymetallic sulfide deposit
Atacamite	$Cu_2(OH)_3Cl$	Bright green, dark emerald-green to blackish green. Transparent to translucent. Adamantine to vitreous.	Polymorphous with botallackite, clinoatacamite and paratacamite.	An oxidation product of other copper minerals, especially under arid, saline conditions; in fumarolic deposits; a weathering product of sulfides in subsea black smoker deposits, an alteration of bronze and copper objects of antiquity
Azurite	$Cu_3(CO_3)_2(OH)_2$	Very dark to pale blue. Transparent to translucent, vitreous to subadamantine	-	In the oxidized zones of copper deposits associated with carbonate rocks
Calcite	$CaCO_3$	Transparent to opaque. Colorless or white, also gray, yellow, green and other colors depending on contamination	Trimorphous with aragonite and vaterite; forms a series with rhodochrosite.	A major rock-forming mineral; in limestones, marbles, chalks
Clinoatacamite	$Cu_2(OH)_3Cl$	Green to dark greenish-black. Rarely greenish-blue. Transparent to translucent. Adamantine to vitreous.	Polymorphous with atacamtie, botallackite, and paratacamite	An oxidation product of other copper minerals
Coesite	SiO_2	Colorless and transparent, vitreous	Polymorphous with quartz, tridymite, cristolbalite, stishovite	Formed in pressures in excess of 20 kbar, and is found as fine-grained ingrowths with quarz and silica glass in impact metamorphosed rocks and tektites.
Cristobalite	SiO_2	Colorless, white, transparent, vitreous	Polymorphic with quartz, tridymite, coesite and stishovite	A late-crystalizing phase in basaltic to rhyolitic volcanic rocks and more
Cuprite	Cu_2O	Cochineal-red, ruby-red, purplish-red to nearly black. Transparent to translucent, adamantine to submetallic, earthy.	-	A common mineral in the oxidized portions of many copper deposits
Diopside	$CaMg(SiO)_3$	Colorless, white, yellow, pale to dark green, black. Transparent to translucent, vitreous or dull	Forms in two series, with hedenbergite and with johannsenite.	Typical of metamorphosed siliceous Ca, Mg-rich rocks of the pyroxene-hornfels or epidote-amphibolite facies;

				common in skarns, Ca, Mg-rich gneisses and schists, and some kimberlites and peridotites. Less common in alkali olivine basalts and andesites.
Dolomite	$CaMg(CO_3)_2$	Colorless, white, yellow, brown, pale pink; transparent to translucent; vitreous to pearly	Forms to series with ankerite and with kutnohorite	Formed by diagenesis or hydrothermal metasomatism of limestone; a primary phase in hypersaline sedimentary environments; a major component of some contact metamorphic rocks and marbles; a gangue in hydrothermal veins; in carbonatites and ultramafic rocks.
Graphite	C	Iron-black to steel-grey; opaque; metallic, may be dull, earthy	Polymorphous with chaoite, diamond and lonsdaleite	Formed by metamorphism of sedimentary carbonaceous material, but the reduction of carbon compounds; a primary constituent in igneous rocks.
Halite	NaCl	Colorless or white when pure; transparent; vitreous	-	Typically in sedimentary rocks of evaporate association, may form immense beds; also as volcanic sublimates, efflorescences, cave deposits. Crystals common in multiphase fluid inclusions; may be in other minerals as product of intermediate-grade metamorphism.
Jadeite	$Na(Al,Fe^{3+})Si_2O_6$	Apple-green, emerald-green, bluish-green, leek-green, greenish-white, white, may show green spots, rarely blue or violet; translucent; subvitreous, pearly on cleavages	-	In high-pressure metamorphic rocks of the glaucophane facies; a component of eclogite.
Paratacamite	$Cu_2(OH)_3Cl$	Green to dark green, greenish black; translucent to nearly opaque; vitreous	Polymorphous with atacamite, botallackite and clinoatacamite	An oxidation product of other copper minerals, especially under acid, saline conditions; in fumarolic deposits; a weathering product of sulfides in subsea black smoker deposits

Pyromorphite	$Pb_5(PO_4)_3Cl$	Dark grass-green, green, yellow, yellow-orange, reddish orange, yellow-brown, brown, tan, grayish, may be colorless; transparent to translucent; resinous to subadamantine	-	A secondary mineral in the oxidized zone of lead deposits; rarely a volcanic sublimate
Quartz	SiO_2	Colorless, white; transparent to nearly opaque; vitreous, waxy to dull when massive	Polymorphous with cristobalite, tridymite, coesite and stishovite	In hydrothermal veins, epithermal to alpine; characteristic of granite and granite pegmatites; in sandstones and quartzites, less abundant in other rock types; in hydrothermal metal deposits. Common in carbonate rocks; a residual mineral in soils and sediments.
Sodalite	$Na_8(Al_6Si_6O_{24})Cl_2$	Colorless, white, yellowish, greenish, light to dark blue, reddish; transparent to translucent, vitreous to greasy	-	Formed in nepheline syenites, phonolites, and related rock types. In metasomatized calcareous rocks, and in cavities in ejectec volcanic blocks.
Tenorite	CuO	Steel-gray, iron-gray, black; opaque; metallic	-	Commonly in the oxidized zone of hydrothermal copper deposits; a volcanic sublimate

Table 7.9: Chemical and visual descriptions of the non-malachite minerals identified in the samples, and formation details (Anthony *et al.* 2003).

7.2. MALACHITE $\delta^{18}O$ AND $\delta^{13}C$ RESULTS

7.2.1. Presentation of Raw Data and Descriptive Statistics

Full results for oxygen-18 and carbon-13 ratios from the 49 B1 archaeological malachite samples are presented in **table 7.10** and plotted in **figure 7.5**. The $\delta^{18}O$ values (VSMOW) range from 21.1‰ to 30.1‰ (mean = 26.3‰, SD = 2.2‰). The $\delta^{13}C$ values (VPDB) of the archaeological malachite range from -18.1‰ to -8.1‰ (mean = -11.5‰, SD = 2.2‰). Batch two consists of 29 archaeological samples in seven geographic groups. The $\delta^{18}O$ and $\delta^{13}C$ results from the carbonate of these malachite samples are provided in the **table 7.11** and plotted on **figure 7.6**. The $\delta^{18}O$ values (VSMOW) range from 22.4‰ to 30.9‰ (mean = 26.2‰, SD = 2.0‰), and the $\delta^{13}C$ values (VPDB) range from -18.2‰ to -6.9‰ (mean = -13.6‰, SD = 2.5‰).

This project's $\delta^{18}O$ data was provided by Cambridge[1] using Vienna Pee Dee Belemnite (VPDB), which is a common reference standard for isotopic measurements on carbonates in paleoclimate studies. However, the standard used among the most recent malachite investigators is Vienna Standard Mean Ocean Water (VSMOW) (Smith and Pandey reported in PDB), which is used when defining the isotopic composition of freshwater. To better compare the malachite $\delta^{18}O$ data to the $\delta^{18}O$ of the formation water, and to be on a par with current investigators, the original $\delta^{18}O$ (VPDB) data was converted to VSMOW using the following equation:

$$\delta^{18}O_{VSMOW} = 1.03091 \cdot \delta^{18}O_{VPDB} + 30.91‰.$$

Tables 7.10 and 7.11 present the $\delta^{18}O$ data in original VPDB and converted VSMOW.

According to Grubb's outlier test, only the B1 English data set has a significant outlier. The $\delta^{18}O$ value for sample E3, marked with an asterisk in **table 7.10**, has a *p*-value equal to 0.04. The B2 dataset has no outliers. Isotope data in **tables 7.10 and 7.11** with light grey boxes represent values furthest from the rest in their geographical group, however apart from E3, they are not significant outliers. Dark grey boxes signify values furthest from the rest in the full data set. Geographically grouped data is further described statistically (standard deviation and standard error) in **tables 7.12 and 7.13,** and visualized in 95% confidence interval plots in **figures 7.1 and 7.2**.

[1] Stable isotope measurements were carried out at the Godwin Laboratory for Paleoclimate Research in the Department of Earth Sciences at the University of Cambridge. Standard procedure at the Godwin Laboratory is to run a single sample on the GasBench as reproducibility is usually very good with no need for replicates. The GasBench runs sample gas ten times, with calculated average and standard deviations for peaks 4 to 8 being better than 0.1 (Rolfe 2019).

Batch One Stable Isotope Data from Archaeological Malachite Samples

Sample ID	Sample Provenance	$\delta^{18}O_{(VPDB)}$, ‰	$\delta^{18}O_{(VSMOW)}$, ‰	$\delta^{13}C_{(VPDB)}$, ‰
H1	Hungary (exact location unknown)	-4.5	26.2	-13.9
H2	Hungary (exact location unknown)	-4.3	26.5	-12.3
H3	Hungary (exact location unknown)	-4.5	26.3	-12.4
H4	Hungary (exact location unknown)	-5.5	25.2	-13.0
H5	Hungary (exact location unknown)	-4.2	26.6	-12.4
H6	Hungary (exact location unknown)	-6.8	24.0	-13.8
H7	Hungary (exact location unknown)	-5.5	25.3	-13.4
H8	Hungary (exact location unknown)	-6.1	24.6	-13.6
H9	Hungary (exact location unknown)	-6.0	24.8	-14.1
H10	Hungary (exact location unknown)	-3.6	27.2	-13.5
H11	Hungary (exact location unknown)	-6.5	24.2	-14.0
US1	Sitka, Alaska, USA	-4.5	26.3	-13.0
US2	Sitka, Alaska, USA	-5.1	25.7	-15.7
US3	Sitka, Alaska, USA	-4.1	26.7	-15.9
US5	Sitka, Alaska, USA	-4.4	26.4	-14.9
US6	Sitka, Alaska, USA	-4.4	26.4	-14.7
P2	Batán Grande, Lambayeque, Peru	-5.7	25.1	-15.0
P3	Batán Grande, Lambayeque, Peru	-5.8	24.9	-14.9
RC4	Pyla-Kokkinokremmos, Cyprus	-3.2	27.6	-12.6
RC7	Episkopi, Cyprus	-3.1	27.7	-9.9
RC8	Episkopi, Cyprus	-3.2	27.6	-10.0
SES9	Las Pilas, Almería, Spain	-2.4	28.5	-11.9
E2	Malmsbury, Wiltshire, England	-1.4	29.5	-18.0
E3	Pewsey, Wiltshire, England	-4.1*	26.7*	-16.3
E4	Boldre, Hampshire, England	-1.1	29.8	-16.7
E6	London, England	-0.8	30.1	-18.1
E7	London, England	-2.3	28.5	-14.4
EC2	Canterbury, Kent, England	-1.5	29.4	-16.5
EC4	Canterbury, Kent, England	-1.2	29.6	-16.1
EC5	Canterbury, Kent, England	-2.6	28.2	-16.7
EC7	Canterbury, Kent, England	-1.8	29.0	-14.6
EC8	Canterbury, Kent, England	-1.6	29.3	-15.9
EO2	Oxford, Oxfordshire, England	-2.2	28.7	-15.8
I1	Tel Gezer, Israel	-3.5	27.3	-13.2
I2	Tel Gezer, Israel	-3.8	27.0	-14.1
I4	Tel Gezer, Israel	-3.2	27.6	-14.9
CGN2	Gansu, China (exact location unknown)	-3.3	27.5	-12.1
CGS2	Guangxi, China (exact location unknown)	-6.6	24.2	-12.4
CGS3	Guangxi, China (exact location unknown)	-7.9	22.8	-16.0
CGS4	Guangxi, China (exact location unknown)	-7.2	23.5	-11.7
CGS5	Guangxi, China (exact location unknown)	-8.2	22.5	-15.1
CJN	Jiangsu, China (exact location unknown)	-4.1	26.7	-16.5
CJS	Jiangxi, China (Niucheng)	-3.5	27.3	-11.6
CNM1	Ningxia, China (exact location unknown)	-5.9	24.8	-11.4
CNW1	Ningxia, China (from west, near Gobi Desert)	-8.5	22.1	-9.5
CNW2	Ningxia, China (from west, near Gobi Desert)	-6.6	24.2	-8.1
CNW3	Ningxia, China (from west, near Gobi Desert)	-3.9	26.9	-11.8
CNW4	Ningxia, China (from west, near Gobi Desert)	-9.5	21.1	-12.2
CNW5	Ningxia, China (from west, near Gobi Desert)	-8.9	21.8	-11.5
	Mean	-4.5	26.3	-13.8
	SD	2.2	2.2	2.2
	CV (%)	48.4	8.4	16.0

Table 7.10: Full results for $\delta^{18}O$ and $\delta^{13}C$ values from the archaeological malachite samples. The $\delta^{18}O$ values (VSMOW) range from 21.1‰ – 30.1‰, and the $\delta^{13}C$ values (VPDB) range from -18.1‰ to -8.1‰. Overall mean, standard deviation and coefficient of variation for each data column is shown at the bottom of the table. Data from sample CNW4 is furthest from the rest (in the dark grey boxes), but not an outlier as $p > 0.05$. Apart from the $\delta^{18}O$ values for sample E3, values in grey boxes are furthest from the rest in their geographical group, however not significant outliers (a group requires more than four samples to carry out a Grubb's test). The $\delta^{18}O$ values for sample E3, marked with an asterisk, are significant outliers with $p = 0.04$.

Batch Two Stable Isotope Data on Archaeological Malachite

Sample ID	Sample Provenance	$\delta^{18}O_{(VPDB)}$, ‰	$\delta^{18}O_{(VSMOW)}$, ‰	$\delta^{13}C_{(VPDB)}$, ‰
B2H1	Hungary (exact location unknown)	-4.9	25.9	-12.9
B2H2	Hungary (exact location unknown)	-4.4	26.4	-12.1
B2H3	Hungary (exact location unknown)	-4.7	26.1	-11.8
B2H4	Hungary (exact location unknown)	-5.1	24.6	-12.6
B2H5	Hungary (exact location unknown)	-4.3	26.5	-12.1
B2H6	Hungary (exact location unknown)	-5.3	25.5	-11.6
B2H7	Hungary (exact location unknown)	-5.4	25.3	-13.0
B2H8	Hungary (exact location unknown)	-5.2	25.5	-13.1
B2H9	Hungary (exact location unknown)	-5.4	25.4	-12.0
B2H10	Hungary (exact location unknown)	-4.5	26.3	-12.5
B2H11	Hungary (exact location unknown)	-5.2	25.5	-12.9
B2US1	Sitka, Alaska, USA	-6.0	24.8	-12.9
B2US2	Sitka, Alaska, USA	-5.8	25.0	-16.3
B2US3	Sitka, Alaska, USA	-4.4	26.4	-16.1
B2US5	Sitka, Alaska, USA	-3.9	26.9	-14.4
B2US6	Sitka, Alaska, USA	-5.1	25.7	-15.8
B2P2	Batán Grande, Lambayeque, Peru	-5.3	25.5	-14.9
B2E2	Malmsbury, Wiltshire, England	-1.4	29.5	-18.2
B2E6	London, England	-0.8	30.1	-18.1
B2EC2	Canterbury, Kent, England	-1.8	29.0	-13.5
B2EC4	Canterbury, Kent, England	-1.4	29.5	-16.3
B2EC5	Canterbury, Kent, England	-3.5	27.3	-16.6
B2EO	Oxford, Oxfordshire, England	-0.01	30.9	-15.6
B2CGS3	Guangxi, China (exact location unknown)	-7.3	23.4	-15.9
B2CGS4	Guangxi, China (exact location unknown)	-7.3	23.4	-11.2
B2CJN	Jiangsu, China (exact location unknown)	-3.1	27.8	-13.6
B2CNM1	Ningxia, China (exact location unknown)	-6.0	24.8	-11.3
B2CNW1	Ningxia, China (from west, near Gobi Desert)	-8.3	22.4	-9.6
B2CNW2	Ningxia, China (from west, near Gobi Desert)	-5.9	24.8	-6.9
	Mean	-4.5	26.2	-13.6
	SD	1.9	2.0	2.5
	CV (%)	42.3	7.6	18.3

Table 7.11: Full results for oxygen-18 and carbon-13 values from the Batch Two archaeological malachite samples. The $\delta^{18}O$ values (VSMOW) range from 22.4‰ to 30.9‰, and the $\delta^{13}C$ values (VPDB) range from -18.2‰ to -6.9‰. Overall mean, standard deviation and coefficient of variation for each data column is shown at the bottom of the table. The $\delta^{18}O$ value from sample B2EO and $\delta^{13}C$ value from B2CNW2 are furthest from the rest (dark grey boxes), but not outliers as $p > 0.05$. Isotope values in light grey boxes are furthest from the rest in their geographical group (a group requires more than four samples to carry out a Grubb's test), however not significant outliers. The B2 data set has no outliers.

$\delta^{18}O$

The following descriptive statistics and confidence interval plots are focused on the B1 and B2 malachite $\delta^{18}O$ results, grouped geographically. The purpose of this information is to determine the strength of central tendencies within raw data sets and quantify the amount of dispersion. The mean for the B1 $\delta^{18}O$ data ranges from 23.5 ± 2.2‰ (Ningxia, China) to 29.0 ± 0.9‰ (England), (refer to **table 7.12** for B1 descriptive statistics). Cyprus has the lowest standard deviation and coefficient of variation, meaning its data points are close to the mean. Ningxia has the highest standard deviation and coefficient of variation, meaning its data points are farthest spread. There are multiple reasons why some data sets range more broadly than others. For this

project, it most likely has to do with sample quality (purity), provenance accuracy and the number of samples in a set.

B1 Descriptive Statistics for Malachite $\delta^{18}O$

Site	N	Mean (‰, VSMOW)	SD (‰)	CV (%)	SE	95% CI Lower Bound	95% CI Upper Bound
Hungary	11	25.5	1.1	4.2	0.3	24.8	26.3
Alaska, USA	5	26.3	0.4	1.5	0.2	25.8	26.7
Peru	2	25.0	0.1	0.4	0.1	24.0	25.9
Cyprus	3	27.6	0.04	0.1	0.03	27.5	27.7
Spain	1	28.5	-	-	-	-	-
England	11	29.0	0.9	3.2	0.3	28.3	29.6
England w/o E3	10	29.2	0.6	2.1	0.2	28.8	29.6
Israel	3	27.3	0.3	1.3	0.2	26.4	28.1
Gansu, China	1	27.5	-	-	-	-	-
Guangxi, China	4	23.2	0.8	3.3	0.4	22.0	24.4
Jiangsu, China	1	26.7	-	-	-	-	-
Jiangxi, China	1	27.3	-	-	-	-	-
Ningxia, China	6	23.5	2.2	9.3	0.9	21.2	25.8

Table 7.12: Geographically grouped B1 $\delta^{18}O$ descriptive statistics for malachite. England is presented twice; first using all isotopic data, second excluding the outlying sample (E3).

The B2 data set serves to assess the necessity of meticulous picking, and as an indirect way of analyzing common impurities. The mean for the B2 $\delta^{18}O$ data set ranges from 23.4 ± 0.0‰ (Guangxi, China) to 29.4 ± 1.2‰ (England), (refer to **table 7.13** for B2 descriptive statistics). Guangxi also has the lowest standard deviation and coefficient of variation, meaning its data points are close to the mean. Ningxia has the highest standard deviation and coefficient of variation, meaning its data points are farthest spread in both the B1 and B2 datasets.

B2 Descriptive Statistics for Malachite $\delta^{18}O$

Site	N	Mean (‰,VSMOW)	SD (‰)	CV (%)	SE	95% CI Lower Bound	95% CI Upper Bound
Hungary	11	25.7	0.6	2.2	0.2	25.4	26.1
Alaska, USA	5	25.7	0.9	3.5	0.4	24.6	26.8
Peru	1	25.0	-	-	-	-	-
England	6	29.4	1.2	4.1	0.5	28.1	30.7
Guangxi, China	2	23.4	<0.0005	<0.0005	<0.0005	23.4	23.4
Jiangsu, China	1	27.8	-	-	-	-	-
Ningxia, China	3	24.0	1.4	5.8	0.8	20.5	27.4

Table 7.13: Geographically grouped B2 $\delta^{18}O$ descriptive statistics for malachite.

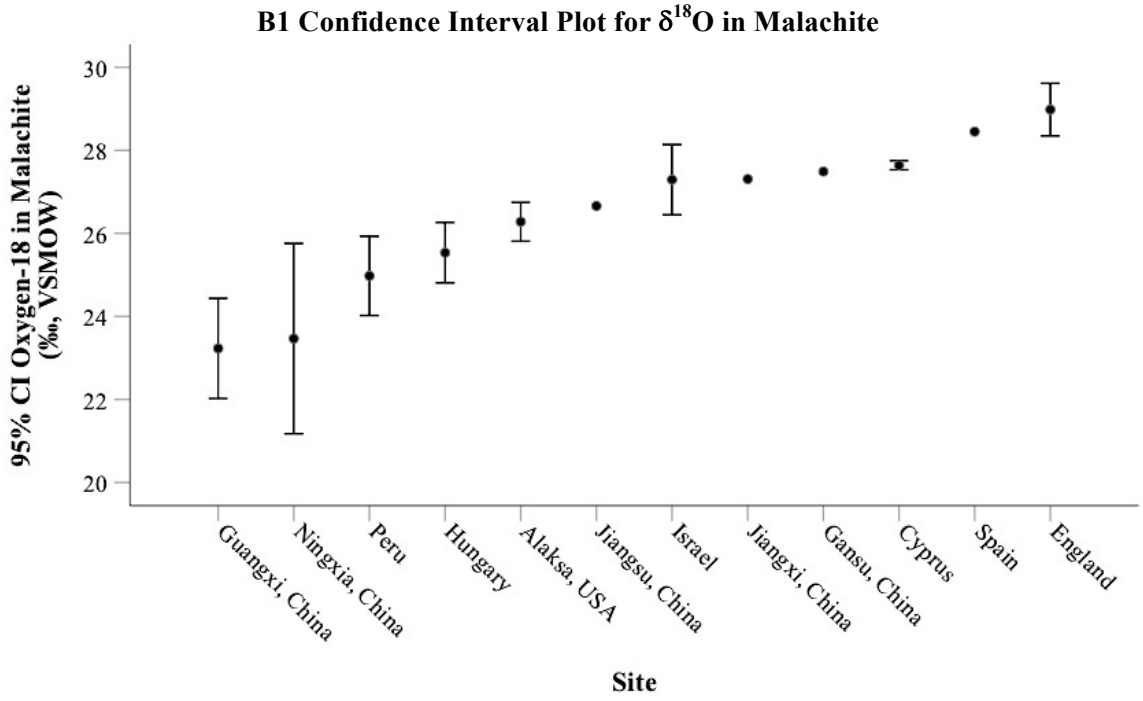


Figure 7.1: Plot showing the B1 malachite $\delta^{18}O$ means (central tendency) for each site represented by a dot, and the lines representing the precision of the estimate of the mean (variability, with a 95% confidence interval), plotted in order of increasing mean value. This order remains the same when plotted without the English outlier (E3), however the error bars shorten slightly. Jiangsu, Jiangxi, Gansu and Spain are only represented by dots because there is only one data point for each of these geographic groups.

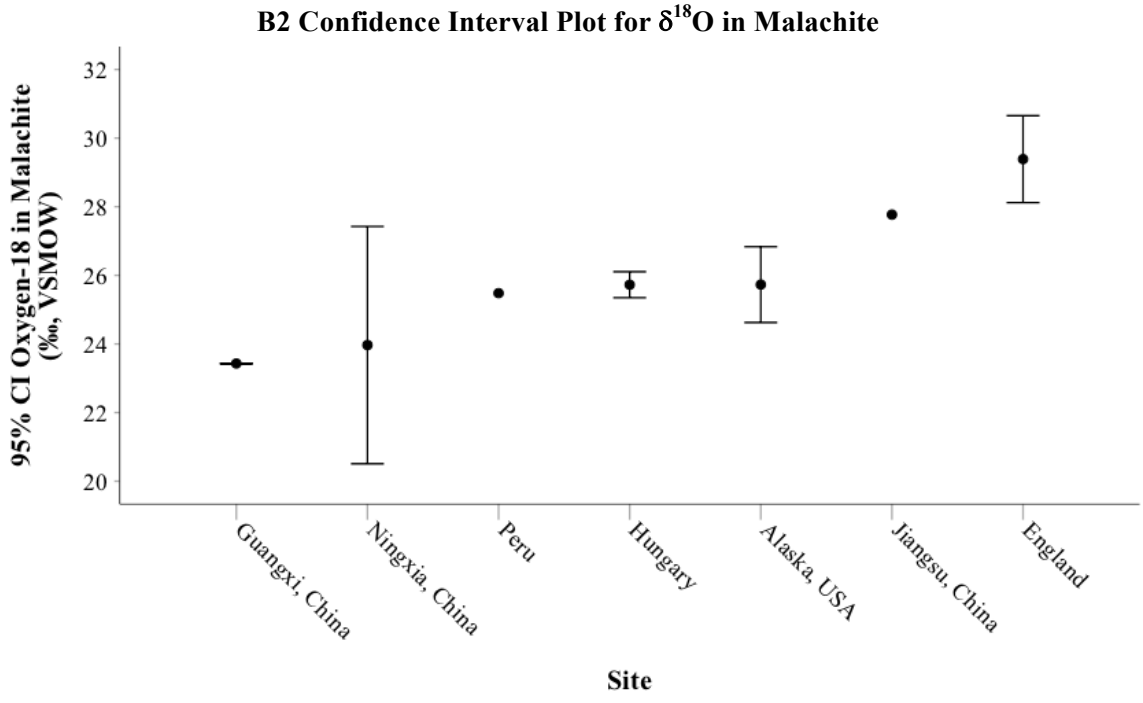


Figure 7.2: Plot showing the B2 malachite $\delta^{18}O$ means (central tendency) for each site represented by a dot, and the lines representing the precision of the estimate of the mean (variability, with a 95% confidence interval), plotted in order of increasing mean value. Peru and Jiangsu are only represented by dots because there is just one data point for each of these geographic groups.

All 29 B1 and B2 $\delta^{18}O_{malachite}$ pairs, along with the mean, standard deviation and coefficient of variation, are presented in **table 7.14**, below. Each B1 and B2 sample pair has small standard deviations (most are below one) and coefficients of variation, meaning they are close to their mean. The widest variation is between the B1 and B2 $\delta^{18}O$ values for sample EO (29.8 ± 1.6‰, CV = 5.3%), and the closest data is for sample CNM1 (24.8 ± 0.02‰, CV = 0.09%). Starting with the null hypothesis that here is no difference between the populations from which the B1 and B2 $\delta^{18}O$ malachite pairs come, and using a 5% (0.05) critical significance level, a paired *t*-value was generated for the batches. The results confirm that there is no significant statistical difference between the B1 and B2 malachite populations for $\delta^{18}O$ (paired *t*-test, two-tailed: $t_{28} = 0.7$, $p = 0.5$, 95% CI [-0.4, 0.2]). Since the critical significance level of 0.05 is smaller than the value of 0.5 of *p*, the stated null hypothesis must be accepted. This suggests that meticulous picking does not significantly impact the oxygen isotope results in archaeological malachite samples.

B1 and B2 $\delta^{18}O$ Pairs for Malachite

Sample ID	B1 $\delta^{18}O_{(VSMOW)}$, ‰	B2 $\delta^{18}O_{(VSMOW)}$, ‰	Mean	SD, ‰	CV, %
H1	26.2	25.9	26.1	0.3	1.0
H2	26.5	26.4	26.4	0.1	0.3
H3	26.3	26.1	26.2	0.1	0.5
H4	25.2	24.6	24.9	0.4	1.8
H5	26.6	26.5	26.5	0.1	0.4
H6	24.0	25.5	24.7	1.1	4.4
H7	25.3	25.3	25.3	0.03	0.1
H8	24.6	25.5	25.1	0.7	2.6
H9	24.8	25.4	25.1	0.4	1.7
H10	27.2	26.3	26.8	0.6	2.4
H11	24.2	25.5	24.9	0.9	3.7
US1	26.3	24.8	25.5	1.1	4.3
US2	25.7	25.0	25.3	0.5	1.9
US3	26.7	26.4	26.5	0.2	0.7
US5	26.4	26.9	26.6	0.3	1.3
US6	26.4	25.7	26.1	0.5	2.0
P2	25.1	25.5	25.3	0.3	1.2
E2	29.5	29.5	29.5	0.04	0.1
E6	30.1	30.1	30.1	0.1	0.2
EC2	29.4	29.0	29.2	0.2	0.8
EC4	29.6	29.5	29.6	0.1	0.4
EC5	28.2	27.3	27.8	0.6	2.3
EO	28.7	30.9	29.8	1.6	5.3
CGS3	22.8	23.4	23.1	0.5	2.0
CGS4	23.5	23.4	23.5	0.1	0.3
CJN	26.7	27.8	27.2	0.8	2.9
CNM1	24.8	24.8	24.8	0.02	0.1
CNW1	22.1	22.4	22.2	0.2	0.8
CNW2	24.2	24.8	24.5	0.4	1.8
N	29	29			
Mean	26.1	26.2			
SD, ‰	2.02	2.0			
CV, %	7.7	7.6			

Table 7.14: Showing the 29 B1 and B2 $\delta^{18}O$ pairs for archaeological malachite. The mean, standard deviation and coefficient of variation are included to show the strength of central tendencies within pairs and batch data sets, and quantify the amount of dispersion.

To collectively determine whether group means differ, one-way Anova statistics were carried out for the malachite $\delta^{18}O$ data. For B1, the critical significance level of 0.05 is larger than the < 0.0005 value of *p*, meaning the $\delta^{18}O$ values in malachite show a statistically significant difference between the twelve geographic groups surveyed (one-way Anova: $F_{11, 37} = 13.6$, $p < 0.0005$). However, a significant difference result using Anova, as is the case here, simply indicates that at least two of the samples differ by more than chance alone (Hawkins 2019, 194). Where the significant differences lie is suggested in the confidence interval plot shown in **figure 7.1**, where samples with confidence intervals overlap the least. The Anova results are similar when the English outlier is removed (E3), maintaining that there is a statistically significant difference between the groups ($F_{11, 36} = 15.5$, $p < 0.0005$). For B2, the same conclusion is reached, statistically confirming that there is a significant difference between the geographic groups ($F_{6, 22} = 20.5$, $p < 0.0005$).

$\delta^{13}C$

The following descriptive statistics and confidence interval plots are focused on the B1 and B2 malachite $\delta^{13}C$ results, grouped geographically. The mean for B1 $\delta^{13}C$ data ranges from -16.5‰ (based on one sample, Jiangsu, China) to -10.7 ± 1.6‰ (Ningxia, China). Peru has the lowest standard deviation and coefficient of variation, and Guangxi has the highest. Refer to **table 7.15** for B1 $\delta^{13}C$ descriptive statistics.

B1 Descriptive Statistics for Malachite $\delta^{13}C$

Site	N	Mean (‰, VPDB)	SD (‰)	CV (%)	SE	95% CI Lower Bound	95% CI Upper Bound
Hungary	11	-13.3	0.7	5.2	0.2	-13.8	-12.8
Alaska, USA	5	-14.8	1.1	7.8	0.5	-16.3	-13.4
Peru	2	-15.0	0.04	0.3	0.03	-15.3	-14.6
Cyprus	3	-10.9	1.5	14.1	0.9	-14.7	-7.1
Spain	1	-11.9	-	-	-	-	-
England	11	-16.3	1.1	2.1	0.3	-17.0	-15.5
Israel	3	-14.1	0.8	6.0	0.5	-16.2	-12.0
Gansu, China	1	-12.1	-	-	-	-	-
Guangxi, China	4	-13.8	2.1	15.0	1.0	-17.1	-10.5
Jiangsu, China	1	-16.5	-	-	-	-	-
Jiangxi, China	1	-11.6	-	-	-	-	-
Ningxia, China	6	-10.7	1.6	14.9	0.7	-12.4	-9.1

Table 7.15: Geographically grouped B1 $\delta^{13}C$ descriptive statistics for malachite.

The mean for the B2 $\delta^{13}C$ data set ranges from -16.4 ± 1.7‰ (England) to -9.3 ± 2.3‰ (Ningxia, China) (refer to **table 7.16** for B2 descriptive statistics). Ningxia is also at the highest extreme of the range for the B1 data set. Guangxi has the highest B2 standard deviation and coefficient of variation, meaning its data points are farthest from the mean. Guangxi also has the highest standard deviation and coefficient of variation in the B1 data set. Hungary has the lowest B2 standard deviation and coefficient of variation, meaning its data points are closest.

B2 Descriptive Statistics for Malachite $\delta^{13}C$

Site	N	Mean (‰,VPDB)	SD (‰)	CV (%)	SE	95% CI Lower Bound	95% CI Upper Bound
Hungary	11	-12.4	0.5	4.3	0.2	-12.8	-12.05
Alaska, USA	5	-15.0	1.4	8.7	0.6	-16.9	-13.3
Peru	1	-14.9	-	-	-	-	-
England	6	-16.4	1.7	10.7	0.7	-18.2	-14.5
Guangxi, China	2	-13.5	3.3	24.5	2.3	-43.3	16.3
Jiangsu, China	1	-13.6	-	-	-	-	-
Ningxia, China	3	-9.3	2.3	24.4	1.3	-14.9	-3.7

Table 7.16: Geographically grouped B2 $\delta^{13}C$ descriptive statistics for malachite.

The following confidence interval plots show the B1 and B2 malachite $\delta^{13}C$ means (central tendency) for each site represented by a dot, and lines representing the precision of the estimate of the mean (variability, with a 95% confidence interval), plotted in order of increasing mean value.

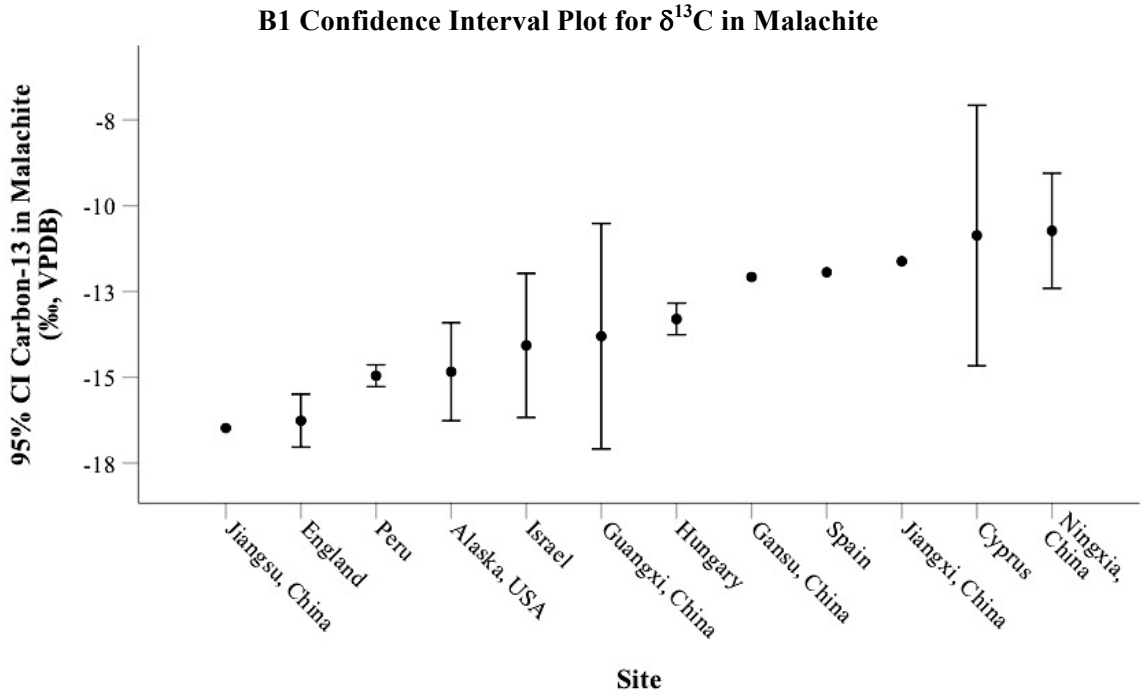


Figure 7.3: Plot showing the B1 malachite $\delta^{13}C$ data, plotted in order of increasing mean value. Jiangsu, Jiangxi, Gansu and Spain are only represented by dots because there is just one data point for each of these geographic groups.

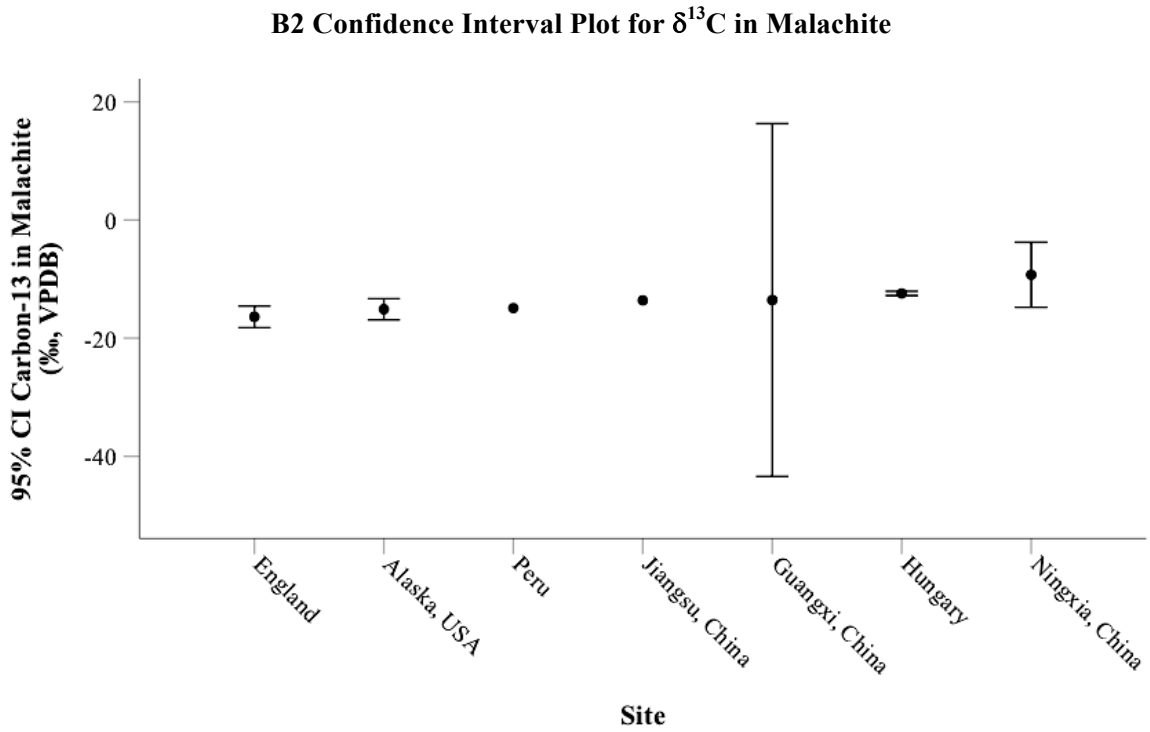


Figure 7.4: Plot showing the B2 malachite $\delta^{13}C$ data, plotted in order of increasing mean value. Jiangsu and Peru are only represented by dots because there is just one data point for each of these geographic groups.

All 29 B1 and B2 $\delta^{13}C_{malachite}$ pairs, along with the mean, standard deviation and coefficient of variation, are presented in **table 7.17**. The widest variation is between the B1 and B2 $\delta^{18}O$ values for sample EC2 (-15.0 ± 2.09‰, CV = 14.0%), and the closest data is for sample CNM1 (-11.3 ± 0.02‰, CV = 0.2%). Sample EC2 also has the largest CV-value, but Hungarian sample H7 has the smallest at CV = 0.02%. Starting with the null hypothesis that here is no difference between the populations from which the B1 and B2 $\delta^{13}C$ malachite pairs come, and using a 5% (0.05) critical significance level, a paired *t*-value was calculated for the batches. The results show that there is a significant statistical difference between the B1 and B2 malachite populations for $\delta^{13}C$ (paired *t*-test, two-tailed: $t_{28} = 3.2$, $p = 0.004$, 95% CI [-0.9, -0.2]). Since the critical significance level of 0.05 is larger than the value of 0.004 of *p*, the stated null hypothesis must be rejected. This suggests that meticulous picking has a significant impact on the carbon isotope results in archaeological malachite samples, which is opposite of the oxygen isotope *t*-test result.

B1 and B2 $\delta^{13}C$ Pairs for Malachite

Sample ID	B1 $\delta^{13}C_{(VPDB)}$, ‰	B2 $\delta^{13}C_{(VPDB)}$, ‰	Mean	SD, ‰	CV, %
H1	-13.9	-12.9	-13.4	0.7	5.1
H2	-12.3	-12.1	-12.2	0.1	1.2
H3	-12.4	-11.8	-12.1	0.4	3.5
H4	-13.0	-12.6	-12.8	0.3	2.3
H5	-12.4	-12.1	-12.2	0.2	1.9
H6	-13.8	-11.6	-12.7	1.5	12.2
H7	-13.4	-13.0	-13.2	0.3	0.02
H8	-13.6	-13.1	-13.3	0.4	2.7
H9	-14.1	-12.0	-13.1	1.5	11.3
H10	-13.5	-12.5	-13.0	0.7	5.6
H11	-14.0	-12.9	-13.4	0.8	6.0
US1	-13.0	-12.9	-12.9	0.1	0.5
US2	-15.7	-16.3	-16.0	0.5	2.9
US3	-15.9	-16.1	-16.0	0.1	0.8
US5	-14.9	-14.4	-14.6	0.4	2.5
US6	-14.7	-15.8	-15.3	0.7	4.7
P2	-15.0	-14.9	-15.0	0.04	0.3
E2	-18.0	-18.2	-18.1	0.2	1.0
E6	-18.1	-18.1	-18.1	0.03	0.2
EC2	-16.5	-13.5	-15.0	2.1	14.0
EC4	-16.1	-16.3	-16.2	0.1	0.7
EC5	-16.7	-16.6	-16.6	0.1	0.4
EO	-15.8	-15.6	-15.7	0.1	0.9
CGS3	-16.0	-15.9	-15.9	0.1	0.6
CGS4	-11.7	-11.2	-11.5	0.4	3.2
CJN	-16.5	-13.6	-15.0	2.1	13.6
CNM1	-11.4	-11.3	-11.3	0.02	0.2
CNW1	-9.5	-9.6	-9.6	0.1	0.8
CNW2	-8.1	-6.9	-7.5	0.8	11.4
N	29	29			
Mean	-14.1	-13.6			
SD, ‰	2.3	2.5			
CV, %	16.1	18.3			

Table 7.17: Showing the 29 B1 and B2 $\delta^{13}C$ pairs for archaeological malachite. The mean, standard deviation and coefficient of variation are included to show the strength of central tendencies within pairs and batch data sets, and quantify the amount of dispersion.

To collectively determine whether group means differ, one-way Anova statistics were carried out for the malachite $\delta^{13}C$ data. The null hypothesis states that there is no difference between the geographic groups from which the samples come. For B1, the critical significance level of 0.05 is larger than the < 0.0005 value of *p*, meaning we can reject the null hypothesis and conclude that $\delta^{13}C$ values in malachite show a statistically significant difference between the twelve geographic groups surveyed (one-way Anova: $F_{11, 37} = 11.0$, $p < 0.0005$). The B2 malachite $\delta^{13}C$ data yields a similar result, also rejecting the null hypothesis and concluding that $\delta^{13}C$ values in malachite show a statistically significant difference between each geographic group (one-way Anova: $F_{6,22} = 10.06$, $p < 0.0005$).

Isotopic Impact of Azurite and Atacamite

Trends cannot be assessed directly because there is no pure azurite or atacamite samples to compare with malachite samples in this study. Regardless, hints of isotopic tendencies were sought out to better understand this project's data.

B1 and B2 Samples with Azurite

Sample	B1 $\delta^{18}O_{(VSMOW)}$, ‰	B2 $\delta^{18}O_{(VSMOW)}$, ‰	B1 $\delta^{13}C_{(VPDB)}$, ‰	B2 $\delta^{13}C_{(VPDB)}$, ‰
H3	26.3	26.1*	-12.4	-11.8*
H5	26.6	26.5*	-12.4	-12.1*
H9	24.8	25.4*	-14.1	-12.0*
H11	24.2	25.5*	-14.0	-12.9*
EO2	28.7	30.9*	-15.8	-15.6*
CGS3	22.8*	23.4	-16.0*	-15.9
CNM1	24.8*	24.8	-11.4*	-11.3

Table 7.18: Showing the $\delta^{18}O$ and $\delta^{13}C$ results for the B1 and B2 malachite samples that contained azurite in one of the pairs. Asterisks identify the azurite-containing samples.

XRD Results for B1 and B2 Samples with Azurite

Sample	XRD (B1)	XRD (B2)
H3	84% malachite, 16% quartz **or** 77% malachite, 14% quartz, 9% tenorite	60% malachite, 23% quartz, 13% azurite, 4% cuprite + more
H5	69% malachite, 19% graphite, 12% halite	40% malachite, 29% quartz, 17% jadeite, 14% azurite
H9	100% malachite	66% malachite, 15% quartz and 19% azurite
H11	46% malachite, 54% sodalite	44% malachite, 35% SiO_2, 15% azurite, 7% tenorite
EO2	64% malachite, 3% cristobalite, 33% atacamite	36% malachite, 61% azurite, 3% SiO_2
CGS3	81% malachite, 19% azurite + one unidentified peak	100% malachite
CNM1	42% malachite, 38% azurite, 20% quartz	3% malachite, 87% SiO_2

Table 7.19: Showing the B1 and B2 sample pairs that contained azurite, and their quantitative XRD material characterizations.

Four of the seven azurite-containing samples included in this study yielded heavier $\delta^{18}O$ values compared to their corresponding samples (H9, H11, EO2 and CNM1). As well, five of the seven samples yielded heavier $\delta^{13}C$ values than their corresponding samples (H3, H5, H9, H11 and EO2). Starting with the null hypothesis that there is no difference between the azurite-containing samples and the samples that do, a paired *t*-test was calculated using 0.05 as the critical significance level. The *t*-test results show that azurite has no significant impact on the $\delta^{18}O$ values in the malachite samples: $t_6 = 1.2$, $p = 0.3$, 95% CI [-1.4, 0.5]. Another *t*-test suggests that azurite also has no significant impact on the $\delta^{13}C$ values in archaeological malachite: $t_6 = 2.0$, $p = 0.09$, 95% CI [-1.3, 0.1].

B1 and B2 Samples with Atacamite

Sample	B1 $\delta^{18}O_{(VSMOW)}$, ‰	B2 $\delta^{18}O_{(VSMOW)}$, ‰
H6	23.96	25.50
US1	26.31	24.77
US6	26.42	25.67
P2	25.05	25.48
EC5	28.22	27.31
EO	28.67	30.92
CNW2	24.16	24.79

Table 7.20: Showing the $\delta^{18}O$ results for the B1 and B2 samples that contained atacamite or the related minerals; paratacamite and clinoatacamite. Asterisks identify the samples with more copper (II) chloride hydroxide-containing minerals than the counterpart sample.

XRD Results for B1 and B2 Samples with Atacamite

Sample	XRD (B1)	XRD (B2)
H6	100% malachite	23% malachite, 23% quartz, 55% atacamite
US1	43% malachite, 57% atacamite	21% malachite, 5% cuprite, 52% calcite, 7% quartz, 14% atacamite,
US6	38% malachite, 47% atacamite, 16% quartz	39% malachite 28% quartz, 23% cuprite, 10% atacamite
P2	26% malachite, 28% atacamite, 41% SiO_2, 5% cuprite	29% malachite, 24% paratacamite, 38% atacamite and 8% quartz
EC5	36% malachite, 8% quartz, 56% atacamite	54% malachite, 46% atacamite
EO	64% malachite, 3% cristobalite, 33% atacamite	36% malachite, 61% azurite, 3% SiO_2
CNW2	87% malachite, 2% paratacamite, 12% dolomite	59% malachite, 39% azurite, 2% clinoatacamite

Table 7.21: Showing the B1 and B2 sample pairs that contained a copper (II) chloride hydroxide mineral (atacamite, paratacamite, and clinoatacamite), and their quantitative XRD material characterizations.

Atacamite does not contain carbon, so if influential, it is only possible to impact the overall oxygen-18 ratios in mix-phase samples. **Table 7.20** provides the oxygen isotope data for the B1 and B2 sample pairs that contained a copper (II) chloride hydroxide mineral (atacamite, paratacamite, and clinoatacamite). Except with sample B1H6, these minerals are present in both the B1 and B2 samples, meaning it is not possible to compare samples with copper (II) chloride hydroxide minerals to those without. Instead, the samples with more copper (II) chloride hydroxide minerals are compared to those with less. In some cases (EC5 and CNW2) the amounts present are comparable between the B1 and B2 sample pairs. Moreover, all of these samples contain potentially consequential amounts of other contaminants, including azurite (EO and

CNW2). All samples except EO2 appear to show that higher concentrations of atacamite, along with related minerals like paratacamite and clinoatacamite, will result in overall heavier oxygen-18 ratios in mixed phase malachite samples. However, a paired *t*-test was calculated, which suggests that atacamite has no significant impact on the $\delta^{18}O$ values in archaeological malachite: $t_6 = 1.0$, $p = 0.3$, 95% CI [-1.7, 0.7]. Ultimately, since most samples included in this study are mixed phase, it is not possible to make confident conclusions on the isotopic impact of various contaminants.

$\delta^{18}O$ and $\delta^{13}C$

The B1 scatterplot for archaeological malachite $\delta^{18}O$ against $\delta^{13}C$ data shows a negative linear relationship and some clustering within sample sites (**figure 7.5**). The best model of these data is the equation for the straight line $y = -0.4x - 2.4$. This model explains a significant relationship in $\delta^{18}O$ and $\delta^{13}C$ values in malachite (based on the null hypothesis that $\delta^{18}O$ does not show a linear relationship with $\delta^{13}C$): $F_{1,47} = 11.0$, $p = 0.002$. In the case of regression, the F statistic reflects the variance accounted for by the regression line relative to the remaining variance, otherwise known as an error variance or residual variance (Hawkins 2019, 219). If the line does not account for any variance, these two values will be the same and F will equal one (*ibid.*). To determine whether a regression F-value is significant, a critical value needs to be found on an F-table, based on the degrees of freedom. In this case, $F_{critical}$ is around 4.0, which is smaller than the calculated F-value of 11.0, and the statistic is considered significant.

The relationship between B1 $\delta^{18}O$ and $\delta^{13}C$ was investigated using Pearson product-moment correlation coefficient (r) and Spearman's Rank Order Correlation (rho), with a variation between the isotopes in the archaeological malachite samples analyzed, $r = -0.4$ ($R^2 = 0.2$), rho = -0.4. In other words, 20% of the variability in one isotope is matched by the variability in the other isotope. When the English outlier (E3) is removed from the dataset, all the regression analysis key information remains very similar, and can be summarized as $y = -0.4x - 2.5$, $F_{1,46} = 10.9$, $p = 0.002$, $R^2 = 0.2$.

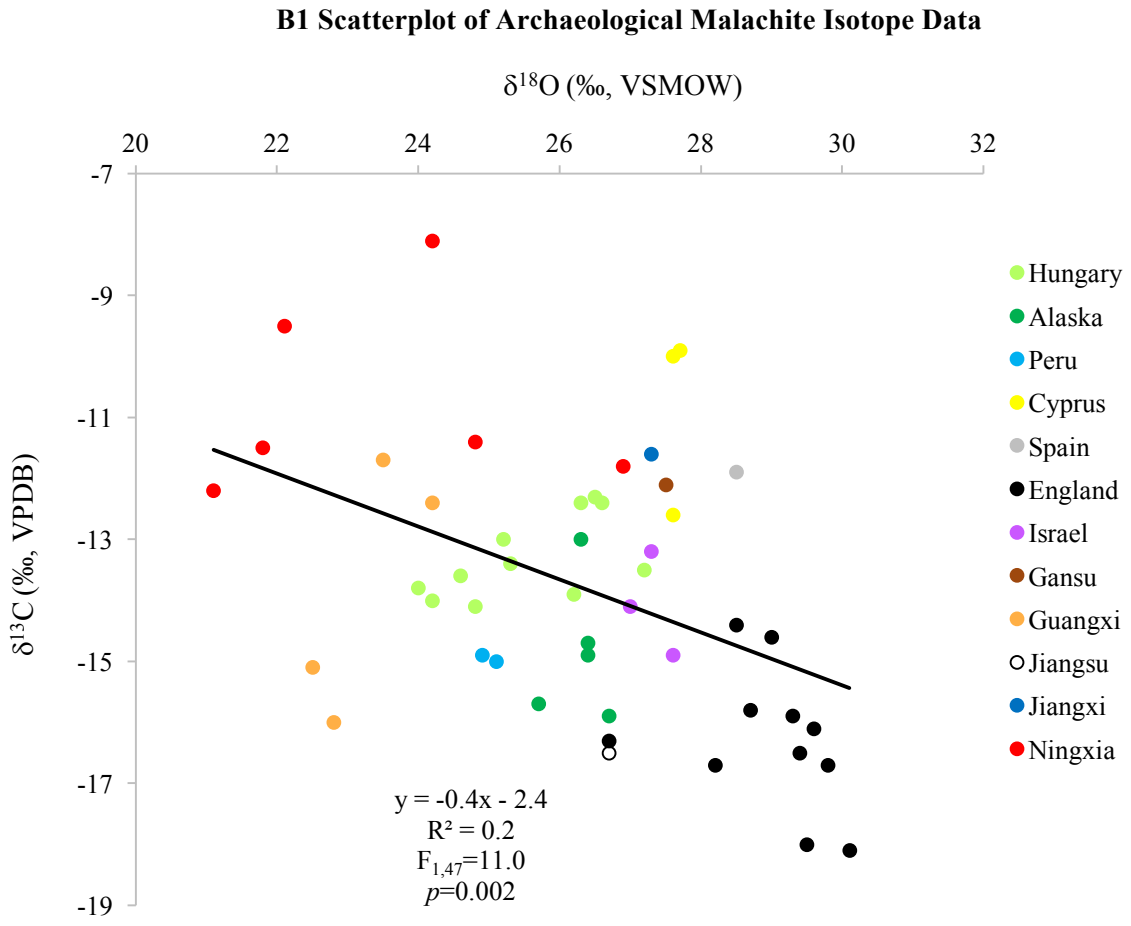


Figure 7.5: In this scatterplot, there a statistically significant linear correlation between B1 $\delta^{18}O$ and $\delta^{13}C$ from the carbonate in archaeological malachite (y= -0.4x–2.4, $F_{1,47}$=11.0, p=0.002, R^2=0.2).

All the key information from the regression analyses for each geographic group in **figure 7.5** can be summarized as follows:

Hungary (n = 11): y = 0.4x – 22.9, $F_{1,9}$ = 4.9, p = 0.05, R^2 = 0.4

Alaska, USA (n = 5): y = 0.3x – 23.6, $F_{1,3}$ = 0.04, p = 0.9, R^2 = 0.01

Peru (n = 2): y = -0.3x – 6.6, R^2 = 1.0 (further regression statistics requires minimum of n = 3)

Cyprus (n = 3): y = 15.08x – 427.6, $F_{1,1}$ = 0.2, p = 0.7, R^2 = 0.2

Spain (n = 1): regression statistics not possible when n = 1

England (n = 11): y = -0.4x – 4.2, $F_{1,9}$ = 1.2, p = 0.3, R^2 = 0.1

England (without outlier, E3) (n = 10): y = -1.2x + 17.4, $F_{1,8}$ = 3.9, p = 0.09, R^2 = 0.3

Israel (n = 3): y = -1.3x + 22.0, $F_{1,1}$ = 0.4, p = 0.6, R^2 = 0.3

Gansu, China (n = 1): regression statistics not possible when n = 1

Guangxi, China (n = 4): y = 2.3x – 66.1, $F_{1,2}$ = 4.3, p = 0.2, R^2 = 0.7

Jiangsu, China (n = 1): regression statistics not possible when n = 1

Jiangxi, China (n = 1): regression statistics not possible when n = 1

Ningxia, China (n = 6): y = 0.002x – 11.3, $F_{1,4}$ = 0.004, p = 1.0, R^2 = 0.001

Although the combined malachite $\delta^{18}O$ against $\delta^{13}C$ B1 data shows a negative linear relationship, this is not always maintained when considering the regression analyses of the geographic groups independently. The best example of this is with England and Hungary, which have regression trends in opposite directions. The Hungarian data shows a positive correlation, meaning the $\delta^{18}O$ values increase as the $\delta^{13}C$ values increase. But the English data shows a negative correlation, suggesting that the $\delta^{13}C$ values decrease as the $\delta^{18}O$ values increase. This can be interpreted in many ways, but ultimately more data is necessary to unravel and understand this inconsistency. Complications such as sample quality (purity), provenance accuracy, and the impact of various environmental parameters also play a role.

The B2 scatterplot for archaeological malachite $\delta^{18}O$ against $\delta^{13}C$ data also shows a negative linear regression and some clustering within sample sites, particularly within Hungary, England and Alaska, which is also the case for B1 (**figures 7.5 and 7.6**). The best model of these data is the equation for the straight line $y = -0.7x + 5.6$. This model explains a significant relationship in B2 $\delta^{18}O$ and $\delta^{13}C$ values in malachite (based on the null hypothesis that $\delta^{18}O$ does not show a linear relationship with $\delta^{13}C$): $F_{1,27} = 14.1$, $p = 0.001$, where $F_{critical}$ is 5.6). Additionally, the relationship between B2 $\delta^{18}O$ and $\delta^{13}C$ was investigated using Pearson product-moment correlation coefficient (r) and Spearman's Rank Order Correlation (rho), with a variation between the isotopes in the B2 archaeological malachite samples analyzed ($r = -0.6$ [$R^2 = 0.3$], $rho = -0.6$). Therefore, since the B2 data has a greater F-statistic and a smaller *p*-value than B1, it is statistically more significant. B2 also has a greater R^2-value, with 30% of the variability in one isotope being matched by the variability in the other, as opposed to B1's 20%. Moreover, B2 has a stronger correlation than B1, with rho = -0.6 compared to B1's rho = -0.4. Unexpectedly, considering that the B2 samples are less pure than the B1 samples, the B2 statistics are stronger. However, when considering the statistics of each geographic group, the B1 data is still stronger for Hungary and England, which are the study's largest datasets. All the key information from the regression analyses for each geographic group in **figure 7.6** can be summarized as follows:

Hungary: $y = 0.3x - 20.6$, $F_{1,9} = 1.1$, $p = 0.3$, $R^2 = 0.1$

Alaska, USA: $y = -0.3x - 7.2$, $F_{1,3} = 0.1$, $p = 0.8$, $R^2 = 0.04$

Peru (n = 1): regression statistics not possible when n = 1

England: $y = -0.1x - 12.9$, $F_{1,4} = 0.03$, $p = 0.9$, $R^2 = 0.007$

Guangxi (n = 2): regression statistics cannot be calculated because the two samples have the same $\delta^{18}O$ value (refer to **table 7.11**)

Jiangsu (n = 1): regression statistics not possible when n = 1

Ningxia, China: $y = 0.3x - 15.3$, $F_{1,1} = 0.02$, $p = 0.9$, $R^2 = 0.02$

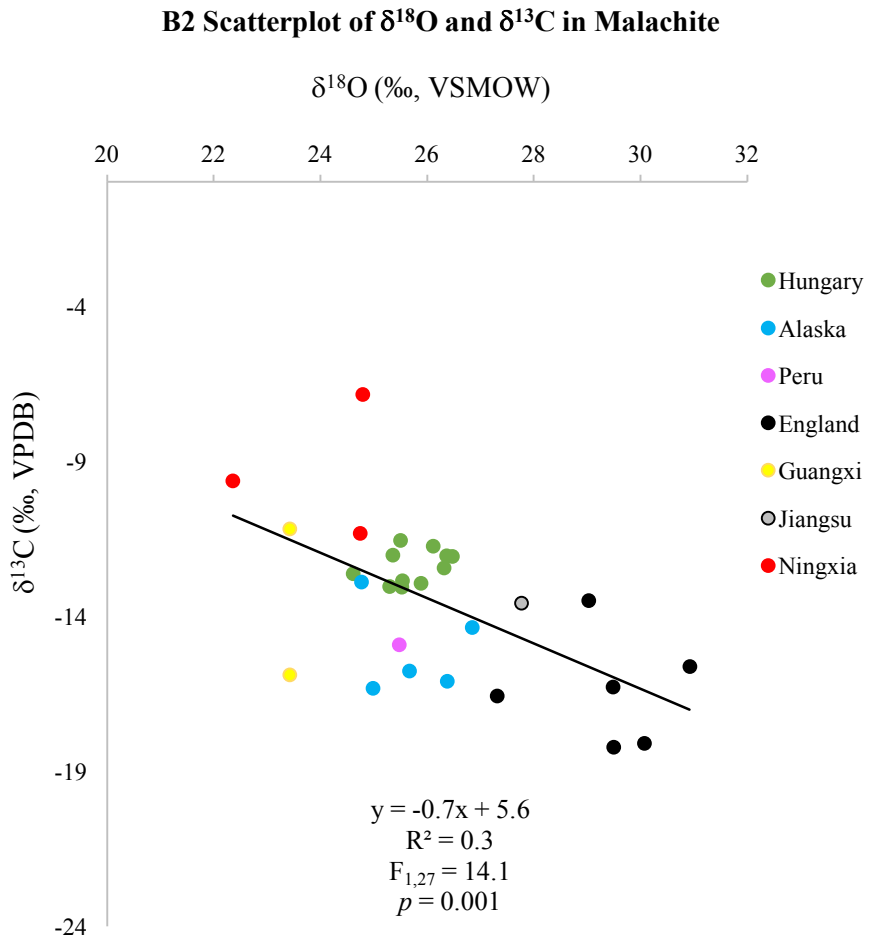


Figure 7.6: In this B2 scatterplot, there is a negative linear regression between the $\delta^{18}O$ and $\delta^{13}C$ in the carbonate of archaeological malachite ($y = -0.7x+5.6$, $F_{1,27} = 14.1$, $p = 0.001$, $R^2 = 0.3$).

In review, Anova statistics show that group means differ between the isotope data. This work was carried out for $\delta^{18}O$, $\delta^{13}C$, B1, B1 without the outlier, and B2. In all data sets, Anova results suggest significant differences between the geographic groups surveyed. Moreover, the B1 and B2 scatterplots of $\delta^{18}O$ versus $\delta^{13}C$ show statistically significant linear correlations with some clustering within sample sites. Interestingly, some of these site clusters show regression trends in opposite directions, and the impact of various environmental parameters may play a role. To understand what controls the isotope ratios in archaeological malachite, further statistical analyses were carried out using linear regression with the $\delta^{18}O$ in local precipitation, surface temperature, and a multidimensional approach by way of climate. This is the topic of the following sections.

7.2.2. Oxygen Isotope Results: Incorporating Environmental Parameters

Table 7.22 presents the B1 $\delta^{18}O$ weighted mean of modern meteoric water used for each sample, along with the average surface air temperature at the corresponding site. These are the values used in calculations, the results from which are also presented in **table 7.22**.

B1 Estimated and Calculated Formation Water $\delta^{18}O$ and Temperature Values

Sample ID	Calculated $\delta^{18}O_{(VSMOW)}$ of Formation Water, ‰	$\delta^{18}O_{(VSMOW)}$ Weighted Mean of Modern Meteoric Water, ‰	Calculated Formation Temperature (ºC)	Average Surface Air Temperature (ºC)
H1	-9.7	-7.7	20.2	10.6
H2	-9.5	-7.7	19.1	10.6
H3	-9.7	-7.7	19.9	10.6
H4	-10.7	-7.7	24.9	10.6
H5	-9.4	-7.7	18.4	10.6
H6	-11.9	-7.7	31.3	10.6
H7	-10.7	-7.7	24.8	10.6
H8	-11.3	-7.7	28.0	10.6
H9	-11.2	-7.7	27.2	10.6
H10	-8.8	-7.7	15.8	10.6
H11	-11.7	-7.7	29.4	10.6
US1	-10.4	-11.4	3.4	7.4
US2	-11.1	-11.4	6.0	7.4
US3	-10.1	-11.4	2.1	7.4
US5	-10.4	-11.4	3.2	7.4
US6	-10.3	-11.4	3.0	7.4
P2	-8.6	-5.1	39.6	21.0
P3	-8.8	-5.1	40.4	21.0
RC4	-6.5	-5.9	22.1	19.5
RC7	-6.6	-5.9	21.8	18.7
RC8	-6.6	-5.9	22.2	18.7
SES9	-5.5	-5.6	20.2	20.0
E2	-6.8	-7.3	8.03	10.0
E3	-9.4	-7.3	19.9	10.0
E4	-6.3	-7.3	6.7	10.9
E6	-5.5	-7.3	5.3	12.9
E7	-7.0	-7.3	11.9	12.9
EC2	-6.9	-7.3	8.4	10.0
EC4	-6.6	-7.3	7.3	10.0
EC5	-8.0	-7.3	13.2	10.0
EC7	-7.2	-7.3	9.9	10.0
EC8	-7.0	-7.3	8.9	10.0
EO2	-7.4	-7.3	11.3	10.7
I1	-6.8	-5.2	27.5	19.4
I2	-7.1	-5.2	29.1	19.4
I4	-6.5	-5.2	25.7	19.4
CGN2	-9.2	-5.7	23.6	7.9
CGS2	-9.9	-6.2	38.6	19.0
CGS3	-11.2	-6.2	46.6	19.0
CGS4	-10.5	-6.2	42.1	19.0
CGS5	-11.5	-6.2	48.4	19.0
CJN	-8.1	-8.0	16.7	16.0
CJS	-7.0	-5.6	25.2	18.4
CNM1	-11.1	-7.2	29.4	10.9
CNW1	-13.7	-7.2	44.2	10.9
CNW2	-11.7	-7.2	32.9	10.9
CNW3	-9.1	-7.2	19.7	10.9
CNW4	-14.6	-7.2	50.2	10.9
CNW5	-14.0	-7.2	46.4	10.9

Table 7.22: Table of each sample's estimated formation water $\delta^{18}O$ (based on the data reported in the site profiles section in Chapter 5) and formation temperature (based on the average surface air temperature at or near the sample's assumed excavation site). Also presented in this table are the calculated formation water $\delta^{18}O$ and temperatures, which were obtained using the estimated values.

Estimating $\delta^{18}O$ of the Formation Water

Earlier studies on malachite suggest its formation is dominantly controlled by temperature and the isotopic composition of the water from which it precipitates (Melchiorre *et al.* 1999, 245; Smith 1978, 132; Haßler *et al*. 2014, 10). Moreover, the reported $\delta^{18}O$ values for malachite ore correlate with values of modern meteoric waters and surface temperatures, qualifying them as suitable proxies for groundwater and soil temperature when considering young samples (*ibid.*). Melchiorre found that plotting the $\delta^{18}O$ in malachite ore samples against the $\delta^{18}O$ of modern meteoric water shows a linear relation, demonstrating that most malachite is precipitated from water with $\delta^{18}O$ very close to the modern values (refer to **figure 7.7**) (Melchiorre 1998, 248 & 250).

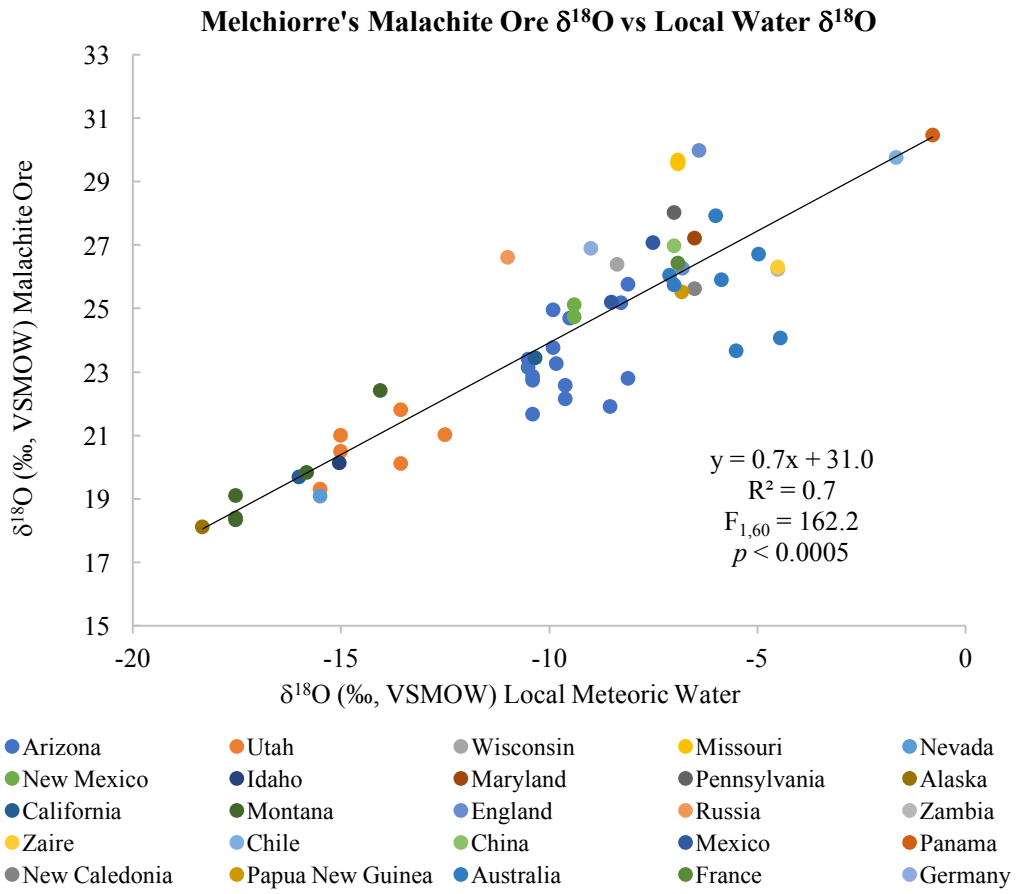


Figure 7.7: Scatterplot of Melchiorre's malachite project, showing that plotting the $\delta^{18}O$ in malachite ore samples against the $\delta^{18}O$ of modern meteoric water has a positive linear relation, and demonstrating that most malachite is precipitated from water with $\delta^{18}O$ very close to the modern values (Melchiorre data obtained from table 2.2 in Melchiorre 1998, 97-100). About 70% ($R^2 = 0.7$) of the variability in $\delta^{18}O_{malachite}$ is matched by the variability in the $\delta^{18}O_{water}$, with an apparent pattern that is statistically significant ($p < 0.0005$).

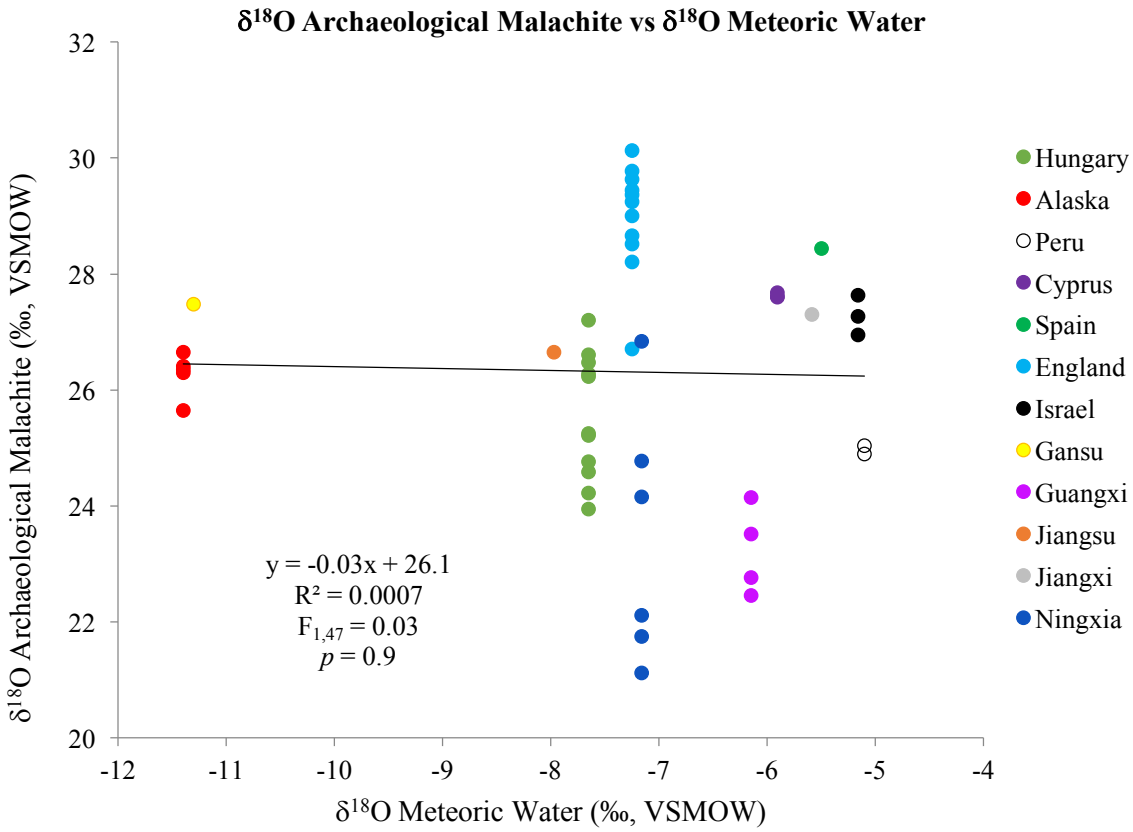


Figure 7.8: Scatterplot showing that plotting the $\delta^{18}O$ in archaeological malachite samples against the $\delta^{18}O$ of modern meteoric water does not suggest a linear relation (p = 0.9, statistically insignificant).

The $\delta^{18}O$ of the archaeological malachite was plotted against the $\delta^{18}O$ in local meteoric water (**figure 7.8**, above). It does not suggest a linear relation ($y = -0.03x + 26.1$, $R^2 = 0.0007$, $F_{1,47} = 0.03$, $p = 0.9$, statistically insignificant). When using the strongest data sets of this study, based on having a known formation site (Alaska, Peru, Cyprus, Spain, England, Israel, Jiangxi and Ningxia), the regression analysis can be summarized as: $y = 0.1x + 27.7$, $R^2 = 0.007$, $F_{1,29} = 0.2$, $p = 0.6$. These statistics are an improvement, but still insignificant, suggesting the data used in this study is either not representative or that there is no correlation between $\delta^{18}O$ in archaeological malachite and $\delta^{18}O$ of modern proxy waters. Since there is no statistically significant difference between the B1 and B2 $\delta^{18}O$ values in malachite, it is assumed that the relationship between the B2 $\delta^{18}O$ in malachite and the $\delta^{18}O$ in the local water shows the same regression result as when using the B1 data, which is that there is no correlation.

The linear regression distribution presented by Melchiorre (**figure 7.7**, $y = 0.7x + 31.0$, $R^2 = 0.7$, $F_{1,60} = 162.2$, $p < 0.0005$) looks very good due to a set of values above (from South America) and below (from western USA and one Russian) -10‰ and -5‰, but demonstrates variance and little correlation between these values (regression becomes $y = 0.7x + 31.2$, $R^2 = 0.2$, $F_{1,32} = 6.4$, $p = 0.02$). This relation is still better than that of the archaeological malachite, having small statistical significance ($p > 0.05$). However, this zone is a prevalent plot region for $\delta^{18}O_{malachite}$ and $\delta^{18}O_{water}$, and it is too unrefined for practical use. At best, having more accurate provenance for the

water samples and cleaner malachite could result in a slightly significant relation like Melchiorre's data.

Estimating Formation Temperature

The two main environmental parameters that control the oxygen isotopic composition of the carbonate in malachite are the $\delta^{18}O$ in the water from which it precipitated and the formation temperature. Previous investigations on artificially grown malachite have shown excellent correlation between the $\delta^{18}O$ in malachite and formation temperatures, showing a decreasing fractionation effect with increasing temperature (Smith 1978, 130). This work was carried out using small pieces of copper foil suspended at various temperatures in water, which had been saturated with a CO_2/air mixture (1:1) (Smith 1979, 126). A plot of $\delta^{18}O$ against temperature for Smith's studies on malachite precipitation is given below (**figure 7.9**). The plot shows a very good correlation ($r = 0.999$, $r^2 = 0.998$), with a temperature coefficient of −0.22‰ per ºC (Smith 1978, 127). This is in excellent agreement with the value of −0.23‰ per ºC obtained for calcium carbonate (McCrea 1950).

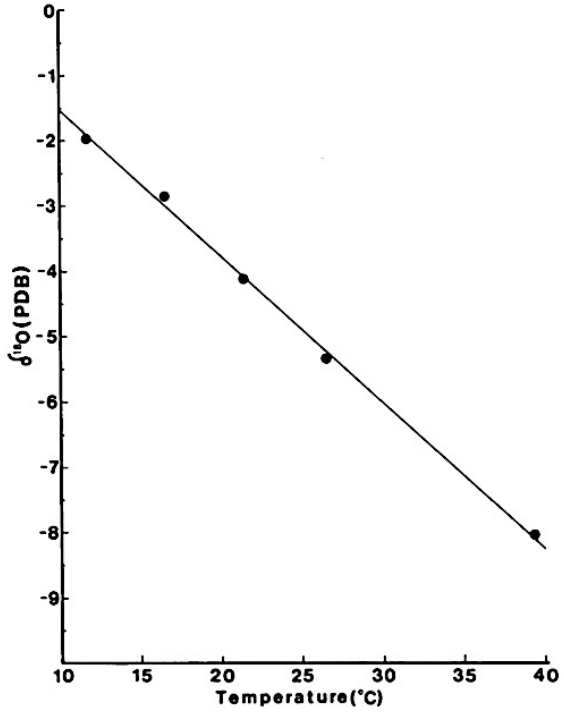


Figure 7.9: A plot of Smith's malachite precipitation results, showing $\delta^{18}O$ against formation temperature. There is a strong, negative, linear correlation ($r = 0.999$, $r^2 = 0.998$) with a temperature coefficient of −0.22‰ per ºC (Smith 1978, 127 & 130).

The modern surface temperatures used as proxies for this study's archaeological malachite formation temperatures are reported in **table 7.22**. These temperatures are for the sample excavation site (where known and available) or for a representative location near the sample excavation site (where the excavation site is not exactly known or suitable temperature recordings have not been recorded). These locations and the locations of each sample's corresponding proxy site are not the same location (details provided in the site profile sections of chapter 5).

Plotting the B1 archaeological malachite $\delta^{18}O$ against the surface temperature of a representative site (refer to **figure 7.10**) produces a statistically insignificant linear regression ($y = -0.05x+27.0$, $R^2 = 0.01$, $F_{1,47} = 0.5$, $p = 0.5$). Although it does not show any simple relationships, it does not mean that one does not exist. As already addressed, in several cases the exact provenance of some samples is not known. In these cases, representative sites were chosen, but it is possible that the true excavation site of a malachite sample has a very different surface temperature. Moreover, there are many complexities to consider when estimating formation temperature (refer to section 3.3.1). Among them, the fact that surface temperature and soil temperature can be very different at the same location. For this reason, rather than using surface temperatures, the decision was made to calculate the formation temperature of malachite through a geothermometer equation developed by Melchiorre. These temperatures are reported and compared to the surface temperatures in the following section.

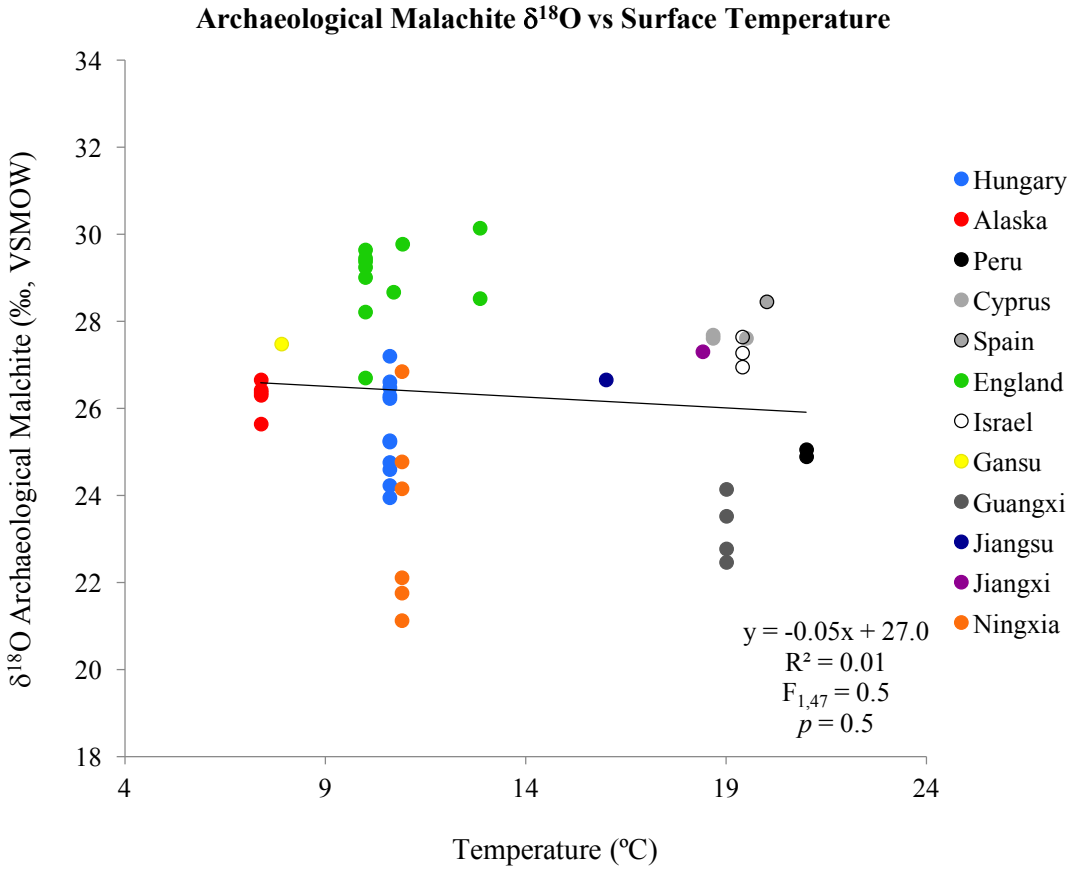


Figure 7.10: Scatterplot of archaeological malachite $\delta^{18}O$ data against modern surface temperatures from representative sites. No simple correlations are apparent; suggesting the use of modern surface temperatures will not always serve as suitable proxies for the formation temperature of malachite.

Calculating for Temperature of Formation Using Meteoric Water $\delta^{18}O$ Values

The equilibrium $\delta^{18}O$ fractionation between malachite and water was determined by Melchiorre through slow precipitation experiments over the temperature range 0-50 degrees Celsius, expressed with the equation:

$$1000\ln\alpha_{\text{malachite-water}} = 2.66\ (10^6/T^2) + 2.66$$

where T is the temperature in Kelvin and α is the fractionation factor between water and malachite ($\alpha = \frac{1000+\delta^{18}O_{\text{malachite}}}{1000+\delta^{18}O_{\text{water}}}$) (Melchiorre 1998, 185). The strong temperature dependence makes this equation an excellent geothermometer, which can be used to either estimate the oxygen isotope composition of water in equilibrium with the malachite at a given temperature or, vice versa, the temperature of formation, when the $\delta^{18}O$ value of the water during formation is known.

Published $\delta^{18}O$ values for local meteoric water were used to calculate the temperature of formation through Melchiorre's malachite geothermometer. These temperatures were compared to the surface temperatures. The scatterplot of the estimated formation temperature against the calculated formation temperature suggests a statistically significant, positive linear relationship ($y = 1.6x+2.0$, $R^2 = 0.3$, $F_{1,47} = 17.9$, $p = <0.0005$) (**figure 7.11**, following page). When only considering samples with known formation sites[1], the regression maintains the same R^2 value, indicating that the difference is due entirely to sample size ($y = 1.5x - 0.5$, $R^2 = 0.3$, $F_{1,29} = 10.4$, $p = 0.003$) (**figure 7.12**, following page). The malachite geothermometer equation is quite sensitive in the 0-50ºC range, and several factors can cause an inaccurate formation temperature result. Some malachite may be so old that modern meteoric water is a poor proxy for the water of formation, but this is not likely when dealing with relatively young, archaeological samples. Alternatively, it is possible that the malachite did not form at equilibrium. It has also been speculated that malachite formation in high sulfide deposits are warmer than ambient temperatures due to the generated heat by the decomposition of sulfides (Thomas 1949 and Sheppard *et al.* 1969 in Melchiorre *et al.* 1999, 255).

[1] Regression statistics do not include data from Hungary, Gansu, Guangxi, Jiangsu and one of the Ningxia samples (CNM1) because these malachite samples do not have known formation sites within their geographic region.

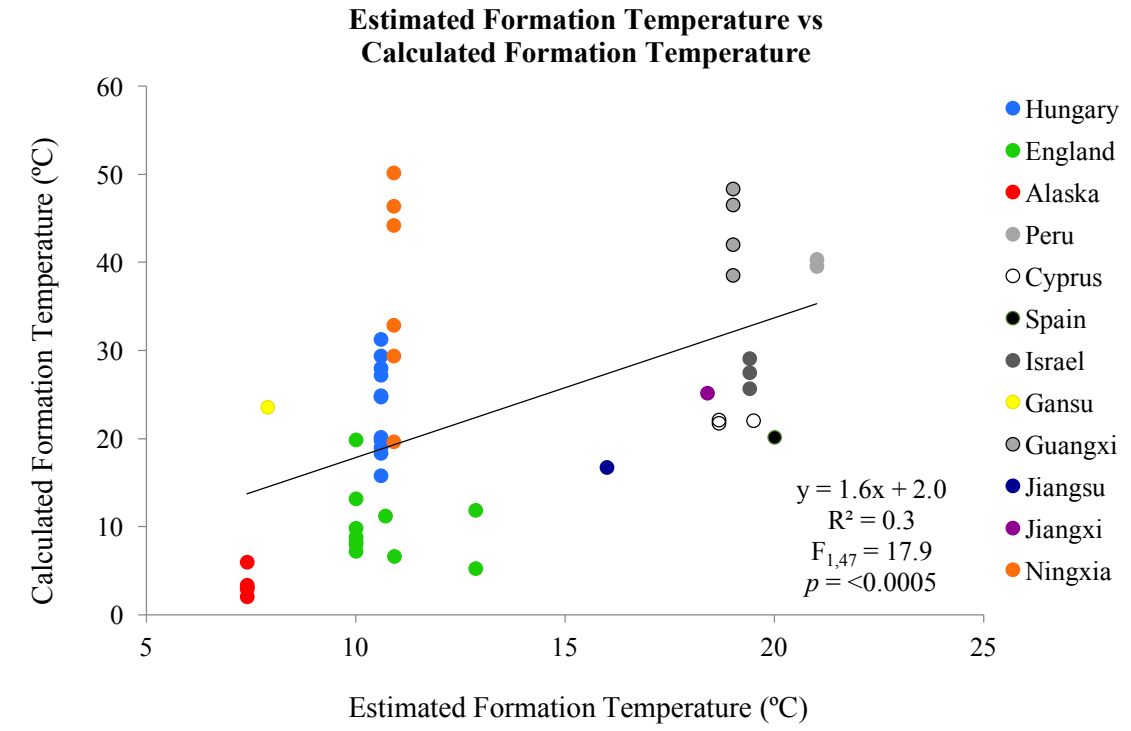


Figure 7.11: Scatterplot of the estimated formation temperature, based on average yearly surface temperature, against the calculated formation temperature, determined using $\delta^{18}O$ of local meteoric water.

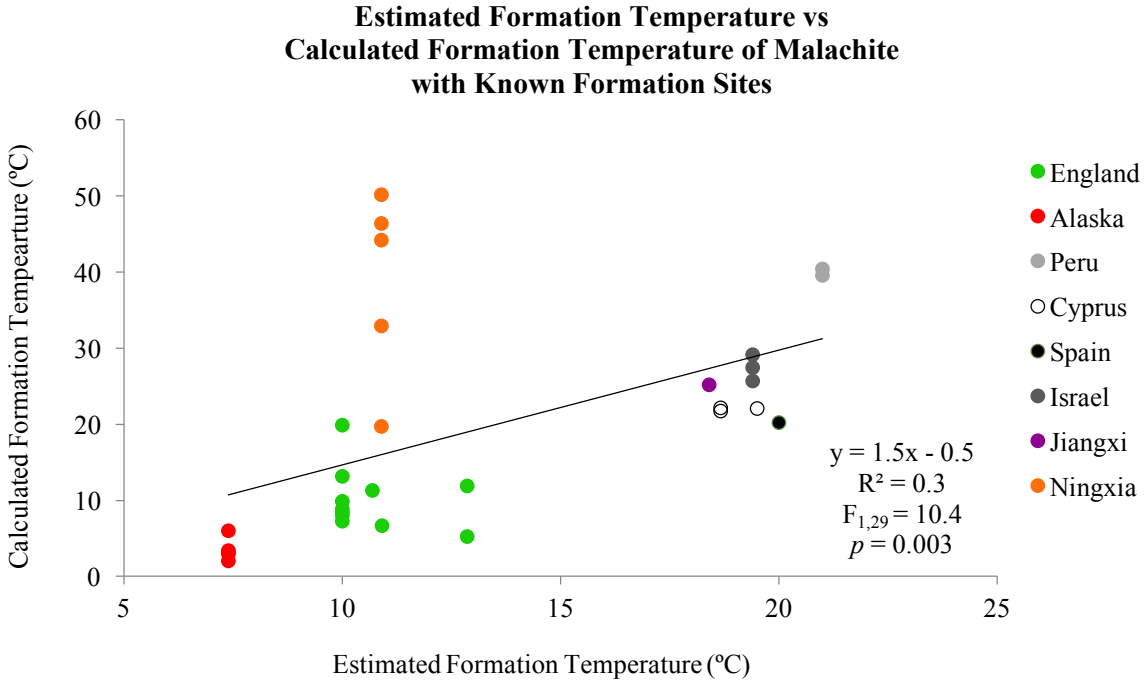


Figure 7.12: Only considering samples with known formation sites, this scatterplot is of the estimated formation temperature, based on average yearly surface temperature, against the calculated formation temperature, determined using $\delta^{18}O$ of local meteoric water.

Calculating for $\delta^{18}O$ of the Formation Water Using Surface Temperatures

Due to financial and time limitations, water samples were not collected for this study. All the $\delta^{18}O_{water}$ data used in this project was estimated based on published data for locations near the malachite formation site, if known. Previous investigators have benefitted from having precise provenance for their malachite samples and from collecting their own water samples to analyze isotopically. Consequently, their estimates for $\delta^{18}O$ in the formation water were more accurate than their formation temperature estimates. This is not necessarily the case for the current study, which is based on archaeological malachite samples that were not personally excavated or collected from the object. Many of the samples have vague formation provenance, which creates issues with estimating both formation temperature and $\delta^{18}O$ of the formation water. Surface temperatures and $\delta^{18}O$ in meteoric water data were selected based on a substitute site, which could be unrepresentative of the true site. Still, it is possible that temperature estimates based on the true site can yield $\delta^{18}O$ in formation water results using Melchiorre's geothermometer equation that are more accurate than the $\delta^{18}O$ of water estimates from proxy sites or indirect sources (Peru's $\delta^{18}O_{water}$ data is based on published studies on $\delta^{18}O$ in archaeological human bone carbonate, for instance. More details are available in the site profiles section of Chapter 5). Considering the unfortunate reality of many archaeological remains, which often have incomplete histories and excavation records, and the uncertainties involved with using published $\delta^{18}O$ values for meteoric water from proxy formation sites, it is worthwhile testing the oxygen isotope thermometer equation used in the reverse direction.

Modern surface temperatures were used to calculate the $\delta^{18}O$ of the formation water through the oxygen isotope thermometer equation. These values are reported in **table 7.22**, along with the $\delta^{18}O$ values of local meteoric water. A scatterplot (**figure 7.13)** of the calculated formation water $\delta^{18}O$ values against the estimated $\delta^{18}O$ meteoric water values suggests that there is a statistically significant, positive linear correlation ($y = 0.5x - 5.8$, $R^2 = 0.1$, $F_{1,47} = 6.05$, $p = 0.02$). When only considering samples with known formation sites, the linear correlation remains similar: $y = 0.5x - 4.5$, $R^2 = 0.2$, $F_{1,29} = 6.5$, $p = 0.02$. This significant difference means that the calculated $\delta^{18}O$ in formation water is not comparable to the estimated $\delta^{18}O$ in meteoric water.

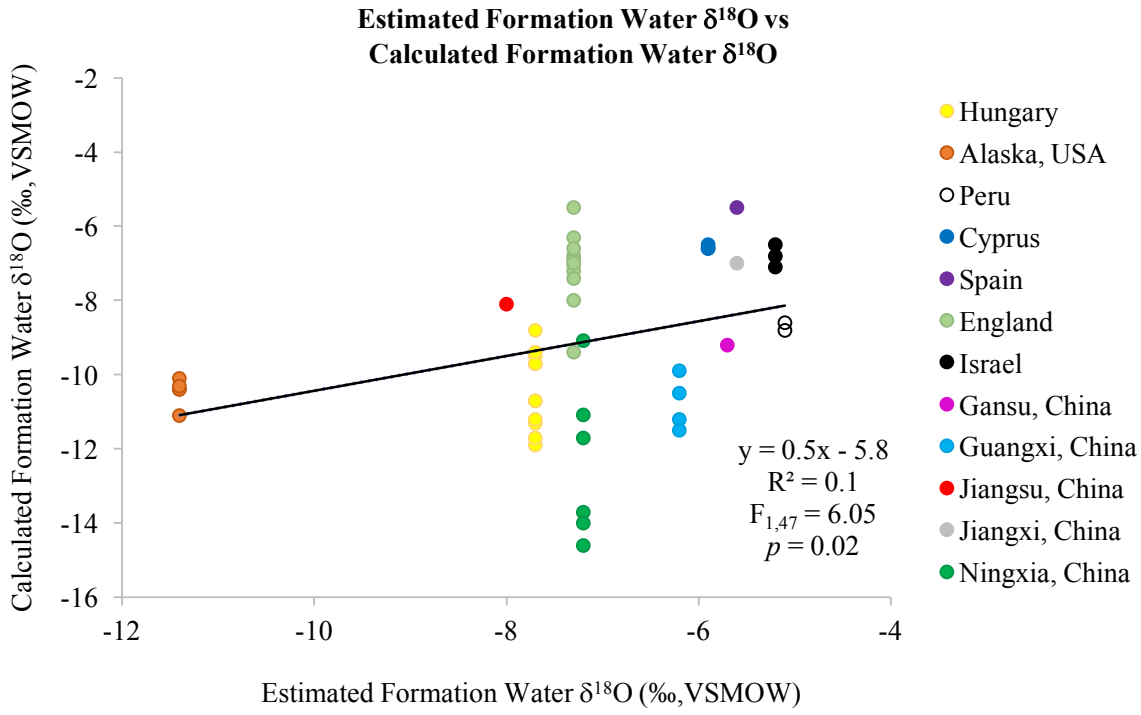


Figure 7.13: Scatterplot of the calculated $\delta^{18}O$ in formation water, based on surface temperatures near the formation site, against the estimated $\delta^{18}O$ in local meteoric water.

The current study has encountered a situation where the $\delta^{18}O$ of the water from which malachite precipitated can be estimated using local meteoric water as a proxy, or calculated using the oxygen isotope thermometer equation and modern surface temperatures. Depending on the circumstances surrounding the accuracy of environmental parameters at a formation provenance, one approach could be better than the other. In cases of unprovenanced malachite, the $\delta^{18}O$ in the carbonate alone will not offer sufficient information to be able to reliably and consistently estimate the $\delta^{18}O$ in the formation water or temperature. Although the isotopic ratios in malachite are in large part determined by these parameters, too many others are also influential. For this reason, a broader approach was pursued, involving the comparison of $\delta^{18}O$ in malachite to collections of environmental parameters. More specifically, the aim was to determine whether the $\delta^{18}O$ in malachite could be used to estimate the formation climate or soil type.

A Multidimensional Approach by Way of Climate

Both temperature and the meteoric water conditions can be considered simultaneously through comprehensive forms of environmental classifications. Climate is the best option because there are several classification systems that can be used for defining them and they tend to be well documented around the world. Among the most common and generally approved is the Köppen Climate Classification system, which is described in detail in section 5.2.4, page 97. As a reminder, the Köppen system uses five major climate types, which are defined by the first, capital

letter (in bold in **table 7.23**). Subsequent letters describe subtypes, which are based on seasonal precipitation (second letter) and temperature (third letter) characteristics (Chen 2017).

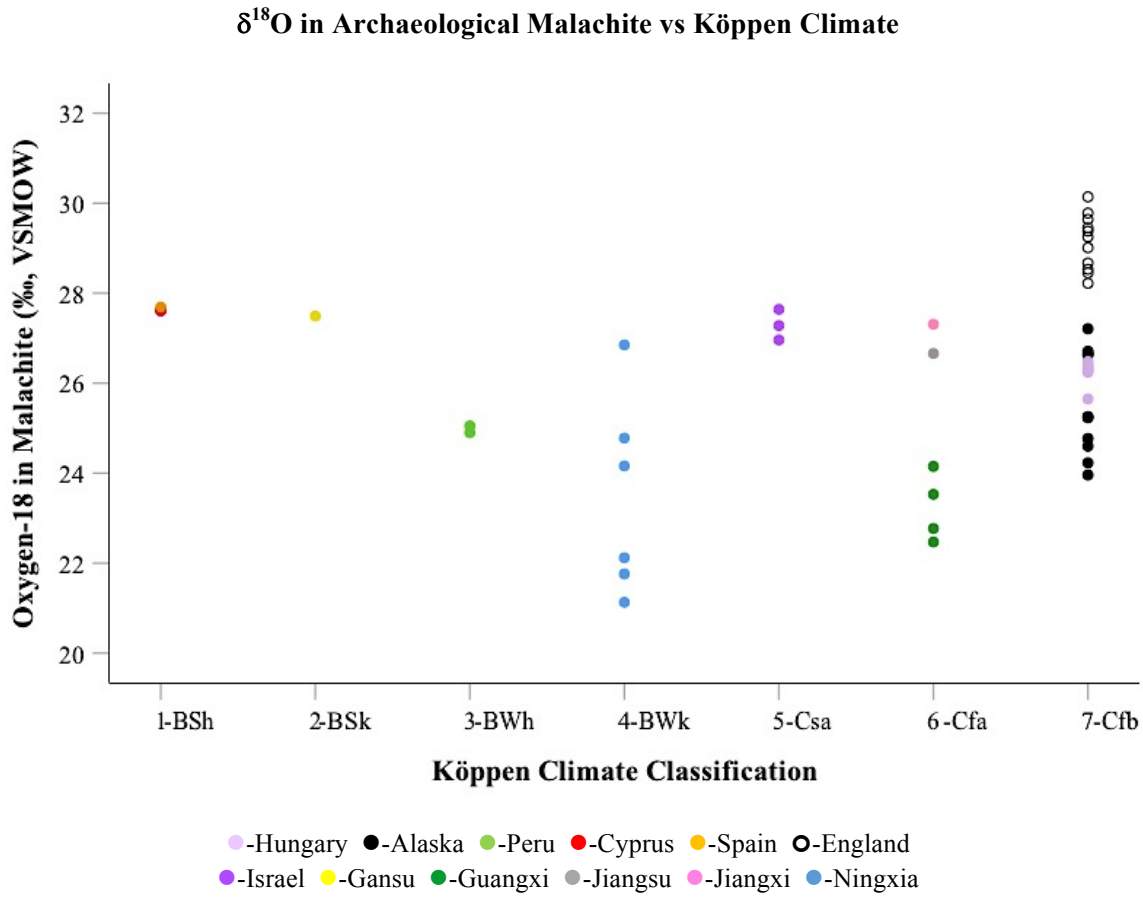


Figure 7.14: Classification plot of archaeological malachite $\delta^{18}O$ values grouped by Köppen climate type, and presented in hierarchal order.

The archaeological malachite $\delta^{18}O$ values are plotted against Köppen climate type and presented in **figure 7.14**, above. It is difficult to rank climate while maintaining an impartial perspective because the full sense of a climate can be compromised with ranking (i.e. ranking by increasing temperature, for example, focuses on one parameter within the climate category). For this reason, the mean $\delta^{18}O$ values where used to put the climates into an order that should elucidate any possible correlations (**table 7.23**). The resulting climate sequence from the broader Köppen classification hints at a few approximate concurrencies. In general, it appears that the temperate climates (beginning with C) are concentrated in the center of the sequence. The two desert climates (BW) are together and associated with lighter $\delta^{18}O_{malachite}$ means. The semi-arid climates (BS) are also grouped, but at the opposite end of the sequence. Obviously, the sequence begins and ends with temperate climates, which goes against the general observations discussed thus far. Uncertain sample provenance, or a parameter not included in the climate classification criteria could be causing this inconsistency. Malachite forms in soils, where additional factors can play a major role in isotope behavior, including pH.

Köppen Climate	Site	N	Mean (‰, VSMOW)	SD
Cfa	Guangxi, China	4	23.2	0.8
BWk	Ningxia, China	6	23.5	2.2
BWh	Peru	2	25.0	0.1
Cfb	Hungary	11	25.5	1.1
Cfb	Alaska, USA	5	26.3	0.4
Cfa	Jiangsu, China	1	26.7	-
Csa	Israel	3	27.3	0.3
Cfa	Jiangxi, China	1	27.3	-
BSk	Gansu, China	1	27.5	-
BSh	Cyprus	3	27.6	0.04
BSh	Spain	1	28.5	-
Cfb	England	11	29.0	0.9
Cfb	England w/o E3	10	29.2	0.6

Table 7.23: Table showing Köppen climate classification order for the $\delta^{18}O$ in malachite ranked by increasing mean value. The first letter, in bold, defines the major climate type. Subsequent letters describe climate subtypes.

7.2.3. Carbon Isotope Results: Incorporating Environmental Parameters

The carbon isotope study cannot be approached in the same way as the oxygen isotopes because there is no known global database for $\delta^{13}C$ values in soils, and carbon-to-carbon comparisons cannot be done directly. Moreover, Melchiorre's isotope geothermometer equation is not applicable and there is no known equivalent equation for malachite that uses $\delta^{13}C$ values. The $\delta^{13}C$ in malachite can still be compared with the average yearly surface temperatures at the formation site, as well as site latitude and altitude.

Previous studies on the controls on $\delta^{13}C$ values in malachite have always focused on the carbon reservoirs, and the distinction between inorganic and organic sources. Improving on these investigations has struggled because there is little data and much discrepancy on carbon isotope fractionation factors for many heavy metal carbonate minerals like malachite, especially at lower (ambient) temperatures (Hasßler *et al.* 2014, 8). This is a shame because the only single environmental parameter that is presently available and can be estimated with a numerical value for use in calculations with the $\delta^{13}C$ values in malachite is formation temperature. This also explains why previous investigations have hardly examined the impact temperature has on the $\delta^{13}C$ in malachite. Melchiorre *et al.* is the only known research project that attempted and published a fractionation factor for carbon in slowly precipitated malachite as a function of temperature (1999). It is beyond the scope of this project to calibrate carbon isotope fractionation, however Melchiorre's carbon equation was used to calculate $\delta^{13}C$ values in local soil CO_2. Furthermore, the carbon isotope data from this study was explored through linear regression to look for statistical relationships with the $\delta^{18}O$ in local meteoric water, estimated formation temperatures, and the calculated $\delta^{13}C$ values in local soil CO_2.

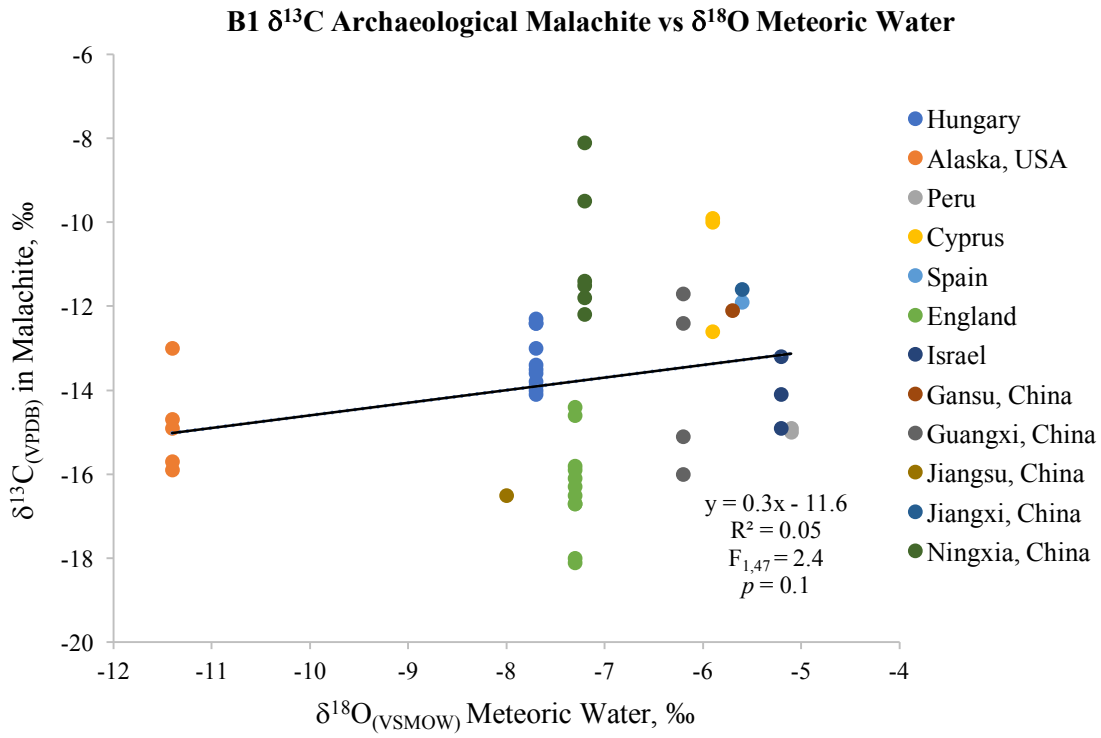


Figure 7.15: Scatterplot showing that plotting the B1 $\delta^{13}C_{malachite}$ against the $\delta^{18}O$ of modern meteoric water does not suggest a linear relation (p = 0.1, statistically insignificant). Only about 5% (R^2 = 0.05) of the variability in $\delta^{13}C_{malachite}$ is matched by the variability in the $\delta^{18}O_{water}$.

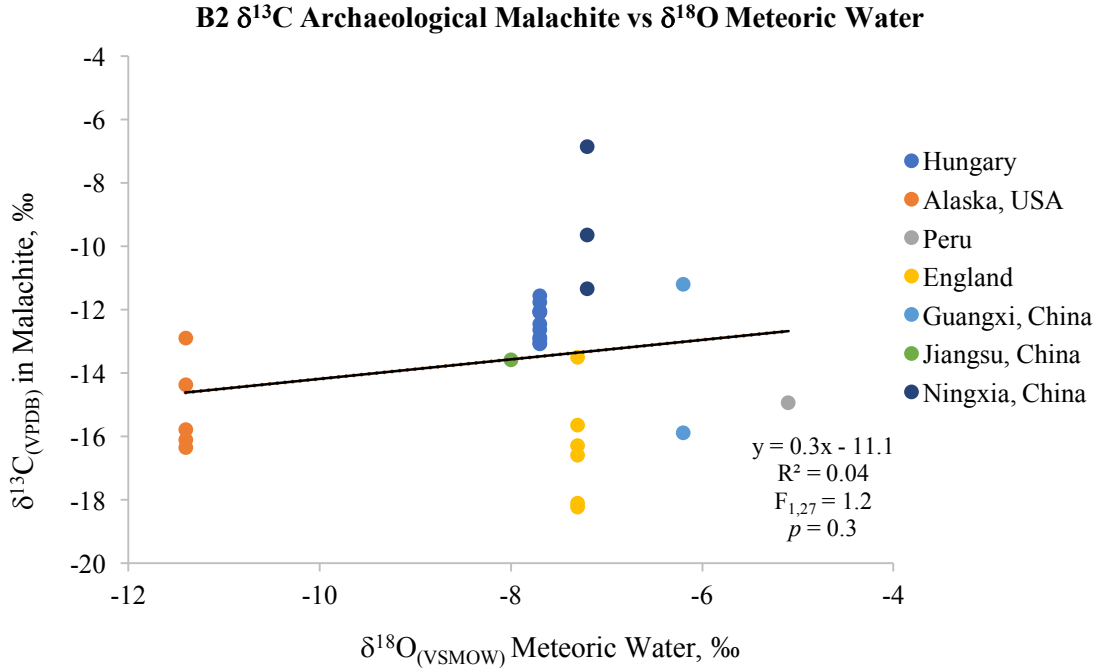


Figure 7.16: Scatterplot showing that plotting the B2 $\delta^{13}C_{malachite}$ against the $\delta^{18}O$ of modern meteoric water does not suggest a linear relation (p = 0.3, statistically insignificant). Only about 4% (R^2 = 0.04) of the variability in $\delta^{13}C_{malachite}$ is matched by the variability in the $\delta^{18}O_{water}$.

The B1 $\delta^{13}C$ in archaeological malachite is plotted against the $\delta^{18}O$ in local meteoric water (**figure 7.15**). The fact that the scatterplot does not show a linear relationship suggests that the $\delta^{18}O$ in the estimated formation water has no statistically significant impact on the $\delta^{13}C$ in

malachite: $y = 0.3x - 11.6$, $R^2 = 0.05$, $F_{1,47} = 2.4$, $p = 0.1$. When using the strongest data sets of this study, based on having a known formation site (Alaska, Peru, Cyprus, Spain, England, Israel, Jiangxi and Ningxia), the regression analysis can be summarized as: $y = 0.3x-11.8$, $R^2 = 0.05$, $F_{1,29} = 1.6$, $p = 0.2$. The B2 scatterplot (**figure 7.16**) shows the least significant relationship of the three regressions: $y = 0.3X - 11.1$, $R^2 = 0.04$, $F_{1,27} = 1.2$, $p = 0.3$. These statistics suggest that the data used in this study is either not representative or that there is no statistically significant correlation between $\delta^{13}C$ in archaeological malachite and $\delta^{18}O$ of modern proxy waters.

The scatterplot (**figure 7.17**) of B1 malachite $\delta^{13}C$ against modern surface temperatures from correlating sites does not suggest a linear relation ($y = 0.08x - 14.9$, $R^2 = 0.03$, $F_{1,47} = 1.3$, $p = 0.3$). Only about 3% of the variability in $\delta^{13}C_{malachite}$ is matched by the variability in the surface temperature. This suggests that the use of estimated modern surface temperatures will not always serve as suitable proxies for the formation temperature of malachite, or that temperature does not significantly influence the isotopes in CO_2-malachite. When only considering samples with known formation sites, the regression becomes as follows: $y = 0.2x-16.2$, $R^2 = 0.09$, $F_{1,27} = 3.0$, $p = 0.09$. These statistics show an improved relationship between $\delta^{13}C$ in malachite and the surface temperature at the estimated site of formation, however it is still considered insignificant because $p > 0.05$. Since the B1 and B2 $\delta^{13}C$ data is significantly different, another scatterplot (**figure 7.18**) was statistically assessed using B2 $\delta^{13}C$ values against surface temperature. This resulted in the least significant linear relation: $y = 0.03x - 13.9$, $R^2 = 0.002$, $F_{1,27} = 0.05$, $p = 0.8$. Although none of these data sets have a significant linear relationship with surface temperature, it is interesting how much the results vary. The strongest relationship is with the B1 data using only samples with known formation sites. With a larger data set and cleaner malachite samples, it is possible that a slight relationship may become apparent.

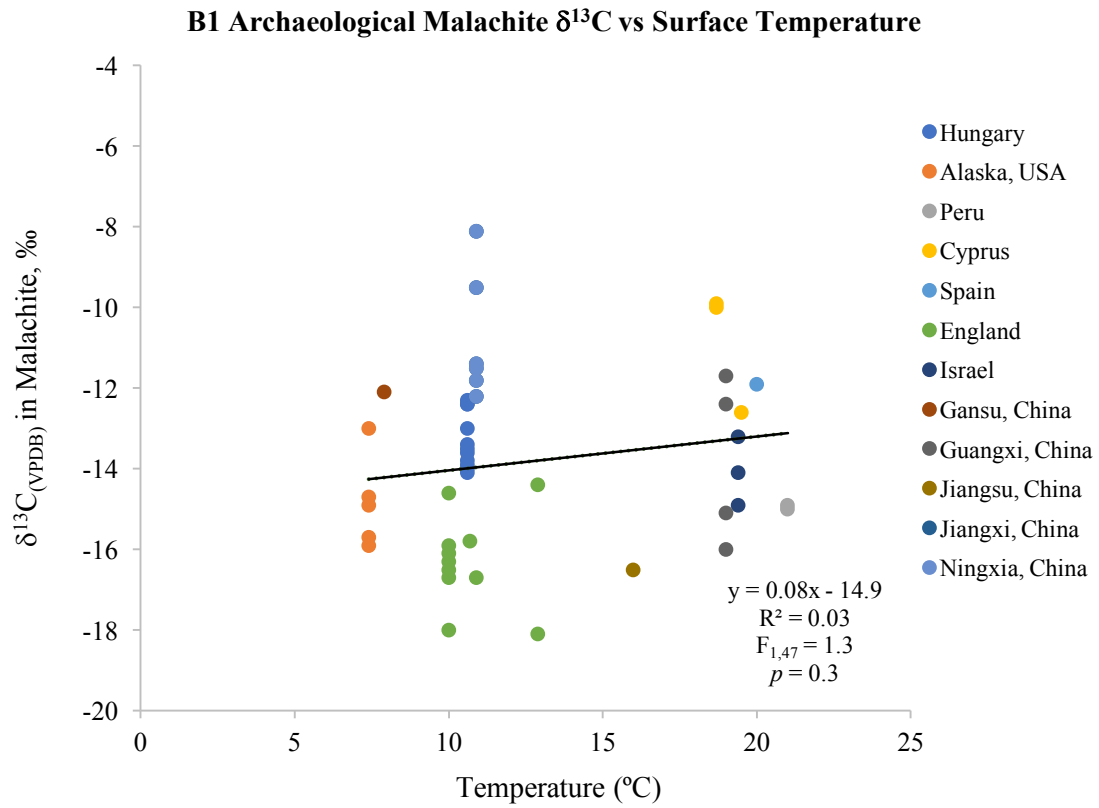


Figure 7.17: Scatterplot of B1 malachite $\delta^{13}C$ against modern surface temperatures from sites does not suggest a linear relation (p = 0.3, statistically insignificant). Only about 3% (R^2 = 0.03) of the variability in $\delta^{13}C_{malachite}$ is matched by the variability in the surface temperature. This suggests that the use of modern surface temperatures will not always serve as suitable proxies for the formation temperature of malachite.

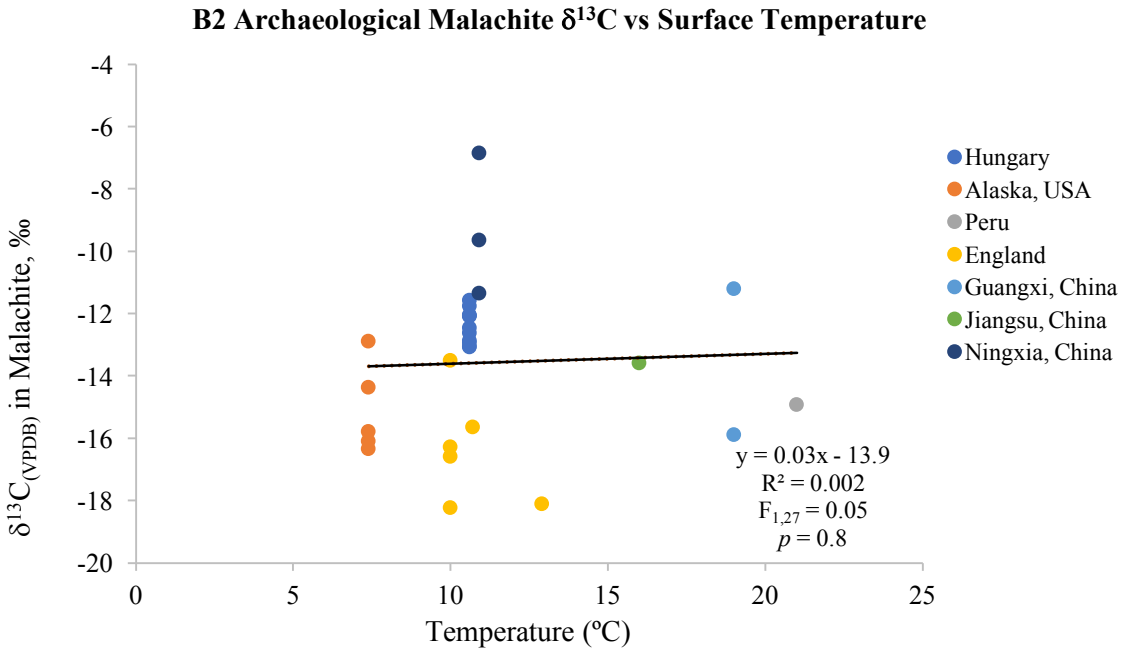


Figure 7.18: Scatterplot of B2 malachite $\delta^{13}C$ against modern surface temperatures from sites does not suggest a linear relation (p = 0.8, statistically insignificant). Only about 0.2% (R^2 = 0.002) of the variability in $\delta^{13}C_{malachite}$ is matched by the variability in the surface temperature. This suggests that the use of modern surface temperatures will not always serve as suitable proxies for the formation temperature of malachite.

Exploring A Carbon Fractionation Factor for Malachite as a Function of Temperature

The equilibrium $\delta^{13}C$ fractionation between malachite and soil $CO_{2(g)}$ was attempted by Melchiorre through slow precipitation experiments over the temperature range 0-50 degrees Celsius, expressed with the equation:

$$1000\ln\alpha_{\text{malachite-soil CO2}} = -1.85\ (10^6/T^2) + 10.51$$

where T is the temperature in Kelvin and the definition of α is the function of δ-values, in this case the fractionation factor between soil CO_2 and malachite ($\alpha = \frac{1000+\delta^{13}C_{\text{malachite}}}{1000+\delta^{13}C_{\text{soil CO2}}}$) (Melchiorre *et al.* 1999, 248). Unlike the oxygen isotope geothermometer, it is difficult to assess the strength of the carbon isotope equation because the actual $\delta^{13}C$ of the formation soil CO_2 is not known and there are no databases like GNIP that can be used to create estimates, all of which prevent comparisons with calculated values from being possible. Moreover, this equation is based on Melchiorre's belief that carbon fractionations between CO_2 and calcite, as defined by Bottinga (1968, refer to footnote), is virtually identical with malachite and therefore the same generalizations can be used to describe their genesis behaviors.[1] However, Haßler *et al.* (2014) came to a different conclusion, with results indicating that malachite is depleted by about Δ = -6‰ relative to calcite (9). Nevertheless, Melchiorre's carbon isotope equation was used to calculate $\delta^{13}C$ in soil CO_2 at the formation site of the archaeological malachite samples using estimated formation temperatures (provided on **table 7.24** for B1 and **table 7.25** for B2). Not a lot can be done with the calculated results since comparisons with estimated values are not possible. However, the results could make suggestion of the realistic possibility that a sample formed at a given biome (Melchiorre *et al.* 1999, 250).

Tables 7.24 and 7.25, on the following pages, present the measured archaeological malachite $\delta^{13}C$ values next to the calculated $\delta^{13}C$ in local soil CO_2, as determined using Melchiorre's ^{13}C fractionation equation. Also presented are the $\delta^{18}O$ weighted mean of modern meteoric water used for each sample, along with the average surface air temperatures at the site of excavation, which were used in calculations.

[1] The carbon fractionation for CO_2-calcite as observed by Bottinga (1968, Fig. 5, Table 3) is defined with the equation below. Melchiorre's values for $1000 ln\alpha_{\text{CO2-malachite}}$ differ by less than 0.16‰ from the values reported by Bottinga (Melchiorre 1999, 250).

$$1000\ ln\ \alpha_{\text{CO2-calcite}} = -2.9880\left(\frac{10^6}{T^2}\right) + 7.6663\left(\frac{10^3}{T}\right) - 2.4612$$

B1 Table of Results for Calculated $\delta^{13}C$ in Soil CO_2

Sample ID	Measured $\delta^{13}C_{(VPDB)}$ in Malachite, ‰	Calculated $\delta^{13}C_{(VPDB)}$ of Soil CO_2, ‰	$\delta^{18}O_{(VSMOW)}$ Weighted Mean of Modern Meteoric Water, ‰	Average Surface Air Temperature (ºC)
H1	-13.9	-26.1	-7.7	10.6
H2	-12.3	-24.5	-7.7	10.6
H3	-12.4	-24.5	-7.7	10.6
H4	-13.0	-25.2	-7.7	10.6
H5	-12.4	-24.6	-7.7	10.6
H6	-13.8	-25.9	-7.7	10.6
H7	-13.4	-25.6	--7.7	10.6
H8	-13.6	-25.7	-7.7	10.6
H9	-14.1	-26.3	-7.7	10.6
H10	-13.5	-25.6	-7.7	10.6
H11	-14.0	-26.2	-7.7	10.6
US1	-13.0	-25.8	-11.4	7.4
US2	-15.7	-28.4	-11.4	7.4
US3	-15.9	-28.6	-11.4	7.4
US5	-14.9	-27.6	-11.4	7.4
US6	-14.7	-27.5	-11.4	7.4
P2	-15.0	-25.6	-5.1	21.0
P3	-14.9	-25.6	-5.1	21.0
RC4	-12.6	-23.5	-5.9	19.5
RC7	-9.9	-21.0	-5.9	18.7
RC8	-10.0	-21.1	-5.9	18.7
SES9	-11.9	-23.2	-5.6	20.0
E2	-18.0	-30.2	-7.3	10.0
E3	-16.3	-28.6	-7.3	10.0
E4	-16.7	-28.8	-7.3	10.9
E6	-18.1	-29.9	-7.3	12.9
E7	-14.4	-26.2	-7.3	12.9
EC2	-16.5	-28.7	-7.3	10.0
EC4	-16.1	-28.4	-7.3	10.0
EC5	-16.7	-29.0	-7.3	10.0
EC7	-14.6	-26.9	-7.3	10.0
EC8	-15.9	-28.2	-7.3	10.0
EO2	-15.8	-28.0	-7.3	10.7
I1	-13.2	-24.1	-5.2	19.4
I2	-14.1	-25.0	-5.2	19.4
I4	-14.9	-25.8	-5.2	19.4
CGN2	-12.1	-24.5	-5.7	7.9
CGS2	-12.4	-23.3	-6.2	19.0
CGS3	-16.0	-26.9	-6.2	19.0
CGS4	-11.7	-22.7	-6.2	19.0
CGS5	-15.1	-25.9	-6.2	19.0
CJN	-16.5	-27.8	-8.0	16.0
CJS	-11.6	-22.7	-5.6	18.4
CNM1	-11.4	-23.6	-7.2	10.9
CNW1	-9.5	-21.8	-7.2	10.9
CNW2	-8.1	-20.3	-7.2	10.9
CNW3	-11.8	-24.0	-7.2	10.9
CNW4	-12.2	-24.4	-7.2	10.9
CNW5	-11.5	-23.7	-7.2	10.9

Table 7.24: The measured B1 archaeological malachite $\delta^{13}C$ values are presented next to the calculated $\delta^{13}C$ in local soil CO_2, as determined using Melchiorre's ^{13}C fractionation equation. Each sample's estimated formation water $\delta^{18}O$ (based on the data reported and cited in the site profiles section in Chapter 5) and formation temperature (based on the average surface air temperature at or near the sample's assumed excavation site) is also presented.

B2 Table of Results for Calculated $\delta^{13}C$ in Soil CO_2

Sample ID	Measured $\delta^{13}C_{(VPDB)}$ in Malachite, ‰	Calculated $\delta^{13}C_{(VPDB)}$ of Soil CO_2, ‰	$\delta^{18}O_{(VSMOW)}$ Weighted Mean of Modern Meteoric Water, ‰	Average Surface Air Temperature (°C)
H1	-12.93	-25.2	-7.7	10.6
H2	-12.06	-24.3	-7.7	10.6
H3	-11.75	-24.0	-7.7	10.6
H4	-12.62	-24.8	-7.7	10.6
H5	-12.08	-24.3	-7.7	10.6
H6	-11.56	-23.8	-7.7	10.6
H7	-13.04	-25.2	--7.7	10.6
H8	-13.06	-25.2	-7.7	10.6
H9	-12.04	-24.2	-7.7	10.6
H10	-12.45	-24.6	-7.7	10.6
H11	-12.86	-25.0	-7.7	10.6
US1	-12.89	-25.7	-11.4	7.4
US2	-16.33	-29.0	-11.4	7.4
US3	-16.09	-28.8	-11.4	7.4
US5	-14.36	-27.1	-11.4	7.4
US6	-15.77	-28.5	-11.4	7.4
P2	-14.92	-25.6	-5.1	21.0
E2	-18.22	-30.5	-7.3	10.0
E6	-18.10	-29.9	-7.3	12.9
EC2	-13.49	-25.8	-7.3	10.0
EC4	-16.28	-28.6	-7.3	10.0
EC5	-16.57	-28.8	-7.3	10.0
EO2	-15.63	-27.8	-7.3	10.7
CGS3	-15.88	-26.8	-6.2	19.0
CGS4	-11.19	-22.2	-6.2	19.0
CJN	-13.58	-25.0	-8.0	16.0
CNM1	-11.33	-23.5	-7.2	10.9
CNW1	-9.64	-21.9	-7.2	10.9
CNW2	-6.85	-19.1	-7.2	10.9

Table 7.25: The measured B2 archaeological malachite $\delta^{13}C$ values are presented next to the calculated $\delta^{13}C$ in local soil CO_2, as determined using Melchiorre's ^{13}C fractionation equation. Each sample's estimated formation water $\delta^{18}O$ (based on the data reported and cited in the site profiles section in Chapter 5) and formation temperature (based on the average surface air temperature at or near the sample's assumed excavation site) is also presented.

Starting with the null hypothesis that there is no difference between the populations from which the B1 and B2 $\delta^{13}C$ soil CO_2 pairs come, and using a 5% (0.05) critical significance level, a paired *t*-value was calculated for the batches. The results show that there is a significant statistical difference between the B1 and B2 malachite populations for $\delta^{13}C_{soil}$ (paired *t*-test, two-tailed: t_{28} = 3.2, p = 0.004, 95% CI [-0.9, -0.2]). Since the critical significance level of 0.05 is larger than the value of 0.004 of p, the stated null hypothesis must be rejected. This result is identical to that of the B1 and B2 $\delta^{13}C_{malachite}$, which is unsurprising considering these data were used to calculate the $\delta^{13}C_{soil}$.

$\delta^{13}C$ Correlations with Climate

Multidimensional categories like climate, which considers environmental parameters like temperature and precipitation conditions simultaneously, were explored for statistical use with the $\delta^{13}C$ results. The Köppen Climate Classification system served well with the $\delta^{18}O$ study (refer to pages 184-186), thus was explored again with $\delta^{13}C$ values in malachite. When the mean $\delta^{13}C$ in malachite is ranked by decreasing value, a provenance order with the following climate sequence is presented:

Site	N	Mean $\delta^{13}C$ (‰, VPDB)	SD	Köppen Climate
Ningxia, China	6	-10.7	1.6	**B**Wk
Cyprus	3	-10.9	1.5	**B**Sh
Jiangxi, China	1	-11.6	-	**C**fa
Spain	1	-11.9	-	**B**Sh
Gansu, China	1	-12.1	-	**B**Sk
Hungary	11	-13.3	0.7	**C**fb
Guangxi, China	4	-13.8	2.1	**C**fa
Israel	3	-14.1	0.8	**C**sa
Alaska, USA	5	-14.8	1.1	**C**fb
Peru	2	-15.0	0.04	**B**Wh
England	11	-16.3	1.1	**C**fb
Jiangsu, China	1	-16.4	-	**C**fa

Table 7.26: Table showing Köppen climate classification order for the $\delta^{13}C$ in malachite ranked by decreasing mean value. The first letter, in bold, defines the major climate type. Subsequent letters describe climate subtypes.

Except for Peru, all the arid and semi-arid climates (beginning with B) are on the heavy half of the $\delta^{13}C$ rank table (**table 7.26**). Otherwise, there are no clearly defined patterns in this sequence. The two plots (**figures 7.19 and 7.20**) on the following page categorize the $\delta^{13}C$ in malachite with their correlating Köppen climate, presented in hierarchical order, which generally ranks dry climates above humid ones. However, an impartial perspective must be maintained for this study since the full sense of a climate can be compromised with ranking. For this reason, the mean $\delta^{13}C$ values were used to put the climates into an order that may elucidate any possible correlations (**table 7.26**). Moreover, varying proportions of carbon sources can dominate at a given time. The carbon isotopes in malachite are complicated by plant densities, mixed vegetation types, soil porosity, water residence times, seasonal fluctuations in precipitation, temperature, and contribution from inorganic carbon reservoirs. It may be the case that the arid and semi-arid climates were grouped only because they offer extreme, yet more stable environments, and this is apparent in the $\delta^{13}C$ values and climate ranking.

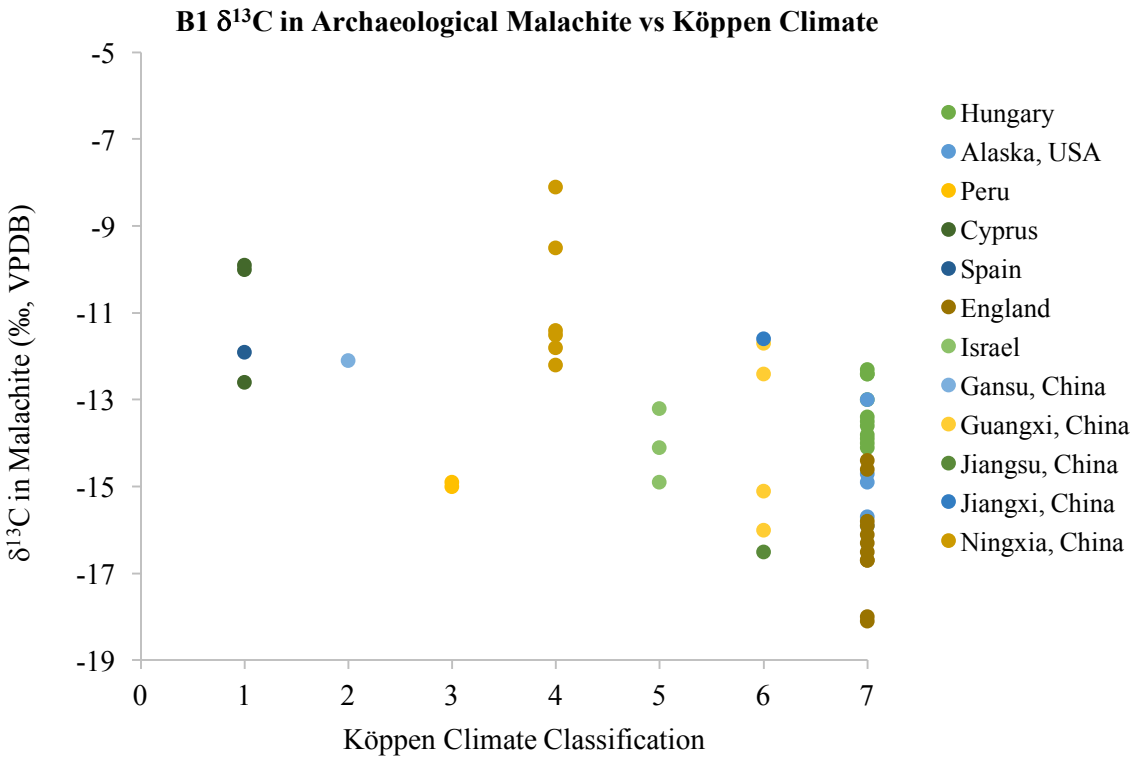


Figure 7.19: Classification plot of archaeological malachite B1 $\delta^{13}C$ values grouped by Köppen climate type, and presented in hierarchical order. Code: 1-BSh, 2-BSk, 3-BWh, 4-BWk, 5-Csa, 6-Cfa, 7-Cfb.

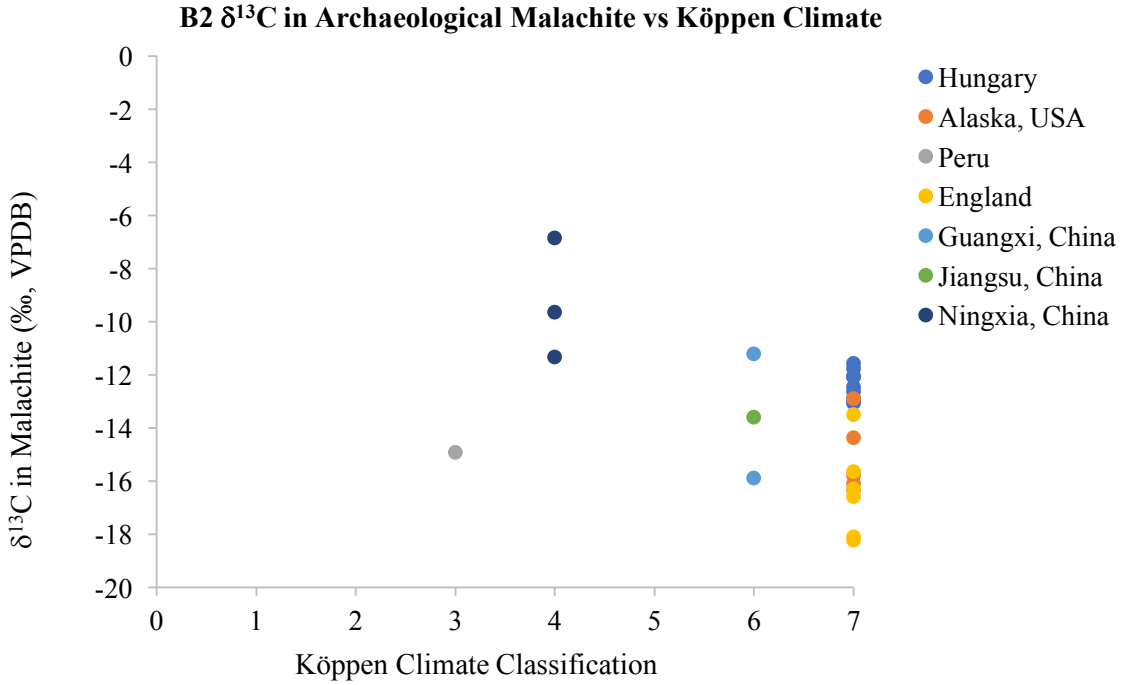


Figure 7.20: Classification plot of archaeological malachite B2 $\delta^{13}C$ values grouped by Köppen climate type, and presented in hierarchical order. Code: 1-BSh, 2-BSk, 3-BWh, 4-BWk, 5-Csa, 6-Cfa, 7-Cfb (the B2 set only has samples from BWh, BWk, Cfa and Cfb).

7.3. Summary

Powder XRD material characterizations of the 49 B1 and 29 B2 malachite samples analyzed isotopically are presented in **tables 7.1 – 7.8**. The B1 $\delta^{18}O$ and $\delta^{13}C$ results are presented in **table 7.10**. According to Grubb's test, the B1 data has one significant outlier in the English set. The B2 $\delta^{18}O$ and $\delta^{13}C$ results are presented in **table 7.11**; this dataset has no outliers. Azurite and copper (II) chloride hydroxide minerals do not significantly impact the isotope ratios in archaeological malachite.

To collectively determine whether group means differ, one-way Anova statistics were carried out for the malachite isotope data. For all datasets, the $\delta^{18}O$ and $\delta^{13}C$ values in malachite consistently show a statistically significant difference between the geographic groups surveyed. Where the significant differences lie is suggested in the confidence interval plots shown in **figures 7.1 and 7.3**, where samples overlap the least.

A two-tailed, paired *t*-test shows that there is no significant difference between the 29 B1 and B2 $\delta^{18}O_{malachite}$ pairs. This suggests that meticulous picking does not significantly impact the oxygen isotope results in archaeological malachite samples. Yet, for the $\delta^{13}C$ data, the paired *t*-test results suggest that there is a significant difference between the B1 and B2 pairs. This suggests that meticulous picking has a significant impact on the carbon isotope results in archaeological malachite samples, which is opposite to the oxygen isotope *t*-test result.

Although the B1 and B2 scatterplots (**figures 7.5 and 7.6**) for $\delta^{18}O$ against $\delta^{13}C$ in malachite show a significant linear relationship with clustering within sites, this is not always maintained when considering the regression analyses of the geographic groups independently. The best example of this is with England and Hungary, which have regression trends in opposite directions. The Hungarian data shows a positive correlation, meaning the $\delta^{18}O$ values increase as the $\delta^{13}C$ values increase. But the English data shows a negative correlation, suggesting that the $\delta^{13}C$ values decrease as the $\delta^{18}O$ values increase. This can be interpreted in many ways, but ultimately more data is necessary to unravel and understand this inconsistency. Complications such as sample quality (purity), provenance accuracy, and the impact of various environmental parameters also play a role.

The B2 scatterplot for $\delta^{18}O$ against $\delta^{13}C$ in malachite has a greater F-statistic and a smaller *p*-value than B1, meaning it is statistically more significant. B2 also has a greater R^2-value, with 30% of the variability in one isotope being matched by the variability in the other, as opposed to B1's 20%. Moreover, B2 has a stronger correlation than B1, with rho = -0.6 compared to B1's rho = -0.4. Unexpectedly, considering that the B2 samples are less pure than the B1 samples, the B2 statistics are stronger. However, when considering the statistics of each geographic group, the B1 data is still stronger for Hungary and England, which are the study's largest datasets.

Plotting the $\delta^{18}O_{malachite}$ against the $\delta^{18}O$ in modern meteoric water (**figure 7.8**) does not suggest a linear relation. Likewise, the B1 and B2 plots for $\delta^{13}C_{malachite}$ against the $\delta^{18}O$ of modern

meteoric water do not suggest a linear relation (**figures 7.15 and 7.16**). However, having more accurate provenance for the water samples and cleaner malachite could result in a slightly significant relation, as previous studies using malachite ores have shown.

Plotting the B1 $\delta^{18}O_{malachite}$ against the surface temperature of a representative site (refer to **figure 7.10**) produces a statistically insignificant linear regression. The scatterplots (**figure 7.17 and 7.18**) of B1 and B2 $\delta^{13}C_{malachite}$ against modern surface temperatures from correlating sites also do not suggest a linear relation. Since surface temperature and soil temperature can be very different at the same location, the formation temperature of malachite was calculated using estimated $\delta^{18}O_{water}$ data through a geothermometer equation developed by Melchiorre. The scatterplot of the estimated formation temperature against the calculated formation temperature suggests a statistically significant linear relationship (**figure 7.8**). This is suspicious considering that the linear regression for B1 $\delta^{18}O_{malachite}$ against the surface temperature produces a statistically insignificant linear regression. Inconsistencies could be due to poor assignment of proxy sites for malachite samples with uncertain formation provenance.

In reverse, modern surface temperatures were used to calculate the $\delta^{18}O$ of the formation water through the oxygen isotope thermometer equation. A scatterplot (**figure 7.13)** of the calculated formation water $\delta^{18}O$ values against the estimated $\delta^{18}O$ meteoric water values suggests that there is a statistically significant difference, meaning that the calculated $\delta^{18}O$ in formation water is not comparable to the estimated $\delta^{18}O$ in meteoric water. These findings show that the geothermometer equation will only work with accurate data. This was not the case for this study, which depends on estimated environmental data.

When the mean $\delta^{18}O$ values in malachite are arranged in decreasing order (**table 7.19**), the resulting Köppen climate sequence hints at a few approximate concurrencies. In general, it appears that the temperate climates are concentrated in the center of the sequence. The two desert climates are together and associated with lighter $\delta^{18}O_{malachite}$ means. The semi-arid climates are also grouped, but at the opposite end of the sequence. For $\delta^{13}C$, all but one of the arid and semi-arid climates are on the heavy half of the $\delta^{13}C$ rank table (**table 7.26**). Otherwise, there are no clearly defined patterns because varying proportions of carbon sources can dominate at a given time. It may be the case that the arid and semi-arid climates were grouped only because they offer extreme, yet more stable environments, and this is apparent in the malachite isotope ratios and climate ranking.

CHAPTER 8

Discussion and Conclusion

8.1. Thesis Overview

As the product of a metal and its environment, corrosion is a valuable source of historical material evidence. The possibility of creating a methodology that could be used to identify the corrosion location of copper minerals is tested, for eventual use on archaeological bronzes that formed in the soil. This doctoral project focuses on the correlations between two of the most common copper corrosion minerals, brochantite and malachite, and their formation environment using $\delta^{18}O$, $\delta^{13}C$ and $\delta^{2}H$.

Oxygen is central to this project as the principal cause of copper corrosion by way of oxidation-reduction reactions. Oxygen is highly chemically reactive and spontaneously forms covalent bonds with atoms of all other elements (except the noble gases) to create oxides that are thermodynamically stable over large temperature ranges. Atmospheric molecular oxygen has a constant isotopic composition with an $\delta^{18}O$ value of 23.5±0.3‰ relative to ocean water (SMOW) (Kroopnick & Craig 1972, 54). Measurement of $\delta^{18}O$ in brochantite and malachite is applied to determine whether the geographic region in which these minerals formed by be identified to some extent when the $\delta^{18}O$ is a function of the $\delta^{18}O$ in local meteoric water and formation temperature. Meteoric processes that provide a characteristic fingerprint of their origin affect the stable isotope composition of water (refer to section 3.2), which then serves as a natural tracer that can be used in provenance studies. As peripheral sub-studies, the hydroxyl-$\delta^{2}H$ in brochantite and $\delta^{13}C$ in malachite are also explored to determine whether they could supplement or alter the $\delta^{18}O$ project.

The aim for the brochantite study is to measure $\delta^{18}O_{SO4}$ in natural samples from geographically distinct locations to determine whether there is isotopic variation between sites, as there is in meteoric waters. Additionally, the hydroxyl-$\delta^{2}H$, which should be entirely meteoric in origin, is measured in larger samples to determine if it may be helpful to the $\delta^{18}O$ study. The data is processed using statistics to determine the significance of the results and identify the most influential environmental factors and trends. Finally, the percent contributions from aqueous and gaseous formation pathways in the brochantite samples are calculated to identify the main reactions taking place during formation.

Using two groups, called Batch One and Batch Two, the malachite study aims to measure $\delta^{18}O$ in archaeological samples from geographically distinct locations to determine whether there is isotopic variation between sites, as there is in meteoric waters. Batch Two is not as pure as Batch One, and is explored to determine the necessity of a meticulous sample cleaning process. The $\delta^{13}C$ is also measured to determine whether this information can be used to supplement the $\delta^{18}O$ study.

The isotope data from archaeological malachite is compared to $\delta^{18}O$ in local meteoric water, surface temperature and climate to identify the controls on isotope ratios during formation. Finally, the archaeological data is compared to previous work on malachite ores to determine whether there is a detectable isotopic difference between archaeological and ore formations.

8.2. $\delta^{18}O_{SO4}$ STUDY ON HISTORIC BROCHANTITE

Brochantite samples were isolated from scrapings off patinated copper roofs with known geographic locations (Oxford, Vienna, Ottawa and Tuscaloosa). Powder XRD confirmed that the mineral phase present is brochantite (**table 6.1**). Samples were dissolved in 1 M hydrochloric acid. Several filtrations were carried out to remove any non-sulfate minerals. $BaCl_2$ was added to yield $BaSO_4$ to isolate the sulfate ion of interest. The $BaSO_4$ was converted to CO and analyzed using a TC/EA-IR-MS. Later, some of the $BaSO_4$ samples were analyzed with FTIR to check the purity. There was concern about carbonate contaminates, but only the sulfate was present.

Excluding outliers (refer to the following paragraph), the mean $\delta^{18}O_{SO4}$ of brochantite samples from each city are Tuscaloosa: 7.4‰, Oxford: 7.7‰, Vienna: 7.9‰ and Ottawa: 7.0‰ (**table 6.2**). The $\delta^{18}O_{SO4}$ results were statistically analyzed using paired *t*-tests, Anova and linear regression. Since all *p*-values are greater than the critical value of 0.05, the conclusion is that there is no statistically significant difference between the $\delta^{18}O_{SO4}$ values in brochantite (**table 6.4**). Moreover, Anova results show that the brochantite $\delta^{18}O_{SO4}$ variances are roughly equal among the cities: $F_{3, 27} = 1.7$, $p = 0.2$.

Grubb's outlier test identified two outliers in the brochantite data that are difficult to explain (Presidential Hall in Tuscaloosa and Oriel Library in Oxford). These samples could have more oxygen sourced from the atmosphere or ozone, in which case the homogeneous pathway must have been favored. It is possible that most of this brochantite formed during a drought. However, there are other samples of similar age from the same city (and therefore comparable environmental histories) that fit within range, suggesting another factor is responsible. The most influential environmental factors that affect isotope ratios in meteoric water and brochantite are pH and temperature. Tuscaloosa's Presidential Hall is difficult to understand because the building has been demolished and the original location of the sample on the roof is unknown. The sample may have come from near a chimney or some other ventilation/drainage location, which could explain the outlying point. Alternatively, local concentrations of bird (pigeon) droppings, i.e., could result in values consistent with the direction of the observed outliers, though this contact would need to be prolonged in the same area to impact brochantite formation. The increased acidity could also result in preference for metal catalyzed formations where heterogeneous pathways occurred.

There is no statistically significant correlation between brochantite $\delta^{18}O_{SO4}$ and the yearly weighted mean $\delta^{18}O_{H2O}$ in local precipitation: $y=7.9+0.05x$, $R^2=0.01$, $p=0.5$ (**figure 6.3**). The correlation between $\delta^{18}O_{H2O}$ in local precipitation and $\delta^{18}O_{SO4}$ in brochantite improves slightly

when only considering summer precipitation, though ultimately it is still insignificant: y=8.3+0.1x, R^2=0.03, *p*=0.4 (**figure 6.4**).

The isotopic data available on GNIP for Tuscaloosa's precipitation only covers a three-year period between 2005 and 2008. Considering that the three observed years included El Niño and La Niña events (these cause changes in temperature and rainfall), it is possible that the $\delta^{18}O$-H_2O data used for Tuscaloosa is not entirely representative. Still, the oxygen-18 data from brochantite sulfate, when compared to the oxygen-18 of the local meteoric water at all sites included in this study, does not correlate enough to be able to use this information for identifying a specific provenance when working with a sample that could be from anywhere in the world. However, if given four sets of samples from four different cities with meteoric waters that vary considerably in $\delta^{18}O$ values, then it might be possible to allocate each sample set to the correct city.

Scatterplots for brochantite $\delta^{18}O_{SO4}$ against the yearly mean precipitation amount, pH, surface temperature, latitude, and age of deposit (**figures 6.5 – 6.9**) were also analyzed and show no significant correlations. The strongest linear correlation is between $\delta^{18}O_{SO4}$ and the pH in meteoric water (y=7.9-(2.3x10^4)x, R^2=0.05, *p*=0.2), and the weakest is between $\delta^{18}O_{SO4}$ and latitude (y=6.8+0.01x, R^2=0.009, *p*=0.6).

About 50% of brochantite's sulfate oxygen is sourced from the local meteoric water (**table 6.6**). The water-oxygen is most likely to react into the sulfate product through a combination of three chemical pathways involving the oxidation and hydrolysis of sulfur dioxide. The predominant oxidizers are H_2O_2, O_2 (metal catalyzed), and O_3. These oxidizers yield sulfates with different ratios of oxygen from water and other oxygen sources (refer to section 4.2.3). Using the values with this study's experimental brochantite data, a percent range of oxygen sourced from water via each pathway can be estimated. As part of the brochantite study, a $SO_2 \rightarrow SO_4$ Pathway Flowchart was created to guide in calculating these estimations (**figure 6.10**). About 44-91% of the water sourced oxygen in brochantite's sulfate was incorporated through an aqueous-phase reaction pathway from SO_2 (**tables 6.7 – 6.13)**. This range may be narrowed when focusing on one city. For Tuscaloosa, the range is reduced to 65-91%, for Vienna it is 44-74%, Ottawa is 46-78%, and Oxford is 53-84%. Values closer to 44% would suggest O_2 is the favored mechanism, whereas values nearer 91% would imply H_2O_2 is predominant. There is no known way, however, to calculate how much water-oxygen is incorporated through all heterogeneous pathways together (refer to section 6.2.3). It is only possible to determine contribution amounts when focusing on one heterogeneous pathway at a time. To determine which heterogeneous pathway is most likely, the pH of the local precipitation must be considered. If the pH is greater than 5, the O_2 (metal catalyzed) pathway is favored. If the pH is less than 5, the H_2O_2 pathway is favored. It is believed that both heterogeneous pathways are contributing, with preference of unknown magnitude for H_2O_2.

The isotopic mechanism for heterogeneous oxidation by ozone remains controversial and needs resolution. Ozone and H_2O_2 concentrations in the troposphere are not uniform and vary from

day-to-day and place-to-place (refer to section 3.4.4). Ozone is a main oxidizer of SO_2 to sulfate and therefore, it was originally assumed that ozone would contribute through an aqueous-phase pathway yielding one oxygen from water and another three from other sources (presumably atmospheric oxygen). This value, however, when used in the equations provided (R1 and R2, refer to section 6.2.3), creates mathematical errors that suggest the pathway is not a realistic option. An exception to this is if ozone were used as an oxidizer via a gas-phase pathway, in which case the result would be the same as the dominant one presented in the $SO_2 \rightarrow SO_4$ Pathway Flowchart (one oxygen from water, three from other sources, (refer to **figure 6.10**). Therefore, the only imaginable way for ozone to be involved in the SO_2 to sulfate reaction would be through a homogeneous pathway.

A pilot study was carried out for the analysis of δ^2H from the hydroxyl groups in brochantite (**table 6.14**). There is no statistically significant correlation between brochantite δ^2H and the $\delta^{18}O$ in local meteoric water, pH, average surface temperature, latitude, or amount of precipitation for the cities included in the study (**figures 6.13 – 6.18**). Ultimately, the δ^2H pilot study consists of little data and analyzing the δ^2H alone is insufficient. The hydroxyl study would benefit from analyzing the hydroxyl oxygen as well, but the brochantite samples collected are not big enough to carry out a full study on the sulfate oxygen and hydroxyl hydrogen.

8.3. $\delta^{18}O$ and $\delta^{13}C$ IN ARCHAEOLOGICAL MALACHITE

The malachite study is larger than the brochantite study, with data sets representing 12 different geographic regions. The exact formation site within the region of many of the malachite samples included in this study is not known. Moreover, details on the objects from which the samples were collected are sometimes lacking. Consequently, it should be taken into consideration that several assumptions and estimations were made to process the malachite data. These assumptions and estimations are identified in the site profiles section of Chapter 5 (section 5.2.5) and throughout the thesis.

This work also focused on finding statistical correlations between the $\delta^{18}O$ and $\delta^{13}C$ data collected from archaeological malachite samples and a set of environmental parameters, including the $\delta^{18}O$ in local meteoric water, to determine which are most influential for an empirical understanding of what controls the $\delta^{18}O$ and $\delta^{13}C$ compositions in archaeological malachite.

8.3.1. Comparing to Data from Previous Investigations

Comparison to the previous investigations was conducted to create a larger database that altogether may elucidate narratives otherwise not detectable, and to determine the applicability of previous work on synthetic and geological malachite.

There is considerable variety between the results reported by different investigators on malachite samples (**table 8.1**). Statistically significant relationships are calculated for the B1 study (labeled as Boos Pedroza), Haßler *et al.* (2014) study, Melchiorre *et al.* (1999) study, and the Smith

(1978) study. The work carried out by Pandey and Melchiorre's data on historical malachite do not produce significant correlations between $\delta^{18}O$ and $\delta^{13}C$. The data from these two investigations was small enough not to adversely affect the grouped results, which maintain that there is a relationship between $\delta^{18}O$ and $\delta^{13}C$ even after combining data from these studies (**table 8.1**).

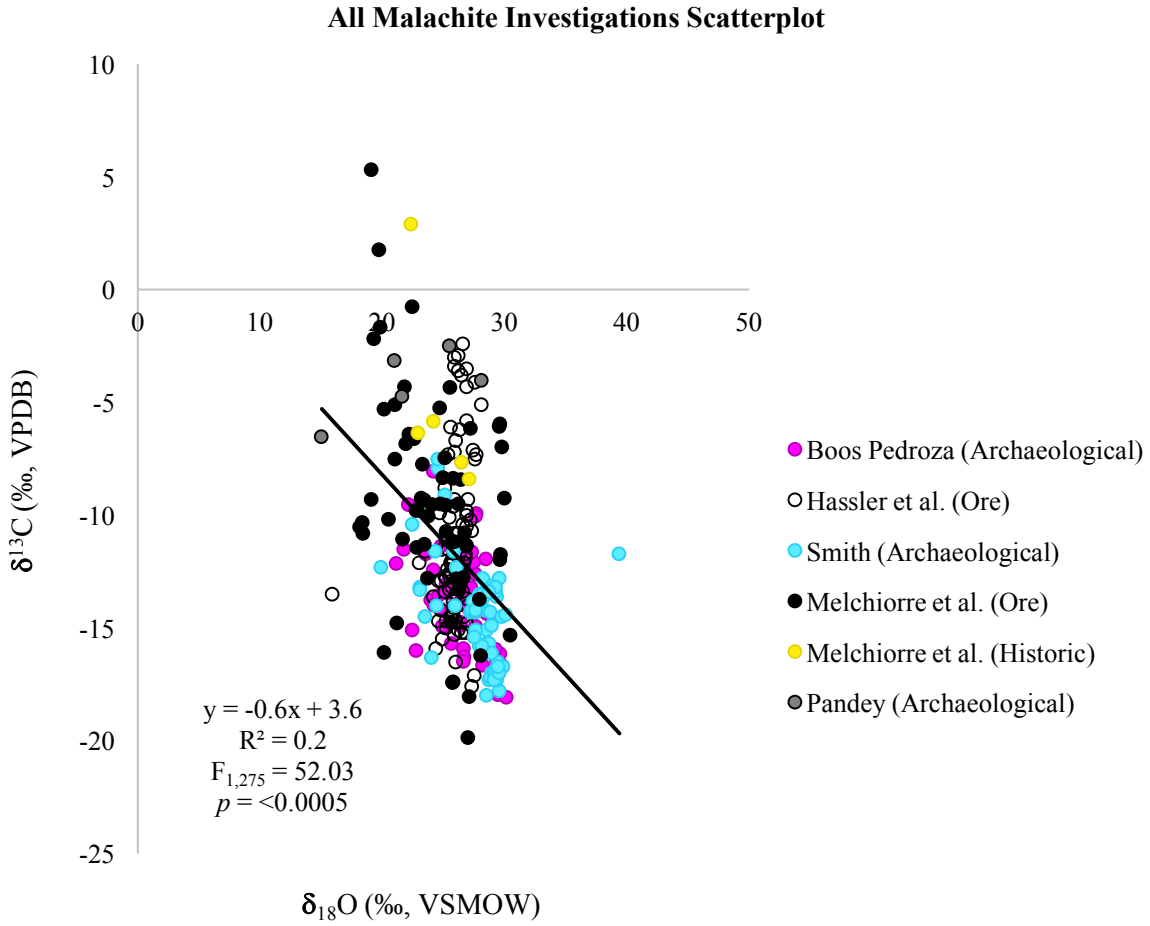


Figure 8.1: Scatterplot displaying isotopic data from all known malachite investigations. Altogether, the linear correlation between $\delta^{18}O$ and $\delta^{13}C$ can be summarized as: $y = -0.6x + 3.6$, $R^2 = 0.2$, $F_{1,275} = 52.03$, $p = <0.0005$. Independent studies vary in correlation strength, with details available in **table 8.1**.

All Malachite Investigations, $\delta^{18}O$ and $\delta^{13}C$ Relationship Statistics

Study	N	Regression Line	R^2	F	*p*
Boos Pedroza (Archaeological)	49	y = -0.4x – 2.4	0.2	11.0	0.002
Haßler *et al.* (Ores)	94	y = 0.6x – 27.3	0.05	5.3	0.02
Smith (Archaeological)	62	y = -0.3x – 4.8	0.2	11.3	0.001
Melchiorre *et al.* (Ores)	62	y = -0.5x + 3.4	0.1	10.4	0.002
Melchiorre *et al.* (Historic)	5	y = -1.6x + 34.5	0.6	3.7	0.2
Pandey (Archaeological)	5	y = 0.2x – 9.2	0.5	3.2	0.2
All Investigations Combined	277	y = -0.6x + 3.6	0.2	52.03	< 0.0005
All Ore Samples	156	y = -0.4x – 1.1	0.05	8.0	0.005
All Archaeological Samples	116	y = -0.5x – 0.07	0.2	34.4	< 0.0005
All Archaeological & Historic	121	y = -0.6x + 3.0	0.2	39.0	< 0.0005

Table 8.1: Displaying the number of malachite samples (n) analyzed and statistical interpretations on the relationships between $\delta^{18}O$ and $\delta^{13}C$ for each project or combination of projects shown in **figure 8.1**.

This study is the first to report a statistically significant relationship between the $\delta^{18}O$ and $\delta^{13}C$ in archaeological malachite, which is also apparent in the large studies on malachite ores, but not presented in publications. The most likely reason this correlation was not found in previous archaeological malachite studies is sample purity. These results show that some OM isolation on malachite crystals is an important and necessary step. Furthermore, filtrations by way of instrumental material characterization is worthwhile for the identification and removal of unsuitable samples, however this processing results in the elimination of about 75% of patina samples.

$\delta^{13}C$ in Malachite

To estimate the $\delta^{13}C$ values in a microenvironment, the following information is needed: 1) exact provenance, 2) vegetation present at site, 3) soil type and details of soil carbonate chemistry. These details are presented in the site profiles section in Chapter 5, but the information is largely assumed or estimated. The purpose of this peripheral study is to determine whether $\delta^{13}C$ in malachite shows potential to supplement or alter the $\delta^{18}O$-focused methodology, in which case recommendation for a future comprehensive investigation could be made.

As described in section 3.6.4, previous investigations have assumed a fractionation for malachite that would result in $\delta^{13}C$ values around 2.2‰ if derived entirely from atmospheric CO_2, and values between -21.8‰ and -12.8‰ in those that incorporate carbon from soil CO_2. At present, a way to quantitatively estimate the contributions from each carbon source in heavy metal carbonates like malachite is not known. The mean $\delta^{13}C$ in the archaeological malachite data is -13.8 ± 2.2‰, ranging between -18.1‰ and -8.1‰ (**table 7.10**). Seventeen of the 49 samples have $\delta^{13}C$ values higher than -12.8‰. This study's archaeological malachite $\delta^{13}C$ data range suggests the carbon source is an inconsistent mixture (with varying contribution amounts) of vegetation-respired soil CO_2 and inorganic carbon sources with higher values. Since many processes can affect the $\delta^{13}C$ value of a sample, blurring the distinction between the plant types (C_3, C_4, CAM),

no attempt is made to infer specific vegetation type source of carbon for individual malachite samples.

Considering the statistically significant relationship between $\delta^{18}O$ and $\delta^{13}C$ shown in **figure 7.5** and discussed in the previous section, it is likely that another study into the $\delta^{13}C$ ratios of malachite would be worthwhile. When considering the regression analyses of the geographic groups independently, the relationship between $\delta^{18}O$ and $\delta^{13}C$ is not consistent with that of the combined data. This can be interpreted in many ways, and ultimately more data is necessary to understand the complexities involved. A formation pathway flowchart like the one created for the brochantite study could be beneficial for determining percent carbon contributions from the above-listed sources, and help in understanding the measured $\delta^{13}C$ values in malachite. To do this, work on carbon isotope fractionation factors for heavy metal carbonates like malachite is necessary, but at present only limited attempts have been made, especially at lower temperatures. These potentially interesting projects are substantial and better suited as independent research investigations.

The Batch Studies and Contaminants

The necessity of a meticulous picking process was assessed by also analyzing a small, less-pure batch of malachite-containing patinas known as batch two (B2) samples. Surprisingly, *t*-tests show that there is no significant difference between the B1 and B2 $\delta^{18}O$ pairs, but there is a difference for the $\delta^{13}C$ data. This trend, however, is not always observed when considering B1 and B2 data on a site-by-site basis (discussed later, in section 8.3.2, "Discussion by Geographic Group"). There was no consistency in the degree of contamination allowed for the B2 samples, which could contribute to this irregularity. Ultimately, since there is no statistically significant difference between the B1 and B2 data sets, the conclusion is that meticulous picking is not especially beneficial. A reasonable picking is still advised, as the results from this study are better than those of previous investigations on archaeological malachite (refer to previous section). Although picking is proven helpful, the samples used in this study were often clearly contaminated, which probably resulted in some mixed isotope data.

The narrative offered by the B2 results included information on common contaminants and their isotopic influence on mix-phase samples, particularly with azurite and atacamite. This is valuable because soil samples were not collected or available for this study, and sample contaminants were not analyzed independently. Although the soil in which the artifacts were discovered cannot be regarded as the initial one in which they were left or buried, the current soils remain informative and likely comparable.

Most recently, Melchiorre & Enders (2003) and Haßler *et al.* (2014) isotopically studied malachite and azurite ores from the same site. Both studies indicate that azurite is isotopically heavier than malachite, unless the minerals come from the same hand specimen (Haßler *et al.* 2014, 5-6; Melchiorre & Enders 2003, 607). Although malachite and azurite from the same site can

differ significantly in no systematic way in their $\delta^{13}C$, malachite-azurite pairs from the same hand specimen yield almost identical $\delta^{13}C$ values (based on three samples, Haßler *et al.* 2014, 8). This is credited to a coeval formation under disequilibrium or simply carbon from the same source. Even on the same hand specimen, it is very unlikely for malachite and azurite to form in equilibrium since this would require a specific and unique set of environmental parameters, in particular pH, temperature and carbonate activity. There are no known studies on azurite to malachite pseudomorphs.

Using paired *t*-tests, this study suggests that azurite has no significant impact on the $\delta^{18}O$ or $\delta^{13}C$ values in the malachite samples. This agrees with the work by previous investigators since the azurite in this study was most likely formed on the same hand specimen as the malachite.

There are no known studies on the relationship between atacamite and malachite isotope compositions. This study suggests that atacamite has no significant impact on the $\delta^{18}O$ values in archaeological malachite.

Since most samples included in this study are mixed phase, it is not possible to make confident conclusions on the isotopic impact of various contaminants. This study suggests that moderate amounts of azurite (up to 61%) and atacamite (up to 59%) have no statistically significant impact on the $\delta^{18}O$ and $\delta^{13}C$ compositions in archaeological malachite samples, but other contaminants could be more effective. The picking technique for malachite crystal isolation from mixed-phase patinas needs improvement, but a way to do this without risking oxygen-isotope exchange is not known.

Incorporation of Environmental Parameters

$\delta^{18}O$ in Local Meteoric Water

The relationship between $\delta^{18}O$ in malachite and $\delta^{18}O$ in the local meteoric water is addressed relative to the previous work done by Melchiorre in Chapter 7. The linear regression distribution presented by Melchiorre (**figure 7.7**) looks very good due to a set of values above and below -10‰ and -5‰, but demonstrates variance and little correlation between these values. Melchiorre clearly made a point to collect malachite samples from regions with distinctly low (significantly below -10‰) and high (significantly above -5‰) $\delta^{18}O$ values in precipitation to expand the range and improve the regression shown in **figure 7.7**, which is easy to accomplish in the US, where there is good latitudinal effect (refer to **figure 3.4**). This project did not collect samples from regions with more extreme $\delta^{18}O$ values in precipitation. Consequently, this study does not suggest a statistically significant relationship between the $\delta^{18}O$ in archaeological malachite and the $\delta^{18}O$ in local meteoric water. It is possible that cleaner archaeological malachite, water sample collection, and including more samples from regions very high or low in $\delta^{18}O$ values could result in a small relationship between $\delta^{18}O_{malachite}$ and $\delta^{18}O_{water}$, but this is still not good enough for confident provenance investigations. At most, if a malachite sample needs to be

allocated to one of a few sites with radically different $\delta^{18}O$ values in precipitation, this work may be used as a guide.

Temperature

Plotting the B1 $\delta^{18}O_{malachite}$ against the surface temperature of a representative site (refer to **figure 7.10**) produces a statistically insignificant linear regression. The scatterplots (**figure 7.17 and 7.18**) of B1 and B2 $\delta^{13}C_{malachite}$ against modern surface temperatures from correlating sites also do not suggest a linear relation. These data are plotted because previous investigations have reported that the calculated formation temperatures of malachite are often close to modern ambient air temperatures when using $\delta^{18}O$ values of local meteoric water (Haßler *et al.* 2014, 15; Melchiorre *et al.* 1999, 255).

To demonstrate the relationship between calculated formation temperature and surface temperature, Melchiorre's temperature data on malachite ores are plotted (**figure 8.2**) and as claimed, present a significant linear relationship. Using this study's archaeological malachite data, a significant regression is again demonstrated (**figure 7.8**). However, this result is suspicious given that the isotopes in archaeological malachite do not show any significant trends with surface temperature (**figures 7.10 and 7.17**). For this reason, regression analyses for $\delta^{18}O$ and $\delta^{13}C$ versus surface temperatures on Melchiorre's data was carried out. The results on Melchiorre's data show that there are no significant relationships between surface temperature and the $\delta^{18}O$ or $\delta^{13}C$ values in malachite ores ($\delta^{18}O$: $y = 0.05x + 23.3$, $R^2 = 0.009$, $F_{1,60} = 0.6$, $p = 0.5$; $\delta^{13}C$: $y = -0.09x + 7.8$, $R^2 = 0.01$, $F_{1,60} = 0.8$, $p = 0.4$) (**figures 8.3 and 8.4**).

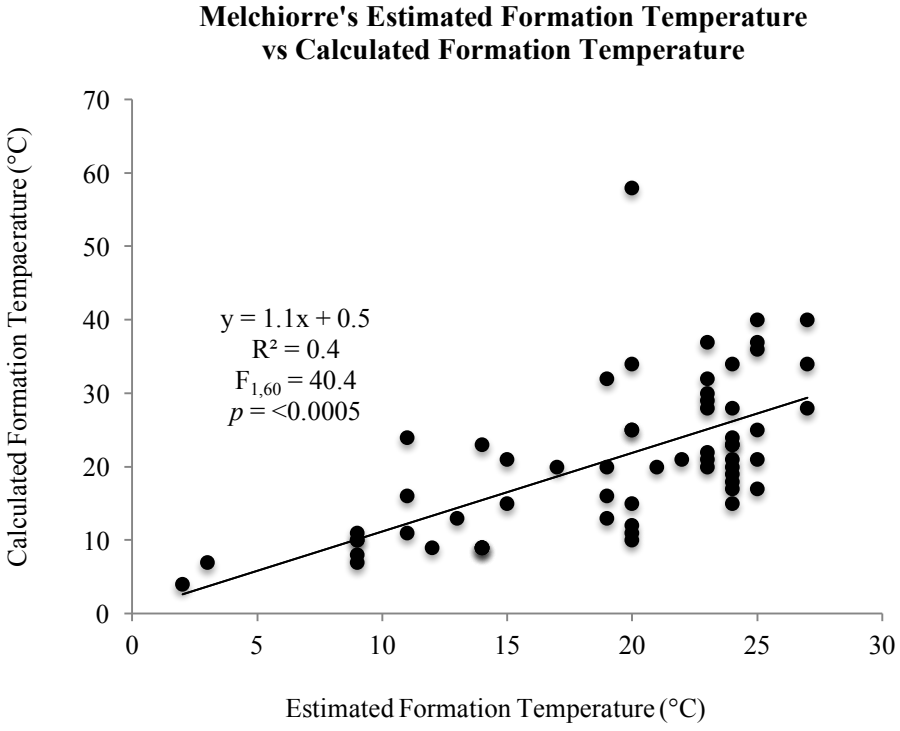


Figure 8.2: Scatterplot for Melchiorre's malachite ore data, showing calculated formation temperatures against average modern surface temperatures. A statistically significant linear correlation is apparent. Data from Melchiorre 1998, 97-100.

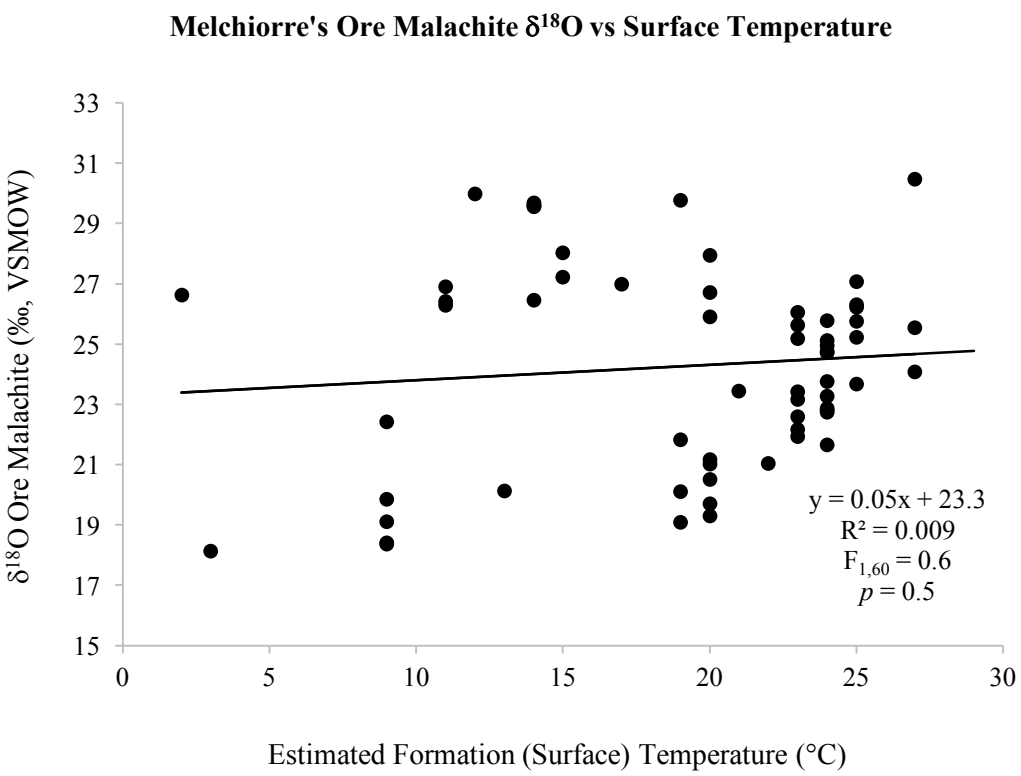


Figure 8.3: Scatterplot of Melchiorre's data on $\delta^{18}O$ in malachite ores versus surface temperatures, showing that there is no significant relationship.

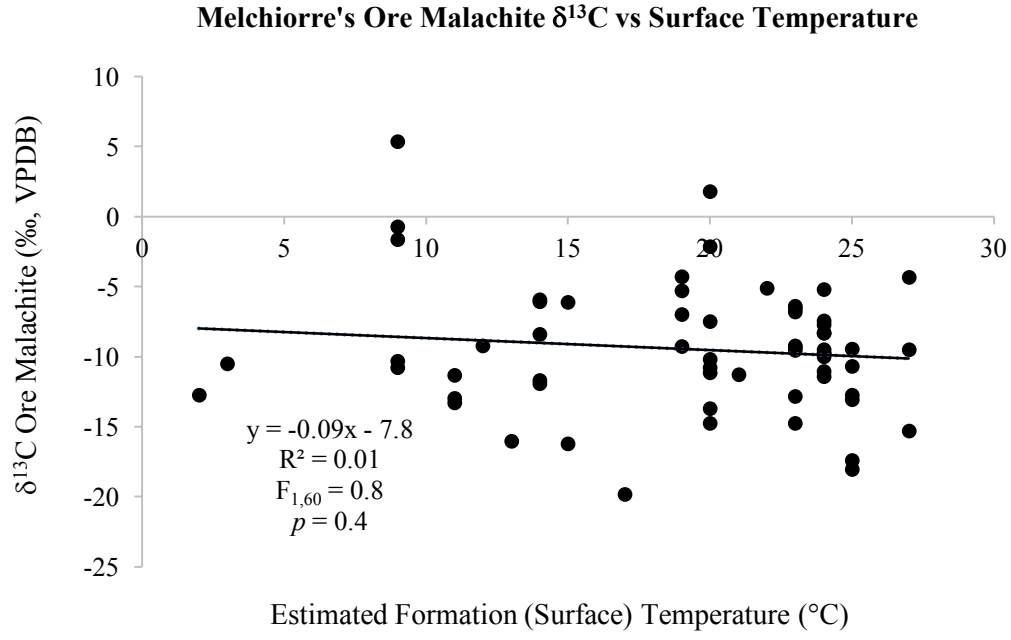


Figure 8.4: Scatterplot of Melchiorre's data on $\delta^{13}C$ in malachite ores versus surface temperatures, showing that there is no significant relationship.

Malachite usually forms in soils, where temperatures are constantly fluctuating through daily and seasonal cycles, and are affected by meteorological events. When factors such as geographic location, vegetation and soil water conditions are added, predicting soil temperature

becomes even more complicated and difficult. Moreover, we can question how representative a soil at the time of excavation is of the formation soil. It is important to remember that objects move in the ground, sometimes to different soil horizons with different temperatures. There are samples in the current study (from Ningxia) that were picked off the ground surface. It is unlikely that the malachite formed at the surface because this environment is more likely to form other copper corrosion minerals (brochantite). More likely, the objects resurfaced recently, and the malachite formed on them while in the ground.

Altogether, these results on temperature indicate that, although there is a correlation between the surface temperatures and calculated formation (soil) temperatures at the same location, the use of surface temperatures extends too far for this type of work, and they will not always serve as a suitable proxy for the formation temperature of malachite. It is probable that for this reason, previous investigations have focused on estimating formation temperatures by calculation using $\delta^{18}O$ in local meteoric water. These investigations then compared the calculated formation temperatures to estimated average surface temperatures at the site of interest to gauge the reliability of the calculated temperatures. The reliability of this approach, however, is misleading.

Köppen Climate

When the mean $\delta^{18}O$ values in malachite are arranged in increasing order (**table 7.23**), the resulting Köppen climate sequence hints at a few trends. In general, it appears that the temperate climates are concentrated in the center of the sequence. The two desert climates are together and associated with lower $\delta^{18}O_{malachite}$ means. Grouping of desert and semi-arid climates suggests that the amount of precipitation is more influential on isotopes than temperature during the formation of malachite. The reverse seems the case for temperate climates, which appear more sensitive isotopically to seasonal temperature changes. Climates with hot summers are at the center of the sequence and are bracketed by warm summer climates, followed by the arid and semi-arid. Obviously, the sequence begins and ends with temperate climates, which goes against the general observations discussed thus far. These climates are associated with Guangxi (Cfa) and England (Cfb). The malachite samples from Guangxi used in this study have unknown provenance within Guangxi, with one sample potentially from outside Guangxi (refer to site profiles section in Chapter 5). It is therefore possible that the samples are from more than one site. The best explanation is that the true formation climate of the Guangxi samples analyzed is not Cfa. This argument cannot be used to explain why England (Cfb) is not listed more centrally in the climate sequence. It is possible that a parameter not included in the climate classification criteria is causing this variation. Malachite forms in soils, where additional factors can play a major role in isotope behavior, including pH.

For $\delta^{13}C$, all but one of the arid and semi-arid climates are on the high half of the $\delta^{13}C$ rank table (**table 7.26**). Otherwise, there are no clearly defined patterns. Likewise, Melchiorre's desert malachite samples from Arizona, Utah and Chile consistently had higher $\delta^{13}C$ values (Melchiorre

et al. 1999, 252). Smith's highest samples precipitated in what he described as sandy soils (1978, 131). Because both hot and cold deserts are listed similarly, it is not likely that temperature is the controlling parameter. It may be the case that the arid and semi-arid climates were grouped only because they offer extreme, yet more stable environments, and this is apparent in the $\delta^{13}C$ values and climate ranking. Ultimately, $\delta^{13}C$ is complicated by multiple factors, and climate alone is not the main controlling parameter for $\delta^{13}C$ values in malachite. Plant densities, mixed vegetation types, soil porosity, water residence times and contribution from inorganic carbon reservoirs all make a significant impact.

Climate as a multidimensional approach is considered in place of multivariate analyses, and the outcome suggests the controlling environmental variables are different for each climate. This is important for future investigations because it means a general framework cannot be applied. To determine the controlling parameters, a climate-focused approach needs to be considered, perhaps beginning with collecting desert malachite samples from around the world.

8.3.2. Discussion by Geographic Group

Hungary

The Hungarian malachite samples came from a collection of corroded bronze objects sold together as a hoard, but their excavation site is unknown. The implication is that the bronzes were found together and corroded in the same spot. This further implies that the isotopic ratios derived from the malachite on these bronzes should be approximate to one another.

Since there is no known excavation site for the samples within Hungary, Debrecen is chosen as a proxy for estimating most environmental parameters. Debrecen has a yearly daily air temperature mean of 10.6ºC and $\delta^{18}O$ in meteoric water of -7.7‰ (refer to **table 5.2**). For calculations, this data is used as proxies for the formation $\delta^{18}O$ and temperature of the Hungarian malachite samples. Based on the GNIP map that places Hungary in a zone with $\delta^{18}O$ in meteoric water ranging between -11‰ and -8‰, these calculations yield a realistic yet broad range of $\delta^{18}O$ in formation water from -11.9‰ to -8.8‰ (refer to **figure 5.11** and **table 7.22**). The calculated formation temperatures range from 15.8ºC to 31.3ºC, which is warm and suggests the malachite samples primarily formed nearer the surface during the spring and summer months.

The broad range in calculated temperature and $\delta^{18}O$ values suggests that the samples did not corrode in the same temperature and water, and more likely have varying provenance within Hungary. This does not mean that they were not excavated as a hoard. It is possible that the hoard was assembled in antiquity using objects that were already corroded, and the corrosion preserved the isotopic information of the formation environment.

The malachite $\delta^{13}C$ values range from -14.1‰ to -12.1‰, which is a central range when considering the full study's $\delta^{13}C$ data (refer to **table 7.10**). The biome in most of Hungary is dominated by deciduous forest, brown earth soils and Cfb climate (**table 5.2**). Most woody trees

are C_3, which tend to yield low $\delta^{13}C$ values compared to C_4 and CAM plants (refer to section 3.6). Based on this estimated environmental information, one could assume that the $\delta^{13}C$ values from the Hungarian samples would scale relatively low when considering all data, but instead the $\delta^{13}C$ data suggests a considerable contribution from heavier carbon sources like atmospheric CO_2 and soil DIC. Moreover, the $\delta^{13}C$ data varies enough to further support the theory that these samples may not have corroded together as a hoard.

The possibility that the data spread could simply be due to the variation in sample purity was explored. According to micro-sample XRD analysis, the Hungarian samples ranged from 46% to 100% malachite, with the typical contaminants being tenorite (CuO), quartz (SiO_2) and, in one sample, sodalite ($Na_8Al_6Si_6O_{24}Cl_2$) (refer to **table 7.1**). It is not likely that these impurities impact $\delta^{13}C$ results in malachite because they do not contain carbon. Other carbonate phases, however, can alter the $\delta^{13}C$ data. Sample H5 contained 21% dolomite ($CaMg(CO_3)_2$), which could be why its $\delta^{13}C$ value is on the higher end of the Hungarian $\delta^{13}C$ data set, however it is not an outlier (refer to section 7.2.1).

A paired *t*-test suggests that there is no significant difference between the B1 and B2 $\delta^{18}O$ datasets (refer to section 7.2.1 and **table 7.14**). However, a paired *t*-test focused on the Hungarian $\delta^{18}O$ data does show a significant difference: $t_{10} = 0.8$, $p = 0.4$, 95% CI [-0.7, 0.3]. The B1 and B2 datasets for $\delta^{13}C$ had a different *t*-test result, suggesting that there is a significant difference, but the Hungarian B1-B2 $\delta^{13}C$ *t*-test result does not support this: $t_{10} = 4.3$, $p = 0.002$, 95% CI [-1.4, 0.4]. In other words, the Hungarian B1 and B2 datasets suggest the opposite of the full B1 and B2 study, which is that meticulous picking matters for $\delta^{18}O$ analysis, but not $\delta^{13}C$. In each case, the B2 sample yielded a higher $\delta^{13}C$ value, which is likely due to the degree and type of contamination in the samples.

Sitka, Alaska, USA

The Alaskan samples were collected from objects excavated at the Castle Hill rock outcrop in Sitka, which is a historical site of Tlingit and Russian forts. Since these samples came from the same place, their isotopic ratios were expected to be approximate. Sitka has a yearly daily air temperature mean of 7.4ºC and $\delta^{18}O$ in stream water of -11.4‰ (**table 5.2**). This data is used as proxies for the formation $\delta^{18}O$ and temperature of the Alaskan malachite samples and are used in calculations. These calculations yield a range of data for $\delta^{18}O$ in formation water from -11.1‰ to -10.1‰, and a formation temperature range from 2.1ºC to 6.0ºC, which is lower than the ambient mean (**table 7.22**). This is sensible since soils are typically cooler than surface temperatures (refer to section 3.3.1).

Although -11.4‰ for $\delta^{18}O$ in meteoric water is a relatively low value, it is high for the latitudinal zone, which more commonly has values between -22 and -18‰ (refer to the GNIP map in **figure 5.23**). It is likely that Sitka's climate, which has been significantly moderated by its

coastal position in the south, has had a stronger influence on the isotopes in the meteoric water than the latitude effect.

When considering this study's full $\delta^{13}C$ dataset, the Alaskan malachite samples have relatively centrally scaled $\delta^{13}C$ values, ranging from -15.9‰ to -13.0‰. Alaska has a Cfb climate, lithosol and boggy soils, and a coastal alpine biome (**table 5.2**). This implies the presence of woody trees, which often use the C_3 pathway (refer to section 3.6.3). These environmental factors should theoretically lend to lower $\delta^{13}C$ values, but it seems the Alaskan malachite samples inherited considerable $\delta^{13}C$ from heavier carbon sources like atmospheric CO_2 and soil DIC.

The possibility that the isotopic spread of relatively low $\delta^{13}C$ values could simply be due to a variation in sample purity was explored. According to micro-sample XRD analysis, the Alaskan samples ranged from 38% to 100% malachite, with the only contaminants being atacamite ($Cu_2Cl(OH)_3$) and quartz (SiO_2) (refer to **table 7.2**). Three of the five samples were reported as 100% malachite. These impurities do not likely impact $\delta^{13}C$ results in malachite because they do not contain carbon. However, visual descriptions for some of the Alaskan samples contained organic material (refer to the microscope photographs in Appendix E), which would not be revealed by XRD, but may impact the $\delta^{13}C$ values. The variation in $\delta^{13}C$ values suggests each sample must have corroded in unique microenvironments within the fort. There are several important environmental factors that could be causing this variation, but they cannot be explored due to a lack of information, such as burial depth, the degree of corrosion and the type of fill that was used in the fort.

A paired *t*-test suggests that there is no significant difference between the B1 and B2 $\delta^{18}O$ datasets. Yet, a paired *t*-test focused on the Hungarian $\delta^{18}O$ data does show a significant difference: $t_4 = 1.7$, $p = 0.2$, 95% CI [-0.4, 1.4]. The B1 and B2 datasets for $\delta^{13}C$ had a different *t*-test result, suggesting that there is a significant difference, and the Alaskan B1-B2 $\delta^{13}C$ *t*-test result supports this: $t_4 = 0.9$, $p = 0.4$, 95% CI [-0.5, 1.0]. In other words, the Alaskan B1-B2 $\delta^{18}O$ and $\delta^{13}C$ *t*-test results suggest that meticulous picking has a significant impact both isotope studies.

It is assumed that the pairs with larger $\delta^{13}C$ variations are due to the degree of contamination in the samples, especially if another carbonate impurity was involved. Sample B2US1 contained calcite ($CaCO_3$), which resulted in a slightly higher overall $\delta^{13}C$ value than the B1 sample. Samples US6/B2US6 produced the greatest difference between $\delta^{13}C$ values, but neither sample contained carbon-containing phases other than the malachite. As stated before, however, this sample was especially mixed-phase and XRD analysis struggles once more than three phases are present. Moreover, organic carbons are often not revealed by XRD.

Variation between Alaska's B1 and B2 malachite samples in the $\delta^{18}O$ values was different from the variation observed in the $\delta^{13}C$ data. Every Alaskan B2 sample produced a lower $\delta^{18}O$ value than the B1 sample. It is likely that there is a common oxygen-containing contaminant in these samples that has a low $\delta^{18}O$ value. Interestingly, the largest $\delta^{18}O$ difference is between US5

and B2U5, which were both reported as 100% malachite by XRD analysis. XRD has many detection limitations, and the computerized search matching that was used for this project is not perfect. This method is sensitive to sample quality, which was low for most of the mix-phase malachite samples studied (Cullity & Stock 2014, 297). These computer programs can identify phases that are actually absent, or vice versa, fail to suggest phases that are present, even if a sample contains more than 50% of the unidentified phase (Cullity & Stock 2014, 297 & 301). It is possible that this technical error can explain the difference between US5 and B2US5, but sample quality is more likely the issue.

Batán Grande, Lambayeque, Peru

The patinated copper samples used for analysis were excavated by looters from a massive burial in northern coastal Peru known as the Huaca Loro East tomb. Their exact context within the tomb is therefore not known, but it is possible that they were exposed to a microenvironment isotopically lightened by buried organics like textiles and corpses, as well as the microbes that assisted with decomposition. The yearly daily temperature mean at Chiclayo, which is Batán Grande's nearest town, is 21ºC (**table 5.2**). When this value is used as the estimate for formation temperature in the oxygen isotope thermometer equation, the $\delta^{18}O$ of the formation water in the two Peruvian samples is calculated to be -8.6‰ and -8.8‰ (**table 7.22**). These values are lower than the suggested -2‰ to -6‰ range represented by the orange zones on the GNIP map of South America in **figure 5.26**, but is consistent with exposure to isotopically lighter burial environments.

A formula-based estimate of $\delta^{18}O$ for the imbibed water in human bone carbonate from ancient individuals buried at Lambayeque are determined to have a mean of -5.1‰ (Turner *et al.* 2013, 33). This value is used as the estimate for formation $\delta^{18}O_{water}$ in the malachite samples, which yielded hot formation temperatures of 39.6ºC and 40.4ºC (**table 7.22**). Chiclayo does not maintain these high temperatures during any time of the year, and it is suspected that the $\delta^{18}O_{water}$ data used as an estimate for the formation water is too high to be properly representative.

Despite having different compositions, the $\delta^{13}C$ values from the Peruvian malachite samples are closely comparable (-15.0‰ and -14.9‰). These are moderately high values when considering the full $\delta^{13}C$ dataset, which is sensible for a mixed contribution from a coastal BWh climate with dry sand and a desert shrub (C_4 pathway) biome (refer to section 3.6.3 and **table 5.2**). According to XRD analysis, sample P2 contained just 26% malachite and sample P3 contained 48%, with the main impurities being quartz (SiO_2), atacamite ($Cu_2Cl(OH)_3$) and cuprite (CuO), which are typical of coastal desert climates (refer to **table 7.3**). These impurities do not likely impact $\delta^{13}C$ results in malachite because they do not contain carbon. This is supported further by sample B2P2, which has slightly more malachite than P2 (B2P2 = 29% malachite, P2 = 26% malachite). Most this sample is atacamite, yet the $\delta^{13}C$ value is -14.9‰, which is very close to the P2 result. The $\delta^{18}O$ values for B1P2 and B2P2 are also comparable (25.1‰ and 25.5‰,

respectively). There is no B2 sample for P3. With only one B1-B2 pair, there is insufficient data for comparative statistics like *t*-tests.

Two malachite ore samples found at Batán Grande are analyzed isotopically. These samples are much cleaner (P6g was 100% malachite and P7g was 82% malachite with the rest quartz) and, like with the Ningxia ores (discussed later), yield $\delta^{13}C$ values lower than the archaeological malachite samples (-15.2‰ and -15.8‰, respectively). The formation site of the ores found in the tomb at Batán Grande is not known, but it is possible that it offered an isotopically lighter carbon reservoir. The oxygen-18 ratios in the malachite ores are higher than the archaeological samples, yielding 28.5‰ for P6g and 26.5‰ for P7g. It is possible that oxygen-containing impurities are responsible for the variation in $\delta^{18}O$ values, or that they formed at very different times or soil depths, but their comparable $\delta^{13}C$ values support that they formed in similar soils.

Episkopi and Pyla-Kokkinokremos, Cyprus

Three samples from two sites were combined to represent southern, coastal Cyprus. The estimated formation temperatures, however, are based on the surface temperatures at towns near the excavation site (Limassol/Episkopi) = 18.7ºC, Larnaca/Pyla-Kokkinokremos) = 19.5ºC) (**table 5.2**). Using these temperatures in the geothermometer equation, the resulting $\delta^{18}O$ values for formation water ranges from -6.5‰ to -6.6‰ (**table 7.2**). These values fit within the range presented in the GNIP isoscape map of Europe (**figure 5.22**), which shows Cyprus in a zone with $\delta^{18}O$ values in precipitation between -8‰ and -5‰. This suggests that using surface temperatures as estimations for formation temperature works for the Cypriot samples. Considering that most of the Cypriot samples had to be eliminated from the study for containing brochantite, which is mainly an atmospheric mineral, it is suspected that the samples formed near the ground surface, where temperatures are warmer and the soil has more contact with the air.

Using Nicosia as a proxy site, the $\delta^{18}O$ in meteoric water (-5.9‰) yielded a realistic yet warm formation temperature range between 21.8 – 22.2ºC through the geothermometer equation (**table 5.2, table 7.22**). These temperatures are slightly higher than the ambient mean temperatures at the archaeological sites, suggesting that the malachite formed during the summer, in lighter water, or both.

The $\delta^{13}C$ values of the Cypriot samples are among the highest of this study (mean = -10.9 ± 1.5‰), as is expected of semi-arid coastal climates dominated by a chaparral biome (C_4 pathway) and calcaric soils (refer to sections 3.6.3, 5.2.4 and **table 5.2**). The malachite sample from Pyla-Kokkinokremos is the lowest out of the three. The possibility that this could simply be due to a variation in sample purity was explored. According to micro-sample XRD analysis, the Cypriot samples ranged from 27% to 68% malachite, with the contaminants being copper (II) chloride hydroxides and calcite ($CaCO_3$), which are both typical of arid climates and coastal regions like Cyprus (**table 7.4**). Copper (II) chloride hydroxides do not likely impact $\delta^{13}C$ results in malachite,

which makes sense because they do not contain carbon. Other carbonate phases like calcite, however, will alter the $\delta^{13}C$ values. Each Cypriot sample contained calcite. The samples from Episkopi had the same proportions of malachite and calcite, therefore yielding comparable $\delta^{13}C$ values. It was difficult to determine the proportions of each phase present in the sample from Pyla, with possibilities ranging from 27-57% malachite and the rest copper (II) chloride hydroxides and calcium carbonates. This sample yielded a lower $\delta^{13}C$ value than the two from Espikopi with less malachite, suggesting that a lower proportion of calcium carbonate is present, offset by the copper (II) chloride hydroxides that were not present in the Episkopi samples. Alternatively, the soil CO_2 at Pyla-Kokkinokremos is significantly lighter than at Episkopi. Contaminations cannot be explored further because there are no B2 samples for Cyprus.

Las Pilas, Mojácar, Spain

This study included one malachite sample from Spain, collected from an axe head excavated near the modern city of Mojácar in Almería. Mojácar is in the most arid region of Europe, with a yearly daily mean surface temperature of 20ºC. When this temperature is used as an estimate for the formation temperature of the malachite sample, a formation water $\delta^{18}O$ value of -5.5‰ is calculated using the oxygen isotope geothermometer equation, which matches the local meteoric water data from a GNIP meteoric station in Almería (-5.5‰). When the $\delta^{18}O$ value of the meteoric water is used to calculate formation temperature, the result is 20.1ºC.

The Spanish sample was 100% malachite and yielded a $\delta^{13}C$ of -11.9‰, which is relatively high compared with all the other malachite samples included in this study. This makes sense considering it formed in a chaparral (dominated by grasses and shrubs that prefer the C_4 pathway) with sierozem soil, which lends to heavier isotopes from inorganic carbon sources (refer to section 3.6.3).

There are no B2 samples for Spain, but there are two malachite ore samples, which yielded $\delta^{13}C$ values of -11.6‰ and -9.1‰, and $\delta^{18}O$ values of 27.1‰ and 27.0‰, respectively. Like the B1 Spanish sample, the ores were also 100% malachite. These samples are not from the same site; all that is known is that they are also from southeastern Spain. Two different, yet similar formation locations would explain the variation in carbon isotope ratios, but similarity in oxygen isotope ratios. The malachite ore samples are higher for $\delta^{13}C$ and lower for $\delta^{18}O$ than the archaeological sample, which is opposite to the examples from Peru and Ningxia. However, with so few samples and non-specific formation sites, there is hesitation to suggest confident explanations based on this data.

Southern England

The same meteoric water $\delta^{18}O$ value is used as an estimate for the formation water of all English samples, which is -7.3‰ (Wallingford, Oxfordshire). The estimated formation temperatures used for each sample, however, is based on the atmospheric temperatures of the

excavation site. Calculating formation temperature using the oxygen isotope thermometer equation and the estimated $\delta^{18}O$ for formation water suggests that the English malachite samples formed in a considerable range of temperatures (5.3ºC – 19.9ºC) (**table 7.22**). Outlier sample (E3) produced the 19.9ºC, so the temperature range can be reduced to 5.3ºC to 13.2ºC. Sample E3 was collected from a coin in a hoard found in Pewsey, Wiltshire. When in current circulation, coins are constantly exchanged in transactions and moving geographically. It is possible that this coin corroded in another environment. Alternatively, it is possible that the coin corroded during a hot summer nearer the surface. No other coins from this hoard were sampled for comparison.

When surface air temperatures are used as estimates for formation temperature in the oxygen isotope thermometer equation, the following range of $\delta^{18}O$ in formation water is calculated: -5.5‰ to -9.4‰ (**table 7.22**). Outlier E3 is responsible for the -9.4‰ value, and when removed, the range is reduced to -5.5‰ to -8.0‰. Most of the samples are higher than the yearly average $\delta^{18}O$ value of meteoric water in Wallingford. This suggests that Wallingford is not representative for all sites in southern England. Sample E3's low $\delta^{18}O$ value again suggests it formed at a warmer temperature.

The lowest $\delta^{13}C$ values found in the full study are from the English samples. Smith analyzed 41 English malachite samples, creating the most extensive known dataset for England, which yielded a mean average of -15.2‰, PDB (1978, 128-9). As with the current study, these samples make up Smith's lowest collection on $\delta^{13}C$, but Smith's data is much lower than what was obtained for this study. England has a Cfb climate, brown calcareous earths, and a biome historically consisting of woody trees (refer to section 3.6.3 and **table 5.2**). These environmental factors are not expected to lend to the low $\delta^{13}C$ values. The best explanation for this inconsistency is that these malachite samples inherited considerable $\delta^{13}C$ from heavier carbon sources like atmospheric CO_2 and soil DIC. The latter is a strong possibility given the soil type.

The reliability of this study's $\delta^{13}C$ values is examined by assessing sample purity. According to micro-sample XRD analysis, the English samples ranged from 25% to 100% malachite, with the typical contaminants being atacamite ($Cu_2Cl(OH)_3$) and quartz (SiO_2), and two samples containing other carbonate phases: azurite ($Cu_3(CO_3)_2(OH)_2$) and calcite ($CaCO_3$) (refer to **table 7.6**). It is not likely that atacamite or quartz impact the $\delta^{13}C$ results in malachite because they do not contain carbon. Other carbonate phases will alter the $\delta^{13}C$ values, however it is not apparent in the two samples containing carbonate minerals (E3 and EC2) because their $\delta^{13}C$ values still fit within range of the other English samples. E3 is from Pewsey, Wiltshire, and has already been mentioned for having an uncharacteristic $\delta^{18}O$ value suggestive of a suspiciously warm formation temperature. E3 is predominantly azurite (41% malachite, 59% azurite), and therefore the isotope signatures being reported for E3 are probably more representative of azurite rather than malachite, though this study suggests that azurite does not have a significant impact on isotope measurements. EC2 is from Canterbury and is roughly comprised of equal parts malachite, quartz and calcite. It is

difficult to understand how this sample's isotope signatures compare to the others from Canterbury because they are spread out within the $\delta^{13}C$ range for England. Although they are from the same city, these samples are not from the same site, perhaps explaining the variation.

Sample EC2 is also the only sample contaminated with a carbonate mineral other than azurite. B2EC2 yielded a higher $\delta^{13}C$ value of -13.5‰ (EC2 was -16.5‰), suggesting that calcite can have a considerable impact on the overall $\delta^{13}C$ value reported. This is not the case for all carbonate phases, as azurite does not seem to have a significant impact. Sample pairs EC5/B2EC5 and EO2/B2EO2 were more heterogeneous than ideal, which made XRD analysis challenging.

A paired *t*-test suggests that there is no significant difference between the B1 and B2 $\delta^{18}O$ datasets. The paired *t*-test focused on the English $\delta^{18}O$ data agrees that there is no significant difference: $t_5 = 0.3$, $p = 0.8$, 95% CI [-1.3, 1.0]. The B1 and B2 datasets for $\delta^{13}C$ had a different *t*-test result, suggesting that there is a significant difference, but the English B1-B2 $\delta^{13}C$ *t*-test result does not support this: $t_5 = 1.0$, $p = 0.4$, 95% CI [-1.8, 0.8]. In other words, there is no statistical difference between the B1-B2 datasets for England, suggesting that they did not benefit from meticulous picking.

Tel Gezer, Israel

Three Israeli samples from Tel Gezer, located halfway between Jerusalem and Tel Aviv, were analyzed isotopically. The $\delta^{18}O$ values in the malachite samples range from 27.0‰ – 27.6‰, and the $\delta^{13}C$ range from -14.9‰ to -13.2‰ (**table 7.10**).

Estimated surface temperatures and $\delta^{18}O$ in meteoric water are from Bet Dagan, which is close to Tel Gezer, but on the coastal plain closer to Tel Aviv. Bet Dagan has a weighted mean $\delta^{18}O$ in precipitation of -5.2‰, and mean surface temperature of 19.4ºC (**table 5.2**). When this data is used in the geothermometer equation, a calculated formation temperature range of 25.7ºC – 29.1ºC and calculated formation $\delta^{18}O$ range of -7.1‰ – -6.5‰ is produced (**table 7.22**). The calculated formation temperatures are warm, suggesting the malachite samples primarily formed during the spring and summer months, or in water with lower $\delta^{18}O$ values than what was used as a proxy. The calculated $\delta^{18}O$ values are lower than the weighted mean $\delta^{18}O$ in precipitation at Bet Dagan, which suggests that the estimated value is too coastal, where isotopically heavier rain tends to fall. The continental effect on isotopes varies in intensity around the world, but in the case of the Israeli malachite samples used in the current study, it appears that Bet Dagan is too close to the coast to serve as a suitable proxy for formation water $\delta^{18}O$ estimates of malachite precipitated in Tel Gezer.

The $\delta^{13}C$ values for Israel are varying enough to support a theory that these samples may not have corroded simultaneously at Tel Gezer, which was active for about 3,000 years (Bullard 1969, 1). When considering this study's full $\delta^{13}C$ dataset, Israel's values are centrally scaled, which is sensible for a mixed carbon contribution from the Csa climate, rendzina soils, and with a

grassland (C_4 pathway) biome (refer to section 3.6.3 and **table 5.2**). The possibility that the isotopic spread could simply be due to the variation in sample purity was explored. According to micro-sample XRD analysis, the Israeli samples ranged from 43% to 47% malachite, with the typical contaminants being atacamite ($Cu_2Cl(OH)_3$) and quartz (SiO_2) (refer to **table 7.7**). It is unlikely that these impurities impact $\delta^{13}C$ results in malachite because they do not contain carbon. Other carbonate phases, however, will alter the $\delta^{13}C$ values. Although no peaks indicative of carbonate phases appeared in the XRD spectra, sample I2 had a couple of unidentified peaks and I4 contained more than three phases. It is possible that a carbon-containing mineral was present in these samples and altered the overall $\delta^{13}C$ signatures, or else the bronze objects on which they formed were abandoned in different ways at different times and in zones with varying blends of carbon sources. There are no B2 samples for comparative analyses.

Gansu, China

There is only one sample assumed to be from Gansu, and its excavation site within Gansu is unknown. Gansu is a long province in north-central China with considerable latitudinal, climate and soil type range. On the GNIP isoscape map of China, Gansu is predominantly located in a zone defined with a $\delta^{18}O$ in precipitation range between -6‰ and -10‰, but it is also partly in a higher zone ranging between -2‰ to -6‰ (**table 5.21**). There are several studies reporting a considerable range of weighted mean $\delta^{18}O$ in precipitation around Gansu (**table 5.1**). Lanzhou was chosen as a proxy site for the sample only because it is the capital city of Gansu. When calculating for formation temperature using GNIP's $\delta^{18}O$ data for Lanzhou precipitation (-4.8‰), the result is a very warm 28.5ºC. This is possible, but difficult to interpret in a region with extreme temperature ranges. Either this malachite sample really did form at a warm temperature, or it formed from water with a much lower $\delta^{18}O$ than in the precipitation at Lanzhou. **Table 5.1** offers several alternative proxy sites with lower $\delta^{18}O$ in precipitation. Jiuquan has the lowest $\delta^{18}O$ in precipitation (-11.3‰), which would suggest a formation temperature below freezing when used in the geothermometer equation (-0.7ºC). Any of the Gansu cities with $\delta^{18}O$ in precipitation ranging between Lanzhou's -4.8‰ and Jiuquan's -11.3‰ could serve as representative of the formation site by yielding calculated formation temperature results in the geothermometer equation that are realistically possible. More data is needed to guide estimating formation provenance.

The single sample from Gansu yielded a $\delta^{13}C$ value of -12.1‰. This is a moderately high value when compared to the full $\delta^{13}C$ dataset, suggesting formation in an arid area with C_3 plants like grasses and shrubs, and a stronger influence from atmospheric CO_2 and soil DIC. This description fits most of Gansu. XRD analysis suggests that this malachite sample was pure, at 100% malachite. Although perfect for isotope studies using MS, the lack of contaminants that could guide in the identification of soil type makes it challenging to narrow down provenance within Gansu. There is no B2 sample for Gansu.

Guangxi, China

There are four malachite samples from Guangxi, but their exact formation sites are unknown. Guangxi is in south-central China, where it is partly mountainous and in a monsoon influenced subtropical climate. GNIP's $\delta^{18}O_{water}$ isoscape presented in **figure 5.32** shows Guangxi in a zone defined as having precipitation $\delta^{18}O$ between -6‰ and -10‰. There are two known cities in Guangxi with meteoric stations, which are Guilin and Liuzhou. Neither of these stations is representative for any of the Guangxi malachite samples because the formation temperatures that are calculated when using $\delta^{18}O$ in precipitation data from them are very high. The $\delta^{18}O$ in precipitation at Guilin is -6.2‰, which yields a formation temperature range of 38.6ºC – 48.4ºC with the oxygen isotope thermometer equation (**table 7.22**). Liuzhou has similar $\delta^{18}O$ in precipitation data that also yields suspiciously high formation temperatures. Although it is possible for malachite to form in these temperature ranges, they are not likely found within Guangxi's soil profile. The Guangxi malachite samples more likely formed at cooler temperatures that reflect the local air temperatures using water with lower $\delta^{18}O$ values. The average yearly air temperature at Guilin is 21.8ºC, which suggests $\delta^{18}O$ in formation water of -11.0‰ to -9.3‰ (**table 7.22**). There are no meteoric stations in or near Guangxi with $\delta^{18}O$ in precipitation that are this low. This does not mean that these values are not possible in Guangxi, but only that there are no stations in representative locations for the sample sites. Lower $\delta^{18}O$ values are often found inland, and at higher altitude and latitude. It is possible that these samples are from one of the mountainous areas of Guangxi. Alternatively, they formed in non-meteoric water, like groundwater or a river carrying a mix of water from various origins.

The $\delta^{13}C$ values in the Guangxi malachite samples range from -16.0‰ to -11.7‰, which is varying enough to support a theory that these samples may not have corroded at the same site (**table 7.11**). Guangxi is in a Cfa climate dominated by rainforest and an alpine biome at higher altitudes (**table 5.2**). There are two main soil types in Guangxi, which are red earths and limestone soils. These contrast considerably with regard to carbonate presence (limestone soils have it in abundance), and it is therefore reasoned that the samples with higher $\delta^{13}C$ values (CGS2 and CGS4) formed in the limestone soil regions. Nonetheless, the possibility that this could simply be due to the variation in sample purity was explored. According to micro-sample XRD analysis, the Guangxi samples ranged from 62% to 100% malachite, with the typical contaminants being azurite ($Cu_3(CO_3)_2(OH)_2$), quartz (SiO_2) and in one sample, pyromorphite ($Pb_5(PO_4)_3Cl$) (**table 7.9**). Apart from CGS4, which was reported to be 100% malachite, each sample contained at least three different phases and had unidentified peaks. It is unlikely that carbon-free phases impact $\delta^{13}C$ results in malachite. This study has statistically suggested that azurite, although it contains carbon, does not significantly impact the isotope ratios of the analyzed samples. Therefore, the contaminants present in the Guangxi samples are not likely responsible for this isotopic spread.

There are two B2 samples for Guangxi. The B2 sample for CGS3 yielded a XRD spectrum for 100% malachite, whereas the supposedly purer B1 sample was only 81% malachite and the rest azurite (**table 7.9**). The fact that XRD analysis suggested that the roughly picked B2 sample is 100% pure, when the visual description using a binocular microscope notes what looks like cuprite, clay and calcite as contaminants, is suspicious. If another carbonate mineral like calcite was truly present, but somehow was not detected by XRD, then it is possible that the measured $\delta^{13}C$ data is not representative. What is certain is that sample B2CGS3 was not 100% malachite. With the other B1-B2 pair, CGS4 was 100% malachite and the B2 sample was contaminated with 11% cuprite.

A paired *t*-test suggests that there is no significant difference between the B1 and B2 $\delta^{18}O$ datasets. The paired *t*-test focused on the Guangxi $\delta^{18}O$ data also does not show a significant difference: $t_1 = 0.7$, $p = 0.6$, 95% CI [-4.7, 4.2]. The B1 and B2 datasets for $\delta^{13}C$ had a different *t*-test result, suggesting that there is a significant difference, but the Guangxi B1-B2 $\delta^{13}C$ *t*-test result did not support this: $t_1 = 1.5$, $p = 0.4$, 95% CI [-2.8, 2.2]. In other words, the Guangxi B1-B2 $\delta^{18}O$ and $\delta^{13}C$ *t*-test results suggest that meticulous picking does not have a significant impact on either isotope studies.

In all, the isotope data for the Guangxi samples are suspicious because they yield extreme formation temperatures up to 48.4ºC. These samples have no known site within Guangxi, but instead of agreeing with the suggestion that they formed in Guangxi, isotopic analyses are suggesting that these samples may not even be from southern China.

Jiangsu, China

One malachite sample is labeled from Jiangsu, but its exact provenance is unknown. The GNIP $\delta^{18}O$ in precipitation isoscape of Asia shows Jiangsu in a -6‰ to -10‰ zone (**figure 5.32**). The capital of Jiangsu, Nanjing, was used as a site proxy for the formation environment. The mean annual air temperature used in calculations is 16.0ºC, and the long-term weighted mean $\delta^{18}O$ in precipitation is -8.0‰ (**table 5.2**). When this value is used as a proxy for the $\delta^{18}O$ in the formation water, a formation temperature of 16.7ºC is calculated using the oxygen isotope thermometer equation. This value is close to the air temperature in Nanjing, but a bit warmer, suggesting the malachite may have formed nearer the surface in the spring and summer months. Alternatively, the malachite sample may have formed in water with a lower $\delta^{18}O$, perhaps someplace more northern where the latitudinal effect can yield such values. There are no other meteoric stations in or near Jiangsu that measure $\delta^{18}O$ in precipitation. Nevertheless, the calculated results are sensible and there is no doubt that the malachite sample could be from Jiangsu.

After England, the second to lowest $\delta^{13}C$ sample is the one from Jiangsu (-16.5‰). A low $\delta^{13}C$ value is expected in carbonates formed in a Cfa climate with deciduous forest biome (refer to section 3.6.3). It is possible that this sample inherited a larger portion of its $\delta^{13}C$ from organic soil

CO_2. The reliability of this value was evaluated by considering its purity. According to micro-sample XRD analysis, the Jiangsu sample was 94% malachite and the rest sodalite (blue mineral, $Na_8Al_6Si_6O_{24}Cl_2$) (**table 7.10**). It is unlikely that these minerals impact $\delta^{13}C$ results in malachite because they do not contain carbon. It is unclear how the oxygen in the sodalite may have affected the $\delta^{18}O$ values. It could be that it lowered the overall value, and the Nanjing data is more representative than it appears.

There is a B2 sample for Jiangsu, which was comprised of 24% malachite, 71% azurite ($Cu_3(CO_3)_2(OH)_2$) and 5% quartz (SiO_2), and yielded a $\delta^{13}C$ value of -13.6‰ (**table 7.10**). This study statistically shows that azurite does not tend to yield higher $\delta^{13}C$ values in the samples, but this case may be different because there was significantly more azurite, in fact being the dominant mineral present. The $\delta^{18}O$ value in B2CJN is also considerably higher than in the B1 sample, but again this could be due to the dominance of azurite in the sample.

Jiangxi, China

Jiangxi is represented by one malachite sample, found at the Niucheng archaeological site in Xingan. The average surface temperature of the nearest city, Ji'an, is used as an estimate for the formation temperature. This results in a $\delta^{18}O$ in formation water of -7.0‰ when inserted into the geothermometer equation. This value fits within one of the GNIP isoscape zones in Jiangxi, which is defined by a range between -6‰ and -10‰ (**figure 5.32**). The calculated value is lower than the average $\delta^{18}O$ value in precipitation from either of the two meteoric stations in Jiangxi, but closest to that of Yingtan, which is -5.6‰. This suggests that the $\delta^{18}O$ in precipitation at Niucheng is lower than at Yingtan and Qianyanzhou.

The single sample from Jiangxi yielded a $\delta^{13}C$ value of -11.6‰. This is relatively high, which is surprising for a carbonate that formed in a Cfa rainforest climate (refer to section 3.6.3). This malachite sample inherited a significant amount of $\delta^{13}C$ from atmospheric CO_2 and soil DIC. XRD analysis suggests that this malachite sample was exceptionally pure, at 100% malachite. Although perfect for isotope studies using MS, the lack of contaminants that could guide in the identification of soil type makes it impossible to confirm Niucheng as the formation site. There is no B2 sample for Jiangxi, but Melchiorre included one sample from Hunan province, which neighbors Jiangxi to the west. This malachite sample yielded Melchiorre's lowest $\delta^{13}C$ value at -19.9‰, which is a drastic contrast to the Jiangxi value, but more sensible considering the climate and biome. It is not understood why these samples inherited such strongly opposing $\delta^{13}C$ values, and there are no other samples to represent either province for comparison.

Ningxia, China

Five of the six malachite samples from Ningxia were collected from slag fragments found on the ground surface at the west of the region near the Gobi Desert. The sixth sample is from a

museum object, with no known site and is only suspected to be from Ningxia. On the GNIP isoscape map in **figure 5.32**, Ningxia is in a zone defined with $\delta^{18}O$ in precipitation ranging between -6‰ and 10‰. Environmental data was collected from the meteoric station in the Shapotou district, Zhongwei, which is noted for the Tengger Desert, and boarders Inner Mongolia to the north. The average yearly surface temperature at this station is 10.9ºC, and the mean $\delta^{18}O$ value in precipitation is -7.2‰, which fits within the range suggested by the GNIP isoscape (**table 5.2**).

When the estimated formation temperature is used in the oxygen isotope thermometer equation to calculate for $\delta^{18}O$ in formation water, the result is a range between -14.6‰ and -9.1‰ (**table 7.22**). The estimated $\delta^{18}O$ in precipitation yields calculated formation temperatures ranging from 19.7ºC to 50.2ºC (**table 7.22**). This suggests that either the samples formed in suspiciously hot temperatures, or in waters with much lower $\delta^{18}O$ averages than at the station in Shapotou, Zhongwei. Since the Earth's surface does not usually reach and maintain temperatures around 50ºC, it is more likely that the malachite formed in isotopically lighter water, and the station at Shapotou, Zhongwei is not representative.

The highest $\delta^{13}C$ samples of this study are from Ningxia (mean average is -10.7‰ with the highest being -8.1‰). This is sensible because this region is dominated by carbonate-rich soils, C_4 plants (e.g. grass and shrubs) and lacks in precipitation, which facilitates the dissolution and movement of isotopically lighter carbon. Moreover, if the Ningxia malachite formed at or near the surface, then atmospheric carbon likely made a significant contribution. According to micro-sample XRD analysis, the Ningxia samples ranged from 42% to 93% malachite, with the main contaminant being SiO_2, but most of them consisting of multiple phases (**table 7.12**). It is not likely that carbon-free mineral impurities impact $\delta^{13}C$ results in malachite, but other carbonate phases could. Sample CNM1 contained 38% azurite ($Cu_3(CO_3)_2(OH)_2$), CNW2 contained 12% dolomite ($CaMg(CO_3)_2$), CNW3 contained 21% calcite ($CaCO_3$), and CNW5 had some unidentified peaks (**table 7.12**). Dolomite appears to have the strongest impact on the overall $\delta^{13}C$ value, resulting in CNW2 being the highest sample of the entire study at -8.1‰.

Three archaeological malachite samples from Ningxia were roughly picked and analyzed towards the B2 study. B2CNM1 merely consisted of 13% malachite and 87% quartz. CNW1 and B2CNW1 had the same minerals present, but in different proportions (93% malachite and 7% SiO_2, 84% malachite and 16% SiO_2, respectively), and their $\delta^{13}C$ values are comparable (-9.5‰ and -9.6‰, respectively), suggesting that these concentrations of malachite will yield reliable results with SiO_2 minerals as contaminants. The samples for CNW2 and B2CNW2 had more phases present, and the $\delta^{13}C$ values reflect this. CNW2 contained more malachite (87%), but was contaminated with 12% dolomite and 2% copper (II) chloride hydroxides (typical of arid regions), while B2CNW2 only had 59% malachite and was contaminated with 39% azurite and 2% copper

(II) chloride hydroxides. The $\delta^{13}C$ values between these samples do not compare well, with CNW2 yielding -8.1‰ and B2CNW2 yielding -6.9‰.

A paired *t*-test suggests that there is no significant difference between the B1 and B2 $\delta^{18}O$ datasets. The paired *t*-test focused on the Ningxia $\delta^{18}O$ data also does not show a significant difference: $t_2 = 1.7$, $p = 0.2$, 95% CI [-1.0, 0.4]. The B1 and B2 datasets for $\delta^{13}C$ had a different *t*-test result, suggesting that there is a significant difference, but the Ningxia B1-B2 $\delta^{13}C$ *t*-test result does not support this: $t_2 = 1.0$, $p = 0.4$, 95% CI [-2.1, 1.3]. In other words, the Ningxia B1-B2 $\delta^{18}O$ and $\delta^{13}C$ *t*-test results suggest that meticulous picking had no significant impact on either isotope studies.

Four malachite ore samples were collected from Ningxia for comparison to the archaeological malachite samples. The Ningxia ores have a mean $\delta^{13}C$ of -13.1‰, which is significantly lower than the archaeological samples analyzed. The ores were found at the ground surface near the Gobi Desert, as were the archaeological samples, but this is not likely the formation site of the ores. The ores probably formed someplace nearby where the $\delta^{13}C$ in soil CO_2 is lower.

8.4. In Conclusion

This doctoral project aims to apply a refined methodological approach that uses light stable isotopes in meteoric water to determine the formation location of copper corrosion minerals, for the eventual use on unprovenanced archaeological bronzes that corroded in the soil environment. This thesis is focused on the correlations between two of the most common copper corrosion minerals, brochantite and malachite, and their formation environment using $\delta^{18}O$, and to a lesser extent, $\delta^{13}C$ and $\delta^{2}H$.

Brochantite

This study suggests that there is no significant difference between the $\delta^{18}O_{SO4}$ values of the brochantite samples, and the brochantite $\delta^{18}O_{SO4}$ variances are roughly equal among the cities included in this study. Furthermore, there is no statistically significant correlation between $\delta^{18}O_{SO4}$ and the yearly weighted means $\delta^{18}O$ in local precipitation, yearly mean precipitation amount, pH, surface temperature, latitude, or age of deposit (**figures 6.5 – 6.9**). This is also the case for hydroxyl-$\delta^{2}H$, which shows no correlations to the listed environmental parameters.

It is determined that about 50% of brochantite's sulfate oxygen is sourced from the local meteoric water. The created $SO_2 \rightarrow SO_4$ Pathway Flowchart can be used as a guide to estimate percent oxygen contributions, however it is only possible to calculate water-oxygen contribution amounts for one heterogeneous pathway at a time. The only way for ozone to be involved in the $SO_2 \rightarrow SO_4$ reaction would be through a homogeneous pathway.

In conclusion, it is possible to determine the percent oxygen contributions for two of the $SO_2 \rightarrow SO_4$ pathways involved in brochantite formation at a time, but the $\delta^{18}O_{SO4}$ and hydroxyl-$\delta^{2}H$

cannot be used confidently in formation location studies. A larger study on $\delta^{18}O_{SO4}$ in brochantite could lead to more significant statistical correlations with the formation environment, but this would still not be good enough for practical use in provenance studies.

Malachite

Considering all samples, the malachite concentrations ranged from 25% to 100% malachite, with an assortment of possible contaminants in varying proportions. Due to the inconsistencies in purity of the mix-phase samples, it is difficult to assess the impact of most of these minerals. The Batch (B1 and B2) studies and statistical data comparisons to previous investigations suggests that picking the patina samples is a critical step, however this process does not need to be meticulous, as it will not significantly refine isotopic results. Picking will leave unwanted material in the samples, and a better method of isolating the malachite in mix-phase patina samples without risking isotope exchange needs to be developed. This would be especially helpful for archaeological studies, since the patinas that form on archaeological bronzes are often a heterogeneous mix of small crystals and more likely to have had conservation treatment.

This study benefits from having malachite samples from several different sites with good longitudinal geographic variance. Although the malachite datasets ($\delta^{18}O$, $\delta^{13}C$, B1, B1 without outlier, and B2) are statistically processed and show significant difference between the geographic groups surveyed, there is room for improvement. As seen in **figure 5.9**, this project could benefit from improved latitudinal geographic variance (most of the samples came from yellow or near yellow regions). Consequently, this study does not suggest a statistically significant relationship between the $\delta^{18}O$ in archaeological malachite and the $\delta^{18}O$ in local meteoric water. This is also the case for $\delta^{13}C$ in malachite, which does not show significant correlations with $\delta^{18}O$ in local water or estimated surface temperatures.

By exploring the possibility of isotopic relationships between the formation environment and brochantite or malachite, this study has generated new archaeological applications, including:

1. Instead of a global approach, this work could be focused for use on hoard studies. The Hungarian malachite data suggests that the samples, which were assumed to have corroded together, may have corroded in different locations in Hungary. This does not mean that the objects were not found together; it is possible that they were already corroded when grouped in antiquity.
2. Rather than using this procedure for locating a corrosion formation site for unprovenanced bronzes, this work may be better suited to confirm whether an assumed formation site is reasonable. This study shows that the malachite samples suspected to be from Guangxi, China have isotope ratios that suggest they may not even be from southern China. Therefore, this work may be used to identify incorrectly provenanced objects or forgeries.

Further investigations could also focus on the following:

1. An empirical, multidimensional approach by way of Köppen climate suggests this work could benefit from a climate-focused project, which may help identify the controlling

parameters for $\delta^{18}O$ and $\delta^{13}C$ under certain environmental conditions. Deserts and semi-arid climates appear to be good observation sites to begin such studies.

2. A significant, negative relationship is apparent between $\delta^{18}O$ and $\delta^{13}C$ with some clustering within sample sites (as shown in **figure 7.5** and discussed in section 8.3.1). However, this is not always maintained when considering the regression analyses of the geographic groups independently. The reason for this is unclear, but it does show that a comprehensive study into the $\delta^{13}C$ values of malachite would be worthwhile.

To refine the methodology used in this study, future researchers are advised to begin by focusing on the following areas:

1. Isolating malachite, or the carbonate within it, from mixed-phase patina samples.
2. Ascertain local environmental data, rather than relying on estimations. This includes collecting and isotopically analyzing meteoric water samples from the sites of interest for at least 3 years, while recording the amount of precipitation, soil pH, and soil temperature at various depths. Soil type descriptions and vegetation present at the site would also be helpful, particularly for a $\delta^{13}C$ study.
3. Collecting samples with broader latitudinal geographic variance.

In conclusion, this work cannot be used to determine the formation location of copper corrosion minerals when they are totally unknown. However, this study has shown that the malachite and brochantite methodologies tested may eventually be used practically to confirm whether a suggested provenance seems like a reasonable possibility, or to identify forgeries.

Works Cited

Al-Aasm, I. H., Taylor, B. E. and South, B. (1990) 'Stable isotopic analysis of multiple carbonate samples using selective acid extraction,' *Chemical Geology*, 80, pp. 119-125.

Alberts, B., Bray, D., Hopkin, K., Johnson, A., Lewis, J., Roberts, K., Raff, M. and Walter, P. (2004) *Essential Cell Biology*. 2nd ed. New York: Garland Publishing, Taylor Francis Group.

Amundson, R. G., Chadwick, O. A., Sowers, J. M. and Doner, H. E. (1988) 'Relationship between climate and vegetation and the stable carbon isotope chemistry of soils in the eastern Mojave Desert, Nevada,' *Quat. Res.*, 29, pp. 245-254.

Angert, A. and Luz, B. (2001) 'Fractionation of Oxygen Isotopes by Root Respiration: Implications for the Isotopic Composition of Atmospheric O_2,' *Geochimica et Cosmochimica Acta*, 65 (11), pp. 1695-1701.

Anthony, J. W., Bideaux, R. A., Bladh, K. W. and Nichols, M. C. (2003) *Handbook of Mineralogy Volume 5: Borates, Carbonates, Sulfates*. Tucson, Arizona: Mineral Data Publishing.

Appelo, C. A. J. and Postma, D. (2005) *Geochemistry, groundwater and pollution*. 2nd ed. Leiden: Balkema.

Araguas-Araguas, L. J. and Diaz Teijeiro, M. F. (2005) 'Isotope Composition of Precipitation and Water Vapour in the Iberian Peninsula: First Results of the Spanish Network of Isotopes in Precipitation,' *IAEA-TECDOC-1453.* International Atomic Energy Agency (IAEA).

Arizona Board of Regents (2005) *Sustainability of Semi-Arid Hydrology and Riparian Areas: Oxygen*. Available at: http://web.sahra.arizona.edu/programs/isotopes/oxygen.html.

Ashman, M. and Puri, G. (2002) *Essential Soil Science: A Clear and Concise Introduction to Soil Science.* Oxford: Blackwell Science.

Baker, A., Ito, E., Smart, P. L. and McEwan, R. F. (1997) 'Elevated and variable values of in speleothems in a British cave system,' *Chemical Geology*, 136, pp. 263-270.

Bao, H. (2005) 'Oxygen-17 Anomaly in Terrestrial Minerals: An Update,' *Geochimica et Cosmochimica Acta*, 69 (10), pp. A443.

Bao, H. and Reheis, M. C. (2003) 'Multiple Oxygen and Sulfur Isotopic Analysis on Water-Soluble Sulfate in Bulk Atmospheric Deposition from the Southwestern United States,' *Journal of Geophysical Research*, 108 (D14), pp. 9-1 – 9-9.

Bao, H. and Thiemens, M. H. (2000) 'Generation of O_2 from $BaSO_4$ Using a CO_2-Laser Fluorination System for Simultaneous Analysis of $\delta^{18}O$ and $\delta^{17}O$,' *Analytical Chemistry*, 72 (17), pp. 4029-4032.

Bao, H., Thiemens, Mark H., Farquhar, J., Campbell, D. A., Lee, C. C.-W., Heine, K. and Loope D. B. (2000) 'Anomalous ^{17}O Compositions in Massive Sulphate Deposits on the Earth,' *Nature*, 406, pp. 176-178.

Barkan, E. and Luz, B. (2003) 'High-Precision Measurements of $^{17}O/^{16}O$ and $^{18}O/^{16}O$ of O_2 and O_2/Ar Ratio in Air,' *Rapid Communications in Mass Spectrometry*, 17, pp. 2809-2814.

Barkan, E. and Luz, B. (2005) 'High Precision Measurements of $^{17}O/^{16}O$ and $^{18}O/^{16}O$ Ratios in H_2O,' *Rapid Communications in Mass Spectrometry*, 19, pp. 3737-3742.

Baumann, K. (2011) 'Atmosphere,' in Schütze, M., Feser, R., Bender, R. (eds) *Corrosion Resistance of Copper and Copper Alloys*. Frankfurt, Germany: DECHEMA e. V., Society for Chemical Engineering and Biotechnology, pp. 119-152.

Ben, R.G. (2009) *Isotopes and half-life*. Available at: http://en.wikipedia.org/wiki/File:Isotopes_and_half-life.svg.

Bender, M. (2006) *The Distribution of O_2 in Air*. Available at: http://geoweb.princeton.edu/people/bender/lab/research_o2n2.html (Accessed: 24 June 2013).

Berner, E. K. and Berner, R. A. (2012) *Global Environment: Water, Air, and Geochemical Cycles*. 2nd ed. Princeton, New Jersey: Princeton University Press.

Biomes Group (2004) 'The World's Biomes,' in Pullen, S. and Ballard, K. (eds) *Biology*. Available at: http://www.ucmp.berkeley.edu/glossary/gloss5/biome/ (Accessed: 15 June 2018).

Blunier, T., Barnett, B., Bender, M. L., Hendricks, M. B. (2002) 'Biological Oxygen Productivity During the Last 60,000 Years from Triple Oxygen Isotope Measurements,' in Reeburgh, W. S. (ed) *Global Biogeochemical Cycles: An International Journal for Global Change*, 16 (3), pp. 3-1 – 3-14.

Brasseur, G. P. and Holland, E. A. H. (2001) 'Uncertainties in the Atmospheric Chemical System,' in Schulze, E.-D., Heimann, M., Harrison, S., Holland, E., Lloyd, J., Prentice, I. C. and Schimel, D. (eds) *Global Biogeochemical Cycles in the Climate System*. San Diego: Academic Press, pp. 31-39.

Bridges, E. M., Batjes, N. H. and Nachtergaele, F. O. (1998) *World reference base for soil resources: atlas.* Leuven: Acco.

Broadgate, J. (2001) *An Assessment of the Preservation of Archaeological Data in Buried Bronze*. Unpublished master's thesis. University of Oxford, Research Laboratory for Archaeology and the History of Art.

Buol, S. W., Southard, R. J., Graham, R. C. and McDaniel, P. A. (2011) *Soil Genesis and Classification*. 6th ed. Chichester: Wiley-Blackwell.

Burton, M. A. S. (1987) *Terrestrial and biome types.* London: GEMS-Monitoring and Assessment Research Centre.

Business Insider, Inc (2013) *Statue of Liberty Quiz*. Available at: http://www.businessinsider.com/statue-of-liberty-quiz-2013-5 (Accessed: 02 December 2013).

Cao, X., Liu, Y. (2011) 'Equilibrium Mass-Dependent Fractionation Relationships for Triple Oxygen Isotopes,' *Geochimica et Cosmochimica Acta*, 75, pp. 7435-7445.

Cao, X., Zhang, J., Tang, M. and Liu, Y. (2011) 'The Accurate Estimation of Mass Dependent Fractionation Line of Oxygen Isotopes,' *Geochimica et Cosmochimica Acta*, 40 (2), pp. 147-155.

Chang, L. L. Y., Howie, R. A. and Zussman, J. (1996) 'Non-silicates: Sulphates, Carbonates, Phosphates, Halides,' *Rock-Forming Minerals*, 5B. 2nd ed. Essex: Longman Group Limited.

Chen, F., Zhang, M., Ma, Q., Wang, S., Li, X. and Zhu, X. (2015) 'Stable isotopic characteristics of precipitation in Lanzhou City and its surrounding areas, Northwest China,' *Environmental Earth Sciences*, 73, pp. 4671-4680.

Cheng, H. (2017) *Köppen climate classification: As a diagnostic tool to quantify climate variation and change*. Available at: http://hanschen.org/koppen/.

Cerling, T. E. (1984) 'The stable isotopic composition of modern soil carbonate and its relationship to climate' *Earth and Planetary Science Letters*, 71, pp. 229-240.

Cicek, V. and Al-Numan, B. (2011) *Corrosion Chemistry*. Co-published by Hoboken, New Jersey: John Wiley & Sons and Salem: Massachusetts: Scrivener Publishing LLC.

Clark, I. D. and Fritz, P. (1997) *Environmental Isotopes in Hydrogeology*. Boca Raton: CRC Press/Lewis Publishers.

Cole, I. S. (2010) 'Atmospheric Corrosion,' in Cottis, R. A., Graham, M. J., Lindsay, R., Lyon, S. B., Richardson, J. A., Scantlebury, J. D. and Stott, F. H. (eds), *Shreir's Corrosion, Volume 2: Corrosion in Liquids, Corrosion Evaluation*. 4th ed. Amsterdam: Elsevier, pp. 1051-1093.

Coleman, M. L., Shepherd, T. J., Durham, J. J., Rouse, J. E. and Moore, G. R. (1982) 'Reduction of Water with Zinc for Hydrogen Isotope Analysis,' *Analytical Chemistry*, 54, pp 993-995.

Coplen, T. B., Herczeg, A. L. and Barnes, C. (2000) 'Isotope engineering - using stable isotopes of the water molecule to solve practical problems,' in Cook, P. G. and Herczeg, A. L. (eds) *Environmental Tracers in Subsurface Hydrology*. Boston: Kluwer Academic Publishers, pp. 79–110.

Cronyn, J. M. (1990) *The Elements of Archaeological Conservation*. Oxon, UK: Routledge.

Cullity, B. D. and Stock, S. R. (2014) *Elements of X-Ray Diffraction*. 3rd ed. Essex: Pearson Education Limited.

DasSharma, S. D., Patil, D. J. and Gopalan, K. (2002) 'Temperature dependence of oxygen isotope fractionation of CO_2 from magnesite-phosphoric acid reaction,' *Geochim Cosmochim Acta*, 66, pp. 589-593.

Dedering, U. (2011) *China edcp location map*. Available at: https://commons.wikimedia.org/wiki/File:Gansu_in_China_(%2Ball_claims_hatched).svg (Accessed on: 06 May 2019).

De Putter, T., Mees, F., Decrée, S. and Dewaele, S. (2010) 'Malachite, an indicator of major Pliocene Cu Mobilization in a karstic environment (Katanga, Democratic Republic of Congo),' *Ore Geology Reviews*, 38, pp. 90-100.

Derrick, M. R., Stulik, S., Landry and J. M. (1999) *Infrared Spectroscopy in Conservation Science*. Los Angeles: Getty Conservation Institute.

Eash, N. S., Sauer, T., Razvi, A. and Walker, F. (2015) *Soil Science Simplified*. 6th ed. Chichester: Wiley-Blackwell.

Edwards, R. (1998) 'The effects of changes in groundwater geochemistry on the survival of buried metal artefacts,' in Corfield, M., Hinton, P., Nixon, T. and Pollard, A. M. (eds) *Preserving Archaeological Remains In-Situ: Proceedings of the Conference of 1st-3rd April 1996.* London: Museum of London Archaeology Service, pp. 86-92.

Eggert, G. (2007) 'Pseudomorph or corrosion? The enigma of the curly malachite,' *Metal 07: When Archaeometry and conservation meet*, 1, pp. 57-60.

Ehleringer, J. R. and Vogel, J. C. (1993) 'Historical Aspects of Stable Isotopes in Plant Carbon and Water Relations,' in Ehleringer, J. R., Hall, A. E. and Farquhar, G. D. (eds) *Stable*

Isotopes and Plant Carbon-Water Relations. San Diego; London: Academic Press, INC., pp. 9-18.

Elsner, G. (2011) 'Soil (Underground Corrosion),' in Schütze, M., Feser, R. and Bender, R. (eds) *Corrosion Resistance of Copper and Copper Alloys*. Frankfurt: DECHEMA c. V., pp. 553-558.

Farquhar, G. D. and Lloyd, J. (1993) 'Carbon and Oxygen Isotope Effects in the Exchange of Carbon Dioxide Between Terrestrial Plants and the Atmosphere,' in Ehleringer, J. R., Hall, A. E. and Farquhar, G. D. (eds) *Stable Isotopes and Plant Carbon-Water Relations*. San Diego; London: Academic Press, INC., pp. 47-70.

Farquhar, G. D., Lloyd, J., Taylor, J. A., Flanagan, L. B., Syvertsen, J. P., Hubick, K. T., Wong, S. C. and Ehleringer, J. R. (1993) 'Vegetation Effects on the Isotope Composition of Oxygen in Atmospheric CO_2,' in *Nature*, 363, pp. 439-443.

Faure, G. (1986) *Principles of Isotope Geology*. 2nd ed. New York: John Wiley & Sons, Inc.

Ferronsky, V. I. and Polyakov, V. A. (2012) *Isotopes of the Earth's Hydrosphere.* New York: Springer.

FitzGerald, K. P., Nairn, J., Skennerton, G. and Atrens, A. (2006) 'Atmospheric corrosion of copper and the colour, structure and composition of natural patinas on copper,' *Corrosion Science*, 48, pp. 2480-2509.

FossilEra Minerals (2017) *3.7" Malachite and Azurite with Quartz – Morocco.* Available at: https://www.fossilera.com/minerals/3-7-malachite-and-azurite-with-quartz-morocco. (Accessed: 08 November 2017).

Frankel, G. S. and Landolt, D. (2003) 'Thermodynamics,' in Bard, A. J., Stratmann, M. and Frankel, G. S. (eds) *Encyclopedia of Electrochemistry: Corrosion and Oxide Films*, 4. Weinheim, Germany: Wiley-VCH, pp. 9-24.

Fraser, D. (2011) *Crystals and Minerals*. Lecture notes distributed and supplemented by Boos Pedroza, D. (student) in Fundamentals of Geology I at the University of Oxford, Department of Earth Sciences, Michaelmas term 2011.

Friedman, H. (2015) *Smithsonian National Museum of Natural History: Part 6 – Carbonates*. Available at: http://news.minerals.net/2015/11/22/default (Accessed: 08 Nov. 2017).

Frost, R. L., Ding, Z., Kloprogge, J. T. and Martens, W. N. (2002) 'Thermal stability of azurite and malachite in relation to the formation of mediaeval glass and glazes,' *Thermochimica Acta 390*, pp. 133-144.

Fyfe, D. (1994) 'The Atmosphere,' in Shreir, L. L., Jarman, R. A. and Burstein, G.T. (eds) *Corrosion: Metal/Environment Reactions*. 3rd ed. Oxford, UK: Butterworth-Heinemann Ltd.

Garber, M. (2011) 'The Counties of Great Britain & Northern Ireland,' *The Association of British Counties,* 2nd ed. Available at: https://abcounties.com/counties/ (Accessed 19 May 2019).

Gat, J. R., Ben-Mair, R. Yam, D., Yakir, D. and Wernli, H. 'The Isotope Composition of Atmospheric Waters in Israel's Coastal Plain,' *IAEA-TECDOC-1453.* International Atomic Energy Agency (IAEA).

Gat, J. R. and Dansgaard, W. (1972) 'Stable Isotope Survey of the Fresh Water Occurrences in Israel and the Northern Jordan Rift Valley,' *Journal of Hydrology*, 16, pp. 177-212.

Geology In (2014) *Malachite Stalactites from Mashamba.* Available at: https://www.geologyin.com/2014/03/mashamba.html (Accessed: 08 November 2017).

Gilg, H. A., Boni, M., Hochleitner, R. and Struck, U. (2008) 'Stable isotope geochemistry of carbonate minerals in supergene oxidation zones of Zn-Pb deposits,' *Ore Geology Reviews*, 33, pp. 117-133.

Gilg, H. A., Girard, J.-P. and Sheppard, S. M. F. (2004) 'Conventional and Less Conventional Techniques for Hydrogen and Oxygen Isotope Analysis of Clays, Associated Minerals and Pore Waters in Sediments and Soils,' *Handbook of Stable Isotope Techniques*, 1, pp. 38-61.

Girard, J.-P. and Savin, S. M. (1996) 'Intracrystalline fractionation of oxygen isotopes between hydroxyl and non-hydroxyl sites in kaolinite measured by thermal dihydroxylation and partial fluorination,' *Geochimica et Cosmochimica Acta*, 60 (3), pp. 469-487.

Google Maps (2019) *Israel*, Google. Available at: https://www.google.com/maps/place/Israel/@32.0488078,34.8627974,10.47z/data=!4m5!3m4!1s0x1500492432a7c98b:0x6a6b422013352cba!8m2!3d31.046051!4d34.851612 (Accessed on 04 May 2019).

Graedel, T. E., Nassau, J. P. and Franey, J. P. (1987) 'Copper patinas formed in the atmosphere – I. Introduction,' *Corrosion Science*, 27 (7), pp. 639-657.

Guy, R. D., Fogel, M. L. and Berry, J. A. (1993) 'Photosynthetic Fractionation of the Stable Isotopes of Oxygen and Carbon,' *Plant Physiology*, 101, pp. 37-47.

Hall, D. O. and Rao, K. K. (1999) *Photosynthesis*. 6th ed. Cambridge, UK: Cambridge University Press.

Harris, J. O. and Eyre, D. (1994) 'Soil in the Corrosion Process,' in Shreir, L. L., Jarman, R. A. and Burstein, G. T. (eds) *Corrosion: Metal/Environment Reactions*. 3rd ed. Oxford: Butterworth-Heinemann Ltd., pp. 2:73-2:86.

Haßler, K., Taubald, H. and Markl, G. (2014) 'Carbon and oxygen isotope composition of Pb-, Cu- and Bi-carbonates of the Schwarzwald mining district: Carbon sources, first data on bismutite and the discovery of an oxidation zone formed by ascending thermal water,' *Geochimica et Cosmochimica Acta*, 133, pp. 1-16.

Hawkins, D. (2019) *Biomeasurement: A Student's Guide to Biological Statistics.* 4th ed. Oxford: Oxford University Press.

Heaton, T. (theh@nigl.nerc.ac.uk). 10 November 2014. Results of hydrogen isotope analysis of brochantite. Email to D. Boos Pedroza (d.boospedroza@rlaha.ox.ac.uk).

Herczeg, A. L. and Edmunds, W. M. (2000) 'Inorganic Ions as Tracers,' in Cook, P. G. and Herczeg, A. L. (eds) *Environmental Tracers in Subsurface Hydrology*. Boston: Kluwer Academic Publishers, pp. 31-77.

Heimann, M. (2001) 'The Cycle of Atmospheric Molecular Oxygen and its Isotopes,' in Schulze, E.-D., Heimann, M., Harrison, S., Holland, E., Lloyd, J., Prentice, I. C. and Schimel, D. (eds) *Global Biogeochemical Cycles in the Climate System*. San Diego: Academic Press, pp. 235-243.

Henderson, J. (2000) *The science and archaeology of materials: an investigation of inorganic materials.* London: Routledge.

Hoefs, J. (1997) *Stable Isotope Geochemistry*. 4th ed. Heidelberg: Springer-Verlag.

Holt, B. D., Cunningham, P. T. and Engelkemeir, A. G. (1978) 'Application of oxygen-18 analysis to the study of atmospheric sulfate formation," in Robinson, B. W. (ed) *Stable Isotopes in the Earth Sciences*. Wellington, New Zealand: Science Information Division, DSIR.

Holt, B. D., Cunningham, P. T., Engelkemeir, A. G., Graczyk, D. G. and Kumar, R. (1983) 'Oxygen-18 Study of Nonaqueous-Phase Oxidation of Sulfur Dioxide,' *Atmospheric Environment*, 17 (3), pp. 625-632.

Holt, B. D., Cunningham, P. T. and Kumar, R. (1979) 'Seasonal Variations of Oxygen-18 in Atmospheric Sulfates,' *International Journal of Environmental Analytical Chemistry*, 6:1, pp. 43-53.

Holt, B. D. and Kumar, R. (1991) 'Oxygen Isotope Fractionation for Understanding the Sulfur Cycle,' in Krouse, H. R. and Grinenko, V. A. (eds) *Stable Isotopes in the Assessment of Natural and Anthropogenic Sulphur in the Environment*. John Wiley & Sons Ltd.

Holt, B. D., Cunningham, P. T. and Kumar, R. (1981a) 'Oxygen Isotopy of Atmospheric Sulfates,' *Environmental Science and Technology*, 15 (7), pp. 804-808.

Holt, B. D., Kumar, R. and Cunningham, P. T. (1981b) 'Oxygen-18 Study of the Aqueous-Phase Oxidation of Sulfur Dioxide,' *Atmospheric Environment*, 15, pp. 557-566.

Holt, B. D., Kumar, R. and Cunningham, P. T. (1982) 'Primary Sulfates in Atmospheric Sulfates: Estimation by Oxygen Isotope Ratio Measurements,' *Science*, 217 (4554), pp. 51-53.

Hometown (2013) *Hometown Roofing Contractors: The Ultimate Guide to Copper Roofing*. Available at: http://www.hometownroofingcontractors.com/metal-roofing/copper-roofing.html (Accessed: 13 December 2013).

Hu, K., Chen, H., Nie, Y., Yang, J. and Wang, K. (2013) 'Characteristics of seasonal variation of deuterium and oxygen-18 isotope composition of precipitation in karst peak-cluster depression area, northwest Guangxi of China,' *Transactions of the Chinese Society of Agricultural Engineering*, 29(5), pp. 53-62.

IAEA (1998-2013) 'International Atomic Energy Agency,' *Isotope Hydrology Section*. Last updated 2010. Available at: http://www- naweb.iaea.org/na/index.html (Accessed: 24 April 2019).

IUPAC (1997) *Compendium of Chemical Terminology.* 2nd ed. Compiled by McNaught, A. D. and A. Wilkinson. Oxford: Blackwell Scientific Publications.

Jouzel, J., Hoffmann, G., Parrenin, F. and Waelbroeck, C. (2002) 'Atmospheric Oxygen 18 and Sea Level Changes,' *Quaternary Science Reviews*, 21, pp. 307-314.

Karageorghis, V. and Demas, M. (1984) *Pyla-Kokkinokremos: a late 13th-century B.C. fortified settlement in Cyprus.* Nicosia: Republic of Cyprus by the Department of Antiquities.

Kendall, C. and Doctor, D. H. (2011) 'Stable Isotope Applications in Hydrologic Studies,' in Holland, H. D. and Turekian, K. K. (eds) *Isotope Geochemistry: From the Treatise on Geochemistry.* London: Academic Press.

Klighoffer, M. (2011) *BISC 103 Midterm 1.* Available at: http://www.studyblue.com/notes/note/n/bisc-103-midterm-i/deck/1084064 (Accessed: 24 April 2013).

Kloppmann, W., Bromblet, P., Vallet, J. M., Vergès-Belmin, V., Rolland, O., Guerrot, C. and Gosselin, C (2011) 'Building materials as intrinsic sources of sulphate: A hidden face of salt weathering of historical monuments investigated through multi-isotope tracing (C, O, S),' *Science of the Total Environment*, 409, pp. 1658-1669.

Kloppmann, W., LeRoux, L., Bromblet, P., Guerrot, C., Proust, E., Cooper, A. H., Worley, N., Smeds, S.-A. and Bengtsson, H. (2014) 'Tracing Medieval and Renaissance Alabaster Works of Art Back to Quarries: A Multi-Isotope (Sr, S, O) Approach,' *Archaeometry*, 56 (2), pp. 203-219.

Knapp, B. J. (1996) *Oxygen*. Henley-on-Thames, Oxon: Atlantic Europe Publishing Company Limited.

Koga, N., Criado, J. M. and Tanaka, H. (1997) 'Reaction Pathway and Kinetics of the Thermal Decomposition of Synthetic Brochantite,' *Journal of Thermal Analysis: An international forum for thermal studies*, 49, pp. 1467-1475.

Koga, N., Criado, J. M. and Tanaka, H. (1999) 'Apparent kinetic behavior of the thermal decomposition of synthetic malachite,' *Thermochimica Acta*, 340-341, pp. 387-394.

Koga, N. and Yamada, S. (2005) 'Influences of Product Gases on the Kinetics of Thermal Decomposition of Synthetic Malachite Evaluated by Controlled Rate Evolved Gas Analysis Coupled with Thermogravimetry,' *Wiley InterScience.*

Kramar, S., Mirtič, B., Knöller, K. and Rogan-Šmuc, N. (2011) 'Weathering of the black limestone of historical monuments (Ljubljana, Slovenia): Oxygen and sulfur isotope composition of sulfate salts,' *Applied Geochemistry*, 26, pp.1632-1638.

Krätschmer, A., Wallinder, O. I. and Leygraf, C. (2002) 'The evolution of outdoor copper patina,' *Corrosion Science*, 44, pp. 425-450.

Kroopnick, P. and Craig, H. (1972) 'Atmospheric Oxygen: Isotopic Composition and Solubility Fractionation,' *Science*, 175 (4017), pp. 54-55.

Lachniet, M. S., Lawson, D. E., Stephen, H., Sloat, A. R. and Patterson, W. P. (2016) 'Isoscapes of $\delta^{18}O$ and $\delta^{2}H$ reveal climatic forcings on Alaska and Yukon precipitation,' *Water Resources Research*, 52, pp. 6575-6586.

Lane, N. (2002) *Oxygen: The Molecules that Made the World*. New York: Oxford University Press.

Langmuir, D. (1997) *Aqueous environmental geochemistry.* Upper Saddle River, New Jersey: Prentice Hall.

Lebedev, A. T. (2012) 'General Principles of Mass Spectrometry,' in Lebedev, A. T. (ed) *Comprehensive Environmental Mass Spectrometry*. Hertfordshire: ILM Publications, pp. 1-20.

Lee, C. C.-W., Savarino, J., Cachier, H., Thiemens, M. H. (2002) 'Sulfur (^{32}S, ^{33}S, ^{34}S, ^{36}S) and oxygen (^{16}O, ^{17}O, ^{18}O) isotopic ratios of primary sulfate produced from combustion processes,' *Tellus*, 54B, pp. 193-200.

Lee, C. C.-W. and Thiemens, M. H. (2001) 'The $\delta^{17}O$ and $\delta^{18}O$ measurements of atmospheric sulfate from a coastal and high alpine region: A mass-independent isotopic anomaly,' *Journal of Geophysical Research*, 106 (D15), pp. 17359-17373.

Leibundgut, C., Maloszewski, P. and Külls, C. (2009) *Tracers in Hydrology*. Chichester: Wiley-Blackwell.

Leygraf, C. and Graedel, T. (2000) *Atmospheric Corrosion*. New York: John Wiley & Sons, Inc.

Li, X. (1995) *Chinese Bronzes: A General Introduction*. Beijing: Foreign Languages Press.

Li, X., Bao, H., Gan, Y., Zhou, A. and Liu, Y. (2013) 'Multiple oxygen and sulfur isotope compositions of secondary atmospheric sulfate in a mega-city in central China,' *Atmospheric Environment*, 81, pp. 591-599.

Little, B. and Lee, J. (2007) *Microbiologically Influenced Corrosion.* Hoboken, New Jersey: John Wiley & Sons, Inc.

Little, B., Wagner, P., and Jones-Meehan, J. (1994) 'Sulfur Isotope Fractionation in Sulfide Corrosion Products as an Indicator for Microbiologically Influenced Corrosion (MIC),' in Kearns, J. and Little, B. (eds.) *Microbiologically Influenced Corrosion Testing, ASTM STP 1232*, Philadelphia: American Society for Testing and Materials, pp. 180-187.

Liu, J., Song, X., Yuan, G., Sun, X. and Yang, L. (2014) 'Stable isotopic compositions of precipitation in China,' *Tellus B: Chemical and Physical Meteorology*, 66(1), pp. 1-17.

Marin Mineral (2017) *Malachite from Kasompi Mine, Katanga Prov., Congo*. Available at: http://www.marinmineral.com/s_present.php?mode=present&sid=B170&cur=euro (Accessed: 08 November 2017).

Mays, L. W. (2012) *Ground and Surface Water Hydrology*. Hoboken, NJ: Wiley & Sons, Inc.

McEwan, C. (2000) *Precolombian Gold: Technology, Style and Iconography*, London: The Trustees of the British Museum.

McNeil, M. B. and Little, B. J. (1992) 'Corrosion Mechanisms for Copper and Silver Objects in Near-Surface Environments,' *Journal of the American Institute for Conservation*, 313 (3) 7, pp. 355-366.

McNeil, M. and Selwyn, L. S. (2001) 'Electrochemical processes in metallic corrosion,' in Brothwell, D. R. and Pollard, A. M. (eds) *Handbook of Archaeological Sciences*. Chichester: Wiley, pp. 605-614.

Melchiorre, E. B. (1998) *Chemical Studies of Low Temperature Fluids in Diverse Geological Settings*. Unpublished doctoral dissertation. Washington University in St. Louis, Department of Earth and Planetary Sciences.

Melchiorre, E. B., Criss, R. E. and Rose, T. P. (1999) 'Oxygen and Carbon Isotope Study of Natural and Synthetic Malachite,' *Economic Geology*, 94(2), pp. 245-260.

Melchiorre, E. B. and Enders, M. S. (2003) 'Stable Isotope Geochemistry of Copper Carbonates at the Northwest Extension Deposit, Morenci District, Arizona: Implications for Conditions of Supergene Oxidation and Related Mineralization,' *Economic Geology*, 98(3), pp. 607-621.

Melchiorre, E. B., Huss, G. R. and Lopez, A. (2013) 'Carbon and hydrogen stable isotope microanalysis and data correction for rare carbonate minerals: Case studies for stichtite ($Mg_6Cr[(OH)_{16}|CO_3]\cdot H_2O$) and malachite ($Cu_2CO_3(OH)_2$),' *Chemical Geology*, 367, pp. 63-69.

Merkel, J. Lecturer, IOA, UCL. Personal Communication 18 September 2015.

Miller, M. F. (2002) 'Isotopic Fractionation and the Quantification of ^{17}O Anomalies in the Oxygen Three-Isotope System: An Appraisal and Geochemical Significance,' *Geochimica et Cosmochimica Acta*, 66 (11), pp. 1881-1889.

Mizutani, Y. (1971) 'An Improvement in the Carbon-Reduction Method for the Oxygen Isotopic Analysis of Sulpates,' *Geochemical Journal*, 5, pp. 69-77.

Mook, W. G. (2006) *Introduction to Isotope Hydrology: stable and radioactive isotopes of hydrogen, oxygen and carbon*. London: Taylor & Francis.

Morin, S., Sander, R. and Savarino, J. (2011) 'Simulation of the Diurnal Variations of the Oxygen Isotope Anomaly ($\Delta^{17}O$) of Reactive Atmospheric Species,' *Atmospheric Chemistry and Physics*, 11, pp. 3653-3671.

Murillo Barroso, M. Post-graduate Researcher, IOA, UCL. Personal Communication 20 July 2015.

Musy, A. and Higy, C. (2011) *Hydrology: A Science of Nature*. New York: Routledge.

Nassau, K., Miller, A. E. and Graedel, T E. (1987) 'The Reaction of Simulated Rain with Copper, Copper Patina, and Some Copper Compounds,' *Corrosion* Science, 21 (7), pp. 703-719.

Nesse, W. D. (2012) *Introduction to mineralogy*. 2nd ed. Oxford: Oxford University Press.

Nord, A. G., Tronner, K. and Boyce, A. J. (2001) 'Atmospheric Bronze and Copper Corrosion as an Environmental Indicator: A Study Based on Chemical and Sulphur Isotope Data,' *Water, Air, and Soil Pollution*, 127, pp. 193-204.

Northover, P. Senior Research Fellow, Retired, Oxford Materials Characterisation Service, University of Oxford. Personal Communication 03 October 2014.

Novák, M., Mitchell, M. J., Jačková, I., Buzek, F., Schweigstillová, J., Erbanová, L., Přikryl, R. and Fottová, D. (2007) 'Processes Affecting Oxygen Isotope Ratios of Atmospheric and Ecosystem Sulfate in Two Contrasting Forest Catchments in Central Europe,' *Environmental Science and Technology*, 41 (3), pp. 703-709.

O'Leary, M. H. (1993) 'Biochemical Basis of Carbon Isotope Fractionation,' in Ehleringer, J. R., Hall, A. E. and Farquhar, G. D. (eds) *Stable Isotopes and Plant Carbon-Water Relations*. San Diego, CA: Academic Press, Inc., pp. 19-28.

Padías, A. B. (2007) *Making the Connections: A How-To Guide for Organic Chemistry Lab Techniques*. Plymouth, MI: Hayden-McNeil Publishing.

Pandey, S. (2005) *Stable Isotope Tracer Studies of Corrosion of Copper in Burial Environment*. M.Sc. dissertation submitted to the University of Oxford (unpublished).

Piccardo, P. and Robbiola, L. (2007) 'Tin and copper oxides in corroded archaeological bronzes,' in Dilliman, P., Béranger, G. and Piccardo, P. (eds) *Corrosion of metallic heritage artefacts: Investigation, conservation and prediction for long-term behavior*, 48, pp. 239-261.

Polikreti, K., Argyropoulos, V., Charalambous, D., Vossou, A., Perdikatsis, V. and Apostolaki, C. (2009) 'Tracing correlations of corrosion products and microclimate data on outdoor bronze monuments by Principle Component Analysis,' *Corrosion Science*, 51, pp. 2416-2422.

Pollard, A. M. and Heron, C. (1996) *Archaeological Chemistry*. Cambridge, UK: The Royal Society of Chemistry.

Pollard, M., Batt, C., Stern, B. and Young, S. M. M. (2007) *Analytical Chemistry in Archaeology*. Cambridge: Cambridge University Press.

Prio Cyprus (2011) *Routes of Displacement and Resettlement: From 1958 to Present.* Available at: http://www.prio-cyprus-displacement.net/default.asp?id=245 (Accessed: 03 May 2019).

Procter, D. A. (2000) 'Corrosion and Thermodynamics,' in Revie, W. R. (ed) *Uhlig's Corrosion Handbook*. 2nd ed. New York: John Wiley & Sons, Inc., pp. 1-11.

Quade, J., Cerling, T. E. and Bowman, J. R. (1989) 'Systematic variations in the carbon and oxygen Isotopic composition of pedogenic carbonate along transects in the Southern Great Basin, United States,' *Geol. Soc. Am.* Bull, 101, pp. 464-475.

Ralph, C. (2013) *Brochantite*. Available at: https://www.mindat.org/min-779.html.

Rapp, G. R. (2002) *Archaeomineralogy*. New York: Springer.

Rapp, Jr., G. and Hill, C. L. (1998) *Geoarchaeology: The Earth-Science Approach to Archaeological Interpretation*. New Haven: Yale University Press.

Rawson, J. (1987) *Chinese Bronzes: Art and Ritual*. London: British Museum Publications Ltd.

Reading, M. and Dollimore, D. (1994) 'The application of constant rate thermal analysis to the study of the thermal decomposition of copper hydroxyl carbonate,' *Thermochimica Acta*, 240, pp. 117-127.

Robbiola, L., Blengino, J.-M. and Fiaud, C. (1998) 'Morphology and Mechanisms of Formation of Natural Patinas on Archaeological Cu-Sn Alloys,' *Corrosion Science*, 40 (12), pp. 2083-2111.

Robbiola, L. and Hurtel, L. (1997) 'Standard nature of the passive layers buried archaeological bronze: the example of two Roman half-length portraits,' in MacLeod, I., Pennec, S. and Robbiola, L. (eds) *Metal 95*. Proceedings of the International Conference on Metals Conservation, James and James, London. pp. 109-117.

Rolfe, J. (jer21@cam.ac.uk). 03 June 2019. Labels on a couple Chinese samples. Email to D. Boos Pedroza (d.boospedroza@rlaha.ox.ac.uk).

Rivas, T., Pozo, S. and Paz, M. (2014) 'Sulphur and oxygen isotope analysis to identify sources of Sulphur in gypsum-rich black rusts developed on granites,' *Science of the Total Environment*, 482-483, pp. 137-147.

Salomons, W. and Mook, W. G. (1986) 'Isotope Geochemistry of Carbonates in the Weathering Zone,' in Fritz, P. and Fontes J. C. (eds) *Handbook of Environmental Isotope Geochemistry, Volume 2, The Terrestrial Environment, B*. Amsterdam: Elsevier Science Publishers B. V., pp. 239-269.

Savarino, J., Lee, C. C.-W. and Thiemens, M. H. (2000) 'Laboratory oxygen isotopic study of sulfur (IV) oxidation: Origin of the mass-independent oxygen isotopic anomaly in atmospheric sulfates and sulfate mineral deposits on Earth,' *Journal of Geophysical Research*, 105 (D23), pp. 29079-29088.

Sawyer, D. T. (1991) *Oxygen Chemistry*. Oxford: Oxford University Press.

Schwartz, F. W. and Zhang, H. (2003) *Fundamentals of Ground Water*. New York: Wiley & Sons, Inc.

Scott, D. A. (1991) *Metallography and microstructure of ancient and historic metals*. Marina del Rey, California: Getty Conservation Institute in association with Archetype Books.

Scott, D. A. (2002) *Copper and Bronze in Art: Corrosion, Colorants, Conservation*. Los Angeles: The J. Paul Getty Trust.

Scully, J. C. (1990) *The fundamentals of corrosion*. 3rd ed. Oxford: Pergamon Press Inc.

Seal II, R. R., Alpers, C. N. and Rye, R. O. (2000) 'Stable Isotope Systematics of Sulfate Minerals,' in Alpers, C. N., Jambor, J. L. and Nordstrom, D. K. (eds) *Sulfate Minerals: Crystallography, Geochemistry, and Environmental Significance*, 40, Washington, DC: Mineralogical Society of America, Geochemical Society.

Selwyn, L. S., Binnie, N. E., Poitras, J., Laver, M. E. and Downham, D. A. (1996) 'Outdoor Bronze Statues: Analysis of Metal and Surface Samples,' *Studies in Conservation*, 41 (4), pp. 205-228.

Selwyn, L. (2004) *Metals and Corrosion: A Handbook for Conservation Professionals.* Ottowa: Canadian Conservation Institute.

Sena, Y. C. (2019) *Bronze and Stone: The Cult of Antiquity in Song Dynasty China*, Seattle: University of Washington Press.

Sharp, Z. (2007) *Principles of Stable Isotope Geochemistry*. Upper Saddle River, NJ: Pearson Education, Inc.

Shimada, I. (1995) *Cultura Sicán: Dios, riqueza y poder en la costa norte del Perú*, Lima: Fundación del Banco Continental para el fomento de la educación y la cultura, Edubanco.

Shimada, I. and Griffin, J. A. (1994) 'Precious Metal Objects of the Middle Sicán,' *Scientific American*, 270(4), pp. 60-67.

Shimada, I., Griffin, J. A. and Gordus, A. (2000) 'The Technology, Iconography and Social Significance of Metals: A Multi-Dimensional Analysis of Middle Sicán Objects,' In: McEwan, C. (ed.) *Precolombian Gold: Technology, Style and Iconography*, London: The Trustees of the British Museum, pp. 28-61.

Shimada, I. and Merkel, J. F. (1991) 'Copper-Alloy Metallurgy in Ancient Perú,' *Scientific American*, 265(1), pp. 80-86.

Shorter, A. H., Ravenhill, W. L. D. and Gregory, K. J. (1969) *Southwest England*, London: Nelson.

Shreir, L. L. (1994) 'Appendix 1.1A – Classification of Corrosion Processes,' in Shreir, L. L., Jarman, R. A. and Burstein, G. T. (eds) *Corrosion: Metal/Environmental Reactions*, 1, 3rd ed. Oxford: Butterworth-Heinemann Ltd, pp. 1:16 – 1:21.

Silberberg, M. S. (2003) *Chemistry: The Molecular Nature of Matter and Change.* 3rd ed. New York: McGraw-Hill.

Smith, A. W. (1978) Stable Carbon and Oxygen Isotope Ratios of Malachite from the Patinas of Ancient Bronze Objects,' *Archaeometry*, 20 (2), pp. 123-133.

Soteriades, C. G., Grivas, G. C. (1970) *General soil map of Cyprus: soil survey.* cartographic material, 1:200000, Nicosia: Republic of Cyprus Department of Land and Surveys.

Spellman, F. R. (2009) *The Science of Air: Concepts and Applications*. 2nd ed. Boca Raton, Florida: CRC Press, Taylor & Francis Group, LLC.

Spiro, T. G., Purvis-Roberts, K. and Stigliani, W. M. (2012) *Chemistry of the Environment.* 3rd ed. Mill Valley, Califonia: University Science Books.

State of Alaska (2018) 'Baranof Castle: State Historic Site,' *Alaska department of natural resources, division of parks and outdoor recreation*. Available at: http://dnr.alaska.gov/parks/aspunits/southeast/baranofcastle.htm. (Accessed: 07 September 2018).

Stott, J. F. D. and John, G. (2010) 'Corrosion in Soils,' in Cottis, B., Graham, M., Lindsay, R., Lyon, S., Richardson, T., Scantlebury, D. and Stott, H. (eds) *Shrier's Corrosion: Corrosion in Liquids, Corrosion Evaluation,* 2, pp. 1149-1167.

Strandberg, H. (1998) 'Reactions of Copper Patina Compounds – I. Influence of Some Air Pollutants,' *Atmospheric Environment*, 32 (20), pp. 3511-3520.

Stuart, B. H. (2004) *Infrared Spectroscopy: Fundamentals and Applications*. Chichester: J. Wiley.

Talibova, A., Tokarev, M. and Hilkert, A. (2012) 'Isotope Ratio Mass Spectrometry,' in Lebedev, A. T. (ed) *Comprehensive Environmental Mass Spectrometry*. Hertfordshire: ILM Publications, pp. 475-490.

Tanaka, H. and Koga, N. (1990) 'The Thermal Decomposition of Basic Copper (II) Sulfate: An Undergraduate Thermal Analysis Experiment,' *Journal of Chemical Education,* 67 (7), pp. 612-614.

Tanaka, N., Rye, D. M., Xiao, Y. and Lasaga, A. (1994) 'Use of stable sulfur isotope systematics for evaluating oxidation reaction pathways and in-cloud-scavenging of sulfur dioxide in the atmosphere,' *Geophysical Research Letters*, 21 (14), pp. 1519-1522.

Tang, Y., Pang, H., Zhang, W., Li, Y. (2015) 'Effects of Changes in Moisture Source and the Upstream Rainout on Stable Isotopes in Precipitation – A Case Study in Nanjing, Eastern China,' *Hydrology and Earth System Sciences*, 19, pp. 4293-4306.

Tel Gezer Project (2019) 'Project Overview,' *Southwestern Baptist Theological Seminary.* Available at: http://www.telgezer.com/overview/ (Accessed on 04 May 2019).

Terzer, S., Wassenaar, L. I, Araguás-Araguás, L. J. and Aggarwal, P. K. (2013) 'Global isoscapes $\delta^{18}O$ and $\delta^{2}H$ in precipitation: improved prediction using regionalized climatic regression models,' *Hydrology and Earth System Sciences*, 17, pp 4713-4728.

Thiemens, M. H. (2002) 'Mass-Independent Isotope Effects and their Use in Understanding Natural Processes,' *Israel Journal of Chemistry*, 42, pp. 43-54.

TimeLine Auctions Limited (2017) *Malachite*. Available at: https://timelineauctions.com/lot/malachite-stalactite-cross-section/39656/ (Accessed: 08 November 2017).

Trethewey, K. R. and Chamberlain, J. (1995) *Corrosion for Science and Engineering*. 2nd ed. Essex: Longman Group Limited.

Turner, B. L., Klaus, H. D., Livengood, S. V. and Brown, L. E. (2013). 'The Variable Roads to Sacrifice: Isotopic Investigations of Human Remains from Chotuna-Huaca de los Sacrificios, Lambayeque, Peru,' *American Journal of Physical Anthropology*, 151, pp. 22-37.

University of Szeged (2010) *Hungary, City of Szeged*. Available at: http://www.pharm.u-szeged.hu/english/for-parents/hungary-city-of-szeged (Accessed : 02 May 2019).

Utah State University (2013) *Water Quality: Water Cycle Lesson Plans.* Available at: https://extension.usu.edu/waterquality/educator-resources/lessonplans/wc.

Van Stempvoort, D. R. and Krouse, H. R. (1994) 'Controls of $\delta^{18}O$ in Sulfate: Review of Experimental Data and Application to Specific Environments,' *Environmental Geochemistry of Sulfide Oxidation*, pp. 446-480.

Vedal, S. and Sullivan, J. (2007) 'Particulate Matter,' in Rom, W. and Markowitz, S. (eds) *Environmental and Occupational Medicine*. 4th ed. Philadelphia: Lippincott Williams & Wilkins, pp. 1487-1506.

Vink, B. W. (1986) 'Stability relations of malachite and azurite,' *Mineralogical Magazine*, 50, pp. 41-47.

Vodila, G., Palcsu, L., Futó, I. and Szántó, Zs. (2011) 'A 9-year record of stable isotope ratios of precipitation in Eastern Hungary: Implications on isotope hydrology and regional palaeoclimatology,' *Journal of Hydrology*, 400, pp. 144-153.

Wagner, D., Dakoronia, F., Ferguson, C., Fischer, W. R., Hills, C., Kars, I. and Meijers, R. (1997) '"Soil Archive" Classification in Terms of Impacts of Conservability of Archaeological Heritage,' in MacLeod, I., Pennec, S. and Robbiola, L. (eds) *Metal 95*. Proceedings of the International Conference on Metals Conservation, James and James, London. pp. 21-26.

Ward, R. C. and Robinson, M. (2000) *Principles of Hydrology*. 4th ed. London: McGraw-Hill.

Williams, J. (1990) *Water*. Hove: Wayland.

Wilmott, M. J. and Jack, T. R. (2000) 'Corrosion by Soils,' in Revie, W. R. (ed) *Uhlig's Corrosion Handbook*. 2nd ed. New York: John Wiley & Sons, Inc., pp. 329-347.

Wilson, L. (2004) *Approaches to Understanding* In Situ *Archaeological Diagenesis: Application of soil solution chemistry and geochemical modelling to investigate diagenetic pathways in inorganic and bioinorganic archaeological materials*. Unpublished doctoral dissertation. School of Archaeological, Geographical and Environmental Sciences, University of Bradford.

Woods, T. L. and Garrels, R. M. (1986) 'Use of oxidized copper minerals as environmental indicators,' *Applied Geochemistry*, 1, pp. 181-187.

Wu, J., Ding, Y., Ye, B., Yang, Q., Zhang, X. and Wang, J. (2010) 'Spatio-temporal variation of stable isotopes in precipitation in the Heihe River Basin, Northwestern China,' *Environmental Earth Sciences*, 61, pp. 1123-1134.

Yakir, D. (2011) 'The Stable Isotopic Composition of Atmospheric CO_2,' in Holland, H. D. and Turekian K. K. (eds) *Isotope Geochemistry: From the Treatise on Geochemistry*. London: Elsevier Ltd, pp. 113-150.

Yakir, D., Berry, J. A., Giles, L. and Osmond, C. B. (1993) 'The ^{18}O of Water in the Metabolic Compartment of Transpiring Leaves,' in Ehleringer, J. R., Hall, A. E. and Farquhar, G. D. (eds) *Stable Isotopes and Plant Carbon-Water Relations*. San Diego; London: Academic Press, INC., pp. 529-540.

Zhang, M. and Wang, S. (2016) 'A review of precipitation isotope studies in China: Basic pattern and hydrological processes,' *Journal of Geographical Sciences*, 26(7), pp. 921-938.

Zhang, M., Zhu, X., Wu, X., Yin, J. and Pan, M. (2015) '$\delta^{18}O$ characteristics of meteoric precipitation and its water vapor sources in the Guilin area of China,' *Environmental Earth Sciences*, 74, pp. 953-976.

Zheng, Y.-F. (1998) 'Oxygen isotope fractionation between hydroxide minerals and water,' *Physics and Chemistry of Minerals*, 25, pp. 213-221.

Zittlau, A. H., Quan, S., Boerio-Goates, J. and Majzlan, J. (2013) 'Thermodynamics of the Basic Copper Sulfates Antlerite, Posnjakite, and Brochantite,' *Chemie der Erde – Geochemistry*, 73 (1), pp. 39-50.

APPENDIX A:

Sample Catalog for the Brochantite and Malachite Studies

All brochantite and malachite samples considered for the doctoral project are listed, including those eliminated during processing. Different information is available for each sample, but everything known is provided. The extent of analysis carried out for each sample and reason for exclusion (if relevant) is reported.

BROCHANTITE SAMPLES

Almost 70 samples were collected from patinated roofs and historic objects, but due to time and financial restraints, only 33 were used for isotopic analysis. All samples were analyzed using XRD (refer to the digital Appendix in Volume II for spectra) to select the purest for processing and mass spectrometry. The aim was to have a batch of 5-10 samples to represent each site. Samples included in the isotope study are marked with an asterisk.

Ottawa

Building/Sample	Description	Analyses
*American Embassy	Roof sample, 1930s	OM, XRD, MS
*Booth House	Roof sample, 1906	OM, XRD, MS
Bruyère Hospital 1	Roof sample, 1866, excluded – contaminated	OM, XRD
*Bruyère Hospital 2	Roof sample, 1866	OM, XRD, MS
*Center Block (W) *Center Block (S1) Center Block (S2)	Roof samples, 1889, one 'S' was excluded for being extra, 'W' was included	OM, XRD, MS
*Confederation Building	Roof sample, 1931	OM, XRD, MS
Handicap Sign	Roadside sign, excluded – no brochantite	OM, XRD
*Hotel Lord Elgin	Roof sample, 1941	OM, XRD, MS
Justice Building	Roof sample, excluded from study-limitations	OM, XRD
Langevin Block	Roof sample, excluded from study-limitations	OM, XRD
*St. Joseph's Parish	Roof sample	OM, XRD, MS
Supreme Court	Roof sample, excluded – contaminated	OM, XRD
*Wellington Building	Roof sample, 1930s	OM, XRD, MS
West Block	Roof sample, excluded – contaminated	OM, XRD
West Memorial	Roof sample, excluded – contaminated	OM, XRD

Oxford

Building/Sample	Description	Analyses
*Corpus Christi	Roof sample, 1960s, XRD, MS	OM, XRD, MS
Magdalene Jesus' Calf	Statue sample, 1963, excluded – no brochantite	OM, XRD
*New College	Roof sample	OM, XRD, MS
*Old Observatory	Roof sample, 1875	OM, XRD, MS
*Oriel Library	Roof sample, 1930s	OM, XRD, MS
Oriental Institute	Roof sample, excluded-limitations	OM, XRD
*Philosophy Centre	Roof sample, 1930-1950s	OM, XRD, MS
*Rhodes House (Oriel)	Roof sample, 1911	OM, XRD, MS
*Rhodes Mandela House	Cupola sample, 1928	OM, XRD, MS
Sheldonian Theatre Cupola Urn, left	Urn sample, Excluded – no brochantite or suspected contamination	OM, XRD
Sheldonian Theatre Cupola Urn, right	Urn sample, Excluded – no brochantite or suspected contamination	OM, XRD
St. Catherine's	Door sample, Excluded – no brochantite	OM, XRD
*St. Cross Law	Roof sample and vent sample, 1964	OM, XRD, MS
The Ox, Rail Station	Statue sample, 2001, too small to proceed	OM
Flore, Maison Française	Statue sample, too small to proceed	OM

APPENDIX A: SAMPLE CATALOG FOR THE BROCHANTITE AND MALACHITE STUDIES

Berne

Building/Sample	Description	Analyses
Parliament Building	Roof sample. Not personally collected. Excluded from study for being only sample to represent Berne.	OM, XRD

Tuscaloosa

Building/Sample	Description	Analyses
BB Comer	Roof sample, excluded – contaminate	OM, XRD
*Bidgood Hall	Roof sample, 1928	OM, XRD, MS
*Bryce Hospital (women's admin)	Gutter sample, 1859	OM, XRD, MS
*Bryce Hospital (receiving office)	Awning sample, 1859	OM, XRD, MS
Bryce Hospital (unknown)	Roof sample, excluded – contaminated	OM, XRD
*Carmichael Hall vent	Vent sample, 1925	OM, XRD, MS
Carmichael Hall 2	Roof sample, 1925, excluded-limitations	OM, XRD
*Farrah Hall	Roof sample, 1927	OM, XRD, MS
*Gallalee Hall	Roof sample, 1949	OM, XRD, MS
Gallalee Hall Dome	Dome sample, 1949, excluded-limitations	OM, XRD
Mystery U of A	Unknown roof sample, excluded-limitations	OM, XRD
*Presidential Hall 1, 2, 3	Roof samples, replaced, only one sample used, other extra	OM, XRD, MS
Rowan-Johnson	Roof Sample, excluded-limitations	OM, XRD
*Wilson Hall	Roof sample	OM, XRD, MS

Vienna

Building/Sample	Description	Analyses
*Burgtheater Chimney	Chimney sample, 1888	OM, XRD, MS
Hofburg Helmet	Statue sample, excluded-tiny sample	OM, XRD
*Hofburg Angel Base	Statue sample, 1881	OM, XRD, MS
Hofburg Butterfly House	Roof sample, excluded-small	OM, XRD
Hofburg Cupola Door	Door sample, excluded – contaminated	OM, XRD
Hofburg Leaf Decoration	Statue sample, excluded-small	OM, XRD
Hofburg Temple	Roof sample, excluded – contaminated	OM, XRD
Karlskirche Drain Pipe	Drain pipe sample, excluded-small	OM, XRD
*Karlskirche Vent Hood	Vent sample	OM, XRD, MS
*Linke Sheet	Removed roof sample	OM, XRD, MS
Linke Gilded Sheet	Removed roof, excluded – contaminated	OM, XRD
*Peterskirche	Roof sample,	OM, XRD, MS
*Vienna Tech. Uni.	Roof sample	OM, XRD, MS
Vienna Tech. Uni. Sheet	Removed roof sample, excluded-small	OM, XRD
*Votivekirche	Roof sample	OM, XRD, MS

MALACHITE SAMPLES

205 samples were collected from archaeological objects, but due to time and financial restraints, only 56 were used for isotopic analysis. Many samples were analyzed using FTIR and XRD (refer to the digital Appendices in Volume II for spectra) to select the purest for processing and mass spectrometry. The aim was to have a batch of 5-10 samples to represent each site. Samples included in the isotope study are marked with an asterisk.

"Asia"

Sample	Description	Analyses
A1	Duo bell, Museum of Asian Art, Wiltshire, BATEA 231, removed-too contaminated	OM, FTIR
A2	Dagger axe, Museum of Asian Art, Wiltshire, BATEA 232, aka 'A,' removed- one insufficient representation of vague provenance, limitations	OM, FTIR, XRD
A3	Oil burner, Museum of Asian Art, Wiltshire, BATEA 245, removed-too contaminated	OM

China

Sample	Site	Description	Analyses
CHS1	Hunan	Spearhead, 11th cen. BC, removed-no malachite	OM, FTIR
CHS2	Hunan	11th cen. BC, removed-no malachite	OM, FTIR
CHS3	Hunan	11th cen. BC, removed-no malachite	OM, FTIR
CHN1	Panlongcheng, Hubei	Vessel, 1600-1300 BC- removed-contained sulfur	OM, FTIR, XRD
CHN2	Panlongcheng, Hubei	Vessel, 1600-1300 BC- removed-contained sulfur	OM, FTIR, XRD
*CJS	Niucheng in Jiangxi	Vessel, 13-11th cen. BC	OM, FTIR, XRD, MS
CGS1	Guangxi	Unidentified object, removed-contained sulfur	OM, FTIR, XRD
*CGS2	Guangxi	interior base	OM, FTIR, XRD, MS
*CGS3	Guangxi	Ding vessel	OM, FTIR, XRD, MS
*CGS4	Guangxi?	Ding external belly	OM, FTIR, XRD, MS
*CGS5	Guangxi	Hu vessel	OM, FTIR, XRD, MS
*CJN	Jiangsu	Ding leg	OM, FTIR, XRD, MS
CGN1	Gansu?	Unidentified object, removed – contained sulfur	OM, FTIR, XRD
*CGN2	Gansu?	Ding internal surface vessel	OM, FTIR, XRD, MS
CGN3	Gansu, Hena	Pen vessel, removed – contained sulfur	OM, FTIR, XRD
*CNM1	Ningxia Museum mystery site	Tube Fragment, Chinese?	OM, FTIR, XRD, MS
CNM2	Ningxia Museum mystery site	Mirror Fragment, Chinese?, removed – contained sulfur	OM, FTIR, XRD
*CNW1	West Ningxia near Gobi desert	slag	OM, FTIR, XRD, MS
*CNW2	West Ningxia near Gobi desert	slag	OM, FTIR, XRD, MS
*CNW3	West Ningxia near Gobi desert	slag	OM, FTIR, XRD, MS
*CNW4	West Ningxia near Gobi desert	slag	OM, FTIR, XRD, MS
*CNW5	West Ningxia near Gobi desert	slag	OM, FTIR, XRD, MS
CNWg1	West Ningxia near Gobi desert	ore	OM, FTIR, XRD, MS
CNWg2	West Ningxia near Gobi desert	ore	OM, FTIR, XRD, MS

CNWg3	West Ningxia near Gobi desert	ore	OM, FTIR, XRD, MS
CNWg4	West Ningxia near Gobi desert	ore	OM, FTIR, XRD, MS
CNWg5	West Ningxia near Gobi desert	Ore – removed, contained sulfur	OM, FTIR, XRD
CNY1	Ningxia, Guyuan City, Yuanzhou District	object fragment - looks like chess pawn, Chinese?, removed – no malachite	OM, FTIR
CNY2	Ningxia, Guyuan City, Yuanzhou District	object fragment - looks like musical quarter note, Chinese?, removed – no malachite	OM, FTIR
CNY3	Ningxia, Guyuan City, Yuanzhou District	object fragment - looks like arch fragment, Chinese?	OM, FTIR
CNP	Ningxia, Guyuan City, Pengyang County	object fragment - has 3 circles, Chinese?, removed – no malachite	OM, FTIR, XRD
C1	Niucheng, Jiangxi	Vessel, 13-11th century B.C., too small	OM
C2	Hunan	Vessel, 11th century B.C, removed-too contaminated	OM
C3	Hunan	Vessel, 11th century B.C, removed-too small and contaminated	OM
C4	Hunan	Vessel, 11th century B.C, removed-too small and contaminated	OM
C6	Hunan	Vessel, 11th century B.C, removed-too small and contaminated	OM
C7	Zhouyuan site in Shaanxi	Accessory, 1076-777 B.C., removed-too small and contaminated	OM
C8	Zhouyuan site in Shaanxi	Vessel, 1076-777 B.C., removed-too small and contaminated	OM
C9	Zhouyuan site in Shaanxi	Horse accessory, 1076-777 B.C., removed-too small and contaminated	OM
C10	Zhouyuan site in Shaanxi	Accessory, 1076-777 B.C., removed-too small and contaminated	OM
C11	Zhouyuan site in Shaanxi	Accessory, 1076-777 B.C., removed-too small and contaminated	OM
C14	Panlongcheng, Hubei	Vessel, 1600-1300 B.C., removed, too small and contaminated	OM
CY1	Guangxi	**二糸筒** Double-threaded(?) *tong*-cylinder [vessel type], 001913, removed-too small and/or contaminated.	OM
CY2	Guangxi	**物片** Object piece [artifact type], 001913, removed-too small and/or contaminated.	OM
CY3	Guangxi	001914, removed-too small and/or contaminated.	OM
CY4	Guangxi	002167, **盘** *pan*-dish [vessel type], removed-too small and/or contaminated.	OM
CY5	Guangxi	001917, **簋** *gui*-bowl [vessel type], removed-too small and/or contaminated.	OM
CY6	Guangxi	002178, *lian*-toiletry case [vessel type] 内壁 Inside wall [site on vessel], **府部**Belly [site on vessel, **府** a loan for **腹**? – alternatively it could be **底部** as "base"], removed-too small and/or contaminated.	OM
CY7	Guangxi	002162, 杯 *bei*-cup [vessel type], 内壁 Inner wall [of vessel], removed-too small &/or contaminated.	OM

CY8	Guangxi	001903, **鼎** *ding*-tripod [vessel type], removed-too small and/or contaminated.	OM
CY9	Guangxi	001903, 内壁 Inside wall [site on vessel], **鼎** *ding*-tripod [vessel type], removed-too small and/or contaminated.	OM
CY10	Guangxi?	001911, 鼎腹 *ding*-tripod belly [vessel type and site on vessel], 外壁 Outside wall [site on vessel], Rust, removed-too small and/or contaminated.	OM
CY11	Guangxi?	001911, 鼎底 *ding*-tripod base [vessel type and site on vessel], Rust, removed-too small and/or contaminated.	OM
CY12	Guangxi	002177, **鐎壺** *jiaohu*-jar [vessel type], removed-too small and/or contaminated.	OM
CY13	Guangxi?	002183-1, **堂瓦** hall roof tile [piece type], removed-too small and/or contaminated.	OM
CY14	Guangxi?	002183-1, removed-too small and/or contaminated.	OM
CY15	Unknown China	002183-3, **釜** *fu*-cauldron [vessel type] [alt. **斧**?], removed-need site.	OM
CY16	Unknown China	002183, **灶** *zao*-stove [vessel type], removed-need site.	OM
CY17	Unknown China	1911, 足 Foot [site on vessel], **鼎** *ding*-tripod [vessel type], removed- need site	OM
CY18	Nanning, Guangxi	**盘** *pan*-dish [vessel type], removed-too small and/or contaminated.	OM
CY19	Unknown China	1911, 足内 Inside the foot (interior), removed, need site	OM
CY20	Unknown China	001913, 内土 Inner dirt, 壤 Soil, removed-no malachite	OM
CY21	Jiangsu	**辅甬物片** … piece [vessel/instrument/chariot fitting type], removed-too small and/or contaminated.	OM
CY22	Jiangsu	**鼎腿** *ding*-tripod foot [vessel type and site on vessel], removed-too small and/or contaminated.	OM
CY23	Unknown China	**礼**??**壺圓足** ritual ? *hu*-jar rounded foot, removed-need site.	OM
CY24	Unknown China	1504, **盆** *pen*-basin [vessel type], removed- need site	OM
CY25	Unknown China	3: **第**1523, removed-need site	OM
CY26	Unknown China	**第**(number) 1494, removed-need site	OM
CY27	Unknown China	第(number) 1509, **鼎腹内***ding*-tripod belly, inside [vessel type and site on vessel], removed-need site	OM
CY28	Gansu?	HENA [location] (Should it be Henan? This conflicts with Gansu however…), **盆** *pen*-basin [vessel type], removed-too small and/or contaminated.	OM
CY29	Unknown China	1534 (1123 written upside down, with writing oriented in opposite reading order, immediately next to the first number), 盆 *pen*-basin [vessel type], removed-need site	OM
CY30	Gansu	未知器物片 piece from an unknown vessel [artifact type], removed-too small and/or contaminated.	OM

Cyprus

Sample	Description	Analyses
RC1	No. 84 Episkopi Seraya. excluded-no malachite	OM, FTIR, XRD
*RC2	PK2014.(W. Lobe) R13 under V.S., PK14.68, MS repeated, but no data yield	OM, FTIR, XRD, MS
RC3	Mix-multiple objects, Politiko, plot 487, excluded-no malachite and contained sulfur	OM, FTIR, XRD
*RC4	PK14 W LOBE. R13, PK.14.64	OM, FTIR, XRD, MS
RC5	mix-multiple objects, Tomb No. 28, Polemidia, excluded-no malachite and contained sulfur	OM, FTIR, XRD
RC6	Courion 2003. SW of Barinza, N4.LN219/15, excluded – no malachite	OM, FTIR, XRD
*RC7	Koupio Agios Ermogenis, T64/107, LN267/15	OM, FTIR, XRD, MS
*RC8	Koupio Agios Ermogenis, T64/108. LN.268/15	OM, FTIR, XRD, MS
CYP1	Kalopsida, Bachman 97. Kalop 10 [219], slag, excluded – no malachite	OM, FTIR
CYP2	Kalopsida, Cyprus, Trench 9 – South + Middle part, Kalop 9/3C, slag excluded - contained sulfur	OM, FTIR
CYP3	Kalavassos Region, [429] MAV1, Mauridhia Mine, ore, excluded - no malachite	OM, FTIR
PK.2014.0028	excluded-insufficient malachite	OM
PK.2014.0033	excluded-insufficient malachite	OM
PK.2014.0037	excluded-insufficient malachite	OM
PK.2014.0034	excluded-insufficient malachite	OM
PK.2014.0068	excluded-insufficient malachite	OM
PK.2014.0064	excluded-insufficient malachite	OM

Southern England

Sample	Description	Analyses
E1	21-coin hoard, WLB II, Wiltshire, removed-contained sulfur	OM, FTIR
*E2	Coin hoard, Malmsbury, Wiltshire, 2012, T652	OM, FTIR, XRD, MS
*E3	Coin hoard, Pewsey, Wiltshire, 2014, T255	OM, FTIR, XRD, MS
*E4	Coin hoard, Boldre, Hampshire, 2014, T287	OM, FTIR, XRD, MS
E5	Cu alloy object, Fenchurch Street, 1983, London, FEN 83 [969] <86>, removed-contained sulfur	OM, FTIR, XRD
*E6	Cu alloy object, Fenchurch Street, 1983, London, FEN 83 [2921] <437>	OM, FTIR, XRD, MS
*E7	Cu alloy object, Fleet Valley Project, 1988, London, VAL 88 [4041] <3313>	OM, FTIR, XRD, MS
E8	Barlaston coin sample from British Museum, removed-too contaminated	OM
EC1	Guilded brooch, 3rd cent. Roman, Rhodaus Town Canterbury, Grave 6, removed-contained sulfur	OM, FTIR, XRD
*EC2	Historic wire (1920-30s), South Foreland Lighthouse near Dover, Kent	OM, FTIR, XRD, MS
EC3	Random historic metal detector finds, Little Farthingloe Farm, Dover, Kent, removed-too contaminated	OM, FTIR, XRD
*EC4	Ingot/Cu cake fragment (find 17), mid-late Bronze age, Bogshole Lane, BA hoard, Broomfield, Kent,	OM, FTIR, XRD, MS
*EC5	Ingot/Cu cake fragment (find 16), mid-late Bronze age, Bogshole Lane, BA hoard, Broomfield, Kent,	OM, FTIR, XRD, MS
EC6	Ingot/Cu cake fragment (find 24), mid-late Bronze age, Bogshole Lane, BA hoard, Broomfield, Kent, removed-too contaminated	OM
EC7	Ingot/Cu cake fragment (find 27), mid-late Bronze age, Bogshole Lane, BA hoard, Broomfield, Kent, removed-too contaminated	OM
EC8	Ingot/Cu cake fragment (find 28), mid-late Bronze age, Bogshole Lane, BA hoard, Broomfield, Kent, removed-too contaminated	OM
EC9	Historic metal detector find, fragment, Thanet Earth, Kent, removed-too small and contaminated	OM

EC10	Historic metal detector find, bell fragment, Thanet Earth, Kent, removed-too contaminated	OM
EC11	Wire, Modern/historic metal detector find, Port Farm, Upstreet, Kent, removed-too small and contaminated	OM
*EC12	Alloy globs, modern/historic, Hallets Garage Canterbury, Kent, in study as EC8	OM, FTIR, XRD, MS
*EC13	Alloy fragment, modern/historic, Hallets Garage Canterbury, Kent, in study as EC7	OM, FTIR, XRD, MS
EC14	William and Mary coin (1694), Historic metal detector find, Thanet Earth, Kent, removed-too small and contaminated	OM
EC15	Historic metal detector find, fragment, Thanet Earth, Kent, removed-too small and contaminated	OM
EC16	Historic metal detector find, knob/fitting, Thanet Earth, Kent. removed-too small and contaminated	OM
EC17	Sword fragment, late Bronze Age hoard, Boughton Malherbe (Kent), Maidstone Museum, 2014.13.59, not included-too small and contaminated	OM
EC18	Ingot, late Bronze Age hoard, Boughton Malherbe (Kent), Maidstone Museum, 2014.13.206, not included-too small and contaminated	OM
EC19	Ingot, late Bronze Age hoard, Boughton Malherbe (Kent), Maidstone Museum, 2014.13.213, not included-too small and contaminated	OM
EC20	Ingot, late Bronze Age hoard, Boughton Malherbe (Kent), Maidstone Museum, 2014.13.215, not included-too small and contaminated	OM
EC21	Ingot, late Bronze Age hoard, Boughton Malherbe (Kent), Maidstone Museum, 2014.13.217, not included-too small and contaminated	OM
EC22	Ingot, late Bronze Age hoard, Boughton Malherbe (Kent), Maidstone Museum, 2014.13.221, not included-too small and contaminated	OM
EC23	Ingot, late Bronze Age hoard, Boughton Malherbe (Kent), Maidstone Museum, 2014.13.227, not included-too small and contaminated	OM
EC24	Ingot, late Bronze Age hoard, Boughton Malherbe (Kent), Maidstone Museum, 2014.13.228, not included-too small and contaminated	OM
EO1	Axehead, saturated/treated in 1880s with wax?, hoard from Leopold St, Oxford, AN1881.198, removed-contained sulfur	OM, FTIR, XRD
*EO2	Socketed axehead, saturated/treated in 1880s with wax?, hoard from Leopold St, Oxford, AN1882.3	OM, FTIR, XRD, MS
EO3	Broken blade, part of axehead, saturated/treated in 1880s with wax?, hoard from Leopold St, Oxford, AN1882.8a, removed-contained sulfur	OM, FTIR, XRD
EO4	Axehead, saturated/treated in 1880s with wax?, hoard from Leopold St, Oxford, AN1882.6, removed-too contaminated	OM
EO5	Axehead, saturated/treated in 1880s with wax?, hoard from Leopold St, Oxford, AN1882.5, removed-contained sulfur	OM, FTIR, XRD
EO6	Axehead, saturated/treated in 1880s with wax?, hoard from Leopold St, Oxford, AN1882.7, removed-contained sulfur	OM, FTIR, XRD

Greece

Sample	Description	Analyses
G1	Cu alloy with ceramic I, Phylakopi-Melos (1975), Stos-Gale collection, removed-no malachite	OM, FTIR
G2	Cu alloy with ceramic II, Phylakopi-Melos (1975), Stos-Gale collection, removed-no malachite	OM, FTIR
G3	Cu alloy with ceramic III, Phylakopi-Melos (1975), Stos-Gale collection, removed-no malachite	OM, FTIR

APPENDIX A: SAMPLE CATALOG FOR THE BROCHANTITE AND MALACHITE STUDIES

Hungary

Sample	Description	Analyses
*H1	From sickle handle/part of blade; H41; Szarazd, KurdBVb	OM, FTIR, XRD, MS
*H2	From sickle handle; H50; Pecs Fund II, Kurd BVb	OM, FTIR, XRD, MS
*H3	From part of handle and blade of knife, H53	OM, FTIR, XRD, MS
*H4	From part of sickle blade, H60	OM, FTIR, XRD, MS
*H5	From two pieces of connected strip; H110; Gyermely (Szoke), Kurd BVb	OM, FTIR, XRD, MS
*H6	From sickle, H130	OM, FTIR, XRD, MS
H7	From sickle, H36, Patroha, Kurd BVb, removed-too small and contaminated	OM
H8	From decorated strip, H113, removed-too small and contamintaed	OM
*H9	From pin, H127, in study as H7	OM, FTIR, XRD, MS
H10	From socketed axe, Szentgalosker, Kurd BVb, H5, removed-too contaminated	OM
*H11	From sickle, Keszohidegut, Kurd BVb, H33, in study as H8	OM
*H12	From belt/harness mount, H105, in study as H9	OM, FTIR, XRD, MS
*H13	From sickle, Palotabozsok, Kurd BVb, H47, in study as H10	OM, FTIR, XRD, MS
H14	From sickle, Balatonkiliti, Kurd BVb, H39, removed-too small	OM
H15	From socketed axe, Oreglak, Kurd BVb, H3	
*H16	Sickle handle/part of blade, Kurd, Kurd BVb, H42, in study as H11	OM, FTIR, XRD, MS
H17	Part of bracelet, Bonyhad, Kurd BVb, H87, too contaminated	OM
H18	Sickle blade, H51, too small	OM

Sardinia, Italy

Sample	Description	Analyses
IS1	Sardinian Ores, July 1984, Bag labeled: Mal. + Az [PMI], Peroli Marvas, Iglesias (CA), removed-too contaminated	OM
IS2	Sardinia, September 1984, Castello di Borvei, Montevecchio Museum Samples, Bag labeled: Castello di Borvei Region, removed-too contaminated	OM
IS3	Sardinia 1984, Sa Duchessa; Sa Lilla, Monte Mannu, Bag labeled: Sa Duchessa, SD1006, Domusnovas (CA), removed-too contaminated	OM, FTIR

Kish, Iraq

Sample	Description	Analyses
IQ1	AN1933.1290, removed-too little, or no malachite	OM, FTIR, MS
IQ2	AN1933.1284, possibly new corrosion, removed-too little or no malachite	OM, FTIR
IQ3	ANTN.D528, bracelet, removed-probably not Iraqi, too little or no malachite	OM, FTIR
IQ4	AN1926.527, arrowhead, removed-too little or no malachite	OM, FTIR, MS
IQ5	AN1929.376, removed-too little or no malachite	OM, FTIR
IQ6	AN1926.453, pin, removed-too little or no malachite	OM, FTIR
IQ7	AN1925.196, pot, removed-too little or no malachite	OM, FTIR
IQ8	AN1925.209, chain, removed-too little or no malachite	OM, FTIR
IQ9	AN1926.533, nail head, removed-too little or no malachite	OM, FTIR
IQ10	AN1926.456, nail head, removed-too little or no malachite	OM, FTIR
IQ11	AN1931.414, spoon, removed-too little or no malachite	OM, FTIR
IQ12	AN1931.186, disk object, removed-too little or no malachite	OM, FTIR
IQ13	several objects mixed, removed-prefer single source, too little or no malachite.	OM, FTIR

APPENDIX A: SAMPLE CATALOG FOR THE BROCHANTITE AND MALACHITE STUDIES

Tel Gezer, Israel

Sample	Description	Analyses
I1	included in study as I1	OM, FTIR, XRD, MS
I2	Mix of I2, I3, I5, I9-used in study as I4	OM, FTIR, XRD, MS
I3	Mix of I2, I3, I5, I9-used in study as I4	OM, FTIR, XRD, MS
I4	Used in study as I2,	OM, FTIR, XRD, MS
I5	Mix of I2, I3, I5, I9-used in study as I4	OM, FTIR, XRD, MS
I6	removed-no malachite	OM
I7	removed-no malachite	OM
I8	Used in study as I3	OM, FTIR, XRD, MS
I9	Mix of I2, I3, I5, I9-used in study as I4	OM, FTIR, XRD, MS
I5g	Ore, King Solomon Mine, removed-no malachite	OM, FTIR
I6g	Ore, King Solomon Mine, removed-no malachite	OM, FTIR
I7g	Ore, King Solomon Mine, removed-no malachite	OM, FTIR

Huaca Loro (NE), Batán Grande, Lambayeque, Peru

Sample	Description	Analyses
P1	Crucible and prills, Excavation Area: C-18-1 y 2, Superficie Ocupación: 11, M-7 (b), MS repeated, but no data yield	OM, FTIR, XRD, MS
*P2	Metal spill (gold mix), Excavation Area: D-17-1, Cuadrante SE, Superficie Ocupación: 8, Nivel: 3, Capa: 18, M-48	OM, FTIR, XRD, MS
*P3	Metal Spill, Excavation Area: 5, Cuadrante 9, Superficie Ocupación: 10, OE-63(c)	OM, FTIR, XRD, MS
P4	Metal Spill, Excavation Area: D-17-1, Sector Sur, Estructura 2, Ocupación 8 y 8ª, M-60, MS repeated, but no data yield.	OM, FTIR, XRD, MS
P5	Metal Spill from Crucible, Excavation Area: 5, Cuadrante: 9, Ocupación: 10, OE-63 (a), removed – no malachite	OM, FTIR, XRD
*P6g	Ore sample	OM, FTIR, XRD, MS
*P7g	Sample extracted from SEM mount 2273, ore sample	OM, FTIR, XRD, MS

Spain

Sample	Description	Analyses
*SES1g	Ore sample, aka SA4g, Las Pilas, Mojacar, Almeria	OM, FTIR. XRD, MS
*SES2g	Ore sample, aka SA5g, Las Pilas, Mojacar, Almeria	OM, FTIR, XRD, MS
SES3	metal fragment, Las Pilas, Mojacar, Almeria, MLP94, C5 S.A, 5-8862, F5, removed-no malachite	OM, FTIR, XRD
SES4	Metal fragment, Las Pilas, Mojacar, Almeria, MPL94 C5 SA 5-6740, MS repeated without yield – too small	OM, FTIR, XRD, MS
SES5	Slag, Las Pilas, Mojacar, Almeria, torta, HPL/94, C-5/C, 5-3035, MS repeated without yield – too small	OM, FTIR, XRD, MS
SES6	Slag, Las Pilas, Mojacar, Almeria, MPL/94, C-5/SB 5-11064, MS repeated without yield – too small	OM, FTIR, XRD, MS
SES7	Slag, Las Pilas, Mojacar, Almeria, MPL/94, C-5/SB, 5-5383, MS repeated without yield – too small	OM, FTIR, XRD, MS
SES8	Axehead, AN1896-1908.Pr201, Almeria-Ashmolean sample	OM, FTIR, XRD, MS
*SES9	Axehead, AN1896-1908.Pr202, Almeria-Ashmolean sample	OM, FTIR, XRD, MS
SES10	Mix sample: axehead (AN1896-1908.Pr198), spearhead (AN1896-1908.Pr205), Spear (AN1896-1908.Pr208), Scrap (AN1896-1908.Pr211), Almeria-Ashmolean, removed – no malachite	OM, FTIR, XRD
SWS5	Archaeological sample, formed over metal, San Blas, Badajoz, SB/01, VE.4, Corte Z, 48, 2'69. removed-too small	OM, FTIR, XRD
SWS6	Archaeological decorative leaf, San Blas, Badajoz, SB/03, H22, VE.22, 122. removed-no malachite	OM, FTIR, XRD
SWS1g	Ore sample, aka SRTg, Rio Tinto, good malachite, but removed since no SWS archaeological samples passed for comparison.	OM, FTIR, XRD

SWS2g	Ore sample, San Blas, Badajoz, J17 (2nd compaña), VE.1, SB/02, Corte J-17, bolsa 34. good malachite, but removed since no SWS archaeological samples passed for comparison.	OM, FTIR, XRD
SWS3g	Ore sample, San Blas, Badajoz, SB/02, Corte K-7, NW VE.16, bolsa 213. good malachite, but removed since no SWS archaeological samples passed for comparison.	OM, FTIR, XRD
SWS4g	Ore sample, San Blas, Badajoz, SB/03, U7, VE.7, removed-contained sulfur and no SWS archaeological samples passed for comparison.	OM, FTIR, XRD
SG	Early Bronze Age flat axe, Serra da Capelada, Cedeira (North of Galicia), removed-too small and too contaminated.	OM

Castle Hill, Sitka, Alaska, USA

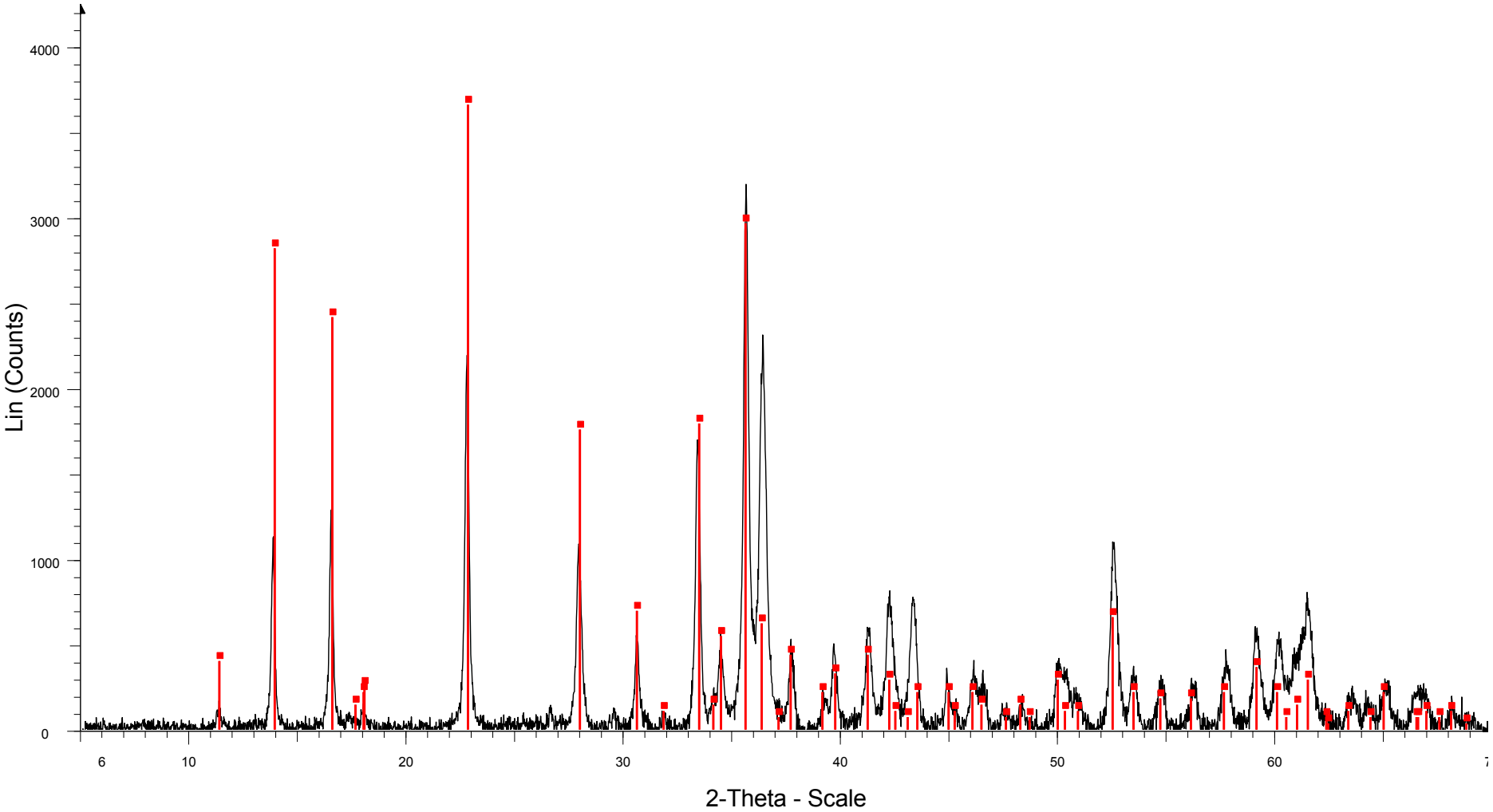
Sample	Description	Analyses
US1	Samovar gate, 98-146, removed-too few/contaminated crystals	OM
US2	copper disk/watch case, 98.5780, removed-too few/contaminated crystals	OM
US3	sheet copper bowl, 98-149, removed-too few/contaminated crystals	OM
*US4	sheet copper lid, 98-005, in study as US1	OM, FTIR, XRD, MS
*US5	sheet copper container, 97-6433, in study as US2	OM, FTIR, XRD, MS
US6	square sheet copper vessel/candle holder, 97-6432, removed-too few/contaminated crystals	OM
US7	round shallow sheet copper vessel, 98-148, removed-too few/contaminated crystals	OM
*US8	square sheet copper vessel, 98-3402, in study as US3	OM, FTIR, XRD, MS
US9	round sheet copper container, 97-6338, aka US4, removed - no malachite	OM, FTIR, XRD
*US10	round sheet copper lid, 98-6834, in study as US5, mixed with US11	OM, FTIR, XRD, MS
*US11	flattened cylindrical sheet copper container, 98-5833, in study as US5, mixed with US10	OM, FTIR, XRD, MS
*US12	sheet copper strap, 98-4755, in study as US6	OM, FTIR, XRD, MS

APPENDIX B:

XRD Spectra of the Brochantite Samples

To create these spectra, the X'Pert Pro PANalytical PW3719 powder diffractometer at University of Oxford's Chemistry Research Laboratories (CRL) was used with EVA 2, a digital library available at Inorganic Chemistry. The mineral phases identified in the samples are listed at the bottom of each spectrum.

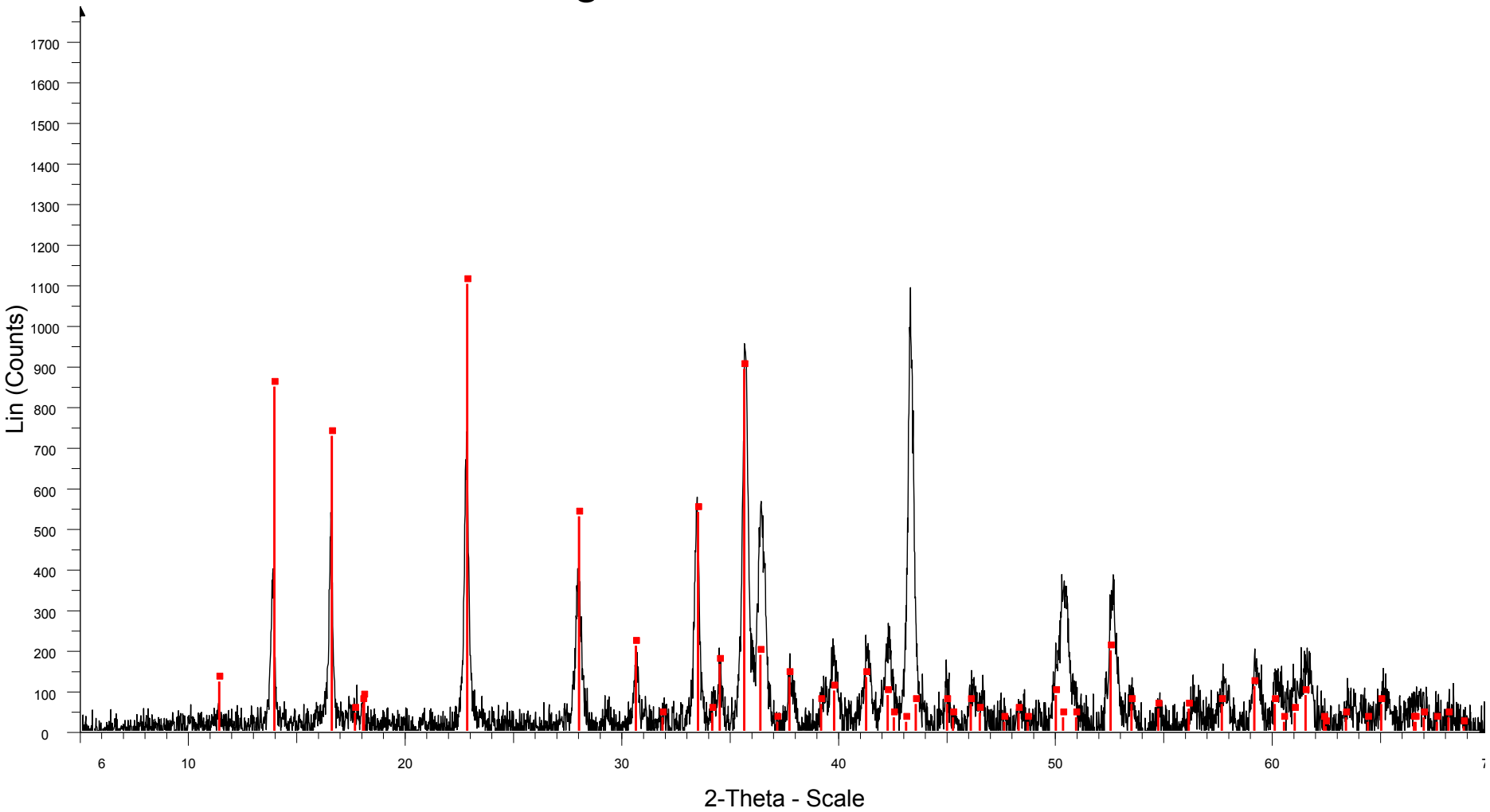
Parliament in Berne, Switzerland



File: Berne Switzerland Parliament.raw - Type: 2Th/Th locked - Start: 5.009 ° - End: 69.999 ° - Step: 0.017 ° - Step time: 2. s - Temp.: 25 °C (Room) - Time Started: 0 s - 2-Theta: 5.009 ° - Theta: 2.505 ° - Phi: 0.00 ° - Operations: Background 1.000,1.000 | Import

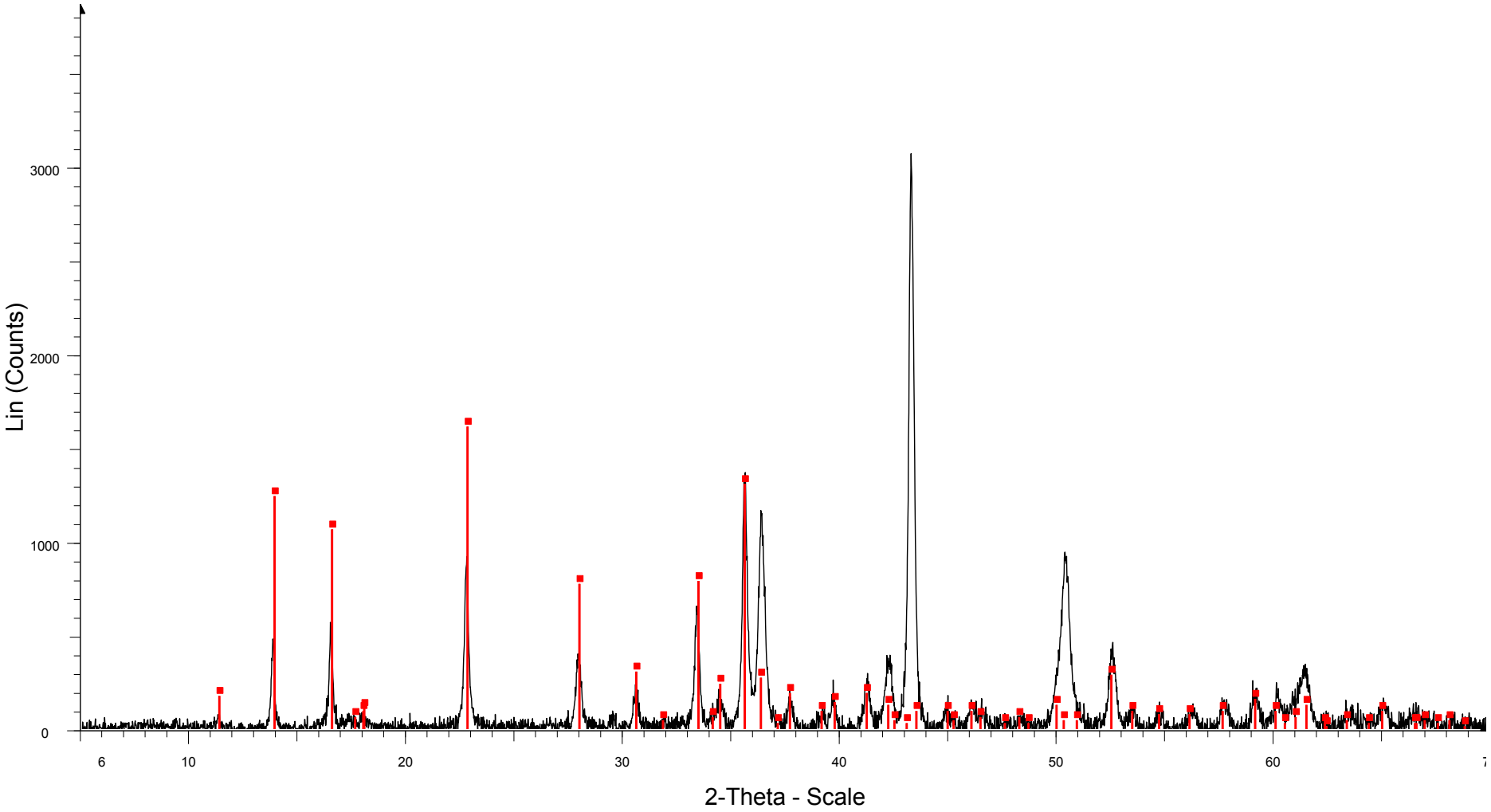
00-043-1458 (I) - Brochantite-M - Cu4+2SO4(OH)6 - Y: 114.69 % - d x by: 1. - WL: 1.5406 - Monoclinic -

Langevin Block, Ottawa



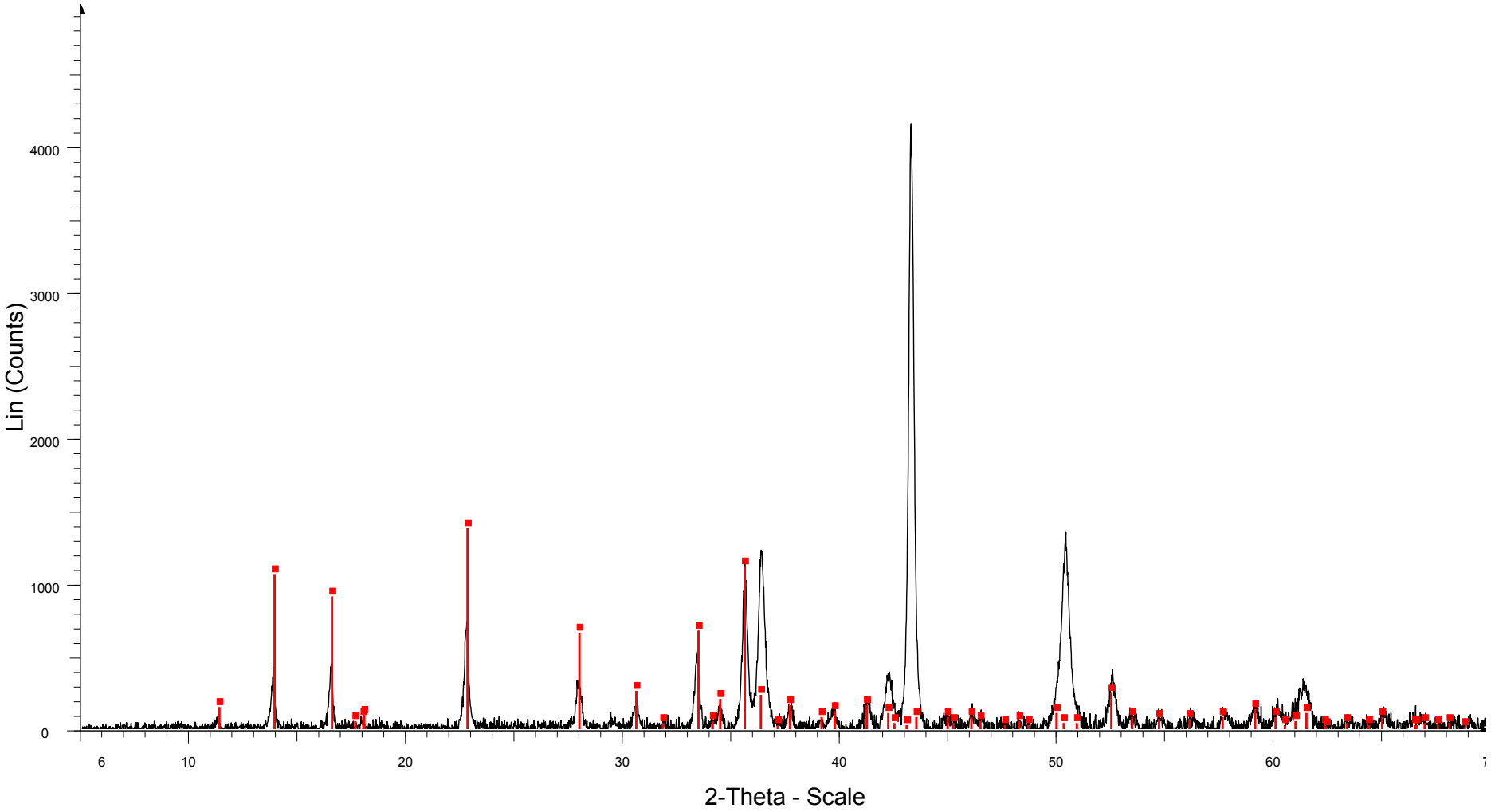
File: Langevin Block,Ottawa.raw - Type: 2Th/Th locked - Start: 5.009 ° - End: 69.999 ° - Step: 0.017 ° - Step time: 2. s - Temp.: 25 °C (Room) - Time Started: 0 s - 2-Theta: 5.009 ° - Theta: 2.505 ° - Phi: 0.00 ° - Aux1: 0
Operations: Background 1.000,1.000 | Import
00-043-1458 (I) - Brochantite-M - Cu4+2SO4(OH)6 - Y: 100.89 % - d x by: 1. - WL: 1.5406 - Monoclinic -

Parliament Block Center, Ottawa, 1

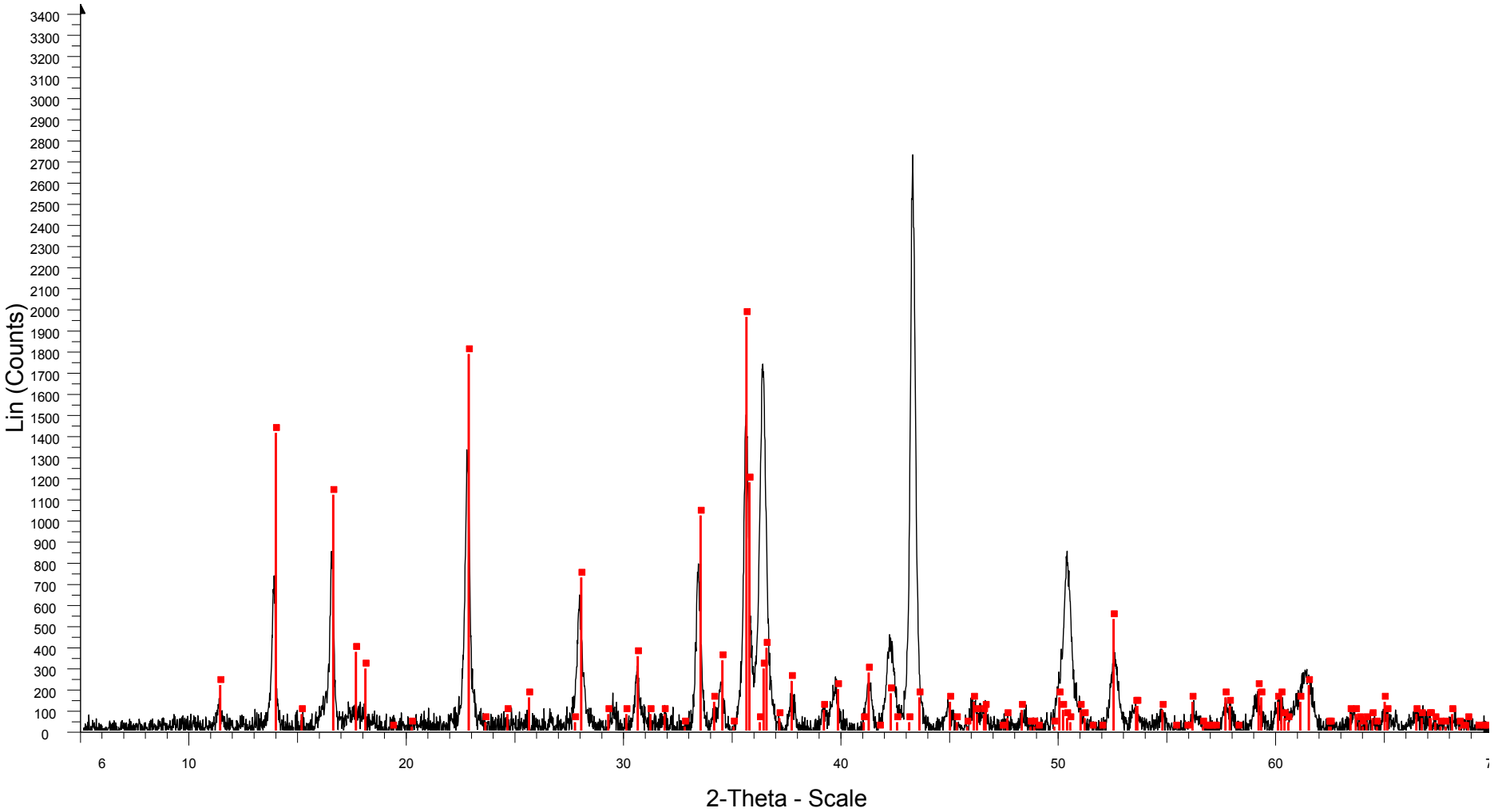


File: Parliament Block Center, Ottawa,1.raw - Type: 2Th/Th locked - Start: 5.009 ° - End: 69.999 ° - Step: 0.017 ° - Step time: 2. s - Temp.: 25 °C (Room) - Time Started: 0 s - 2-Theta: 5.009 ° - Theta: 2.505 ° - Phi: 0.0
Operations: Background 1.000,1.000 | Import
00-043-1458 (I) - Brochantite-M - Cu4+2SO4(OH)6 - Y: 52.62 % - d x by: 1. - WL: 1.5406 - Monoclinic -

Parliament Block Center, Ottawa, 2

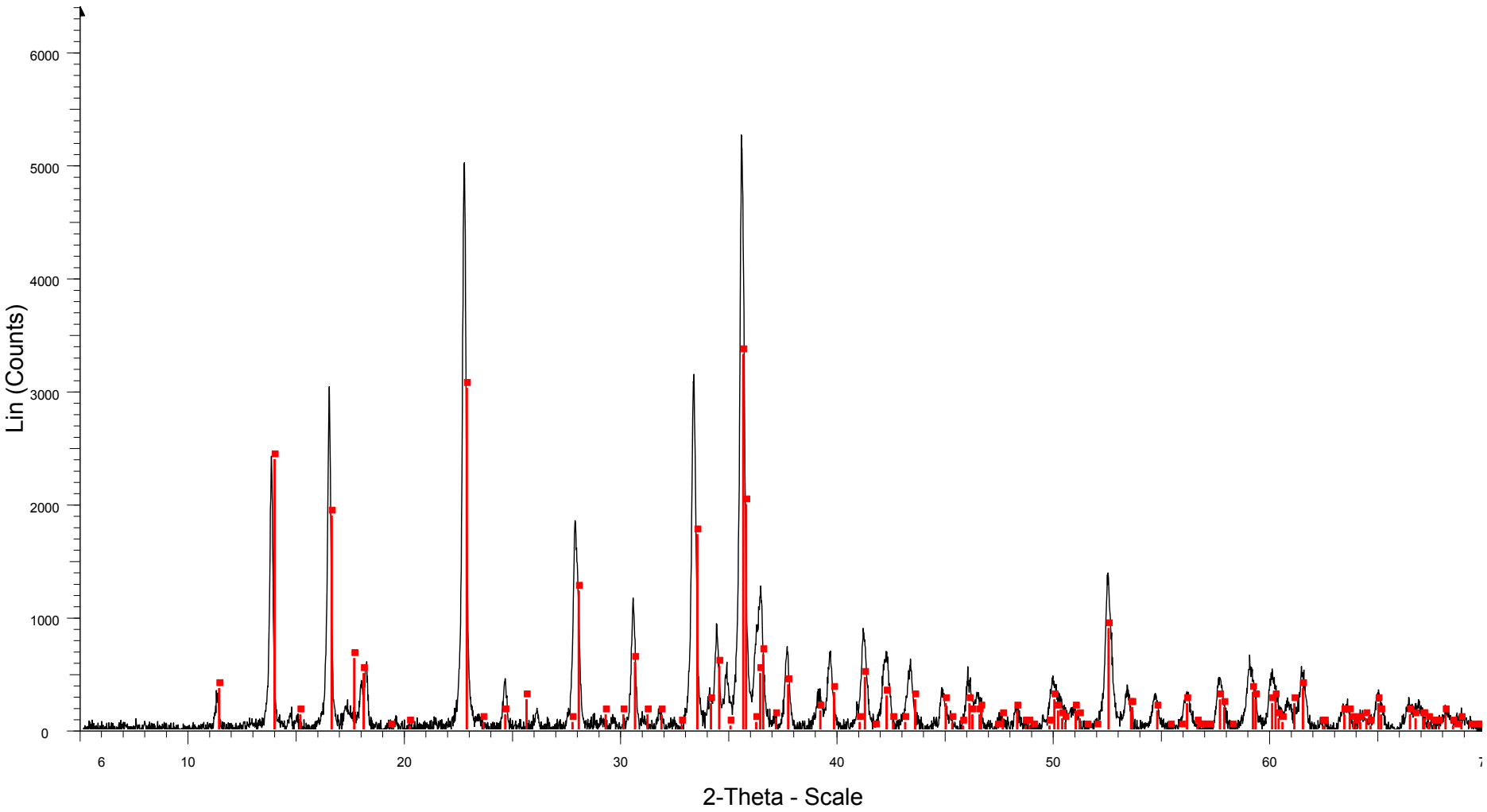


File: Parliament Block Center, Ottawa,2.raw - Type: 2Th/Th locked - Start: 5.009 ° - End: 69.999 ° - Step: 0.017 ° - Step time: 2. s - Temp.: 25 °C (Room) - Time Started: 0 s - 2-Theta: 5.009 ° - Theta: 2.505 ° - Phi: 0.0
Operations: Background 1.000,1.000 | Import
00-043-1458 (I) - Brochantite-M - Cu4+2SO4(OH)6 - Y: 33.23 % - d x by: 1. - WL: 1.5406 - Monoclinic -



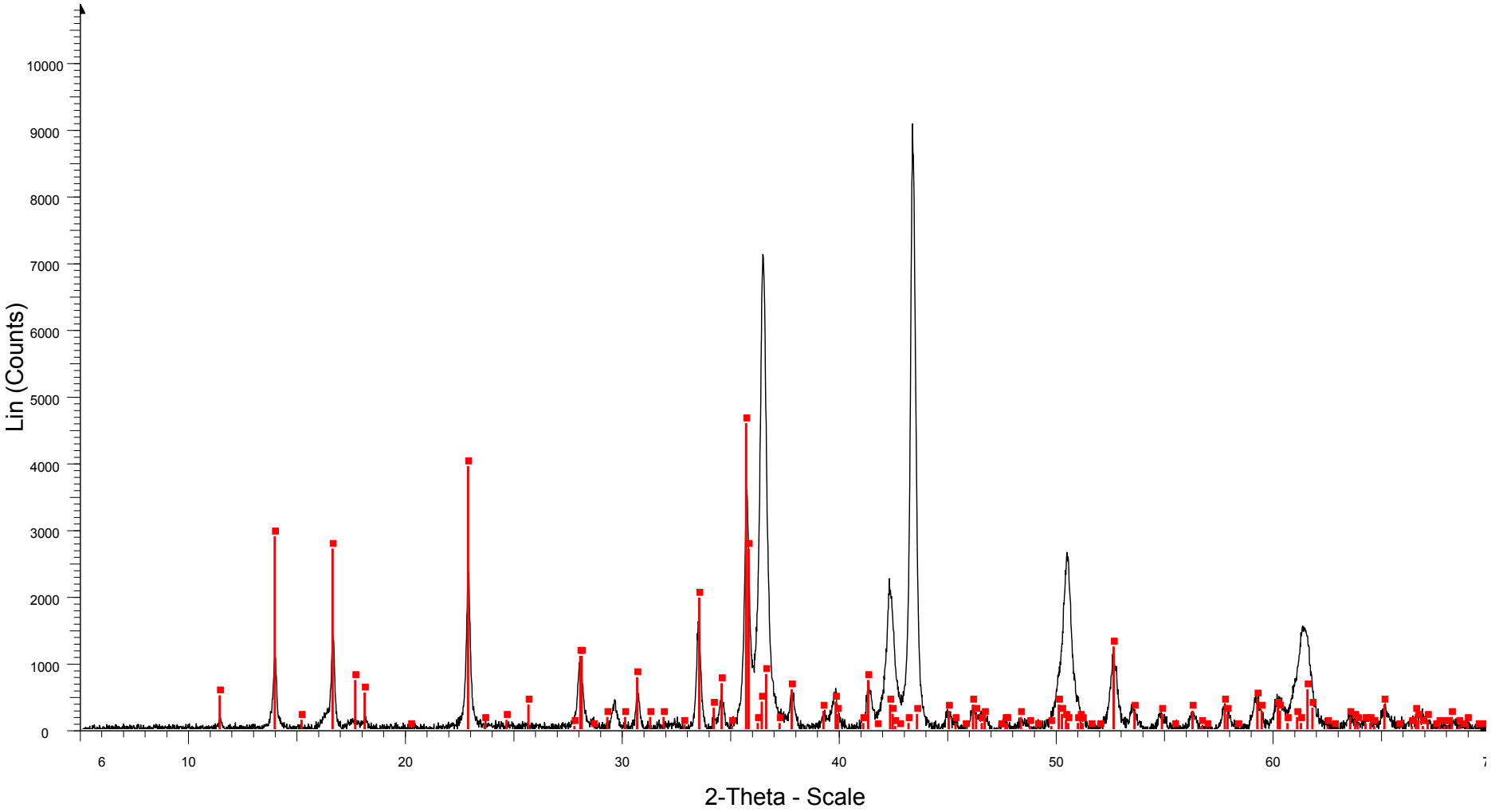
File: American Embassy.raw - Type: 2Th/Th locked - Start: 5.009 ° - End: 69.999 ° - Step: 0.017 ° - Step time: 2. s - Temp.: 25 °C (Room) - Time Started: 0 s - 2-Theta: 5.009 ° - Theta: 2.505 ° - Phi: 0.00 ° - Aux1: 0.0 - Operations: Background 1.000,1.000 | Import

01-085-1316 (C) - Brochantite - Cu4(OH)6SO4 - Y: 71.88 % - d x by: 1. - WL: 1.5406 - Monoclinic - I/Ic PDF 1. -



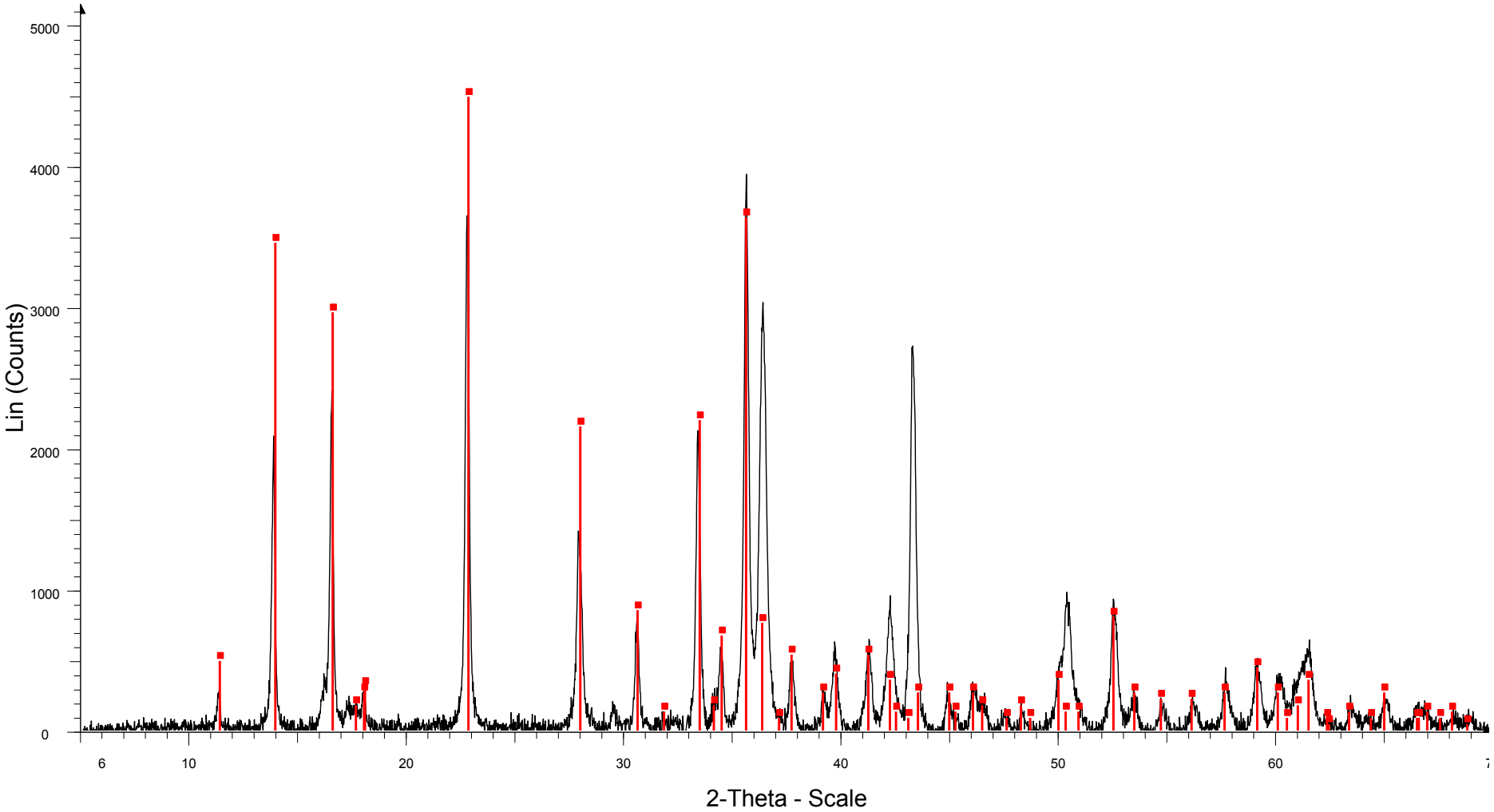
File: Booth House.raw - Type: 2Th/Th locked - Start: 5.009 ° - End: 69.999 ° - Step: 0.017 ° - Step time: 2. s - Temp.: 25 °C (Room) - Time Started: 0 s - 2-Theta: 5.009 ° - Theta: 2.505 ° - Phi: 0.00 ° - Aux1: 0.0 - Aux2:
Operations: Background 1.000,1.000 | Import

01-085-1316 (C) - Brochantite - Cu4(OH)6SO4 - Y: 63.16 % - d x by: 1. - WL: 1.5406 - Monoclinic - I/Ic PDF 1. -



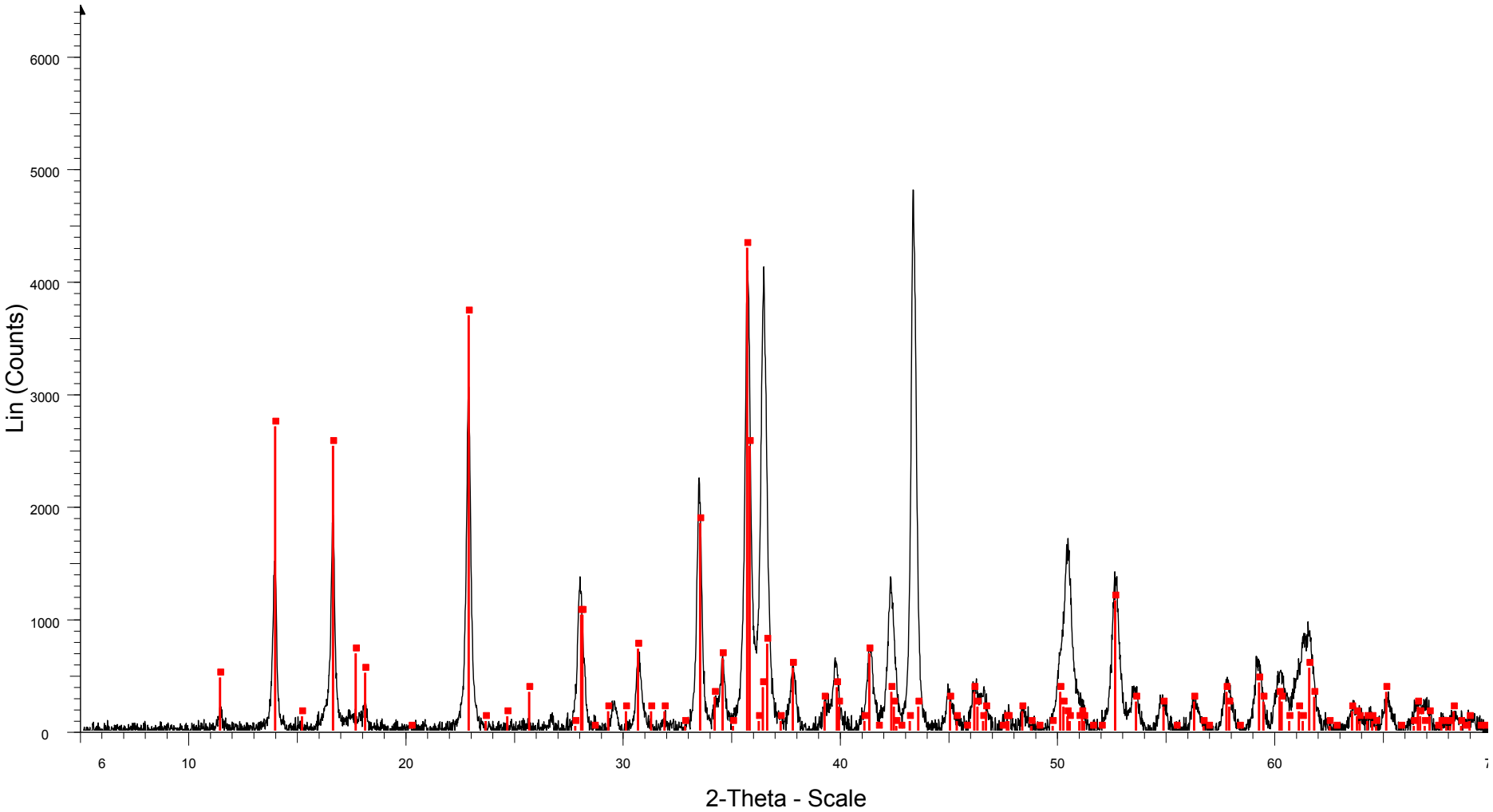
File: Bruyere Hospital 1 (front).raw - Type: 2Th/Th locked - Start: 5.009 ° - End: 69.999 ° - Step: 0.017 ° - Step time: 2. s - Temp.: 25 °C (Room) - Time Started: 0 s - 2-Theta: 5.009 ° - Theta: 2.505 ° - Phi: 0.00 ° - Aux1
Operations: Background 1.000,1.000 | Import

01-087-0454 (C) - Brochantite - Cu4(SO4)(OH)6 - Y: 50.56 % - d x by: 1. - WL: 1.5406 - Monoclinic - I/Ic PDF 1.1 -



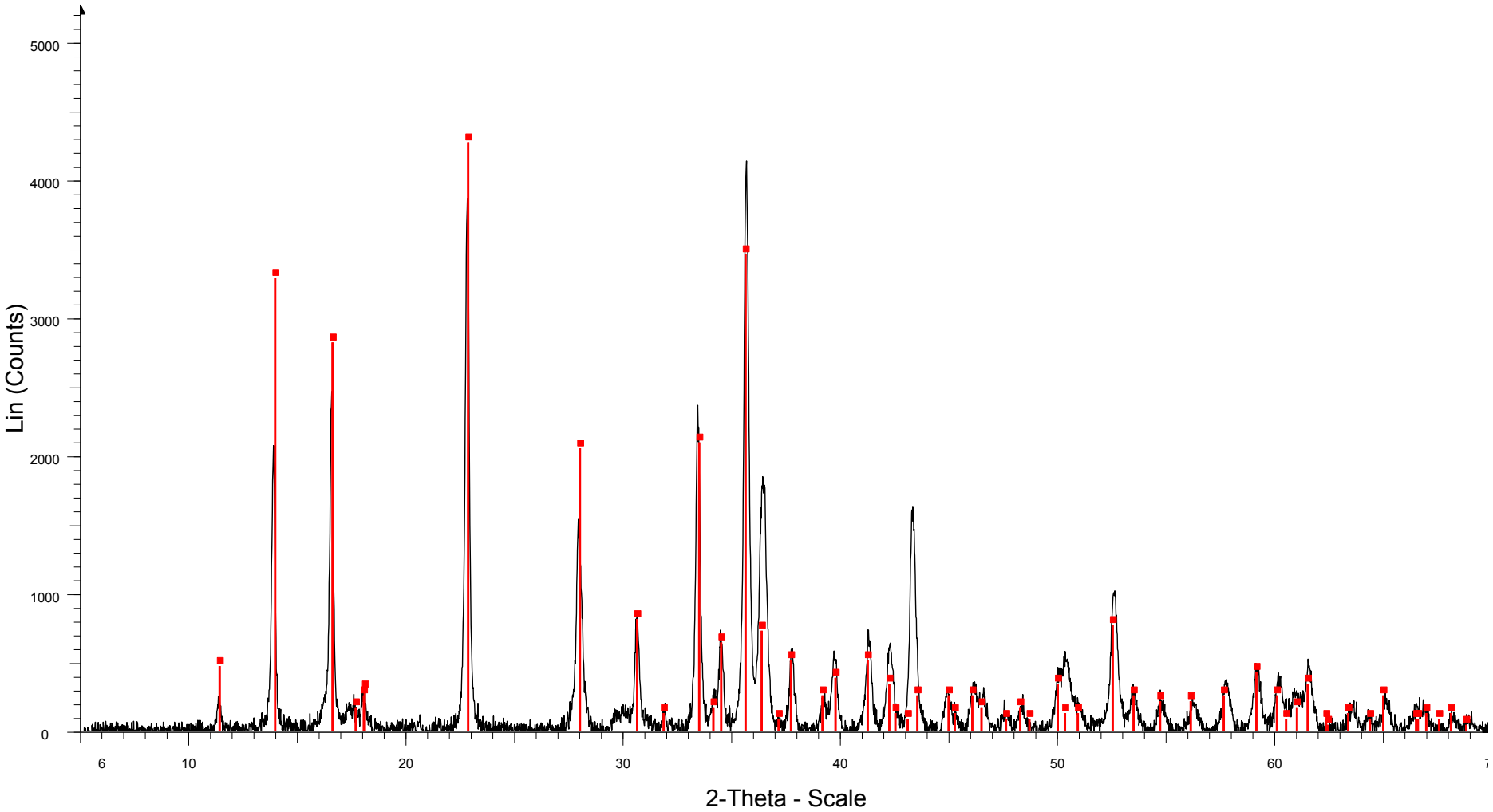
File: Bruyere Hospital, side 2.raw - Type: 2Th/Th locked - Start: 5.009 ° - End: 69.999 ° - Step: 0.017 ° - Step time: 2. s - Temp.: 25 °C (Room) - Time Started: 0 s - 2-Theta: 5.009 ° - Theta: 2.505 ° - Phi: 0.00 ° - Aux1:
Operations: Background 1.000,1.000 | Import

00-043-1458 (I) - Brochantite-M - Cu4+2SO4(OH)6 - Y: 113.92 % - d x by: 1. - WL: 1.5406 - Monoclinic -



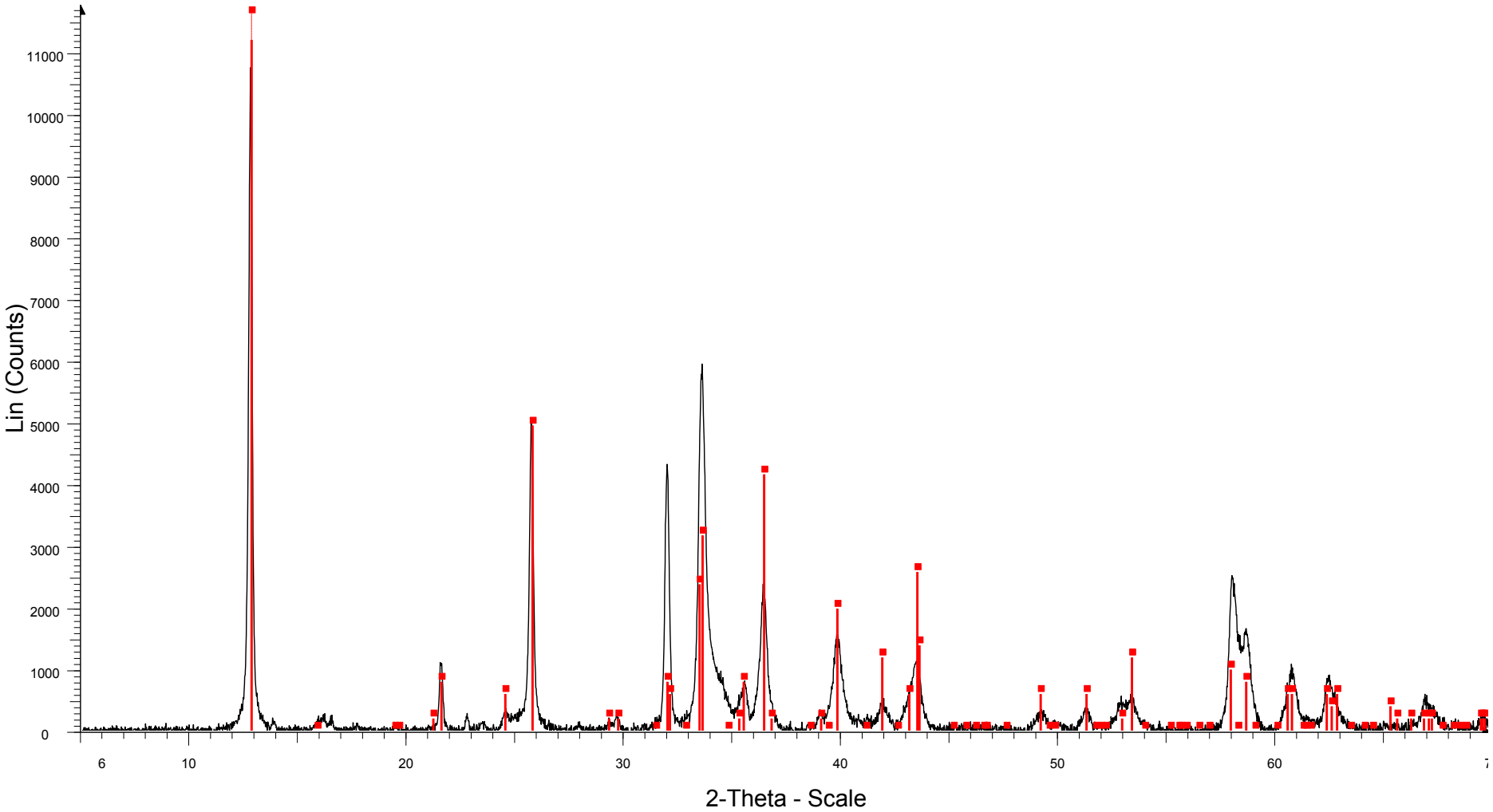
File: Centre Block (Wojdan).raw - Type: 2Th/Th locked - Start: 5.009 ° - End: 69.999 ° - Step: 0.017 ° - Step time: 2. s - Temp.: 25 °C (Room) - Time Started: 0 s - 2-Theta: 5.009 ° - Theta: 2.505 ° - Phi: 0.00 ° - Aux1: 0
Operations: Background 1.000,1.000 | Import

01-087-0454 (C) - Brochantite - Cu4(SO4)(OH)6 - Y: 89.33 % - d x by: 1. - WL: 1.5406 - Monoclinic - I/Ic PDF 1.1 -



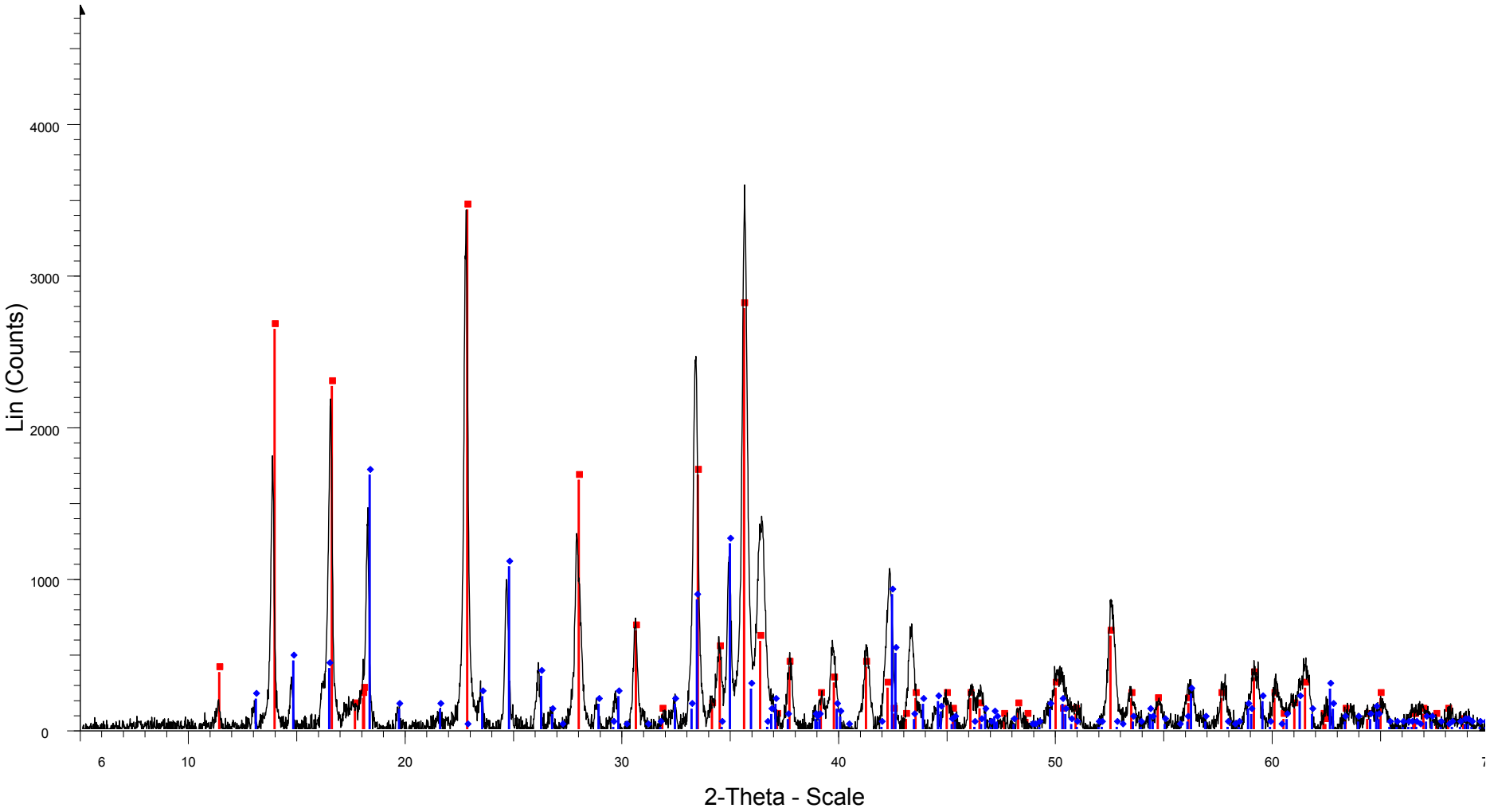
File: Confederation Building.raw - Type: 2Th/Th locked - Start: 5.009 ° - End: 69.999 ° - Step: 0.017 ° - Step time: 2. s - Temp.: 25 °C (Room) - Time Started: 0 s - 2-Theta: 5.009 ° - Theta: 2.505 ° - Phi: 0.00 ° - Aux1: 0
Operations: Background 1.000,1.000 | Import

00-043-1458 (I) - Brochantite-M - Cu4+2SO4(OH)6 - Y: 103.32 % - d x by: 1. - WL: 1.5406 - Monoclinic -



File: Handicap Sign.raw - Type: 2Th/Th locked - Start: 5.009 ° - End: 69.999 ° - Step: 0.017 ° - Step time: 2. s - Temp.: 25 °C (Room) - Time Started: 0 s - 2-Theta: 5.009 ° - Theta: 2.505 ° - Phi: 0.00 ° - Aux1: 0.0 - Aux
Operations: Background 1.000,1.000 | Import

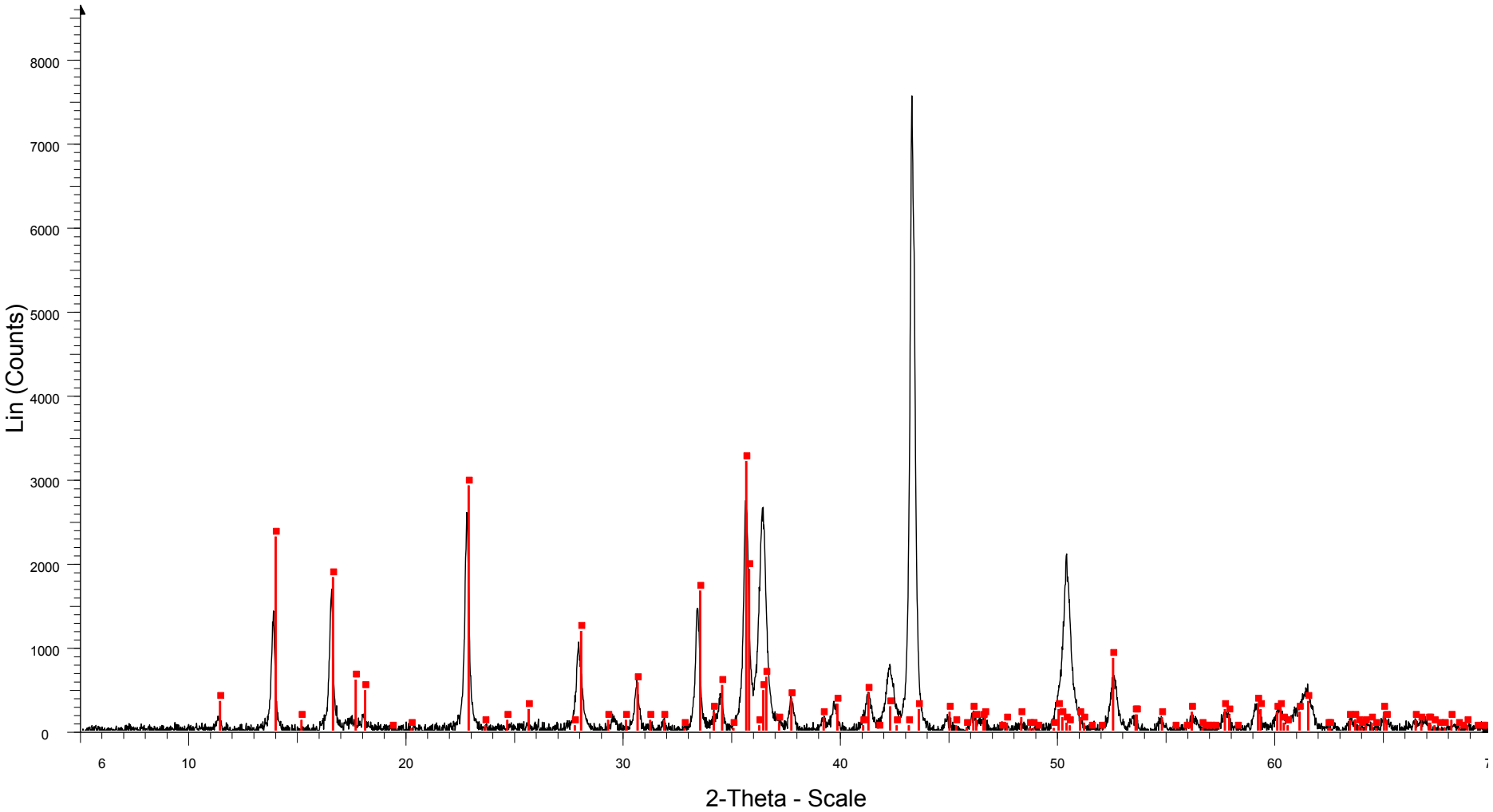
01-075-1779 (C) - Copper Hydroxide Nitrate - Cu2(OH)3(NO3) - Y: 184.19 % - d x by: 1. - WL: 1.5406 - Monoclinic - I/Ic PDF 5. -



File: Hotel Lord Elgin.raw - Type: 2Th/Th locked - Start: 5.009 ° - End: 69.999 ° - Step: 0.017 ° - Step time: 2. s - Temp.: 25 °C (Room) - Time Started: 0 s - 2-Theta: 5.009 ° - Theta: 2.505 ° - Phi: 0.00 ° - Aux1: 0.0 - Au
Operations: Background 1.000,1.000 | Import

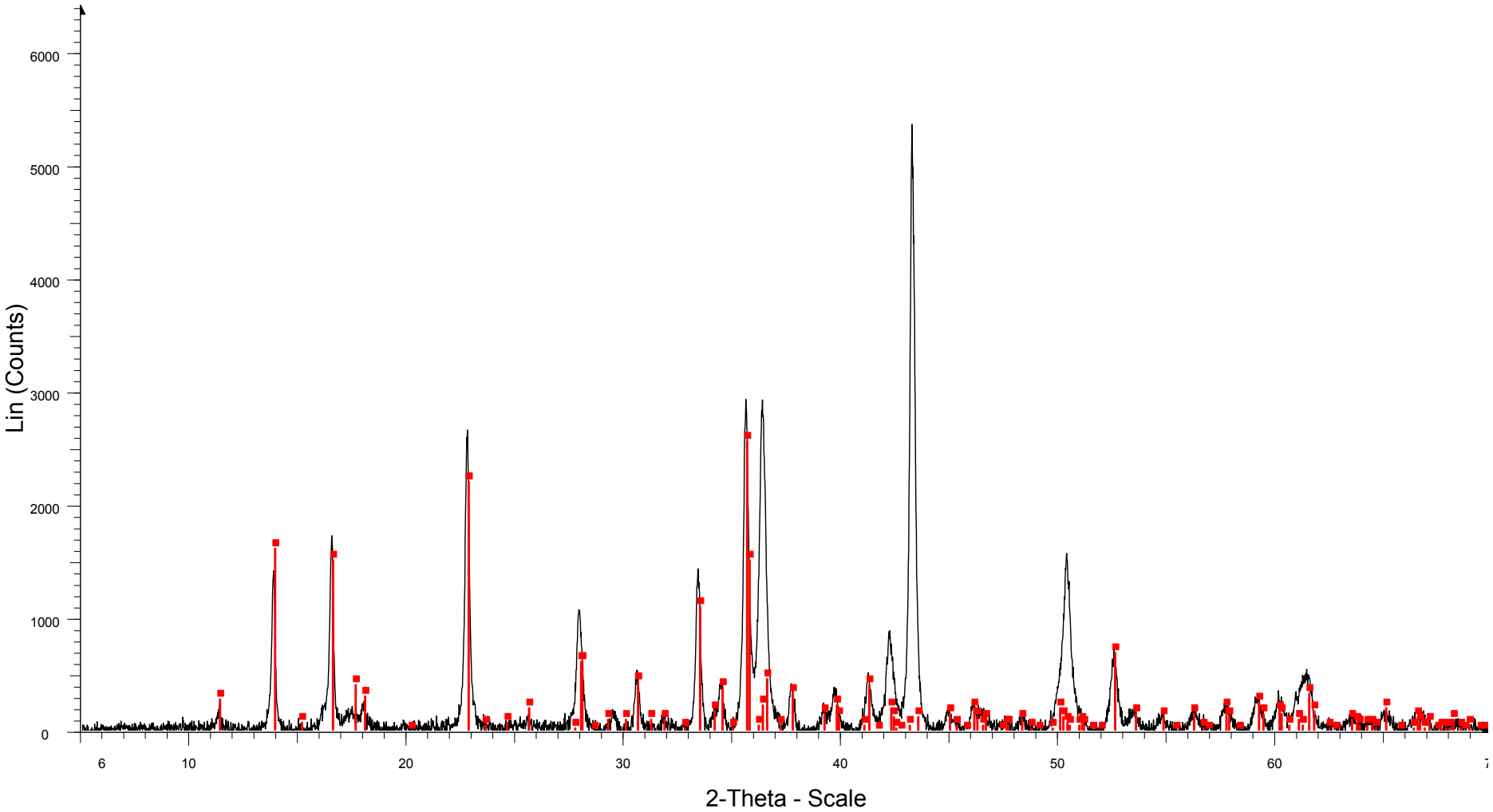
00-043-1458 (I) - Brochantite-M - Cu4+2SO4(OH)6 - Y: 95.53 % - d x by: 1. - WL: 1.5406 - Monoclinic -

01-084-2037 (C) - Antlerite - Cu3(SO4)(OH)4 - Y: 46.81 % - d x by: 1. - WL: 1.5406 - Orthorhombic - I/Ic PDF 1.6 -



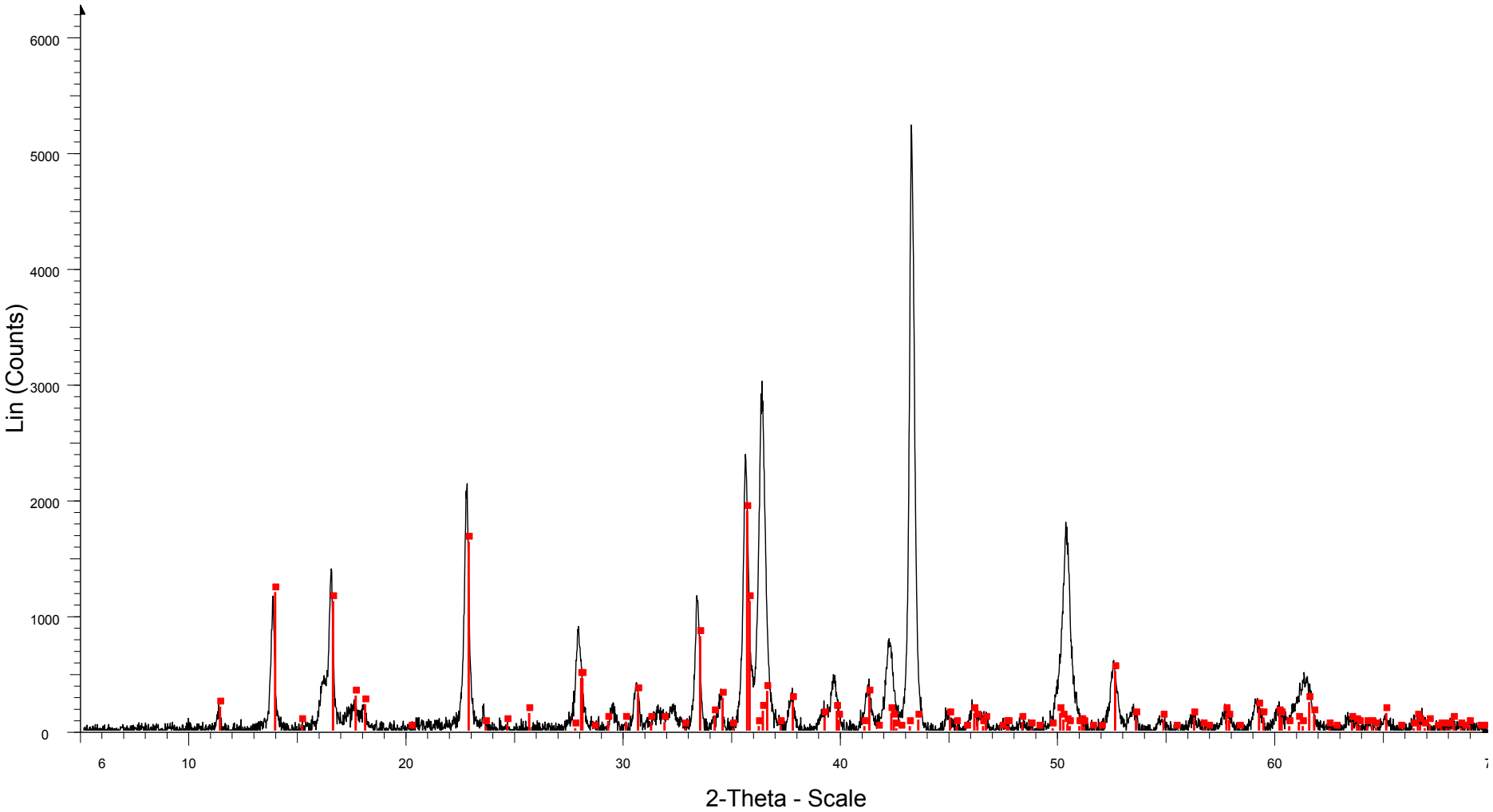
File: Justice Building.raw - Type: 2Th/Th locked - Start: 5.009 ° - End: 69.999 ° - Step: 0.017 ° - Step time: 2. s - Temp.: 25 °C (Room) - Time Started: 0 s - 2-Theta: 5.009 ° - Theta: 2.505 ° - Phi: 0.00 ° - Aux1: 0.0 - Au
Operations: Background 1.000,1.000 | Import

01-085-1316 (C) - Brochantite - Cu4(OH)6SO4 - Y: 42.47 % - d x by: 1. - WL: 1.5406 - Monoclinic - I/Ic PDF 1. -



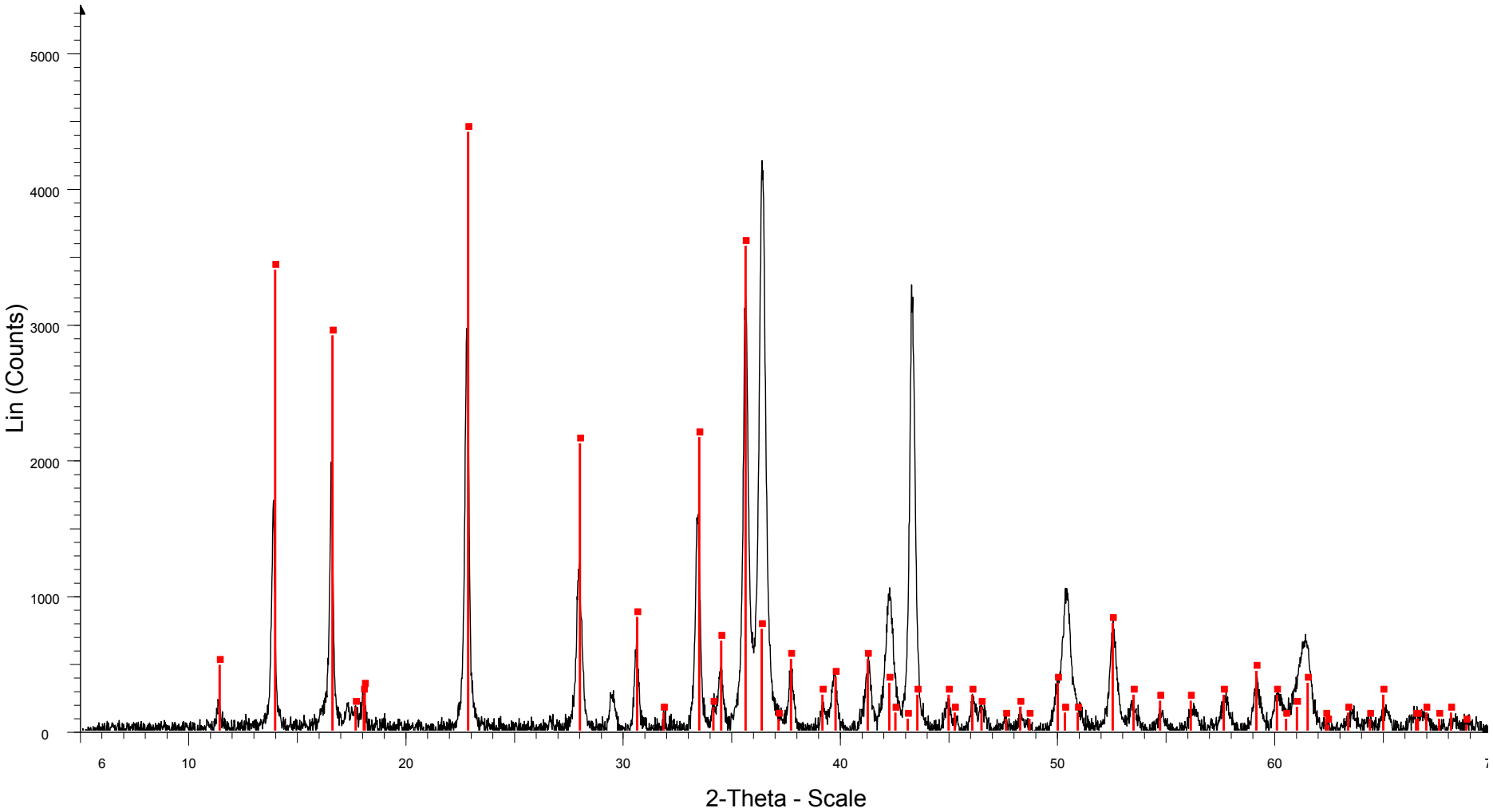
File: St. Joseph's Parish.raw - Type: 2Th/Th locked - Start: 5.009 ° - End: 69.999 ° - Step: 0.017 ° - Step time: 2. s - Temp.: 25 °C (Room) - Time Started: 0 s - 2-Theta: 5.009 ° - Theta: 2.505 ° - Phi: 0.00 ° - Aux1: 0.0 - Operations: Background 1.000,1.000 | Import

01-087-0454 (C) - Brochantite - Cu4(SO4)(OH)6 - Y: 47.86 % - d x by: 1. - WL: 1.5406 - Monoclinic - I/Ic PDF 1.1 -



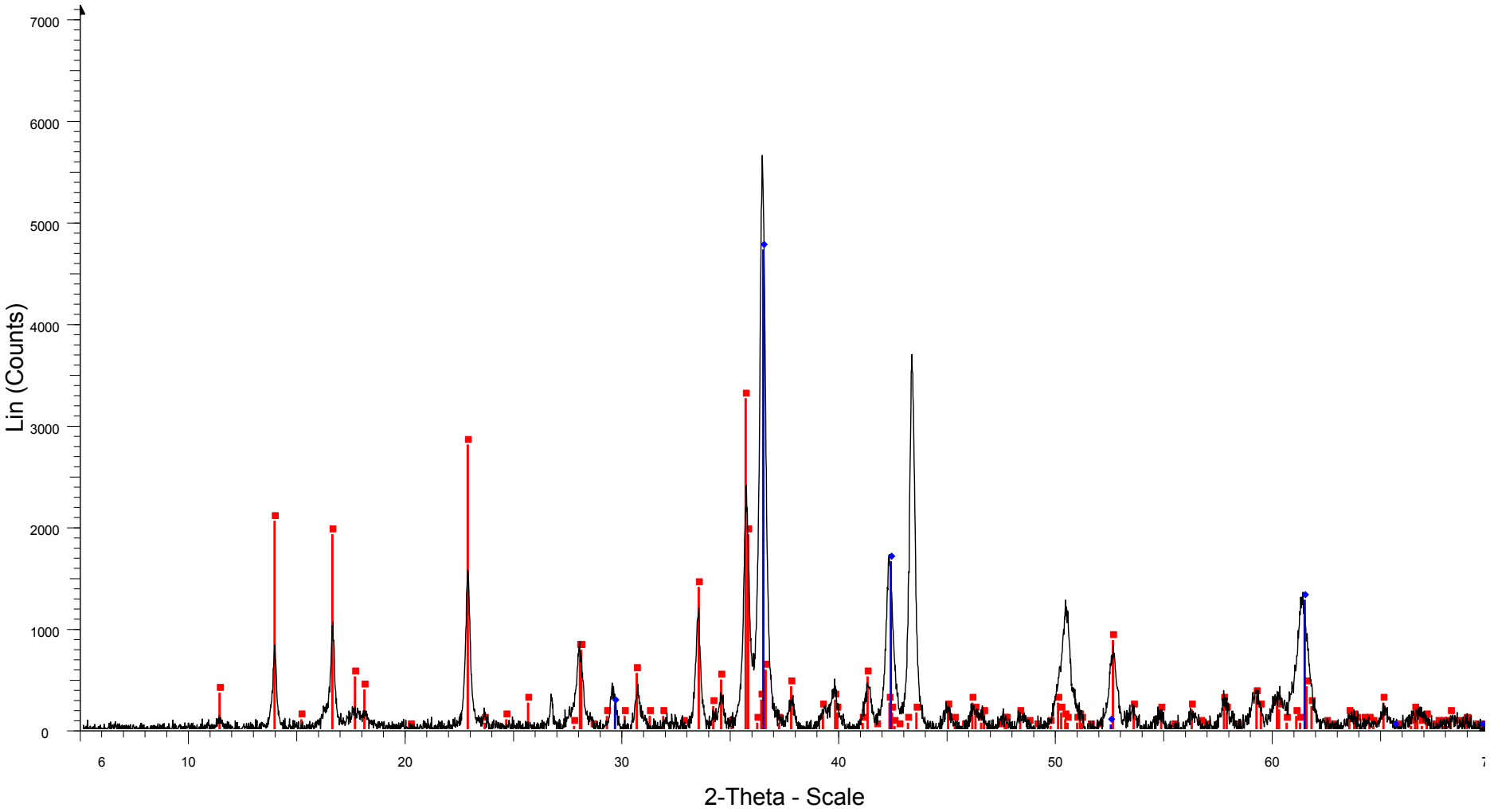
File: Wellington Building.raw - Type: 2Th/Th locked - Start: 5.009 ° - End: 69.999 ° - Step: 0.017 ° - Step time: 2. s - Temp.: 25 °C (Room) - Time Started: 0 s - 2-Theta: 5.009 ° - Theta: 2.505 ° - Phi: 0.00 ° - Aux1: 0.0 - Operations: Background 1.000,1.000 | Import

01-087-0454 (C) - Brochantite - Cu4(SO4)(OH)6 - Y: 36.32 % - d x by: 1. - WL: 1.5406 - Monoclinic - I/Ic PDF 1.1 -



File: West Block, Parliament.raw - Type: 2Th/Th locked - Start: 5.009 ° - End: 69.999 ° - Step: 0.017 ° - Step time: 2. s - Temp.: 25 °C (Room) - Time Started: 0 s - 2-Theta: 5.009 ° - Theta: 2.505 ° - Phi: 0.00 ° - Aux1:
Operations: Background 1.000,1.000 | Import

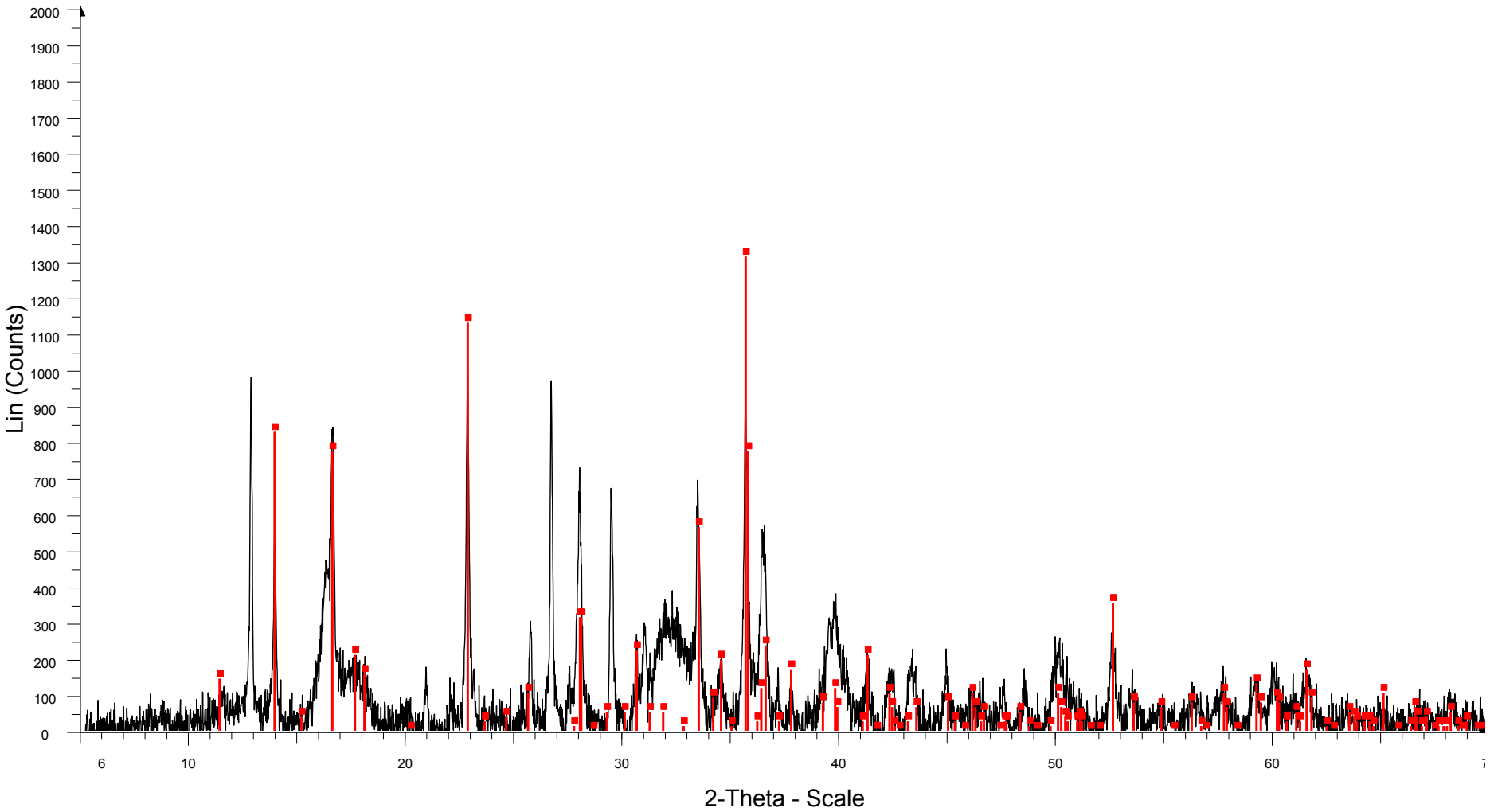
00-043-1458 (I) - Brochantite-M - Cu4+2SO4(OH)6 - Y: 105.07 % - d x by: 1. - WL: 1.5406 - Monoclinic -



File: West Memorial (green vial).raw - Type: 2Th/Th locked - Start: 5.009 ° - End: 69.999 ° - Step: 0.017 ° - Step time: 2. s - Temp.: 25 °C (Room) - Time Started: 0 s - 2-Theta: 5.009 ° - Theta: 2.505 ° - Phi: 0.00 ° - Au
Operations: Background 1.000,1.000 | Import

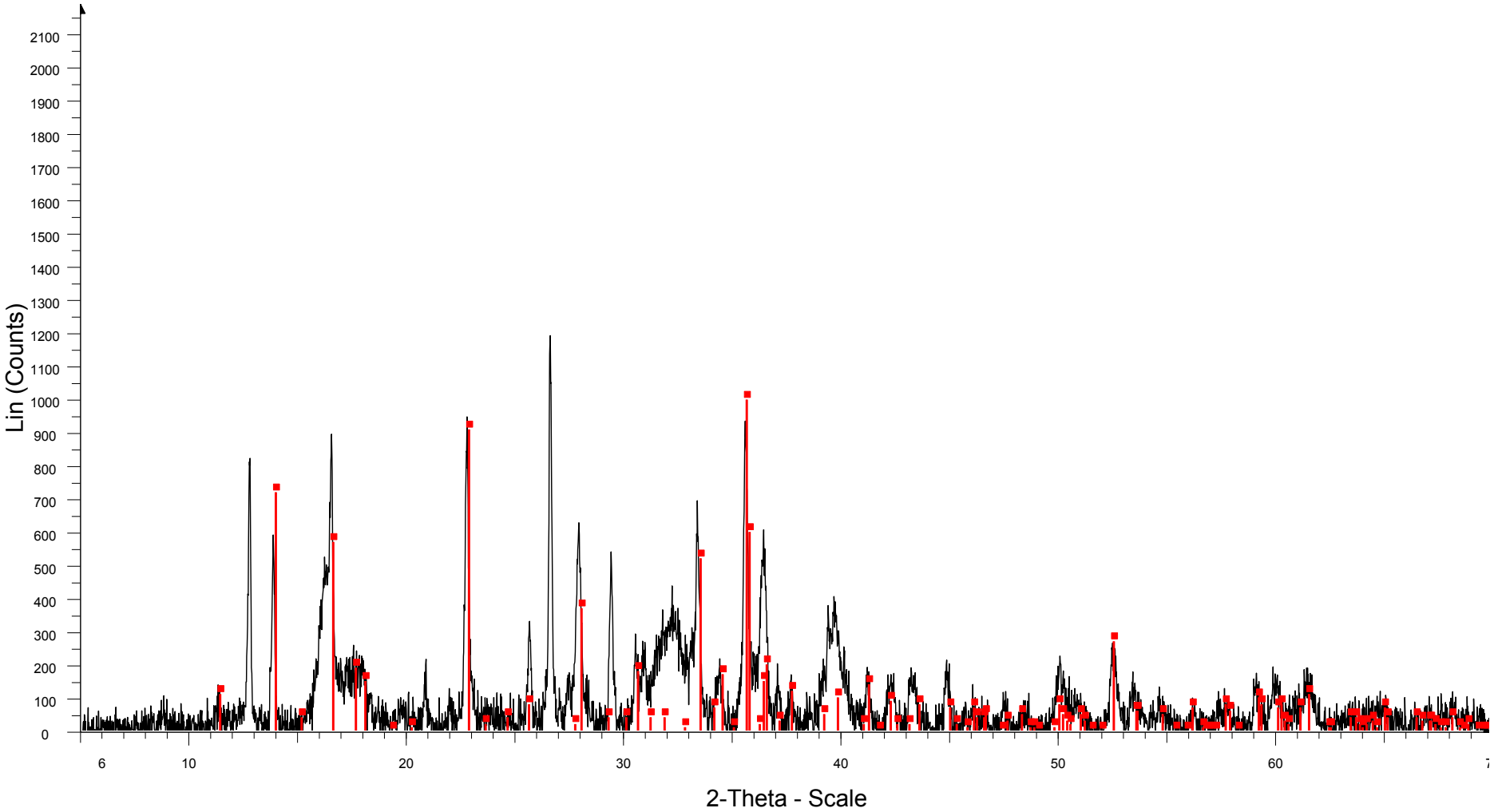
01-087-0454 (C) - Brochantite - Cu4(SO4)(OH)6 - Y: 57.67 % - d x by: 1. - WL: 1.5406 - Monoclinic - I/Ic PDF 1.1 - S-Q 84.2 % -

01-075-1531 (C) - Cuprite - Cu2O - Y: 83.62 % - d x by: 1. - WL: 1.5406 - Cubic - I/Ic PDF 8.3 - S-Q 15.8 % -



File: supreme court repeat.raw - Type: 2Th/Th locked - Start: 5.009 ° - End: 69.999 ° - Step: 0.017 ° - Step time: 2. s - Temp.: 25 °C (Room) - Time Started: 0 s - 2-Theta: 5.009 ° - Theta: 2.505 ° - Phi: 0.00 ° - Aux1: 0.
Operations: Background 1.000,1.000 | Import

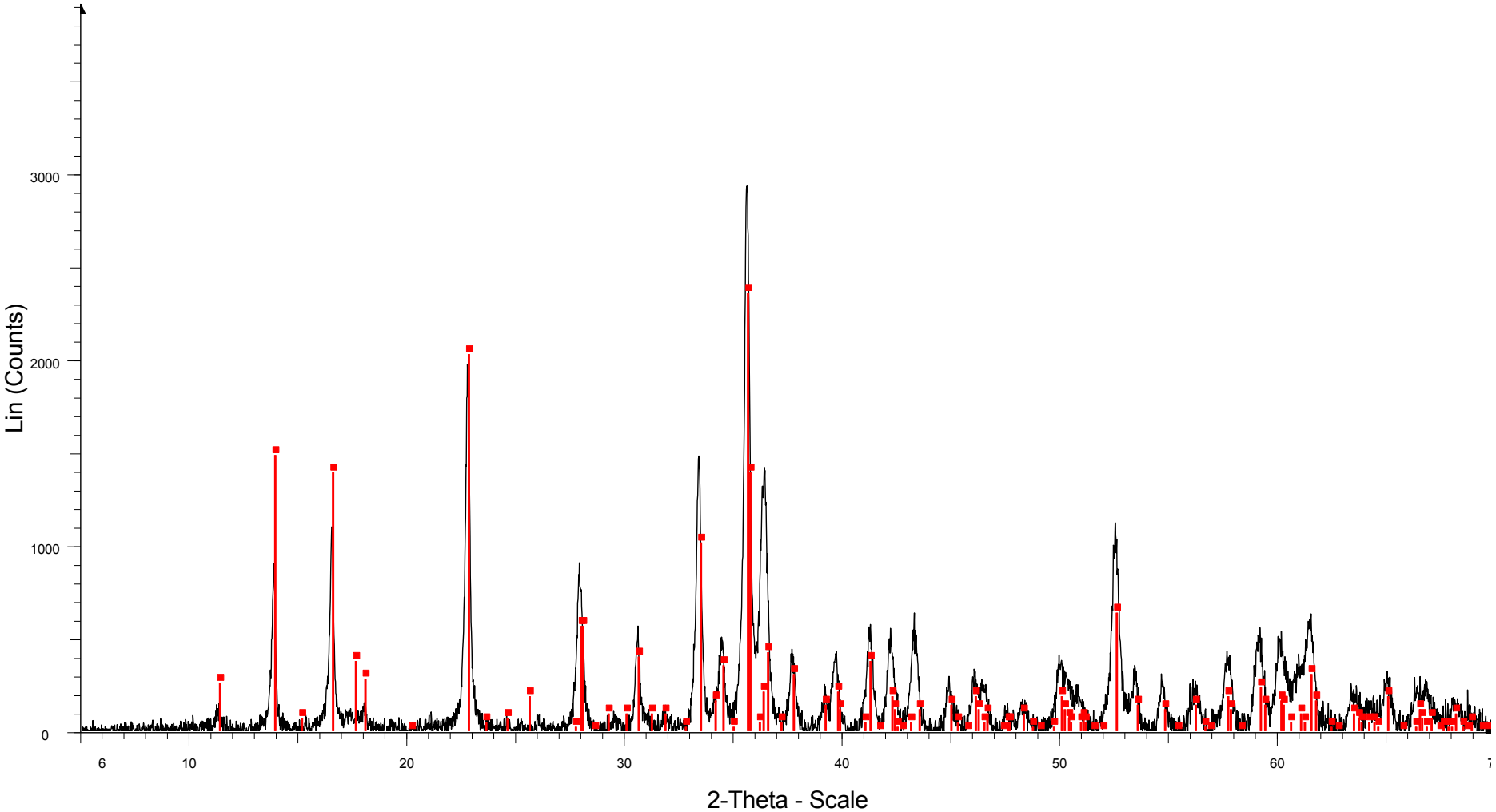
01-087-0454 (C) - Brochantite - Cu4(SO4)(OH)6 - Y: 125.76 % - d x by: 1. - WL: 1.5406 - Monoclinic - I/Ic PDF 1.1 -



File: Supreme Court.raw - Type: 2Th/Th locked - Start: 5.009 ° - End: 69.999 ° - Step: 0.017 ° - Step time: 2. s - Temp.: 25 °C (Room) - Time Started: 0 s - 2-Theta: 5.009 ° - Theta: 2.505 ° - Phi: 0.00 ° - Aux1: 0.0 - Aux
Operations: Background 1.000,1.000 | Import

01-085-1316 (C) - Brochantite - Cu4(OH)6SO4 - Y: 83.86 % - d x by: 1. - WL: 1.5406 - Monoclinic - I/Ic PDF 1. -

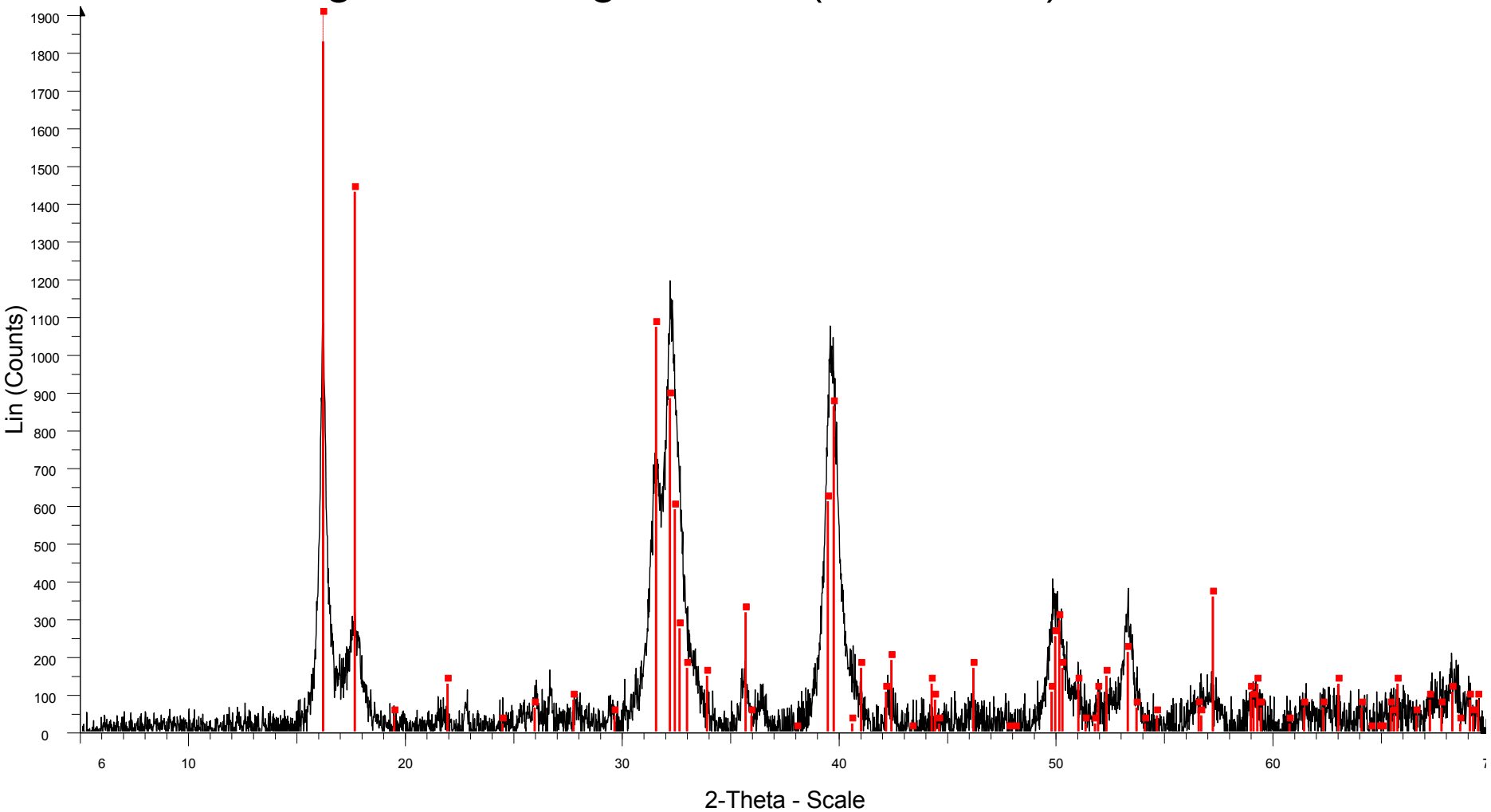
Corpus Christi Roof, Oxford



File: Corpus Christi Roof.raw - Type: 2Th/Th locked - Start: 5.009 ° - End: 69.999 ° - Step: 0.017 ° - Step time: 2. s - Temp.: 25 °C (Room) - Time Started: 0 s - 2-Theta: 5.009 ° - Theta: 2.505 ° - Phi: 0.00 ° - Aux1: 0.0 - Operations: Background 1.000,1.000 | Import

01-087-0454 (C) - Brochantite - Cu4(SO4)(OH)6 - Y: 80.47 % - d x by: 1. - WL: 1.5406 - Monoclinic - I/Ic PDF 1.1 -

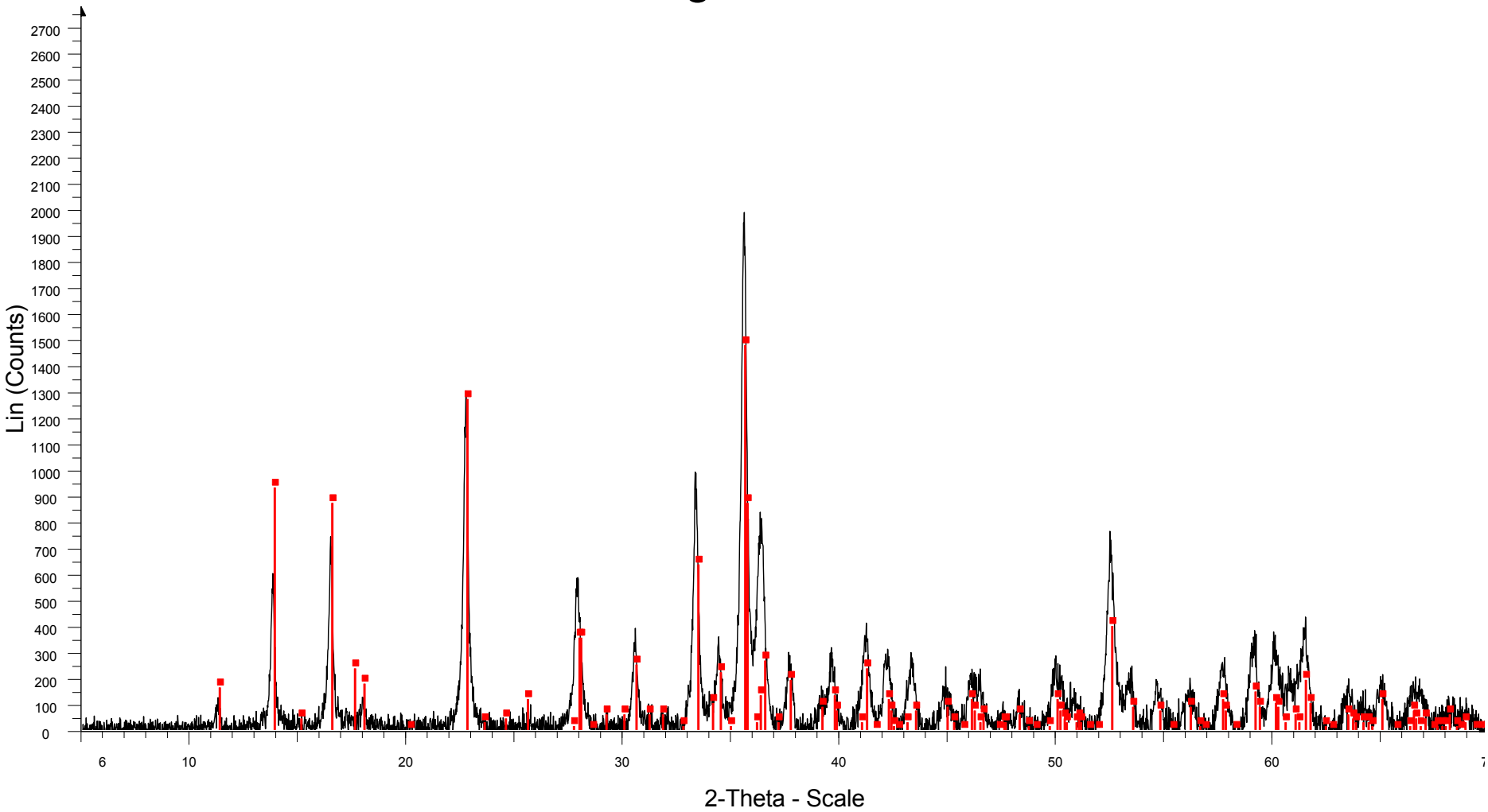
Magdalen College Statue (Jesus' calf), Oxford



File: Magdalen College (Jesus' Calf).raw - Type: 2Th/Th locked - Start: 5.009 ° - End: 69.999 ° - Step: 0.017 ° - Step time: 2. s - Temp.: 25 °C (Room) - Time Started: 0 s - 2-Theta: 5.009 ° - Theta: 2.505 ° - Phi: 0.00 ° - Operations: Background 1.000,1.000 | Import

01-078-0372 (C) - Atacamite - Cu2Cl(OH)3 - Y: 176.12 % - d x by: 1. - WL: 1.5406 - Orthorhombic - I/Ic PDF 2.3 - S-Q 100.0 % -

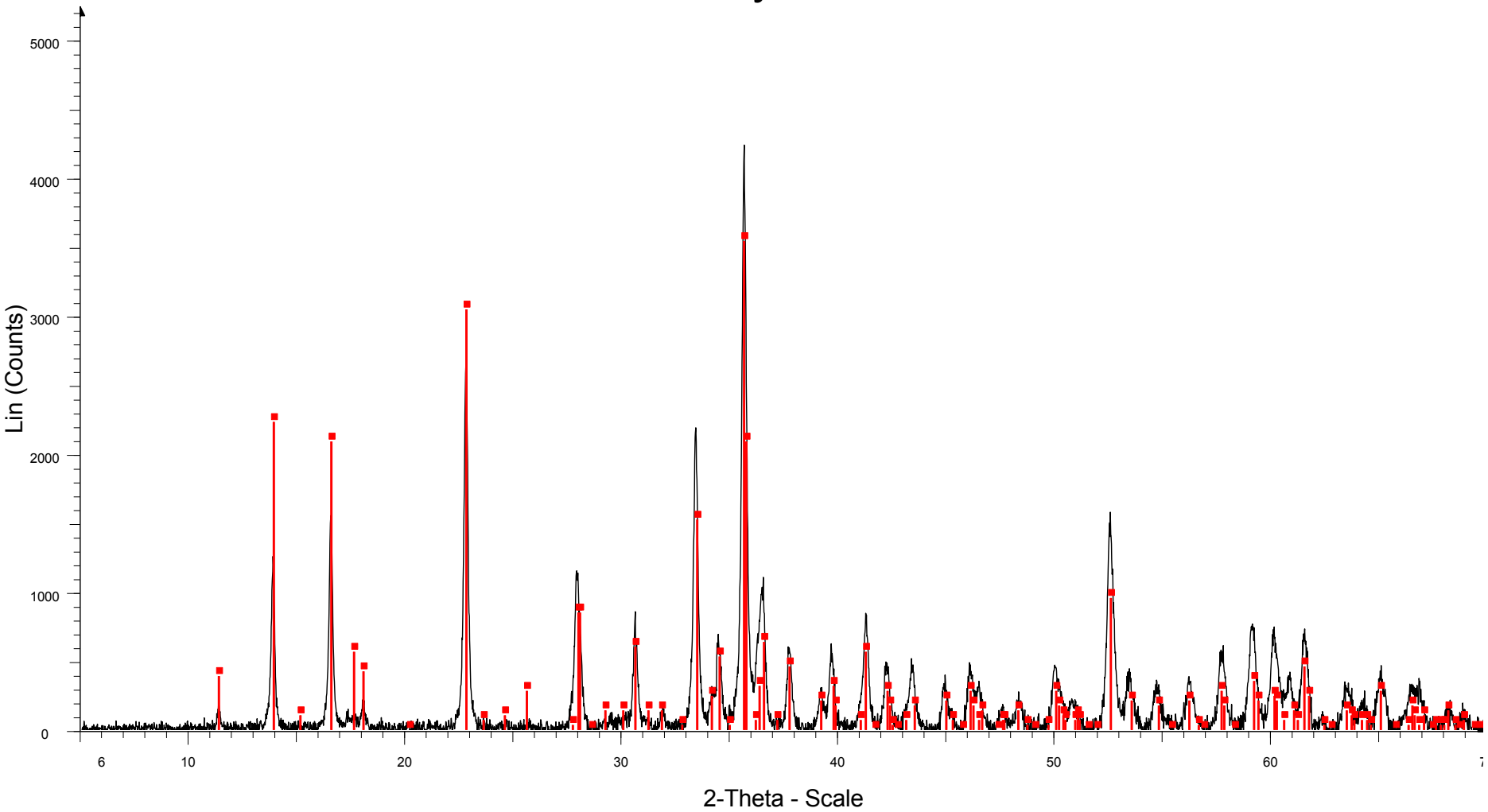
New College Roof, Oxford



File: New College.raw - Type: 2Th/Th locked - Start: 5.009 ° - End: 69.999 ° - Step: 0.017 ° - Step time: 2. s - Temp.: 25 °C (Room) - Time Started: 0 s - 2-Theta: 5.009 ° - Theta: 2.505 ° - Phi: 0.00 ° - Aux1: 0.0 - Aux2:
Operations: Background 1.000,1.000 | Import

01-087-0454 (C) - Brochantite - Cu4(SO4)(OH)6 - Y: 74.41 % - d x by: 1. - WL: 1.5406 - Monoclinic - I/Ic PDF 1.1 -

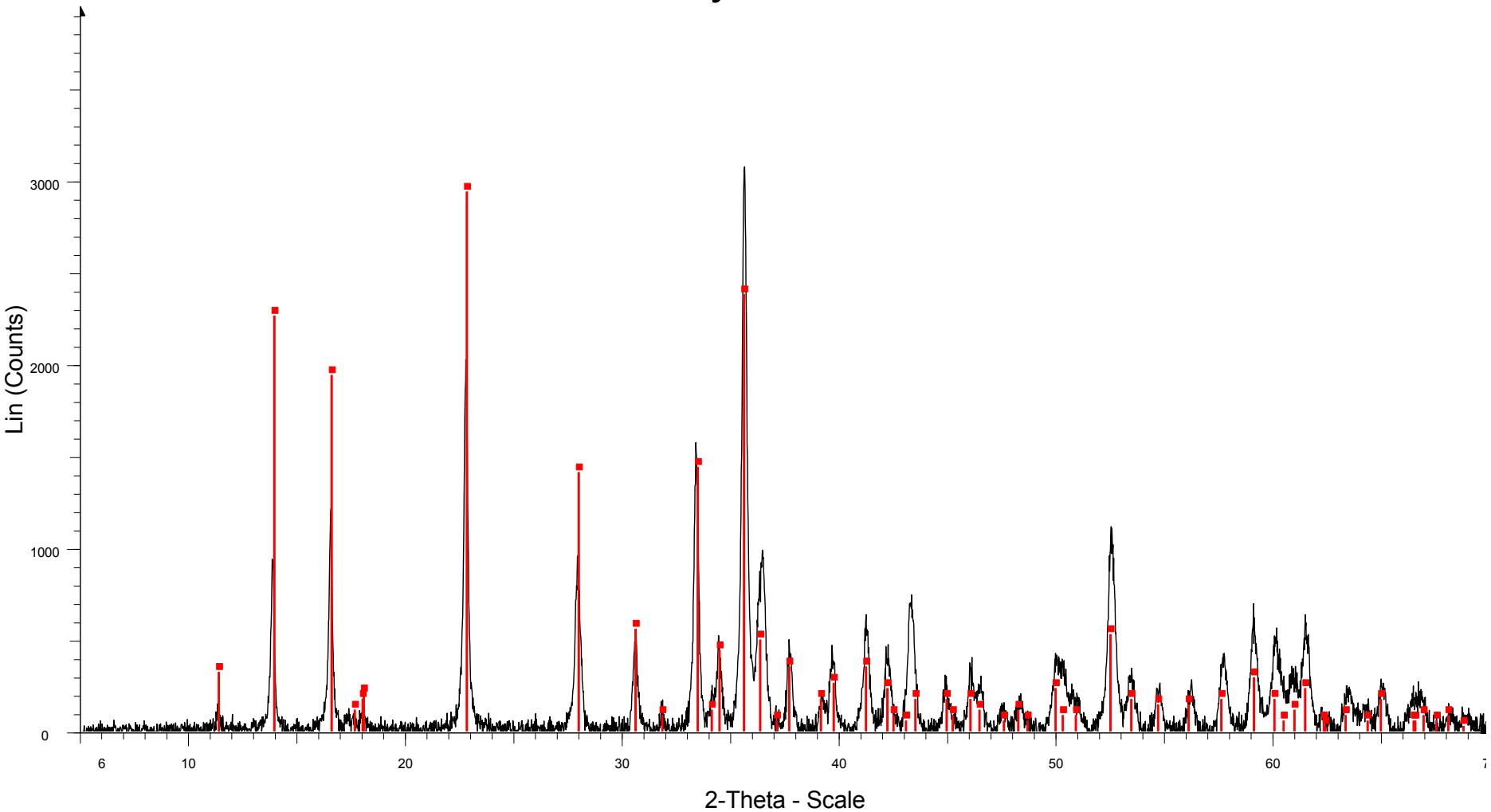
Old Observatory Roof, Oxford



File: Old Observatory.raw - Type: 2Th/Th locked - Start: 5.009 ° - End: 69.999 ° - Step: 0.017 ° - Step time: 2. s - Temp.: 25 °C (Room) - Time Started: 0 s - 2-Theta: 5.009 ° - Theta: 2.505 ° - Phi: 0.00 ° - Aux1: 0.0 - Au
Operations: Background 1.000,1.000 | Import

01-087-0454 (C) - Brochantite - Cu4(SO4)(OH)6 - Y: 83.64 % - d x by: 1. - WL: 1.5406 - Monoclinic - I/Ic PDF 1.1 -

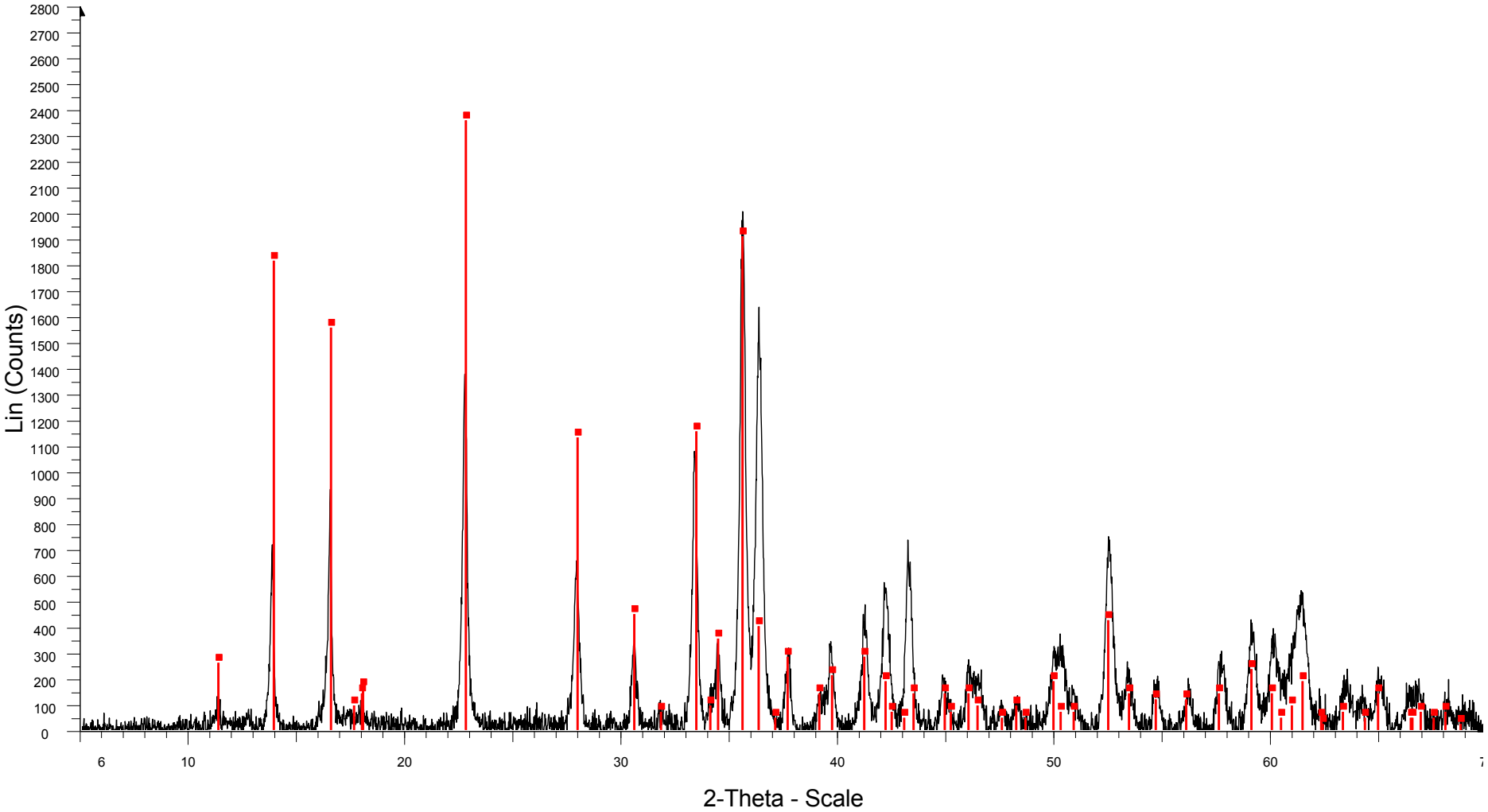
Oriel Library Roof, Oxford



File: Oriel Library.raw - Type: 2Th/Th locked - Start: 5.009 ° - End: 69.999 ° - Step: 0.017 ° - Step time: 2. s - Temp.: 25 °C (Room) - Time Started: 0 s - 2-Theta: 5.009 ° - Theta: 2.505 ° - Phi: 0.00 ° - Aux1: 0.0 - Aux2:
Operations: Background 1.000,1.000 | Import

00-043-1458 (I) - Brochantite-M - Cu4+2SO4(OH)6 - Y: 95.64 % - d x by: 1. - WL: 1.5406 - Monoclinic -

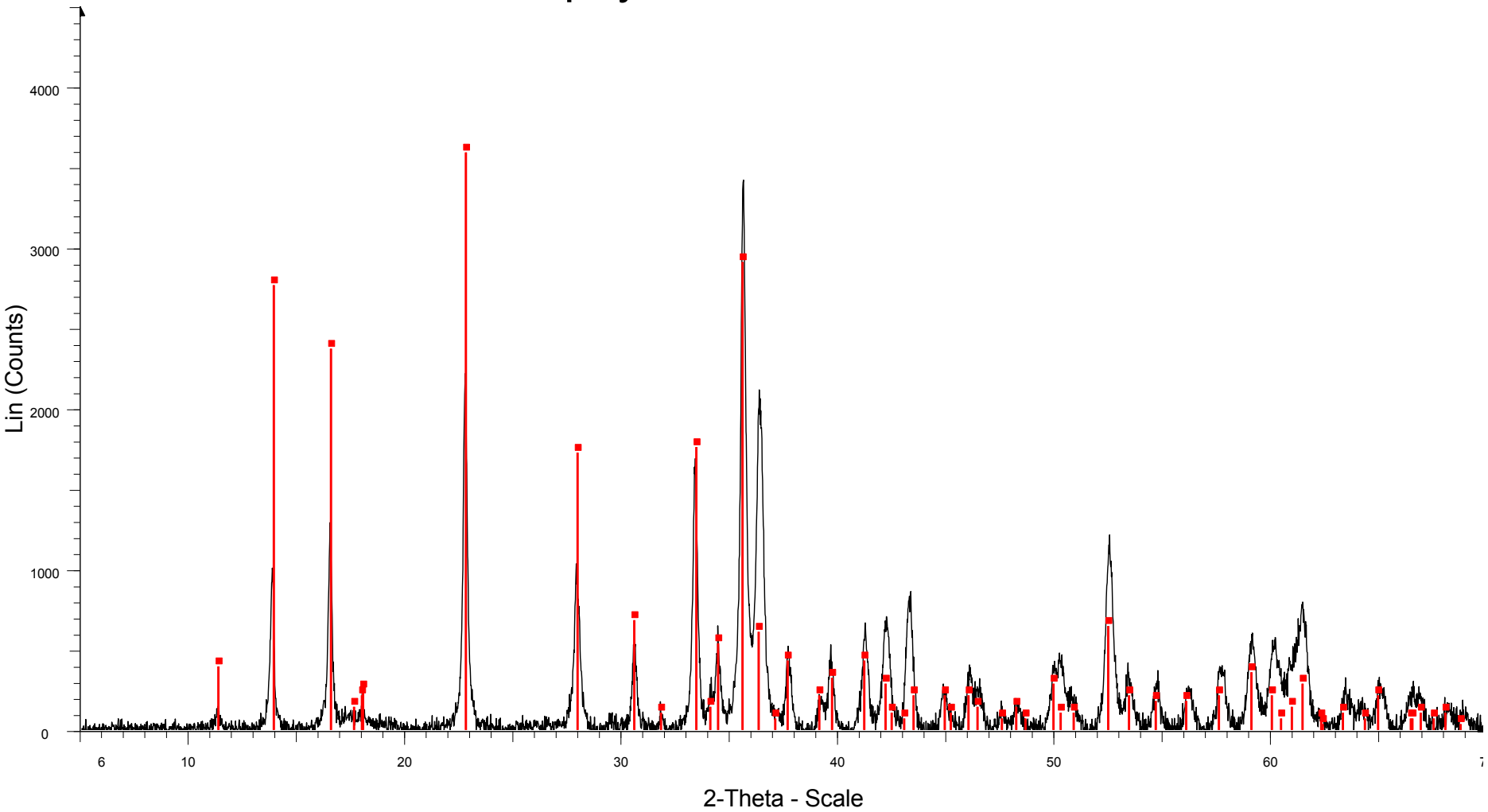
Oriental Institute Roof, Oxford



File: Oriental Institute.raw - Type: 2Th/Th locked - Start: 5.009 ° - End: 69.999 ° - Step: 0.017 ° - Step time: 2. s - Temp.: 25 °C (Room) - Time Started: 0 s - 2-Theta: 5.009 ° - Theta: 2.505 ° - Phi: 0.00 ° - Aux1: 0.0 - Au
Operations: Background 1.000,1.000 | Import

00-043-1458 (I) - Brochantite-M - Cu4+2SO4(OH)6 - Y: 117.62 % - d x by: 1. - WL: 1.5406 - Monoclinic -

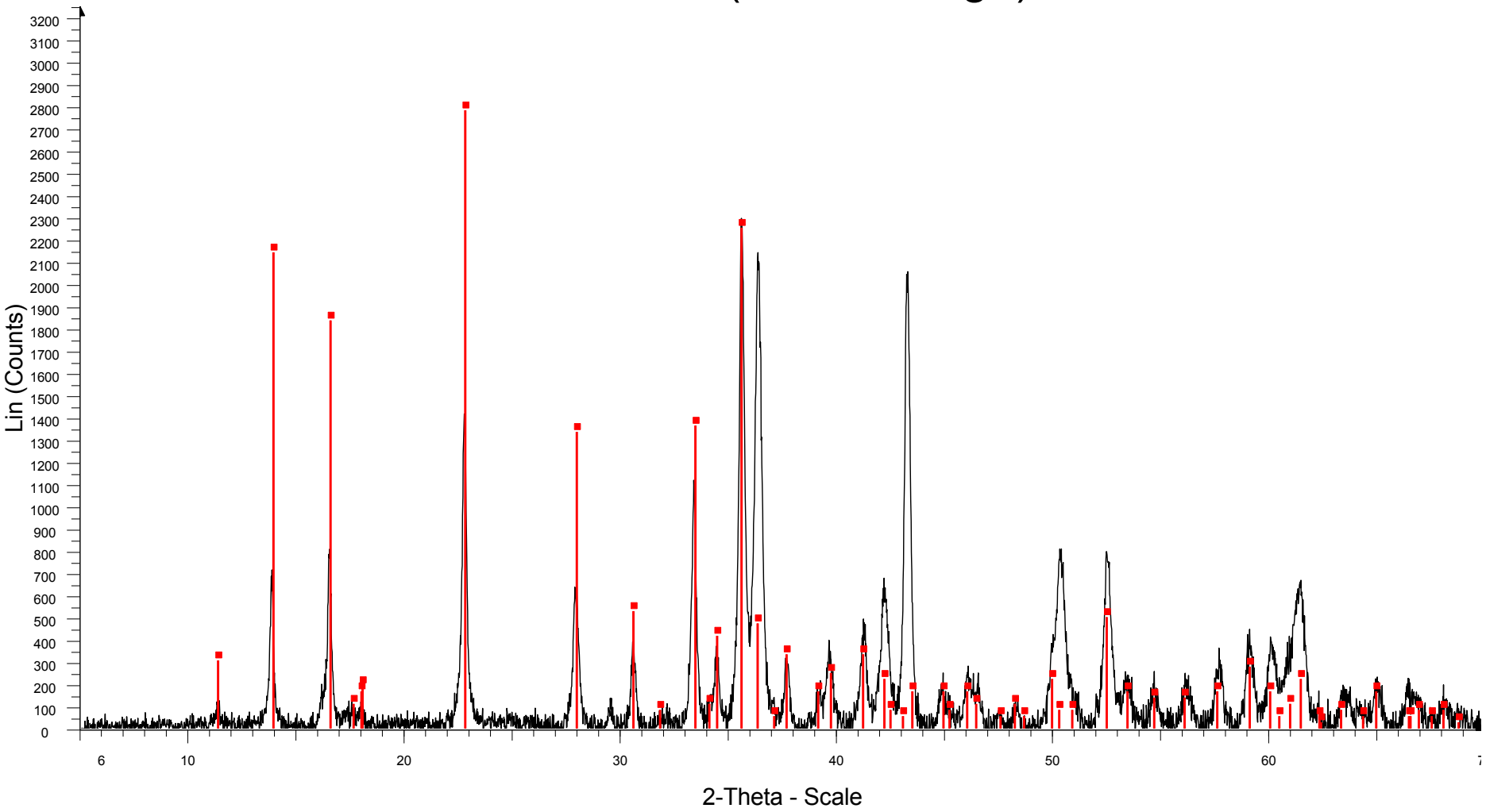
Philosophy Centre Roof, Oxford



File: Philosophy Centre.raw - Type: 2Th/Th locked - Start: 5.009 ° - End: 69.999 ° - Step: 0.017 ° - Step time: 2. s - Temp.: 25 °C (Room) - Time Started: 0 s - 2-Theta: 5.009 ° - Theta: 2.505 ° - Phi: 0.00 ° - Aux1: 0.0 - Operations: Background 1.000,1.000 | Import

00-043-1458 (I) - Brochantite-M - Cu4+2SO4(OH)6 - Y: 105.06 % - d x by: 1. - WL: 1.5406 - Monoclinic -

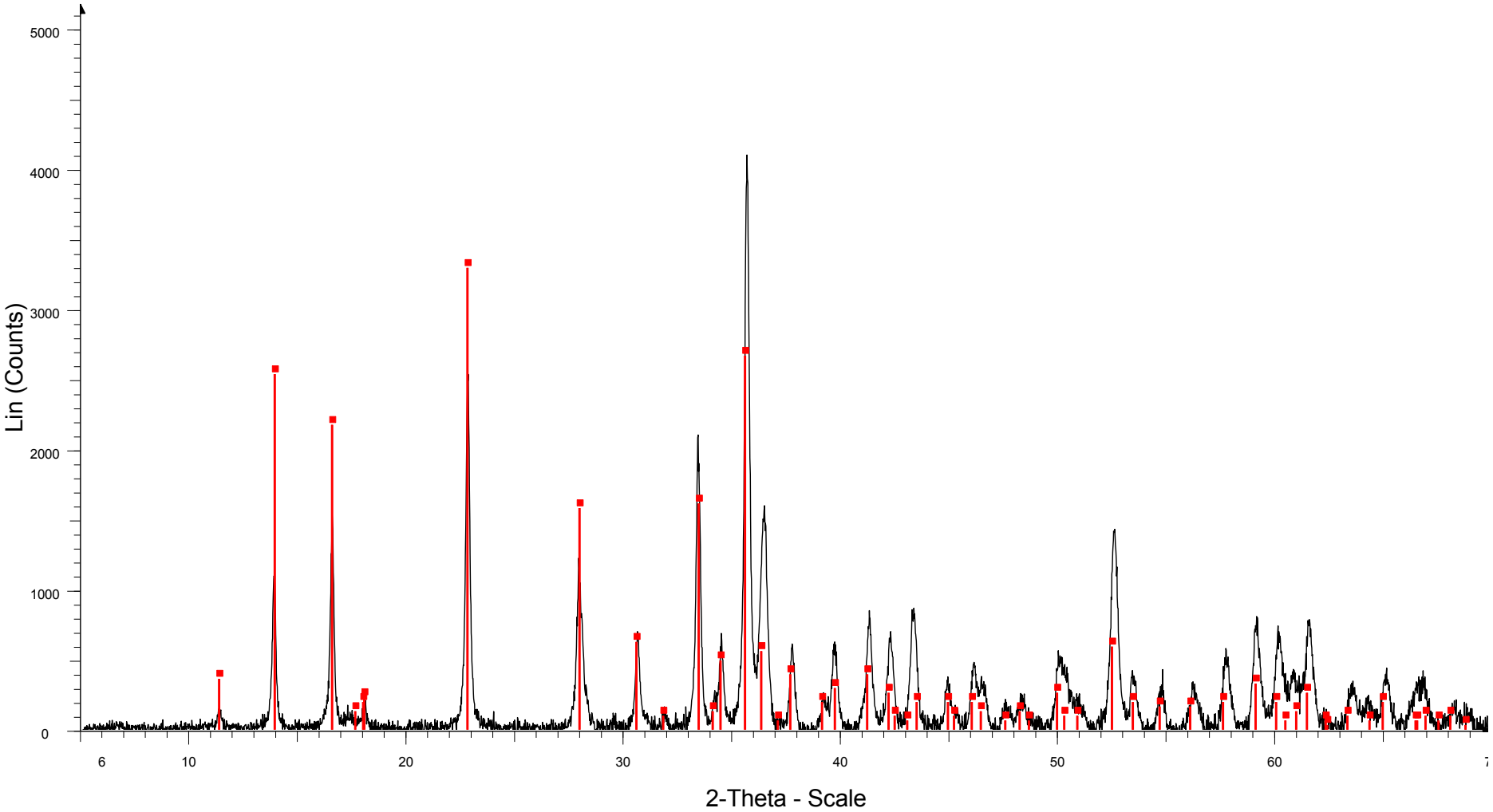
Rhodes House Roof (Oriel College), Oxford



File: Rhodes House ORIEL.raw - Type: 2Th/Th locked - Start: 5.009 ° - End: 69.999 ° - Step: 0.017 ° - Step time: 2. s - Temp.: 25 °C (Room) - Time Started: 0 s - 2-Theta: 5.009 ° - Theta: 2.505 ° - Phi: 0.00 ° - Aux1: 0.
Operations: Background 1.000,1.000 | Import

00-043-1458 (I) - Brochantite-M - Cu4+2SO4(OH)6 - Y: 121.21 % - d x by: 1. - WL: 1.5406 - Monoclinic -

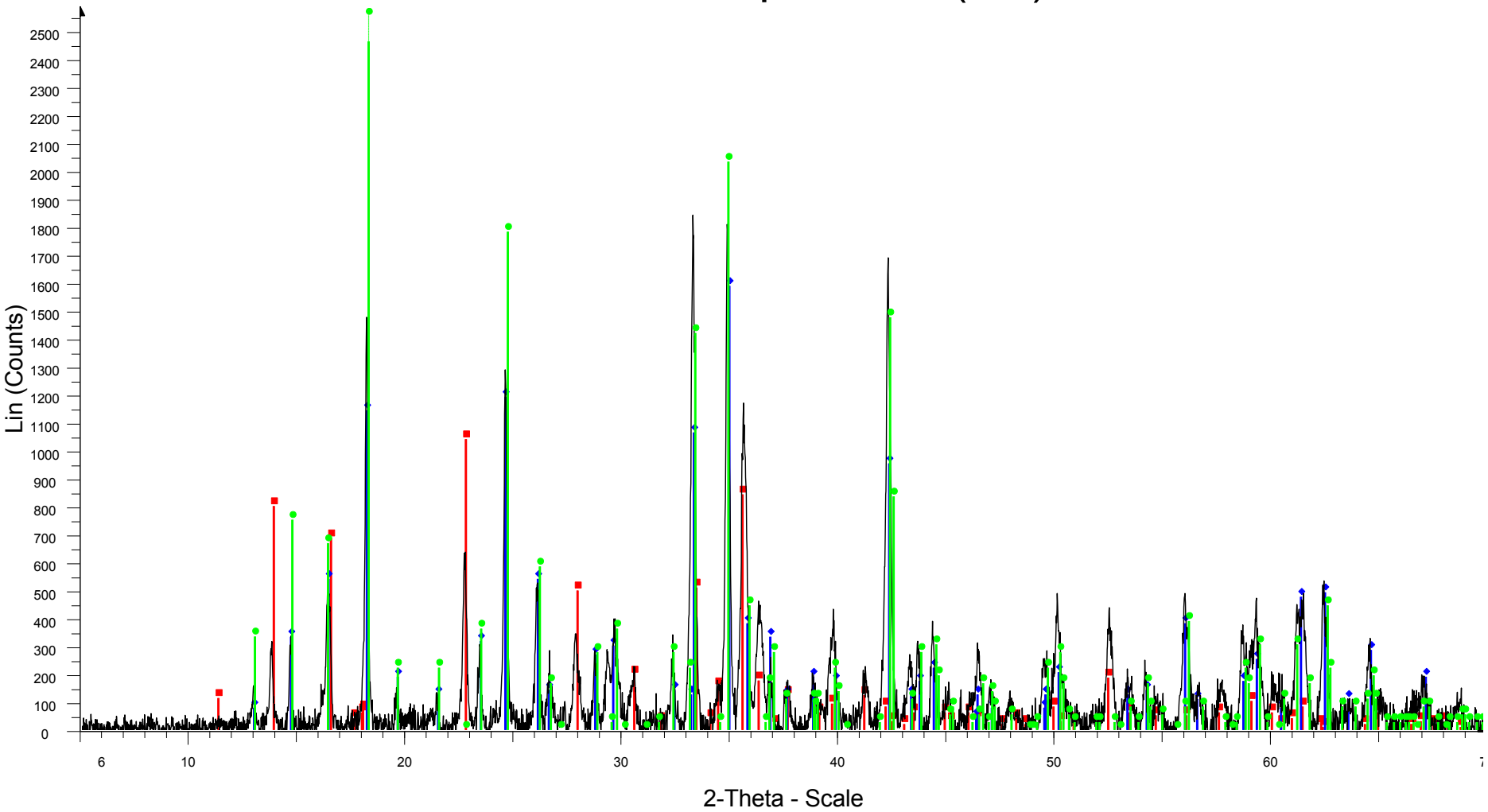
Rhodes Mandela House Cupola, Oxford



File: Rhodes Mandela Cupola.raw - Type: 2Th/Th locked - Start: 5.009 ° - End: 69.999 ° - Step: 0.017 ° - Step time: 2. s - Temp.: 25 °C (Room) - Time Started: 0 s - 2-Theta: 5.009 ° - Theta: 2.505 ° - Phi: 0.00 ° - Aux1: Operations: Background 1.000,1.000 | Import

00-043-1458 (I) - Brochantite-M - Cu4+2SO4(OH)6 - Y: 80.38 % - d x by: 1. - WL: 1.5406 - Monoclinic -

Sheldonian Theatre Cupola Urn (left), Oxford



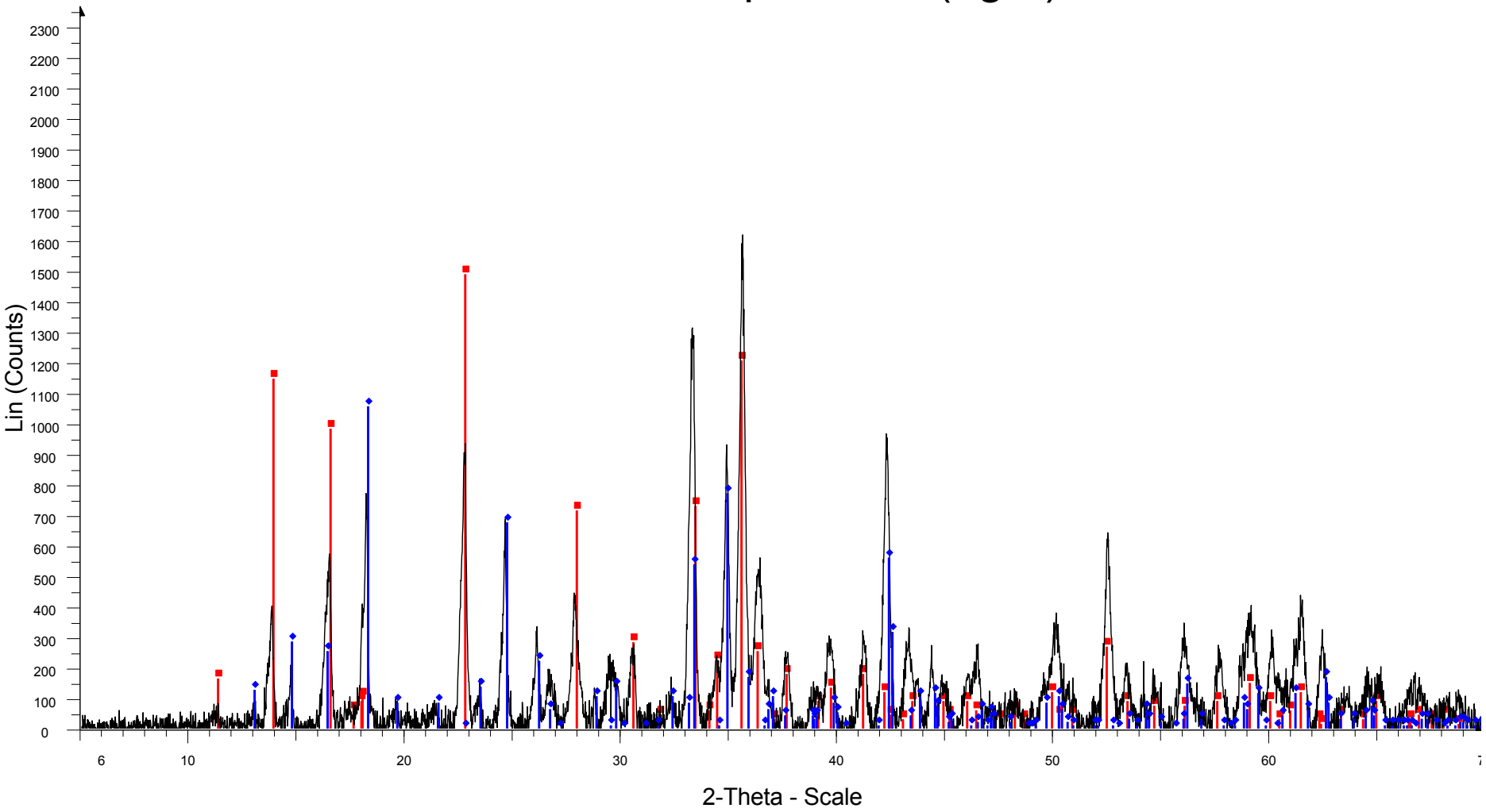
File: Sheldonian Urn Left.raw - Type: 2Th/Th locked - Start: 5.009 ° - End: 69.999 ° - Step: 0.017 ° - Step time: 2. s - Temp.: 25 °C (Room) - Time Started: 0 s - 2-Theta: 5.009 ° - Theta: 2.505 ° - Phi: 0.00 ° - Aux1: 0.0
Operations: Background 1.000,1.000 | Import

00-043-1458 (I) - Brochantite-M - Cu4+2SO4(OH)6 - Y: 56.47 % - d x by: 1. - WL: 1.5406 - Monoclinic -

00-039-0051 (C) - Copper Chromium Oxide Hydrate - Cu3CrO6·2H2O/CuCrO4·2CuO·2H2O - Y: 86.28 % - d x by: 1. - WL: 1.5406 - Orthorhombic -

01-084-2037 (C) - Antlerite - Cu3(SO4)(OH)4 - Y: 151.24 % - d x by: 1. - WL: 1.5406 - Orthorhombic - I/Ic PDF 1.6 -

Sheldonian Theatre Cupola Urn (right), Oxford

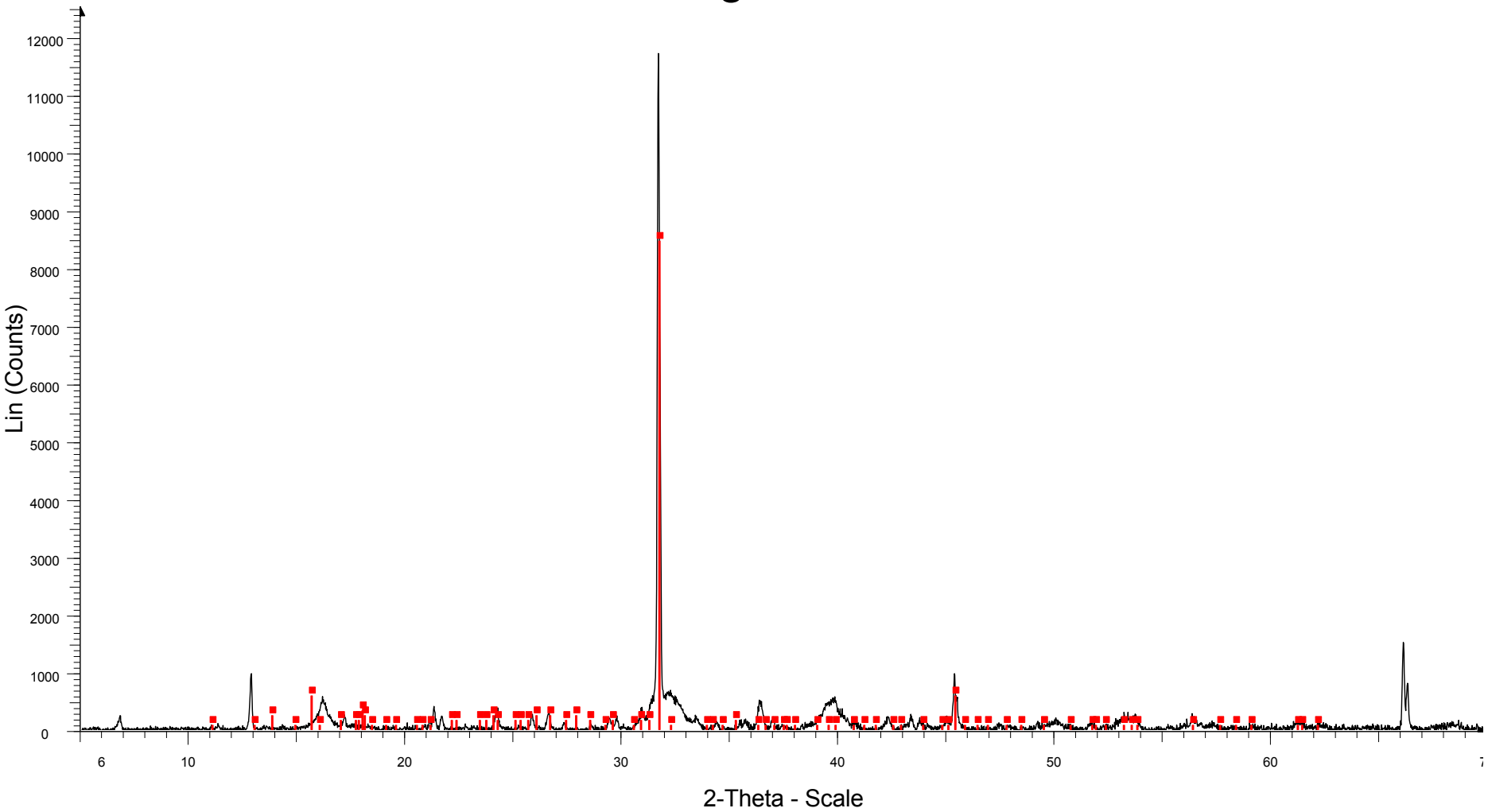


File: Sheldonian Urn Right.raw - Type: 2Th/Th locked - Start: 5.009 ° - End: 69.999 ° - Step: 0.017 ° - Step time: 2. s - Temp.: 25 °C (Room) - Time Started: 0 s - 2-Theta: 5.009 ° - Theta: 2.505 ° - Phi: 0.00 ° - Aux1: 0.
Operations: Background 1.000,1.000 | Import

00-043-1458 (I) - Brochantite-M - Cu4+2SO4(OH)6 - Y: 92.07 % - d x by: 1. - WL: 1.5406 - Monoclinic -

01-084-2037 (C) - Antlerite - Cu3(SO4)(OH)4 - Y: 65.31 % - d x by: 1. - WL: 1.5406 - Orthorhombic - I/Ic PDF 1.6 -

St. Catherine's College Floor Sheet, Oxford

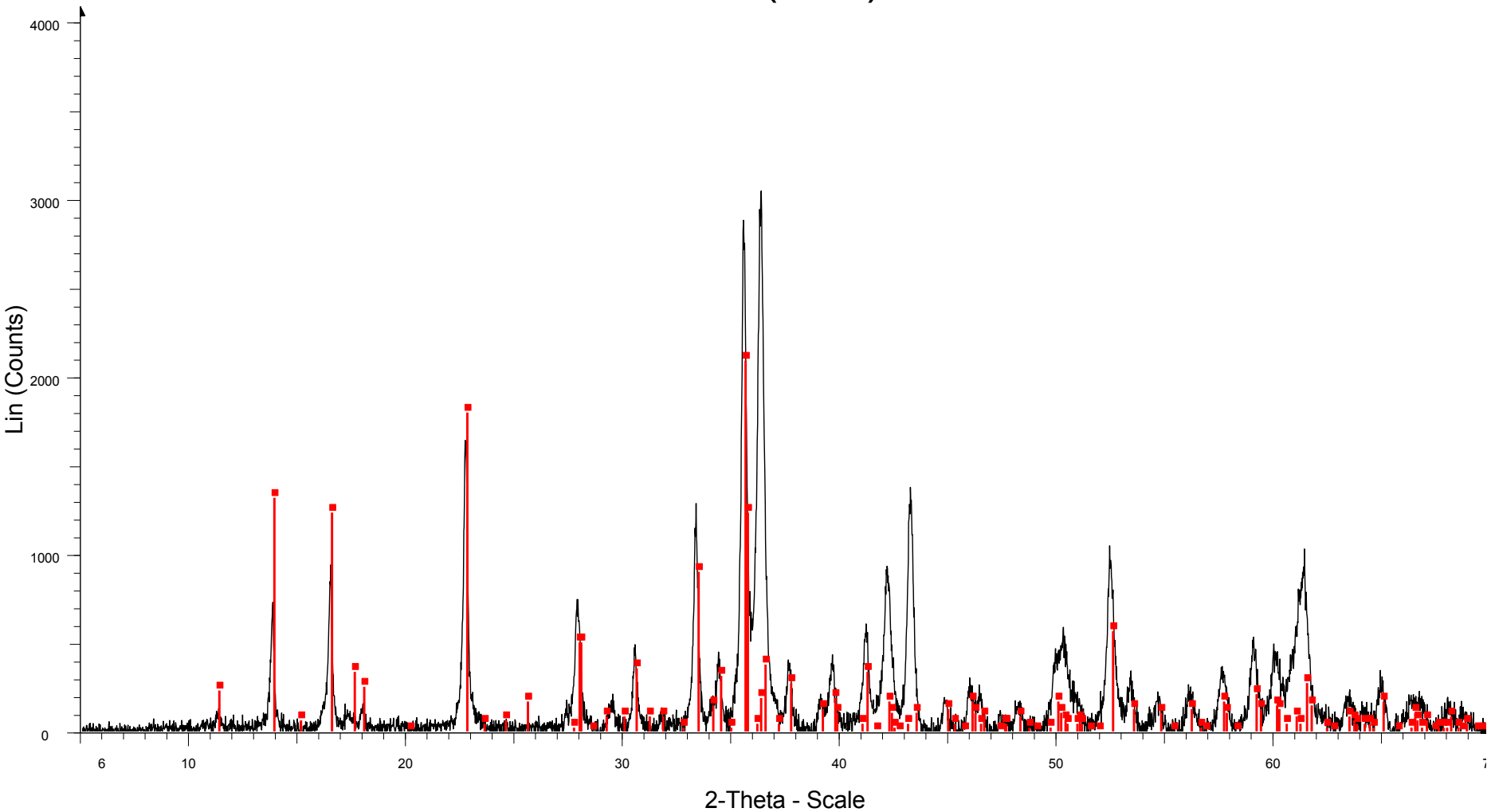


File: St Catherines Floor Sheet.raw - Type: 2Th/Th locked - Start: 5.009 ° - End: 69.999 ° - Step: 0.017 ° - Step time: 2. s - Temp.: 25 °C (Room) - Time Started: 0 s - 2-Theta: 5.009 ° - Theta: 2.505 ° - Phi: 0.00 ° - Aux

Operations: Background 1.000,1.000 | Import

00-050-2011 (I) - Chloro [1,5-bis[1-methylimidazol-2-ylmethyl]-1,5-diazacyclooctane] nickel(2+) - $C_{16}H_{26}ClN_6Ni \cdot ClO_4$ - Y: 72.35 % - d x by: 1. - WL: 1.5406 - Triclinic - I/Ic PDF 2.1 -

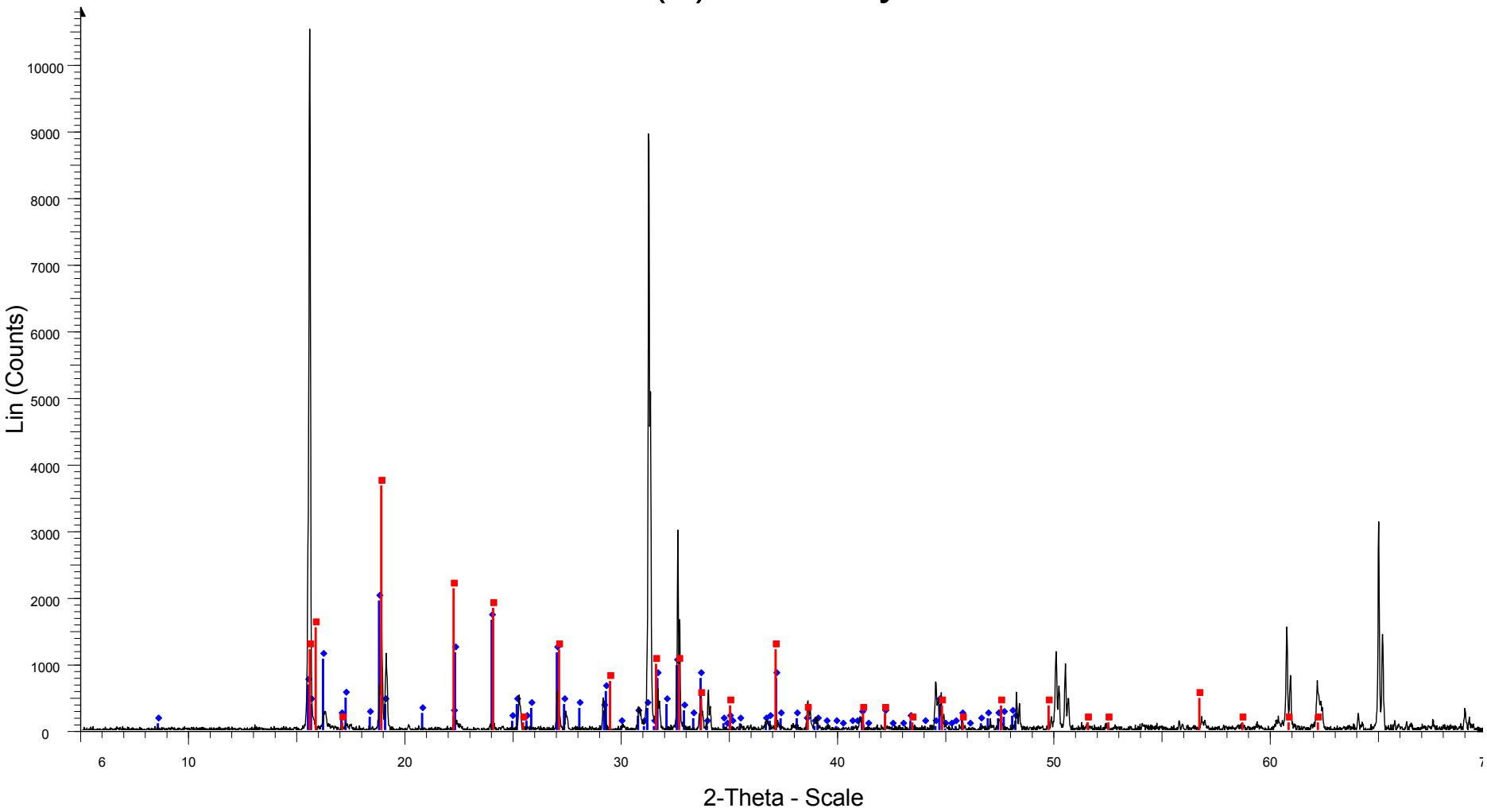
St. Cross Roof (Law), Oxford



File: St Cross Building (Law).raw - Type: 2Th/Th locked - Start: 5.009 ° - End: 69.999 ° - Step: 0.017 ° - Step time: 2. s - Temp.: 25 °C (Room) - Time Started: 0 s - 2-Theta: 5.009 ° - Theta: 2.505 ° - Phi: 0.00 ° - Aux1:
Operations: Background 1.000,1.000 | Import

01-087-0454 (C) - Brochantite - Cu4(SO4)(OH)6 - Y: 68.64 % - d x by: 1. - WL: 1.5406 - Monoclinic - I/Ic PDF 1.1 -

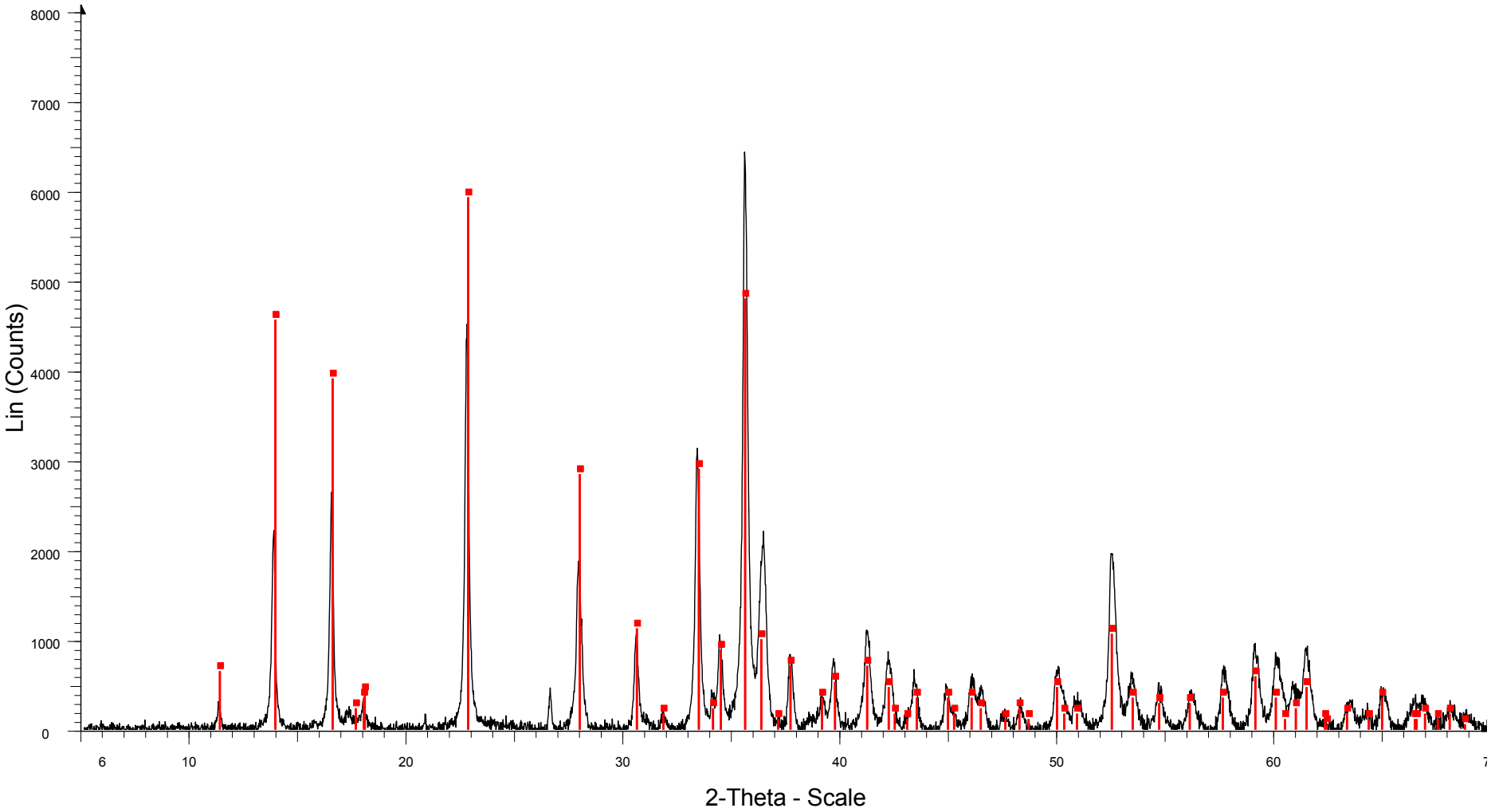
Fisher Cu(II)SO4 - Synthetic



File: Fisher Cu (II) SO4.raw - Type: 2Th/Th locked - Start: 5.009 ° - End: 69.999 ° - Step: 0.017 ° - Step time: 2. s - Temp.: 25 °C (Room) - Time Started: 0 s - 2-Theta: 5.009 ° - Theta: 2.505 ° - Phi: 0.00 ° - Aux1: 0.0 - Operations: Background 1.000,1.000 | Import

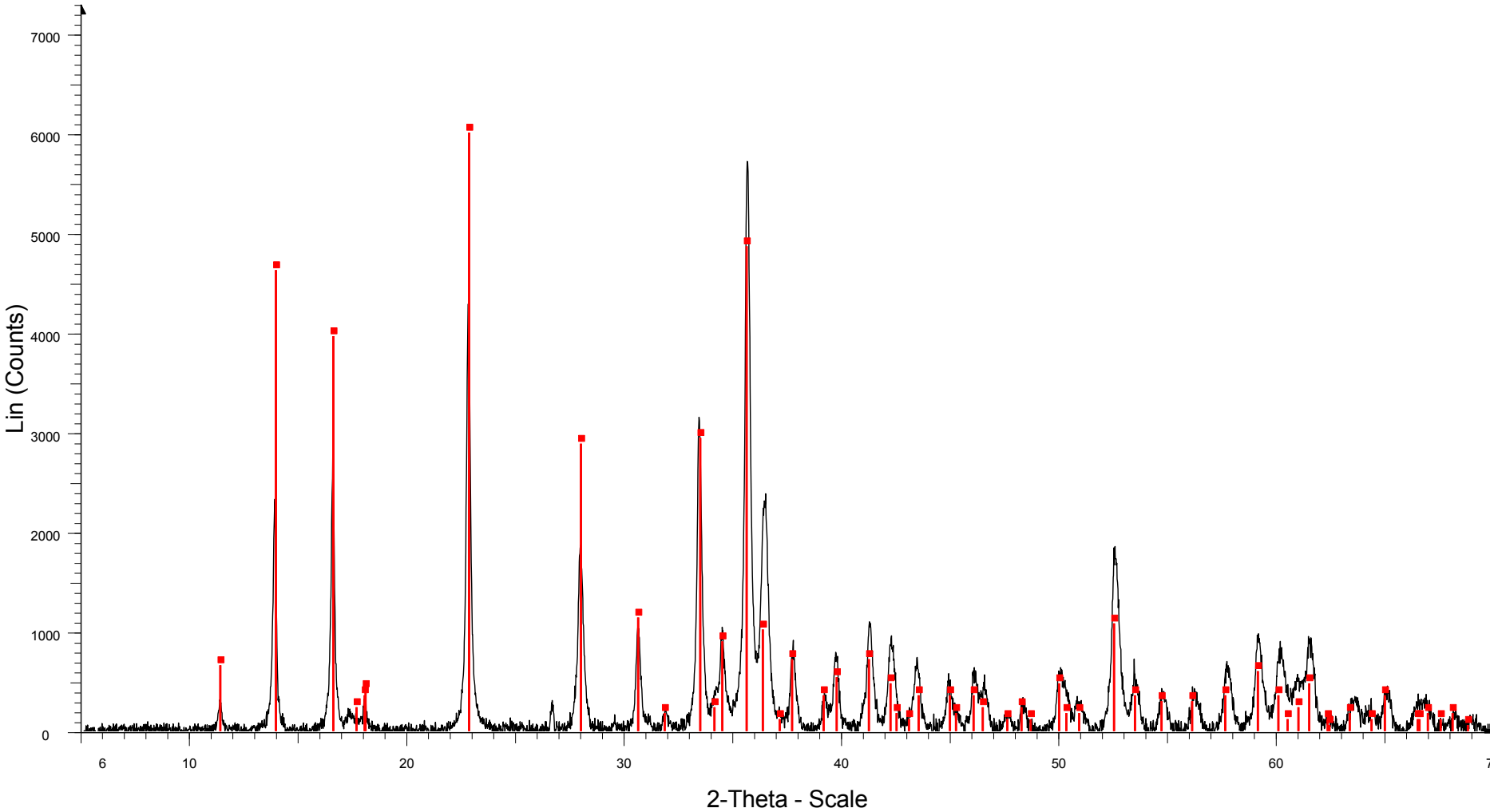
00-011-0646 (*) - Chalcanthite, syn - Cu+2SO4·5H2O - Y: 18.48 % - d x by: 1. - WL: 1.5406 - Triclinic -

00-001-0301 (D) - Chalcanthite - CuSO4·5H2O - Y: 34.86 % - d x by: 1. - WL: 1.5406 - Triclinic -

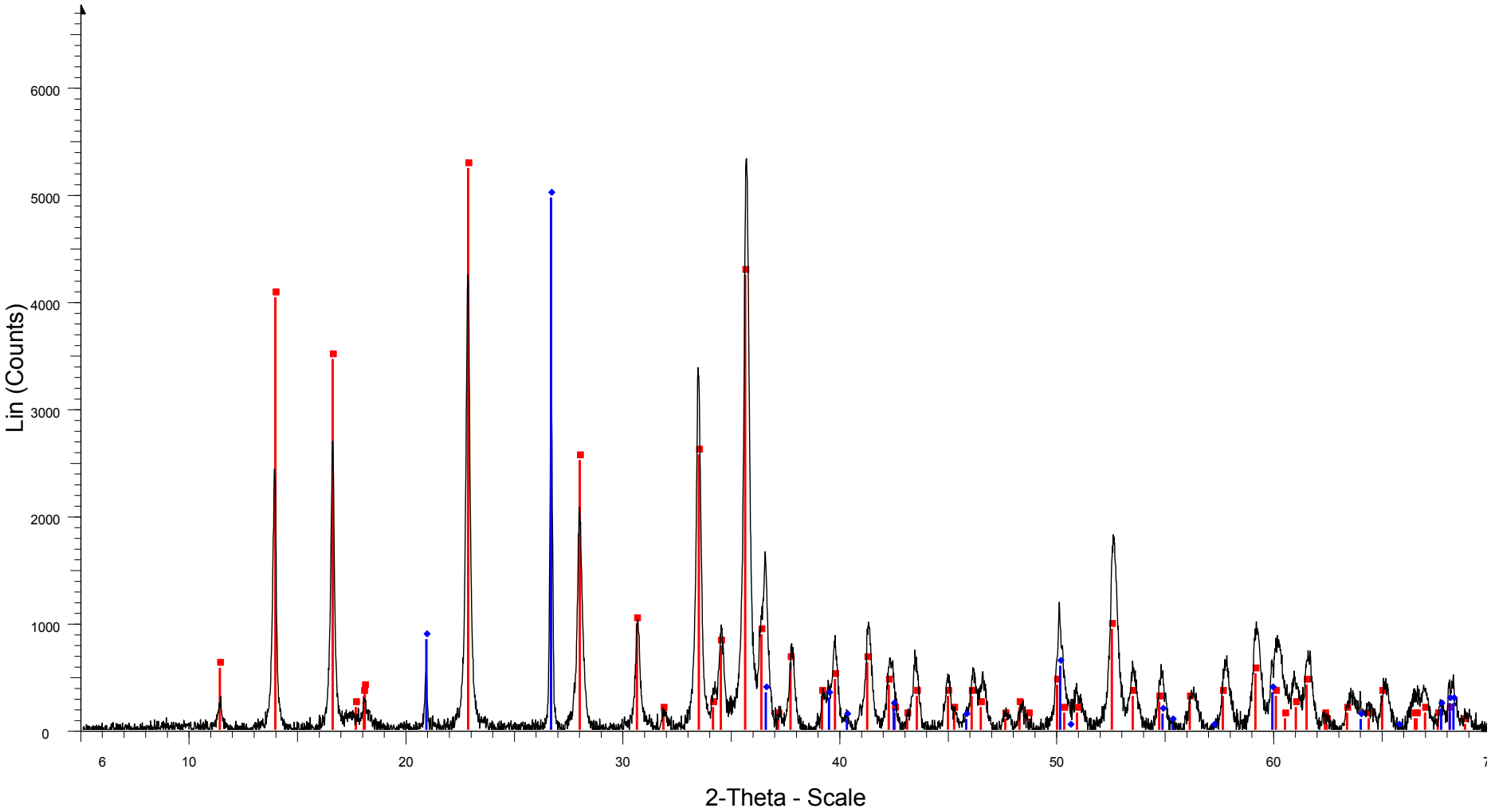


File: Bidgood Hall.raw - Type: 2Th/Th locked - Start: 5.009 ° - End: 69.999 ° - Step: 0.017 ° - Step time: 2. s - Temp.: 25 °C (Room) - Time Started: 0 s - 2-Theta: 5.009 ° - Theta: 2.505 ° - Phi: 0.00 ° - Aux1: 0.0 - Aux2:
Operations: Background 1.000,1.000 | Import

00-043-1458 (I) - Brochantite-M - Cu4+2SO4(OH)6 - Y: 92.20 % - d x by: 1. - WL: 1.5406 - Monoclinic -



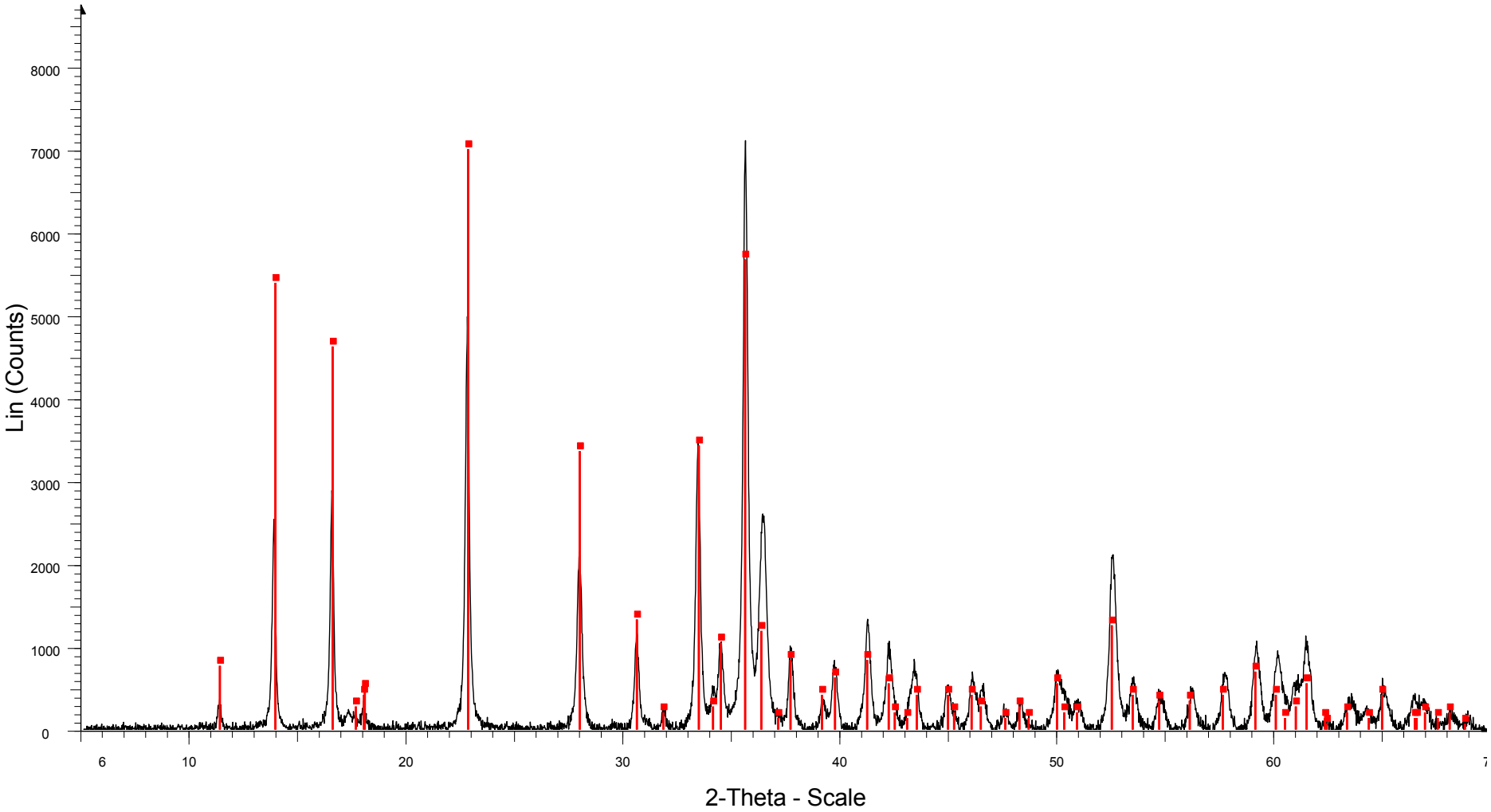
File: Bryce Unknown.raw - Type: 2Th/Th locked - Start: 5.009 ° - End: 69.999 ° - Step: 0.017 ° - Step time: 2. s - Temp.: 25 °C (Room) - Time Started: 0 s - 2-Theta: 5.009 ° - Theta: 2.505 ° - Phi: 0.00 ° - Aux1: 0.0 - Au
Operations: Background 1.000,1.000 | Import
00-043-1458 (I) - Brochantite-M - Cu4+2SO4(OH)6 - Y: 105.13 % - d x by: 1. - WL: 1.5406 - Monoclinic -



File: Carmichael Hall 1.raw - Type: 2Th/Th locked - Start: 5.009 ° - End: 69.999 ° - Step: 0.017 ° - Step time: 2. s - Temp.: 25 °C (Room) - Time Started: 0 s - 2-Theta: 5.009 ° - Theta: 2.505 ° - Phi: 0.00 ° - Aux1: 0.0 - Operations: Background 1.000,1.000 | Import

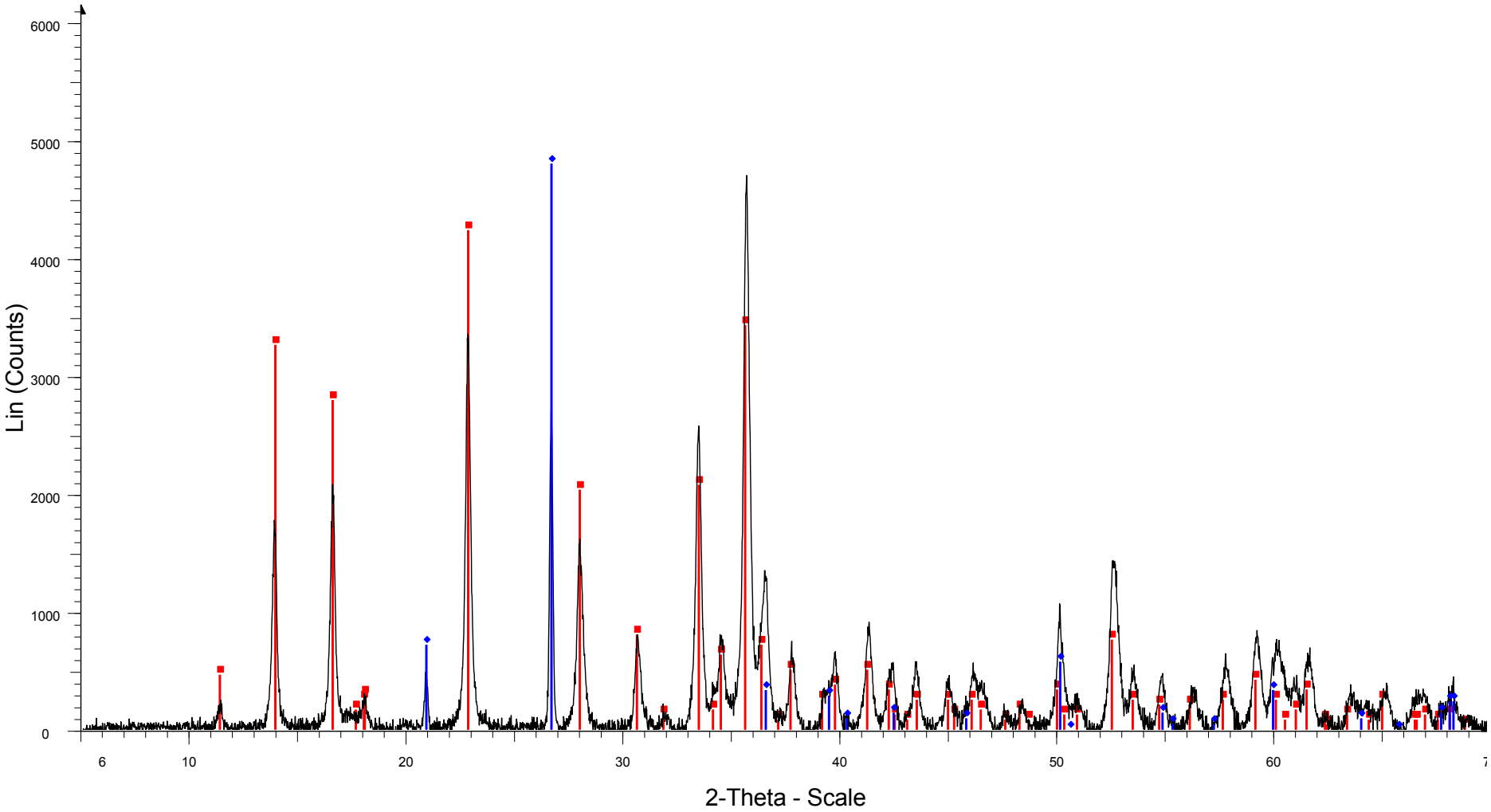
00-043-1458 (I) - Brochantite-M - Cu4+2SO4(OH)6 - Y: 98.39 % - d x by: 1. - WL: 1.5406 - Monoclinic -

01-085-0796 (C) - Quartz - SiO2 - Y: 93.23 % - d x by: 1. - WL: 1.5406 - Hexagonal - I/Ic PDF 3.1 -



File: Carmichael Hall 2.raw - Type: 2Th/Th locked - Start: 5.009 ° - End: 69.999 ° - Step: 0.017 ° - Step time: 2. s - Temp.: 25 °C (Room) - Time Started: 0 s - 2-Theta: 5.009 ° - Theta: 2.505 ° - Phi: 0.00 ° - Aux1: 0.0 - Operations: Background 1.000,1.000 | Import

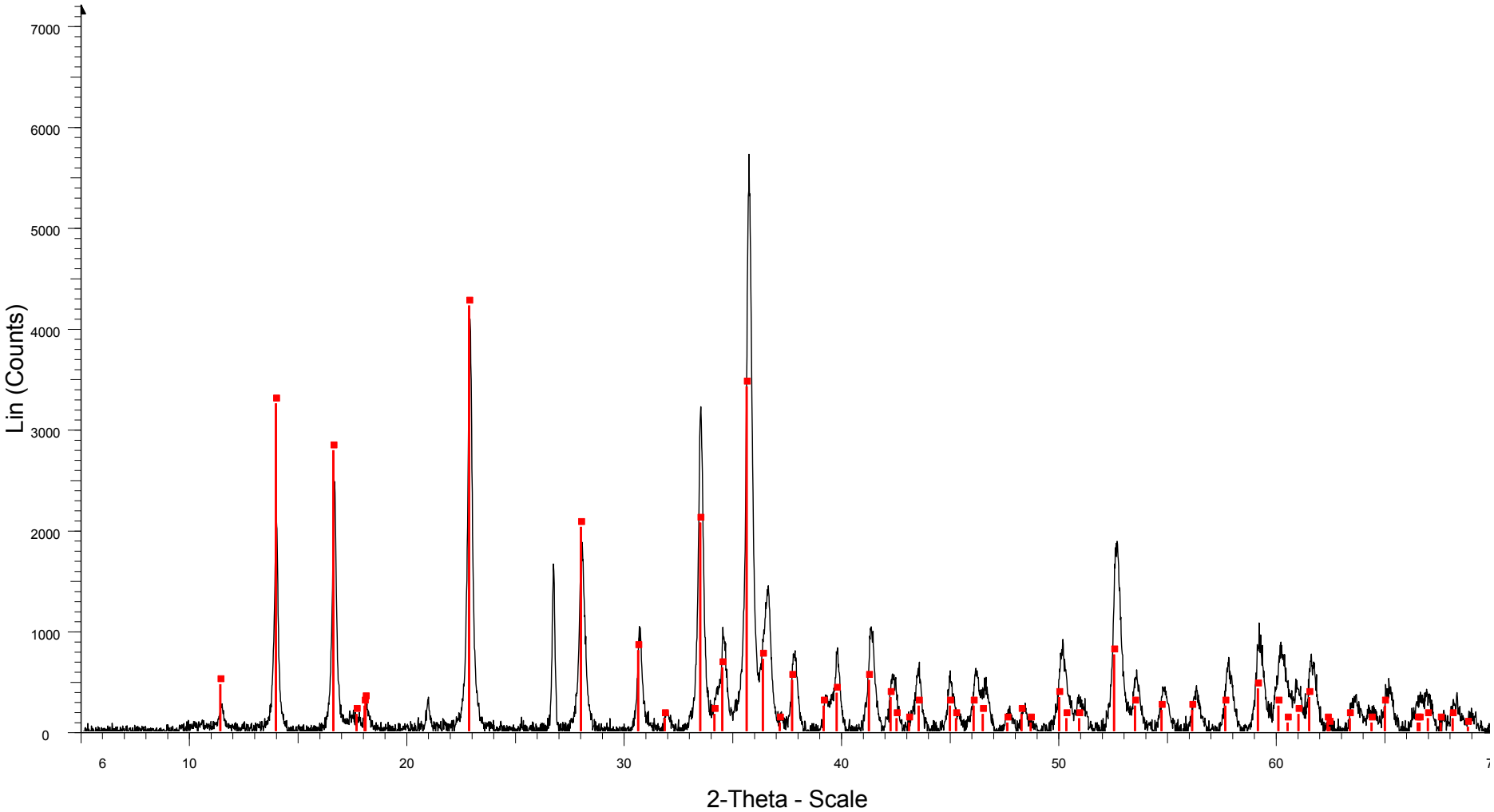
00-043-1458 (I) - Brochantite-M - Cu4+2SO4(OH)6 - Y: 98.59 % - d x by: 1. - WL: 1.5406 - Monoclinic -



File: Farrah Hall.raw - Type: 2Th/Th locked - Start: 5.009 ° - End: 69.999 ° - Step: 0.017 ° - Step time: 2. s - Temp.: 25 °C (Room) - Time Started: 0 s - 2-Theta: 5.009 ° - Theta: 2.505 ° - Phi: 0.00 ° - Aux1: 0.0 - Aux2: 0
Operations: Background 1.000,1.000 | Import

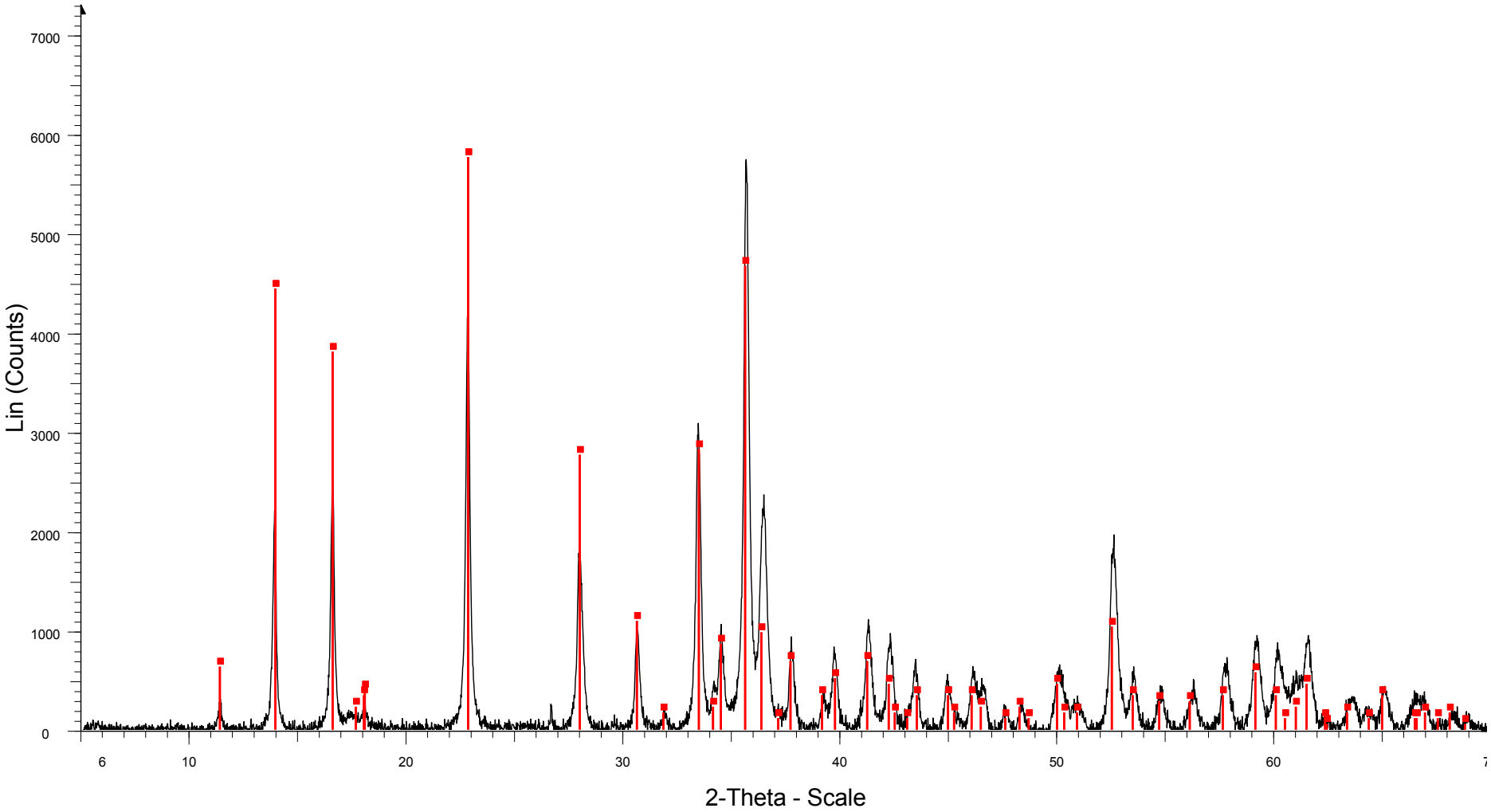
00-043-1458 (I) - Brochantite-M - Cu4+2SO4(OH)6 - Y: 90.17 % - d x by: 1. - WL: 1.5406 - Monoclinic -

01-085-0795 (C) - Quartz - SiO2 - Y: 102.14 % - d x by: 1. - WL: 1.5406 - Hexagonal - I/Ic PDF 3.1 -



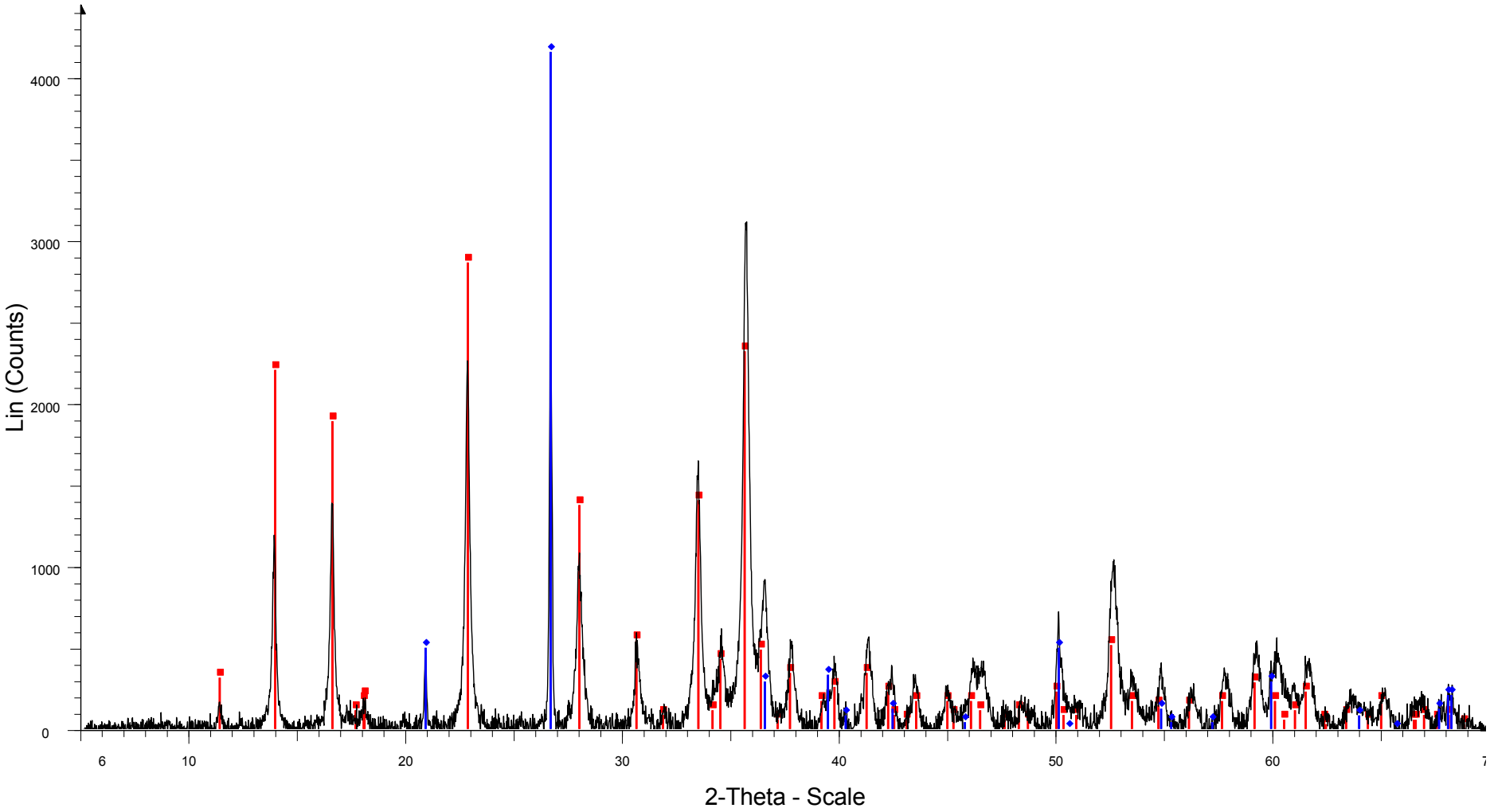
File: Former Bryce Receiving Office.raw - Type: 2Th/Th locked - Start: 5.009 ° - End: 69.999 ° - Step: 0.017 ° - Step time: 2. s - Temp.: 25 °C (Room) - Time Started: 0 s - 2-Theta: 5.009 ° - Theta: 2.505 ° - Phi: 0.00 ° - Operations: Background 1.000,1.000 | Import

00-043-1458 (I) - Brochantite-M - Cu4+2SO4(OH)6 - Y: 73.84 % - d x by: 1. - WL: 1.5406 - Monoclinic -



File: Former Bryce Women's Admin.raw - Type: 2Th/Th locked - Start: 5.009 ° - End: 69.999 ° - Step: 0.017 ° - Step time: 2. s - Temp.: 25 °C (Room) - Time Started: 0 s - 2-Theta: 5.009 ° - Theta: 2.505 ° - Phi: 0.00 ° - Operations: Background 1.000,1.000 | Import

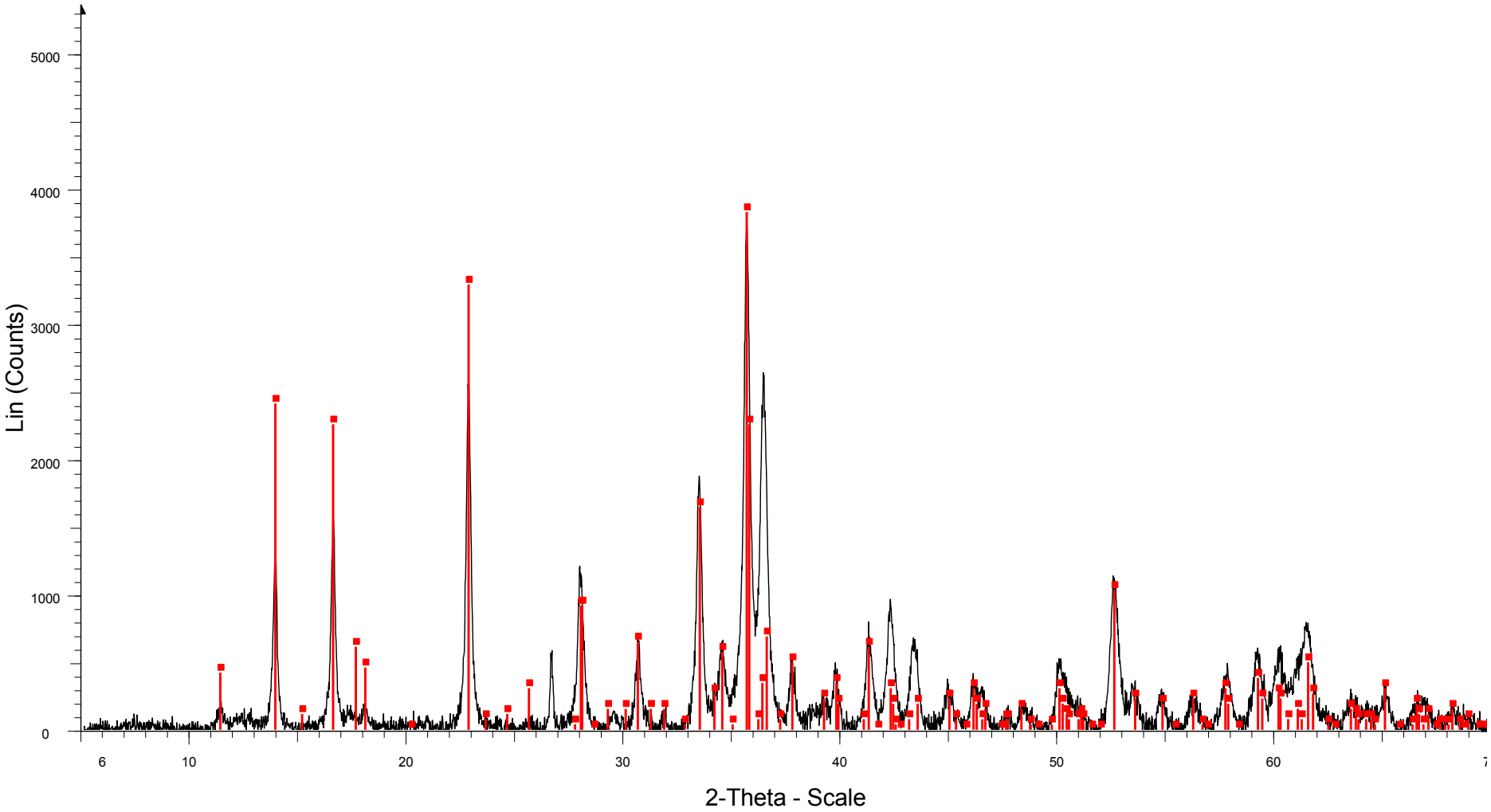
00-043-1458 (I) - Brochantite-M - Cu4+2SO4(OH)6 - Y: 100.49 % - d x by: 1. - WL: 1.5406 - Monoclinic -



File: Gallalee Dome.raw - Type: 2Th/Th locked - Start: 5.009 ° - End: 69.999 ° - Step: 0.017 ° - Step time: 2. s - Temp.: 25 °C (Room) - Time Started: 0 s - 2-Theta: 5.009 ° - Theta: 2.505 ° - Phi: 0.00 ° - Aux1: 0.0 - Aux
Operations: Background 1.000,1.000 | Import

00-043-1458 (I) - Brochantite-M - Cu4+2SO4(OH)6 - Y: 91.99 % - d x by: 1. - WL: 1.5406 - Monoclinic -

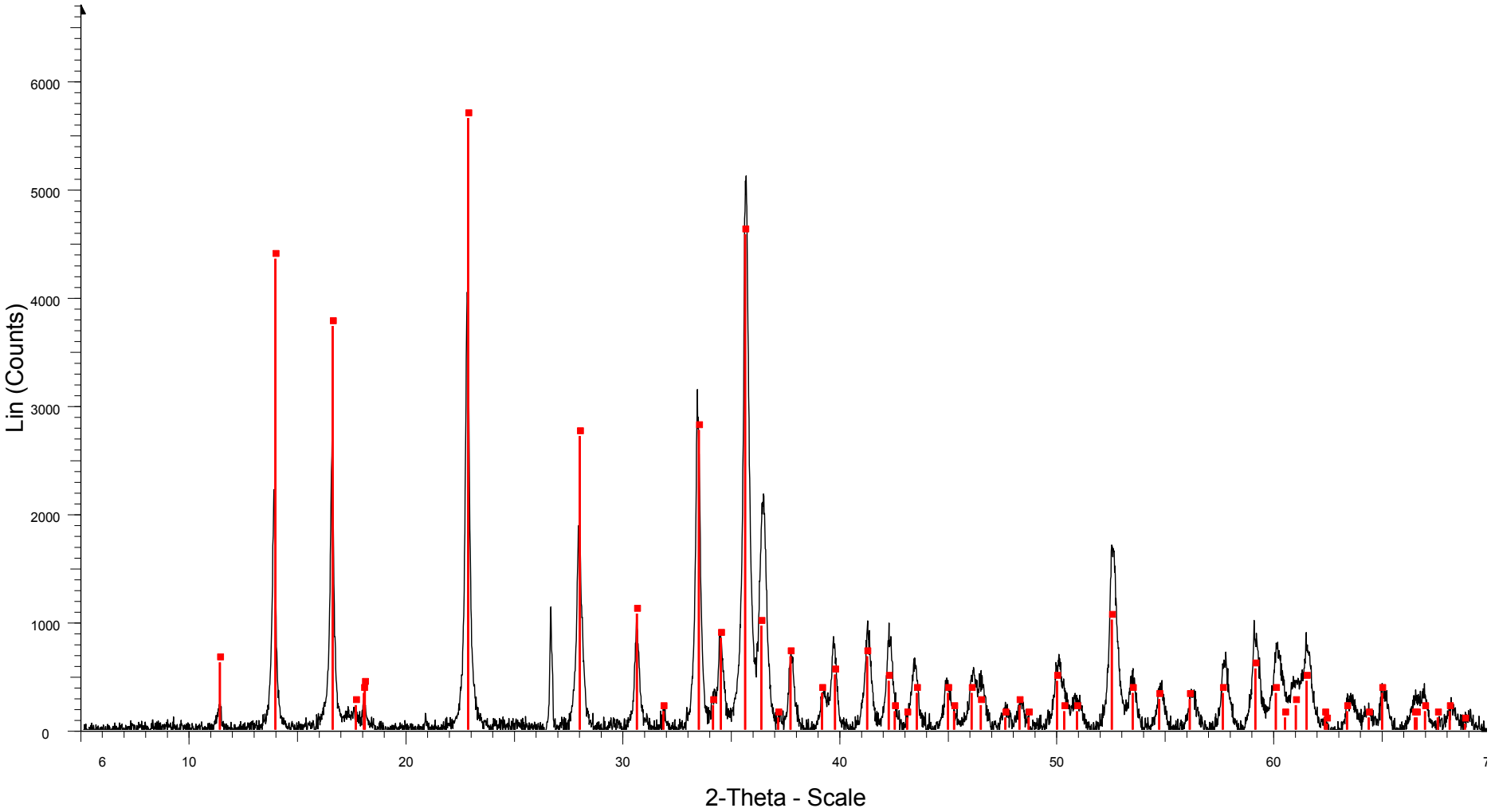
01-085-0798 (C) - Quartz - SiO2 - Y: 133.56 % - d x by: 1. - WL: 1.5406 - Hexagonal - I/Ic PDF 3.3 -



File: Gallalee Hall 1.raw - Type: 2Th/Th locked - Start: 5.009 ° - End: 69.999 ° - Step: 0.017 ° - Step time: 2. s - Temp.: 25 °C (Room) - Time Started: 0 s - 2-Theta: 5.009 ° - Theta: 2.505 ° - Phi: 0.00 ° - Aux1: 0.0 - Aux

Operations: Background 1.000,1.000 | Import

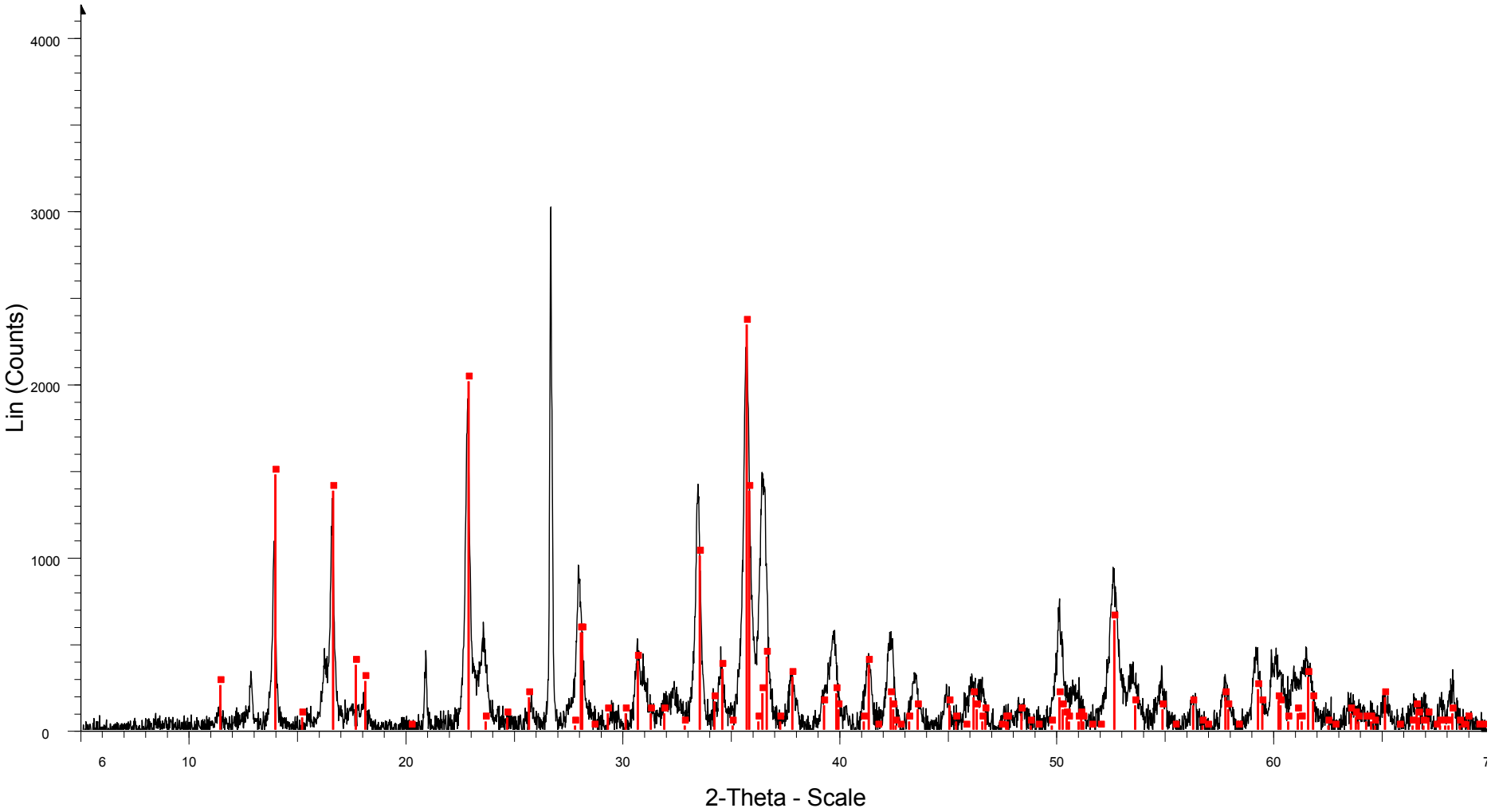
01-087-0454 (C) - Brochantite - Cu4(SO4)(OH)6 - Y: 102.14 % - d x by: 1. - WL: 1.5406 - Monoclinic - I/Ic PDF 1.1 -



File: Mystery Tuscaloosa.raw - Type: 2Th/Th locked - Start: 5.009 ° - End: 69.999 ° - Step: 0.017 ° - Step time: 2. s - Temp.: 25 °C (Room) - Time Started: 0 s - 2-Theta: 5.009 ° - Theta: 2.505 ° - Phi: 0.00 ° - Aux1: 0.0

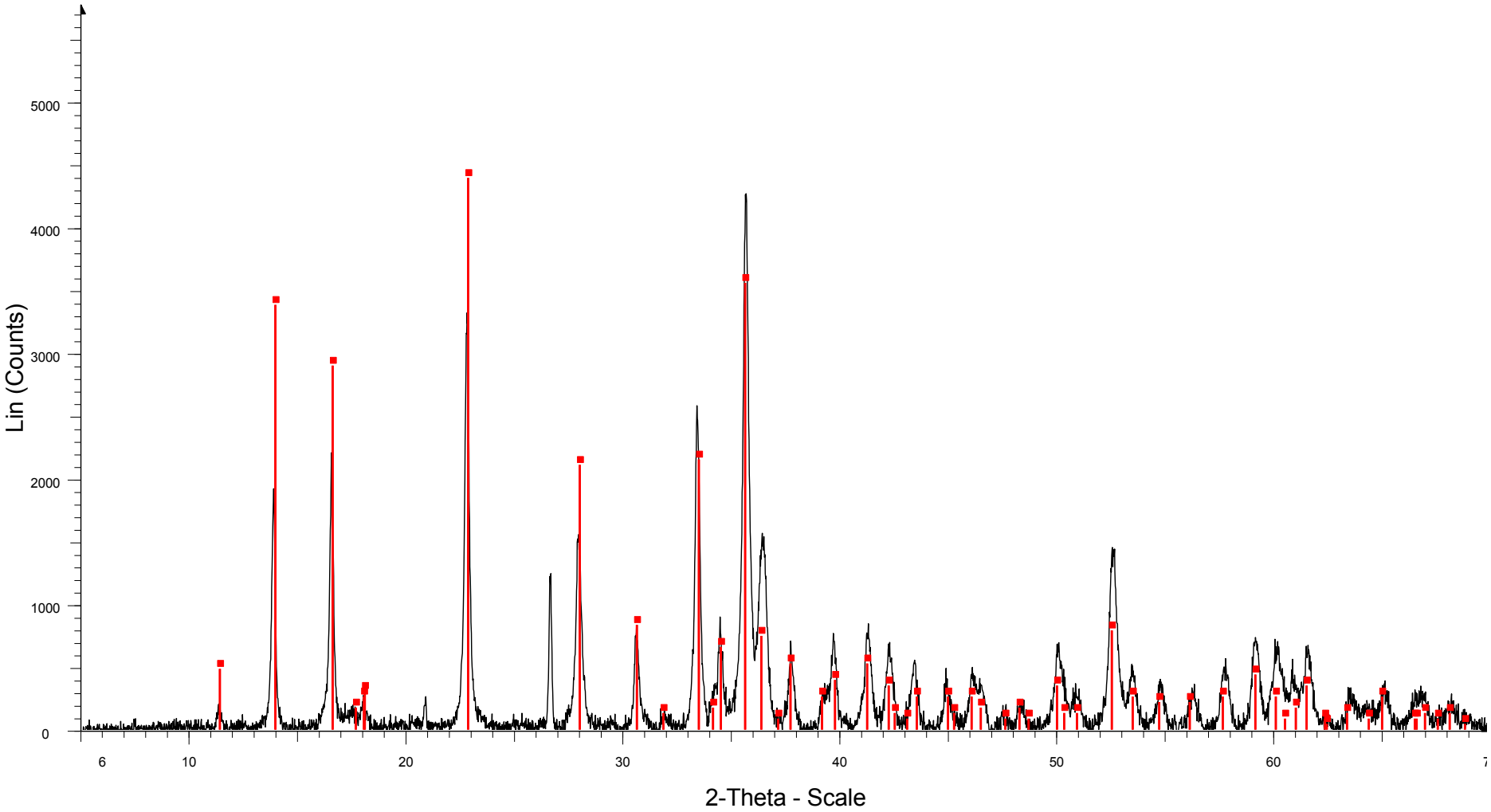
Operations: Background 1.000,1.000 | Import

00-043-1458 (I) - Brochantite-M - Cu4+2SO4(OH)6 - Y: 110.49 % - d x by: 1. - WL: 1.5406 - Monoclinic -



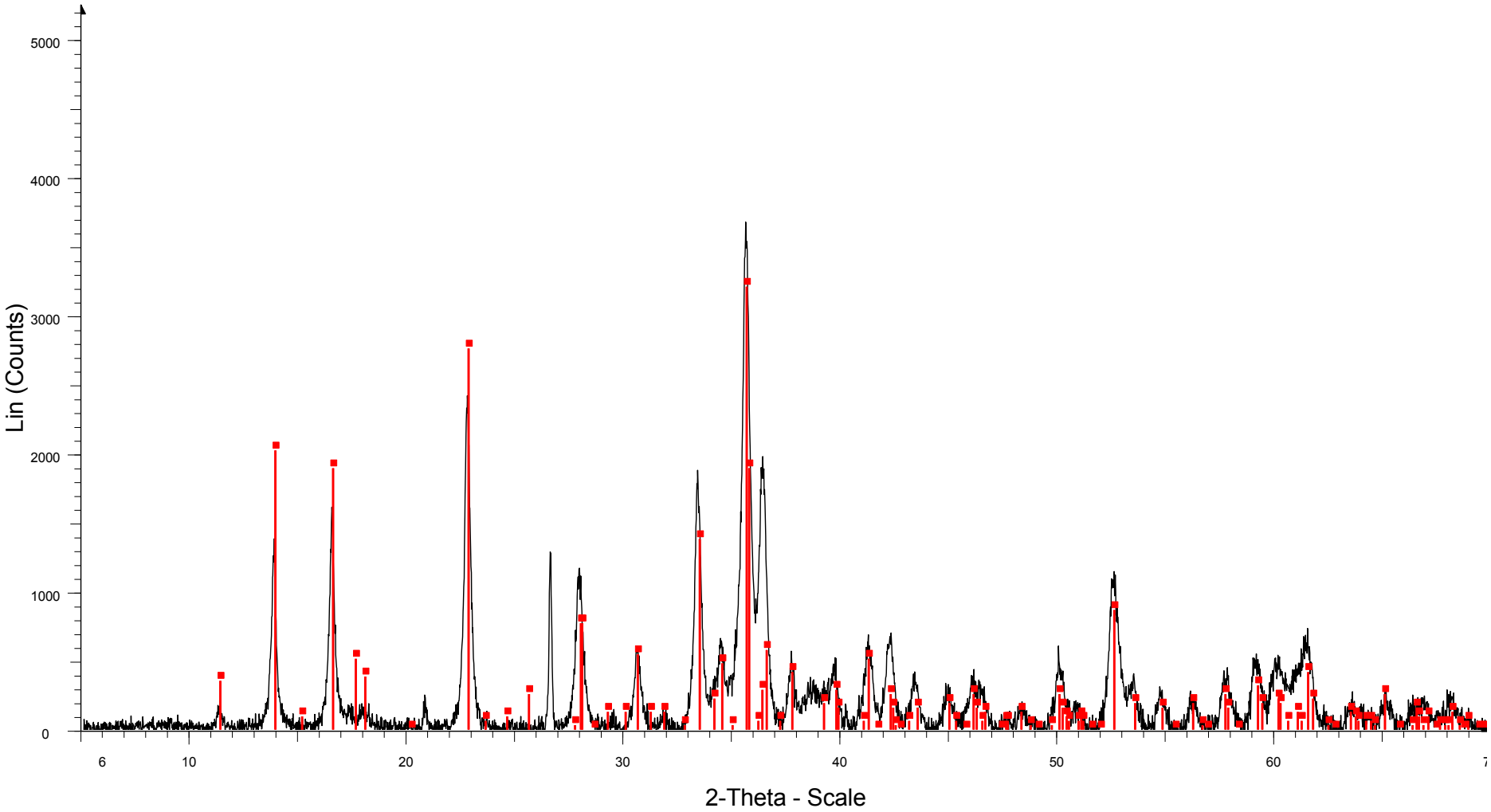
File: Presidential Hall 2.raw - Type: 2Th/Th locked - Start: 5.009 ° - End: 69.999 ° - Step: 0.017 ° - Step time: 2. s - Temp.: 25 °C (Room) - Time Started: 0 s - 2-Theta: 5.009 ° - Theta: 2.505 ° - Phi: 0.00 ° - Aux1: 0.0 -
Operations: Background 1.000,1.000 | Import

01-087-0454 (C) - Brochantite - Cu4(SO4)(OH)6 - Y: 77.51 % - d x by: 1. - WL: 1.5406 - Monoclinic - I/Ic PDF 1.1 -

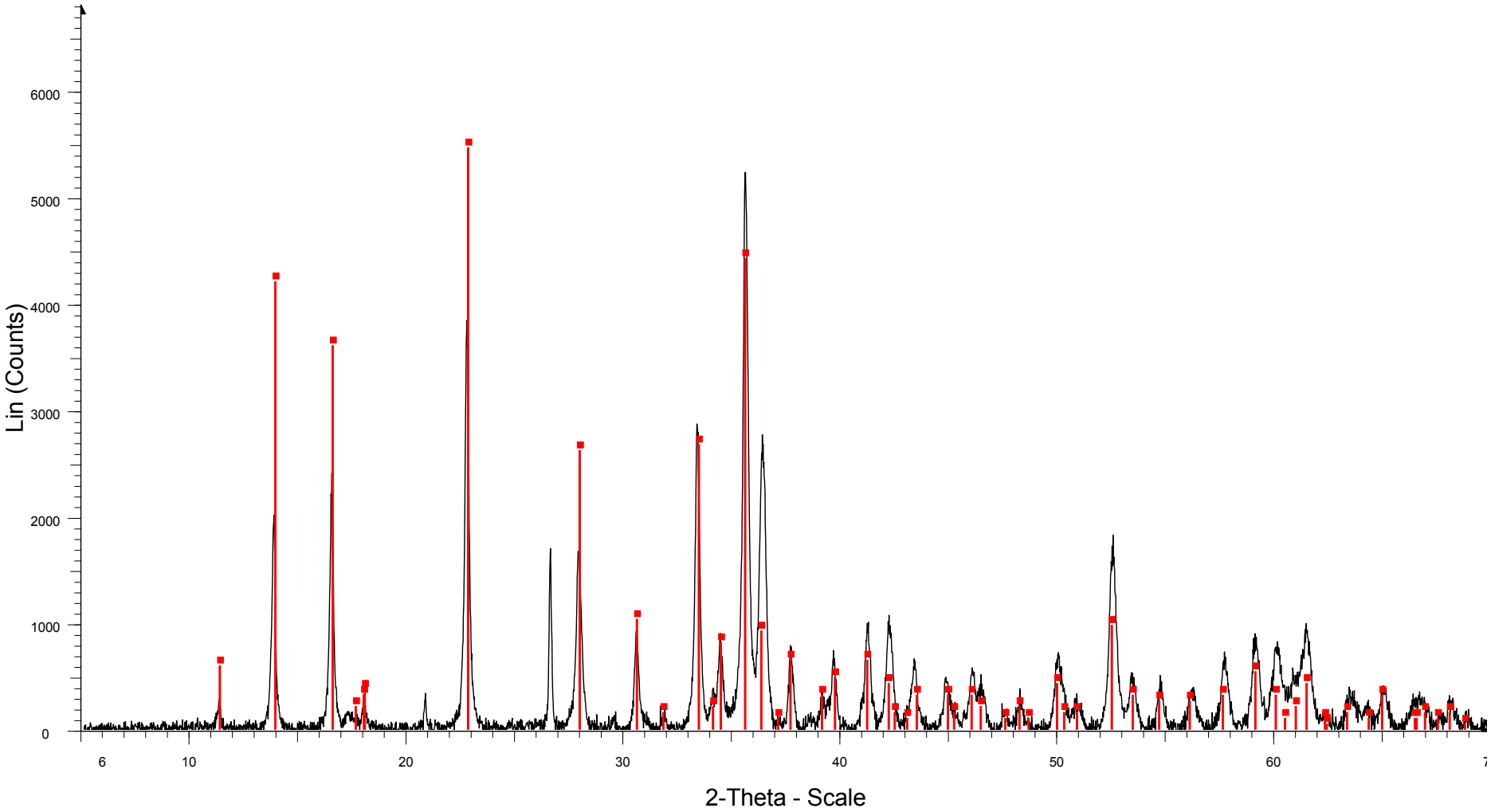


File: Presidential Hall 3.raw - Type: 2Th/Th locked - Start: 5.009 ° - End: 69.999 ° - Step: 0.017 ° - Step time: 2. s - Temp.: 25 °C (Room) - Time Started: 0 s - 2-Theta: 5.009 ° - Theta: 2.505 ° - Phi: 0.00 ° - Aux1: 0.0 -
Operations: Background 1.000,1.000 | Import

00-043-1458 (I) - Brochantite-M - Cu4+2SO4(OH)6 - Y: 102.98 % - d x by: 1. - WL: 1.5406 - Monoclinic -



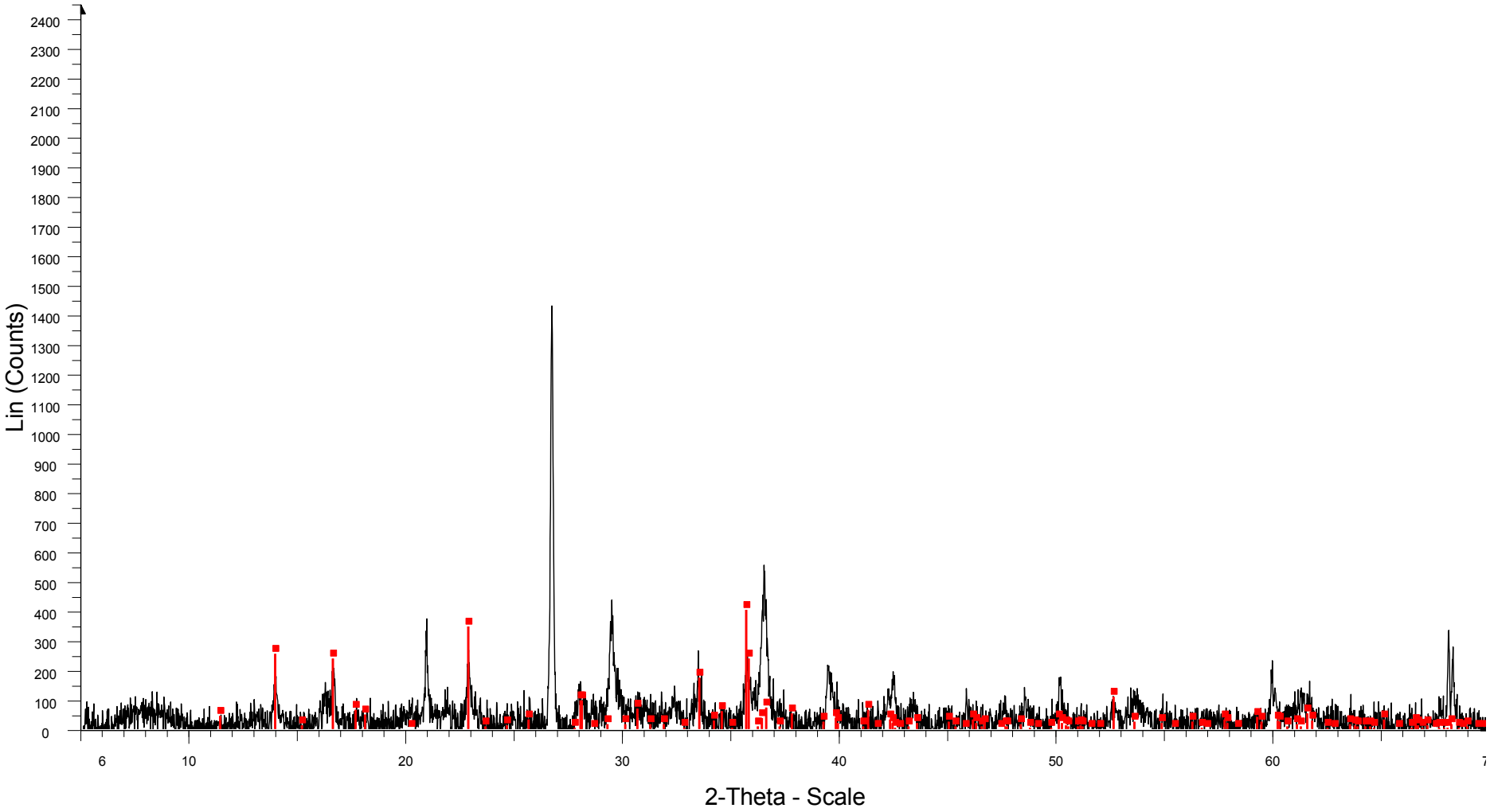
File: Rowan-Johnson.raw - Type: 2Th/Th locked - Start: 5.009 ° - End: 69.999 ° - Step: 0.017 ° - Step time: 2. s - Temp.: 25 °C (Room) - Time Started: 0 s - 2-Theta: 5.009 ° - Theta: 2.505 ° - Phi: 0.00 ° - Aux1: 0.0 - Au
Operations: Background 1.000,1.000 | Import
01-087-0454 (C) - Brochantite - Cu4(SO4)(OH)6 - Y: 87.34 % - d x by: 1. - WL: 1.5406 - Monoclinic - I/Ic PDF 1.1 -



File: Wilson Hall.raw - Type: 2Th/Th locked - Start: 5.009 ° - End: 69.999 ° - Step: 0.017 ° - Step time: 2. s - Temp.: 25 °C (Room) - Time Started: 0 s - 2-Theta: 5.009 ° - Theta: 2.505 ° - Phi: 0.00 ° - Aux1: 0.0 - Aux2: 0

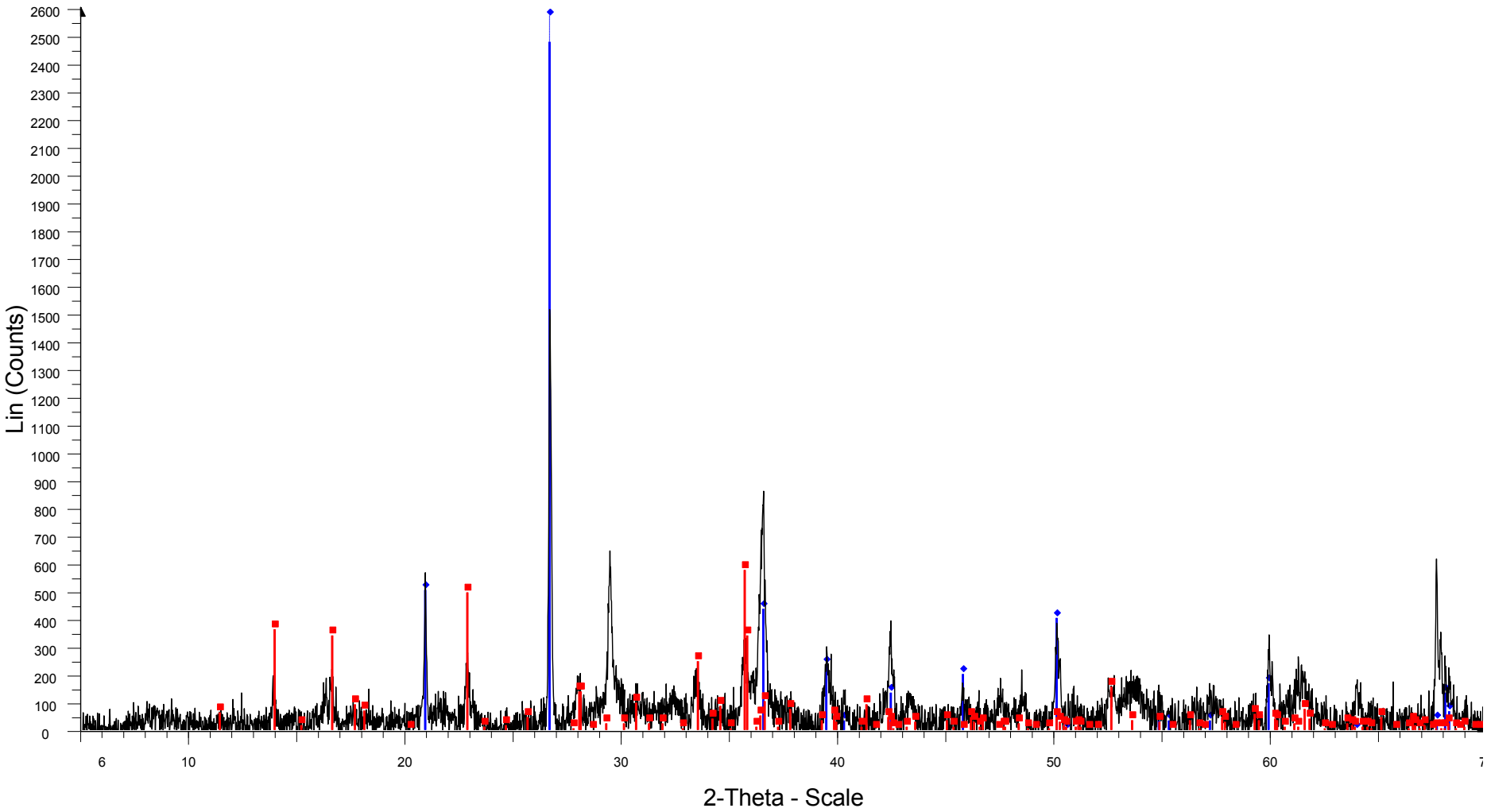
Operations: Background 1.000,1.000 | Import

00-043-1458 (I) - Brochantite-M - Cu4+2SO4(OH)6 - Y: 104.52 % - d x by: 1. - WL: 1.5406 - Monoclinic -



File: BB Comer Repeat.raw - Type: 2Th/Th locked - Start: 5.009 ° - End: 69.999 ° - Step: 0.017 ° - Step time: 2. s - Temp.: 25 °C (Room) - Time Started: 0 s - 2-Theta: 5.009 ° - Theta: 2.505 ° - Phi: 0.00 ° - Aux1: 0.0 -
Operations: Background 1.000,1.000 | Import

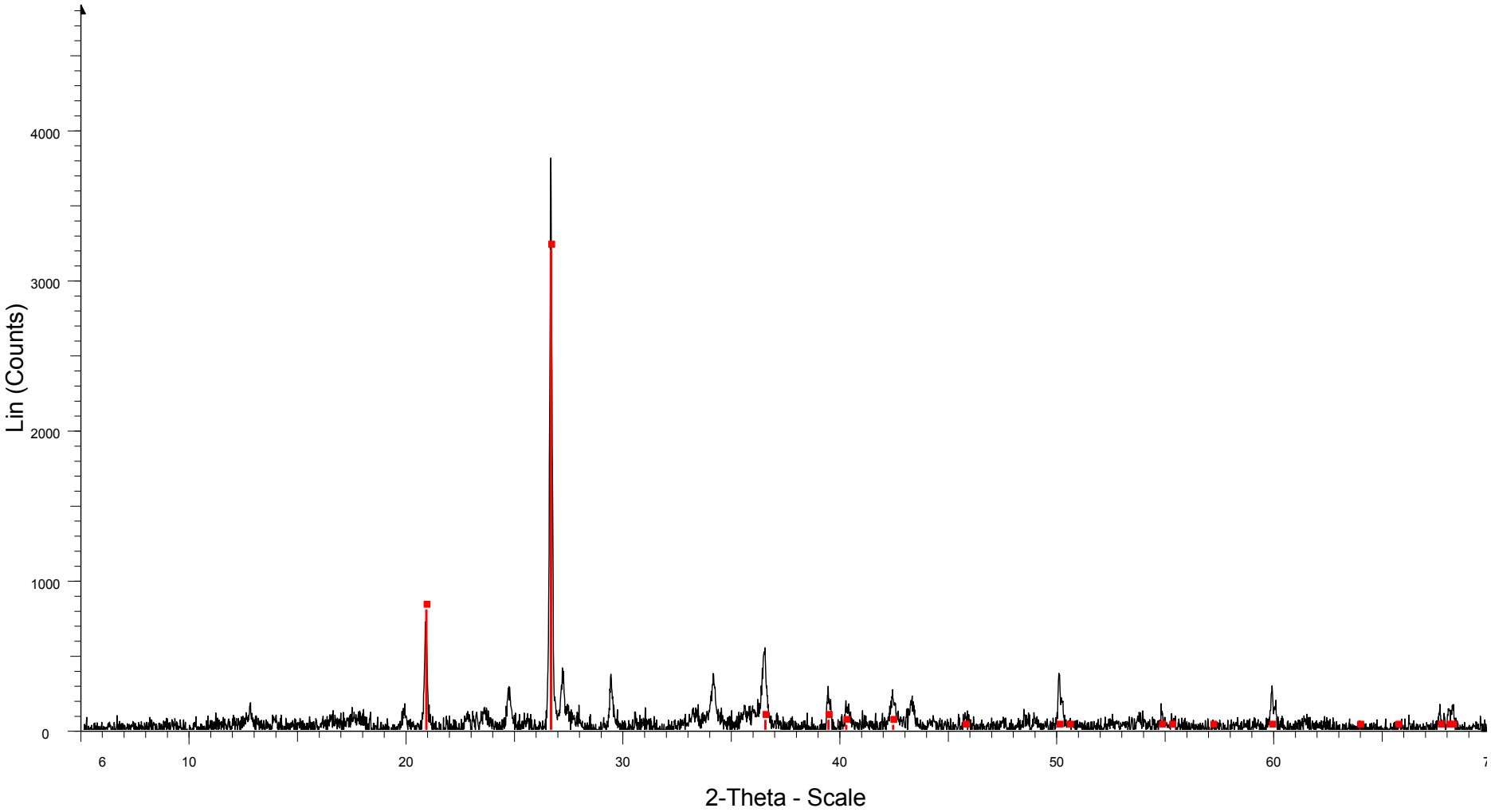
01-087-0454 (C) - Brochantite - Cu4(SO4)(OH)6 - Y: 28.17 % - d x by: 1. - WL: 1.5406 - Monoclinic - I/Ic PDF 1.1 -



File: BB Comer.raw - Type: 2Th/Th locked - Start: 5.009 ° - End: 69.999 ° - Step: 0.017 ° - Step time: 2. s - Temp.: 25 °C (Room) - Time Started: 0 s - 2-Theta: 5.009 ° - Theta: 2.505 ° - Phi: 0.00 ° - Aux1: 0.0 - Aux2: 0.
Operations: Background 1.000,1.000 | Import

01-079-1906 (C) - Quartz - SiO2 - Y: 222.01 % - d x by: 1. - WL: 1.5406 - Hexagonal - I/Ic PDF 4.8 - S-Q 56.8 % -

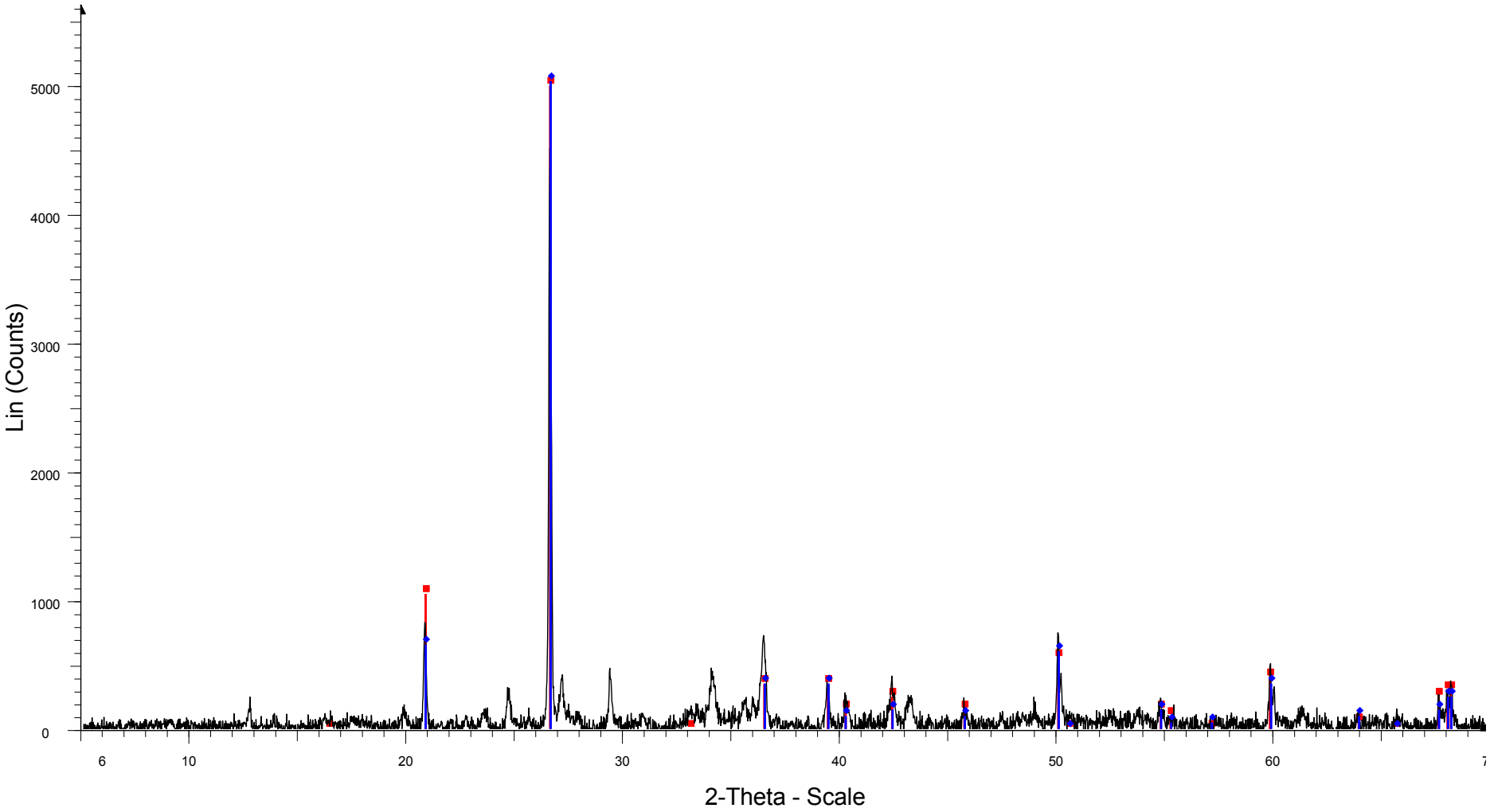
01-087-0454 (C) - Brochantite - Cu4(SO4)(OH)6 - Y: 38.06 % - d x by: 1. - WL: 1.5406 - Monoclinic - I/Ic PDF 1.1 - S-Q 43.2 % -



File: Presidential Hall 1 repeat.raw - Type: 2Th/Th locked - Start: 5.009 ° - End: 69.999 ° - Step: 0.017 ° - Step time: 2. s - Temp.: 25 °C (Room) - Time Started: 0 s - 2-Theta: 5.009 ° - Theta: 2.505 ° - Phi: 0.00 ° - Aux1

Operations: Background 1.000,1.000 | Import

01-085-0335 (C) - Quartz low - SiO2 - Y: 84.03 % - d x by: 1. - WL: 1.5406 - Hexagonal - I/Ic PDF 0.1 -

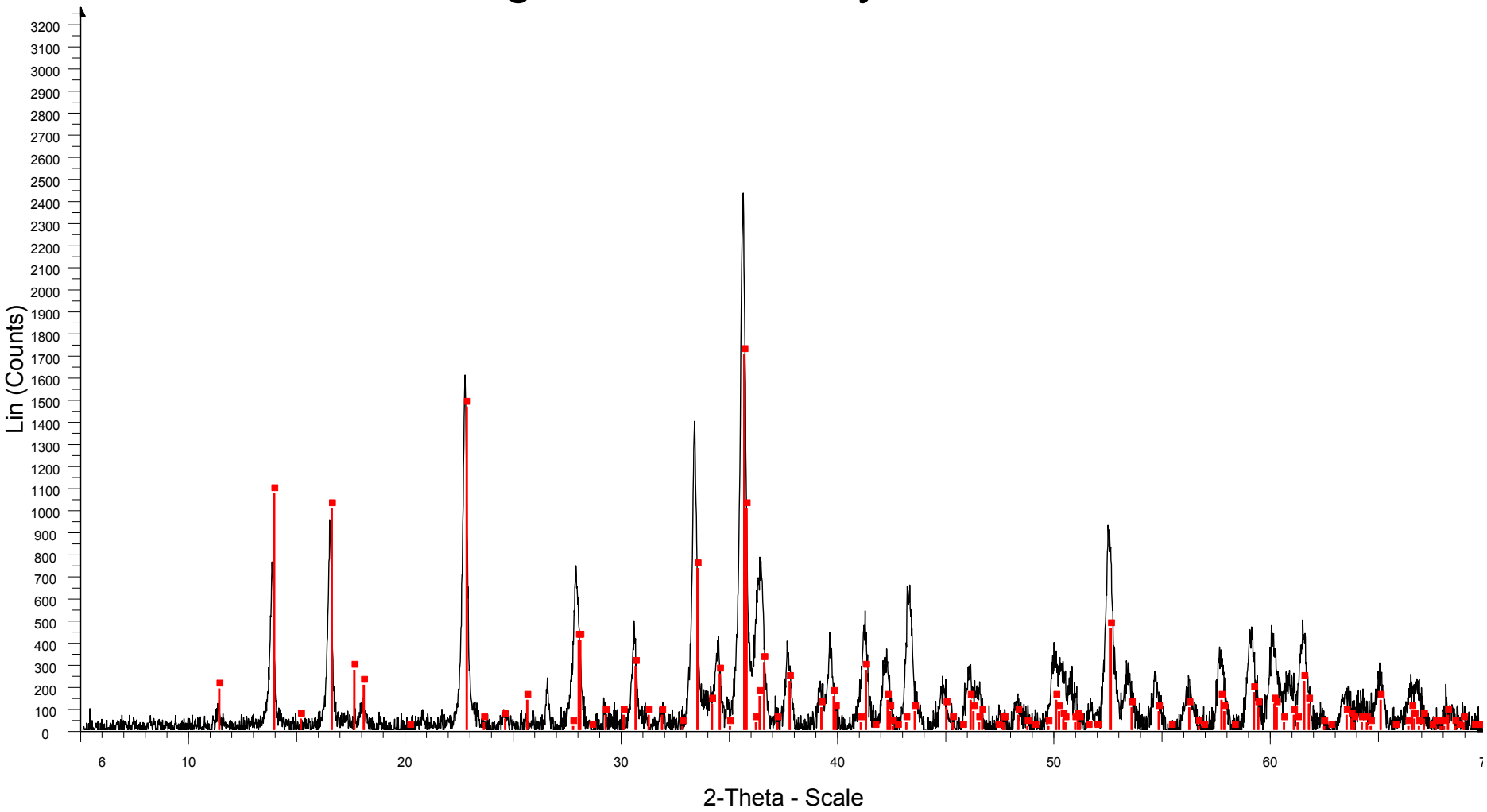


File: Presidential Hall 1 .raw - Type: 2Th/Th locked - Start: 5.009 ° - End: 69.999 ° - Step: 0.017 ° - Step time: 2. s - Temp.: 25 °C (Room) - Time Started: 0 s - 2-Theta: 5.009 ° - Theta: 2.505 ° - Phi: 0.00 ° - Aux1: 0.0 - Operations: Background 1.000,1.000 | Import

01-077-1060 (C) - Silicon Oxide - SiO2 - Y: 110.83 % - d x by: 1. - WL: 1.5406 - Triclinic - I/Ic PDF 1. - S-Q 76.0 % -

01-085-0797 (C) - Quartz - SiO2 - Y: 111.60 % - d x by: 1. - WL: 1.5406 - Hexagonal - I/Ic PDF 3.3 - S-Q 24.0 % -

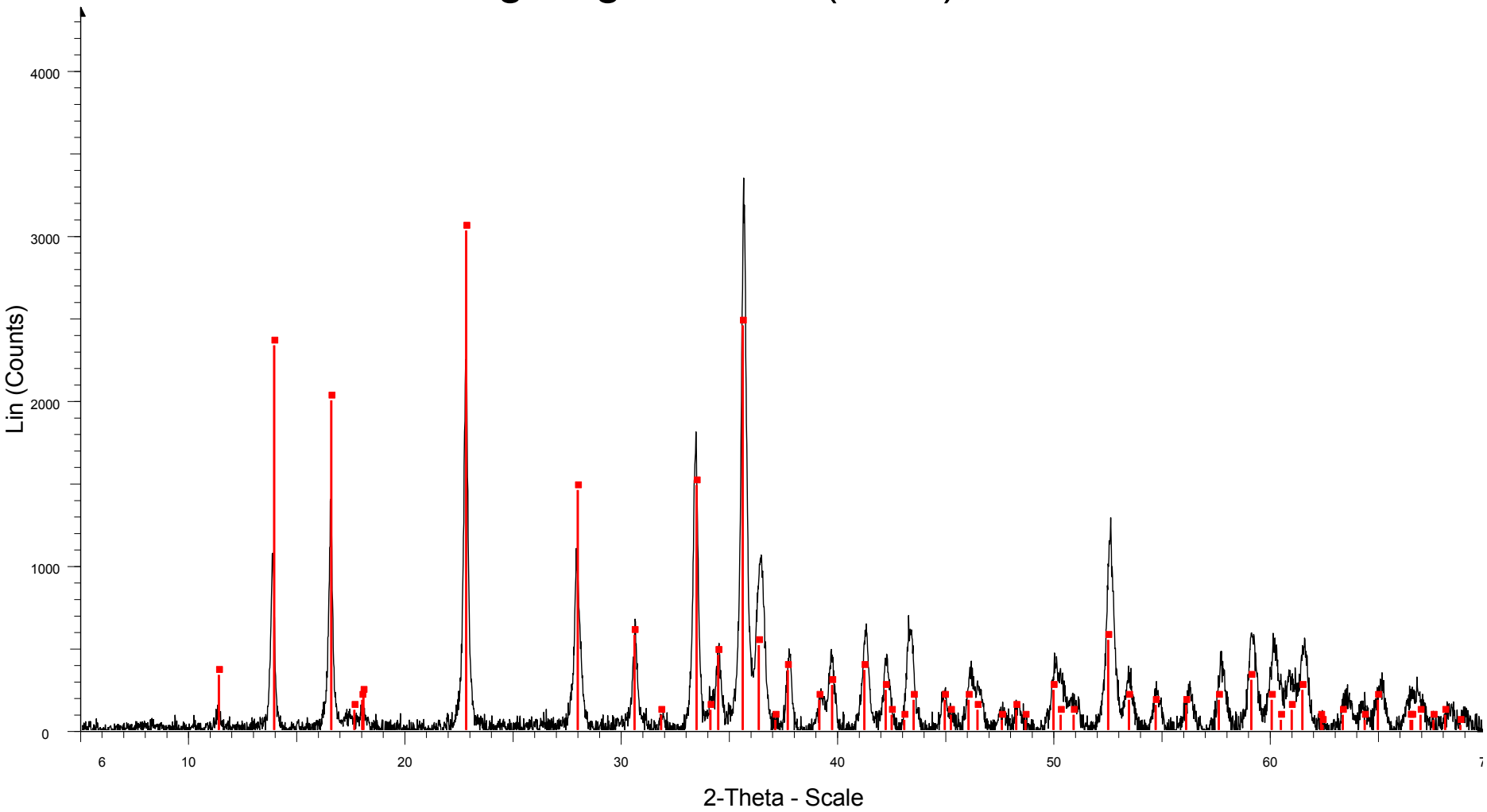
Burgtheater Chimney, Vienna



File: Burgtheater Chimney.raw - Type: 2Th/Th locked - Start: 5.009 ° - End: 69.999 ° - Step: 0.017 ° - Step time: 2. s - Temp.: 25 °C (Room) - Time Started: 0 s - 2-Theta: 5.009 ° - Theta: 2.505 ° - Phi: 0.00 ° - Aux1: 0.0
Operations: Background 1.000,1.000 | Import

01-087-0454 (C) - Brochantite - Cu4(SO4)(OH)6 - Y: 70.06 % - d x by: 1. - WL: 1.5406 - Monoclinic - I/Ic PDF 1.1 -

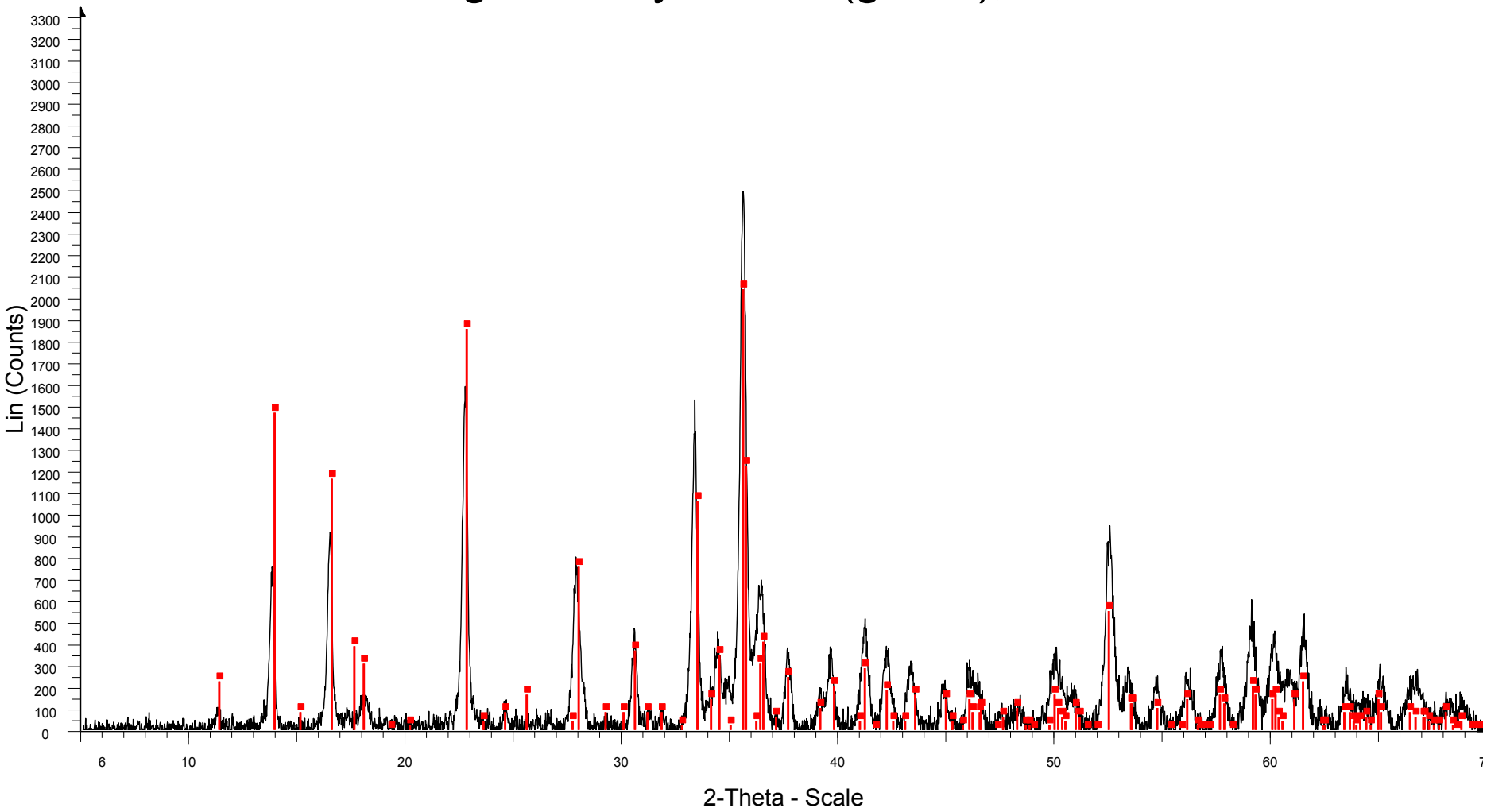
Hofburg Angel Statue (base), Vienna



File: Hofburg Angel Base.raw - Type: 2Th/Th locked - Start: 5.009 ° - End: 69.999 ° - Step: 0.017 ° - Step time: 2. s - Temp.: 25 °C (Room) - Time Started: 0 s - 2-Theta: 5.009 ° - Theta: 2.505 ° - Phi: 0.00 ° - Aux1: 0.0
Operations: Background 1.000,1.000 | Import

00-043-1458 (I) - Brochantite-M - Cu4+2SO4(OH)6 - Y: 90.54 % - d x by: 1. - WL: 1.5406 - Monoclinic -

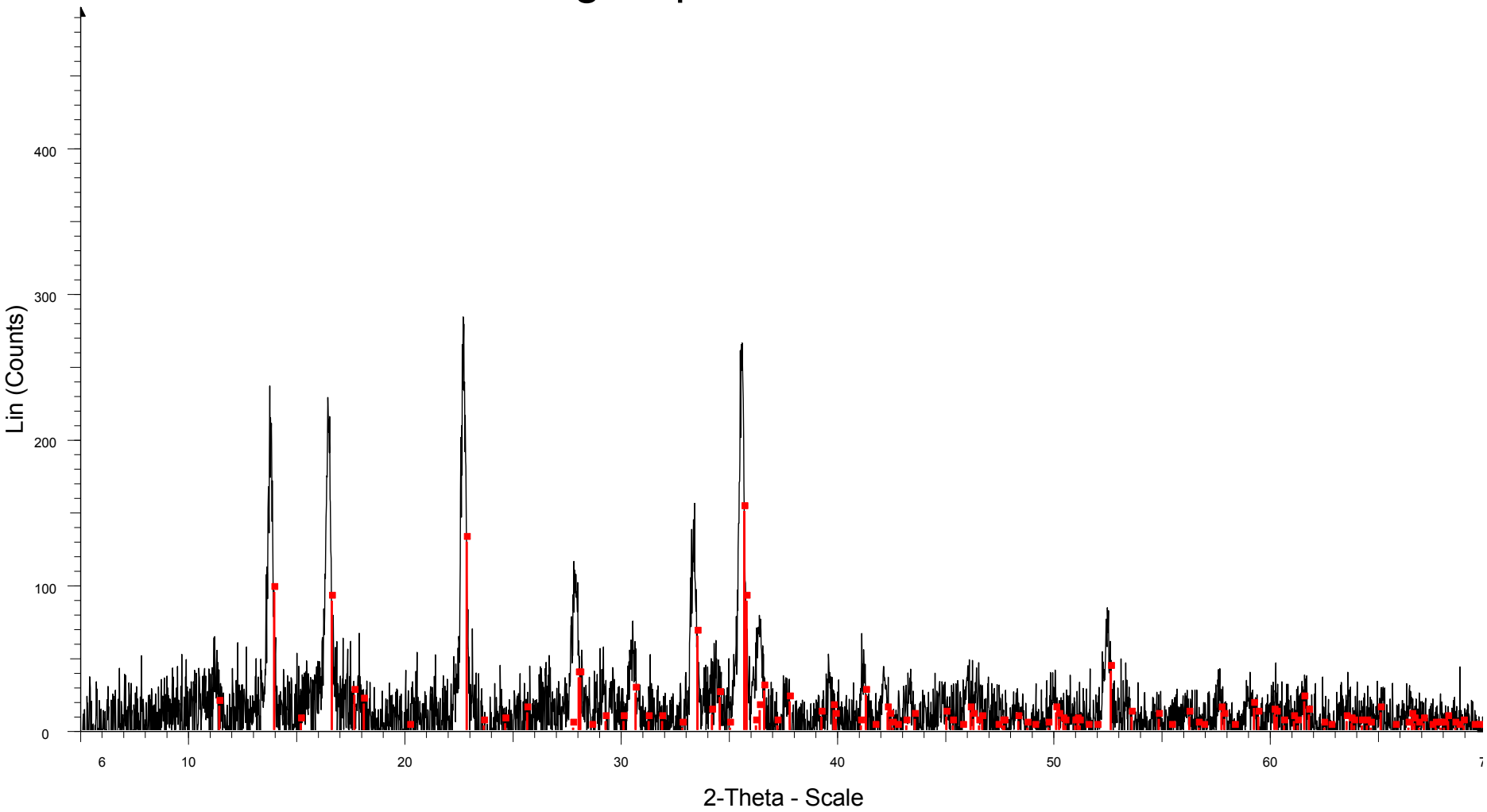
Hofburg Butterfly House (gutter), Vienna



File: Hofburg Butterfly House.raw - Type: 2Th/Th locked - Start: 5.009 ° - End: 69.999 ° - Step: 0.017 ° - Step time: 2. s - Temp.: 25 °C (Room) - Time Started: 0 s - 2-Theta: 5.009 ° - Theta: 2.505 ° - Phi: 0.00 ° - Aux1:
Operations: Background 1.000,1.000 | Import

01-085-1316 (C) - Brochantite - Cu4(OH)6SO4 - Y: 81.85 % - d x by: 1. - WL: 1.5406 - Monoclinic - I/Ic PDF 1. -

Hofburg Cupola Door, Vienna

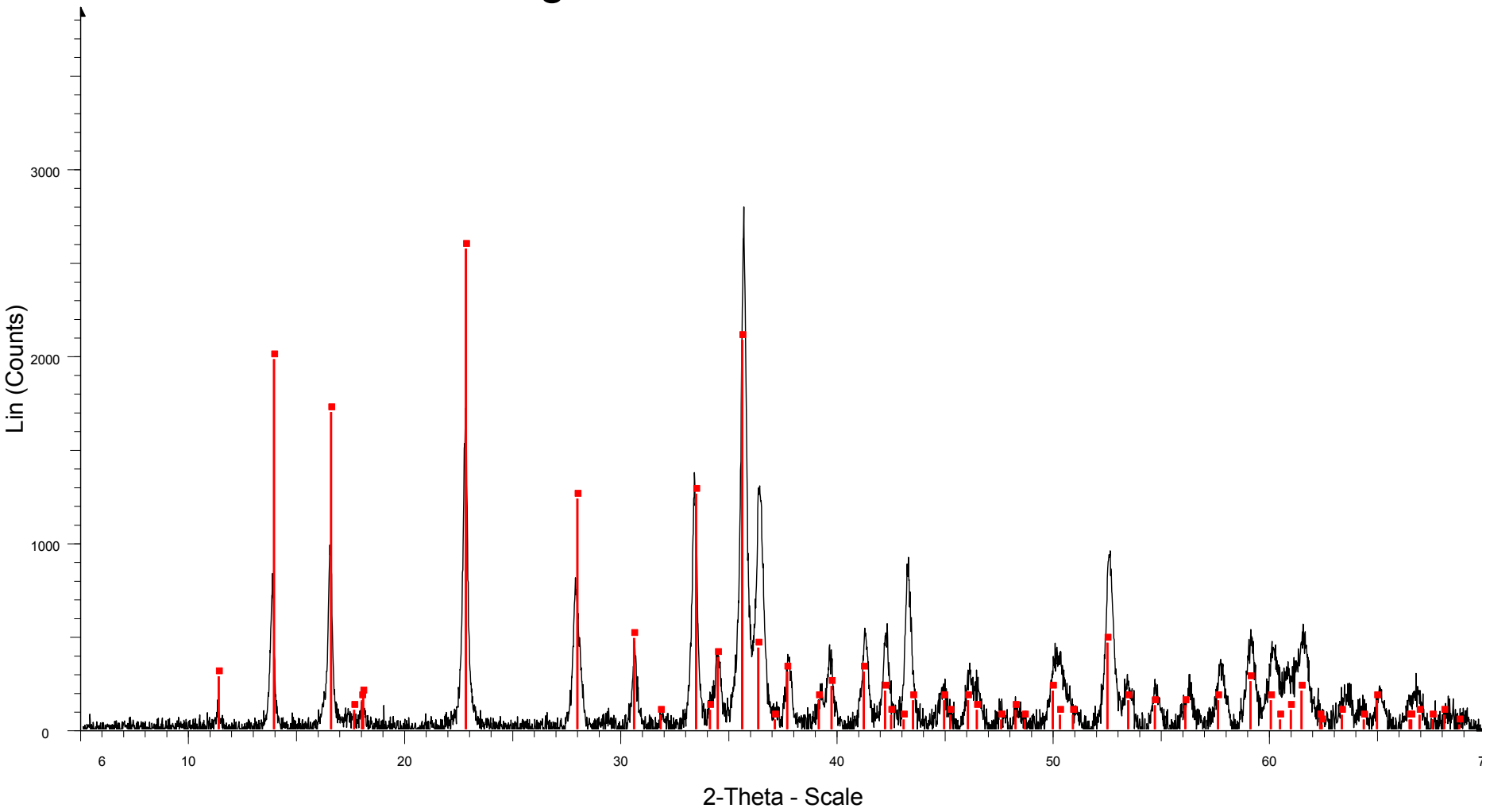


File: Hofburg Cupola Door.raw - Type: 2Th/Th locked - Start: 5.009 ° - End: 69.999 ° - Step: 0.017 ° - Step time: 2. s - Temp.: 25 °C (Room) - Time Started: 0 s - 2-Theta: 5.009 ° - Theta: 2.505 ° - Phi: 0.00 ° - Aux1: 0.0

Operations: Background 1.000,1.000 | Import

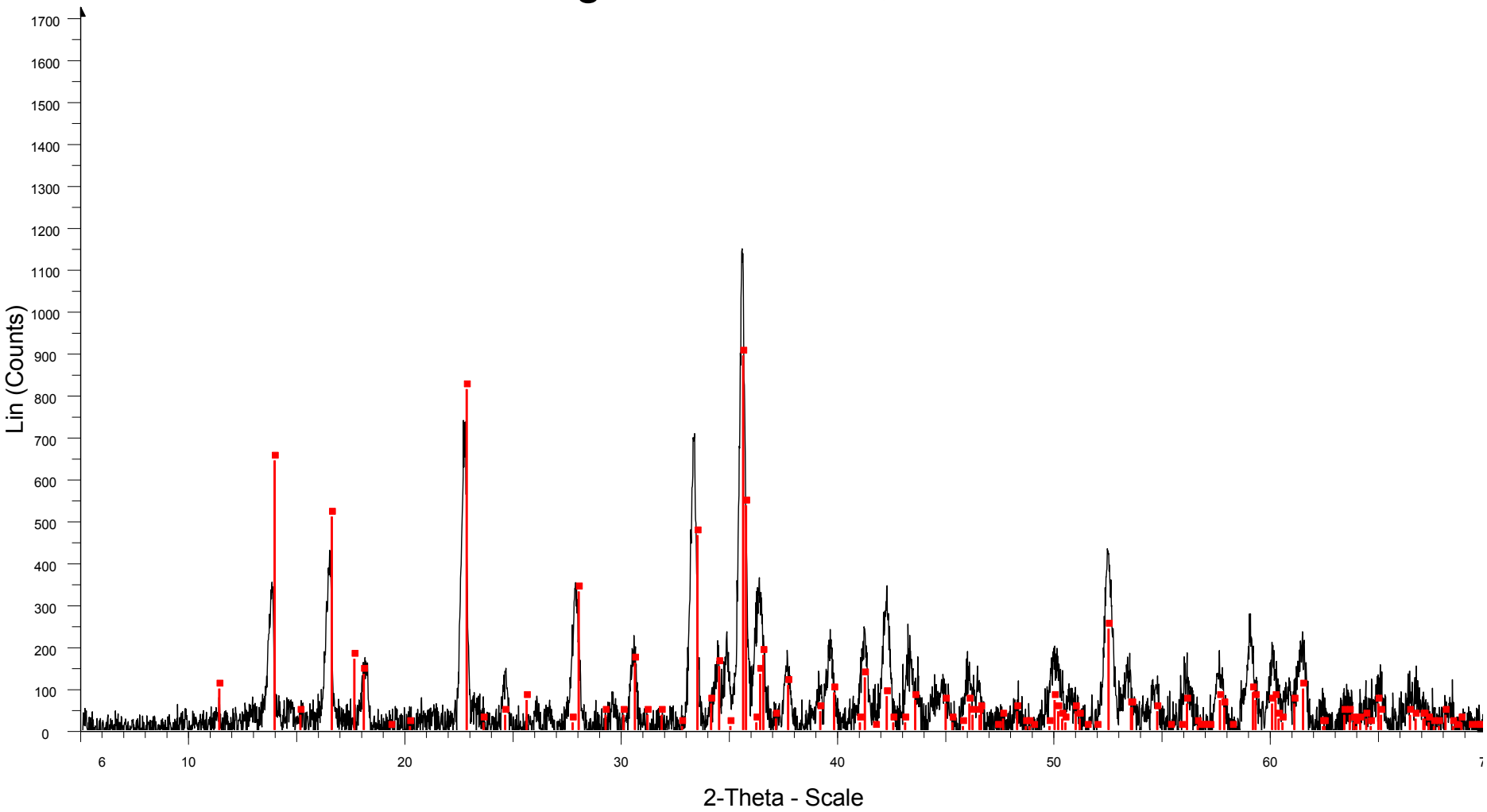
01-087-0454 (C) - Brochantite - Cu4(SO4)(OH)6 - Y: 53.03 % - d x by: 1. - WL: 1.5406 - Monoclinic - I/Ic PDF 1.1 - S-Q 100.0 % -

Hofburg Leaf Decoration, Vienna



File: Hofburg Leaf Decoration_repeat.raw - Type: 2Th/Th locked - Start: 5.009 ° - End: 69.999 ° - Step: 0.017 ° - Step time: 2. s - Temp.: 25 °C (Room) - Time Started: 0 s - 2-Theta: 5.009 ° - Theta: 2.505 ° - Phi: 0.00 °
Operations: Background 1.000,1.000 | Import
00-043-1458 (I) - Brochantite-M - Cu4+2SO4(OH)6 - Y: 92.06 % - d x by: 1. - WL: 1.5406 - Monoclinic -

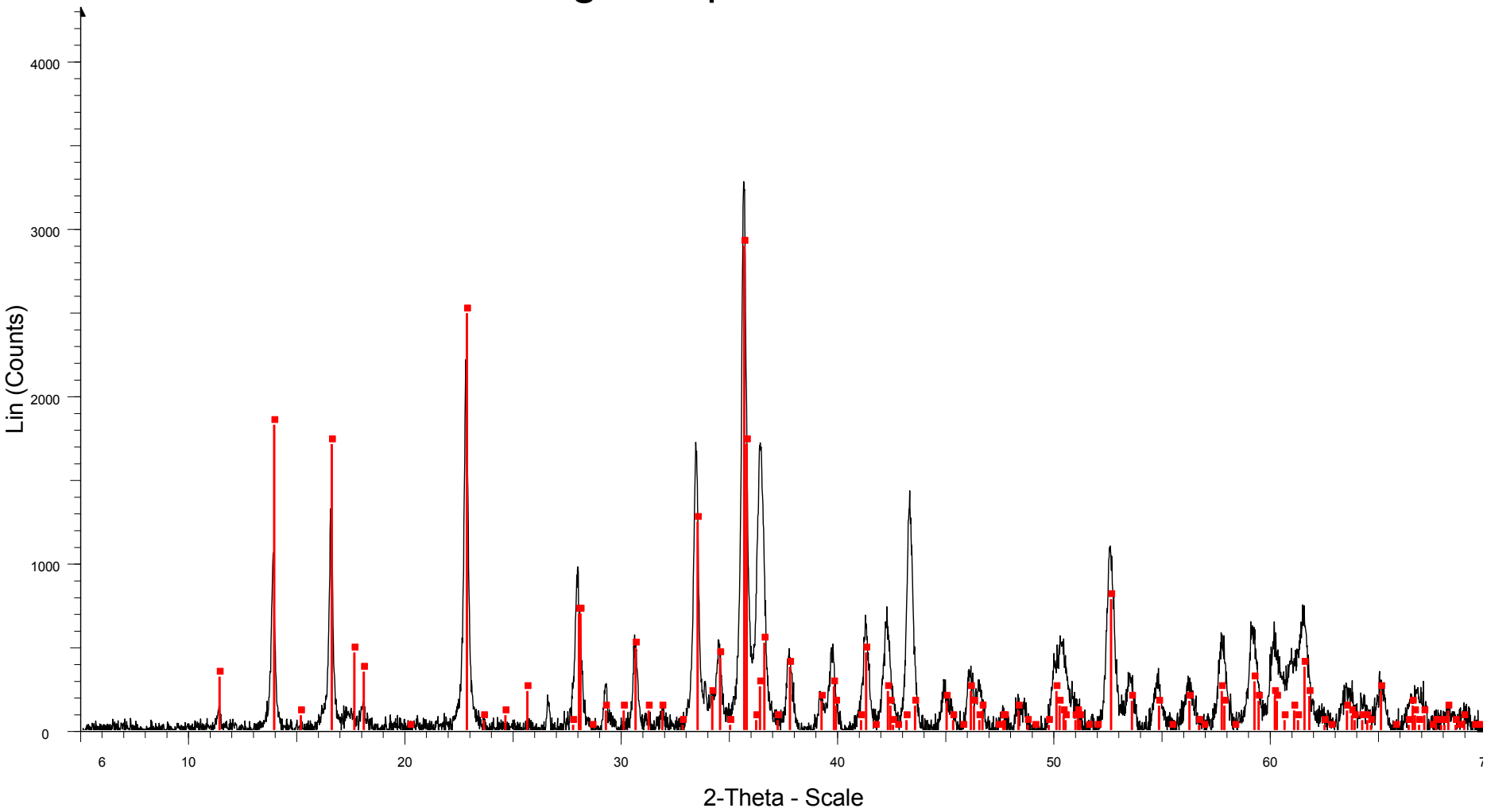
Hofburg Roof Helmet, Vienna



File: Hofburg Roof Helmet_repeat.raw - Type: 2Th/Th locked - Start: 5.009 ° - End: 69.999 ° - Step: 0.017 ° - Step time: 2. s - Temp.: 25 °C (Room) - Time Started: 0 s - 2-Theta: 5.009 ° - Theta: 2.505 ° - Phi: 0.00 ° - A
Operations: Background 1.000,1.000 | Import

01-085-1316 (C) - Brochantite - Cu4(OH)6SO4 - Y: 77.83 % - d x by: 1. - WL: 1.5406 - Monoclinic - I/Ic PDF 1. -

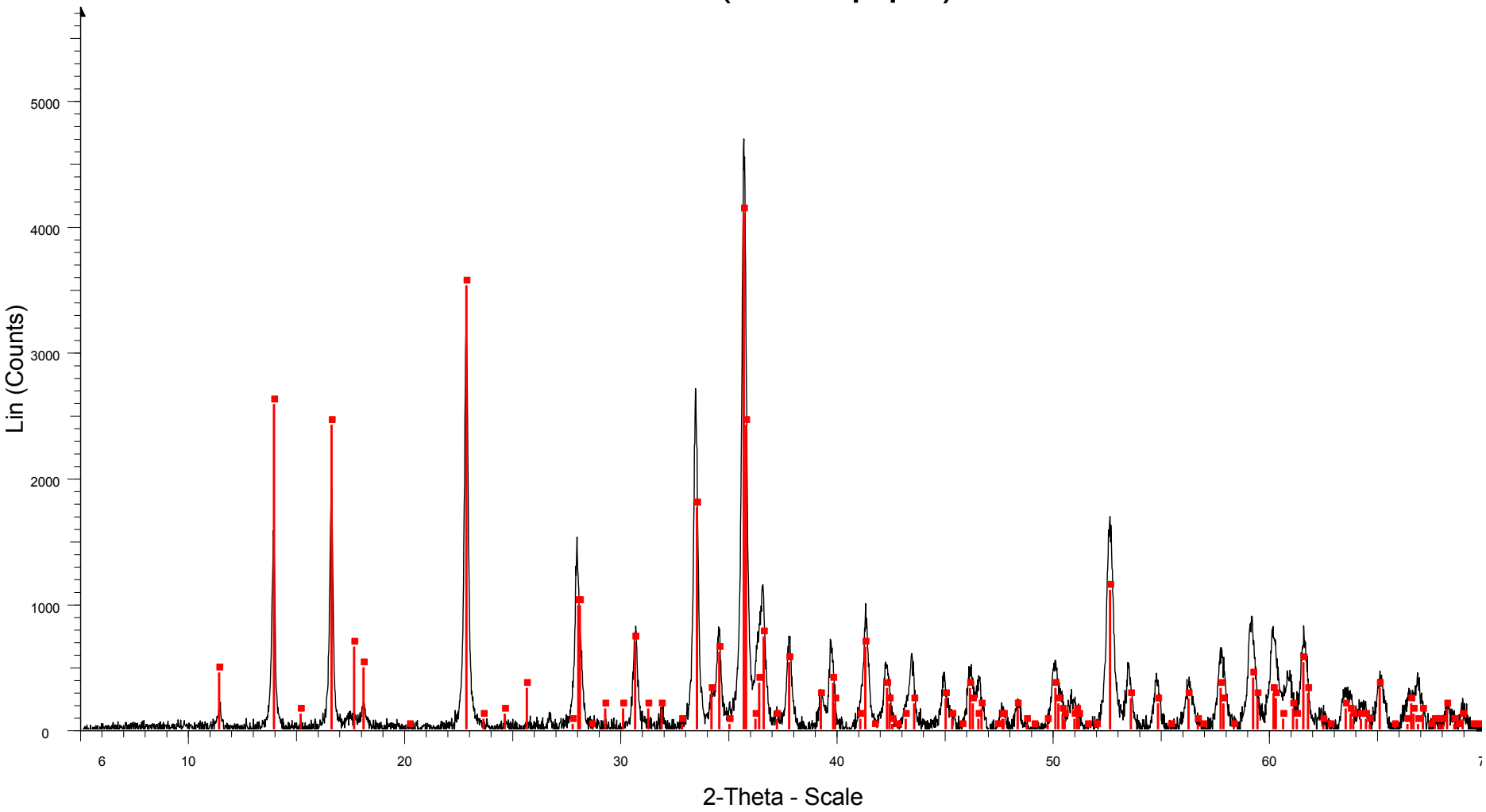
Hofburg Temple Roof, Vienna



File: Hofburg Temple.raw - Type: 2Th/Th locked - Start: 5.009 ° - End: 69.999 ° - Step: 0.017 ° - Step time: 2. s - Temp.: 25 °C (Room) - Time Started: 0 s - 2-Theta: 5.009 ° - Theta: 2.505 ° - Phi: 0.00 ° - Aux1: 0.0 - Au
Operations: Background 1.000,1.000 | Import

01-087-0454 (C) - Brochantite - Cu4(SO4)(OH)6 - Y: 88.36 % - d x by: 1. - WL: 1.5406 - Monoclinic - I/Ic PDF 1.1 -

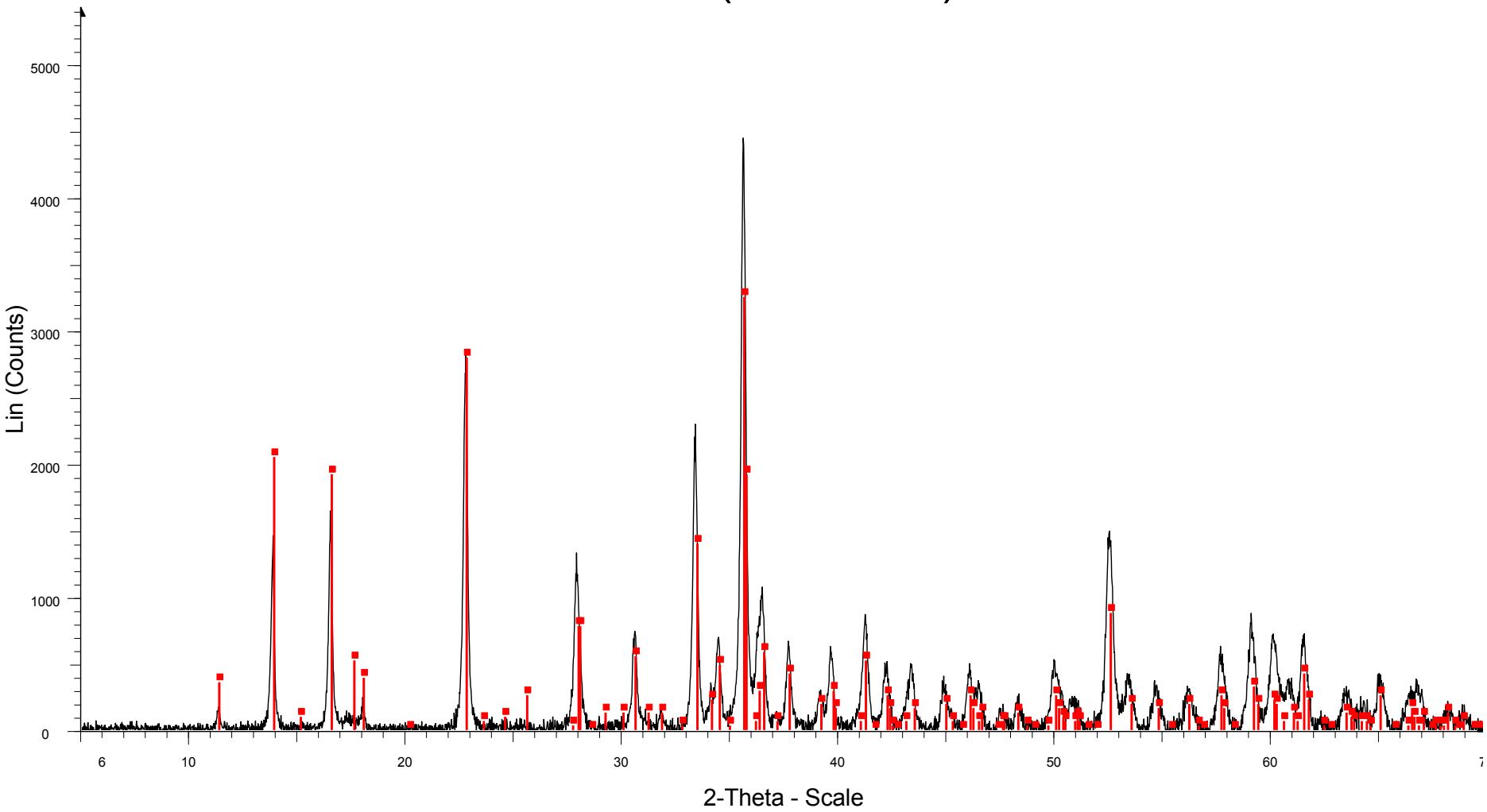
Karlskirche Roof (drain pipe), Vienna



File: Karlskirche Drain Pipe.raw - Type: 2Th/Th locked - Start: 5.009 ° - End: 69.999 ° - Step: 0.017 ° - Step time: 2. s - Temp.: 25 °C (Room) - Time Started: 0 s - 2-Theta: 5.009 ° - Theta: 2.505 ° - Phi: 0.00 ° - Aux1: 0.
Operations: Background 1.000,1.000 | Import

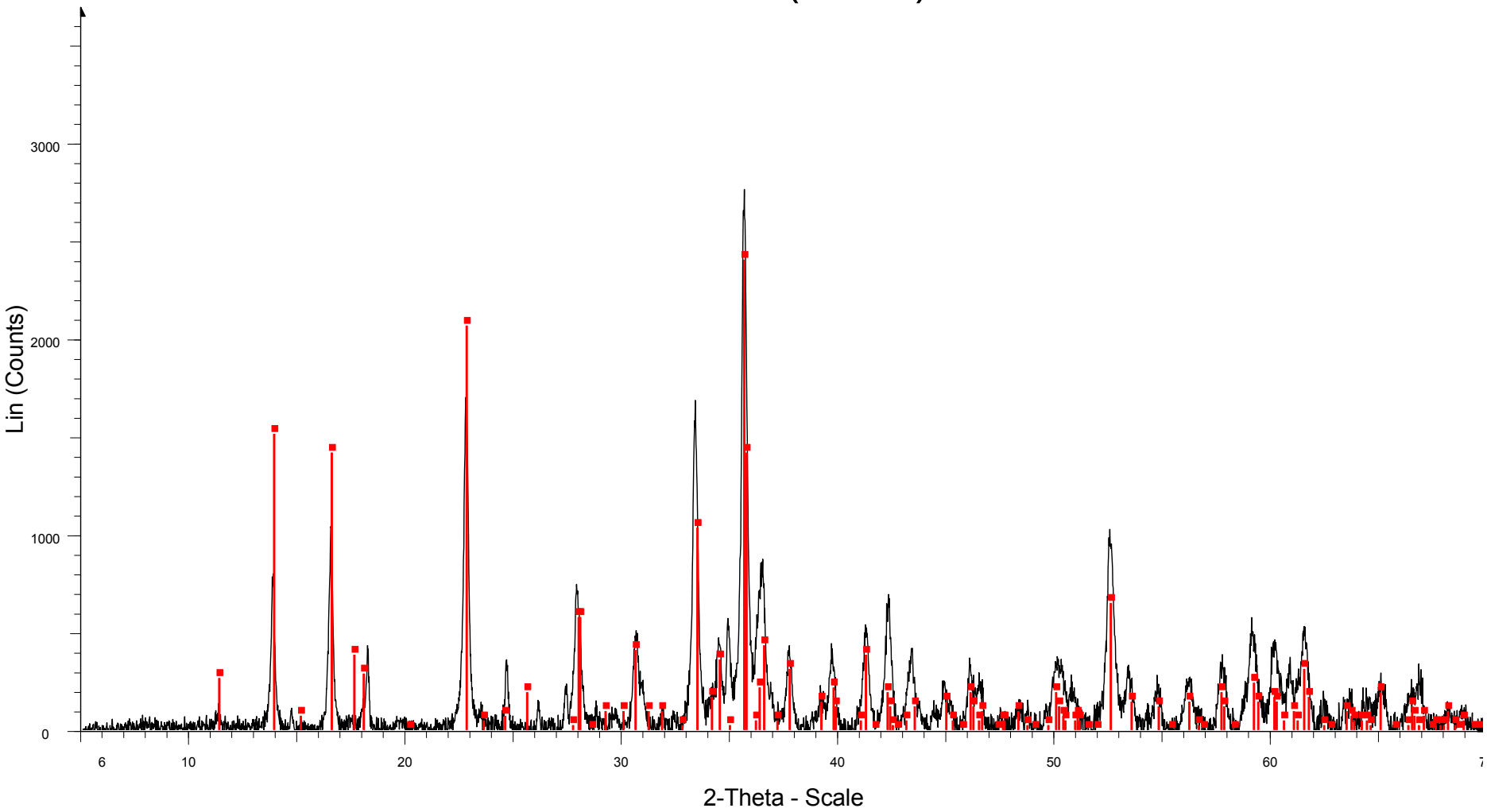
01-087-0454 (C) - Brochantite - Cu4(SO4)(OH)6 - Y: 87.44 % - d x by: 1. - WL: 1.5406 - Monoclinic - I/Ic PDF 1.1 -

Karlskirche Roof (vent hood), Vienna



File: Karlskirche Vent Hood.raw - Type: 2Th/Th locked - Start: 5.009 ° - End: 69.999 ° - Step: 0.017 ° - Step time: 2. s - Temp.: 25 °C (Room) - Time Started: 0 s - 2-Theta: 5.009 ° - Theta: 2.505 ° - Phi: 0.00 ° - Aux1: 0.
Operations: Background 1.000,1.000 | Import
01-087-0454 (C) - Brochantite - Cu4(SO4)(OH)6 - Y: 73.20 % - d x by: 1. - WL: 1.5406 - Monoclinic - I/Ic PDF 1.1 -

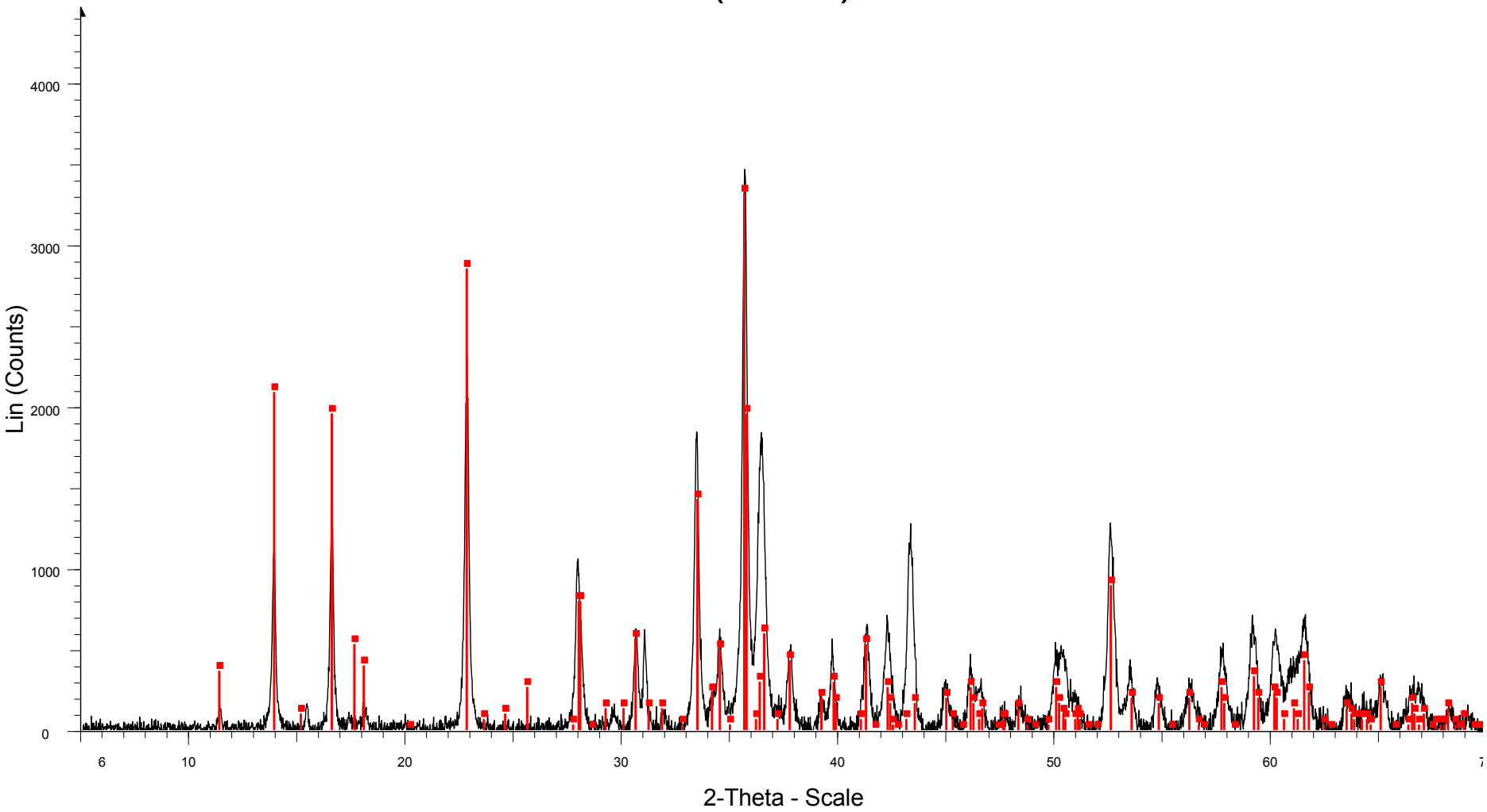
Gilded Roof Sheet (Linke), Vienna



File: Linke Copper Sheet (Guilded).raw - Type: 2Th/Th locked - Start: 5.009 ° - End: 69.999 ° - Step: 0.017 ° - Step time: 2. s - Temp.: 25 °C (Room) - Time Started: 0 s - 2-Theta: 5.009 ° - Theta: 2.505 ° - Phi: 0.00 ° - Operations: Background 1.000,1.000 | Import

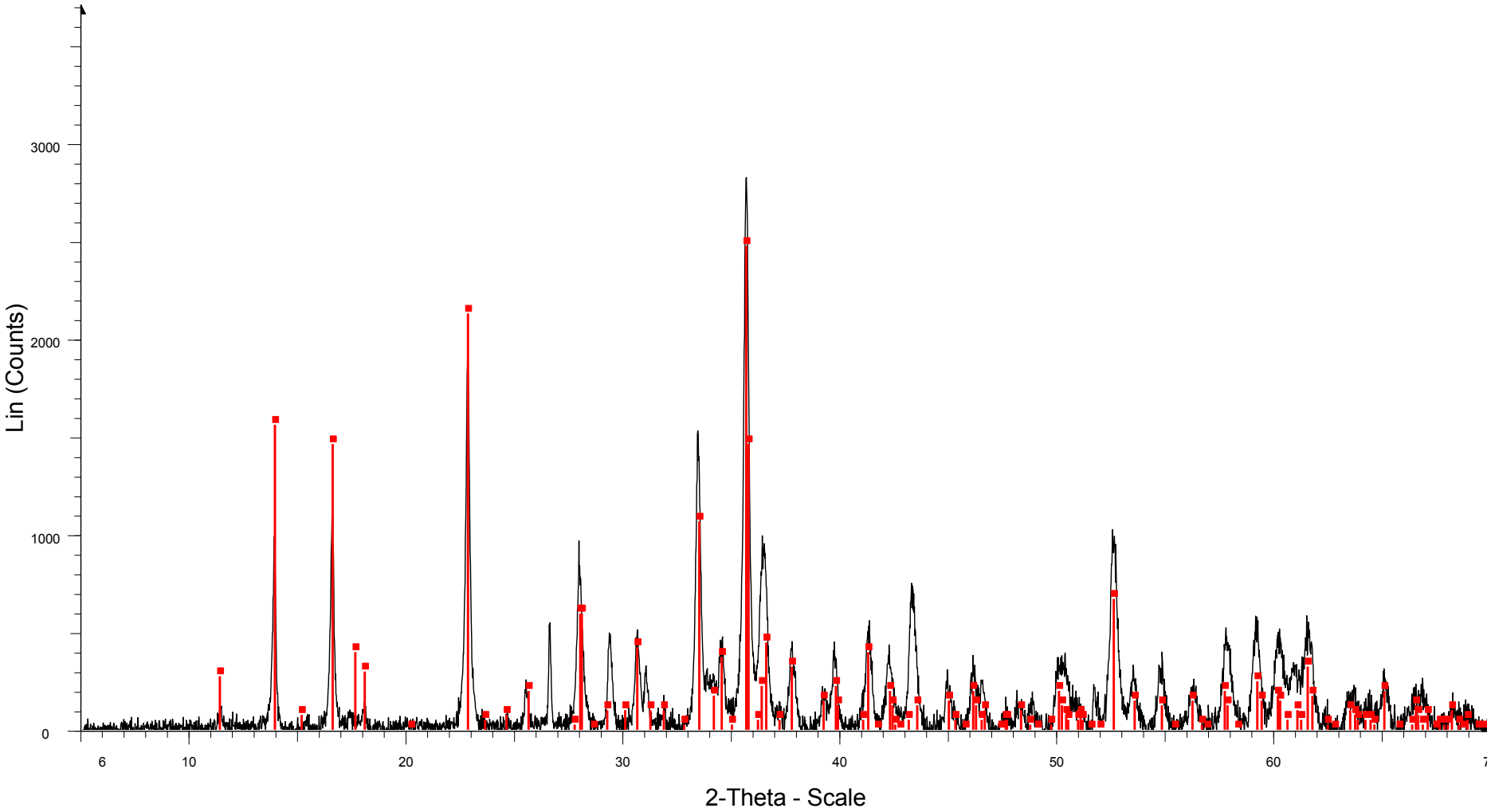
01-087-0454 (C) - Brochantite - Cu4(SO4)(OH)6 - Y: 87.04 % - d x by: 1. - WL: 1.5406 - Monoclinic - I/Ic PDF 1.1 -

Roof Sheet (Linke), Vienna



File: Linke Copper Sheet.raw - Type: 2Th/Th locked - Start: 5.009 ° - End: 69.999 ° - Step: 0.017 ° - Step time: 2. s - Temp.: 25 °C (Room) - Time Started: 0 s - 2-Theta: 5.009 ° - Theta: 2.505 ° - Phi: 0.00 ° - Aux1: 0.0
Operations: Background 1.000,1.000 | Import
01-087-0454 (C) - Brochantite - Cu4(SO4)(OH)6 - Y: 95.74 % - d x by: 1. - WL: 1.5406 - Monoclinic - I/Ic PDF 1.1 -

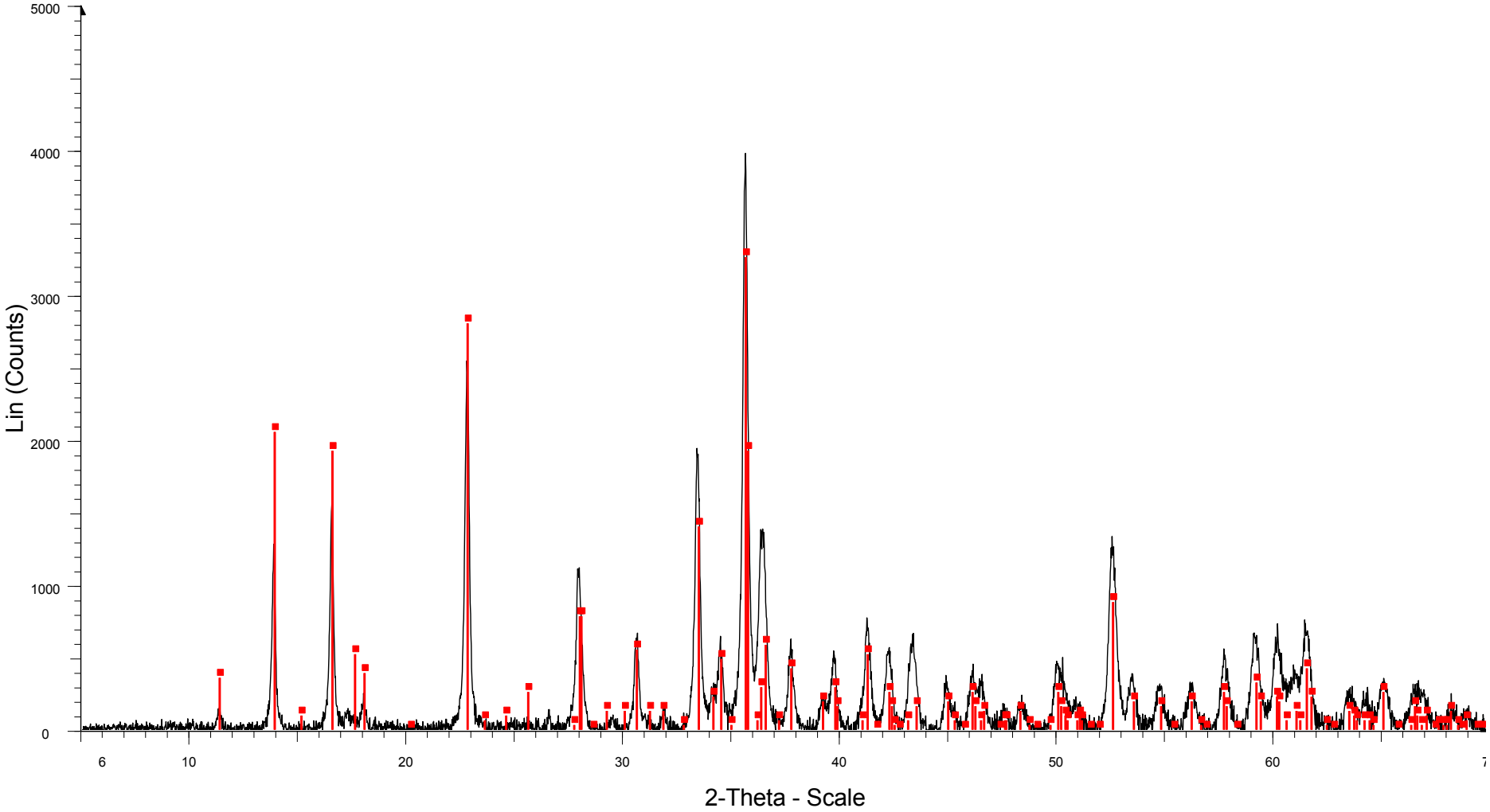
Peterskirche Roof, Vienna



File: Peterskirche (1747).raw - Type: 2Th/Th locked - Start: 5.009 ° - End: 69.999 ° - Step: 0.017 ° - Step time: 2. s - Temp.: 25 °C (Room) - Time Started: 0 s - 2-Theta: 5.009 ° - Theta: 2.505 ° - Phi: 0.00 ° - Aux1: 0.0 - Operations: Background 1.000,1.000 | Import

01-087-0454 (C) - Brochantite - Cu4(SO4)(OH)6 - Y: 87.65 % - d x by: 1. - WL: 1.5406 - Monoclinic - I/Ic PDF 1.1 -

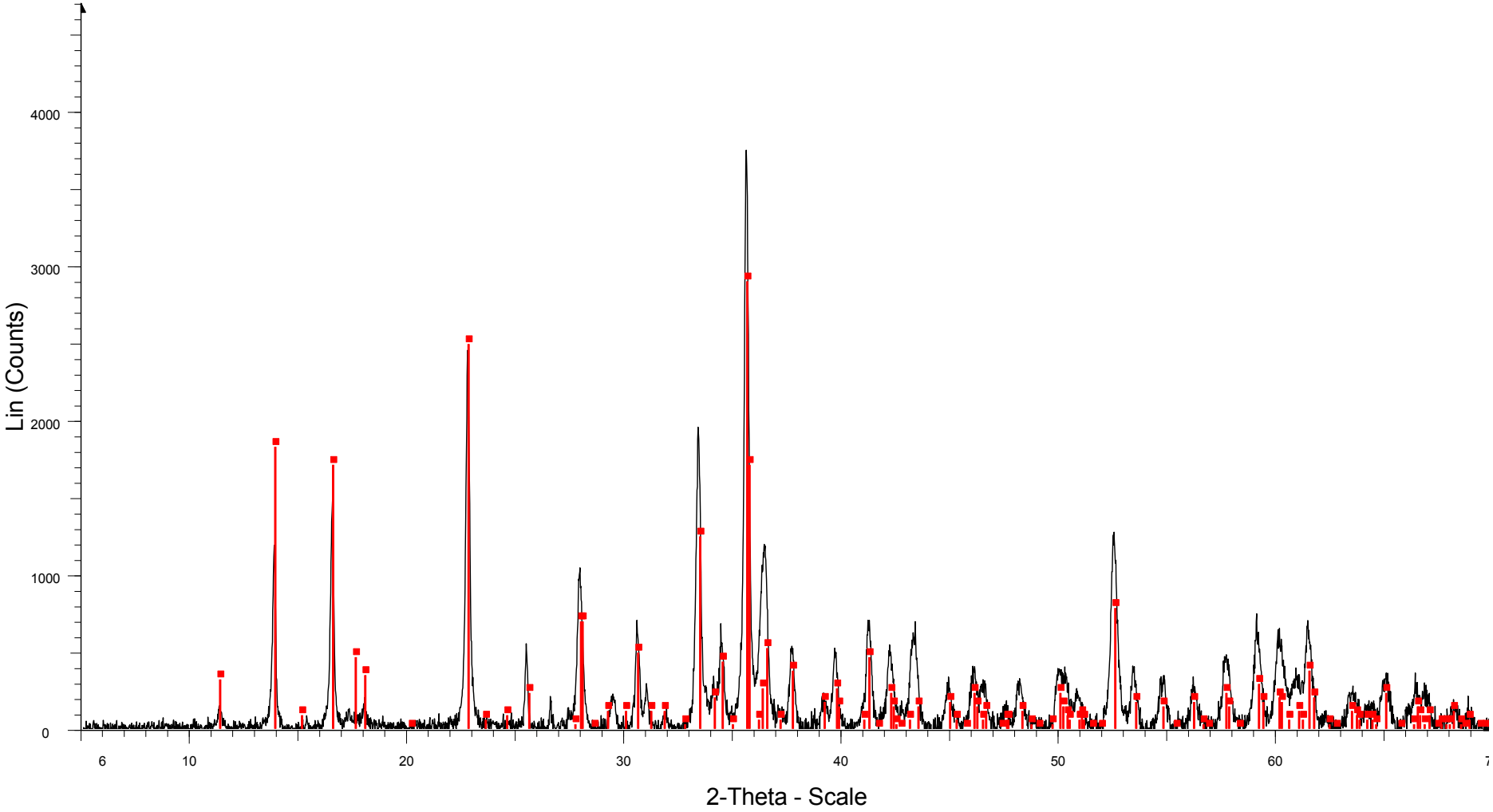
Vienna Tech Uni Roof, Vienna



File: Vienna Tech Uni.raw - Type: 2Th/Th locked - Start: 5.009 ° - End: 69.999 ° - Step: 0.017 ° - Step time: 2. s - Temp.: 25 °C (Room) - Time Started: 0 s - 2-Theta: 5.009 ° - Theta: 2.505 ° - Phi: 0.00 ° - Aux1: 0.0 - A
Operations: Background 1.000,1.000 | Import

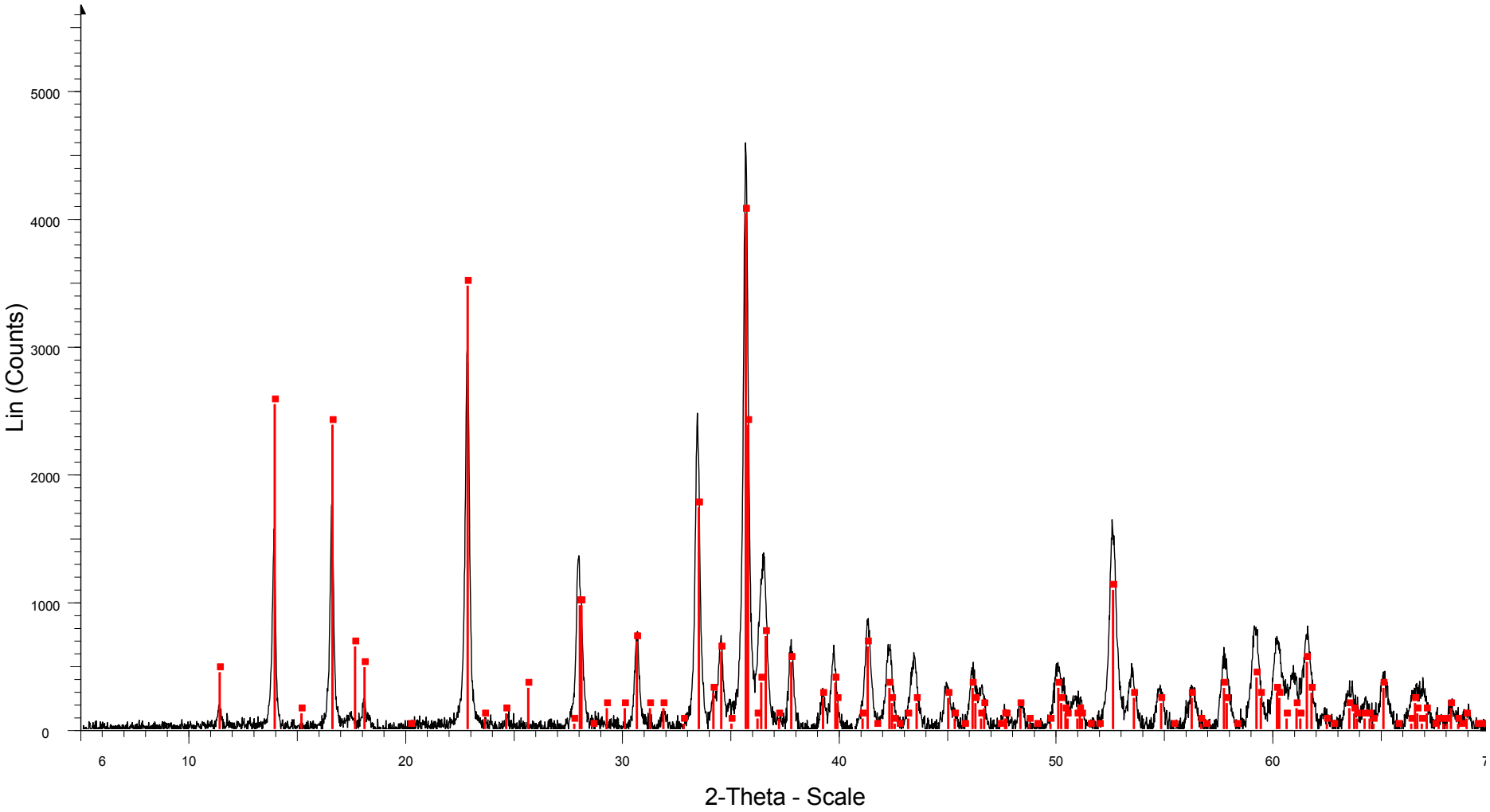
01-087-0454 (C) - Brochantite - Cu4(SO4)(OH)6 - Y: 82.03 % - d x by: 1. - WL: 1.5406 - Monoclinic - I/Ic PDF 1.1 -

Vienna Tech Uni Old Roof (sheet sample), Vienna



File: Vienna Tech Uni-Sheet Sample.raw - Type: 2Th/Th locked - Start: 5.009 ° - End: 69.999 ° - Step: 0.017 ° - Step time: 2. s - Temp.: 25 °C (Room) - Time Started: 0 s - 2-Theta: 5.009 ° - Theta: 2.505 ° - Phi: 0.00 °
Operations: Background 1.000,1.000 | Import
01-087-0454 (C) - Brochantite - Cu4(SO4)(OH)6 - Y: 77.36 % - d x by: 1. - WL: 1.5406 - Monoclinic - I/Ic PDF 1.1 - S-Q 100.0 % -

Votivekirche Roof, Vienna



File: Votivekirche.raw - Type: 2Th/Th locked - Start: 5.009 ° - End: 69.999 ° - Step: 0.017 ° - Step time: 2. s - Temp.: 25 °C (Room) - Time Started: 0 s - 2-Theta: 5.009 ° - Theta: 2.505 ° - Phi: 0.00 ° - Aux1: 0.0 - Aux2:
Operations: Background 1.000,1.000 | Import

01-087-0454 (C) - Brochantite - Cu4(SO4)(OH)6 - Y: 87.99 % - d x by: 1. - WL: 1.5406 - Monoclinic - I/Ic PDF 1.1 -

APPENDIX C:

FTIR Spectra of the Malachite Samples

These results are presented to document additional work that was carried out, but not directly used in this dissertation. These samples were picked under a binocular microscope and analyzed to confirm the presence of malachite. The 'h' in front of each label communicates that the sample was homogenized prior to analysis. Many of these samples did not continue to XRD or MS, usually because they did not contain carbonate or because sulfates were present. Samples containing sulfur were not allowed in the mass spectrometer.

FTIR spectra were characterized by comparing to published FTIR spectra and peak descriptions of malachite and other phases suspected present in the samples. These are as follows:

Chukanov, Nikita V., 2014. *Infrared Spectra of Mineral Species: Extended Library*. Dordrecht, Netherlands: Springer Science + Business Media.

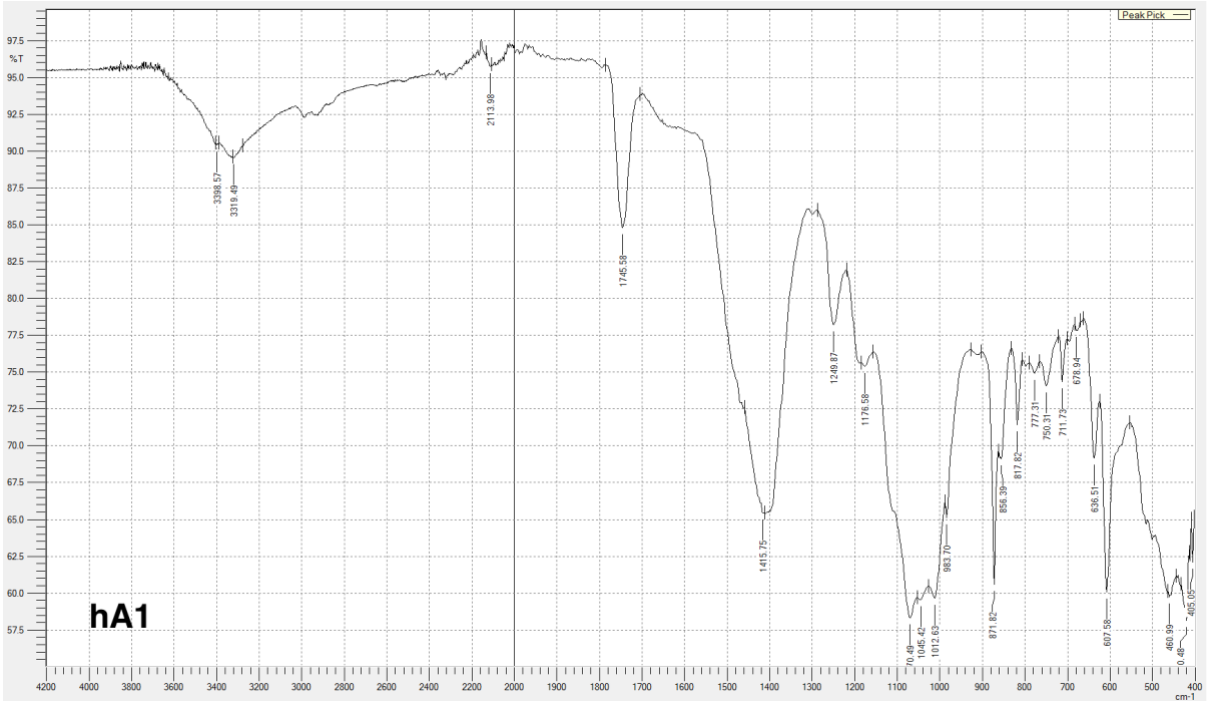
Chukanov, Nikita V.; Chervonnyi, Alexandr D., 2016. *Infrared Spectroscopy of Minerals and Related Compounds.* Cham, Switzerland: Springer International Publishing.

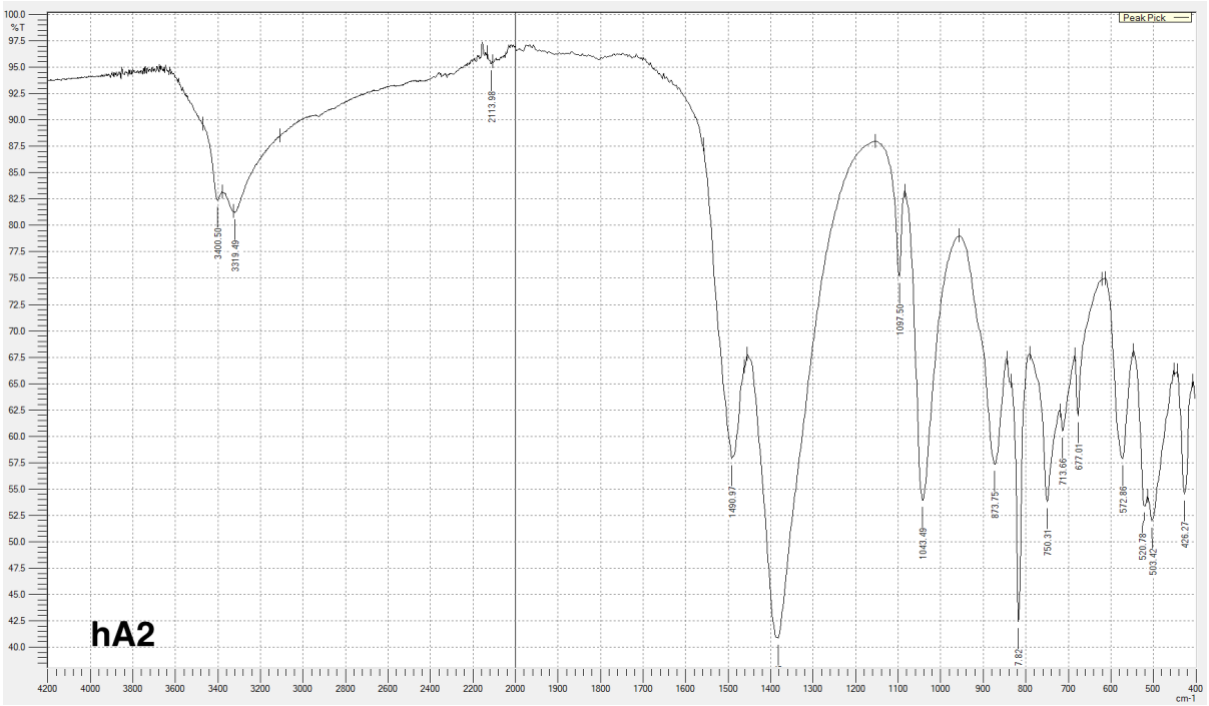
Jones, G.C.; Jackson, B., 1993. *Infrared Transmission Spectra of Carbonate Minerals.* London: Chapman and Hall.

Malachite + Linseed Oil, 2016. Database of ATR-FT-IR spectra of various materials. Institute of Chemistry University of Tartu, Estonia. Available from: http://lisa.chem.ut.ee/IR_spectra/oil_color/malachite-linseed-oil/. Accessed on 08 November, 2016.

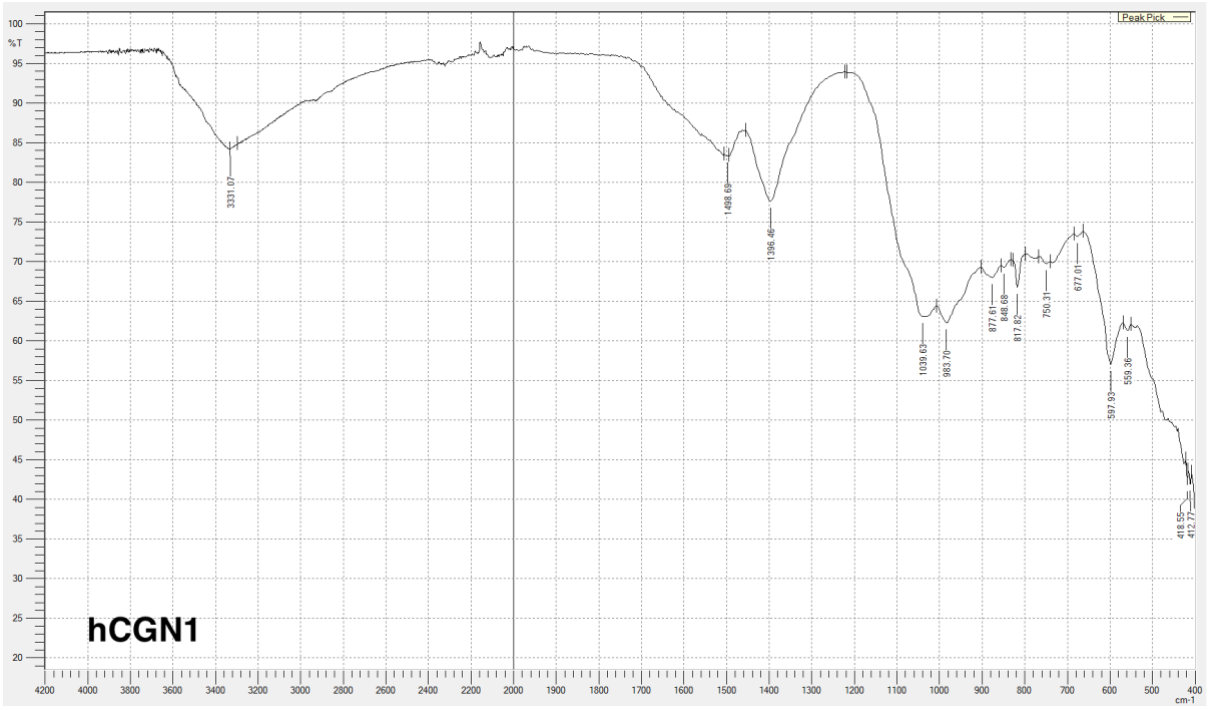
Schuiskii, A. V.; Zorina, M. L., 2013. Infrared Spectra of Natural and Synthetic Malachites. In: *Journal of Applied Spectroscopy*. Vol. 80 (4): 576-580.

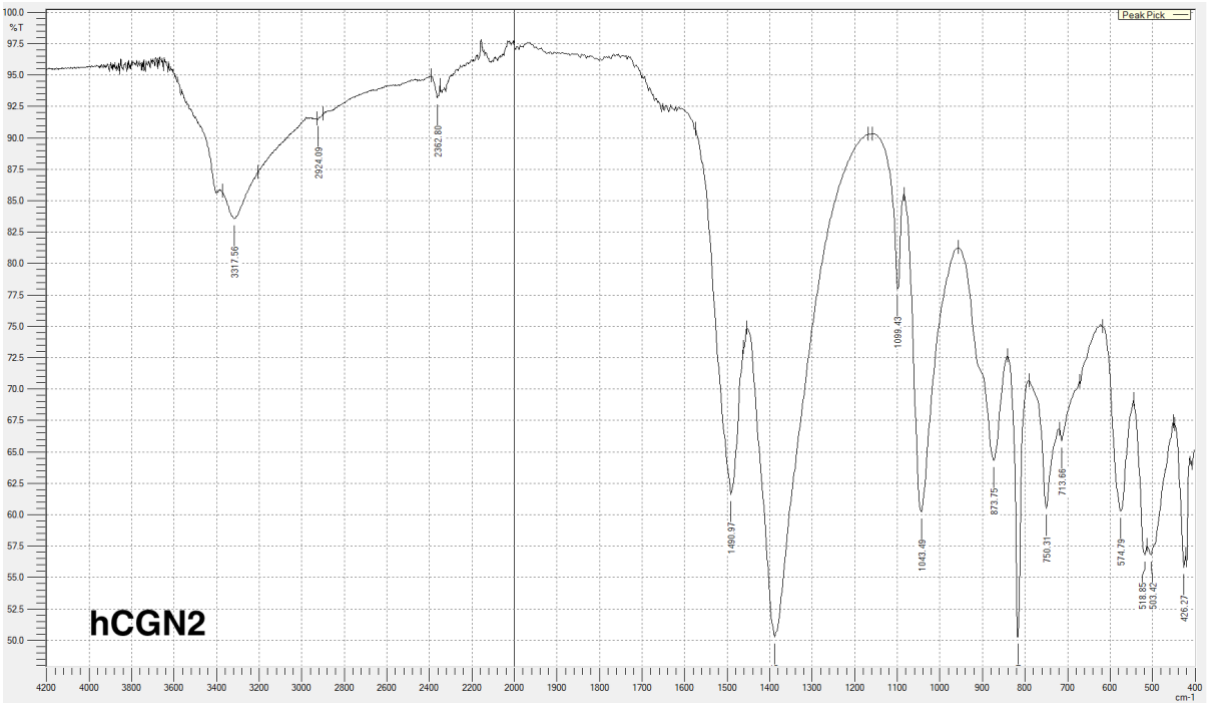
Asia

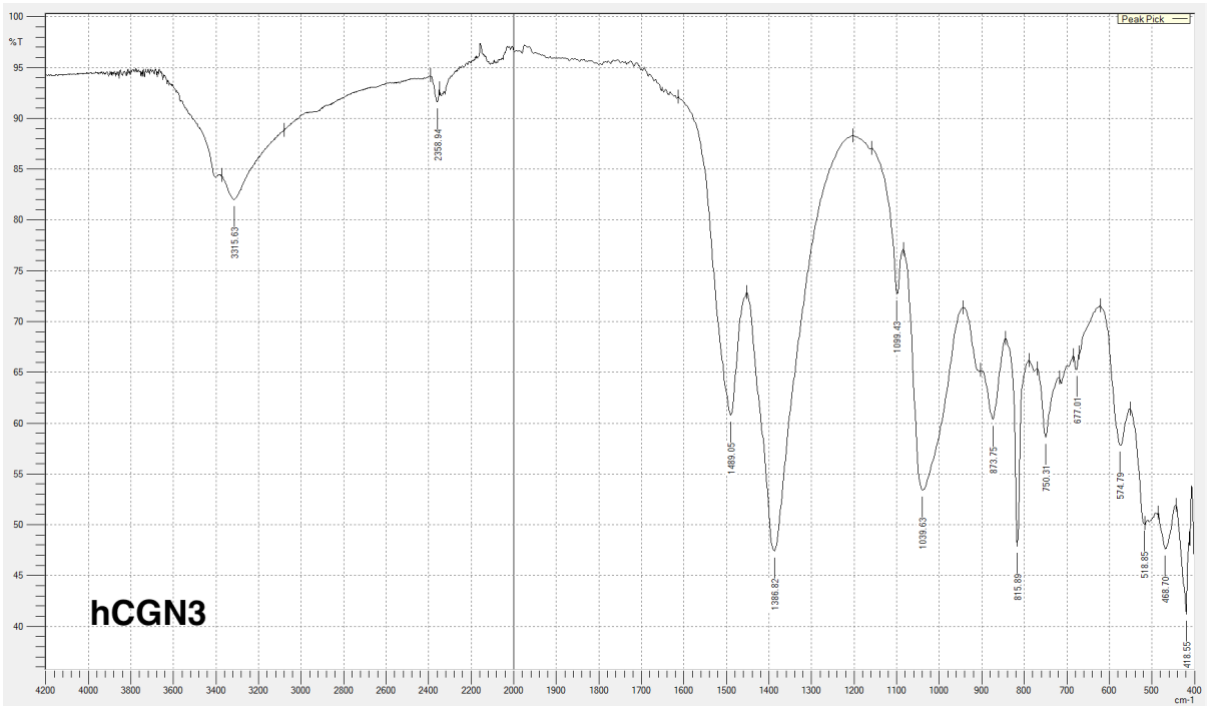

Peak Pick
%T
hA1
3398.57
3319.49
2113.98
1745.58
1415.75
1240.87
1176.58
1045.42
1012.63
983.70
871.82
856.39
817.82
777.31
750.31
711.73
678.94
636.51
607.58
460.99
405.05
cm-1

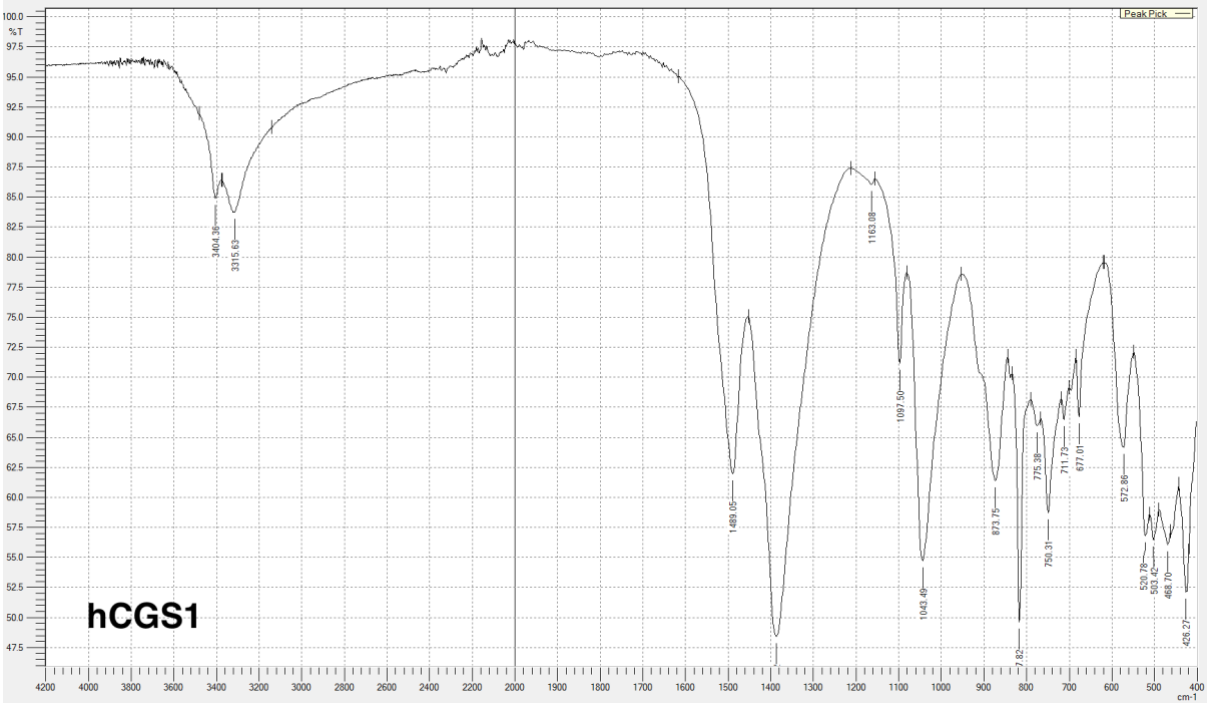

Peak Pick
%T
hA2
3400.50
3319.49
2113.98
1400.97
1097.50
1043.49
873.75
750.31
713.66
677.01
572.86
520.78
503.42
426.27
cm-1

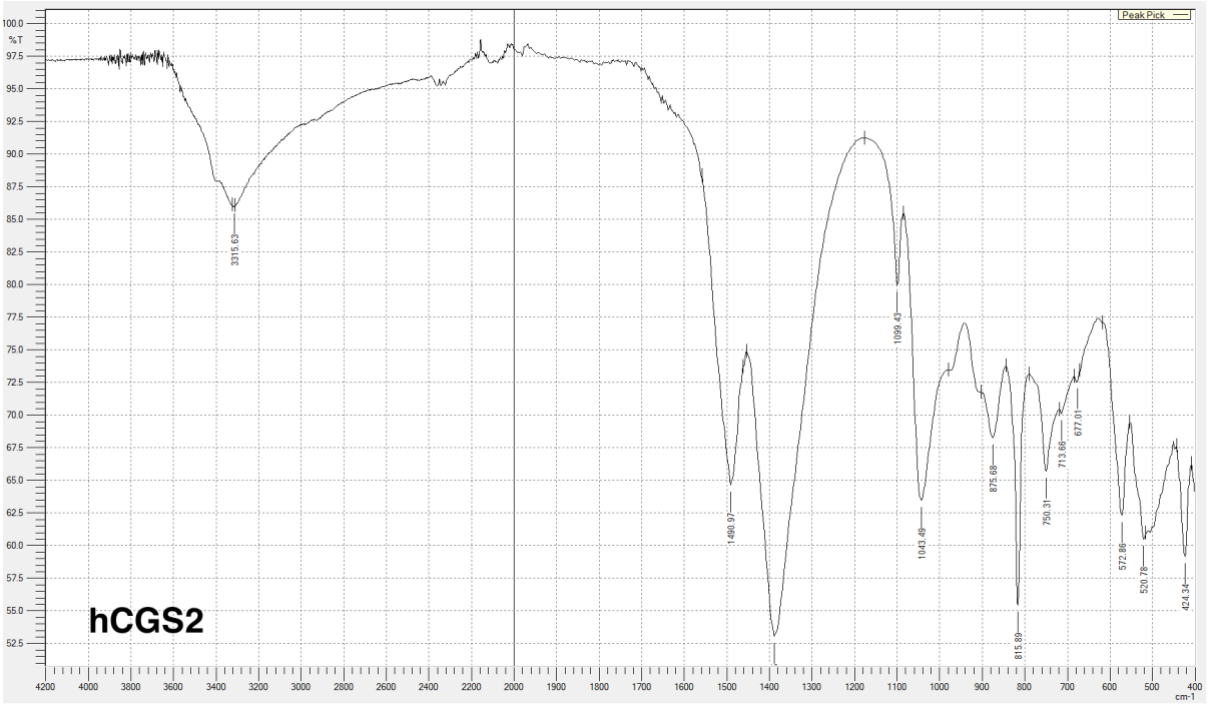
China

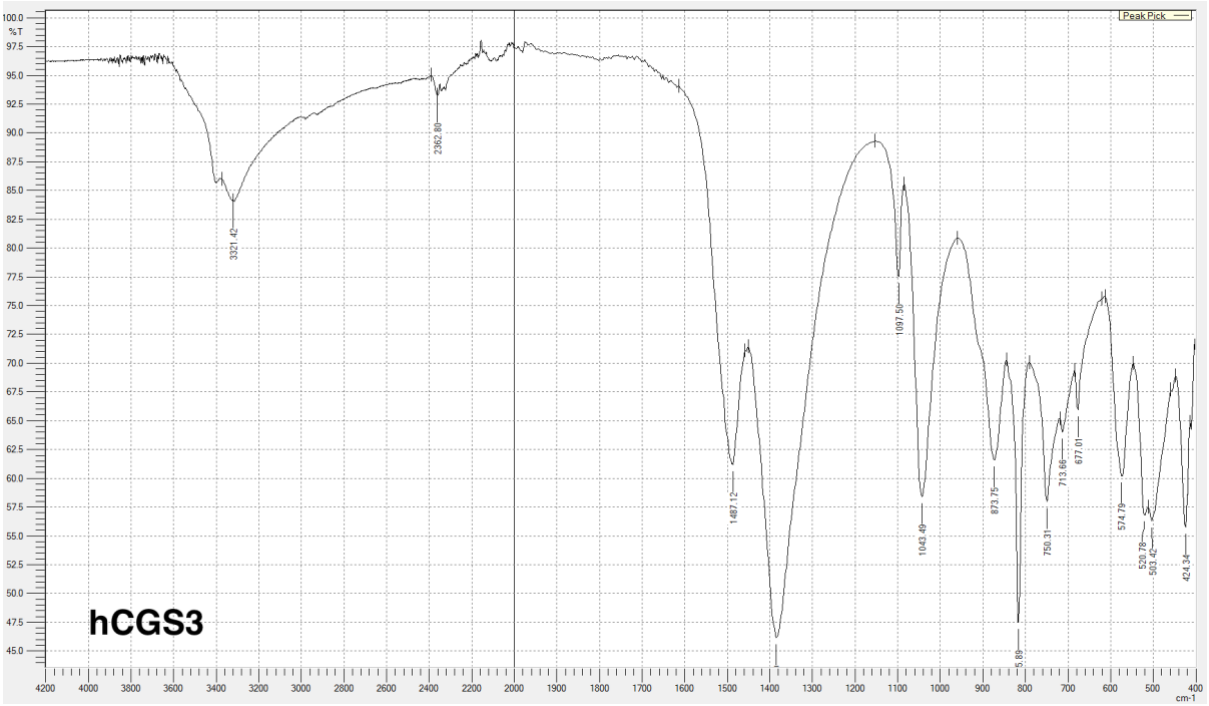

Peak Pick
%T
3331.07
1498.69
1396.46
1039.63
983.70
877.61
848.68
817.82
750.31
677.01
597.93
559.36
418.55
412.77
hCGN1
cm-1

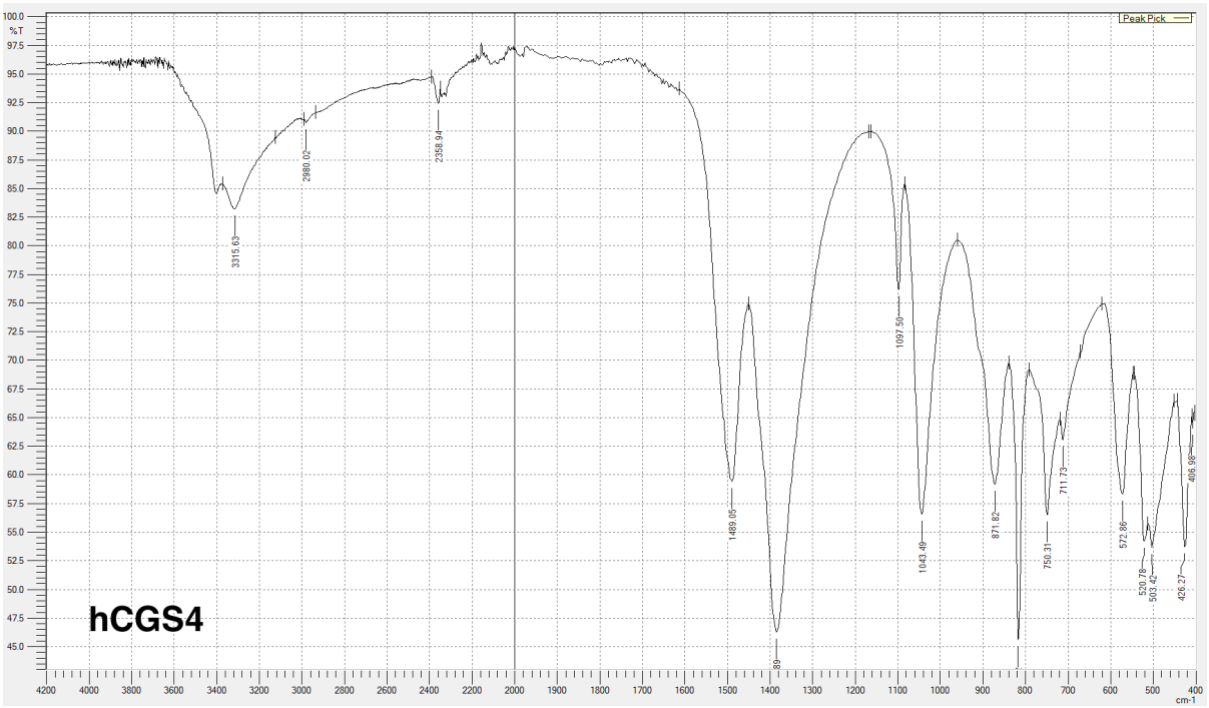

Peak Pick
%T
3317.56
2924.09
2362.80
1460.97
1099.43
1043.49
873.75
750.31
713.66
574.79
518.85
503.42
426.27
hCGN2
cm-1

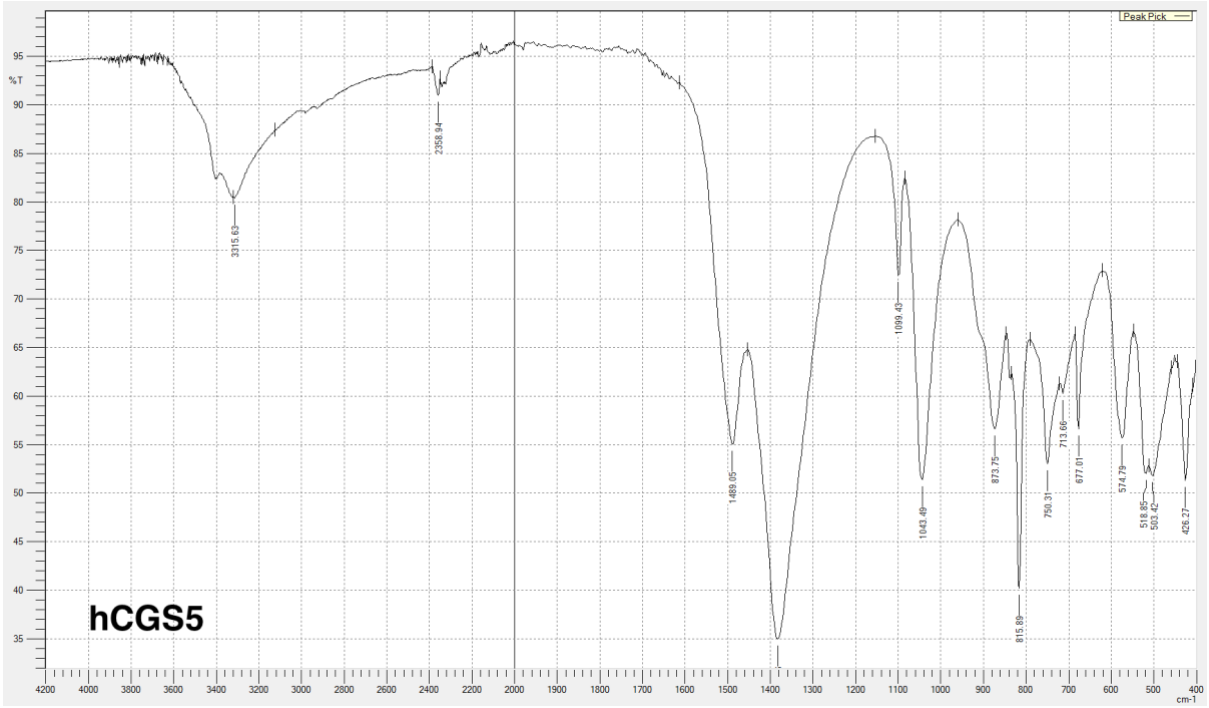

Peak Pick
%T
3315.63
2358.94
1489.05
1386.82
1099.43
1039.63
873.75
815.89
750.31
677.01
574.79
518.85
468.70
418.55
hCGN3
cm-1

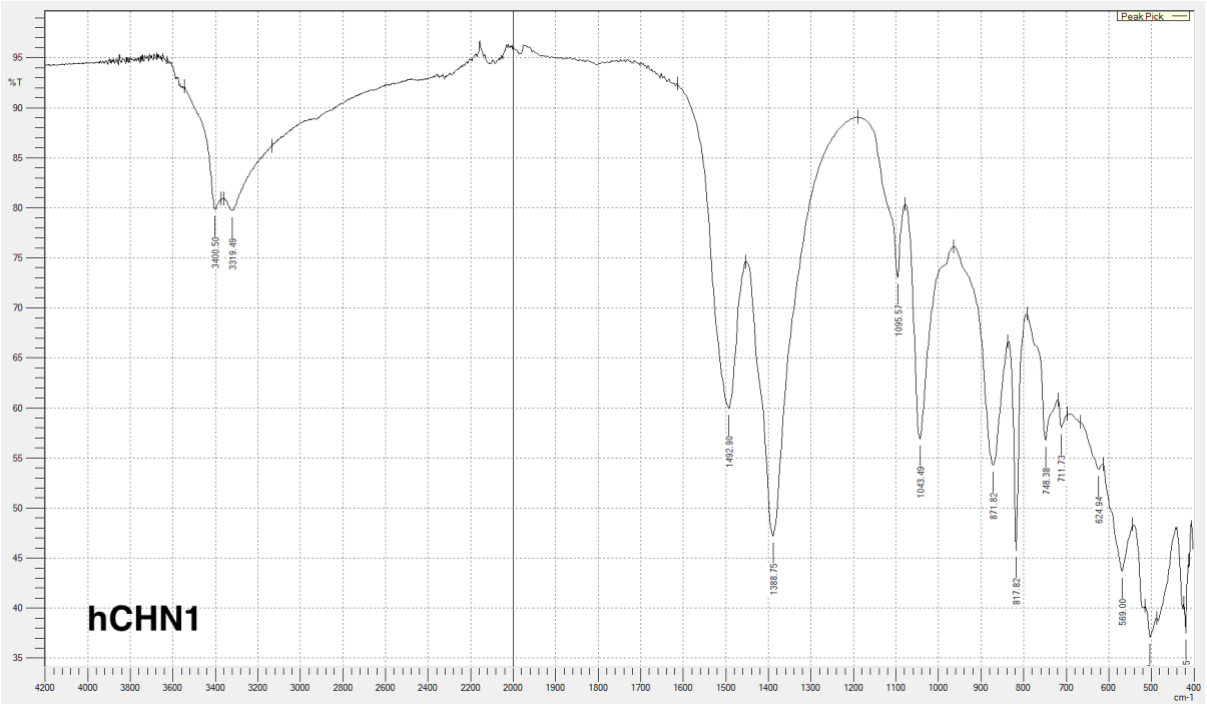

Peak Pick
%T
3404.36
3315.63
1163.08
1097.50
1043.40
1489.05
873.75
782
775.38
750.31
711.73
677.01
572.86
520.78
503.42
468.70
426.27
hCGS1
cm-1

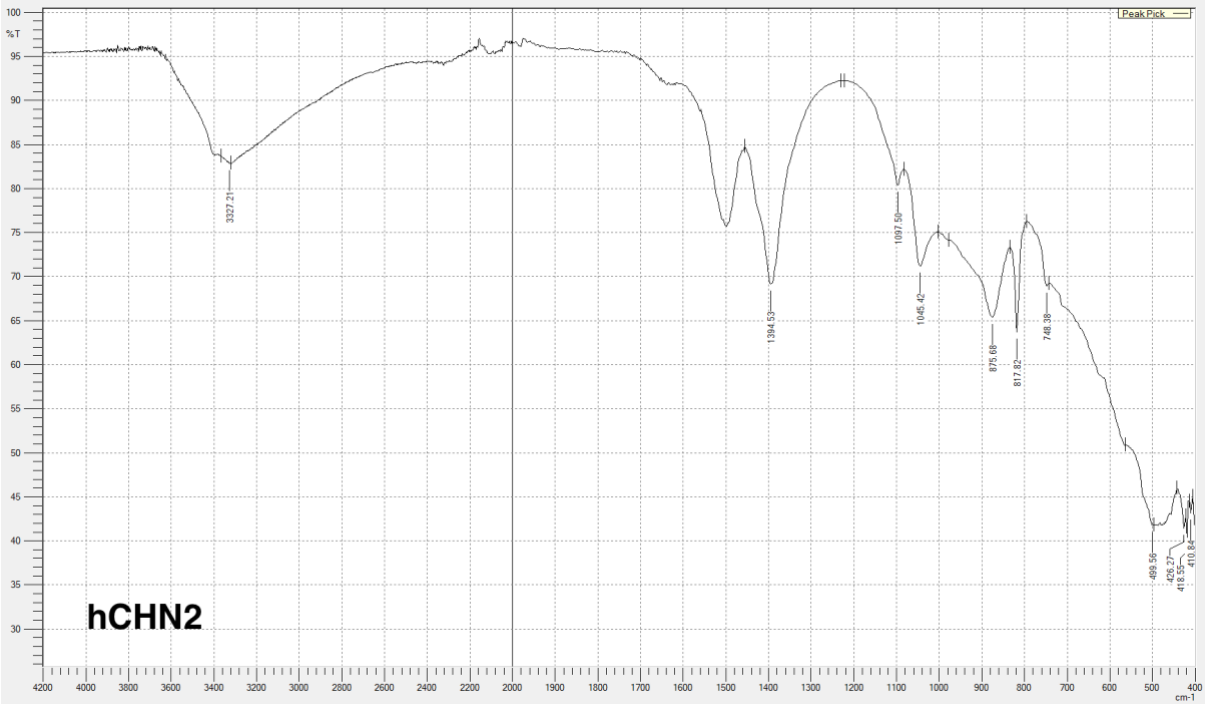

Peak Pick
%T
3315.63
1490.97
1099.43
1043.49
875.68
815.89
750.31
713.66
677.01
572.86
520.78
424.34
hCGS2
cm-1

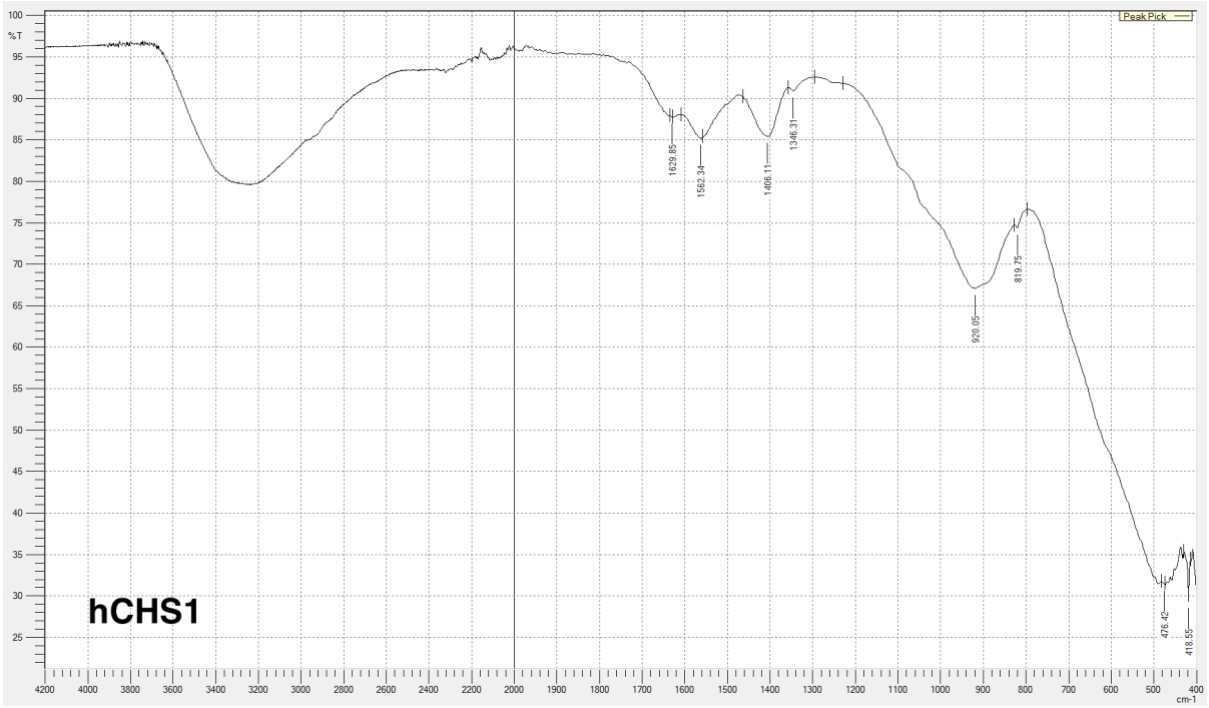

Peak Pick
%T
3321.42
2362.80
1487.12
1097.50
1043.49
873.75
815.89
750.31
713.66
677.01
574.79
520.78
503.42
424.34
hCGS3
cm-1

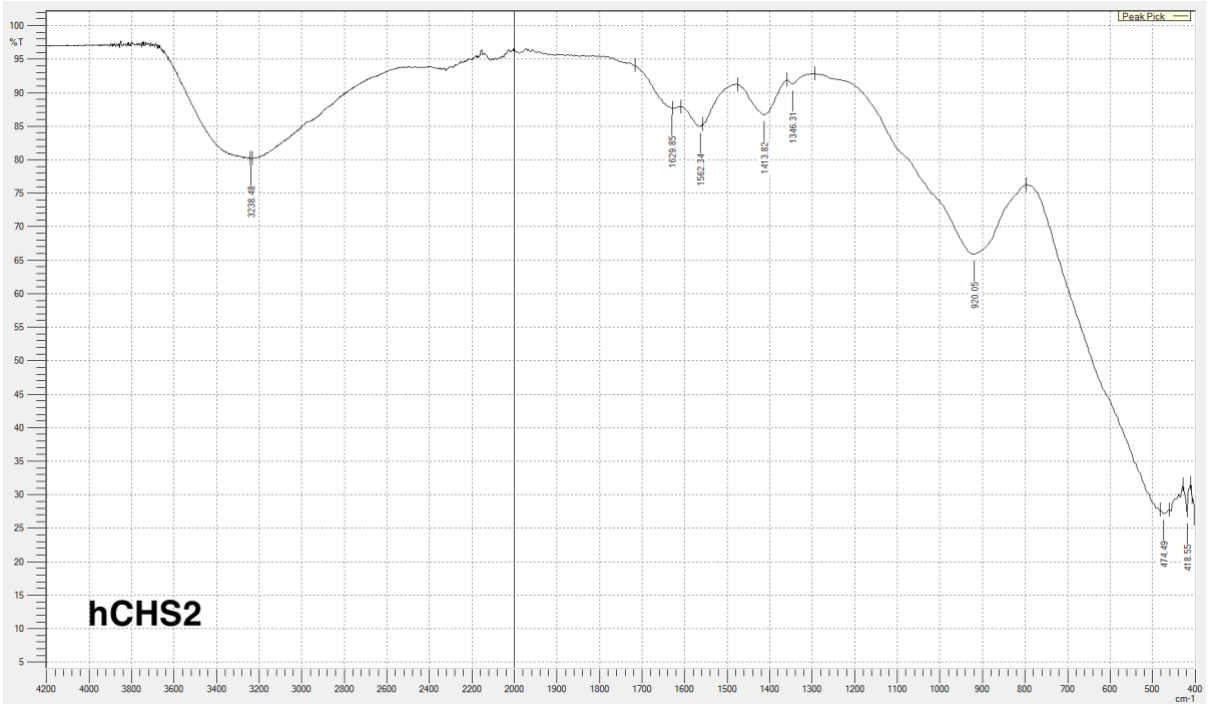

Peak Pick
%T
3315.63
2980.02
2358.94
1489.05
1097.50
1043.49
871.82
750.31
711.73
572.86
520.78
503.42
426.27
406.98
hCGS4
cm-1

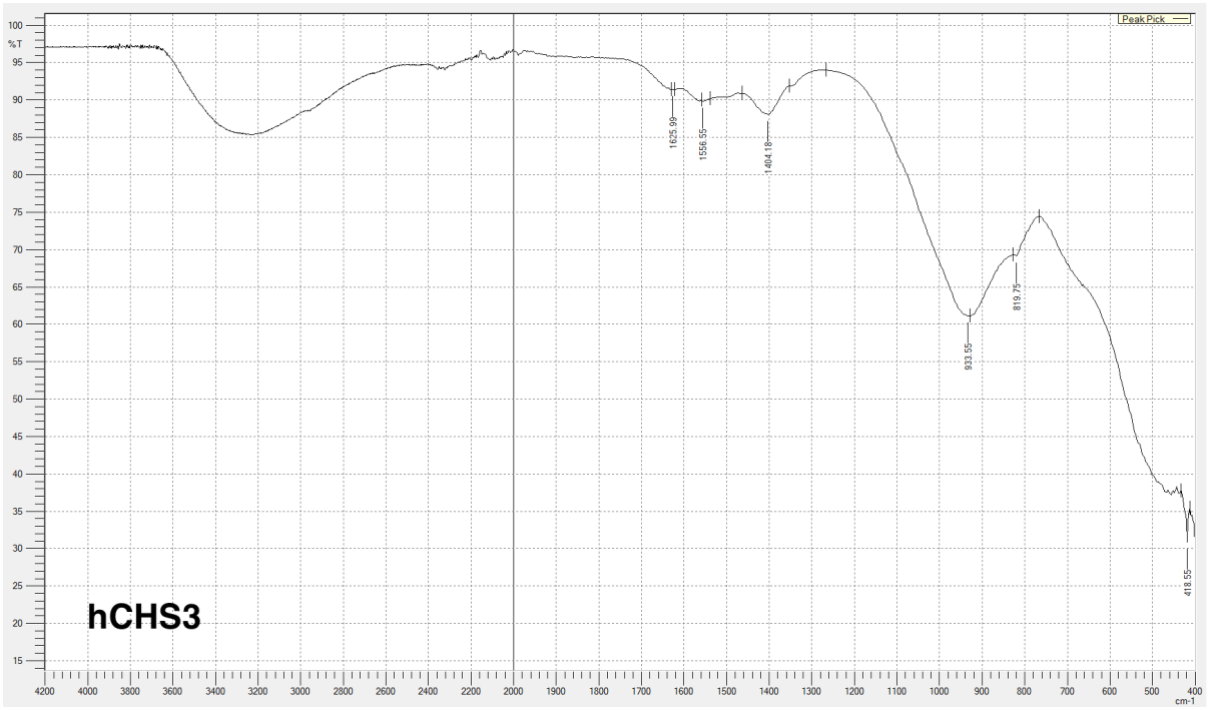

Peak Pick
%T
3315.63
2358.94
1489.05
1099.43
1043.49
873.75
815.89
750.31
713.66
677.01
574.79
518.85
503.42
426.27
hCGS5
cm-1

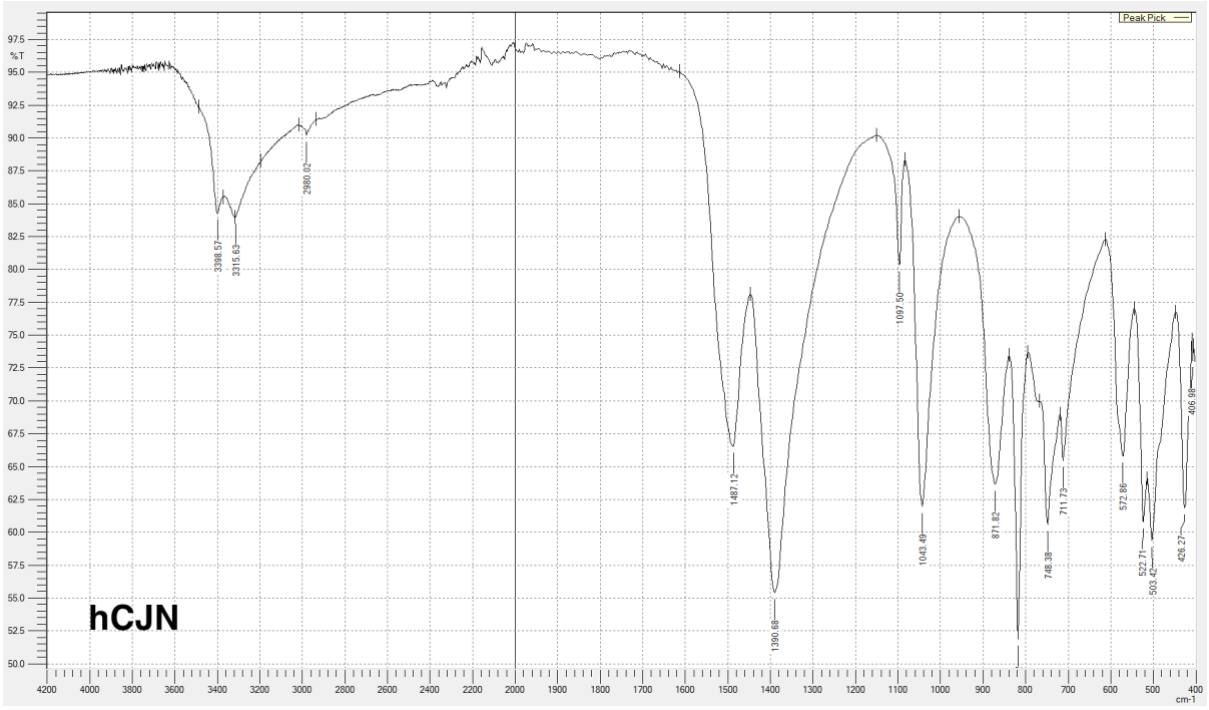

Peak Pick
%T
3400.50
3319.49
1492.96
1388.75
1095.57
1043.49
871.82
817.82
748.38
711.73
624.94
569.00
cm-1
hCHN1

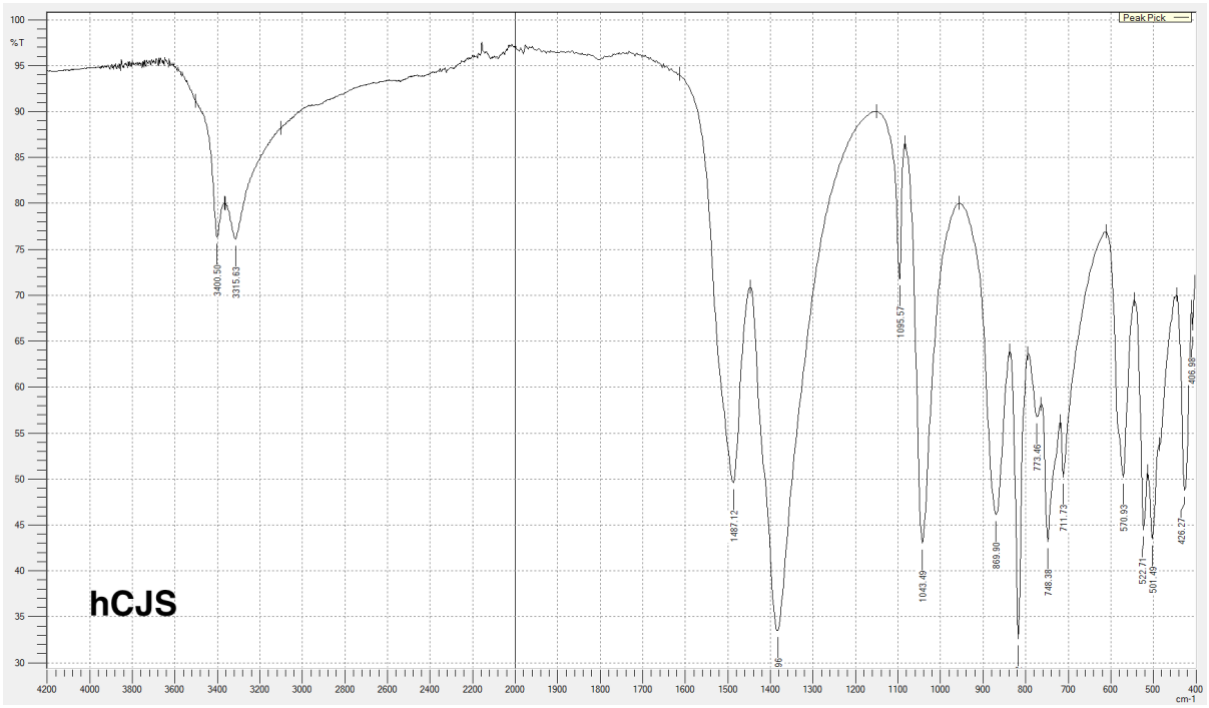

Peak Pick
%T
3327.21
1394.53
1097.58
1046.42
875.68
817.82
748.38
499.56
426.27
418.55
cm-1
hCHN2

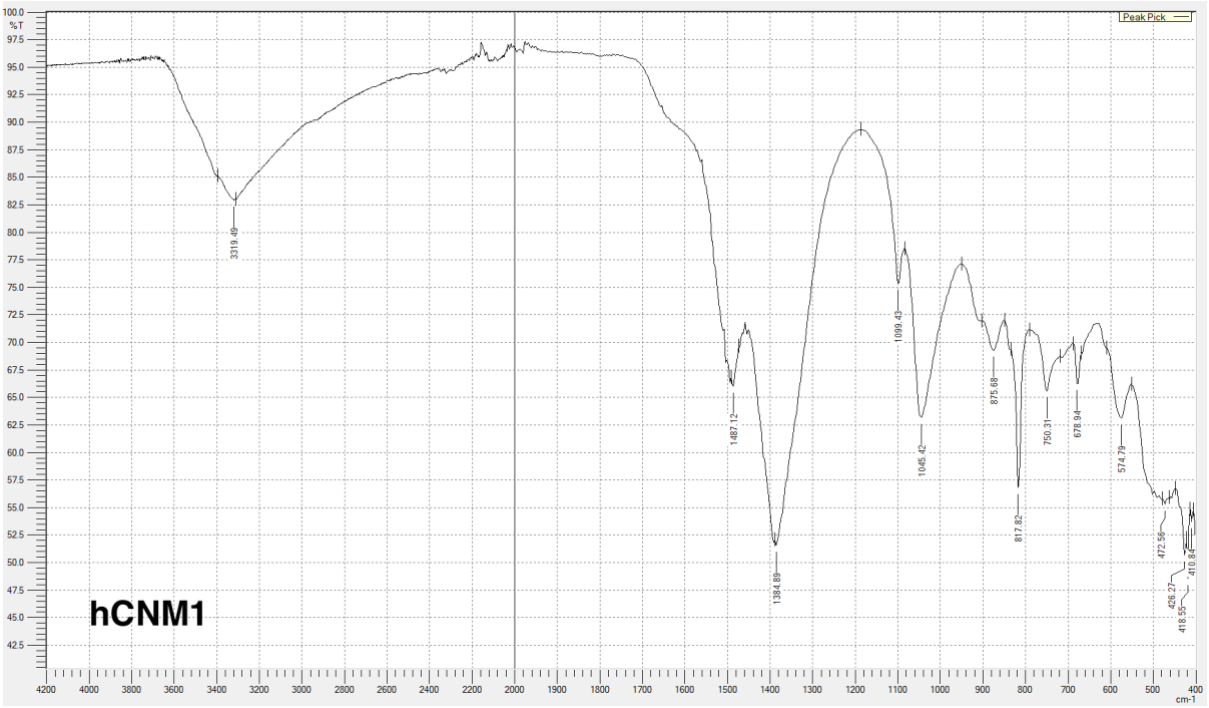

Peak Pick
%T
1629.85
1562.34
1406.11
1346.31
920.05
819.75
476.42
418.55
hCHS1
cm-1

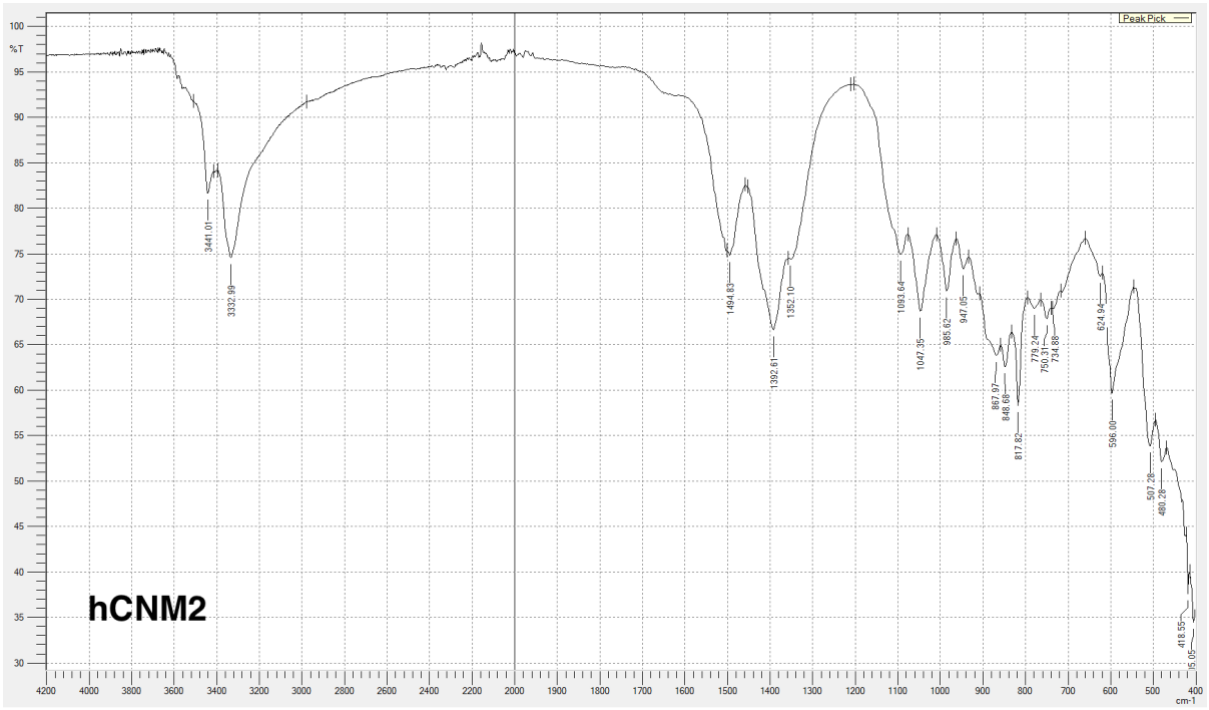

Peak Pick
%T
3238.49
1629.85
1562.34
1413.82
1346.31
920.05
474.49
418.55
hCHS2
cm-1

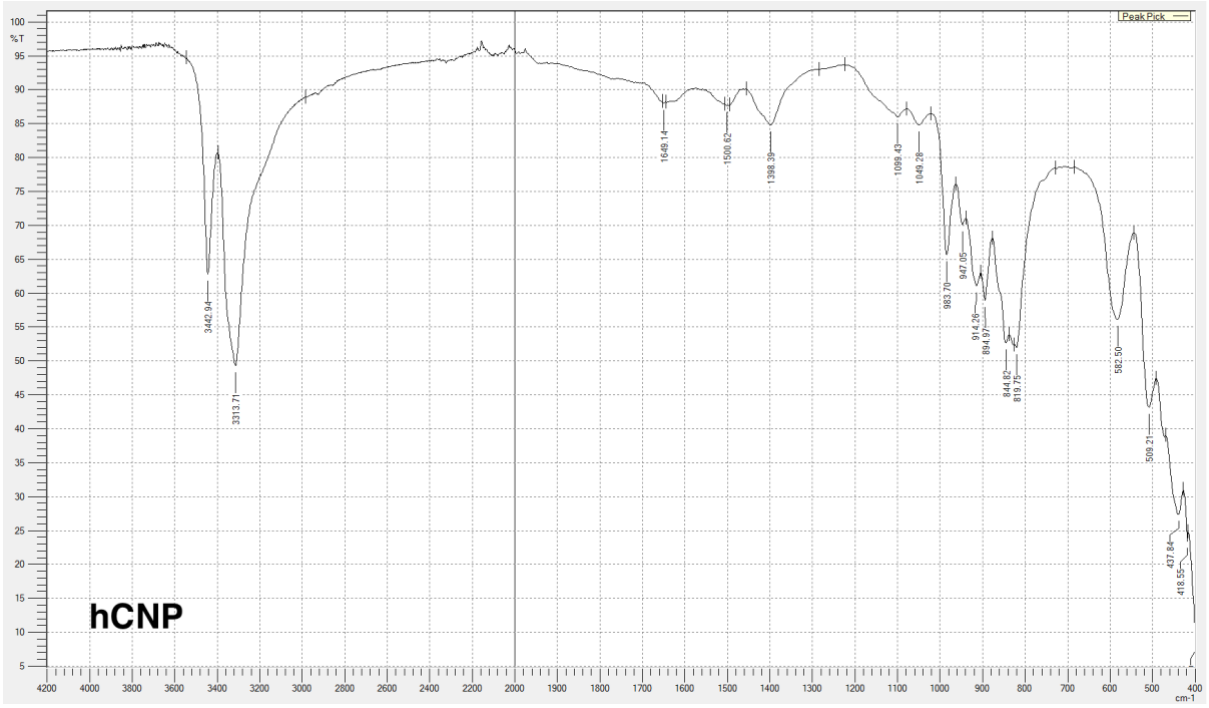

Peak Pick
%T
1625.99
1556.55
1404.18
933.55
819.75
418.55
hCHS3
cm-1

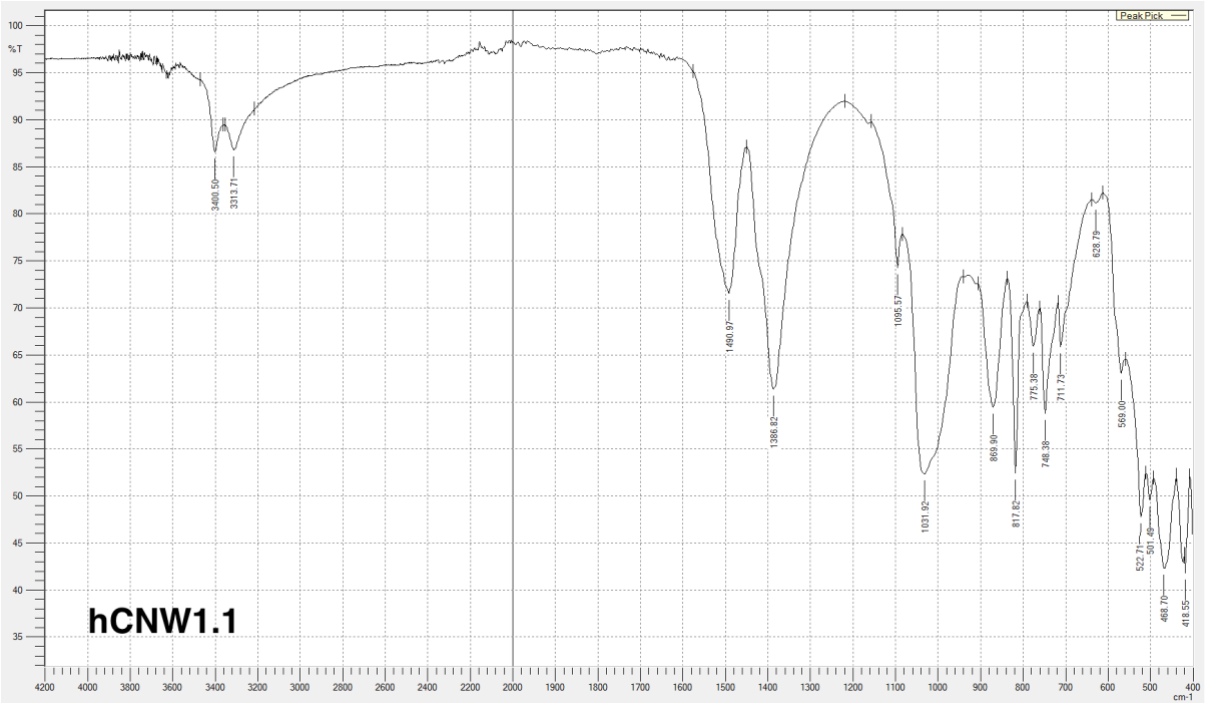

Peak Pick
%T
3398.57
3315.63
2980.02
1487.12
1390.68
1097.50
1043.40
871.82
748.38
711.73
572.86
522.71
503.42
456.27
406.89
hCJN
cm-1

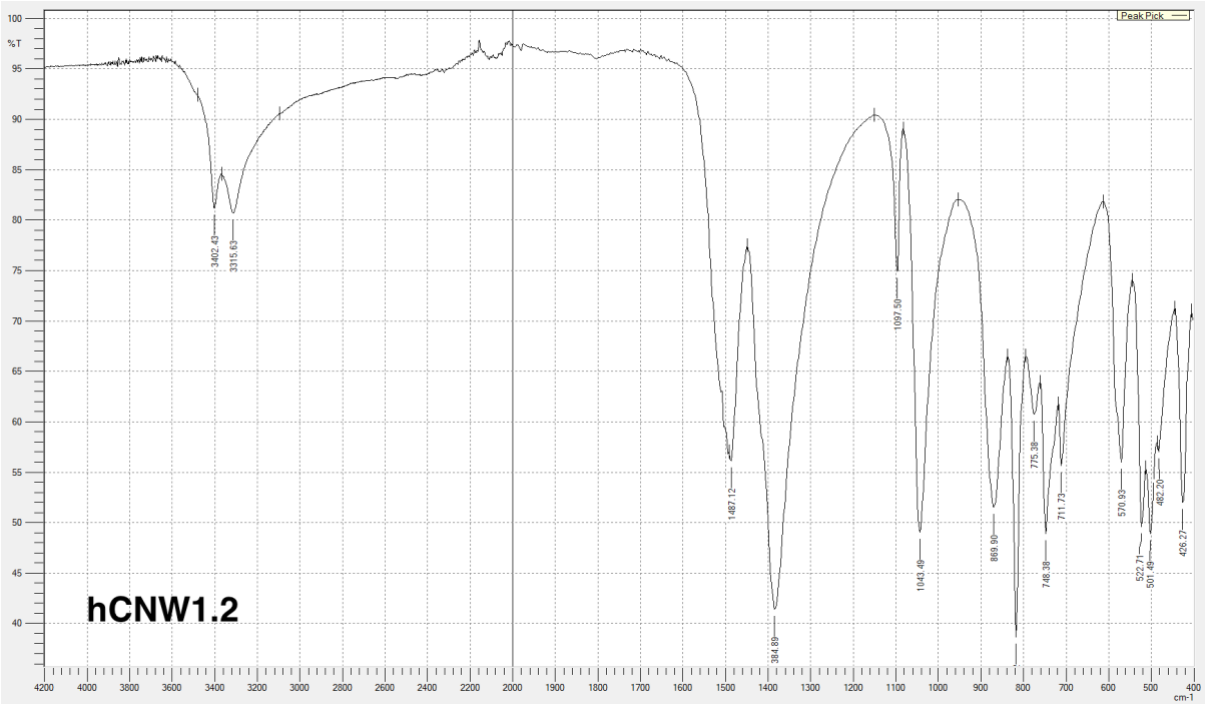

Peak Pick
%T
3400.50
3315.63
1487.12
1095.57
1043.49
869.90
773.46
748.38
711.73
570.93
522.71
501.49
428.27
406.89
hCJS
cm-1

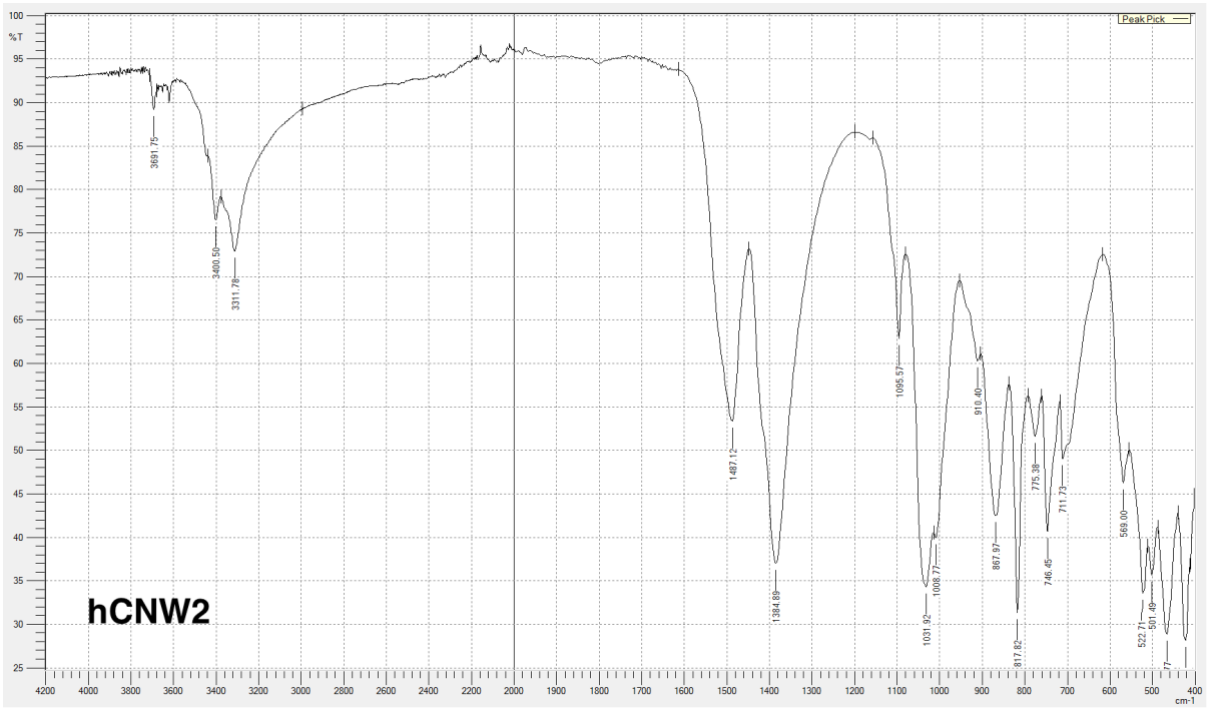

Peak Pick
%T
3319.49
1487.12
1384.89
1089.43
1045.42
875.68
817.82
750.31
678.94
574.79
472.56
428.27
416.55
hCNM1
cm-1

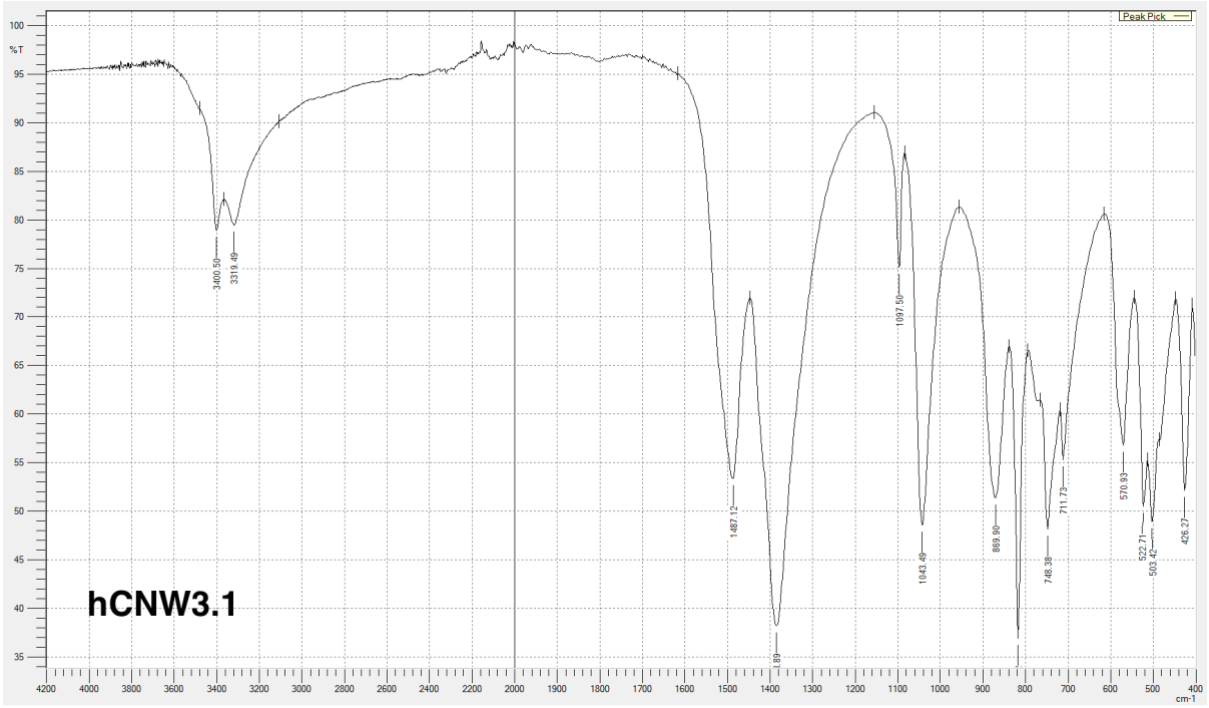

Peak Pick
%T
3441.01
3332.99
1494.83
1392.61
1352.10
1083.64
1047.35
985.62
947.05
867.97
848.68
817.82
779.24
750.31
734.88
624.94
596.00
507.28
480.26
418.55
cm-1
hCNM2

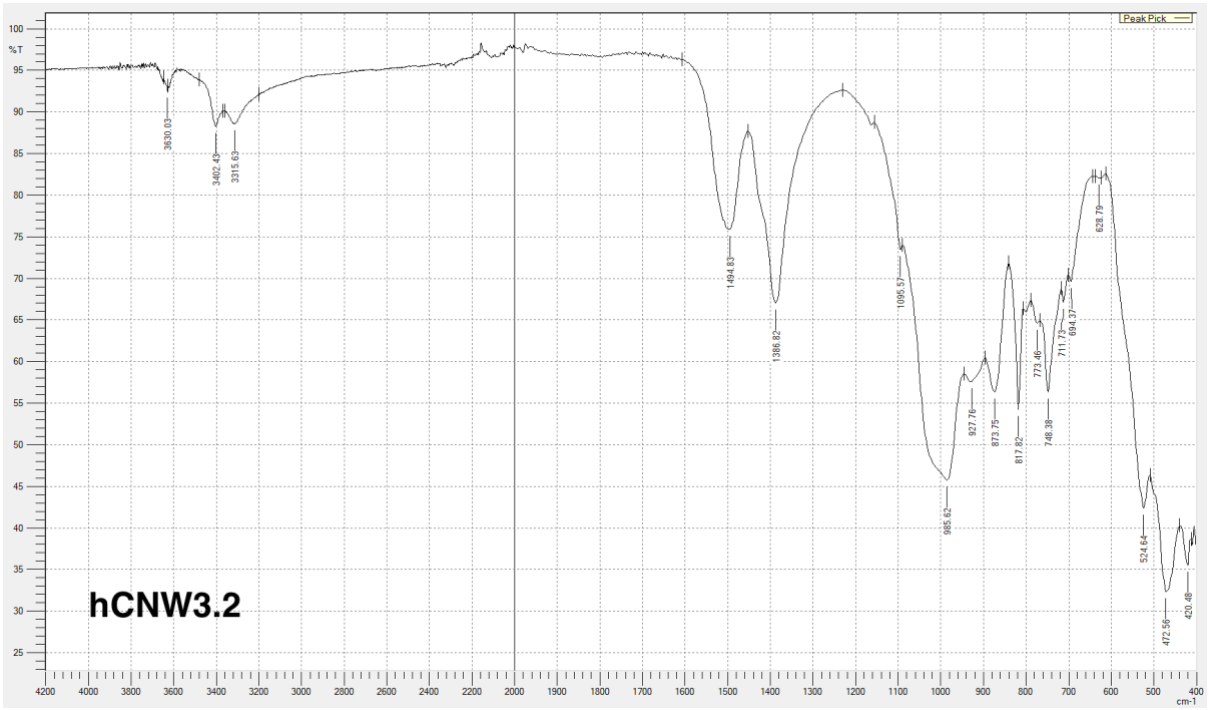

Peak Pick
%T
3442.94
3313.71
1648.14
1500.62
1398.39
1098.43
1049.28
983.70
947.05
914.26
894.97
844.82
819.75
582.50
509.21
437.84
418.55
cm-1
hCNP

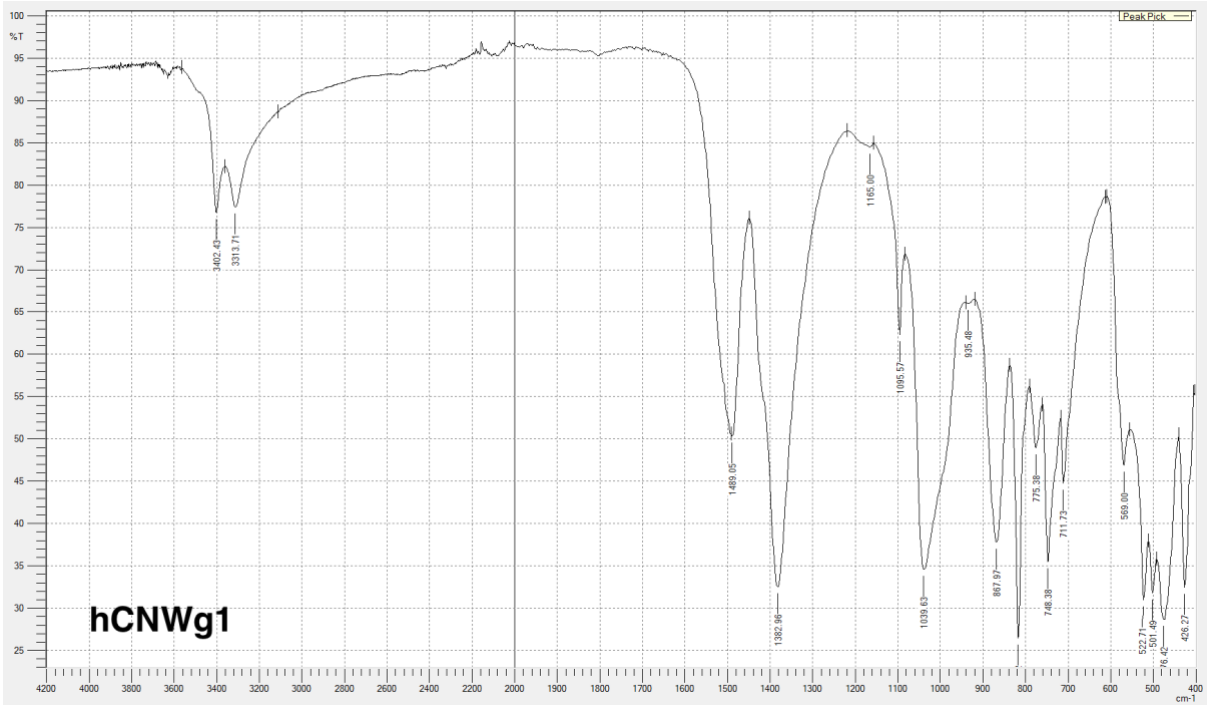

Peak Pick
%T
3400.50
3313.71
1490.97
1386.82
1095.57
1031.92
869.90
817.82
775.38
748.38
711.73
628.79
569.00
522.71
501.49
468.70
418.55
hCNW1.1
cm-1

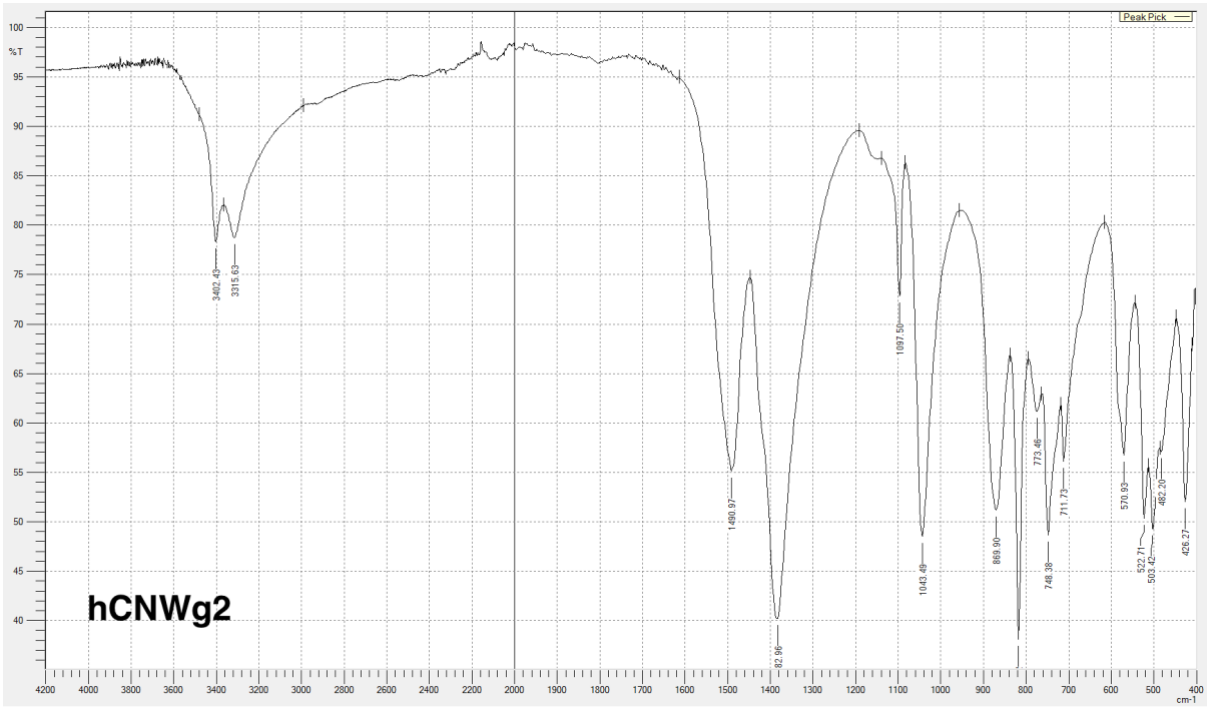

Peak Pick
%T
3402.43
3315.63
1487.12
1384.89
1097.50
1043.49
869.90
775.38
748.38
711.73
570.93
522.71
501.49
482.20
426.27
hCNW1.2
cm-1

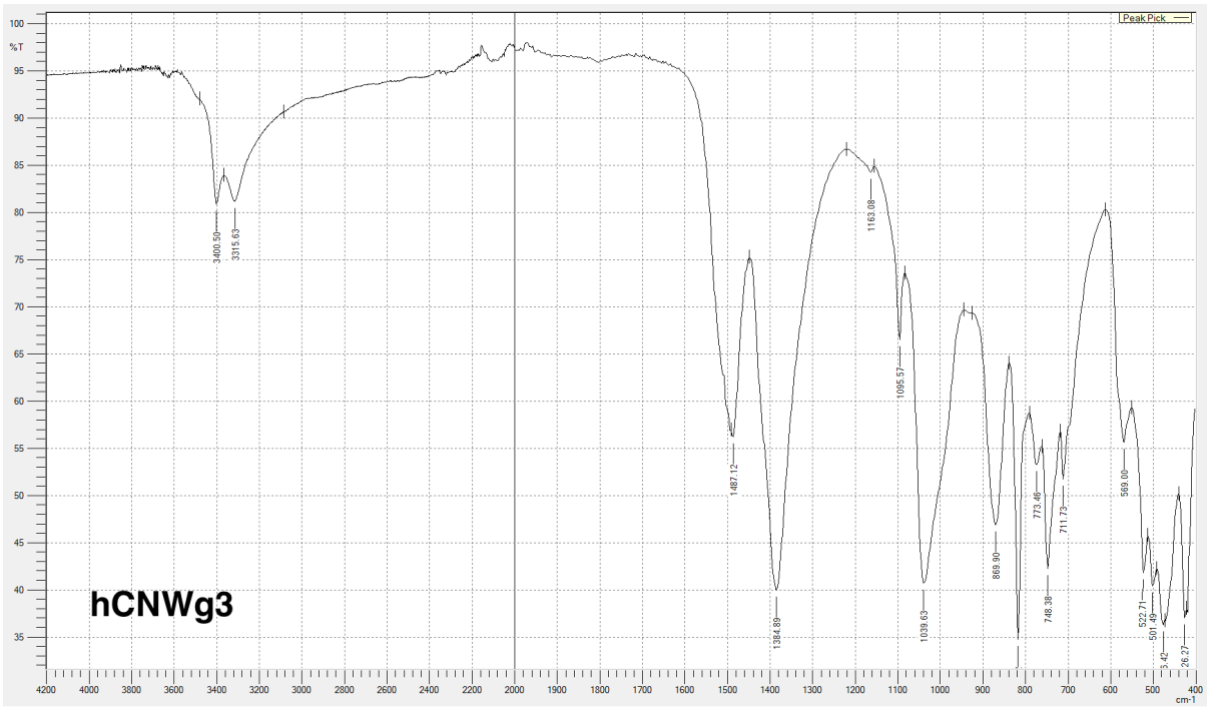

Peak Pick
%T
3691.75
3400.50
3311.76
1487.12
1384.89
1095.57
1031.92
1008.77
910.40
867.97
817.82
775.38
746.45
711.73
568.00
522.71
501.40
hCNW2
cm-1

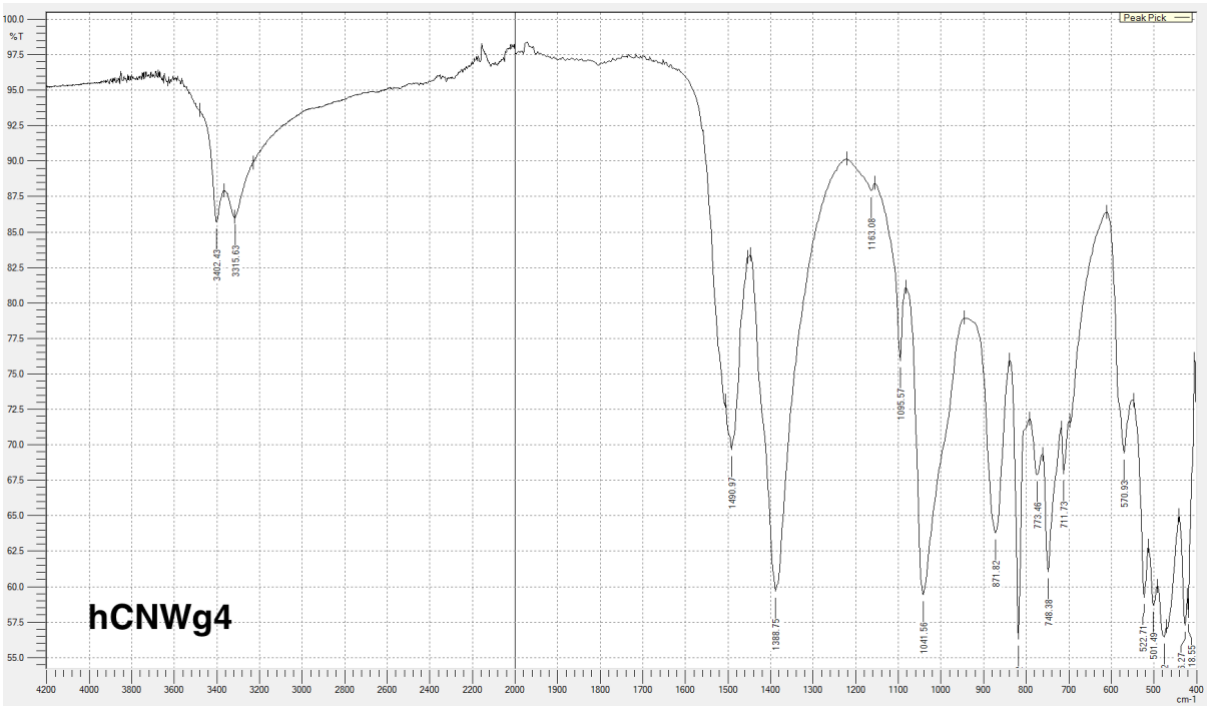

Peak Pick
%T
3400.50
3319.49
1487.12
1097.50
1043.49
869.90
748.38
711.73
570.93
522.71
503.42
426.27
hCNW3.1
cm-1

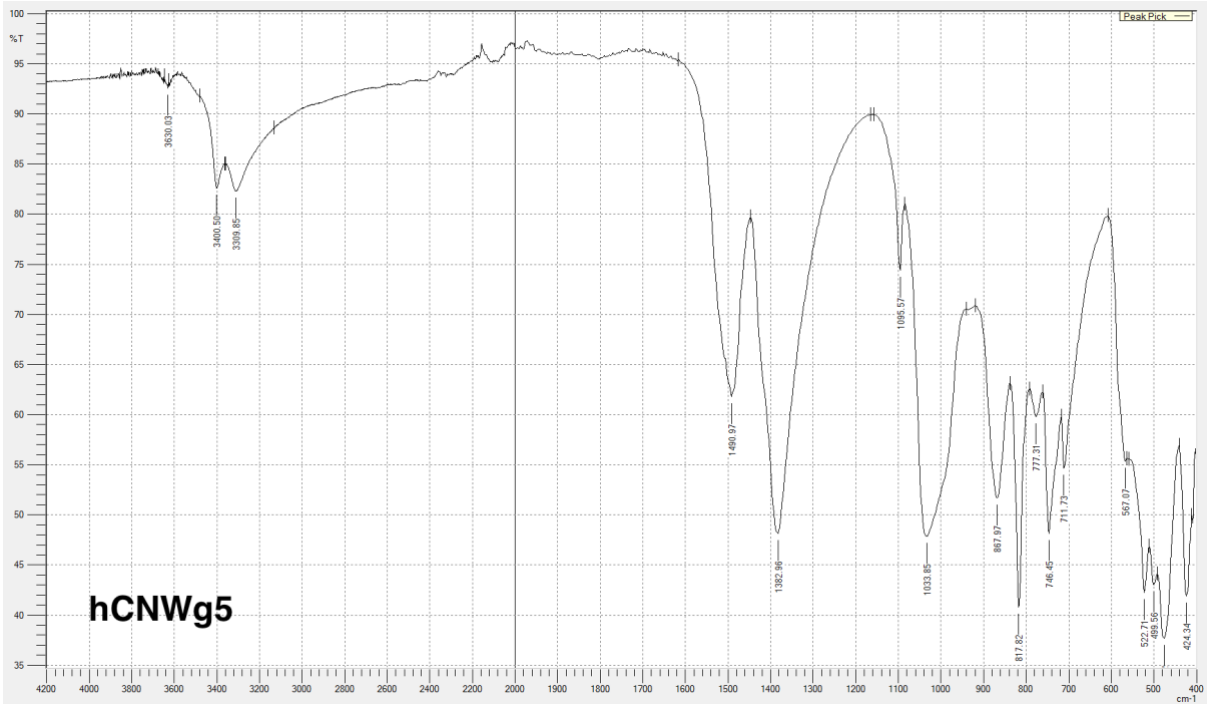

Peak Pick
%T
3630.03
3402.43
3315.63
1494.83
1386.82
1095.57
985.62
927.76
873.75
817.82
773.46
748.38
711.73
694.37
628.79
524.64
472.56
420.48
hCNW3.2
cm-1

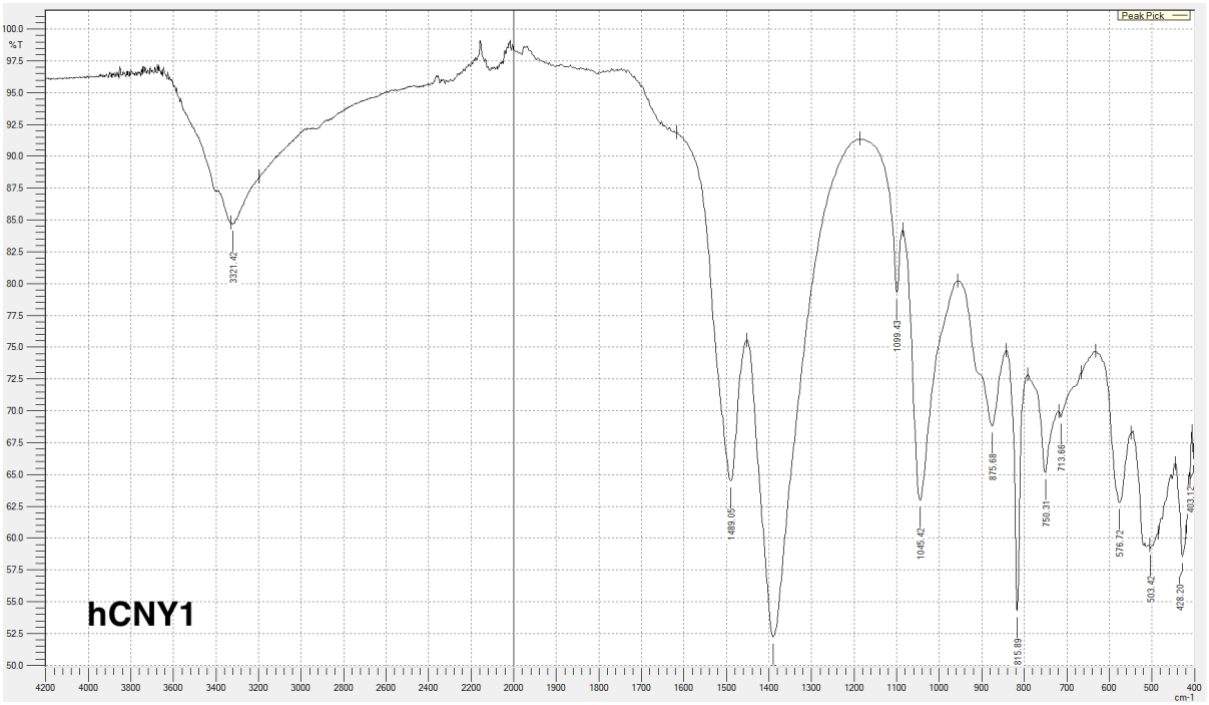

Peak Pick
%T
3402.43
3313.71
1469.05
1382.96
1165.00
1095.57
1039.63
935.48
867.97
775.38
748.38
711.73
569.00
522.71
426.27
hCNWg1
cm-1

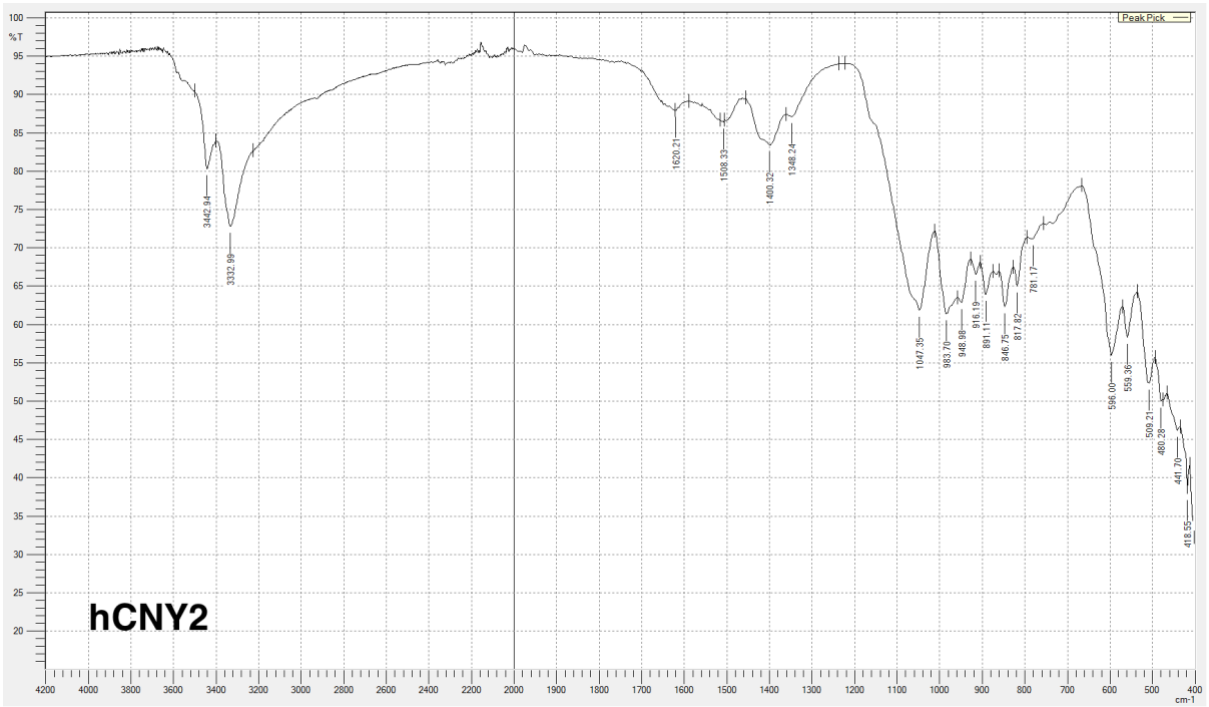

Peak Pick
%T
hCNWg2
3402.43
3315.63
1490.97
1384.89
1087.50
1043.48
869.90
773.46
748.38
711.73
570.93
522.71
503.42
482.20
426.27
cm-1

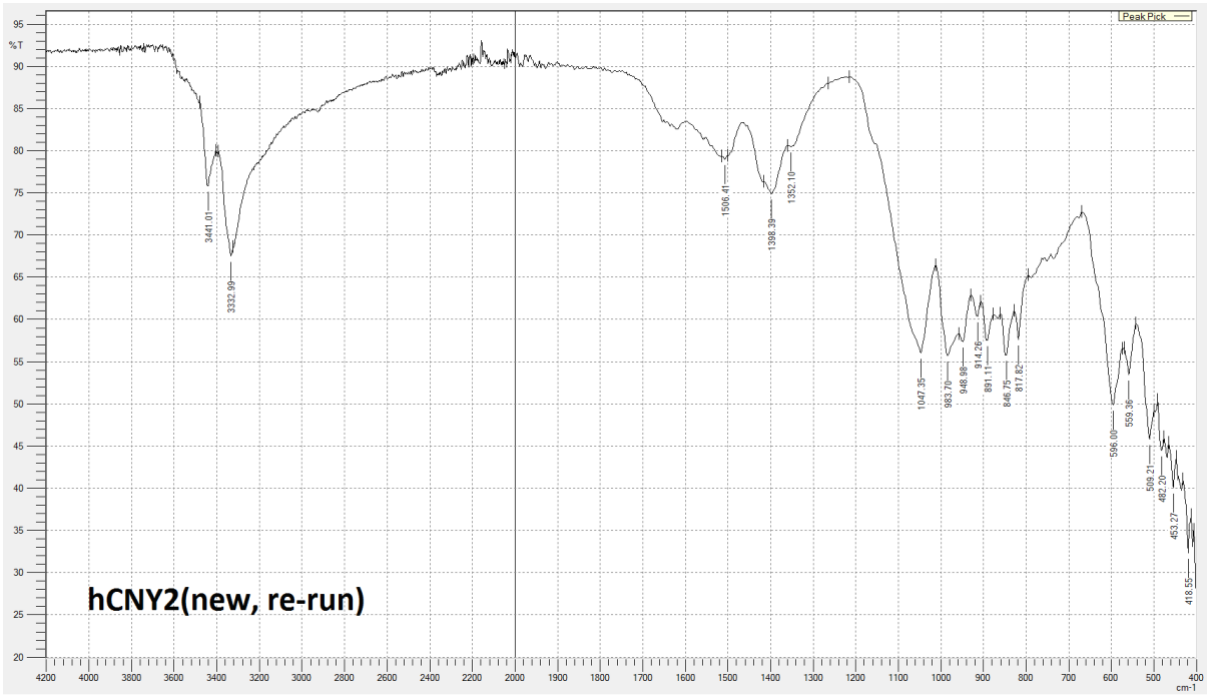

Peak Pick
%T
hCNWg3
3400.50
3315.63
1487.72
1384.89
1163.08
1095.57
1039.63
869.90
773.46
748.38
711.73
569.00
522.71
501.49
426.27
cm-1

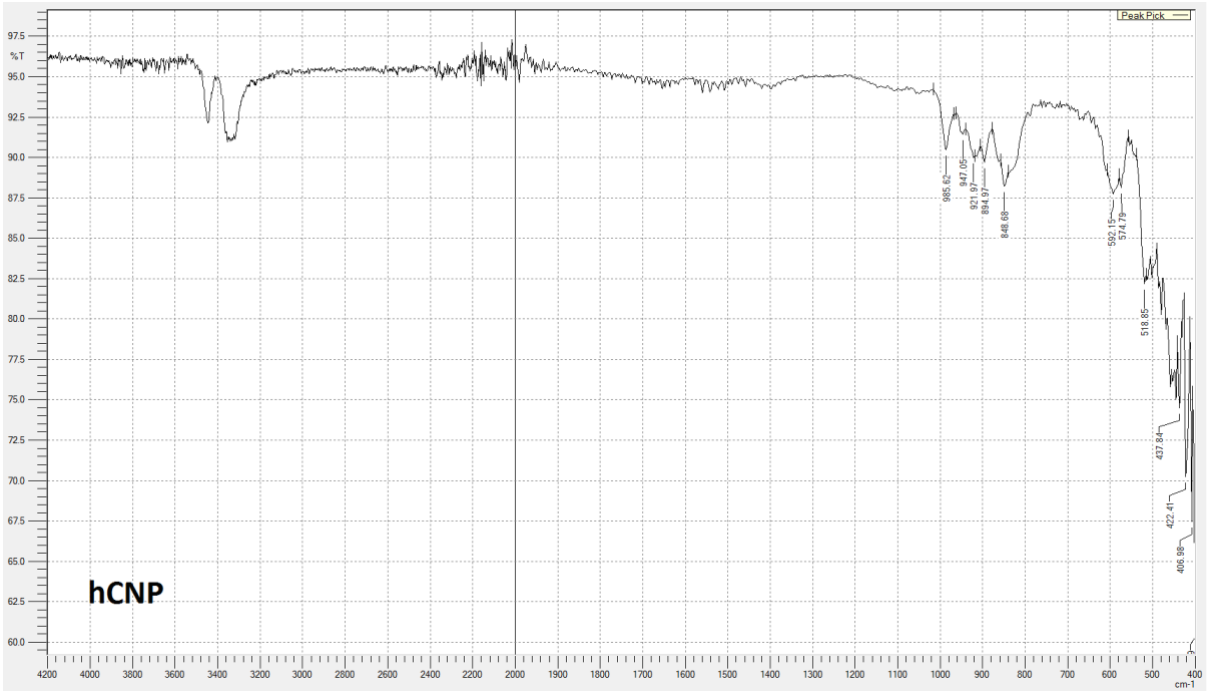

Peak Pick
%T
3402.43
3315.63
1490.97
1388.75
1163.08
1095.57
1041.56
871.82
773.46
748.38
711.73
578.93
522.71
501.49
hCNWg4
cm-1


Peak Pick
%T
3530.03
3400.50
3309.85
1490.97
1382.96
1095.57
1033.85
867.97
817.82
777.31
746.45
711.73
567.87
522.71
468.56
424.34
hCNWg5
cm-1

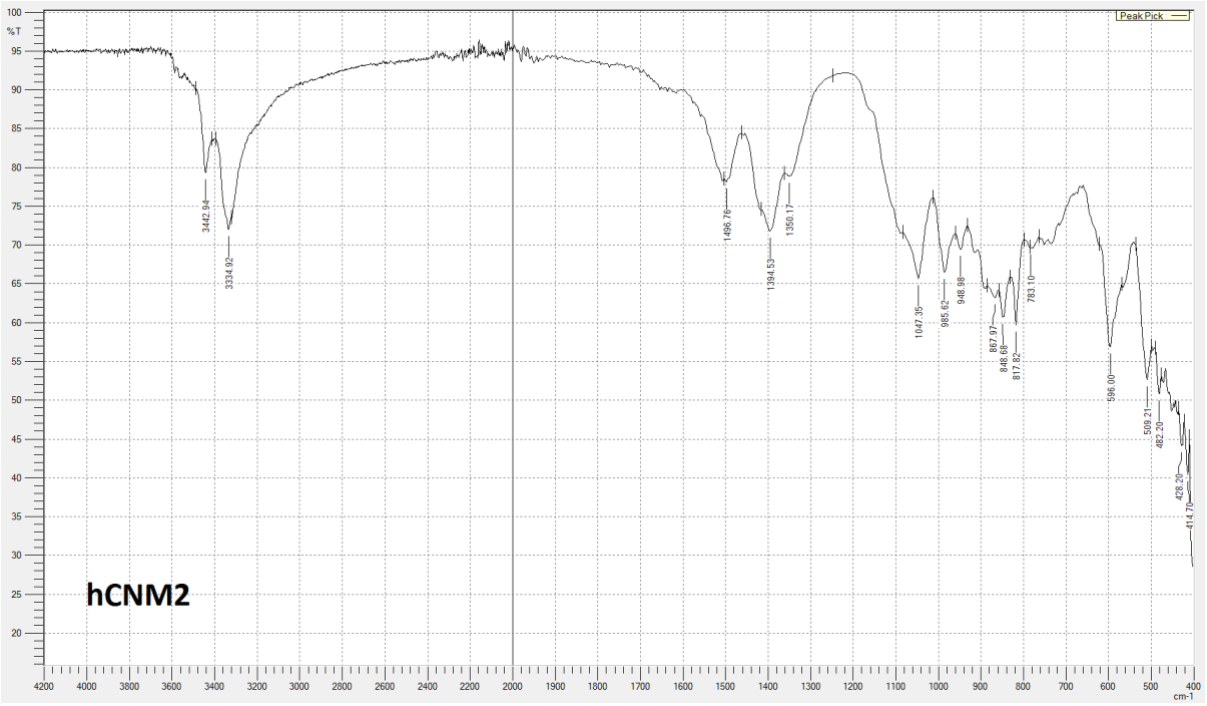

Peak Pick
%T
3321.42
1489.05
1099.43
1045.42
875.68
815.89
750.31
713.66
576.72
503.42
463.12
428.20
hCNY1
cm-1


Peak Pick
%T
3442.94
3332.99
1620.21
1508.33
1400.32
1348.24
1047.35
983.70
948.98
916.19
891.11
846.75
817.82
781.17
596.00
559.36
509.21
480.28
441.70
418.55
hCNY2
cm-1

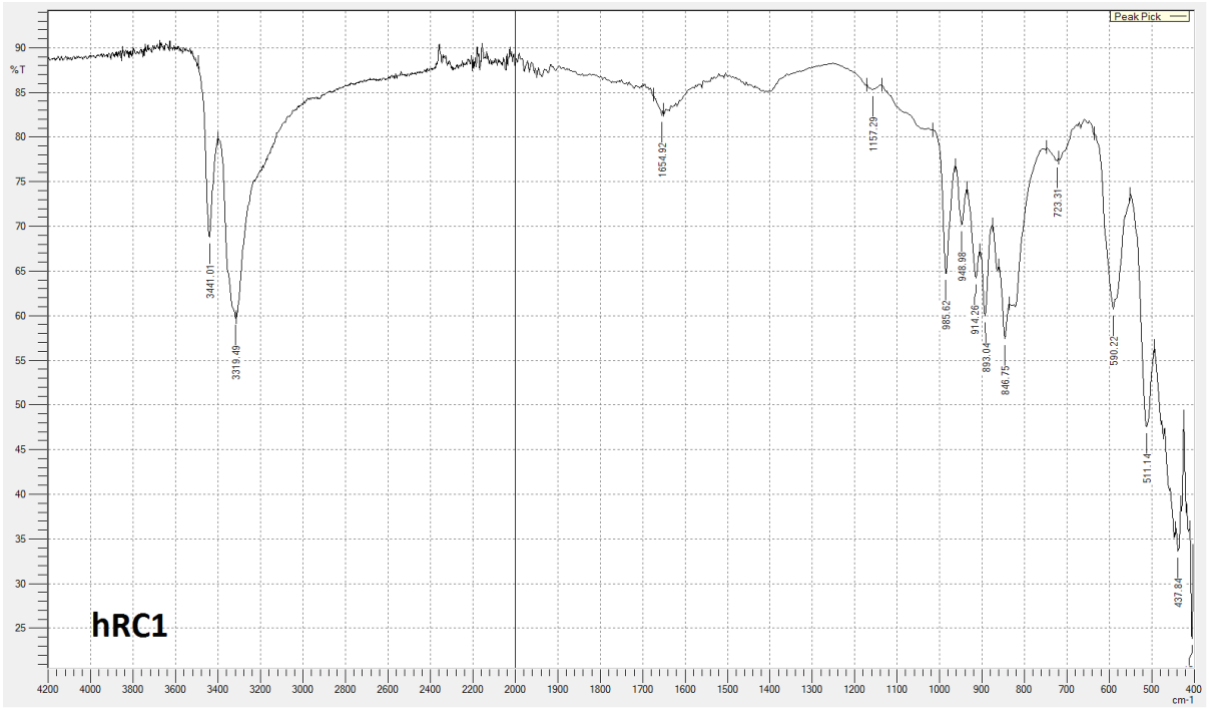

Peak Pick
%T
3441.01
3332.99
1506.41
1398.39
1352.10
1047.35
983.70
948.98
914.26
891.11
846.75
817.82
596.60
559.36
509.21
482.20
453.27
418.55
hCNY2(new, re-run)
cm-1

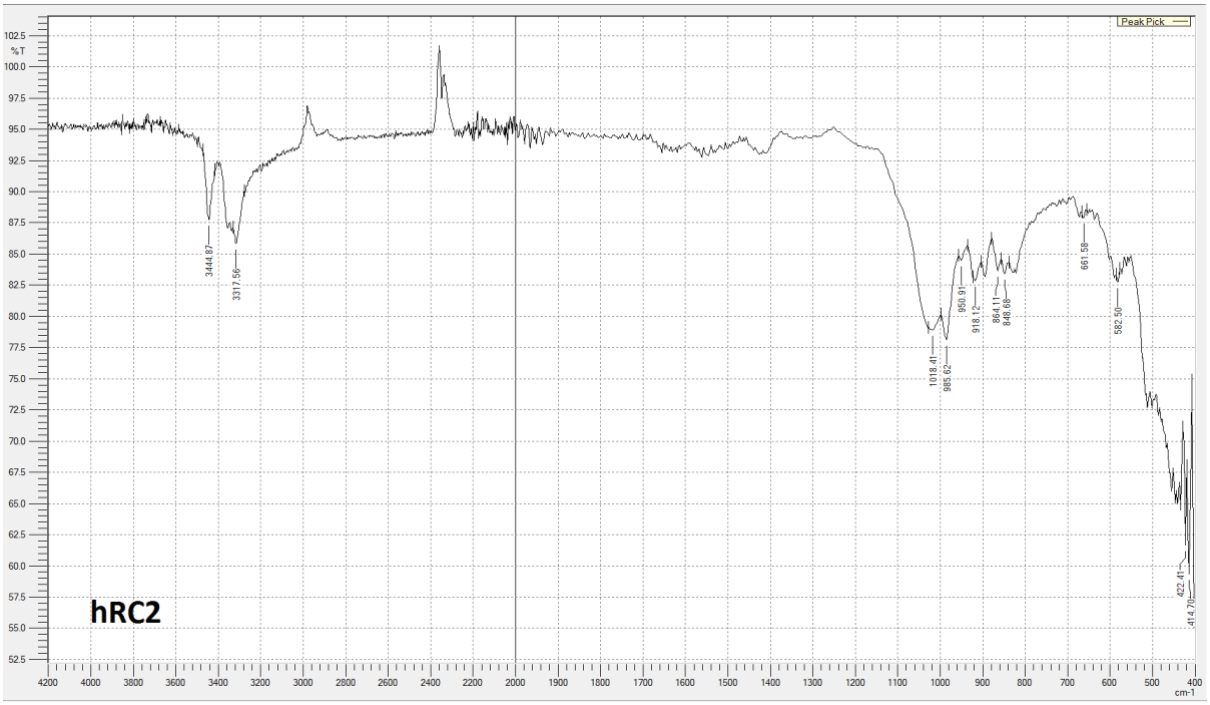

Peak Pick
%T
985.62
947.05
921.97
884.97
848.68
592.15
574.79
518.85
437.84
422.41
406.98
hCNP
cm-1

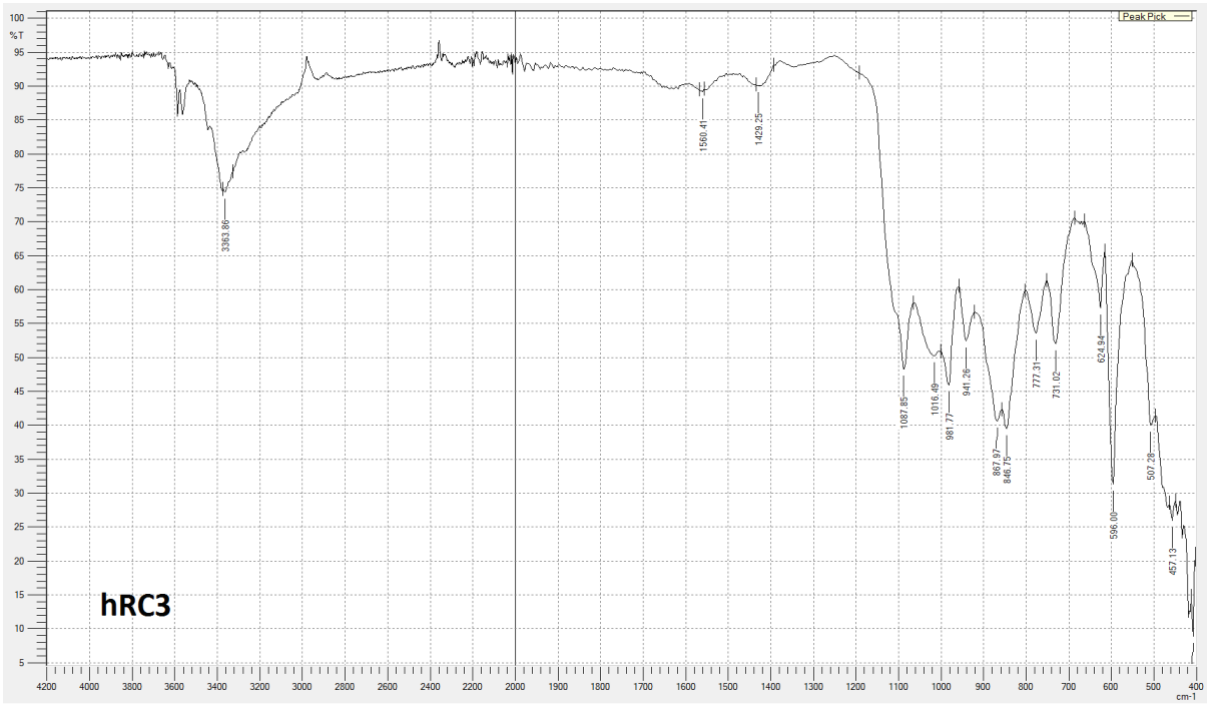
APPENDIX C: FTIR SPECTRA FOR THE MALACHITE SAMPLES

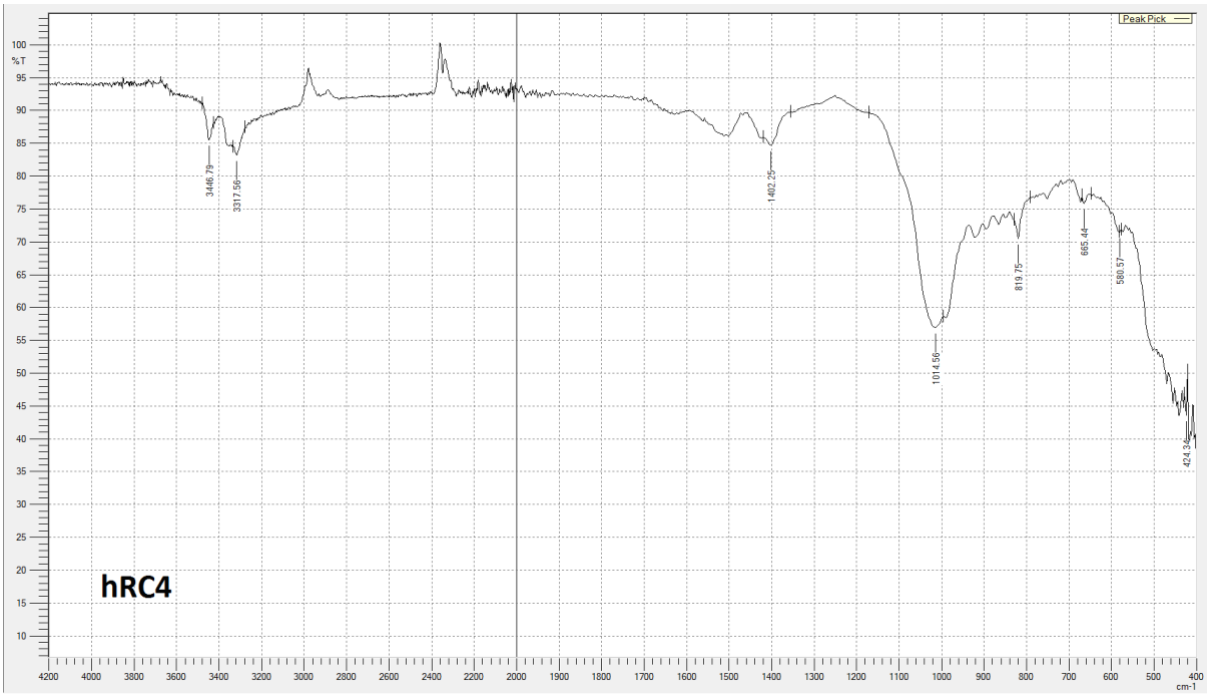


Cyprus

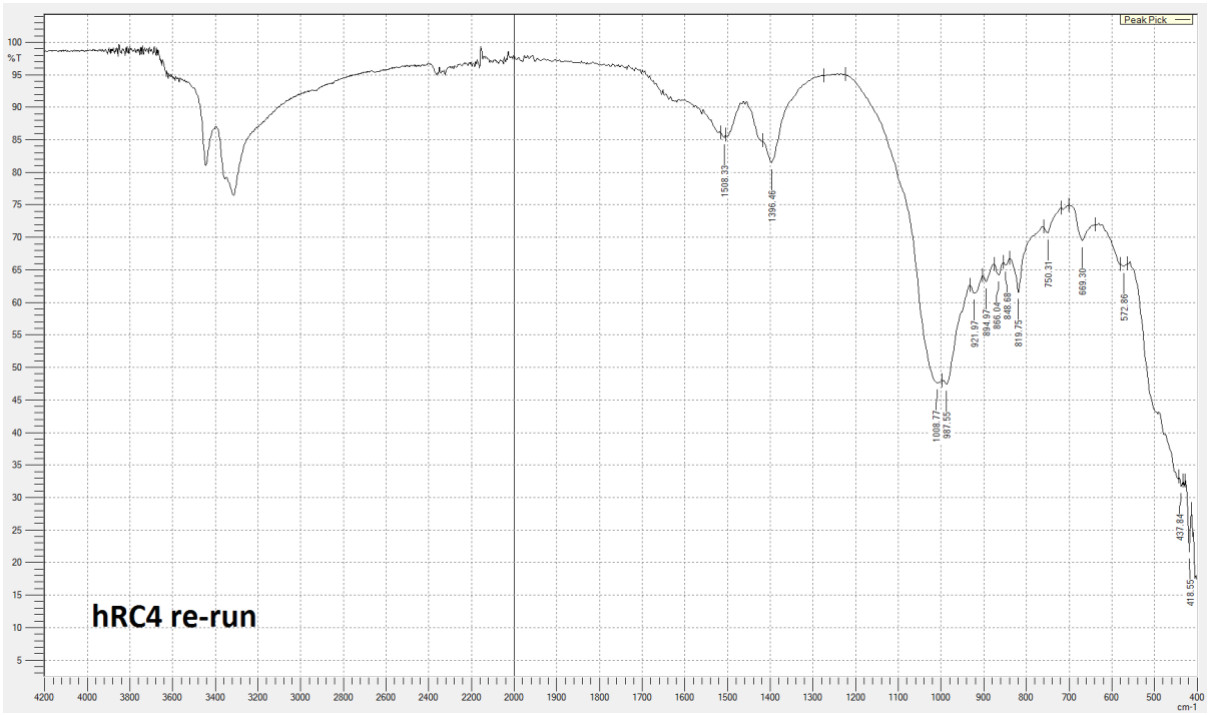

Peak Pick
%T
3441.01
3319.49
1654.92
1157.29
985.62
948.98
914.26
893.04
846.75
723.31
590.22
511.14
437.84
hRC1
cm-1

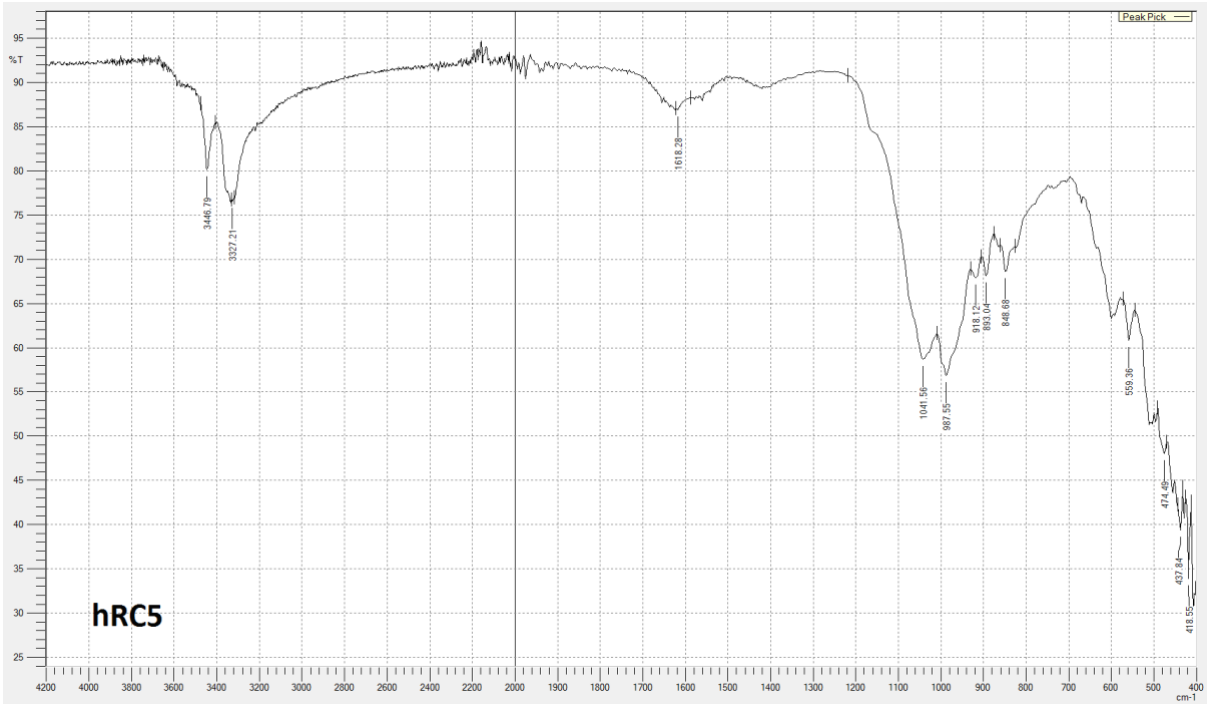

Peak Pick
%T
3444.87
3317.56
1018.41
985.62
950.91
918.12
864.11
848.68
661.58
582.50
422.41
414.70
hRC2
cm-1

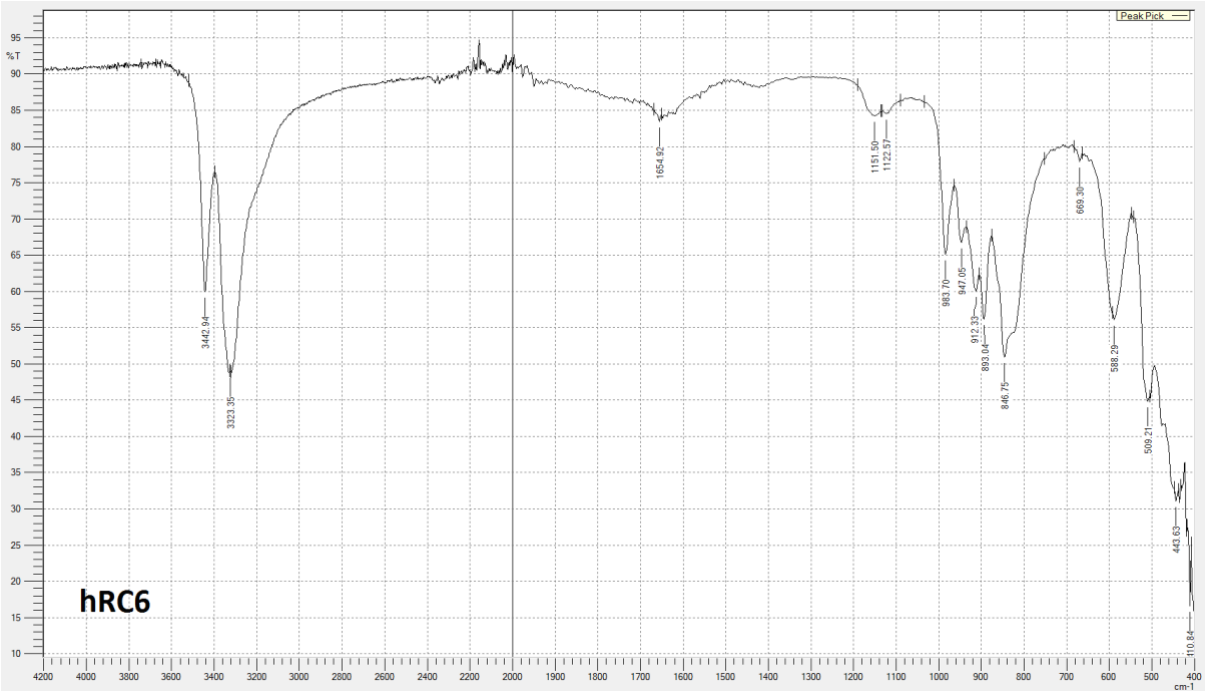

Peak Pick
%T
3363.86
1560.41
1429.25
1087.85
1016.49
981.77
941.26
867.97
846.75
777.31
731.02
624.84
596.00
507.28
457.13
hRC3
cm-1

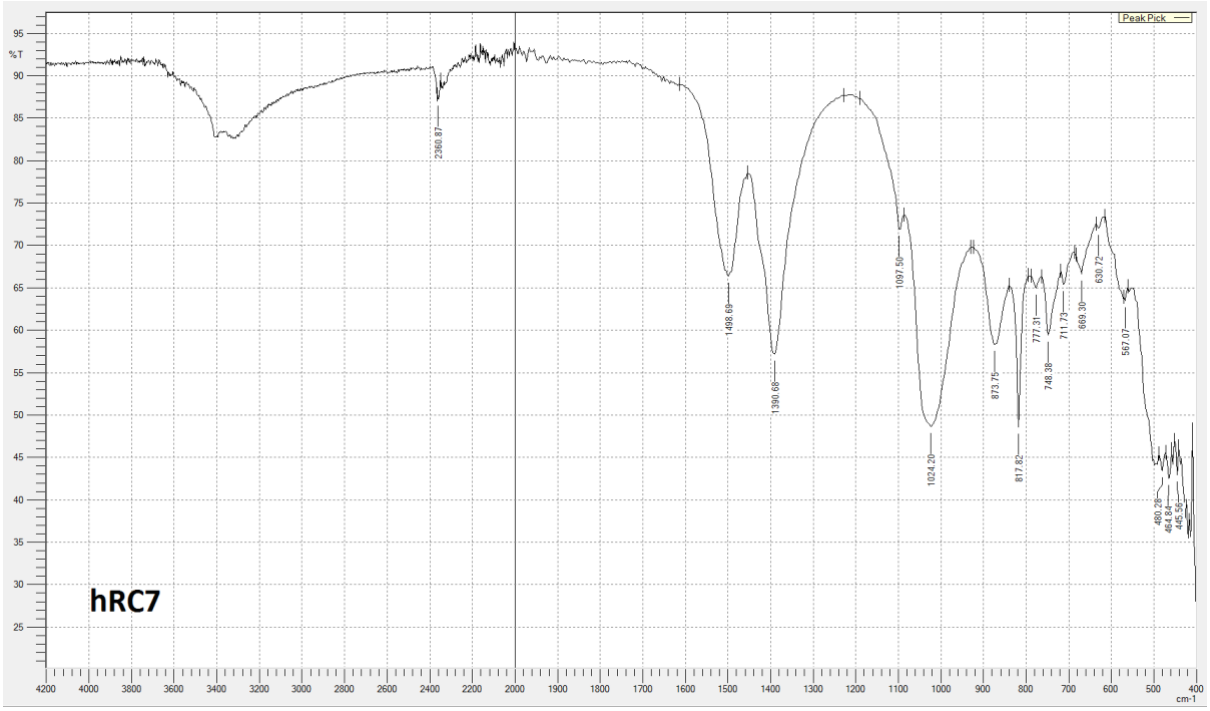

Peak Pick
%T
3446.79
3317.56
1402.25
1014.56
819.75
685.44
580.57
424.38
hRC4
cm-1

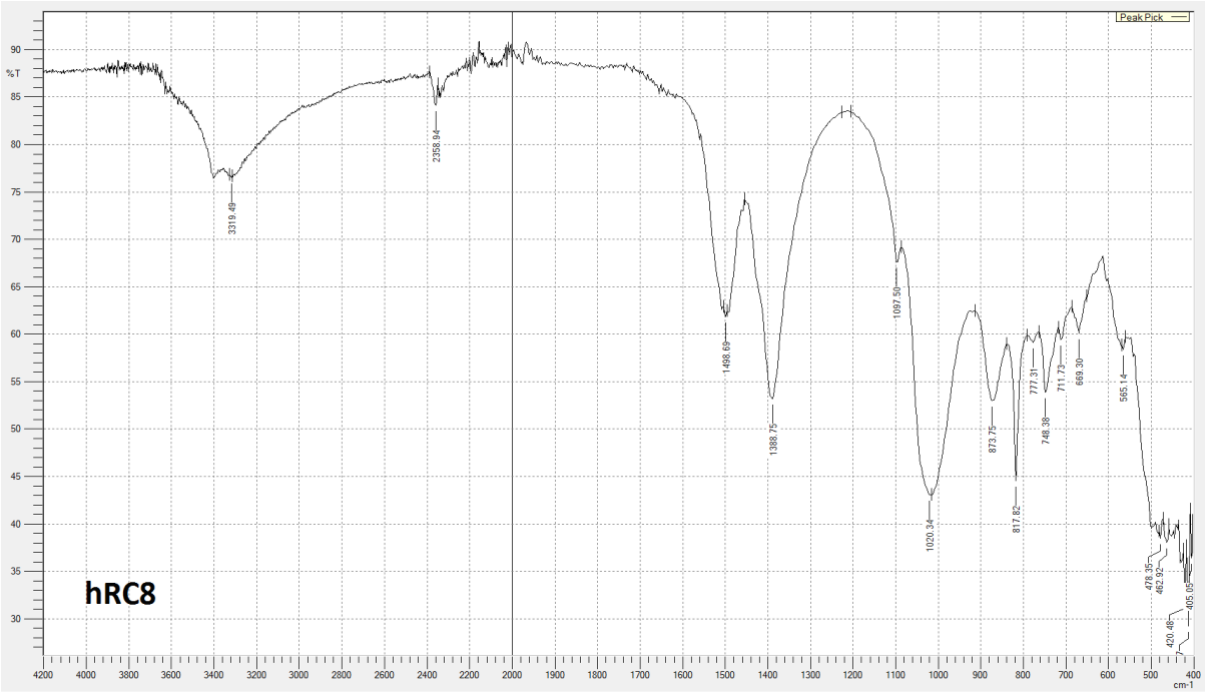
APPENDIX C: FTIR SPECTRA FOR THE MALACHITE SAMPLES



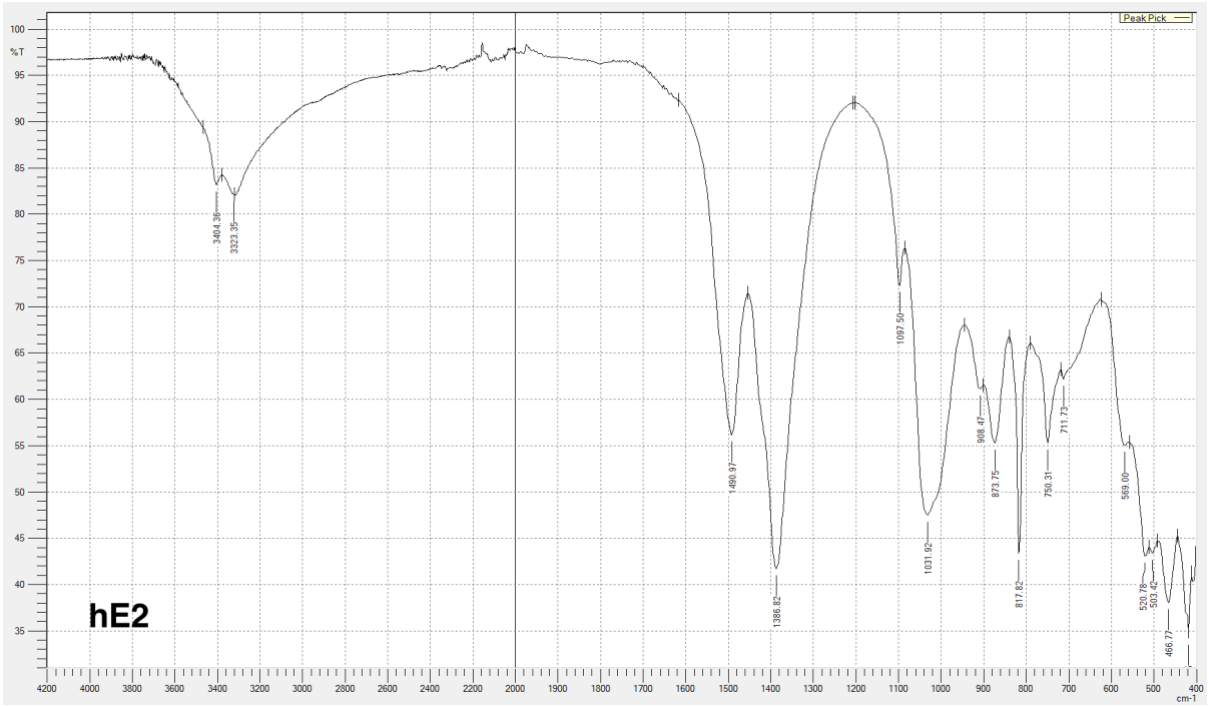


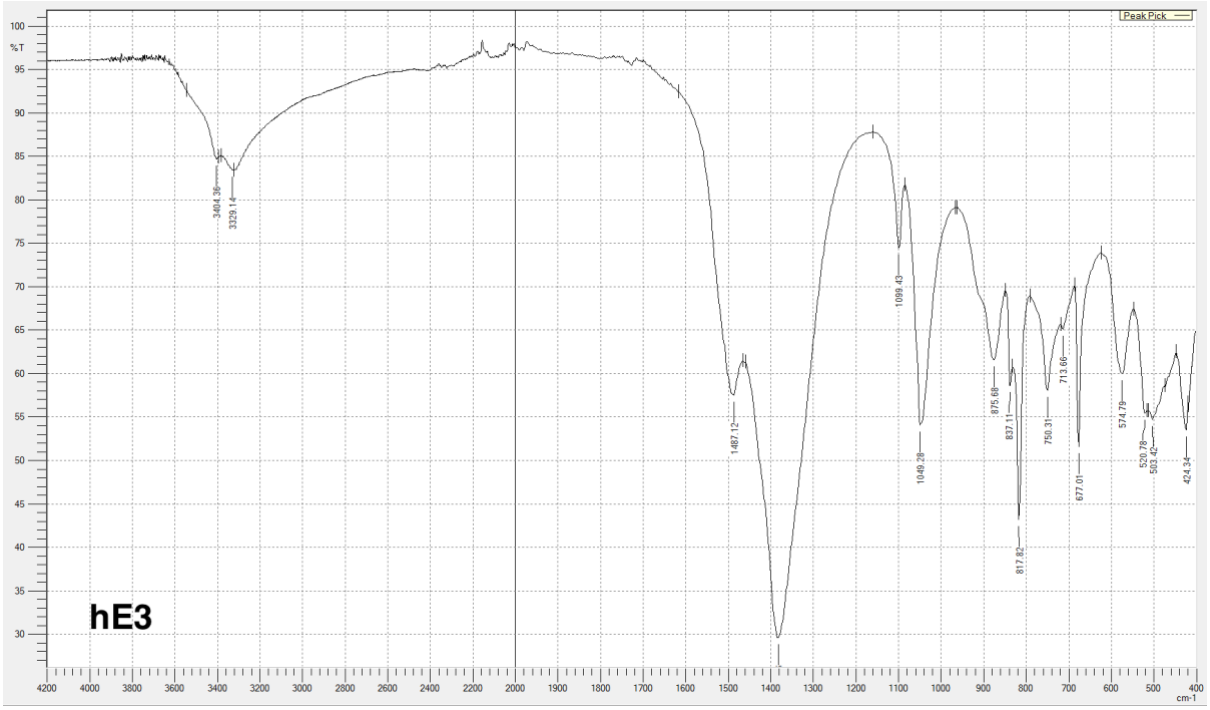

Peak Pick
%T
3442.94
3323.35
1654.92
1151.50
1122.57
983.70
947.05
912.33
893.04
846.75
669.30
588.29
509.21
443.63
410.84
hRC6
cm-1

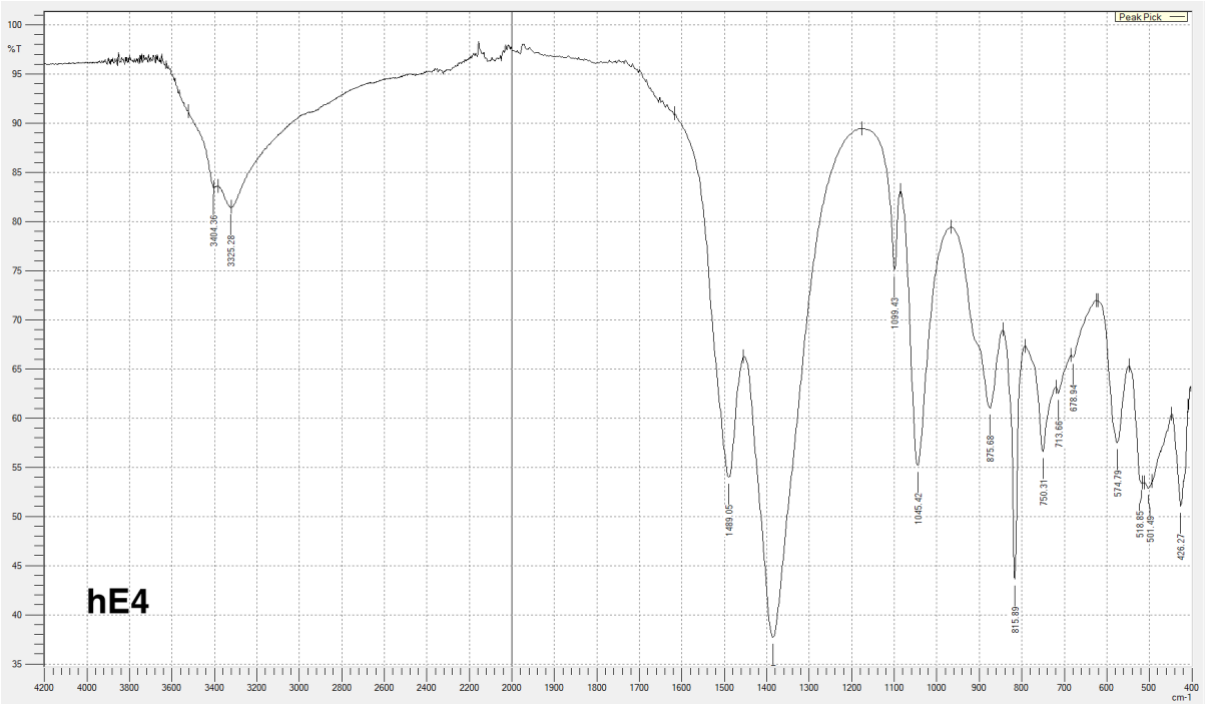

Peak Pick
%T
2360.87
1498.69
1390.66
1097.50
1024.20
873.75
817.82
777.31
748.38
711.73
669.30
630.72
567.07
480.28
454.64
hRC7
cm-1

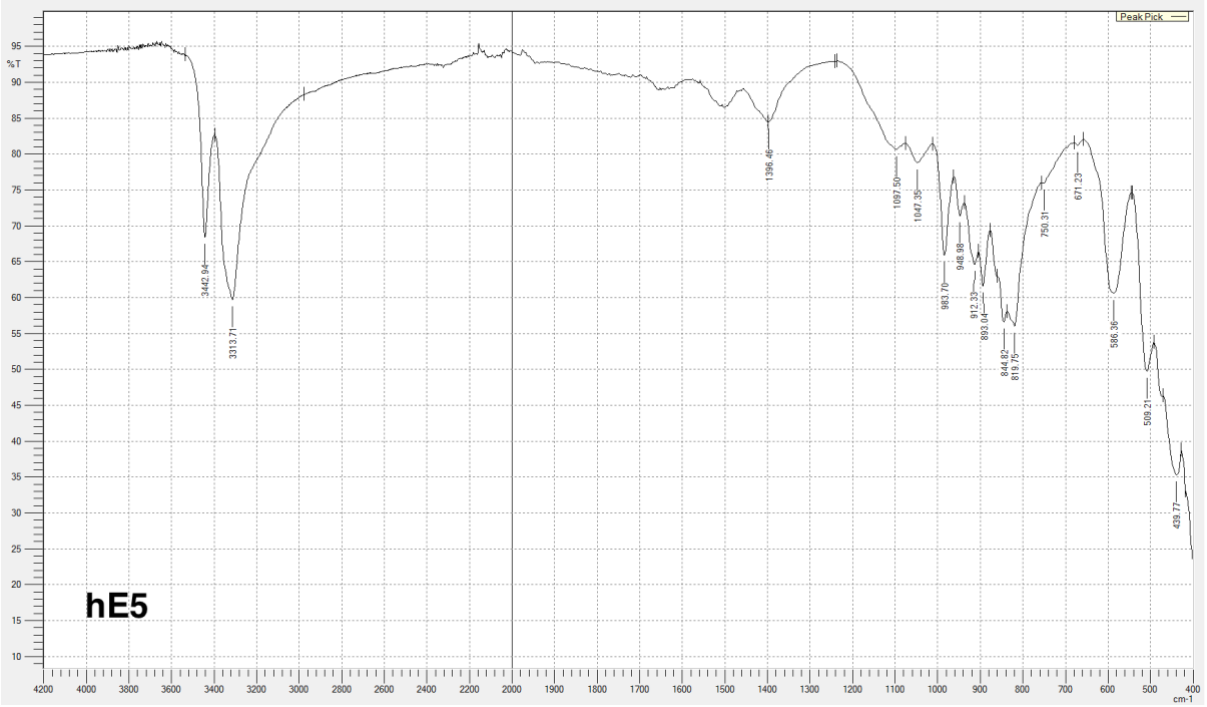

Peak Pick
%T
hRC8
3319.49
2358.94
1498.69
1388.75
1097.50
1020.34
873.75
817.82
777.31
748.38
711.73
669.30
565.14
476.35
462.92
420.48
405.05
cm-1

England

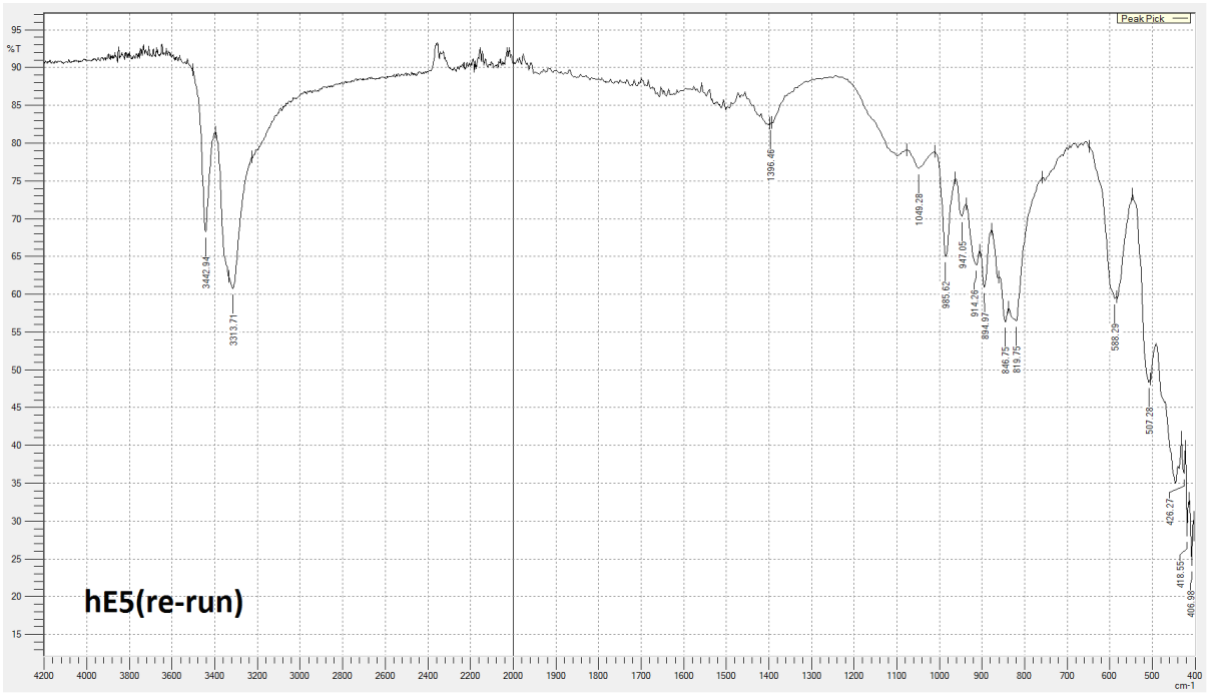

Peak Pick
%T
3404.36
3323.35
1490.97
1386.82
1097.50
1031.82
968.47
873.75
817.82
750.31
711.72
569.00
520.78
503.42
466.77
hE2
cm-1

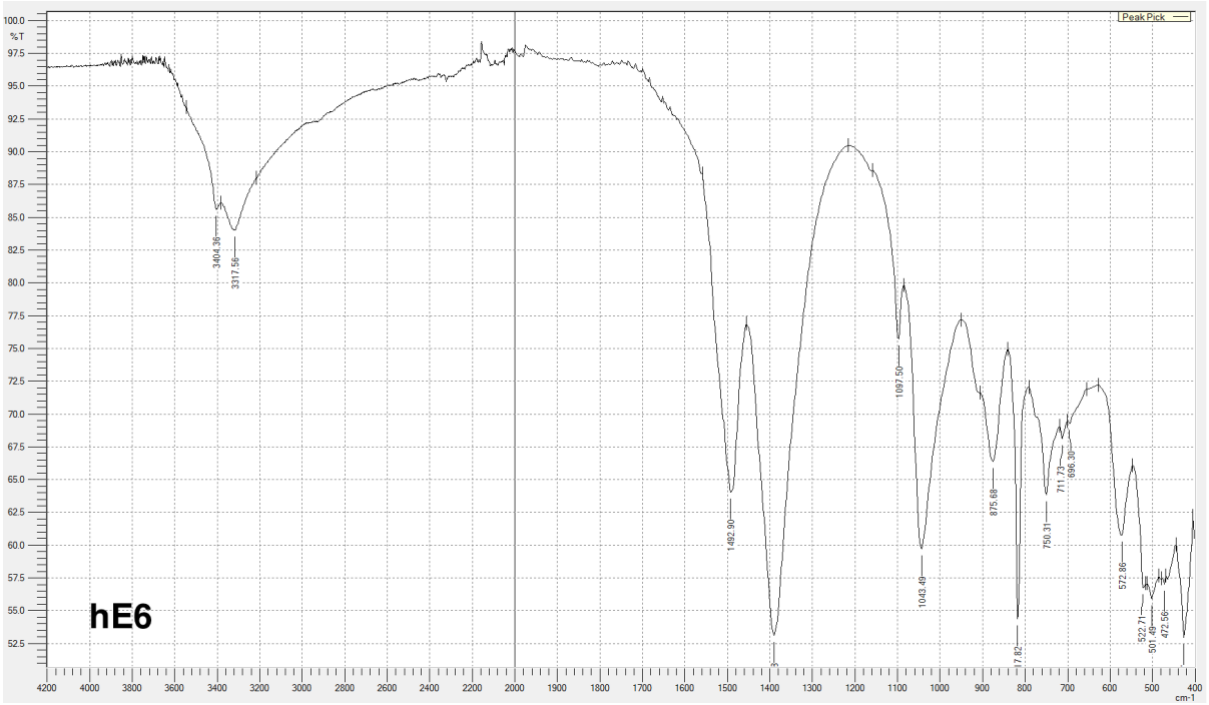

Peak Pick
%T
3404.36
3329.14
1487.12
1099.43
1049.28
875.68
837.11
817.82
750.31
713.66
677.01
574.79
520.78
503.42
424.34
hE3
cm-1


Peak Pick
%T
3404.36
3325.28
1489.05
1099.43
1046.42
875.68
815.89
750.31
713.66
678.84
574.79
518.85
591.48
426.27
hE4
cm-1

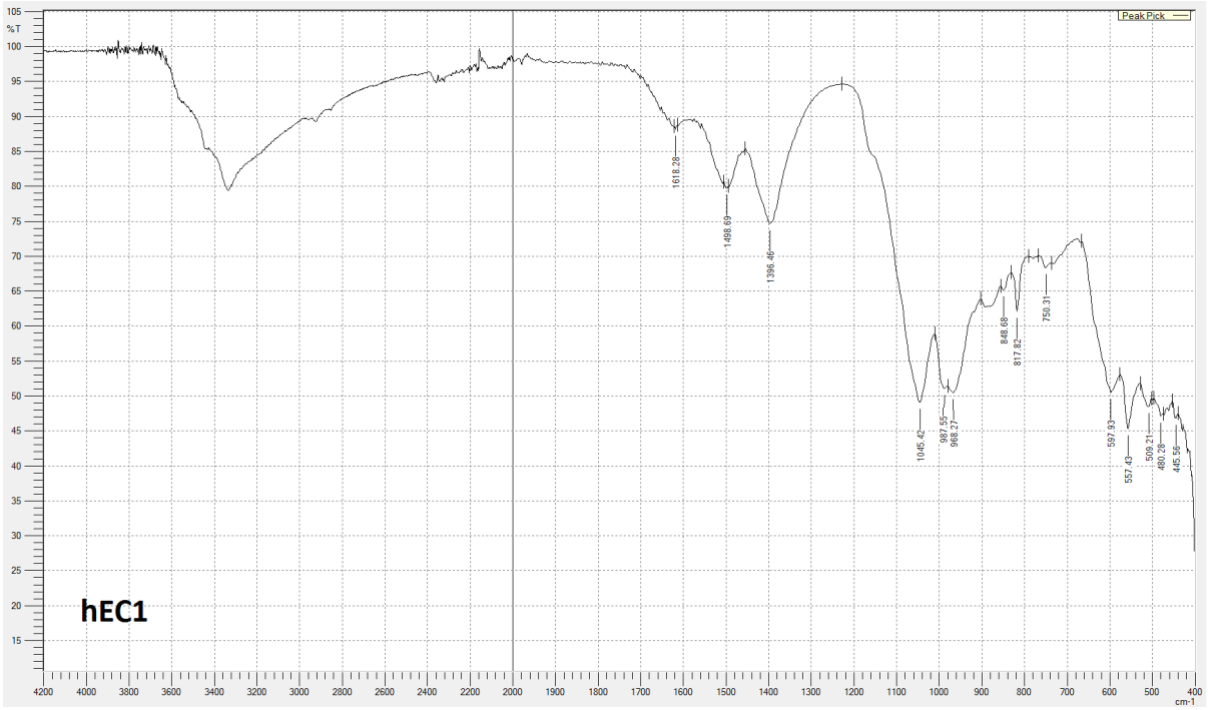

Peak Pick
%T
3442.94
3313.71
1396.46
1097.50
1047.35
983.70
948.88
912.33
893.04
844.82
819.75
750.31
671.23
586.36
509.21
438.77
hE5
cm-1

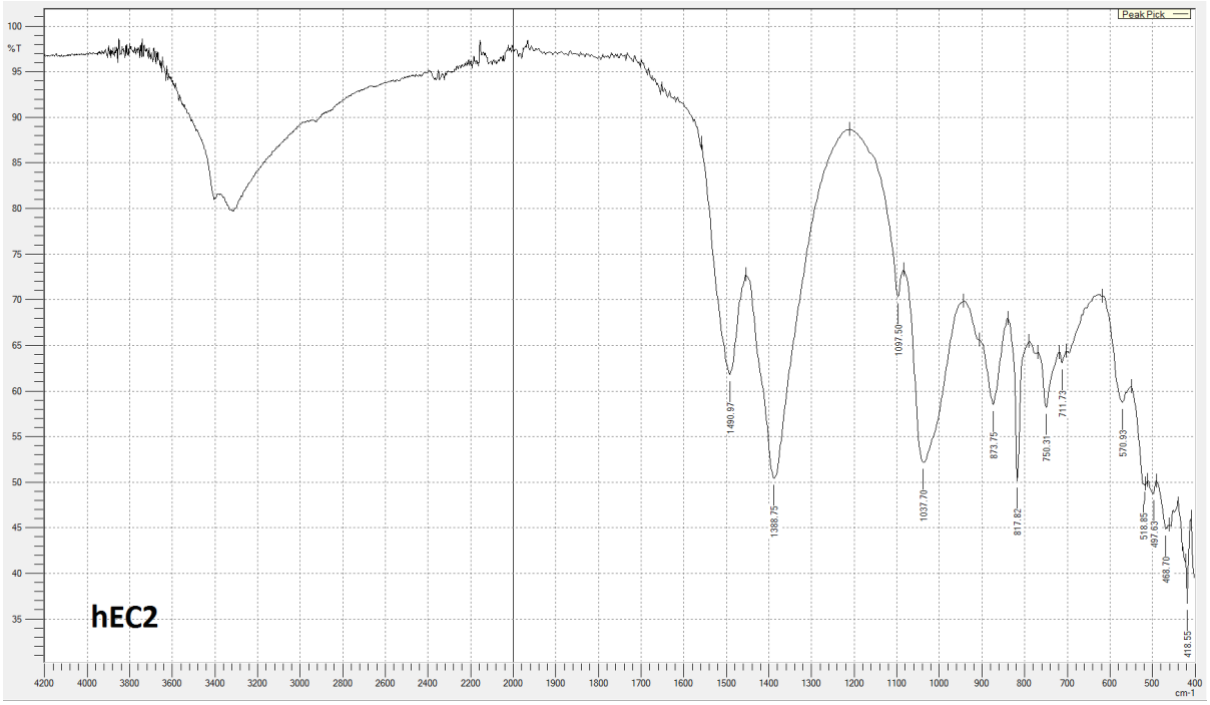
APPENDIX C: FTIR SPECTRA FOR THE MALACHITE SAMPLES

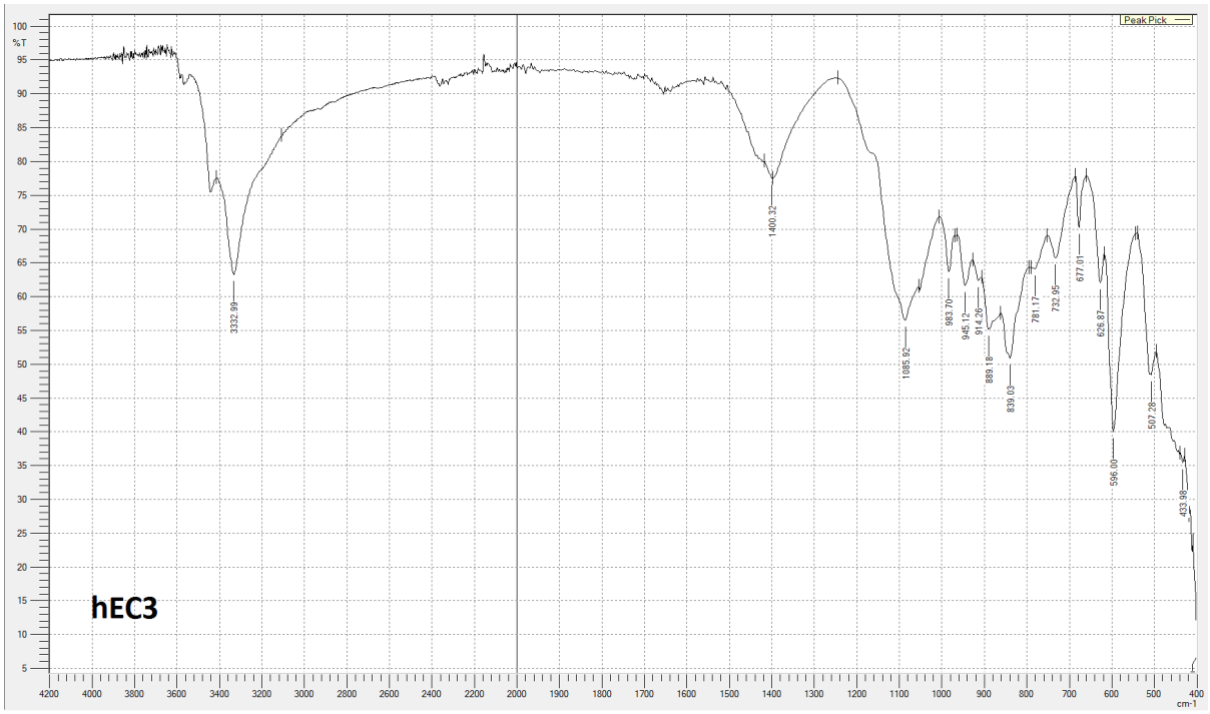


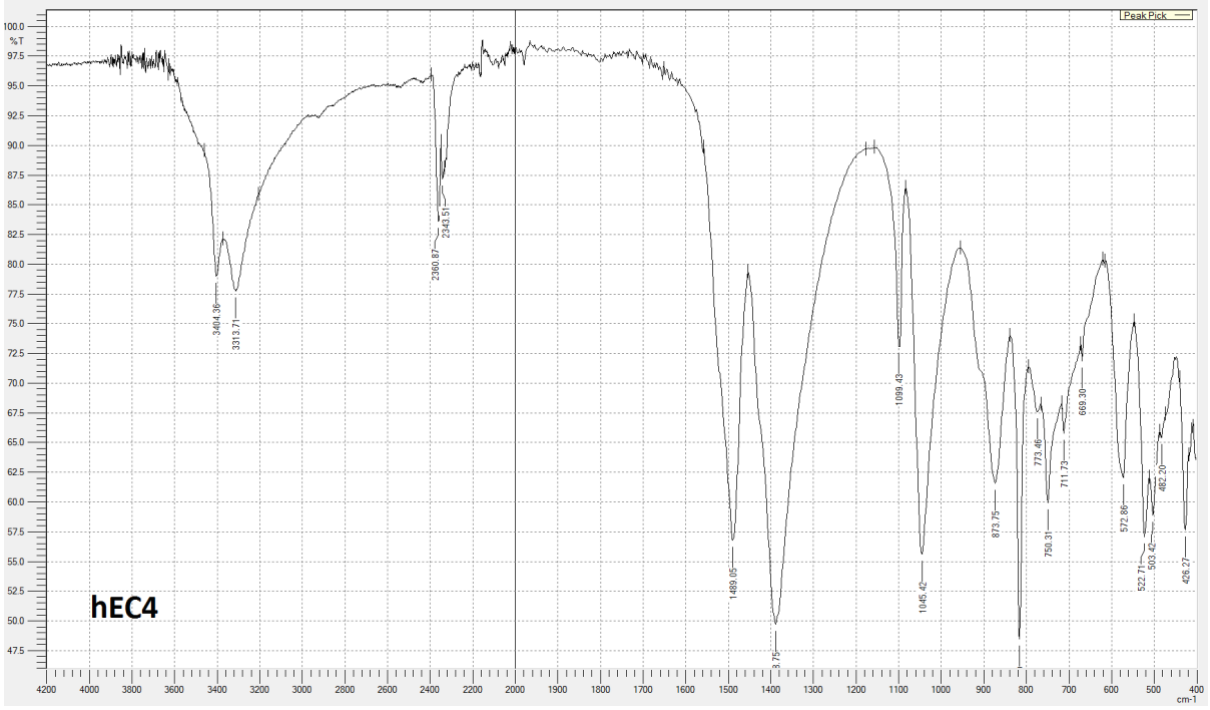


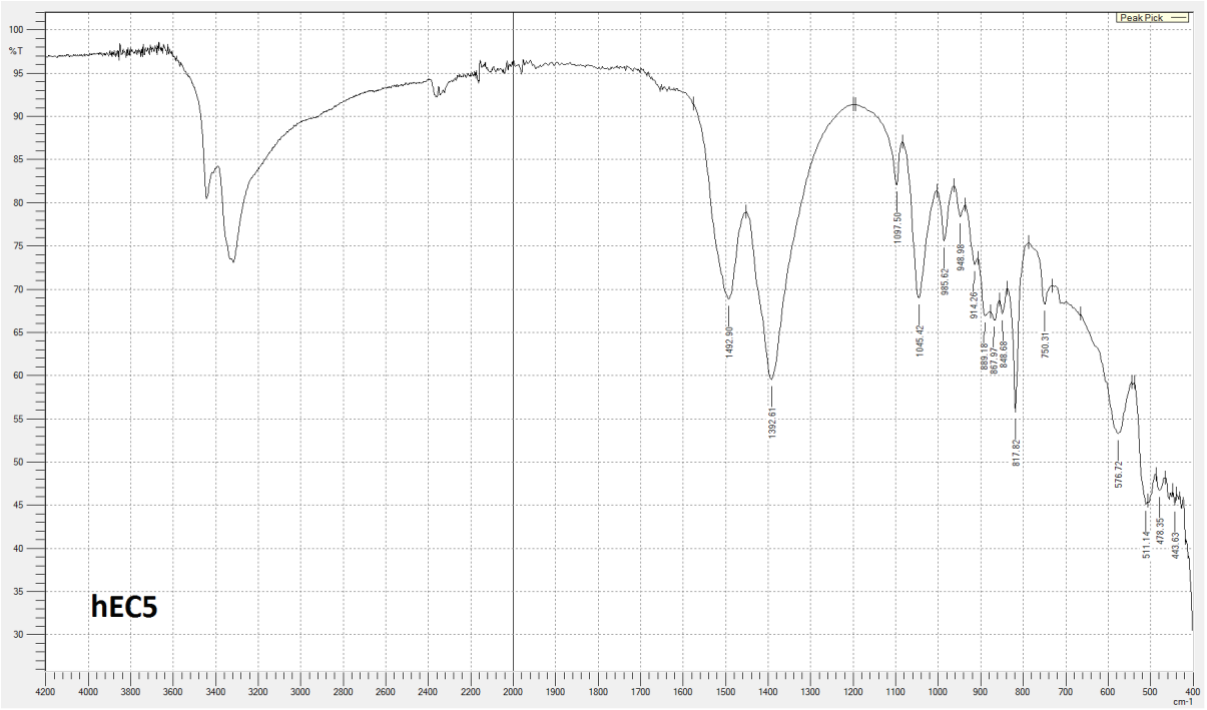
CV

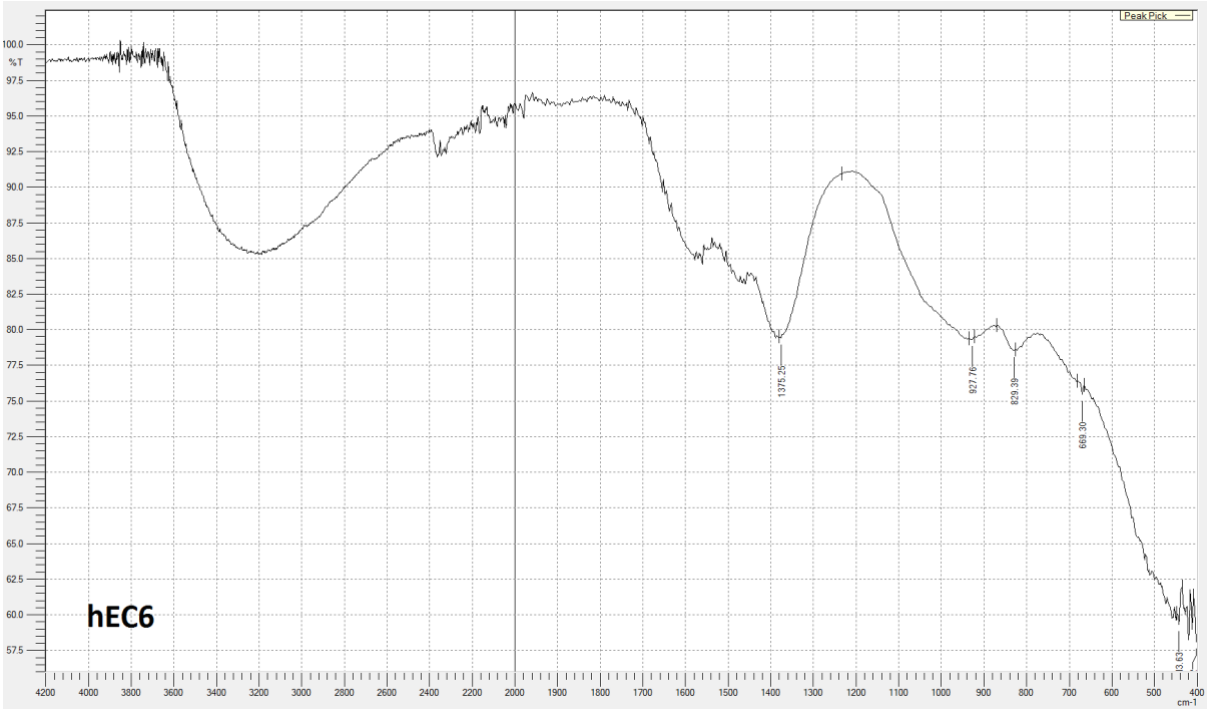

Peak Pick
%T
1618.28
1498.69
1396.46
1045.42
987.55
968.27
848.68
817.82
750.31
597.93
557.43
509.21
480.28
445.56
hEC1
cm-1

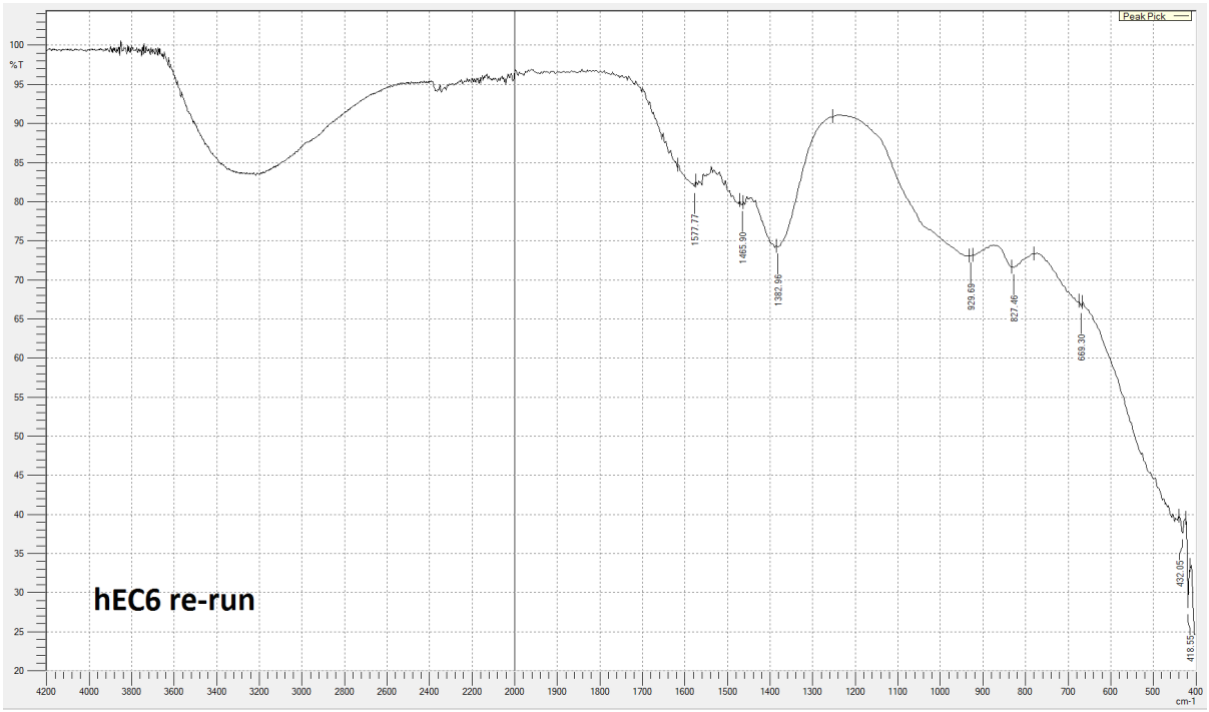

Peak Pick
%T
1490.97
1388.75
1097.50
1037.70
873.75
817.62
750.31
711.73
570.93
518.85
497.63
468.70
418.55
hEC2
cm-1

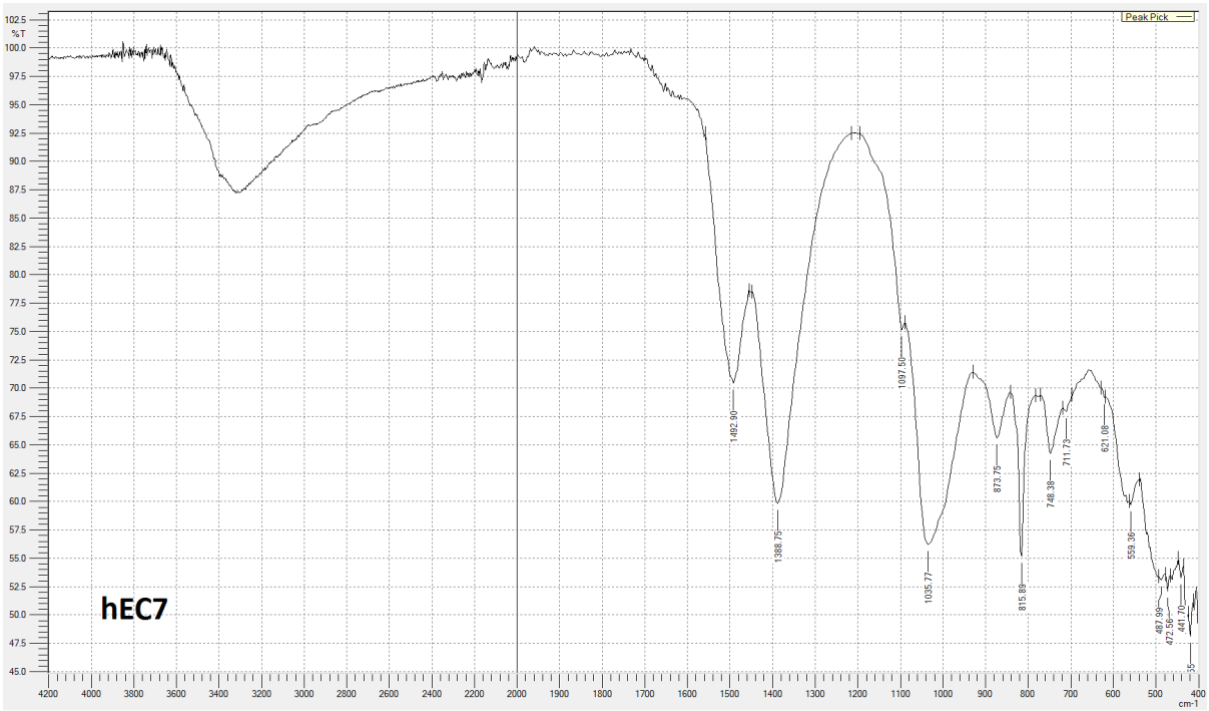

Peak Pick
%T
3332.99
1400.32
1085.92
983.70
945.12
914.26
889.18
839.03
781.17
732.95
677.01
626.87
596.00
507.28
423.95
hEC3
cm-1

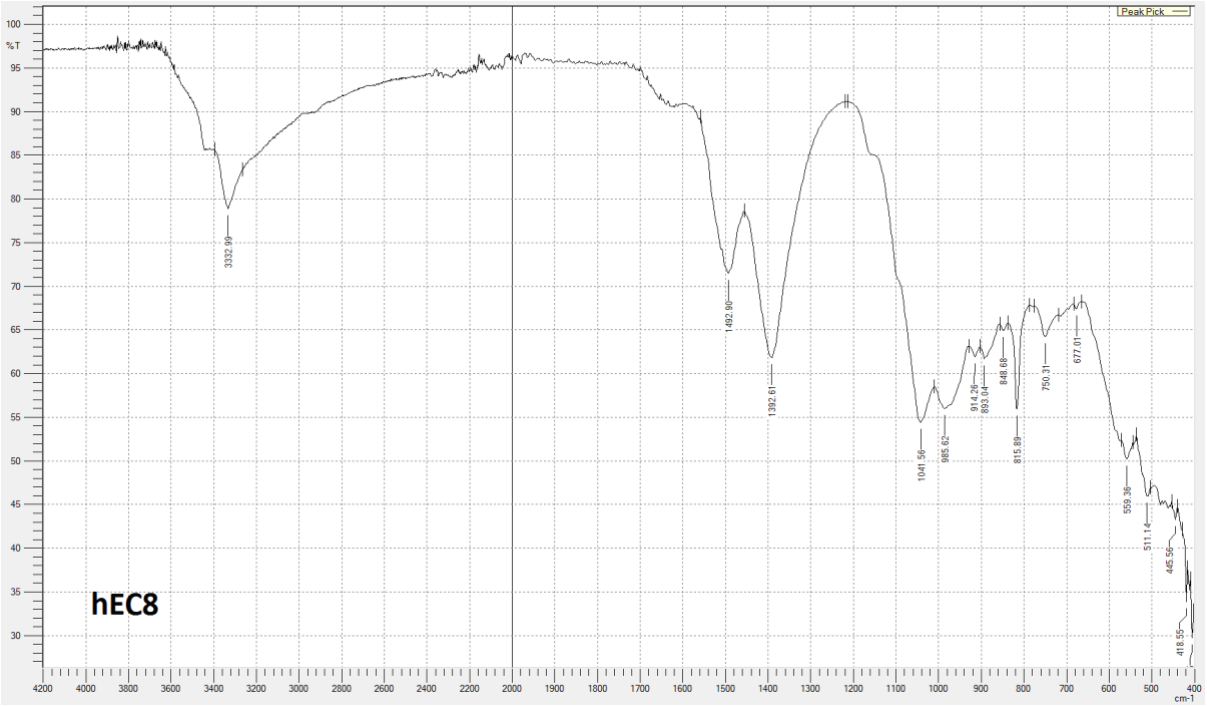

Peak Pick
%T
3404.36
3313.71
2360.87
2343.51
1489.05
1099.43
1045.42
873.75
773.46
750.31
711.73
669.30
572.86
522.71
503.42
482.20
428.27
hEC4
cm-1


Peak Pick
%T
hEC5
1492.90
1392.61
1097.50
1045.42
985.62
948.98
914.20
889.18
867.97
848.69
817.82
750.31
576.72
511.14
478.35
443.63
cm-1

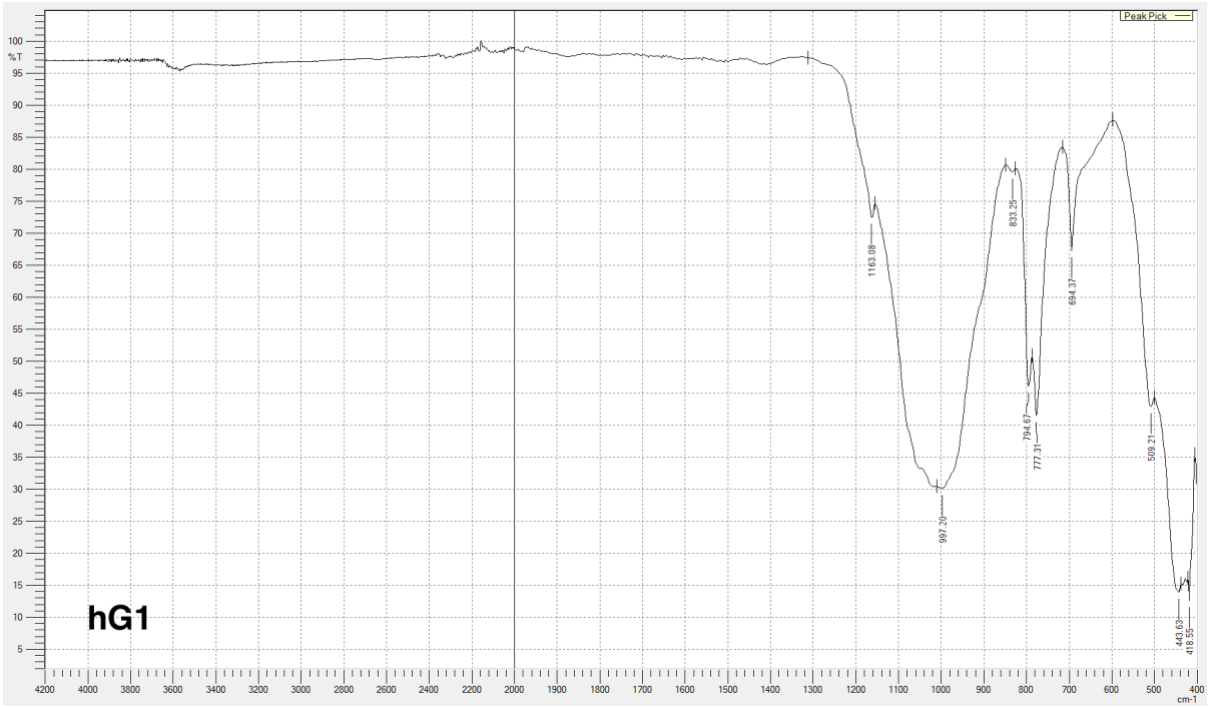

Peak Pick
%T
hEC6
1375.26
927.70
829.39
669.30
cm-1

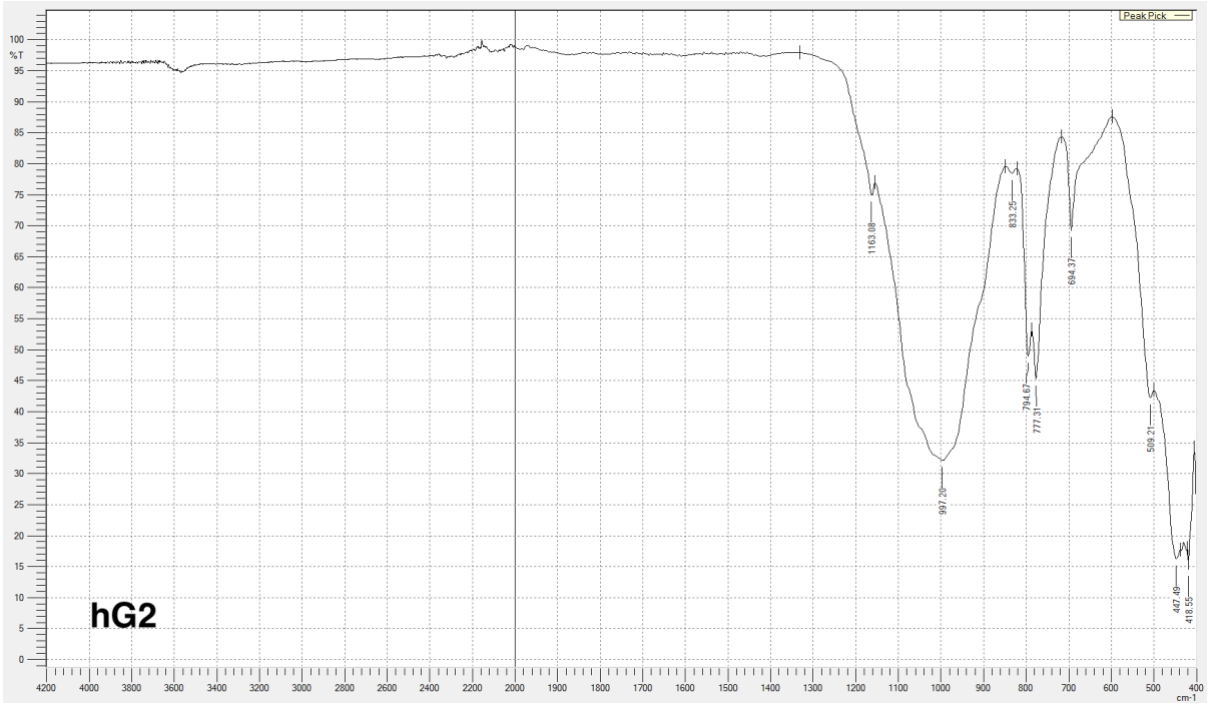

Peak Pick
%T
cm-1
1577.77
1465.90
1382.96
829.69
827.46
669.30
432.05
418.55
hEC6 re-run

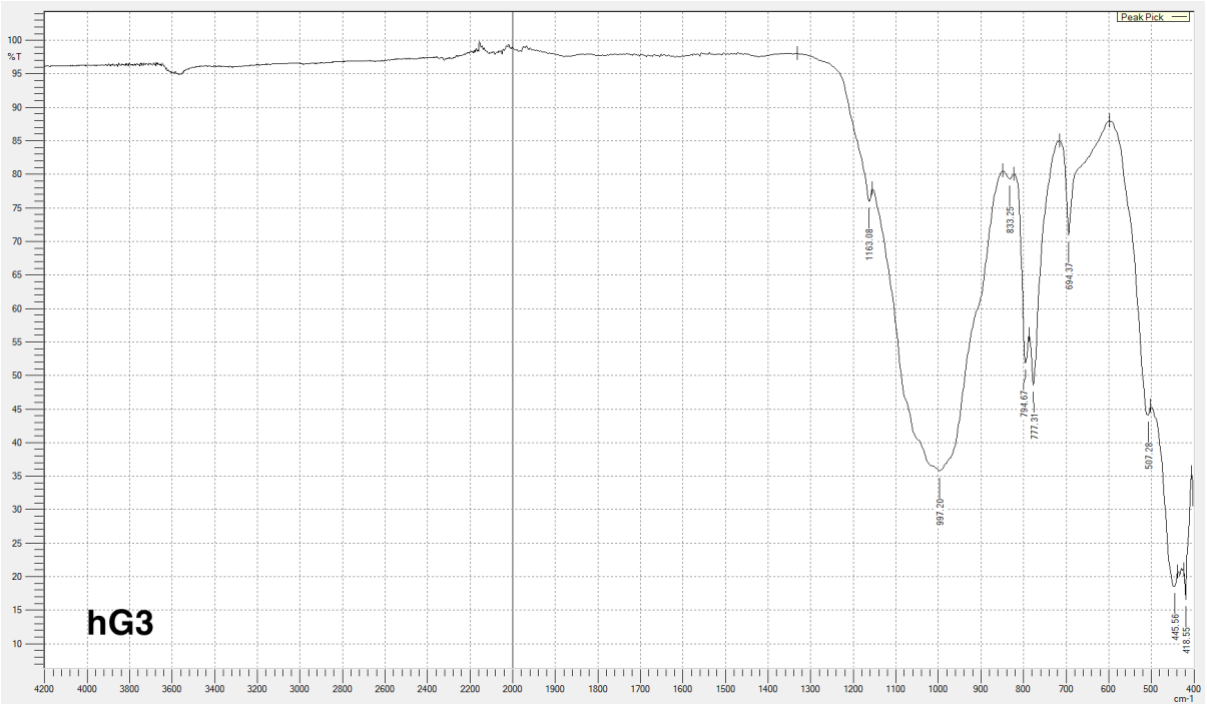

Peak Pick
%T
cm-1
1492.90
1388.75
1097.50
1035.77
873.75
815.89
748.38
711.73
621.08
559.36
497.99
472.56
461.70
hEC7


Peak Pick
%T
hEC8
3332.89
1492.90
1392.61
1041.56
985.62
914.26
893.04
848.68
815.89
750.31
677.01
559.36
511.14
445.56
418.55
cm-1

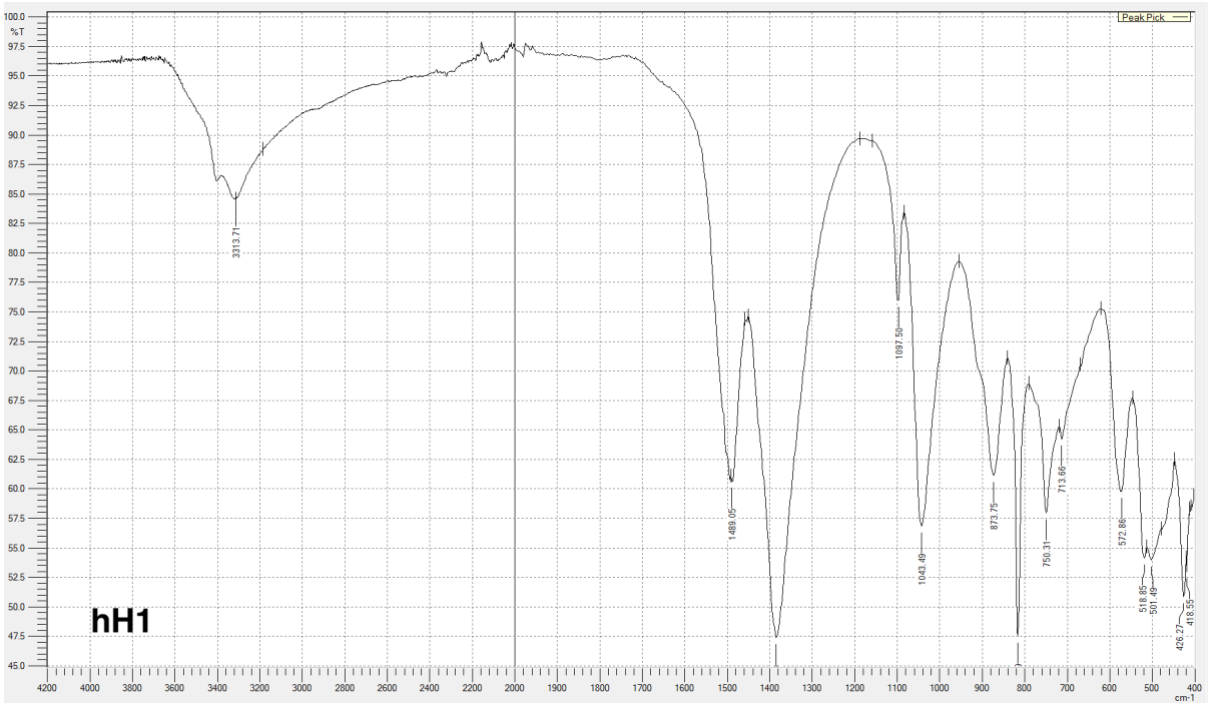
Greece

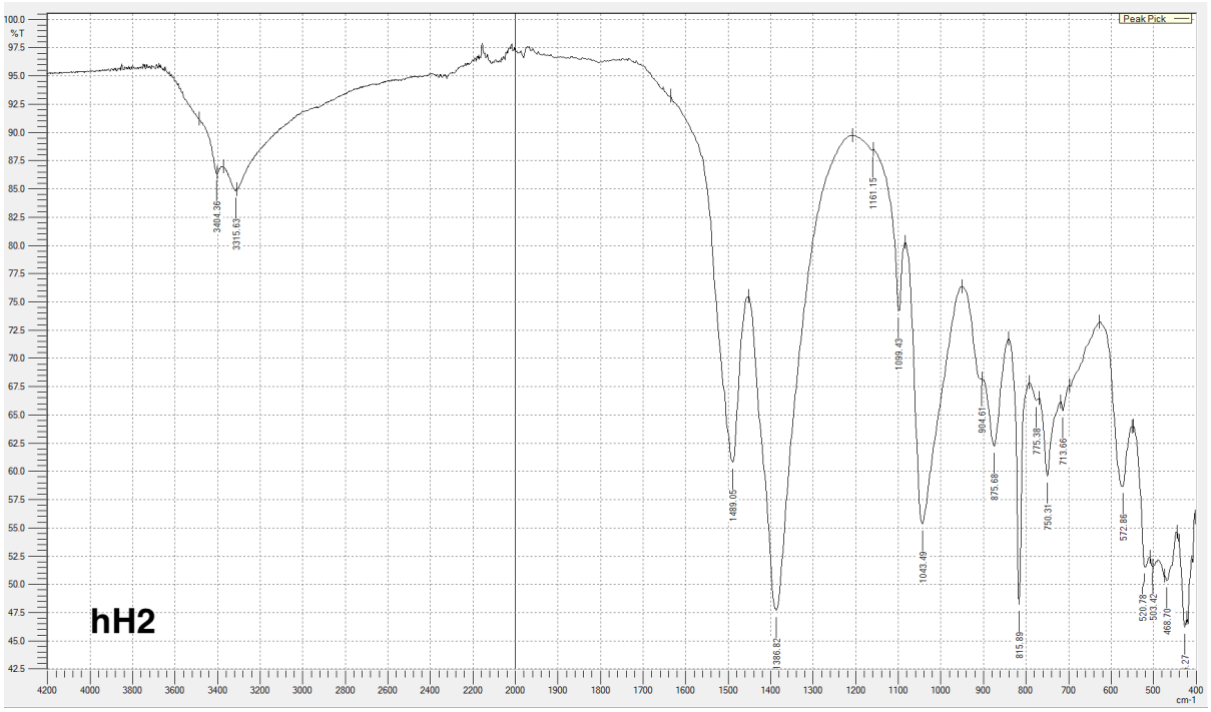

Peak Pick
%T
1163.08
997.20
833.25
794.67
777.31
694.37
509.21
447.63
418.55
hG1
cm-1

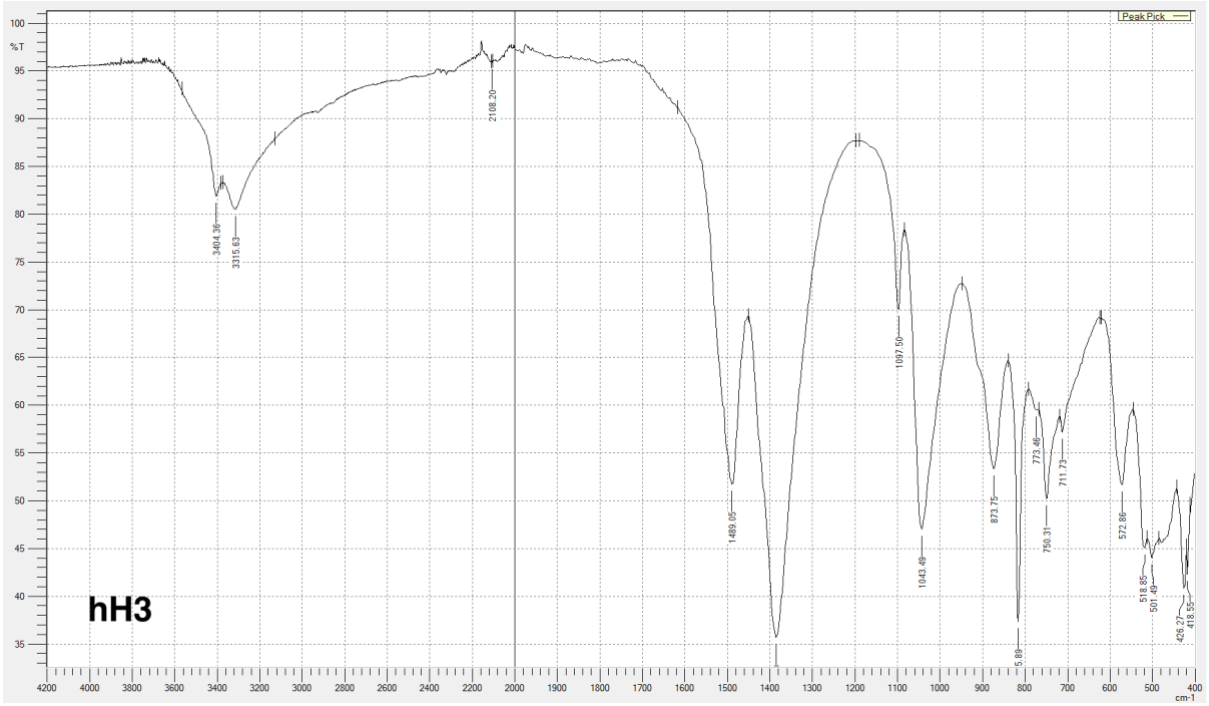

Peak Pick
%T
1163.08
997.20
833.25
794.67
777.31
694.37
509.21
447.49
418.55
hG2
cm-1

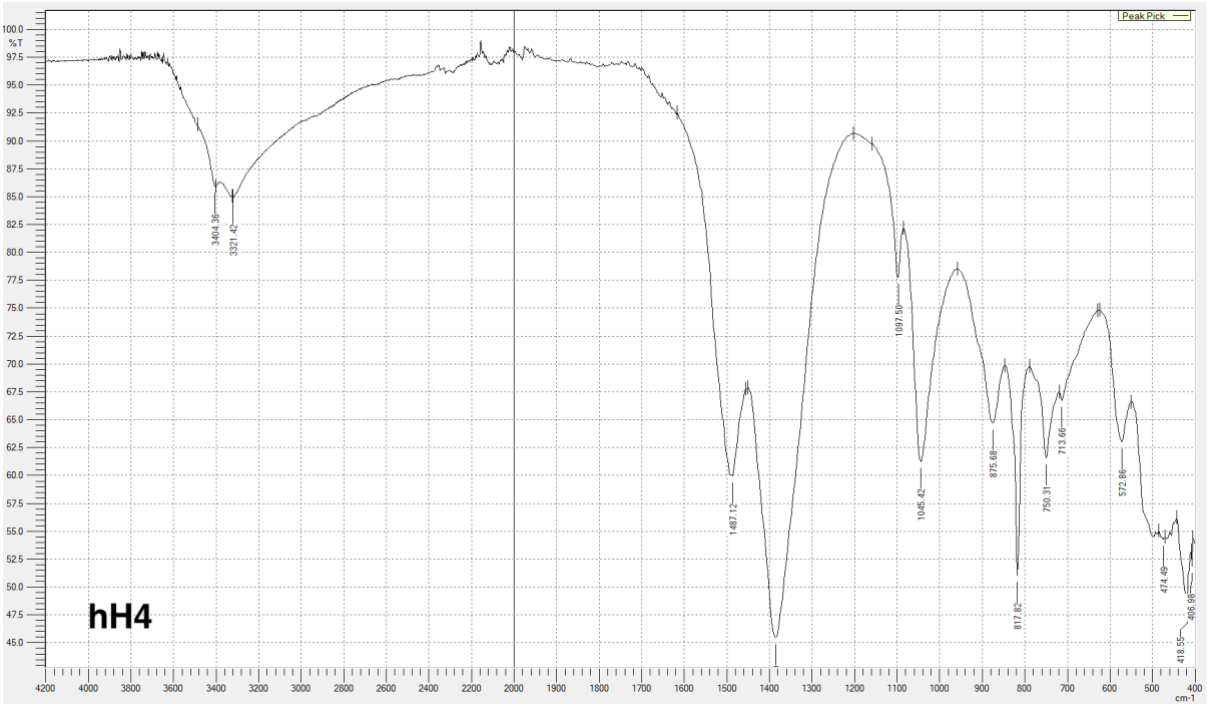

Peak Pick
%T
hG3
1163.08
997.20
833.25
794.67
777.31
694.37
507.28
445.56
418.55
cm-1

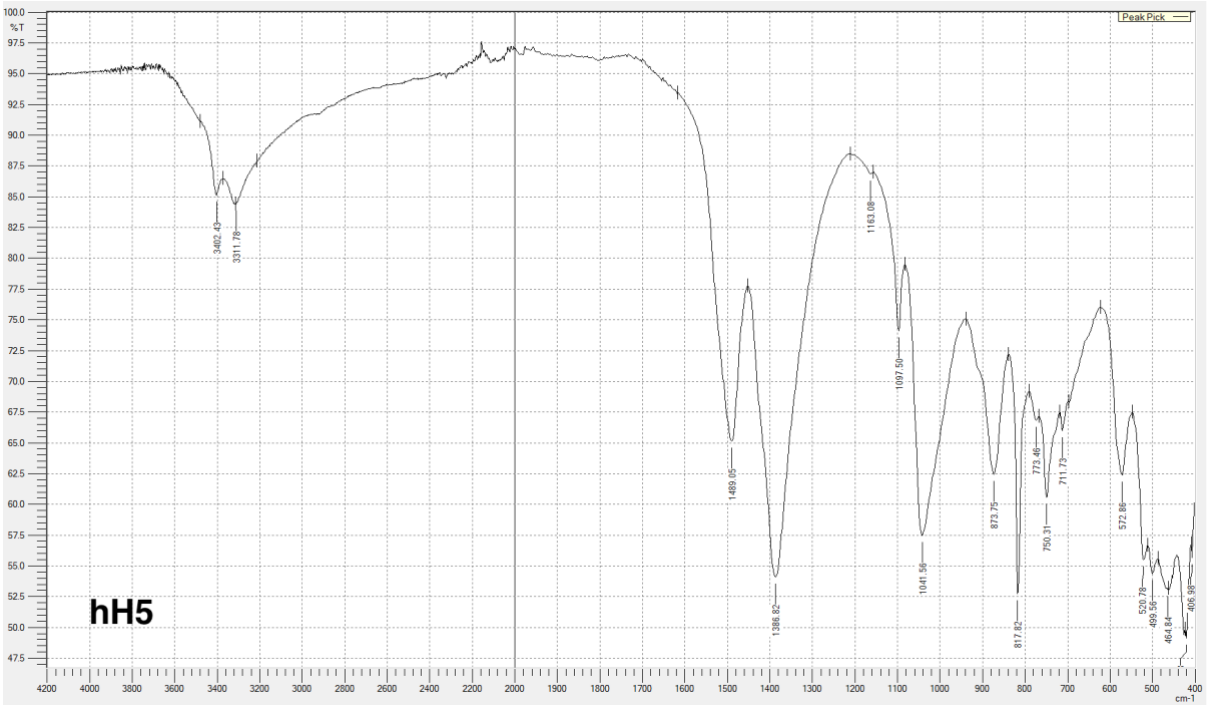
Hungary

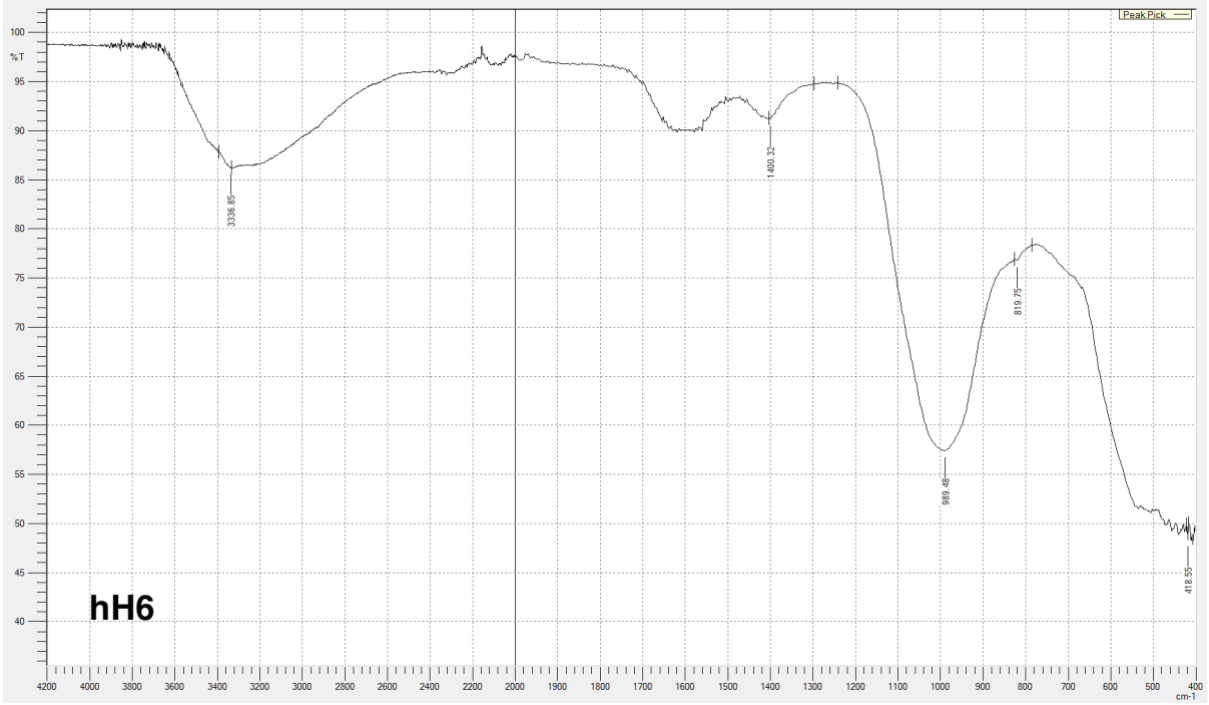

Peak Pick
%T
cm-1
3313.71
1489.05
1097.50
1043.49
873.75
750.31
713.66
572.86
518.85
501.49
426.27
418.55
hH1

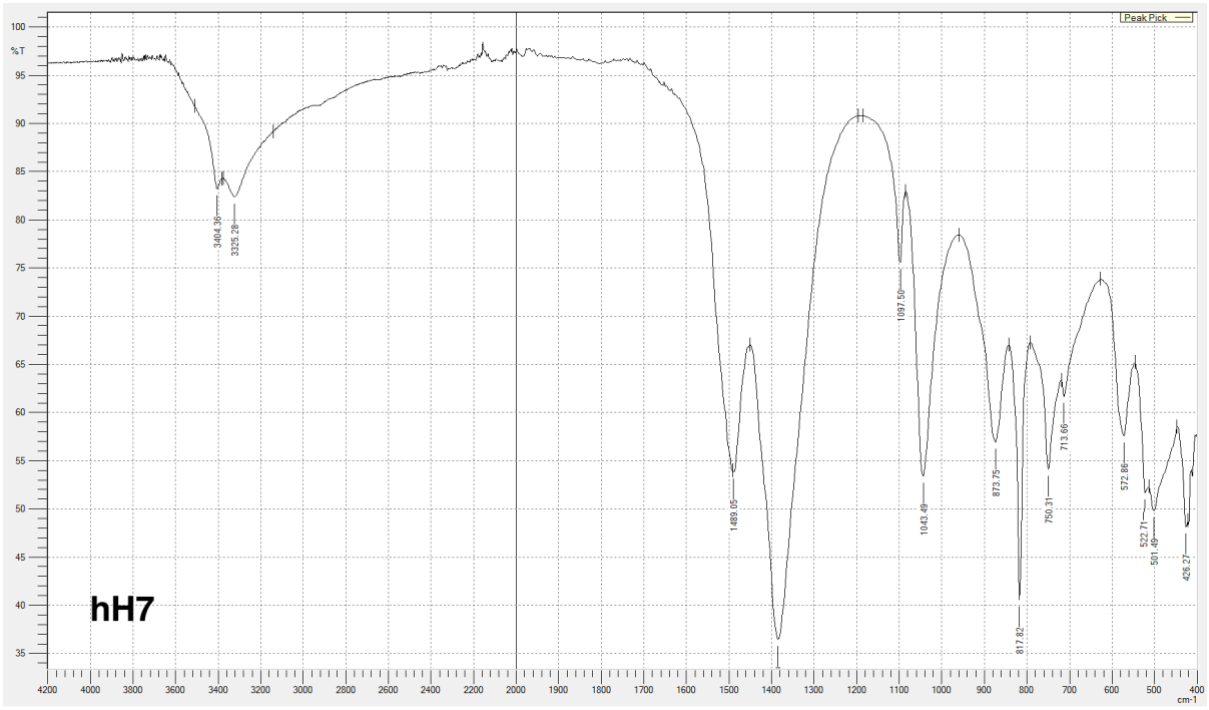

Peak Pick
%T
cm-1
3464.36
3315.63
1161.15
1099.43
1043.49
904.61
875.68
815.89
775.38
750.31
713.66
572.86
520.78
503.42
468.70
386.82
hH2

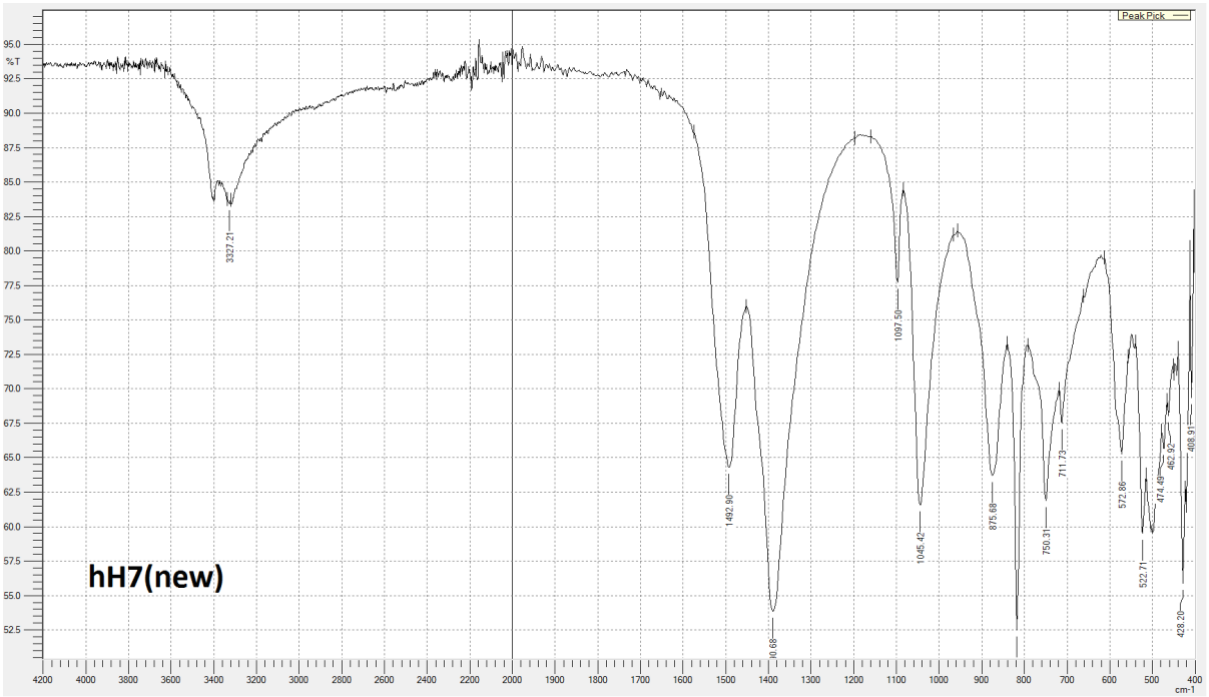

Peak Pick
%T
3404.36
3315.63
2108.20
1489.05
1097.50
1043.49
873.75
773.46
750.31
711.73
572.86
518.85
501.49
426.27
418.55
hH3
cm-1

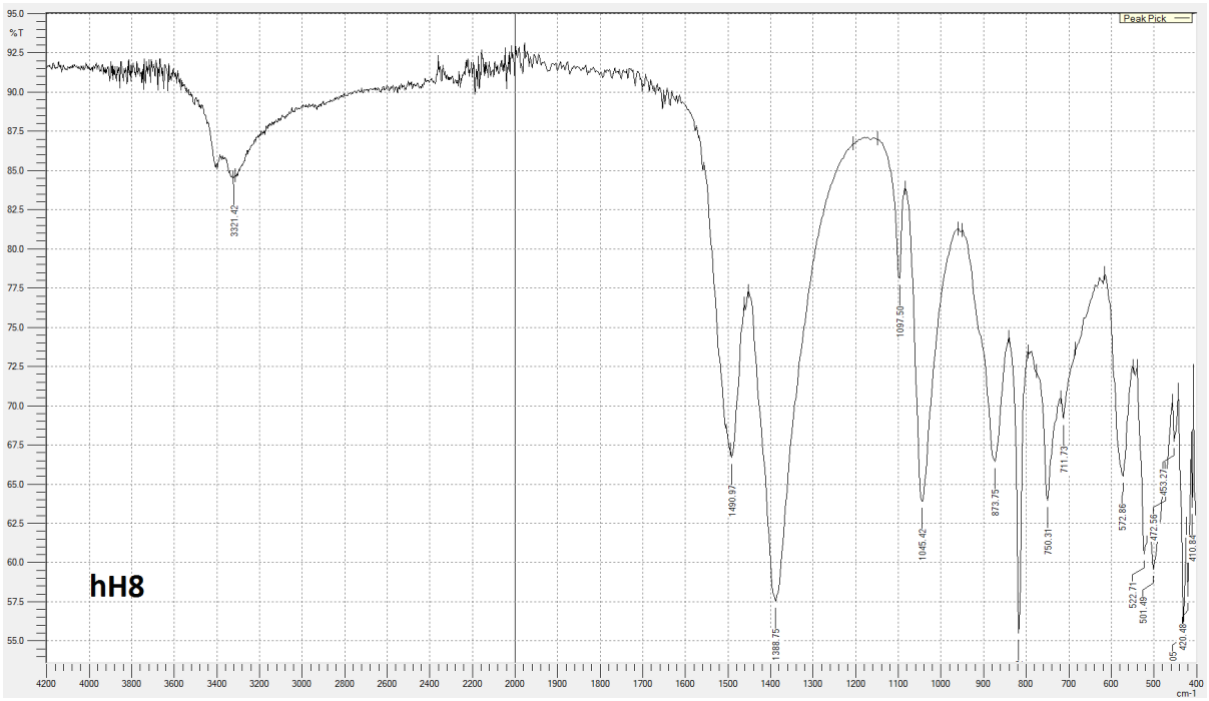

Peak Pick
%T
3404.36
3321.42
1487.12
1097.50
1046.42
875.68
817.82
750.31
713.66
572.86
474.49
406.98
418.55
hH4
cm-1

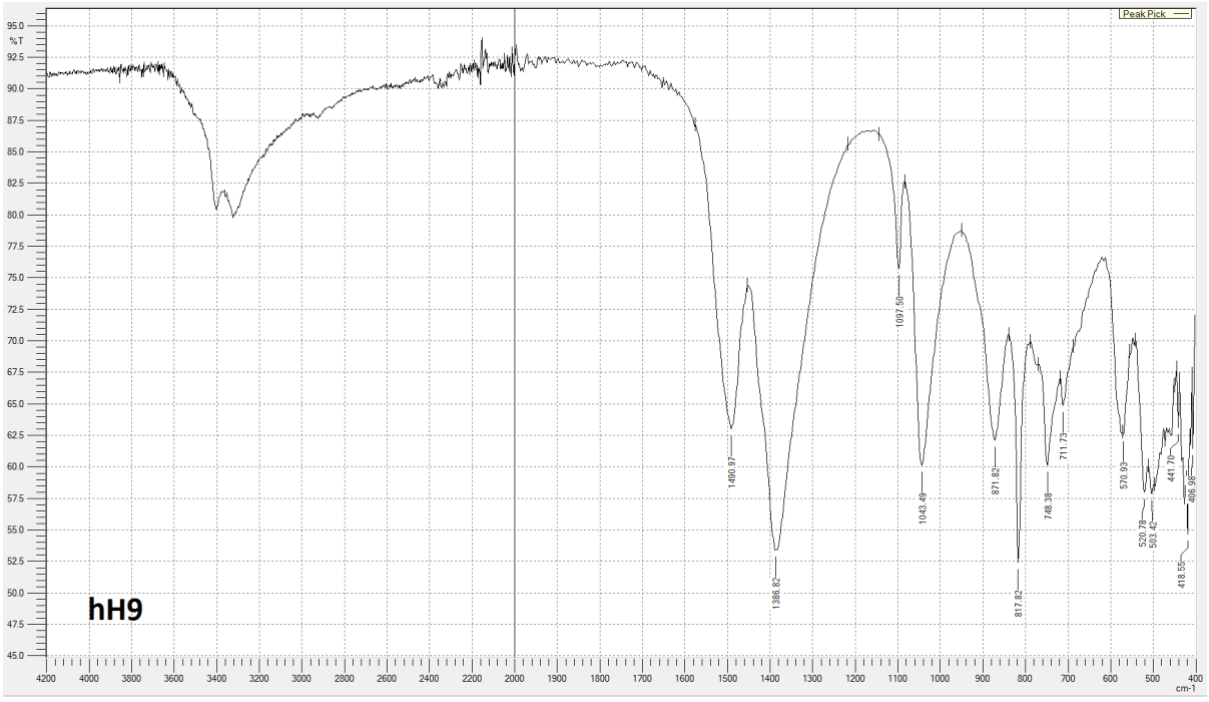

Peak Pick
%T
3402.43
3311.78
1489.05
1386.82
1163.08
1097.50
1041.56
873.75
817.82
773.46
750.31
711.73
572.86
520.78
495.56
464.84
406.98
hH5
cm-1

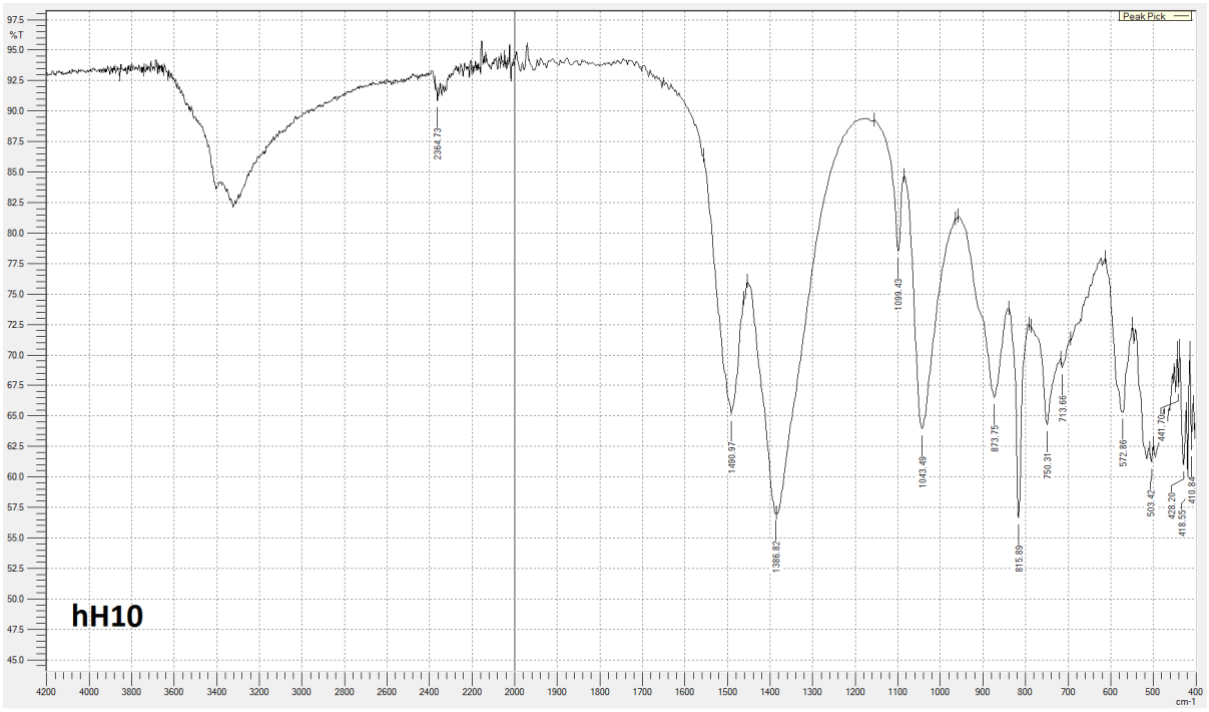

Peak Pick
%T
3336.85
1400.32
989.48
819.75
418.55
hH6
cm-1

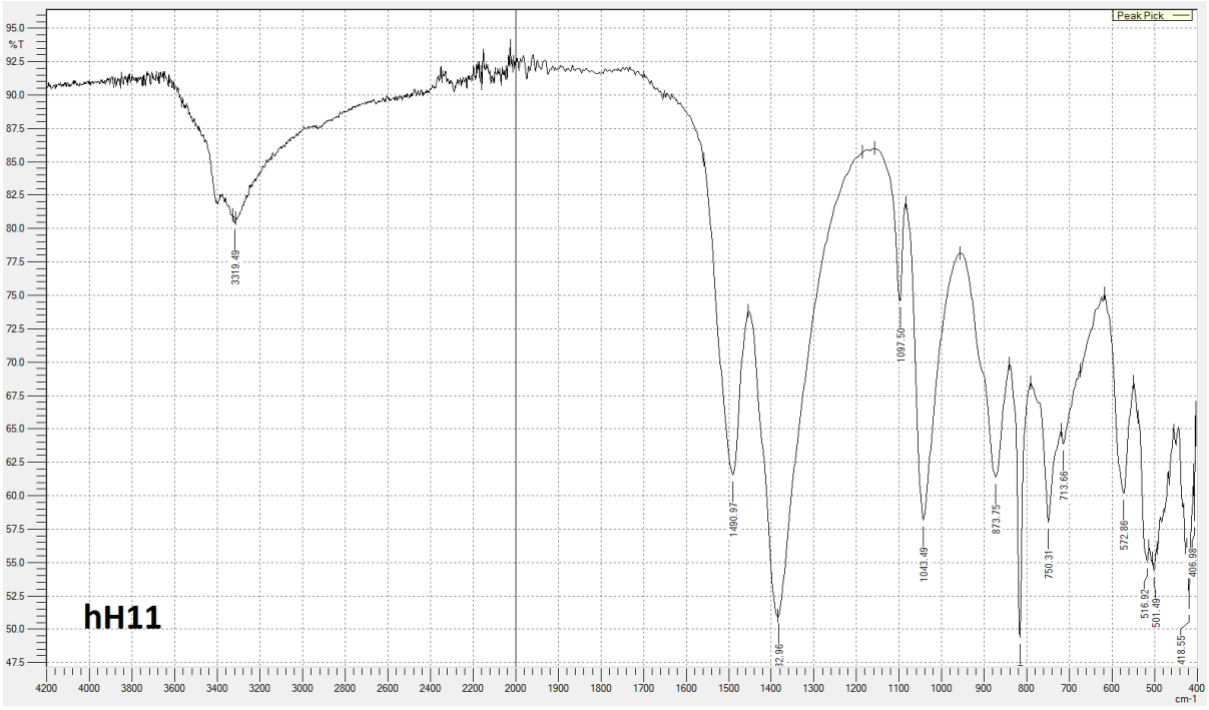

Peak Pick
%T
3404.36
3325.28
1489.05
1097.50
1043.49
873.75
817.82
750.31
713.66
572.86
522.71
501.49
426.27
hH7
cm-1


Peak Pick
%T
3327.21
1492.90
1097.50
1045.42
875.68
750.31
711.73
572.86
522.71
474.49
462.92
428.20
hH7(new)
cm-1

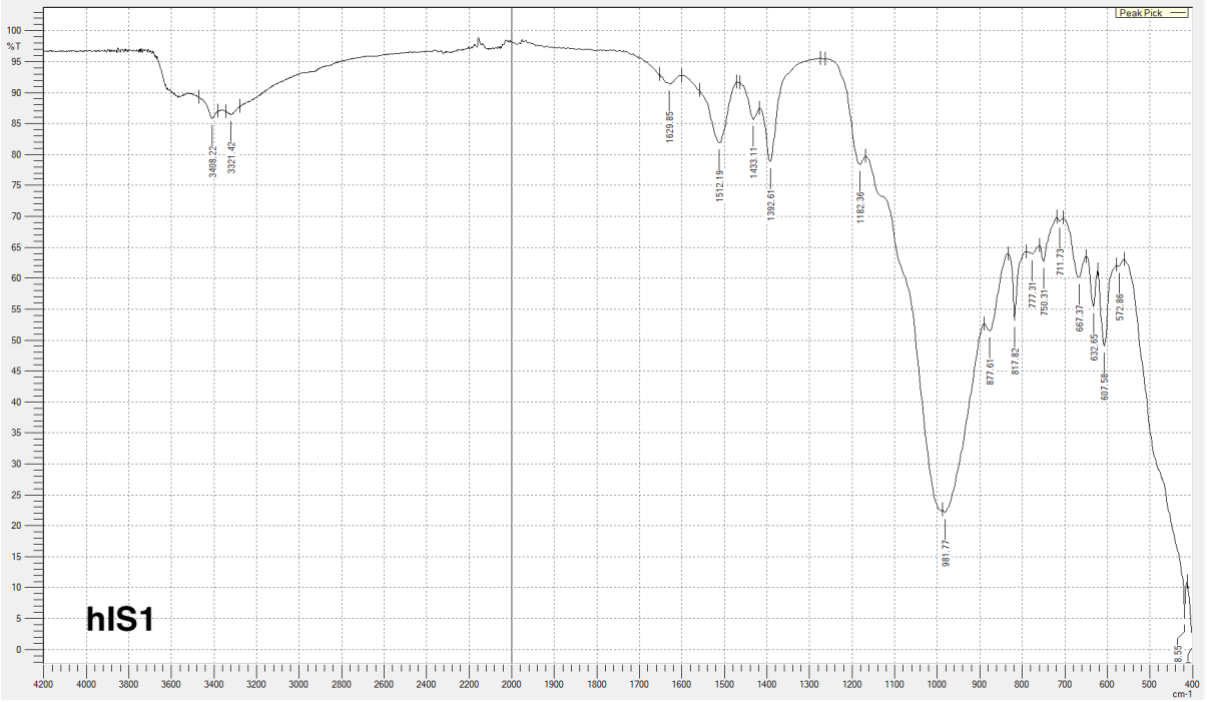

Peak Pick
%T
cm-1
hH8
3321.42
1490.97
1388.75
1097.50
1045.42
873.75
750.31
711.73
572.86
522.71
501.49
453.27
420.48

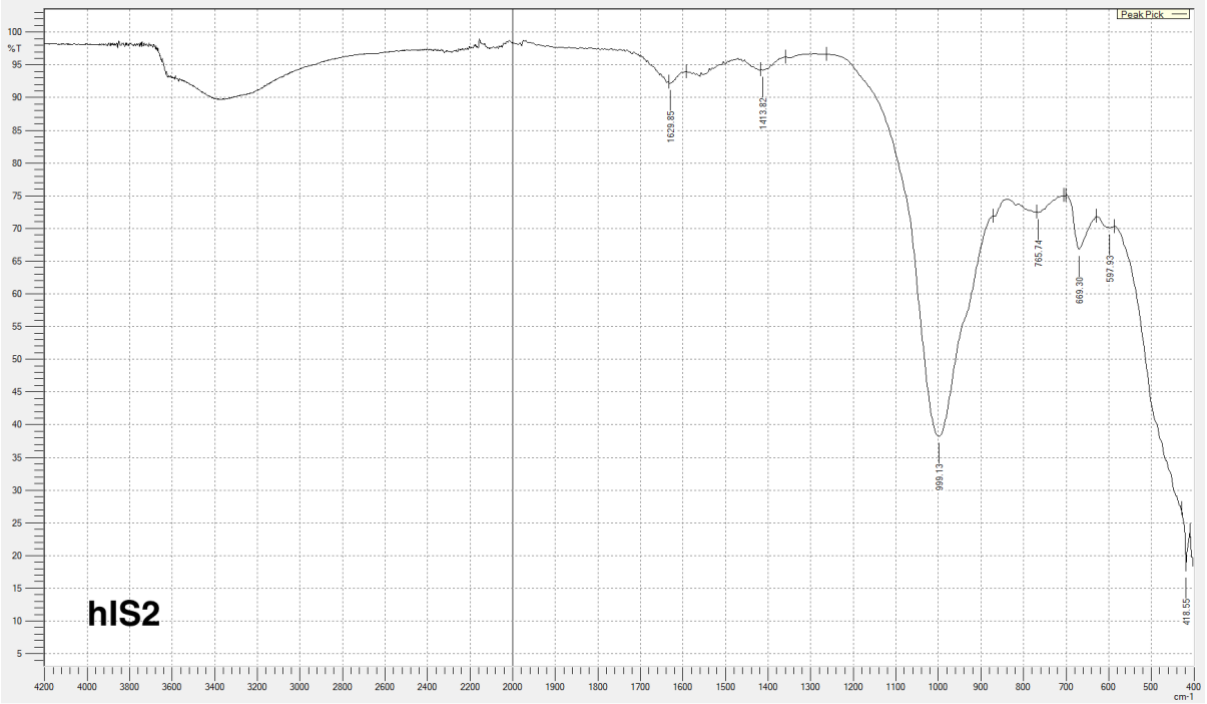

Peak Pick
%T
cm-1
hH9
1490.97
1386.82
1097.50
1043.49
871.82
817.82
748.39
711.73
570.93
520.78
503.42
441.70
418.55

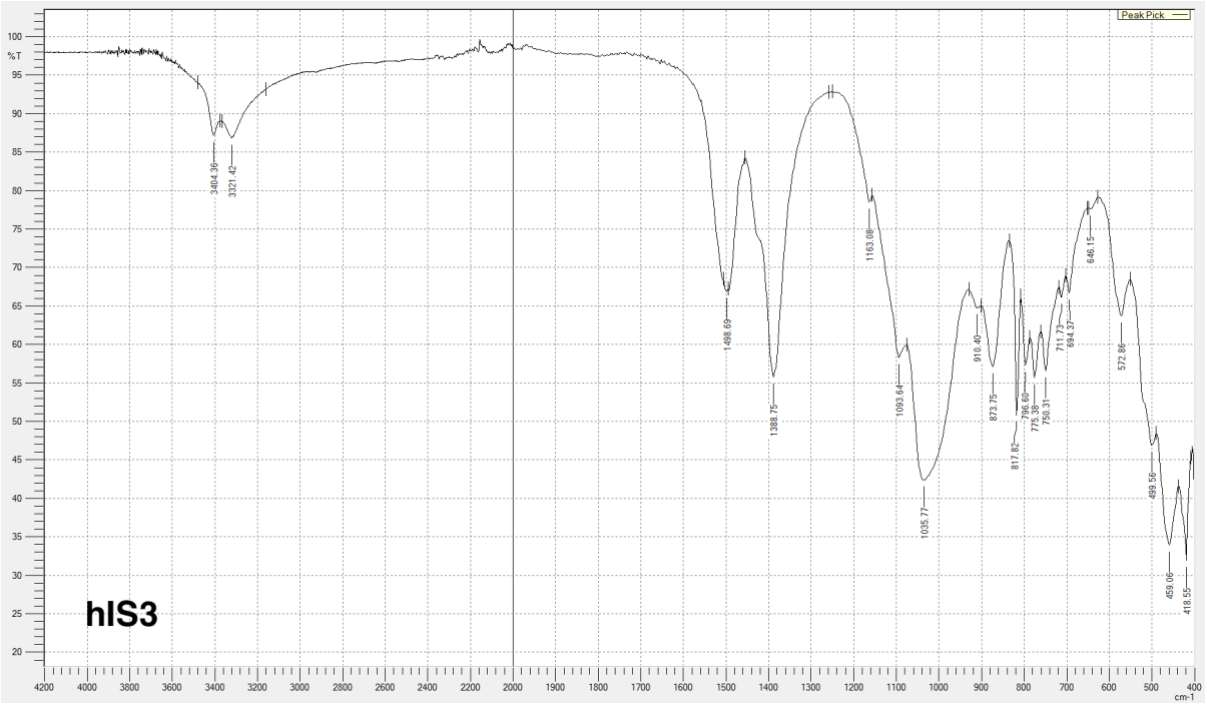

Peak Pick
%T
2364.73
1490.97
1386.82
1099.43
1043.49
873.75
815.89
750.31
713.66
572.86
503.42
441.70
428.26
418.55
410.84
hH10
cm-1


Peak Pick
%T
3319.49
1490.97
1386.96
1097.50
1043.49
873.75
750.31
713.66
572.86
516.92
501.49
418.55
406.98
hH11
cm-1

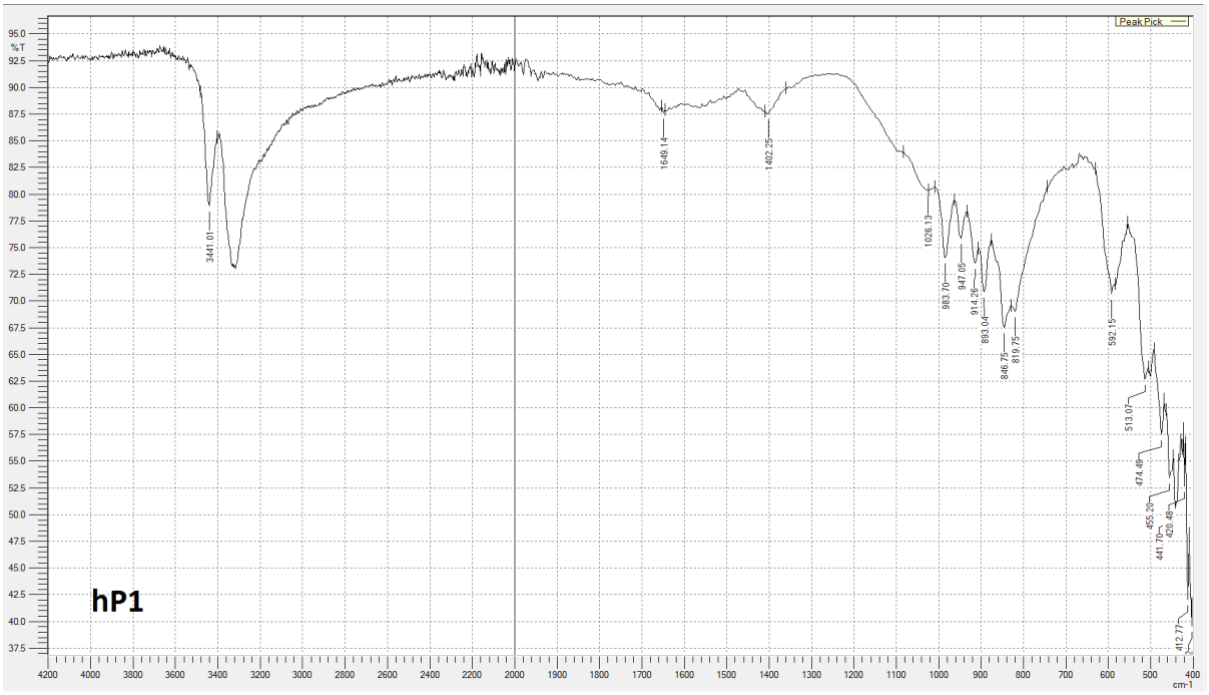
Italy

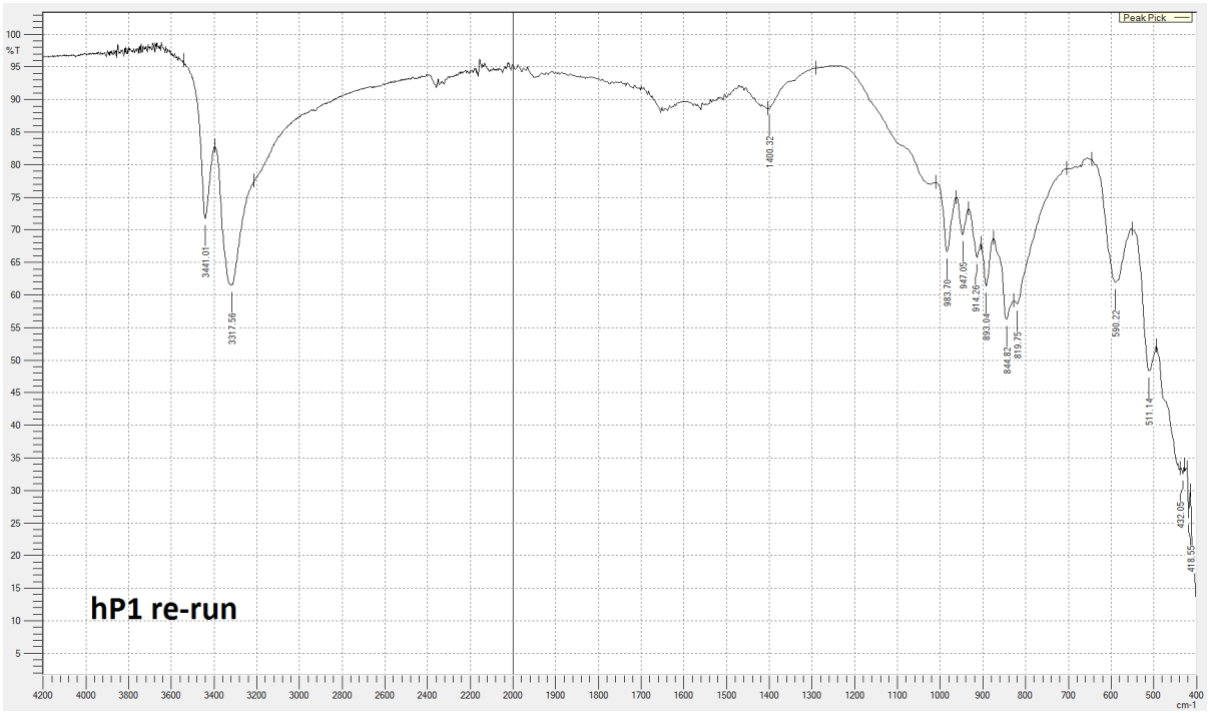

Peak Pick
%T
3468.22
3321.42
1629.85
1512.19
1433.11
1392.61
1182.36
991.77
877.61
817.82
777.31
750.31
711.73
667.37
632.65
607.58
572.86
hIS1
cm-1

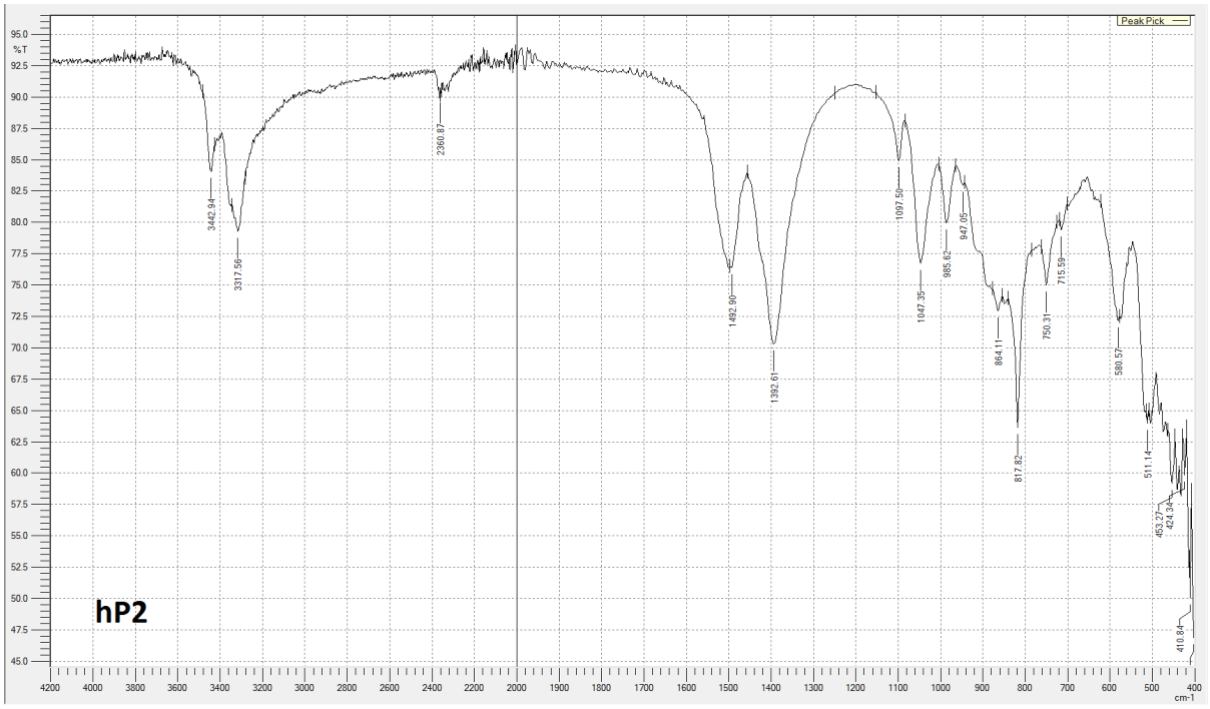

Peak Pick
%T
1629.85
1413.82
999.13
765.74
669.30
597.93
418.55
hIS2
cm-1

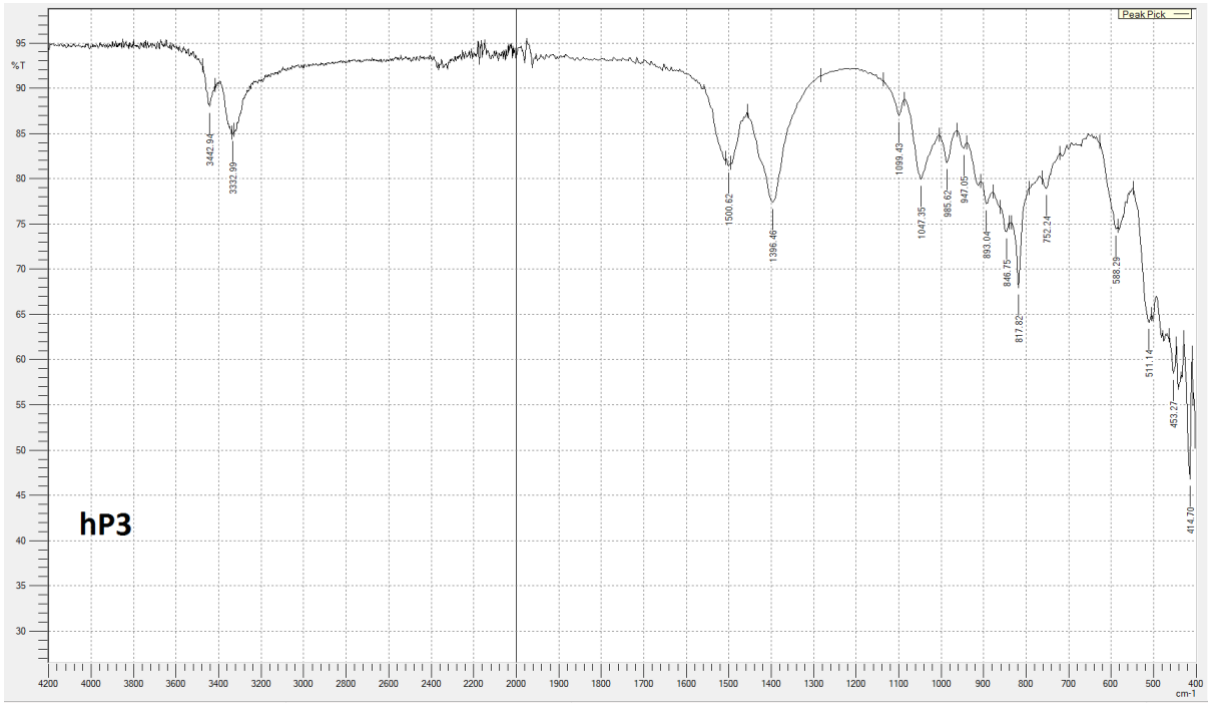

Peak Pick
%T
hIS3
3404.36
3321.42
1466.69
1388.75
1163.08
1093.64
1035.77
910.40
873.75
817.82
796.60
775.38
750.31
711.73
694.37
646.15
572.86
499.56
459.06
418.55
cm-1

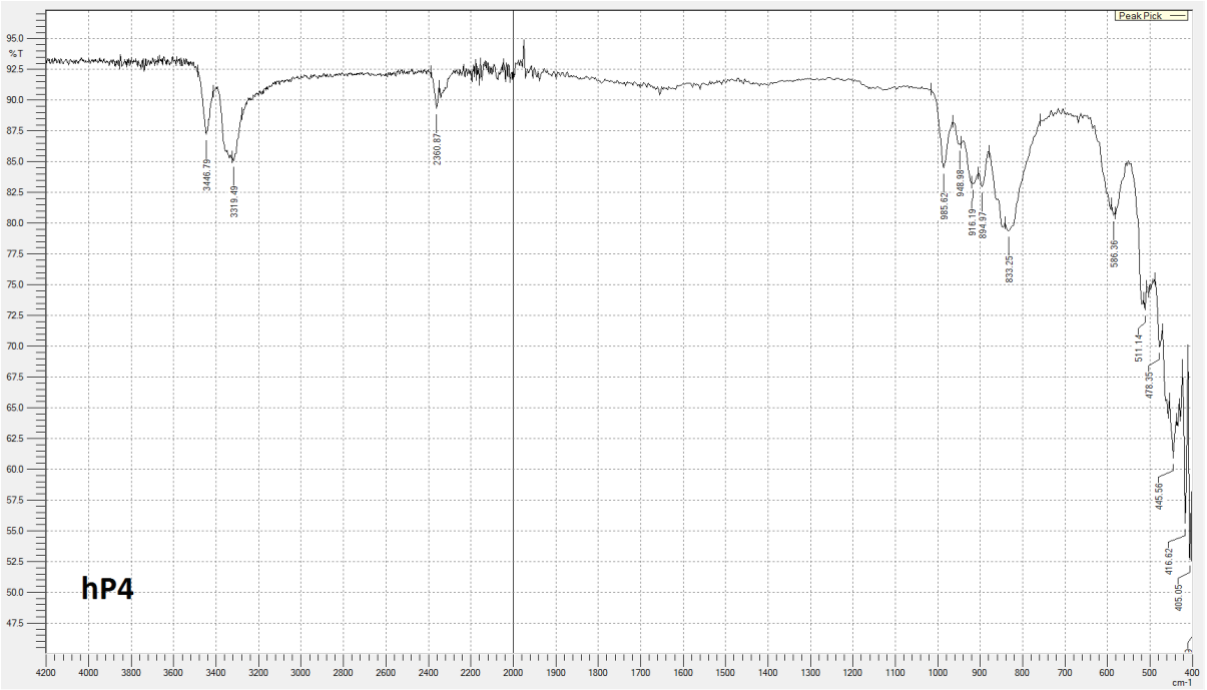
Peru

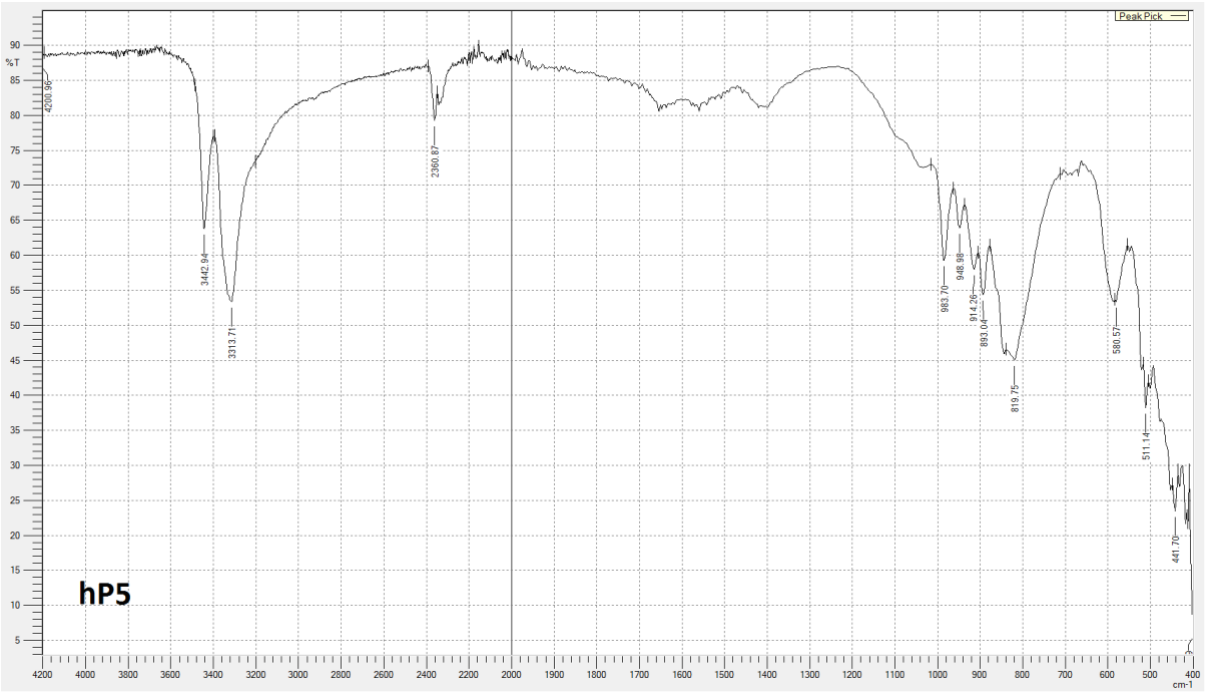

Peak Pick
%T
3441.01
1649.14
1402.25
1026.13
983.70
947.05
914.26
893.04
846.75
819.75
592.15
513.07
474.49
455.29
441.70
420.48
412.77
cm-1
hP1

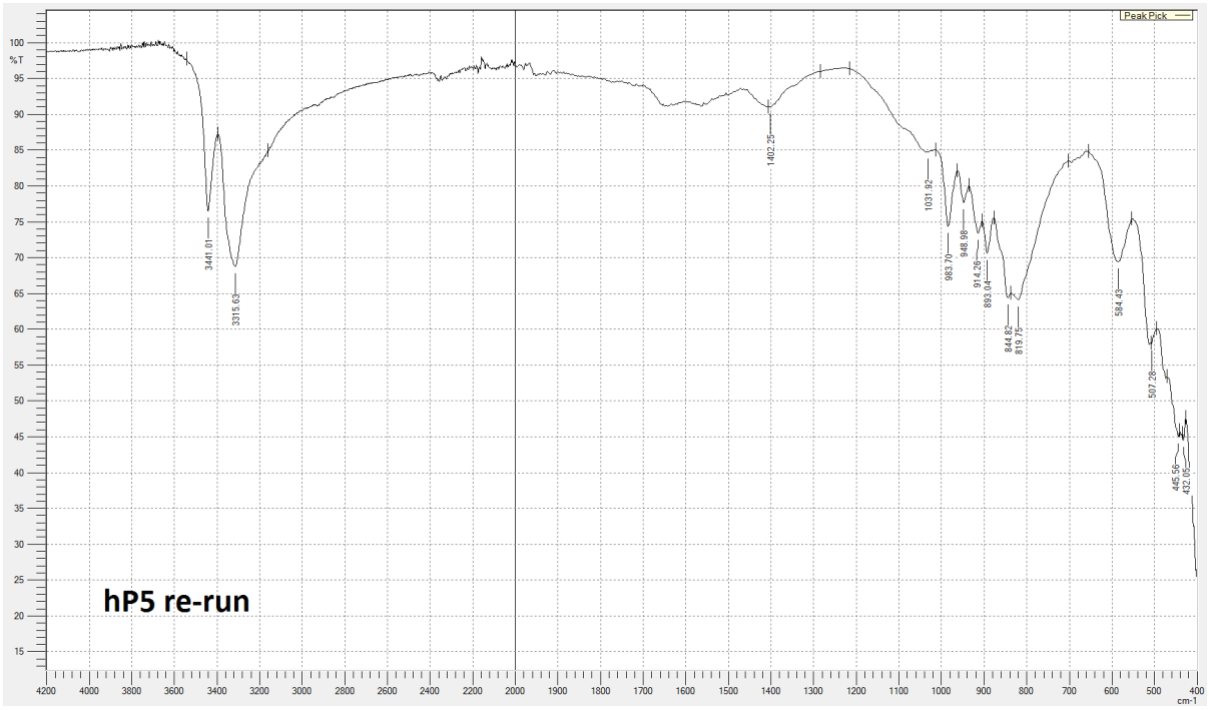

Peak Pick
%T
3441.01
3317.56
1400.32
983.70
947.05
914.26
893.04
844.82
819.75
590.22
511.14
432.05
418.55
cm-1
hP1 re-run

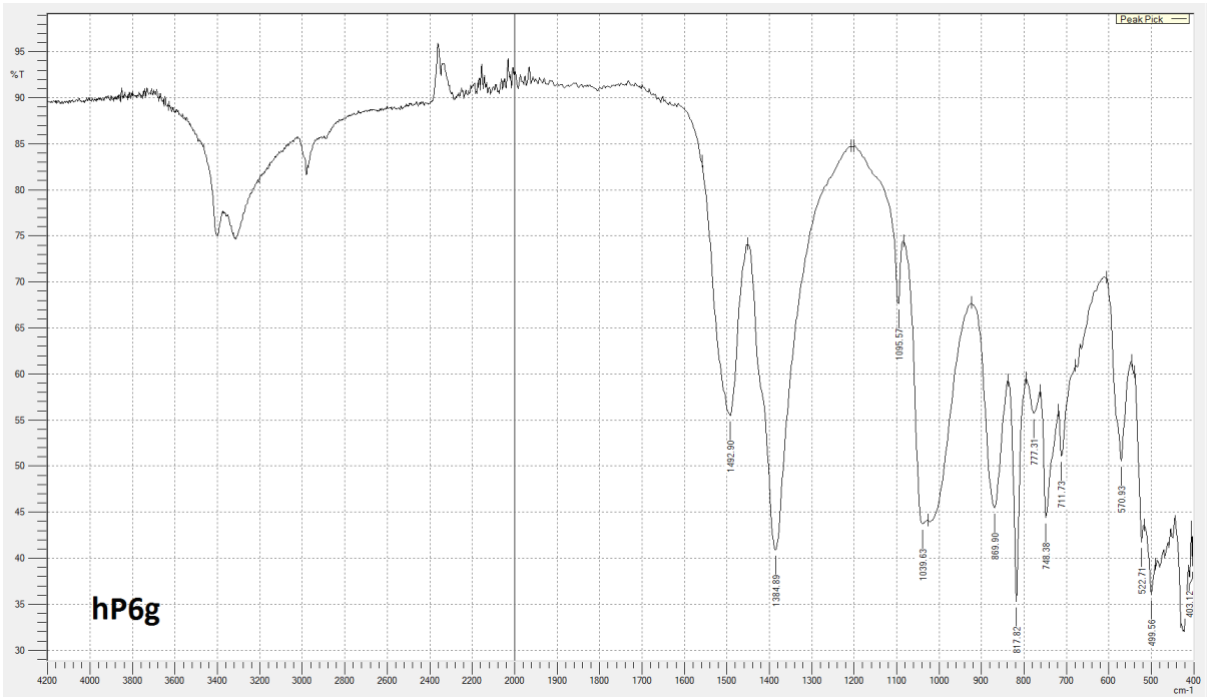

Peak Pick
%T
3442.94
3317.56
2360.87
1492.90
1392.61
1097.50
1047.35
985.62
947.05
864.11
817.82
750.31
715.59
580.57
511.14
453.27
424.34
410.84
hP2
cm-1

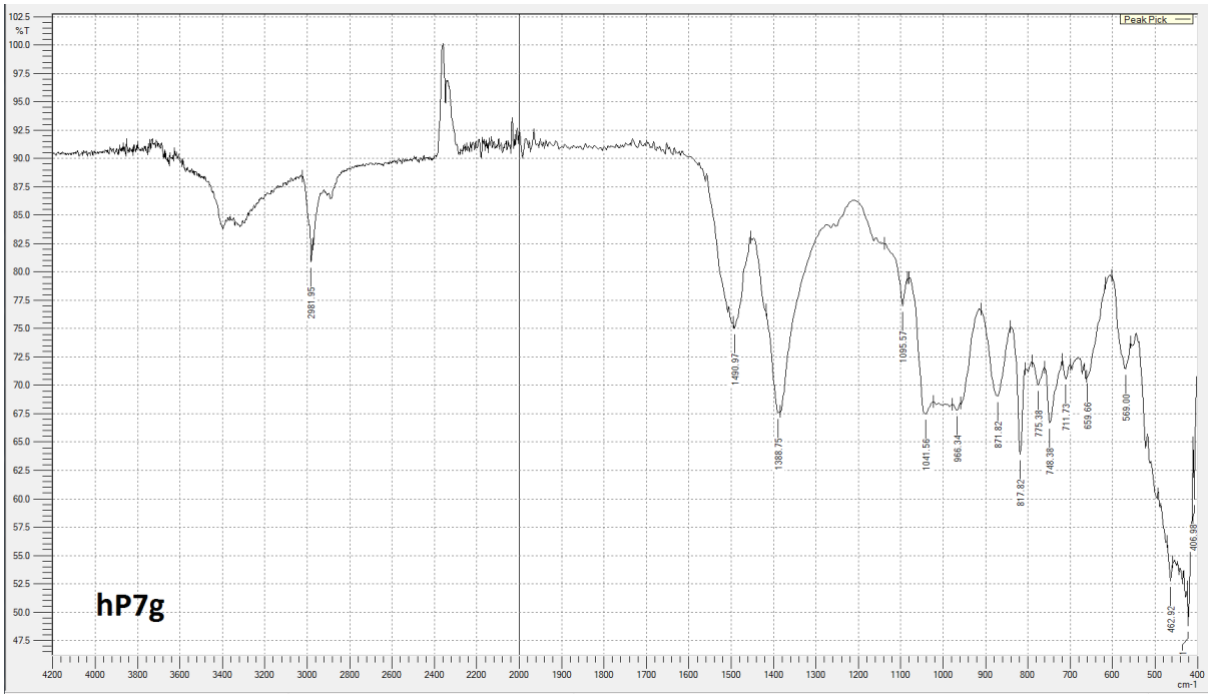

Peak Pick
%T
3442.94
3332.99
1500.62
1396.46
1099.43
1047.35
985.62
947.05
893.04
846.75
817.82
752.24
588.29
511.14
453.27
414.70
hP3
cm-1


Peak Pick
%T
3446.79
3319.49
2360.87
985.62
948.98
916.19
894.97
833.25
586.36
511.14
478.35
445.59
416.82
405.05
hP4
cm-1

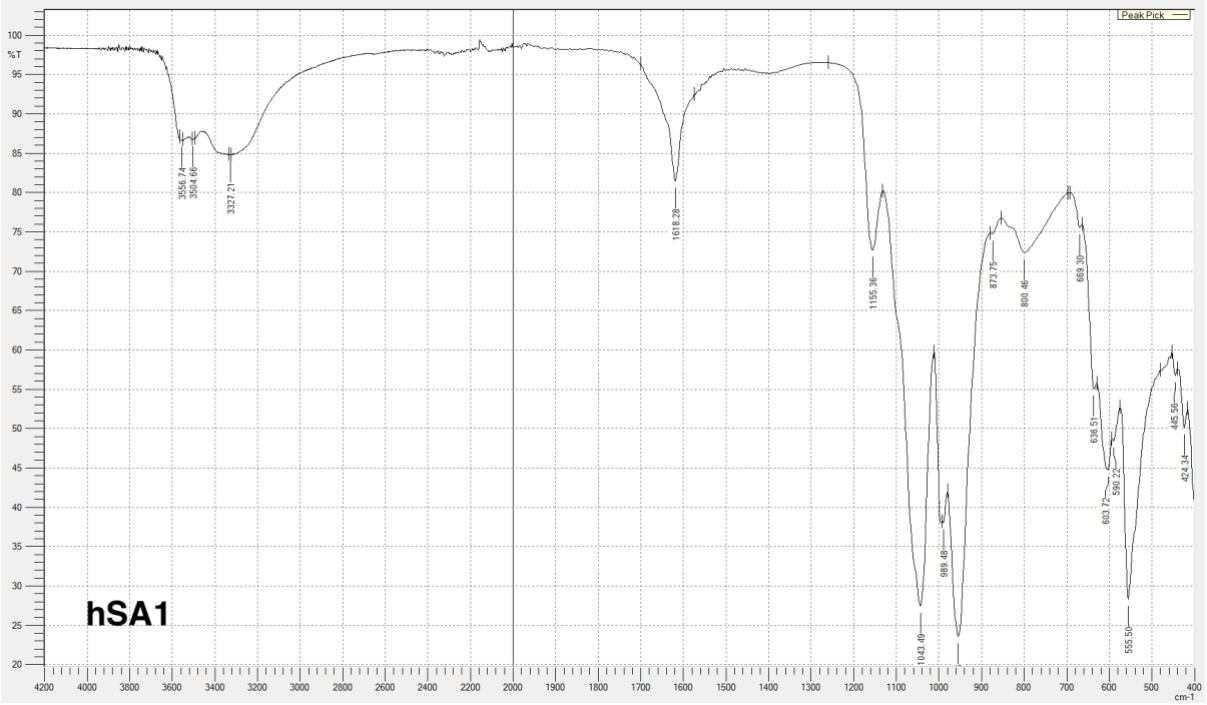

Peak Pick
%T
4200.96
3442.94
3313.71
2360.87
983.70
948.98
914.26
893.04
819.75
580.57
511.14
441.70
hP5
cm-1

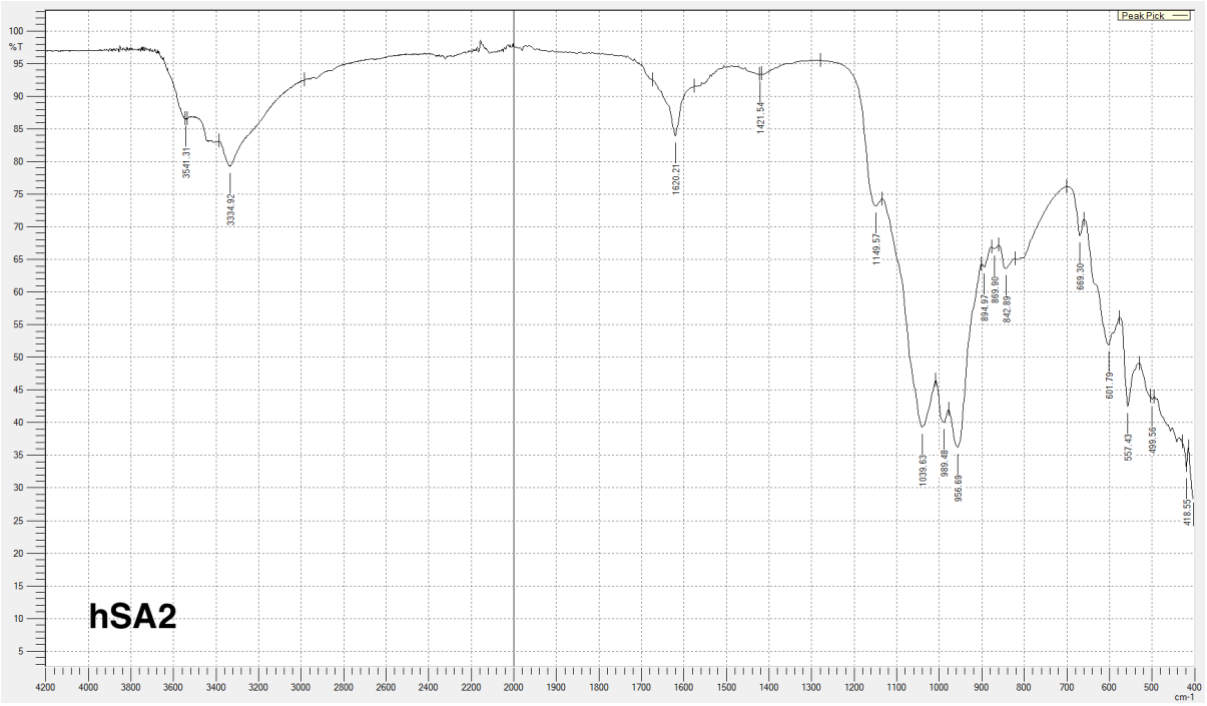

Peak Pick
%T
3441.01
3315.63
1402.25
1031.82
983.70
948.98
914.26
893.04
844.82
819.75
584.43
507.28
445.56
432.05
hP5 re-run
cm-1

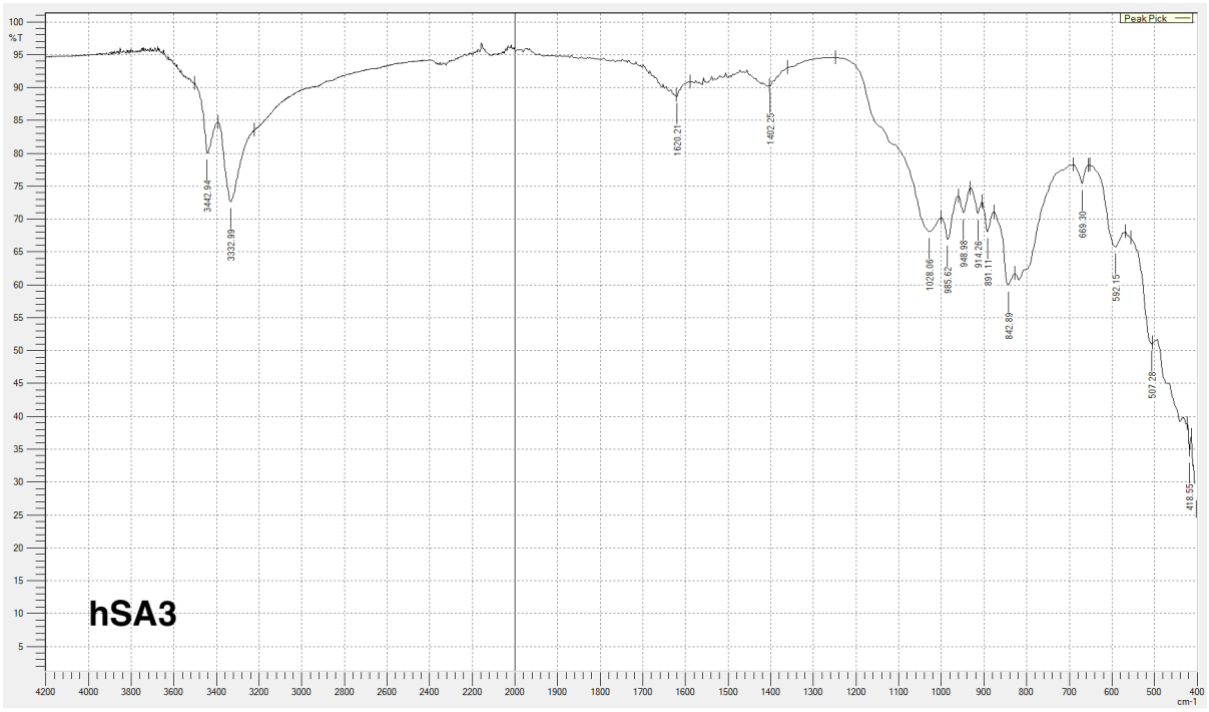

Peak Pick
%T
1492.90
1384.89
1095.57
1039.63
869.90
817.82
777.31
748.38
711.73
570.93
522.71
499.56
403.12
hP6g
cm-1

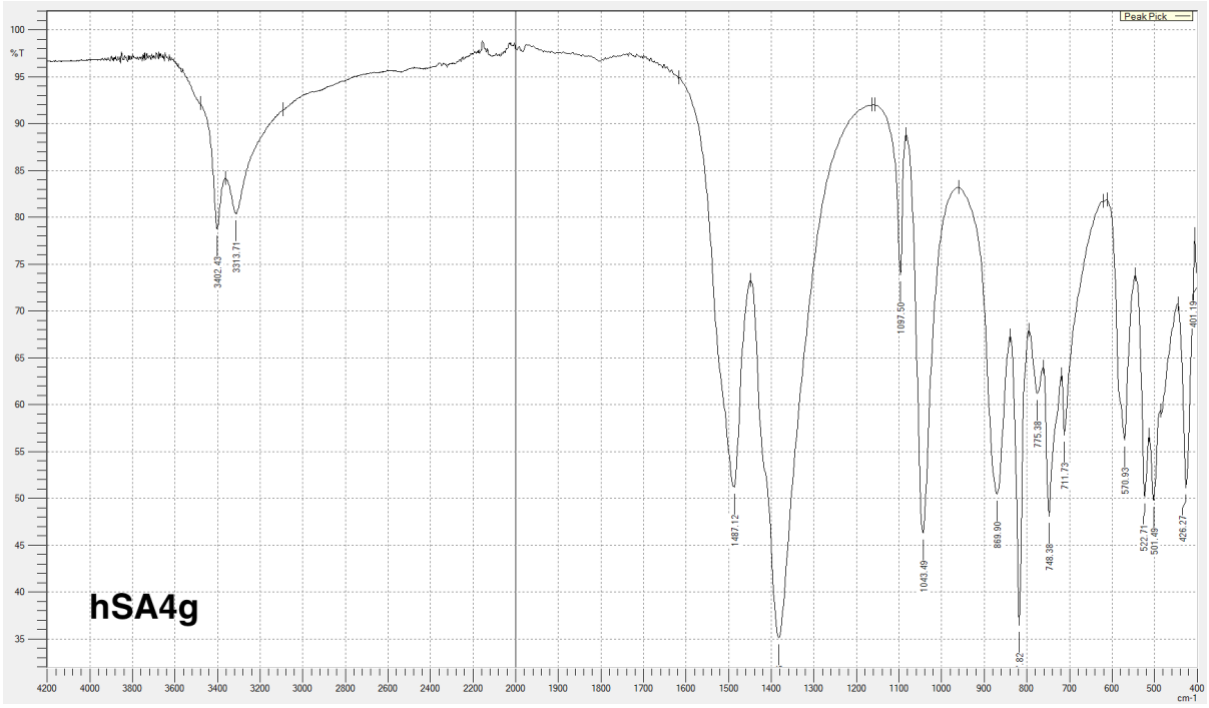

Peak Pick
%T
2981.95
1490.97
1388.75
1095.57
1041.56
966.34
871.82
817.82
775.39
748.38
711.73
659.66
569.00
462.92
406.98
hP7g
cm-1

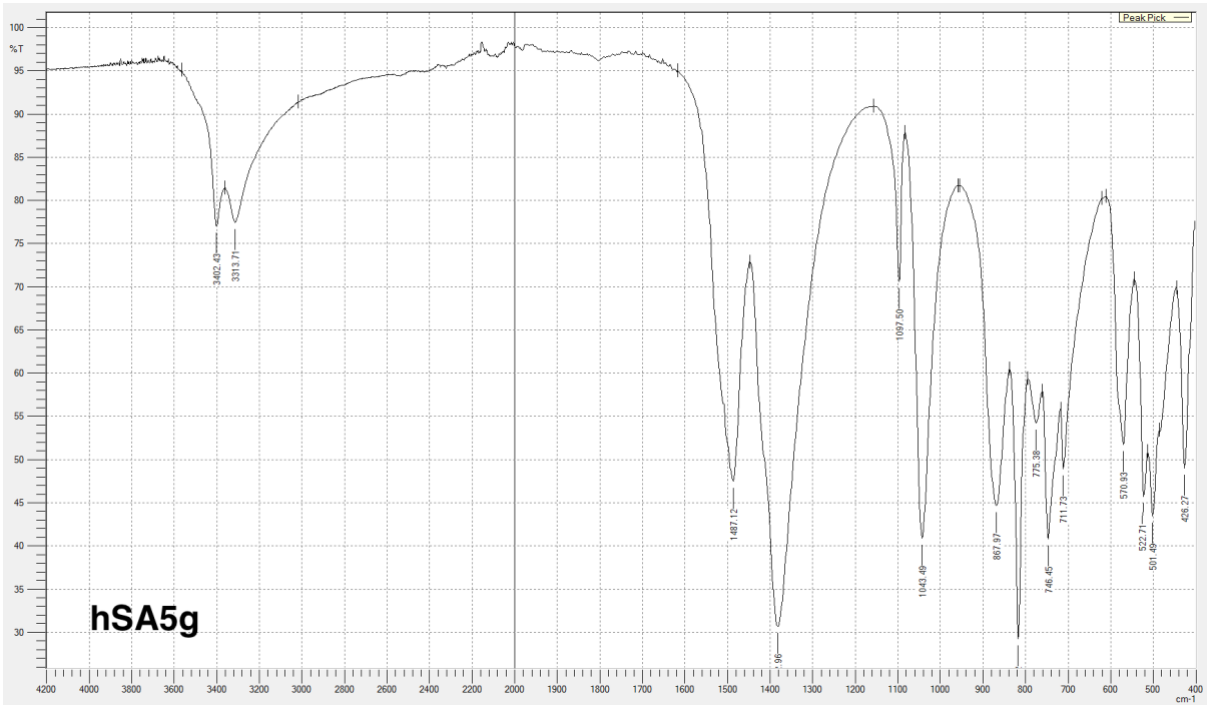
Spain

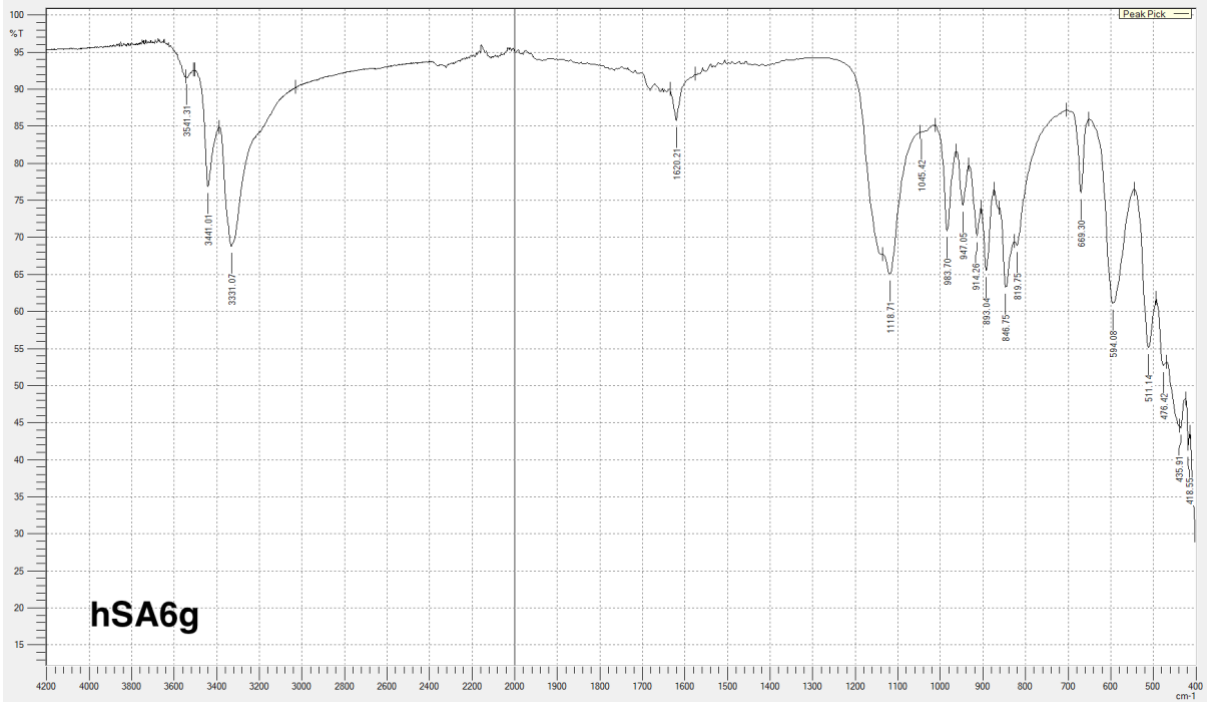

Peak Pick
%T
3556.74
3504.66
3327.21
1618.28
1155.36
1043.49
989.48
873.75
800.46
669.30
636.51
603.72
590.22
555.50
445.56
424.34
hSA1
cm-1

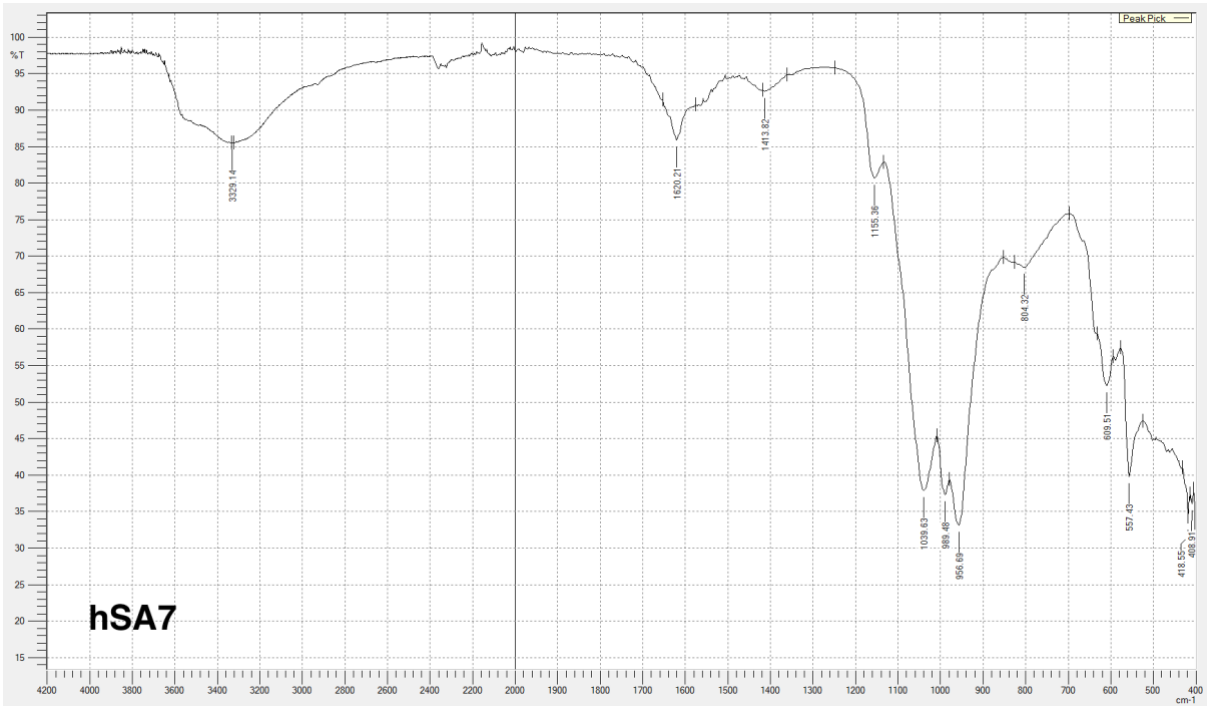

Peak Pick
%T
3541.31
3334.92
1620.21
1421.54
1149.57
1039.63
989.48
956.69
894.97
869.90
842.89
669.30
601.79
557.43
459.56
418.55
hSA2
cm-1

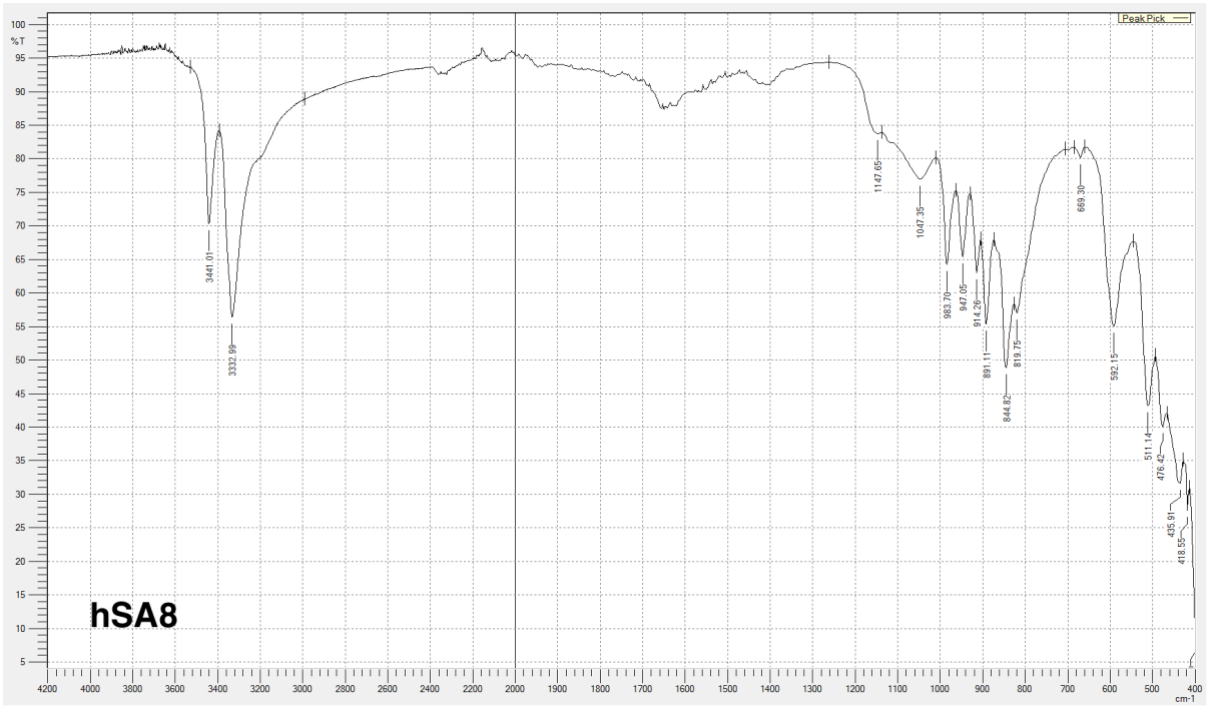

Peak Pick
%T
3442.94
3332.99
1620.21
1402.25
1028.06
985.62
948.98
914.26
891.11
842.89
669.30
592.15
507.28
418.55
hSA3
cm-1

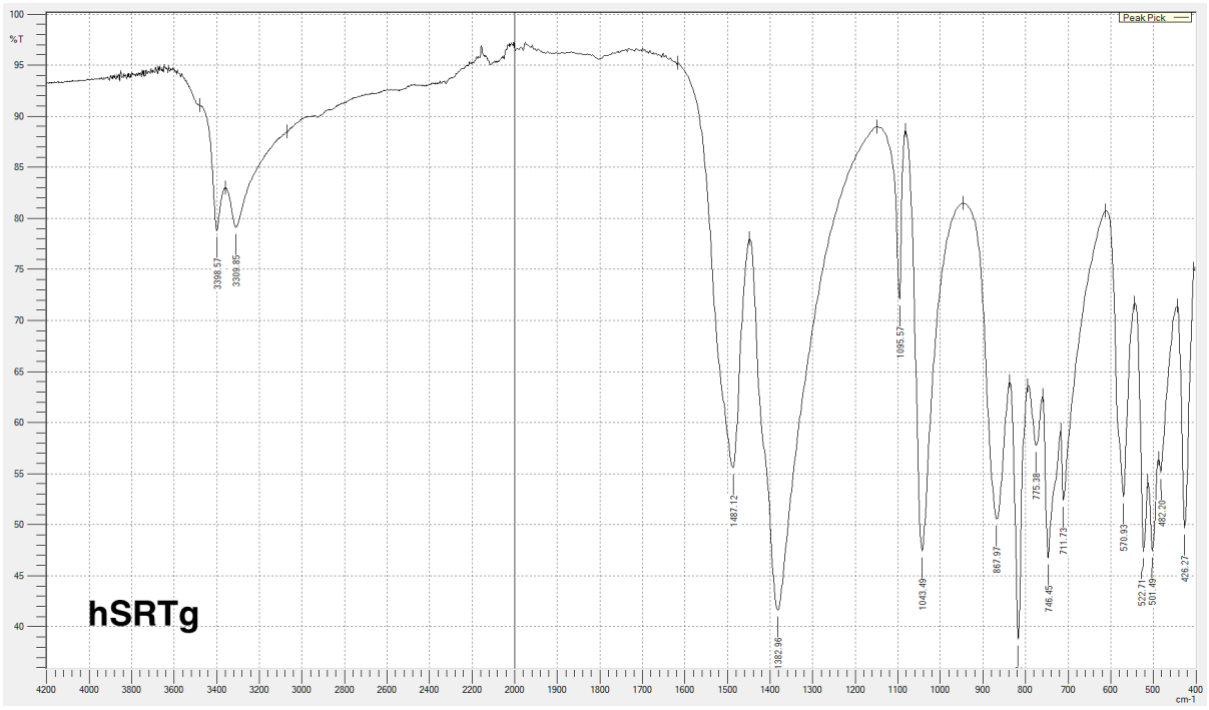

Peak Pick
%T
3402.43
3313.71
1697.50
1487.12
1043.49
869.90
775.38
748.38
711.73
578.93
522.71
501.49
426.27
401.19
hSA4g
cm-1

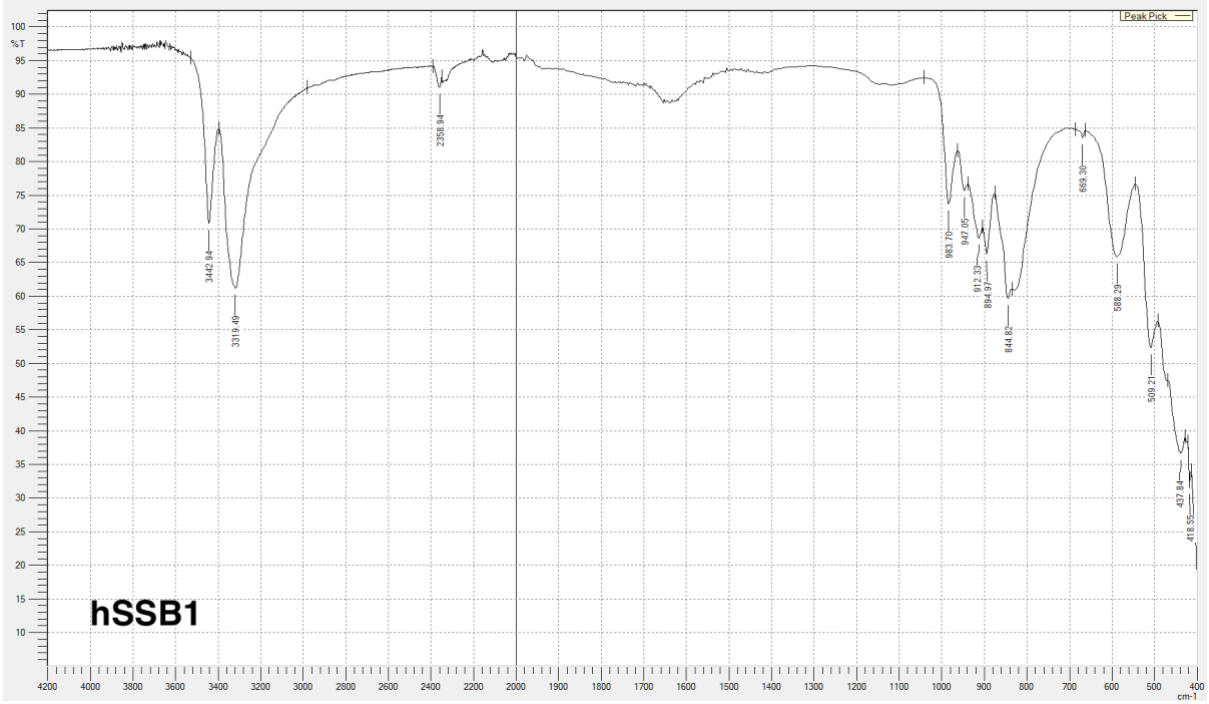

Peak Pick
%T
3402.43
3313.71
1487.12
1087.50
1043.49
867.97
775.38
746.45
711.73
570.93
522.71
501.49
426.27
hSA5g
cm-1

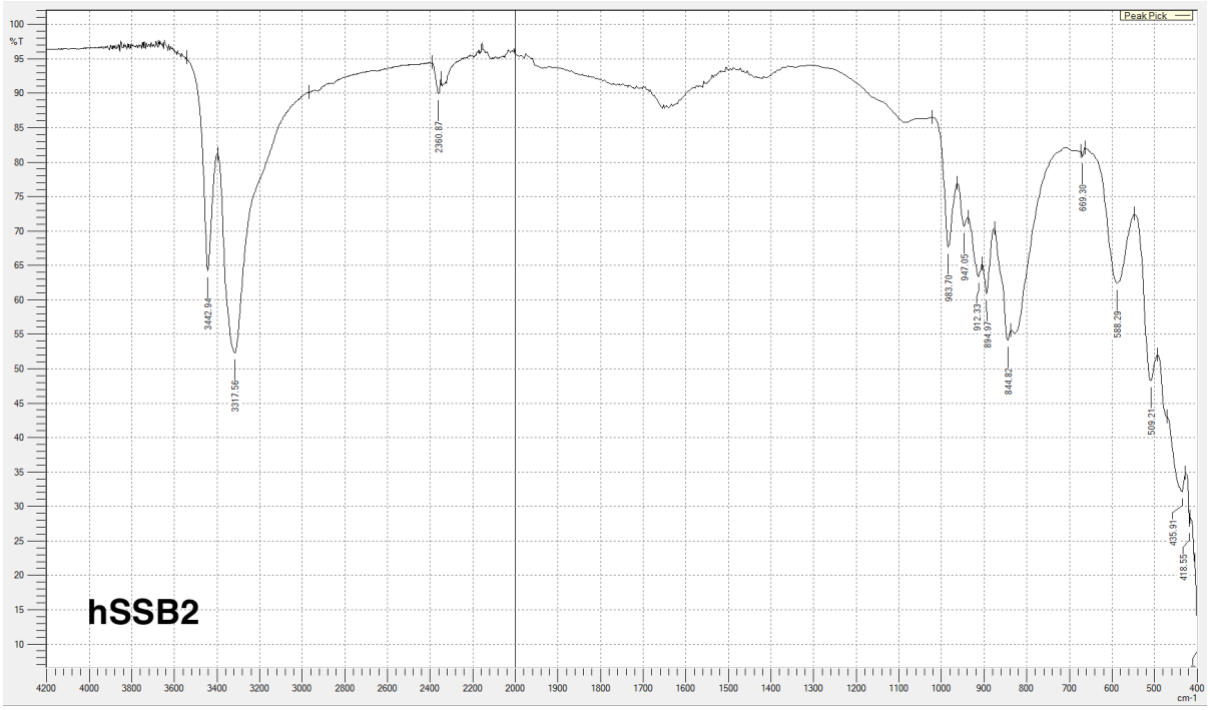

Peak Pick
%T
3541.31
3441.61
3331.07
1620.21
1118.71
1045.42
983.70
947.05
914.26
893.04
846.75
819.75
669.30
594.08
511.14
476.42
435.91
418.55
hSA6g
cm-1

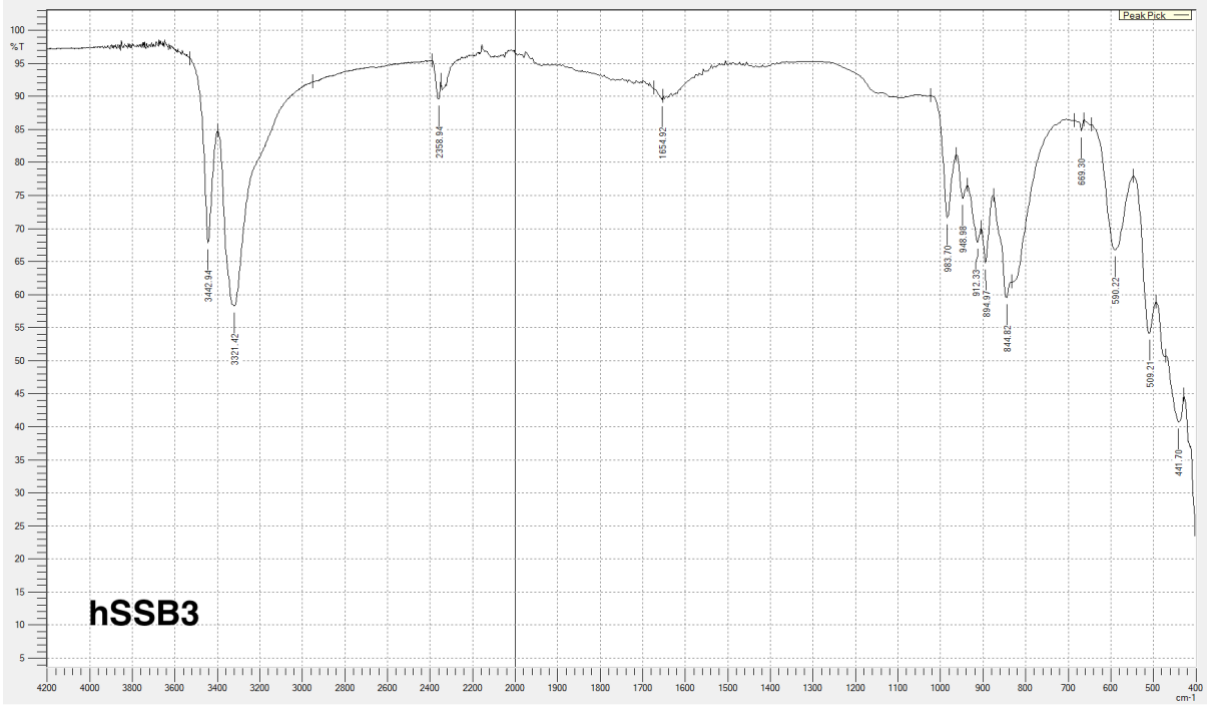

Peak Pick
%T
3329.14
1620.21
1413.82
1155.36
1039.63
989.46
956.69
804.32
609.51
557.43
468.91
418.55
hSA7
cm-1

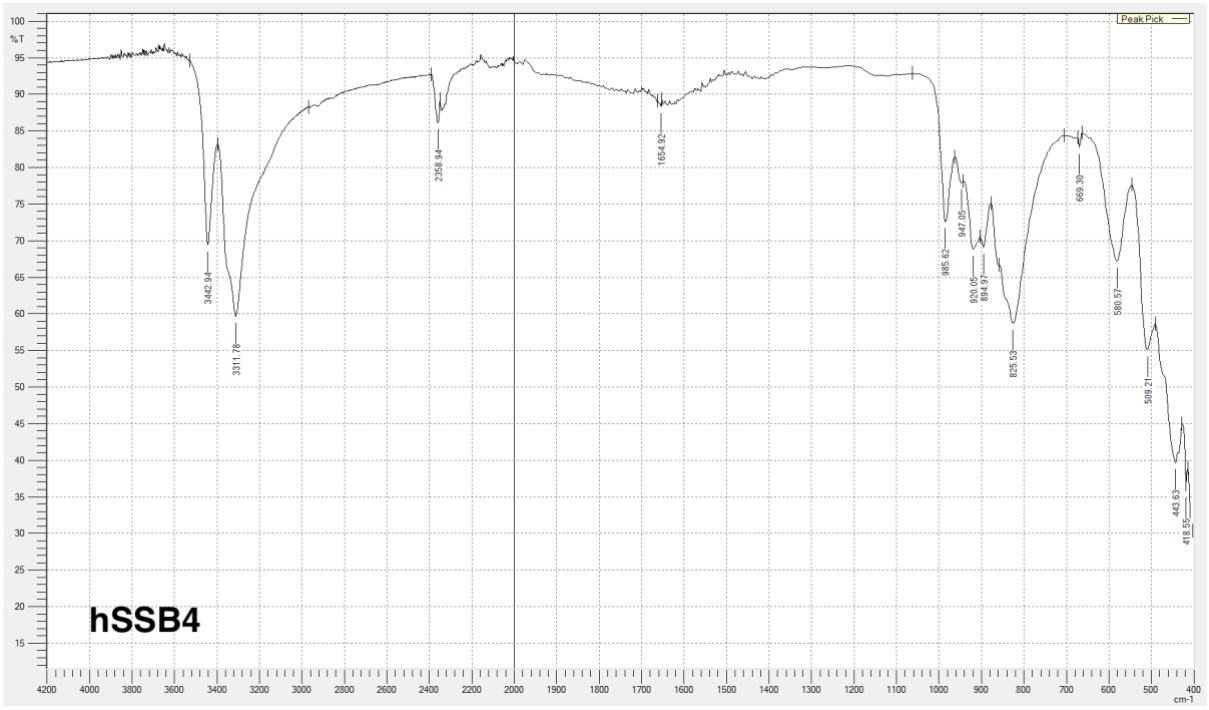

Peak Pick
%T
3441.01
3332.99
1147.65
1047.35
985.70
947.05
914.26
891.11
844.82
819.75
669.30
592.15
511.14
476.42
435.91
418.55
hSA8
cm-1

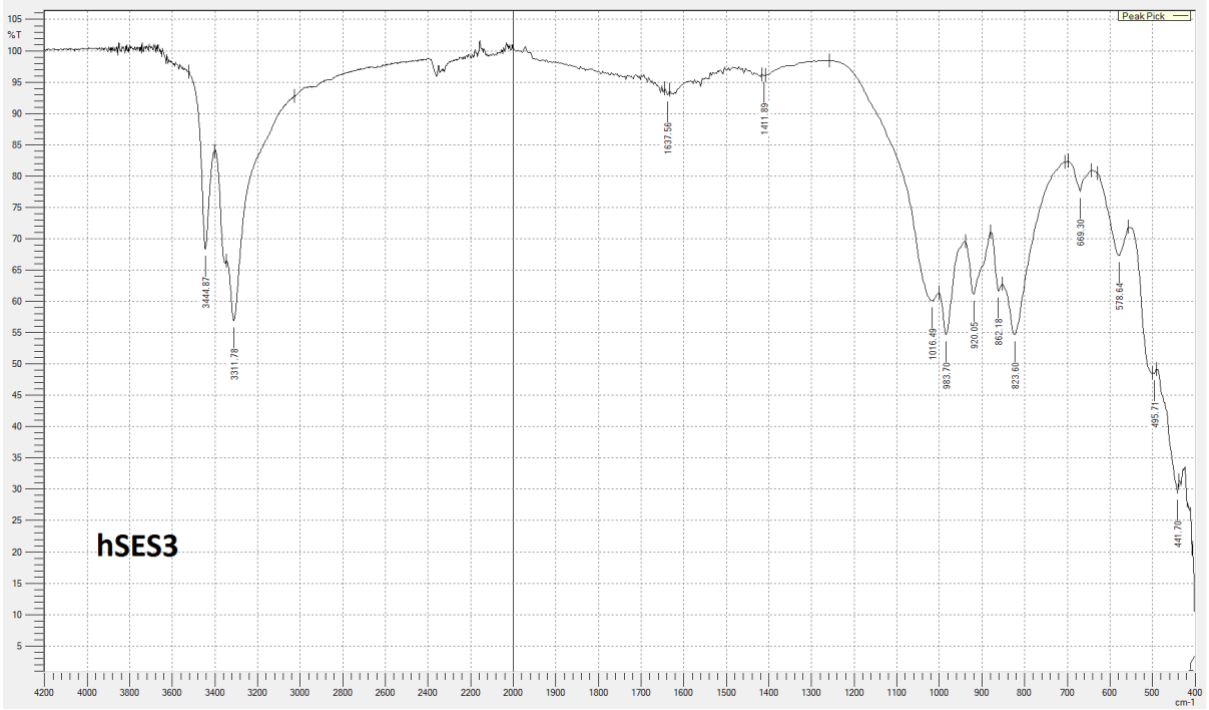

Peak Pick
%T
3398.57
3300.85
1487.12
1382.96
1095.57
1043.49
867.97
775.38
746.45
711.73
576.93
522.71
501.49
482.20
426.27
hSRTg
cm-1

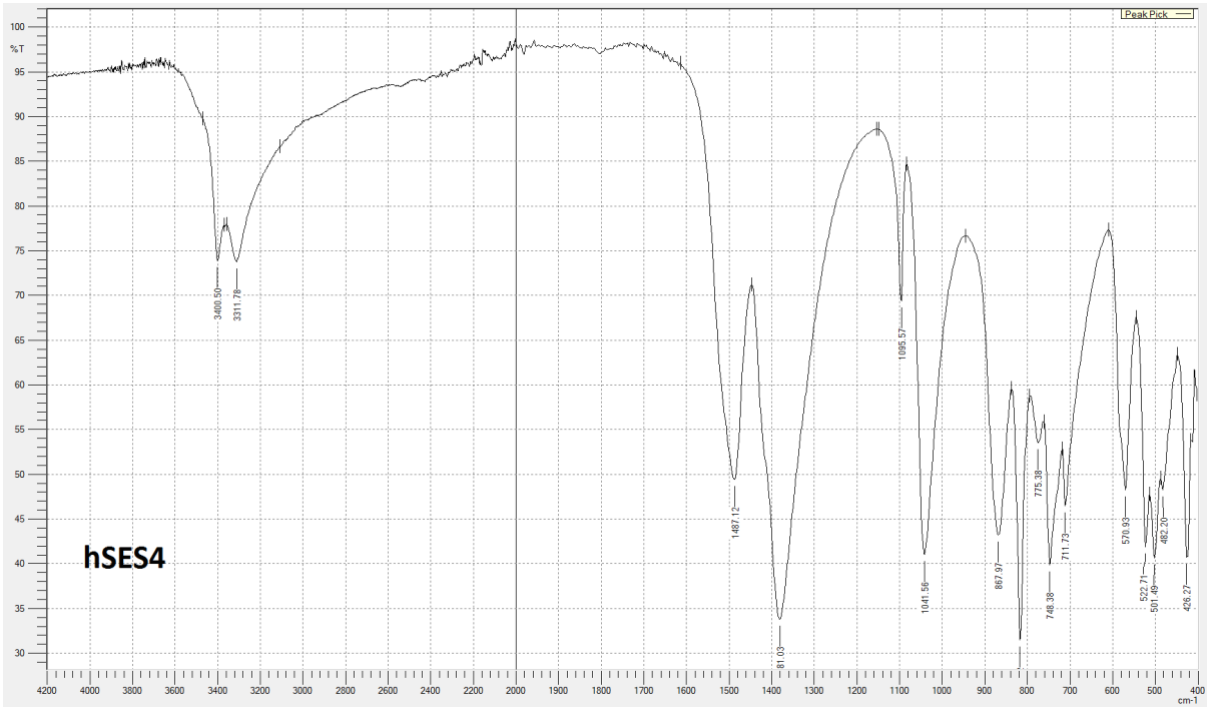

Peak Pick
%T
3442.94
3319.49
2358.94
983.70
947.05
912.33
894.97
844.82
693.30
588.29
509.21
437.84
418.55
hSSB1
cm-1

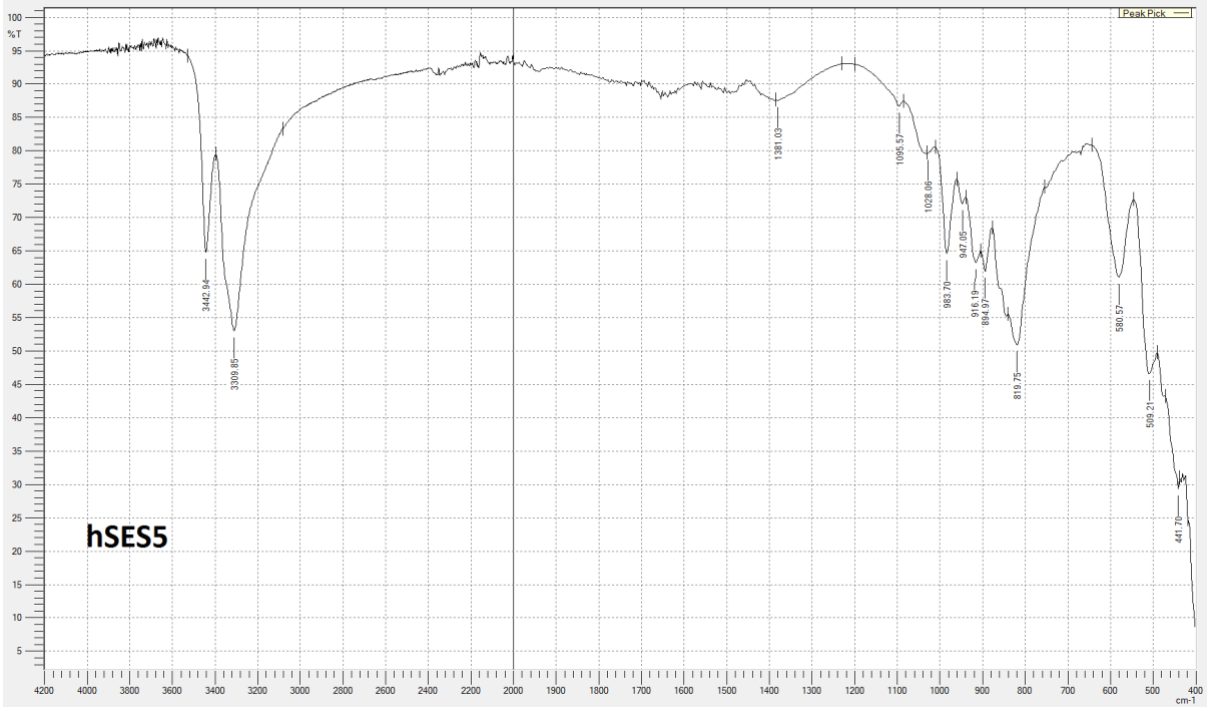

Peak Pick
%T
3442.94
3317.56
2360.87
983.70
947.05
912.33
894.97
844.82
669.30
588.29
509.21
435.91
418.55
hSSB2
cm-1

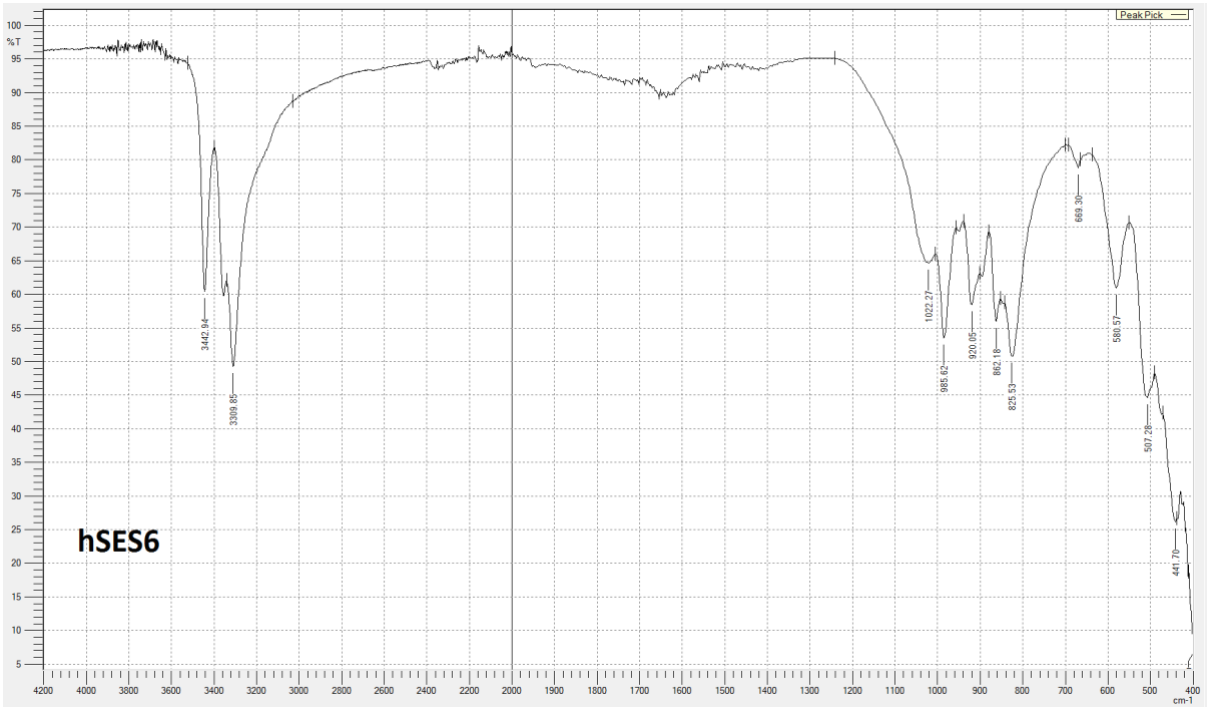

Peak Pick
%T
3442.94
3321.42
2358.84
1654.92
983.70
948.98
912.33
894.97
844.82
669.30
590.22
509.21
441.70
hSSB3
cm-1

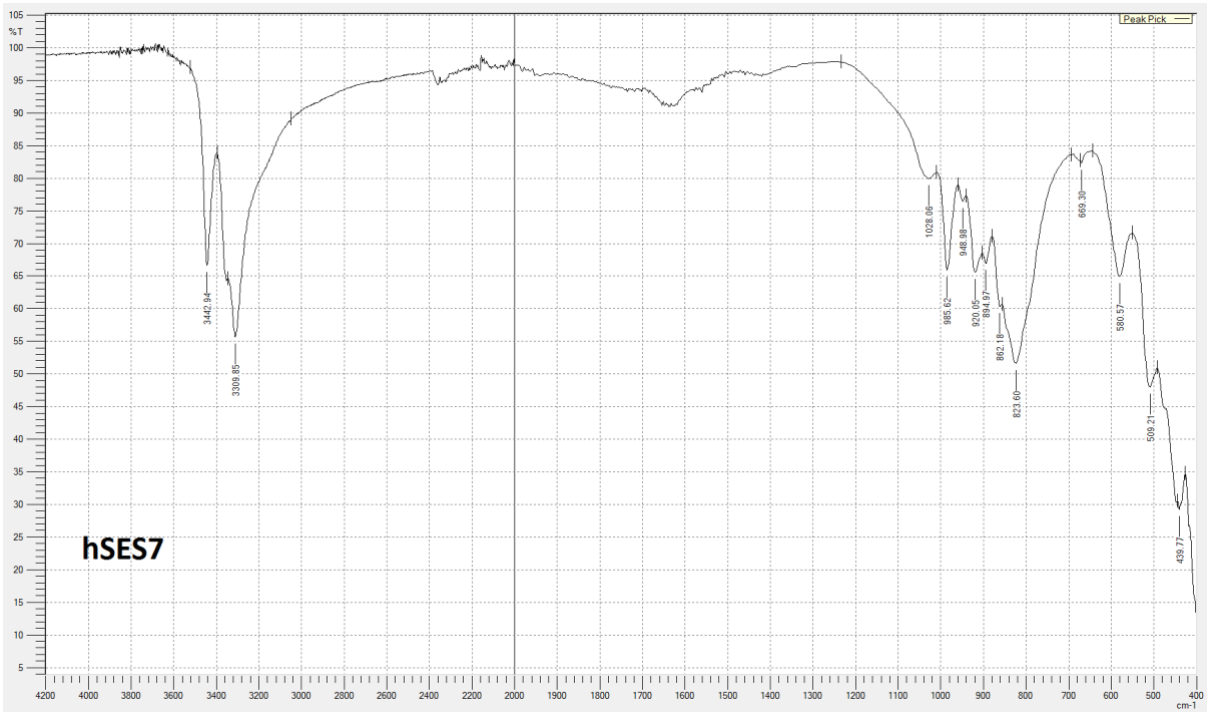

Peak Pick
%T
3442.94
3311.78
2358.94
1654.92
985.62
947.05
920.05
884.97
825.53
669.30
580.57
509.21
443.63
418.55
hSSB4
cm-1

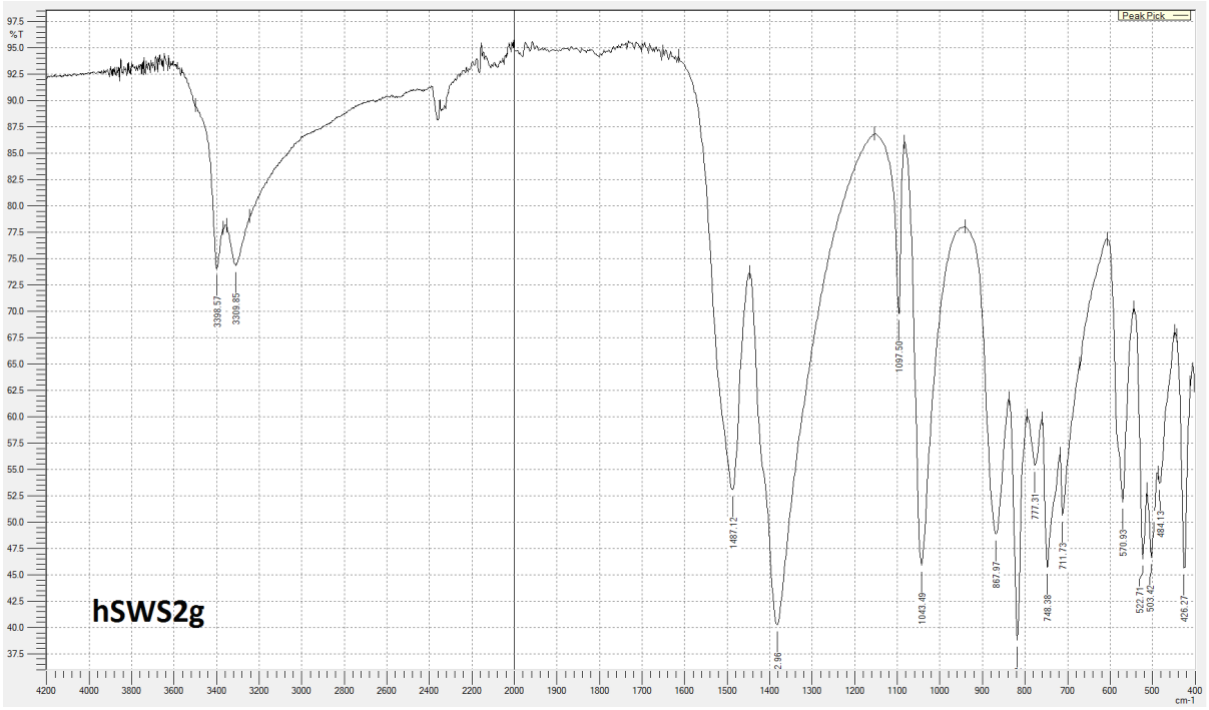

Peak Pick
%T
3444.87
3311.78
1637.56
1411.89
1016.49
983.70
920.05
862.18
823.60
669.30
578.64
495.71
441.70
hSES3
cm-1

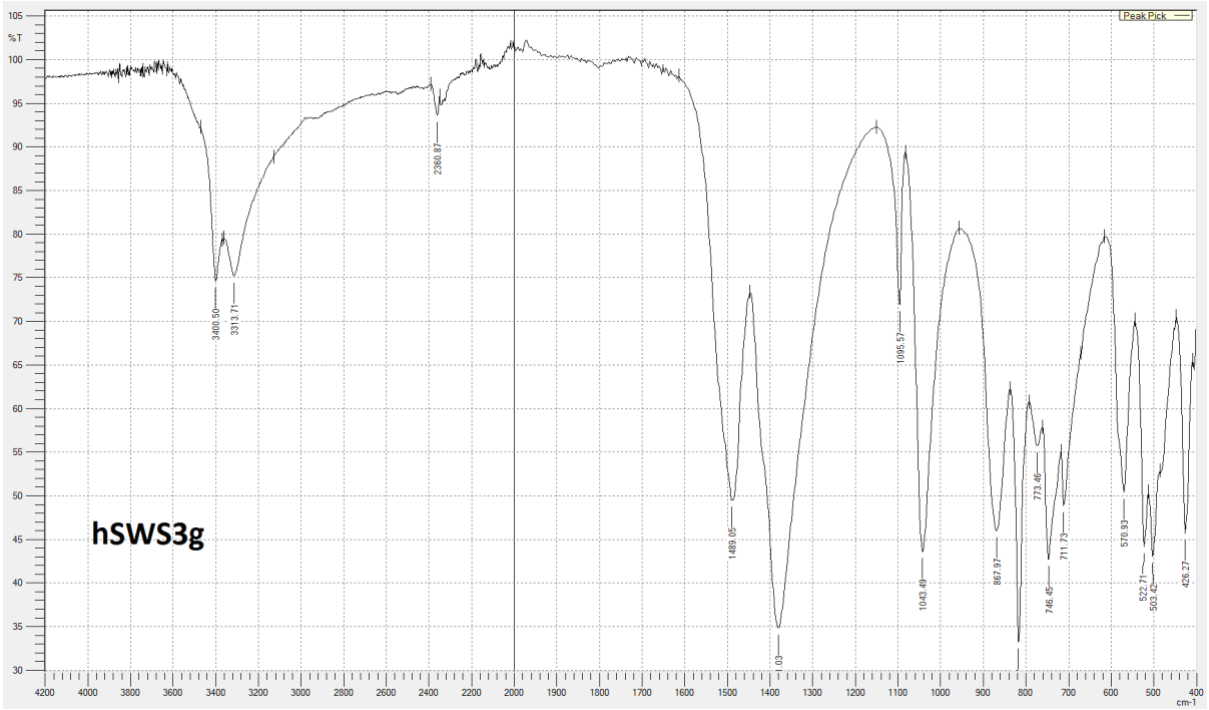

Peak Pick
%T
hSES4
3400.50
3311.78
1487.12
1381.03
1095.57
1041.56
867.97
775.38
748.38
711.73
570.93
522.71
501.49
482.20
426.27
cm-1

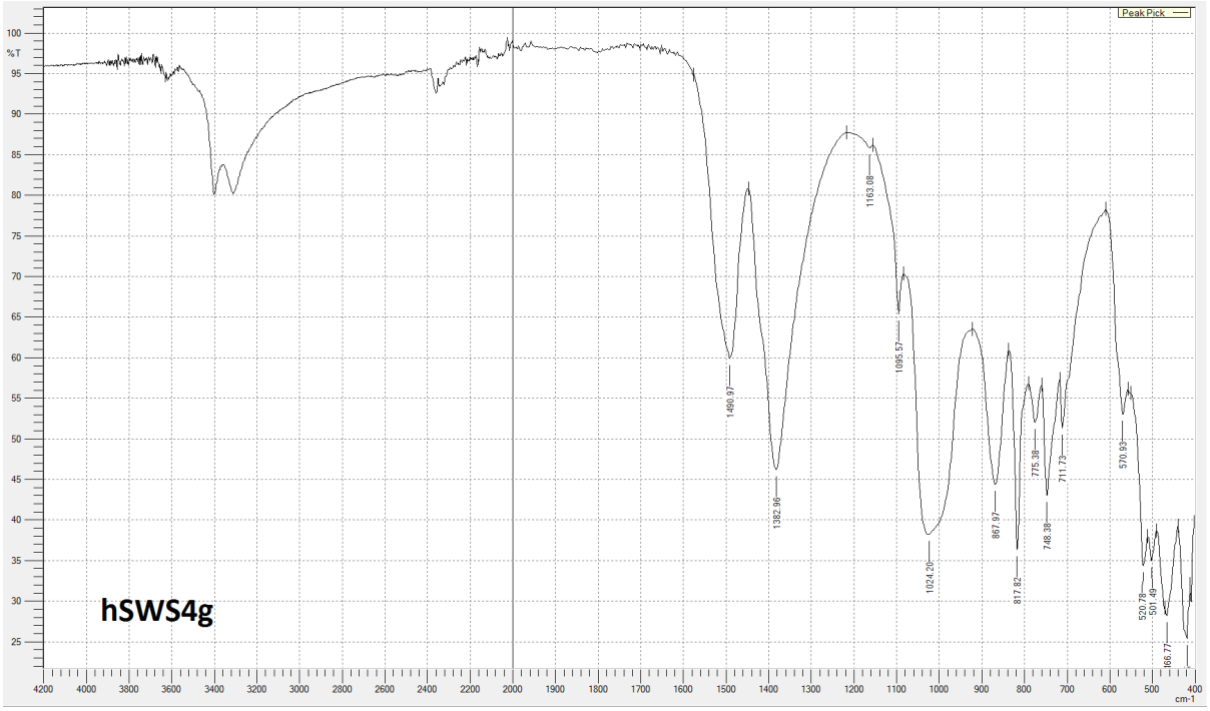

Peak Pick
%T
hSES5
3442.94
3309.85
1381.03
1095.57
1028.06
983.70
947.05
916.19
884.97
819.75
580.57
509.21
441.70
cm-1

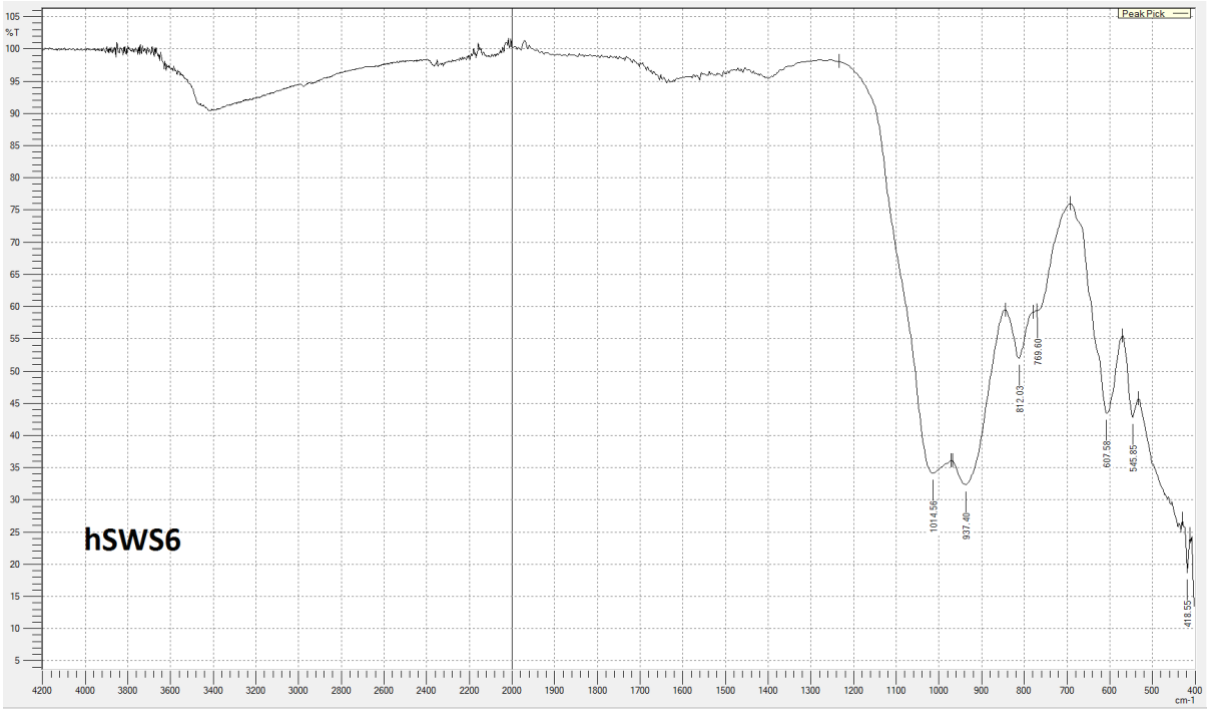

Peak Pick
%T
3442.94
3309.85
1022.27
985.62
920.05
862.18
825.53
669.30
580.57
507.28
441.70
hSES6
cm-1

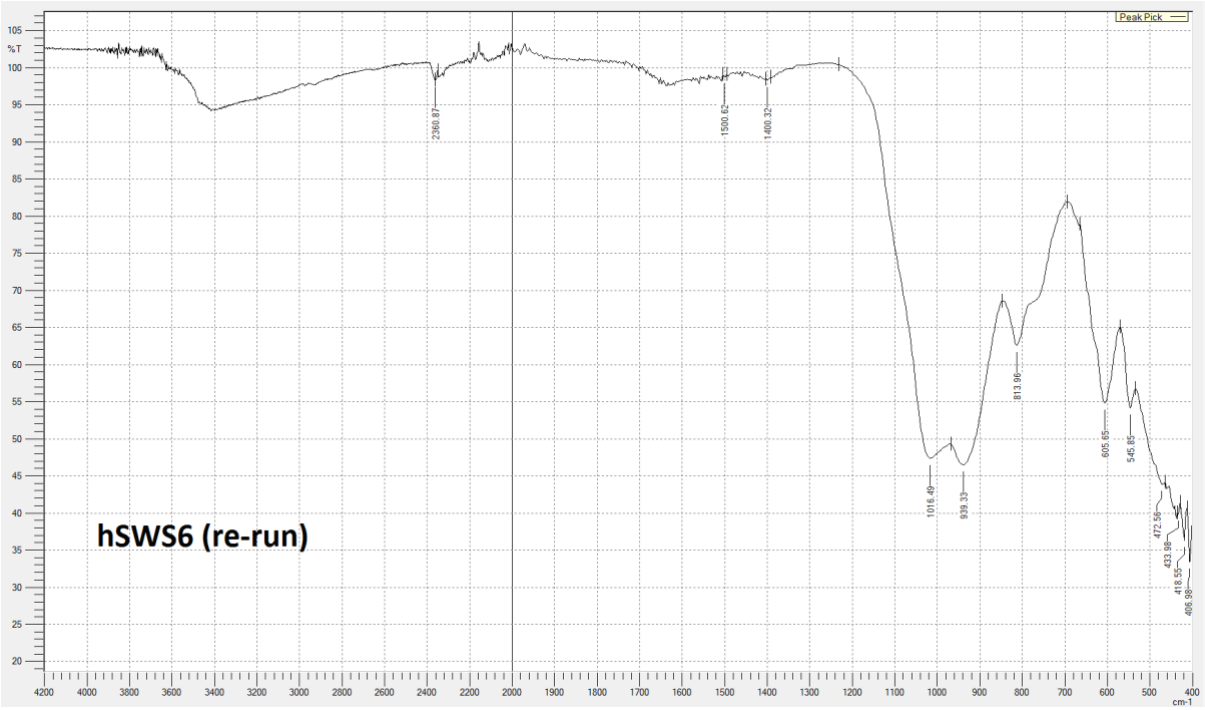

Peak Pick
%T
3442.94
3309.85
1028.06
985.62
948.98
920.05
894.97
862.18
823.60
669.30
580.57
509.21
439.77
hSES7
cm-1


Peak Pick
%T
cm-1
hSWS2g
3398.57
3309.85
1487.12
2.96
1097.50
1043.49
867.97
777.31
748.38
711.73
570.93
522.71
503.42
484.13
426.27

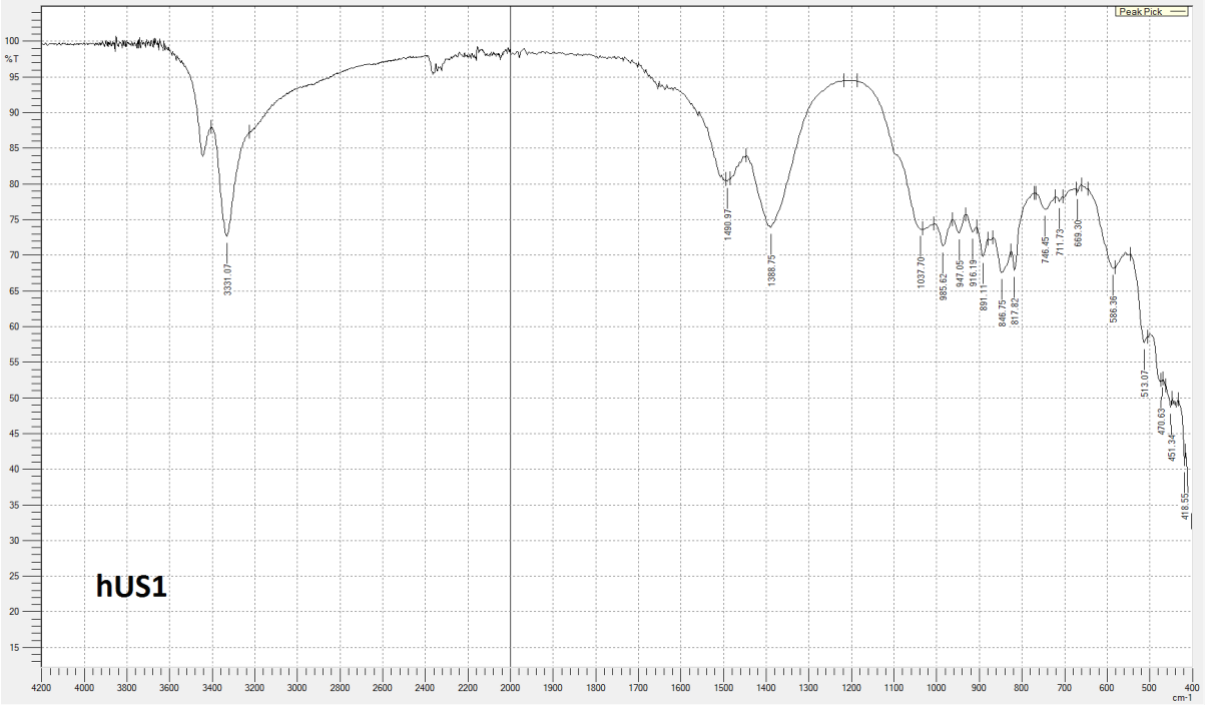

Peak Pick
%T
cm-1
hSWS3g
3400.50
3313.71
2360.97
1489.05
.03
1095.57
1043.49
867.97
773.46
748.45
711.73
570.93
522.71
503.42
426.27

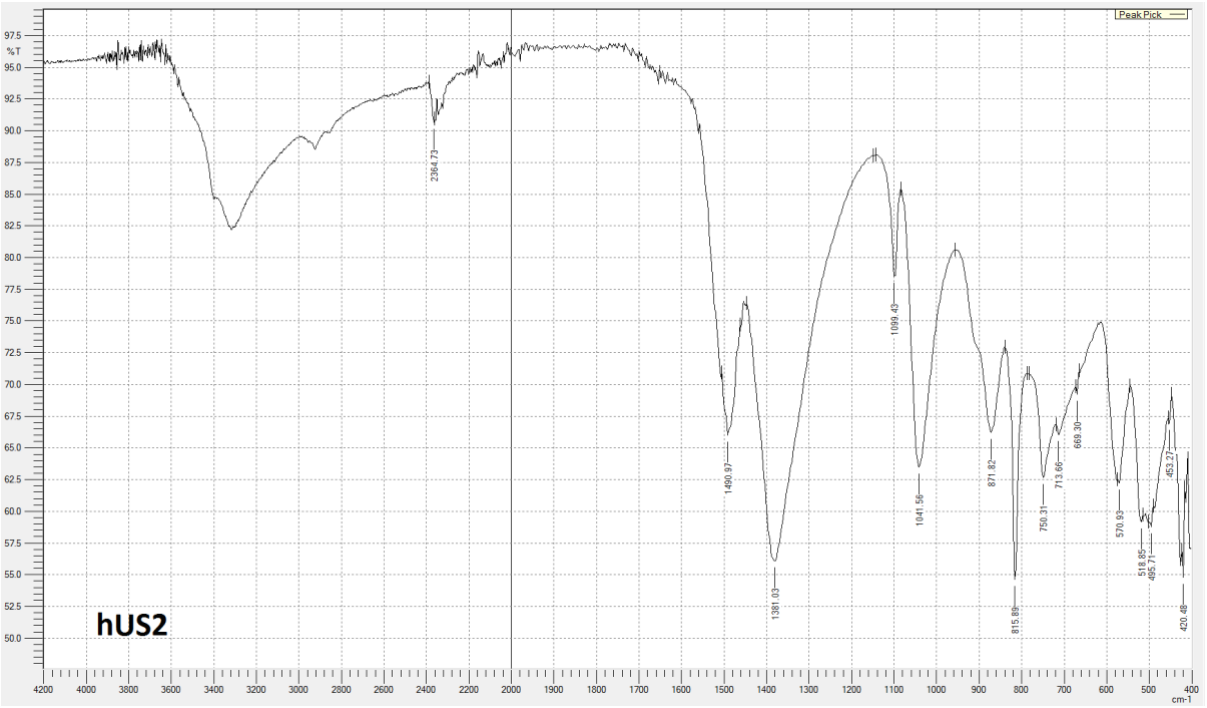

Peak Pick
%T
hSWS4g
1490.97
1382.96
1163.08
1095.57
1024.20
867.97
817.82
775.38
748.38
711.73
570.93
520.78
507.48
466.77
cm-1

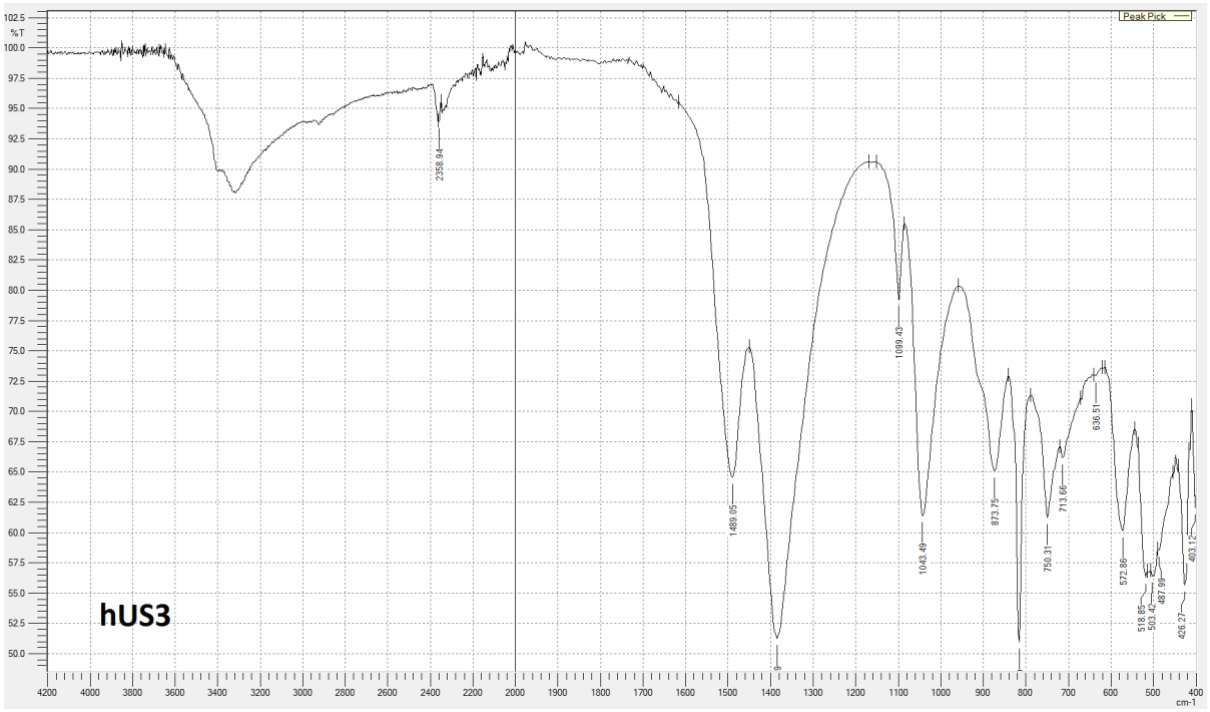

Peak Pick
%T
hSWS6
1014.56
937.49
812.03
769.60
607.58
545.85
418.55
cm-1

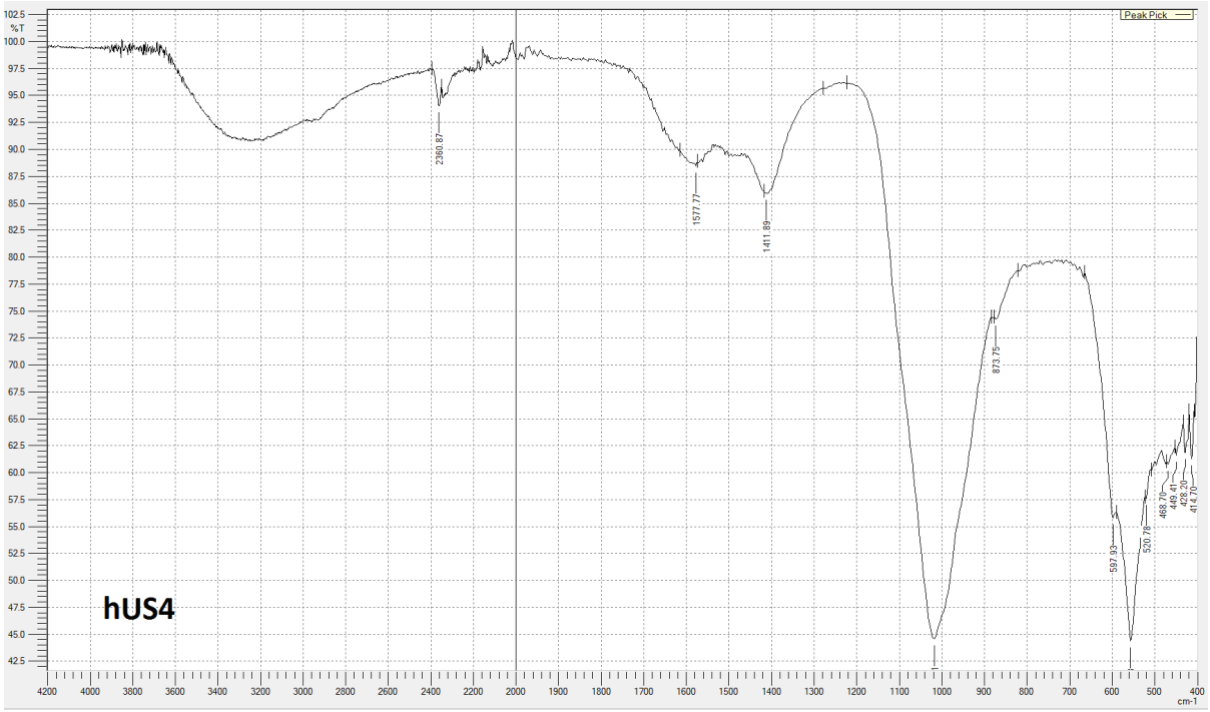

Peak Pick
%T
hSWS6 (re-run)
2360.87
1500.62
1400.32
1016.49
939.33
813.99
605.65
545.85
472.56
433.98
418.55
406.98
cm-1

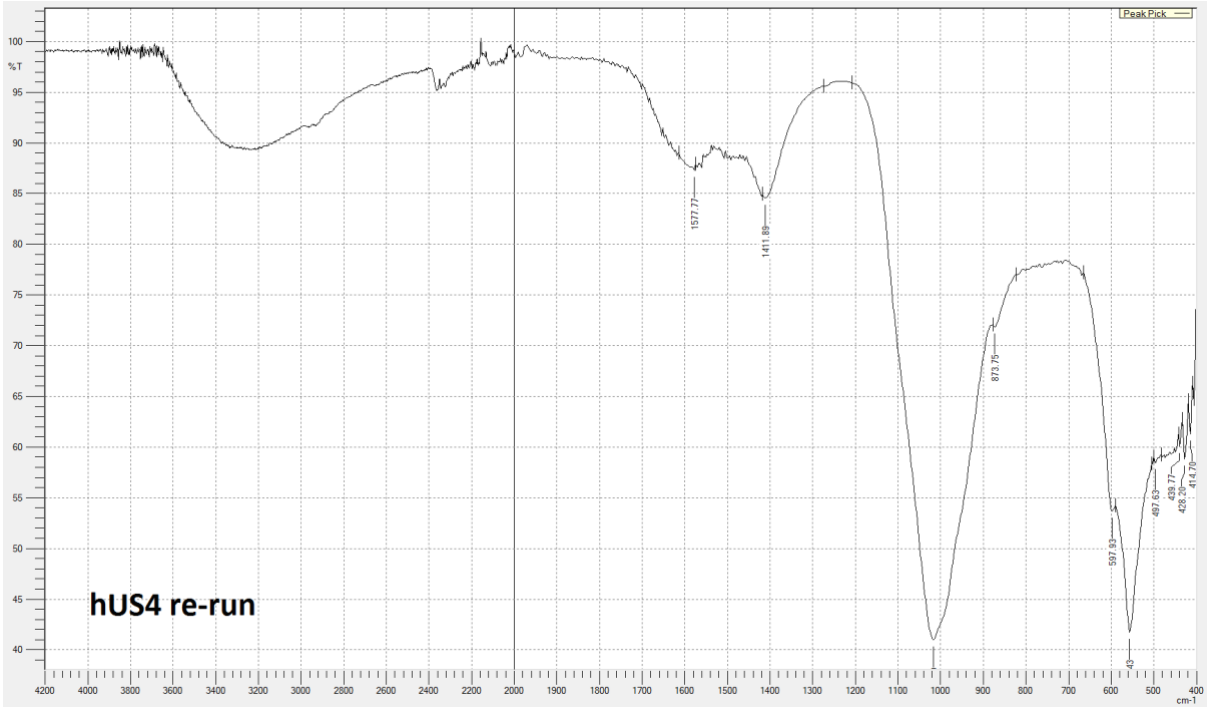
USA

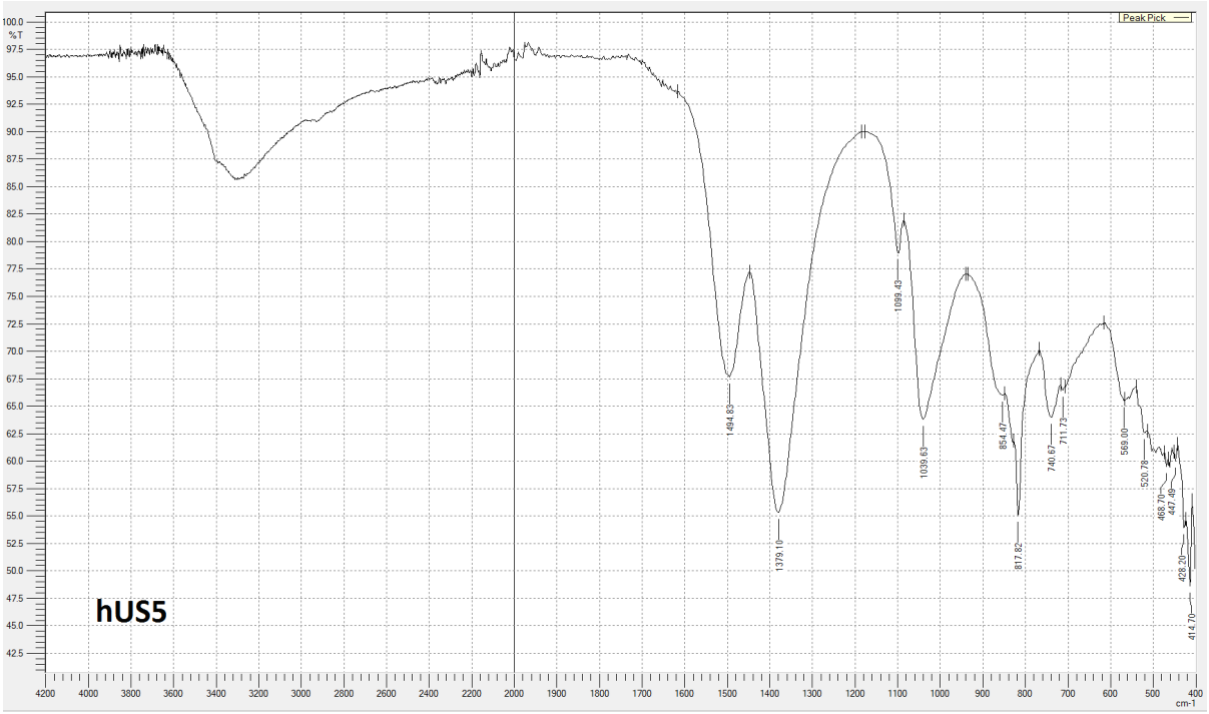

Peak Pick
%T
3331.07
1490.97
1388.75
1037.70
985.62
947.05
916.19
891.11
846.75
817.82
746.45
711.73
669.30
588.36
513.07
470.63
451.34
418.55
hUS1
cm-1


Peak Pick
%T
2364.73
1490.97
1381.03
1099.43
1041.56
871.82
815.89
750.31
713.66
669.30
570.93
518.85
485.71
453.27
420.48
hUS2
cm-1

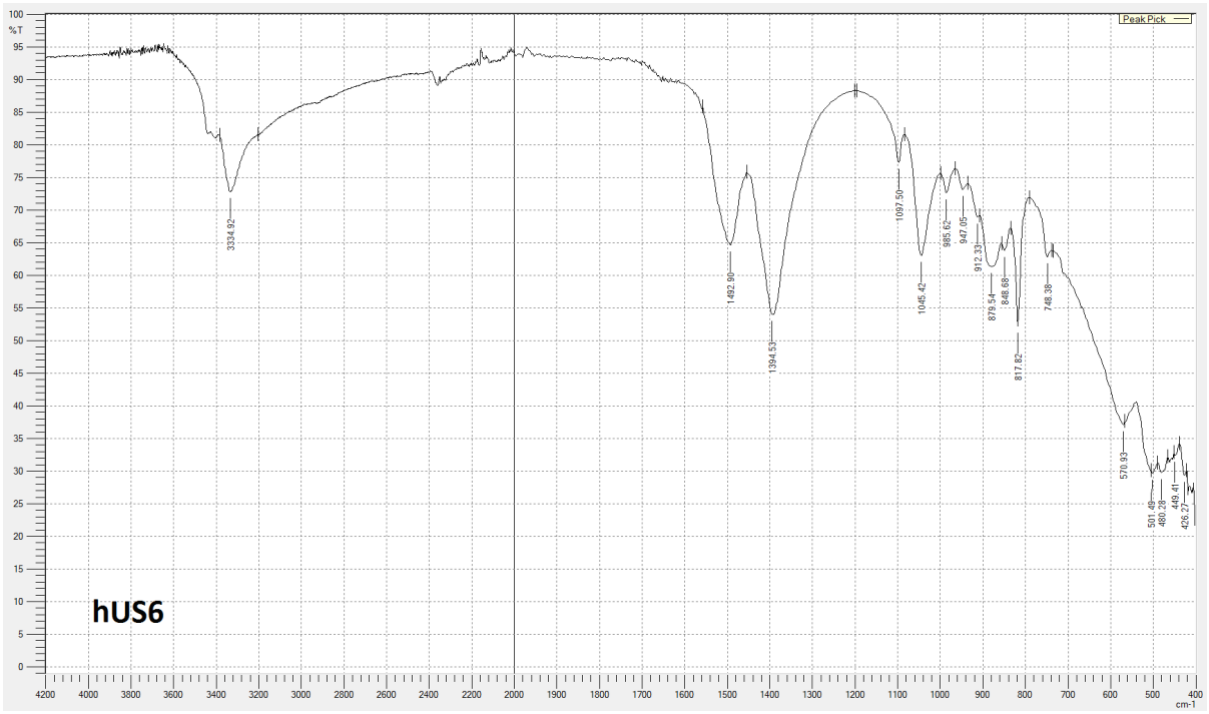

Peak Pick
%T
2358.94
1489.05
1099.43
1043.49
873.75
750.31
713.66
636.51
572.86
518.85
487.99
426.27
hUS3
cm-1


Peak Pick
%T
2360.87
1577.77
1411.89
873.75
597.83
520.78
468.70
449.41
428.20
hUS4
cm-1


Peak Pick
%T
1577.77
1411.89
873.75
597.83
487.63
439.77
428.20
414.70
hUS4 re-run
cm-1


Peak Pick
%T
1494.83
1379.10
1099.43
1039.63
854.47
817.82
740.67
711.73
568.00
520.78
468.70
447.49
428.20
414.70
hUS5
cm-1

APPENDIX C: FTIR SPECTRA FOR THE MALACHITE SAMPLES



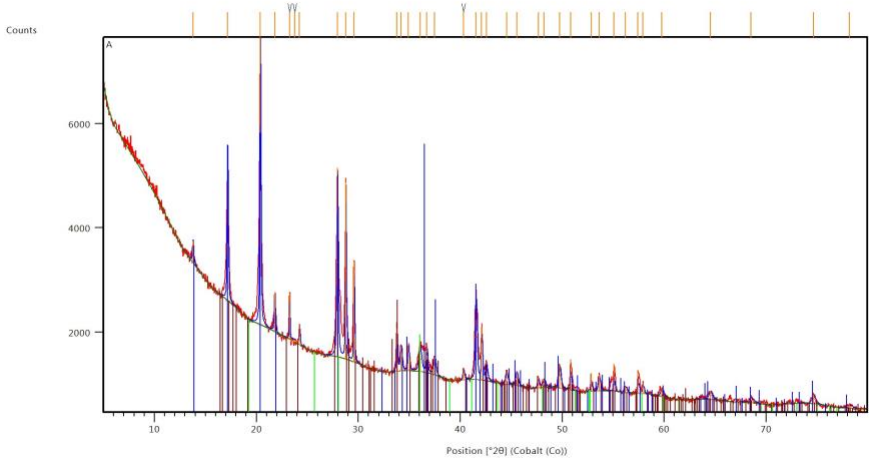
APPENDIX D:

XRD Spectra of the Malachite Samples

Malachite samples were analyzed at the University of Oxford Department of Earth Sciences, using the PANalytical Empyrean Series 2 diffractometer. Diffraction data were reduced using the HighScore Plus software suite, and mineral identifications were based on correspondence to the International Centre for Diffraction Data Powder Diffraction File 4+ database (and quantified through the reference intensity ratio method). Spectra are ordered by country, site or region. The B2 spectra are presented after the B1 samples.

ASIA

A



Pattern List

Ref.Code	Mineral Name	SemiQuant[%]	Score	Compound Name	Scale Fac.	Chem. Formula
00-056-0001	Malachite	51	38	Copper Carbonate H..	0.572	Cu2 +2 (C O3) (..
00-041-0586	Ankerite	5	33	Calcium Iron Magne..	0.093	Ca (Fe +2 , Mg) ..
04-012-1018		44	15	Sodium Aluminum Si..	0.178	Na Al Si3 O8

Peak List

Pos.[°2θ]	Height [cts]	FWHMLeft[°2θ]	d-spacing [Å]	Rel. Int. [%]
13.7961	422.10	0.1535	7.45321	7.68
17.1876	2862.00	0.1279	5.99051	52.05
20.3912	5498.76	0.1279	5.05709	100.00
21.8108	761.86	0.1279	4.73155	13.86
23.2497	890.16	0.0768	4.44239	16.19
23.7431	36.04	0.8187	4.35135	0.66
24.2296	400.66	0.1023	4.26525	7.29
27.9553	3629.61	0.1535	3.70597	66.01
28.7745	3386.98	0.1023	3.60259	61.60
29.5889	1933.05	0.1023	3.50557	35.15
33.7876	811.47	0.1279	3.08038	14.76
34.1968	468.09	0.2047	3.04460	8.51
34.9170	508.93	0.1791	2.98370	9.26
36.0621	471.30	0.3070	2.89196	8.57
36.7129	515.92	0.1535	2.84241	9.38
37.4889	341.97	0.2558	2.78562	6.22
40.3278	206.21	0.1535	2.59686	3.75
41.5488	1623.30	0.1791	2.52377	29.52
42.0998	1022.50	0.1279	2.49221	18.60
42.5619	358.38	0.2047	2.46639	6.52
44.5391	240.90	0.2558	2.36210	4.38
45.5436	267.67	0.2558	2.31269	4.87
47.6493	191.88	0.2047	2.21606	3.49
48.2256	142.30	0.3070	2.19113	2.59
49.7401	448.25	0.2558	2.12847	8.15
50.8189	568.32	0.1023	2.08620	10.34
52.8463	349.67	0.0768	2.01159	6.36
53.6162	306.08	0.2047	1.98480	5.57
55.0708	526.01	0.0768	1.93632	9.57
56.2173	113.78	0.3070	1.89995	2.07
57.4311	449.30	0.1023	1.86311	8.17
57.9224	220.45	0.1535	1.84866	4.01
59.7780	173.37	0.3070	1.79634	3.15
64.5447	157.63	0.4093	1.67649	2.87
68.5162	87.11	0.6140	1.59019	1.58
74.6271	168.39	0.4093	1.47672	3.06
78.1850	59.41	0.6140	1.41959	1.08

ALASKA, USA

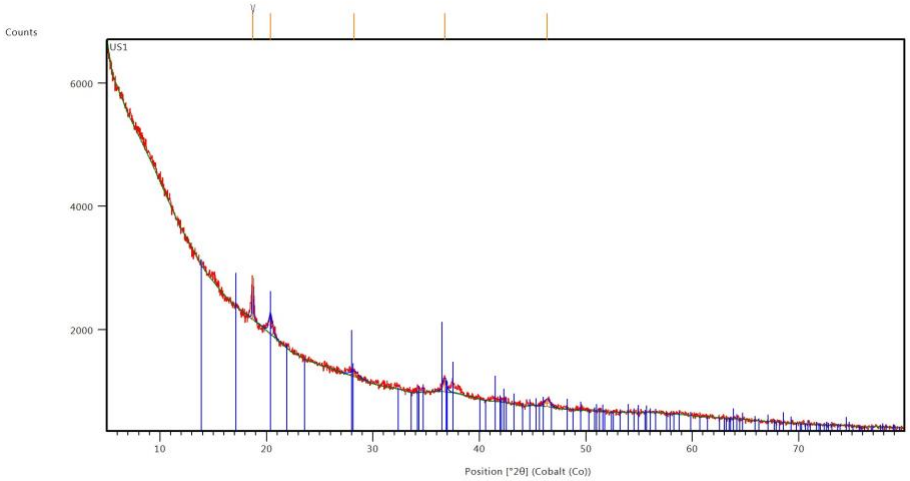
US1

Pattern List

Ref.Code	Mineral Name	SemiQuant[%]	Score	Compound Name	Scale Fac.	Chem. Formula
04-013-7662	Malachite	100	4	Copper Carbonate H..	0.168	Cu2 (C O3) (O H..

Peak List

Pos.[°2θ]	Height [cts]	FWHMLeft[°2θ]	d-spacing [Å]	Rel. Int. [%]
18.6958	696.43	0.1023	5.51105	100.00
20.3836	297.69	0.4093	5.05898	42.75
28.2348	84.20	0.9210	3.67003	12.09
36.7334	216.31	0.4093	2.84087	31.06
46.3443	116.14	0.6140	2.27488	16.68



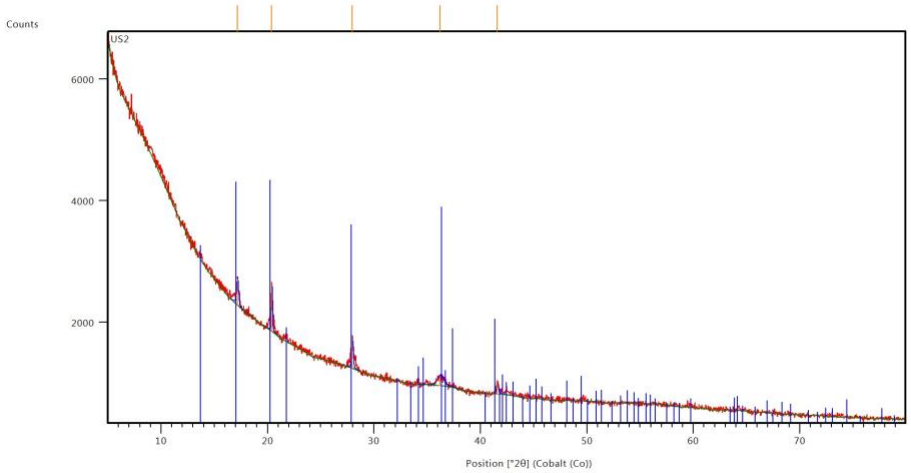
US2

Pattern List

Ref.Code	Mineral Name	SemiQuant[%]	Score	Compound Name	Scale Fac.	Chem. Formula
00-056-0001	Malachite	100	14	Copper Carbonate H..	0.434	Cu2 +2 (C O3) (..

Peak List

Pos.[°2θ]	Height [cts]	FWHMLeft[°2θ]	d-spacing [Å]	Rel. Int. [%]
17.1760	438.76	0.2047	5.99454	53.01
20.4015	827.68	0.1023	5.05457	100.00
27.9632	551.55	0.1535	3.70494	66.64
36.2301	164.75	0.7164	2.87899	19.91
41.5839	198.46	0.1535	2.52173	23.98



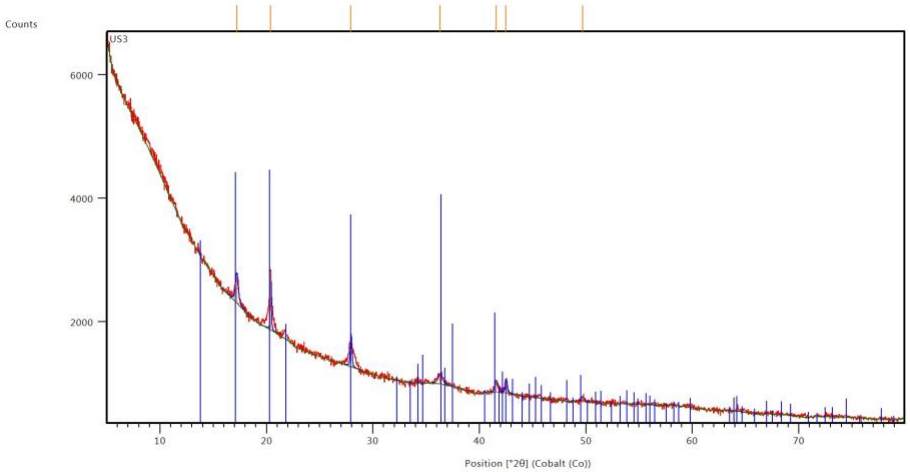
US3

Pattern List

Ref.Code	Mineral Name	SemiQuant[%]	Score	Compound Name	Scale Fac.	Chem. Formula
00-056-0001	Malachite	100	17	Copper Carbonate H..	0.458	Cu2 +2 (C O3) (..

Peak List

Pos.[°2θ]	Height [cts]	FWHM Left[°2θ]	d-spacing [Å]	Rel. Int. [%]
17.2171	455.35	0.3070	5.98033	47.83
20.3912	952.01	0.1023	5.05710	100.00
27.9233	537.90	0.1535	3.71014	56.50
36.2859	138.13	0.5117	2.87471	14.51
41.5689	176.76	0.3070	2.52260	18.57
42.5019	226.09	0.2047	2.46970	23.75
49.6833	84.82	0.3070	2.13075	8.91

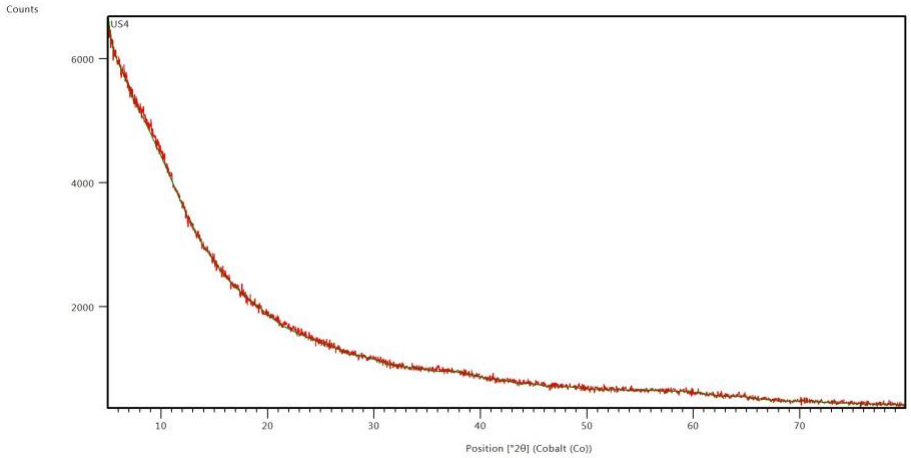


US4

Graphics

No phases detected

Graphics



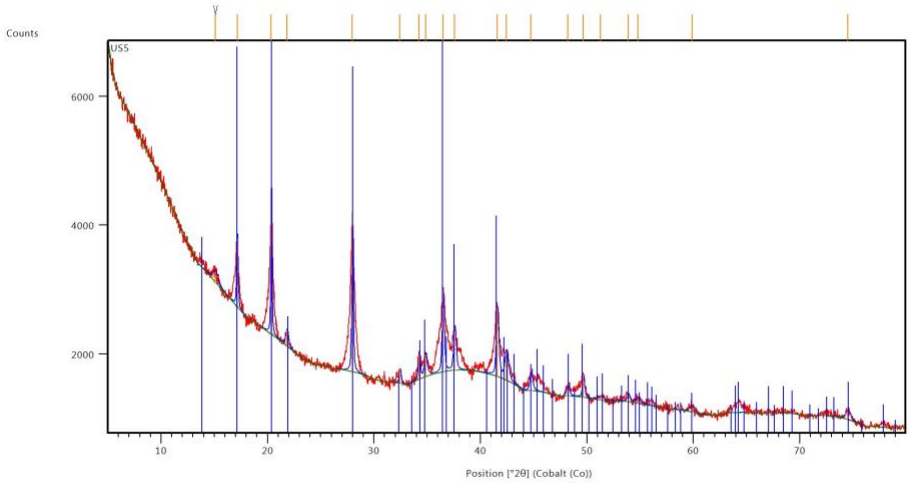
US5

Pattern List

Ref.Code	Mineral Name	SemiQuant[%]	Score	Compound Name	Scale Fac.	Chem. Formula
00-056-0001	Malachite	100	52	Copper Carbonate H..	0.861	Cu2 +2 (C O3) (..

Peak List

Pos.[°2θ]	Height [cts]	FWHMLeft[°2θ]	d-spacing [Å]	Rel. Int. [%]
15.1177	164.50	0.6140	6.80497	6.66
17.1629	1070.78	0.1535	5.99908	43.37
20.3565	2245.17	0.1279	5.06563	90.95
21.8404	245.43	0.3070	4.72522	9.94
27.9737	2468.67	0.1535	3.70358	100.00
32.4388	221.45	0.2047	3.20481	8.97
34.2396	359.80	0.2047	3.04091	14.57
34.8612	340.35	0.3070	2.98833	13.79
36.4845	1244.67	0.2047	2.85959	50.42
37.5864	664.02	0.2558	2.77866	26.90
41.5954	1062.38	0.2558	2.52107	43.03
42.4563	434.09	0.4093	2.47223	17.58
44.7590	271.69	0.3070	2.35109	11.01
48.2021	167.83	0.3070	2.19214	6.80
49.6518	351.65	0.2047	2.13202	14.24
51.2820	57.30	0.6140	2.06862	2.32
53.8933	111.37	0.3070	1.97536	4.51
54.7965	76.75	0.6140	1.94526	3.11
59.8773	90.86	0.6140	1.79363	3.68
74.4977	152.89	0.5117	1.47891	6.19



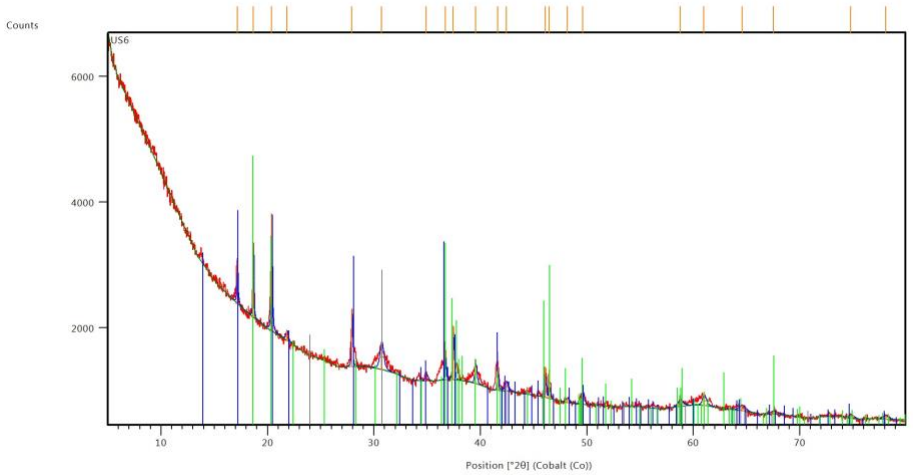
US6

Pattern List

Ref.Code	Mineral Name	SemiQuant[%]	Score	Compound Name	Scale Fac.	Chem. Formula
00-056-0001	Malachite	38	27	Copper Carbonate H..	0.328	Cu2 +2 (C O3) (..
01-077-0116	Atacamite	47	30	Copper Chloride Hy..	0.382	Cu Cl2 (Cu (O H ..
04-006-1757	Quartz	16	24	Silicon Oxide	0.236	Si O2

Peak List

Pos.[°2θ]	Height [cts]	FWHM Left[°2θ]	d-spacing [Å]	Rel. Int. [%]
17.1713	699.62	0.1279	5.99615	37.40
18.6767	1178.74	0.1023	5.51663	63.02
20.4012	1870.54	0.1279	5.05466	100.00
21.8400	151.72	0.2558	4.72531	8.11
27.9315	895.43	0.1279	3.70906	47.87
30.7273	401.12	0.4093	3.37865	21.44
34.9208	110.33	0.3070	2.98338	5.90
36.7010	447.89	0.1023	2.84330	23.94
37.4424	861.60	0.1279	2.78896	46.06
39.5635	319.51	0.2047	2.64495	17.08
41.6082	615.76	0.0768	2.52032	32.92
42.4447	142.28	0.4093	2.47288	7.61
46.0713	488.71	0.1023	2.28762	26.13
46.4449	454.85	0.0768	2.27022	24.32
48.1457	70.50	0.4093	2.19455	3.77
49.6230	211.41	0.2047	2.13317	11.30
58.7558	86.40	0.6140	1.82473	4.62
61.0002	157.95	0.4093	1.76371	8.44
64.5761	78.12	0.7164	1.67576	4.18
67.5010	45.96	0.8187	1.61121	2.46
74.7618	46.96	0.6140	1.47445	2.51
78.0602	56.98	0.6140	1.42149	3.05



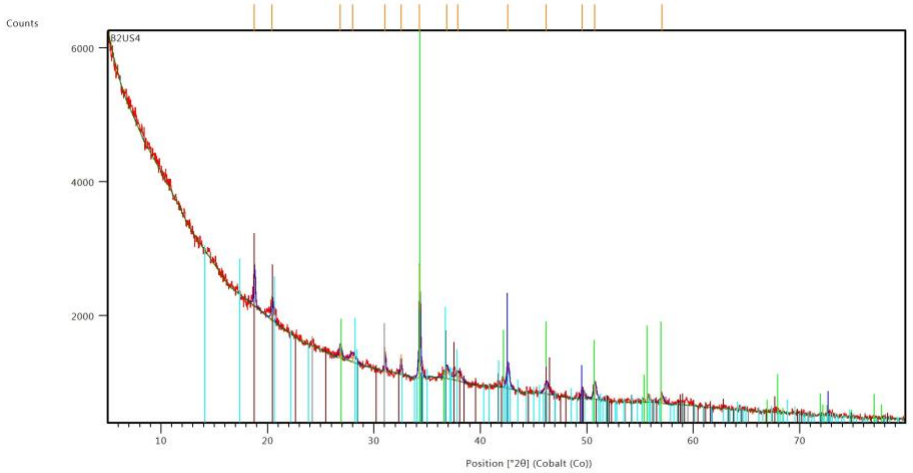
B2US4

Pattern List

Ref.Code	Mineral Name	SemiQuant[%]	Score	Compound Name	Scale Fac.	Chem. Formula
04-007-9767	Cuprite	5	36	Copper Oxide	0.228	Cu2 O
01-083-4609		52	31	Calcium Carbonate	0.955	Ca (C O3)
01-075-8320	Quartz	7	17	Silicon Oxide	0.114	Si O2
04-010-1616	Atacamite	14	14	Copper Chloride Hy..	0.174	Cu2 Cl (O H)3
01-072-8421	Malachite	21	7	Copper Carbonate H..	0.171	Cu2 (O H)2 (C O..

Peak List

Pos.[°2θ]	Height [cts]	FWHMLeft[°2θ]	d-spacing [Å]	Rel. Int. [%]
18.7719	594.64	0.1535	5.48892	35.37
20.4428	348.20	0.2047	5.04448	20.71
26.8380	188.44	0.3070	3.85725	11.21
28.0027	129.00	0.6140	3.69983	7.67
31.0143	360.73	0.1023	3.34813	21.46
32.5432	300.14	0.1023	3.19480	17.85
34.2782	1680.97	0.1279	3.03758	100.00
36.8483	178.15	0.4093	2.83232	10.60
37.8745	123.63	0.6140	2.75828	7.35
42.5787	384.30	0.2558	2.46546	22.86
46.1993	188.63	0.4093	2.28162	11.22
49.5787	115.98	0.3070	2.13496	6.90
50.7458	269.06	0.2558	2.08900	16.01
57.0373	125.03	0.3070	1.87488	7.44



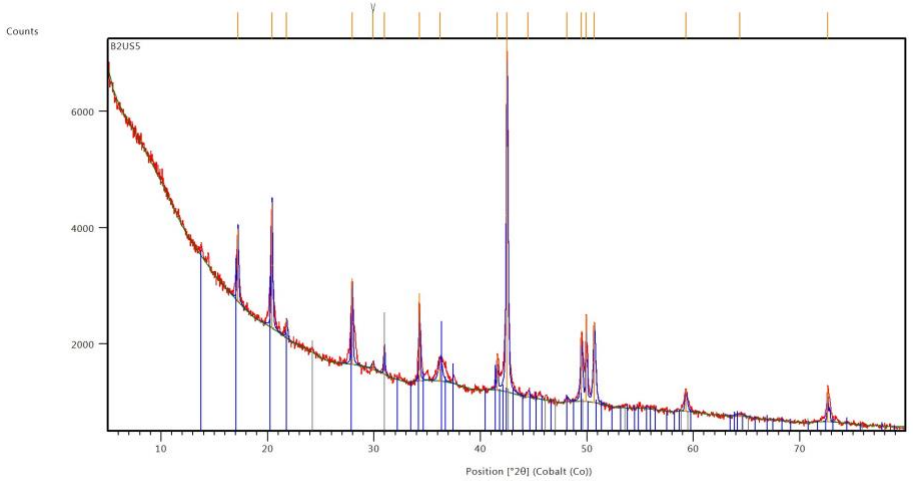
B2US5

Pattern List

Ref.Code	Mineral Name	SemiQuant[%]	Score	Compound Name	Scale Fac.	Chem. Formula
00-056-0001	Malachite	62	21	Copper Carbonate H..	0.142	Cu2 +2 (C O3) (..
01-075-8320	Quartz	38	17	Silicon Oxide	0.146	Si O2

Peak List

Pos. [°2θ]	Height [cts]	FWHM Left [°2θ]	d-spacing [Å]	Rel. Int. [%]
17.2138	1248.58	0.1535	5.98147	20.37
20.4148	2159.31	0.1535	5.05132	35.22
21.7993	325.93	0.1535	4.73401	5.32
27.9360	1466.43	0.1535	3.70848	23.92
29.8889	114.16	0.3070	3.47117	1.86
30.9753	600.87	0.1023	3.35225	9.80
34.2619	1504.99	0.1023	3.03899	24.55
36.2194	376.50	0.4093	2.87982	6.14
41.5615	600.42	0.1023	2.52303	9.79
42.4812	6130.94	0.1791	2.47085	100.00
44.4894	118.80	0.3070	2.36461	1.94
48.1244	85.58	0.3070	2.19547	1.40
49.4693	1156.72	0.1791	2.13938	18.87
49.9334	1481.14	0.1023	2.12076	24.16
50.6846	1374.69	0.2303	2.09136	22.42
59.2891	375.45	0.2047	1.80979	6.12
64.3443	35.91	0.8187	1.68115	0.59
72.6189	609.92	0.1279	1.51171	9.95



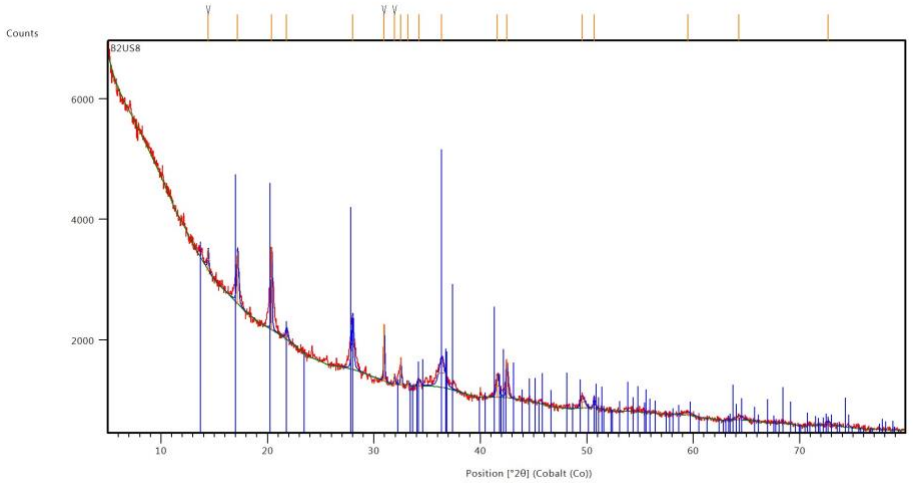
B2US8

Pattern List

Ref.Code	Mineral Name	SemiQuant[%]	Score	Compound Name	Scale Fac.	Chem. Formula
04-015-4888	Malachite	100	16	Copper Carbonate H..	0.566	Cu2 (C O3) (O H..

Peak List

Pos.[°2θ]	Height [cts]	FWHMLeft[°2θ]	d-spacing [Å]	Rel. Int. [%]
14.4256	350.67	0.1535	7.12958	25.48
17.1912	861.68	0.2047	5.98929	62.62
20.3894	1376.07	0.1023	5.05755	100.00
21.7974	180.73	0.3070	4.73443	13.13
27.9870	889.95	0.2303	3.70186	64.67
30.9552	949.20	0.1023	3.35437	68.98
31.9331	160.90	0.1535	3.25420	11.69
32.5250	454.20	0.1023	3.19654	33.01
33.1787	85.87	0.1535	3.13528	6.24
34.2136	98.63	0.3070	3.04315	7.17
36.3660	474.28	0.6140	2.86859	34.47
41.5964	367.49	0.2558	2.52101	26.71
42.4676	646.69	0.1535	2.47161	47.00
49.5843	186.68	0.4093	2.13474	13.57
50.6732	177.04	0.1535	2.09180	12.87
59.5037	49.47	0.8187	1.80385	3.59
64.2750	66.03	0.8187	1.68277	4.80
72.6430	74.10	0.3070	1.51128	5.38



CL

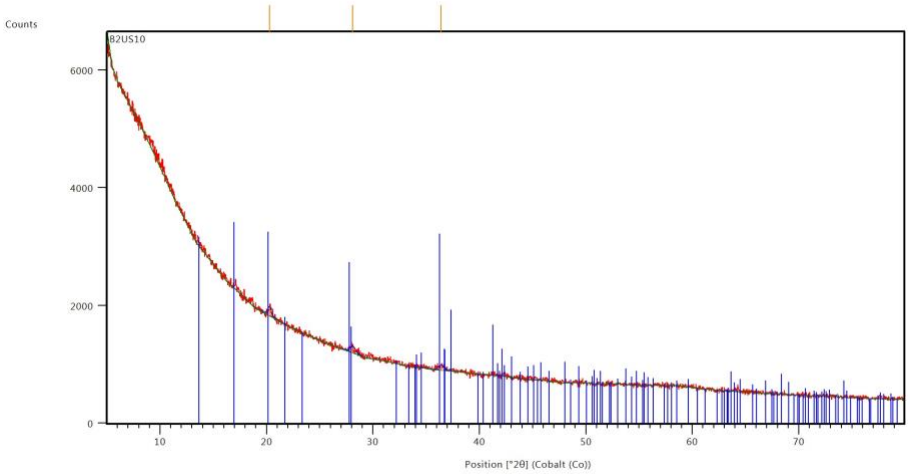
B2US10

Pattern List

Ref.Code	Mineral Name	SemiQuant[%]	Score	Compound Name	Scale Fac.	Chem. Formula
04-013-7662	Malachite	100	6	Copper Carbonate H..	0.348	Cu2 (C O3) (O H..

Peak List

Pos.[°2θ]	Height [cts]	FWHMLeft[°2θ]	d-spacing [Å]	Rel. Int. [%]
20.2693	153.75	0.4093	5.08719	100.00
28.0788	103.68	0.6140	3.69000	67.44
36.3768	81.60	0.6140	2.86777	53.07



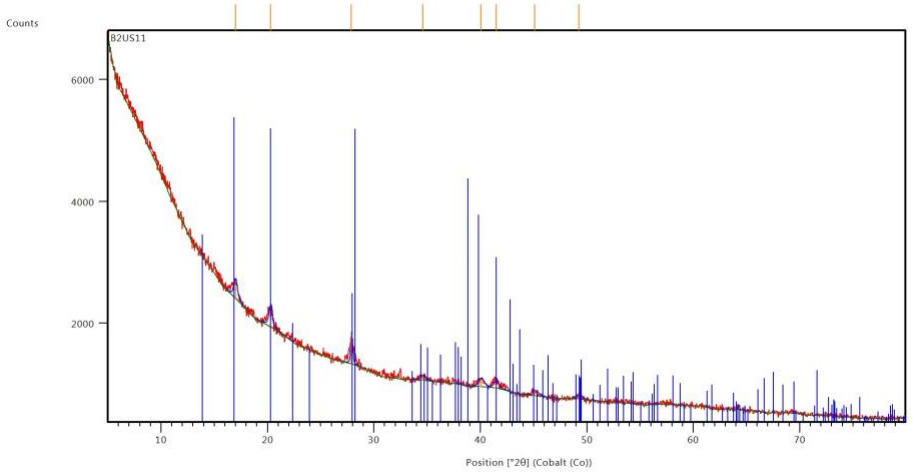
B2US11

Pattern List

Ref.Code	Mineral Name	SemiQuant[%]	Score	Compound Name	Scale Fac.	Chem. Formula
04-019-0179		100	Unmatch	Copper Carbonate H..	0.568	Cu2 (C O3) (O H..

Peak List

Pos.[°2θ]	Height [cts]	FWHMLeft[°2θ]	d-spacing [Å]	Rel. Int. [%]
16.9976	295.81	0.4093	6.05697	57.61
20.3011	340.78	0.4093	5.07931	66.37
27.8901	513.43	0.2047	3.71446	100.00
34.5754	75.63	0.6140	3.01226	14.73
40.0579	129.53	0.6140	2.61363	25.23
41.4815	121.30	0.5117	2.52768	23.62
45.0999	76.83	0.8187	2.33424	14.96
49.2732	55.45	0.6140	2.14736	10.80



CHINA

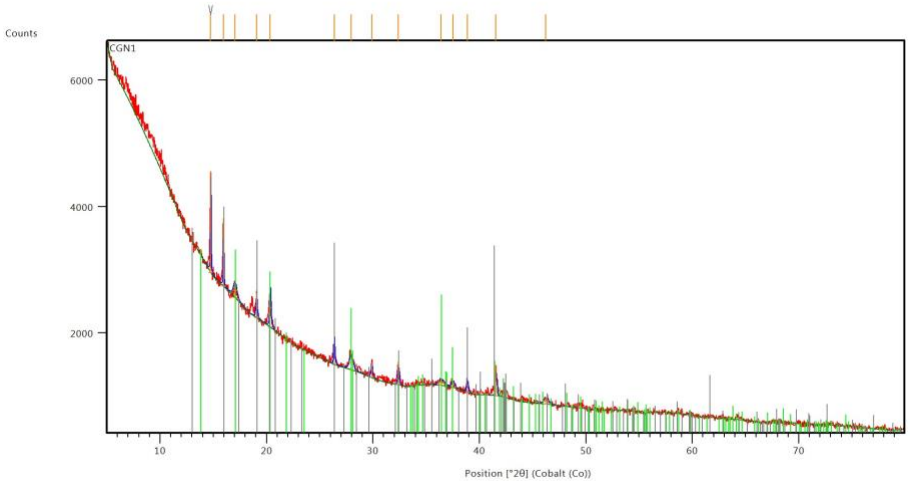
CGN1

Pattern List

Ref.Code	Mineral Name	SemiQuant[%]	Score	Compound Name	Scale Fac.	Chem. Formula
04-015-4888	Malachite	30	9	Copper Carbonate H..	0.216	Cu2 (C O3) (O H..
01-079-6416	Brochantite	70	14	Copper Sulfate Hyd..	0.358	Cu4 (S O4) (O H..

Peak List

Pos.[°2θ]	Height [cts]	FWHMLeft[°2θ]	d-spacing [Å]	Rel. Int. [%]
14.7548	1608.29	0.0768	6.97135	100.00
15.9541	1076.54	0.0768	6.45031	66.94
17.0515	228.58	0.4093	6.03796	14.21
19.0673	387.00	0.1535	5.40465	24.06
20.3536	609.31	0.1535	5.06634	37.89
26.3645	506.88	0.1023	3.92527	31.52
27.9535	223.71	0.4093	3.70621	13.91
29.8792	233.36	0.1535	3.47226	14.51
32.3857	366.04	0.1279	3.20992	22.76
36.3770	93.13	0.6140	2.86776	5.79
37.5037	100.07	0.3070	2.78456	6.22
38.8579	211.13	0.1535	2.69108	13.13
41.5484	485.27	0.1023	2.52379	30.17
46.2363	92.41	0.5117	2.27990	5.75



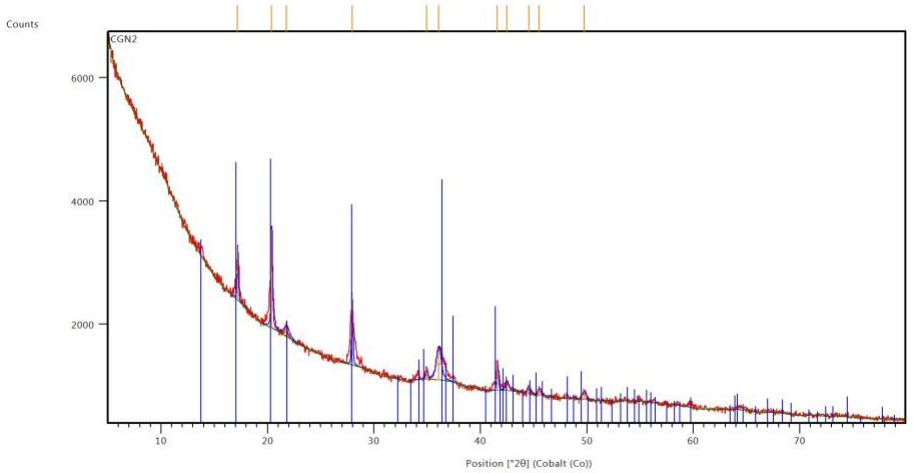
CGN2

Pattern List

Ref.Code	Mineral Name	SemiQuant[%]	Score	Compound Name	Scale Fac.	Chem. Formula
00-056-0001	Malachite	100	22	Copper Carbonate H..	0.482	Cu2 +2 (C O3) (..

Peak List

Pos.[°2θ]	Height [cts]	FWHMLeft[°2θ]	d-spacing [Å]	Rel. Int. [%]
17.1912	867.01	0.1279	5.98927	54.20
20.3983	1599.58	0.1535	5.05535	100.00
21.7873	161.35	0.6140	4.73659	10.09
27.9404	1151.11	0.1279	3.70791	71.96
34.9500	194.19	0.1535	2.98097	12.14
36.0708	506.55	0.5117	2.89128	31.67
41.5883	454.59	0.1535	2.52148	28.42
42.4910	148.78	0.3070	2.47031	9.30
44.5423	127.63	0.3070	2.36194	7.98
45.5289	110.04	0.3070	2.31339	6.88
49.7392	138.60	0.4093	2.12851	8.67



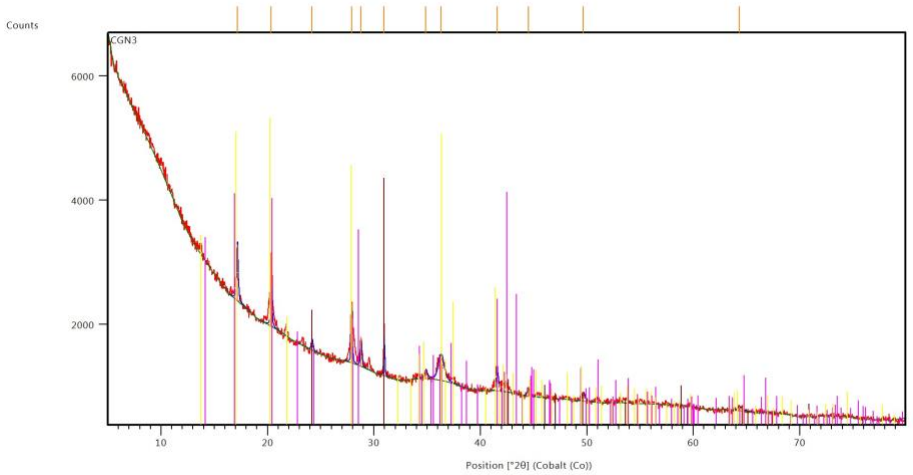
CGN3

Pattern List

Ref.Code	Mineral Name	SemiQuant[%]	Score	Compound Name	Scale Fac.	Chem. Formula
04-016-2085	Quartz	20	26	Silicon Oxide	0.474	Si O2
04-020-9522		40	Unmatch	Copper Carbonate H..	0.481	Cu2 (C O3) (O H..
00-056-0001	Malachite	41	25	Copper Carbonate H..	0.593	Cu2 +2 (C O3) (..

Peak List

Pos.[°2θ]	Height [cts]	FWHMLeft[°2θ]	d-spacing [Å]	Rel. Int. [%]
17.1552	900.37	0.1791	6.00174	76.41
20.3458	1178.36	0.1279	5.06826	100.00
24.1817	174.06	0.2047	4.27357	14.77
27.8946	951.74	0.1279	3.71388	80.77
28.7710	472.53	0.1279	3.60302	40.10
30.9517	805.34	0.0768	3.35475	68.34
34.8715	128.05	0.3070	2.98747	10.87
36.3009	393.27	0.6140	2.87357	33.37
41.5599	450.21	0.1535	2.52313	38.21
44.4931	119.97	0.3070	2.36442	10.18
49.6525	134.38	0.3070	2.13199	11.40
64.3319	64.51	0.6140	1.68144	5.47



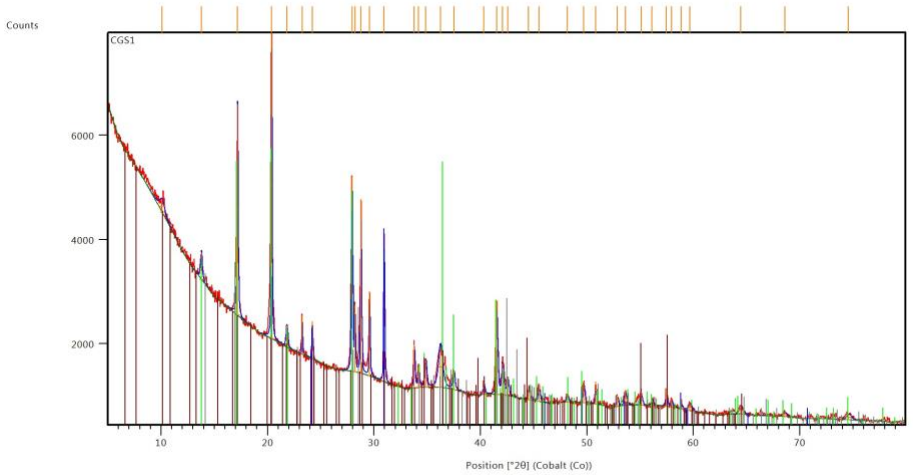
CGS1

Pattern List

Ref.Code	Mineral Name	SemiQuant[%]	Score	Compound Name	Scale Fac.	Chem. Formula
01-075-8320	Quartz	13	37	Silicon Oxide	0.368	Si O2
00-056-0001	Malachite	32	34	Copper Carbonate H..	0.543	Cu2 +2 (C O3) (..
04-020-9522		17	12	Copper Carbonate H..	0.234	Cu2 (C O3) (O H..
04-019-1452	Roxbyite	39	Unmatch	Copper Sulfide	0.172	Cu29 S16

Peak List

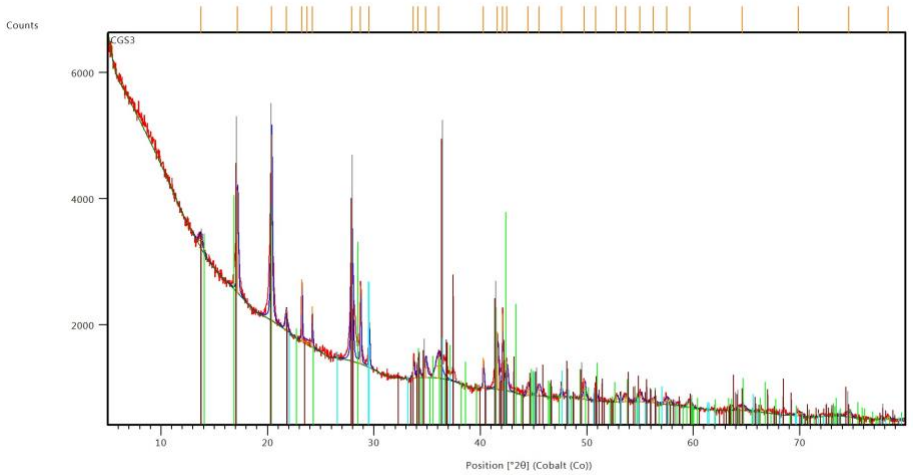
Pos.[°2θ]	Height [cts]	FWHMLeft[°2θ]	d-spacing [Å]	Rel. Int. [%]
10.0948	226.10	0.6140	10.17456	3.84
13.7922	516.53	0.2047	7.45529	8.77
17.1776	4039.92	0.1279	5.99397	68.57
20.3779	5891.93	0.1023	5.06036	100.00
21.8188	409.27	0.2047	4.72984	6.95
23.2502	747.95	0.0768	4.44229	12.69
24.2094	717.46	0.1023	4.26875	12.18
27.9388	3727.05	0.1279	3.70812	63.26
28.2134	1288.48	0.0768	3.67275	21.87
28.7752	3334.92	0.1023	3.60251	56.60
29.5819	1615.33	0.1023	3.50637	27.42
30.9521	2901.08	0.1023	3.35470	49.24
33.7891	826.89	0.1279	3.08024	14.03
34.1969	410.43	0.1535	3.04459	6.97
34.8641	521.42	0.2047	2.98809	8.85
36.2432	778.61	0.4605	2.87799	13.21
37.5005	350.62	0.2047	2.78479	5.95
40.3217	244.55	0.1535	2.59723	4.15
41.5408	1803.73	0.1535	2.52423	30.61
42.0680	593.93	0.2303	2.49400	10.08
42.5527	354.30	0.2047	2.46690	6.01
44.5306	240.54	0.2558	2.36253	4.08
45.4884	342.25	0.1535	2.31535	5.81
48.1620	148.25	0.2047	2.19386	2.52
49.7023	415.60	0.1791	2.12999	7.05
50.8168	428.85	0.1023	2.08628	7.28
52.8695	209.30	0.1535	2.01077	3.55
53.6142	263.34	0.2558	1.98487	4.47
55.1010	265.63	0.1535	1.93534	4.51
56.1274	124.47	0.2047	1.90275	2.11
57.4511	334.53	0.1279	1.86252	5.68
57.9575	133.22	0.2047	1.84764	2.26
58.8694	188.66	0.0768	1.82152	3.20
59.6579	138.07	0.4093	1.79962	2.34
64.4666	151.40	0.4093	1.67830	2.57
68.5902	86.48	0.3070	1.58869	1.47
74.5705	106.88	0.5117	1.47768	1.81



CGS3

Pattern List

Ref.Code	Mineral Name	SemiQuant[%]	Score	Compound Name	Scale Fac.	Chem. Formula
04-020-9522		26	13	Copper Carbonate H..	0.426	Cu2 (C O3) (O H..
00-056-0001	Malachite	31	26	Copper Carbonate H..	0.616	Cu2 +2 (C O3) (..
04-015-4888	Malachite	33	15	Copper Carbonate H..	0.572	Cu2 (C O3) (O H..
04-007-9727	Anhydrite	10	18	Calcium Sulfate	0.204	Ca (S O4)



Peak List

Pos.[°2θ]	Height [cts]	FWHMLeft[°2θ]	d-spacing [Å]	Rel. Int. [%]
13.7433	235.11	0.4093	7.48173	7.98
17.1971	1628.04	0.1535	5.98724	55.27
20.3702	2945.61	0.1791	5.06227	100.00
21.7691	347.29	0.2047	4.74051	11.79
23.2280	984.93	0.0768	4.44648	33.44
23.7094	64.10	0.8187	4.35746	2.18
24.2041	644.53	0.0768	4.26967	21.88
27.9268	2113.23	0.2047	3.70968	71.74
28.7440	1235.84	0.1023	3.60634	41.96
29.5541	738.73	0.1023	3.50960	25.08
33.7081	332.10	0.1023	3.08743	11.27
34.1449	273.90	0.2047	3.04909	9.30
34.8573	306.44	0.2558	2.98865	10.40
36.0793	385.10	0.6140	2.89062	13.07
40.2761	480.76	0.1023	2.60005	16.32
41.5791	909.20	0.1791	2.52201	30.87
42.0725	1211.09	0.1023	2.49375	41.12
42.5028	464.16	0.1535	2.46966	15.76
44.4647	191.82	0.2558	2.36586	6.51
45.5016	189.31	0.3070	2.31471	6.43
47.6233	174.76	0.1535	2.21720	5.93
49.7660	312.29	0.2047	2.12743	10.60
50.8229	232.04	0.2047	2.08604	7.88
52.7813	102.05	0.3070	2.01389	3.46
53.6444	114.48	0.4093	1.98384	3.89
54.9741	146.77	0.4093	1.93946	4.98
56.2645	85.13	0.3070	1.89849	2.89
57.5196	107.15	0.6140	1.86049	3.64
59.6583	121.31	0.4093	1.79961	4.12
64.5704	90.21	0.6140	1.67590	3.06
69.8785	67.75	0.6140	1.56302	2.30
74.5904	117.42	0.4093	1.47734	3.99
78.2957	60.55	0.3070	1.41790	2.06

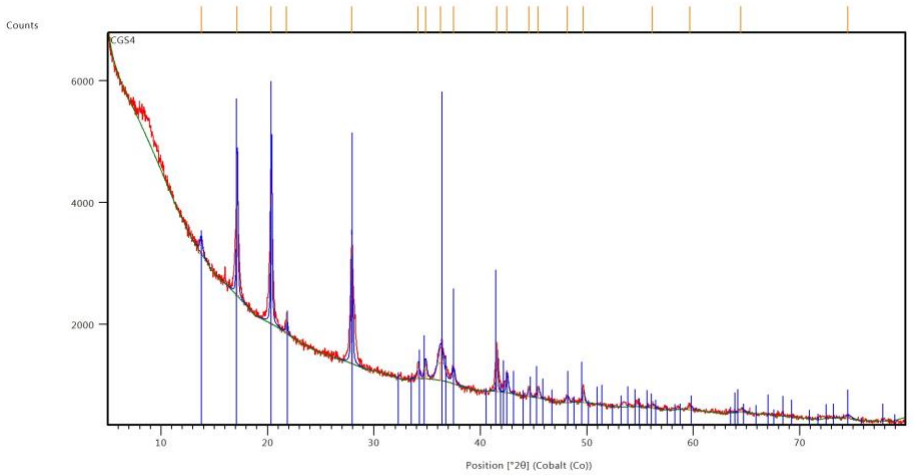
CGS4

Pattern List

Ref.Code	Mineral Name	SemiQuant[%]	Score	Compound Name	Scale Fac.	Chem. Formula
00-056-0001	Malachite	100	37	Copper Carbonate H..	0.697	Cu2 +2 (C O3) (..

Peak List

Pos.[°2θ]	Height [cts]	FWHMLeft[°2θ]	d-spacing [Å]	Rel. Int. [%]
13.7755	266.51	0.3070	7.46430	8.93
17.1521	2330.15	0.1535	6.00283	78.11
20.3565	2983.23	0.1535	5.06562	100.00
21.7985	338.88	0.1535	4.73419	11.36
27.9024	2116.23	0.1791	3.71287	70.94
34.1602	266.40	0.2047	3.04776	8.93
34.8380	305.47	0.2558	2.99025	10.24
36.2553	555.75	0.6140	2.87706	18.63
37.4627	238.35	0.3070	2.78750	7.99
41.5193	821.43	0.1279	2.52548	27.54
42.5010	345.12	0.2047	2.46976	11.57
44.5451	156.36	0.2047	2.36180	5.24
45.4367	198.57	0.2047	2.31784	6.66
48.1531	120.57	0.3070	2.19423	4.04
49.6595	242.99	0.1535	2.13171	8.15
56.1510	61.08	0.6140	1.90201	2.05
59.6900	71.64	0.4093	1.79874	2.40
64.4746	59.25	0.6140	1.67812	1.99
74.5004	57.75	0.6140	1.47887	1.94



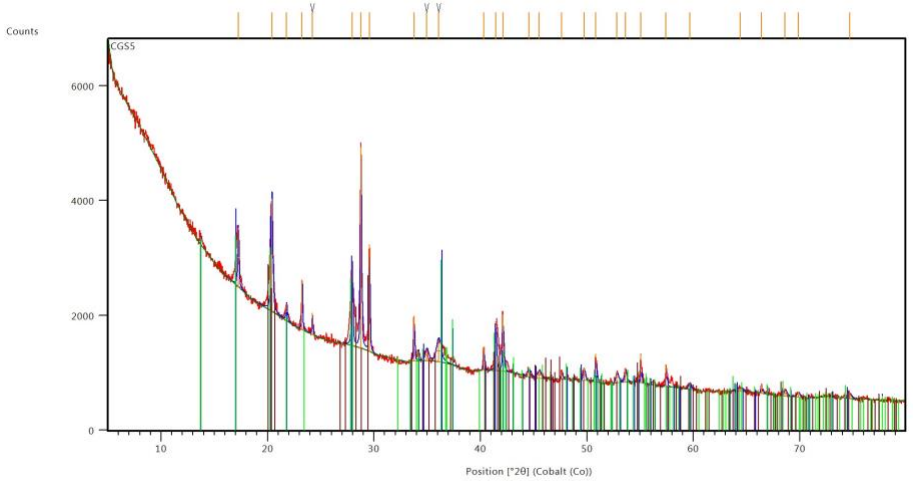
CGS5

Pattern List

Ref.Code	Mineral Name	SemiQuant[%]	Score	Compound Name	Scale Fac.	Chem. Formula
00-056-0001	Malachite	37	18	Copper Carbonate H..	0.287	Cu2 +2 (C O3) (..
04-013-7662	Malachite	40	10	Copper Carbonate H..	0.261	Cu2 (C O3) (O H..
04-015-4757	Azurite	23	Unmatch	Copper Carbonate H..	0.193	Cu3 (C O3)2 (O ..

Peak List

Pos.[°2θ]	Height [cts]	FWHM Left[°2θ]	d-spacing [Å]	Rel. Int. [%]
17.2495	1024.11	0.1535	5.96918	29.23
20.4022	1966.70	0.2047	5.05440	56.13
21.7902	308.07	0.1535	4.73597	8.79
23.2431	873.33	0.1023	4.44363	24.92
24.2019	374.89	0.1023	4.27005	10.70
27.9414	1482.80	0.1535	3.70778	42.32
28.7675	3504.07	0.1279	3.60345	100.00
29.5698	1860.97	0.1023	3.50778	53.11
33.7598	793.01	0.1023	3.08284	22.63
34.9695	198.79	0.3582	2.97936	5.67
36.0778	382.27	0.5117	2.89074	10.91
40.3177	417.71	0.1023	2.59748	11.92
41.4321	844.66	0.1535	2.53056	24.11
42.1094	993.26	0.1279	2.49166	28.35
44.5486	128.32	0.4093	2.36163	3.66
45.5060	127.44	0.4093	2.31450	3.64
47.6431	132.51	0.1535	2.21633	3.78
49.7415	209.68	0.2047	2.12841	5.98
50.8139	489.77	0.1279	2.08639	13.98
52.8251	191.81	0.2558	2.01234	5.47
53.6339	243.85	0.2047	1.98420	6.96
55.0500	488.55	0.0768	1.93699	13.94
57.4356	389.82	0.1023	1.86298	11.12
59.6512	98.65	0.3070	1.79980	2.82
64.4071	57.98	0.6140	1.67969	1.65
66.3865	158.74	0.1535	1.63509	4.53
68.6036	108.88	0.3070	1.58841	3.11
69.8520	84.32	0.3070	1.56354	2.41
74.6756	96.50	0.3070	1.47590	2.75



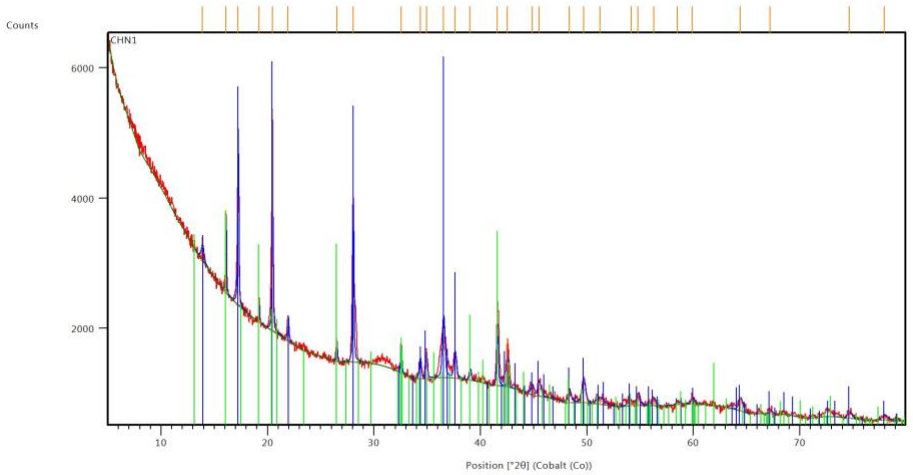
CHN1

Pattern List

Ref.Code	Mineral Name	SemiQuant[%]	Score	Compound Name	Scale Fac.	Chem. Formula
00-056-0001	Malachite	56	57	Copper Carbonate H..	0.752	Cu2 +2 (C O3) (..
04-011-4170	Brochantite	44	24	Copper Sulfate Hyd..	0.362	Cu4 (S O4) (O H..

Peak List

Pos. [°2θ]	Height [cts]	FWHM Left [°2θ]	d-spacing [Å]	Rel. Int. [%]
13.8983	235.22	0.3070	7.39867	6.93
16.1059	1266.16	0.0768	6.38994	37.30
17.2419	2609.76	0.1279	5.97179	76.89
19.2257	357.46	0.0768	5.36051	10.53
20.4630	3394.17	0.1023	5.03955	100.00
21.9332	369.68	0.1535	4.70546	10.89
26.4949	365.35	0.1023	3.90629	10.76
28.0433	2534.73	0.1279	3.69458	74.68
32.5500	507.89	0.1023	3.19415	14.96
34.3432	304.87	0.2047	3.03201	8.98
34.9322	449.14	0.1535	2.98244	13.23
36.5234	927.80	0.2558	2.85665	27.34
37.6180	402.73	0.2558	2.77641	11.87
39.0328	177.89	0.2047	2.67949	5.24
41.5774	1142.52	0.1279	2.52211	33.66
42.5392	751.69	0.1023	2.46764	22.15
44.8680	152.67	0.3582	2.34568	4.50
45.5133	214.17	0.3070	2.31415	6.31
48.3441	205.88	0.3070	2.18608	6.07
49.6794	367.52	0.3582	2.13091	10.83
51.2147	92.51	0.8187	2.07115	2.73
54.1881	64.99	0.8187	1.96542	1.91
54.8220	175.29	0.3070	1.94442	5.16
56.2777	112.27	0.4093	1.89808	3.31
58.4986	44.19	0.4093	1.83204	1.30
59.9022	103.80	0.3070	1.79296	3.06
64.4032	211.23	0.4093	1.67978	6.22
67.2078	50.87	0.3070	1.61741	1.50
74.6444	103.53	0.4093	1.47643	3.05
77.9196	71.00	0.6140	1.42365	2.09



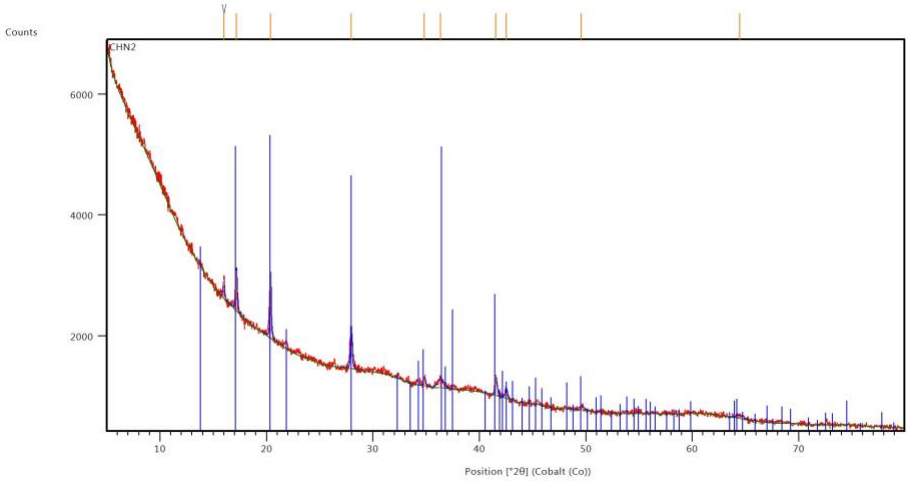
CHN2

Pattern List

Ref.Code	Mineral Name	SemiQuant[%]	Score	Compound Name	Scale Fac.	Chem. Formula
00-056-0001	Malachite	100	24	Copper Carbonate H..	0.578	Cu2 +2 (C O3) (..

Peak List

Pos.[°2θ]	Height [cts]	FWHMLeft[°2θ]	d-spacing [Å]	Rel. Int. [%]
15.9933	319.48	0.1535	6.43461	28.94
17.1704	669.61	0.1791	5.99648	60.66
20.3741	1103.82	0.1279	5.06131	100.00
27.9572	719.05	0.1535	3.70573	65.14
34.8236	132.80	0.2047	2.99145	12.03
36.3387	143.60	0.6140	2.87068	13.01
41.5383	328.28	0.2047	2.52438	29.74
42.5113	163.74	0.2558	2.46919	14.83
49.5603	63.80	0.6140	2.13570	5.78
64.4398	47.94	0.8187	1.67893	4.34



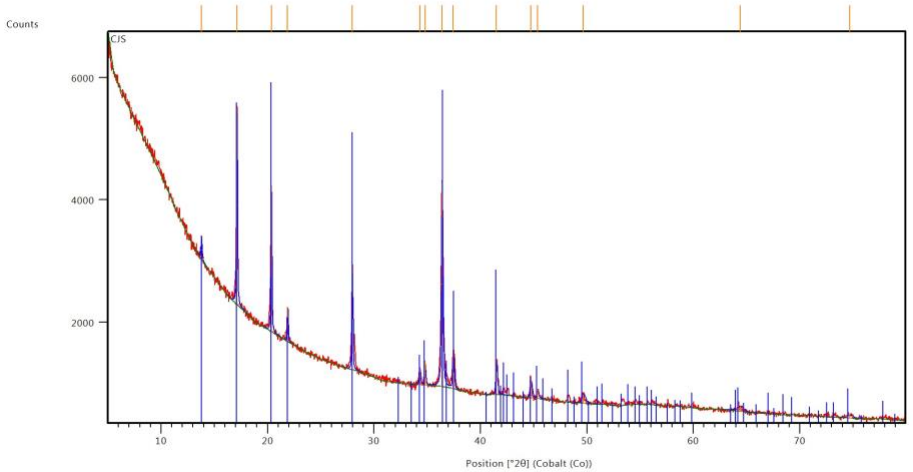
CJS

Pattern List

Ref.Code	Mineral Name	SemiQuant[%]	Score	Compound Name	Scale Fac.	Chem. Formula
00-056-0001	Malachite	100	44	Copper Carbonate H..	0.716	Cu2 +2 (C O3) (..

Peak List

Pos.[°2θ]	Height [cts]	FWHMLeft[°2θ]	d-spacing [Å]	Rel. Int. [%]
13.8031	294.89	0.1535	7.44947	8.81
17.1302	3248.63	0.1023	6.01044	97.06
20.3591	2388.57	0.1023	5.06498	71.36
21.8891	568.93	0.1023	4.71483	17.00
27.9650	1740.01	0.1023	3.70471	51.98
34.3088	254.98	0.1535	3.03495	7.62
34.7940	397.39	0.1023	2.99391	11.87
36.3872	3347.15	0.1535	2.86698	100.00
37.4465	638.38	0.1279	2.78866	19.07
41.4982	584.34	0.1535	2.52671	17.46
44.7580	286.76	0.2047	2.35114	8.57
45.3855	139.05	0.1535	2.32032	4.15
49.6766	141.32	0.4093	2.13102	4.22
64.3888	79.15	0.8187	1.68011	2.36
74.6825	49.11	0.6140	1.47578	1.47



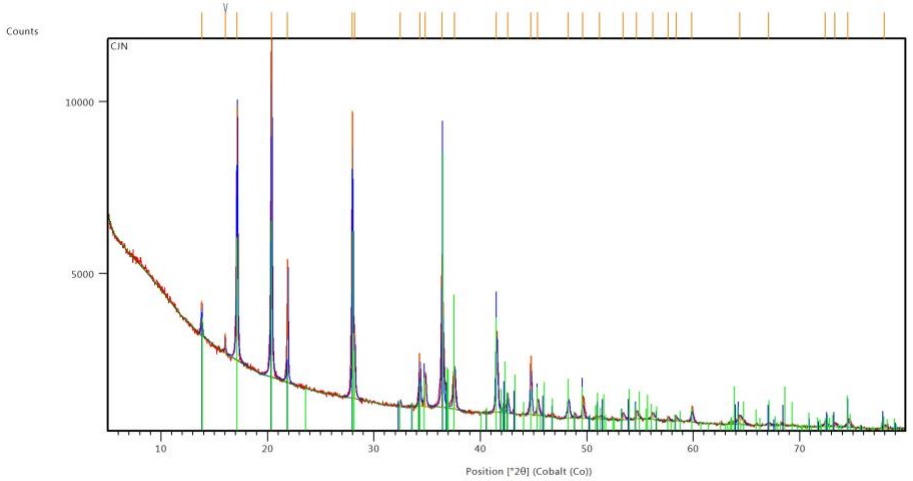
CJN

Pattern List

Ref.Code	Mineral Name	SemiQuant[%]	Score	Compound Name	Scale Fac.	Chem. Formula
00-056-0001	Malachite	49	47	Copper Carbonate H..	0.704	Cu2 +2 (C O3) (..
04-013-7662	Malachite	51	30	Copper Carbonate H..	0.627	Cu2 (C O3) (O H..

Peak List

Pos.[°2θ]	Height [cts]	FWHMLeft[°2θ]	d-spacing [Å]	Rel. Int. [%]
13.8261	1013.80	0.1023	7.43714	10.25
16.0323	575.02	0.0768	6.41906	5.81
17.1480	7418.31	0.1279	6.00424	74.99
20.3722	9891.99	0.1279	5.06176	100.00
21.8897	3599.46	0.1023	4.71472	36.39
27.9771	8367.87	0.1023	3.70314	84.59
28.2053	1888.90	0.0768	3.67379	19.10
32.4875	186.63	0.1535	3.20013	1.89
34.2979	1556.77	0.1279	3.03589	15.74
34.8068	1003.79	0.1791	2.99285	10.15
36.3956	4456.65	0.1535	2.86634	45.05
37.5621	1245.92	0.2047	2.78039	12.60
41.5034	2364.94	0.1791	2.52641	23.91
42.5645	594.71	0.1279	2.46624	6.01
44.7324	1695.55	0.1279	2.35242	17.14
45.3829	465.17	0.2047	2.32044	4.70
48.2623	575.31	0.2303	2.18957	5.82
49.6013	574.93	0.1279	2.13405	5.81
51.2035	80.12	0.6140	2.07157	0.81
53.3993	207.21	0.2558	1.99227	2.09
54.6865	231.71	0.2047	1.94887	2.34
56.1772	206.12	0.3070	1.90120	2.08
57.6332	129.75	0.2047	1.85713	1.31
58.3883	138.39	0.2047	1.83519	1.40
59.8582	442.81	0.1279	1.79415	4.48
64.3655	254.00	0.5117	1.68066	2.57
67.0515	70.02	0.3070	1.62074	0.71
72.4156	180.53	0.2558	1.51537	1.82
73.3171	95.39	0.3070	1.49931	0.96
74.5318	227.99	0.2047	1.47833	2.30
77.9498	96.38	0.3070	1.42318	0.97



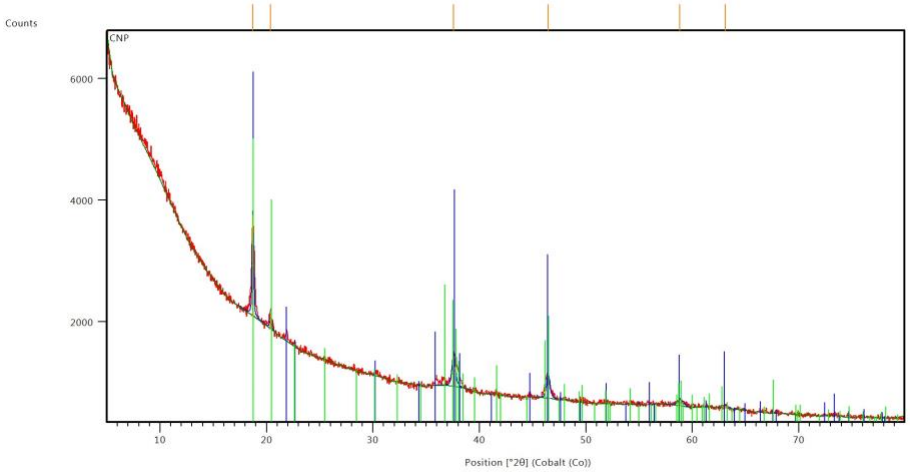
CNP

Pattern List

Ref.Code	Mineral Name	SemiQuant[%]	Score	Compound Name	Scale Fac.	Chem. Formula
01-083-4790		48	40	Copper Zinc Chlori..	0.591	(Cu3.75 Zn0.25) ..
01-080-9252	Atacamite	52	23	Copper Chloride Hy..	0.429	Cu2 Cl (O H)3

Peak List

Pos.[°2θ]	Height [cts]	FWHMLeft[°2θ]	d-spacing [Å]	Rel. Int. [%]
18.7074	1656.70	0.1535	5.50766	100.00
20.3714	291.96	0.1535	5.06196	17.62
37.5663	497.75	0.3582	2.78009	30.04
46.4343	372.24	0.3582	2.27071	22.47
58.8295	100.70	0.6140	1.82265	6.08
63.0852	42.80	0.6140	1.71114	2.58



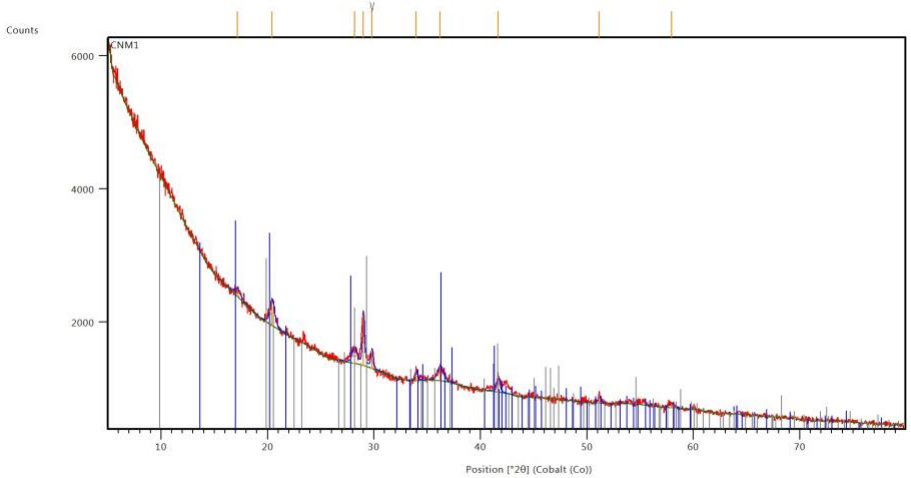
CNM1

Pattern List

Ref.Code	Mineral Name	SemiQuant[%]	Score	Compound Name	Scale Fac.	Chem. Formula
00-056-0001	Malachite	52	10	Copper Carbonate H..	0.260	Cu2 +2 (C O3) (..
04-018-0069		48	5	Copper Carbonate H..	0.264	Cu3 (C O3)2 (O ..

Peak List

Pos.[°2θ]	Height [cts]	FWHMLeft[°2θ]	d-spacing [Å]	Rel. Int. [%]
17.1805	115.87	0.6140	5.99298	15.21
20.4426	365.29	0.5117	5.04453	47.95
28.1636	215.45	0.5117	3.67912	28.28
29.0099	761.85	0.2303	3.57399	100.00
29.8108	272.86	0.2558	3.48006	35.81
33.9472	137.90	0.3070	3.06632	18.10
36.2200	212.64	0.6140	2.87976	27.91
41.6552	228.68	0.3070	2.51761	30.02
51.1670	113.75	0.3070	2.07295	14.93
57.9363	62.36	0.6140	1.84826	8.19



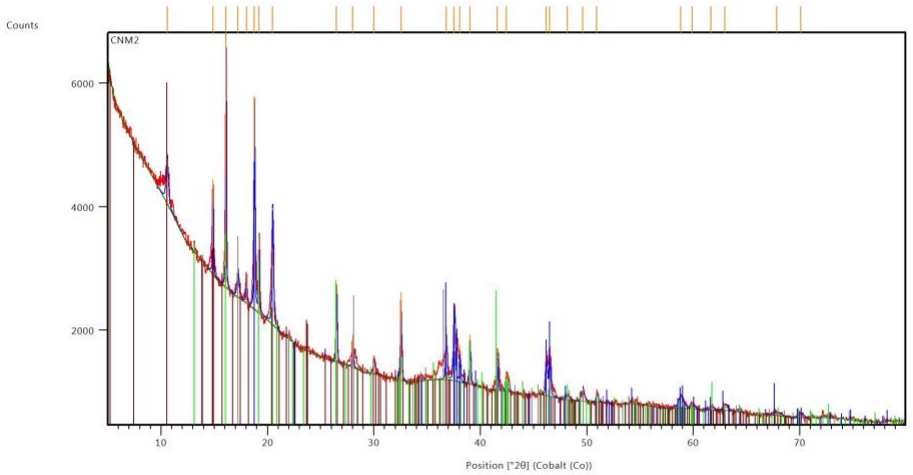
CNM2

Pattern List

Ref.Code	Mineral Name	SemiQuant[%]	Score	Compound Name	Scale Fac.	Chem. Formula
04-010-1616	Atacamite	28	35	Copper Chloride Hy..	0.351	Cu2 Cl (O H)3
01-079-6416	Brochantite	38	25	Copper Sulfate Hyd..	0.238	Cu4 (S O4) (O H..
00-056-0001	Malachite	21	26	Copper Carbonate H..	0.214	Cu2 +2 (C O3) (..
01-089-1668		13	11	Silicon Oxide	0.286	Si O2

Peak List

Pos.[°2θ]	Height [cts]	FWHMLeft[°2θ]	d-spacing [Å]	Rel. Int. [%]
10.5730	733.16	0.2558	9.71556	17.54
14.8670	1541.78	0.1023	6.91906	36.89
16.1023	4178.85	0.0768	6.39135	100.00
17.2211	435.87	0.2047	5.97897	10.43
18.0114	506.37	0.1023	5.71864	12.12
18.7705	3451.63	0.1023	5.48931	82.60
19.2137	1305.07	0.1023	5.36383	31.23
20.4843	1895.74	0.1535	5.03437	45.37
26.4884	1260.65	0.1023	3.90723	30.17
28.0245	459.46	0.1279	3.69701	10.99
30.0024	294.45	0.1535	3.45834	7.05
32.5430	1424.71	0.1023	3.19481	34.09
36.7812	858.53	0.1279	2.83731	20.54
37.5388	1263.44	0.1535	2.78205	30.23
38.0624	600.63	0.0768	2.74517	14.37
38.9989	806.29	0.1279	2.68172	19.29
41.5849	679.62	0.1023	2.52167	16.26
42.4550	283.76	0.1535	2.47231	6.79
46.2001	720.18	0.1279	2.28159	17.23
46.4853	774.58	0.1279	2.26836	18.54
48.1734	64.52	0.5117	2.19336	1.54
49.6083	140.74	0.4093	2.13377	3.37
50.9423	209.14	0.1535	2.08148	5.00
58.8076	195.76	0.5117	1.82327	4.68
59.9189	94.63	0.3070	1.79250	2.26
61.6706	53.95	0.6140	1.74640	1.29
62.9722	98.49	0.4093	1.71390	2.36
67.8310	55.87	0.8187	1.60430	1.34
70.1008	68.40	0.4093	1.55869	1.64



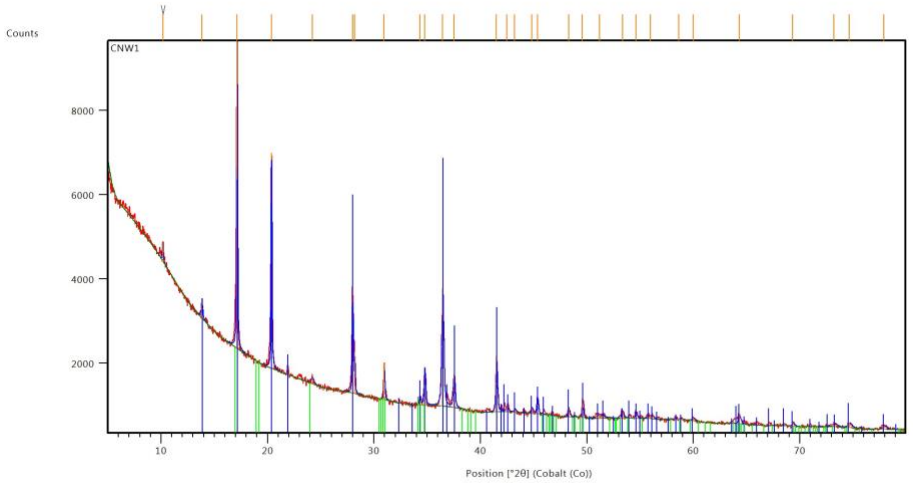
CNW1

Pattern List

Ref.Code	Mineral Name	SemiQuant[%]	Score	Compound Name	Scale Fac.	Chem. Formula
00-056-0001	Malachite	93	50	Copper Carbonate H..	0.609	Cu2 +2 (C O3) (..
04-015-7163		7	6	Silicon Oxide	0.020	Si O2

Peak List

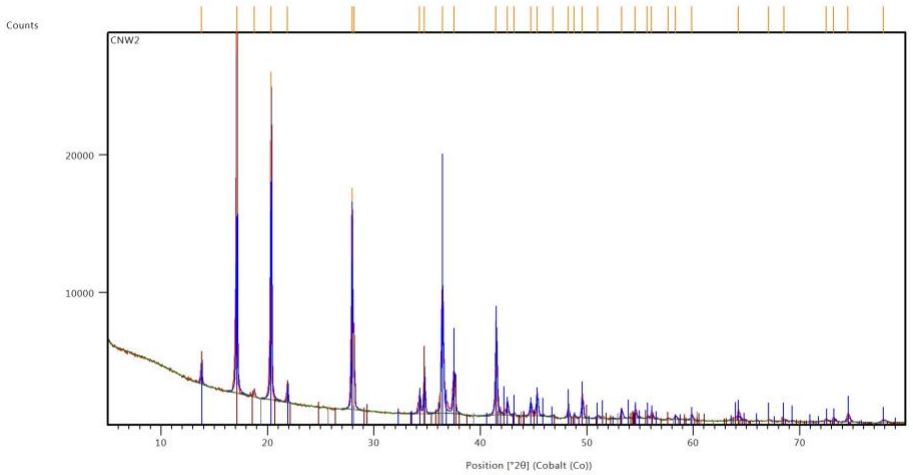
Pos. [°2θ]	Height [cts]	FWHM Left [°2θ]	d-spacing [Å]	Rel. Int. [%]
10.1690	456.59	0.1023	10.10047	6.17
13.8407	435.90	0.1535	7.42929	5.89
17.1427	7395.52	0.1023	6.00610	100.00
20.3742	5121.30	0.1023	5.06128	69.25
24.2124	144.83	0.3070	4.26824	1.96
27.9858	2642.04	0.1023	3.70202	35.72
28.1943	988.61	0.0768	3.67519	13.37
30.9531	873.85	0.1023	3.35460	11.82
34.3287	212.72	0.1535	3.03325	2.88
34.7757	914.18	0.1535	2.99545	12.36
36.4470	2790.96	0.2047	2.86243	37.74
37.5227	788.15	0.1791	2.78321	10.66
41.5131	1329.08	0.1535	2.52584	17.97
42.4869	112.10	0.3070	2.47054	1.52
43.2186	69.49	0.3070	2.43066	0.94
44.8207	147.54	0.2047	2.34802	1.99
45.3502	426.82	0.1535	2.32203	5.77
48.3072	205.47	0.1791	2.18766	2.78
49.5779	457.90	0.1023	2.13499	6.19
51.2123	83.00	0.8187	2.07124	1.12
53.3411	189.48	0.2047	1.99428	2.56
54.5999	170.14	0.1535	1.95172	2.30
55.9631	68.59	0.6140	1.90788	0.93
58.6487	8.50	0.8187	1.82776	0.11
59.9980	71.68	0.3070	1.79036	0.97
64.3082	244.91	0.2047	1.68199	3.31
69.3462	108.66	0.2047	1.57350	1.47
73.2140	69.61	0.6140	1.50112	0.94
74.6632	114.25	0.4093	1.47611	1.54
77.9101	90.47	0.4093	1.42379	1.22



CNW2

Pattern List

Ref.Code	Mineral Name	SemiQuant[%]	Score	Compound Name	Scale Fac.	Chem. Formula
00-056-0001	Malachite	59	61	Copper Carbonate H..	0.651	Cu2 +2 (C O3) (..
04-015-9842		11	18	Calcium Magnesium ..	0.128	Ca Mg (C O3)2
04-020-5889		31	21	Calcium Carbonate	0.170	Ca (C O3)



Peak List

Pos.[°2θ]	Height [cts]	FWHMLeft[°2θ]	d-spacing [Å]	Rel. Int. [%]
13.8055	2402.18	0.1023	7.44814	9.19
17.1103	26133.45	0.1023	6.01736	100.00
18.7457	644.93	0.1279	5.49652	2.47
20.3399	23811.59	0.1023	5.06971	91.12
21.8759	1688.44	0.1023	4.71764	6.46
27.9459	16098.61	0.1023	3.70719	61.60
28.1509	5557.16	0.0512	3.68074	21.26
34.2860	1650.26	0.1279	3.03692	6.31
34.7292	3467.09	0.1279	2.99933	13.27
36.4230	9507.60	0.1791	2.86425	36.38
37.5260	3150.39	0.1791	2.78296	12.05
41.4638	6822.20	0.1791	2.52872	26.11
42.5351	1052.99	0.1535	2.46787	4.03
43.1626	171.65	0.2558	2.43367	0.66
44.7208	982.52	0.2047	2.35299	3.76
45.3115	1711.36	0.1791	2.32390	6.55
46.7922	135.04	0.3070	2.25431	0.52
48.2660	756.04	0.1279	2.18941	2.89
48.7936	283.14	0.1535	2.16716	1.08
49.5560	1792.76	0.1279	2.13588	6.86
50.9965	226.98	0.3070	2.07941	0.87
53.2589	749.81	0.1535	1.99713	2.87
54.5350	876.81	0.1023	1.95386	3.36
55.6721	200.80	0.1535	1.91705	0.77
56.0776	630.58	0.1023	1.90430	2.41
57.6256	99.60	0.3070	1.85736	0.38
58.3204	286.96	0.2047	1.83714	1.10
59.8550	479.31	0.1279	1.79424	1.83
64.2289	797.82	0.1023	1.68385	3.05
67.0784	122.66	0.2558	1.62017	0.47
68.5259	136.09	0.3070	1.58999	0.52
72.4625	134.66	0.3070	1.51452	0.52
73.1701	353.44	0.0936	1.50081	1.35
74.5282	658.07	0.1535	1.47839	2.52
77.8529	209.42	0.5117	1.42467	0.80

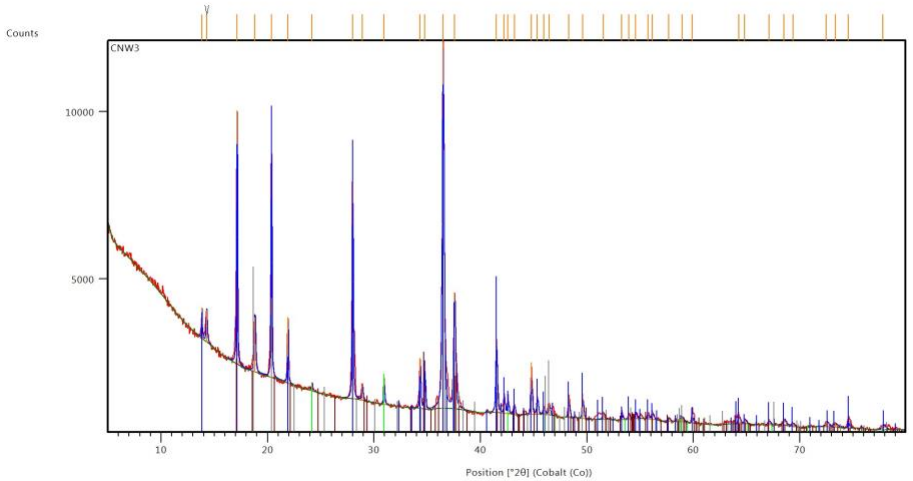
CNW3

Pattern List

Ref.Code	Mineral Name	SemiQuant[%]	Score	Compound Name	Scale Fac.	Chem. Formula
00-056-0001	Malachite	60	65	Copper Carbonate H..	0.795	Cu2 +2 (C O3) (..
01-075-8320	Quartz	3	30	Silicon Oxide	0.075	Si O2
04-013-1385	Atacamite	16	22	Copper Chloride Hy..	0.257	Cu2 Cl (O H)3
04-020-5889		21	14	Calcium Carbonate	0.140	Ca (C O3)

Peak List

Pos.[°2θ]	Height [cts]	FWHMLeft[°2θ]	d-spacing [Å]	Rel. Int. [%]
13.8409	917.53	0.0768	7.42922	8.32
14.2866	952.96	0.1279	7.19860	8.64
17.1400	7567.03	0.1023	6.00703	68.59
18.8152	1629.85	0.1791	5.47639	14.77
20.3725	6822.51	0.1023	5.06169	61.84
21.9239	1959.45	0.1023	4.70744	17.76
24.1812	232.17	0.1535	4.27367	2.10
27.9908	6992.32	0.1023	3.70137	63.38
28.9113	489.74	0.1279	3.58592	4.44
30.9457	714.46	0.1023	3.35537	6.48
34.3343	1507.28	0.1023	3.03277	13.66
34.7684	1199.69	0.1279	2.99605	10.87
36.4824	11031.67	0.1791	2.85975	100.00
37.5702	3476.80	0.1791	2.77981	31.52
41.5017	2212.22	0.1535	2.52651	20.05
42.2308	590.81	0.1023	2.48483	5.36
42.5794	590.31	0.1023	2.46542	5.35
43.1841	315.06	0.1791	2.43251	2.86
44.7743	1544.78	0.1023	2.35033	14.00
45.3369	513.69	0.1535	2.32267	4.66
45.9460	241.16	0.1535	2.29352	2.19
46.4333	341.96	0.1535	2.27076	3.10
48.3098	678.88	0.1023	2.18754	6.15
49.5991	736.28	0.1279	2.13414	6.67
51.5633	201.52	0.2558	2.05809	1.83
53.2840	281.30	0.0768	1.99626	2.55
53.9582	166.56	0.1535	1.97316	1.51
54.5909	194.80	0.2047	1.95202	1.77
55.7330	172.27	0.1535	1.91512	1.56
56.1628	230.65	0.1535	1.90165	2.09
57.6696	129.16	0.2558	1.85606	1.17
58.9500	146.29	0.3070	1.81925	1.33
59.8945	460.62	0.0768	1.79317	4.18
64.2607	330.06	0.1535	1.68310	2.99
64.8215	153.46	0.2558	1.67011	1.39
67.0980	147.59	0.2047	1.61975	1.34
68.5150	196.67	0.3582	1.59022	1.78
69.3524	97.29	0.3070	1.57338	0.88
72.5005	165.95	0.3070	1.51384	1.50
73.3300	113.03	0.4093	1.49908	1.02
74.5639	374.97	0.1023	1.47779	3.40
77.8279	149.18	0.4093	1.42506	1.35



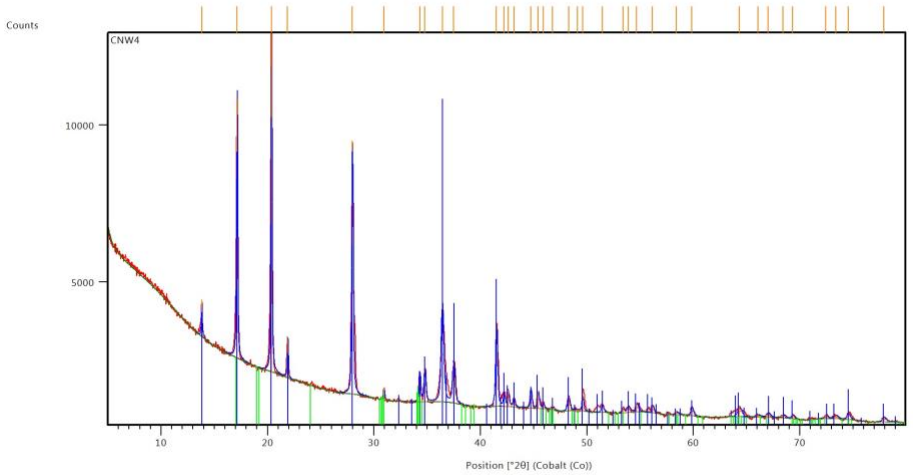
CNW4

Pattern List

Ref.Code	Mineral Name	SemiQuant[%]	Score	Compound Name	Scale Fac.	Chem. Formula
00-056-0001	Malachite	90	58	Copper Carbonate H..	0.745	Cu2 +2 (C O3) (..
04-015-7160		10	12	Silicon Oxide	0.038	Si O2

Peak List

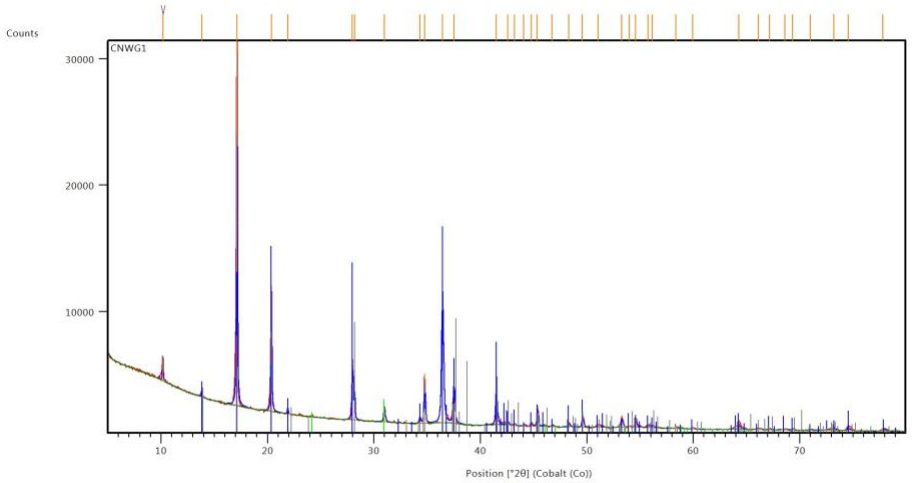
Pos. [°2θ]	Height [cts]	FWHM Left [°2θ]	d-spacing [Å]	Rel. Int. [%]
13.8255	1180.22	0.1023	7.43743	10.92
17.1443	8306.16	0.1279	6.00552	76.82
20.3675	10811.99	0.1279	5.06292	100.00
21.8816	1325.82	0.1279	4.71644	12.26
27.9759	8080.90	0.1535	3.70330	74.74
30.9364	387.06	0.1279	3.35636	3.58
34.2990	995.83	0.1535	3.03580	9.21
34.7641	1029.11	0.2047	2.99641	9.52
36.4167	3009.97	0.2814	2.86473	27.84
37.4723	1281.69	0.2558	2.78681	11.85
41.4976	2570.36	0.2047	2.52675	23.77
42.2145	474.28	0.1535	2.48574	4.39
42.6271	525.30	0.1535	2.46279	4.86
43.1511	277.81	0.2047	2.43428	2.57
44.7421	651.08	0.1791	2.35193	6.02
45.4165	550.23	0.2047	2.31882	5.09
45.9070	211.31	0.1535	2.29536	1.95
46.7643	75.68	0.4093	2.25558	0.70
48.2812	456.89	0.2558	2.18876	4.23
49.1121	21.56	0.8187	2.15397	0.20
49.5892	657.05	0.1279	2.13454	6.08
51.4418	280.18	0.2047	2.06262	2.59
53.3790	187.06	0.1535	1.99297	1.73
53.8974	196.19	0.3070	1.97521	1.81
54.6827	260.03	0.3070	1.94899	2.40
56.1749	234.63	0.2047	1.90127	2.17
58.4161	100.64	0.3070	1.83440	0.93
59.8511	295.07	0.2558	1.79435	2.73
64.3076	318.78	0.4093	1.68201	2.95
66.0802	65.61	0.4093	1.64180	0.61
67.0099	142.80	0.4093	1.62163	1.32
68.4458	101.82	0.4093	1.59163	0.94
69.3471	129.06	0.3070	1.57348	1.19
72.4570	127.90	0.3070	1.51462	1.18
73.3799	107.42	0.4093	1.49820	0.99
74.5498	240.62	0.2558	1.47803	2.23
77.9003	152.59	0.4093	1.42394	1.41



CNWg1

Pattern List

Ref.Code	Mineral Name	SemiQuant[%]	Score	Compound Name	Scale Fac.	Chem. Formula
00-056-0001	Malachite	55	46	Copper Carbonate H..	0.494	Cu2 +2 (C O3) (..
01-086-1560	Quartz	4	20	Silicon Oxide	0.057	Si O2
04-019-0177		41	20	Copper Carbonate H..	0.264	Cu2 (C O3) (O H..



Peak List

Pos.[°2θ]	Height [cts]	FWHMLeft[°2θ]	d-spacing [Å]	Rel. Int. [%]
10.1623	1936.36	0.1023	10.10711	6.67
13.8356	582.72	0.1023	7.43205	2.01
17.1284	29043.33	0.1023	6.01108	100.00
20.3587	9941.34	0.1023	5.06508	34.23
21.9061	459.36	0.1023	4.71122	1.58
27.9763	4906.39	0.1023	3.70325	16.89
28.1682	3135.57	0.0768	3.67853	10.80
30.9689	1262.18	0.1535	3.35293	4.35
34.3154	496.02	0.1279	3.03439	1.71
34.7501	3938.68	0.1279	2.99758	13.56
36.4250	10309.43	0.2047	2.86410	35.50
37.5057	2978.73	0.1791	2.78442	10.26
41.4834	2777.96	0.1791	2.52757	9.56
42.5842	365.24	0.1279	2.46516	1.26
43.2208	159.98	0.1535	2.43055	0.55
44.0729	127.10	0.3070	2.38582	0.44
44.7858	341.66	0.1023	2.34976	1.18
45.3358	1636.13	0.1279	2.32273	5.63
46.7273	162.14	0.2558	2.25726	0.56
48.3072	325.06	0.2047	2.18765	1.12
49.5842	945.71	0.1535	2.13474	3.26
51.0448	206.13	0.4093	2.07758	0.71
53.2700	865.77	0.1279	1.99675	2.98
53.9783	82.16	0.1535	1.97248	0.28
54.5516	710.90	0.1279	1.95331	2.45
55.7356	250.72	0.2047	1.91504	0.86
56.1438	210.90	0.1535	1.90224	0.73
58.3523	148.68	0.1535	1.83623	0.51
59.9328	142.07	0.2558	1.79213	0.49
64.2625	743.12	0.1023	1.68306	2.56
66.1345	61.82	0.6140	1.64061	0.21
67.1405	125.88	0.2047	1.61884	0.43
68.6145	62.62	0.4093	1.58819	0.22
69.3357	130.00	0.2047	1.57371	0.45
70.9930	90.34	0.3070	1.54163	0.31
73.2105	205.00	0.2047	1.50118	0.71
74.5365	382.04	0.1279	1.47825	1.32
77.8206	202.19	0.3582	1.42517	0.70

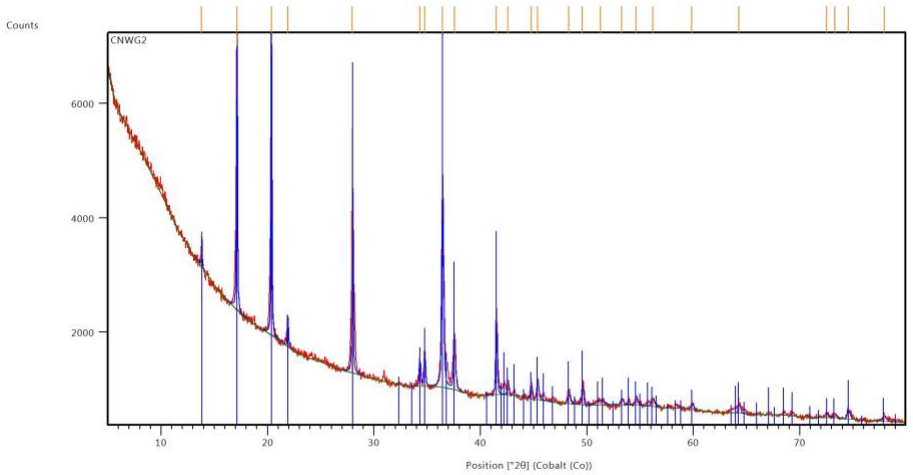
CNWg2

Pattern List

Ref.Code	Mineral Name	SemiQuant[%]	Score	Compound Name	Scale Fac.	Chem. Formula
00-056-0001	Malachite	100	61	Copper Carbonate H..	0.937	Cu2 +2 (C O3) (..

Peak List

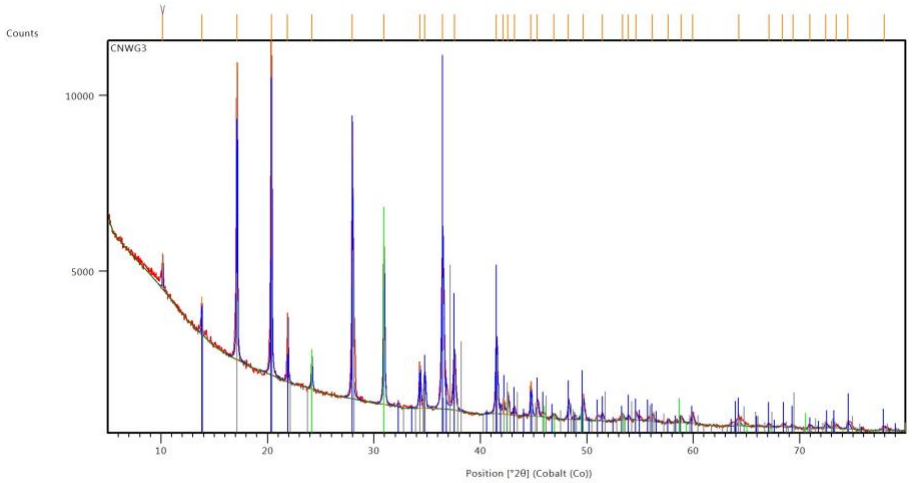
Pos.[°2θ]	Height [cts]	FWHMLeft[°2θ]	d-spacing [Å]	Rel. Int. [%]
13.8138	591.46	0.1023	7.44370	11.14
17.1274	4886.41	0.1023	6.01143	92.02
20.3585	5309.90	0.1023	5.06513	100.00
21.9031	549.68	0.1023	4.71187	10.35
27.9743	4278.85	0.1023	3.70351	80.58
34.3078	460.60	0.1535	3.03505	8.67
34.7587	668.94	0.1279	2.99686	12.60
36.4300	3767.91	0.1791	2.86372	70.96
37.5569	1006.43	0.1791	2.78076	18.95
41.4830	1491.37	0.1279	2.52760	28.09
42.5878	272.03	0.1535	2.46495	5.12
44.7767	360.55	0.1279	2.35021	6.79
45.3561	384.93	0.1791	2.32174	7.25
48.2920	240.84	0.2047	2.18830	4.54
49.5635	449.39	0.1279	2.13557	8.46
51.2861	85.33	0.8187	2.06846	1.61
53.2505	110.07	0.3070	1.99743	2.07
54.6206	137.23	0.3070	1.95104	2.58
56.1851	149.00	0.3070	1.90095	2.81
59.8374	107.29	0.2558	1.79472	2.02
64.2761	236.37	0.1535	1.68274	4.45
72.5221	82.92	0.3070	1.51345	1.56
73.2919	78.04	0.3070	1.49975	1.47
74.5410	203.33	0.2047	1.47818	3.83
77.9206	111.45	0.3070	1.42363	2.10



CNWg3

Pattern List

Ref.Code	Mineral Name	SemiQuant[%]	Score	Compound Name	Scale Fac.	Chem. Formula
00-056-0001	Malachite	54	59	Copper Carbonate H..	0.869	Cu2 +2 (C O3) (..
01-089-8937		18	45	Silicon Oxide	0.484	Si O2
04-019-0176		28	19	Copper Carbonate H..	0.356	Cu2 (C O3) (O H..



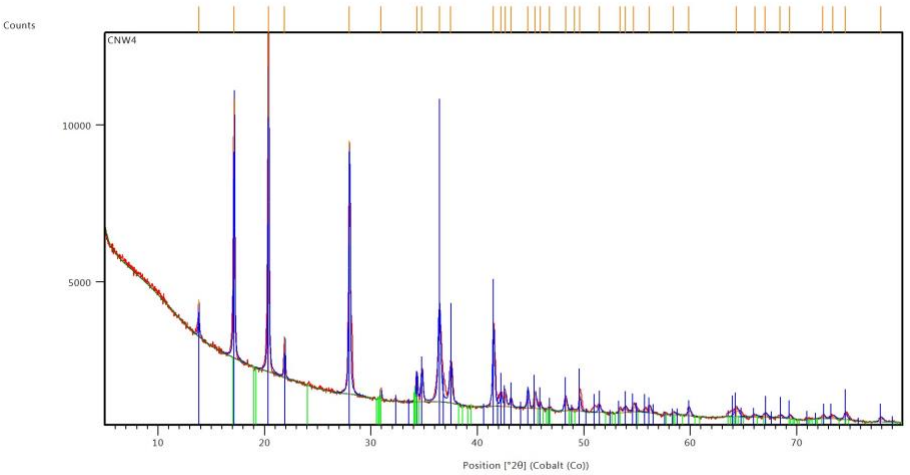
Peak List

Pos.[°2θ]	Height [cts]	FWHMLeft[°2θ]	d-spacing [Å]	Rel. Int. [%]
10.1429	1037.81	0.0768	10.12639	10.92
13.8251	1065.38	0.0768	7.43766	11.21
17.1313	8448.73	0.1023	6.01005	88.91
20.3626	9502.44	0.1023	5.06412	100.00
21.8904	1975.94	0.1023	4.71456	20.79
24.1690	968.55	0.1023	4.27579	10.19
27.9719	7892.33	0.1023	3.70382	83.06
30.9391	4517.59	0.1279	3.35608	47.54
34.3086	1286.21	0.1535	3.03498	13.54
34.7589	1039.57	0.1791	2.99685	10.94
36.4468	5154.10	0.2047	2.86245	54.24
37.5568	1723.34	0.2047	2.78076	18.14
41.4956	2206.48	0.2047	2.52686	23.22
42.1434	378.20	0.1791	2.48974	3.98
42.5857	651.79	0.1535	2.46507	6.86
43.1888	276.73	0.1791	2.43226	2.91
44.7446	990.88	0.1279	2.35181	10.43
45.3453	507.70	0.1279	2.32226	5.34
46.9082	126.23	0.4093	2.24905	1.33
48.2808	611.86	0.1535	2.18878	6.44
49.6388	666.94	0.2558	2.13254	7.02
51.4390	247.72	0.2047	2.06273	2.61
53.3415	191.11	0.2047	1.99427	2.01
53.9063	159.64	0.1535	1.97491	1.68
54.6401	244.18	0.1535	1.95039	2.57
56.1692	206.31	0.2047	1.90145	2.17
57.6387	124.45	0.2047	1.85697	1.31
58.8802	197.47	0.2047	1.82122	2.08
59.9206	294.95	0.2558	1.79246	3.10
64.2700	311.26	0.1535	1.68288	3.28
67.0940	98.84	0.2558	1.61983	1.04
68.3740	95.74	0.3582	1.59309	1.01
69.3494	68.09	0.3070	1.57344	0.72
70.9476	81.76	0.3070	1.54249	0.86
72.4308	158.52	0.2047	1.51510	1.67
73.4200	86.86	0.3070	1.49750	0.91
74.5313	239.82	0.2047	1.47834	2.52
77.9230	107.06	0.4093	1.42359	1.13

CNWg4

Pattern List

Ref.Code	Mineral Name	SemiQuant[%]	Score	Compound Name	Scale Fac.	Chem. Formula
04-016-2085	Quartz	37	55	Silicon Oxide	0.565	Si O2
00-056-0001	Malachite	63	61	Copper Carbonate H..	0.587	Cu2 +2 (C O3) (..



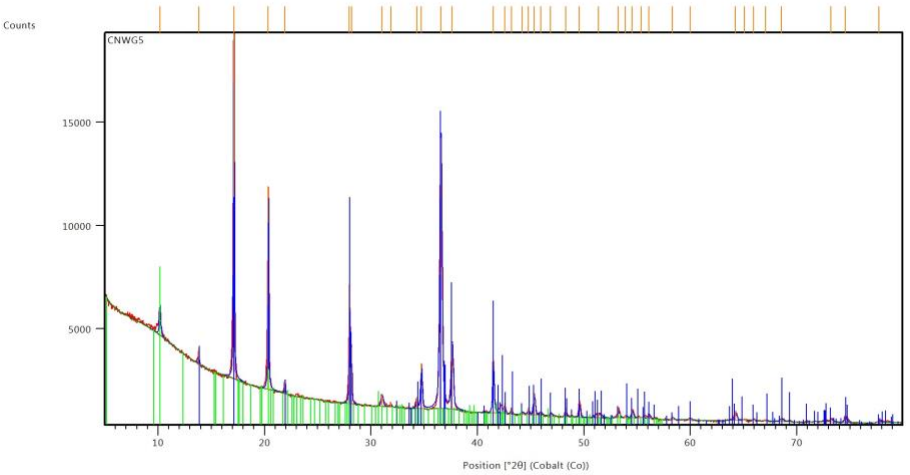
Peak List

Pos. [°2θ]	Height [cts]	FWHM Left [°2θ]	d-spacing [Å]	Rel. Int. [%]
10.1680	1516.31	0.0768	10.10149	15.22
13.8346	807.17	0.1023	7.43255	8.10
17.1453	8625.86	0.1279	6.00519	86.57
20.3713	8460.25	0.1279	5.06200	84.91
21.8974	786.33	0.1279	4.71308	7.89
24.1922	1466.16	0.0768	4.27176	14.71
27.9833	5981.79	0.1279	3.70234	60.03
30.9594	9963.85	0.1023	3.35393	100.00
34.3201	706.56	0.1279	3.03399	7.09
34.7914	1238.48	0.1535	2.99414	12.43
36.4364	4334.41	0.1791	2.86324	43.50
37.5722	1439.62	0.2303	2.77967	14.45
41.5127	2127.13	0.1535	2.52587	21.35
42.2166	393.99	0.1535	2.48563	3.95
42.5999	575.00	0.1535	2.46429	5.77
43.1677	221.50	0.2047	2.43339	2.22
44.7460	413.56	0.2047	2.35174	4.15
45.3701	502.22	0.1791	2.32106	5.04
46.0859	318.82	0.0768	2.28693	3.20
46.9434	80.88	0.4093	2.24746	0.81
48.2970	425.22	0.1279	2.18809	4.27
49.6217	795.91	0.1279	2.13323	7.99
51.4594	210.41	0.3070	2.06196	2.11
53.3303	203.10	0.4093	1.99466	2.04
54.6143	240.88	0.2558	1.95124	2.42
56.1711	205.91	0.2558	1.90139	2.07
58.8657	402.95	0.0768	1.82163	4.04
59.9052	180.49	0.2558	1.79288	1.81
64.2965	366.60	0.2047	1.68227	3.68
67.1040	95.90	0.3070	1.61962	0.96
68.4651	109.40	0.3070	1.59123	1.10
69.3349	101.87	0.3070	1.57372	1.02
70.8768	224.84	0.1023	1.54383	2.26
72.5831	97.10	0.3070	1.51235	0.97
73.3161	84.58	0.3070	1.49932	0.85
74.5591	201.76	0.2047	1.47787	2.02
77.9345	143.31	0.4093	1.42342	1.44

CNWg5

Pattern List

Ref.Code	Mineral Name	SemiQuant[%]	Score	Compound Name	Scale Fac.	Chem. Formula
01-080-8572		92	38	Copper Carbonate H..	0.743	Cu2 (C O3) (O H..
04-011-2637	Devilline	8	8	Calcium Copper Sul..	0.172	Ca Cu4 (S O4)2 (..



Peak List

Pos. [°2θ]	Height [cts]	FWHM Left [°2θ]	d-spacing [Å]	Rel. Int. [%]
10.1831	1367.30	0.1535	10.08657	8.01
13.8369	778.37	0.0768	7.43136	4.56
17.1203	17076.75	0.1023	6.01388	100.00
20.3545	9800.15	0.1023	5.06613	57.39
21.9118	687.90	0.1023	4.71001	4.03
27.9776	5765.23	0.1023	3.70308	33.76
28.1645	2742.76	0.0768	3.67900	16.06
31.0379	546.92	0.2047	3.34565	3.20
31.8801	237.22	0.0768	3.25947	1.39
34.3134	556.39	0.1279	3.03456	3.26
34.7334	2199.63	0.1535	2.99898	12.88
36.5531	13090.05	0.2303	2.85441	76.65
37.6205	3218.89	0.2047	2.77623	18.85
41.4765	2563.65	0.1535	2.52798	15.01
42.5769	476.37	0.0768	2.46556	2.79
43.1883	304.51	0.1279	2.43229	1.78
44.1835	110.61	0.3070	2.38015	0.65
44.7876	330.85	0.1023	2.34967	1.94
45.3158	1062.98	0.1791	2.32370	6.22
45.9472	156.51	0.2047	2.29346	0.92
46.8628	163.85	0.2047	2.25110	0.96
48.2991	405.56	0.1023	2.18800	2.37
49.5633	867.87	0.1023	2.13558	5.08
51.3732	196.62	0.6140	2.06519	1.15
53.2421	490.93	0.1023	1.99772	2.87
53.9151	87.72	0.2047	1.97462	0.51
54.5200	428.75	0.1535	1.95436	2.51
55.3794	34.59	0.8187	1.92637	0.20
56.1299	231.59	0.1535	1.90267	1.36
58.3150	148.74	0.1535	1.83730	0.87
59.9813	100.89	0.2558	1.79081	0.59
64.2170	425.48	0.1791	1.68412	2.49
65.0693	45.53	0.3070	1.66444	0.27
65.9199	56.60	0.3070	1.64534	0.33
67.0549	57.29	0.3070	1.62067	0.34
68.5367	144.52	0.3582	1.58977	0.85
73.2249	165.00	0.2047	1.50093	0.97
74.5425	351.30	0.2047	1.47815	2.06
77.7183	148.75	0.2047	1.42675	0.87

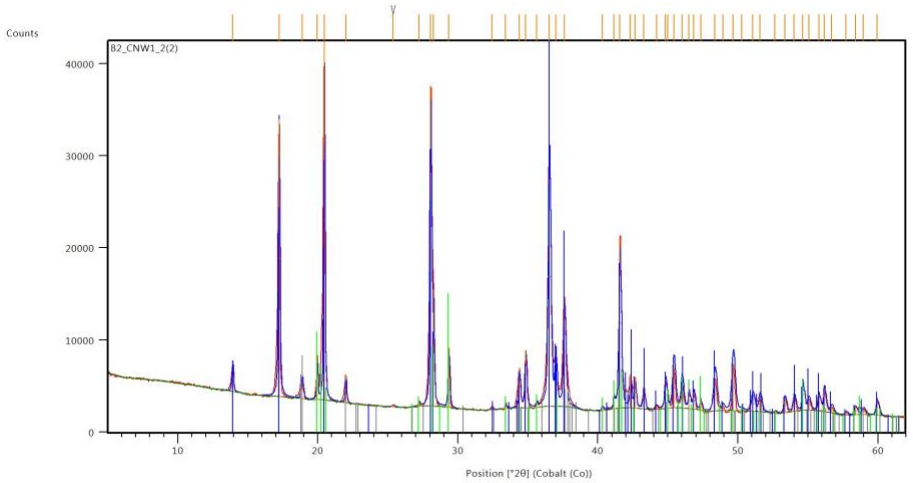
B2CNW1

Pattern List

Ref.Code	Mineral Name	SemiQuant[%]	Score	Compound Name	Scale Fac.	Chem. Formula
04-013-7662	Malachite	77	73	Copper Carbonate H..	1.162	Cu2 (C O3) (O H..
04-015-4757	Azurite	18	54	Copper Carbonate H..	0.291	Cu3 (C O3)2 (O ..
04-012-9781	Clinoatacamite	5	33	Copper Chloride Hy..	0.111	Cu2 Cl (O H)3

Peak List

Pos.[°2θ]	Height [cts]	FWHMLeft[°2θ]	d-spacing [Å]	Rel. Int. [%]
13.9212	3151.10	0.1279	7.38657	8.05
17.2303	30130.71	0.1279	5.97579	76.96
18.8932	2318.33	0.1791	5.45399	5.92
19.9562	4894.64	0.0768	5.16619	12.50
20.4574	39152.73	0.1023	5.04091	100.00
22.0014	3031.52	0.1023	4.69107	7.74
25.3720	215.06	0.3070	4.07614	0.55
27.2405	505.78	0.1023	3.80131	1.29
28.0628	34784.38	0.1279	3.69206	88.84
28.2655	12694.37	0.0768	3.66611	32.42
29.3592	6476.93	0.1279	3.53238	16.54
32.4351	394.17	0.1535	3.20516	1.01
33.4156	586.53	0.0768	3.11367	1.50
34.4030	4335.73	0.1279	3.02689	11.07
34.8497	6247.70	0.1535	2.98928	15.96
35.6262	677.77	0.1023	2.92617	1.73
36.5294	28247.48	0.2047	2.85620	72.15
36.9921	5372.32	0.1535	2.82170	13.72
37.6129	11906.01	0.1791	2.77677	30.41
40.3235	511.25	0.1023	2.59712	1.31
41.1494	1553.84	0.0768	2.54719	3.97
41.5725	18554.17	0.1791	2.52239	47.39
42.3244	3672.77	0.1279	2.47958	9.38
42.6449	3455.13	0.1279	2.46181	8.82
43.2786	2428.73	0.1535	2.42746	6.20
44.1934	446.41	0.1791	2.37964	1.14
44.8366	2906.37	0.1560	2.34553	7.42
44.9931	2083.02	0.0936	2.34287	5.32
45.4253	4397.36	0.2184	2.31671	11.23
46.0113	2879.98	0.1872	2.28878	7.36
46.5141	1780.22	0.1248	2.26539	4.55
46.8561	1773.05	0.1560	2.24978	4.53
47.3456	1253.85	0.0936	2.22784	3.20
48.3642	3599.43	0.2496	2.18365	9.19
48.9340	602.53	0.1248	2.15976	1.54
49.6631	5053.39	0.2496	2.13002	12.91
50.2913	205.60	0.1248	2.10511	0.53
51.0613	1690.61	0.2184	2.07545	4.32
51.5840	1648.05	0.2184	2.05584	4.21
52.6575	206.91	0.1872	2.01683	0.53
53.3594	1553.35	0.1872	1.99221	3.97
54.0179	1598.47	0.1872	1.96971	4.08
54.6446	3190.61	0.1248	1.94883	8.15
55.0638	1207.64	0.2184	1.93514	3.08
55.7885	1768.63	0.1560	1.91198	4.52
56.1888	2542.22	0.1560	1.89946	6.49
56.7007	714.65	0.2496	1.88372	1.83
57.7245	308.84	0.2496	1.85311	0.79
58.3965	927.79	0.1560	1.83363	2.37
58.9614	605.94	0.2496	1.81762	1.55
59.9374	1688.87	0.1560	1.79070	4.31



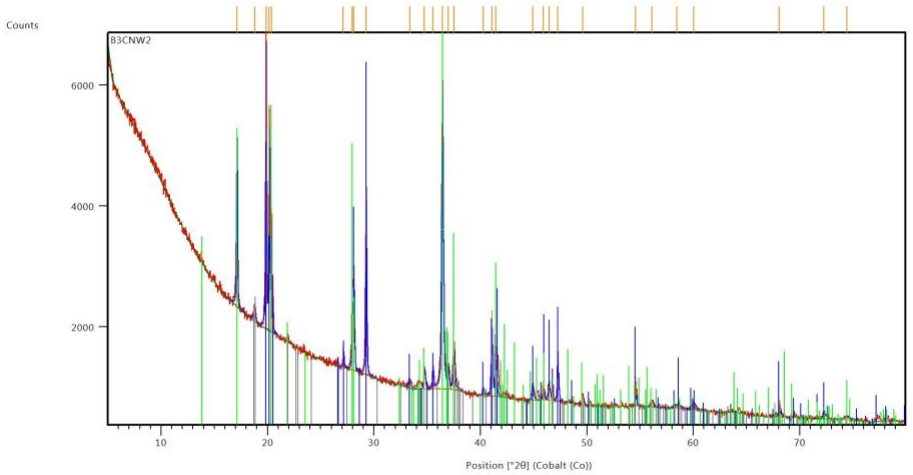
B2CNW2

Pattern List

Ref.Code	Mineral Name	SemiQuant[%]	Score	Compound Name	Scale Fac.	Chem. Formula
01-076-5942	Azurite	39	46	Copper Carbonate H..	0.752	Cu3 (C O3)2 (O ..
01-072-8421	Malachite	59	30	Copper Carbonate H..	0.863	Cu2 (O H)2 (C O..
04-012-9781	Clinoatacamite	2	13	Copper Chloride Hy..	0.062	Cu2 Cl (O H)3

Peak List

Pos.[°2θ]	Height [cts]	FWHMLeft[°2θ]	d-spacing [Å]	Rel. Int. [%]
17.1378	2797.87	0.1023	6.00779	52.92
18.7834	272.12	0.2047	5.48558	5.15
19.8624	4918.79	0.1023	5.19034	93.04
20.1648	3743.31	0.0768	5.11328	70.81
20.3623	2034.73	0.0768	5.06421	38.49
27.1190	349.05	0.1023	3.81801	6.60
27.9560	1320.72	0.0768	3.70588	24.98
28.1115	1658.95	0.1023	3.68579	31.38
29.2595	3258.49	0.1023	3.54415	61.64
33.3640	136.80	0.3070	3.11835	2.59
34.7401	374.76	0.1535	2.99841	7.09
35.5480	399.40	0.1023	2.93240	7.55
36.4280	5286.70	0.1535	2.86388	100.00
36.9848	396.88	0.1535	2.82223	7.51
37.5133	810.08	0.1279	2.78387	15.32
40.2627	136.47	0.1535	2.60088	2.58
41.0667	1407.10	0.1279	2.55209	26.62
41.4538	705.02	0.1279	2.52930	13.34
44.9328	265.80	0.1535	2.34247	5.03
45.9162	322.40	0.0768	2.29493	6.10
46.4452	277.35	0.1535	2.27021	5.25
47.2605	816.46	0.1023	2.23323	15.44
49.6172	138.54	0.2047	2.13341	2.62
54.5596	474.42	0.0768	1.95305	8.97
56.0902	113.45	0.3070	1.90391	2.15
58.4634	59.15	0.6140	1.83304	1.12
60.0312	98.44	0.4093	1.78946	1.86
68.0764	257.10	0.0768	1.59922	4.86
72.2661	122.43	0.2558	1.51808	2.32
74.4120	49.96	0.6140	1.48037	0.94



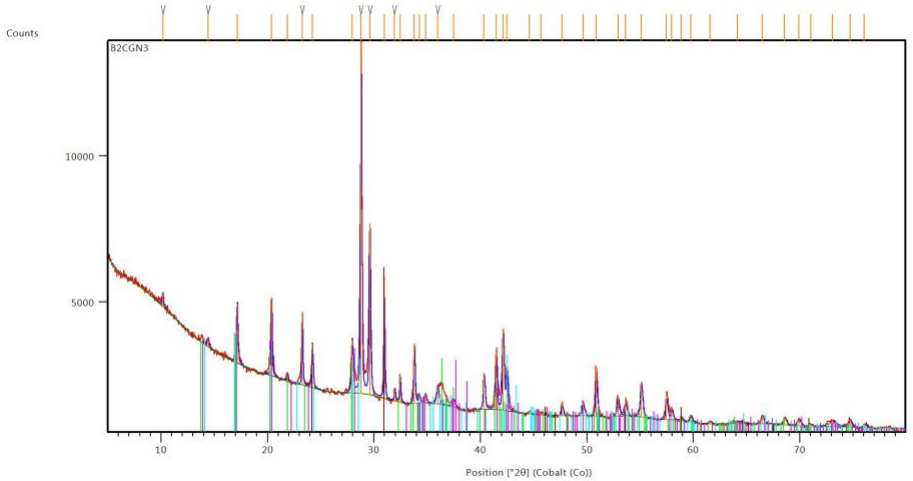
B2CGN3

Pattern List

Ref.Code	Mineral Name	SemiQuant[%]	Score	Compound Name	Scale Fac.	Chem. Formula
01-080-8572		20	20	Copper Carbonate H..	0.112	Cu2 (C O3) (O H..
04-016-2085	Quartz	30	35	Silicon Oxide	0.321	Si O2
04-020-9522		25	18	Copper Carbonate H..	0.137	Cu2 (C O3) (O H..
04-019-0177		25	9	Copper Carbonate H..	0.117	Cu2 (C O3) (O H..

Peak List

Pos.[°2θ]	Height [cts]	FWHMLeft[°2θ]	d-spacing [Å]	Rel. Int. [%]
10.1810	451.55	0.1535	10.08858	3.67
14.4277	293.63	0.2047	7.12852	2.39
17.1569	2012.57	0.1535	6.00114	16.37
20.3765	2690.68	0.1279	5.06072	21.89
21.8825	284.17	0.1791	4.71623	2.31
23.2689	2487.92	0.1023	4.43877	20.24
24.2084	1504.53	0.1535	4.26893	12.24
27.9575	1805.24	0.1791	3.70568	14.68
28.7905	12293.84	0.1279	3.60063	100.00
29.6092	5854.65	0.1535	3.50322	47.62
30.9672	4090.88	0.1023	3.35311	33.28
31.9491	441.44	0.1535	3.25262	3.59
32.4555	970.36	0.1279	3.20320	7.89
33.7984	2037.74	0.1279	3.07942	16.58
34.2597	307.84	0.1535	3.03918	2.50
34.8468	324.81	0.1791	2.98952	2.64
35.9818	600.60	0.2558	2.89819	4.89
37.4989	245.47	0.3070	2.78491	2.00
40.3351	1236.01	0.1791	2.59640	10.05
41.4793	1968.56	0.1535	2.52781	16.01
42.1356	2805.81	0.1791	2.49018	22.82
42.4748	1571.18	0.1279	2.47121	12.78
44.6172	106.76	0.3070	2.35818	0.87
45.6758	88.78	0.6140	2.30635	0.72
47.6633	502.77	0.1279	2.21545	4.09
49.6566	450.91	0.2047	2.13182	3.67
50.8553	1733.25	0.1279	2.08480	14.10
52.9279	718.25	0.2047	2.00872	5.84
53.6382	632.55	0.1279	1.98405	5.15
55.1146	1212.91	0.2303	1.93490	9.87
57.4768	913.14	0.1535	1.86175	7.43
57.9694	417.02	0.2047	1.84729	3.39
58.8778	144.29	0.2047	1.82128	1.17
59.7581	227.12	0.2558	1.79688	1.85
61.5645	93.76	0.3070	1.74911	0.76
64.1524	56.25	0.8187	1.68564	0.46
66.4914	299.15	0.2558	1.63280	2.43
68.5752	255.55	0.2558	1.58899	2.08
69.9265	235.34	0.3582	1.56208	1.91
71.0182	84.58	0.3070	1.54116	0.69
73.0754	193.22	0.7164	1.50357	1.57
74.7273	234.95	0.3070	1.47503	1.91
76.0437	112.66	0.3582	1.45326	0.92



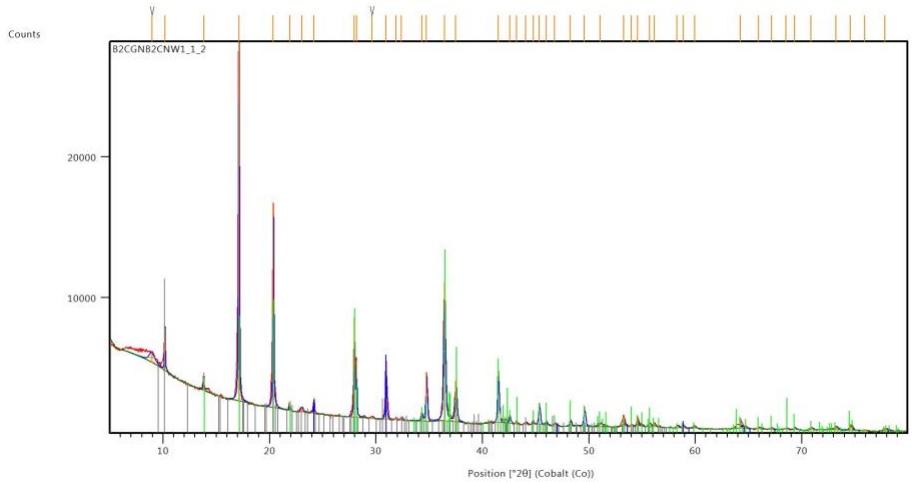
B2CGNB2CNW1

Pattern List

Ref.Code	Mineral Name	SemiQuant[%]	Score	Compound Name	Scale Fac.	Chem. Formula
04-016-2085	Quartz	14	46	Silicon Oxide	0.162	Si O2
01-072-8421	Malachite	73	45	Copper Carbonate H..	0.430	Cu2 (O H)2 (C O..
04-011-2637	Devilline	14	16	Calcium Copper Sul..	0.230	Ca Cu4 (S O4)2 (..

Peak List

Pos.[°2θ]	Height [cts]	FWHMLeft[°2θ]	d-spacing [Å]	Rel. Int. [%]
8.9514	680.39	0.6140	11.47094	2.61
10.1724	2972.55	0.1023	10.09711	11.39
13.8209	1208.05	0.1023	7.43990	4.63
17.1223	26096.99	0.1023	6.01319	100.00
20.3523	14545.49	0.1023	5.06667	55.74
21.8943	573.32	0.1023	4.71372	2.20
23.0323	316.72	0.2558	4.48375	1.21
24.1674	1065.90	0.1023	4.27606	4.08
27.9670	7029.22	0.1023	3.70446	26.93
28.1622	4020.90	0.0768	3.67928	15.41
29.6054	160.85	0.3070	3.50366	0.62
30.9342	4159.66	0.1023	3.35659	15.94
31.8898	166.89	0.1535	3.25850	0.64
32.3984	257.17	0.1791	3.20869	0.99
34.3268	656.19	0.1023	3.03341	2.51
34.7464	3491.22	0.1535	2.99789	13.38
36.4293	9838.46	0.1791	2.86378	37.70
37.4986	2862.66	0.1791	2.78493	10.97
41.4863	3680.25	0.1535	2.52740	14.10
42.5679	613.51	0.1279	2.46606	2.35
43.1954	228.60	0.1535	2.43191	0.88
44.0810	171.24	0.2047	2.38541	0.66
44.7622	339.29	0.0768	2.35093	1.30
45.3372	1537.04	0.1535	2.32266	5.89
45.9845	220.51	0.2047	2.29170	0.84
46.7900	219.42	0.2047	2.25441	0.84
48.2642	431.33	0.1279	2.18948	1.65
49.5831	1381.86	0.1535	2.13478	5.30
51.0571	279.03	0.3070	2.07711	1.07
53.2506	768.75	0.0768	1.99742	2.95
53.9797	120.83	0.1535	1.97243	0.46
54.5625	746.05	0.1023	1.95296	2.86
55.6870	254.29	0.2558	1.91658	0.97
56.1404	290.41	0.1535	1.90234	1.11
58.2943	178.04	0.2558	1.83789	0.68
58.8680	214.76	0.1535	1.82156	0.82
59.9203	182.48	0.2047	1.79247	0.70
64.2473	673.77	0.0768	1.68342	2.58
65.9574	109.96	0.4093	1.64451	0.42
67.1396	125.61	0.3070	1.61886	0.48
68.5343	81.82	0.3070	1.58982	0.31
69.3464	172.40	0.2047	1.57349	0.66
70.8782	178.57	0.2558	1.54380	0.68
73.2138	248.37	0.2558	1.50113	0.95
74.5366	387.86	0.2047	1.47825	1.49
75.9164	53.26	0.3070	1.45533	0.20
77.8115	227.61	0.2558	1.42531	0.87



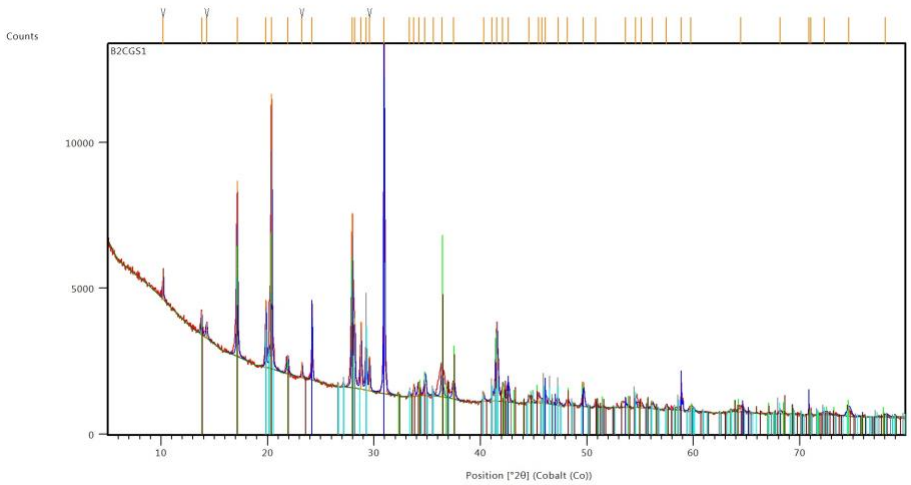
B2CGS1

Pattern List

Ref.Code	Mineral Name	SemiQuant[%]	Score	Compound Name	Scale Fac.	Chem. Formula
04-016-2085	Quartz	35	59	Silicon Oxide	0.992	Si O2
00-056-0001	Malachite	24	42	Copper Carbonate H..	0.414	Cu2 +2 (C O3) (..
04-013-7672	Azurite	13	30	Copper Carbonate H..	0.248	Cu3 (C O3)2 (O ..
01-072-8421	Malachite	19	25	Copper Carbonate H..	0.263	Cu2 (O H)2 (C O..
01-076-5942	Azurite	9	31	Copper Carbonate H..	0.161	Cu3 (C O3)2 (O ..

Peak List

Pos.[°2θ]	Height [cts]	FWHMLeft[°2θ]	d-spacing [Å]	Rel. Int. [%]
10.2048	1048.59	0.0768	10.06516	8.45
13.8161	806.11	0.1023	7.44247	6.50
14.2812	539.97	0.1535	7.20129	4.35
17.1540	6025.13	0.1023	6.00216	48.58
19.8537	2323.19	0.0768	5.19259	18.73
20.3715	9429.47	0.1023	5.06193	76.02
21.9005	615.91	0.1791	4.71241	4.97
23.2393	538.32	0.0768	4.44435	4.34
24.1902	2597.22	0.0768	4.27209	20.94
27.9459	5991.61	0.1023	3.70720	48.31
28.1811	2394.88	0.1023	3.67688	19.31
28.7755	2311.80	0.1023	3.60248	18.64
29.2622	2122.38	0.1023	3.54384	17.11
29.5850	1183.22	0.1023	3.50602	9.54
30.9518	12403.35	0.1023	3.35473	100.00
33.3212	174.08	0.1535	3.12225	1.40
33.7450	419.00	0.1279	3.08415	3.38
34.2096	464.81	0.2047	3.04349	3.75
34.7921	763.08	0.2047	2.99407	6.15
35.5738	163.34	0.1535	2.93034	1.32
36.3773	1186.07	0.1791	2.86773	9.56
37.4911	603.59	0.2558	2.78547	4.87
40.3092	303.12	0.1023	2.59800	2.44
41.0853	472.79	0.0768	2.55099	3.81
41.5168	2716.72	0.2303	2.52563	21.90
42.0938	631.71	0.1791	2.49255	5.09
42.6012	727.52	0.1791	2.46421	5.87
44.5667	261.48	0.2047	2.36071	2.11
45.4506	370.39	0.1791	2.31717	2.99
45.7986	131.14	0.4093	2.30050	1.06
46.0870	499.82	0.1023	2.28688	4.03
47.3013	262.91	0.2047	2.23142	2.12
48.1460	194.78	0.3070	2.19454	1.57
49.6428	848.41	0.1535	2.13238	6.84
50.8421	302.23	0.1535	2.08531	2.44
53.6397	345.97	0.0768	1.98400	2.79
54.5665	518.53	0.0768	1.95282	4.18
55.1041	255.71	0.1535	1.93524	2.06
56.1354	245.62	0.2558	1.90250	1.98
57.4575	184.69	0.2047	1.86233	1.49
58.8730	954.02	0.0768	1.82142	7.69
59.7749	204.18	0.4093	1.79642	1.65
64.4626	194.72	0.4093	1.67840	1.57
68.1337	185.18	0.1535	1.59803	1.49
70.8678	405.41	0.0936	1.54288	3.27
71.0574	269.64	0.0936	1.54265	2.17
72.3023	78.04	0.7488	1.51632	0.63
74.5859	267.94	0.3744	1.47635	2.16
78.0441	82.27	0.4992	1.42071	0.66



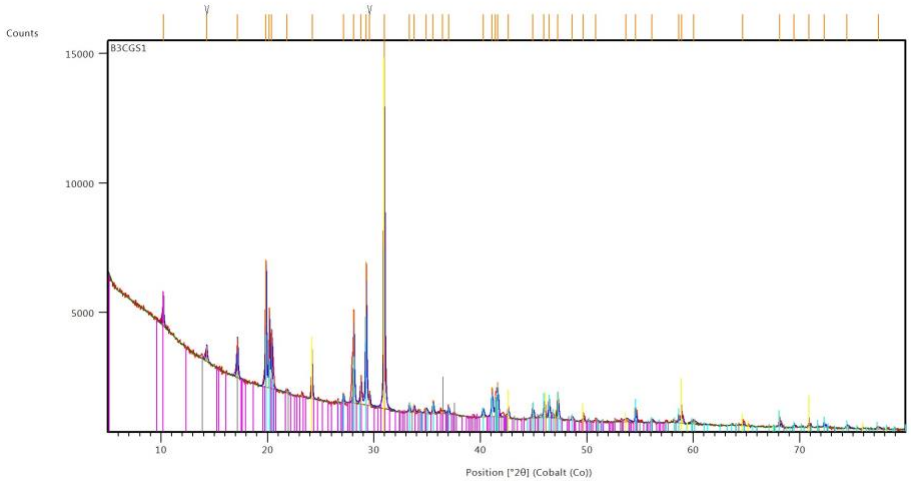
B3CGS1

Pattern List

Ref.Code	Mineral Name	SemiQuant[%]	Score	Compound Name	Scale Fac.	Chem. Formula
00-056-0001	Malachite	11	18	Copper Carbonate H..	0.092	Cu2 +2 (C O3) (..
04-015-4757	Azurite	24	46	Copper Carbonate H..	0.220	Cu3 (C O3)2 (O ..
04-011-2637	Devilline	4	8	Calcium Copper Sul..	0.085	Ca Cu4 (S O4)2 (..
01-070-7344	Quartz	60	46	Silicon Oxide	0.874	Si O2

Peak List

Pos.[°2θ]	Height [cts]	FWHMLeft[°2θ]	d-spacing [Å]	Rel. Int. [%]
10.2126	1270.44	0.1023	10.05744	8.86
14.2828	595.88	0.1535	7.20050	4.16
17.1770	1539.71	0.1279	5.99418	10.74
19.8548	4925.04	0.1023	5.19230	34.35
20.1690	3100.35	0.0768	5.11222	21.62
20.3788	2297.84	0.1023	5.06015	16.03
21.8307	145.46	0.3070	4.72730	1.01
24.1915	1914.58	0.0768	4.27188	13.35
27.1338	377.05	0.1023	3.81598	2.63
28.1054	3581.69	0.1023	3.68657	24.98
28.7782	1135.57	0.1023	3.60214	7.92
29.2679	5516.87	0.1023	3.54316	38.48
29.6046	535.28	0.0768	3.50375	3.73
30.9587	14338.56	0.1023	3.35400	100.00
33.3403	347.86	0.1023	3.12051	2.43
33.7710	310.76	0.1279	3.08185	2.17
34.9200	186.80	0.2558	2.98345	1.30
35.5588	505.72	0.1279	2.93154	3.53
36.4339	121.86	0.4093	2.86342	0.85
37.0069	387.21	0.1023	2.82061	2.70
40.2536	352.19	0.1791	2.60144	2.46
41.0882	1124.15	0.1279	2.55082	7.84
41.4234	884.44	0.1023	2.53107	6.17
41.6314	1305.35	0.1023	2.51898	9.10
42.6152	463.83	0.1023	2.46344	3.23
44.9219	562.18	0.1023	2.34300	3.92
45.9533	637.27	0.0768	2.29317	4.44
46.4433	693.04	0.1023	2.27030	4.83
47.2670	1045.14	0.1023	2.23294	7.29
48.6380	183.96	0.1535	2.17367	1.28
49.6432	341.00	0.0768	2.13236	2.38
50.8103	130.84	0.2047	2.08653	0.91
53.6786	126.36	0.6140	1.98267	0.88
54.5629	679.40	0.0768	1.95294	4.74
56.1122	143.02	0.2047	1.90322	1.00
58.6137	358.96	0.0768	1.82876	2.50
58.9246	380.60	0.1535	1.81997	2.65
60.0230	130.06	0.5117	1.78969	0.91
64.6265	234.10	0.0768	1.67460	1.63
68.0979	414.65	0.0768	1.59877	2.89
69.4640	120.82	0.2047	1.57117	0.84
70.8540	269.64	0.1535	1.54426	1.88
72.2901	193.28	0.0936	1.51654	1.35
74.4421	156.92	0.2047	1.47986	1.09
77.3791	90.77	0.3070	1.43202	0.63



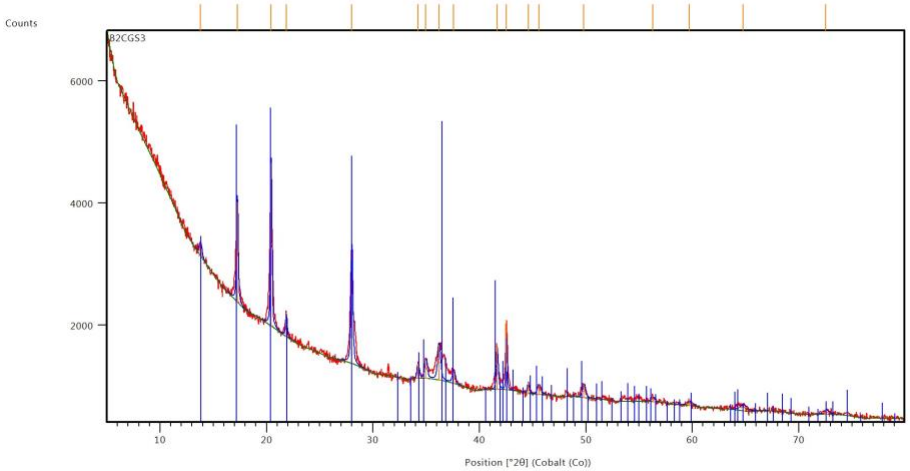
B2CGS3

Pattern List

Ref.Code	Mineral Name	SemiQuant[%]	Score	Compound Name	Scale Fac.	Chem. Formula
00-056-0001	Malachite	100	32	Copper Carbonate H..	0.621	Cu2 +2 (C O3) (..

Peak List

Pos.[°2θ]	Height [cts]	FWHMLeft[°2θ]	d-spacing [Å]	Rel. Int. [%]
13.8021	217.15	0.3070	7.44996	8.14
17.2527	1638.37	0.1791	5.96809	61.40
20.4319	2668.26	0.1535	5.04714	100.00
21.8472	392.08	0.1535	4.72376	14.69
28.0029	1890.56	0.2047	3.69980	70.85
34.2347	244.68	0.2047	3.04133	9.17
34.9600	313.73	0.2558	2.98014	11.76
36.1947	573.24	0.3070	2.88171	21.48
37.5788	215.73	0.3070	2.77920	8.08
41.6582	700.51	0.1791	2.51743	26.25
42.5156	1134.98	0.1023	2.46895	42.54
44.5857	171.47	0.2047	2.35976	6.43
45.5809	152.23	0.4093	2.31090	5.71
49.7998	217.33	0.3582	2.12608	8.15
56.2803	75.45	0.3070	1.89800	2.83
59.7349	65.99	0.6140	1.79752	2.47
64.7613	96.43	0.8187	1.67149	3.61
72.5159	69.18	0.6140	1.51356	2.59



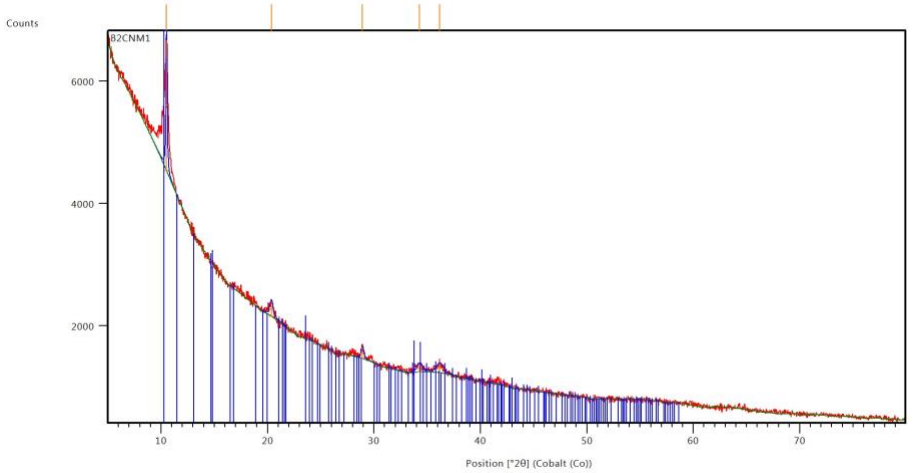
B2CNM1

Pattern List

Ref.Code	Mineral Name	SemiQuant[%]	Score	Compound Name	Scale Fac.	Chem. Formula
01-081-8023	Sampleite	100	6	Sodium Calcium Cop..	0.442	Na Ca Cu5 (P O4)2..

Peak List

Pos.[°2θ]	Height [cts]	FWHMLeft[°2θ]	d-spacing [Å]	Rel. Int. [%]
10.5100	2129.09	0.1535	9.77364	100.00
20.3713	244.63	0.4093	5.06199	11.49
28.9100	188.87	0.3070	3.58607	8.87
34.2697	134.23	0.6140	3.03832	6.30
36.1580	142.69	0.8187	2.88454	6.70



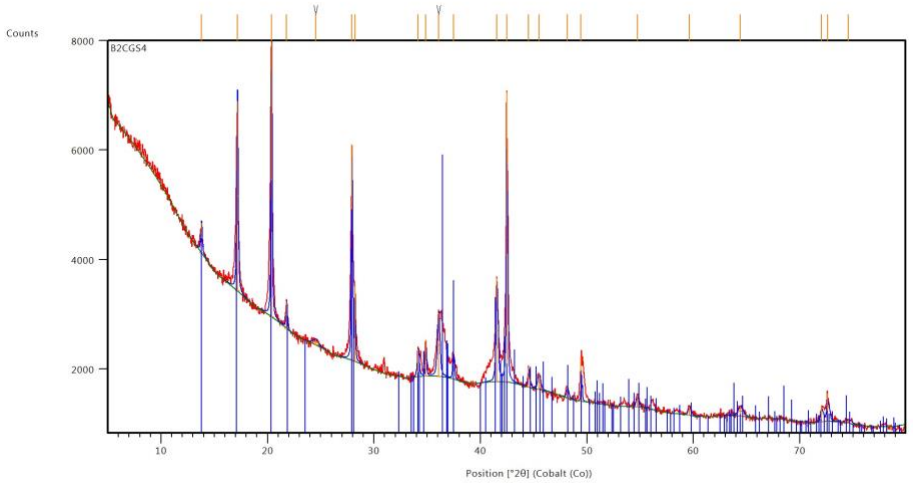
B2CGS4

Pattern List

Ref.Code	Mineral Name	SemiQuant[%]	Score	Compound Name	Scale Fac.	Chem. Formula
04-015-4888	Malachite	100	25	Copper Carbonate H..	0.506	Cu2 (C O3) (O H..

Peak List

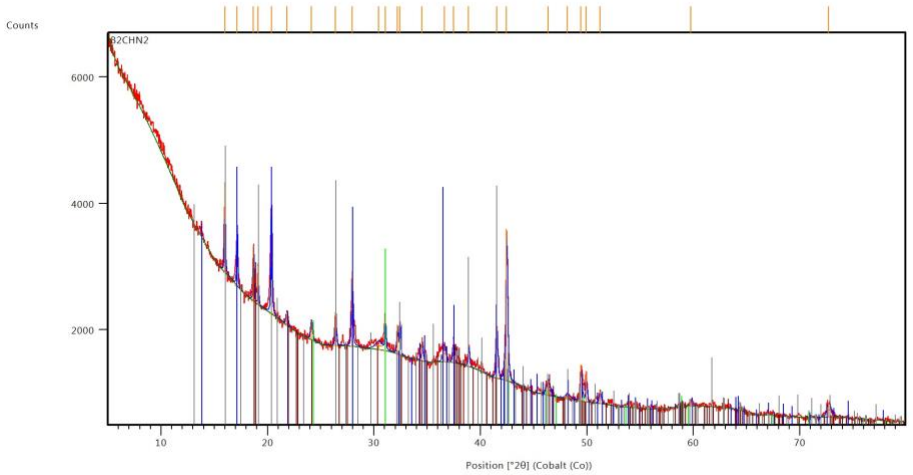
Pos.[°2θ]	Height [cts]	FWHMLeft[°2θ]	d-spacing [Å]	Rel. Int. [%]
13.7996	551.80	0.1791	7.45135	10.44
17.1656	3463.97	0.1535	5.99815	65.52
20.3692	5045.59	0.1279	5.06251	95.43
21.7858	503.28	0.1535	4.73692	9.52
24.5314	100.31	0.6140	4.21357	1.90
27.9210	3943.46	0.1279	3.71044	74.59
28.2099	1375.71	0.0768	3.67320	26.02
34.1431	488.85	0.2047	3.04924	9.25
34.8671	653.81	0.1023	2.98783	12.37
36.0578	1144.44	0.2558	2.89229	21.65
37.4646	491.20	0.1535	2.78736	9.29
41.5327	1874.80	0.2047	2.52470	35.46
42.4617	5287.14	0.1279	2.47194	100.00
44.5308	333.46	0.2047	2.36252	6.31
45.4876	282.67	0.3070	2.31539	5.35
48.1668	199.24	0.2303	2.19365	3.77
49.4514	810.95	0.0768	2.14011	15.34
54.7355	206.74	0.2558	1.94725	3.91
59.6227	155.78	0.3070	1.80058	2.95
64.4096	175.27	0.5117	1.67963	3.31
72.0480	294.16	0.2047	1.52205	5.56
72.6100	507.82	0.2047	1.51187	9.60
74.5754	64.93	0.6140	1.47760	1.23



B2CHN2

Pattern List

Ref.Code	Mineral Name	SemiQuant[%]	Score	Compound Name	Scale Fac.	Chem. Formula
00-056-0001	Malachite	31	26	Copper Carbonate H..	0.412	Cu2 +2 (C O3) (..
01-075-8320	Quartz	11	24	Silicon Oxide	0.241	Si O2
04-013-5988	Brochantite-MDO1	53	20	Copper Sulfate Hyd..	0.454	Cu4 (S O4) (O H..
04-012-9781	Clinoatacamite	5	3	Copper Chloride Hy..	0.095	Cu2 Cl (O H)3



Peak List

Pos.[°2θ]	Height [cts]	FWHMLeft[°2θ]	d-spacing [Å]	Rel. Int. [%]
15.9982	1409.48	0.1023	6.43267	58.65
17.1431	972.77	0.1023	6.00596	40.48
18.6759	871.52	0.1023	5.51687	36.27
19.1229	614.44	0.0768	5.38906	25.57
20.3701	1729.21	0.1279	5.06229	71.95
21.8295	206.26	0.2047	4.72756	8.58
24.1196	294.08	0.2047	4.28442	12.24
26.3889	526.68	0.1279	3.92170	21.92
27.9464	1190.91	0.1535	3.70712	49.56
30.4484	124.35	0.8187	3.40885	5.17
31.0619	498.07	0.1023	3.34314	20.73
32.1917	458.08	0.1279	3.22874	19.06
32.4239	602.14	0.1023	3.20624	25.06
34.5152	313.47	0.1535	3.01736	13.04
36.6086	253.87	0.3070	2.85023	10.56
37.4669	375.59	0.1535	2.78720	15.63
38.8925	334.00	0.1535	2.68877	13.90
41.5302	833.93	0.1535	2.52485	34.70
42.4569	2403.19	0.1791	2.47220	100.00
46.3619	242.00	0.3582	2.27406	10.07
48.1499	73.55	0.6140	2.19437	3.06
49.4423	570.77	0.1535	2.14048	23.75
49.9121	488.47	0.1023	2.12160	20.33
51.2230	187.55	0.2047	2.07083	7.80
59.7800	91.97	0.3070	1.79628	3.83
72.7013	224.95	0.4093	1.51023	9.36

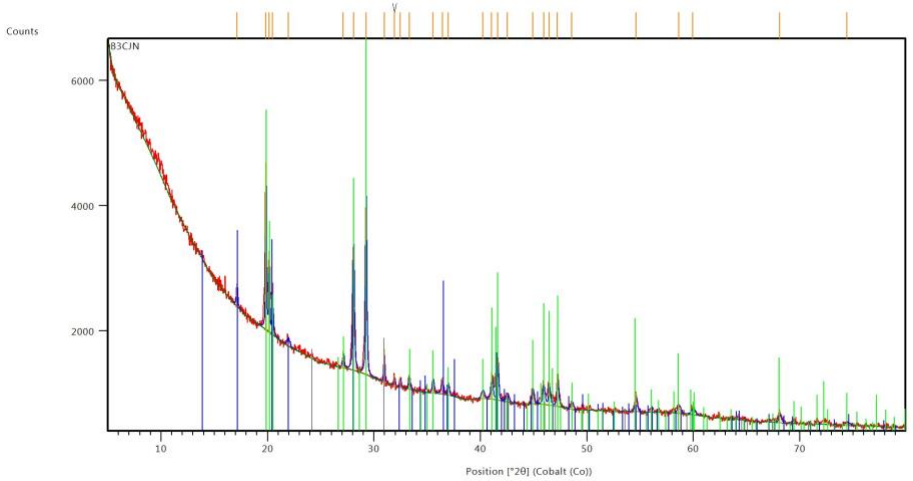
B2CJN

Pattern List

Ref.Code	Mineral Name	SemiQuant[%]	Score	Compound Name	Scale Fac.	Chem. Formula
00-056-0001	Malachite	24	18	Copper Carbonate H..	0.271	Cu2 +2 (C O3) (..
01-076-5942	Azurite	71	48	Copper Carbonate H..	0.880	Cu3 (C O3)2 (O ..
01-070-3755	Quartz	5	15	Silicon Oxide	0.105	Si O2

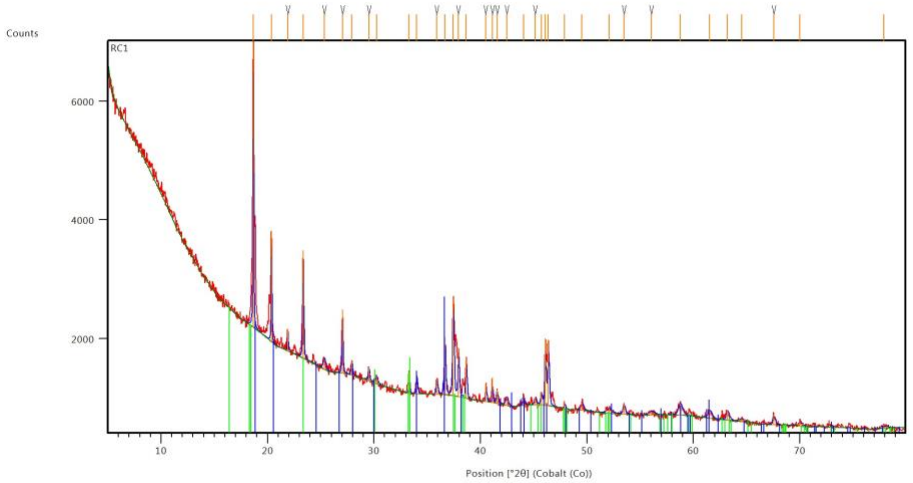
Peak List

Pos.[°2θ]	Height [cts]	FWHMLeft[°2θ]	d-spacing [Å]	Rel. Int. [%]
17.1348	345.99	0.1535	6.00886	11.31
19.8481	2666.55	0.1023	5.19403	87.16
20.1491	1295.97	0.1023	5.11722	42.36
20.4610	836.73	0.1023	5.04003	27.35
21.9641	125.45	0.3070	4.69894	4.10
27.1163	256.46	0.1535	3.81839	8.38
28.0776	1985.85	0.1791	3.69016	64.91
29.2536	3059.32	0.1279	3.54485	100.00
30.9634	528.58	0.1023	3.35350	17.28
31.9301	172.87	0.1023	3.25450	5.65
32.4743	168.83	0.1535	3.20139	5.52
33.3120	239.46	0.1535	3.12309	7.83
35.5524	220.06	0.2047	2.93205	7.19
36.4211	255.22	0.2047	2.86440	8.34
36.9928	196.60	0.1535	2.82165	6.43
40.2180	135.36	0.3070	2.60365	4.42
41.0546	427.36	0.1791	2.55281	13.97
41.6457	691.33	0.1023	2.51815	22.60
42.5418	132.74	0.3070	2.46750	4.34
44.9301	248.58	0.2047	2.34260	8.13
45.9377	331.26	0.2047	2.29391	10.83
46.4620	362.60	0.1535	2.26943	11.85
47.2390	521.04	0.1535	2.23419	17.03
48.5872	119.64	0.3070	2.17580	3.91
54.5969	290.82	0.2047	1.95182	9.51
58.6324	137.38	0.3070	1.82823	4.49
59.9623	106.81	0.4093	1.79133	3.49
68.0935	187.15	0.2047	1.59886	6.12
74.4013	47.38	0.6140	1.48055	1.55



CYPRUS

RC1



Pattern List

Ref.Code	Mineral Name	SemiQuant[%]	Score	Compound Name	Scale Fac.	Chem. Formula
04-016-1459	Akermanite	46	27	Calcium Magnesium ..	0.235	Ca2 Mg (Si2 O7)
04-016-2556	Coesite	54	13	Silicon Oxide	0.087	Si O2

Peak List

Pos.[°2θ]	Height [cts]	FWHM Left[°2θ]	d-spacing [Å]	Rel. Int. [%]
18.6587	4882.44	0.0768	5.52193	100.00
20.3651	1875.39	0.0768	5.06353	38.41
21.8966	372.65	0.0768	4.71324	7.63
23.3434	1820.01	0.1023	4.42481	37.28
25.3466	174.55	0.3070	4.08017	3.58
27.0343	1071.84	0.1023	3.82976	21.95
27.9119	242.97	0.1535	3.71162	4.98
29.5173	224.32	0.1535	3.51388	4.59
30.2403	112.92	0.3070	3.43176	2.31
33.2941	360.19	0.1023	3.12472	7.38
34.0251	288.05	0.1535	3.05950	5.90
35.9148	246.64	0.1535	2.90342	5.05
36.6577	970.65	0.1279	2.84654	19.88
37.4437	1654.81	0.1279	2.78886	33.89
37.9401	823.88	0.1279	2.75369	16.87
38.6631	637.77	0.1279	2.70412	13.06
40.5114	291.59	0.1023	2.58558	5.97
41.1205	421.00	0.0768	2.54890	8.62
41.5669	213.91	0.1535	2.52272	4.38
42.4740	140.79	0.3070	2.47125	2.88
44.0474	177.29	0.1535	2.38714	3.63
45.1483	135.75	0.2047	2.33187	2.78
45.7202	215.00	0.1535	2.30423	4.40
46.0947	1129.67	0.1023	2.28652	23.14
46.3748	1109.54	0.1279	2.27347	22.73
47.9043	102.30	0.1535	2.20495	2.10
49.5274	126.52	0.3070	2.13703	2.59
52.0738	79.68	0.6140	2.03930	1.63
53.4829	156.69	0.2558	1.98938	3.21
56.0424	56.81	0.6140	1.90540	1.16
58.7555	190.40	0.4093	1.82474	3.90
61.5373	126.29	0.4093	1.74981	2.59
63.2100	155.80	0.3070	1.70811	3.19
64.5227	42.36	0.6140	1.67700	0.87
67.5539	168.76	0.2047	1.61010	3.46
69.9952	58.18	0.6140	1.56075	1.19
77.8873	29.46	0.8187	1.42414	0.60

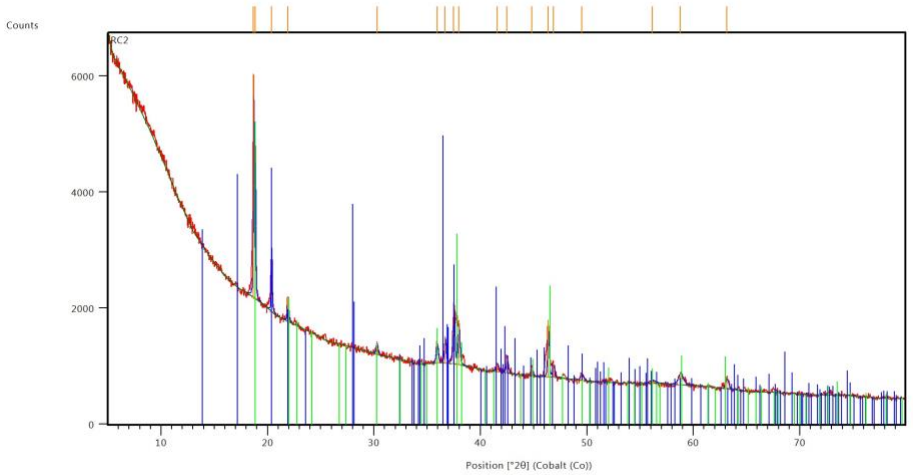
RC2

Pattern List

Ref.Code	Mineral Name	SemiQuant[%]	Score	Compound Name	Scale Fac.	Chem. Formula
01-072-8421	Malachite	68	8	Copper Carbonate H..	0.580	Cu2 (O H)2 (C O..
01-078-7708	Clinoatacamite	32	32	Copper Hydroxide C..	0.451	Cu2 (O H)3 Cl

Peak List

Pos.[°2θ]	Height [cts]	FWHM Left[°2θ]	d-spacing [Å]	Rel. Int. [%]
18.6805	3852.19	0.0768	5.51551	100.00
18.8580	2511.77	0.0768	5.46407	65.20
20.3876	1128.25	0.1023	5.05798	29.29
21.9252	431.78	0.1279	4.70716	11.21
30.2814	193.64	0.2047	3.42721	5.03
35.9369	327.95	0.2047	2.90170	8.51
36.6663	461.78	0.1535	2.84589	11.99
37.4857	1061.66	0.1535	2.78585	27.56
37.9710	748.77	0.1535	2.75154	19.44
41.5672	132.66	0.3070	2.52270	3.44
42.4983	252.69	0.2047	2.46990	6.56
44.8394	150.62	0.1535	2.34709	3.91
46.3568	981.81	0.1279	2.27430	25.49
46.8529	243.12	0.1535	2.25155	6.31
49.5296	110.29	0.3070	2.13694	2.86
56.1500	44.43	0.6140	1.90204	1.15
58.7846	200.06	0.5117	1.82391	5.19
63.1341	206.14	0.2558	1.70995	5.35



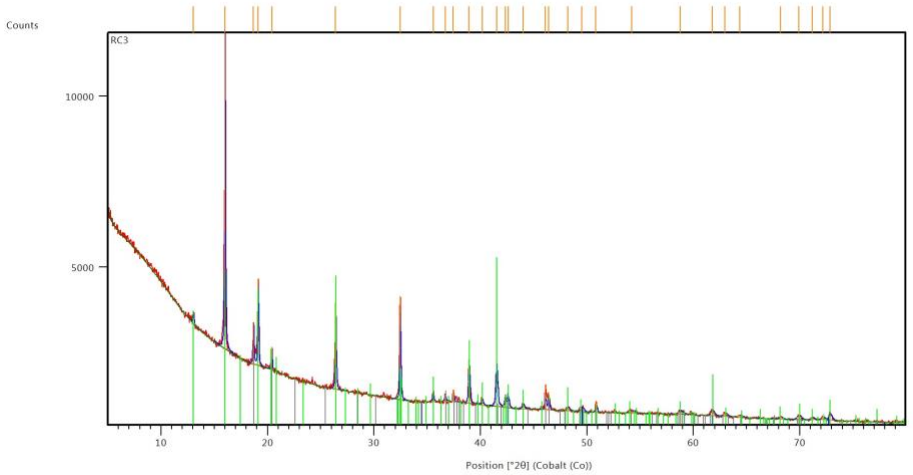
RC3

Pattern List

Ref.Code	Mineral Name	SemiQuant[%]	Score	Compound Name	Scale Fac.	Chem. Formula
04-007-9767	Cuprite	1	33	Copper Oxide	0.036	Cu2 O
04-011-4170	Brochantite	94	39	Copper Sulfate Hyd..	0.367	Cu4 (S O4) (O H..
04-010-1616	Atacamite	5	19	Copper Chloride Hy..	0.039	Cu2 Cl (O H)3

Peak List

Pos.[°2θ]	Height [cts]	FWHMLeft[°2θ]	d-spacing [Å]	Rel. Int. [%]
13.0401	285.46	0.1535	7.88325	3.09
16.0179	9224.29	0.1023	6.42481	100.00
18.6865	1230.40	0.1023	5.51376	13.34
19.1304	2543.78	0.1023	5.38698	27.58
20.4068	671.53	0.1023	5.05329	7.28
26.4013	2525.32	0.1023	3.91989	27.38
32.4631	3019.05	0.1023	3.20247	32.73
35.5596	320.73	0.1023	2.93147	3.48
36.6950	168.07	0.1535	2.84375	1.82
37.4466	348.53	0.0768	2.78866	3.78
38.9310	1265.05	0.1535	2.68622	13.71
40.1747	209.37	0.1535	2.60634	2.27
41.5255	1289.47	0.1791	2.52512	13.98
42.3332	327.34	0.1535	2.47909	3.55
42.6170	356.45	0.1535	2.46334	3.86
44.0084	161.15	0.2047	2.38915	1.75
46.1033	713.73	0.0768	2.28612	7.74
46.3909	518.05	0.1023	2.27272	5.62
48.2354	114.06	0.3070	2.19071	1.24
49.5305	120.44	0.4093	2.13691	1.31
50.8475	291.33	0.1279	2.08510	3.16
54.2161	59.62	0.6140	1.96448	0.65
58.7917	105.33	0.4093	1.82371	1.14
61.7852	165.99	0.3582	1.74347	1.80
62.9552	100.16	0.4093	1.71431	1.09
64.3823	53.44	0.6140	1.68026	0.58
68.1938	78.02	0.3070	1.59679	0.85
69.8983	137.27	0.4093	1.56263	1.49
71.1811	64.12	0.3070	1.53809	0.70
72.1676	78.46	0.3070	1.51987	0.85
72.8327	227.68	0.2558	1.50788	2.47



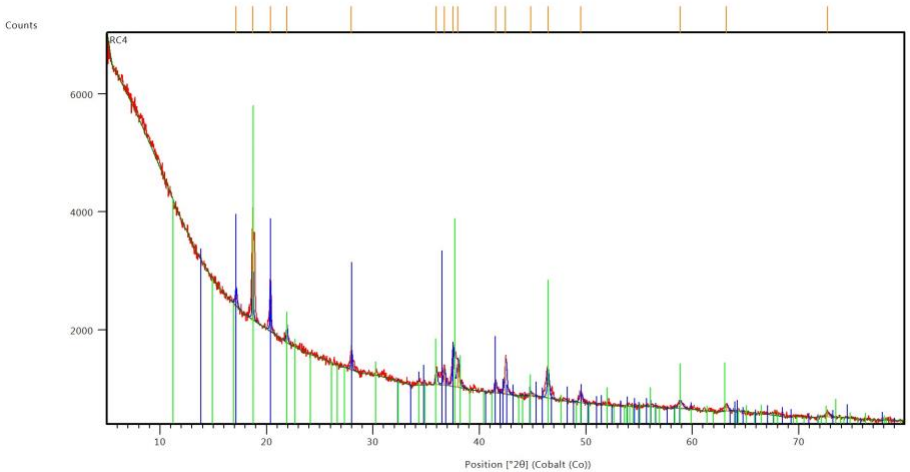
RC4

Pattern List

Ref.Code	Mineral Name	SemiQuant[%]	Score	Compound Name	Scale Fac.	Chem. Formula
00-056-0001	Malachite	57	20	Copper Carbonate H..	0.324	Cu2 +2 (C O3) (..
04-011-3123	Paratacamite	43	37	Copper Chloride Hy..	0.516	Cu2 Cl (O H)3

Peak List

Pos.[°2θ]	Height [cts]	FWHMLeft[°2θ]	d-spacing [Å]	Rel. Int. [%]
17.1459	293.71	0.2047	6.00498	15.53
18.7023	1891.49	0.0768	5.50916	100.00
20.3685	905.81	0.1023	5.06267	47.89
21.9199	262.27	0.1535	4.70828	13.87
27.9737	412.87	0.1279	3.70359	21.83
35.9580	277.23	0.1535	2.90005	14.66
36.6958	335.38	0.1535	2.84369	17.73
37.5271	715.87	0.1535	2.78289	37.85
37.9874	462.53	0.2558	2.75039	24.45
41.5149	207.29	0.2047	2.52574	10.96
42.4591	633.60	0.2047	2.47208	33.50
44.8150	56.03	0.6140	2.34831	2.96
46.4316	545.39	0.1791	2.27084	28.83
49.5173	179.58	0.3070	2.13744	9.49
58.8512	122.58	0.4093	1.82204	6.48
63.2012	117.40	0.3070	1.70833	6.21
72.7242	80.91	0.3070	1.50982	4.28



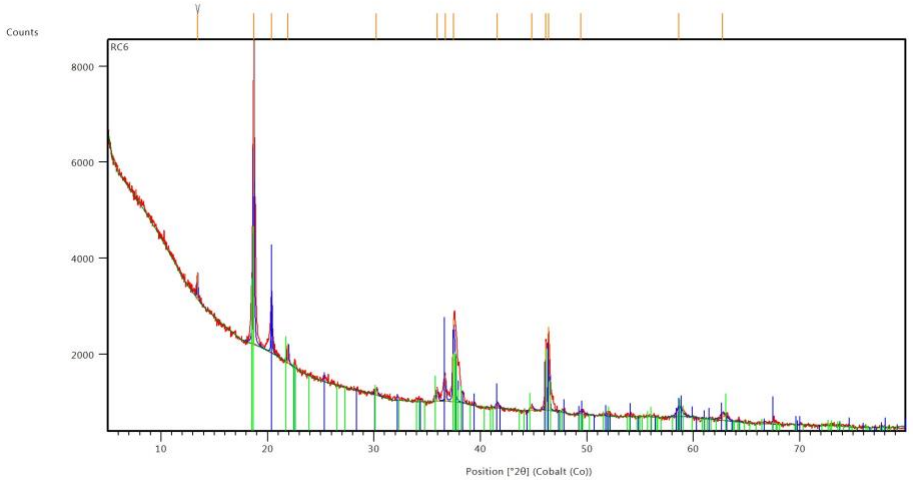
RC6

Pattern List

Ref.Code	Mineral Name	SemiQuant[%]	Score	Compound Name	Scale Fac.	Chem. Formula
01-080-9252	Atacamite	57	41	Copper Chloride Hy..	0.359	Cu2 Cl (O H)3
04-012-9781	Clinoatacamite	43	36	Copper Chloride Hy..	0.286	Cu2 Cl (O H)3

Peak List

Pos.[°2θ]	Height [cts]	FWHMLeft[°2θ]	d-spacing [Å]	Rel. Int. [%]
13.4207	540.27	0.1023	7.66067	8.34
18.6974	6475.03	0.1023	5.51059	100.00
20.3837	1296.83	0.1023	5.05895	20.03
21.9335	405.91	0.1279	4.70542	6.27
30.1933	135.31	0.3070	3.43698	2.09
35.9355	268.18	0.1535	2.90180	4.14
36.6972	529.39	0.1023	2.84358	8.18
37.4943	1729.25	0.1535	2.78523	26.71
41.5630	117.03	0.3070	2.52295	1.81
44.8078	93.03	0.3070	2.34866	1.44
46.1206	1423.72	0.0768	2.28531	21.99
46.4098	1739.80	0.0768	2.27185	26.87
49.4266	68.00	0.6140	2.14112	1.05
58.6494	182.39	0.6140	1.82774	2.82
62.7558	155.26	0.7164	1.71920	2.40



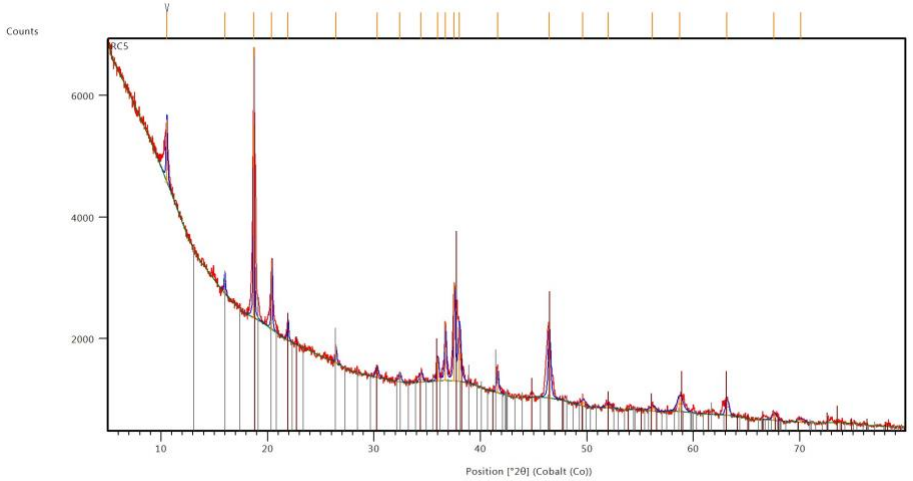
RC5

Pattern List

Ref.Code	Mineral Name	SemiQuant[%]	Score	Compound Name	Scale Fac.	Chem. Formula
01-079-6416	Brochantite	43	8	Copper Sulfate Hyd..	0.102	Cu4 (S O4) (O H..
04-012-5828	Paratacamite	57	39	Copper Chloride Hy..	0.459	Cu2 Cl (O H)3

Peak List

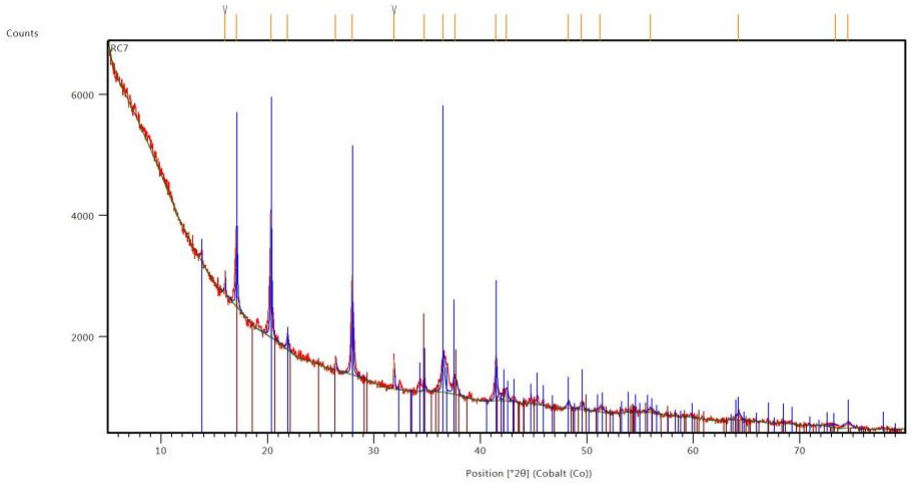
Pos.[°2θ]	Height [cts]	FWHM Left[°2θ]	d-spacing [Å]	Rel. Int. [%]
10.5469	1023.59	0.1535	9.73956	22.94
15.9867	340.95	0.1535	6.43727	7.64
18.7046	4462.21	0.1023	5.50848	100.00
20.3875	1141.96	0.1279	5.05802	25.59
21.9209	334.54	0.1535	4.70808	7.50
26.4251	279.07	0.1535	3.91643	6.25
30.2889	165.75	0.3070	3.42638	3.71
32.4066	128.24	0.3070	3.20790	2.87
34.4128	164.17	0.3070	3.02606	3.68
35.9894	382.05	0.2047	2.89760	8.56
36.6997	973.44	0.1535	2.84340	21.82
37.5275	1609.20	0.1535	2.78286	36.06
38.0168	913.71	0.3070	2.74834	20.48
41.6052	385.82	0.2047	2.52050	8.65
46.4487	1232.11	0.2303	2.27005	27.61
49.6051	99.27	0.6140	2.13390	2.22
52.0033	67.02	0.6140	2.04188	1.50
56.1690	85.02	0.6140	1.90145	1.91
58.7100	256.57	0.6140	1.82603	5.75
63.1407	287.99	0.3070	1.70979	6.45
67.5760	133.76	0.4093	1.60964	3.00
70.0717	55.72	0.6140	1.55926	1.25



RC7

Pattern List

Ref.Code	Mineral Name	SemiQuant[%]	Score	Compound Name	Scale Fac.	Chem. Formula
00-056-0001	Malachite	65	44	Copper Carbonate H..	0.687	Cu2 +2 (C O3) (..
04-020-5889		35	9	Calcium Carbonate	0.186	Ca (C O3)



Peak List

Pos. [°2θ]	Height [cts]	FWHM Left [°2θ]	d-spacing [Å]	Rel. Int. [%]
16.0116	393.46	0.1023	6.42730	19.13
17.1052	1290.02	0.1535	6.01916	62.70
20.3247	2057.30	0.1535	5.07347	100.00
21.8766	242.78	0.2047	4.71749	11.80
26.4010	213.41	0.1535	3.91993	10.37
27.9469	1650.29	0.1535	3.70707	80.22
31.8890	482.07	0.1023	3.25859	23.43
34.7304	189.45	0.1535	2.99923	9.21
36.4898	637.18	0.2558	2.85919	30.97
37.6304	265.74	0.4093	2.77553	12.92
41.4584	749.39	0.1791	2.52903	36.43
42.4321	204.80	0.3070	2.47358	9.95
48.2514	115.68	0.3070	2.19003	5.62
49.4918	145.10	0.2558	2.13847	7.05
51.2529	79.28	0.6140	2.06971	3.85
55.9684	67.99	0.6140	1.90772	3.30
64.2243	118.89	0.4093	1.68395	5.78
73.3244	50.98	0.9210	1.49918	2.48
74.4998	95.57	0.6140	1.47888	4.65

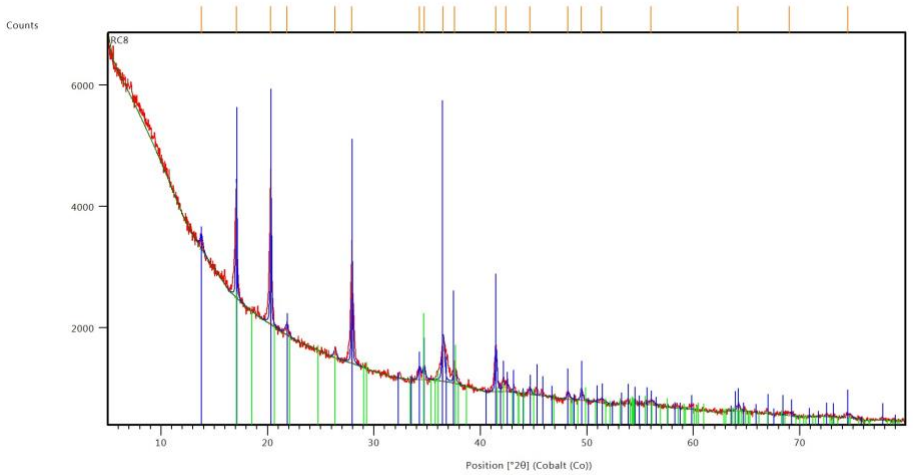
RC8

Pattern List

Ref.Code	Mineral Name	SemiQuant[%]	Score	Compound Name	Scale Fac.	Chem. Formula
00-056-0001	Malachite	68	46	Copper Carbonate H..	0.672	Cu2 +2 (C O3) (..
04-020-5889		32	9	Calcium Carbonate	0.159	Ca (C O3)

Peak List

Pos.[°2θ]	Height [cts]	FWHMLeft[°2θ]	d-spacing [Å]	Rel. Int. [%]
13.7953	225.96	0.3070	7.45366	8.79
17.0651	1897.32	0.1279	6.03321	73.84
20.2996	2569.53	0.1279	5.07969	100.00
21.8053	164.17	0.4093	4.73274	6.39
26.3417	132.72	0.3070	3.92860	5.17
27.9196	2035.93	0.1279	3.71062	79.23
34.2832	197.80	0.2558	3.03716	7.70
34.7046	217.90	0.2558	3.00139	8.48
36.4913	745.30	0.2558	2.85908	29.01
37.5628	359.88	0.2047	2.78034	14.01
41.4445	759.00	0.1791	2.52984	29.54
42.3803	134.54	0.6140	2.47647	5.24
44.6347	99.83	0.3070	2.35730	3.89
48.2303	107.84	0.3070	2.19093	4.20
49.4701	199.96	0.2047	2.13935	7.78
51.3717	61.64	0.8187	2.06525	2.40
56.0068	68.49	0.6140	1.90651	2.67
64.1926	114.56	0.3070	1.68470	4.46
69.0260	53.57	0.6140	1.57989	2.08
74.5193	63.83	0.6140	1.47855	2.48



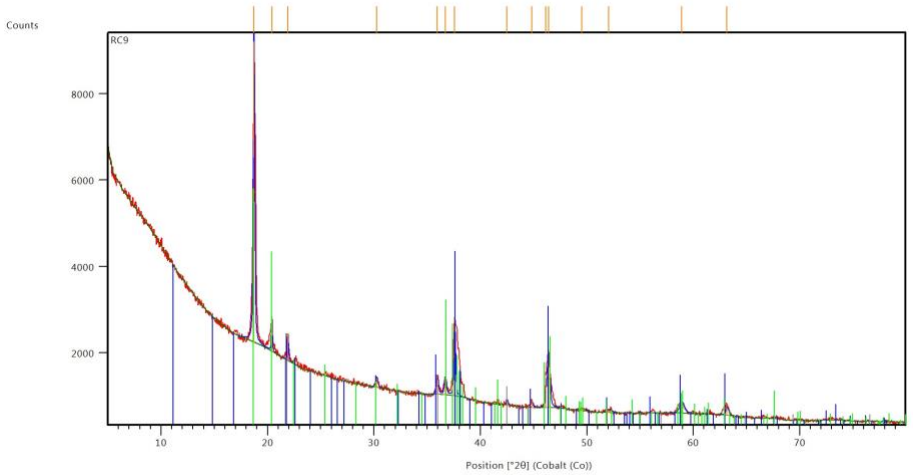
RC9

Pattern List

Ref.Code	Mineral Name	SemiQuant[%]	Score	Compound Name	Scale Fac.	Chem. Formula
04-011-3123	Paratacamite	42	42	Copper Chloride Hy..	0.453	Cu2 Cl (O H)3
01-071-2027	Atacamite	53	31	Copper Chloride Hy..	0.377	Cu2 Cl (O H)3
04-011-8982		5	18	Copper Aluminum Ox..	0.047	Cu Al2 O4

Peak List

Pos.[°2θ]	Height [cts]	FWHMLeft[°2θ]	d-spacing [Å]	Rel. Int. [%]
18.7149	6974.59	0.1535	5.50549	100.00
20.4035	811.11	0.1023	5.05409	11.63
21.9070	632.32	0.1023	4.71102	9.07
30.2420	227.39	0.2558	3.43157	3.26
35.9370	437.65	0.2047	2.90169	6.27
36.6893	397.38	0.2047	2.84418	5.70
37.5594	1797.15	0.1535	2.78058	25.77
42.4899	141.71	0.1535	2.47037	2.03
44.8073	167.46	0.1535	2.34869	2.40
46.1254	736.15	0.0768	2.28508	10.55
46.3928	1334.79	0.2303	2.27263	19.14
49.5179	54.85	0.6140	2.13742	0.79
52.0341	66.22	0.6140	2.04075	0.95
58.9023	246.34	0.5117	1.82060	3.53
63.1438	267.27	0.2047	1.70972	3.83



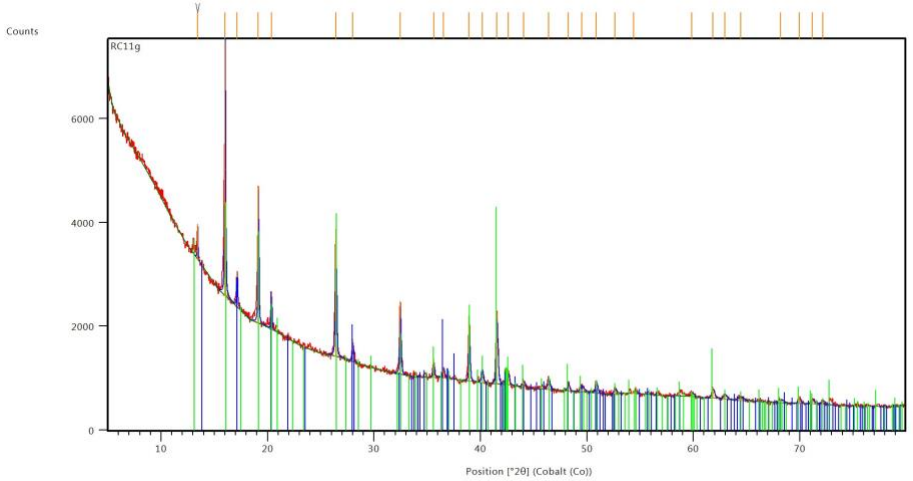
RC11

Pattern List

Ref.Code	Mineral Name	SemiQuant[%]	Score	Compound Name	Scale Fac.	Chem. Formula
01-072-8421	Malachite	20	12	Copper Carbonate H..	0.149	Cu2 (O H)2 (C O..
01-079-6416	Brochantite	80	44	Copper Sulfate Hyd..	0.451	Cu4 (S O4) (O H..

Peak List

Pos. [°2θ]	Height [cts]	FWHM Left [°2θ]	d-spacing [Å]	Rel. Int. [%]
13.4262	654.25	0.0768	7.65759	13.37
16.0199	4892.83	0.1023	6.42399	100.00
17.1403	688.99	0.1023	6.00691	14.08
19.1345	2640.49	0.1023	5.38582	53.97
20.3709	667.70	0.1023	5.06209	13.65
26.4197	2439.21	0.1279	3.91720	49.85
27.9873	415.19	0.1279	3.70182	8.49
32.4627	1401.58	0.1279	3.20251	28.65
35.6049	349.10	0.1279	2.92786	7.13
36.5330	192.06	0.2047	2.85593	3.93
38.9389	1255.20	0.1023	2.68569	25.65
40.1729	263.25	0.2047	2.60645	5.38
41.5496	1381.51	0.1535	2.52372	28.24
42.6286	285.06	0.1535	2.46271	5.83
44.0567	122.07	0.3070	2.38666	2.49
46.4044	239.30	0.2047	2.27209	4.89
48.2399	164.26	0.2047	2.19052	3.36
49.5317	114.60	0.4093	2.13686	2.34
50.8801	240.58	0.2047	2.08385	4.92
52.6405	108.14	0.3070	2.01889	2.21
54.3866	30.70	0.6140	1.95879	0.63
59.8739	80.79	0.3070	1.79373	1.65
61.8264	200.66	0.2558	1.74243	4.10
62.9538	85.76	0.3070	1.71435	1.75
64.4549	67.58	0.6140	1.67857	1.38
68.2017	60.30	0.6140	1.59663	1.23
69.9354	133.94	0.2047	1.56191	2.74
71.1972	92.55	0.3070	1.53779	1.89
72.1681	70.65	0.3070	1.51986	1.44



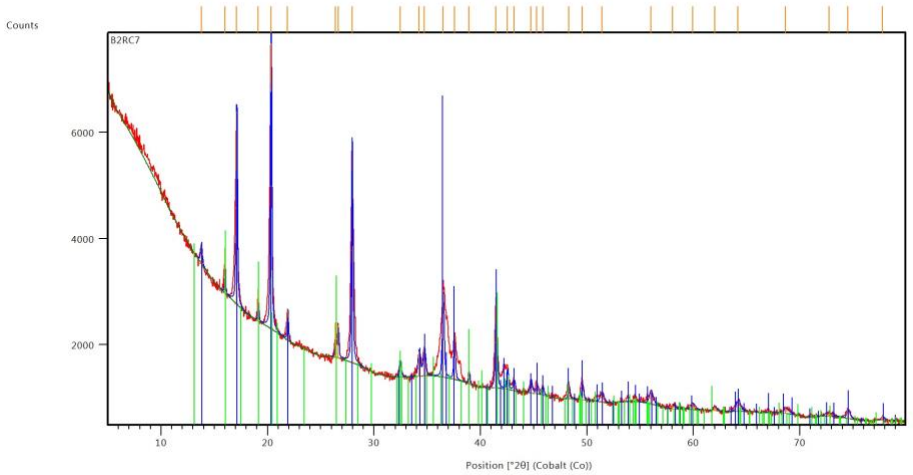
B2RC7

Pattern List

Ref.Code	Mineral Name	SemiQuant[%]	Score	Compound Name	Scale Fac.	Chem. Formula
00-056-0001	Malachite	65	59	Copper Carbonate H..	0.672	Cu2 +2 (C O3) (..
04-013-5988	Brochantite-MDO1	35	24	Copper Sulfate Hyd..	0.228	Cu4 (S O4) (O H..

Peak List

Pos. [°2θ]	Height [cts]	FWHM Left [°2θ]	d-spacing [Å]	Rel. Int. [%]
13.7877	345.31	0.2047	7.45771	6.43
16.0100	851.06	0.0768	6.42796	15.85
17.1016	3618.59	0.1535	6.02041	67.39
19.1246	585.63	0.0768	5.38858	10.91
20.3300	5369.57	0.1535	5.07216	100.00
21.8865	592.18	0.1279	4.71539	11.03
26.4015	655.55	0.1023	3.91986	12.21
26.6347	622.07	0.1279	3.88615	11.59
27.9432	4247.32	0.1535	3.70755	79.10
32.4696	303.48	0.2047	3.20185	5.65
34.2387	469.69	0.2558	3.04099	8.75
34.7271	510.96	0.2558	2.99951	9.52
36.4832	1650.82	0.1791	2.85969	30.74
37.5488	813.41	0.1535	2.78134	15.15
38.9235	242.87	0.1535	2.68672	4.52
41.4579	1701.04	0.1791	2.52906	31.68
42.5426	449.91	0.1535	2.46745	8.38
43.1577	214.61	0.2047	2.43393	4.00
44.7493	264.22	0.2047	2.35158	4.92
45.2850	257.71	0.1535	2.32520	4.80
45.8671	189.87	0.1535	2.29725	3.54
48.2973	289.55	0.1791	2.18808	5.39
49.5739	383.45	0.1535	2.13515	7.14
51.4084	178.41	0.4093	2.06387	3.32
56.0132	240.09	0.4093	1.90631	4.47
58.0619	75.88	0.4093	1.84460	1.41
59.9216	112.04	0.5117	1.79243	2.09
62.0165	75.79	0.3070	1.73762	1.41
64.1883	214.79	0.4093	1.68480	4.00
68.6676	90.61	0.6140	1.58711	1.69
72.7590	55.53	0.8187	1.50920	1.03
74.5330	179.23	0.3070	1.47831	3.34
77.7541	72.10	0.3070	1.42620	1.34



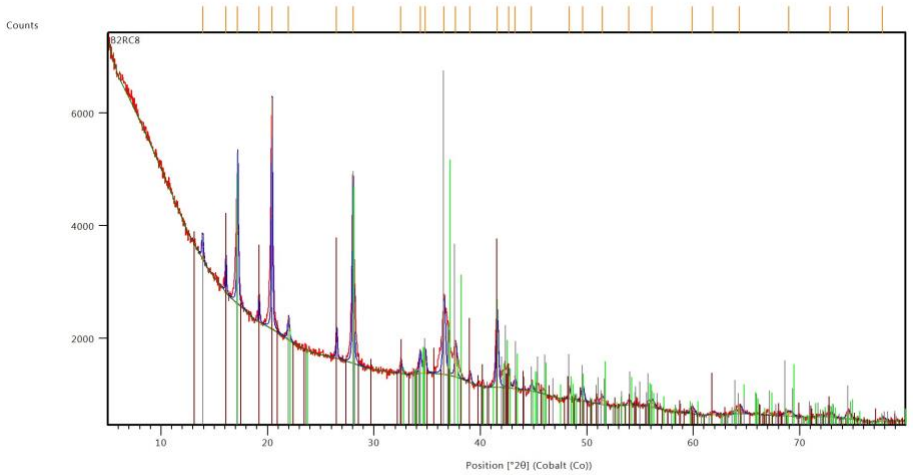
B2RC8

Pattern List

Ref.Code	Mineral Name	SemiQuant[%]	Score	Compound Name	Scale Fac.	Chem. Formula
04-019-0176		31	21	Copper Carbonate H..	0.516	Cu2 (C O3) (O H..
01-072-8421	Malachite	42	37	Copper Carbonate H..	0.726	Cu2 (O H)2 (C O..
01-079-6416	Brochantite	27	29	Copper Sulfate Hyd..	0.355	Cu4 (S O4) (O H..

Peak List

Pos.[°2θ]	Height [cts]	FWHMLeft[°2θ]	d-spacing [Å]	Rel. Int. [%]
13.9098	436.64	0.1791	7.39256	10.62
16.0887	707.18	0.1023	6.39670	17.20
17.1932	2593.09	0.1535	5.98857	63.05
19.2070	519.24	0.1023	5.36569	12.63
20.4152	4112.51	0.1279	5.05121	100.00
21.9719	407.30	0.2047	4.69728	9.90
26.4876	549.15	0.1535	3.90735	13.35
28.0284	3387.70	0.1535	3.69650	82.38
32.5302	285.56	0.1535	3.19604	6.94
34.3467	392.51	0.2047	3.03171	9.54
34.8076	431.46	0.2047	2.99278	10.49
36.5761	1304.68	0.2558	2.85267	31.72
37.6617	638.02	0.2047	2.77330	15.51
39.0188	196.18	0.2047	2.68041	4.77
41.5648	1437.70	0.2047	2.52284	34.96
42.6460	417.27	0.1535	2.46174	10.15
43.2487	199.95	0.2047	2.42905	4.86
44.7983	135.26	0.3070	2.34913	3.29
48.3416	220.89	0.2047	2.18619	5.37
49.5916	286.97	0.2558	2.13444	6.98
51.4528	157.12	0.3070	2.06221	3.82
53.9529	104.50	0.3070	1.97334	2.54
56.0950	136.61	0.5117	1.90376	3.32
59.8862	119.96	0.4093	1.79339	2.92
61.8336	38.52	0.6140	1.74225	0.94
64.3295	154.01	0.4093	1.68150	3.74
68.9649	85.05	0.8187	1.58111	2.07
72.8510	67.10	0.6140	1.50756	1.63
74.5621	152.47	0.4093	1.47782	3.71
77.7720	62.83	0.6140	1.42592	1.53



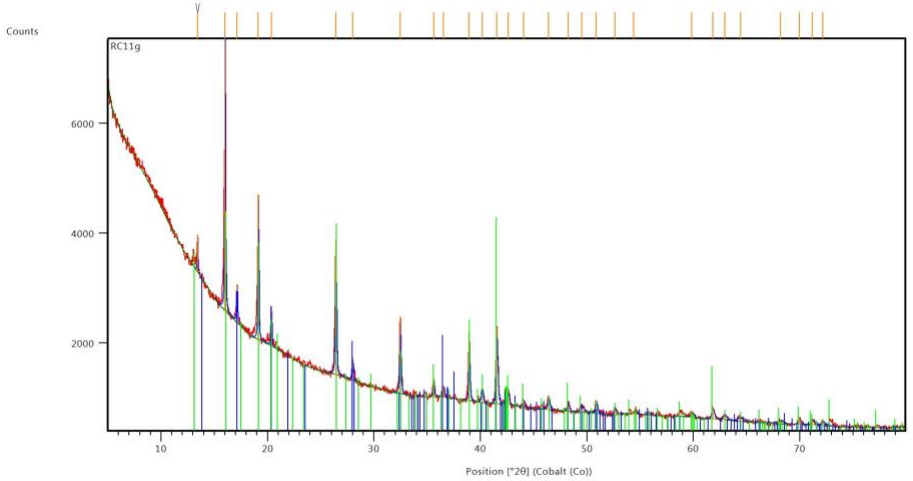
RC11g

Pattern List

Ref.Code	Mineral Name	SemiQuant[%]	Score	Compound Name	Scale Fac.	Chem. Formula
01-072-8421	Malachite	20	12	Copper Carbonate H..	0.149	Cu2 (O H)2 (C O..
01-079-6416	Brochantite	80	44	Copper Sulfate Hyd..	0.451	Cu4 (S O4) (O H..

Peak List

Pos. [°2θ]	Height [cts]	FWHM Left [°2θ]	d-spacing [Å]	Rel. Int. [%]
13.4262	654.25	0.0768	7.65759	13.37
16.0199	4892.83	0.1023	6.42399	100.00
17.1403	688.99	0.1023	6.00691	14.08
19.1345	2640.49	0.1023	5.38582	53.97
20.3709	667.70	0.1023	5.06209	13.65
26.4197	2439.21	0.1279	3.91720	49.85
27.9873	415.19	0.1279	3.70182	8.49
32.4627	1401.58	0.1279	3.20251	28.65
35.6049	349.10	0.1279	2.92786	7.13
36.5330	192.06	0.2047	2.85593	3.93
38.9389	1255.20	0.1023	2.68569	25.65
40.1729	263.25	0.2047	2.60645	5.38
41.5496	1381.51	0.1535	2.52372	28.24
42.6286	285.06	0.1535	2.46271	5.83
44.0567	122.07	0.3070	2.38666	2.49
46.4044	239.30	0.2047	2.27209	4.89
48.2399	164.26	0.2047	2.19052	3.36
49.5317	114.60	0.4093	2.13686	2.34
50.8801	240.58	0.2047	2.08385	4.92
52.6405	108.14	0.3070	2.01889	2.21
54.3866	30.70	0.6140	1.95879	0.63
59.8739	80.79	0.3070	1.79373	1.65
61.8264	200.66	0.2558	1.74243	4.10
62.9538	85.76	0.3070	1.71435	1.75
64.4549	67.58	0.6140	1.67857	1.38
68.2017	60.30	0.6140	1.59663	1.23
69.9354	133.94	0.2047	1.56191	2.74
71.1972	92.55	0.3070	1.53779	1.89
72.1681	70.65	0.3070	1.51986	1.44



ENGLAND

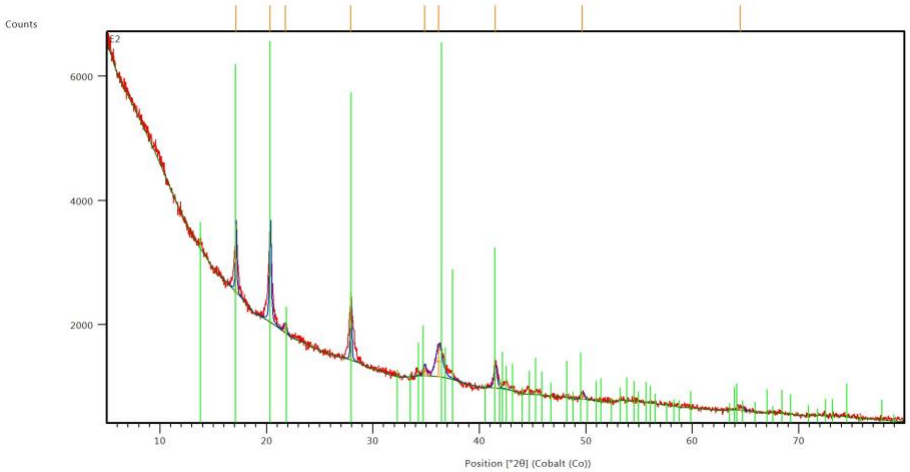
E2

Pattern List

Ref.Code	Mineral Name	SemiQuant[%]	Score	Compound Name	Scale Fac.	Chem. Formula
00-056-0001	Malachite	100	30	Copper Carbonate H..	0.800	Cu2 +2 (C O3) (..

Peak List

Pos.[°2θ]	Height [cts]	FWHMLeft[°2θ]	d-spacing [Å]	Rel. Int. [%]
17.1357	1089.16	0.1535	6.00853	70.55
20.3524	1543.80	0.2047	5.06665	100.00
21.7619	148.23	0.3070	4.74207	9.60
27.9270	1091.17	0.1279	3.70965	70.68
34.8657	165.63	0.3070	2.98795	10.73
36.1873	483.23	0.7164	2.88228	31.30
41.4850	362.13	0.3070	2.52748	23.46
49.6626	131.13	0.3070	2.13158	8.49
64.5004	53.83	0.6140	1.67752	3.49



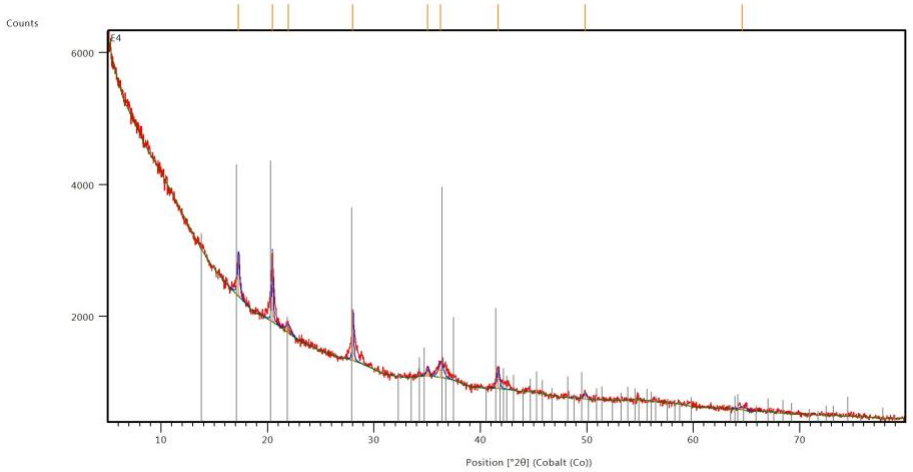
E4

Pattern List

Ref.Code	Mineral Name	SemiQuant[%]	Score	Compound Name	Scale Fac.	Chem. Formula
00-056-0001	Malachite	100	20	Copper Carbonate H..	0.456	Cu2 +2 (C O3) (..

Peak List

Pos.[°2θ]	Height [cts]	FWHMLeft[°2θ]	d-spacing [Å]	Rel. Int. [%]
17.2662	627.66	0.2558	5.96345	58.72
20.4489	1068.96	0.1535	5.04299	100.00
21.9617	113.43	0.6140	4.69943	10.61
28.0090	779.61	0.1535	3.69901	72.93
35.0433	128.43	0.3070	2.97328	12.01
36.2755	224.40	0.5117	2.87551	20.99
41.6523	310.34	0.2558	2.51777	29.03
49.8182	96.32	0.3070	2.12535	9.01
64.6113	45.82	0.8187	1.67495	4.29



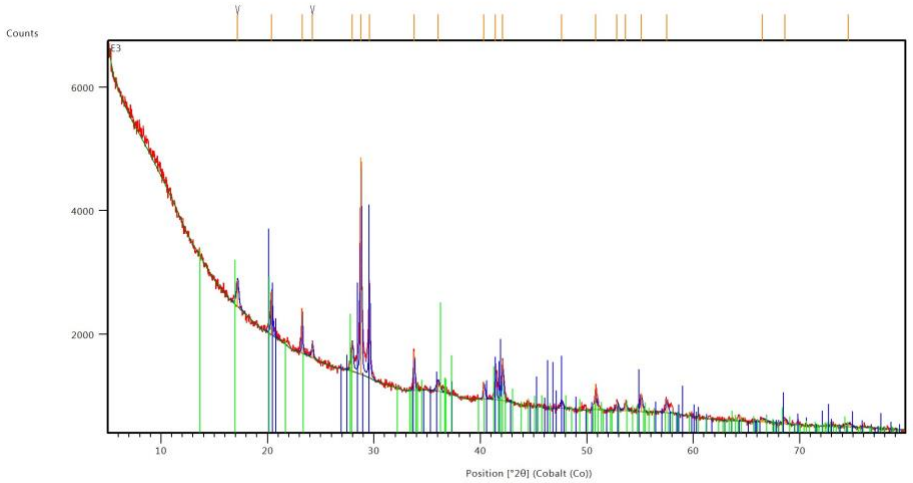
E3

Pattern List

Ref.Code	Mineral Name	SemiQuant[%]	Score	Compound Name	Scale Fac.	Chem. Formula
01-077-5327		59	18	Copper Carbonate H..	0.414	Cu3 (C O3)2 (O ..
01-072-8421	Malachite	41	3	Copper Carbonate H..	0.214	Cu2 (O H)2 (C O..

Peak List

Pos.[°2θ]	Height [cts]	FWHM Left[°2θ]	d-spacing [Å]	Rel. Int. [%]
17.1853	424.42	0.2558	5.99133	12.09
20.3954	703.31	0.1791	5.05608	20.04
23.2526	726.23	0.1023	4.44184	20.69
24.2097	271.97	0.1535	4.26870	7.75
27.9525	474.25	0.2047	3.70634	13.51
28.7696	3509.21	0.1279	3.60320	100.00
29.5738	1587.80	0.1279	3.50731	45.25
33.7632	633.89	0.1279	3.08254	18.06
36.0114	161.00	0.4093	2.89589	4.59
40.3350	270.63	0.1535	2.59641	7.71
41.4197	546.31	0.1023	2.53129	15.57
42.0716	650.20	0.1535	2.49380	18.53
47.6227	124.86	0.3070	2.21723	3.56
50.8424	428.22	0.0768	2.08530	12.20
52.8186	138.43	0.3070	2.01257	3.94
53.6322	153.83	0.2047	1.98425	4.38
55.0962	294.88	0.2047	1.93550	8.40
57.4910	222.20	0.2047	1.86134	6.33
66.4643	56.09	0.6140	1.63339	1.60
68.6095	87.48	0.3070	1.58829	2.49
74.5656	57.27	0.7164	1.47776	1.63



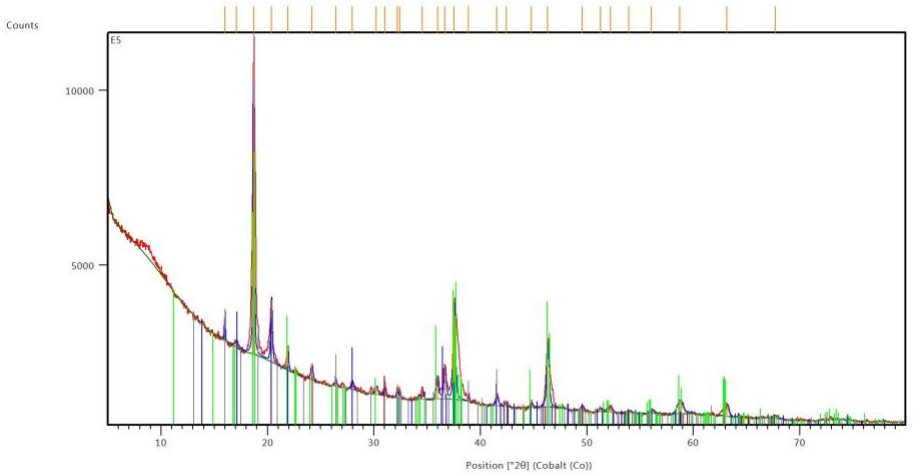
E5

Pattern List

Ref.Code	Mineral Name	SemiQuant[%]	Score	Compound Name	Scale Fac.	Chem. Formula
00-056-0001	Malachite	12	23	Copper Carbonate H..	0.128	Cu2 +2 (C O3) (..
04-016-8161	Anatacamite	71	41	Copper Chloride Hy..	0.497	Cu2 Cl (O H)3
04-013-5988	Brochantite-MDO1	14	12	Copper Sulfate Hyd..	0.089	Cu4 (S O4) (O H..
01-075-8320	Quartz	3	23	Silicon Oxide	0.049	Si O2

Peak List

Pos.[°2θ]	Height [cts]	FWHMLeft[°2θ]	d-spacing [Å]	Rel. Int. [%]
15.9966	904.50	0.0768	6.43330	9.85
17.0670	188.14	0.4093	6.03254	2.05
18.6879	9182.23	0.1279	5.51337	100.00
20.3652	1763.56	0.1791	5.06349	19.21
21.9045	722.86	0.1279	4.71157	7.87
24.1658	431.55	0.2047	4.27635	4.70
26.4131	222.86	0.1535	3.91816	2.43
27.9757	245.72	0.2047	3.70332	2.68
30.2359	210.83	0.3070	3.43225	2.30
31.0087	456.98	0.1023	3.34873	4.98
32.1804	389.54	0.1023	3.22985	4.24
32.4216	355.02	0.0768	3.20646	3.87
34.5647	314.72	0.1535	3.01316	3.43
35.9718	652.98	0.2303	2.89897	7.11
36.6584	945.43	0.2047	2.84649	10.30
37.5395	2801.28	0.2047	2.78200	30.51
38.8938	278.54	0.0768	2.68869	3.03
41.5529	328.04	0.2558	2.52353	3.57
42.4599	132.18	0.3070	2.47203	1.44
44.7931	196.15	0.1535	2.34939	2.14
46.3074	1950.85	0.2303	2.27659	21.25
49.5812	143.46	0.3070	2.13486	1.56
51.2651	109.12	0.3070	2.06925	1.19
52.2243	182.24	0.2558	2.03384	1.98
53.9399	58.98	0.6140	1.97378	0.64
56.0805	106.91	0.5117	1.90421	1.16
58.7120	367.64	0.6140	1.82597	4.00
63.1601	380.40	0.3070	1.70932	4.14
67.6908	77.54	0.5117	1.60723	0.84



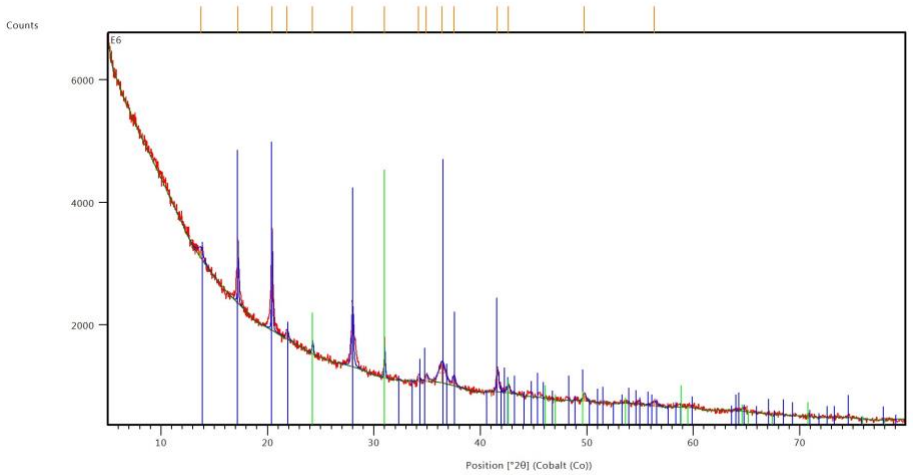
E6

Pattern List

Ref.Code	Mineral Name	SemiQuant[%]	Score	Compound Name	Scale Fac.	Chem. Formula
00-056-0001	Malachite	64	28	Copper Carbonate H..	0.539	Cu2 +2 (C O3) (..
01-075-8320	Quartz	36	27	Silicon Oxide	0.502	Si O2

Peak List

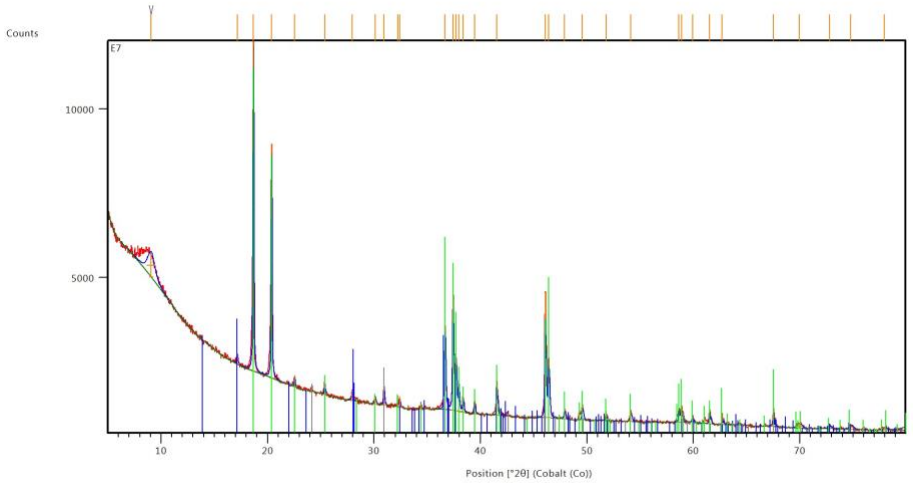
Pos. [°2θ]	Height [cts]	FWHM Left [°2θ]	d-spacing [Å]	Rel. Int. [%]
13.7360	158.18	0.6140	7.48565	9.42
17.2294	1055.04	0.1023	5.97609	62.82
20.4352	1679.39	0.1023	5.04632	100.00
21.8430	141.68	0.3070	4.72466	8.44
24.2270	209.32	0.1535	4.26570	12.46
27.9646	1044.95	0.2047	3.70476	62.22
30.9917	691.58	0.0768	3.35052	41.18
34.2026	109.08	0.2047	3.04410	6.50
34.9214	105.90	0.3070	2.98333	6.31
36.3956	326.38	0.7164	2.86634	19.43
37.5073	148.41	0.3070	2.78430	8.84
41.6043	386.12	0.2047	2.52055	22.99
42.6083	136.51	0.3070	2.46383	8.13
49.7361	121.84	0.3070	2.12863	7.26
56.3248	73.08	0.6140	1.89662	4.35



E7

Pattern List

Ref.Code	Mineral Name	SemiQuant[%]	Score	Compound Name	Scale Fac.	Chem. Formula
01-080-8572		25	14	Copper Carbonate H..	0.183	Cu2 (C O3) (O H..
01-080-9252	Atacamite	68	65	Copper Chloride Hy..	0.745	Cu2 Cl (O H)3
04-016-2085	Quartz	7	20	Silicon Oxide	0.092	Si O2



Peak List

Pos.[°2θ]	Height [cts]	FWHMLeft[°2θ]	d-spacing [Å]	Rel. Int. [%]
9.0705	678.57	0.8187	11.32072	6.94
17.1657	285.33	0.1535	5.99809	2.92
18.6687	9772.91	0.1023	5.51899	100.00
20.3827	6943.65	0.1023	5.05919	71.05
22.5332	344.57	0.1023	4.58174	3.53
25.3764	396.71	0.0768	4.07545	4.06
27.9423	301.51	0.1535	3.70767	3.09
30.1271	201.22	0.1535	3.44435	2.06
30.9450	555.92	0.1023	3.35545	5.69
32.2268	297.83	0.0768	3.22532	3.05
32.4203	319.12	0.0768	3.20658	3.27
36.6660	2599.15	0.1279	2.84592	26.60
37.4290	3428.00	0.1279	2.78992	35.08
37.7064	1637.89	0.1023	2.77014	16.76
37.9622	929.16	0.1023	2.75215	9.51
38.3595	490.32	0.1023	2.72470	5.02
39.4622	400.19	0.1023	2.65147	4.09
41.5515	945.72	0.1023	2.52361	9.68
46.0888	3700.18	0.1023	2.28680	37.86
46.4009	1888.58	0.1279	2.27226	19.32
47.8912	298.00	0.1279	2.20552	3.05
49.5767	456.97	0.1279	2.13504	4.68
51.8029	289.79	0.0768	2.04923	2.97
54.1165	339.17	0.1279	1.96782	3.47
58.6410	438.62	0.0936	1.82666	4.49
58.8925	493.79	0.1023	1.82087	5.05
59.9261	169.52	0.1535	1.79231	1.73
61.5282	456.30	0.1023	1.75004	4.67
62.7004	346.05	0.0768	1.72056	3.54
67.5369	544.93	0.0768	1.61046	5.58
69.9504	125.10	0.5117	1.56162	1.28
72.8198	81.66	0.3070	1.50811	0.84
74.7955	128.24	0.4093	1.47388	1.31
77.9609	66.59	0.6140	1.42301	0.68

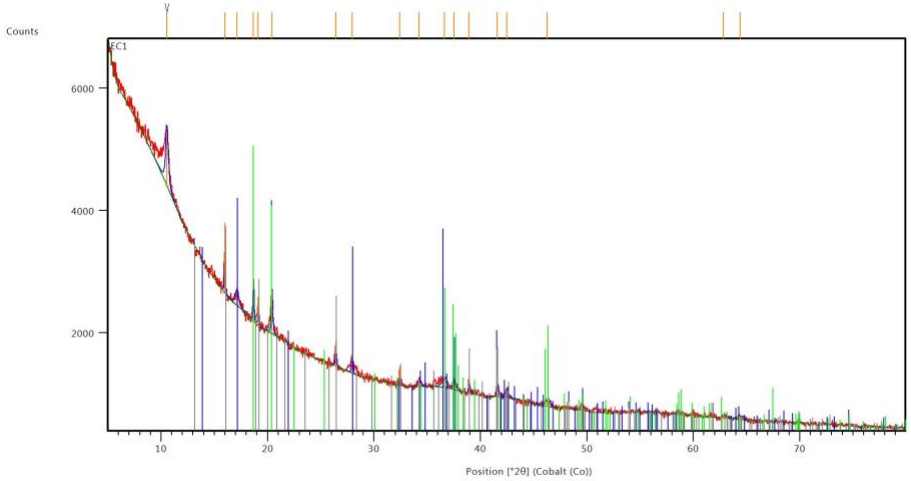
EC1

Pattern List

Ref.Code	Mineral Name	SemiQuant[%]	Score	Compound Name	Scale Fac.	Chem. Formula
00-056-0001	Malachite	40	18	Copper Carbonate H..	0.381	Cu2 +2 (C O3) (..
01-080-9252	Atacamite	33	13	Copper Chloride Hy..	0.418	Cu2 Cl (O H)3
04-013-5989	Brochantite-MDO2	28	8	Copper Sulfate Hyd..	0.170	Cu4 (S O4) (O H..

Peak List

Pos.[°2θ]	Height [cts]	FWHMLeft[°2θ]	d-spacing [Å]	Rel. Int. [%]
10.5552	886.48	0.3070	9.73187	77.02
16.0020	1151.01	0.0768	6.43114	100.00
17.1283	238.55	0.4093	6.01111	20.73
18.6803	657.11	0.0768	5.51557	57.09
19.1271	472.84	0.1023	5.38789	41.08
20.4188	708.63	0.1535	5.05034	61.57
26.4133	404.63	0.1023	3.91813	35.15
27.9421	291.81	0.1535	3.70769	25.35
32.4308	310.45	0.0768	3.20557	26.97
34.2326	115.93	0.3070	3.04151	10.07
36.6350	139.21	0.6140	2.84825	12.09
37.5262	138.76	0.3070	2.78296	12.06
38.9246	205.94	0.1535	2.68664	17.89
41.6003	254.39	0.1535	2.52078	22.10
42.4725	114.34	0.3582	2.47134	9.93
46.2739	100.37	0.6140	2.27815	8.72
62.8461	36.77	0.7164	1.71698	3.19
64.3892	51.24	0.6140	1.68010	4.45



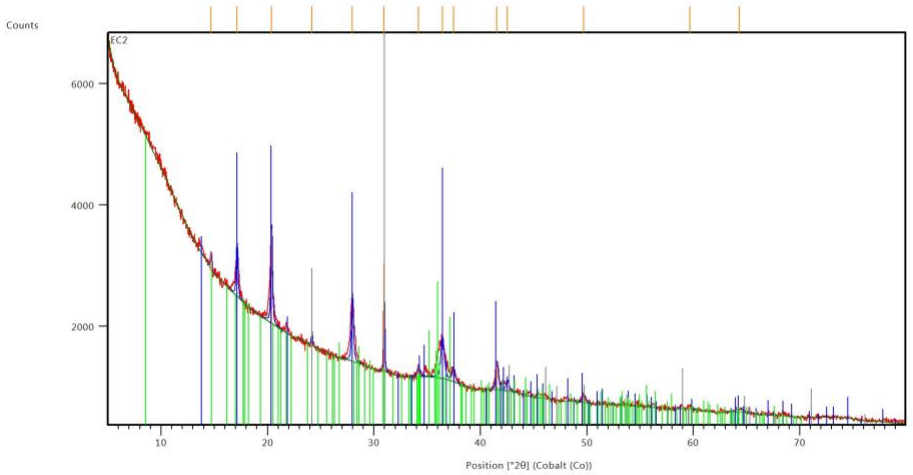
EC2

Pattern List

Ref.Code	Mineral Name	SemiQuant[%]	Score	Compound Name	Scale Fac.	Chem. Formula
00-056-0001	Malachite	33	36	Copper Carbonate H..	0.508	Cu2 +2 (C O3) (..
04-021-1753		33	2	Calcium Carbonate	0.232	Ca (C O3)
04-008-7653		34	28	Silicon Oxide	0.938	Si O2

Peak List

Pos.[°2θ]	Height [cts]	FWHMLeft[°2θ]	d-spacing [Å]	Rel. Int. [%]
14.7003	275.32	0.1535	6.99706	15.44
17.1301	829.70	0.1791	6.01048	46.53
20.3780	1553.06	0.1791	5.06034	87.09
24.1619	190.43	0.1535	4.27703	10.68
27.9678	1081.72	0.2047	3.70435	60.66
30.9553	1783.20	0.0768	3.35436	100.00
34.1802	157.78	0.3070	3.04603	8.85
36.4241	647.47	0.3582	2.86417	36.31
37.4667	214.30	0.3070	2.78721	12.02
41.5556	462.93	0.2558	2.52337	25.96
42.5312	174.62	0.3070	2.46808	9.79
49.6935	122.09	0.4093	2.13034	6.85
59.6908	63.05	0.4093	1.79872	3.54
64.3325	56.22	0.8187	1.68142	3.15



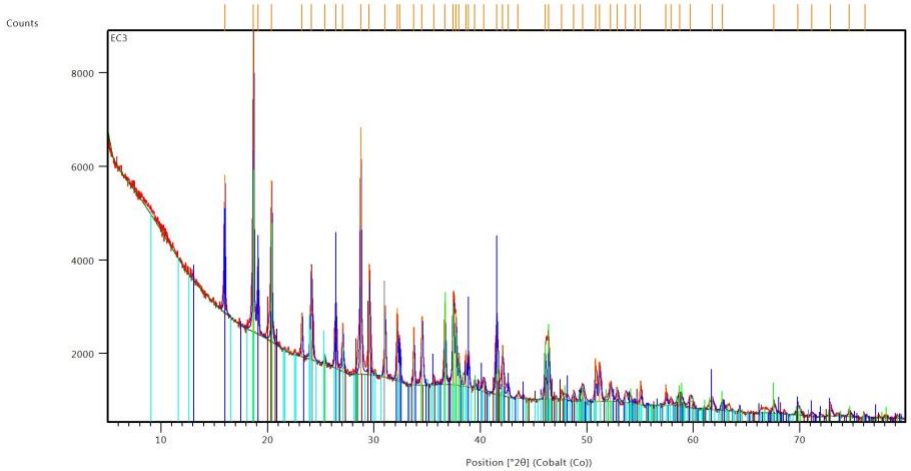
EC3

Pattern List

Ref.Code	Mineral Name	SemiQuant[%]	Score	Compound Name	Scale Fac.	Chem. Formula
04-013-5988	Brochantite-MDO1	46	39	Copper Sulfate Hyd..	0.381	Cu4 (S O4) (O H..
01-080-9252	Atacamite	22	48	Copper Chloride Hy..	0.389	Cu2 Cl (O H)3
01-075-8320	Quartz	11	28	Silicon Oxide	0.231	Si O2
04-015-4845	Azurite	12	13	Copper Carbonate H..	0.176	Cu3 (C O3)2 (O ..
04-008-8461	Tridymite	9	14	Silicon Oxide	0.105	Si O2

Peak List

Pos.[°2θ]	Height [cts]	FWHMLeft[°2θ]	d-spacing [Å]	Rel. Int. [%]
15.9840	2947.34	0.1023	6.43835	44.86
18.6757	6570.33	0.1023	5.51694	100.00
19.1057	1585.46	0.1279	5.39387	24.13
20.3871	3450.42	0.1023	5.05810	52.52
23.2376	951.43	0.1023	4.44466	14.48
24.1181	2016.47	0.1535	4.28468	30.69
25.3758	197.27	0.1535	4.07555	3.00
26.4215	1423.67	0.1535	3.91695	21.67
27.0693	1044.38	0.1023	3.82489	15.90
28.7579	5277.98	0.1023	3.60463	80.33
29.5572	2375.24	0.1023	3.50924	36.15
31.0386	1543.57	0.1279	3.34558	23.49
32.1792	1547.40	0.1023	3.22996	23.55
32.4147	979.26	0.1023	3.20712	14.90
33.7435	1239.68	0.1023	3.08428	18.87
34.5216	1475.43	0.1535	3.01682	22.46
35.6256	182.81	0.1535	2.92622	2.78
36.6684	1766.14	0.1023	2.84574	26.88
37.4449	1945.58	0.1535	2.78878	29.61
37.7077	1552.83	0.1023	2.77004	23.63
37.9822	663.02	0.0768	2.75076	10.09
38.6281	783.31	0.1023	2.70647	11.92
38.8784	774.03	0.1023	2.68971	11.78
39.4718	191.36	0.1535	2.65085	2.91
40.3243	299.88	0.2558	2.59707	4.56
41.5417	1764.48	0.1791	2.52418	26.86
42.0906	1089.73	0.1279	2.49273	16.59
42.6055	324.19	0.1535	2.46398	4.93
43.5235	115.52	0.3070	2.41445	1.76
46.0932	1167.66	0.1279	2.28659	17.77
46.4050	1462.62	0.1023	2.27207	22.26
47.6382	222.97	0.1535	2.21655	3.39
48.7611	210.99	0.2047	2.16852	3.21
49.6019	359.12	0.3582	2.13403	5.47
50.8074	925.63	0.0768	2.08664	14.09
51.1836	850.82	0.1535	2.07232	12.95
52.2226	416.80	0.2047	2.03390	6.34
52.8462	275.99	0.2047	2.01160	4.20
53.6470	255.53	0.2558	1.98375	3.89
54.5070	33.48	0.8187	1.95479	0.51
55.0423	492.48	0.0768	1.93724	7.50
57.4180	406.15	0.0768	1.86350	6.18
57.8997	191.91	0.1535	1.84932	2.92
58.7167	278.27	0.5117	1.82584	4.24
59.7187	267.75	0.3582	1.79796	4.08
61.7916	276.40	0.2047	1.74331	4.21
62.7170	241.49	0.3070	1.72016	3.68
67.5664	251.27	0.2558	1.60984	3.82
69.8046	261.94	0.2558	1.56446	3.99
71.1341	101.11	0.3070	1.53898	1.54
72.8713	290.59	0.1535	1.50720	4.42
74.6504	159.71	0.2558	1.47633	2.43
76.1329	66.28	0.3070	1.45182	1.01



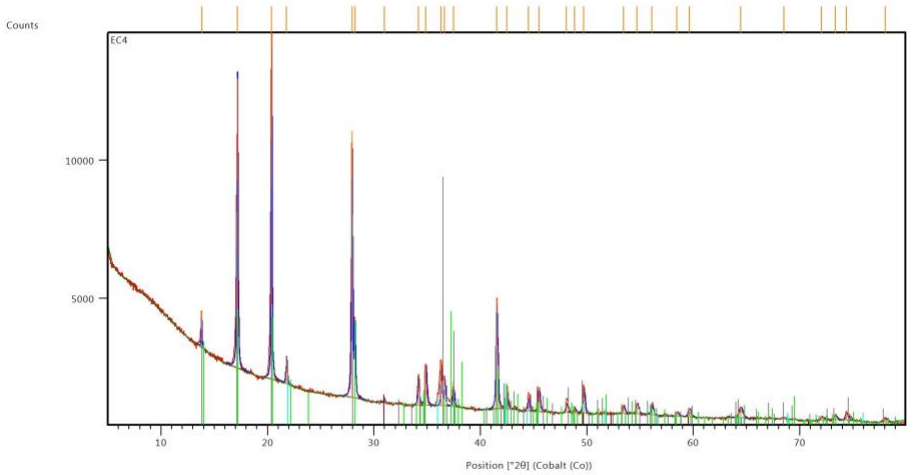
EC4

Pattern List

Ref.Code	Mineral Name	SemiQuant[%]	Score	Compound Name	Scale Fac.	Chem. Formula
04-019-0176		34	21	Copper Carbonate H..	0.234	Cu2 (C O3) (O H..
00-056-0001	Malachite	63	35	Copper Carbonate H..	0.565	Cu2 +2 (C O3) (..
00-041-1487	Graphite-2H	1	18	Carbon	0.021	C
04-014-9664		2	19	Iron Oxide	0.062	Fe3 O4

Peak List

Pos.[°2θ]	Height [cts]	FWHMLeft[°2θ]	d-spacing [Å]	Rel. Int. [%]
13.8164	1338.60	0.0768	7.44233	10.67
17.1739	10487.02	0.1279	5.99525	83.56
20.3814	12550.88	0.1023	5.05950	100.00
21.7852	967.94	0.1535	4.73705	7.71
27.9401	9624.71	0.1279	3.70795	76.69
28.2137	2891.62	0.1023	3.67271	23.04
30.9887	153.29	0.1535	3.35083	1.22
34.1795	1130.19	0.1535	3.04609	9.00
34.8798	1454.73	0.2047	2.98678	11.59
36.3115	1640.57	0.1023	2.87275	13.07
36.6313	1045.76	0.1279	2.84852	8.33
37.4686	893.55	0.1279	2.78708	7.12
41.5375	4000.89	0.1791	2.52442	31.88
42.4863	898.15	0.1535	2.47057	7.16
44.4921	629.42	0.1279	2.36447	5.01
45.4995	901.93	0.2047	2.31481	7.19
48.0786	478.27	0.1279	2.19743	3.81
48.8239	215.83	0.1791	2.16590	1.72
49.7043	1038.12	0.2047	2.12991	8.27
53.4609	310.50	0.2047	1.99014	2.47
54.7223	382.13	0.2558	1.94769	3.04
56.1225	415.07	0.1535	1.90290	3.31
58.4710	170.52	0.2558	1.83283	1.36
59.6426	306.92	0.2558	1.80004	2.45
64.4634	389.34	0.3582	1.67838	3.10
68.4973	56.03	0.3070	1.59058	0.45
72.0443	130.04	0.3070	1.52212	1.04
73.3305	173.96	0.2558	1.49907	1.39
74.3698	307.30	0.2558	1.48109	2.45
78.0541	135.65	0.3582	1.42158	1.08



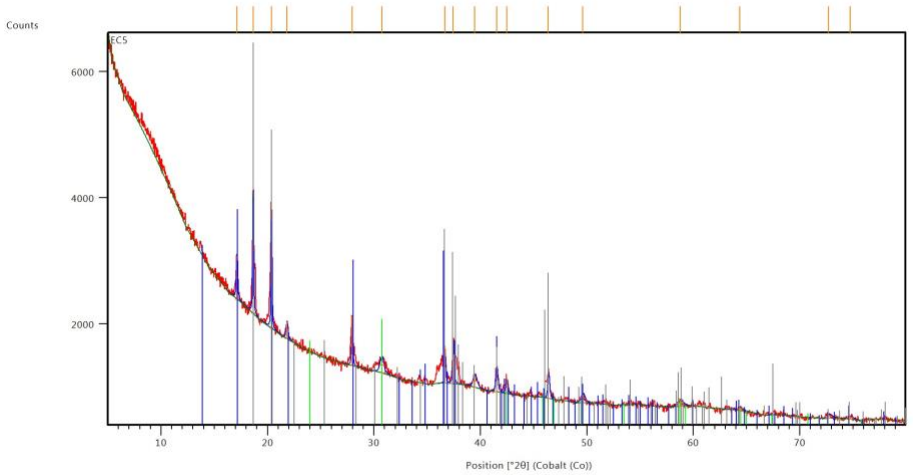
EC5

Pattern List

Ref.Code	Mineral Name	SemiQuant[%]	Score	Compound Name	Scale Fac.	Chem. Formula
00-056-0001	Malachite	36	26	Copper Carbonate H..	0.317	Cu2 +2 (C O3) (..
04-006-1757	Quartz	8	25	Silicon Oxide	0.129	Si O2
01-080-9252	Atacamite	56	32	Copper Chloride Hy..	0.647	Cu2 Cl (O H)3

Peak List

Pos.[°2θ]	Height [cts]	FWHMLeft[°2θ]	d-spacing [Å]	Rel. Int. [%]
17.1310	686.23	0.1535	6.01017	34.30
18.6440	2000.53	0.1023	5.52623	100.00
20.3644	1971.54	0.1023	5.06368	98.55
21.8286	263.45	0.2047	4.72774	13.17
27.9386	786.74	0.1279	3.70814	39.33
30.7341	242.27	0.4093	3.37791	12.11
36.6560	597.07	0.1023	2.84667	29.85
37.4429	728.16	0.1535	2.78892	36.40
39.4827	201.24	0.4093	2.65015	10.06
41.5276	418.33	0.2047	2.52500	20.91
42.4720	239.38	0.2047	2.47137	11.97
46.3822	478.60	0.1535	2.27312	23.92
49.6214	140.87	0.4093	2.13324	7.04
58.7602	91.31	0.6140	1.82460	4.56
64.3505	51.41	0.6140	1.68100	2.57
72.7169	63.22	0.6140	1.50995	3.16
74.7205	45.88	0.6140	1.47514	2.29



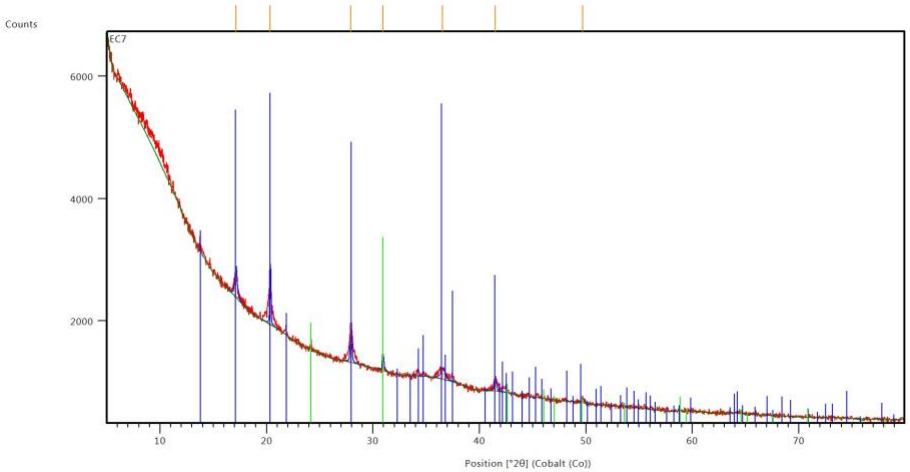
EC7

Pattern List

Ref.Code	Mineral Name	SemiQuant[%]	Score	Compound Name	Scale Fac.	Chem. Formula
00-056-0001	Malachite	77	25	Copper Carbonate H..	0.668	Cu2 +2 (C O3) (..
04-016-2085	Quartz	23	18	Silicon Oxide	0.324	Si O2

Peak List

Pos.[°2θ]	Height [cts]	FWHMLeft[°2θ]	d-spacing [Å]	Rel. Int. [%]
17.1319	465.18	0.2558	6.00985	45.41
20.3477	1024.43	0.1023	5.06779	100.00
27.9158	631.27	0.1535	3.71112	61.62
30.9414	251.49	0.1535	3.35583	24.55
36.5477	167.04	0.5117	2.85482	16.31
41.4699	224.32	0.2047	2.52836	21.90
49.6972	81.46	0.3070	2.13019	7.95



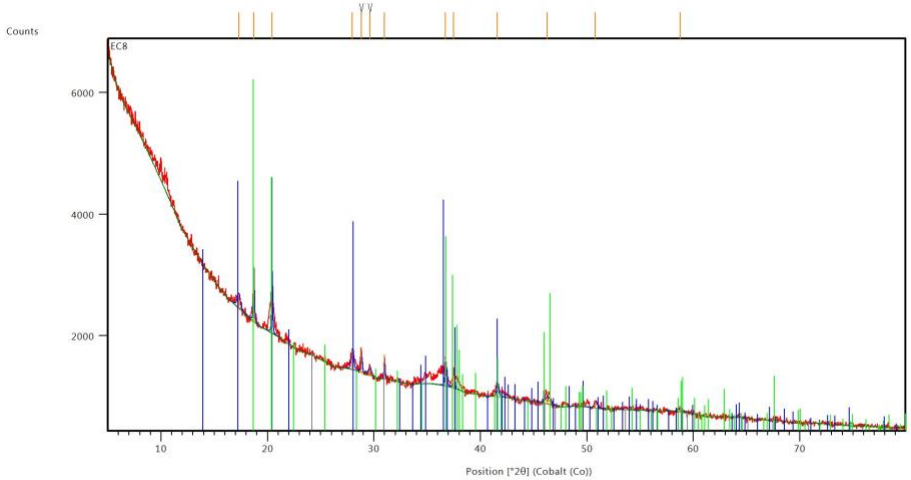
EC8

Pattern List

Ref.Code	Mineral Name	SemiQuant[%]	Score	Compound Name	Scale Fac.	Chem. Formula
00-056-0001	Malachite	50	19	Copper Carbonate H..	0.442	Cu2 +2 (C O3) (..
01-071-2027	Atacamite	48	19	Copper Chloride Hy..	0.575	Cu2 Cl (O H)3
04-015-8431	Quartz	2	16	Silicon Oxide	0.029	Si O2

Peak List

Pos.[°2θ]	Height [cts]	FWHMLeft[°2θ]	d-spacing [Å]	Rel. Int. [%]
17.2934	224.08	0.3582	5.95413	21.44
18.7020	905.15	0.1023	5.50923	86.62
20.4227	1044.96	0.1023	5.04939	100.00
27.9661	323.43	0.2558	3.70457	30.95
28.8172	387.45	0.1023	3.59738	37.08
29.6193	124.42	0.3070	3.50204	11.91
30.9759	391.98	0.1023	3.35219	37.51
36.7274	442.76	0.1535	2.84133	42.37
37.4729	336.08	0.1535	2.78677	32.16
41.6018	232.45	0.2047	2.52070	22.25
46.2924	112.73	0.6140	2.27729	10.79
50.7873	97.13	0.3582	2.08741	9.30
58.7509	52.21	0.6140	1.82487	5.00



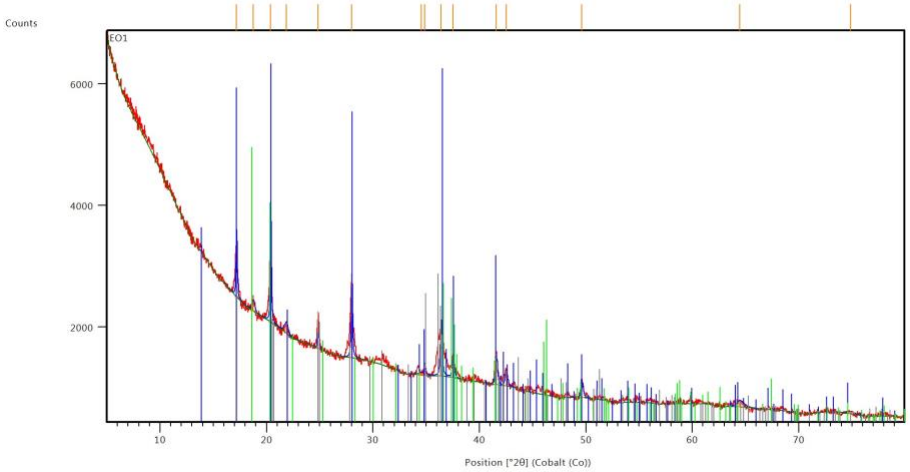
EO1

Pattern List

Ref.Code	Mineral Name	SemiQuant[%]	Score	Compound Name	Scale Fac.	Chem. Formula
00-056-0001	Malachite	55	39	Copper Carbonate H..	0.735	Cu2 +2 (C O3) (..
01-080-9252	Atacamite	22	11	Copper Chloride Hy..	0.389	Cu2 Cl (O H)3
04-007-4282		23	9	Potassium Sulfate	0.244	K2 (S O4)

Peak List

Pos.[°2θ]	Height [cts]	FWHM Left[°2θ]	d-spacing [Å]	Rel. Int. [%]
17.1867	1070.62	0.1279	5.99082	60.69
18.7739	171.18	0.3070	5.48834	9.70
20.3970	1764.17	0.1279	5.05567	100.00
21.8567	177.02	0.4093	4.72173	10.03
24.8508	604.03	0.1023	4.16025	34.24
27.9967	1383.77	0.1535	3.70060	78.44
34.5413	34.57	0.8187	3.01514	1.96
34.8654	192.32	0.1535	2.98797	10.90
36.3979	929.13	0.2047	2.86617	52.67
37.5264	361.52	0.2047	2.78294	20.49
41.5748	501.72	0.2047	2.52226	28.44
42.5149	250.64	0.2558	2.46899	14.21
49.6188	284.42	0.2047	2.13334	16.12
64.4446	94.96	0.8187	1.67881	5.38
74.8960	38.27	0.7164	1.47219	2.17



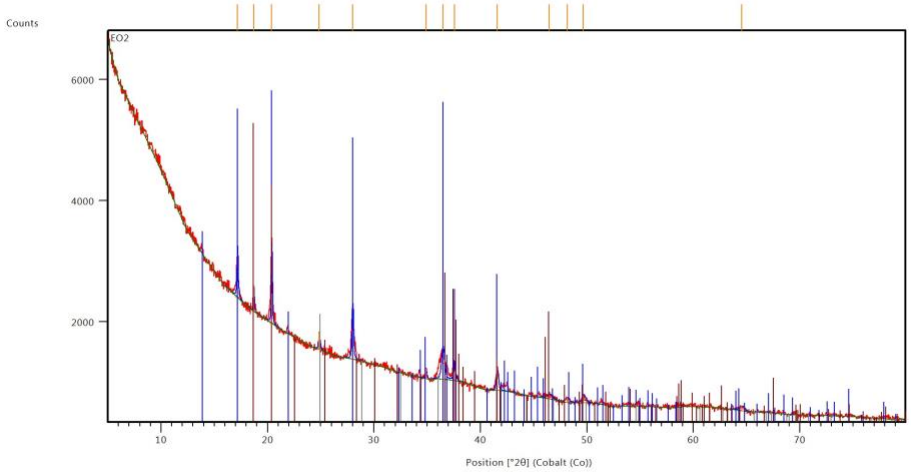
EO2

Pattern List

Ref.Code	Mineral Name	SemiQuant[%]	Score	Compound Name	Scale Fac.	Chem. Formula
00-056-0001	Malachite	64	39	Copper Carbonate H..	0.671	Cu2 +2 (C O3) (..
01-075-0923	Cristobalite	3	0	Silicon Oxide	0.087	Si O2
01-080-9252	Atacamite	33	17	Copper Chloride Hy..	0.455	Cu2 Cl (O H)3

Peak List

Pos.[°2θ]	Height [cts]	FWHM Left[°2θ]	d-spacing [Å]	Rel. Int. [%]
17.1829	840.21	0.1279	5.99213	59.52
18.7104	431.07	0.0768	5.50679	30.53
20.3924	1411.71	0.1023	5.05681	100.00
24.8654	280.84	0.1535	4.15784	19.89
27.9969	940.95	0.1535	3.70058	66.65
34.8911	166.06	0.1535	2.98584	11.76
36.4704	518.11	0.3070	2.86066	36.70
37.5464	317.15	0.2047	2.78151	22.47
41.5753	376.14	0.2047	2.52223	26.64
46.4609	72.63	0.6140	2.26948	5.14
48.1836	82.05	0.4093	2.19293	5.81
49.6719	125.95	0.4093	2.13121	8.92
64.5417	72.93	0.6140	1.67656	5.17



CCV

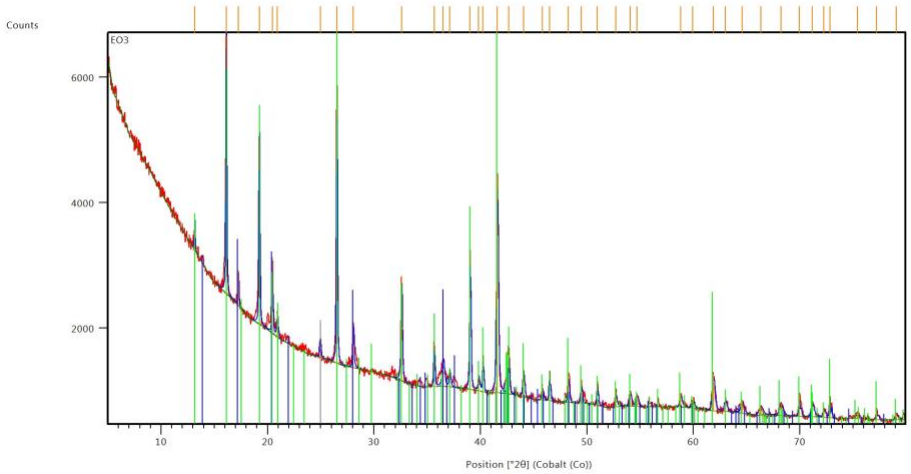
EO3

Pattern List

Ref.Code	Mineral Name	SemiQuant[%]	Score	Compound Name	Scale Fac.	Chem. Formula
00-056-0001	Malachite	12	24	Copper Carbonate H..	0.229	Cu2 +2 (C O3) (..
01-079-6416	Brochantite	86	73	Copper Sulfate Hyd..	1.081	Cu4 (S O4) (O H..
04-007-4908		2	17	Silicon Oxide	0.089	Si O2

Peak List

Pos.[°2θ]	Height [cts]	FWHMLeft[°2θ]	d-spacing [Å]	Rel. Int. [%]
13.1697	508.40	0.0768	7.80606	11.47
16.1233	4104.87	0.1023	6.38306	92.59
17.2607	558.25	0.1023	5.96533	12.59
19.2335	3294.63	0.1023	5.35837	74.31
20.4625	1208.84	0.1023	5.03967	27.27
20.9221	379.81	0.1535	4.93016	8.57
24.9606	298.93	0.1535	4.14223	6.74
26.5157	4433.42	0.1023	3.90328	100.00
28.0577	722.12	0.1279	3.69272	16.29
32.5893	1667.57	0.1535	3.19041	37.61
35.6536	764.43	0.1023	2.92399	17.24
36.4967	419.64	0.2558	2.85867	9.47
37.1211	268.13	0.1535	2.81223	6.05
39.0305	2283.96	0.1279	2.67964	51.52
39.8444	241.56	0.1535	2.62706	5.45
40.2390	585.61	0.1023	2.60234	13.21
41.5888	3505.16	0.1791	2.52145	79.06
42.6666	844.51	0.0768	2.46061	19.05
44.0438	436.67	0.1791	2.38732	9.85
45.8137	223.65	0.1535	2.29978	5.04
46.4952	433.62	0.1279	2.26790	9.78
48.2587	489.42	0.1279	2.18972	11.04
49.4628	374.49	0.1279	2.13965	8.45
50.9793	390.91	0.1023	2.08007	8.82
52.7249	232.88	0.1535	2.01589	5.25
54.0880	212.25	0.2047	1.96878	4.79
54.7287	176.07	0.2558	1.94748	3.97
58.8097	208.24	0.2047	1.82321	4.70
59.9567	105.78	0.3070	1.79148	2.39
61.8940	579.49	0.2558	1.74071	13.07
63.0017	186.20	0.2558	1.71318	4.20
64.5803	210.13	0.3070	1.67567	4.74
66.3270	135.13	0.4093	1.63639	3.05
68.2410	188.38	0.4093	1.59582	4.25
69.9713	358.31	0.1279	1.56121	8.08
71.1637	223.03	0.3070	1.53842	5.03
72.2798	134.72	0.2558	1.51783	3.04
72.8222	350.63	0.0936	1.50698	7.91
75.4047	83.58	0.3070	1.46372	1.89
77.2217	159.33	0.1535	1.43448	3.59
79.0920	94.54	0.3070	1.40593	2.13



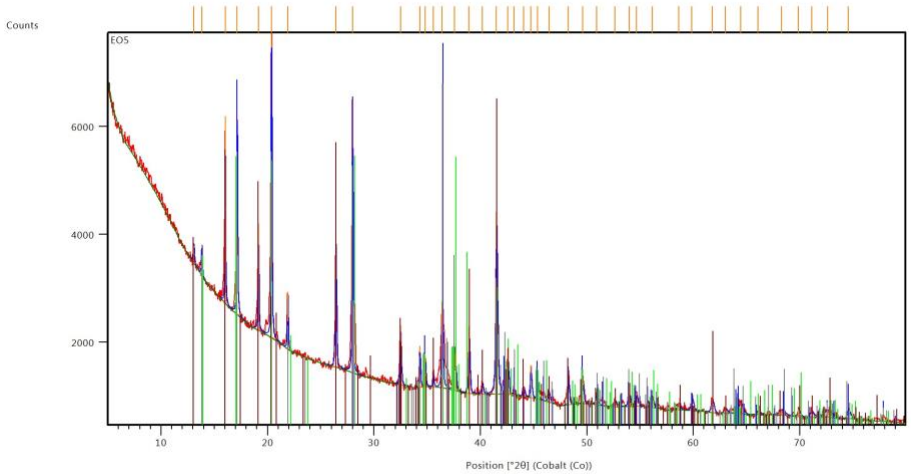
EO5

Pattern List

Ref.Code	Mineral Name	SemiQuant[%]	Score	Compound Name	Scale Fac.	Chem. Formula
00-056-0001	Malachite	23	55	Copper Carbonate H..	0.825	Cu2 +2 (C O3) (..
04-019-0177		22	13	Copper Carbonate H..	0.560	Cu2 (C O3) (O H..
04-015-4888	Malachite	24	36	Copper Carbonate H..	0.728	Cu2 (C O3) (O H..
04-011-4170	Brochantite	32	50	Copper Sulfate Hyd..	0.707	Cu4 (S O4) (O H..

Peak List

Pos.[°2θ]	Height [cts]	FWHMLeft[°2θ]	d-spacing [Å]	Rel. Int. [%]
13.0780	332.45	0.1535	7.86050	5.84
13.8341	568.42	0.1023	7.43282	9.98
16.0306	3464.17	0.0768	6.41975	60.85
17.1513	3637.63	0.1023	6.00309	63.89
19.1396	1977.80	0.1023	5.38441	34.74
20.3779	5693.39	0.1023	5.06036	100.00
21.8961	1059.29	0.1023	4.71335	18.61
26.4198	2350.73	0.1279	3.91719	41.29
27.9871	5119.99	0.1023	3.70184	89.93
32.4962	1100.40	0.1279	3.19930	19.33
34.3174	767.21	0.1023	3.03422	13.48
34.8029	559.91	0.1279	2.99317	9.83
35.5708	360.74	0.0768	2.93058	6.34
36.4058	1601.71	0.1535	2.86557	28.13
37.5862	823.70	0.2047	2.77867	14.47
38.9397	1237.83	0.1279	2.68564	21.74
40.1945	218.87	0.1535	2.60511	3.84
41.5128	3368.88	0.1791	2.52586	59.17
42.5795	843.78	0.1279	2.46541	14.82
43.1680	119.78	0.1535	2.43337	2.10
44.0629	188.43	0.2047	2.38634	3.31
44.7435	601.51	0.1279	2.35187	10.57
45.3808	363.05	0.1279	2.32054	6.38
46.4314	237.14	0.1535	2.27085	4.17
48.2664	638.71	0.1023	2.18939	11.22
49.6115	467.93	0.1279	2.13364	8.22
50.9135	216.06	0.2047	2.08258	3.79
52.6356	115.32	0.3070	2.01907	2.03
53.9837	210.48	0.2558	1.97230	3.70
54.6508	256.58	0.2047	1.95004	4.51
56.1620	187.49	0.2047	1.90167	3.29
58.6118	105.78	0.3070	1.82881	1.86
59.8714	298.14	0.2047	1.79379	5.24
61.7915	253.23	0.2558	1.74331	4.45
63.0025	89.73	0.3070	1.71316	1.58
64.4336	207.95	0.4093	1.67907	3.65
66.0881	66.56	0.4093	1.64163	1.17
68.2792	95.83	0.6140	1.59504	1.68
69.8737	140.61	0.2558	1.56311	2.47
71.1089	115.94	0.3070	1.53945	2.04
72.6120	131.24	0.8187	1.51183	2.31
74.5696	193.57	0.2558	1.47769	3.40



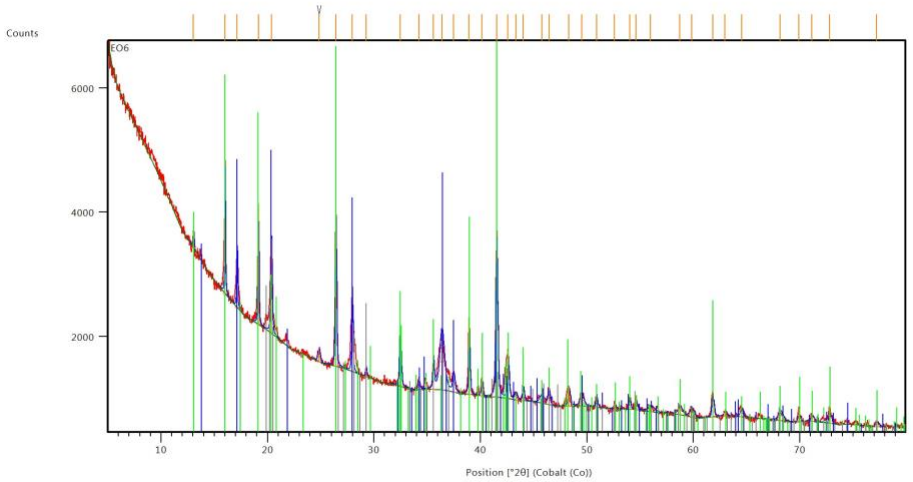
EO6

Pattern List

Ref.Code	Mineral Name	SemiQuant[%]	Score	Compound Name	Scale Fac.	Chem. Formula
00-056-0001	Malachite	22	38	Copper Carbonate H..	0.517	Cu2 +2 (C O3) (..
04-011-4170	Brochantite	71	54	Copper Sulfate Hyd..	1.163	Cu4 (S O4) (O H..
01-076-5942	Azurite	7	11	Copper Carbonate H..	0.174	Cu3 (C O3)2 (O ..

Peak List

Pos.[°2θ]	Height [cts]	FWHMLeft[°2θ]	d-spacing [Å]	Rel. Int. [%]
13.0481	262.63	0.1535	7.87846	9.55
16.0212	2169.80	0.0768	6.42350	78.94
17.1509	1022.90	0.1023	6.00324	37.21
19.1463	1942.93	0.1023	5.38256	70.69
20.3629	1517.62	0.1535	5.06405	55.21
24.8470	213.37	0.2558	4.16087	7.76
26.4271	2514.17	0.1279	3.91613	91.47
27.9626	1407.52	0.1279	3.70503	51.21
29.2666	168.64	0.1535	3.54332	6.14
32.4691	901.03	0.1791	3.20189	32.78
34.2107	182.24	0.1535	3.04340	6.63
35.5886	557.48	0.1279	2.92916	20.28
36.3838	907.14	0.5117	2.86724	33.00
37.4822	309.04	0.2047	2.78610	11.24
38.9351	1238.32	0.1279	2.68594	45.05
40.1274	297.08	0.1535	2.60929	10.81
41.5219	2748.65	0.1791	2.52533	100.00
42.5874	758.25	0.1791	2.46498	27.59
43.3353	121.18	0.3070	2.42443	4.41
44.0203	275.67	0.1535	2.38853	10.03
45.7644	134.80	0.5117	2.30212	4.90
46.4340	267.67	0.2047	2.27073	9.74
48.3122	304.75	0.2303	2.18744	11.09
49.5257	190.24	0.4093	2.13710	6.92
50.9018	162.56	0.1535	2.08303	5.91
52.5833	74.68	0.3070	2.02093	2.72
54.0156	189.89	0.1535	1.97122	6.91
54.6251	199.52	0.1535	1.95089	7.26
55.9870	82.72	0.8187	1.90713	3.01
58.7057	147.85	0.4093	1.82615	5.38
59.8456	140.66	0.5117	1.79450	5.12
61.8182	421.49	0.1791	1.74264	15.33
62.9760	95.92	0.3070	1.71380	3.49
64.5378	137.24	0.3582	1.67665	4.99
68.1480	156.84	0.5117	1.59774	5.71
69.8899	193.98	0.1535	1.56280	7.06
71.1468	116.17	0.3070	1.53874	4.23
72.8052	259.76	0.1535	1.50837	9.45
77.2288	90.57	0.3070	1.43437	3.29



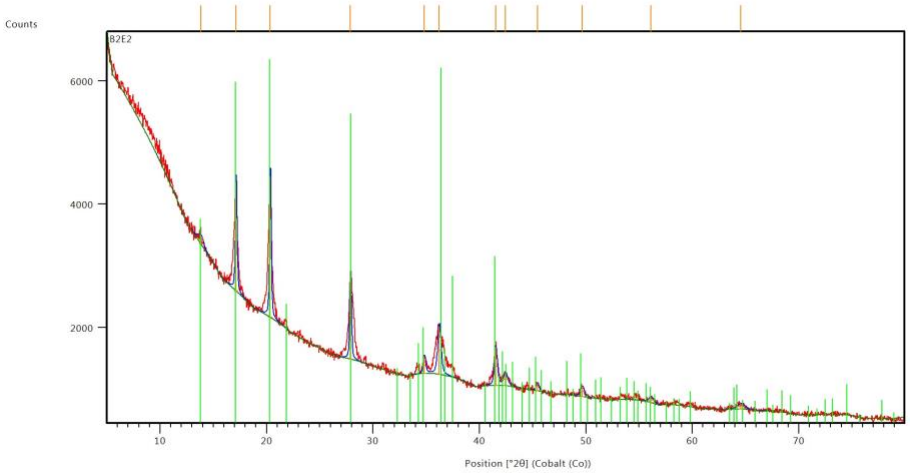
B2E2

Pattern List

Ref.Code	Mineral Name	SemiQuant[%]	Score	Compound Name	Scale Fac.	Chem. Formula
00-056-0001	Malachite	100	33	Copper Carbonate H..	0.731	Cu2 +2 (C O3) (..

Peak List

Pos.[°2θ]	Height [cts]	FWHMLeft[°2θ]	d-spacing [Å]	Rel. Int. [%]
13.8291	145.32	0.6140	7.43553	6.34
17.1456	1771.23	0.1791	6.00509	77.31
20.3554	2291.05	0.1791	5.06591	100.00
27.8830	1430.04	0.1791	3.71539	62.42
34.8182	280.19	0.2558	2.99190	12.23
36.2182	775.42	0.3582	2.87990	33.85
41.5183	619.81	0.3070	2.52554	27.05
42.4408	200.85	0.4093	2.47310	8.77
45.4546	133.69	0.3070	2.31698	5.84
49.6433	163.30	0.4093	2.13236	7.13
56.0982	88.29	0.6140	1.90366	3.85
64.5312	86.84	0.8187	1.67680	3.79



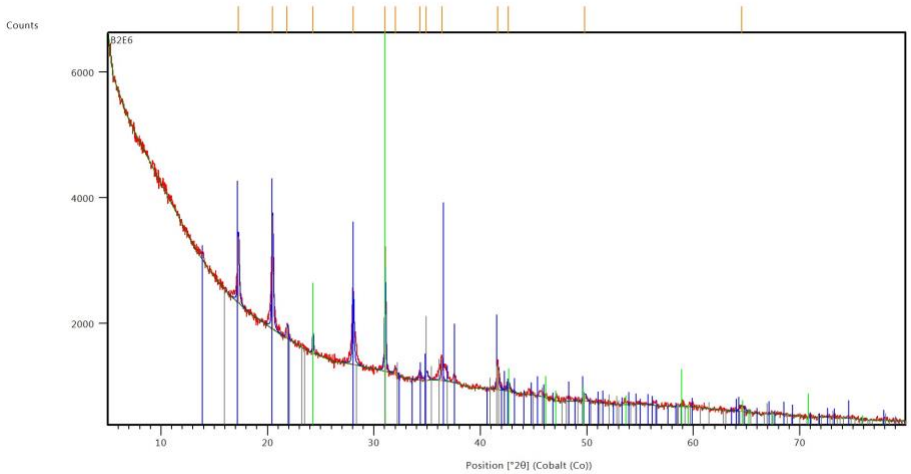
B2E6

Pattern List

Ref.Code	Mineral Name	SemiQuant[%]	Score	Compound Name	Scale Fac.	Chem. Formula
00-056-0001	Malachite	38	24	Copper Carbonate H..	0.428	Cu2 +2 (C O3) (..
01-075-8320	Quartz	45	43	Silicon Oxide	0.847	Si O2
01-071-3828	Diopside	17	9	Calcium Magnesium ..	0.154	Ca Mg (Si O3)2

Peak List

Pos.[°2θ]	Height [cts]	FWHMLeft[°2θ]	d-spacing [Å]	Rel. Int. [%]
17.2649	1049.48	0.1791	5.96391	53.06
20.4770	1801.56	0.1535	5.03613	91.09
21.8363	215.46	0.2047	4.72609	10.89
24.2649	365.20	0.1023	4.25913	18.46
28.0419	1154.87	0.1791	3.69475	58.39
31.0419	1977.79	0.1023	3.34523	100.00
32.0094	98.45	0.3070	3.24665	4.98
34.2962	120.80	0.3070	3.03604	6.11
34.9173	137.53	0.3070	2.98367	6.95
36.3775	361.35	0.1535	2.86771	18.27
41.6075	396.83	0.2047	2.52037	20.06
42.6250	142.04	0.3070	2.46290	7.18
49.8103	116.51	0.3070	2.12566	5.89
64.5508	82.25	0.6140	1.67635	4.16



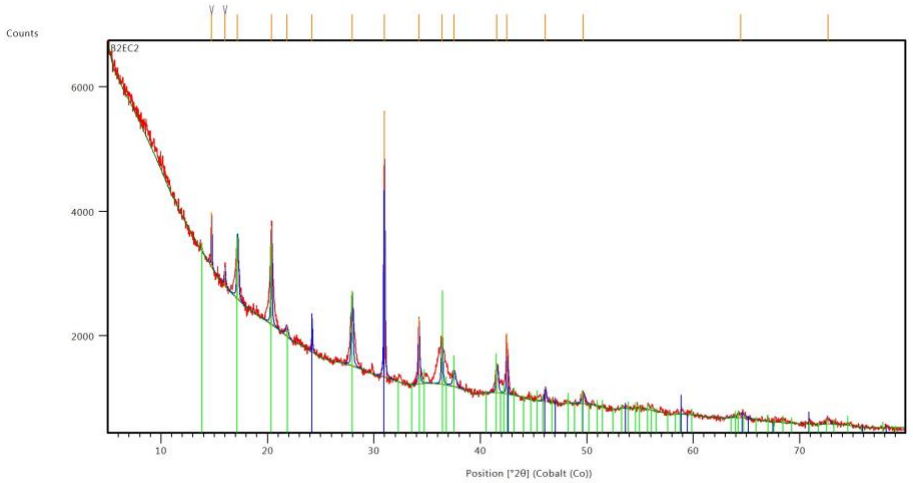
B2EC2

Pattern List

Ref.Code	Mineral Name	SemiQuant[%]	Score	Compound Name	Scale Fac.	Chem. Formula
04-016-2085	Quartz	55	48	Silicon Oxide	0.444	Si O2
00-056-0001	Malachite	45	35	Copper Carbonate H..	0.224	Cu2 +2 (C O3) (..

Peak List

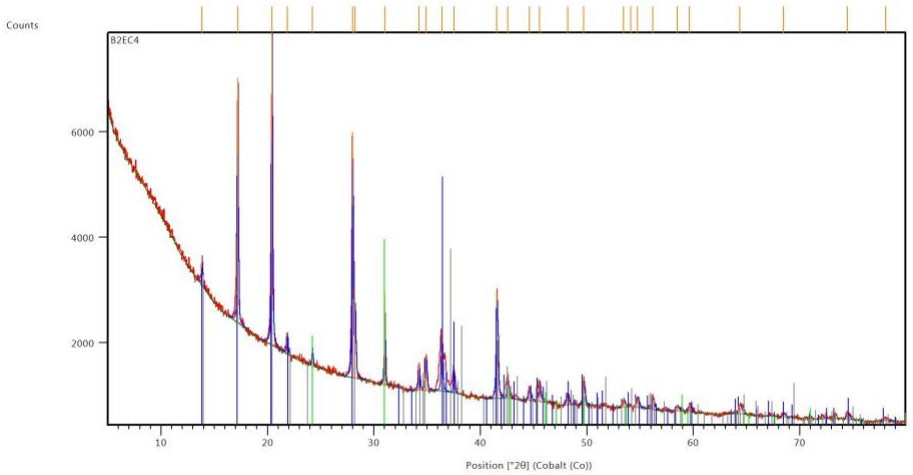
Pos.[°2θ]	Height [cts]	FWHMLeft[°2θ]	d-spacing [Å]	Rel. Int. [%]
14.7418	876.64	0.0768	6.97749	20.62
16.0030	299.88	0.1535	6.43076	7.05
17.1944	981.38	0.1791	5.98818	23.09
20.3622	1579.56	0.1279	5.06423	37.16
21.8046	157.24	0.3070	4.73288	3.70
24.1863	550.55	0.0768	4.27278	12.95
27.9513	1094.42	0.1791	3.70649	25.74
30.9625	4251.13	0.1023	3.35361	100.00
34.2251	1049.78	0.1279	3.04216	24.69
36.3765	768.17	0.1535	2.86779	18.07
37.5353	241.92	0.3070	2.78230	5.69
41.5526	449.41	0.2047	2.52355	10.57
42.4627	979.05	0.1023	2.47188	23.03
46.0870	225.54	0.2047	2.28688	5.31
49.6720	166.78	0.3582	2.13120	3.92
64.4643	67.46	0.8187	1.67836	1.59
72.6508	106.05	0.3070	1.51114	2.49



B2EC4

Pattern List

Ref.Code	Mineral Name	SemiQuant[%]	Score	Compound Name	Scale Fac.	Chem. Formula
00-056-0001	Malachite	45	37	Copper Carbonate H..	0.517	Cu2 +2 (C O3) (..
04-006-1757	Quartz	18	32	Silicon Oxide	0.350	Si O2
04-019-0176		38	13	Copper Carbonate H..	0.345	Cu2 (C O3) (O H..



Peak List

Pos.[°2θ]	Height [cts]	FWHMLeft[°2θ]	d-spacing [Å]	Rel. Int. [%]
13.8603	570.51	0.1023	7.41883	9.61
17.2114	4641.06	0.1023	5.98229	78.17
20.4210	5937.44	0.1279	5.04980	100.00
21.8573	418.66	0.1279	4.72161	7.05
24.2144	380.04	0.1023	4.26789	6.40
27.9837	4666.43	0.1279	3.70228	78.59
28.2465	1417.35	0.1023	3.66854	23.87
31.0058	1727.60	0.1023	3.34903	29.10
34.2256	513.99	0.1535	3.04211	8.66
34.8951	695.47	0.1791	2.98551	11.71
36.3746	1193.79	0.1535	2.86794	20.11
37.4997	560.53	0.1023	2.78485	9.44
41.5559	2011.66	0.1791	2.52336	33.88
42.5715	478.57	0.1279	2.46585	8.06
44.5939	247.57	0.2558	2.35935	4.17
45.5601	425.96	0.1791	2.31190	7.17
48.2030	232.21	0.2558	2.19210	3.91
49.7057	538.68	0.1791	2.12985	9.07
53.4579	133.94	0.3070	1.99024	2.26
54.1289	10.03	0.8187	1.96740	0.17
54.7446	183.73	0.3070	1.94696	3.09
56.2119	256.00	0.2047	1.90012	4.31
58.4792	107.55	0.3070	1.83259	1.81
59.6338	137.61	0.3070	1.80028	2.32
64.3846	194.43	0.2558	1.68021	3.27
68.4865	72.30	0.3070	1.59080	1.22
74.4740	131.74	0.2558	1.47931	2.22
78.0654	46.78	0.6140	1.42141	0.79

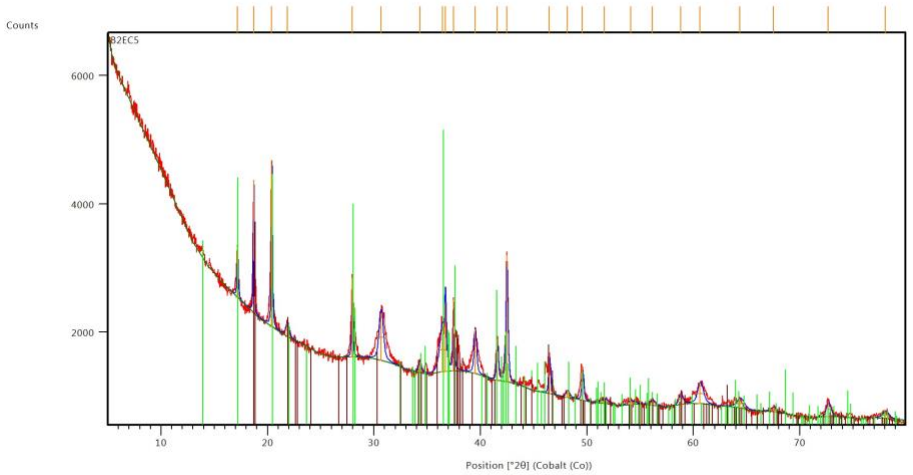
B2EC5

Pattern List

Ref.Code	Mineral Name	SemiQuant[%]	Score	Compound Name	Scale Fac.	Chem. Formula
01-072-8421	Malachite	82	32	Copper Carbonate H..	0.564	Cu2 (O H)2 (C O..
04-012-9781	Clinoatacamite	18	24	Copper Chloride Hy..	0.216	Cu2 Cl (O H)3

Peak List

Pos.[°2θ]	Height [cts]	FWHM Left[°2θ]	d-spacing [Å]	Rel. Int. [%]
17.1750	800.24	0.1279	5.99488	30.82
18.6923	2074.22	0.1023	5.51209	79.89
20.4009	2596.23	0.1279	5.05473	100.00
21.8771	209.45	0.4093	4.71739	8.07
27.9538	1228.22	0.1279	3.70616	47.31
30.6682	725.76	0.4605	3.38500	27.95
34.3043	162.01	0.3070	3.03535	6.24
36.4299	686.92	0.6140	2.86373	26.46
36.7072	1048.01	0.1023	2.84283	40.37
37.4780	1108.73	0.1279	2.78640	42.71
39.4963	684.33	0.2558	2.64927	26.36
41.5708	635.83	0.1791	2.52249	24.49
42.4657	1966.37	0.2047	2.47171	75.74
46.4737	644.80	0.1791	2.26889	24.84
48.1747	106.40	0.4093	2.19331	4.10
49.5805	530.88	0.1791	2.13489	20.45
51.6334	65.65	0.8187	2.05549	2.53
54.1125	57.30	0.8187	1.96796	2.21
56.1508	71.74	0.6140	1.90202	2.76
58.8052	160.48	0.4093	1.82333	6.18
60.6362	312.49	0.6140	1.77328	12.04
64.3819	141.26	0.8187	1.68027	5.44
67.5146	66.18	0.6140	1.61093	2.55
72.6533	240.00	0.4093	1.51109	9.24
78.0268	111.75	0.7164	1.42200	4.30



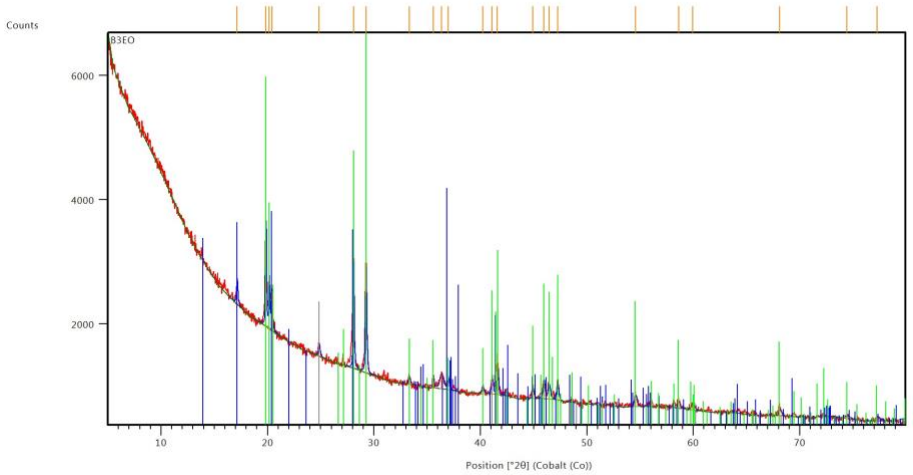
B2EO

Pattern List

Ref.Code	Mineral Name	SemiQuant[%]	Score	Compound Name	Scale Fac.	Chem. Formula
04-011-5196	Malachite	36	10	Copper Carbonate H..	0.484	Cu2 (C O3) (O H..
01-076-5942	Azurite	61	46	Copper Carbonate H..	1.007	Cu3 (C O3)2 (O ..
01-077-8631		3	16	Silicon Oxide	0.131	Si O2

Peak List

Pos.[°2θ]	Height [cts]	FWHMLeft[°2θ]	d-spacing [Å]	Rel. Int. [%]
17.1489	388.44	0.1535	6.00395	19.69
19.8519	1756.09	0.1023	5.19304	89.03
20.1476	853.90	0.1023	5.11759	43.29
20.4022	628.24	0.1535	5.05442	31.85
24.8564	208.54	0.1535	4.15933	10.57
28.0830	1972.37	0.1023	3.68946	100.00
29.2549	1830.27	0.1279	3.54470	92.80
33.3431	112.82	0.2047	3.12025	5.72
35.5733	194.12	0.1535	2.93038	9.84
36.3545	227.00	0.4093	2.86947	11.51
36.9874	201.85	0.1535	2.82205	10.23
40.2178	138.54	0.1535	2.60366	7.02
41.0922	294.48	0.1535	2.55058	14.93
41.6023	652.94	0.1023	2.52067	33.10
44.9281	208.75	0.1535	2.34270	10.58
45.9716	315.73	0.2047	2.29231	16.01
46.4387	249.65	0.2047	2.27051	12.66
47.2436	325.82	0.1535	2.23399	16.52
54.5558	219.77	0.2047	1.95318	11.14
58.6151	157.36	0.1535	1.82872	7.98
59.9480	88.33	0.4093	1.79171	4.48
68.1275	127.69	0.2047	1.59816	6.47
74.4095	41.76	0.6140	1.48041	2.12
77.2726	55.91	0.6140	1.43368	2.83



HUNGARY

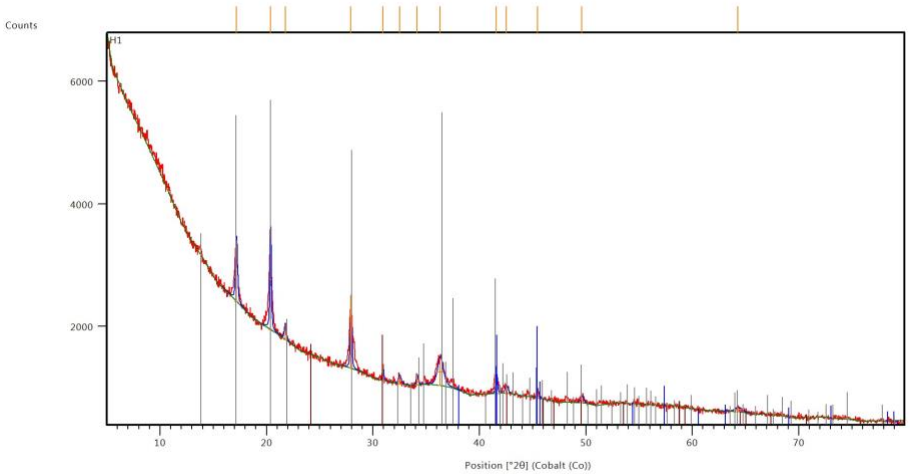
H1

Pattern List

Ref.Code	Mineral Name	SemiQuant[%]	Score	Compound Name	Scale Fac.	Chem. Formula
04-004-4916		10	21	Copper Oxide	0.172	Cu O
00-056-0001	Malachite	84	33	Copper Carbonate H..	0.655	Cu2 +2 (C O3) (..
01-089-1961	Quartz, syn	6	15	Silicon Oxide	0.109	Si O2

Peak List

Pos.[°2θ]	Height [cts]	FWHMLeft[°2θ]	d-spacing [Å]	Rel. Int. [%]
17.1792	996.88	0.2047	5.99343	60.86
20.3734	1638.10	0.1535	5.06148	100.00
21.7590	255.53	0.2047	4.74267	15.60
27.9195	1178.13	0.1535	3.71063	71.92
30.9312	275.15	0.1023	3.35691	16.80
32.4956	134.52	0.3070	3.19935	8.21
34.1379	167.31	0.2047	3.04969	10.21
36.3209	441.97	0.6140	2.87203	26.98
41.5727	422.43	0.1535	2.52238	25.79
42.5342	124.28	0.3070	2.46792	7.59
45.4785	107.41	0.3070	2.31582	6.56
49.6255	116.08	0.3070	2.13307	7.09
64.2742	71.27	0.8187	1.68279	4.35



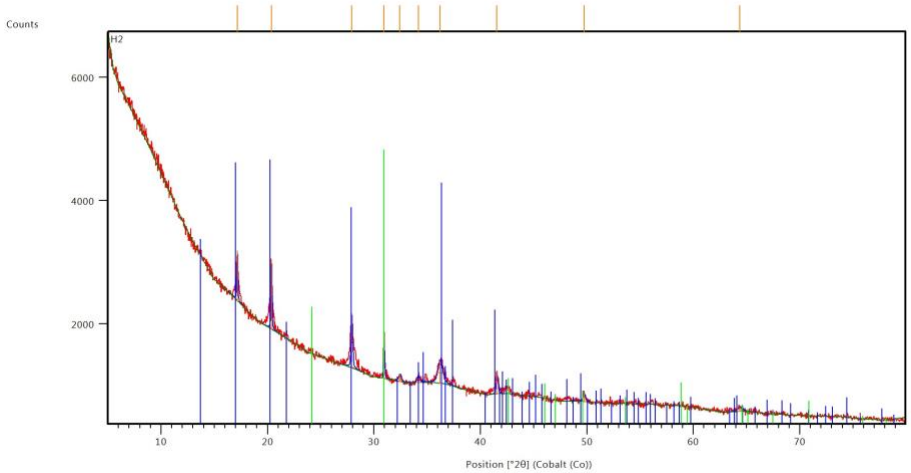
H2

Pattern List

Ref.Code	Mineral Name	SemiQuant[%]	Score	Compound Name	Scale Fac.	Chem. Formula
00-056-0001	Malachite	59	20	Copper Carbonate H..	0.482	Cu2 +2 (C O3) (..
04-016-2085	Quartz	41	18	Silicon Oxide	0.550	Si O2

Peak List

Pos.[°2θ]	Height [cts]	FWHMLeft[°2θ]	d-spacing [Å]	Rel. Int. [%]
17.1543	812.38	0.1023	6.00206	72.73
20.3578	1116.96	0.1023	5.06531	100.00
27.9094	870.47	0.1535	3.71195	77.93
30.9508	701.69	0.0768	3.35483	62.82
32.4422	110.11	0.3070	3.20447	9.86
34.1674	106.01	0.3070	3.04714	9.49
36.2241	347.39	0.5117	2.87945	31.10
41.5374	377.05	0.1535	2.52443	33.76
49.7250	123.48	0.3070	2.12908	11.06
64.3823	65.15	0.6140	1.68026	5.83



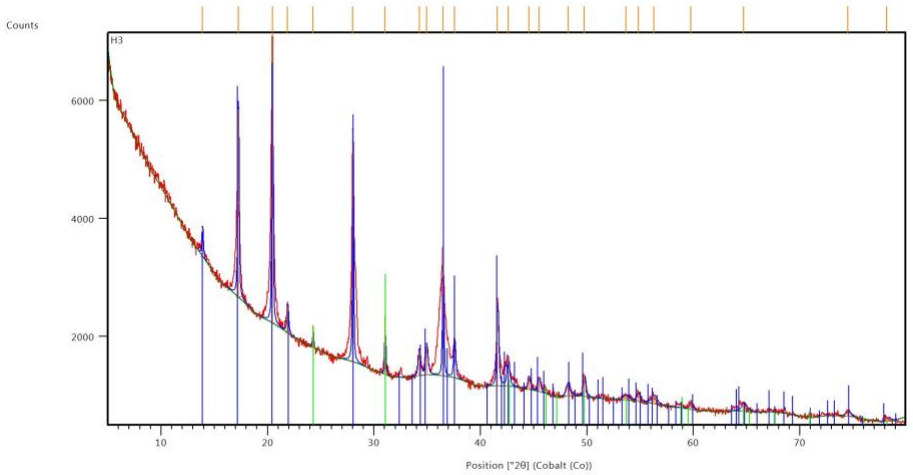
H3

Pattern List

Ref.Code	Mineral Name	SemiQuant[%]	Score	Compound Name	Scale Fac.	Chem. Formula
00-056-0001	Malachite	84	48	Copper Carbonate H..	0.732	Cu2 +2 (C O3) (..
01-075-0443	Quartz	16	24	Silicon Oxide	0.238	Si O2

Peak List

Pos.[°2θ]	Height [cts]	FWHMLeft[°2θ]	d-spacing [Å]	Rel. Int. [%]
13.8998	481.94	0.1535	7.39785	9.74
17.2553	3182.60	0.1535	5.96720	64.30
20.4552	4949.39	0.1279	5.04145	100.00
21.8878	456.27	0.2047	4.71510	9.22
24.2746	354.79	0.0768	4.25747	7.17
28.0085	3911.57	0.1279	3.69908	79.03
31.0331	984.90	0.1023	3.34616	19.90
34.2522	431.25	0.2558	3.03982	8.71
34.9462	507.61	0.2558	2.98128	10.26
36.4689	2202.34	0.1279	2.86077	44.50
37.5652	663.81	0.2047	2.78017	13.41
41.6017	1423.99	0.2047	2.52070	28.77
42.5975	485.78	0.2558	2.46442	9.81
44.5387	224.14	0.2558	2.36212	4.53
45.4918	250.58	0.2558	2.31518	5.06
48.2440	221.83	0.4093	2.19035	4.48
49.7596	363.41	0.2558	2.12769	7.34
53.6606	79.02	0.6140	1.98328	1.60
54.8482	132.97	0.4093	1.94356	2.69
56.2897	136.12	0.6140	1.89771	2.75
59.7508	130.02	0.3070	1.79708	2.63
64.7432	125.80	0.6140	1.67191	2.54
74.5287	81.56	0.5117	1.47839	1.65
78.1686	60.61	0.6140	1.41983	1.22



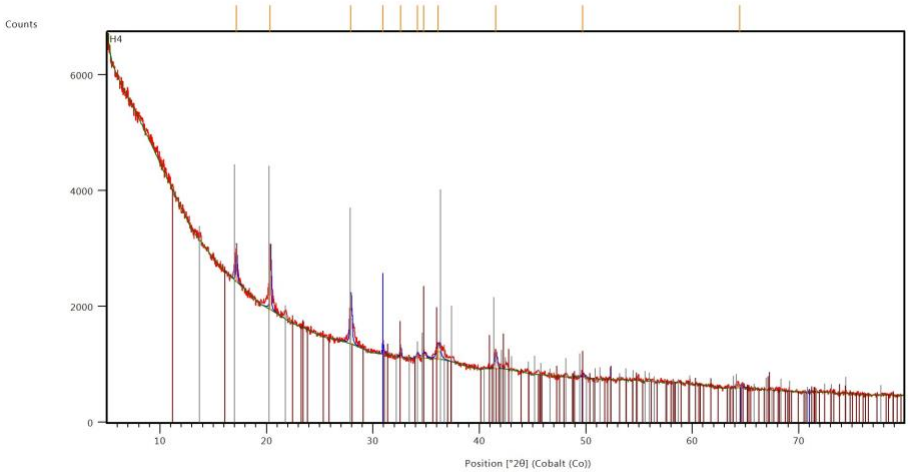
H4

Pattern List

Ref.Code	Mineral Name	SemiQuant[%]	Score	Compound Name	Scale Fac.	Chem. Formula
04-016-6288	Graphite-2H	17	23	Carbon	0.207	C
00-056-0001	Malachite	48	16	Copper Carbonate H..	0.434	Cu2 +2 (C O3) (..
01-078-5155		34	6	Calcium Magnesium ..	0.184	(Fe0.253 Mg0.747 ..

Peak List

Pos.[°2θ]	Height [cts]	FWHMLeft[°2θ]	d-spacing [Å]	Rel. Int. [%]
17.1716	641.22	0.1279	5.99605	57.09
20.3558	1123.08	0.1279	5.06580	100.00
27.9259	857.97	0.2047	3.70980	76.39
30.9430	181.96	0.1535	3.35566	16.20
32.5925	191.87	0.1535	3.19010	17.08
34.1840	84.89	0.3070	3.04570	7.56
34.7806	96.99	0.3582	2.99503	8.64
36.1429	258.73	0.4093	2.88571	23.04
41.5319	314.81	0.2047	2.52475	28.03
49.7111	77.46	0.3070	2.12963	6.90
64.4669	43.48	0.6140	1.67830	3.87



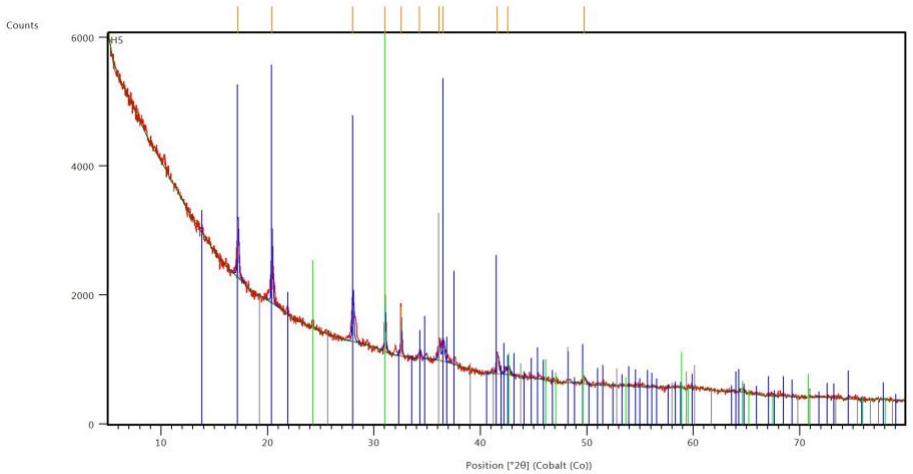
H5

Pattern List

Ref.Code	Mineral Name	SemiQuant[%]	Score	Compound Name	Scale Fac.	Chem. Formula
00-056-0001	Malachite	46	30	Copper Carbonate H..	0.722	Cu2 +2 (C O3) (..
01-075-8320	Quartz	33	26	Silicon Oxide	0.863	Si O2
04-015-9848		21	16	Calcium Magnesium ..	0.375	Ca Mg (C O3)2

Peak List

Pos.[°2θ]	Height [cts]	FWHMLeft[°2θ]	d-spacing [Å]	Rel. Int. [%]
17.2291	903.71	0.1535	5.97621	77.76
20.4245	1162.14	0.1279	5.04894	100.00
28.0210	789.79	0.1535	3.69746	67.96
31.0361	906.83	0.1023	3.34584	78.03
32.5427	765.95	0.1023	3.19485	65.91
34.2902	120.91	0.3070	3.03655	10.40
36.1050	353.89	0.1535	2.88863	30.45
36.5041	333.55	0.2047	2.85811	28.70
41.5995	316.08	0.2047	2.52083	27.20
42.5866	127.38	0.4093	2.46502	10.96
49.7486	97.59	0.4093	2.12813	8.40



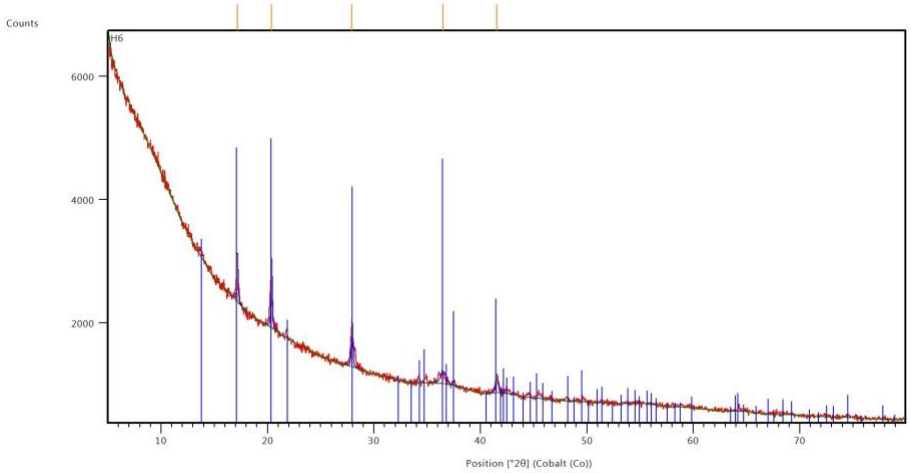
H6

Pattern List

Ref.Code	Mineral Name	SemiQuant[%]	Score	Compound Name	Scale Fac.	Chem. Formula
00-056-0001	Malachite	100	27	Copper Carbonate H..	0.541	Cu2 +2 (C O3) (..

Peak List

Pos.[°2θ]	Height [cts]	FWHMLeft[°2θ]	d-spacing [Å]	Rel. Int. [%]
17.1698	770.62	0.1279	5.99668	68.02
20.3712	1132.98	0.1279	5.06201	100.00
27.9247	777.61	0.1535	3.70996	68.63
36.4911	180.96	0.6140	2.85909	15.97
41.5209	305.55	0.2558	2.52539	26.97



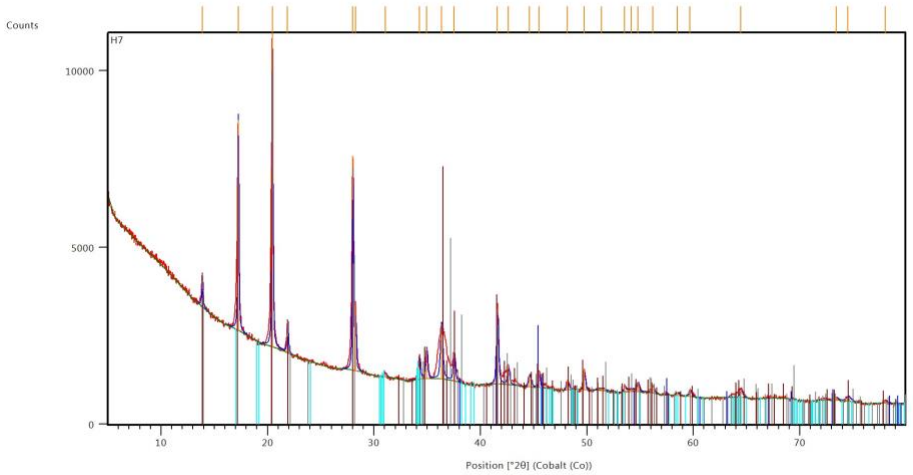
H7

Pattern List

Ref.Code	Mineral Name	SemiQuant[%]	Score	Compound Name	Scale Fac.	Chem. Formula
01-073-6234	Tenorite	6	20	Copper Oxide	0.159	Cu O
04-019-0176		39	18	Copper Carbonate H..	0.362	Cu2 (C O3) (O H..
00-056-0001	Malachite	46	36	Copper Carbonate H..	0.543	Cu2 +2 (C O3) (..
04-015-7160		8	16	Silicon Oxide	0.047	Si O2

Peak List

Pos.[°2θ]	Height [cts]	FWHMLeft[°2θ]	d-spacing [Å]	Rel. Int. [%]
13.8707	904.33	0.1535	7.41334	10.14
17.2475	5945.40	0.1279	5.96987	66.69
20.4491	8914.60	0.1279	5.04293	100.00
21.8778	919.65	0.1535	4.71724	10.32
28.0042	6072.58	0.1279	3.69963	68.12
28.2902	1838.01	0.0768	3.66299	20.62
31.0750	103.53	0.3070	3.34175	1.16
34.2582	702.20	0.2047	3.03931	7.88
34.9488	866.69	0.2047	2.98106	9.72
36.3410	1551.12	0.2558	2.87050	17.40
37.5175	805.52	0.2047	2.78358	9.04
41.5793	2120.12	0.2047	2.52200	23.78
42.6114	555.92	0.2047	2.46365	6.24
44.6071	350.61	0.3070	2.35869	3.93
45.5165	458.21	0.1279	2.31399	5.14
48.1766	247.41	0.2558	2.19323	2.78
49.7600	597.25	0.1279	2.12768	6.70
51.3572	59.09	0.8187	2.06579	0.66
53.5583	191.79	0.1535	1.98679	2.15
54.1827	65.08	0.8187	1.96560	0.73
54.7999	257.78	0.2558	1.94514	2.89
56.2127	216.50	0.2047	1.90010	2.43
58.5043	84.05	0.3070	1.83188	0.94
59.6879	175.04	0.2558	1.79880	1.96
64.4558	223.14	0.2558	1.67855	2.50
73.4169	85.47	0.3070	1.49756	0.96
74.5145	140.30	0.5117	1.47863	1.57
78.0373	76.37	0.3070	1.42184	0.86



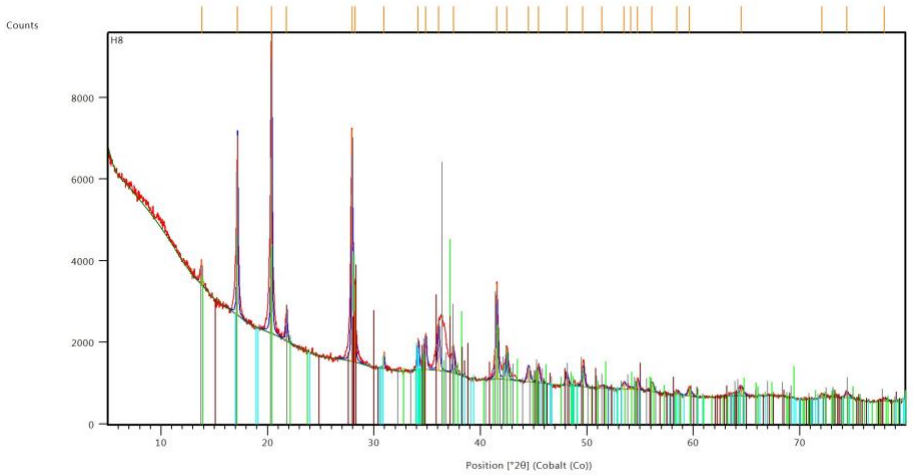
H8

Pattern List

Ref.Code	Mineral Name	SemiQuant[%]	Score	Compound Name	Scale Fac.	Chem. Formula
04-019-0176		26	20	Copper Carbonate H..	0.340	Cu2 (C O3) (O H..
00-056-0001	Malachite	32	37	Copper Carbonate H..	0.533	Cu2 +2 (C O3) (..
04-018-0239		33	17	Silicon Oxide	0.250	Si O2
01-077-8640		9	22	Silicon Oxide	0.071	Si O2

Peak List

Pos.[°2θ]	Height [cts]	FWHMLeft[°2θ]	d-spacing [Å]	Rel. Int. [%]
13.8219	615.33	0.0768	7.43934	8.35
17.1707	4404.95	0.1279	5.99635	59.81
20.3674	7365.45	0.1279	5.06294	100.00
21.7886	854.36	0.1535	4.73632	11.60
27.9359	5684.87	0.1535	3.70849	77.18
28.2253	1897.32	0.0768	3.67123	25.76
30.9454	411.24	0.1023	3.35540	5.58
34.1531	753.46	0.1535	3.04837	10.23
34.8607	902.36	0.1791	2.98837	12.25
36.0662	1222.51	0.2047	2.89164	16.60
37.4565	689.58	0.1535	2.78794	9.36
41.5215	2337.57	0.1791	2.52536	31.74
42.4727	794.45	0.1791	2.47133	10.79
44.4969	398.29	0.3070	2.36423	5.41
45.4449	493.62	0.1791	2.31744	6.70
48.1052	315.11	0.2558	2.19629	4.28
49.6305	602.39	0.1791	2.13287	8.18
51.4376	74.25	0.6140	2.06278	1.01
53.4695	177.34	0.3070	1.98985	2.41
54.1347	42.01	0.8187	1.96721	0.57
54.7708	267.45	0.2047	1.94610	3.63
56.1303	244.48	0.2558	1.90266	3.32
58.4756	108.71	0.3070	1.83269	1.48
59.6316	206.16	0.3070	1.80034	2.80
64.4928	241.82	0.3582	1.67769	3.28
72.0707	94.64	0.3070	1.52163	1.28
74.4118	163.42	0.3070	1.48037	2.22
77.9362	72.64	0.6140	1.42339	0.99



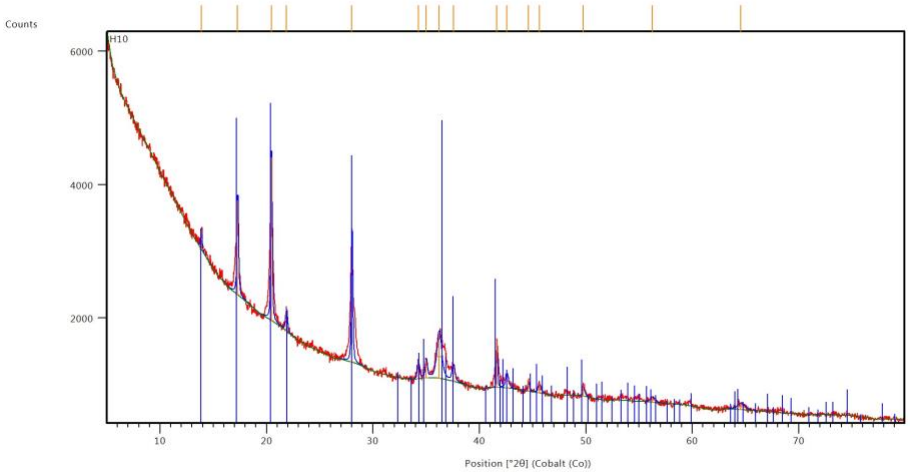
H10

Pattern List

Ref.Code	Mineral Name	SemiQuant[%]	Score	Compound Name	Scale Fac.	Chem. Formula
00-056-0001	Malachite	100	28	Copper Carbonate H..	0.614	Cu2 +2 (C O3) (..

Peak List

Pos.[°2θ]	Height [cts]	FWHMLeft[°2θ]	d-spacing [Å]	Rel. Int. [%]
13.8764	283.16	0.1535	7.41029	11.57
17.2873	1411.35	0.1791	5.95622	57.67
20.4621	2447.28	0.1535	5.03978	100.00
21.8689	320.61	0.2047	4.71914	13.10
28.0188	2007.95	0.1535	3.69774	82.05
34.2522	267.52	0.2047	3.03982	10.93
35.0018	269.86	0.2047	2.97669	11.03
36.2102	652.81	0.5117	2.88052	26.67
37.5471	232.44	0.3070	2.78146	9.50
41.6300	730.80	0.1023	2.51906	29.86
42.5732	215.82	0.3070	2.46576	8.82
44.6067	170.36	0.1535	2.35871	6.96
45.6353	129.53	0.3070	2.30829	5.29
49.7631	133.34	0.2558	2.12755	5.45
56.2627	71.31	0.6140	1.89854	2.91
64.5329	95.11	0.8187	1.67677	3.89



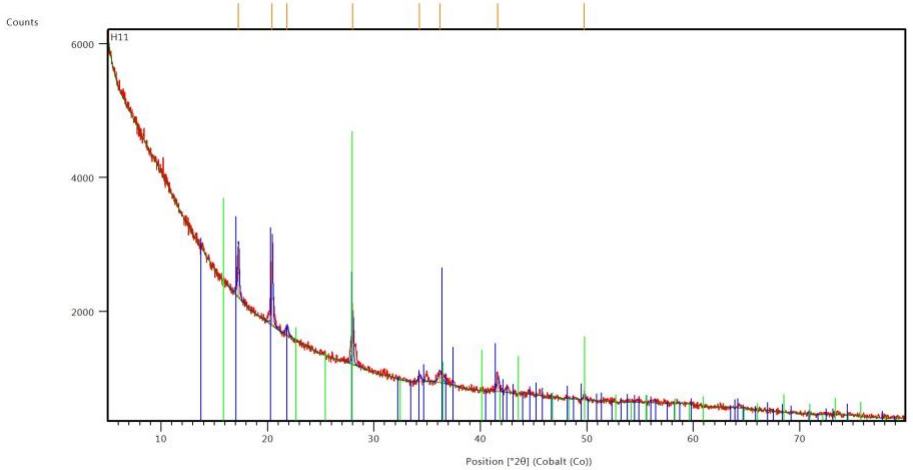
H11

Pattern List

Ref.Code	Mineral Name	SemiQuant[%]	Score	Compound Name	Scale Fac.	Chem. Formula
00-056-0001	Malachite	46	11	Copper Carbonate H..	0.277	Cu2 +2 (C O3) (..
04-014-6618		54	21	Sodium Aluminum Ch..	0.560	Na8 Al6 (Si O4)6..

Peak List

Pos.[°2θ]	Height [cts]	FWHMLeft[°2θ]	d-spacing [Å]	Rel. Int. [%]
17.2594	792.97	0.1791	5.96577	58.15
20.4438	1363.56	0.1279	5.04423	100.00
21.8264	149.44	0.3070	4.72822	10.96
27.9862	902.75	0.1279	3.70197	66.21
34.2931	102.88	0.3070	3.03631	7.54
36.2315	159.48	0.4093	2.87888	11.70
41.6244	253.29	0.2047	2.51939	18.58
49.7449	125.52	0.1535	2.12828	9.21



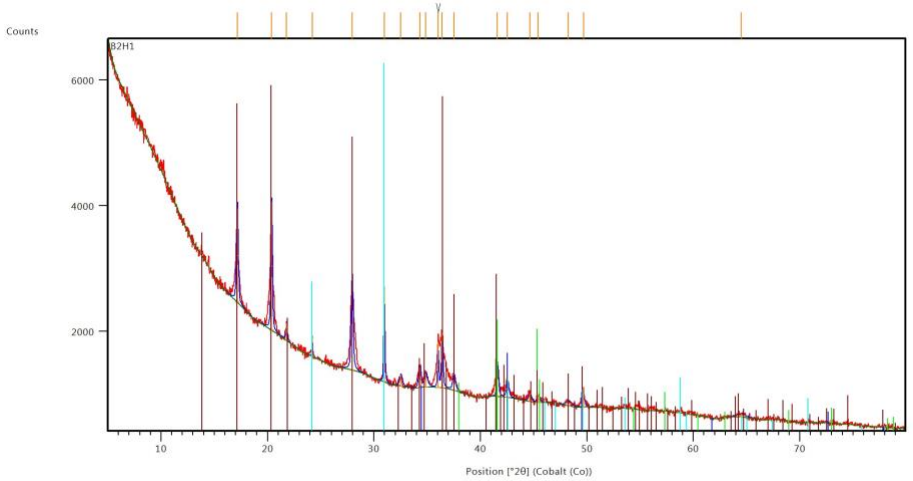
B2H1

Pattern List

Ref.Code	Mineral Name	SemiQuant[%]	Score	Compound Name	Scale Fac.	Chem. Formula
04-007-9767	Cuprite	2	30	Copper Oxide	0.106	Cu2O
00-005-0661	Tenorite, syn	14	17	Copper Oxide	0.182	CuO
00-056-0001	Malachite	57	36	Copper Carbonate H..	0.695	Cu2 +2 (CO3) (..
01-089-1961	Quartz, syn	27	33	Silicon Oxide	0.760	SiO2

Peak List

Pos.[°2θ]	Height [cts]	FWHMLeft[°2θ]	d-spacing [Å]	Rel. Int. [%]
17.1606	1490.23	0.1791	5.99989	72.93
20.3701	2043.32	0.1535	5.06229	100.00
21.7829	276.60	0.1535	4.73755	13.54
24.1991	291.35	0.0768	4.27055	14.26
27.9380	1478.73	0.2047	3.70822	72.37
30.9601	1516.70	0.1023	3.35386	74.23
32.5265	175.70	0.3070	3.19640	8.60
34.3035	320.39	0.2558	3.03541	15.68
34.8811	216.60	0.3070	2.98667	10.60
36.0107	715.68	0.1023	2.89595	35.03
36.3928	873.24	0.1535	2.86655	42.74
37.5138	237.17	0.3070	2.78384	11.61
41.5919	547.56	0.1791	2.52127	26.80
42.5384	259.37	0.2558	2.46769	12.69
44.6340	122.52	0.3070	2.35734	6.00
45.4273	107.65	0.3070	2.31830	5.27
48.2682	77.65	0.6140	2.18932	3.80
49.6873	207.89	0.1535	2.13059	10.17
64.4946	53.73	0.8187	1.67765	2.63



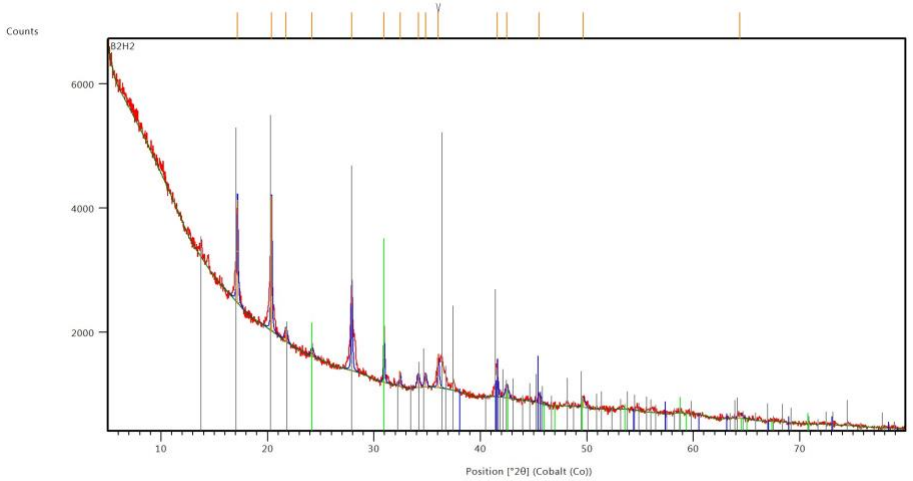
B2H2

Pattern List

Ref.Code	Mineral Name	SemiQuant[%]	Score	Compound Name	Scale Fac.	Chem. Formula
04-004-5425	Tenorite	7	19	Copper Oxide	0.113	Cu O
01-089-1961	Quartz, syn	18	32	Silicon Oxide	0.344	Si O2
00-056-0001	Malachite	75	22	Copper Carbonate H..	0.611	Cu2 +2 (C O3) (..

Peak List

Pos.[°2θ]	Height [cts]	FWHM Left[°2θ]	d-spacing [Å]	Rel. Int. [%]
17.1610	1657.54	0.1535	5.99975	76.37
20.3623	2170.50	0.1279	5.06422	100.00
21.7421	221.69	0.3070	4.74632	10.21
24.1840	140.41	0.3070	4.27318	6.47
27.9031	1526.62	0.1279	3.71277	70.34
30.9537	795.22	0.1023	3.35453	36.64
32.4591	230.33	0.1535	3.20285	10.61
34.1708	220.23	0.2558	3.04684	10.15
34.8480	211.09	0.2047	2.98942	9.73
36.0476	518.74	0.1535	2.89308	23.90
41.5905	453.22	0.1023	2.52135	20.88
42.4654	219.79	0.3070	2.47173	10.13
45.5283	130.15	0.4093	2.31342	6.00
49.6609	158.40	0.3070	2.13165	7.30
64.3830	69.81	0.5117	1.68025	3.22



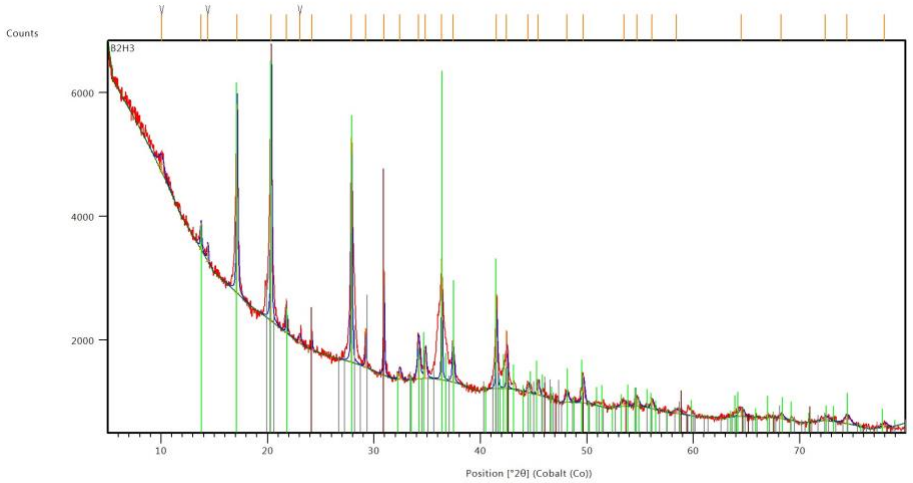
B2H3

Pattern List

Ref.Code	Mineral Name	SemiQuant[%]	Score	Compound Name	Scale Fac.	Chem. Formula
00-056-0001	Malachite	62	40	Copper Carbonate H..	0.729	Cu2 +2 (C O3) (..
01-076-5942	Azurite	14	7	Copper Carbonate H..	0.173	Cu3 (C O3)2 (O ..
04-006-1757	Quartz	24	29	Silicon Oxide	0.487	Si O2

Peak List

Pos.[°2θ]	Height [cts]	FWHMLeft[°2θ]	d-spacing [Å]	Rel. Int. [%]
10.0537	253.40	0.6140	10.21601	5.68
13.7585	439.57	0.1535	7.47346	9.86
14.3889	285.56	0.1535	7.14765	6.40
17.1427	3053.94	0.1535	6.00609	68.47
20.3423	4460.25	0.1279	5.06912	100.00
21.7639	552.89	0.1023	4.74162	12.40
23.0510	140.94	0.3070	4.48015	3.16
24.1653	322.30	0.0768	4.27643	7.23
27.8880	3635.22	0.1279	3.71474	81.50
29.2041	621.42	0.1023	3.55074	13.93
30.9320	1705.00	0.1023	3.35683	38.23
32.4336	176.54	0.3070	3.20530	3.96
34.1853	678.06	0.2558	3.04559	15.20
34.8283	492.09	0.2047	2.99106	11.03
36.3565	1939.94	0.1023	2.86932	43.49
37.4196	681.75	0.1791	2.79059	15.28
41.4954	1520.27	0.1279	2.52687	34.08
42.4575	940.86	0.1023	2.47217	21.09
44.4729	171.04	0.2047	2.36544	3.83
45.4297	255.65	0.2047	2.31818	5.73
48.1225	175.91	0.3070	2.19555	3.94
49.6537	440.11	0.2558	2.13194	9.87
53.4806	84.35	0.6140	1.98946	1.89
54.6945	147.81	0.4093	1.94860	3.31
56.1243	159.83	0.3070	1.90284	3.58
58.3946	64.17	0.7164	1.83501	1.44
64.4807	146.27	0.5117	1.67798	3.28
68.2523	79.59	0.4093	1.59559	1.78
72.3760	64.43	0.8187	1.51609	1.44
74.4252	140.08	0.6140	1.48014	3.14
77.9195	69.49	0.6140	1.42365	1.56



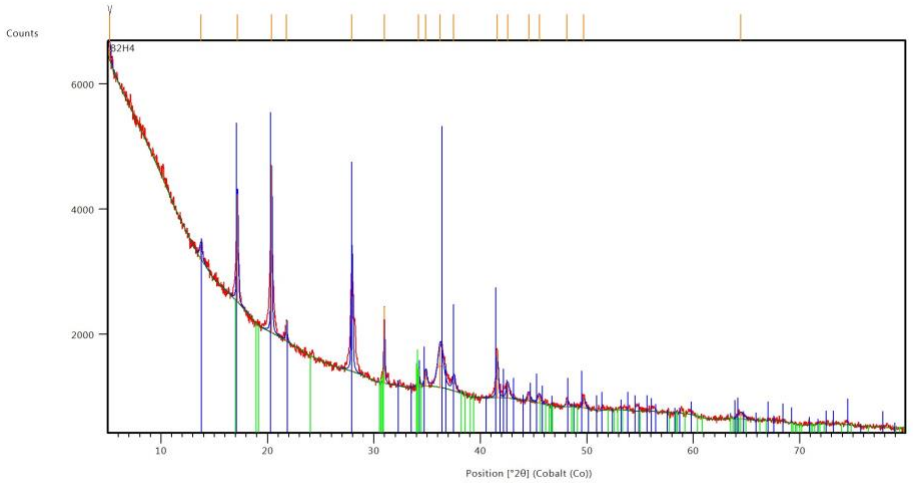
B2H4

Pattern List

Ref.Code	Mineral Name	SemiQuant[%]	Score	Compound Name	Scale Fac.	Chem. Formula
00-056-0001	Malachite	77	31	Copper Carbonate H..	0.624	Cu2 +2 (C O3) (..
04-015-7160		23	14	Silicon Oxide	0.088	Si O2

Peak List

Pos. [°2θ]	Height [cts]	FWHM Left [°2θ]	d-spacing [Å]	Rel. Int. [%]
5.1557	272.10	0.3070	19.90262	10.13
13.7550	251.00	0.3070	7.47539	9.35
17.1723	1722.37	0.1535	5.99583	64.15
20.3775	2684.98	0.1279	5.06046	100.00
21.7700	317.81	0.1535	4.74032	11.84
27.9267	2045.99	0.1535	3.70970	76.20
30.9666	1217.61	0.1023	3.35317	45.35
34.1847	267.54	0.1535	3.04565	9.96
34.8572	246.72	0.2558	2.98866	9.19
36.2353	666.35	0.6140	2.87859	24.82
37.4850	241.70	0.3070	2.78590	9.00
41.5627	757.60	0.1791	2.52296	28.22
42.5538	251.47	0.3070	2.46683	9.37
44.5393	132.98	0.3070	2.36209	4.95
45.5345	141.72	0.3582	2.31313	5.28
48.1310	115.12	0.3070	2.19518	4.29
49.6992	186.43	0.2047	2.13011	6.94
64.4489	102.50	0.6140	1.67871	3.82



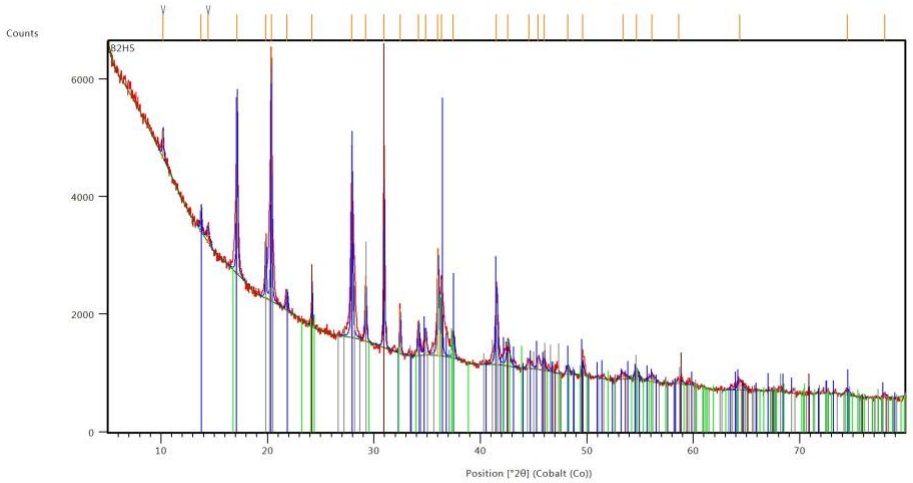
B2H5

Pattern List

Ref.Code	Mineral Name	SemiQuant[%]	Score	Compound Name	Scale Fac.	Chem. Formula
00-056-0001	Malachite	40	43	Copper Carbonate H..	0.659	Cu2 +2 (C O3) (..
04-015-8186		17	19	Sodium Aluminum Si..	0.158	Na Al Si2 O6
01-077-5327		14	14	Copper Carbonate H..	0.254	Cu3 (C O3)2 (O ..
04-016-2085	Quartz	29	42	Silicon Oxide	0.776	Si O2

Peak List

Pos.[°2θ]	Height [cts]	FWHMLeft[°2θ]	d-spacing [Å]	Rel. Int. [%]
10.1813	463.64	0.1535	10.08827	10.76
13.7643	427.64	0.1535	7.47036	9.93
14.4280	246.67	0.3070	7.12840	5.73
17.1407	3027.36	0.1279	6.00678	70.27
19.8373	1115.46	0.1023	5.19684	25.89
20.3580	4308.31	0.1023	5.06527	100.00
21.8365	332.26	0.1791	4.72605	7.71
24.1763	778.58	0.1023	4.27452	18.07
27.9147	3256.01	0.1535	3.71126	75.58
29.2227	1107.45	0.1279	3.54852	25.71
30.9426	3399.71	0.1023	3.35570	78.91
32.4591	767.29	0.1279	3.20286	17.81
34.1830	607.04	0.1791	3.04579	14.09
34.8418	436.59	0.2303	2.98993	10.13
36.0037	1828.25	0.1535	2.89649	42.44
36.3452	1308.65	0.1279	2.87018	30.38
37.4342	460.00	0.1791	2.78955	10.68
41.4941	1395.78	0.2047	2.52695	32.40
42.5933	432.34	0.3070	2.46465	10.04
44.5649	131.36	0.4093	2.36081	3.05
45.4355	235.34	0.2558	2.31790	5.46
45.9926	193.75	0.2558	2.29132	4.50
48.2133	159.66	0.3070	2.19166	3.71
49.6097	443.69	0.0768	2.13371	10.30
53.3827	103.14	0.6140	1.99284	2.39
54.6583	183.32	0.3582	1.94979	4.26
56.1103	111.98	0.6140	1.90328	2.60
58.6456	78.82	0.6140	1.82785	1.83
64.3679	157.38	0.5117	1.68060	3.65
74.4538	95.51	0.4093	1.47966	2.22
78.0044	71.26	0.3070	1.42235	1.65



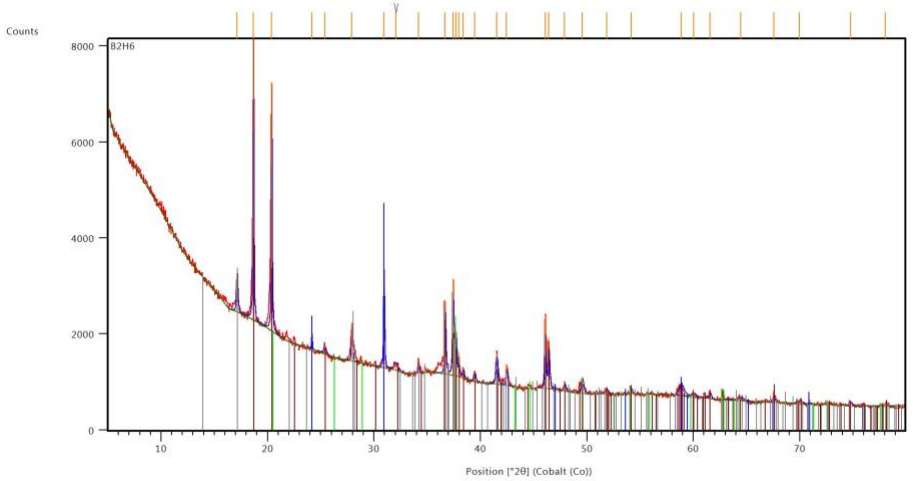
B2H6

Pattern List

Ref.Code	Mineral Name	SemiQuant[%]	Score	Compound Name	Scale Fac.	Chem. Formula
04-007-9911	Quartz	33	41	Silicon Oxide	0.419	Si O2
01-083-5738		16	27	Calcium Magnesium ..	0.153	Ca Mg (C O3)2
01-080-8572		29	22	Copper Carbonate H..	0.186	Cu2 (C O3) (O H..
04-010-1616	Atacamite	23	46	Copper Chloride Hy..	0.209	Cu2 Cl (O H)3

Peak List

Pos.[°2θ]	Height [cts]	FWHMLeft[°2θ]	d-spacing [Å]	Rel. Int. [%]
17.1504	811.43	0.1535	6.00341	13.79
18.6685	5885.85	0.1023	5.51904	100.00
20.3839	5156.49	0.1023	5.05890	87.61
24.1642	352.39	0.0768	4.27663	5.99
25.3905	146.08	0.3070	4.07322	2.48
27.9163	754.25	0.1279	3.71104	12.81
30.9400	2052.12	0.1023	3.35599	34.87
32.0516	146.00	0.4093	3.24248	2.48
34.1712	320.38	0.0768	3.04681	5.44
36.6732	1538.44	0.1279	2.84538	26.14
37.4360	2011.85	0.1279	2.78942	34.18
37.7077	951.21	0.1023	2.77004	16.16
37.9613	511.17	0.0768	2.75221	8.68
38.3812	209.89	0.1535	2.72322	3.57
39.4634	195.27	0.2047	2.65139	3.32
41.5276	643.38	0.1791	2.52500	10.93
42.4418	432.84	0.1279	2.47304	7.35
46.0758	1520.61	0.1023	2.28740	25.83
46.4021	1077.24	0.1279	2.27220	18.30
47.9005	175.92	0.2047	2.20512	2.99
49.5807	321.42	0.2047	2.13488	5.46
51.8724	87.46	0.3070	2.04667	1.49
54.1473	151.71	0.1535	1.96678	2.58
58.8736	216.09	0.5117	1.82140	3.67
60.0263	81.52	0.3070	1.78959	1.38
61.5661	142.72	0.1535	1.74907	2.42
64.4382	66.43	0.6140	1.67896	1.13
67.5628	255.07	0.0768	1.60991	4.33
69.9758	56.56	0.6140	1.56112	0.96
74.7733	82.09	0.3070	1.47425	1.39
78.0304	46.49	0.6140	1.42195	0.79



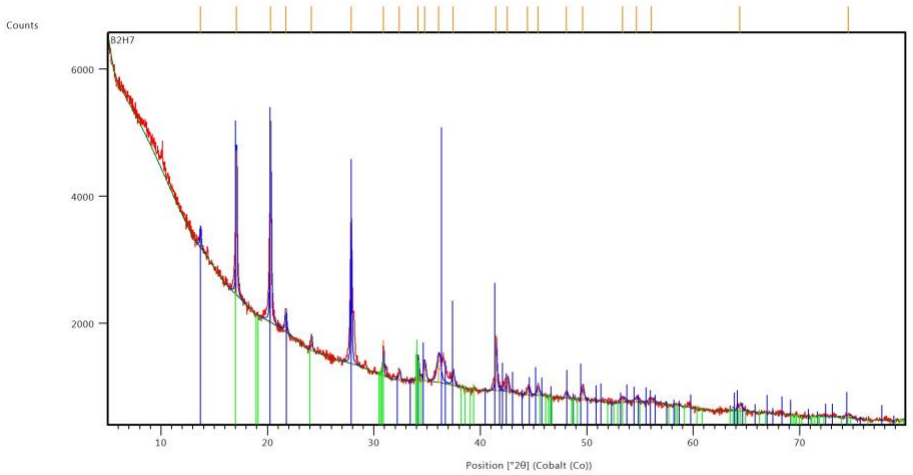
B2H7

Pattern List

Ref.Code	Mineral Name	SemiQuant[%]	Score	Compound Name	Scale Fac.	Chem. Formula
00-056-0001	Malachite	75	33	Copper Carbonate H..	0.610	Cu2 +2 (C O3) (..
04-015-7160		25	20	Silicon Oxide	0.098	Si O2

Peak List

Pos.[°2θ]	Height [cts]	FWHMLeft[°2θ]	d-spacing [Å]	Rel. Int. [%]
13.7062	326.56	0.1535	7.50188	10.31
17.0857	2273.61	0.1279	6.02596	71.77
20.2928	3167.90	0.1279	5.08136	100.00
21.7143	351.11	0.2047	4.75233	11.08
24.1314	247.77	0.1535	4.28235	7.82
27.8538	2268.42	0.1279	3.71921	71.61
30.8849	556.79	0.1023	3.36182	17.58
32.3940	161.95	0.2047	3.20912	5.11
34.1510	334.20	0.2047	3.04856	10.55
34.7595	306.64	0.2558	2.99680	9.68
36.0926	433.26	0.4093	2.88959	13.68
37.4278	254.70	0.2047	2.79000	8.04
41.4460	844.16	0.1535	2.52975	26.65
42.5474	236.96	0.2558	2.46718	7.48
44.4320	102.78	0.3582	2.36751	3.24
45.4016	168.34	0.2047	2.31954	5.31
48.0667	104.65	0.3070	2.19794	3.30
49.5963	217.98	0.2558	2.13425	6.88
53.3647	73.38	0.6140	1.99347	2.32
54.6669	67.66	0.6140	1.94951	2.14
56.0519	58.36	0.6140	1.90510	1.84
64.3550	93.41	0.5117	1.68090	2.95
74.5562	55.24	0.6140	1.47792	1.74



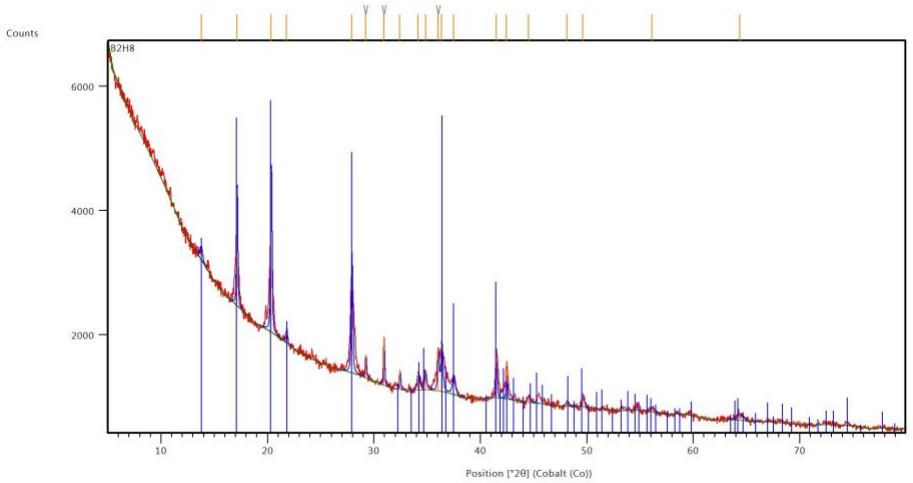
B2H8

Pattern List

Ref.Code	Mineral Name	SemiQuant[%]	Score	Compound Name	Scale Fac.	Chem. Formula
00-056-0001	Malachite	100	38	Copper Carbonate H..	0.659	Cu2 +2 (C O3) (..

Peak List

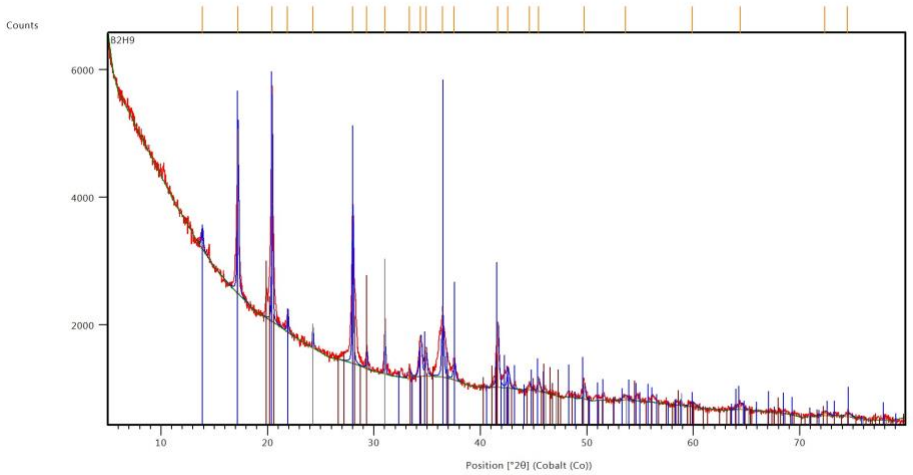
Pos.[°2θ]	Height [cts]	FWHMLeft[°2θ]	d-spacing [Å]	Rel. Int. [%]
13.7764	203.31	0.3070	7.46382	7.77
17.1444	1888.25	0.1279	6.00549	72.19
20.3456	2615.69	0.1535	5.06831	100.00
21.7907	242.60	0.1535	4.73588	9.27
27.9191	1956.88	0.1535	3.71069	74.81
29.2335	365.42	0.1279	3.54724	13.97
30.9363	781.61	0.1023	3.35637	29.88
32.4287	320.35	0.1279	3.20577	12.25
34.1557	270.60	0.2558	3.04815	10.35
34.8423	283.99	0.2047	2.98990	10.86
36.0305	646.72	0.1535	2.89441	24.72
36.3624	758.73	0.2047	2.86887	29.01
37.4877	288.19	0.3070	2.78570	11.02
41.4731	708.27	0.1279	2.52817	27.08
42.4406	499.03	0.1023	2.47311	19.08
44.5316	94.01	0.3070	2.36248	3.59
48.1334	89.47	0.3070	2.19508	3.42
49.6257	207.86	0.2047	2.13307	7.95
56.1205	66.60	0.6140	1.90296	2.55
64.3712	101.70	0.6140	1.68052	3.89



B2H9

Pattern List

Ref.Code	Mineral Name	SemiQuant[%]	Score	Compound Name	Scale Fac.	Chem. Formula
00-056-0001	Malachite	66	39	Copper Carbonate H..	0.708	Cu2 +2 (C O3) (..
01-070-3755	Quartz	15	25	Silicon Oxide	0.274	Si O2
04-013-7672	Azurite	19	13	Copper Carbonate H..	0.222	Cu3 (C O3)2 (O ..



Peak List

Pos.[°2θ]	Height [cts]	FWHMLeft[°2θ]	d-spacing [Å]	Rel. Int. [%]
13.8840	314.70	0.2047	7.40624	8.47
17.2210	2584.75	0.1535	5.97900	69.53
20.4379	3717.27	0.1023	5.04568	100.00
21.8894	359.66	0.1535	4.71477	9.68
24.2656	340.56	0.0768	4.25901	9.16
28.0016	2642.96	0.1279	3.69997	71.10
29.3243	385.79	0.1023	3.53649	10.38
31.0258	875.19	0.0768	3.34692	23.54
33.3351	130.81	0.3070	3.12098	3.52
34.3767	613.75	0.2558	3.02914	16.51
34.9050	431.59	0.1535	2.98469	11.61
36.4462	1030.38	0.2047	2.86249	27.72
37.5356	311.49	0.2047	2.78228	8.38
41.6135	1032.88	0.2303	2.52002	27.79
42.5924	326.86	0.2047	2.46470	8.79
44.6017	99.72	0.4093	2.35896	2.68
45.4734	213.29	0.2047	2.31607	5.74
49.7287	293.88	0.1535	2.12893	7.91
53.6284	74.23	0.6140	1.98439	2.00
59.9029	72.03	0.6140	1.79294	1.94
64.3919	99.40	0.6140	1.68004	2.67
72.3477	66.28	0.6140	1.51660	1.78
74.4781	56.49	0.6140	1.47925	1.52

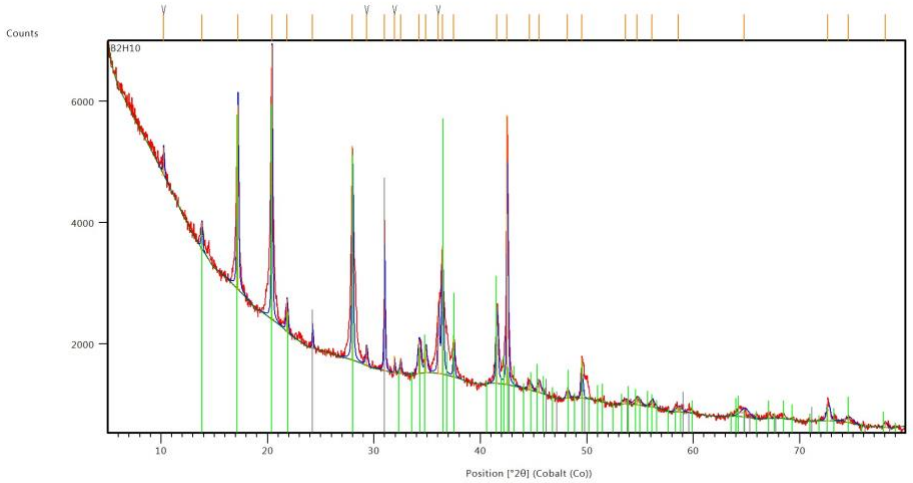
B2H10

Pattern List

Ref.Code	Mineral Name	SemiQuant[%]	Score	Compound Name	Scale Fac.	Chem. Formula
00-056-0001	Malachite	70	44	Copper Carbonate H..	0.601	Cu2 +2 (C O3) (..
04-008-7653		30	31	Silicon Oxide	0.454	Si O2

Peak List

Pos. [°2θ]	Height [cts]	FWHM Left [°2θ]	d-spacing [Å]	Rel. Int. [%]
10.2404	448.81	0.1535	10.03024	9.93
13.8415	435.76	0.1535	7.42888	9.64
17.2117	3037.28	0.1791	5.98219	67.21
20.4171	4519.17	0.1279	5.05076	100.00
21.8305	538.12	0.1791	4.72734	11.91
24.2262	421.39	0.1023	4.26584	9.32
27.9777	3528.53	0.1535	3.70306	78.08
29.3054	327.18	0.2047	3.53873	7.24
30.9942	2452.99	0.1023	3.35026	54.28
31.9392	280.47	0.0768	3.25360	6.21
32.5096	237.85	0.1535	3.19801	5.26
34.2489	558.73	0.3070	3.04011	12.36
34.8783	442.94	0.2047	2.98690	9.80
36.0551	1164.77	0.1535	2.89250	25.77
36.4227	2107.33	0.1791	2.86428	46.63
37.4930	682.03	0.1279	2.78533	15.09
41.5455	1261.93	0.2047	2.52396	27.92
42.5063	4442.04	0.1279	2.46946	98.29
44.6226	142.24	0.4093	2.35791	3.15
45.5158	201.38	0.3070	2.31403	4.46
48.1840	139.28	0.3070	2.19291	3.08
49.5099	667.85	0.1279	2.13774	14.78
53.6188	74.17	0.6140	1.98471	1.64
54.7188	120.39	0.6140	1.94780	2.66
56.1129	125.87	0.4093	1.90320	2.79
58.5993	91.10	0.6140	1.82917	2.02
64.7758	137.86	0.9210	1.67116	3.05
72.6329	343.04	0.3070	1.51146	7.59
74.5618	87.96	0.8187	1.47783	1.95
78.0219	99.00	0.3070	1.42208	2.19



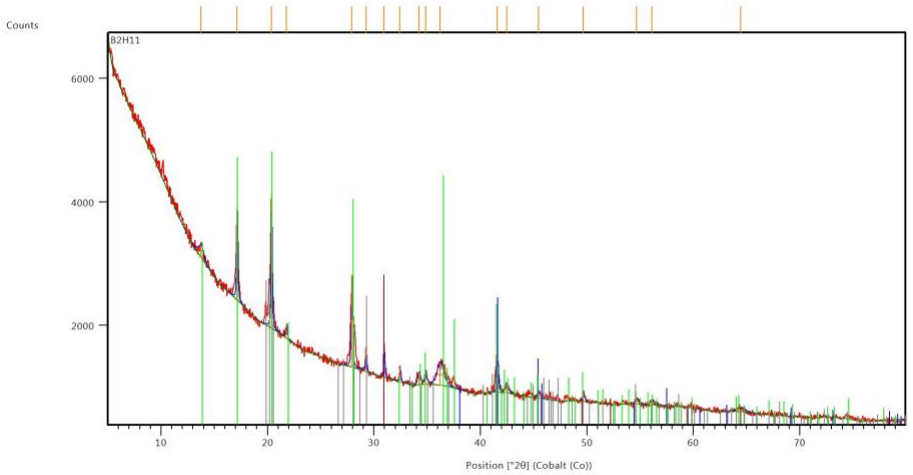
B2H11

Pattern List

Ref.Code	Mineral Name	SemiQuant[%]	Score	Compound Name	Scale Fac.	Chem. Formula
03-065-2309	Tenorite, syn	10	19	Copper Oxide	0.228	Cu O
00-056-0001	Malachite	63	28	Copper Carbonate H..	0.504	Cu2 +2 (C O3) (..
01-070-1579	Azurite	21	Unmatch	Copper Hydroxide C..	0.182	Cu3 (O H)2 (C O..
00-041-1487	Graphite-2H	7	29	Carbon	0.246	C

Peak List

Pos.[°2θ]	Height [cts]	FWHMLeft[°2θ]	d-spacing [Å]	Rel. Int. [%]
13.7702	184.18	0.6140	7.46714	8.46
17.1502	1502.27	0.1279	6.00350	68.97
20.3716	2178.04	0.1279	5.06192	100.00
21.7857	222.89	0.1535	4.73694	10.23
27.9172	1493.17	0.1535	3.71093	68.56
29.2584	372.09	0.1279	3.54429	17.08
30.9455	547.86	0.1023	3.35540	25.15
32.4427	210.66	0.1535	3.20443	9.67
34.2390	188.53	0.3070	3.04096	8.66
34.8473	209.91	0.2047	2.98948	9.64
36.2197	343.68	0.7164	2.87979	15.78
41.5958	618.25	0.1535	2.52104	28.39
42.4841	154.98	0.3070	2.47069	7.12
45.4773	112.71	0.3070	2.31588	5.17
49.6605	144.28	0.2047	2.13166	6.62
54.6684	102.56	0.3070	1.94946	4.71
56.1090	72.36	0.6140	1.90332	3.32
64.4600	65.29	0.8187	1.67846	3.00



IRAQ

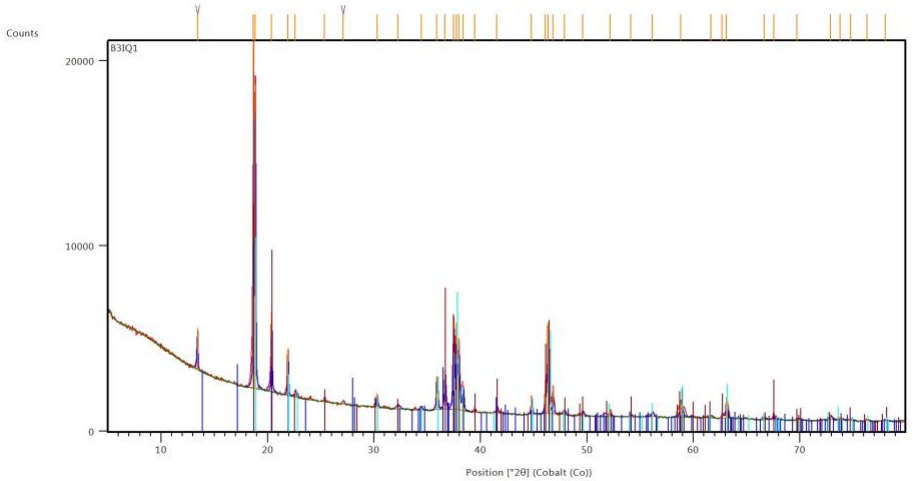
IQ1

Pattern List

Ref.Code	Mineral Name	SemiQuant[%]	Score	Compound Name	Scale Fac.	Chem. Formula
04-013-7662	Malachite	18	9	Copper Carbonate H..	0.108	Cu2 (C O3) (O H..
04-010-1616	Atacamite	55	39	Copper Chloride Hy..	0.471	Cu2 Cl (O H)3
04-012-5828	Paratacamite	26	31	Copper Chloride Hy..	0.387	Cu2 Cl (O H)3

Peak List

Pos.[°2θ]	Height [cts]	FWHMLeft[°2θ]	d-spacing [Å]	Rel. Int. [%]
13.4110	2254.86	0.1023	7.66623	12.04
18.6785	18729.83	0.0768	5.51611	100.00
18.8575	16404.15	0.0768	5.46423	87.58
20.3834	4249.36	0.1023	5.05902	22.69
21.9122	2527.64	0.1023	4.70993	13.50
22.6065	412.66	0.1535	4.56707	2.20
25.3613	275.43	0.1535	4.07783	1.47
27.1142	206.18	0.2047	3.81868	1.10
30.3000	695.92	0.1279	3.42515	3.72
32.2460	217.36	0.4093	3.22345	1.16
34.4489	200.20	0.2047	3.02299	1.07
35.8981	1790.89	0.1279	2.90473	9.56
36.6609	2112.49	0.1535	2.84630	11.28
37.4779	4899.50	0.1279	2.78641	26.16
37.7558	4696.07	0.0768	2.76664	25.07
37.9778	3810.46	0.1279	2.75106	20.34
38.3589	1568.88	0.1279	2.72474	8.38
39.4540	331.13	0.0768	2.65200	1.77
41.5497	448.68	0.1023	2.52372	2.40
44.7942	1010.39	0.0768	2.34934	5.39
46.1115	1827.29	0.0768	2.28573	9.76
46.3412	4909.77	0.1279	2.27502	26.21
46.8052	1570.21	0.0768	2.25372	8.38
47.8823	288.94	0.1791	2.20591	1.54
49.6326	264.70	0.2047	2.13279	1.41
52.1923	378.88	0.0768	2.03500	2.02
54.1160	164.89	0.1535	1.96783	0.88
56.1653	268.54	0.2047	1.90157	1.43
58.8281	873.39	0.2558	1.82269	4.66
61.6374	138.53	0.3070	1.74724	0.74
62.7013	266.32	0.1535	1.72054	1.42
63.1070	1124.43	0.1279	1.71061	6.00
66.6651	178.14	0.2047	1.62904	0.95
67.5484	386.54	0.0768	1.61022	2.06
69.7504	85.30	0.7164	1.56553	0.46
72.8927	236.63	0.2558	1.50681	1.26
73.7928	74.74	0.4093	1.49100	0.40
74.7985	87.96	0.4093	1.47383	0.47
76.3201	86.26	0.3070	1.44880	0.46
78.0169	71.89	0.6140	1.42215	0.38



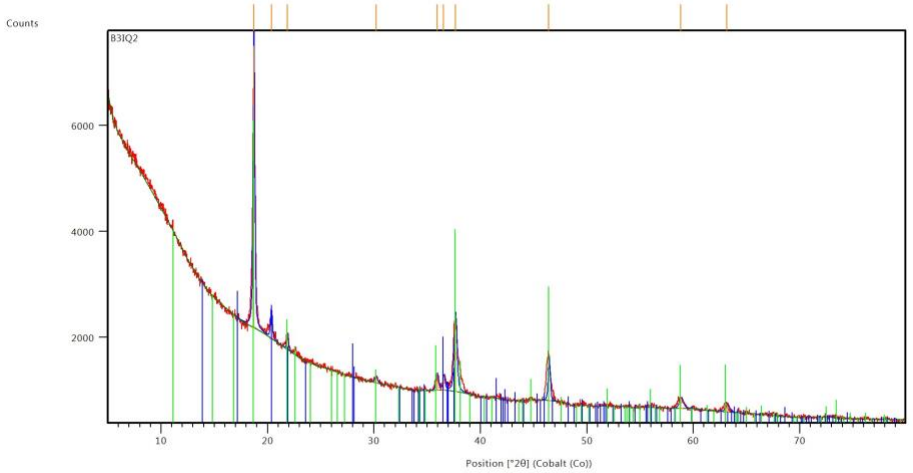
IQ2

Pattern List

Ref.Code	Mineral Name	SemiQuant[%]	Score	Compound Name	Scale Fac.	Chem. Formula
01-072-8421	Malachite	40	7	Copper Carbonate H..	0.130	Cu2 (O H)2 (C O..
04-011-3123	Paratacamite	60	52	Copper Chloride Hy..	0.501	Cu2 Cl (O H)3

Peak List

Pos.[°2θ]	Height [cts]	FWHM Left[°2θ]	d-spacing [Å]	Rel. Int. [%]
18.7104	5319.76	0.1791	5.50678	100.00
20.3625	499.70	0.2047	5.06416	9.39
21.8658	321.32	0.1535	4.71980	6.04
30.2027	120.75	0.3070	3.43592	2.27
35.9342	315.82	0.2558	2.90191	5.94
36.5511	275.47	0.2047	2.85456	5.18
37.6439	1442.35	0.2814	2.77457	27.11
46.4246	901.11	0.1791	2.27116	16.94
58.8297	203.94	0.4093	1.82264	3.83
63.1598	146.21	0.4093	1.70933	2.75



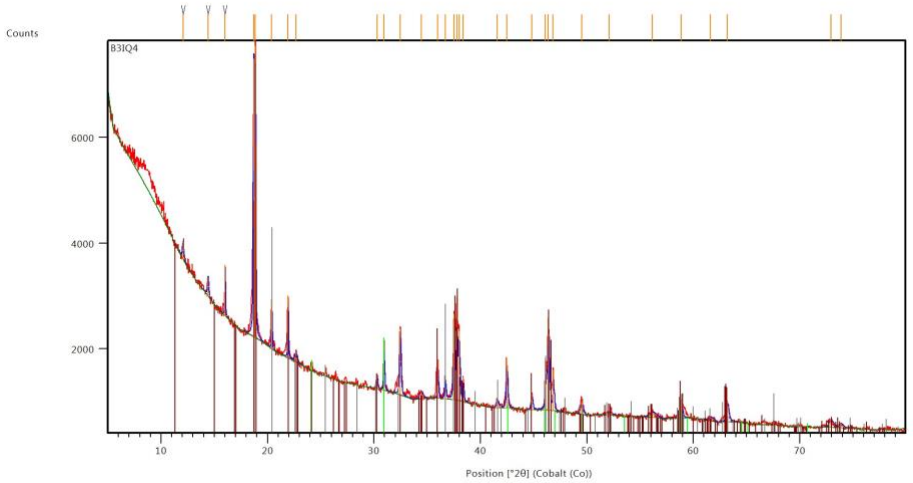
IQ4

Pattern List

Ref.Code	Mineral Name	SemiQuant[%]	Score	Compound Name	Scale Fac.	Chem. Formula
01-075-8320	Quartz	7	21	Silicon Oxide	0.127	Si O2
01-080-9252	Atacamite	28	30	Copper Chloride Hy..	0.402	Cu2 Cl (O H)3
04-016-8161	Anatacamite	64	47	Copper Chloride Hy..	0.467	Cu2 Cl (O H)3

Peak List

Pos.[°2θ]	Height [cts]	FWHMLeft[°2θ]	d-spacing [Å]	Rel. Int. [%]
12.0629	323.81	0.1535	8.51922	5.86
14.4180	358.22	0.1535	7.13329	6.48
16.0204	967.37	0.0768	6.42380	17.50
18.6946	5258.88	0.1023	5.51140	95.14
18.8587	5527.76	0.0768	5.46388	100.00
20.3976	931.64	0.0768	5.05553	16.85
21.9320	1179.04	0.0768	4.70572	21.33
22.6820	164.46	0.3070	4.55207	2.98
30.2917	287.79	0.1279	3.42607	5.21
30.9511	907.31	0.0768	3.35481	16.41
32.4502	1248.17	0.1535	3.20371	22.58
34.4471	127.72	0.4093	3.02314	2.31
35.9956	736.68	0.0768	2.89712	13.33
36.6970	394.09	0.1279	2.84360	7.13
37.5060	1627.06	0.1279	2.78440	29.43
37.7725	1951.77	0.1023	2.76546	35.31
37.9968	1310.47	0.1279	2.74973	23.71
38.3886	460.12	0.0768	2.72271	8.32
41.5945	133.51	0.3070	2.52112	2.42
42.4642	946.42	0.1279	2.47180	17.12
44.8169	300.82	0.1535	2.34821	5.44
46.1092	968.28	0.0768	2.28584	17.52
46.3714	1751.17	0.1791	2.27362	31.68
46.8328	780.47	0.1023	2.25247	14.12
49.5183	232.89	0.2558	2.13740	4.21
52.0832	50.66	0.6140	2.03896	0.92
56.1621	94.20	0.8187	1.90167	1.70
58.8428	354.04	0.2047	1.82227	6.40
61.6297	68.11	0.6140	1.74744	1.23
63.1779	378.25	0.2558	1.70889	6.84
72.9275	136.90	0.4093	1.50620	2.48
73.8776	75.63	0.4093	1.48953	1.37



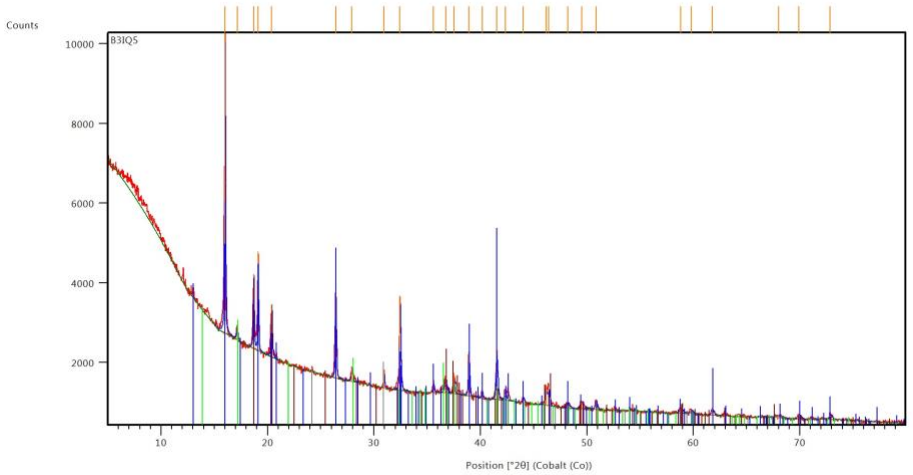
IQ5

Pattern List

Ref.Code	Mineral Name	SemiQuant[%]	Score	Compound Name	Scale Fac.	Chem. Formula
04-011-4170	Brochantite	74	38	Copper Sulfate Hyd..	0.418	Cu4 (S O4) (O H..
00-056-0001	Malachite	8	14	Copper Carbonate H..	0.073	Cu2 +2 (C O3) (..
01-070-7345	Quartz	4	21	Silicon Oxide	0.064	Si O2
01-071-2027	Atacamite	14	21	Copper Chloride Hy..	0.172	Cu2 Cl (O H)3

Peak List

Pos.[°2θ]	Height [cts]	FWHMLeft[°2θ]	d-spacing [Å]	Rel. Int. [%]
16.0122	7569.61	0.1023	6.42708	100.00
17.1552	361.04	0.1279	6.00175	4.77
18.6963	1864.67	0.1023	5.51090	24.63
19.1243	2486.34	0.0768	5.38867	32.85
20.3907	1311.64	0.1279	5.05723	17.33
26.4146	2251.36	0.1023	3.91795	29.74
27.9272	340.63	0.1535	3.70963	4.50
30.9518	455.11	0.0768	3.35473	6.01
32.4465	2373.33	0.1279	3.20406	31.35
35.6021	303.66	0.1023	2.92809	4.01
36.7377	412.46	0.1791	2.84056	5.45
37.5012	515.82	0.1023	2.78474	6.81
38.9093	1108.87	0.1279	2.68766	14.65
40.1700	198.89	0.1535	2.60663	2.63
41.5403	1235.15	0.1535	2.52426	16.32
42.3344	269.13	0.1535	2.47903	3.56
44.0311	135.29	0.2047	2.38798	1.79
46.1640	519.27	0.1279	2.28327	6.86
46.4253	460.31	0.1535	2.27113	6.08
48.2255	137.36	0.3070	2.19114	1.81
49.5220	160.30	0.4093	2.13725	2.12
50.8677	224.16	0.2047	2.08433	2.96
58.8158	136.52	0.3070	1.82304	1.80
59.8041	86.76	0.3070	1.79563	1.15
61.7780	164.32	0.2558	1.74366	2.17
68.0055	44.41	0.8187	1.60068	0.59
69.9223	112.27	0.4093	1.56217	1.48
72.8655	154.64	0.2047	1.50730	2.04



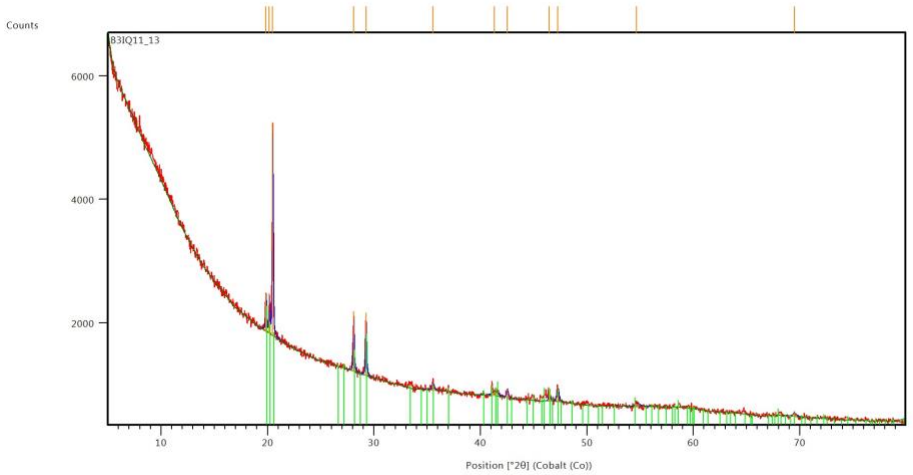
IQ11-13

Pattern List

Ref.Code	Mineral Name	SemiQuant[%]	Score	Compound Name	Scale Fac.	Chem. Formula
04-013-7672	Azurite	100	10	Copper Carbonate H..	0.101	Cu3 (C O3)2 (O ..

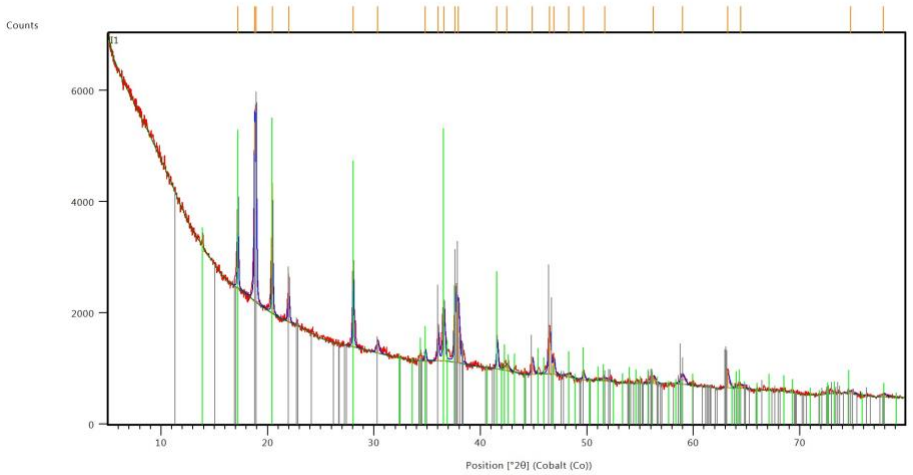
Peak List

Pos.[°2θ]	Height [cts]	FWHMLeft[°2θ]	d-spacing [Å]	Rel. Int. [%]
19.8417	602.39	0.1023	5.19570	17.48
20.1523	641.72	0.0768	5.11642	18.62
20.4855	3445.71	0.1023	5.03407	100.00
28.0870	967.84	0.1023	3.68895	28.09
29.2470	1019.46	0.1023	3.54564	29.59
35.5196	93.63	0.3070	2.93466	2.72
41.3217	72.17	0.6140	2.53703	2.09
42.5075	128.17	0.2047	2.46939	3.72
46.4412	161.87	0.1535	2.27039	4.70
47.2549	234.07	0.2047	2.23348	6.79
54.6620	44.62	0.6140	1.94967	1.29
69.5011	46.06	0.4093	1.57043	1.34



ISRAEL

I1



Pattern List

Ref.Code	Mineral Name	SemiQuant[%]	Score	Compound Name	Scale Fac.	Chem. Formula
00-056-0001	Malachite	43	42	Copper Carbonate H..	0.594	Cu2 +2 (C O3) (..
04-016-8161	Anatacamite	57	41	Copper Chloride Hy..	0.537	Cu2 Cl (O H)3

Peak List

Pos.[°2θ]	Height [cts]	FWHMLeft[°2θ]	d-spacing [Å]	Rel. Int. [%]
17.2200	1673.07	0.1023	5.97932	46.41
18.7946	3224.02	0.1279	5.48234	89.44
18.9388	3604.58	0.0768	5.44098	100.00
20.4488	2347.09	0.1023	5.04300	65.11
21.9845	863.16	0.1279	4.69462	23.95
28.0537	1581.02	0.1023	3.69323	43.86
30.3534	204.62	0.3070	3.41927	5.68
34.8187	224.74	0.1791	2.99186	6.23
36.0136	664.26	0.1279	2.89572	18.43
36.5579	1110.36	0.1791	2.85405	30.80
37.6132	1345.69	0.1279	2.77674	37.33
37.9124	1105.03	0.2558	2.75563	30.66
41.5554	646.73	0.1279	2.52339	17.94
42.4943	106.16	0.5117	2.47013	2.95
44.8807	316.26	0.2047	2.34505	8.77
46.4844	853.99	0.2303	2.26840	23.69
46.8825	352.91	0.1535	2.25021	9.79
48.2812	58.74	0.6140	2.18876	1.63
49.6800	156.70	0.2047	2.13088	4.35
51.6940	51.44	0.8187	2.05325	1.43
56.2538	130.35	0.4093	1.89882	3.62
58.9739	182.11	0.4093	1.81858	5.05
63.2551	312.92	0.2047	1.70702	8.68
64.4575	63.30	0.6140	1.67851	1.76
74.7832	50.59	0.6140	1.47409	1.40
77.8706	52.47	0.6140	1.42440	1.46

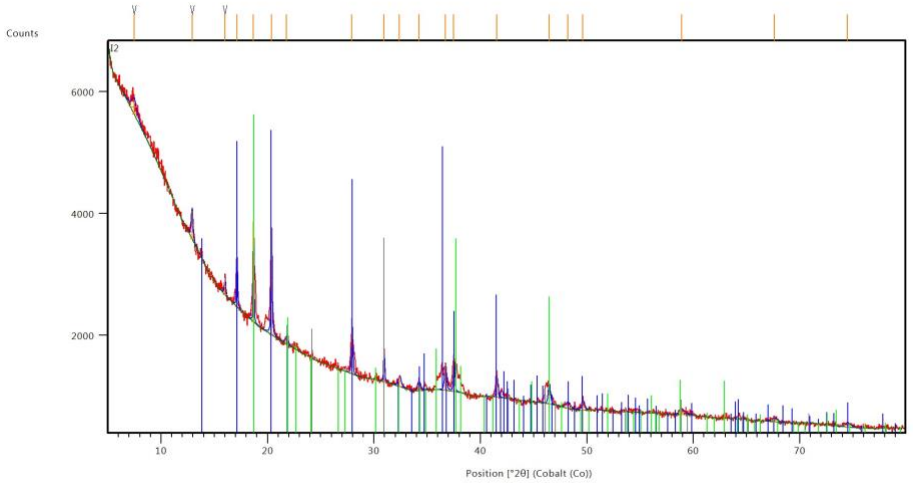
I2

Pattern List

Ref.Code	Mineral Name	SemiQuant[%]	Score	Compound Name	Scale Fac.	Chem. Formula
00-056-0001	Malachite	50	30	Copper Carbonate H..	0.584	Cu2 +2 (C O3) (..
01-078-7708	Clinoatacamite	32	24	Copper Hydroxide C..	0.498	Cu2 (O H)3 Cl
04-016-2085	Quartz	18	20	Silicon Oxide	0.345	Si O2

Peak List

Pos.[°2θ]	Height [cts]	FWHMLeft[°2θ]	d-spacing [Å]	Rel. Int. [%]
7.4742	242.54	0.6140	13.73379	13.76
12.9149	470.16	0.2047	7.95937	26.68
16.0070	279.09	0.1535	6.42914	15.83
17.1237	839.82	0.1023	6.01272	47.65
18.6800	1645.16	0.0768	5.51568	93.34
20.3698	1762.49	0.1279	5.06236	100.00
21.7964	129.16	0.3070	4.73464	7.33
27.9256	909.98	0.1279	3.70983	51.63
30.9454	518.53	0.1023	3.35541	29.42
32.3940	171.07	0.3070	3.20912	9.71
34.2284	145.15	0.3070	3.04187	8.24
36.6992	426.14	0.2047	2.84343	24.18
37.4947	599.73	0.1279	2.78520	34.03
41.5396	439.58	0.1279	2.52430	24.94
46.4366	342.55	0.2047	2.27061	19.44
48.1997	95.45	0.5117	2.19224	5.42
49.6232	146.78	0.3070	2.13317	8.33
58.9007	79.14	0.6140	1.82064	4.49
67.6020	62.38	0.6140	1.60909	3.54
74.4768	62.83	0.6140	1.47927	3.56



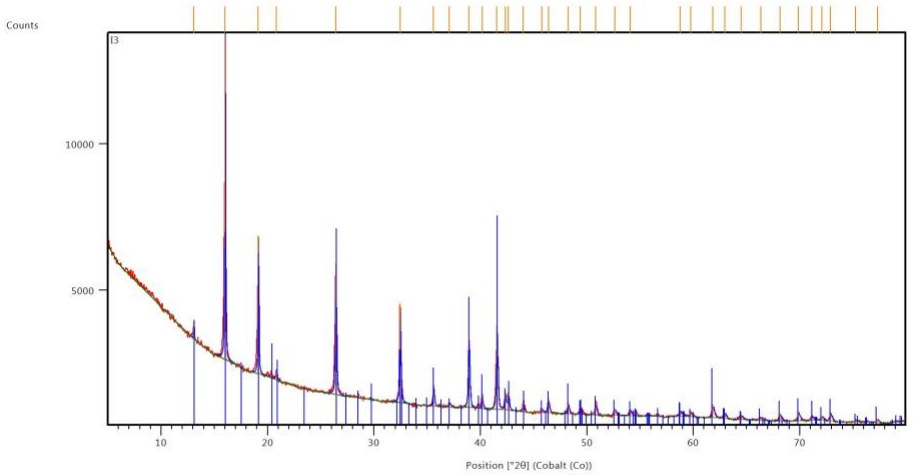
I3

Pattern List

Ref.Code	Mineral Name	SemiQuant[%]	Score	Compound Name	Scale Fac.	Chem. Formula
04-013-5988	Brochantite-MDO1	100	52	Copper Sulfate Hyd..	0.479	Cu4 (S O4) (O H..

Peak List

Pos.[°2θ]	Height [cts]	FWHMLeft[°2θ]	d-spacing [Å]	Rel. Int. [%]
13.0823	589.17	0.0768	7.85793	5.32
16.0214	11069.66	0.1023	6.42340	100.00
19.1364	4713.81	0.1023	5.38530	42.58
20.8424	327.32	0.1535	4.94880	2.96
26.4161	4473.89	0.1279	3.91773	40.42
32.4535	3400.73	0.1279	3.20339	30.72
35.6027	701.12	0.1279	2.92804	6.33
37.0900	128.83	0.3070	2.81451	1.16
38.9193	2338.68	0.1535	2.68700	21.13
40.1696	534.13	0.1023	2.60666	4.83
41.5467	2865.57	0.1535	2.52389	25.89
42.3266	637.71	0.1023	2.47946	5.76
42.6105	626.90	0.1535	2.46370	5.66
44.0359	386.68	0.0768	2.38773	3.49
45.7787	122.51	0.1535	2.30145	1.11
46.3941	478.67	0.1535	2.27257	4.32
48.2423	399.60	0.1279	2.19042	3.61
49.3681	334.69	0.0768	2.14349	3.02
50.8374	515.96	0.1023	2.08549	4.66
52.6178	204.34	0.2558	2.01970	1.85
54.0873	198.26	0.2047	1.96880	1.79
58.7583	155.51	0.4093	1.82466	1.40
59.7687	163.78	0.1535	1.79659	1.48
61.8415	408.84	0.2047	1.74204	3.69
62.9730	193.75	0.2047	1.71388	1.75
64.4810	130.79	0.4093	1.67797	1.18
66.3636	81.34	0.6140	1.63559	0.73
68.1651	205.07	0.2558	1.59739	1.85
69.8878	294.27	0.2047	1.56284	2.66
71.1432	152.39	0.2558	1.53880	1.38
72.0806	140.36	0.2558	1.52145	1.27
72.8888	253.27	0.2558	1.50688	2.29
75.2361	63.70	0.4093	1.46652	0.58
77.2900	120.10	0.2558	1.43341	1.08



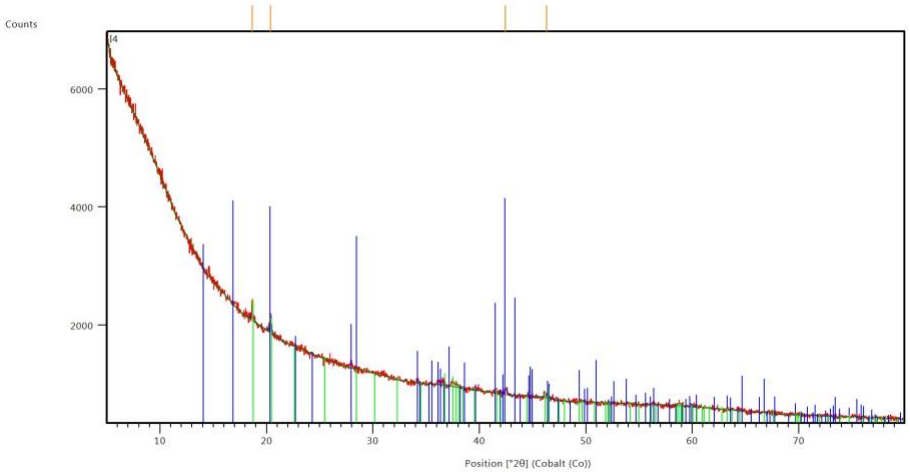
I4

Pattern List

Ref.Code	Mineral Name	SemiQuant[%]	Score	Compound Name	Scale Fac.	Chem. Formula
04-020-9522		94	Unmatch	Copper Carbonate H..	0.477	Cu2 (C O3) (O H..
01-080-9252	Atacamite	6	Unmatch	Copper Chloride Hy..	0.051	Cu2 Cl (O H)3

Peak List

Pos.[°2θ]	Height [cts]	FWHMLeft[°2θ]	d-spacing [Å]	Rel. Int. [%]
18.6650	365.84	0.1023	5.52008	100.00
20.3841	309.40	0.1535	5.05884	84.57
42.4613	104.34	0.3070	2.47196	28.52
46.3076	55.45	0.5117	2.27658	15.16



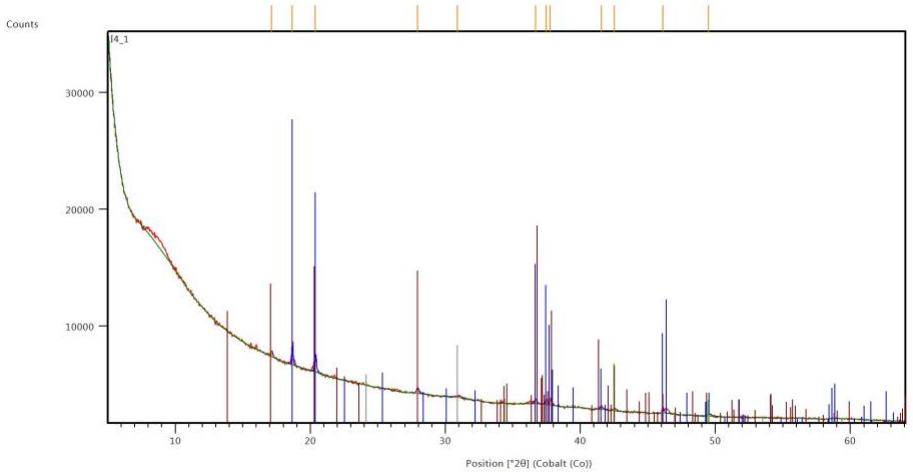
I4 re-run

Pattern List

Ref.Code	Mineral Name	SemiQuant[%]	Score	Compound Name	Scale Fac.	Chem. Formula
01-080-9252	Atacamite	43	29	Copper Chloride Hy..	0.597	Cu2 Cl (O H)3
04-007-9767	Cuprite	2	19	Copper Oxide	0.114	Cu2 O
01-075-8320	Quartz	7	11	Silicon Oxide	0.128	Si O2
04-011-5196	Malachite	47	14	Copper Carbonate H..	0.433	Cu2 (C O3) (O H..

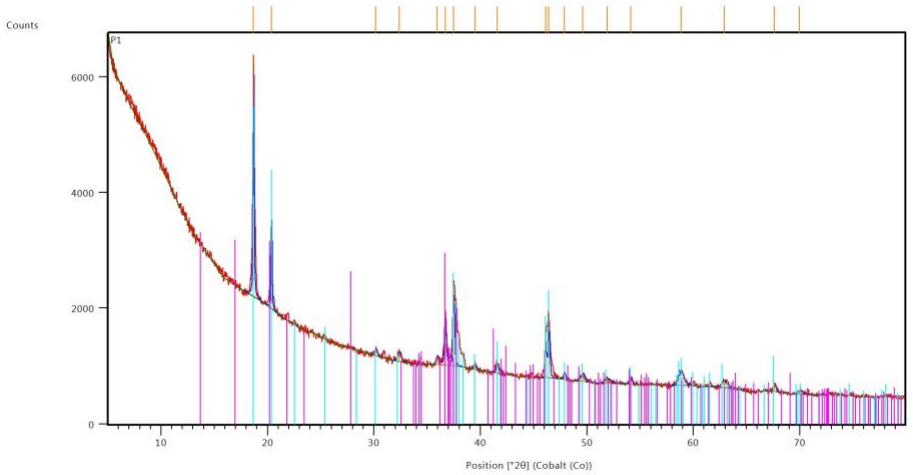
Peak List

Pos.[°2θ]	Height [cts]	FWHMLeft[°2θ]	d-spacing [Å]	Rel. Int. [%]
17.1427	473.04	0.1535	6.00607	23.57
18.6748	2006.88	0.0768	5.51721	100.00
20.3719	1600.17	0.1279	5.06185	79.73
27.9398	466.53	0.2047	3.70799	23.25
30.9043	130.36	0.6140	3.35976	6.50
36.6883	446.07	0.1535	2.84425	22.23
37.4646	469.48	0.1535	2.78736	23.39
37.7716	642.20	0.1023	2.76553	32.00
41.5473	354.85	0.1535	2.52385	17.68
42.5068	177.28	0.3070	2.46944	8.83
46.1105	594.14	0.0768	2.28578	29.61
49.4788	184.37	0.4093	2.13900	9.19



PERU

P1



Pattern List

Ref.Code	Mineral Name	SemiQuant[%]	Score	Compound Name	Scale Fac.	Chem. Formula
01-080-9252	Atacamite	53	51	Copper Chloride Hy..	0.485	Cu2 Cl (O H)3
04-011-5196	Malachite	47	6	Copper Carbonate H..	0.286	Cu2 (C O3) (O H..

Peak List

Pos.[°2θ]	Height [cts]	FWHMLeft[°2θ]	d-spacing [Å]	Rel. Int. [%]
18.6857	4186.58	0.1023	5.51401	100.00
20.3819	1566.56	0.1023	5.05938	37.42
30.1774	121.05	0.3070	3.43874	2.89
32.3899	159.69	0.4093	3.20951	3.81
35.9529	143.73	0.3070	2.90044	3.43
36.6875	968.59	0.1535	2.84431	23.14
37.4846	1433.89	0.1279	2.78593	34.25
39.4846	103.71	0.3070	2.65003	2.48
41.6030	168.77	0.2558	2.52062	4.03
46.1326	802.78	0.1023	2.28475	19.18
46.4060	1157.54	0.1279	2.27202	27.65
47.9149	137.37	0.1535	2.20450	3.28
49.6147	134.72	0.4093	2.13351	3.22
51.9048	79.74	0.6140	2.04549	1.90
54.1220	102.54	0.3070	1.96764	2.45
58.8381	239.24	0.5117	1.82241	5.71
62.9121	117.14	0.6140	1.71537	2.80
67.6152	146.03	0.2047	1.60881	3.49
69.9752	59.96	0.6140	1.56114	1.43

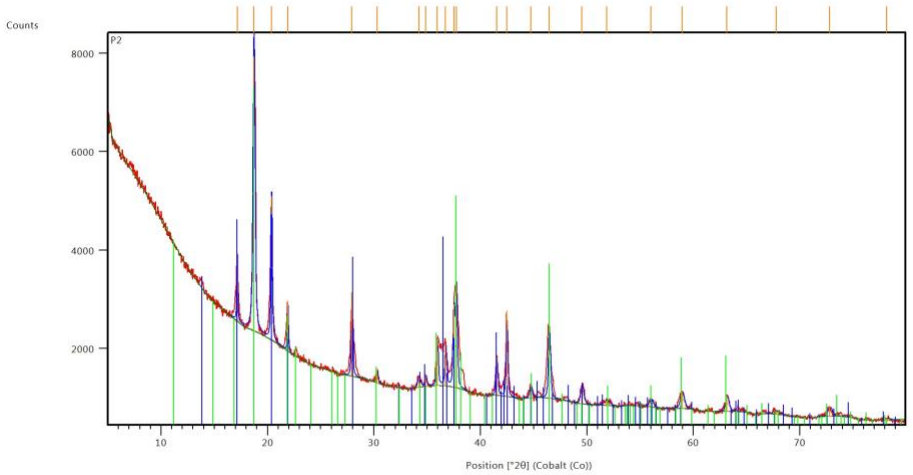
P2

Pattern List

Ref.Code	Mineral Name	SemiQuant[%]	Score	Compound Name	Scale Fac.	Chem. Formula
00-056-0001	Malachite	56	36	Copper Carbonate H..	0.360	Cu2 +2 (C O3) (..
04-011-3123	Paratacamite	44	55	Copper Chloride Hy..	0.589	Cu2 Cl (O H)3

Peak List

Pos. [°2θ]	Height [cts]	FWHM Left [°2θ]	d-spacing [Å]	Rel. Int. [%]
17.1564	1386.71	0.1023	6.00135	24.89
18.7211	5571.03	0.2303	5.50368	100.00
20.3732	2921.74	0.1535	5.06152	52.45
21.8932	1008.21	0.1023	4.71396	18.10
27.9305	1698.46	0.1535	3.70920	30.49
30.3211	261.72	0.1535	3.42282	4.70
34.2285	191.81	0.3070	3.04186	3.44
34.8710	210.82	0.2047	2.98751	3.78
35.9396	931.74	0.1791	2.90148	16.72
36.7265	854.05	0.1791	2.84139	15.33
37.5033	1683.93	0.1791	2.78459	30.23
37.7394	2154.06	0.1535	2.76780	38.67
41.5251	764.97	0.1791	2.52515	13.73
42.4630	1741.94	0.1535	2.47186	31.27
44.7526	221.98	0.3070	2.35141	3.98
46.4569	1471.08	0.2047	2.26967	26.41
49.5306	379.69	0.3070	2.13690	6.82
51.8893	96.87	0.6140	2.04605	1.74
56.0368	152.49	0.4093	1.90557	2.74
58.9452	337.07	0.4093	1.81939	6.05
63.1574	324.70	0.3070	1.70939	5.83
67.7829	71.46	0.6140	1.60531	1.28
72.8003	180.38	0.4605	1.50846	3.24
78.1575	35.24	0.6140	1.42000	0.63



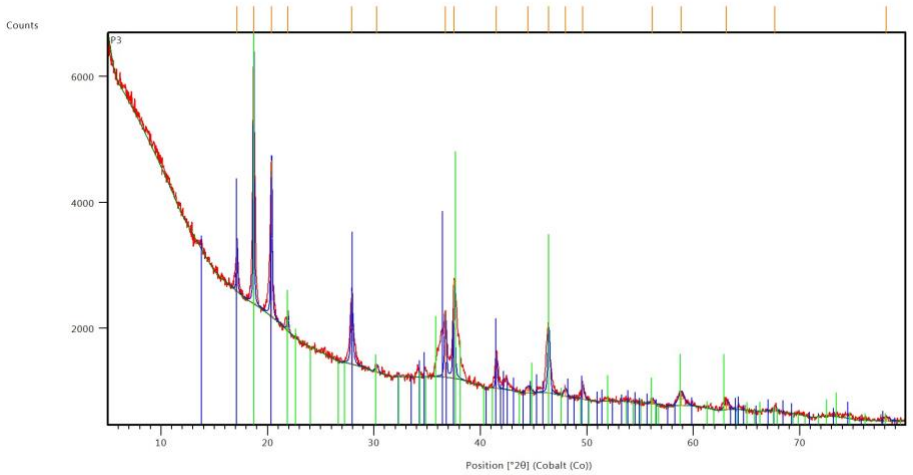
P3

Pattern List

Ref.Code	Mineral Name	SemiQuant[%]	Score	Compound Name	Scale Fac.	Chem. Formula
00-056-0001	Malachite	42	30	Copper Carbonate H..	0.392	Cu2 +2 (C O3) (..
01-078-7708	Clinoatacamite	58	42	Copper Hydroxide C..	0.727	Cu2 (O H)3 Cl

Peak List

Pos. [°2θ]	Height [cts]	FWHM Left [°2θ]	d-spacing [Å]	Rel. Int. [%]
17.1318	825.41	0.1279	6.00987	20.02
18.6923	4123.42	0.1023	5.51207	100.00
20.3696	2477.75	0.1535	5.06240	60.09
21.8984	319.95	0.1535	4.71287	7.76
27.9122	1153.71	0.2303	3.71158	27.98
30.2500	114.71	0.3070	3.43069	2.78
36.6904	1060.72	0.1791	2.84410	25.72
37.5010	1559.88	0.1791	2.78475	37.83
41.4831	559.45	0.1535	2.52759	13.57
44.4593	104.86	0.5117	2.36613	2.54
46.4021	1116.72	0.2047	2.27220	27.08
47.9726	119.03	0.3070	2.20200	2.89
49.6122	253.68	0.2047	2.13361	6.15
56.1410	85.15	0.3070	1.90232	2.07
58.8387	214.03	0.6140	1.82239	5.19
63.1145	136.87	0.5117	1.71043	3.32
67.6575	86.73	0.3070	1.60793	2.10
78.1144	58.41	0.6140	1.42066	1.42



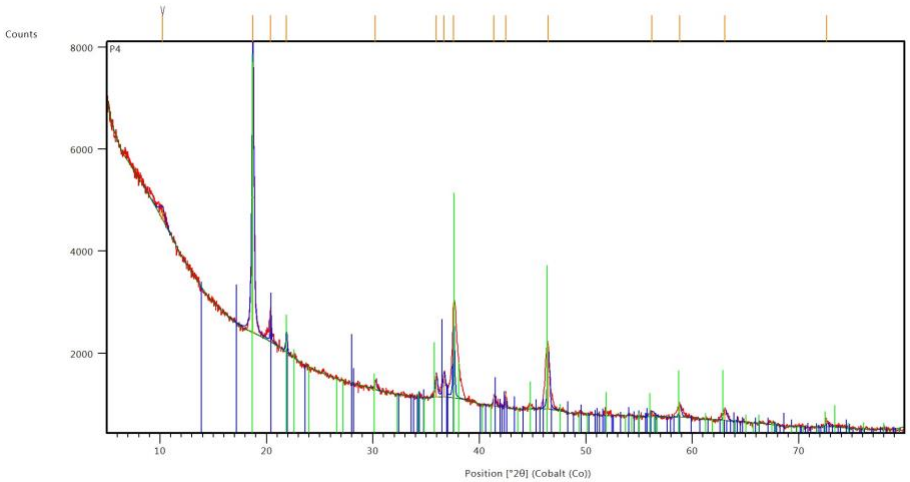
P4

Pattern List

Ref.Code	Mineral Name	SemiQuant[%]	Score	Compound Name	Scale Fac.	Chem. Formula
01-072-8421	Malachite	32	13	Copper Carbonate H..	0.188	Cu2 (O H)2 (C O..
01-078-7708	Clinoatacamite	68	46	Copper Hydroxide C..	0.670	Cu2 (O H)3 Cl

Peak List

Pos.[°2θ]	Height [cts]	FWHM Left[°2θ]	d-spacing [Å]	Rel. Int. [%]
10.2117	223.17	0.6140	10.05832	4.21
18.7113	5300.84	0.2303	5.50652	100.00
20.3834	674.14	0.1023	5.05902	12.72
21.8635	403.19	0.1535	4.72028	7.61
30.2283	166.59	0.2558	3.43309	3.14
35.9432	444.39	0.2047	2.90120	8.38
36.6758	453.70	0.3070	2.84518	8.56
37.5640	1863.16	0.1279	2.78025	35.15
41.3778	203.46	0.2558	2.53374	3.84
42.4616	274.56	0.1023	2.47194	5.18
46.4542	1257.90	0.2047	2.26979	23.73
56.1911	94.89	0.6140	1.90077	1.79
58.8168	273.26	0.2047	1.82300	5.15
63.0517	225.01	0.3070	1.71196	4.24
72.6072	158.04	0.1535	1.51192	2.98



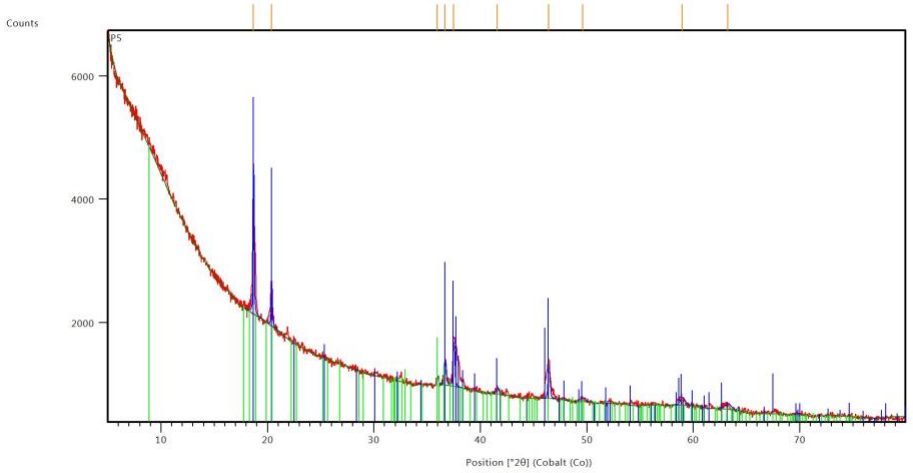
P5

Pattern List

Ref.Code	Mineral Name	SemiQuant[%]	Score	Compound Name	Scale Fac.	Chem. Formula
01-080-9252	Atacamite	57	39	Copper Chloride Hy..	0.520	Cu2 Cl (O H)3
04-021-5194		43	9	Silicon Oxide	0.115	Si O2

Peak List

Pos.[°2θ]	Height [cts]	FWHM Left[°2θ]	d-spacing [Å]	Rel. Int. [%]
18.6866	2445.45	0.1023	5.51373	100.00
20.3924	672.86	0.1279	5.05682	27.51
35.9618	152.63	0.1535	2.89975	6.24
36.6785	425.91	0.1535	2.84498	17.42
37.4875	779.99	0.1535	2.78573	31.90
41.5827	110.64	0.3070	2.52180	4.52
46.4128	649.53	0.1535	2.27170	26.56
49.5894	59.46	0.6140	2.13453	2.43
58.9526	120.11	0.5117	1.81918	4.91
63.2259	88.30	0.6140	1.70773	3.61



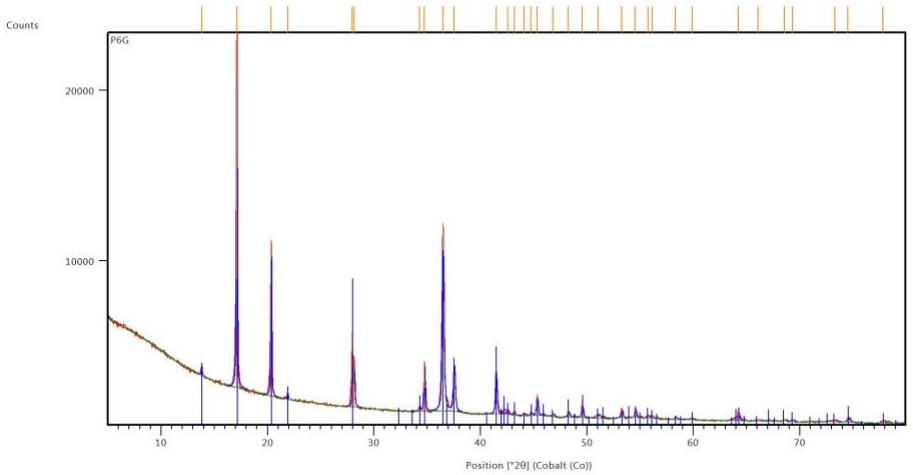
P6g

Pattern List

Ref.Code	Mineral Name	SemiQuant[%]	Score	Compound Name	Scale Fac.	Chem. Formula
00-056-0001	Malachite	100	58	Copper Carbonate H..	0.402	Cu2 +2 (C O3) (..

Peak List

Pos.[°2θ]	Height [cts]	FWHMLeft[°2θ]	d-spacing [Å]	Rel. Int. [%]
13.8223	634.73	0.1023	7.43916	3.00
17.1197	21165.58	0.1023	6.01410	100.00
20.3473	9172.77	0.1023	5.06789	43.34
21.8974	433.58	0.1023	4.71308	2.05
27.9591	4429.97	0.0768	3.70548	20.93
28.1511	2826.88	0.1023	3.68071	13.36
34.2730	327.33	0.1279	3.03803	1.55
34.7389	2947.05	0.1535	2.99852	13.92
36.4773	10978.60	0.1791	2.86014	51.87
37.5439	2741.46	0.1791	2.78169	12.95
41.4724	2468.32	0.1791	2.52821	11.66
42.5784	297.32	0.1535	2.46547	1.40
43.2023	200.44	0.1535	2.43153	0.95
44.0976	112.98	0.3070	2.38455	0.53
44.7470	215.33	0.1535	2.35169	1.02
45.3211	1246.73	0.1535	2.32344	5.89
46.8291	160.85	0.2558	2.25263	0.76
48.2781	327.83	0.2047	2.18889	1.55
49.5540	946.67	0.1279	2.13596	4.47
51.0381	198.84	0.5117	2.07783	0.94
53.2500	564.96	0.1279	1.99744	2.67
54.5432	633.16	0.1023	1.95359	2.99
55.7408	187.82	0.1535	1.91488	0.89
56.1330	207.59	0.1535	1.90257	0.98
58.3336	203.15	0.1535	1.83676	0.96
59.8960	97.17	0.3070	1.79313	0.46
64.2314	615.63	0.1023	1.68379	2.91
66.0944	55.42	0.6140	1.64149	0.26
68.5529	114.91	0.3070	1.58944	0.54
69.3261	100.47	0.3070	1.57390	0.47
73.3018	119.36	0.4093	1.49958	0.56
74.5274	290.78	0.2047	1.47841	1.37
77.7889	196.92	0.2558	1.42566	0.93



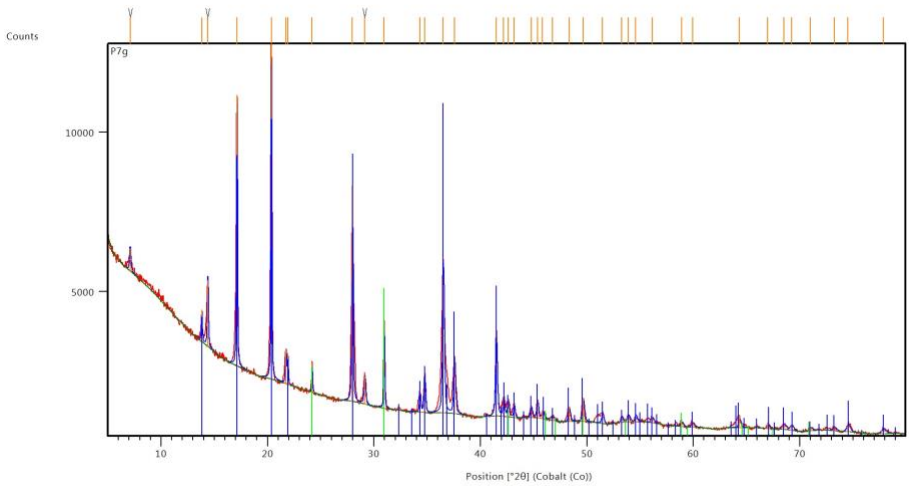
P7g

Pattern List

Ref.Code	Mineral Name	SemiQuant[%]	Score	Compound Name	Scale Fac.	Chem. Formula
00-056-0001	Malachite	82	65	Copper Carbonate H..	0.758	Cu2 +2 (C O3) (..
04-002-3600	Quartz	18	41	Silicon Oxide	0.295	Si O2

Peak List

Pos. [°2θ]	Height [cts]	FWHM Left [°2θ]	d-spacing [Å]	Rel. Int. [%]
7.1026	710.73	0.1535	14.45151	6.75
13.8281	1001.92	0.1023	7.43603	9.52
14.3833	2070.87	0.1279	7.15045	19.68
17.1268	8495.15	0.1023	6.01161	80.73
20.3570	10523.14	0.1023	5.06550	100.00
21.7238	1077.57	0.1279	4.75028	10.24
21.8952	969.75	0.0768	4.71354	9.22
24.1885	937.25	0.0768	4.27240	8.91
27.9684	6759.22	0.1279	3.70427	64.23
29.1376	874.36	0.1791	3.55865	8.31
30.9578	2799.59	0.1023	3.35409	26.60
34.3146	686.82	0.1279	3.03446	6.53
34.7604	1258.93	0.1535	2.99672	11.96
36.5051	4826.56	0.1791	2.85803	45.87
37.5591	1823.29	0.1791	2.78060	17.33
41.4840	2663.89	0.1791	2.52753	25.31
42.1690	617.94	0.1535	2.48830	5.87
42.6166	574.06	0.1791	2.46337	5.46
43.1704	464.56	0.1279	2.43325	4.41
44.7700	350.35	0.2047	2.35054	3.33
45.3517	584.93	0.1791	2.32195	5.56
45.8420	262.68	0.2047	2.29844	2.50
46.7634	110.26	0.5117	2.25562	1.05
48.3292	466.85	0.2047	2.18672	4.44
49.6533	745.68	0.2047	2.13196	7.09
51.4678	372.68	0.2047	2.06165	3.54
53.2783	192.00	0.2047	1.99646	1.82
53.9022	218.40	0.2558	1.97505	2.08
54.5886	217.62	0.2047	1.95209	2.07
56.1325	175.32	0.3070	1.90259	1.67
58.9239	144.35	0.3070	1.81999	1.37
59.9340	163.67	0.3070	1.79210	1.56
64.3209	391.03	0.1791	1.68170	3.72
67.0017	181.28	0.2047	1.62180	1.72
68.5165	155.24	0.4093	1.59019	1.48
69.2287	173.35	0.3070	1.57584	1.65
71.0144	106.36	0.3070	1.54123	1.01
73.2515	112.35	0.3070	1.50046	1.07
74.5250	251.05	0.3070	1.47845	2.39
77.8436	162.62	0.4093	1.42482	1.55



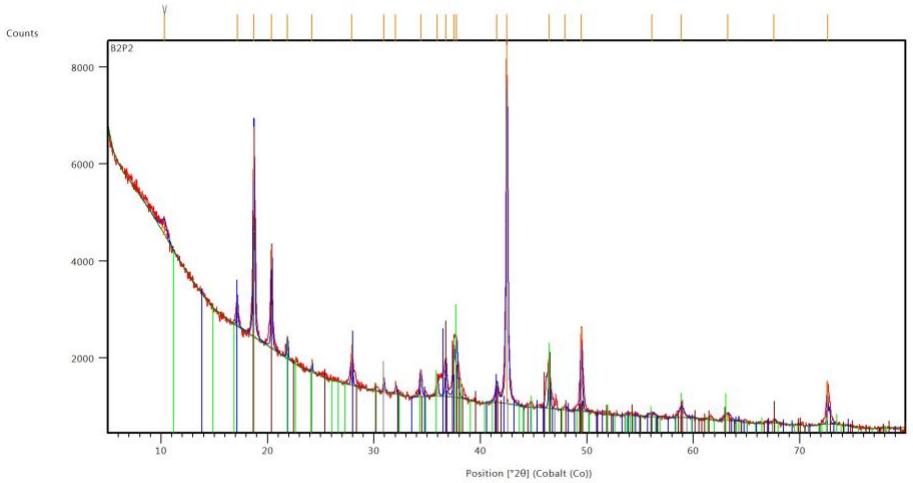
B2P2

Pattern List

Ref.Code	Mineral Name	SemiQuant[%]	Score	Compound Name	Scale Fac.	Chem. Formula
00-056-0001	Malachite	29	24	Copper Carbonate H..	0.164	Cu2 +2 (C O3) (..
04-011-3123	Paratacamite	24	42	Copper Chloride Hy..	0.286	Cu2 Cl (O H)3
01-070-3755	Quartz	8	17	Silicon Oxide	0.075	Si O2
01-071-2027	Atacamite	38	36	Copper Chloride Hy..	0.293	Cu2 Cl (O H)3

Peak List

Pos.[°2θ]	Height [cts]	FWHMLeft[°2θ]	d-spacing [Å]	Rel. Int. [%]
10.3056	289.01	0.6140	9.96698	3.91
17.1709	626.82	0.1279	5.99629	8.48
18.7071	4334.48	0.1535	5.50776	58.63
20.3862	2136.04	0.1279	5.05834	28.89
21.8615	472.26	0.1279	4.72072	6.39
24.1712	275.95	0.1023	4.27540	3.73
27.9135	837.23	0.1279	3.71142	11.32
30.9318	251.85	0.1535	3.35684	3.41
32.0188	277.28	0.1023	3.24571	3.75
34.3902	574.11	0.1791	3.02799	7.77
35.9315	445.38	0.1535	2.90212	6.02
36.7520	817.08	0.1535	2.83949	11.05
37.5051	1191.53	0.1279	2.78446	16.12
37.7590	1215.08	0.1791	2.76642	16.43
41.5329	401.16	0.2558	2.52469	5.43
42.4636	7393.40	0.1791	2.47183	100.00
46.4450	1016.20	0.1279	2.27022	13.74
47.9409	103.77	0.3070	2.20337	1.40
49.4613	1718.78	0.1279	2.13971	23.25
56.1128	75.05	0.6140	1.90320	1.02
58.8617	228.94	0.5117	1.82174	3.10
63.2151	149.02	0.6140	1.70799	2.02
67.5825	94.79	0.3070	1.60950	1.28
72.6109	883.13	0.1279	1.51185	11.94



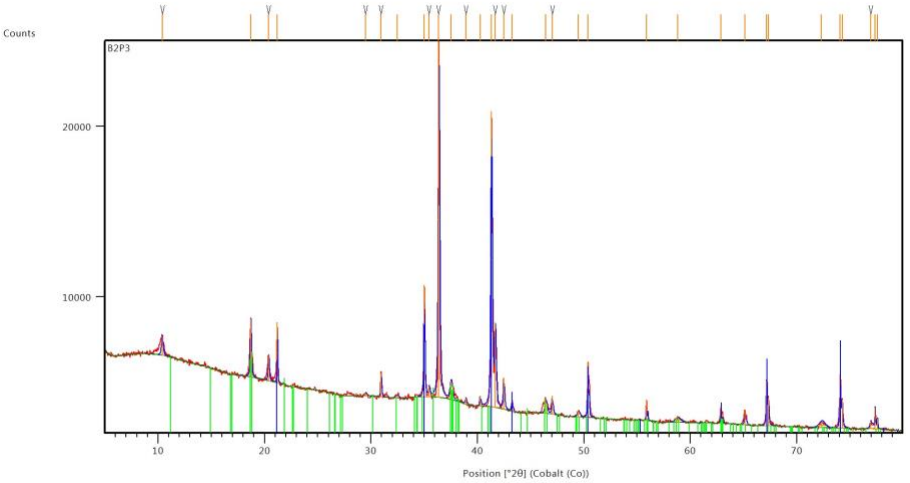
B2P3

Pattern List

Ref.Code	Mineral Name	SemiQuant[%]	Score	Compound Name	Scale Fac.	Chem. Formula
04-015-8211		71	74	Iron Oxide	0.586	Fe3 O4
04-016-8161	Anatacamite	29	24	Copper Chloride Hy..	0.059	Cu2 Cl (O H)3

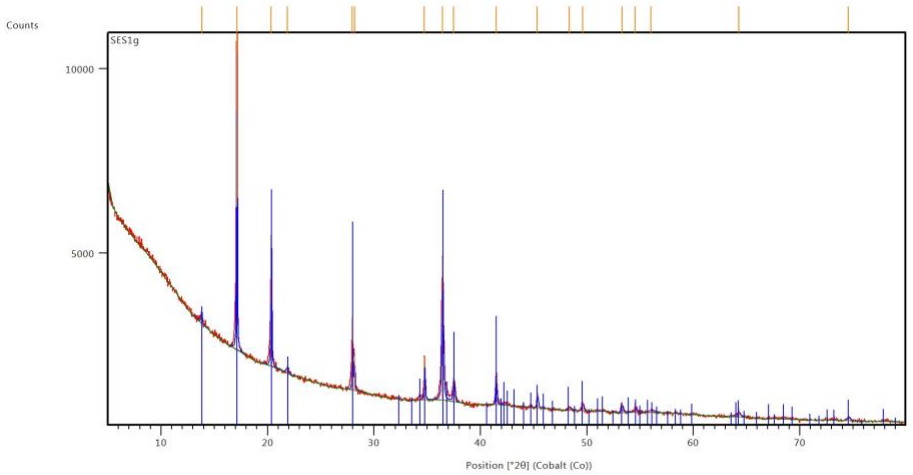
Peak List

Pos.[°2θ]	Height [cts]	FWHM Left[°2θ]	d-spacing [Å]	Rel. Int. [%]
10.3972	1081.84	0.1791	9.87941	5.13
18.7080	3418.47	0.1279	5.50748	16.23
20.3884	1515.91	0.1279	5.05779	7.19
21.2003	3489.89	0.0768	4.86618	16.56
29.5132	157.98	0.3070	3.51436	0.75
30.9573	1374.95	0.1023	3.35415	6.53
32.4504	184.82	0.3070	3.20368	0.88
35.0067	6547.51	0.1023	2.97629	31.08
35.4616	634.91	0.1279	2.93931	3.01
36.3709	21069.06	0.1535	2.86822	100.00
37.5307	1081.97	0.2558	2.78263	5.14
38.9116	333.40	0.2047	2.68751	1.58
40.2510	615.48	0.1023	2.60160	2.92
41.3140	17347.31	0.1535	2.53748	82.34
41.6827	4979.73	0.1535	2.51602	23.64
42.4688	1861.64	0.1279	2.47154	8.84
43.2426	714.11	0.1023	2.42938	3.39
46.4106	878.70	0.2047	2.27181	4.17
47.0179	1059.40	0.1279	2.24410	5.03
49.4800	356.57	0.2558	2.13895	1.69
50.3821	3256.92	0.1023	2.10308	15.46
55.8758	1239.13	0.0768	1.91062	5.88
58.8115	273.97	0.5117	1.82316	1.30
62.8708	1024.45	0.1023	1.71638	4.86
65.1182	843.44	0.1279	1.66333	4.00
67.1756	2617.73	0.1248	1.61692	12.42
67.3531	1606.98	0.0936	1.61667	7.63
72.3251	296.29	0.6240	1.51591	1.41
74.0830	3160.71	0.1248	1.48492	15.00
74.2903	1671.65	0.0936	1.48459	7.93
76.9621	439.77	0.1872	1.43752	2.09
77.3754	1264.77	0.0936	1.43104	6.00
77.5786	624.94	0.0936	1.43098	2.97



SPAIN

SES1g



Pattern List

Ref.Code	Mineral Name	SemiQuant[%]	Score	Compound Name	Scale Fac.	Chem. Formula
00-056-0001	Malachite	100	43	Copper Carbonate H..	0.519	Cu2 +2 (C O3) (..

Peak List

Pos.[°2θ]	Height [cts]	FWHMLeft[°2θ]	d-spacing [Å]	Rel. Int. [%]
13.8215	316.32	0.1535	7.43957	3.57
17.1203	8870.76	0.0768	6.01389	100.00
20.3488	3557.29	0.1023	5.06753	40.10
21.8737	164.84	0.3070	4.71812	1.86
27.9636	1950.10	0.0768	3.70489	21.98
28.1620	984.89	0.0768	3.67931	11.10
34.7452	1171.95	0.1023	2.99799	13.21
36.4287	3867.19	0.1535	2.86383	43.59
37.4871	642.23	0.1535	2.78575	7.24
41.4694	794.73	0.1023	2.52839	8.96
45.3374	414.72	0.1279	2.32265	4.68
48.3591	78.43	0.3070	2.18545	0.88
49.6042	217.05	0.2047	2.13393	2.45
53.2897	244.99	0.2047	1.99606	2.76
54.5509	251.78	0.0768	1.95334	2.84
56.0371	53.84	0.8187	1.90557	0.61
64.2651	207.83	0.1535	1.68300	2.34
74.5685	105.96	0.3070	1.47771	1.19

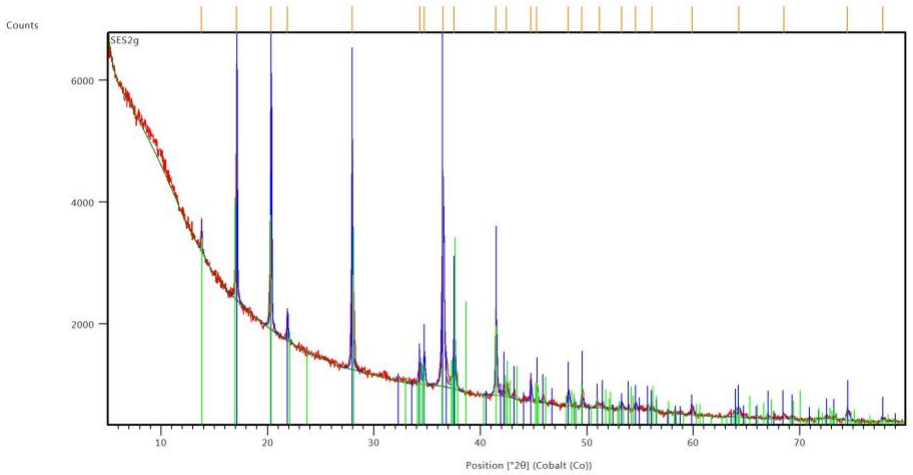
SES2g

Pattern List

Ref.Code	Mineral Name	SemiQuant[%]	Score	Compound Name	Scale Fac.	Chem. Formula
00-056-0001	Malachite	66	59	Copper Carbonate H..	0.972	Cu2 +2 (C O3) (..
04-019-0177		34	12	Copper Carbonate H..	0.366	Cu2 (C O3) (O H..

Peak List

Pos. [°2θ]	Height [cts]	FWHM Left [°2θ]	d-spacing [Å]	Rel. Int. [%]
13.8070	559.12	0.0768	7.44736	12.69
17.1070	3884.17	0.1023	6.01853	88.14
20.3388	4407.06	0.1023	5.06999	100.00
21.8820	497.98	0.1023	4.71634	11.30
27.9544	3895.13	0.1023	3.70609	88.38
34.2992	562.89	0.1023	3.03578	12.77
34.7127	575.42	0.1535	3.00071	13.06
36.4794	3555.10	0.1791	2.85998	80.67
37.5429	1048.59	0.1535	2.78176	23.79
41.4625	1414.65	0.1535	2.52879	32.10
42.4577	165.16	0.3070	2.47216	3.75
44.7477	383.11	0.1023	2.35166	8.69
45.2957	332.02	0.1535	2.32468	7.53
48.2711	272.56	0.2047	2.18919	6.18
49.5300	403.44	0.0768	2.13693	9.15
51.1918	62.70	0.6140	2.07201	1.42
53.2645	121.46	0.2047	1.99694	2.76
54.5700	117.45	0.2047	1.95271	2.67
56.1179	126.24	0.1535	1.90304	2.86
59.8995	151.39	0.2047	1.79303	3.44
64.2878	160.41	0.3070	1.68247	3.64
68.5090	77.51	0.3070	1.59034	1.76
74.4678	200.58	0.2558	1.47942	4.55
77.8275	57.53	0.3070	1.42506	1.31



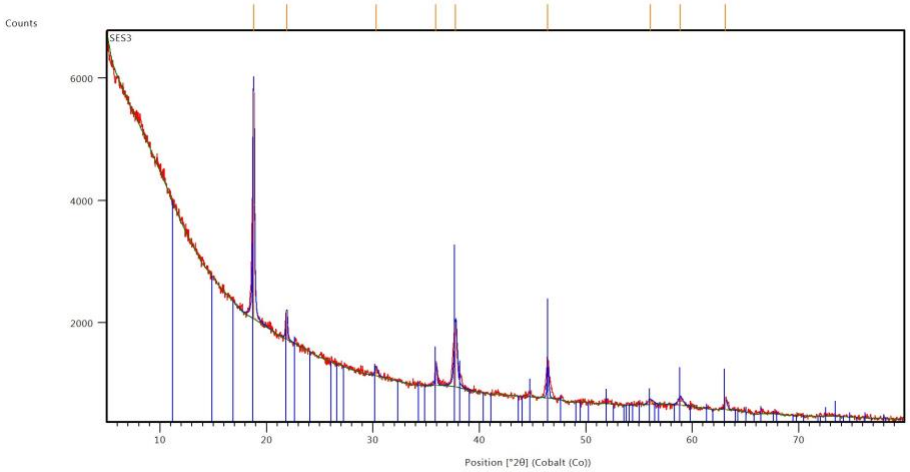
SES3

Pattern List

Ref.Code	Mineral Name	SemiQuant[%]	Score	Compound Name	Scale Fac.	Chem. Formula
04-011-3123	Paratacamite	100	55	Copper Chloride Hy..	0.436	Cu2 Cl (O H)3

Peak List

Pos.[°2θ]	Height [cts]	FWHMLeft[°2θ]	d-spacing [Å]	Rel. Int. [%]
18.7785	3709.26	0.1791	5.48699	100.00
21.8943	459.13	0.1791	4.71374	12.38
30.3046	146.16	0.3070	3.42465	3.94
35.9011	393.98	0.1535	2.90449	10.62
37.7490	1061.59	0.3070	2.76712	28.62
46.3991	691.41	0.1279	2.27234	18.64
56.0452	71.88	0.6140	1.90531	1.94
58.8431	134.64	0.5117	1.82226	3.63
63.1190	185.04	0.2047	1.71032	4.99



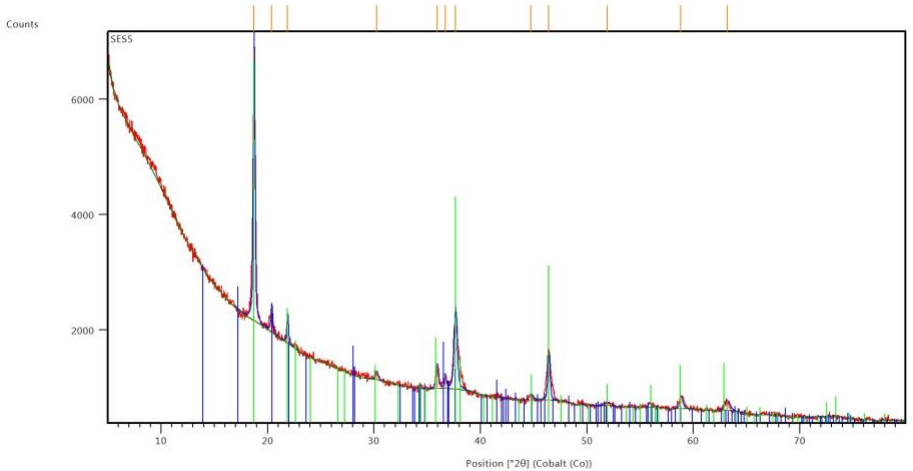
SES5

Pattern List

Ref.Code	Mineral Name	SemiQuant[%]	Score	Compound Name	Scale Fac.	Chem. Formula
01-072-8421	Malachite	23	9	Copper Carbonate H..	0.112	Cu2 (O H)2 (C O..
01-078-7708	Clinoatacamite	77	54	Copper Hydroxide C..	0.627	Cu2 (O H)3 Cl

Peak List

Pos.[°2θ]	Height [cts]	FWHMLeft[°2θ]	d-spacing [Å]	Rel. Int. [%]
18.7289	4718.28	0.1791	5.50141	100.00
20.3935	445.84	0.2047	5.05654	9.45
21.8855	500.35	0.1535	4.71560	10.60
30.2533	138.95	0.3070	3.43031	2.94
35.9394	401.60	0.2558	2.90150	8.51
36.6934	253.87	0.1535	2.84387	5.38
37.6489	1354.99	0.3070	2.77421	28.72
44.7454	97.61	0.4093	2.35177	2.07
46.3991	894.61	0.2047	2.27234	18.96
51.9249	52.01	0.8187	2.04475	1.10
58.8243	224.76	0.3070	1.82279	4.76
63.1875	165.14	0.5117	1.70866	3.50



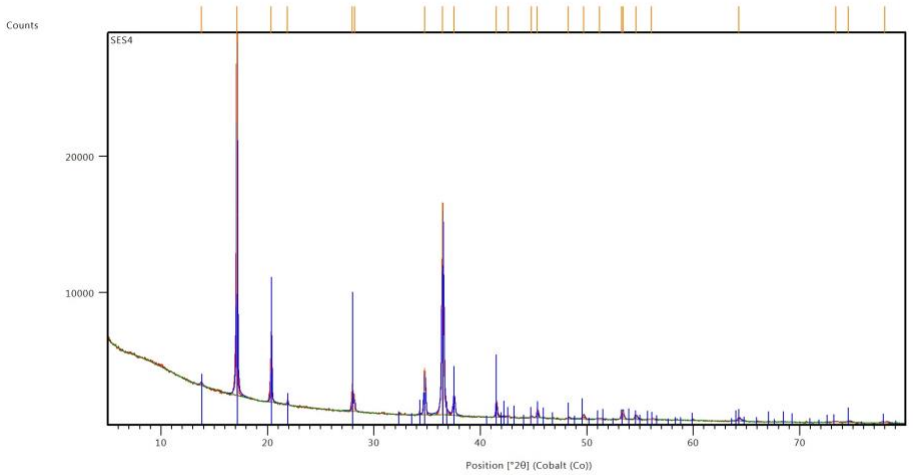
SES4

Pattern List

Ref.Code	Mineral Name	SemiQuant[%]	Score	Compound Name	Scale Fac.	Chem. Formula
00-056-0001	Malachite	100	32	Copper Carbonate H..	0.375	Cu2 +2 (C O3) (..

Peak List

Pos.[°2θ]	Height [cts]	FWHMLeft[°2θ]	d-spacing [Å]	Rel. Int. [%]
13.7848	219.38	0.3070	7.45927	0.82
17.1277	26730.59	0.1023	6.01133	100.00
20.3558	5172.53	0.1023	5.06580	19.35
21.8790	400.41	0.1023	4.71699	1.50
27.9675	2039.89	0.1023	3.70439	7.63
28.1640	1256.90	0.0768	3.67906	4.70
34.7486	3426.73	0.1535	2.99770	12.82
36.4471	15562.03	0.1791	2.86243	58.22
37.5196	1485.94	0.1535	2.78342	5.56
41.4827	1210.10	0.1023	2.52761	4.53
42.6137	134.98	0.1535	2.46352	0.50
44.7704	138.94	0.1535	2.35052	0.52
45.3245	624.33	0.1279	2.32328	2.34
48.2600	128.54	0.3070	2.18967	0.48
49.6832	385.94	0.2047	2.13075	1.44
51.2082	64.91	0.6140	2.07139	0.24
53.2582	675.54	0.0936	1.99571	2.53
53.4195	599.20	0.0768	1.99157	2.24
54.6029	307.47	0.2558	1.95162	1.15
56.0419	49.36	0.6140	1.90542	0.18
64.2925	281.10	0.2047	1.68236	1.05
73.3756	27.68	0.6140	1.49828	0.10
74.5419	160.03	0.1535	1.47816	0.60
78.0038	86.90	0.6140	1.42235	0.33



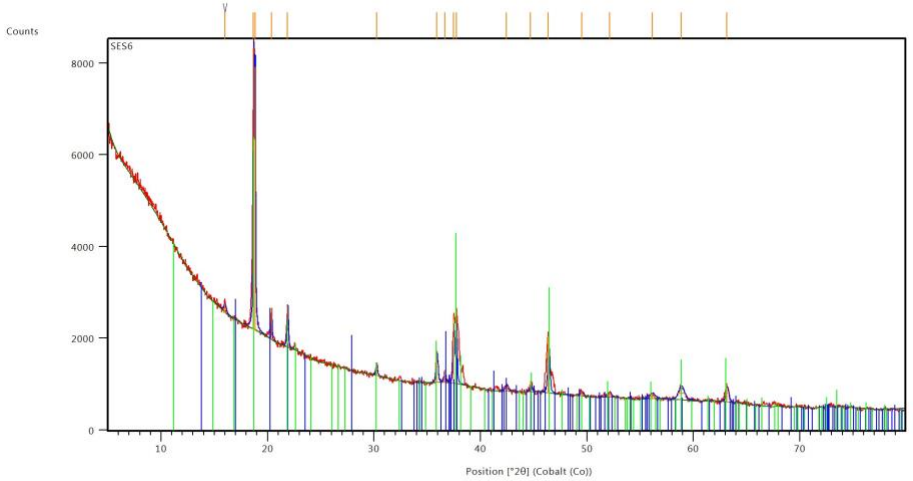
SES6

Pattern List

Ref.Code	Mineral Name	SemiQuant[%]	Score	Compound Name	Scale Fac.	Chem. Formula
04-011-5196	Malachite	39	5	Copper Carbonate H..	0.131	Cu2 (C O3) (O H..
04-011-3123	Paratacamite	61	51	Copper Chloride Hy..	0.490	Cu2 Cl (O H)3

Peak List

Pos.[°2θ]	Height [cts]	FWHMLeft[°2θ]	d-spacing [Å]	Rel. Int. [%]
16.0196	177.35	0.3070	6.42413	2.89
18.6747	6133.20	0.1023	5.51722	100.00
18.8240	5733.51	0.1023	5.47384	93.48
20.3842	693.16	0.0768	5.05883	11.30
21.8854	900.98	0.1535	4.71563	14.69
30.2539	254.67	0.1535	3.43026	4.15
35.9117	680.37	0.1791	2.90366	11.09
36.6525	279.53	0.1535	2.84693	4.56
37.4840	1480.96	0.1279	2.78597	24.15
37.7296	1654.54	0.1023	2.76849	26.98
42.4385	135.38	0.4093	2.47323	2.21
44.7152	192.86	0.1791	2.35328	3.14
46.3845	1230.66	0.1791	2.27302	20.07
49.5149	91.22	0.3070	2.13754	1.49
52.1478	103.07	0.3070	2.03661	1.68
56.1315	116.13	0.5117	1.90262	1.89
58.8585	284.82	0.6140	1.82183	4.64
63.1620	379.46	0.2558	1.70928	6.19



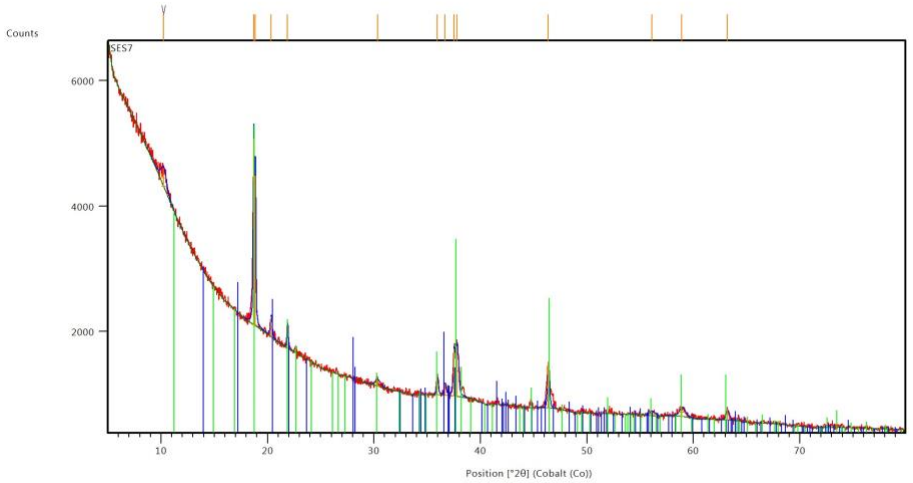
SES7

Pattern List

Ref.Code	Mineral Name	SemiQuant[%]	Score	Compound Name	Scale Fac.	Chem. Formula
04-013-7662	Malachite	44	6	Copper Carbonate H..	0.152	Cu2 (C O3) (O H..
04-011-3123	Paratacamite	56	46	Copper Chloride Hy..	0.481	Cu2 Cl (O H)3

Peak List

Pos. [°2θ]	Height [cts]	FWHM Left [°2θ]	d-spacing [Å]	Rel. Int. [%]
10.2499	285.89	0.6140	10.02094	9.63
18.6973	2968.76	0.1279	5.51060	100.00
18.8498	2389.81	0.1023	5.46643	80.50
20.3468	329.14	0.2047	5.06802	11.09
21.8799	424.27	0.1023	4.71678	14.29
30.3373	96.82	0.6140	3.42104	3.26
35.9527	330.25	0.1535	2.90046	11.12
36.6675	182.82	0.2047	2.84581	6.16
37.5230	752.59	0.1535	2.78318	25.35
37.8025	801.78	0.2558	2.76334	27.01
46.3618	712.98	0.1791	2.27407	24.02
56.0957	65.98	0.6140	1.90373	2.22
58.9215	138.87	0.6140	1.82006	4.68
63.1922	161.37	0.3070	1.70854	5.44



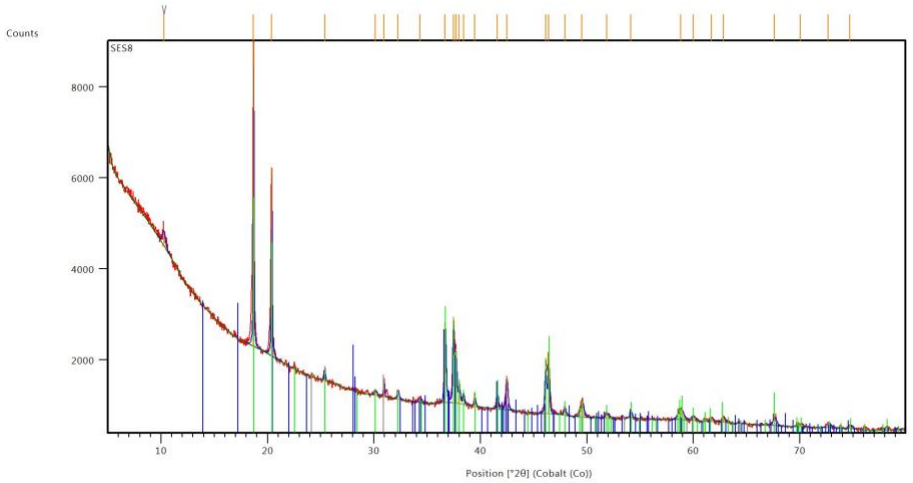
SES8

Pattern List

Ref.Code	Mineral Name	SemiQuant[%]	Score	Compound Name	Scale Fac.	Chem. Formula
01-072-8421	Malachite	40	12	Copper Carbonate H..	0.178	Cu2 (O H)2 (C O..
04-013-1385	Atacamite	54	50	Copper Chloride Hy..	0.362	Cu2 Cl (O H)3
01-075-8320	Quartz	6	17	Silicon Oxide	0.053	Si O2

Peak List

Pos.[°2θ]	Height [cts]	FWHMLeft[°2θ]	d-spacing [Å]	Rel. Int. [%]
10.2808	307.24	0.3070	9.99096	4.43
18.6785	6938.43	0.0768	5.51611	100.00
20.3831	4129.13	0.1023	5.05909	59.51
25.3706	319.71	0.1023	4.07637	4.61
30.1357	105.95	0.3070	3.44339	1.53
30.9377	411.80	0.1023	3.35623	5.94
32.2513	198.42	0.2047	3.22294	2.86
34.3131	107.61	0.3070	3.03458	1.55
36.6794	1761.43	0.1535	2.84492	25.39
37.4645	1886.60	0.1279	2.78737	27.19
37.7159	1185.80	0.1023	2.76946	17.09
37.9887	489.68	0.1279	2.75030	7.06
38.4061	241.88	0.1535	2.72152	3.49
39.4758	226.94	0.1535	2.65060	3.27
41.5830	457.59	0.1279	2.52179	6.60
42.4635	705.37	0.2047	2.47183	10.17
46.1225	1125.75	0.1535	2.28522	16.22
46.3870	1361.30	0.1023	2.27290	19.62
47.9274	185.35	0.2047	2.20395	2.67
49.5434	351.53	0.3070	2.13638	5.07
51.8780	104.03	0.3070	2.04647	1.50
54.1189	175.25	0.2047	1.96774	2.53
58.7991	232.03	0.5117	1.82351	3.34
59.9717	90.78	0.4093	1.79107	1.31
61.6841	94.10	0.3070	1.74605	1.36
62.8086	128.14	0.3070	1.71790	1.85
67.6063	198.02	0.3070	1.60900	2.85
70.0297	57.20	0.5117	1.56007	0.82
72.6822	109.10	0.4093	1.51058	1.57
74.7002	69.22	0.4093	1.47549	1.00



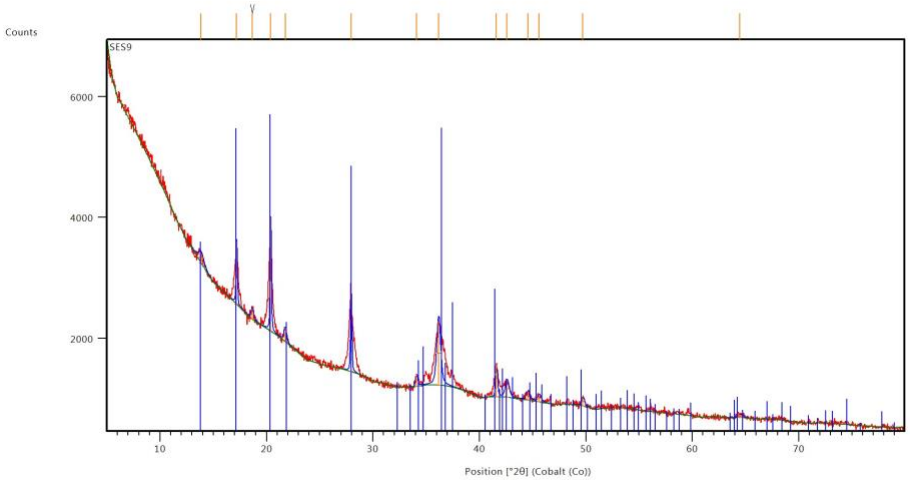
SES9

Pattern List

Ref.Code	Mineral Name	SemiQuant[%]	Score	Compound Name	Scale Fac.	Chem. Formula
00-056-0001	Malachite	100	31	Copper Carbonate H..	0.613	Cu2 +2 (C O3) (..

Peak List

Pos.[°2θ]	Height [cts]	FWHMLeft[°2θ]	d-spacing [Å]	Rel. Int. [%]
13.8527	171.57	0.6140	7.42288	9.13
17.1917	1039.97	0.1279	5.98910	55.35
18.6620	175.52	0.3070	5.52095	9.34
20.3883	1879.05	0.1279	5.05782	100.00
21.7579	227.27	0.3070	4.74293	12.10
27.9379	1394.49	0.1279	3.70823	74.21
34.0917	192.50	0.2047	3.05371	10.24
36.1574	1061.42	0.4093	2.88459	56.49
41.5945	527.67	0.1791	2.52112	28.08
42.5796	279.56	0.4093	2.46541	14.88
44.5572	141.84	0.4093	2.36119	7.55
45.6005	117.70	0.4093	2.30996	6.26
49.7157	144.58	0.3070	2.12945	7.69
64.4647	55.89	0.6140	1.67835	2.97



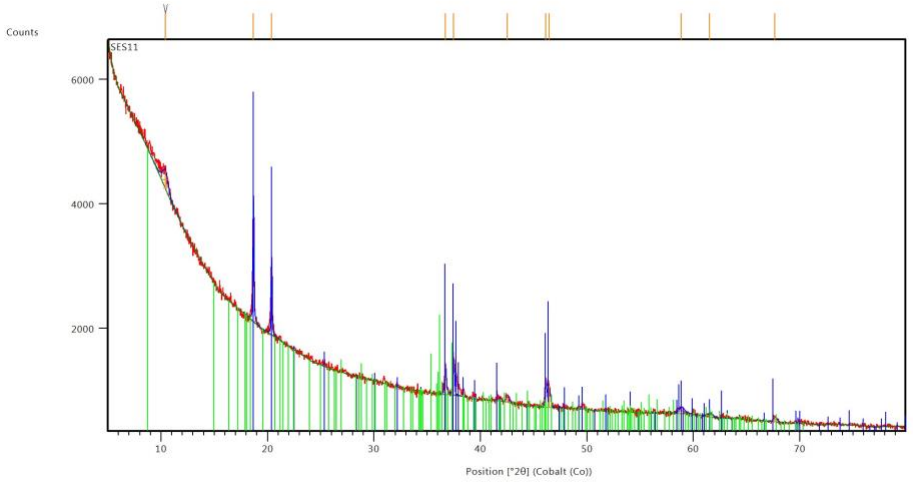
SES11

Pattern List

Ref.Code	Mineral Name	SemiQuant[%]	Score	Compound Name	Scale Fac.	Chem. Formula
01-080-9252	Atacamite	49	32	Copper Chloride Hy..	0.554	Cu2 Cl (O H)3
04-021-1753		51	2	Calcium Carbonate	0.193	Ca (C O3)

Peak List

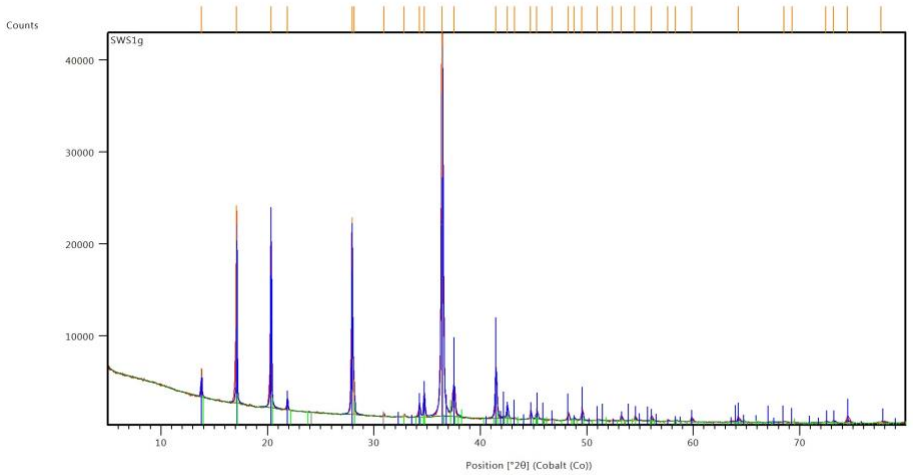
Pos.[°2θ]	Height [cts]	FWHMLeft[°2θ]	d-spacing [Å]	Rel. Int. [%]
10.4054	277.30	0.6140	9.87159	13.77
18.6754	2013.75	0.1023	5.51700	100.00
20.3810	1259.84	0.1023	5.05961	62.56
36.6994	512.04	0.1535	2.84342	25.43
37.4600	686.49	0.1279	2.78770	34.09
42.5232	115.82	0.3070	2.46852	5.75
46.1384	487.44	0.1535	2.28447	24.21
46.4623	353.06	0.1535	2.26942	17.53
58.8592	102.93	0.6140	1.82181	5.11
61.5316	59.19	0.6140	1.74995	2.94
67.6679	87.11	0.3070	1.60771	4.33



SWS1g

Pattern List

Ref.Code	Mineral Name	SemiQuant[%]	Score	Compound Name	Scale Fac.	Chem. Formula
00-056-0001	Malachite	91	48	Copper Carbonate H..	0.602	Cu2 +2 (C O3) (..
04-019-0176		8	15	Copper Carbonate H..	0.040	Cu2 (C O3) (O H..
01-075-8320	Quartz	1	17	Silicon Oxide	0.013	Si O2



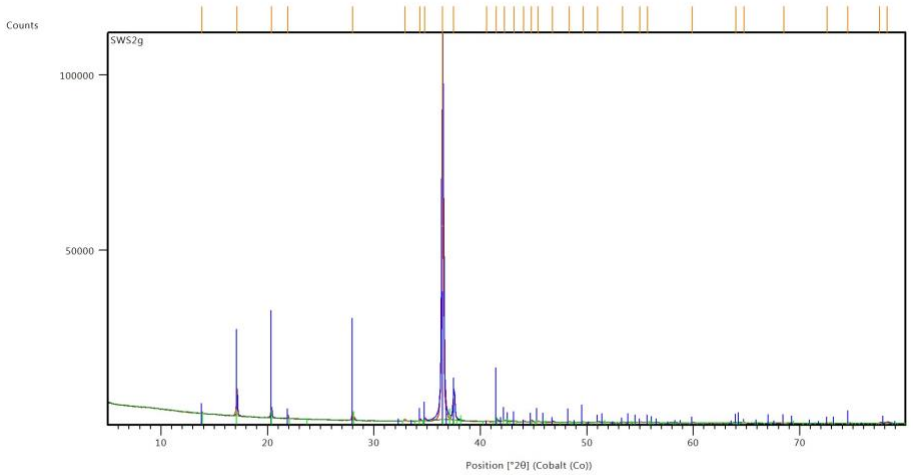
Peak List

Pos.[°2θ]	Height [cts]	FWHMLeft[°2θ]	d-spacing [Å]	Rel. Int. [%]
13.8010	3124.75	0.1023	7.45057	7.49
17.0950	21475.35	0.0768	6.02272	51.48
20.3254	19608.91	0.1023	5.07331	47.01
21.8690	1369.42	0.1023	4.71912	3.28
27.9402	21403.90	0.1023	3.70793	51.31
28.1460	3718.15	0.0512	3.68137	8.91
30.9276	366.91	0.1023	3.35729	0.88
32.8483	269.96	0.1535	3.16593	0.65
34.2793	1606.81	0.1023	3.03749	3.85
34.7122	2904.39	0.1279	3.00075	6.96
36.3941	41715.58	0.1791	2.86645	100.00
37.5121	3297.39	0.2047	2.78396	7.90
41.4441	5605.47	0.1791	2.52986	13.44
42.5201	1507.83	0.1535	2.46870	3.61
43.1860	151.86	0.2047	2.43241	0.36
44.7168	920.11	0.1279	2.35320	2.21
45.2892	1162.88	0.1535	2.32499	2.79
46.7075	98.76	0.4093	2.25817	0.24
48.2577	899.79	0.1279	2.18976	2.16
48.8108	234.99	0.1535	2.16644	0.56
49.5277	1482.71	0.1279	2.13702	3.55
50.9739	114.35	0.5117	2.08027	0.27
52.4245	84.60	0.1535	2.02662	0.20
53.2199	630.76	0.1279	1.99849	1.51
54.4946	517.11	0.1023	1.95520	1.24
56.0596	681.45	0.0768	1.90486	1.63
57.6131	123.43	0.1535	1.85773	0.30
58.3059	156.96	0.2047	1.83756	0.38
59.8466	497.45	0.1023	1.79447	1.19
64.2114	640.19	0.1023	1.68426	1.53
68.5138	97.48	0.4093	1.59024	0.23
69.2960	62.22	0.3070	1.57450	0.15
72.4225	183.83	0.2047	1.51525	0.44
73.1706	295.47	0.0936	1.50080	0.71
74.4813	805.92	0.1023	1.47919	1.93
77.6434	158.86	0.5117	1.42791	0.38

SWS2g

Pattern List

Ref.Code	Mineral Name	SemiQuant[%]	Score	Compound Name	Scale Fac.	Chem. Formula
00-056-0001	Malachite	90	22	Copper Carbonate H..	0.325	Cu2 +2 (C O3) (..
04-019-0176		10	14	Copper Carbonate H..	0.028	Cu2 (C O3) (O H..



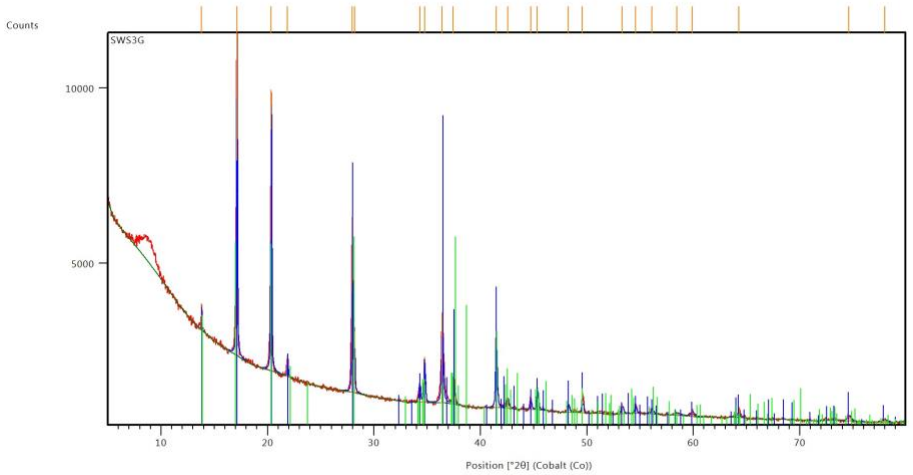
Peak List

Pos.[°2θ]	Height [cts]	FWHMLeft[°2θ]	d-spacing [Å]	Rel. Int. [%]
13.8389	417.59	0.1279	7.43029	0.37
17.1475	7878.27	0.0768	6.00441	6.97
20.3774	3235.20	0.1023	5.06050	2.86
21.9075	1053.17	0.1023	4.71092	0.93
27.9899	2578.84	0.1023	3.70148	2.28
32.9009	678.33	0.1023	3.16101	0.60
34.3332	732.14	0.1023	3.03287	0.65
34.7694	934.83	0.1279	2.99597	0.83
36.4302	113046.40	0.1791	2.86371	100.00
37.4975	8985.47	0.1535	2.78501	7.95
40.5940	143.94	0.4093	2.58054	0.13
41.5140	810.71	0.1535	2.52579	0.72
42.2555	203.96	0.1535	2.48344	0.18
43.1687	140.79	0.2047	2.43334	0.12
44.0604	404.33	0.1279	2.38647	0.36
44.7661	688.91	0.1791	2.35074	0.61
45.4030	255.57	0.1535	2.31947	0.23
46.7755	378.80	0.1279	2.25507	0.34
48.3292	222.02	0.2047	2.18672	0.20
49.6416	243.49	0.2047	2.13243	0.22
51.0253	230.30	0.2047	2.07832	0.20
53.3568	200.92	0.2047	1.99374	0.18
55.0015	177.68	0.2047	1.93857	0.16
55.6952	76.98	0.3070	1.91632	0.07
59.9094	119.85	0.3070	1.79276	0.11
63.9974	107.86	0.5117	1.68929	0.10
64.7777	110.80	0.2047	1.67111	0.10
68.5199	102.62	0.4093	1.59012	0.09
72.5757	29.06	0.3070	1.51249	0.03
74.5112	124.17	0.3070	1.47868	0.11
77.4995	253.35	0.2047	1.43014	0.22
78.2129	406.27	0.3070	1.41916	0.36

SWS3g

Pattern List

Ref.Code	Mineral Name	SemiQuant[%]	Score	Compound Name	Scale Fac.	Chem. Formula
00-056-0001	Malachite	55	52	Copper Carbonate H..	0.707	Cu2 +2 (C O3) (..
04-019-0177		45	17	Copper Carbonate H..	0.413	Cu2 (C O3) (O H..



Peak List

Pos. [°2θ]	Height [cts]	FWHM Left [°2θ]	d-spacing [Å]	Rel. Int. [%]
13.8145	754.60	0.0768	7.44333	8.08
17.1246	9337.43	0.1023	6.01240	100.00
20.3501	8037.65	0.1023	5.06721	86.08
21.8774	604.83	0.1023	4.71734	6.48
27.9557	5013.89	0.1023	3.70592	53.70
28.1664	1746.63	0.0768	3.67875	18.71
34.3005	546.44	0.1535	3.03567	5.85
34.7537	1291.08	0.1279	2.99728	13.83
36.4086	2550.84	0.1791	2.86535	27.32
37.4451	733.60	0.1791	2.78876	7.86
41.4786	2099.16	0.1535	2.52785	22.48
42.5584	301.43	0.2047	2.46658	3.23
44.7356	345.72	0.1023	2.35226	3.70
45.3456	618.74	0.1791	2.32225	6.63
48.2639	218.11	0.2047	2.18950	2.34
49.5719	577.21	0.1023	2.13524	6.18
53.3086	236.47	0.2047	1.99541	2.53
54.5617	280.95	0.1279	1.95298	3.01
56.1134	185.58	0.2047	1.90318	1.99
58.4556	56.54	0.6140	1.83327	0.61
59.8801	150.93	0.3070	1.79356	1.62
64.2658	326.09	0.0768	1.68298	3.49
74.6042	164.80	0.4093	1.47711	1.76
77.9667	72.15	0.6140	1.42292	0.77

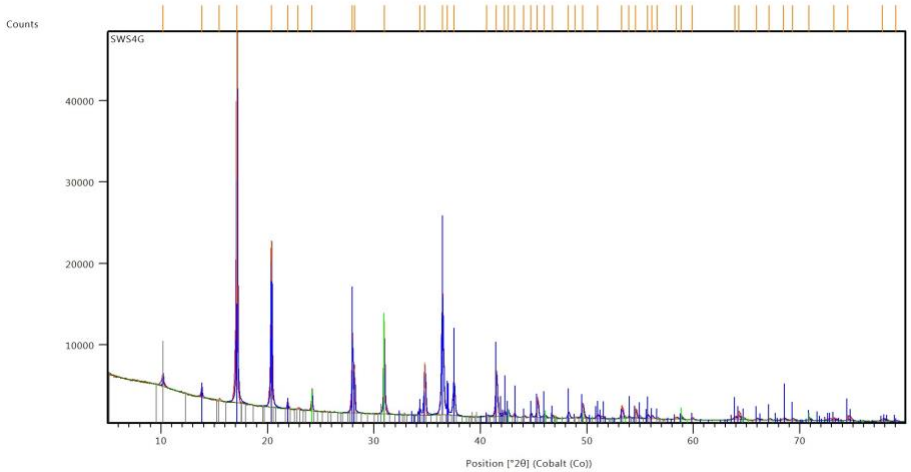
SWS4g

Pattern List

Ref.Code	Mineral Name	SemiQuant[%]	Score	Compound Name	Scale Fac.	Chem. Formula
01-072-8421	Malachite	76	47	Copper Carbonate H..	0.505	Cu2 (O H)2 (C O..
04-008-8228	Quartz	18	48	Silicon Oxide	0.255	Si O2
04-011-2637	Devilline	6	16	Calcium Copper Sul..	0.115	Ca Cu4 (S O4)2 (..

Peak List

Pos.[°2θ]	Height [cts]	FWHMLeft[°2θ]	d-spacing [Å]	Rel. Int. [%]
10.1986	1588.96	0.1023	10.07129	3.46
13.8366	1264.07	0.1023	7.43147	2.75
15.4737	247.88	0.1535	6.64930	0.54
17.1415	45916.34	0.1023	6.00649	100.00
20.3703	20379.44	0.1279	5.06224	44.38
21.9034	899.42	0.0768	4.71180	1.96
22.8668	210.65	0.3582	4.51575	0.46
24.1911	2705.83	0.0768	4.27195	5.89
27.9798	10158.66	0.1023	3.70279	22.12
28.1795	5444.70	0.0768	3.67707	11.86
30.9597	11394.71	0.1023	3.35390	24.82
34.3025	950.20	0.1023	3.03549	2.07
34.7671	6483.96	0.1535	2.99616	14.12
36.4255	14822.76	0.1791	2.86407	32.28
36.8933	1308.51	0.1023	2.82899	2.85
37.5032	4120.58	0.1791	2.78460	8.97
40.5846	198.03	0.2558	2.58111	0.43
41.4974	5666.80	0.1791	2.52675	12.34
42.2624	750.55	0.1535	2.48306	1.63
42.6041	933.36	0.1279	2.46406	2.03
43.2026	548.93	0.1023	2.43152	1.20
44.0658	227.42	0.2047	2.38619	0.50
44.7517	535.34	0.1279	2.35146	1.17
45.3469	2465.98	0.1279	2.32219	5.37
46.0008	360.42	0.2558	2.29093	0.78
46.7792	331.54	0.2047	2.25490	0.72
48.2791	805.57	0.1535	2.18885	1.75
48.8773	82.74	0.2047	2.16368	0.18
49.5976	1873.38	0.2047	2.13420	4.08
51.0102	458.03	0.3070	2.07889	1.00
53.2777	1575.50	0.1279	1.99648	3.43
53.9419	335.49	0.1023	1.97371	0.73
54.5673	1292.92	0.1279	1.95280	2.82
55.7158	525.81	0.1791	1.91567	1.15
56.1130	464.57	0.1791	1.90320	1.01
56.6014	186.88	0.1535	1.88811	0.41
58.4173	265.38	0.2303	1.83436	0.58
58.8693	560.36	0.0768	1.82153	1.22
59.9025	240.29	0.2047	1.79295	0.52
63.9318	422.63	0.1535	1.69084	0.92
64.2653	1124.69	0.1023	1.68300	2.45
65.9593	262.22	0.2047	1.64447	0.57
67.1069	226.51	0.2558	1.61956	0.49
68.4794	296.76	0.3070	1.59094	0.65
69.3372	229.35	0.2558	1.57368	0.50
70.8690	511.80	0.1023	1.54398	1.11
73.2144	360.33	0.1023	1.50112	0.78
74.5338	650.78	0.1023	1.47830	1.42
77.7808	299.51	0.3582	1.42578	0.65
79.0357	136.04	0.3070	1.40677	0.30



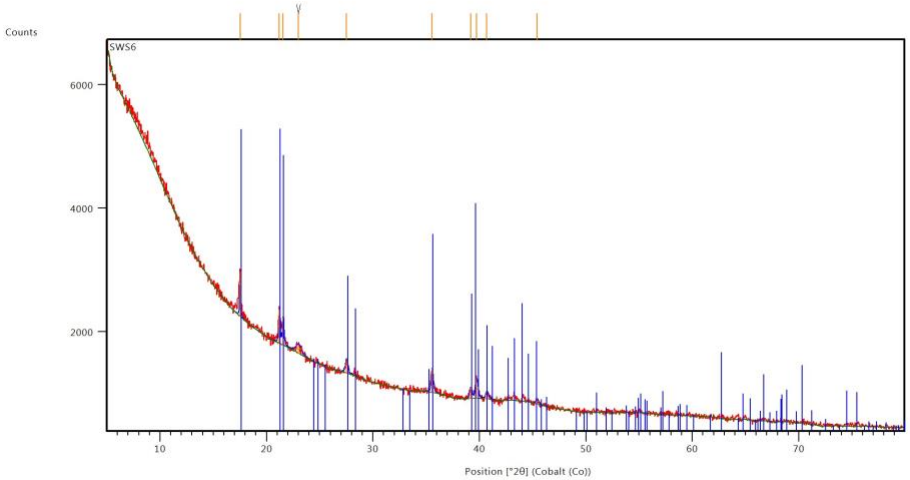
SWS6g

Pattern List

Ref.Code	Mineral Name	SemiQuant[%]	Score	Compound Name	Scale Fac.	Chem. Formula
01-072-0592	Libethenite	100	16	Copper Phosphate H..	0.516	Cu2 (P O4) (O H)

Peak List

Pos.[°2θ]	Height [cts]	FWHMLeft[°2θ]	d-spacing [Å]	Rel. Int. [%]
17.5217	719.00	0.1023	5.87717	100.00
21.2060	545.57	0.1535	4.86488	75.88
21.5586	447.84	0.1535	4.78625	62.29
23.0096	137.44	0.6140	4.48810	19.12
27.5059	225.79	0.2558	3.76533	31.40
35.5497	386.65	0.2047	2.93226	53.78
39.1729	183.02	0.2047	2.67027	25.45
39.7255	315.81	0.2558	2.63460	43.92
40.7008	111.08	0.3070	2.57405	15.45
45.4075	83.78	0.3070	2.31925	11.65



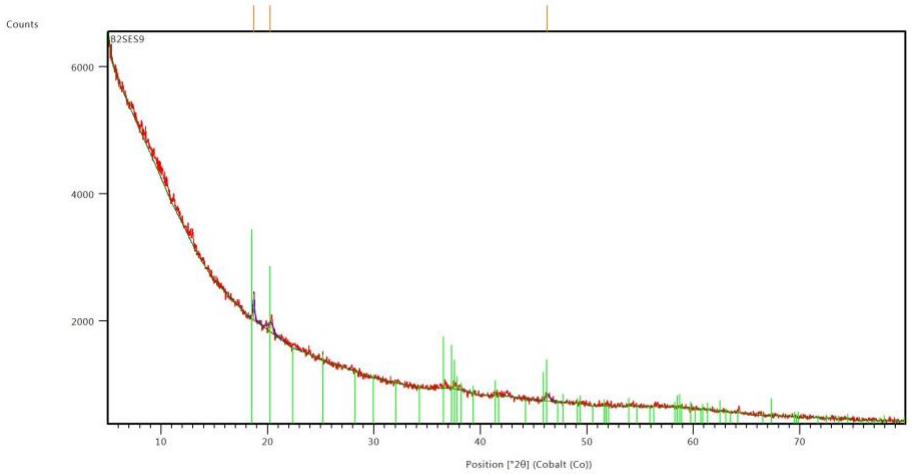
B2SES9

Pattern List

Ref.Code	Mineral Name	SemiQuant[%]	Score	Compound Name	Scale Fac.	Chem. Formula
01-080-9252	Atacamite	100	Unmatch	Copper Chloride Hy..	0.215	Cu2 Cl (O H)3

Peak List

Pos.[°2θ]	Height [cts]	FWHMLeft[°2θ]	d-spacing [Å]	Rel. Int. [%]
18.7040	416.86	0.1535	5.50865	100.00
20.2644	140.37	0.6140	5.08841	33.67
46.2808	101.94	0.4093	2.27783	24.46



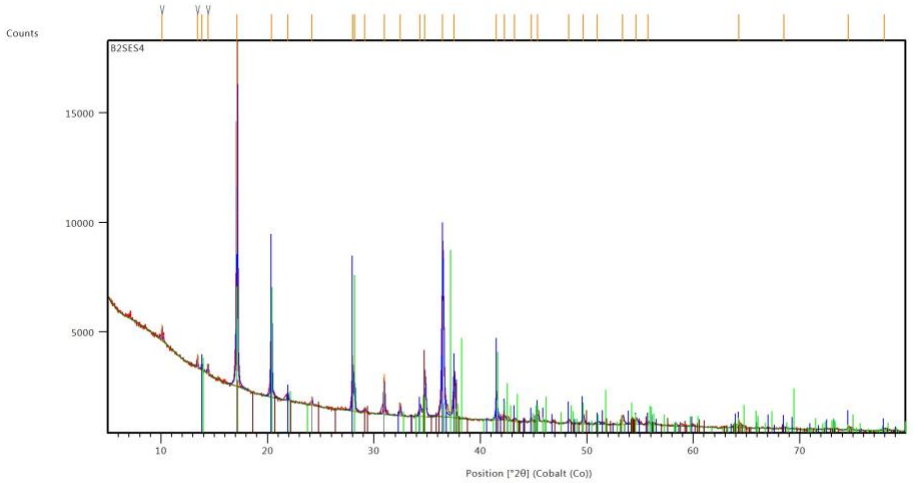
B2SES4

Pattern List

Ref.Code	Mineral Name	SemiQuant[%]	Score	Compound Name	Scale Fac.	Chem. Formula
00-056-0001	Malachite	35	47	Copper Carbonate H..	0.484	Cu2 +2 (C O3) (..
04-019-0176		38	16	Copper Carbonate H..	0.416	Cu2 (C O3) (O H..
01-075-8320	Quartz	3	32	Silicon Oxide	0.078	Si O2
04-020-5889		24	15	Calcium Carbonate	0.165	Ca (C O3)

Peak List

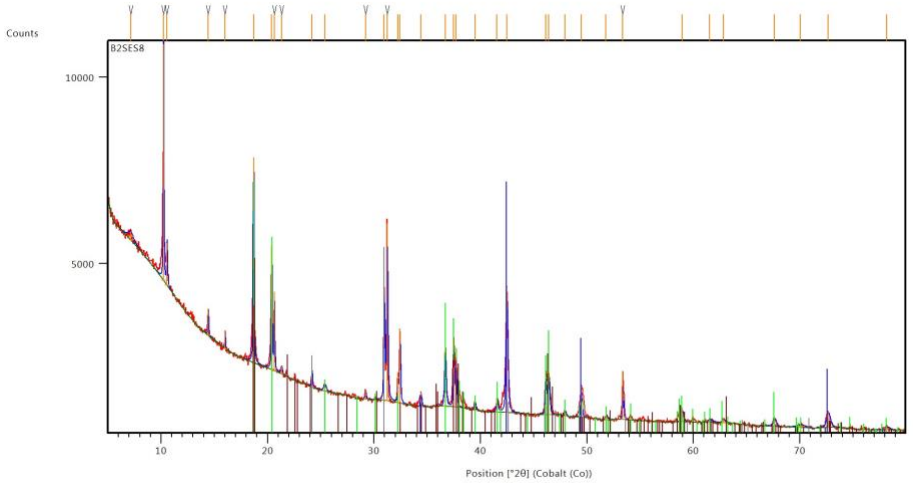
Pos.[°2θ]	Height [cts]	FWHMLeft[°2θ]	d-spacing [Å]	Rel. Int. [%]
10.0903	732.95	0.0768	10.17906	4.57
13.4181	602.52	0.0768	7.66215	3.76
13.8365	265.51	0.1535	7.43156	1.66
14.4058	442.44	0.1023	7.13934	2.76
17.1442	16024.39	0.1023	6.00558	100.00
20.3736	5037.99	0.1023	5.06142	31.44
21.8986	346.11	0.1535	4.71281	2.16
24.1903	360.10	0.0768	4.27209	2.25
27.9867	2550.36	0.1023	3.70190	15.92
28.1840	1527.93	0.0768	3.67651	9.54
29.1342	246.54	0.1535	3.55906	1.54
30.9602	1826.24	0.1023	3.35384	11.40
32.4555	593.19	0.1279	3.20320	3.70
34.3260	525.48	0.1535	3.03348	3.28
34.7652	2179.01	0.1791	2.99632	13.60
36.4578	8105.85	0.1535	2.86162	50.58
37.5394	2134.92	0.1535	2.78201	13.32
41.5114	1305.21	0.1535	2.52594	8.15
42.2416	251.14	0.1535	2.48422	1.57
43.2136	133.22	0.3070	2.43093	0.83
44.7873	144.63	0.1535	2.34968	0.90
45.3502	570.92	0.1023	2.32203	3.56
48.2965	172.19	0.2047	2.18811	1.07
49.6426	366.64	0.2047	2.13239	2.29
50.9812	142.05	0.3070	2.08000	0.89
53.3541	438.78	0.2047	1.99383	2.74
54.6328	320.53	0.1535	1.95064	2.00
55.7428	125.49	0.3070	1.91481	0.78
64.2648	380.12	0.0768	1.68301	2.37
68.5250	77.32	0.3070	1.59001	0.48
74.5445	199.23	0.1535	1.47812	1.24
77.9232	91.71	0.4093	1.42359	0.57



B2SES8

Pattern List

Ref.Code	Mineral Name	SemiQuant[%]	Score	Compound Name	Scale Fac.	Chem. Formula
04-007-9767	Cuprite	14	51	Copper Oxide	0.564	Cu2 O
01-080-9252	Atacamite	38	53	Copper Chloride Hy..	0.443	Cu2 Cl (O H)3
04-016-2085	Quartz	26	38	Silicon Oxide	0.374	Si O2
04-013-3625	Clinoatacamite, syn	21	21	Copper Chloride Hy..	0.256	Cu2 Cl (O H)3



Peak List

Pos.[°2θ]	Height [cts]	FWHMLeft[°2θ]	d-spacing [Å]	Rel. Int. [%]
7.1430	209.27	0.6140	14.36972	3.30
10.2315	6334.65	0.0768	10.03894	100.00
10.5619	1143.69	0.1023	9.72571	18.05
14.4292	709.85	0.1023	7.12781	11.21
16.0178	484.06	0.0768	6.42485	7.64
18.6877	5508.45	0.1023	5.51343	86.96
20.3931	3297.17	0.1023	5.05663	52.05
20.6435	2120.09	0.0768	4.99596	33.47
21.3251	222.48	0.1535	4.83803	3.51
24.1831	472.79	0.1023	4.27333	7.46
25.3871	172.56	0.3070	4.07377	2.72
29.2052	236.20	0.1535	3.55061	3.73
30.9548	3090.92	0.1023	3.35441	48.79
31.2324	4763.34	0.1279	3.32534	75.20
32.2420	811.25	0.0768	3.22384	12.81
32.4410	1956.41	0.1023	3.20459	30.88
34.4211	361.21	0.1279	3.02535	5.70
36.6890	1505.31	0.1535	2.84420	23.76
37.4813	1874.20	0.1023	2.78617	29.59
37.7151	1296.91	0.1023	2.76951	20.47
39.4999	227.47	0.1535	2.64904	3.59
41.5451	376.98	0.1535	2.52398	5.95
42.4631	3358.16	0.1791	2.47186	53.01
46.1356	1158.97	0.1279	2.28460	18.30
46.4087	1185.42	0.1279	2.27189	18.71
47.9563	138.72	0.1535	2.20270	2.19
49.4613	833.68	0.1279	2.13971	13.16
51.7900	110.50	0.3070	2.04970	1.74
53.3586	1305.46	0.0768	1.99368	20.61
58.9280	355.94	0.2047	1.81987	5.62
61.5229	70.24	0.6140	1.75018	1.11
62.8240	100.40	0.3070	1.71752	1.58
67.5928	231.82	0.3070	1.60928	3.66
70.0616	70.29	0.8187	1.55946	1.11
72.6512	420.37	0.3582	1.51113	6.64
78.1586	73.34	0.6140	1.41999	1.16

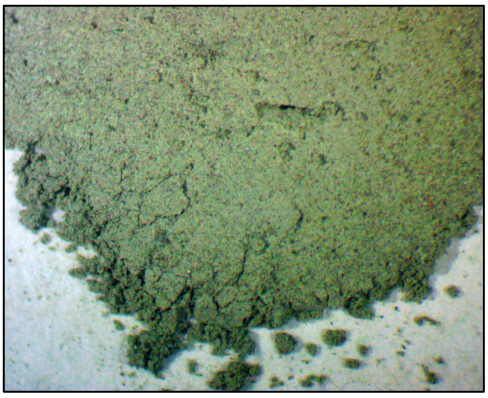
APPENDIX E:

Binocular Microscope Photographs of the Brochantite and Malachite Samples

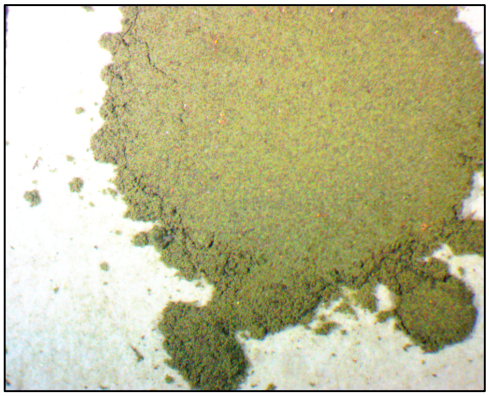
All brochantite and malachite samples considered for the doctoral project are listed, including those eliminated during processing. Refer to Appendix A for context details on the samples, and Appendices B, C and D for instrumental material characterizations. Photographs of samples were taken before processing. All images are scaled to approximately one centimeter in width.

BROCHANTITE SAMPLES

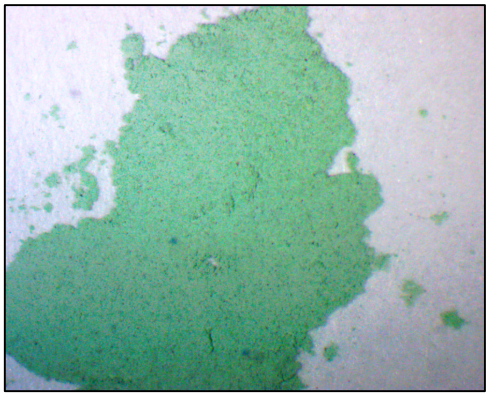
Berne, Switzerland



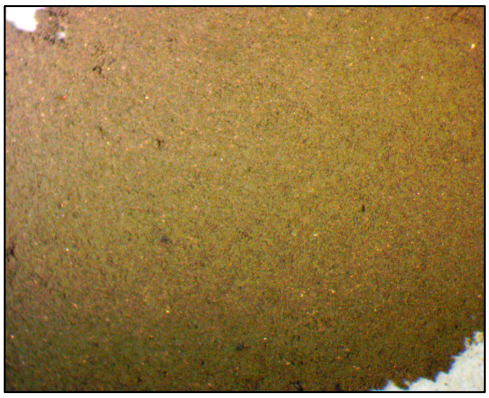
Ottawa, Canada



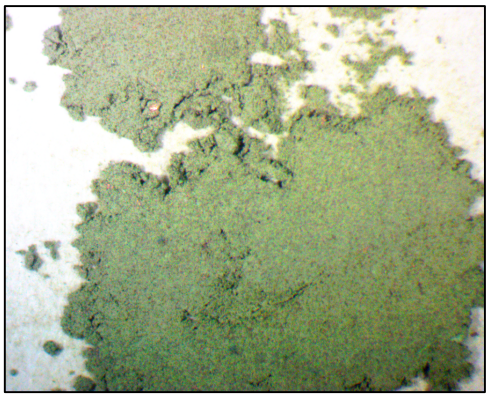
American Embassy Roof



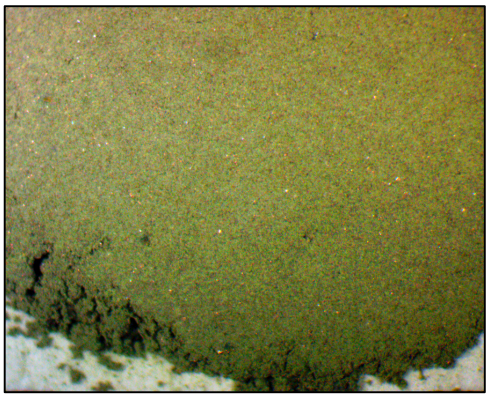
Booth House Roof



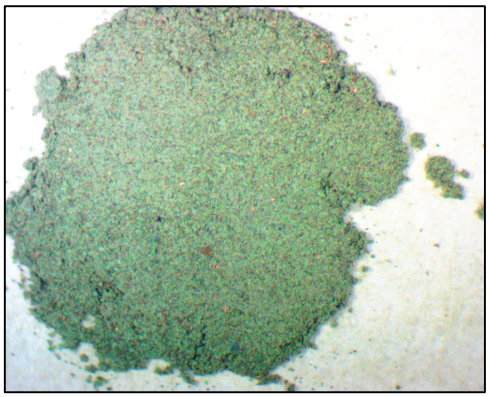
Bruyère Hospital Roof 1



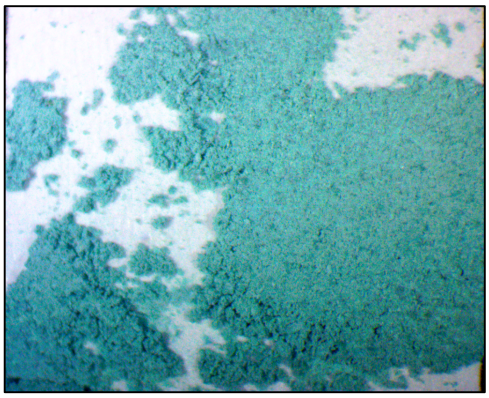
Bruyère Hospital Roof 2



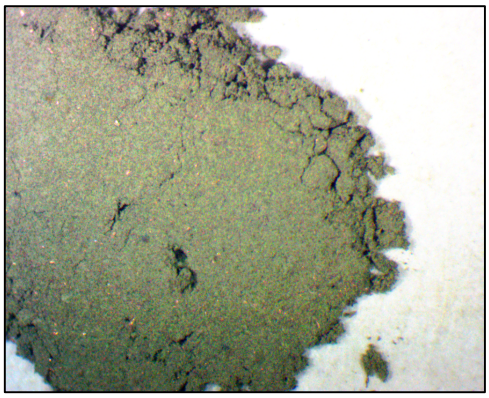
Center Block Building Roof 1



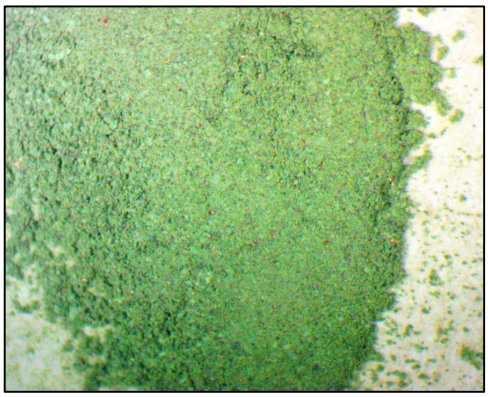
Center Block Building Roof 2



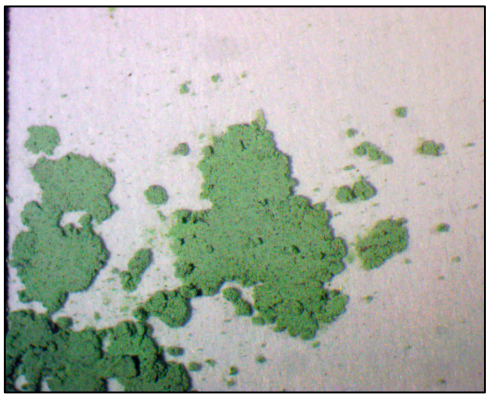
Roadside Handicap Sign



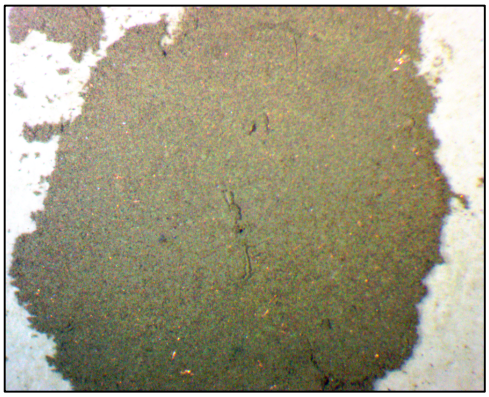
Justice Building Roof



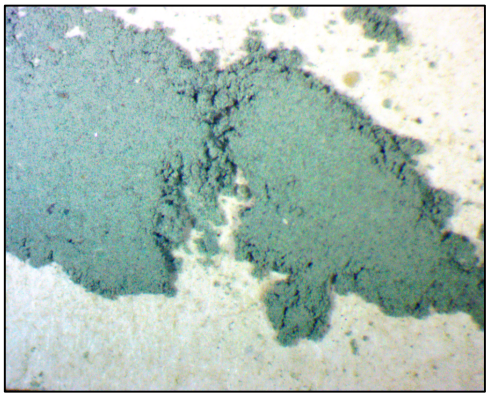
Langevin Block Building Roof



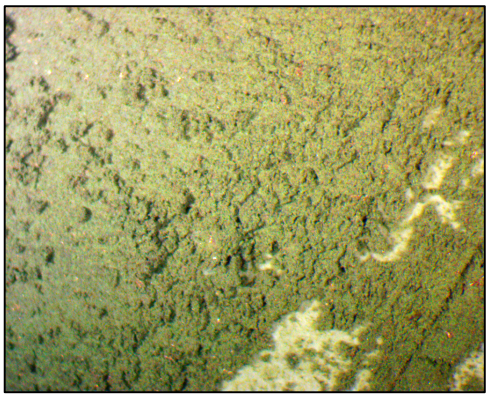
Hotel Lord Elgin Roof



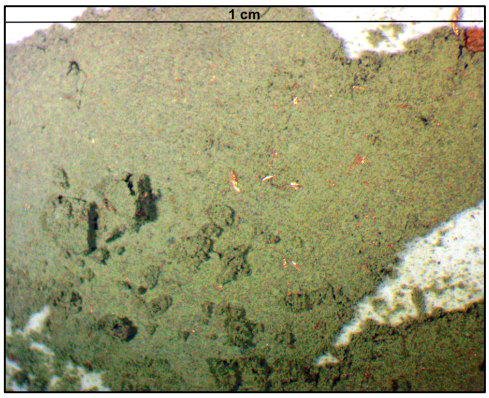
Mystery Building Roof



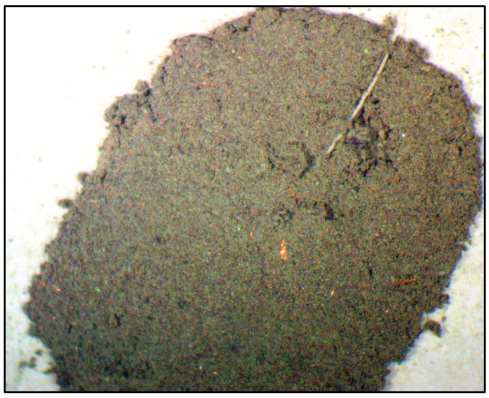
Supreme Court Building Roof



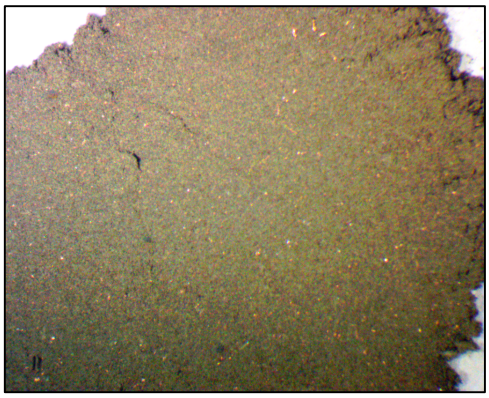
Wellington Building Roof



West Block Building Roof

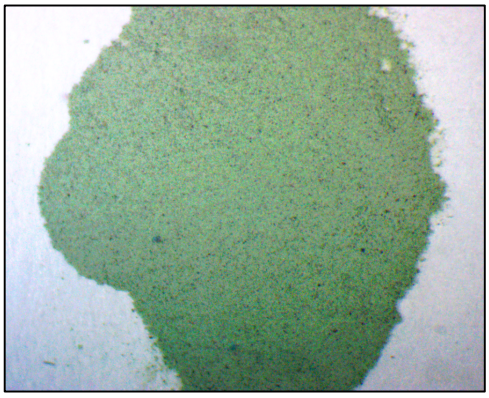


West Memorial Building Roof 1

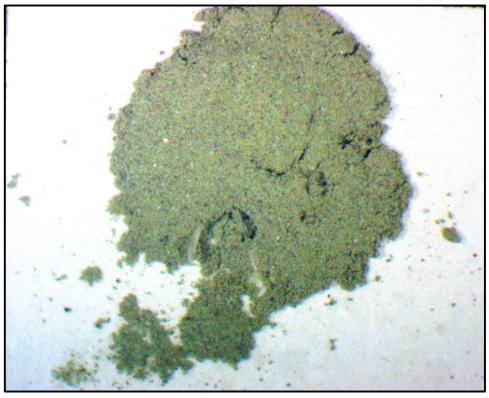


West Memorial Building Roof 2

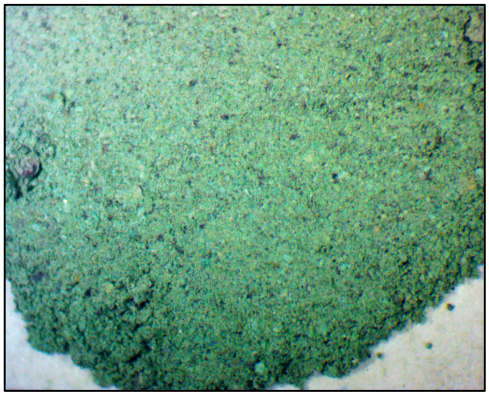
Oxford, England



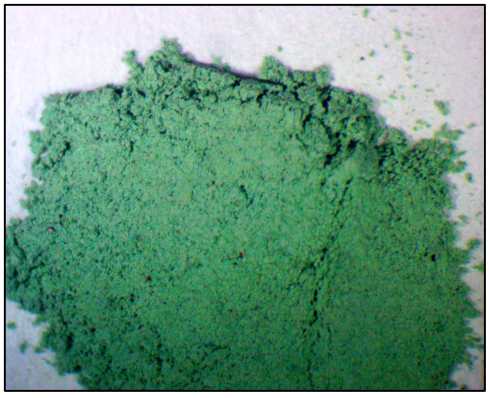
Corpus Christi College Roof



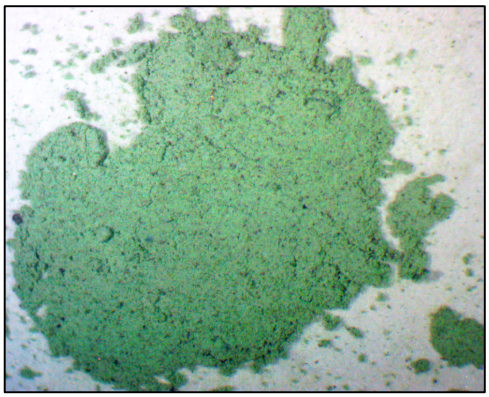
Flore Statue, Maison Française



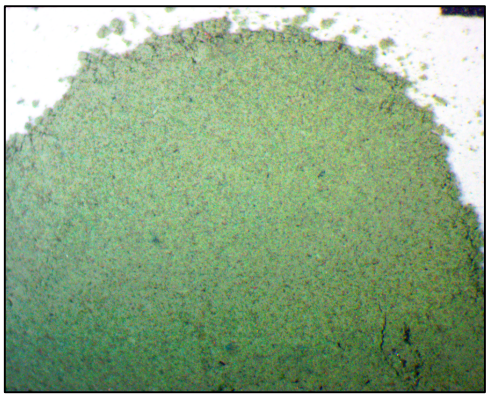
Jesus Statue, Magdalen College



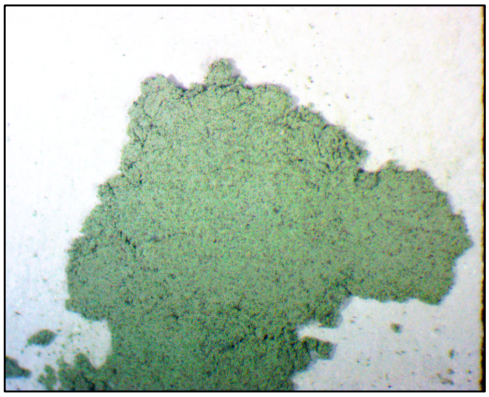
Old Observatory Roof



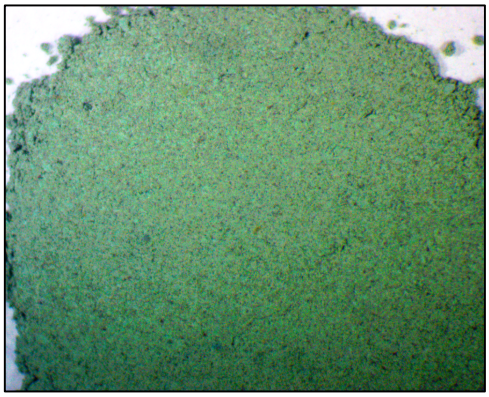
Oriel Library Roof



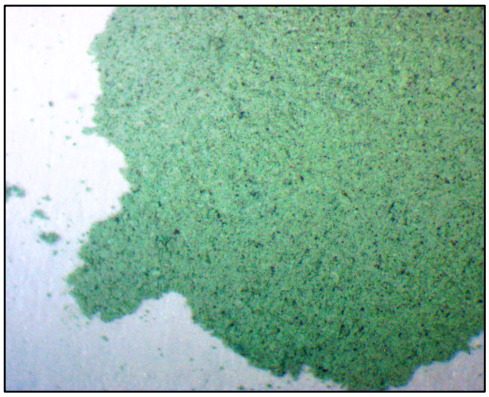
Oriental Institute Roof



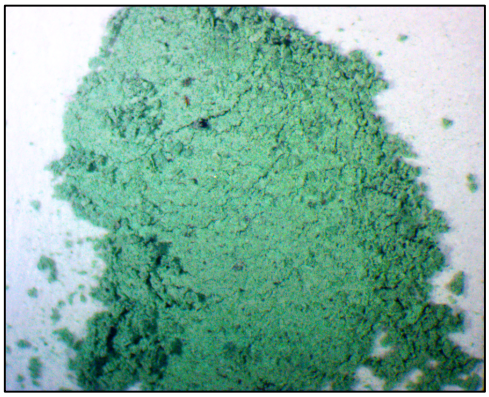
Philosophy Centre Roof



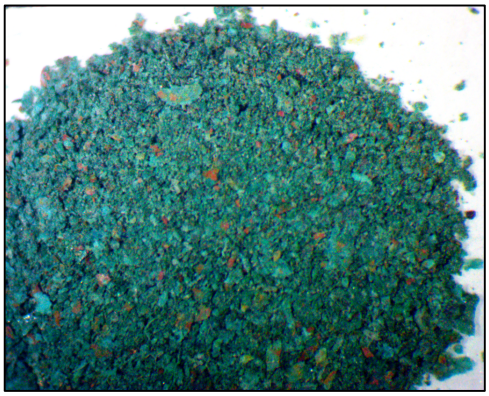
Rhodes Mandela House Cupola



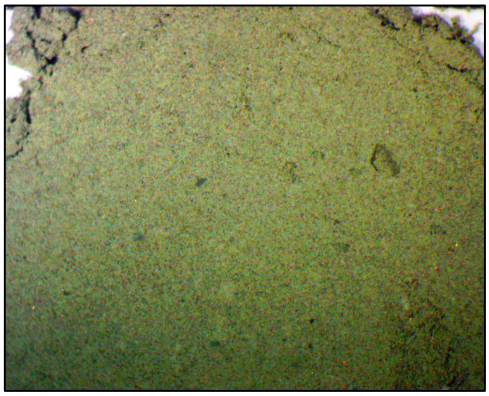
Sheldonian Urn Left



Sheldonian Urn Right

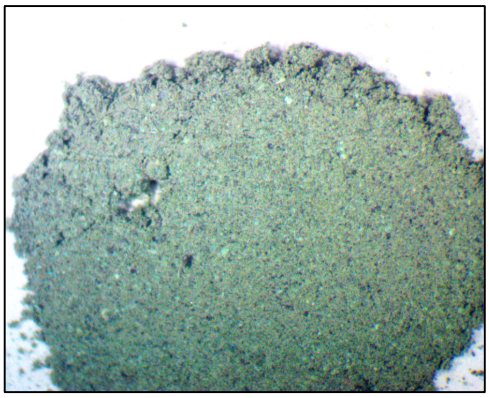


St. Catherine's College Door Hinge Plate

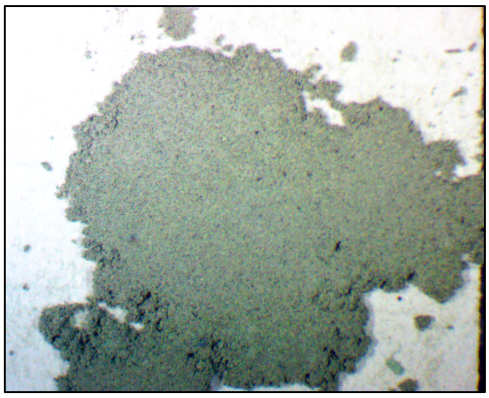


St. Cross Law Building Roof

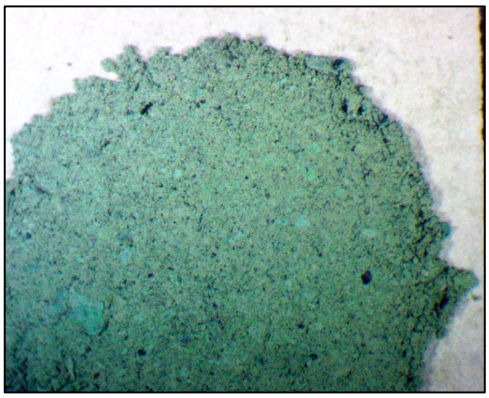
Tuscaloosa, Alabama, USA



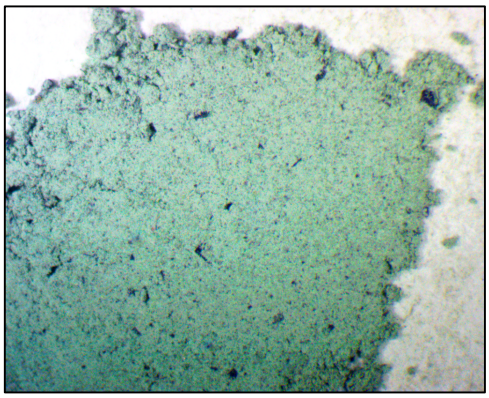
B. B. Comer Building Roof



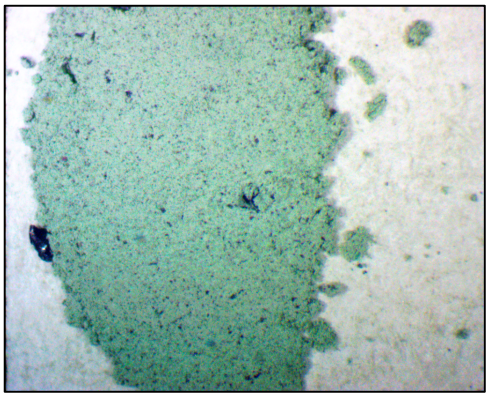
Bidgood Hall Roof



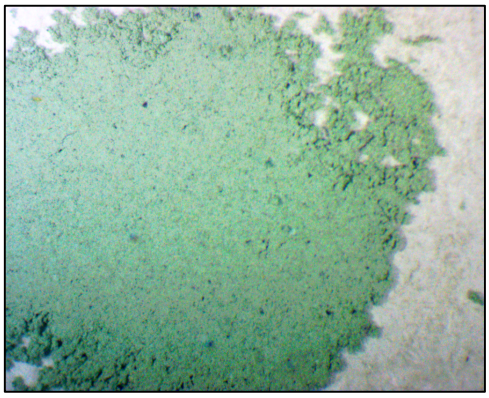
Bryce Hospital (Receiving Office) Awning



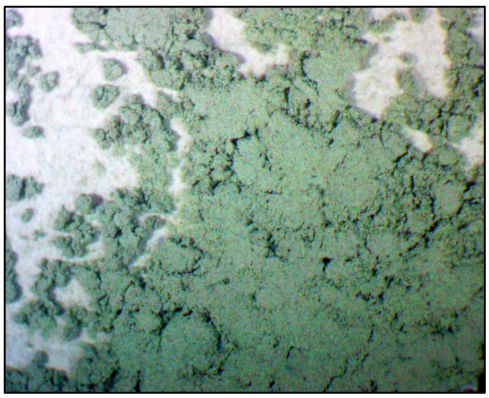
Bryce Hospital, Unknown Roof



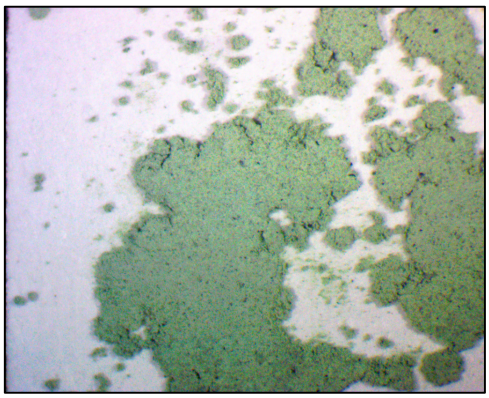
Bryce Hospital (Women's Administration) Gutter



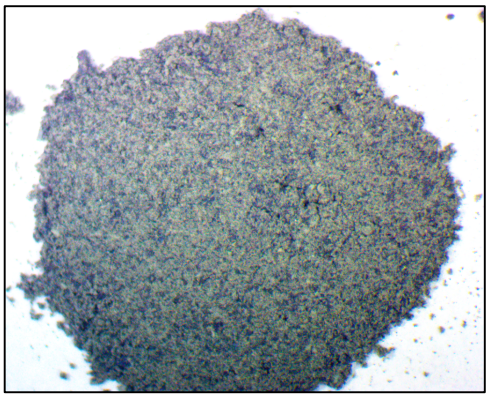
Carmichael Hall Roof



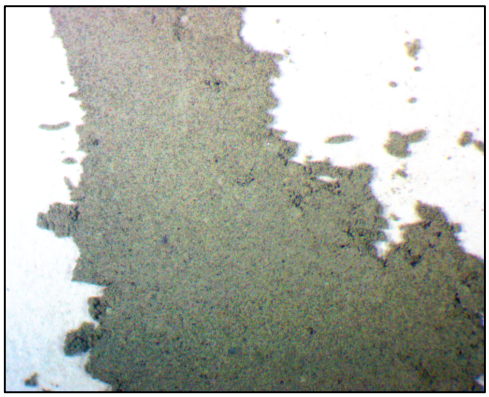
Carmichael Hall Roof Vent



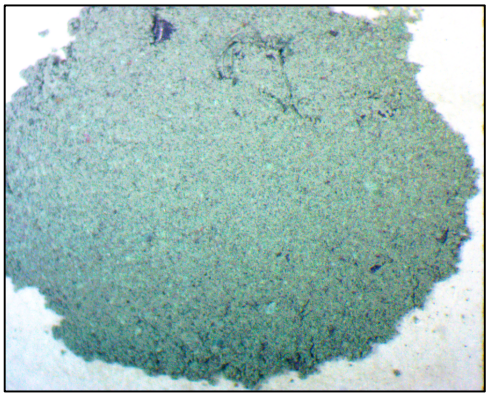
Farrah Hall Roof



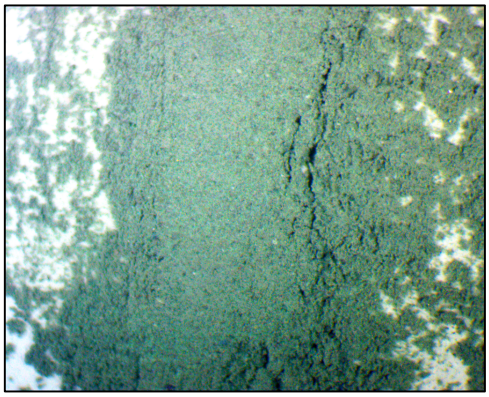
Gallalee Hall Roof



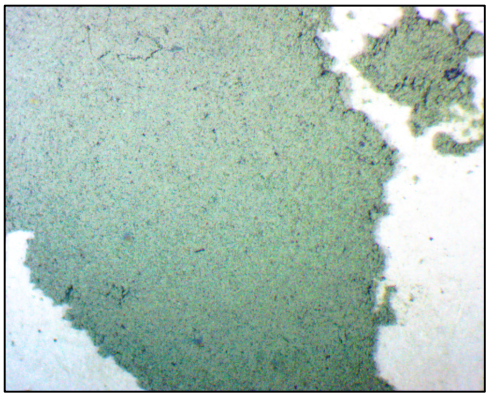
Gallalee Hall Roof Vent



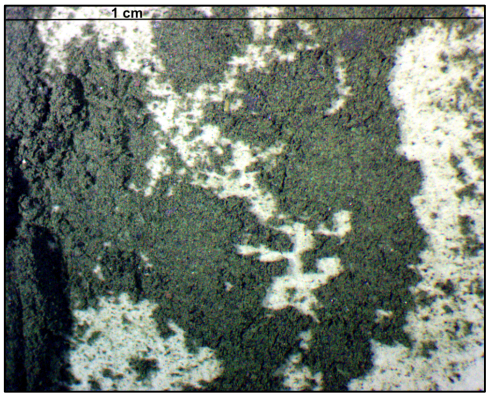
Mystery Tuscaloosa Roof



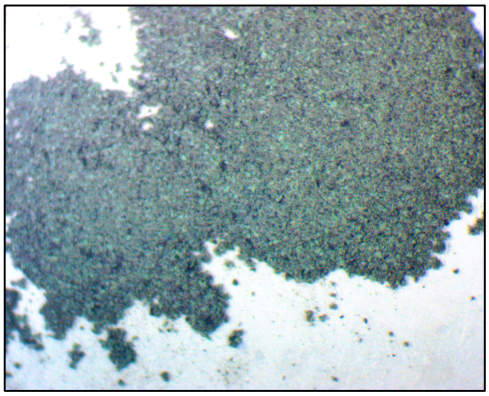
Presidential Hall Roof 1



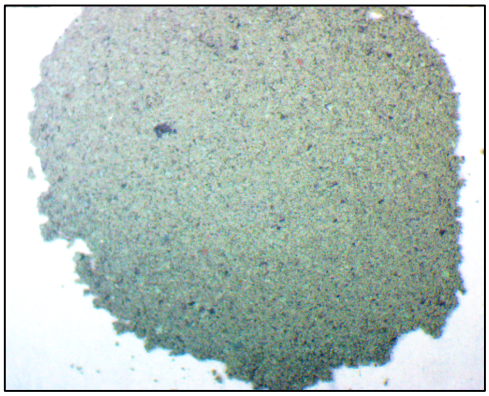
Presidential Hall Roof 2



Presidential Hall Roof 3

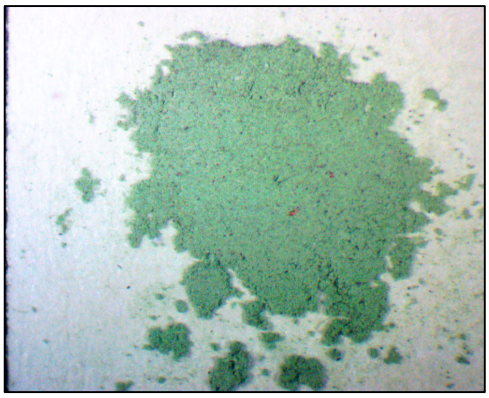


Rowan-Johnson Building Roof

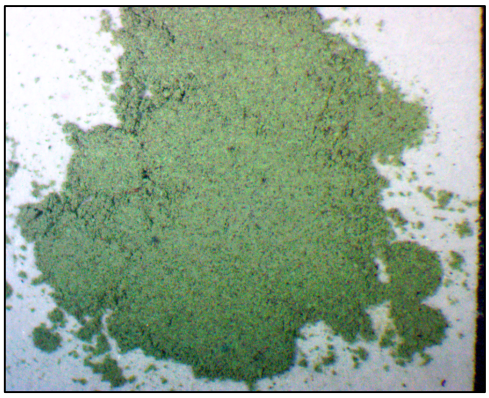


Wilson Hall Roof

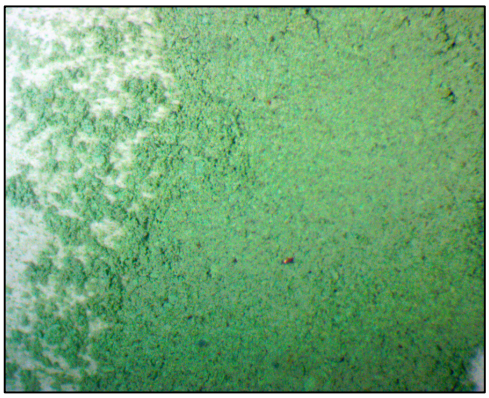
Vienna, Austria



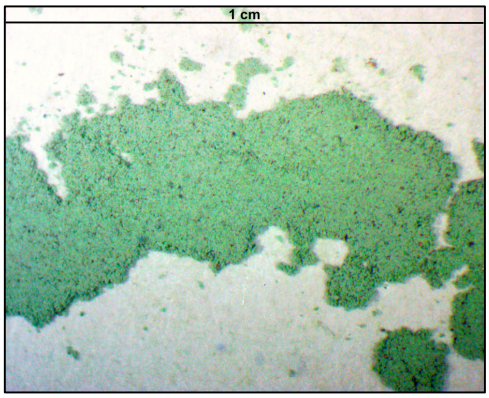
Burgtheater Chimney



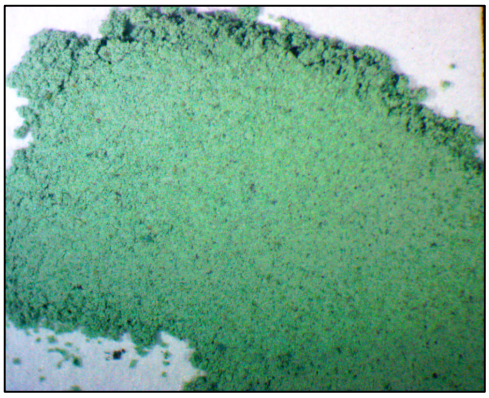
Linke Copper Sheet



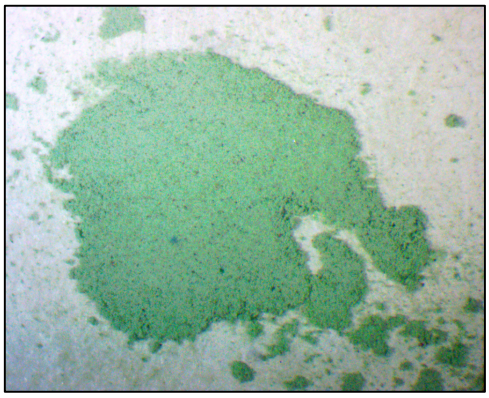
Linke Gilded Copper Sheet



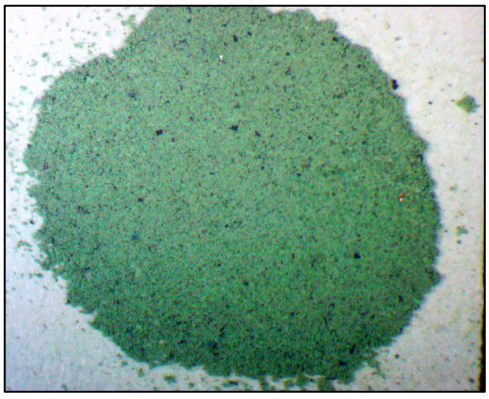
Hofburg Angel Statue



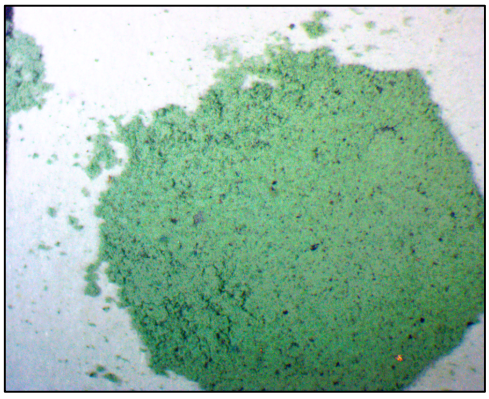
Hofburg Butterfly House Roof



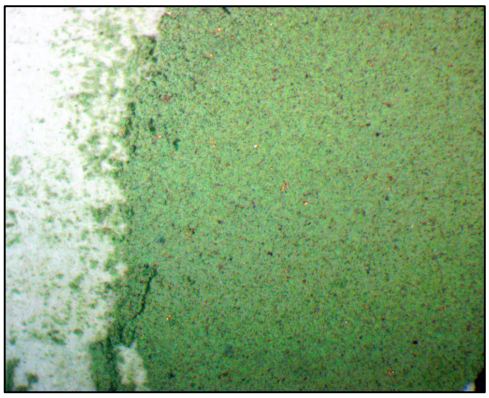
Hofburg Cupola Door



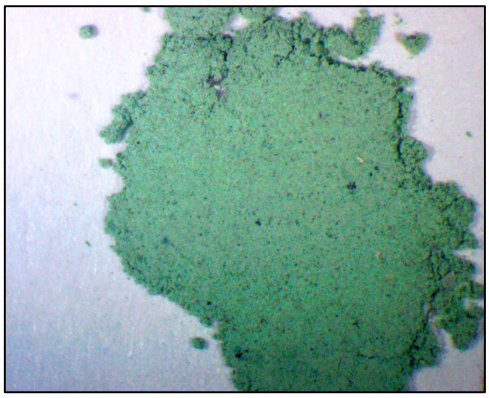
Hofburg Leaf Decoration



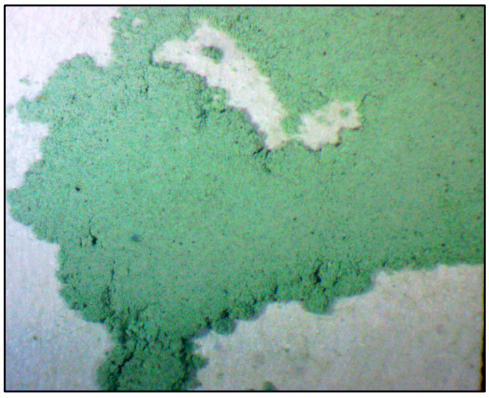
Hofburg Helmet



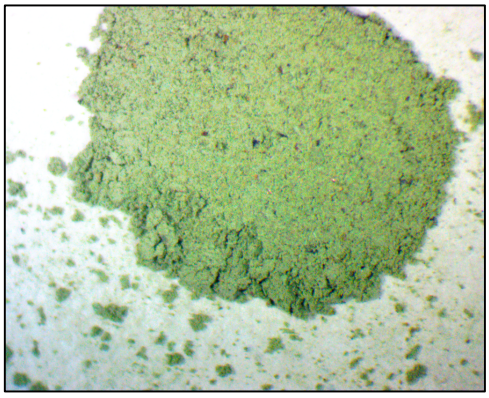
Hofburg Temple Roof



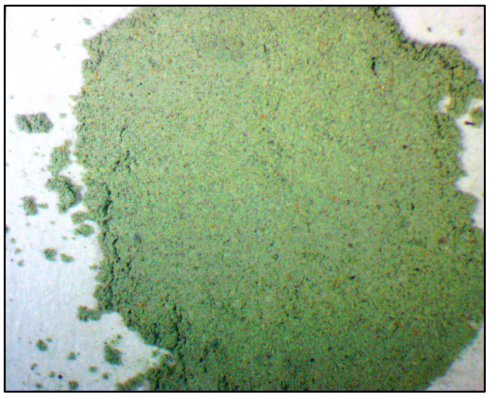
Karlskirche Roof Drain



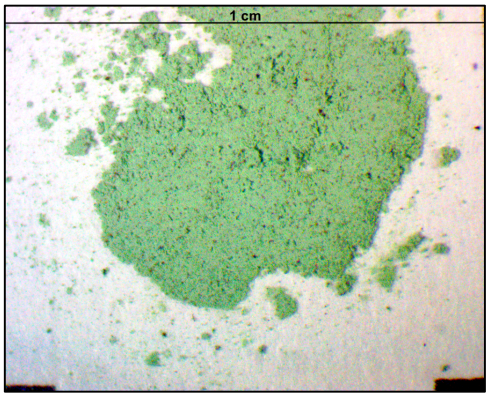
Karlskirche Roof Vent



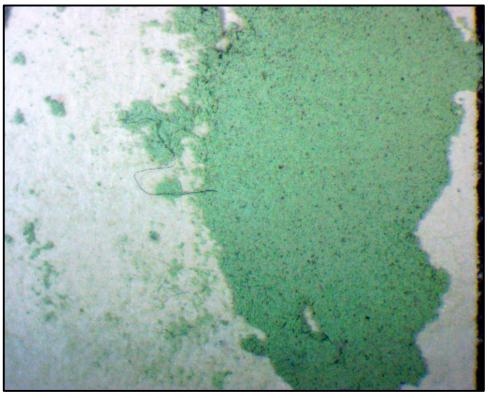
Peterskirche Roof



Vienna Tech University Roof Sheet



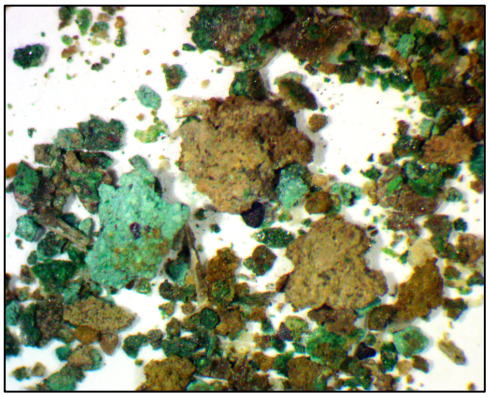
Vienna Tech University Roof



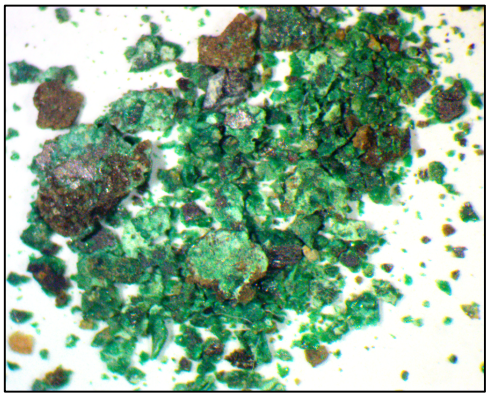
Votivekirche Roof

MALACHITE SAMPLES

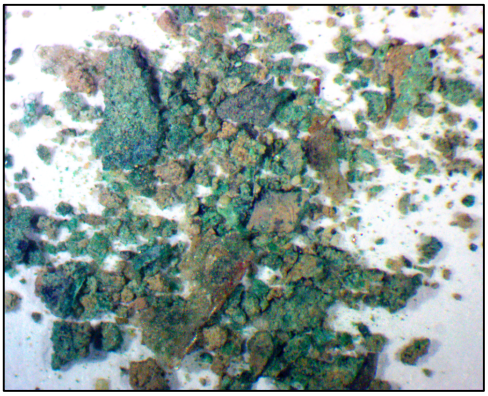
"Asia"



A1-Duo Bell

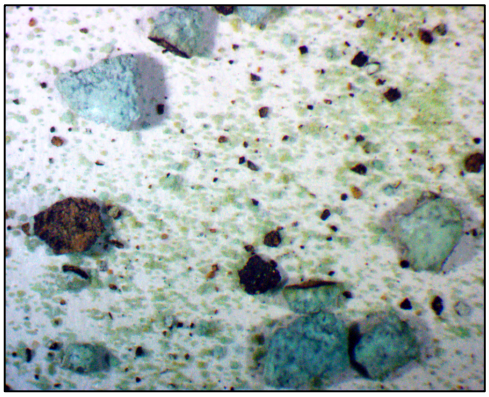


A2-Dagger Axe

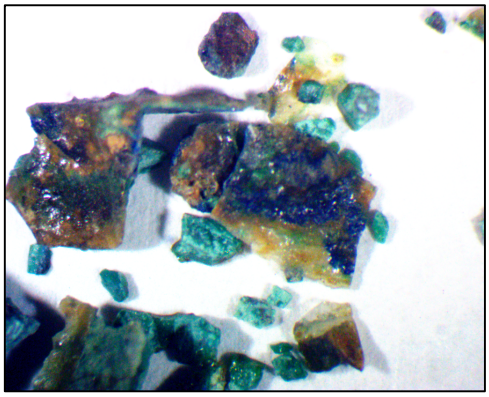


A3-Oil Burner

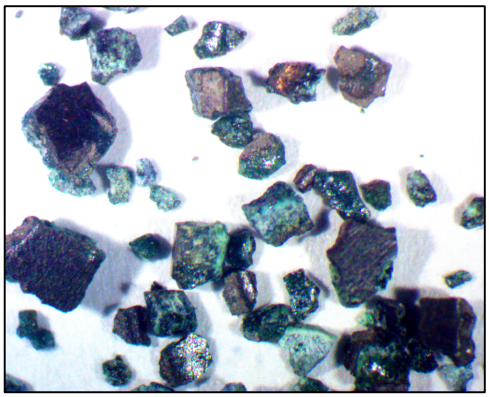
China



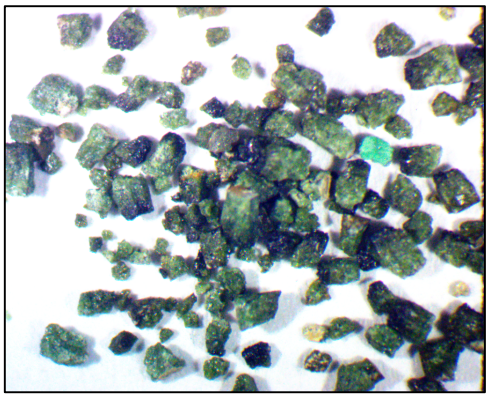
C1-Niucheng, Jiangxi



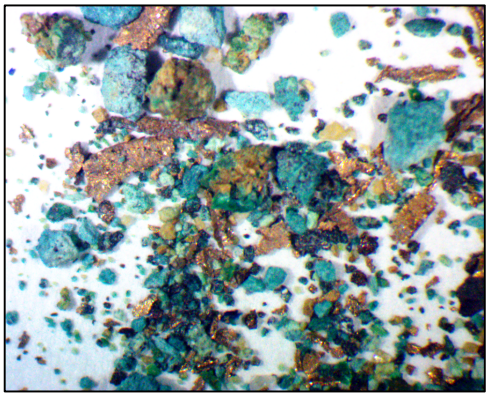
C2-Hunan



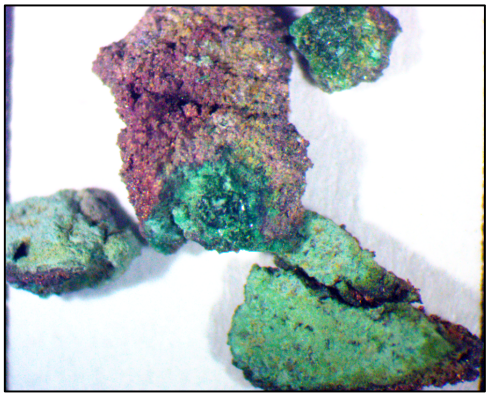
C3-Hunan



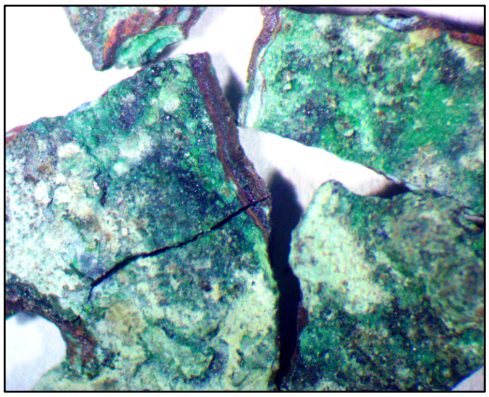
C4-Hunan



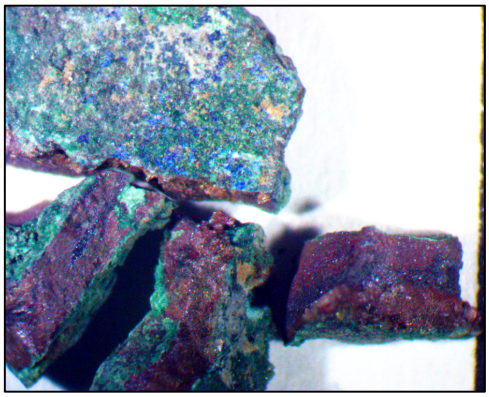
C5-Hunan



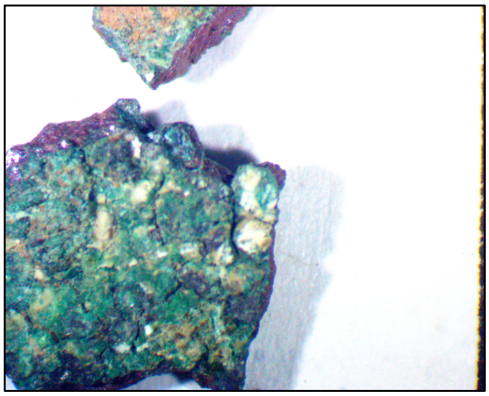
C6-Hunan



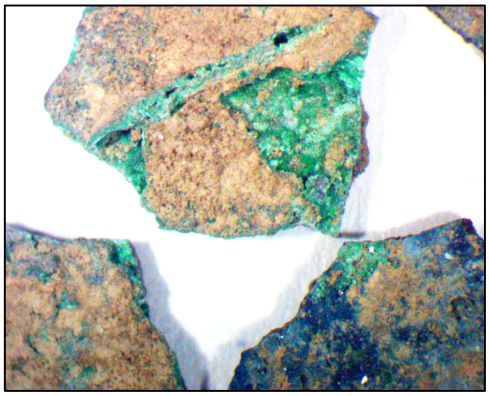
C7-Shaanxi



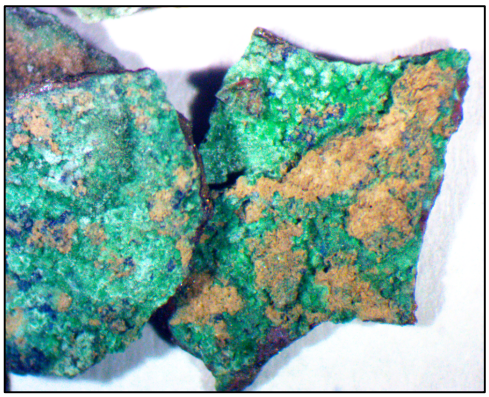
C8-Shaanxi



C9-Shaanxi



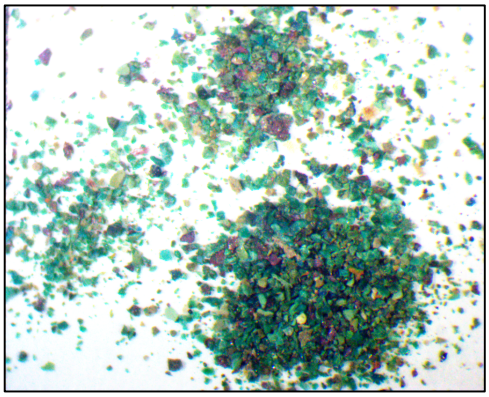
C10-Shaanxi



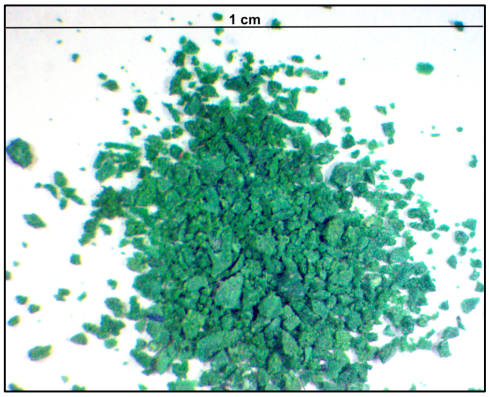
C11-Shaanxi



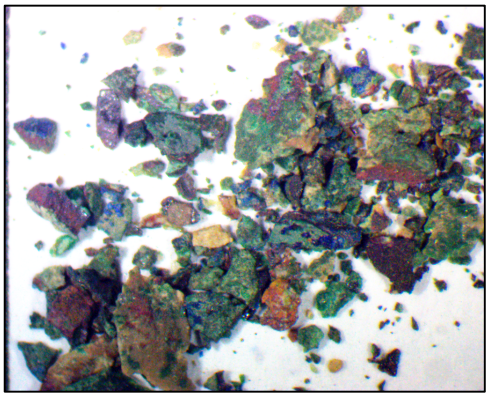
C14-Hubei



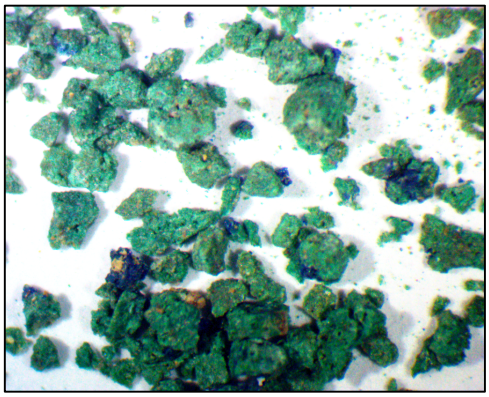
CGN1-Gansu?



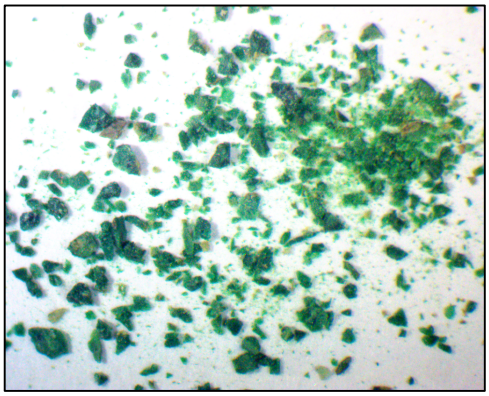
CGN2-Gansu?



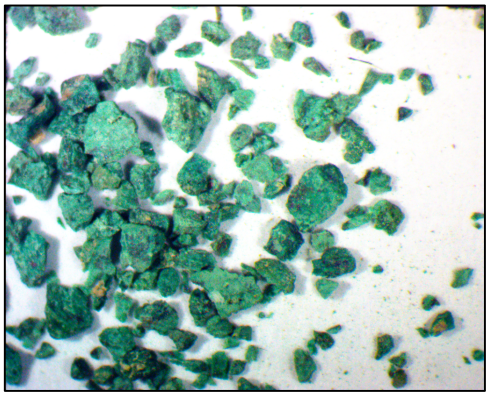
CGN3-Gansu



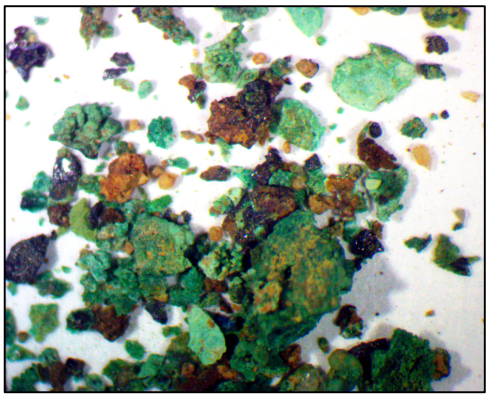
CGS1-Guangxi



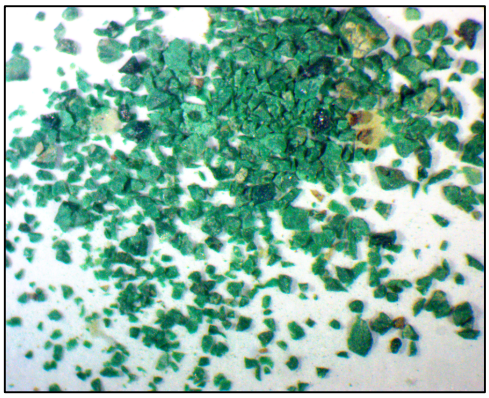
CGS2-Guangxi



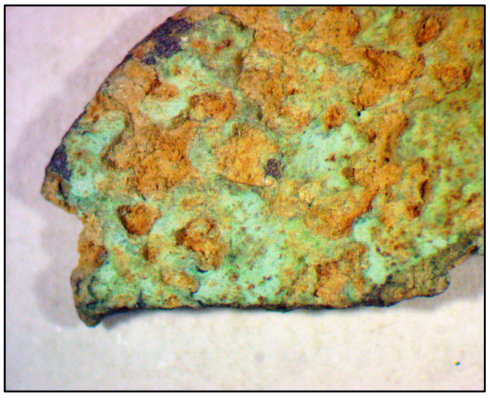
CGS3-Guangxi



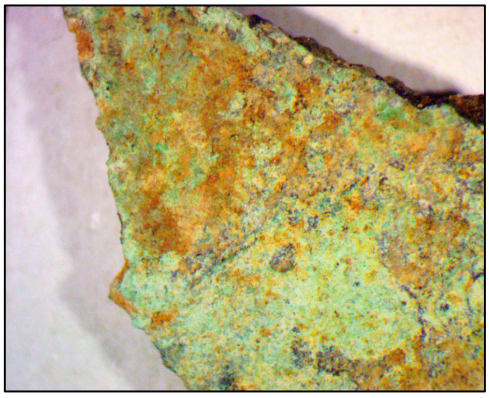
CGS4-Guangxi?



CGS5-Guangxi



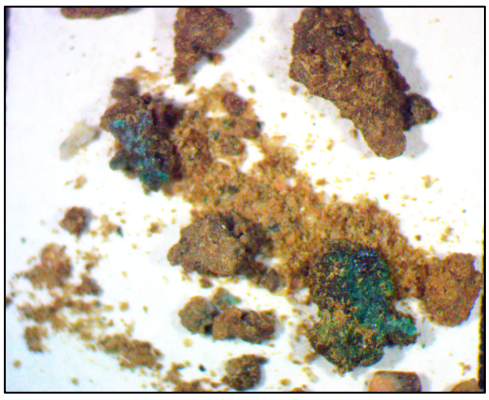
CY1-Guangxi



CY2-Guangxi



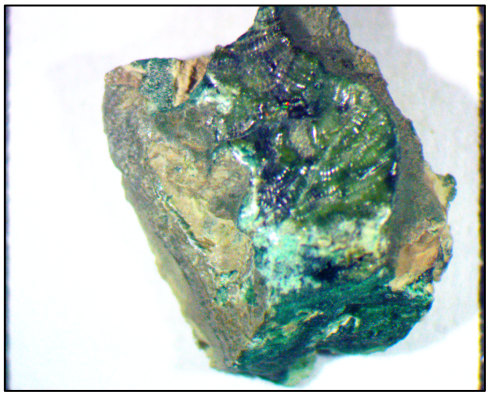
CY3-Guangxi



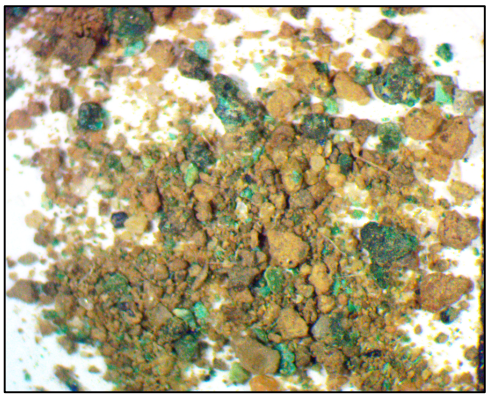
CY4-Guangxi



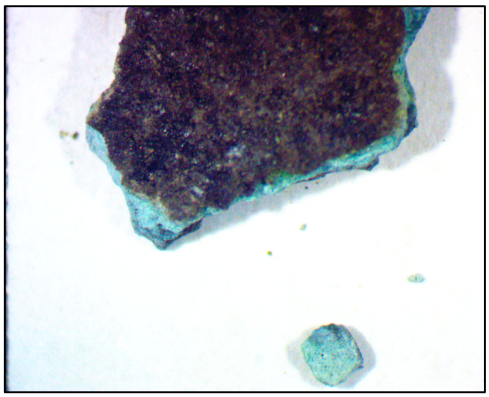
CY5-Guangxi



CY6-Guangxi



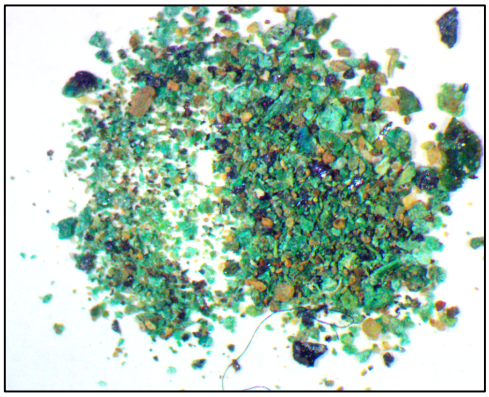
CY7-Guangxi



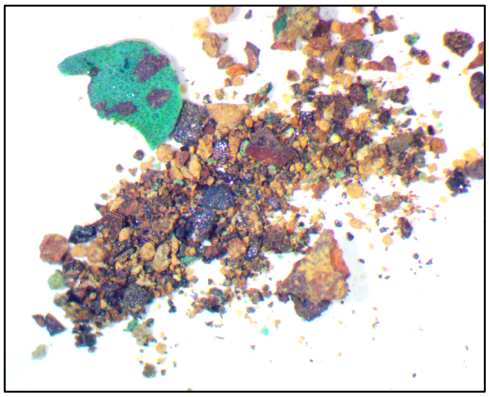
CY8-Guangxi



CY9-Guangxi



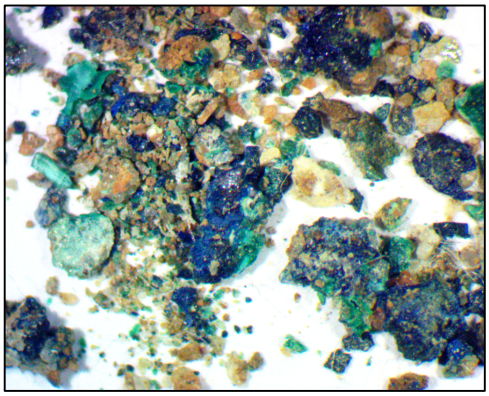
CY10-Guangxi



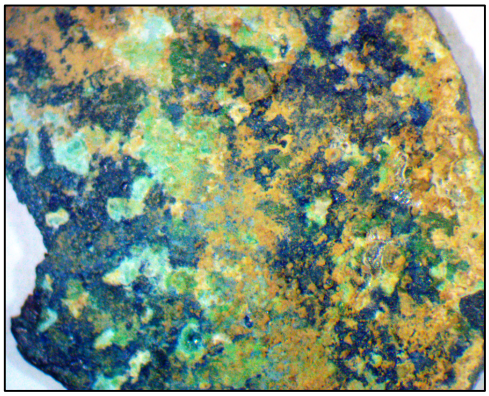
CY11-Guangxi?



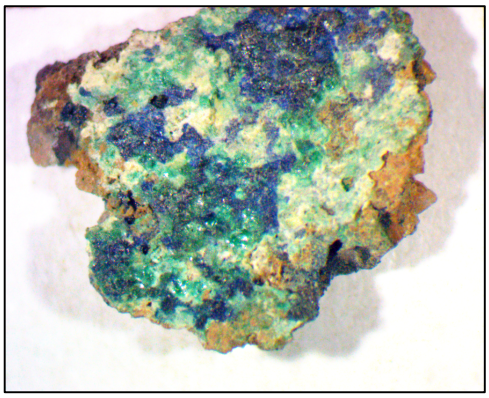
CY12-Guangxi



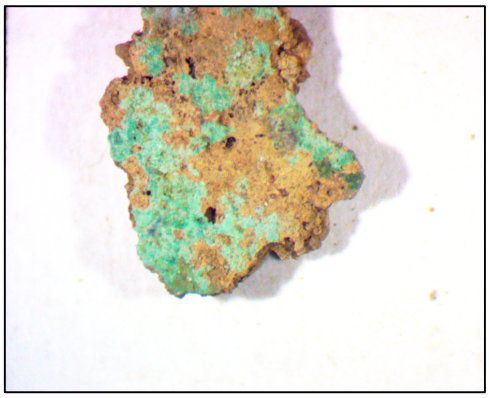
CY13-Guangxi?



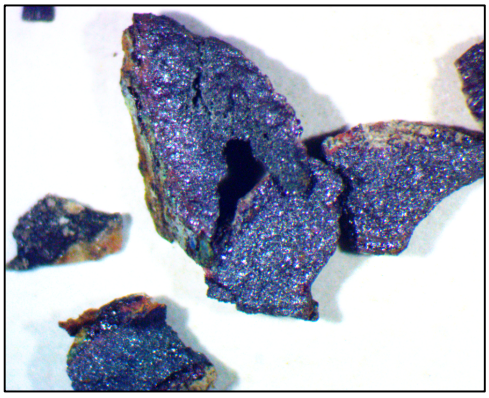
CY14-Guangxi?



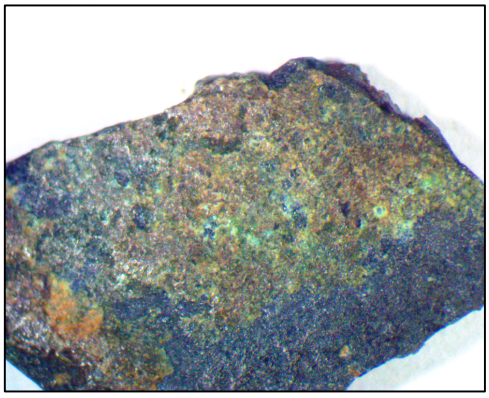
CY15-Unknown China



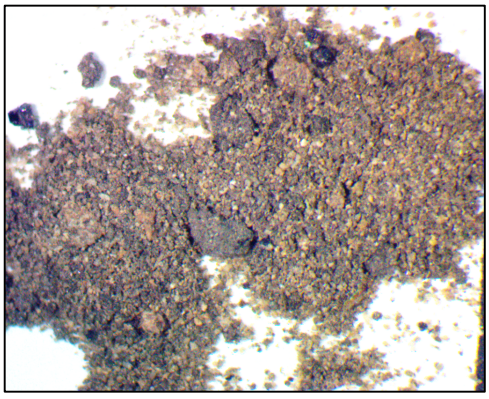
CY16-Unknown China



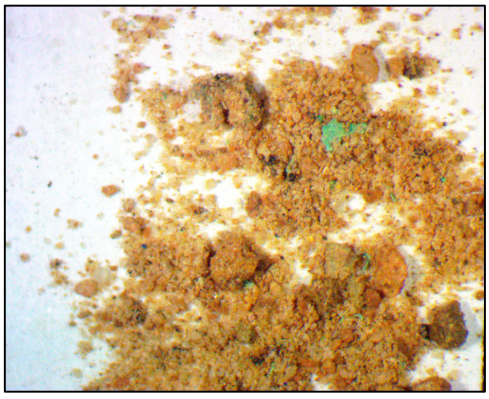
CY17-Unknown China



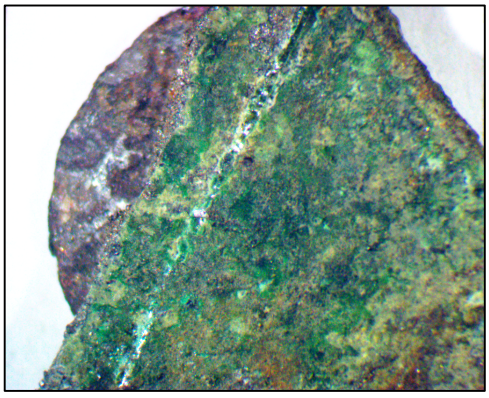
CY18-Guangxi



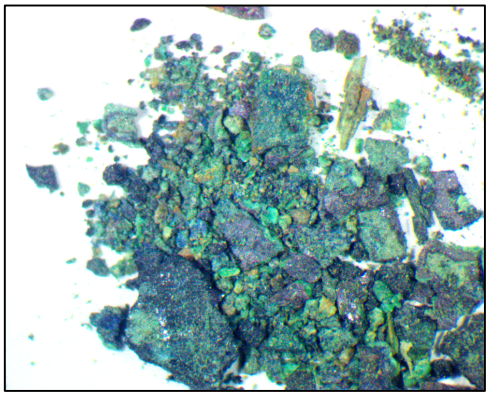
CY19-Unknown China



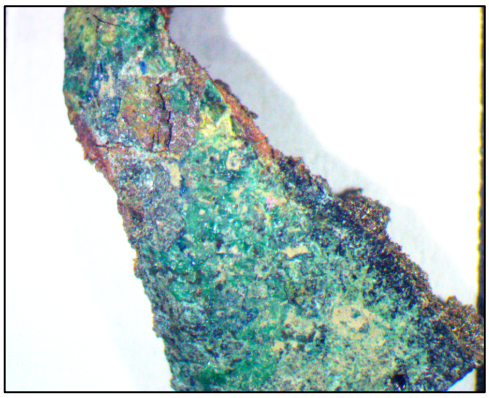
CY20-Unknown China



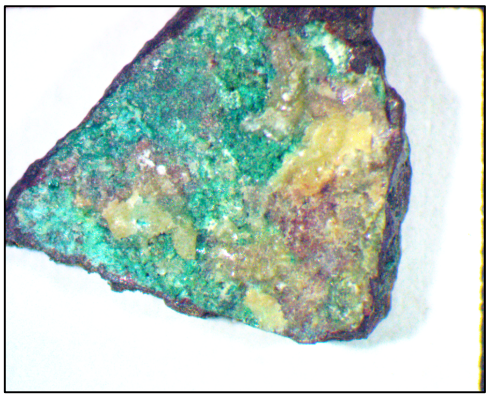
CY21-Jiangsu



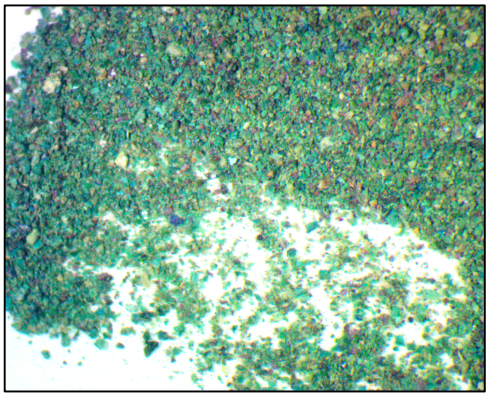
CY22-Jiangsu



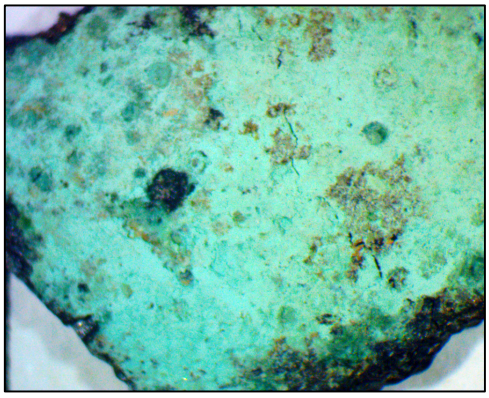
CY23-Unknown China



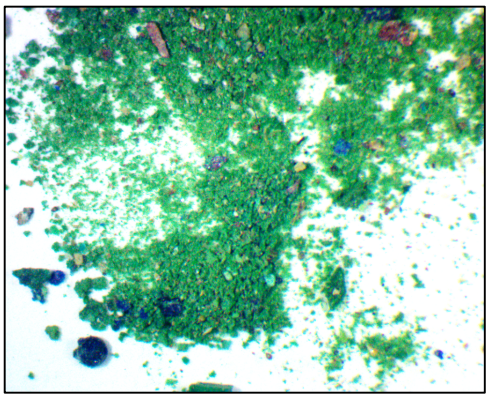
CY24-Unknown China



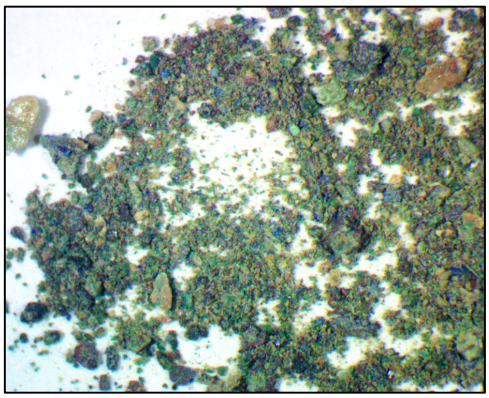
CY25-Unknown China



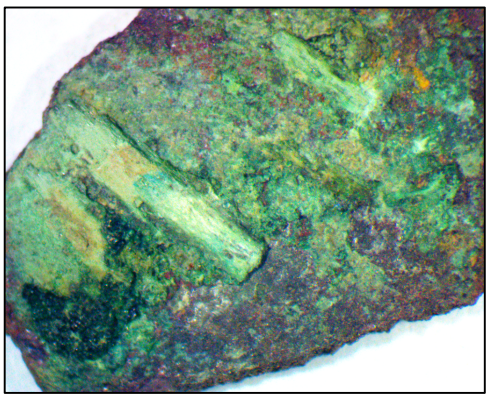
CY26-Unknown China



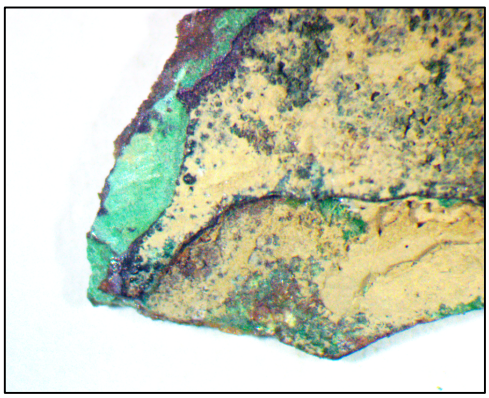
CY27-Unknown China



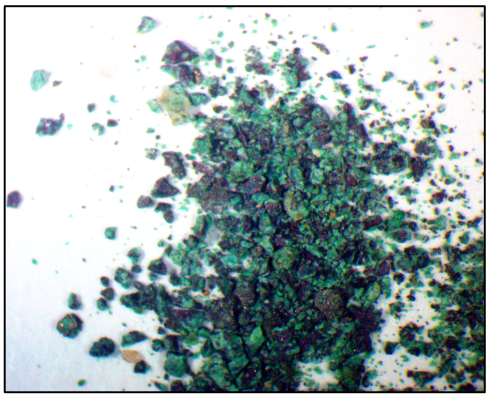
CY28-Gansu?



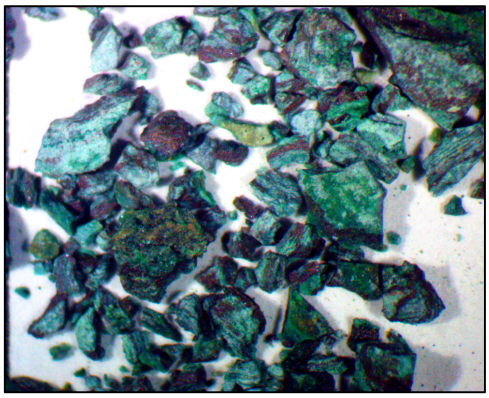
CY29-Unknown China



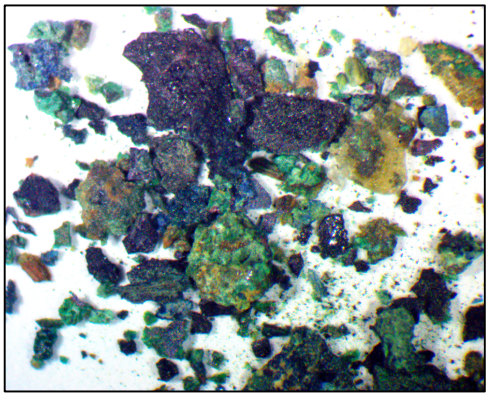
CY30-Gansu



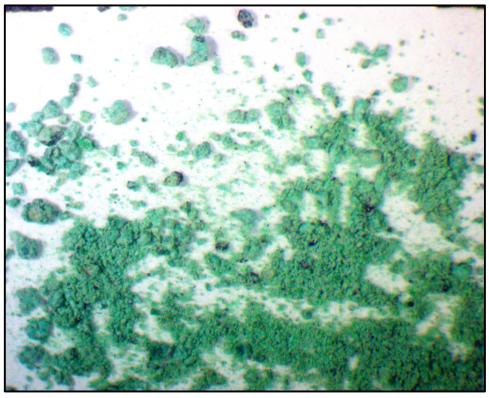
CHN1-Hubei



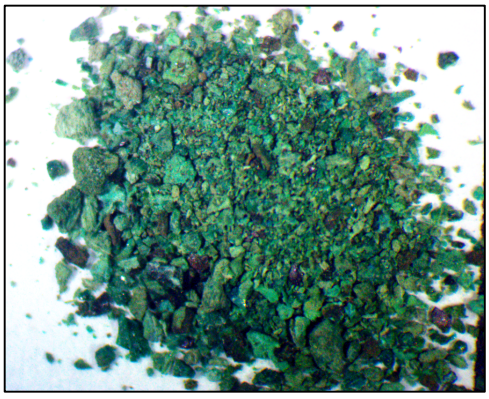
CHN2-Hubei



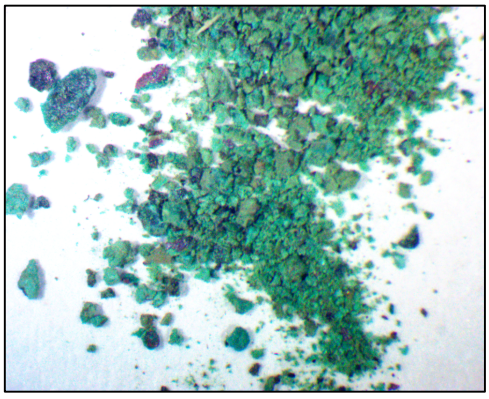
CJN-Jiangsu



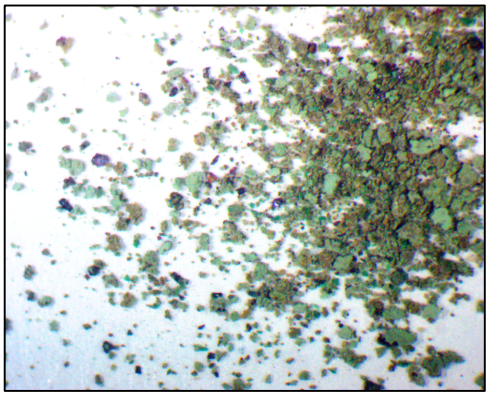
CJS-Jiangxi



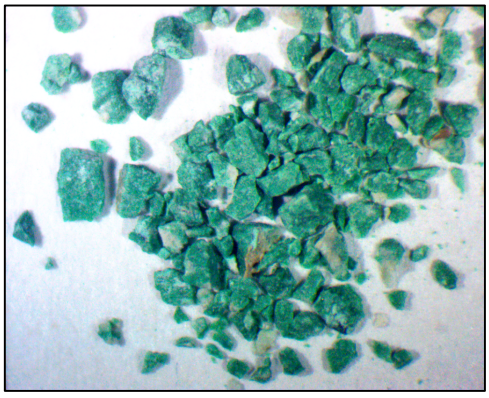
CNM1-Unknown China, Ningxia?



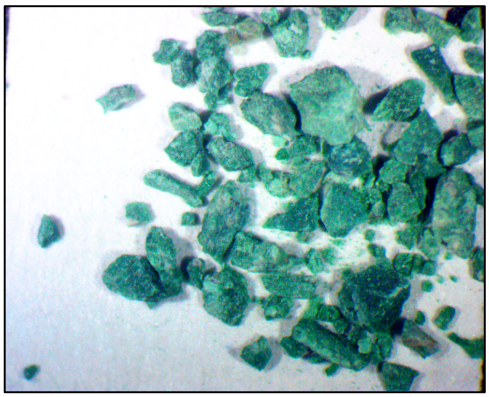
CNM2-Unknown China, Ningxia?



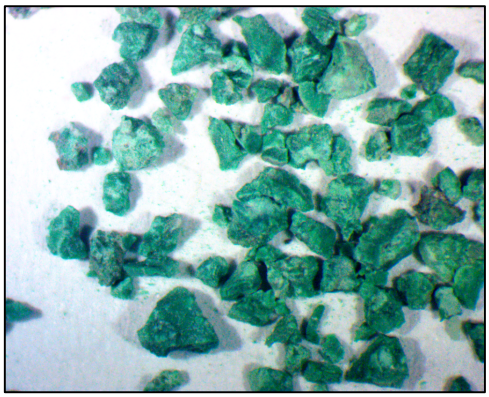
CNP-Ningxia



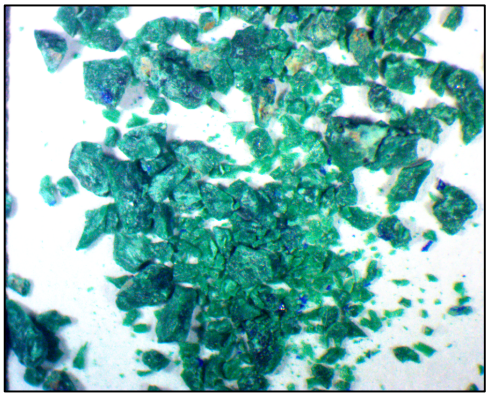
CNW1-West Ningxia



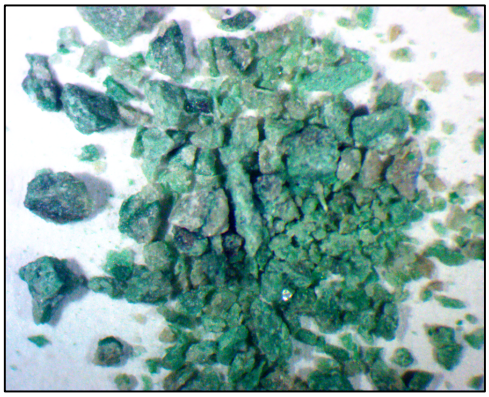
CNW2-West Ningxia



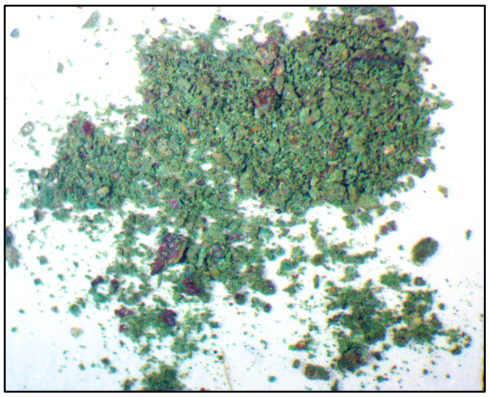
CNW3-West Ningxia



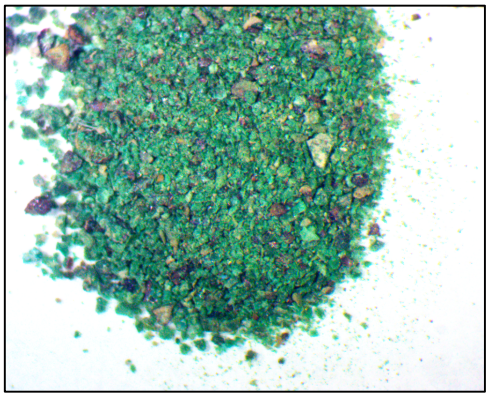
CNW4-West Ningxia



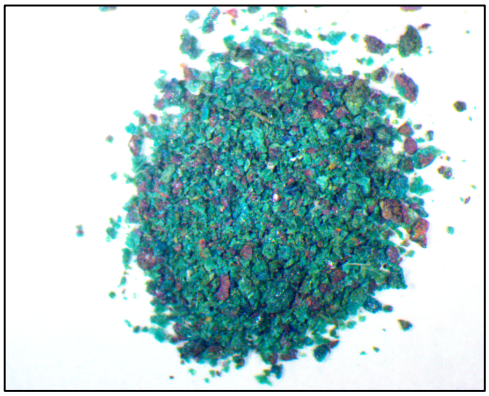
CNW5-West Ningxia



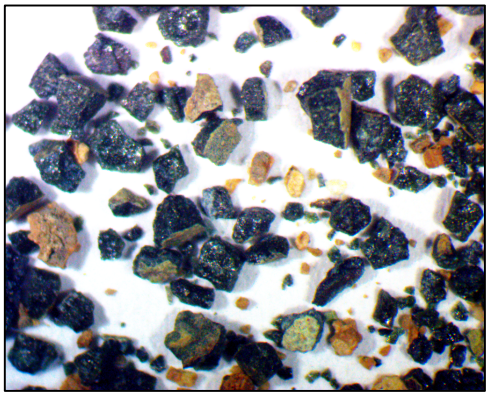
CNY1-Ningxia



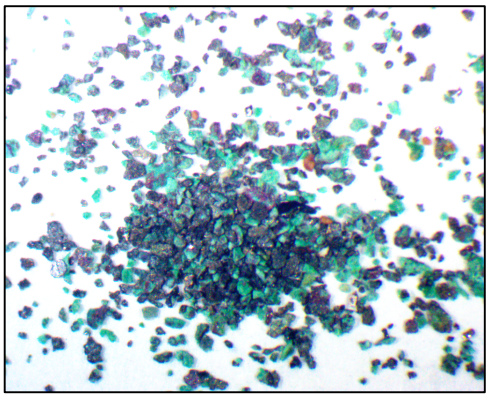
CNY2-Ningxia



CNY3-Ningxia



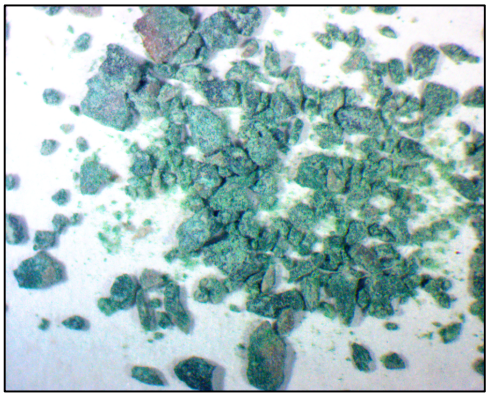
CHS1-Hunan



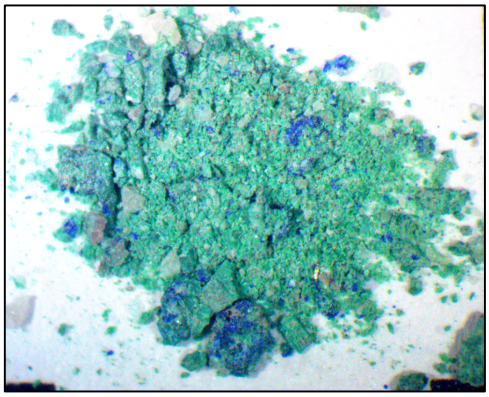
CHS2-Hunan



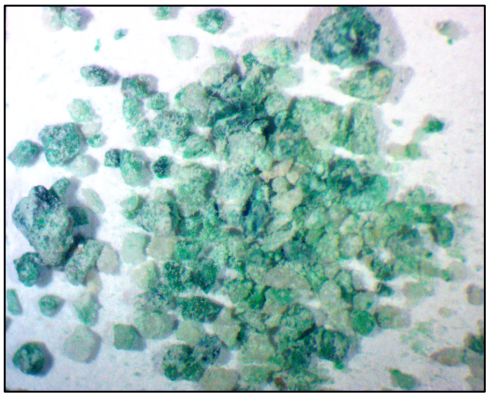
CHS3-Hunan



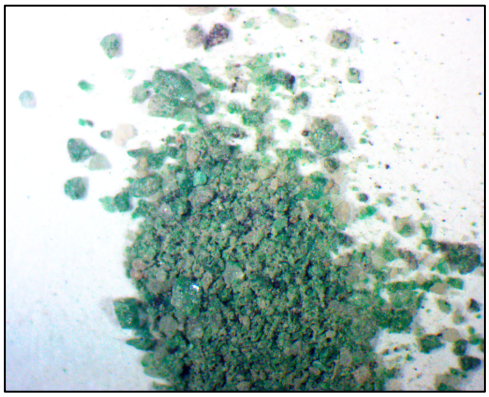
CNWg1-Ninxgia Ore



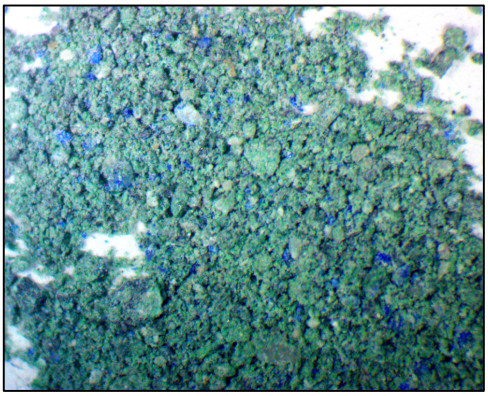
CNWg2-Ningxia Ore



CNWg3-Ningxia Ore

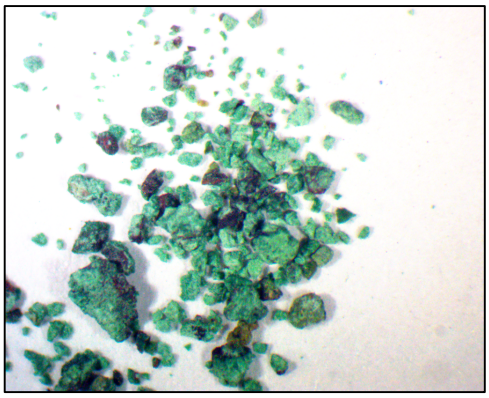


CNWg4-Ningxia Ore

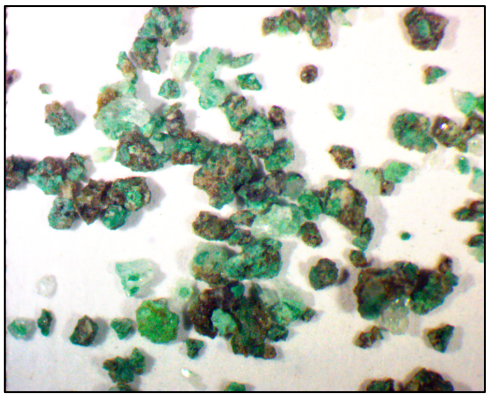


CNWg5-Ningxia Ore

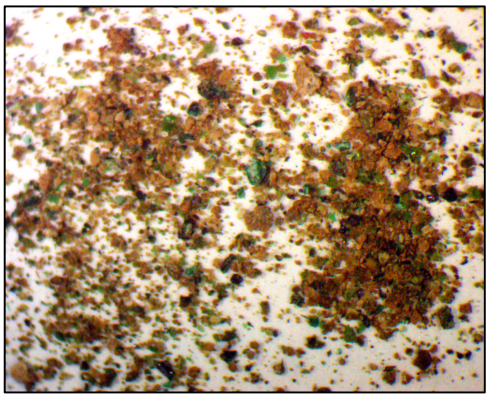
Cyprus



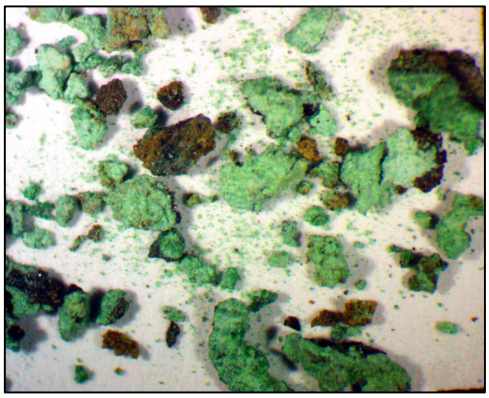
CYP1-Kalopsida



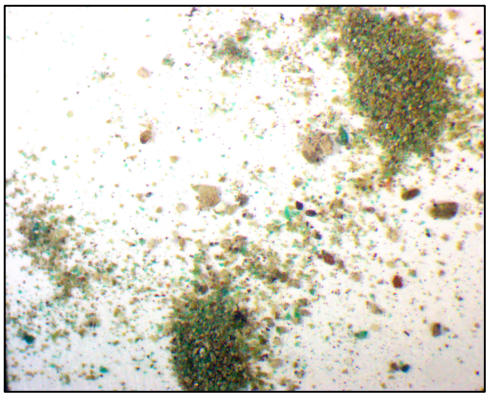
CYP2-Kalopsida



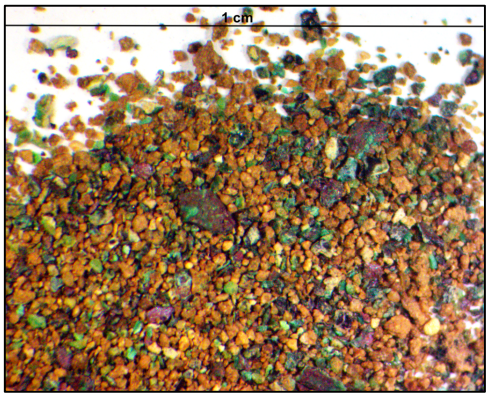
RC1-Episkopi Seraya



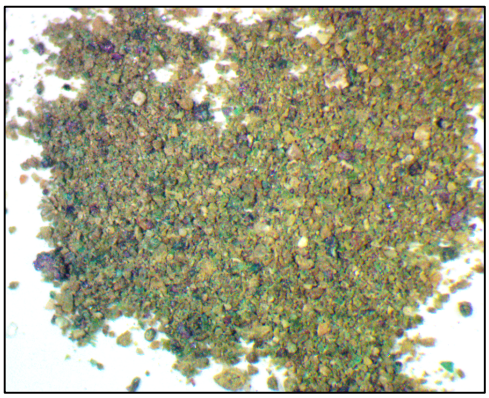
RC2-Pyla Kokkinokremos



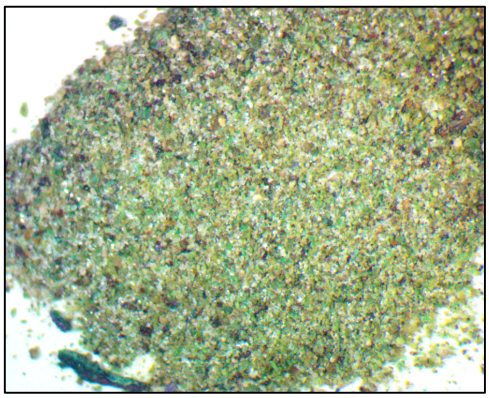
RC3-Politiko



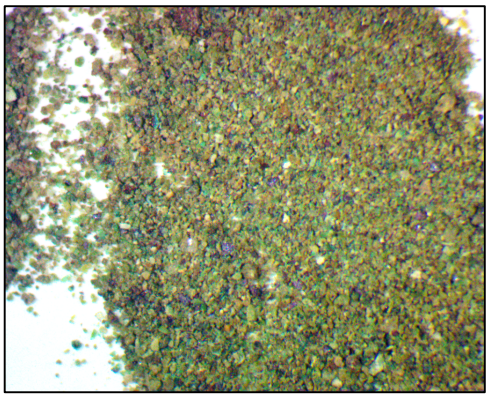
RC4-Pyla Kokkinokremos



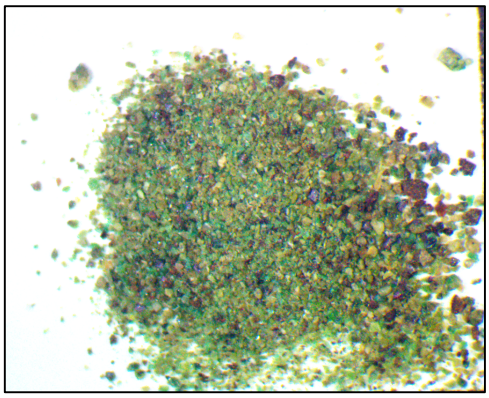
PK.2014.0028



PK.2014.0033

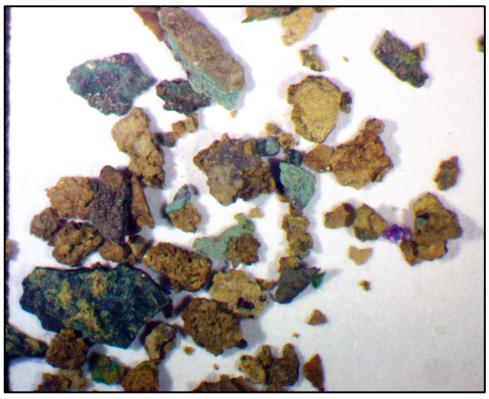


PK.2014.0034

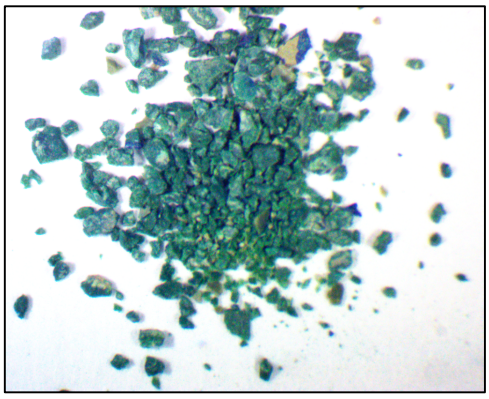


PK.2014.0037

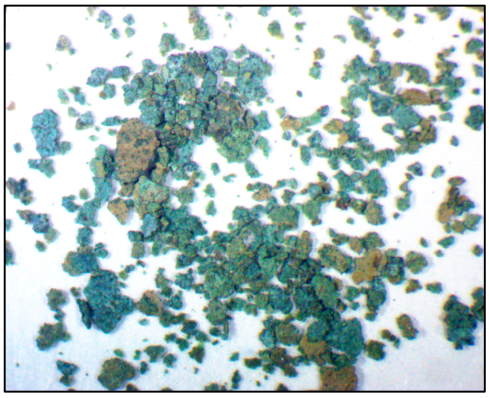
Southern England



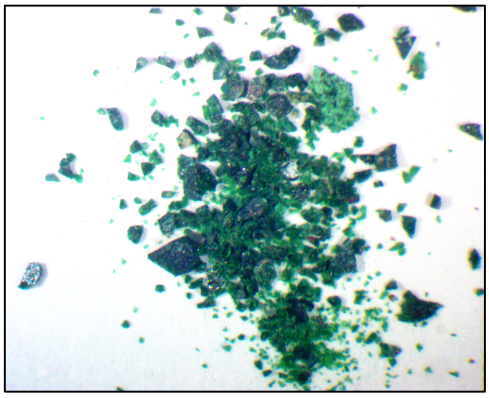
E1- Wiltshire



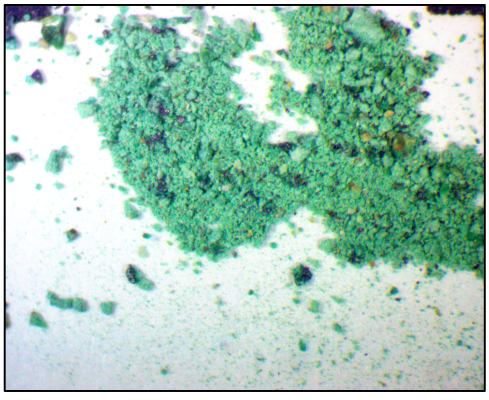
E2- Malmsbury, Wiltshire



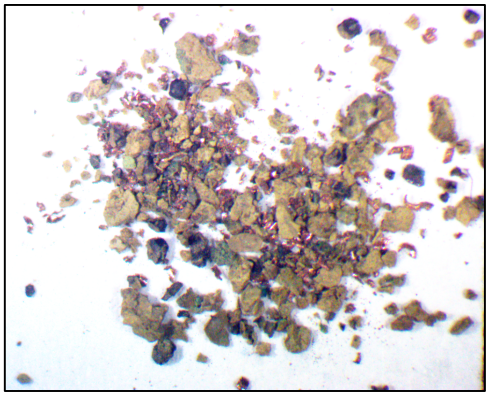
E3- Pewsey, Wiltshire



E4-Boldre, Hampshire



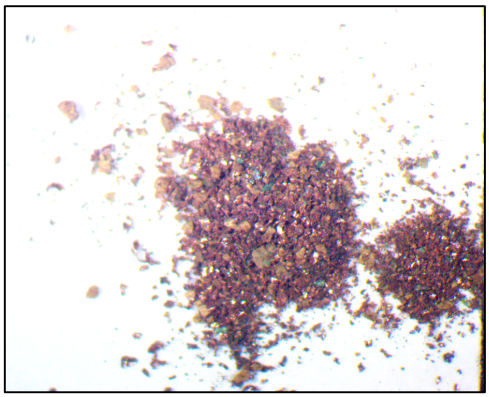
E5-London



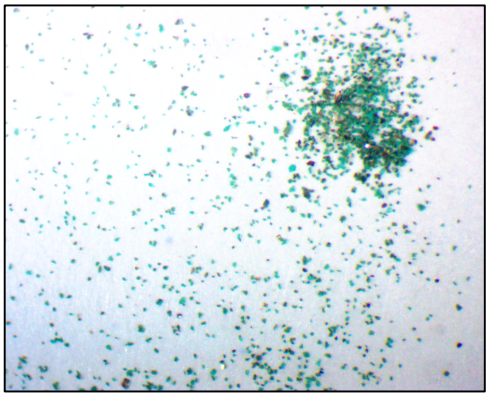
E6-London



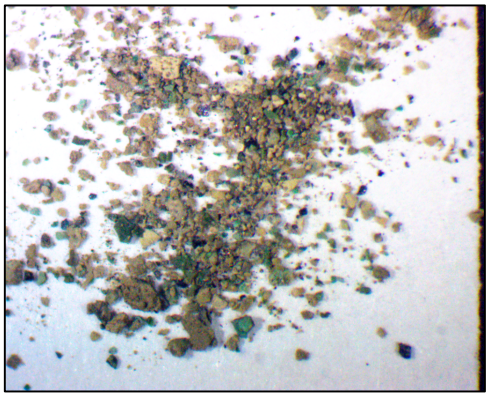
E7-London



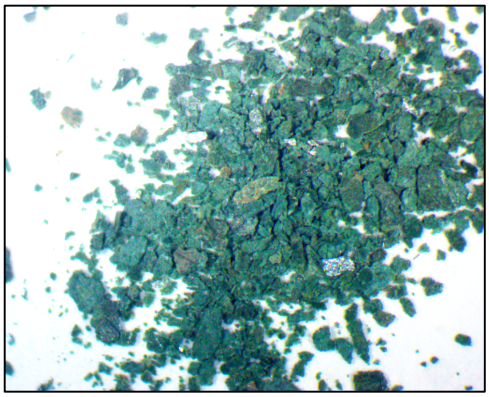
E8-London



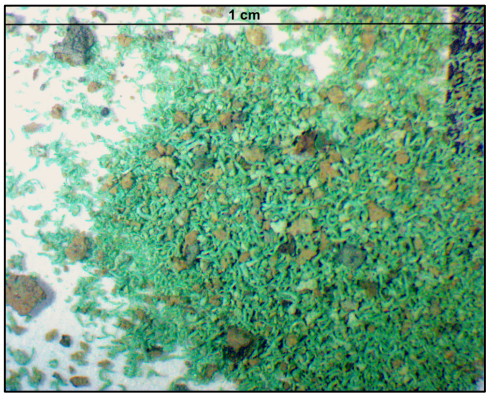
EC1-Canturbury



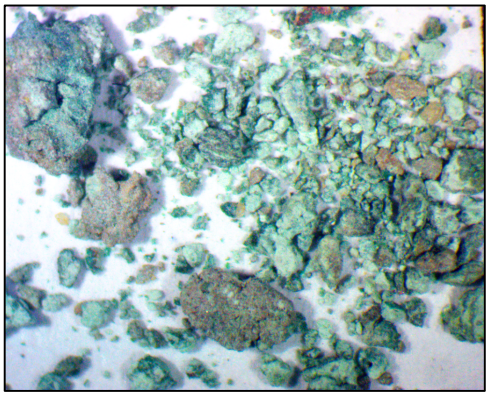
EC2-Dover



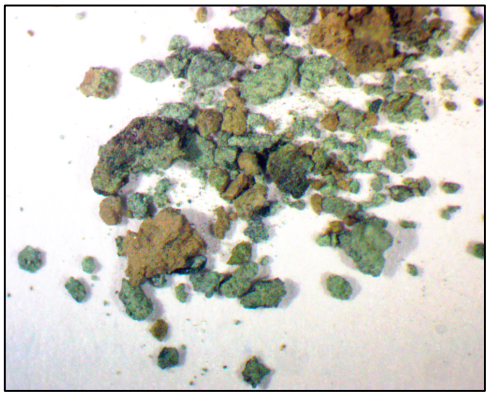
EC3-Dover



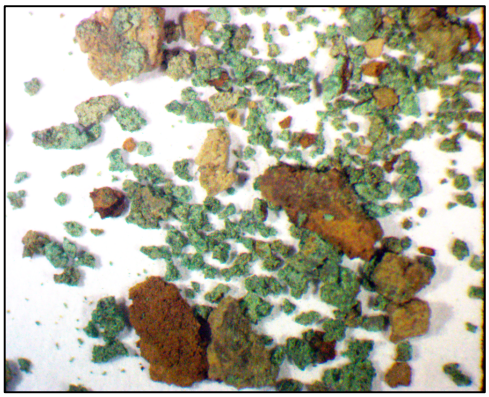
EC4-Broomfield



EC5-Broomfield



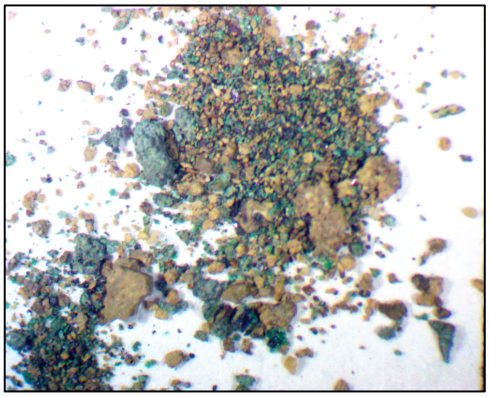
EC6-Broomfield



EC7-Broomfield



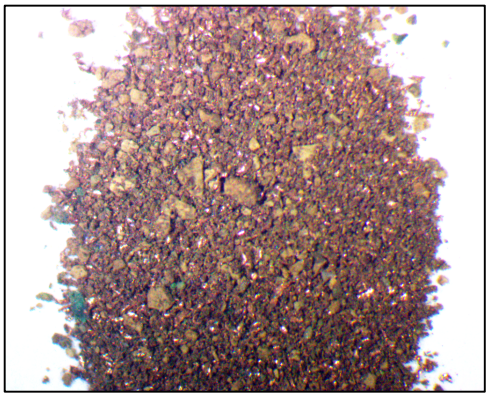
EC8-Broomfield



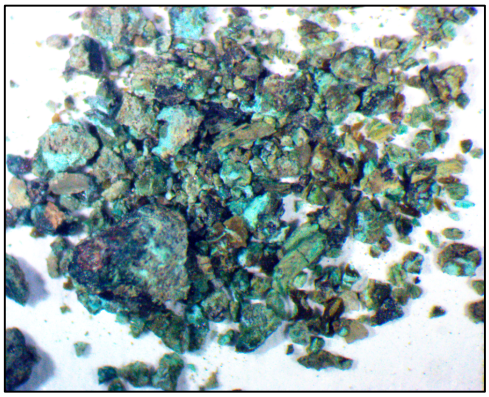
EC9-Thanet



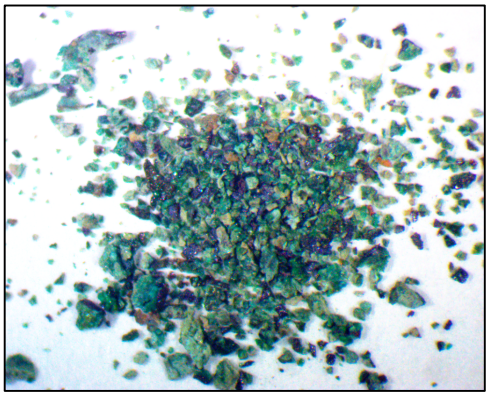
EC10-Thanet



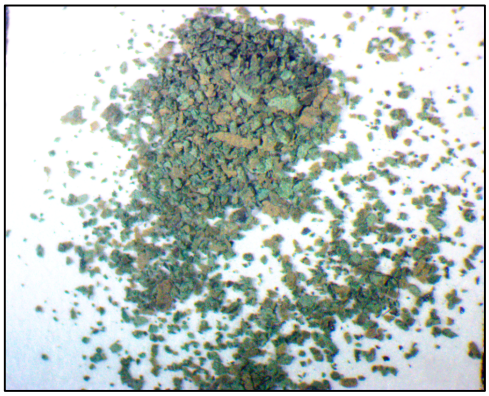
EC11-Upstreet



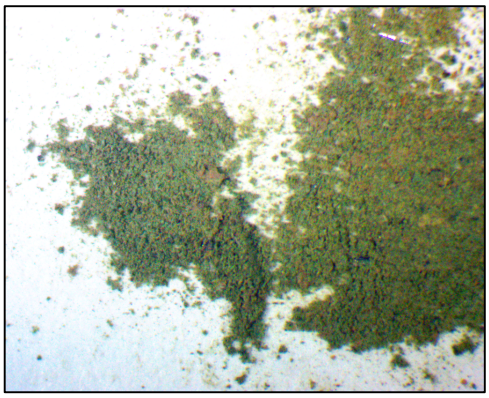
EC12-Canterbury



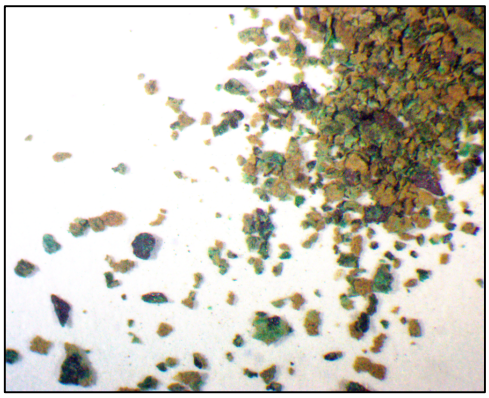
EC13-Canterbury



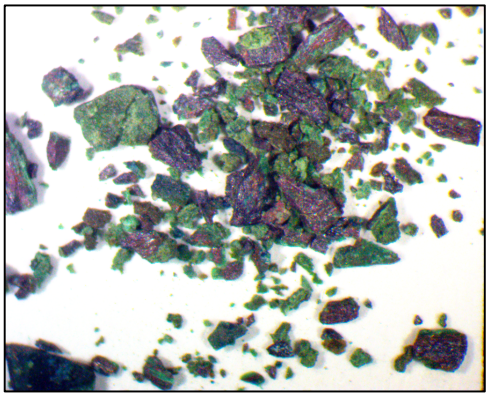
EC14-Thanet



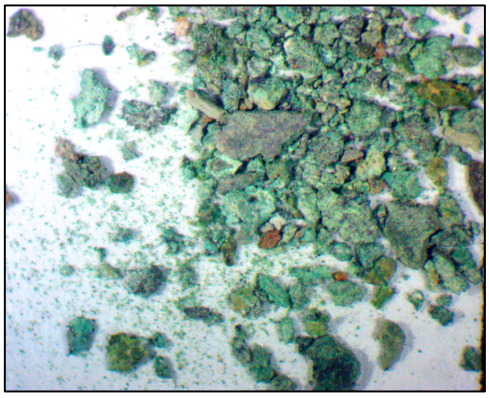
EC15-Thanet



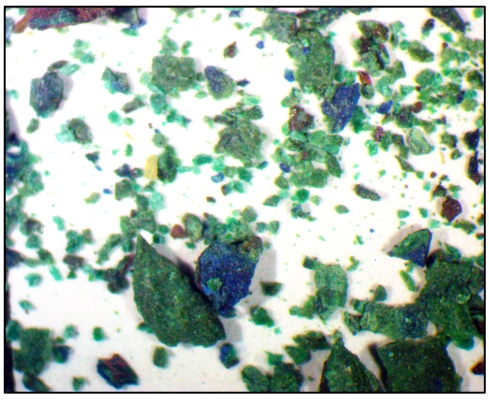
EC16-Thanet



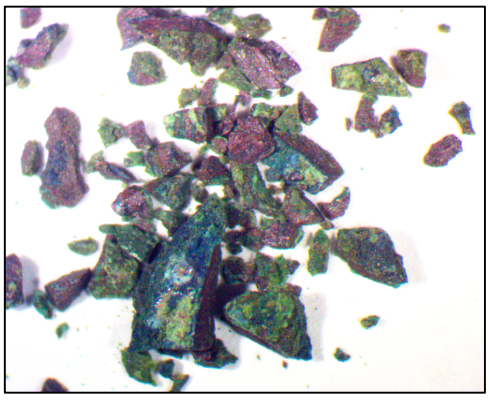
EO1-Oxford



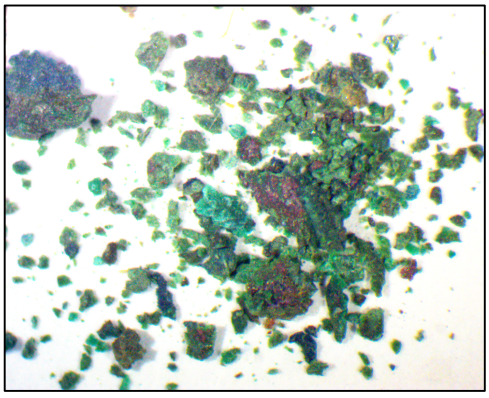
EO2- Oxford



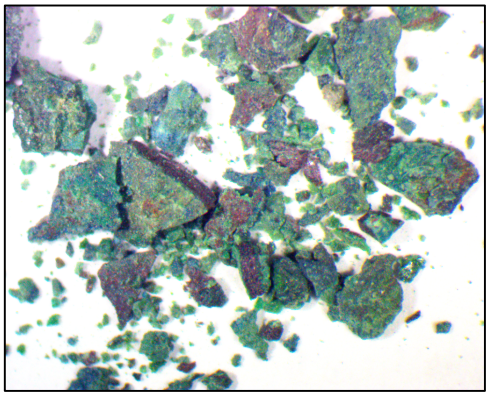
EO3-Oxford



EO4-Oxford

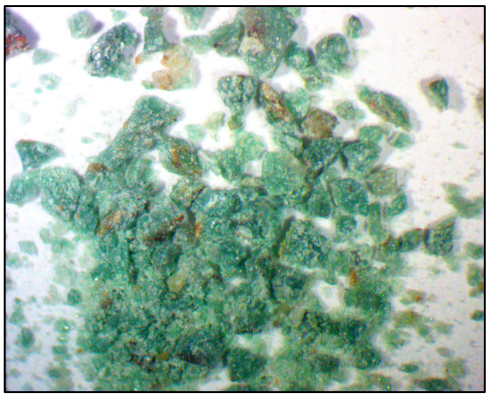


EO5-Oxford

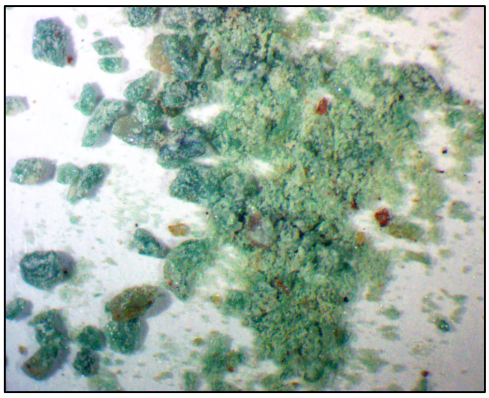


EO6-Oxford

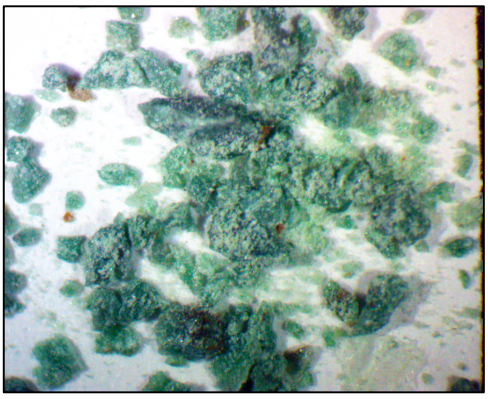
Greece



G1-Phylakopi-Melos

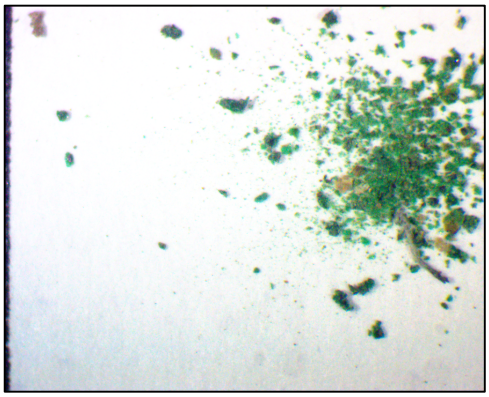


G2-Phylakopi-Melos

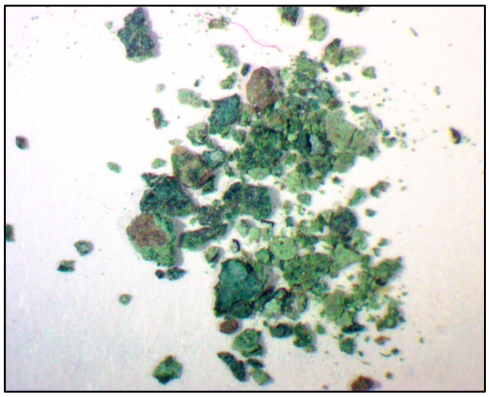


G3-Phylakopi-Melos

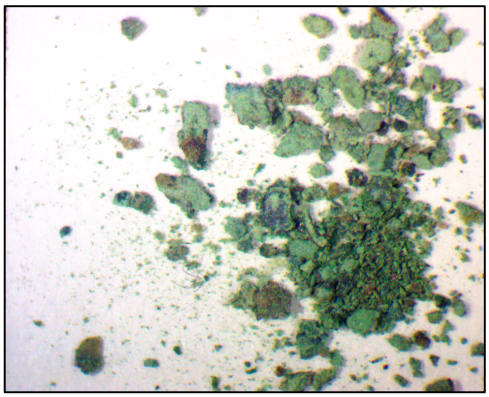
Hungary



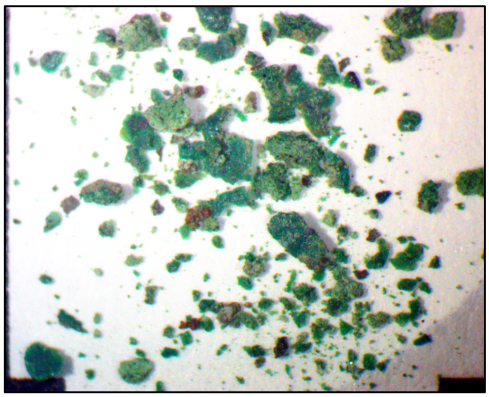
H1



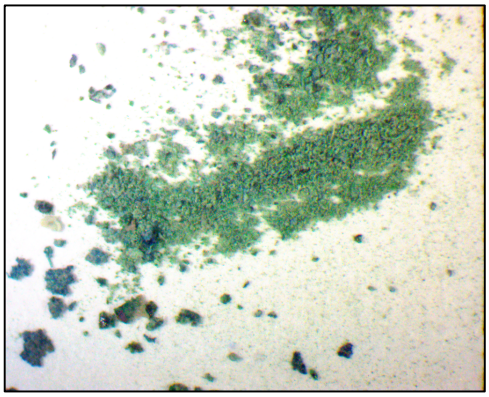
H2



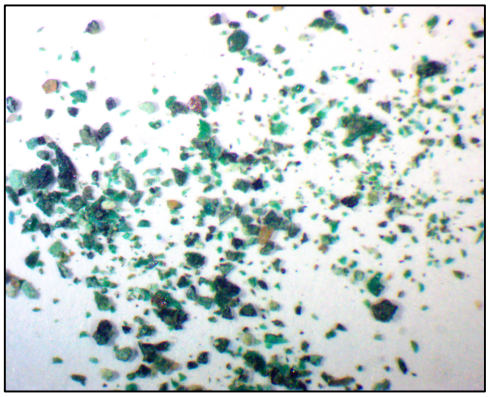
H3



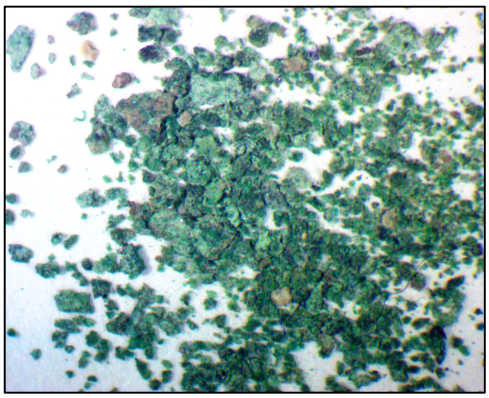
H4



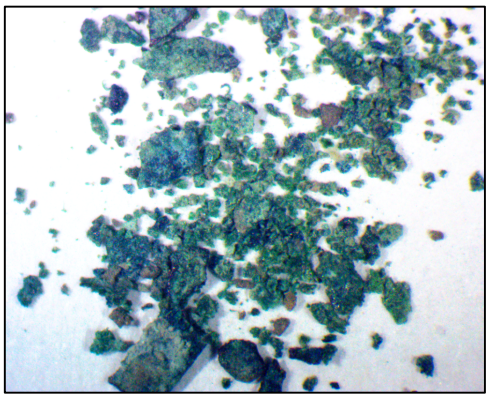
H5



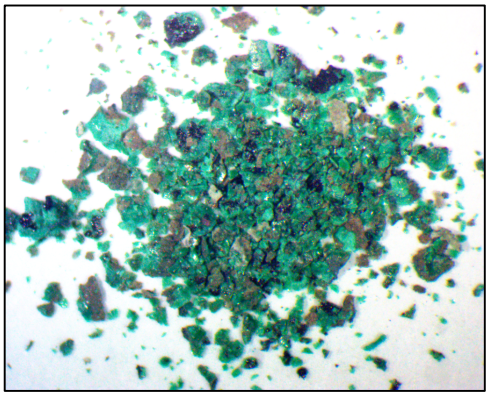
H6



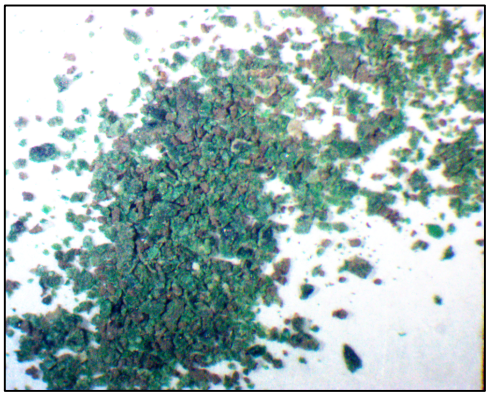
H7



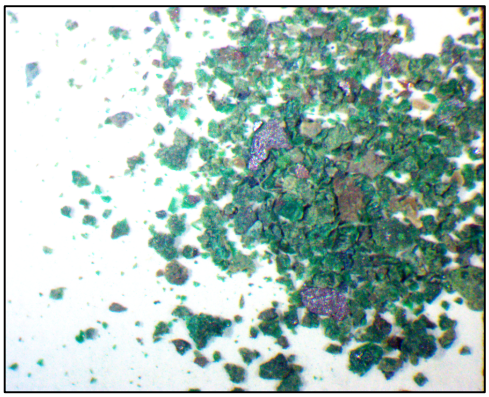
H8



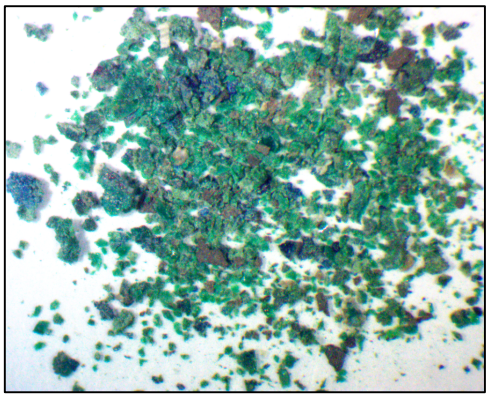
H9



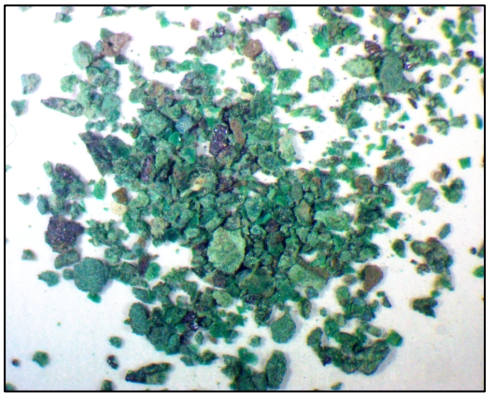
H10



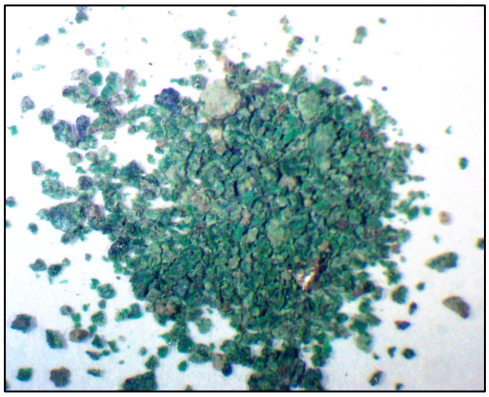
H11



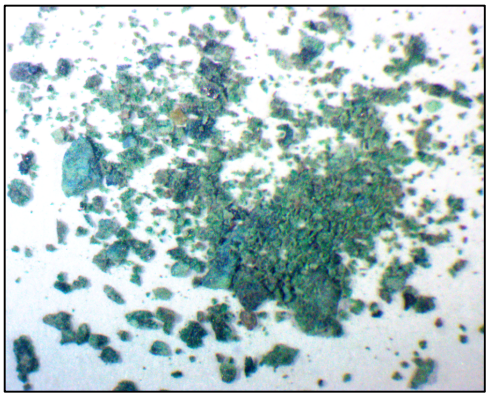
H12



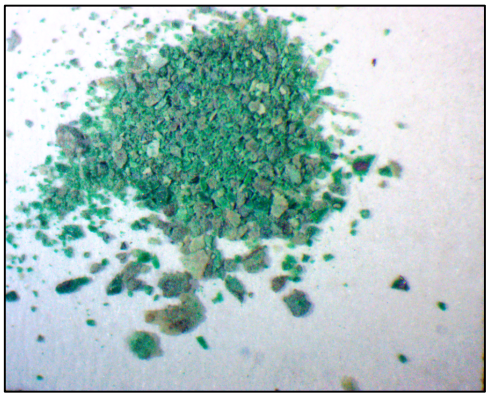
H13



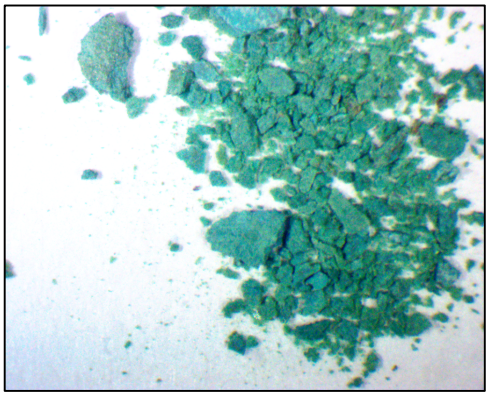
H14



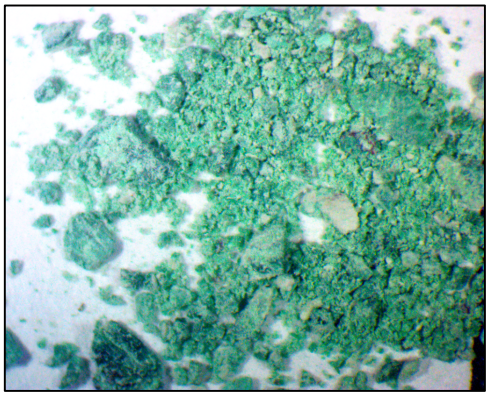
H15



H16

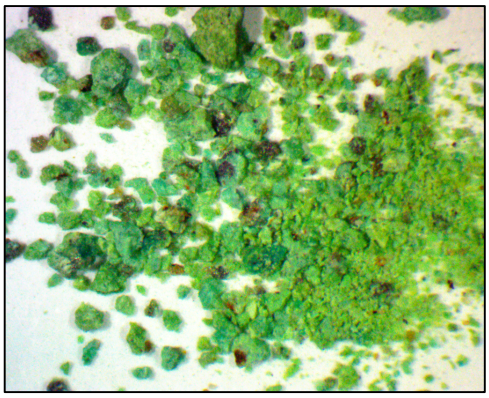


H17

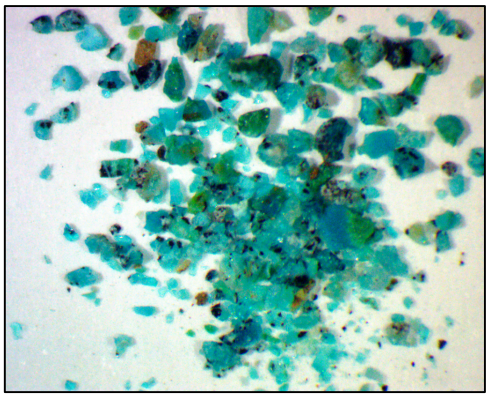


H18

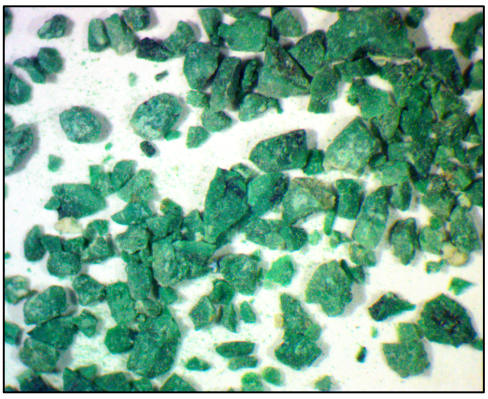
Sardinia, Italy



IS1-Sardinia

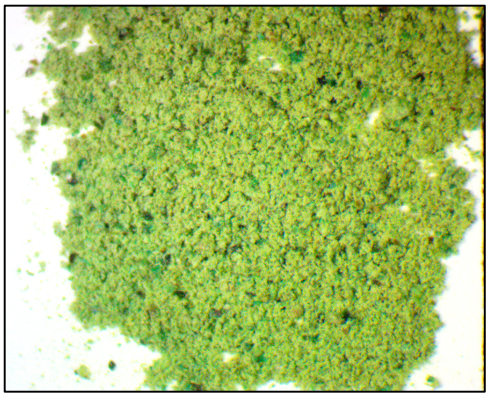


IS2-Castello de Borvei Region

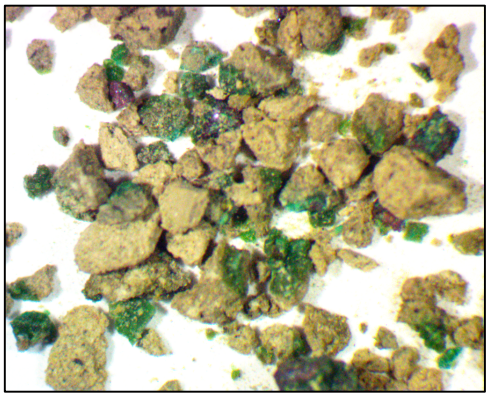


IS3-Sa Duchessa

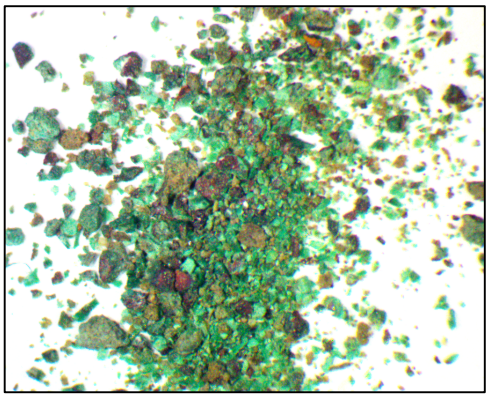
Kish, Iraq



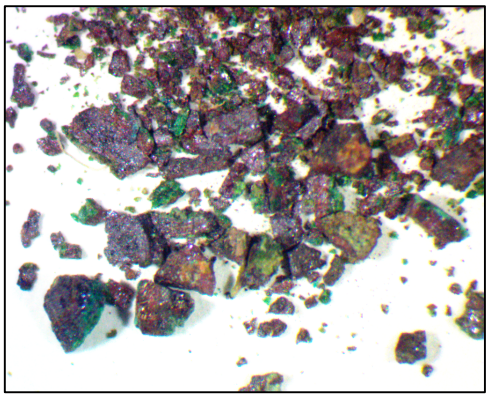
IQ3-Probably not Iraq



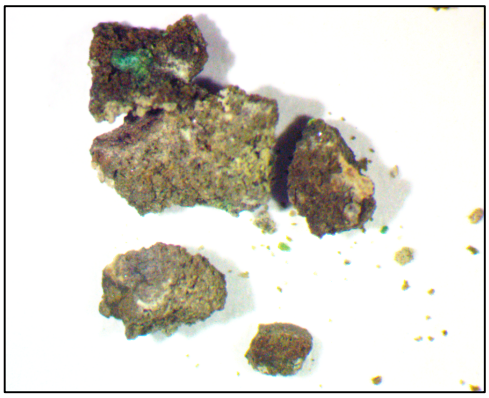
IQ5-AN1929.376



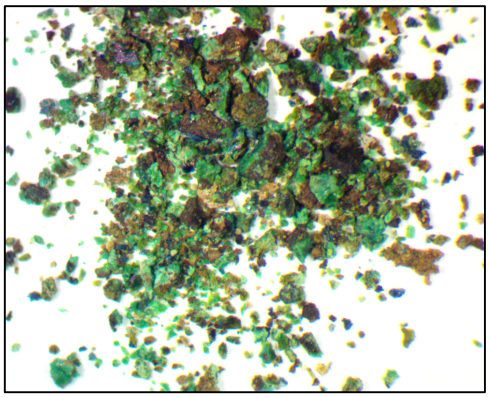
IQ6-AN1926.453



IQ7-AN1925.196

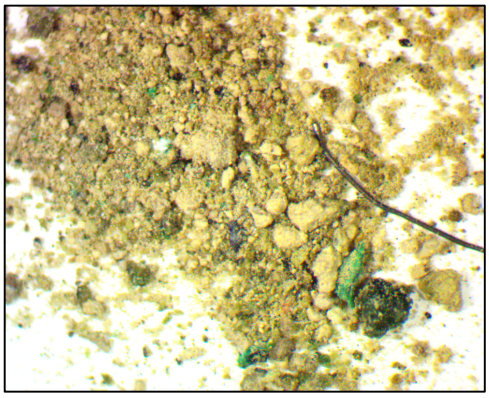


IQ11-AN1931.414

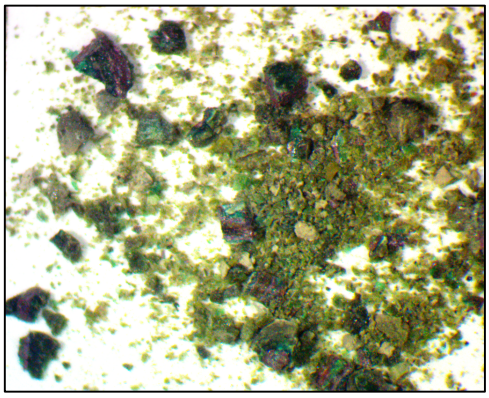


IQ12-1932.186

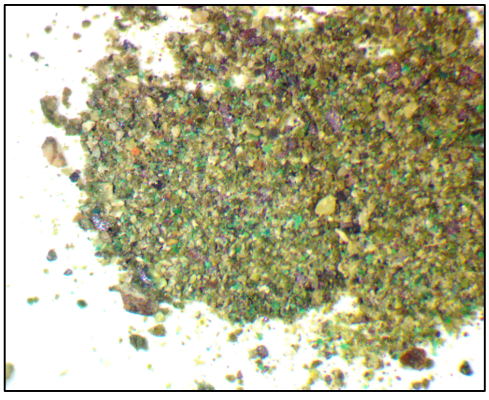
Tel Gezer, Israel



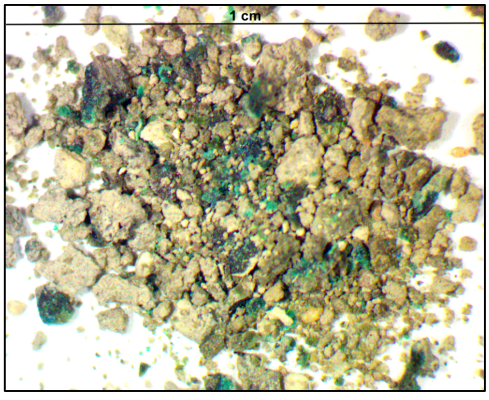
I1



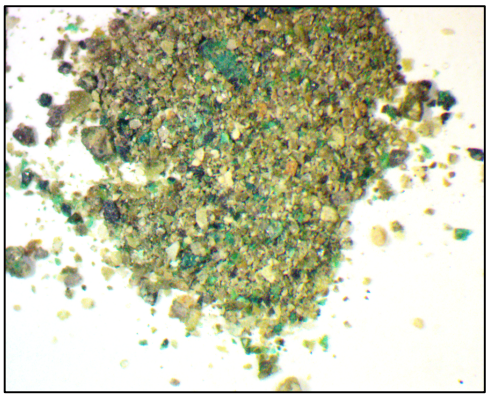
I2



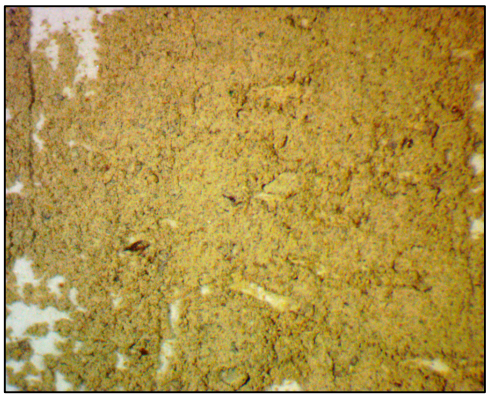
I3



I4



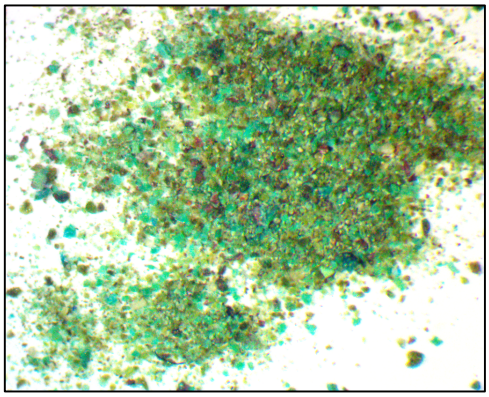
I5



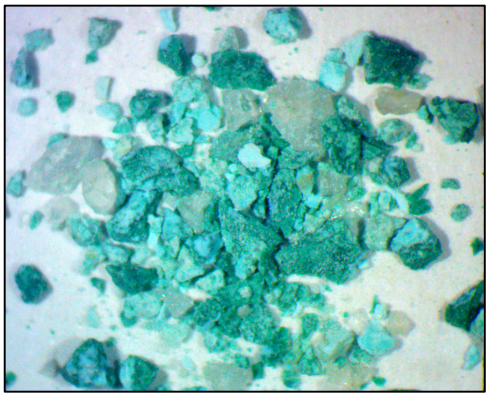
I6



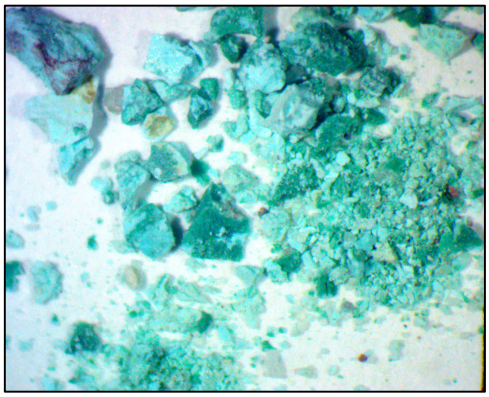
I7



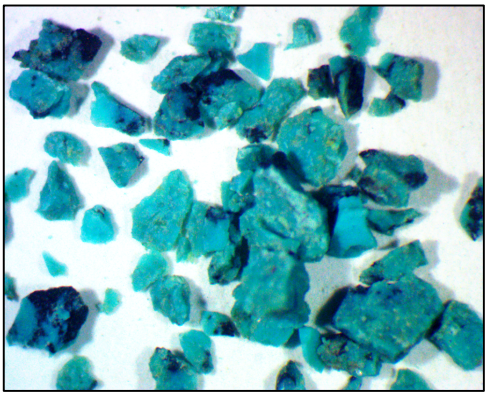
I8



I5g-King Solomon Ore

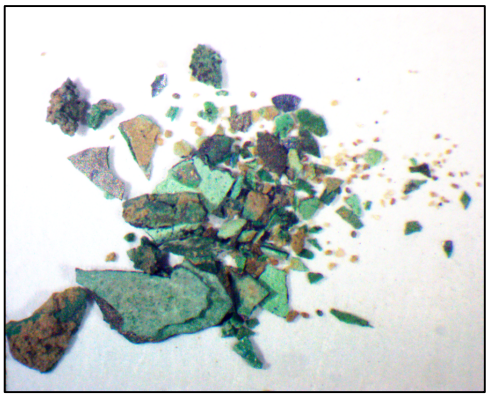


I6g-King Solomon Ore

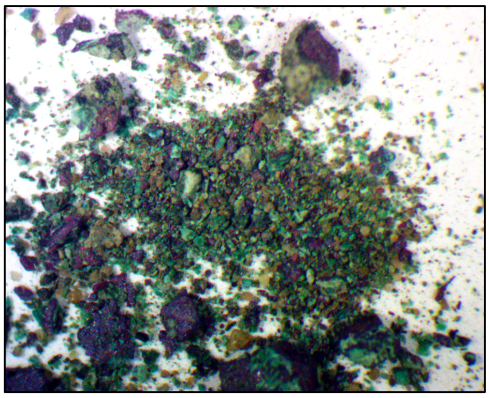


I7g-King Solomon Ore

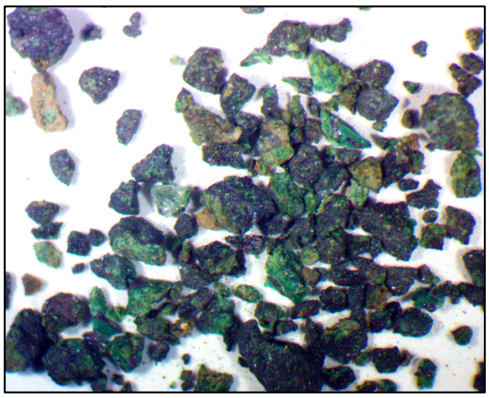
Batán Grande, Peru



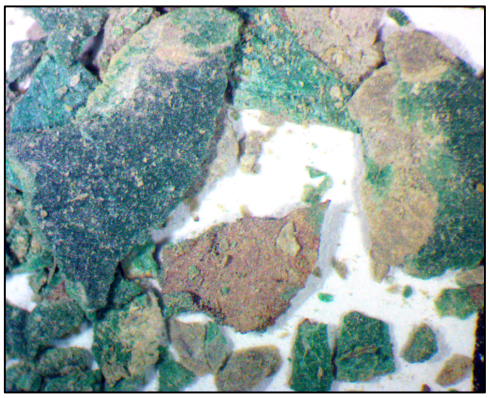
P1



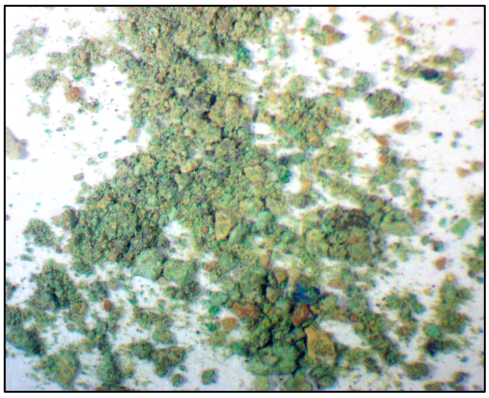
P2



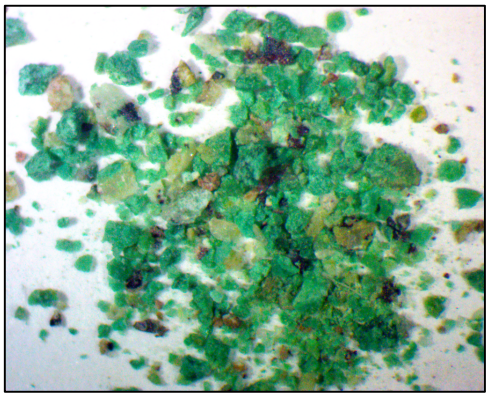
P3



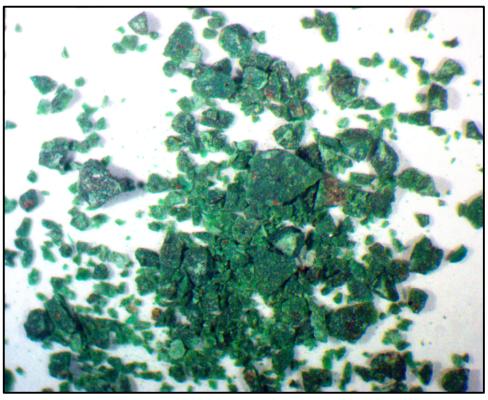
P4



P5

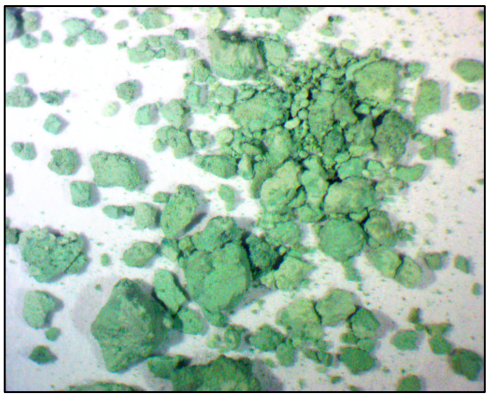


P6g-Ore

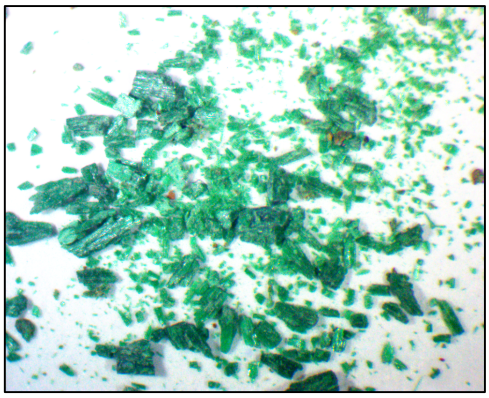


P7g-Ore

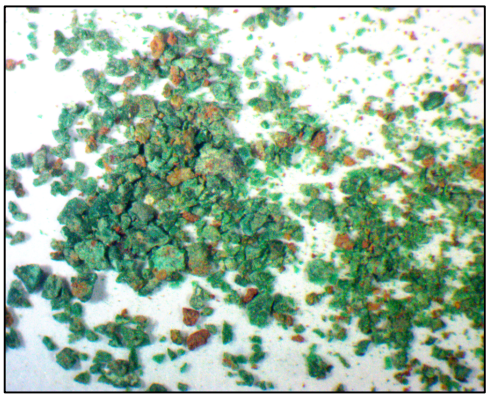
Spain



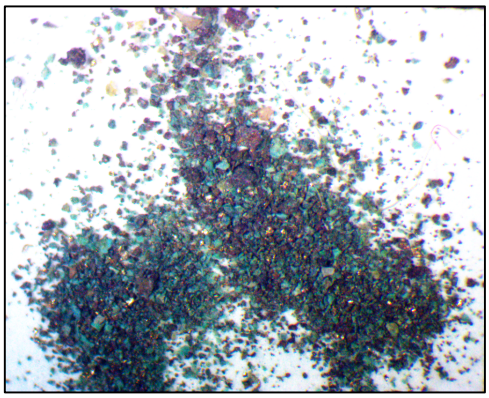
SES3-Las Pilas



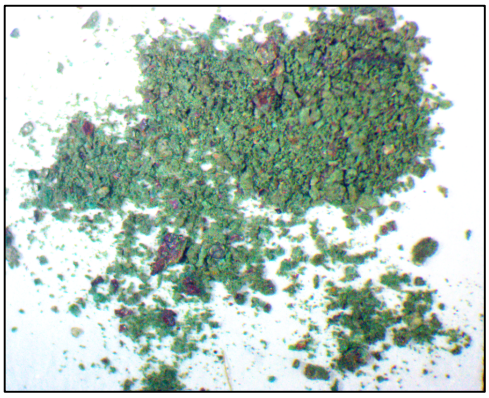
SES4- Las Pilas



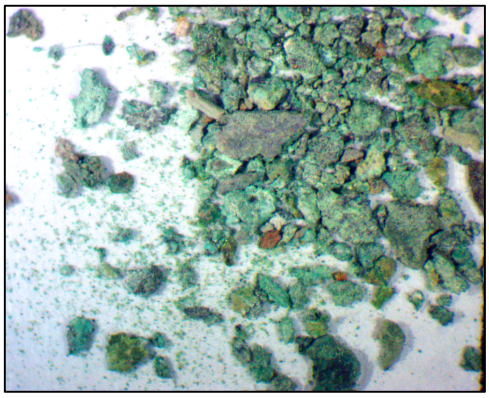
SES5-Las Pilas



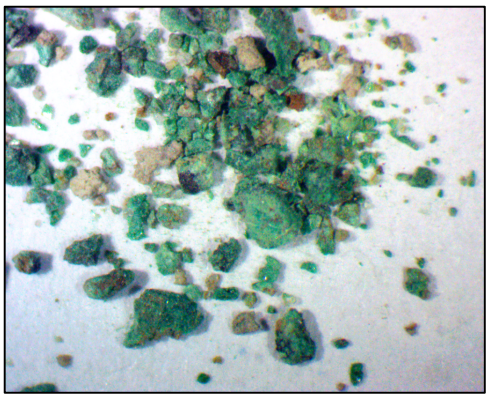
SES6-Las Pilas



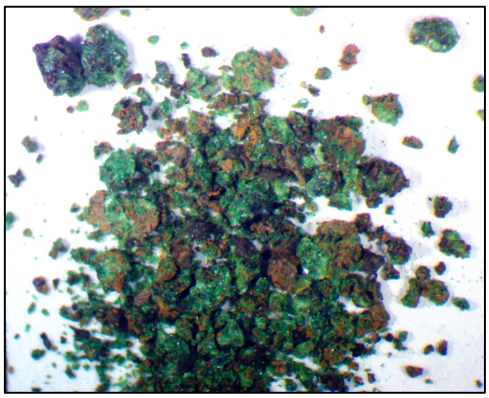
SES7-Las Pilas



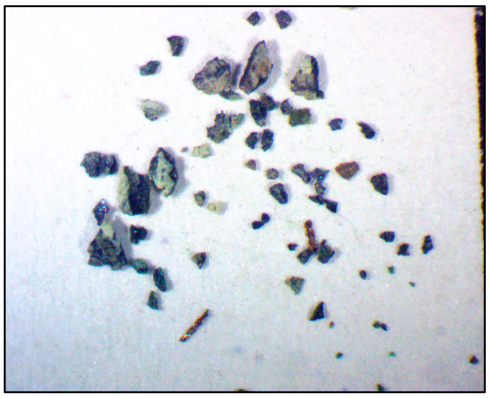
SES8-Almeria



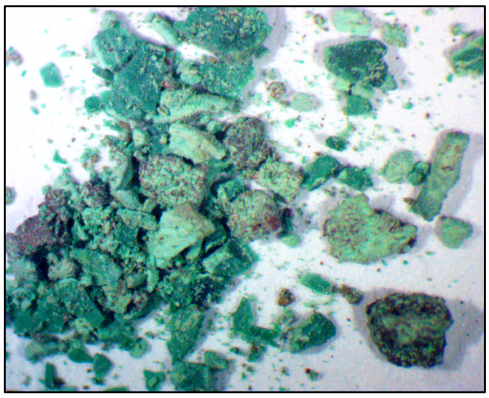
SES9-Almeria



SES10-Almeria

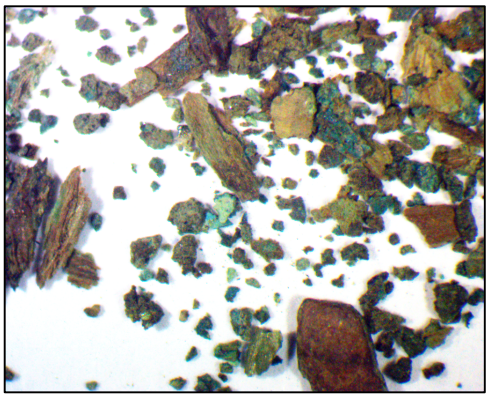


SWS5-Badajoz

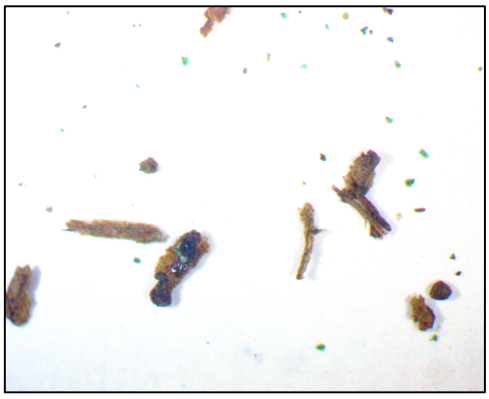


SWS6-Badajoz

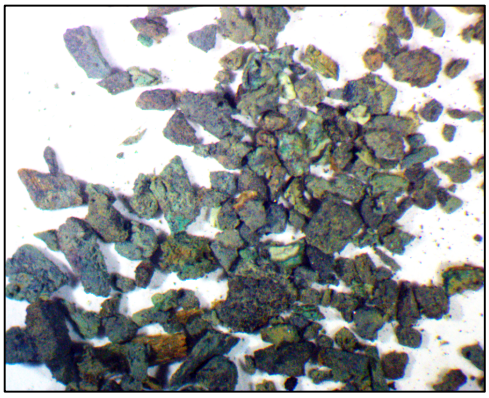
Sitka, Alaska, USA



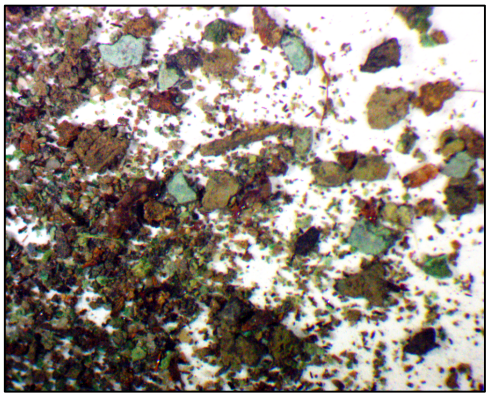
US1



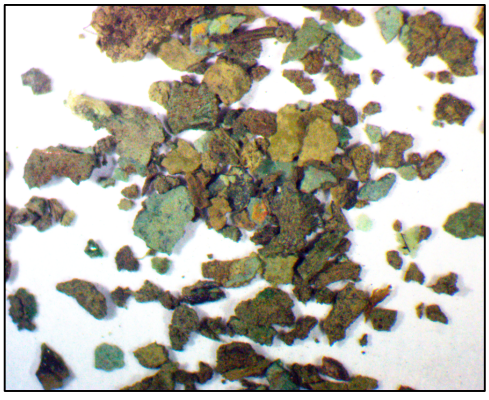
US2



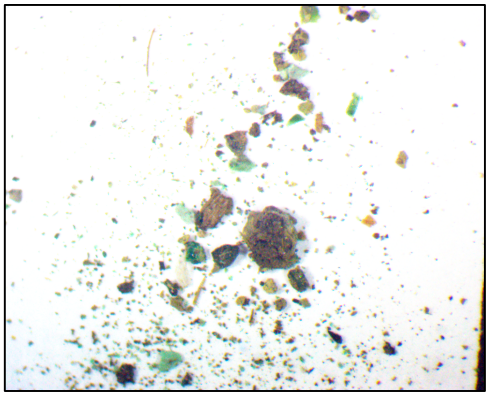
US3



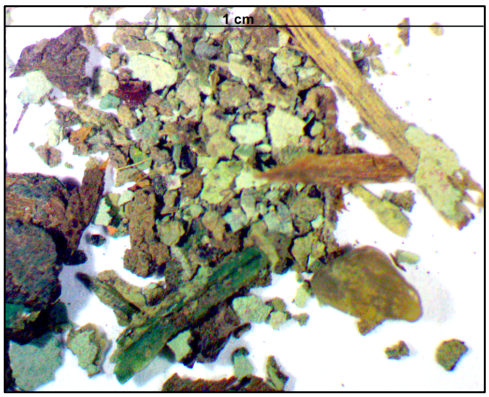
US4



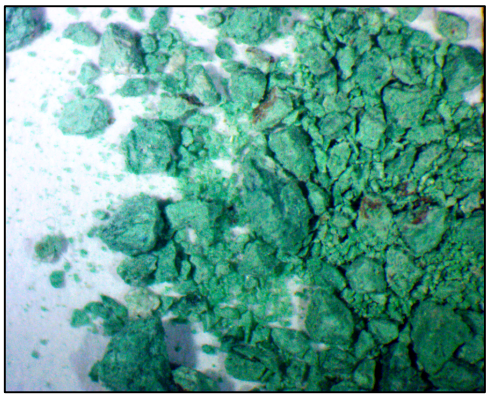
US5



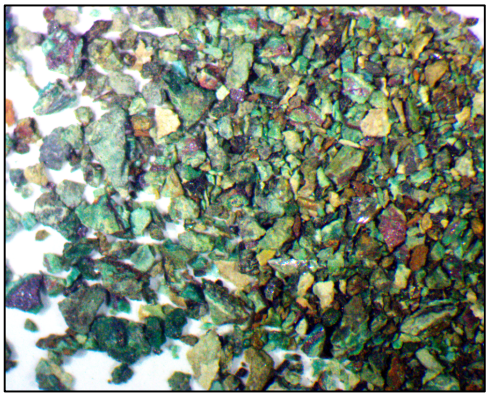
US6



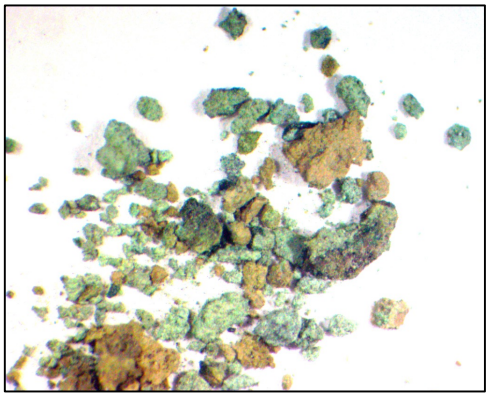
US7



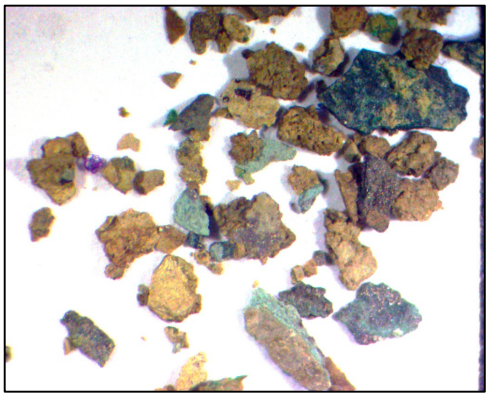
US8



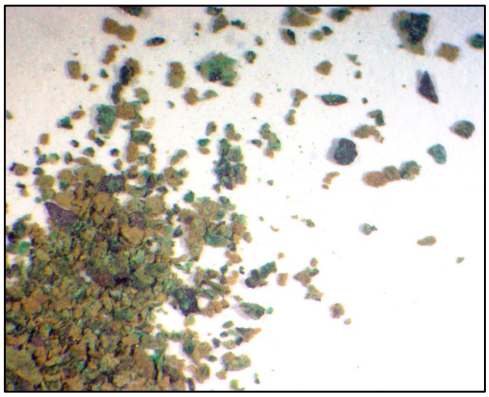
US9



US10



US11



US12

APPENDIX F:
References for the Environmental Data on Table 5.2

Hungary

Budapest, Hungary. Temperature. Available from: http://met.hu/eghajlat/magyarorszag_eghajlata/varosok_jellemzoi/Budapest/. Accessed on 16 April 2018.

Dudal, R.; Tavernier, R.; Osmond. D, 1966. *Soil Map of Europe, 1:2,500,000: Explanatory Text*. Rome: Food and Agriculture Organization of the United Nations.

Möller, Detlev and Zierath, Reinhard, 1986. On Composition of precipitation water and its acidity. In: *Tellus*. Vol. 38B: 44-50.

Radó, Sándor (ed.), 1967. *National Atlas of Hungary*. Budapest: "Offset,, Printing House.

Sitka, Alaska, USA

Kellog, Charles E. and Nygard, Iver J., 1951. *Exploratory Study of The Principle Soil Groups of Alaska.* Agriculture Monograph No. 7. Washington, D. C,: United States Department of Agriculture.

Neal, Edward G.; Brabets, Timothy P.; Frenzel, Steven A., 2004. *Water Quality and Streamflow of the Indian River, Sitka, Alaska, 2001-02.* U.S. Geological Survey Scientific Investigation Report 04-5023, 34 p.

Sitka, Alaska, USA. Temperature. Available from: http://w2.weather.gov/climate/xmacis.php?wfo=pajk. Accessed on 16 April 2018.

Northern Peru

Chiclayo, Peru. Temperature. Available from: https://en.climate-data.org/location/3932/. Accessed on 12 February 2018.

Cyprus

Dudal, R.; Tavernier, R.; Osmond. D, 1966. *Soil Map of Europe, 1:2,500,000: Explanatory Text*. Rome: Food and Agriculture Organization of the United Nations.

Karageorghis, V.; Demas, M., 1984. *Pyla-Kokkinokremos: A Late 13th – Century B.C. Fortified Settlement in Cyprus*. Nicosia: Chr. Nicolaou & Sons Ltd.

Larnaca, Cyprus. Temperature. Available from: http://www.holiday-weather.com/larnaca/averages/. Accessed on 17 September 2017.

Limassol, Cyprus. Temperature. Available from: http://www.holiday-weather.com/limassol/averages/. Accessed on 17 September 2017.

Republic of Cyprus, 2018. The Climate of Cyprus. Ministry of Agriculture, Rural Development and Environment: Department of Meteorology. Available from: http://www.moa.gov.cy/moa/ms/ms.nsf/DMLcyclimate_en/DMLcyclimate+en?OpenDocument. Accessed on 04 April 2018.

Spain

Araguas-Araguas, L. J. and DiazTeijeiro, M. F., 2005. Isotope Composition of Precipitation and Water Vapour in the Iberian Peninsula: First Results of the Spanish Network of Isotopes in Precipitation. In: *Isotopic composition of precipitation in the Mediterranean Basin in relation to air circulation patterns and climate: Final report of a coordinated research project 2000-2004*. Vienna: IAEA: 173-190.

Castro, Pedro; Gili, Sylvia; Lull, Vicente; Micó, Rafael; Rihuete, Cristina; Risch, Roberto; Sanahuja Yll, Ma. Encarna; Chapman, Robert, 2000. Archaeology an Desertification in the Vera Basin (Almería, South-East Spain). In: *European Journal of Archaeology*. Vol. 3(2): 147-166.

Dudal, R.; Tavernier, R.; Osmond. D, 1966. *Soil Map of Europe, 1:2,500,000: Explanatory Text*. Rome: Food and Agriculture Organization of the United Nations.

Mojácar, Spain. Temperature. Available from: https://en.climate-data.org/location/828587/. Accessed on 04 April 2018.

Murillo-Barroso, Mercedes; Martinón-Torres, Marcos; Camalich Massieu, Ma Dolores; Martín Socas, Dimas; Molina González, Fernando, 2017. Early metallurgy in SE Iberia. The workshop of Las Pilas (Mojácar, Almería, Spain). In: *Archaeology Anthropology Science*. Vol 9: 1539-1569.

Southern England

Canterbury, UK. Temperature. Available from: https://www.yr.no/place/United_Kingdom/England/Canterbury/statistics.html. Accessed on 22 Sept. 2017.

Dudal, R.; Tavernier, R.; Osmond. D, 1966. *Soil Map of Europe, 1:2,500,000: Explanatory Text*. Rome: Food and Agriculture Organization of the United Nations.

Mochlinski, K., 1969. *Assessment of Soil Ambient Temperatures, Report No. 5289*. Leatherhead, Surry, UK: The Electrical Research Association.

Oxford, UK. Temperature. Available from: https://www.metoffice.gov.uk/public/weather/climate/gcpn7mp10#averagesTable. Accessed on 22 Sept. 2017.

London, UK. Temperature. Available from: https://en.tutiempo.net/climate/ws-37790.html. Accessed on 22 September 2017.

Malmsbury and Pewsey, UK. Temperature. Available from: https://www.metoffice.gov.uk/climate/uk/regional-climates/sw. Accessed on 22 Sept. 2017.

Lymington/Boldre, UK. Temperature. Available from: http://www.holidayweather.com/lymington_gb/averages/. Accessed on 22 Sept. 2017.

Israel

Bet Dagan, Israel. Temperature. Available from: http://www.weatherbase.com/weather/weatherall.php3?s=591686&units. Accessed on 07 February 2017.

Climate Gezer: Temperature, Climograph, Climate Table for Gezer. Available from https://en.climate-data.org/location/202254. Accessed on 04 April 2018.

Gat, J. R.; Ben-Mair, R.; Yam R.; Yakir, D.; Wernli, H., 2005. The Isotope Composition of Atmospheric Waters in Israel's Coastal Plain. In: *Isotopic composition of precipitation in the Mediterranean Basin in relation to air circulation patterns and climate: Final report of a coordinated research project 2000-2004.* Vienna: IAEA.

Itkin, Danny; Crouvi, Onn; Monger, H. Curtis; Shaanan, Uri; Goldfus, Haim, 2018. Pedology of archaeological soils in tells of the Judean Foothills, Israel. In: *Catena*. April 2018: 1-15.

Shapiro, M. B., 2006. Soils of Israel. In: *Eurasian Soil Science: Genesis and Geography of Soils*. Vol. 39 (11): 1170-1175.

Stewart Macalister, R. A., 1912. *The Excavation of Gezer 1902 – 1905 and 1907 – 1909.* London: John Murray.

Gansu

Lanzhou, Gansu. Temperature. Available from: http://www.weather.com.cn/html/cityintro/101160101.shtml. Accessed on 24 July 2017.

Guangxi

Nanning, Guangxi. Temperature. Available from: https://web.archive.org/web/20090716061113/http://cdc.cma.gov.cn/shuju/index3.jsp?tpcat=SURF&dsid=SURF_CLI_CHN_MUL_MMON_19712000_CES&pageid=3. Accessed on 24 July 2017.

Jiangsu

Nanjing, Jiangsu. Temperature. Available from: https://web.archive.org/web/20150302053152/http://cdc.cma.gov.cn/home.do. Accessed from: 16 April 2018.

Jiangxi

Ji'an, Jiangxi. Temperature. Available from: http://oldcdc.cma.gov.cn/shuju/search1.jsp?dsid=SURF_CLI_CHN_MUL_MMON_19712000_CES&tpcat=SURF&type=table&pageid=3 . Accessed on 16 April 2018.

Ningxia

Yinchuan, Ningxia. Temperature. Available from: http://oldcdc.cma.gov.cn/shuju/search1.jsp?dsid=SURF_CLI_CHN_MUL_MMON_19712000_CES&tpcat=SURF&type=table&pageid=3. Accessed on 16 April 2018.